Patricia Bassereau · Pierre Sens *Editors*

Physics of Biological Membranes

Springer

Physics of Biological Membranes

Patricia Bassereau • Pierre Sens
Editors

Physics of Biological Membranes

Springer

Editors
Patricia Bassereau
PhysicoChimie Curie (UMR CNRS 168)
Institut Curie
Paris, France

Pierre Sens
PhysicoChimie Curie (UMR CNRS 168)
Institut Curie
Paris, France

ISBN 978-3-030-00628-0 ISBN 978-3-030-00630-3 (eBook)
https://doi.org/10.1007/978-3-030-00630-3

Library of Congress Control Number: 2018964272

This Springer imprint is published by the registered company Springer Nature Switzerland AG
The registered company address is: Gewerbestrasse 11, 6330 Cham, Switzerland

Preface

In searching for optimal boundaries to separate living cells from their environment and to compartmentalize eukaryotic cells into regions of different properties, evolution has selected a design that appears universal: a bilayer made of lipid molecules. This design has physical properties that are particularly advantageous for the versatile boundary of a highly dynamical system that is in constant exchange with its environment. Lipid bilayers spontaneously self-assemble, owing to the amphiphilic nature of the lipids, and are rather impermeable to ions and large macromolecules. At physiological temperatures, they are fluid and deformable, allowing for large shape changes, and they are able to undergo fusion and scission without leakage. According to the fluid mosaic model of Singer and Nicholson (1972), the lipid bilayer provides the membrane with fluidity and elasticity, while most of the biological functions are performed by membrane-associated proteins. Since then our view of biomembranes has greatly evolved, and lipids themselves are now known to actively participate in many biological functions, either by directed interaction with other cellular components or by providing particular micro-environments for the proper functioning of proteins.

Lipid membranes with fairly well-controlled compositions and mechanical states can easily be produced *in vitro*. As two-dimensional fluid objects, they constitute fascinating structures for physicists, experimentalists, and theorists alike. The world of fluid membranes has been a particularly productive meeting place for physicists and biologists. Much knowledge about the interactions between membranes and proteins, and the large-scale mechanics of biomembranes, has emerged from these multidisciplinary interactions, which has improved our understanding of a variety of membrane-related physiological processes. This development has been made possible by efforts from both communities to find a common language required to share fundamental concepts from both fields. By combining the physical and biological point of views on biomembranes, the landmark handbook *Structure and Dynamics of Membranes*, edited by R. Lipowsky and E. Sackmann in 1995, has been particularly influential in developing this common language.

This book follows the same spirit of interdisciplinarity. It aims to provide the reader with state-of-the-art overviews of contemporary subjects that have

emerged over the last twenty years in the biological physics of biomembranes by combining theoretical and experimental aspects together with general point of views from leading biologists. The direct exchanges and collaborations between biologists and physicists have clearly improved in the past two decades. There is now a new generation of scientists who feel at ease with concepts both from physics and biology, and an increasing number of young scientists trained in physics who are pursuing careers in cell and developmental biology labs. With this book, we seek to provide this interdisciplinary community with a broad overview of our current knowledge of the physics of biological membranes. We also wish to show that interactions between physicists and biologists constitute a true exchange. The improved awareness of physicists about the biological context within which biological membranes operate has greatly broadened the scope of biological problems that are being studied from a physics point of view and has improved the impact such studies can have on the biological community. On the other side, many biologists now integrate basic physical concepts, such as membrane tension and spontaneous curvature in their understanding of biological situations. Biologists are also increasingly acknowledging the relevance of *in vitro* reconstituted systems to the study of the molecular couplings between membrane and proteins and how this leads to large-scale protein self-organization and membrane reshaping. In many of these topics, experimental progress, both *in vitro* and in cells, has improved or suggested theoretical models. In particular, reconstituted membrane systems, which have been particularly influential in shaping our understanding of the physics of membranes, are now playing a crucial role in shaping our understanding and quantification of biological membranes.

This book begins with personal perspectives by R. Lipowsky and E. Sackmann on the major evolution in the field over the past two decades, discussing physical phenomena and biological processes that could be inspirational to physicists, respectively. The introduction ends with a reference chapter by Rob Phillips that gives an overview of the orders of magnitude pertaining to many characteristics of the membrane, and how these numbers are related to particular cellular functions.

The main body of this book is separated into two parts. The first deals with membrane heterogeneities, starting with a general biological introduction (Simons), followed by two chapters describing thermodynamic concepts relevant to membrane heterogeneities (Schick, Veatch & Cicuta). The next two chapters (Marguet & Salomé, Démery & Lacoste) describe diffusion in membranes from the experimental and theoretical points of view, respectively. The last two chapters (Rautu & Turner, Frey & Schwille) introduce concepts of out-of-equilibrium physics, including energy-consuming fluxes of membrane components, and then show their relevance for the maintenance of membrane heterogeneities and the emergence of pattern formation in cell membranes.

The second part of the book deals with several aspects of membrane mechanics and their involvement in various cell functions. The section starts with a description of the importance of mechanical stresses in cell biology (Disher), taking the biophysical determinants of blood formation as an example while focusing on the cortical protein meshworks that underlie membranes and consequently

contribute to membrane properties and processes therein. One theoretical chapter (Kozlov) follows dealing with stress distribution in membranes and addressing the fundamental concept of spontaneous curvature. The next two chapters (Bitbol & Constantin & Fournier, Simunovic & Voth) describe the physics of membrane–protein interaction at different scales from both an analytical and numerical perspective. Next, two chapters (Foret, Tareste & Roux) describe mechanical aspects implicated in cellular transport, such as budding, fission, and fusion. Three chapters (Auth & Dasgupta & Gompper, Sengupta & Smith, Biswas & Groves) then describe the mechanical aspects of the cell's interaction with particles (colloids or pathogens), the cell's interaction with a substrate (cell adhesion), and the mechanical aspects of signal transduction in the cell membrane. This second part of the book ends with two chapters reporting on new developments in active membranes, namely membranes for which behavior is controlled by the exchange of matter and energy with the surrounding. The first of these two chapters (Kumar & Laradji) discusses the way complex membrane structures can be generated by active protein exchange with the cytosol or by active cytoskeleton contraction, and the second discusses the fluctuations of active membranes described from both an experimental and theoretical perspective (Turlier & Betz). The book ends with our personal views on the outstanding remaining questions that are of both crucial physiological relevance and intrinsic interest for the physics of membranes.

Paris, France

Patricia Bassereau
Pierre Sens

Contents

Part I
Introduction

Understanding Membranes and Vesicles: A Personal Recollection of the Last Two Decades

Reinhard Lipowsky

Denken ohne Erfahrung ist leer, Erfahrung ohne Denken ist blind.
(*Thought without experience is empty, experience without thought is blind.*)

Immanuel Kant

Abstract Biomembranes consist of fluid bilayers built up from many lipid and protein components. The membrane fluidity has two important consequences. First, the molecular components can undergo fast lateral transport within the membranes, a necessary prerequisite for the formation and remodelling of intramembrane compartments. Second, the fluidity leads to unusual elastic properties of the membranes that allow them to "escape into the third dimension." Intramembrane compartments can be formed by lipid phase separation, now observed for many ternary lipid mixtures, or by heterogeneous environments that lead to an ambience-induced segmentation of the membranes. Because of their unusual elastic properties, the membranes can attain many different shapes and undergo striking shape transformations, which reflect their ability to respond locally to external perturbations by changes in their curvature. Several molecular mechanisms for local curvature generation have been identified including membrane-anchored polymers, adsorption or depletion layers of solutes, and membrane-bound proteins. The local curvature generation is intimately related to the concept of a preferred or spontaneous curvature that describes the asymmetry between the two leaflets of the bilayer membrane. New methods to determine the spontaneous curvature in a reliable manner have been recently developed, based on spontaneous or force-induced tubulation of giant vesicles. The spontaneous curvature plays a pivotal role both for the engulfment of nanoparticles by membranes and for the wetting of membranes by aqueous droplets, two membrane processes that remain to be further elucidated.

R. Lipowsky (✉)
Theory & Bio-Systems, Max Planck Institute of Colloids and Interfaces, Potsdam, Germany
e-mail: lipowsky@mpikg.mpg.de

P. Bassereau, P. Sens (eds.), *Physics of Biological Membranes*,
https://doi.org/10.1007/978-3-030-00630-3_1

The spontaneous curvature also determines the exergonic or endergonic nature of membrane fusion and fission.

Keywords Biomembranes · Curvature · Tubulation · Nanoparticle engulfment · Membrane wetting

1 Introduction

Patricia Bassereau and Pierre Sens asked me to write an introductory chapter that provides a personal account of the "most interesting and surprising developments in membrane physics" during the last two decades, i.e., since the publication of the "green book" in 1995 [1]. The latter book on "Structure and Dynamics of Membranes" was edited by Erich Sackmann and myself, a longsome process that took several years. During the last decade, we discussed, once in a while, the possibility of a new edition but I never found the time to think seriously about such a venture. The present chapter gives me the opportunity to briefly review a few aspects of membranes and vesicles that I would definitely want to include in a putative new edition of the "green book."

The chapter is organized as follows. The following Sects. 2–5 address several aspects that caught my attention already in the 1990s and underwent important developments during the last 20 years: Fluid domains or rafts in fluid membranes; segmentation of membranes by heterogeneous environments; emergence of membrane curvature on nanoscopic scales; as well as local curvature generation and spontaneous curvature. At the end of Sect. 3, it is argued that intracellular heterogeneities close to the membranes act to suppress the separation and coexistence of lipid phases in vivo. In Sect. 5, membrane-bound proteins are viewed as Janus particles with strongly nonspherical shapes.

The subsequent Sects. 6–9 deal with four aspects that I found particularly interesting during the last couple of years: Two distinct mechanisms for the formation of membrane nanotubes as provided by spontaneous curvature and locally applied forces; the interplay between these two tubulation mechanisms; the engulfment of nanoparticles by membranes; and the wetting of membranes by aqueous two-phase systems. Section 7 describes the interplay of spontaneous and force-induced tubulation in a quantitative manner. Section 9 emphasizes that all lipid compositions and aqueous two-phase systems that have been studied so far undergo complete-to-partial wetting transitions and that the nucleation and growth of droplets at membranes depends strongly on the spontaneous curvature. Finally, Sect. 10 explains how this curvature affects the exergonic or endergonic nature of membrane fusion and fission, the most important topology-transforming membrane processes. At the end, I give a brief summary and a short outlook on open questions and future studies. In order to produce a readable piece, I had to focus on a few aspects of membranes and vesicles and, thus, had to omit other intriguing aspects, many of which will be covered in later chapters of this book.

The presentation is intuitive and largely nontechnical but, as a theoretical physicist, I cannot refrain from displaying some equations. Following the motto "As simple as possible but not simpler" of Albert Einstein, all displayed equations are short and provide simple relationships between a small number of parameters. In addition, all of these parameters can now be measured in experiments and/or simulations. One such parameter that plays a prominent role in the following is the spontaneous (or preferred) curvature which describes the local asymmetry between the two leaflets of bilayer membranes. A much more detailed account of the underlying theory will be given elsewhere [2].

2 Fluid Domains and Rafts in Fluid Membranes

Biological and biomimetic membranes are fluid, contain several molecular components, and represent two-dimensional systems. As a consequence, they should be able to undergo phase separation into two types of fluid domains, in close analogy to macroscopic liquid mixtures in three dimensions. This conclusion seems quite obvious from a theoretical point of view but, at the beginning of the 1990s, it was rather difficult to find experimental evidence for it. In fact, when I first submitted my theory on domain-induced budding [3, 4] to *Nature*, the editors finally rejected it after an extended review process because they thought that the underlying idea of fluid-fluid coexistence in bilayer membranes was "too speculative."

2.1 Intramembrane Domains in Ternary Lipid Mixtures

This situation has now changed completely because many ternary lipid mixtures have been identified which exhibit two coexisting fluid phases, a liquid-ordered and a liquid-disordered phase, see Fig. 1. These mixtures consist of a saturated lipid such as sphingomyelin, an unsaturated phospholipid, and cholesterol. The intense experimental study of these mixtures was triggered by the proposal [8] that biological membranes contain intramembrane domains or rafts that are rich in sphingomyelin and cholesterol. In order to directly visualize the different domains formed in lipid vesicles, it was also crucial to find appropriate fluorescent probes that have a preference for one of the two fluid phases [6, 9–11].

Direct evidence for the formation of two types of fluid domains was provided by single particle tracking that showed that both phases exhibit relatively fast lateral diffusion [10]. In addition, using giant unilamellar vesicles, several theoretical predictions [3, 5, 12, 13] could be directly confirmed: the growth and coalescence of small domains into larger ones [11]; the budding of the more flexible domains [6, 11]; and the shift of the domain boundary away from the neck of the bud [14, 15]. So far, this domain boundary shift provides the only method to estimate the difference between the Gaussian curvature moduli for the two types of membrane domains.

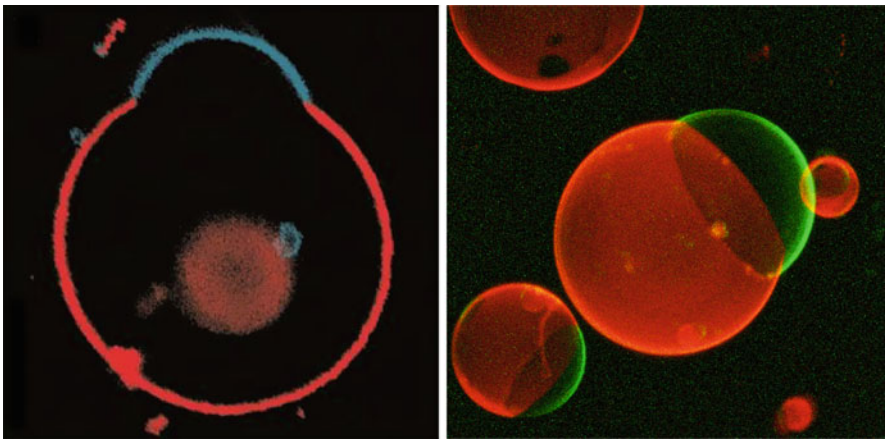

Fig. 1 Domain-induced budding of vesicles as theoretically predicted in [3, 5] and observed by fluorescence microscopy in [6, 7]: (left) cross section through a vesicle that formed two domains after a decrease in temperature [6]; and (right) three-dimensional confocal scan of a two-domain vesicle that was formed by electrofusion [7]. In both cases, the vesicle membrane is composed of DOPC, sphingomyelin, and cholesterol, doped with small concentrations of two fluorescent probes

Phase separation in ternary lipid mixtures has now been observed for a variety of membrane systems including giant vesicles [6, 10, 11, 15–17], solid-supported membranes [18–20], hole-spanning (or black lipid) membranes [21], as well as pore-spanning membranes [22]. The phase diagrams of such three-component membranes have been determined using spectroscopic methods [23] as well as fluorescence microscopy of giant vesicles and X-ray diffraction of membrane stacks [24–27]. Somewhat surprisingly, fluid–fluid coexistence has even been found in giant plasma membrane vesicles that contain a wide assortment of different lipids and proteins [28, 29].

2.2 Lipid Phase Domains or Rafts In Vivo

As far as biological membranes are concerned, the existence and size of sphingomyelin- and cholesterol-enriched rafts as proposed in [8] is still a matter of ongoing debate. It is generally accepted that the diameter of these rafts is below the diffraction limit of conventional optical microscopy, i.e., below 200 nm, see, e.g., [30]. However, even superresolution microscopy methods such as STED [31, 32] could not provide a reliable estimate but only an upper bound for the raft size: the STED measurements indicated that, for the plasma membranes of mammalian cells, the raft diameter does not exceed 20 nm [31]. The search for rafts in biological membranes as pursued with different experimental techniques has been critically reviewed in [33].

2.3 Intramembrane Domains Arising from Protein Clusters

In contrast to lipid phase domains, the formation of intramembrane domains via the clustering of membrane proteins is frequently observed in vivo. One example is provided by clathrin-dependent endocytosis which is used to internalize membrane-bound receptors as well as cargo such as receptor-bound ligands or nanoparticles. During this process, a strongly asymmetric membrane domain is formed with receptors or receptor–ligand complexes on its outer (exoplasmic) face and a thick protein coat consisting of adaptor proteins and clathrin triskelions on its inner (cytoplasmic) face. Therefore, clathrin-dependent endocytosis can be understood as a domain-induced budding process that is governed by the membrane's spontaneous curvature. When the endocytic vesicles contain nanoparticles or other types of cargo, the uptake of this cargo becomes maximal at a certain, optimal cargo size [34] as experimentally observed for the uptake of gold nanoparticles by HeLa cells [35, 36]. The mechanism of domain-induced budding should also be responsible for membrane budding arising from the clustering of Shiga toxin [37] and from the sequential adsorption of ESCRT proteins [38].

3 Segmentation of Membranes by Heterogeneous Environments

As we move along a biological membrane, we typically encounter changes in the molecular composition of the aqueous environment and, thus, changes in the local interactions between this environment and the membrane molecules. One interesting example is provided by the interactions between the plasma membrane of a eukaryotic cell and its cytoskeletal cortex. Because different membrane molecules differ in their affinity to the cytoskeletal proteins, the membrane is partitioned into different segments in which certain lipids and/or membrane proteins are enriched or depleted.

3.1 Lateral Diffusion in Cell Membranes

This ambience-induced segmentation of the plasma membrane can be revealed by studying the lateral diffusion of the membrane molecules using single particle tracking [39–42], see Fig. 2. This figure displays a typical diffusive trajectory of a single gold nanoparticle with a diameter of 40 nm. The particle was coated by transferrin and bound to transferrin receptors within the plasma membrane of a fibroblast [39]. Each color in Fig. 2 represents the confined diffusion of the nanoparticle within a certain membrane segment until the particle escapes to an adjacent segment where it again undergoes confined diffusion, etc. In this example,

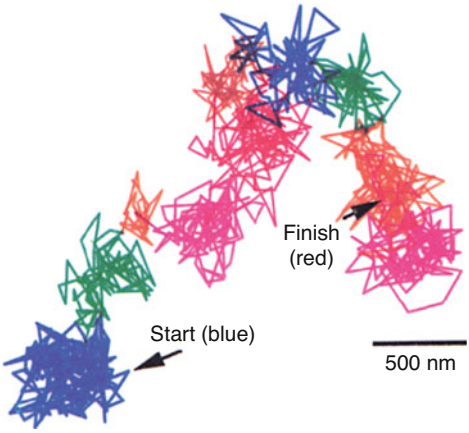

Fig. 2 Diffusive motion of a transferrin-coated gold particle bound to transferrin receptors on the plasma membrane of a fibroblast [39]. The membrane-bound particle undergoes confined diffusion in separate membrane segments, corresponding to the different colors, until it escapes to an adjacent segment. The average size of these segments was 280 nm, the average residence time of the particle in one of these segments was 29 s

the membrane segments had an average radius of 280 nm and the particles remained within one of these segments for an average residence time of 29 s.

The confined diffusion implies that the complex of nanoparticle and receptor molecules encounters some obstacles that prevent its free lateral diffusion. In fact, two types of obstacles have been proposed [40, 42]. First, cytoskeletal proteins that are immobile over the diffusive time scales may act as "corrals" or "fences" for diffusing membrane proteins that have an ectodomain protruding into the cytosol. Second, the cytoskeletal cortex may also directly bind transmembrane proteins and these transiently bound proteins can then act as "rows of pickets" that impede even the diffusion of lipid molecules in the outer leaflet of the bilayer membrane. More recent studies have corroborated the influence of the actin cortex on the lateral diffusion of membrane-anchored receptors. While the diffusion of some receptors was confined to the voids of the actin–myosin meshwork [43, 44], other receptors were observed to undergo quasi-one-dimensional diffusion, reflecting attractive interactions between the latter receptors and the meshwork [45].

3.2 Ambience-Induced Segmentation of Membranes

The skeleton-induced partitioning of cell membranes represents an important but relatively complex example for ambience-induced segmentation of membranes. Much simpler examples are provided by adhering vesicles, hole- or pore-spanning membranes, and membranes supported by chemically patterned surfaces [46, 47].

In these latter systems, the membrane molecules are exposed to two different environments which generate different molecular fields within the adjacent membrane segments. Likewise, vesicle–vesicle adhesion combined with vesicle–substrate adhesion can easily lead to ambience-induced partitioning of a vesicle membrane into more than two segments [48]. For a one-component membrane, the different segments will exhibit different molecular densities which are necessarily small and, thus, difficult to detect experimentally. For a multicomponent membrane, the different segments will also differ in their molecular composition. It then follows from general theoretical considerations that phase domains can only form in one of the membrane segments but not in several segments simultaneously [46, 47].

3.3 Impeded Formation of Intramembrane Domains

The environment of a cell membrane is rather heterogeneous, and the effective molecular fields acting on the membrane molecules change on nanoscopic scales. The skeleton-induced membrane segmentation as probed by single particle tracking (Fig. 2) implies that we can distinguish at least two types of membrane segments, contact segments that interact with the cytoskeletal proteins and noncontact segments that do not experience such interactions. However, different contact segments will, in general, be exposed to cytoskeletal structures that differ in their molecular composition of actin-binding proteins [49, 50] and noncontact segments involve additional supramolecular structures such as the protein scaffolds formed during clathrin-dependent endocytosis that have a lifetime in the range between 20 and 80 s [51, 52]. Thus, cell membranes are expected to be partitioned into many distinct membrane segments that are exposed to different molecular environments. If lipid phase domains form in such a cell membrane, this domain formation is necessarily restricted to one of the membrane segments and, thus, hard to detect [48]. In the limiting case in which the environmental heterogeneities of the cell membrane act as long-lived random fields, these heterogeneities would completely destroy domain formation and phase separation, in analogy to the two-dimensional Ising model with random fields [53–55].

4 Emergence of Membrane Curvature on Nanoscopic Scales

Because of their fluidity, biomembranes are rather flexible and can easily change their shape. Indeed, one fascinating aspect of membranes and vesicles is that they can attain many different nonspherical shapes. When viewed under the optical microscope, these shapes appear to be rather smooth, see the examples in Fig. 1. Therefore, on the micrometer scale, membranes can be described as smoothly curved surfaces and then characterized by their curvature. However, this smoothness does not persist to molecular scales, i.e., when we resolve the molecular structure of a bilayer membrane as in Fig. 3.

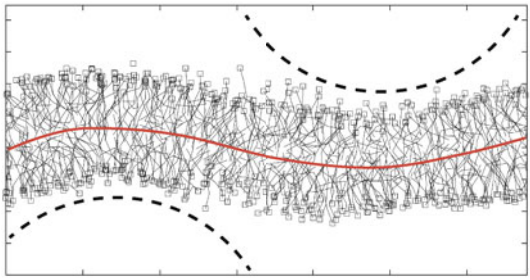

Fig. 3 Emergence of membrane curvature in molecular dynamics simulations of a tensionless membrane [56]. The lipid bilayer has a thickness of about 4 nm, the smallest curvature radius of its midsurface (red) was observed to be about 6 nm. For comparison, two circles (broken lines) with a radius of 6 nm are also displayed

4.1 Basic Aspects of Membrane Curvature

Because membranes are immersed in liquid water, each lipid and protein molecule undergoes thermal motion with displacements both parallel and perpendicular to the membrane. The perpendicular displacements represent molecular protrusions that roughen the two interfaces bounding the membrane, see Fig. 3. Therefore, in order to characterize a lipid/protein bilayer by its curvature, one has to consider small membrane patches and to average over the molecular conformations within these patches. The minimal lateral size of these patches can be determined from the analysis of the bilayer's shape fluctuations and was found, from molecular dynamics simulations of a one-component lipid bilayer, to be about 1.5 times the membrane thickness, see Fig. 3 [56]. For a membrane with a thickness of 4 nm, this minimal size is about 6 nm. Because such a membrane patch contains 80–100 lipid molecules, membrane curvature should be regarded as an emergent property arising from the collective behavior of a large number of lipid molecules.

4.2 Tensionless States of Membranes

The curvature just discussed applies to the midsurface of the bilayer membrane, i.e., to the surface between the two leaflets of the bilayer. Furthermore, for a membrane segment with midsurface area A and bending rigidity κ, curved conformations as in Fig. 3 are only possible if the membrane is "tensionless" in the sense that the mechanical membrane tension as obtained from the stress profile across the bilayer [57] is small compared to κ/A. For the example displayed in Fig. 3, the latter tension scale is found to be $\kappa/A = 0.08\,\mathrm{mN/m}$. Such tensionless states, which represent the natural reference states of the membranes, can be used to determine the bending rigidity from the undulation spectrum [56, 58–60] and the Gaussian

curvature modulus from the stress profile [61, 62], and the spontaneous curvature induced by the interactions with small solutes such as ions or monosaccharides [63, 64]. Attractive interactions between the solutes and the membrane lead to adsorption layers adjacent to the two leaflets, repulsive interactions to depletion layers. The spontaneous curvatures generated by depletion and adsorption have opposite signs [65]. Furthermore, both attractive and repulsive membrane-solute interactions generate a spontaneous curvature that varies linearly with the solute concentration difference between the exterior and interior solution [63, 64], in agreement with our analytical theories.

4.3 Simulations of More Complex Membrane Processes

During the last 20 years, molecular simulations of membranes have become a rather popular tool. Indeed, up to 1995, about 300 publications had been published on the molecular dynamics of membranes but, during the last 20 years, the same topic was addressed in about 25,000 publications. Using such simulations, one can study molecular remodelling processes such as membrane fusion [66–70] or membrane adhesion via membrane-anchored receptors and ligands [71–73]. In addition, simulation snapshots provide useful insights into the typical molecular conformations of the membrane systems and allow to compare the free energies of different conformations. One recent example is provided by the adsorption of PEG molecules onto liquid-ordered and liquid-disordered membranes [74].

5 Local Curvature Generation and Spontaneous Curvature

During the 1990s, I thought about a variety of ways to generate membrane curvature locally by membrane-bound macromolecules and adhesive nanoparticles. One simple example is provided by a flexible polymer that is anchored with one of its ends to the membrane, see Fig. 4a [75, 76]. Such an anchored polymer generates curvature by entropic forces because it can increase its configurational entropy by curving the membrane away from it. Another simple example are adhesive nanoparticles that are partially engulfed by the membrane, see Fig. 4b [34, 65, 77]. Here, the rigid particle imposes the curvature of its surface directly onto the membrane provided that the particle size is large compared to the membrane thickness. Curvature can also be generated by the adsorption of nanoparticles that are small compared to the membrane thickness, see Fig. 4c [65, 78]. In fact, small adhesive solutes with a diameter below 1 nm can generate spontaneous curvatures as large as 1/(20 nm) as recently shown by molecular dynamics simulations [63]. In these simulations, the adsorbed solutes increased the molecular area per lipid. The opposite effect is also possible, arising from the condensation of the lipid head groups. The two effects lead to opposite signs of the spontaneous curvature as proposed for the adsorption of calcium cations onto negatively charged membranes [80, 81].

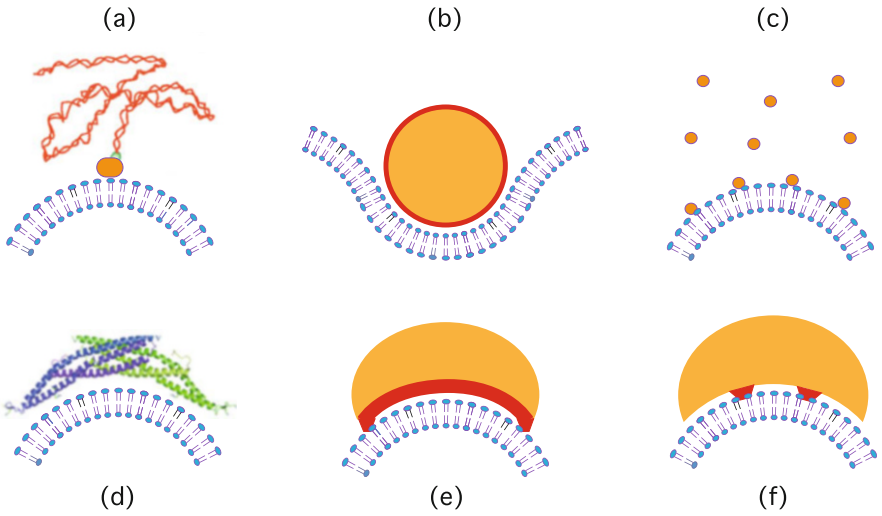

Fig. 4 Different mechanisms for local generation of membrane curvature: (**a**) Flexible polymer with one end anchored to the membrane [75] such as biotinylated DNA (red) linked to membrane-anchored avidin (orange) [76]; (**b**) spherical nanoparticle (orange) with an adhesive surface (red) partially engulfed by the membrane [34, 65, 77]. The particle radius is about 2.5 times the membrane thickness; (**c**) asymmetric adsorption of solutes that are small compared to the membrane thickness [63, 65, 78]; (**d**) N-BAR-domain protein with a curvature radius of about 11 nm [79] bound to the membrane; (**e**) BAR-mimetic nanoparticle with a large adhesive surface domain (red) that generates curvature via an induced-fit mechanism; and (**f**) BAR-mimetic nanoparticle with relatively small adhesive surface domains (red) which generate curvature via conformational selection [48]. Note that the sign of the local curvature in (**b**) is opposite to the sign of the local curvature in all other panels

5.1 Local Curvature Generated by Membrane-Bound Proteins

At the end of the 1990s, several labs started to use a simple experimental criterion to assess the curvature-generating capabilities of certain proteins. This criterion was based on the transformation of liposomes into tubular structures via protein adsorption and was used to identify, in a qualitative manner, a variety of curvature-generating proteins: N-BAR proteins such as amphiphysin [79] and endophilin [82], see Fig. 4d, F-BAR proteins such as pacsin/syndapin [83], and other proteins involved in endocytosis such as epsin [84]. The discovery of proteins that generate membrane curvature provides another rather interesting connection between biophysics and molecular cell biology.

The membrane-binding proteins are usually quite rigid and can be regarded as adhesive nanoparticles with two characteristic properties: (i) their shape is typically nonspherical and often banana-like or convex–concave; and (ii) their surface contains a more or less complex pattern of adhesive and nonadhesive surface domains. Thus, the membrane-binding proteins can be regarded as nonspherical

Janus-like nanoparticles. If the planar membrane can bind to some of the adhesive surface domains of the protein, this protein generates membrane curvature via an induced-fit mechanism, see Fig. 4e. In contrast, if the adhesive surface domains can only be reached by an appropriately curved membrane as in Fig. 4f, the protein senses and stabilizes membrane curvature via conformational selection [48].

5.2 From Local to Spontaneous Curvature

If the membrane is decorated by many bound solutes or "particles," it will acquire a certain spontaneous curvature that depends both on the local particle-induced curvature and on the particle coverages on the two leaflets of the bilayer membrane [85, 86]. Thus, if a single particle that is bound to the outer leaflet of the bilayer induces the local curvature M_1 in a membrane patch of area A_1, the spontaneous curvature m is given by

$$m = A_1 M_1 (\Gamma_{\rm ex} - \Gamma_{\rm in}) \tag{1}$$

where the coverages $\Gamma_{\rm ex}$ and $\Gamma_{\rm in}$ are defined by the numbers of particles bound to the outer and inner leaflets per unit area. The product $A_1 M_1 = \int dA\, M_{\rm si}$ can be determined by first calculating the local, position-dependent mean curvature $M_{\rm si}$ as generated by a single particle bound to the outer leaflet of an asymptotically flat membrane [85]. In contrast to other elastic membrane parameters such as the bending rigidity or the area compressibility modulus, the spontaneous curvature can vary over more than three orders of magnitude, from the inverse size of giant vesicles, which is of the order of $1/(50\,\mu{\rm m})$, to half the inverse membrane thickness, which is of the order of $1/(10\,{\rm nm})$.

5.3 Short History of Spontaneous Curvature

The spontaneous (or preferred) curvature m considered here describes the local bilayer asymmetry arising from the intermolecular interactions. Such a curvature was first discussed by Bancroft for surfactant monolayers in water–oil emulsions [87, 88]. It was also included by Frank, as the so-called splay term, in his theory for the curvature elasticity of liquid crystals [89]. In the context of lipid bilayers, spontaneous curvature as a local elastic parameter was first considered by Helfrich [90], in analogy to the liquid crystal case. The corresponding bending energy of the membrane is now known as the spontaneous curvature model [91].

If the membrane molecules cannot undergo flip-flops between the two leaflets, the number of molecules is fixed within each leaflet, and the quenched difference between these two numbers leads to a preferred area difference between the leaflets. This constraint was originally considered by Evans [92], incorporated

into the bilayer-coupling model of Svetina and Zeks [91, 93], and generalized in terms of the area-difference-elasticity model by Wortis and coworkers [94, 95]. As shown in these latter studies, the stationary shapes of the area-difference-elasticity model are also stationary shapes of the spontaneous curvature model provided that one defines an effective spontaneous curvature that includes a nonlocal, shape-dependent contribution. The latter contribution can be calculated explicitly for limit shapes that consist of two spherical membrane segments connected by a closed membrane neck [2]. Furthermore, the constraints on the area difference should be irrelevant if the bilayer membranes contain molecules such as cholesterol that can easily undergo flip-flops and, thus, relax local stresses induced by the bending deformations [96, 97]. In addition, even in the absence of flip-flops, the area-difference-elasticity term represents a small correction term whenever the (local) spontaneous curvature m is large compared to the inverse vesicle size. The latter separation of length scales applies, in particular, to the processes of nanotube formation and particle engulfment as considered in the following.

5.4 Sign of Spontaneous Curvature

It is important to note that the spontaneous curvature can be positive or negative. Within the spontaneous curvature model, the energy density of a membrane segment is proportional to $(M - m)^2$ which depends on the mean curvature M of this segment. It then follows that the spontaneous curvature is positive (negative) if the segment prefers to attain a positive (negative) mean curvature M. Furthermore, we need a convention to distinguish the two possible signs of the mean curvature in a unique manner. Here and below, I use the convention that the mean curvature M of a membrane segment is *positive* if it bulges towards the *exterior* aqueous compartment and negative if it bulges towards the interior compartment. Thus, if the exterior compartment in Fig. 4 is located on top of the membrane segments, the mean curvature of these segments is positive for panels (a) and (c)–(f) but negative for panel (b).

6 Two Mechanisms for the Formation of Membrane Nanotubes

Now, consider a membrane segment with area A and assume that this segment has a spontaneous curvature m that is large compared to $1/\sqrt{A}$. The membrane can then minimize its free energy by forming a long tube with a diameter of the order of $1/|m|$. More precisely, it may form a necklace-like tube consisting of small spheres with radius $1/|m|$, connected by closed membrane necks, a cylindrical tube with radius $1/(2|m|)$, or unduloids that interpolate between the necklace and the cylinder [74, 78].

6.1 Spontaneous Tubulation of Membranes

Recent experimental studies on supported lipid bilayers and giant vesicles have indeed shown that unilamellar membrane systems can undergo spontaneous tubulation, i.e., can form membrane tubules or nanotubes without the application of external forces. In the case of supported lipid bilayers, the tube formation was induced by the adsorption of antimicrobial peptides [98, 99]. In the case of giant vesicles, spontaneous tubulation was observed for a variety of binary and ternary lipid mixtures when the two leaflets of the vesicle membrane were exposed to aqueous polymer solutions that differed in their composition [74, 100].

Depending on the phase behavior of the aqueous polymer solution, the GUV membranes form different patterns of flexible nanotubes as shown in Fig. 5 for the liquid-disordered phase of a three-component membrane. All tubes were observed to be in-tubes protruding into the interior of the vesicles. For the liquid-disordered membranes, the morphology of the tubes could not be resolved because the tube diameter was below the optical diffraction limit. However, short and long tubes are theoretically predicted to be necklace-like and cylindrical, respectively [74].

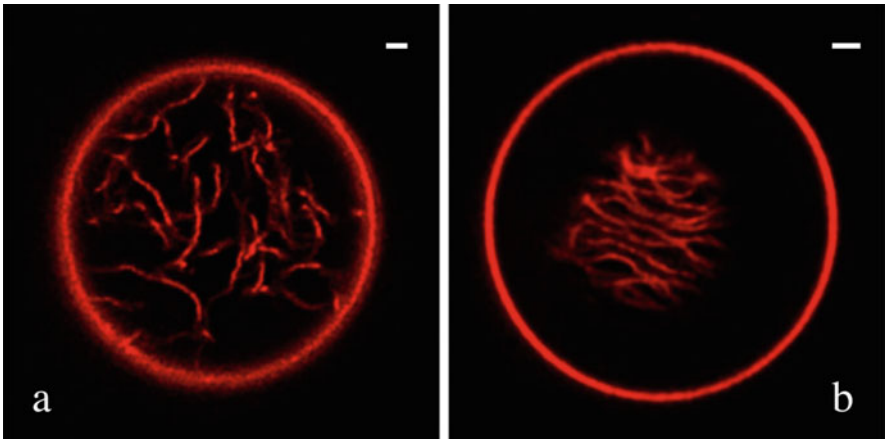

Fig. 5 Patterns of flexible nanotubes formed by liquid-disordered membranes exposed to aqueous solutions of PEG and dextran. All tubes are in-tubes in the sense that they protrude into the vesicle interior: (**a**) Disordered pattern of in-tubes freely suspended within the PEG-rich droplet enclosed by the vesicle; and (**b**) Thin layer of tubes adhering to the interface between the PEG-rich and the dextran-rich phase, with some short-range orientational order arising from crowding. The diameter of the tubes is below the diffraction limit but the tubes are theoretically predicted to be necklace-like and cylindrical in panels (**a**) and (**b**), respectively [74]. Scale bars: 2 μm

6.2 Necklace-to-Cylinder Transformation of Nanotubes

In fact, according to our theory, the tubes undergo a novel shape transformation from necklace-like to cylindrical tubes at a certain critical tube length, consistent with experimental observations for liquid-ordered membranes. Using the parameters of the liquid-disordered membranes, the tubes in Fig. 5a, b are predicted to be necklace-like and cylindrical, respectively. Furthermore, the spontaneous curvature of all tubes shown in Fig. 5 is about 1/(125 nm) as deduced via three distinct and independent methods of image analysis [74].

The presence of a necklace–cylinder transformation at a critical tube length can be understood as follows. Both the necklace-like tube and the main body of the cylindrical tube have zero bending energy. The two endcaps of the cylindrical tube contribute a bending energy of the order of $2\pi\kappa$. Therefore, the bending energy of the membrane disfavors the cylindrical tube. On the other hand, the necklace-like tube has a larger volume compared to the cylindrical one and the osmotic pressure difference across the membranes acts to compress the tubes when they protrude into the interior of the vesicles. Therefore, such an in-tube can lower its energy by reducing its volume which favors the cylindrical tube. The volume work is proportional to the tube length whereas the bending energy of the endcaps is independent of this length. It then follows from the competition between these two energies that short tubes are necklace-like whereas long tubes are cylindrical. Using superresolution microscopy such as STED, it should be possible to directly resolve the tube morphologies underlying the tube patterns in Fig. 5.

6.3 Increased Robustness of Tubulated Vesicles

The nanotubes arising from spontaneous tubulation provide the mother vesicle with a large reservoir of membrane area. Therefore, the mother vesicle can respond to mechanical perturbations by exchanging area with the tubes and then behaves much like a liquid droplet with variable surface area. This increased mechanical robustness of the mother vesicle has been recently demonstrated by micropipette aspiration [101]. The initial aspiration for small suction pressure directly reveals the spontaneous tension [78]

$$\sigma \equiv 2\kappa m^2 \tag{2}$$

of the vesicle membranes which represents the intrinsic tension scale of a membrane with bending rigidity κ and spontaneous curvature m. When the suction pressure reaches a σ-dependent critical value, the tubulated vesicles start to flow into the micropipette, thereby behaving like liquid droplets with an effective interfacial tension that is provided by the spontaneous tension σ [101].

6.4 Force-Induced Tubulation of Membranes

A second, quite different mechanism for the formation of membrane nanotubes is provided by external forces that are locally applied to the membranes of cells and giant vesicles. In order to generate such forces, one has to "grab" the cell or vesicle, e.g., by an adhesive surface or by a micropipette, and then apply some localized force which often acts onto a membrane-bound bead or nanoparticle. A variety of such force-generating methods have been used over the years: hydrodynamic flow applied to adhering cells [102–104], aspirated cells [105, 106], aspirated vesicles [107, 108], and vesicles attached to the tip of a micro-rod [109]; relative displacement of two micropipettes, one of which holds a membrane-bound bead while the other aspirates a cell [105] or GUV [110, 111]; gravity acting on a bead attached to an aspirated vesicle [112]; laser traps acting on a bead attached to cells [113–115], aspirated vesicles [80, 116, 117], and adhering vesicles [118]; as well as magnetic tweezers acting on a bead bound to aspirated vesicles [119] and adhering cells [120]. In addition, networks of membrane tubules have been generated by molecular motors moving along microtubules [121–124] as well as by manipulating adhering vesicles by micropipettes [125, 126]. A particularly instructive set-up for force-induced tubulation is provided by micropipette aspiration of a GUV combined with a membrane-bound nanobead to which one can apply a pulling force f via magnetic tweezers [119] or optical traps [80, 116, 117], as schematically depicted in Fig. 6. This set-up will now be considered in order to discuss the interplay between spontaneous and force-induced tubulation in a quantitative manner.

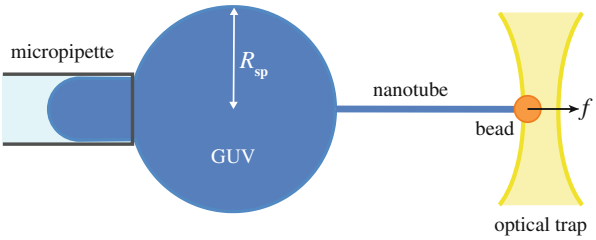

Fig. 6 Pulling a membrane nanotube attached to a bead from a giant unilamellar vesicle (GUV) by an optical trap: The weakly curved GUV is aspirated by the micropipette; the right end of the strongly curved nanotube experiences the pulling force f arising from the optical trap. The force f is taken to be positive for an out-tube as shown here and negative for an in-tube

7 Interplay Between Spontaneous and Force-Induced Tubulation

7.1 Tube Width Determined by Composite Curvature

In general, the diameter of a membrane nanotube depends both on the spontaneous curvature m and on the pulling force f [78]. It will be convenient to take the force f to be positive and negative if it points towards the exterior and interior aqueous solution, respectively (this convention is different from the one used in [78], where f described the absolute value of the pulling force for both pulling directions). To be specific, let us consider a cylindrical out-tube that protrudes from a GUV with a large spherical segment of radius $R_{\rm sp}$ as in Fig. 6. We can then distinguish different parameter regimes depending on the relative magnitudes of the composite curvature

$$m_{\rm com} \equiv m + \frac{f}{4\pi\kappa} \quad \text{and } 1/R_{\rm sp}. \tag{3}$$

The composite curvature $m_{\rm com}$ represents the superposition of the spontaneous curvature m with the rescaled pulling force $f/(4\pi\kappa)$ and directly describes the interplay of the two tubulation mechanisms. Indeed, the composite curvature can be positive or negative depending on the sign of m and f. As mentioned before, I use the sign convention that the spontaneous curvature m of a membrane segment is positive if this segment prefers to bulge towards the exterior compartment.

If the composite curvature is positive and much larger than the inverse vesicle radius, i.e., if $m_{\rm com} \gg 1/R_{\rm sp}$, the vesicle membrane can form cylindrical out-tubes with the mean curvature [78]

$$M_{\rm cy} \approx m_{\rm com} - \frac{1}{4R_{\rm sp}} = m + \frac{f}{4\pi\kappa} - \frac{1}{4R_{\rm sp}} \tag{4}$$

for small values of $1/(R_{\rm sp}\, m_{\rm com})$ as follows from the Euler–Lagrange equation (or shape equation) of the spontaneous curvature model and the force balance at the tube end.[1] Here and below, the symbol $\approx$ stands for "asymptotically equal" in the limit in which a certain parameter becomes small (or large). The relation (4) also applies to cylindrical in-tubes which form for negative composite curvatures with

[1] More precisely, the relation (4) is obtained for the mechanical equilibrium between a spherical membrane segment with mean curvature $M_{\rm sp} = 1/R_{\rm sp}$ and a cylindrical segment with mean curvature $M_{\rm cy}$, coexisting on the same vesicle, by combining the two Euler–Lagrange equations for these membrane segments with the force balance at the tube end, see [78].

$m_{\rm com} \ll -1/R_{\rm sp}$. In both cases, the tube radius is given by

$$R_{\rm cy} \approx \frac{1}{2|m_{\rm com}|} = \frac{1}{\left|2m + \frac{f}{2\pi\kappa}\right|} \quad \text{for } |m_{\rm com}| \gg 1/R_{\rm sp}. \tag{5}$$

Thus, in this parameter regime, the tube radius $R_{\rm cy}$ is directly determined by the composite curvature $m_{\rm com}$, i.e., by the combined action of the two tubulation mechanisms provided by spontaneous curvature m and pulling force f. If m and f have the same sign, these two mechanisms act synergistically whereas they act antagonistically if m and f have opposite sign. In both cases, the radius is primarily determined by the spontaneous curvature in the parameter regime with $|m| \gg |f|/(4\pi\kappa)$ and by the pulling force for $|f| \gg 4\pi\kappa|m|$.

7.2 Composite Curvature and Total Membrane Tension

The mechanical equilibrium between a cylindrical tube and a large spherical mother vesicle [78] also implies the relation

$$m_{\rm com} = m + \frac{f}{4\pi\kappa} \approx \pm\left(\frac{\hat{\Sigma}}{2\kappa}\right)^{1/2} - \frac{1}{4R_{\rm sp}} \quad \text{for large } R_{\rm sp}/R_{\rm cy} \tag{6}$$

where the plus and minus sign applies to out- and in-tubes, respectively, with the total membrane tension

$$\hat{\Sigma} \equiv \Sigma + \sigma = \Sigma + 2\kappa m^2 \tag{7}$$

which represents the superposition of the mechanical tension Σ and the spontaneous tension σ as defined in (2).

It has been recently shown that it is possible to pull both out- and in-tubes via an optical trap from the same aspirated GUV [108, 127]. One can then measure the two forces $f_{\rm ex}$ and $f_{\rm in}$ that generate out- and in-tubes for the same aspiration pressure. Both cases are described by (6) with f replaced by $f_{\rm ex}$ for the plus sign and by $f_{\rm in}$ for the minus sign. The sum of these two relations leads to the simple expression

$$m \approx -\frac{f_{\rm ex} + f_{\rm in}}{8\pi\kappa} - \frac{1}{4R_{\rm sp}} \tag{8}$$

for the spontaneous curvature m. In this way, one can determine the spontaneous curvature m by force-induced tubulation regardless of the membrane tension. For symmetric bilayers as studied in [108], the spontaneous curvature vanishes and the relation (8) implies that $f_{\rm in} = -f_{\rm ex}$. For GUVs containing a binary mixture of POPC and GM1, on the other hand, the out- and in-pulling forces, $f_{\rm ex}$ and $f_{\rm in}$, were observed to have different magnitudes, i.e., $f_{\rm in} \neq -f_{\rm ex}$ which implies a nonzero spontaneous curvature [127].

7.3 Total Membrane Tension Versus Aspiration Tension

The relationship between the composite curvature and the total membrane tension as given by (6) involves the total membrane tension $\hat{\Sigma}$ defined in (7). In some experimental studies, [80, 117] the relation (6) was used with the total membrane tension replaced by the aspiration tension

$$\Sigma_{\rm asp} \equiv \frac{(P_{\rm ex} - P_{\rm pip})R_{\rm pip}}{2(1 - R_{\rm pip}/R_{\rm sp})} \,. \tag{9}$$

which can be directly obtained from measured values of the suction pressure $P_{\rm ex} - P_{\rm pip}$ of the micropipette and the radii $R_{\rm pip}$ and $R_{\rm sp}$ of the pipette and the nonaspirated membrane segment. The expression (9) follows from the Laplace equation for the spherical endcap of the fully aspirated membrane tongue with mean curvature $M_{\rm cap} = 1/R_{\rm pip}$, see, e.g., [128]. However, the Laplace equation represents a truncation of the full Euler–Lagrange (or shape equation) for a spherical membrane segment. As a consequence, the total membrane tension $\hat{\Sigma}$ in (6) is not equal to the aspiration tension $\Sigma_{\rm asp}$ but satisfies, for $M_{\rm cap} = 1/R_{\rm pip}$, the more general relation

$$\hat{\Sigma} = \Sigma_{\rm asp} + \Delta\hat{\Sigma} \tag{10}$$

with the additional tension term

$$\Delta\hat{\Sigma} \equiv 2\kappa m \left(\frac{1}{R_{\rm pip}} + \frac{1}{R_{\rm sp}}\right) . \tag{11}$$

As an example, let us consider a GUV membrane with bending rigidity $\kappa = 10^{-19}$ J and spontaneous curvature $m = \tilde{m}/\mu$m. Let us further assume that the GUV is aspirated by a micropipette of radius $R_{\rm pip} = 3\,\mu$m and that the nonaspirated membrane segment forms a spherical segment of radius $R_{\rm sp} = 6\,\mu$m. The additional tension term $\Delta\hat{\Sigma}$ then has the magnitude $0.1\tilde{m}\,\mu$N/m which is equal to $1\,\mu$N/m for $\tilde{m} = 10$ or $m = 1/(100\,{\rm nm})$. The magnitude of $\Delta\hat{\Sigma}$ should be compared to the smallest values of the aspiration tension which are also of the order of $1\,\mu$N/m for the considered geometry, corresponding to the smallest accessible suction pressures of about 1 Pa. Therefore, we conclude that the additional tension term $\Delta\hat{\Sigma}$ can only be ignored for suction pressures that are much larger than 1 Pa and for spontaneous curvatures m that are much smaller than $1/(100\,{\rm nm})$.

7.4 Different Parameter Regimes

As emphasized before, both the spontaneous curvature m and the pulling force f can be positive or negative. Irrespective of the signs of m and f, the expressions (4)–(6)

are valid as long as $\left|m + \frac{f}{4\pi\kappa}\right| \gg 1/R_{\rm sp}$. The latter inequality is not fulfilled: (i) if both $|m|$ and $|f|/(4\pi\kappa)$ are smaller than or comparable to the inverse vesicle radius $1/R_{\rm sp}$ or (ii) if m and $f/(4\pi\kappa)$ have opposite sign and (almost) cancel each other. In case (i), the vesicle membrane cannot form nanotubes at all. In case (ii), nanotubes are still possible but only if the curvature ratio $|m|/M_{\rm sp} = |m|R_{\rm sp} \gtrsim 10^3$. In the latter case, the mean curvature of the tube behaves as $M_{\rm cy} \approx \pm(|m|M_{\rm sp}^2/4)^{1/3}$ and, thus, depends strongly on the vesicle size as follows from the theory in [78]. The different regimes for the interplay between spontaneous and force-induced tubulation can be probed experimentally by first pulling a tube from a GUV membrane with no spontaneous curvature and subsequently generating a positive or negative spontaneous curvature in this membrane, e.g., by adsorption of macromolecules or nanoparticles.

8 Engulfment of Nanoparticles by Membranes

One process for which the spontaneous curvature represents a key parameter is the engulfment of nanoparticles by membranes [34]. These particles are widely used to deliver drugs, imaging agents, and toxins to biological cells [129–131]. The cellular uptake of such a particle requires the adhesion of this particle to the cell membrane and its subsequent engulfment by this membrane, a process that is governed by the competition between particle adhesion and membrane bending [34, 65, 77]. The same process is misused by viruses that enter the host cell by receptor-mediated endocytosis and by enveloped viruses that exit the host cell by exocytosis.

8.1 Nanoparticles in Contact with Membranes

An adhesive nanoparticle that comes into contact with a membrane can remain in a free, nonadhering state or can become engulfed by the membrane. In the latter case, the membrane may cover only part of the particle surface or engulf the particle completely. These three different states of the nanoparticle are illustrated in Fig. 7. In order to understand the energetics of these states, it is rather instructive to consider the stability (i) of the free state against the onset of membrane spreading and (ii) of the completely engulfed state against the opening of the closed membrane neck. This stability analysis can be performed in a systematic manner and leads to two relatively simple stability relations [34] which have a number of interesting consequences [132–134] as briefly summarized in the following subsections.

The stability of the free, nonadhering state in Fig. 7a depends only on three parameters: the mean curvature M of the membrane segment that comes into contact with the particle, see Fig. 7a; the particle size $R_{\rm pa}$; and the adhesion length

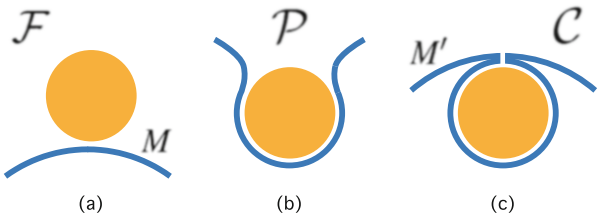

Fig. 7 Three possible states of a nanoparticle (orange) in contact with a membrane segment (blue): (**a**) free, nonadhering state $\mathscr{F}$ in which the membrane does not spread over the particle surface in spite of the attractive membrane–particle interactions; (**b**) partially engulfed state $\mathscr{P}$ in which the membrane covers some part of the particle surface; and (**c**) completely engulfed state $\mathscr{C}$ in which the membrane covers the whole particle surface and forms a closed neck that connects the bound membrane segment to the unbound membrane of the mother vesicle. The particles originate from the exterior aqueous solution corresponding to endocytic engulfment. The membrane segment in (**a**) has mean curvature M, and the unbound membrane segment in (**c**) has mean curvature M'. All bound membrane segments have the mean curvature $-1/R_{\rm pa}$ [34]

$$R_W \equiv \sqrt{2\kappa/|W|} \tag{12}$$

which represents a material parameter that is independent of the membrane geometry and encodes the competition between the bending rigidity κ of the membrane and the adhesive strength $|W|$ of the membrane–particle interactions [135]. Depending on the chemical composition of the membrane and the nanoparticle, the adhesion length R_W can vary from about 10 nm for strong adhesion to a couple of micrometers for ultra-weak adhesion [34]. The adhesion length R_W provides the basic length scale for engulfment processes and the most interesting engulfment behavior is found for nanoparticle sizes of the order of R_W.

8.2 *(In)stability of Free Particle State and Onset of Adhesion*

To be specific, consider the endocytic engulfment of spherical nanoparticles of radius $R_{\rm pa}$ dispersed in the exterior aqueous compartment. When such a particle comes close to a membrane segment with mean curvature M,[2] this segment does *not* adhere to the particle, even in the presence of attractive membrane–particle interactions, if [34, 132]

$$M \geq M_{\rm fr} \equiv -\frac{1}{R_{\rm pa}} + \frac{1}{R_W} \quad \text{(no adhesion, endocytic process)}, \tag{13}$$

[2] As explained before, the mean curvature M of a membrane segment is taken to be positive (negative) if this segment bulges towards the exterior (interior) compartment.

i.e., if the membrane's mean curvature M exceeds the threshold value $M_{\rm fr}$ that depends on the particle radius and the adhesion length. The stability criterion (13) implies that the free, nonadhering particle state is stable for all particle sizes if the membrane curvature $M \geq 1/R_W$, i.e., a membrane segment with a sufficiently large positive curvature M does not start to spread onto a particle of any size. Note that the threshold value $M_{\rm fr}$ is independent of the spontaneous curvature m of the membrane, which is somewhat counterintuitive. On the other hand, if the mean curvature is below this threshold value and within the range [34, 132]

$$-\frac{1}{R_{\rm pa}} < M < M_{\rm fr} = -\frac{1}{R_{\rm pa}} + \frac{1}{R_W} \quad \text{(onset of adhesion, endocytic process)}, \tag{14}$$

the membrane segment starts to spread over the particle surface. The first inequality $-1/R_{\rm pa} < M$ ensures that membrane segment and particle can come into direct contact without intersecting each other, compare Fig. 8c1. Note that the curvature range as given by (14) becomes rather small if the adhesion length R_W is large compared to the particle size $R_{\rm pa}$. In such a situation, one has to fine-tune the parameters in order to observe the onset of adhesion experimentally. The stability relations (13) and (14) are illustrated in Fig. 8a–c.

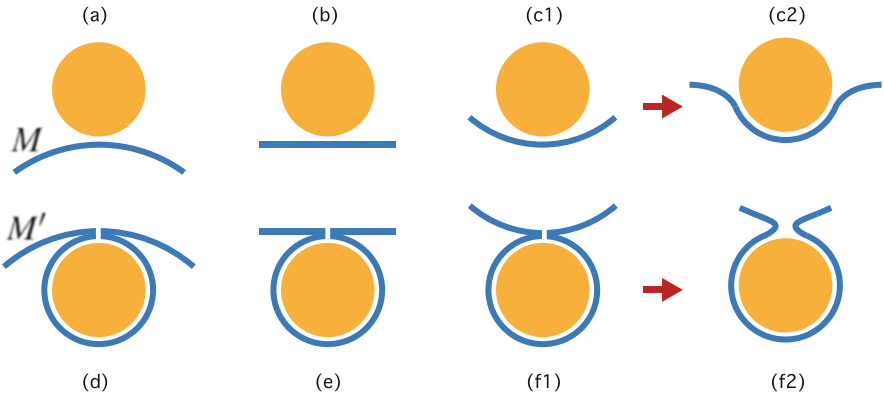

Fig. 8 Endocytic engulfment of nanoparticles (orange) originating from the exterior solution: (**a**)–(**c**) The top row illustrates the (in)stability of the free, nonadhering particle state for curvature threshold $M_{\rm fr} = 0$, see (13) and (14). The free state is stable in (**a**) with membrane curvature $M > 0$, marginally stable in (**b**) with $M = 0$, and unstable in (**c1**) with $M < 0$. The instability of (**c1**) leads to the onset of adhesion and to the partially engulfed state in (**c2**). (**d**)–(**f**) The bottom row illustrates the (in)stability of the completely engulfed state with a closed membrane neck for curvature threshold $M_{\rm ce} = 0$, see (16) and (15). The latter state is stable in (**d**) with curvature $M' > 0$ of the unbound membrane, marginally stable in (**e**) with curvature $M' = 0$, and unstable in (**f1**) with $M' < 0$. The instability of (**f1**) leads to an opening of the membrane neck and to the partially engulfed state in (**f2**)

8.3 (In)stability of Completely Engulfed Particle State

The stability of the completely engulfed state in Fig. 7c depends on four parameters: in addition to the three parameters that are also relevant for the onset of adhesion, the stability of the completely engulfed state depends on the spontaneous curvature m as well. Now, consider a completely engulfed state with a closed membrane neck that connects the bound membrane segment in contact with the nanoparticle to the adjacent segment of the unbound vesicle membrane. The latter membrane segment has the mean curvature M' as in Fig. 7c. The closed membrane neck starts to open up if M' satisfies the inequality [34, 132]

$$M' < M_{\rm ce} \equiv 2m + \frac{1}{R_{\rm pa}} - \frac{1}{R_W} \quad \text{(neck opening, endocytic process)}, \tag{15}$$

i.e., if the mean curvature M' is below the threshold value $M_{\rm ce}$ that depends on the spontaneous curvature, the particle size, and the adhesion length. The instability criterion (15) implies that the completely engulfed state is unstable for all particle sizes if the membrane curvature $M' < 2m - 1/R_W$ which is always fulfilled for a sufficiently large negative value of M'. On the other hand, the closed neck is stable if the curvature M' is above the threshold value $M_{\rm ce}$ and within the range [34, 132]

$$M_{\rm ce} = 2m + \frac{1}{R_{\rm pa}} - \frac{1}{R_W} \le M' < \frac{1}{R_{\rm pa}} \quad \text{(closed neck, endocytic process)}. \tag{16}$$

The last inequality $M' < 1/R_{\rm pa}$ ensures that the vesicle membrane and the particle do not intersect each other.

In biological cells, many processes that lead to the formation of membrane buds with closed necks involve proteins that generate constriction forces onto the necks [133]. In the case of endocytosis, proteins such as dynamin [136] or ESCRTs [38, 137, 138] are typically involved in neck closure and fission. In phagocytic engulfment by macrophages, a contractile ring composed of actin and myosin motors is formed around the neck [139]. Now, if a spherical nanoparticle with radius $R_{\rm pa}$, adhering to the outer leaflet of the vesicle membrane, is fully engulfed by the membrane, the bound membrane segment forms a spherical bud with mean curvature $M_{\rm bud} = -1/R_{\rm pa}$. In the presence of a radial constriction force $f > 0$ that acts to decrease the neck radius, the closed neck is stable if [133]

$$f + f_{\rm eng} \ge 0 \quad \text{with} \quad f_{\rm eng} \equiv 4\pi\kappa \left(M' + M_{\rm bud} + \frac{1}{R_W} - 2m \right) \tag{17}$$

which generalizes the stability condition (16) and describes the enhanced neck stability in the presence of constriction forces.

Table 1 The (in)stabilities of the free state $\mathscr{F}$ and the completely engulfed state $\mathscr{C}$ as described by the (in)stability conditions (13)–(16) define four engulfment regimes $\mathscr{F}_{\rm st}$, $\mathscr{C}_{\rm st}$, $\mathscr{B}_{\rm st}$, and $\mathscr{P}_{\rm st}$

State $\mathscr{F}$	Stable	Unstable	(Meta)stable	Unstable
State $\mathscr{C}$	Unstable	Stable	(Meta)stable	Unstable
Regime	$\mathscr{F}_{\rm st}$	$\mathscr{C}_{\rm st}$	$\mathscr{B}_{\rm st}$	$\mathscr{P}_{\rm st}$

8.4 Engulfment Regimes of Single Nanoparticles

When we combine the (in)stability conditions for the free particle states $\mathscr{F}$ as given by (13) and (14) with the (in)stability conditions for the completely engulfed particle states $\mathscr{C}$ as described by (15) and (16), we obtain four combinations which define four different engulfment regimes, $\mathscr{F}_{\rm st}$, $\mathscr{C}_{\rm st}$, $\mathscr{B}_{\rm st}$, and $\mathscr{P}_{\rm st}$, as summarized in Table 1.

First, the engulfment regime $\mathscr{F}_{\rm st}$ corresponds to a stable free state $\mathscr{F}$ and an unstable completely engulfed state $\mathscr{C}$ as described by the combination of (13) and (15). Second, the complete engulfment regime $\mathscr{C}_{\rm st}$ is defined by an unstable state $\mathscr{F}$ and a stable state $\mathscr{C}$, i.e., by the combination of (14) and (16). Third, if both the free and the completely engulfed states are stable, one has to combine the stability relations (13) and (16) which leads to the bistable engulfment regime $\mathscr{B}_{\rm st}$. Finally, the partial engulfment regime $\mathscr{P}_{\rm st}$ is obtained by combining the instability conditions (14) and (15) corresponding to the situation in which both the free and the completely engulfed states are unstable.

The (in)stability conditions as given by (13)–(16) depend on the local mean curvatures M and M', which characterize the membrane geometry close to the nanoparticle, see Fig. 7, and on three material parameters, the particle size $R_{\rm pa}$, the adhesion length R_W, and the spontaneous curvature m. In fact, close inspection of these (in)stability conditions reveals that they depend on particle size and adhesion length only via the contact mean curvature $M_{\rm co} \equiv 1/R_W - 1/R_{\rm pa}$. Furthermore, in the small particle limit, i.e., if the nanoparticles are much smaller than the vesicle size, one may identify the local mean curvatures M and M' [132, 134]. In this limit, one is left with a three-dimensional parameter space defined by the local mean curvature M, the contact mean curvature $M_{\rm co}$, and the spontaneous curvature m. The different engulfment regimes can then be visualized by two-dimensional sections through the three-dimensional parameter space [34, 132, 134, 140].

8.5 Engulfment Regimes and Local Energy Landscapes

The (in)stability relations as given by (13)–(16) are intimately related to the local energy landscapes for engulfment as a function of an appropriate reaction coordinate. Convenient reaction coordinates are the wrapping angle for axisymmetric engulfment geometries [34, 77] and the area fraction of the membrane-covered particle surface for non-axisymmetric geometries [133]. The engulfment regimes

$\mathscr{F}_{\rm st}$ are characterized by local energy landscapes with a single minimum at the free state $\mathscr{F}$ and a single maximum at the completely engulfed state $\mathscr{C}$. Likewise, the complete engulfment regime $\mathscr{C}_{\rm st}$ is described by local energy landscapes with a single minimum at $\mathscr{C}$ and a single maximum at $\mathscr{F}$. Within the bistable engulfment regime $\mathscr{B}_{\rm st}$, the local energy landscapes exhibit two (meta)stable minima at the particle states $\mathscr{F}$ and $\mathscr{C}$ separated by an energy barrier. Finally, within the partial engulfment regime $\mathscr{P}_{\rm st}$, the only extrema of the local energy landscapes are provided by a single minimum corresponding to a partially engulfed state $\mathscr{P}$ and by maxima at the particle states $\mathscr{F}$ and $\mathscr{C}$.

In the preceding discussion, we have implicitly assumed that the energy landscapes do not exhibit any additional minima or maxima. The latter feature is always valid in the small particle limit [134]. In general, one may have additional satellite minima close to the free or completely engulfed states as found by numerical energy minimization for zero spontaneous curvature [140].

8.6 Exocytic Engulfment of Interior Nanoparticles

The (in)stability relations as given by (13)–(16) and the corresponding engulfment regimes described in the previous subsection apply to *endocytic* engulfment of exterior nanoparticles which are dispersed in the exterior aqueous solution and adhere to the outer leaflet of the membranes. The corresponding relations for *exocytic* engulfment of nanoparticles originating from the vesicle interior and adhering to the inner membrane leaflet can be obtained by replacing M, M', and m in (13)–(16) by $-M$, $-M'$, and $-m$, i.e., by changing the sign of all curvatures that appear in these relations. One then finds, in particular, that a membrane segment with $M < -1/R_W$ does not adhere to any particle and that completely engulfed states are impossible for an unbound membrane segment with $M' > 2m + 1/R_W$, irrespective of the size of the particles.

8.7 Engulfment Patterns and Curvature-Induced Forces

The four stability relations (13)–(16) which define the four engulfment regimes depend on the local mean curvatures M and M' of the membrane, with $M = M'$ in the small particle limit. Therefore, when a nonspherical vesicle with variable curvature M is exposed to many nanoparticles, the vesicle membrane can be decomposed, in general, into several membrane segments that belong to different engulfment regimes. As a consequence, nonspherical vesicles exhibit distinct engulfment patterns corresponding to different combinations of the engulfment regimes. However, not all combinations of the four engulfment regimes can be present on a single vesicle but only 10 out of 15 such combinations [132].

When a membrane-bound nanoparticle diffuses within a membrane segment that belongs to the partial engulfment regime $\mathscr{P}_{\mathrm{st}}$, its binding energy depends on the local mean curvature M of the membrane. This M-dependence of the binding energy defines a global energy landscape for the diffusing particle, and the gradient of this global energy landscape provides a curvature-induced force acting on the particle [134]. As a consequence, the nanoparticle undergoes biased diffusion towards membrane segments of lower or higher mean curvature, depending on whether the particle adheres to the outer or inner membrane leaflet, respectively. The partial engulfment of nanoparticles with a chemically uniform surface requires fine-tuning of particle size and adhesiveness with respect to the properties of the membrane. In contrast, Janus particles with one strongly adhesive and one nonadhesive surface domain are always partially engulfed. Therefore, the curvature-induced forces that have been predicted theoretically [134] should be directly accessible to experimental studies when the vesicles are exposed to such Janus particles.

8.8 Further Aspects of Membrane-Nanoparticle Interactions

In the preceding subsections, spherical nanoparticles interacting with uniform membranes have been considered. These membrane–particle systems are governed by the (in)stability conditions (13)–(16) which lead to four engulfment regimes, ten different engulfment patterns, and curvature-induced forces acting on partially engulfed nanoparticles. Generalized (in)stability conditions have also been derived for membranes with two types of intramembrane domains that differ in their fluid-elastic properties [34]. These generalized conditions provide a quantitative description for the nonmonotonic size dependence of clathrin-dependent endocytosis as observed experimentally in [35, 36]. The (in)stability conditions can also be extended to nonspherical particles [133] as studied in [141] by Monte-Carlo simulations. Furthermore, for vanishing spontaneous curvature, another intriguing effect has been observed in simulations: when the membrane–particle adhesion was parametrized in terms of a short-ranged potential well, the nanoparticles were found to assemble into linear aggregates that are enclosed by membrane in-tubes [142–144].

9 Wetting of Membranes by Aqueous Droplets

My renewed interest in spontaneous curvature was triggered by the spontaneous tube formation as observed in aqueous two-phase systems (Fig. 5). I first came across these systems in 2001 when I gave a talk at Penn State and met Christine Keating who was studying lipid vesicles in aqueous PEG-dextran solutions [145]. These solutions can undergo aqueous phase separation and then form PEG-rich and dextran-rich droplets. Such aqueous two-phase systems have been frequently used

in biochemical analysis and biotechnology to separate and purify biomolecules, organelles, and membranes [146]. As explained in the present section, they also provide insight into the wetting behavior of membranes and vesicles, a new research topic which turns out to be rather interesting.

9.1 Transitions Between Distinct Wetting Morphologies

Two experimental methods have been used to induce aqueous phase separation of PEG-dextran solutions within GUVs: temperature changes [145, 147] and osmotic deflation [74, 100, 148, 149]. After the phase separation has been completed, the vesicle contains two aqueous droplets consisting of the PEG-rich phase α and the dextran-rich phase β, which are both separated by the membrane from the exterior phase γ, see insets in Fig. 9. In general, we can distinguish three different wetting morphologies for a membrane in contact with two aqueous phases α and β: the

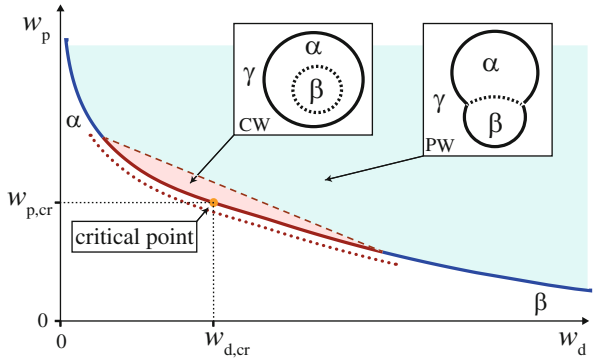

Fig. 9 Phase diagram and membrane wetting behavior of aqueous PEG-dextran solutions as a function of the weight fractions w_p and w_d for the two polymers. The critical demixing point (orange dot) is located at $(w_{d,cr}, w_{p,cr}) = (0.0451, 0.0361)$ [74]. The coexistence region of the PEG-rich phase α and the dextran-rich phase β consists of two subregions, CW (pink) and PW (turquois). In the pink CW subregion close to the critical point, the membrane is completely wetted by the PEG-rich phase α which encloses the dextran-rich phase β, see left inset where γ denotes the exterior phase, and gravitational effects arising from the mass densities of the different phases have been ignored. The CW subregion is separated from the one-phase region (white) by the red segment of the binodal line. In the turquois PW subregion, the membrane is partially wetted by both phases, see right inset. The PW subregion is separated from the one-phase region by the blue segment of the binodal line. The boundary between the CW and PW subregions is provided by a certain tie line (red dashed line), the precise location of which depends on the lipid composition of the membrane. Along this tie line, the system undergoes a complete-to-partial wetting transition. Furthermore, if one approaches the red CW segment of the binodal line from the one-phase region, a wetting layer of the α phase starts to form at the membrane (red dotted line) and becomes mesoscopically thick as one reaches the red CW segment of the binodal line. No such layer is formed along the blue PW segment of the binodal

membrane is wetted (i) completely by the α phase, (ii) completely by the β phase, or (iii) partially by both phases. For the PEG-dextran solutions, both complete wetting by the PEG-rich phase α and partial wetting by both phases have been observed. The corresponding phase diagram is displayed in Fig. 9. As shown in this figure, the two-phase coexistence region of these systems typically consists of two subregions corresponding to complete and partial wetting of the membrane by the PEG-rich phase α. These two subregions are separated by a certain tie line, at which the system undergoes a complete-to-partial wetting transition. The precise location of this tie line depends on the lipid composition of the membranes and has been elucidated for binary lipid mixtures consisting of DOPC and GM1 [100, 148] as well as for ternary mixtures containing DOPC, DPPC, and cholesterol [74]. In general, the wetting transition along this tie line can be continuous or discontinuous depending on the manner in which the contact angle vanishes as we approach the transition from the partial wetting regime. So far, the experimental data do not allow us to draw firm conclusions about the continuous or discontinuous nature of the transition.

A particularly interesting class of aqueous droplets is provided by biomolecular condensates, also known as membraneless organelles, that have been discovered in vivo and are enriched in intrinsically disordered proteins such as FUS [150]. Quite recently, we studied GUVs exposed to such droplets and found that these droplets undergo two distinct wetting transitions: from complete wetting of the membrane by the FUS-poor phase to partial wetting to complete wetting by the FUS-rich phase [151].

9.2 Partial Wetting and Apparent Contact Angles

For partial wetting of a vesicle membrane, both the α and the β droplets are in contact with this membrane (right inset of Fig. 9). As a consequence, the $\alpha\beta$ interface between the two aqueous phases forms a contact line with the membrane that partitions this membrane into two segments, an $\alpha\gamma$ and a $\beta\gamma$ segment, as shown in Fig. 10. Because the two membrane segments are exposed to different aqueous environments, they will in general have different spontaneous curvatures $m_{\alpha\gamma}$ and $m_{\beta\gamma}$ and different bending rigidities $\kappa_{\alpha\gamma}$ and $\kappa_{\beta\gamma}$. Furthermore, the $\alpha\beta$ interface exerts capillary forces onto the vesicle membrane which are counterbalanced by the tensions within the two membrane segments.

The membrane deformations arising from these capillary forces depend on the interfacial tension $\Sigma_{\alpha\beta}$, on the mechanical tensions and fluid-elastic properties of the two membrane segments, as well as on the sizes of the α and β droplets, which are conveniently defined via $(3V_\alpha/4\pi)^{1/3}$ and $(3V_\beta/4\pi)^{1/3}$. So far, the experimental studies have explored the regime in which the α and β droplets were large compared to the length scales $(\kappa_{\alpha\gamma}/\Sigma_{\alpha\beta})^{1/2}$ and $(\kappa_{\beta\gamma}/\Sigma_{\alpha\beta})^{1/2}$. In such a situation, the two membrane segments form two spherical caps which meet the spherical $\alpha\beta$ interface along an apparent contact line as shown in Fig. 10a. This three-spherical-cap geometry is determined by the curvature radii of the three

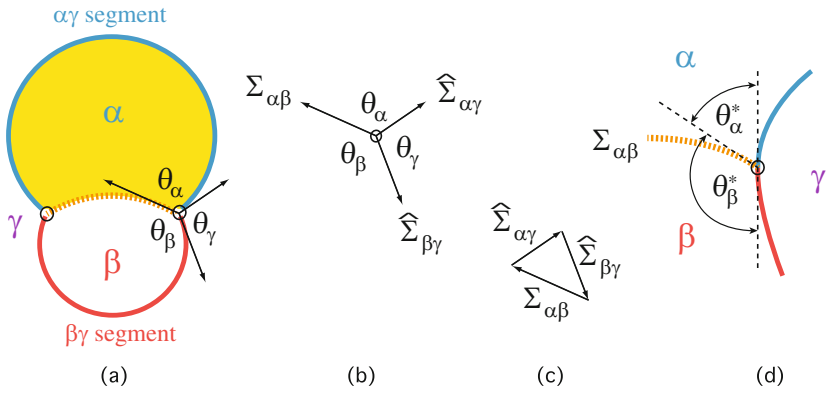

Fig. 10 Vesicle (blue/red) enclosing two aqueous droplets of α and β phase (yellow and white) immersed in the exterior liquid γ corresponding to partial wetting of the membrane by both α and β. The latter two phases are separated by the $\alpha\beta$ interface (broken orange) with interfacial tension $\Sigma_{\alpha\beta}$. This interface partitioned the vesicle membrane into two segments, the $\alpha\gamma$ segment (blue) and the $\beta\gamma$ segment (red). Because the two membrane segments are exposed to two different aqueous environments, they will in general differ in their spontaneous curvatures. (**a**) Vesicle shape consisting of three surface segments that have a spherical shape when viewed with optical resolution. The extrapolation of the spherical membrane segments defines an apparent contact line (black circles) and three apparent contact angles θ_α, θ_β, and θ_γ; [78, 152] (**b**) for certain parameter regimes, see main text, the total membrane tensions $\hat{\Sigma}_{\alpha\gamma}$ and $\hat{\Sigma}_{\beta\gamma}$ balance the interfacial tension $\Sigma_{\alpha\beta}$ along the apparent contact line; (**c**) force balance in (**b**) redrawn as a triangle; and (**d**) enlarged view of the true contact line at which the membrane bends smoothly, and the effective membrane segments have a common tangent plane (vertical broken line). The angles between this common tangent plane and the plane tangential to the $\alpha\beta$ interface represent the intrinsic contact angles θ^*_α and θ^*_β with $\theta^*_\alpha + \theta^*_\beta = \pi$

spherical surface segments and the radius of the apparent contact line [152].[3] Along the contact line, one can measure three apparent contact angles θ_α, θ_β, and θ_γ, see Fig. 10a. Combining the Laplace equation for the $\alpha\beta$ interface with the Euler–Lagrange (or shape) equations for the two membrane segments, one obtains the general relationship [152]

$$M_{\alpha\gamma}\left(\frac{\Sigma^{\rm eff}_{\alpha\gamma}}{\Sigma_{\alpha\beta}} - \frac{\sin\theta_\beta}{\sin\theta_\gamma}\right) = M_{\beta\gamma}\left(\frac{\Sigma^{\rm eff}_{\beta\gamma}}{\Sigma_{\alpha\beta}} - \frac{\sin\theta_\alpha}{\sin\theta_\gamma}\right) \tag{18}$$

[3] In addition, one also has to specify whether the three cap centers are located above or below the plane that contains the contact line.

between the mean curvatures $M_{\alpha\gamma}$ and $M_{\beta\gamma}$ of the two membrane segments, the apparent contact angles $\theta_\alpha, \theta_\beta, \theta_\gamma$ and the effective segment tensions

$$\Sigma_{j\gamma}^{\mathrm{eff}} \equiv \hat{\Sigma}_{j\gamma} - 2\kappa_{j\gamma}\, m_{j\gamma}\, M_{j\gamma} = \Sigma_{j\gamma} + \sigma_{j\gamma} - 2\kappa_{j\gamma}\, m_{j\gamma}\, M_{j\gamma}\,. \tag{19}$$

with $j = \alpha$ or β. The effective tension $\Sigma_{j\gamma}^{\mathrm{eff}}$ consists of the total segment tension $\hat{\Sigma}_{j\gamma} = \Sigma_{j\gamma} + \sigma_{j\gamma}$ and of the curvature-dependent term $2\kappa_{j\gamma}\, m_{j\gamma}\, M_{j\gamma}$. The mechanical segment tensions $\Sigma_{j\gamma}$ can be further decomposed into the overall mechanical stress experienced by the whole membrane, corresponding to the Lagrange multiplier conjugate to the total membrane area, and into the adhesion free energy densities of the two membrane segments [152]. The overall mechanical stress represents a hidden parameter which cannot be measured directly but depends on the vesicle geometry. In order to eliminate this parameter, one may apply the relation (18) to several droplets on the same vesicle.

For certain regions of the parameter space, the force balance along the apparent contact line can be described in a self-consistent manner and then leads to curvature-independent relationships between the apparent contact angles and the total membrane tensions. For each membrane segment $j\gamma$, we can define a regime of small bending energies and a regime of large spontaneous curvatures. Segment $j\gamma$ belongs to the *regime of small bending energy* if the bending energy of this segment is small compared to the interfacial free energy of the $\alpha\beta$ interface. The latter condition is fulfilled if the spontaneous curvature $m_{j\gamma}$ is comparable to or smaller than the mean curvature $M_{j\gamma}$ of the membrane segment and if the water–water interface is large compared to $18\pi\kappa_{j\gamma}/\Sigma_{\alpha\beta}$. On the other hand, segment $j\gamma$ belongs to the *regime of large spontaneous curvature* if the spontaneous curvature $m_{j\gamma}$ is large compared to the mean curvature $M_{j\gamma}$ of this segment. If each membrane segment belongs to the small bending or to the large spontaneous curvature regime, one obtains the force balance conditions [152]

$$\frac{\Sigma_{\alpha\beta}}{\sin\theta_\gamma} = \frac{\hat{\Sigma}_{\alpha\gamma}}{\sin\theta_\beta} = \frac{\hat{\Sigma}_{\beta\gamma}}{\sin\theta_\alpha} \tag{20}$$

along the apparent contact line which relate the total membrane tensions $\hat{\Sigma}_{\alpha\gamma}$ and $\hat{\Sigma}_{\beta\gamma}$ of the two membrane segments to the apparent contact angles and the interfacial tension $\Sigma_{\alpha\beta}$. The conditions in (20) are equivalent to the tension ratios

$$\frac{\hat{\Sigma}_{\alpha\gamma}}{\Sigma_{\alpha\beta}} = \frac{\sin\theta_\beta}{\sin\theta_\gamma} \quad \text{and} \quad \frac{\hat{\Sigma}_{\beta\gamma}}{\Sigma_{\alpha\beta}} = \frac{\sin\theta_\alpha}{\sin\theta_\gamma}\,. \tag{21}$$

as used in [48, 78]. These equations represent the law of sines for a triangle with the three sides $\Sigma_{\alpha\beta}$, $\hat{\Sigma}_{\alpha\gamma}$, and $\hat{\Sigma}_{\beta\gamma}$ as displayed in Fig. 10b, c. Therefore, in the parameter regimes of small bending energies and/or large spontaneous curvatures, the total membrane tensions can be deduced from the measured values of the apparent contact angles and of the interfacial tension $\Sigma_{\alpha\beta}$.

If one membrane segment, say the $\alpha\gamma$ segment, forms nanotubes, the mean curvature $M_{\alpha\gamma}$ of the $\alpha\gamma$-segment is much smaller than the mean curvature of the tubes which is of the order of the spontaneous curvature $m_{\alpha\gamma}$. In such a situation, the mechanical tension $\Sigma_{\alpha\gamma}$ turns out to be much smaller than the spontaneous tension $\sigma_{\alpha\gamma}$ [78] and the total membrane tension $\hat{\Sigma}_{\alpha\gamma} \approx \sigma_{\alpha\gamma} = 2\kappa_{\alpha\gamma}\, m_{\alpha\gamma}^2$. When we combine this asymptotic equality with the first relationship in (21), we obtain the spontaneous curvature

$$m_{\alpha\gamma} = -\left(\frac{\Sigma_{\alpha\beta}}{2\kappa_{\alpha\gamma}}\,\frac{\sin(\theta_\beta)}{\sin(\theta_\gamma)}\right)^{1/2} \tag{22}$$

where the minus sign reflects the experimental observation that the nanotubes protrude into the interior compartment of the vesicle as in Fig. 5. The $m_{\alpha\gamma}$-values obtained from (22) have been confirmed in [74] by two other, completely independent methods to deduce the spontaneous curvature.

9.3 Intrinsic Contact Angles

If the spherical cap geometry shown in Fig. 10a persisted to nanoscopic scales, the vesicle membrane would have a kink along the true contact line. Such a kink would lead to an infinite bending energy of the membrane. Therefore, along the true contact line, the membrane should be smoothly curved and the geometry is then characterized by intrinsic contact angles [149, 152]. As shown in Fig. 10d, the common tangent plane to the two membrane segments along the true contact line defines two intrinsic angles θ_α^* and θ_β^* which are related via $\theta_\alpha^* + \theta_\beta^* = \pi$.

The total (free) energy of the system consists of the bending energy of the membrane, the interfacial free energy of the water–water interface, and the line energy of the three-phase contact line. The latter contribution is proportional to the line tension $\lambda_{\rm co}$ of the contact line. Minimizing this free energy for axisymmetric morphologies, one obtains the balance condition [152]

$$\Sigma_{\beta\gamma} - \Sigma_{\alpha\gamma} = \Sigma_{\alpha\beta}\cos\theta_\alpha^* + \lambda_{\rm co}\,\frac{\cos\psi_{\rm co}}{R_{\rm co}} + \Delta_{\Sigma,{\rm co}} \tag{23}$$

between the mechanical segment tensions $\Sigma_{\beta\gamma}$ and $\Sigma_{\alpha\gamma}$, the interfacial tension $\Sigma_{\alpha\beta}$, and the line tension $\lambda_{\rm co}$. The parameter $R_{\rm co}$ is the radius of the true contact line, and $\psi_{\rm co}$ is the tilt angle between the symmetry axis and the common tangent plane of the two membrane segment at the true contact line. The additional term $\Delta_{\Sigma,{\rm co}}$ depends on the local curvatures of the two membrane segments along this contact line, compare Fig. 10d, and vanishes if the two membrane segments have the same curvature-elastic properties [152]. In the latter case, the balance condition (23) along

the true contact line simplifies and becomes

$$\Sigma_{\beta\gamma} - \Sigma_{\alpha\gamma} = \hat{\Sigma}_{\beta\gamma} - \hat{\Sigma}_{\alpha\gamma} = \Sigma_{\alpha\beta} \cos\theta_\alpha^* + \lambda_{\rm co} \frac{\cos\psi_{\rm co}}{R_{\rm co}} \,. \tag{24}$$

If both segments belong to the small bending energy regime or to the large spontaneous curvature regime, we can combine the balance condition (24) with the tension ratios in (21) which then describes the force balance along the apparent contact line. As a result, we obtain the simple relation

$$\cos\theta_\alpha^* = \frac{\sin\theta_\alpha - \sin\theta_\beta}{\sin\theta_\gamma} - \frac{\lambda_{\rm co}}{\Sigma_{\alpha\beta}} \frac{\cos\psi_{\rm co}}{R_{\rm co}} \tag{25}$$

between the intrinsic contact angle θ_α^* that is not accessible to conventional optical microscopy and the apparent contact angles that can be obtained from the microscopy images.

In [149], the relation (25) was originally derived for the special case of vanishing spontaneous curvatures for both membrane segments, i.e., $m_{\alpha\gamma} = m_{\beta\gamma} = 0$, and was then used to analyze the shapes of vesicles that enclosed one PEG-rich and one dextran-rich droplet. Even though the apparent contact angles of these vesicles were quite different, the relation (25) led to a fairly constant value for the intrinsic contact angle θ_α^*. Later experiments revealed, however, that the spontaneous curvatures $m_{\alpha\gamma}$ must be quite large because the $\alpha\gamma$ membrane segments in contact with the PEG-rich phase formed nanotubes with a suboptical width as in Fig. 5 [74, 100]. Furthermore, the experimental data as well as molecular dynamics simulations provided strong evidence that this large spontaneous curvature was generated by asymmetric adsorption of PEG molecules. Therefore, it is tempting to assume that the spontaneous curvature $m_{\beta\gamma}$ of the $\beta\gamma$ membrane segments in contact with the dextran-rich phase was comparatively small. A small value of $m_{\beta\gamma}$ and a large value of $m_{\alpha\gamma}$ would justify the use of (21) to describe the force balance along the apparent contact line but it would not justify the use of (24) to describe the force balance along the true contact line because (24) is based on the assumption that both membrane segments have essentially the same spontaneous curvature. On the other hand, if we assumed that the spontaneous curvature $m_{\beta\gamma}$ is large as well and comparable to $m_{\alpha\gamma}$, we could justify the use of both relations (21) and (24).

9.4 Nucleation and Growth of Nanodroplets at Membranes

For complete wetting of the vesicle membrane by the α phase, the intrinsic contact angle θ_α^* vanishes which implies that the phase separation starts via the formation of a thin α layer at the vesicle membrane (broken red line in Fig. 9). For partial wetting, on the other hand, the intrinsic contact angle $\theta_\alpha^* > 0$, and the phase separation starts with the nucleation of α droplets at the membrane surface as shown in Fig. 11a,

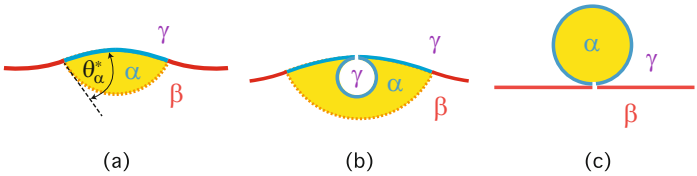

Fig. 11 Nucleation and growth of an α droplet (yellow) that is formed at a vesicle membrane (blue/red). As in Fig. 10, the two aqueous phases α and β are in contact with the inner membrane leaflet, and γ denotes the exterior aqueous phase: (**a**) The $\alpha\beta$ interface (broken orange) between the α droplet and the other interior phase β has the shape of a spherical cap and forms the intrinsic contact angle θ_α^* with the adjacent $\alpha\gamma$ segment (blue) of the membrane. Because the latter segment is now exposed to an asymmetric environment, it can acquire an appreciable spontaneous curvature $m_{\alpha\gamma}$. Of particular interest is the case for which the curvature $m_{\alpha\gamma}$ is large compared to the spontaneous curvature $m_{\beta\gamma}$ of the $\beta\gamma$ membrane segment (red); (**b**) for negative values of $m_{\alpha\gamma}$, the $\alpha\gamma$ membrane segment prefers to form a spherical in-bud that is filled with exterior γ phase; and (**c**) for positive values of $m_{\alpha\gamma}$, the $\alpha\gamma$ membrane segment prefers to engulf the α droplet provided that the volume of the droplet matches the preferred bud size. Complete engulfment leads to a closed membrane neck that replaces the $\alpha\beta$ interface, thereby eliminating the contribution of this interface to the system's free energy

corresponding to a critical nucleus with a radius of tens of nanometers. For such a small droplet, the intrinsic contact angle will be affected by the line tension λ_{co} of the contact line. The line tension can be positive or negative, in contrast to the line tension λ of domain boundaries which is always positive. In fact, recent molecular simulations indicate that the contact line tension λ_{co} is typically negative [153].

After an α droplet as in Fig. 11a has been formed, the $\alpha\gamma$ segment of the membrane, which is in contact with this droplet, is exposed to an asymmetric environment and can acquire an appreciable spontaneous curvature $m_{\alpha\gamma}$. In order to simplify the following discussion, let us assume that the curvature $m_{\alpha\gamma}$ is large compared to the spontaneous curvature $m_{\beta\gamma}$ of the $\beta\gamma$ segment and that the latter curvature is small and can be ignored.

If the spontaneous curvature $m_{\alpha\gamma}$ is *negative* as in the case of PEG-dextran solutions that undergo aqueous phase separation within the vesicles, the membrane prefers to curve towards the inner leaflet and to form a spherical in-bud of radius $R_\gamma \simeq 1/(2|m_{\alpha\gamma}|)$ that is filled with the exterior γ phase as in Fig. 11b. Such an in-bud represents a limit shape with a closed neck that can be characterized by the condition [78, 91] $M_a + M_b = 2m_{\alpha\gamma}$ where $M_a = -1/R_\gamma$ and M_b are the mean curvatures of the two membrane segments a and b adjacent to the neck. The in-bud displaces some volume of α phase and *increases* the area of the $\alpha\beta$ interface which implies that the α droplet has to reach a volume large compared to $4\pi R_\gamma^3/3$ before the in-bud becomes energetically favorable. After such an in-bud has formed, the bud radius increases until the spherical shape becomes unstable and transforms into a short necklace-like tube [74, 101].

On the other hand, if the droplet-induced curvature $m_{\alpha\gamma}$ is *positive*, the $\alpha\gamma$ membrane segment prefers to curve towards the outer leaflet of the vesicle membrane and to form a spherical out-bud of radius $R_\alpha \simeq 1/m_{\alpha\gamma}$ that is filled with α phase as in

Fig. 11c. Such an out-bud with a closed membrane neck reduces the free energy of the membrane-droplet system by (i) adapting the mean curvature of the $\alpha\gamma$ segment to its spontaneous curvature $m_{\alpha\gamma}$ and (ii) replacing the $\alpha\beta$ interface by a closed membrane neck which implies a strong reduction of the interfacial free energy. Spherical buds with closed necks are also formed during domain-induced budding in the absence of aqueous phase separation [3, 5]. Compared to domain-induced budding, the closed neck in Fig. 11c is further stabilized by the formation of an $\alpha\beta$ interface during neck opening. For an axisymmetric neck, the area of this interface depends quadratically on the neck radius $R_{\rm ne}$ which implies a free energy increase proportional to $\Sigma_{\alpha\beta} R_{\rm ne}^2$ and the same closed neck condition as for domain-induced buds [152]. However, recent simulations revealed that negative line tensions break the axisymmetry and lead to tight-lipped membrane necks [153].

Even in the absence of budding, the existence of a complete-to-partial wetting transition implies some interesting behavior of the aqueous droplets. Thus, consider again a droplet as in Fig. 11a and assume that we now change the conditions from partial to complete wetting. The localized droplet will then be transformed into a delocalized film that covers the whole membrane, and this morphological transformation can be used to redistribute molecules within the aqueous subcompartment.

10 Topological Transformations of Membranes

In the previous sections, I focused on processes that do not change the topology of the membranes. Now, let us briefly consider two important topology-transforming processes, membrane fusion and membrane fission (or scission). During membrane fusion, two separate membranes are combined into a single one; during fission, a single membrane is divided up into two separate ones. These processes are ubiquitous in eukaryotic cells: Both the outer cell membrane and the inner membranes of organelles act (i) as donor membranes that continuously produce vesicles via budding and fission and (ii) as acceptor membranes that integrate such vesicles via adhesion and fusion. One example for fission is provided by the closure of autophagosomes which are double-membrane organelles [154, 155].

10.1 Free Energy Landscapes of Fusion and Fission

It is instructive to consider the free energy landscapes for fusion and fission as schematically depicted in Fig. 12. Fusion is exergonic, if the free energy G_2 of the 2-vesicle state exceeds the free energy G_1 of the 1-vesicle state. In the opposite case with $G_1 > G_2$, fission is exergonic. Exergonic fusion or fission processes occur spontaneously but the kinetics of these processes is governed by the free energy barriers Δ between the 1-vesicle and the 2-vesicle state, see Fig. 12. Because these barriers are typically large compared to $k_{\rm B}T$, even exergonic fusion and fission

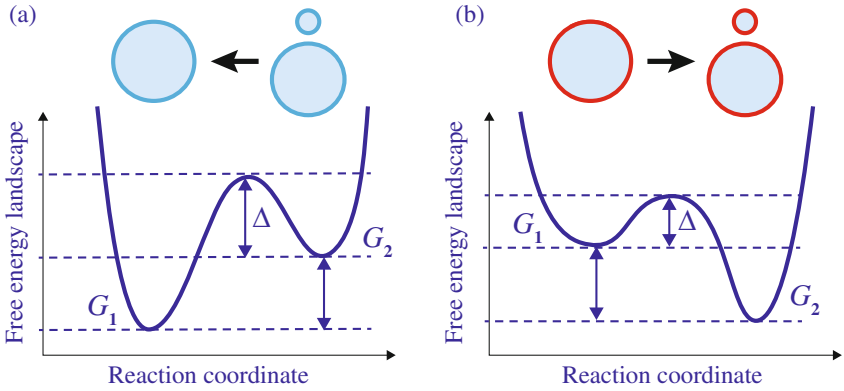

Fig. 12 Free energy landscapes for membrane fusion and fission (or scission): (**a**) schematic landscape for an exergonic fusion process. In this case, the free energy G_2 of the 2-vesicle state exceeds the free energy G_1 of the 1-vesicle state; and (**b**) schematic landscape for an exergonic fission process. In the latter case, the free energy G_1 of the 1-vesicle state is larger than the free energy G_2 of the 2-vesicle state. The cartoons (top row) show a 1-vesicle state on the left and a 2-vesicle state on the right; both states have the same membrane area. The small vesicle of the 2-vesicle state has the radius R_{ss} which is much smaller than the radius of the large vesicle. The dark blue membranes in (**a**) have a spontaneous curvature with magnitude $|m| \ll 1/R_{ss}$ whereas the red membranes in (**b**) have a large spontaneous curvature with $m \simeq 1/(2R_{ss})$. In both (**a**) and (**b**), the free energy difference $G_2 - G_1$ determines the direction in which the processes can proceed spontaneously (black arrows), while the kinetics of these processes is governed by the free energy barriers Δ

processes will be rather slow unless coupled to other molecular processes that act to reduce these barriers. Indeed, in the living cell, the fusion and fission of biomembranes is controlled by membrane-bound proteins such as SNAREs and dynamin as will be discussed in later chapters of this book. It should also be emphasized that the free energy landscape may involve several barriers as has been observed in molecular dynamics simulations of tension-induced fusion [67, 69].

The free energy difference $G_2 - G_1$ between the 2-vesicle and the 1-vesicle state can be estimated by the corresponding changes in curvature energy [156]. Because of the topological changes, we need to take the Gaussian curvature and the associated Gaussian curvature modulus κ_G into account [90]. Stability arguments indicate that $-2 < \kappa_G/\kappa < 0$ [157]. For the following considerations, it will be sufficient to use the rough estimate $\kappa_G \simeq -\kappa$ which is consistent with both experimental [158, 159] and simulation [62] studies. A small spherical vesicle that is cleaved off from a donor membrane then changes the total curvature energy by a certain amount that can be used to estimate the free energy difference $G_2 - G_1$. It is important to realize, however, that this change in curvature energy depends strongly on the magnitude of the spontaneous curvature as shown in the next subsections.

10.2 Exergonic Fusion for Small Spontaneous Curvatures

Let us consider a 1-vesicle state corresponding to a spherical GUV that acts as the donor membrane and a 2-vesicle state obtained from this GUV by cleaving off a much smaller spherical vesicle, see top row of Fig. 12. Both states have the same membrane area. The small vesicle of the 2-vesicle state has the radius R_{ss} which is taken to be much smaller than the radius of the GUV. We may then ignore any constraints on the vesicle volumes and assume that the large vesicle of the 2-vesicle state has a spherical shape as well. If the GUV membrane is uniform, and the magnitude $|m|$ of its spontaneous curvature is much smaller than the inverse size, $1/R_{ss}$, of the small vesicle, the free energy difference between the 2-vesicle and 1-vesicle state is *positive* and has the form

$$G_2 - G_1 = 8\pi\kappa + 4\pi\kappa_G \simeq +4\pi\kappa \quad \text{for } |m| \ll 1/R_{ss} \tag{26}$$

where the estimate $\kappa_G \simeq -\kappa$ has been used. In this case, the fission process is endergonic whereas the fusion process is exergonic, see the corresponding free energy landscape in Fig. 12a. For the typical rigidity value $\kappa \simeq 20\, k_B T$, the relation (26) leads to the large free energy difference $G_2 - G_1 \simeq +250\, k_B T$!

10.3 Exergonic Fission for Large Spontaneous Curvatures

On the other hand, if the magnitude $|m|$ of the spontaneous curvature is large, the GUV can form a small spherical bud with radius $R_{ss} \simeq 1/(2|m|)$ as in Fig. 12b as follows from the closed neck condition for the corresponding limit shape.[4] If this bud is cleaved off, the free energy difference between the resulting 2-vesicle state and the initial 1-vesicle state is now *negative* and given by

$$G_2 - G_1 = 8\pi\kappa(1 - 2R_{ss}|m|) + 4\pi\kappa_G \simeq 4\pi\kappa_G \simeq -4\pi\kappa \quad \text{for } R_{ss} \simeq 1/(2|m|). \tag{27}$$

In the latter case, the fission process is exergonic and the fusion process is endergonic, corresponding to a free energy landscape as in Fig. 12b. Now, the free energy difference $G_2 - G_1 \simeq -250\, k_B T$ for the typical value $\kappa \simeq 20\, k_B T$ of the bending rigidity.

[4] For $m > 0$ and $m < 0$, this limit shape involves a spherical out- and in-bud, respectively, corresponding to the shapes L^{pear} and L^{sto} in [91].

10.4 Free Energy Difference for Domain-Induced Fission

Biological membranes often form intramembrane domains with an appreciable spontaneous curvature $m_{\rm do}$. One example for this latter case is provided by clathrin-dependent endocytosis which leads to membrane domains with a spontaneous curvature $m_{\rm do} \simeq -1/(40\,{\rm nm})$ [34]. Now, consider a GUV with a small membrane domain with an appreciable spontaneous curvature $m_{\rm do}$ whereas the spontaneous curvature of the remaining GUV membrane is again negligible. The membrane domain can then form a small spherical bud of size $R_{\rm ss} = 1/|m_{\rm do}|$ as follows from the closed neck condition for domain-induced budding [5]. If the latter bud is cleaved off, the free energy difference between the resulting 2-vesicle state and the initial 1-vesicle state is again negative and now has the form

$$G_2 - G_1 = 8\pi\kappa(1-2R_{\rm ss}|m_{\rm do}|) + 4\pi\kappa_G - 4\pi\frac{\lambda}{|m_{\rm do}|} \simeq -12\pi\kappa - 4\pi\frac{\lambda}{|m_{\rm do}|} \qquad (28)$$

where λ denotes the line tension of the domain boundary. Because this line tension has to be positive, the fission of a domain-induced bud is an exergonic process that leads to an even larger free energy gain $|G_2 - G_1| > 12\pi\kappa \gtrsim 750\,k_{\rm B}T$ for bending rigidity $\kappa \simeq 20\,k_{\rm B}T$.

11 Summary and Outlook

During the last 20 years, we have seen a fair number of rather interesting developments related to the biophysics of membranes and vesicles. One important development was the identification of several lipid mixtures that can separate into two fluid phases. This development was triggered by the proposal that cellular membranes contain lipid rafts enriched in sphingomyelin and cholesterol [8]. So far, we do not have any images of such phase domains in vivo. On the other hand, cell membranes are expected to be partitioned into many distinct membrane segments that are exposed to different molecular environments. Long-lived components of these heterogeneous environments arise from the cytoskeletal cortex as revealed by single particle tracking of membrane-bound nanoparticles [42]. If lipid phase domains form in such a cell membrane, the domain formation is necessarily restricted to one of the membrane segments and, thus, hard to detect [48]. In the limiting case in which the environmental heterogeneities of the cell membrane act as long-lived random fields, membrane phase separation would be completely destroyed.

Another development that had a large impact on the field was the identification of proteins that generate local membrane curvature. These proteins can be viewed as Janus particles with strongly nonspherical shapes (Fig. 4). It should be rather interesting to synthesize such Janus particles and to study their interactions with

lipid membranes. In the last couple of years, reliable methods have been developed to determine the spontaneous curvature of membranes from their spontaneous [74, 100] or force-induced [117] tubulation. Using the relation (1), we can then deduce the locally generated curvature of single membrane-bound "particles" from the coverages on the two leaflets of the membranes [85, 86]. Furthermore, because the nanotubes provide a reservoir for membrane area, the mother vesicles of tubulated vesicles exhibit an increased robustness against mechanical perturbations as recently demonstrated by micropipette aspiration [101].

Membrane nanotubes are also formed within eukaryotic cells and provide ubiquitous structural elements of many membrane-bound organelles such as the endoplasmic reticulum, the Golgi, the endosomal network, and mitochondria [160–162]. These intracellular nanotubes are used for molecular sorting, signalling, and transport. Intercellular (or "tunneling") nanotubes formed by the plasma membranes of two or more cells provide long-distance connections for cell–cell communication, intercellular transport, and virus infections [163–165]. It seems rather plausible to assume that these tubes are also generated by spontaneous curvature and/or locally applied forces but the relative importance of these two tubulation mechanisms remains to be elucidated for cellular membranes.

As far as the engulfment of nanoparticles by membranes is concerned, we now have a rather detailed theory which leads to the stability conditions (13)–(16) and predicts several critical particle sizes for the engulfment process [34], complex engulfment patterns on GUVs [132], and curvature-induced forces leading to biased diffusion of partially engulfed particles [134]. The theory has been extended to the engulfment by membrane domains [34] and can then explain the nonmonotonic size dependence of clathrin-dependent endocytosis as observed for the uptake of gold particles by HeLa cells [35, 36]. In addition, the stability conditions for closed membrane necks have been generalized to include constriction forces, see the closed neck condition (17), and applied to a variety of membrane systems such as giant plasma membrane vesicles formed by eukaryotic cells and outer membrane vesicles secreted by bacteria [133]. I am rather curious to see experimental studies that scrutinize these predictions.

Another fairly interesting topic that has been hardly explored at all is the wetting behavior of membranes and vesicles in contact with several aqueous phases. So far, this behavior has only been studied for three lipid compositions exposed to aqueous solutions of PEG and dextran [74, 100, 148] as well as to aqueous droplets or membraneless organelles enriched in the intrinsically disordered FUS protein [151] but, quite unexpectedly, all of these systems were found to exhibit wetting transitions (Fig. 9). Another aspect of wetting that remains to be elucidated in a systematic manner, both theoretically and experimentally, is the nucleation and growth of nanodroplets at membranes (Fig. 11).

In the context of synthetic biology, GUVs have long been discussed as possible micro-compartments for the bottom-up assembly of artificial protocells. One practical problem that has impeded research in this direction is the limited robustness of GUVs against mechanical perturbations. Very recently, this limitation has been overcome by two different strategies. One strategy is based on the formation of

GUVs within microfluidic emulsion droplets that support and stabilize the GUVs [166]. The other strategy uses the special properties of tubulated GUVs which can respond to external perturbations by exchanging membrane area between the nanotubes and the mother vesicles [101]. Compared to conventional GUVs, both droplet-stabilized and tubulated GUVs are much more robust against mechanical forces and thus provide new modules for the bottom-up assembly of artificial cells.

Acknowledgements I thank all my coworkers for enjoyable collaborations and Jaime Agudo-Canalejo for a critical reading of the manuscript.

References

1. Lipowsky R, Sackmann E (eds) (1995) Handbook of biological physics, vol 1. Elsevier, Amsterdam
2. Lipowsky R (2019) In: Dimova R, Marques C (eds) The giant vesicle book. Taylor & Francis
3. Lipowsky R (1992) J Phys II France 2:1825
4. Lipowsky R (1993) Biophys J 64:1133
5. Jülicher F, Lipowsky R (1993) Phys Rev Lett 70:2964
6. Baumgart T, Hess S, Webb W (2003) Nature 425:821
7. Riske KA, Bezlyepkina N, Lipowsky R, Dimova R (2006) Biophys Rev Lett 1:387
8. Simons K, Ikonen E (1997) Nature 387:569
9. Korlach J, Schwille P, Webb W, Feigenson G (1999) Proc Natl Acad Sci USA 96:8461
10. Dietrich C, Bagatolli L, Volovyk Z, Thompson N, Levi M, Jacobson K, Gratton E (2001) Biophys J 80:1417
11. Veatch S, Keller S (2003) Biophys J 85:3074
12. Jülicher F, Lipowsky R (1996) Phys Rev E 53:2670
13. Kumar S, Gompper G, Lipowsky R (2001) Phys Rev Lett 86:3911
14. Baumgart T, Das S, Webb WW, Jenkins JT (2005) Biophys J 89:1067
15. Semrau S, Idema T, Holtzer L, Schmidt T, Storm C (2008) Phys Rev Lett 100:088101
16. Bacia K, Schwille P, Kurzchalia T (2005) Proc Natl Acad Sci USA 102:3272
17. Dimova R, Riske KA, Aranda S, Bezlyepkina N, Knorr RL, Lipowsky R (2007) Soft Matter 3:817
18. Jensen MH, Morris EJ, Simonsen AC (2007) Langmuir 23:8135
19. Garg S, Rühe J, Lüdtke K, Jordan R, Naumann CA (2007) Biophys J 92:1263
20. Kiessling V, Wan C, Tamm LK (2009) Biochim Biophys Acta 1788:64
21. Collins MD, Keller SL (2008) Proc Natl Acad Sci USA 105(1):124
22. Orth A, Johannes L, Römer W, Steinem C (2012) Chem Phys Chem 13:108
23. David JH, Clair JJ, Juhasz J (2009) Biophys J 96:521
24. Veatch SL, Gawrisch K, Keller SL (2006) Biophys J 90:4428
25. Vequi-Suplicy C, Riske K, Knorr R, Dimova R (2010) Biochim Biophys Acta 1798:1338
26. Uppamoochikkal P, Tristram-Nagle S, Nagle JF (2010) Langmuir 26(22):17363
27. Pataraia S, Liu Y, Lipowsky R, Dimova R (2014) Biochim Biophys Acta 1838:2036
28. Baumgart T, Hammond AT, Sengupta P, Hess ST, Holowka DA, Baird BA, Webb WW (2007) Proc Natl Acad Sci USA 104:3165
29. Veatch SL, Cicuta P, Sengupta P, Honerkamp-Smith A, Holowka D, Baird B (2008) ACS Chem Biol 3:287
30. Owen DM, Williamson DJ, Magenau A, Gaus K (2012) Nat Commun 3:1256
31. Eggeling C, Ringemann C, Medda R, Schwarzmann G, Sandhoff K, Polyakova S, Belov VN, Hein B, von Middendorff C, Schönle A, Hell SW (2009) Nature 457:1159

32. Mueller V, Ringemann, C, Honigmann A, Schwarzmann G, Medda R, Leutenegger M, Polyakova S, Belov VN, Hell SW, Eggeling C (2011) Biophys J 101:1651
33. Klotzsch E, Schütz GJ (2013) Philos Trans R Soc B 368:20120033
34. Agudo-Canalejo J, Lipowsky R (2015) ACS Nano 9:3704
35. Chithrani BD, Ghazani AA, Chan WCW (2006) Nano Lett 6(4):662
36. Chithrani BD, Chan WCW (2007) Nano Lett 7(6):1542
37. Pezeshkian W, Gao H, Arumugam S, Becken U, Bassereau P, Florent JC, Ipsen JH, Johannes L, Shillcock JC (2016) ACS Nano 11:314
38. Avalos-Padilla Y, Knorr RL, Lipowsky R, Dimova R (2018) Front Cell Infect Microbiol 8:53. https://doi.org/10.3389/fcimb.2018.00053
39. Sako Y, Kusumi A (1994) J Cell Biol 125(6):1251
40. Saxton MJ, Jacobson K (1997) Annu Rev Biophys Biomol Struct 26:373–399
41. Fujiwara T, Ritchie K, Murakoshi H, Jacobson K, Kusumi A (2002) J Cell Biol 157(6):1071
42. Kusumi A, Nakada C, Ritchie K, Murase K, Suzuki K, Murakoshi H, Kasai RS, Kondo J, Fujiwara T (2005) Annu Rev Biophys Biomol Struct 34:351
43. Andrews NL, Lidke KA, Pfeiffer JR, Burns AR, Wilson BS, Oliver JM, Lidke DS (2008) Natl Cell Biol 10(8):955
44. Treanor B, Depoil D, Gonzalez-Granja A, Barral P, Weber M, Dushek O, Bruckbauer A, Batista FD (2010) Immunity 32:187
45. Jaqaman K, Kuwata H, Touret N, Collins R, Trimble WS, Danuser G, Grinstein S (2011) Cell 146:593
46. Rouhiparkouhi T, Weikl TR, Discher DE, Lipowsky R (2013) Int J Mol Sci 14:2203
47. Lipowsky R, Rouhiparkouhi T, Discher DE, Weikl TR (2013) Soft Matter 9:8438
48. Lipowsky R (2014) Biol Chem 395:253
49. Skau CT, Kovar DR (2010) Curr Biol 20:1415
50. Michelot A, Drubin DG (2011) Curr Biol 21:R560
51. Loerke D, Mettlen M, Yarar D, Jaqaman K, Jaqaman H, Danuser G, Schmid SL (2009) PLOS Biol 7(3):e1000057
52. Cureton DK, Harbison CE, Parrish CR, Kirchhausen T (2012) J Virol 86(9):5330
53. Binder K (1983) Z Phys B 50:343
54. Aizenman M, Wehr J (1989) Phys Rev Lett 62:2503
55. Fischer T, Vink RLC (2011) J Chem Phys 134:055106
56. Goetz R, Gompper G, Lipowsky R (1999) Phys Rev Lett 82:221
57. Goetz R, Lipowsky R (1998) J Chem Phys 108:7397
58. Brandt EG, Braun AR, Sachs JN, Nagle JF, Edholm O (2011) Biophys J 100:2104
59. Watson MC, Penev ES, Welch PM, Brown FLH (2011) J Chem Phys 135:244701
60. Tarazona P, Chacon E, Bresme F (2013) J Chem Phys 139:094902
61. Orsi M, Haubertin DY, Sanderson WE, Essex JW (2008) J Phys Chem B 112:802
62. Hu M, Briguglio JJ, Deserno M (2012) Biophys J 102(6):1403
63. Rózycki B, Lipowsky R (2015) J Chem Phys 142:054101
64. Rózycki B, Lipowsky R (2016) J Chem Phys 145:074117
65. Lipowsky R, Döbereiner HG (1998) Europhys Lett 43:219
66. Shillcock J, Lipowsky R (2005) Nat Mater 4:225
67. Grafmüller A, Shillcock J, Lipowsky R (2007) Phys Rev Lett 98:218101
68. Gao L, Lipowsky R, Shillcock JC (2008) Soft Matter 4:1208
69. Grafmüller A, Shillcock JC, Lipowsky R (2009) Biophys J 96:2658
70. Smirnova Y, Marrink S, Lipowsky R, Knecht V (2010) J Am Chem Soc 132:6710
71. Hu J, Lipowsky R, Weikl TR (2013) Proc Natl Acad Sci USA 110:15283
72. Xu GK, Hu J Lipowsky R, Weikl TR (2015) J Chem Phys 143:243136
73. Hu J, Xu GK, Lipowsky R, Weikl TR (2015) J Chem Phys 143:243137
74. Liu Y, Agudo-Canalejo J, Grafmüller A, Dimova R, Lipowsky R (2016) ACS Nano 10:463
75. Lipowsky R (1995) Europhys Lett 30:197
76. Nikolov V, Lipowsky R, Dimova R (2007) Biophys J 92:4356
77. Deserno M (2004) Phys Rev E 69:031903

78. Lipowsky R (2013) Faraday Discuss 161:305
79. Peter BJ, Kent HM, Mills IG, Vallis Y, Butler PJG, Evans PR, McMahon HT (2004) Science 303:495
80. Simunovic M, Yee C. K, Lee, Bassereau P (2015) Soft Matter 11:5030
81. Graber ZT, Shi Z, Baumgart T (2017) Phys Chem Chem Phys 19:15285
82. Farsad K, Ringstad N, Takei K, Floyd SR, Rose K, Camilli PD (2001) J Cell Biol 155(2):193
83. Wang Q, Navarro VAS, Peng G, Molinelli E, Goh SL, Judson BL, Rajashankar KR, Sondermann H (2009) Proc Natl Acad Sci USA 106(31):12700
84. Ford MG, Mills IG, Peter BJ, Vallis Y, Praefcke GJ, Evans PR, McMahon HT (2002) Nature 419:361
85. Breidenich M, Netz R, Lipowsky R Europhys Lett (2000) 49:431
86. Lipowsky R (2002) J Biol Phys 28:195
87. Bancroft WD (1913) J Phys Chem 17:501
88. Bancroft W, Tucker C (1927) J Phys Chem 31:1681
89. Frank FC (1958) Discuss Faraday Soc 25:19
90. Helfrich W (1973) Z Naturforsch 28C:693
91. Seifert U, Berndl K, Lipowsky R (1991) Phys Rev A 44:1182
92. Evans E (1974) Biophys J 14:923
93. Svetina S, Zeks B (1989) Eur Biophys J 17:101
94. Miao L, Seifert U, Wortis M, Döbereiner HG (1994) Phys Rev E 49:5389
95. Döbereiner HG, Evans E, Kraus M, Seifert U, Wortis M (1997) Phys Rev E 55(4):4458
96. Lipowsky R (1999) In: Reguera D, Rubi JM, Vilar JMB (eds) Statistical mechanics of biocomplexity. Lecture notes in physics. Springer, Berlin, pp 1–23
97. Bruckner RJ, Mansy SS, Ricardo A, Mahadevan L, Szostak JW (2009) Biophys J 97:3113
98. Domanov YA, Kinnunen PKJ (2006) Biophys J 91:4427
99. Arouni A, Kiessling V, Tamm L, Dathe M, Blume A (2011) J Phys Chem 115:158
100. Li Y, Lipowsky R, Dimova R (2011) Proc Natl Acad Sci USA 108:4731
101. Bhatia T, Agudo-Canalejo J, Dimova R, Lipowsky R (2018) ACS Nano 12:4478
102. Hochmuth R, Mohandas N, Blackshear PL Jr (1973) Biophys J 13:747
103. Schmidtke DW, Diamond SL (2000) J Cell Biol 149:719
104. Dopheide SM, Maxwell JJ, Jackson SP (2002) Blood 99:159
105. Hochmuth RM, Wiles HC, Evans EA, McCown JT (1982) Biophys J 39:83
106. Brochard-Wyart F, Borghi N, Cuvelier D, Nassoy P (2006) Proc Natl Acad Sci USA 103:7660
107. Waugh RE Biophys J 38:29 (1982)
108. Dasgupta R, Dimova R (2014) J Phys D Appl Phys 47:282001
109. Borghi N, Rossier O, Brochard-Wyart F (2003) Europhys Lett 64:837
110. Tian A, Capraro BR, Esposito C, Baumgart T (2009) Biophys J 97:1636
111. Zhu C, Das SL, Baumgart T (2012) Biophys J 102:1837
112. Bo L, Waugh RE (1989) Biophys J 55:509
113. Ashkin A, Dziedzic JM (1989) Proc Natl Acad Sci USA 86:7914
114. Dai J, Sheetz MP (1995) Biophys J 68:988
115. Hochmuth RM, Shao JY, Dai J, Sheetz MP (1996) Biophys J 70:358
116. Cuvelier D, Derenyi I, Bassereau P, Nassoy P (2005) Biophys J 88:2714
117. Sorre B, Callan-Jones A, Manzi J, Goud B, Prost J, Bassereau P, Roux A (2012) Proc Natl Acad Sci USA 109(1):173
118. Dimova R, Seifert U, Pouligny B, Förster S, Döbereiner HG (2002) Eur Phys J B 7:241
119. Heinrich V, Waugh RE (2006) Ann Biomed Eng 24:595
120. Hosu BG, Sun M, Marga F, Grandbois M, Forgacs G (2007) Phys Biol 4:67
121. Terasaki M, Chen LB, Fujiwara K (1986) J Cell Biol 103:1557
122. Vale RD, Hotani H (1988) J Cell Biol 107:2233
123. Roux A, Cappello G, Cartaud J, Prost J, Goud B, Bassereau P (2002) Proc Natl Acad Sci USA 100:15583
124. Koster G, Duijn MV, Hofs B, Dogterom M (2003) Proc Natl Acad Sci USA 100:15583

125. Karlsson A, Karlsson R, Karlsson M, Cans AS, Strömberg A, Ryttsén F, Orwar O (2001) Nature 409:150
126. Karlsson M, Sott K, Cans AS, Karlsson A, Karlsson R, Orwar O (2001) Langmuir 17:6754
127. Dasgupta R, Miettinen M, Lipowsky R, Dimova R (2018) Proc Nat Acad Sci USA 115:5756
128. Evans E, Needham D (1987) J Phys Chem 91:4219
129. Petros RA, DeSimone JM (2010) Nat Rev Drug Discov 9:615
130. Rodriguez PL, Harada T, Christian DA, Pantano DA, Tsai RK, Discher DE (2013) Science 339:971
131. Mahmoudi M, Meng J, Xue X, Liang XJ, Rahmand M, Pfeiffer C, Hartmann R, Gil PR, Pelaz B, Parak WJ, del Pino P, Carregal-Romero S, Kanaras AG, Selvan ST (2014) Biotechnol Adv 32:679
132. Agudo-Canalejo J, Lipowsky R (2015) Nano Lett 15:7168
133. Agudo-Canalejo J, Lipowsky R (2016) Soft Matter 12:8155
134. Agudo-Canalejo J, Lipowsky R (2017) Soft Matter 13:2155
135. Seifert U, Lipowsky R (1990) Phys Rev A 42:4768
136. Antonny B, Burd C, De Camilli P, Chen E, Daumke O, Faelber K, Ford M, Frolov VA, Frost A, Hinshaw JE, Kirchhausen T, Kozlov MM, Lenz M, Low HH, McMahon H, Merrifield C, Pollard TD, Robinson PJ, Roux A, Schmid S (2016) EMBO J 35:2270
137. Schöneberg J, Lee IH, Iwasa JH, Hurley JH (2017) Nat Rev Mol Cell Biol 18:5
138. Agudo-Canalejo J, Lipowsky R (2018) PLoS Comput Biol 14:e1006422
139. Sosale N, Rouhiparkouhi T, Bradshaw AM, Dimova R, Lipowsky R, Discher DE (2015) Blood 125:542
140. Bahrami AH, Lipowsky R, Weikl TR (2016) Soft Matter 12:581
141. Dasgupta S, Auth T, Gompper G (2014) Nano Lett 14:687
142. Bahrami AH, Lipowsky R, Weikl TR (2012) Phys Rev Lett 109:188102
143. Šarić A, Cacciuto A (2012) Phys Rev Lett 109:188101
144. Bahrami AH, Raatz M, Agudo-Canalejo J, Michel R, Curtis EM, Hall CK, Gradzielski M, Lipowsky R, Weikl TR (2014) Adv Colloid Interface Sci 208:214
145. Helfrich M, Mangeney-Slavin L, Long M, Djoko K, Keating C J Am Chem Soc 124:13374 (2002)
146. Albertsson PA (1986) Partition of cell particles and macromolecules: separation and purification of biomolecules, cell organelles membranes, and cells in aqueous polymer two-phase systems and their use in biochemical analysis and biotechnology, 3rd edn. Wiley, New York
147. Long MS, Cans AS, Keating CD (2008) J Am Chem Soc 130:756
148. Li Y, Lipowsky R Dimova R (2008) J Am Chem Soc 130:12252
149. Kusumaatmaja H, Li Y, Dimova R, Lipowsky R (2009) Phys Rev Lett 103:238103
150. Brangwynne CP, Eckmann CR, Courson DS, Rybarska A, Hoege C, Gharakhani J, Jülicher F, Hyman AA (2009) Science 324:1729
151. Knorr RL, Franzmann T, Feeney M, Frigerio L, Hyman A, Dimova R, Lipowsky R (manuscript in preparation)
152. Lipowsky R (2018) J Phys Chem B. 122:3572
153. Satarifard V, Grafmüller A, Lipowsky R ACS Nano (in press)
154. Knorr RL, Dimova R, Lipowsky R (2012) PLoS One 7:e32753
155. Knorr RL, Lipowsky R, Dimova R (2015) Autophagy 11:2134
156. Lipowsky R (2013) Faraday Discuss 161:571
157. Helfrich W, Harbich W (1987) Physics of amphiphilic layers. In: Meunier J, Langevin D, Boccara N (eds) Springer proceedings in physics, vol 21. Springer, Berlin, pp 58–63
158. Derzhanski A, Petrov AG, Mitov MD (1978) Ann Phys 3:297
159. Lorenzen S, Servuss RM, Helfrich W (1986) Biophys J 50:565
160. Marchi S, Patergnani S, Pinton P (2014) Biochim Biophys Acta 1837:461–469
161. van Weering JRT, Cullen PJ (2014) Semin Cell Dev Biol 31:40
162. Westrate LM, Lee JE, Prinz WA, Voeltz GK (2015) Annu Rev Biochem 84:791
163. Wang X, Gerdes HH (2015) Cell Death Differ 22:1181

164. He K, Luo W, Zhang Y, Liu F, Liu D, Xu L, Qin L, Xiong C, Lu Z Fang X, Zhang Y (2010) ACS Nano 6:3015
165. Sowinski S, Jolly C, Berninghausen O, Purbhoo MA, Chauveau A, Köhler K, Oddos S, Eissmann P, Brodsky FM, Hopkins C, Önfelt B, Sattenta Q, Davis DM (2008) Natl Cell Biol 10(2):211
166. Weiss M, Benk LT, Frohnmayer JP, Haller B, Janiesch JW, Heitkamp T, Börsch M, de Lira R, Dimova R, Lipowsky R, Bodenschatz E, Baret JC, Vidakovic-Koch T, Sundmacher K, Platzman I, Spatz JP (2018) Nat Mater 17:89

Advanced Concepts and Perspectives of Membrane Physics

Erich Sackmann

Abstract Highly effective pathways of transmembrane signal transmission are realized by functional membrane domain formation through logistically controlled recruitment of functional proteins to specific sites on cytoplasmic membrane leaflets. Sites of assembly are selected by priming membranes through master switches generating local swarms of super affinity lipid anchors, such as PI(3,4,5)P3 and diacylglycerol (DAG).

Formation and activation of functional domains are regulated by agonistically or antagonistically cooperating molecular switches. We consider here the agonistic Rab4/Rab 5 tandem, serving the rapid receptor recycling, and the antagonistic pair of GTPases Rac-1 and Rho A, controlling the state of the actin cortex. To avoid over-excitations of cells (implying the danger of tumorigenesis), the omnipresent phosphoinositide anchors are protected by layers of the polybasic protein MACKS recruited by electrostatic-hydrophobic forces.

The universality of cell control systems is exemplified by the observation that extrinsic forces and hormones can trigger the generation of very similar types of transmembrane signal transmission centers assembled around receptor tyrosine kinases (RTK). These signal amplifying domains can regulate cellular membrane processes simultaneously through fast biochemical signals, eliciting the rapid structural change of the composite cell envelope, and slow, genetically controlled processes for adapting the mechanical impedances of cells and tissues.

Membrane-based reactions can be controlled via the access of reaction spaces by constituents or enzymes. They can be regulated over large distances by contacting distant membranes through synaptic contacts (such as endoplasmic and of immunological synapses).

Hopefully, insights in the analogy of technical and biological control mechanism may teach us how to generate new self-healing composite materials in logistic ways.

E. Sackmann (✉)
Technical University Munich, Munich, Germany

Physics Department E22/E27, Garching, Germany
e-mail: sackmann@ph.tum.de

P. Bassereau, P. Sens (eds.), *Physics of Biological Membranes*,
https://doi.org/10.1007/978-3-030-00630-3_2

Keywords Functional membrane domain formation · Membrane-associated protein recruitment by electrostatic hydrophobic forces · Transmembrane signal amplifying domains · MARCKS protein-controlled membrane processes · Reticulons controlled tubular membrane networks · Immunological and endoplasmic synapses

Abbreviations

DAG	Diacylglycerol
GAP	Guanine hydrolyzing protein accelerating the deactivation of GTPase
GEF	Guanine exchange factor accelerating the activation of GTPases by replacement of GDP by GTP
GIP	Guanine exchange inhibitor that maintains GTPases in the resting state
P(4,5)P2, P(3,4,5)P3	Phosphoinositol (4,5)-diphosphate, Phosphatidylinositol (3,4,5)-trisphosphate
PCK	Protein kinase C, a regulator of filopoida formation
PI-3K	Protein kinase 3 that catalyzes the phosphorylation of the $3'$-OH position on the inositol ring
PSL-γ	Phospholipase gamma, the generator of DAG lipids

1 Introduction

The first 30 years of membrane physics were dominated by two major questions. The first was whether the structure and physiological functions of multicomponent cell membranes can be explained in terms of the classical thermodynamics of mixtures. The second, closely related question, was whether phase separation modulated by specific lipid protein interaction mechanisms plays a role for the self-organization of functional domains (reviewed in [1, 2]). The interest of physicists in membrane research was greatly stimulated by the bending elasticity theories of soft shells developed in the early 1970s by Wolfgang Helfrich (see [3, 4] and Evan Evans [5]). Here it became apparent that many vital cell functions are controlled by the membrane bending elasticity, such as cell adhesion [6, 7], pearling instabilities [8], and the control of intracellular trafficking by budding-fission-fusion sequences [9]. Rigorous theories of bending fluctuations of closed shells by the groups of F. Brochard and S. Safran paved the way for high precision measurements of membrane bending moduli of vesicles and erythrocytes [10–12]. These questions stimulated the development of sophisticated new experimental techniques for high precision measurements of elastic moduli of giant vesicles and composite cell envelopes [13, 14].

The heterogeneous shell model proposed by physicists already in 1972 [1] was recognized by biologists in the mid-1990s after the discovery of Triton-insoluble membrane fragments (called lipid rafts). The mosaic model of membranes has now gained further impetus by the discovery that the micro-organization and

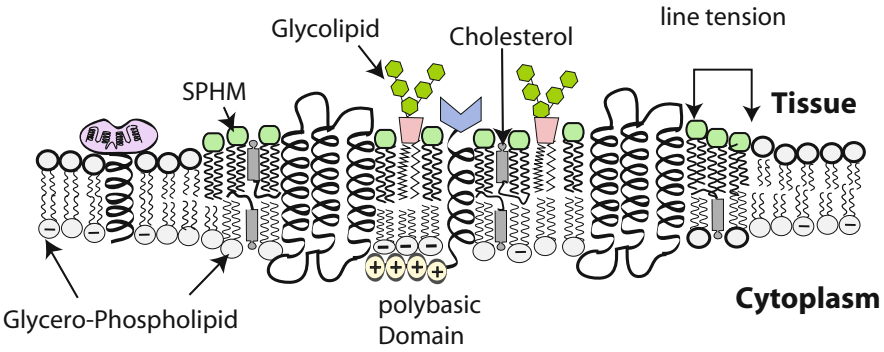

Fig. 1 Hypothetic structure of lipid–protein bilayer of the plasma membrane undergoing segregation into a condensed domain enriched in a SPHM/cholesterol-rich phase and a more loosely packed fluid phase composed of zwitterionic and acidic glycerol lipids. Some intracellular segments of integral proteins can expose polybasic domains and couple to the cytoplasmic leaflets of cell organelles via electrostatic forces. Typical PM-located proteins are glycophorin with 24 hydrophobic domains ($h_P \approx 3.6$ nm) and transferrin receptors ($h_P \approx 4$ nm). Neutron scattering experiments suggest that cholesterol can modulate the bilayer thickness to accommodate proteins with different hydrophobic lengths (see [2])

function of biomembranes is determined by the recruitment of extrinsic proteins through electrostatic and hydrophobic forces as extensively discussed in the chapter "Membranes by the numbers."

It is still a great challenge to understand the structural organization and functions of cell membranes in terms of the thermodynamics of mixtures. At present, the result of countless systematic studies of lipid–lipid and lipid–protein–phase diagrams can be summarized as follows (see Fig. 1 and [2]).

- The phospholipid moiety of mammalian cells can be considered as quasi-binary mixture of two classes of constituents, namely, glycerol lipids and sphingomyelins (SPHM), including gangliosides. The SPHM fraction exposes mainly long hydrophobic chains exhibiting only one or two non-saturated bonds (such as C18:0, C18:1, and C22:0) and undergoes a gel-to-fluid transition close to the physiological temperature [15]. In contrast, the glycerol lipids exhibit shorter chains with one to three double bonds (C16:1, C18:2) exhibiting chain melting phase transitions around 0 °C. This low melting phospholipid fraction can be considered as a single component forming a fluid phase, L_α, and exhibiting a very broad chain melting transition at $T_m < 10$ °C.
- Cholesterol associates preferentially with saturated lipids and acts as fluidizer of solid membranes. It thus forms a strongly condensed saturated solution with the SPHM fraction. (This densely packed phase is called liquid condensed phase $L_{\alpha c}$.)

The physiological role of the quasi-binary lipid mixture (of the L_α and $L_{\alpha c}$ phases) became evident by a survey of the lengths (h_P) of the hydrophobic domains of integral proteins in the plasma and the *trans*-Golgi membrane, respectively. It showed that the membrane spanning hydrophobic domains of proteins residing in the PM are by about 0.5 nm longer than those in the Golgi (see [2, 16]). As suggested by MC calculations, the energy costs for the insertion of a protein in a bilayer exhibiting a hydrophobic mismatch of $\Delta h \approx \pm$ 0.5 nm are $\Delta g \approx 2\ k_BT$ per lipid [17]. For the case of the anion exchange protein Band III of erythrocytes, this corresponds to an energy cost of 20 k_BT. The MC calculations showed further that, at thermal equilibrium, the protein is surrounded by a shell of about 30 length-adapted lipids. Taken together, these observations strongly suggest that the lipid and protein distribution between cellular organelles is partially regulated by the concept of hydrophobic matching.

A possible example of lipid–protein sorting by the hydrophobic mismatch is the transfer of Fe^{3+} ions into the cell. Fe^{3+} bound to transferrin is recognized by transferrin receptor (TFR) and internalized by coated pit endocytosis (summarized in [2]). After fusion of the vesicles with early endosomes Fe^{3+} dissociates from transferrin under the acidic conditions and the endosomal membrane decays into a SPHM/cholesterol-rich phase containing the TFRs and a domain composed of glycerol lipid. The membrane loaded with the receptor is captured by the Rab 4 GTPase and directly transferred back to the plasma membrane. Thereby the detour of the lipid protein sorting over the multi-lamellar lipid bodies is circumvented (see Fig. 2).

2 The Composite Cell Membrane a Multipurpose Machine

During the last 20 years, it has become evident that an astonishing large number of basic cellular processes, such as cell adhesion and locomotion, are membrane-based processes which are controlled by the interactive cross talk between the lipid/protein bilayer and the associated actin cortex. The communication with other cells and with tissues is controlled by a few classes of cell surface proteins called *c*ell *a*dhesion *m*olecules (CAM), two of which are shown in Fig. 3. They include integrins, selectins, cadherins, and various intracellular adhesion molecules such as the superfamilies of immunoglobulins (including ICAM and VCAM) and several families of glycoproteins (Fig. 3a). The latter class of proteins behaves like Janus Heads by acting both as buffers that prevent sticking of cells to surfaces and as CAMs mediating the coupling of cells to the tissue or to other cells. Important examples are CD43 (which can recognize ICAMs), syndecans (which bind collagen), and CD44. CD44 is also a receptor for the giant acidic polyelectrolyte hyaluronic acid (HA) which can separate cells over distances of some 100 nm. The intermembrane

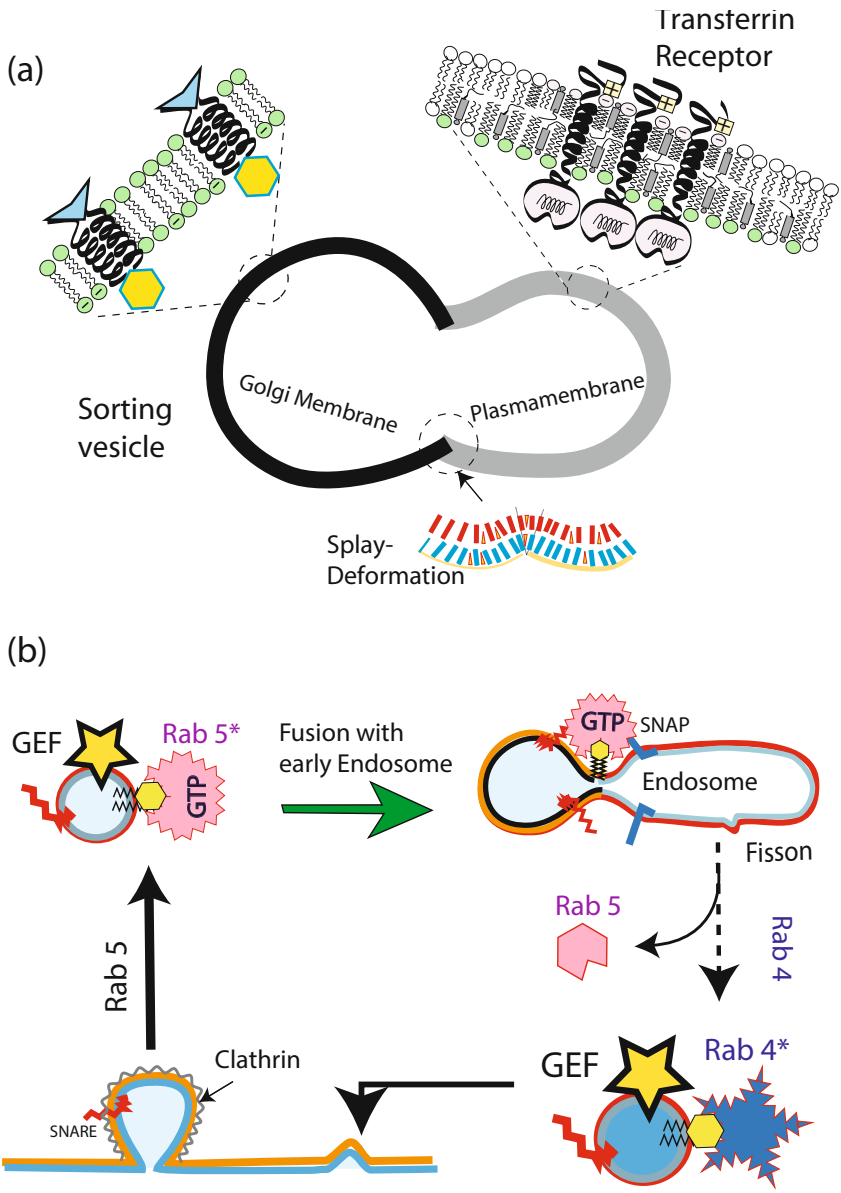

Fig. 2 On the recycling of transferrin receptors after fusion with acidic early endosomes. (**a**) Model of sorting of lipids and integral proteins of the plasma membrane in early endosomes by lateral phase separation into domains enriched in a glycerol lipid- and a SPHM/cholesterol-rich fraction, respectively. The envelope of the organelle will eventually become unstable resulting in the abscission of the SPHM-rich vesicle as suggested by in vitro experiments of bio-analogue lipid mixtures [18]. (**b**) The directed sorting and recycling is assumed to be mediated by two specific GTPases of the Rab family, namely, Rab-4 and Rab-5. The tandem Rab-4/Rab-5 mediates the rapid recycling of the transferrin receptors back to the PM and can thus circumvent the slow pathway via multi-lamellar lipid bodies. For evidence, see [19]

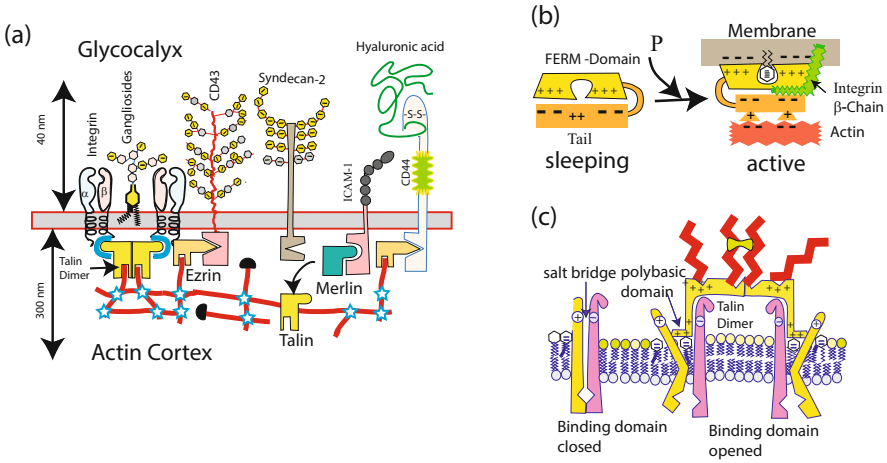

Fig. 3 The composite cell envelope stabilization by talin actin coupling. (**a**) Stratified structure of the cell plasma membrane showing some of the major membrane proteins, which serve the communication with the environment, called cell adhesion molecules (CAM) in the following. The CAMs are generally coupled with their intracellular domains to the actin cortex through coupling proteins exposing FERM homology domains. (**b**) Switching of membrane recruitment of talin by electrostatic-hydrophobic forces after phosphorylation-induced exposure of polybasic peptide sequence and binding pocket for phosphoinositide PI(4,5)P2 lipid anchoring. In the sleeping state, the binding motifs are hidden by internal complex formation. The other actin membrane coupling proteins are activated in similar ways. (**c**) Coupling of actin-integrin linker talin to cytoplasmic tail of beta chain of integrin following [20]. The left side shows the low-affinity state of integrin stabilized by a salt bridge. The right side shows the high-affinity state triggered by binding of a talin dimer both to the integrin beta chain (breaking up the salt bridge) and to the membrane through electrostatic-hydrophobic forces (explained in Fig. 4). Please note that talin exposes several binding sites for F-actin

distance is further determined by entropic surface pressures mediated by membrane bending undulations [21].[1]

All cell surface proteins involved in adhesion can be coupled to the actin cytoskeleton via three families of coupling proteins exposing FERM domains. These include talin, ezrin/moesin, merlin, and band IV.1, which exhibit some specific preferences.

- Talin binds preferentially to beta-chains of integrin, thereby enhancing the binding affinity of these CAMs by about a factor of five (see Fig. 3c and [20]). In the presence of PI(3,4,5)P3, the membrane binding of talin can be complemented and enforced by kindlin. While talin binds to PI(4,5)P2 via a PH domain, kindlin binds specifically to PI(3,4,5)P3 via a fivefold charged peptide loop [22]. Finally, talin harbors several binding sites for F-actin and can thus assemble actin gel patches by crosslinking the actin filaments coupled to integrin.

[1]Please note: I do not discuss the cell–cell interaction mediated by homophilic CAMs of the cadherin family which couples to the actin cortex via the linker cadherin.

- Ezrin and moesin bind preferentially to the glycoproteins and can couple these proteins also to microtubules (see Fig. 6b).
- A unique feature of merlin is that it is devoid of actin binding sites and can thus abolish the actin membrane coupling by the other FERM exposing proteins. This is a major reason for its function as tumor suppressing protein.

A common feature of all these coupling proteins is that, in the resting state of cells, they reside in the cytoplasm in a self-inhibited conformation. They have to be activated by changing the state of phosphorylation of specific domains as shown for talin in Fig. 3b and for the phosphoinositide-3-kinase (PI-3K) in Fig. 4b.

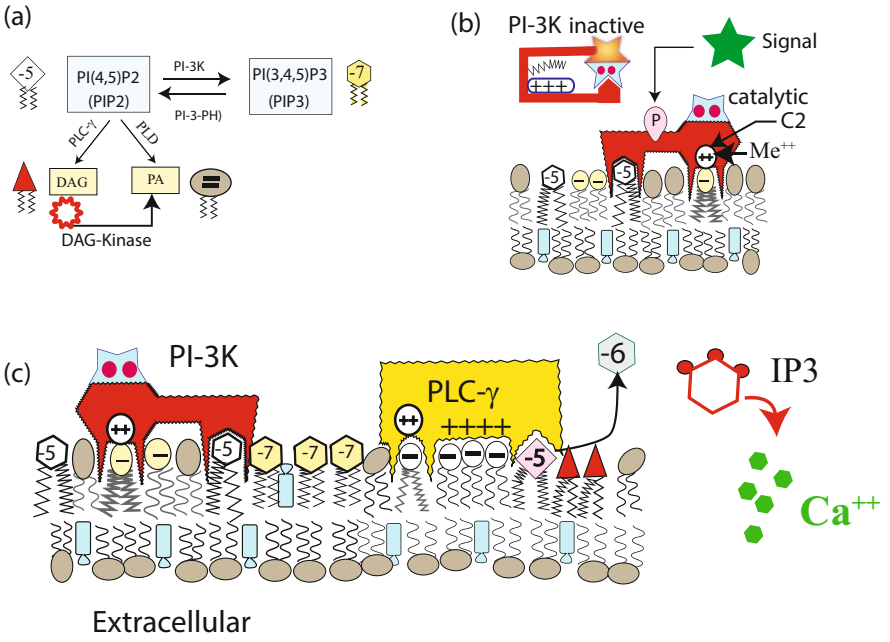

Fig. 4 Switching of activity of cytoplasmic proteins by membrane recruitment through electro-hydrophobic forces. (**a**) Top: Control of relative density of the lipid anchors PI(4,5)P2 and PI(3,4,5)P3 by the kinase-phosphatase tandem: PI-3K and PI-3PH. Bottom: generation of functional lipids diacylglycerol (DAG) and phosphatidic acid (PA). (**b**) PI-3 kinase as a paradigm of the activation of proteins sleeping in the cytoplasm by membrane recruitment. Insert upper left: PI-3K kept in an inactive state by internal complex formation. Bottom: activation of kinase by receptor tyrosine kinases (see Fig. 5) and recruitment to the membrane by anchoring via C2 homology domains resulting in binding constants of $K_d \sim 0.03$ nM [23]. (**c**) An example of the interrelationship of protein functions by the concept of induced membrane recruitment via electro-hydrophobic forces. Shown is the membrane recruitment of phospholipase Cγ by burst of PI(3,4,5)P3 anchors generated by PI-3Kinase (PI-3K). Please note that PI-3K couples a phosphate group ($-OPO_3^{2-}$) to the 3′-OH Position at the inositol ring, thus enhancing the negative charge of the head group from −5 to −7.

3 Generation of Functional Membrane Domains by Electrostatic-Hydrophobic Recruitment of Proteins

Electrostatically induced phase changes and domain formation by adsorption of polybasic proteins have fascinated physicists for many years [24, 25]. Numerous papers on charge-induced phase separation and lipid–protein interaction have been published (see [26]). The interests, raised by the potential control of membrane structure and functions by electrostatic forces, led to improved Poisson–Boltzmann theories of electrified membranes by [27, 28].

A major breakthrough came during the last 10 years with the discovery that cytoplasmic proteins can become integral parts of membranes by recruitment to the cytoplasmic leaflets of the plasma membrane and intracellular organelles by electrostatic-hydrophobic forces (called electro-hydrophobic forces below) (for an example, see Fig. 4c). The electrostatic membrane coupling is mediated non-specifically by binding of polybasic sequences (comprising 5–10 basic amino acids) to acidic lipids comprising about 20% of the lipids in the cytoplasmic leaflets. The hydrophobic binding is mediated by various hydrophobic anchors. These include, first, phosphoinositides, such as PI(4,5)P2 and PI(3,4,5)P3 (Fig. 4a), second, fatty acids such as palmitic acid and prenyl-prenyl chains, and third, membrane penetrating loops formed by hydrophobic amino acid sequences called C domains (see Fig. 4b and [29]). The fatty acid chains are often coupled to the proteins post-translationally, as in the process shown in Fig. 2b. The anchoring through amino acid loops is often enforced by bivalent ions (Ca^{2+}, Mn^{2+}, Zn^{++}) which form salt bridges between the protein and acidic lipids as shown in Fig. 4b, c. They resemble the zinc-finger proteins.

In the resting state of cells, most of the membrane-associated proteins reside in sleeping conformations in the cytoplasm due to internal complex formation, thus hiding the membrane binding modules. The internal complex formation is broken by phosphorylation and/or PI(4, 5)P2 binding, resulting in the exposure of the membrane binding constituents, as shown in Fig. 3b for talin and in Fig. 5b for the src-like kinases.

A paradigm of electro-hydrophobic protein binding is the MARCKS protein [30]. It exposes a sequence of 13 basic amino acids interrupted by four serine groups that can be rendered acidic by phosphorylation [via Protein Kinase C (PKC)]. The binding energy to membranes of natural composition is determined by the subtle balance of the gain in energy by electrostatic binding ($\Delta G \approx -40\ k_BT$) and the hydrophobic effect ($\Delta G \approx -12\ k_BT$ for myristic acid chains). This gain in energy is reduced by the entropic energy cost of the two hydrophilic peptide sequences, one of which is free while the other is anchored at the bilayer by a myristic acid chain [31]. Due to the balance of energies, the effective gain in binding energy is about $\Delta G \approx -15\ k_BT$.

By phosphorylation of the serine groups, the effective binding energy is reduced drastically to $\Delta G_{tot} \approx -5\ k_BT$. MARCKS is now only very weakly bound and can be easily displaced by other proteins binding via electro-hydrophobic forces. The important biological role of MARCKS is discussed below (see Fig. 8).

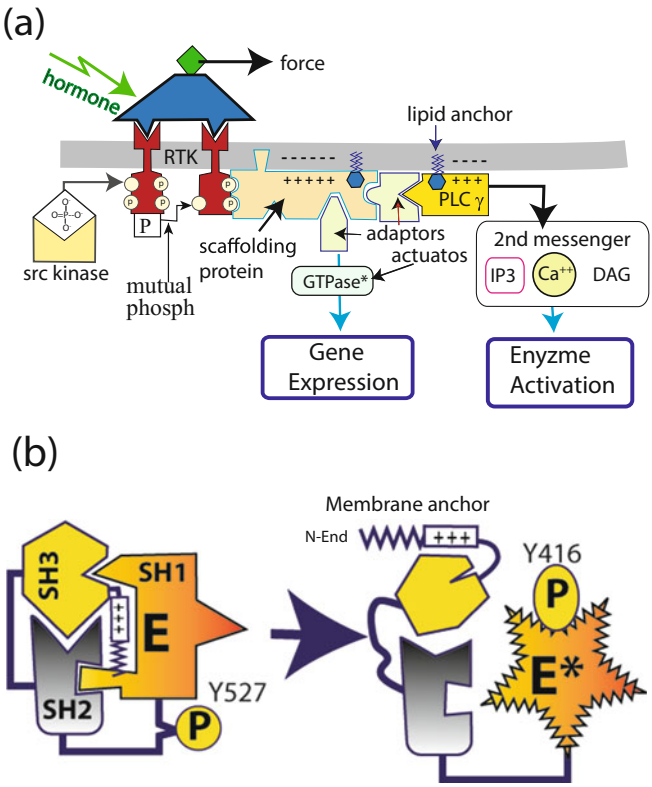

Fig. 5 General scheme of translation of external signals (hormones or forces) into intracellular structural reorganizations via rapid pathways mediated by second messengers and slow processes involving genetic expressions. (**a**) Universal mechanism of signal transduction across membranes mediated by RTKs exposing tyrosine-phosphorylated (and therefore active) binding pockets. Scaffold proteins serve the coupling and switching on of several activators. These are often docked on via so-called adapters but can also couple to the RTKs themselves. On the far right, the production of important messenger substances by the phospholipase Cγ is shown, and in the middle the initiation of gene expression which will not be discussed further here. Please note that the activators are called effectors in the biological literature. (**b**) Switching on of src kinase sleeping in the cytoplasm by dephosphorylation of the tyrosine group Y527 which results in the exposure of polybasic sequences and a hydrophobic anchor. The kinase binds to the membrane and enforces the activation of the RTKs as shown on the right side of (**a**)

4 Transmembrane Signal Transmission by Remodeling of Plasma Membranes

External cues (such as exogenous forces and binding of hormones to receptors) are generally transformed into intracellular biochemical processes by the generation of functional membrane domains acting as signal amplifiers. This conversion of signals is called transmembrane signal transmission. It is generally mediated by recruitment

of specific sets of functional proteins to the intracellular leaflet of the composite plasma membrane. Two key proteins mediating the signal transmission are, first, the kinase PI-3K acting as PI(4,5)P2→PI(3,4,5)P3 transformer (Fig. 4a) and, second, the phospholipase PLC-Cγ which generates the lipid anchor diacylglycerol (DAG) and the two second messengers IP3 and Ca^{++}. Below we consider two important examples of the switching of protein activities by recruitment to the membrane after binding to these specific lipid anchors.

- A key functional protein which is switched on by the DAG-generator PLC-γ is the protein kinase C (PKC) which controls the function of many proteins (see Fig. 8) and is involved in cancerogenesis. PKC enzymes are activated by all events inducing an increase in the concentration of diacylglycerol (DAG). It is strongly anchored in the membrane. First, by two C1 domains which bind to DAG and, second, by a C2 domain. Since C2 penetrates the membrane with two hydrophobic loops, the binding is enforced by Ca^{++}or Zn^{++} [29]. Based on this property, C2 can act as a strongly binding calcium sensor.
- A second very important example is the activation of the molecular switches of the GTPase superfamily by recruitment to membranes through regulatory proteins, such as guanine exchange proteins (GEF) described in Appendix. While GTPases are mobile and randomly distributed throughout the cytoplasm, the helper proteins (such as GEF) are recruited to membrane surface at specific sites, such as adhesion domains [32]. In this way, membrane processes can be controlled in a logistic way. One example is the triggering of solitary actin gelation pulses at the front of migrating cells by GEF-induced recruitment of the actin polymerization promotor Rac-1, as described in [33]. In this case, the location is determined by the generation of a cloud of PI(3,4,5) anchors by PI-3K as shown in Fig. 4a.

4.1 Regulation of PI(4,5)P2-PI(3,4,5)P3 Equilibrium by the Tandem PTEN and PI-3K (Fig. 4a)

To respond sensitively to external signals, the density of the high-affinity messenger lipid PI(3,4,5)P3 must be kept at a very low level (<0.02%) in resting cells. This state is maintained by the PI-3-phosphatase PTEN which binds strongly to membranes ($K_d \approx 10^{-9}$ M) and dissociates very slowly: $k_{off} \approx 10^{-3}\ s^{-1}$. The strong membrane binding is mediated by a hydrophobic C2 domain, which can penetrate into the membrane with or without Ca^{++} [34]. Ca^{++} controls the off-rate of the C2 domains which is 100 times faster in the absence of Ca^{++}. The binding of PLC-γ to this anchor is two orders of magnitude stronger than to PI(4,5)P2. This ensures that the functional proteins find the locally generated selective anchors, although PI(4,5)P2 is present in 100-fold excess.

In summary, the specific lipid anchors such as DAG and PI(3,4,5)P3 act as a kind of second messengers that control the activity of enzymes in a network

of interrelated enzymes. In this way, the activities of many enzymes involved in transmembrane signal transmission are interrelated by binding to the same functional membrane domains (see also Fig. 5).

4.2 The Access of Protein Binding Pockets to PI(3,4,5)P2 Is Controlled by Peptide Segments Acting as Sentinel

How can the enzyme PI-3K find the small fraction of PI(3,4,5)P3 hidden within the 100-fold excess of PI(4,5)P2? The selectivity is achieved by a specific structural feature of the binding pocket for the lipid anchor. It exposes a negatively charged amino acid (glutamate) at the entry of the binding pocket. This acts as sentinel which impairs the binding to PI(4,5)P2 [35]. In contrast, PI(3,4,5)P3 can overcome the negative potential owing to its higher negative charge and the 100 times larger binding constant ($K_d \approx 14$ nM). A life-saving example of this super-strong binding is protein kinase B (Akt). Activated Akt provides a survival signal that protects cells from apoptosis induced by various stresses. Removal of the negative charge of the sentinel peptide in Akt results in the ongoing cell division and cancer.

4.3 Transmembrane Signal Transduction by Membrane-Bound Domains Acting as Signal Amplifiers

Many membrane-based signal transmission processes triggered by hormones, growth factors, or mechanical forces are mediated by the family of receptor tyrosine kinases (RTK), often in combination with src kinases. The activated receptors trigger the self-assembly of functional nano-domains acting as signal amplifiers. As an example I consider the activation of the phospholipase Cγ (abbreviated as PLC-Cγ), a key activator of the signal transmission across plasma membranes (see Fig. 5). RTKs can be triggered by mechanical forces or hormone-induced activation of receptor tyrosine kinases following the scheme of Fig. 5.

The first step consists in the activation of tyrosine-exposing binding pockets of the cytoplasmic domains of the receptors by two universal mechanisms: first, by mutual phosphorylation of the tyrosine groups which is mediated by kinases associated with the RTKs (Fig. 5a) and, second, by so-called src kinases dissolved in the cytoplasm (Fig. 5b). Some RTKs (such as the insulin receptor) possess the capacity of self-phosphorylation. It is important to note that in these cases the activation requires the formation of dimers (as shown in Fig. 5a) or cluster formation by cell–cell adhesion. The tyrosine-phosphorylated binding pockets attract and thereby activate scaffolding proteins which in turn can attract and activate several activators of intracellular processes, such as PLC-γ the generator of two second

messengers DAG and Ca^{++}. The former acts as specific lipid anchor for cytoplasmic proteins exposing C2 domains such as protein kinase C.

Due to the high affinity of RTKs for specific hormones, very low hormone concentrations (10^{-9}–10^{-11} M) are often sufficient to control the proliferation of cells. The response of the RTK-induced processes is usually very slow and often lasts several hours. The long lifetime of the excited state of RTKs is essential for the switching of genetic expressions indicated in Fig. 5a.

5 Cell Adhesion Controlled Assembly of Biochemical Reaction Platforms

Cell adhesion is a complex biological process implying a rich physics and sharing some concepts with heterogeneous wetting processes [36]. A common feature of cell–cell and cell–tissue adhesion is the formation of domains of tight adhesion separated by weakly adhering zones. Biomimetic experiments provided strong evidence that the decay of the adhesion zone is an inevitable consequence of the competition between short-range attraction forces between pairs of[2] cell adhesion molecules (CAM) and long-range repulsion forces mediated by glycoprotein of the glycocalyx and bending fluctuations [37]. In a secondary step, the nuclei of CAM–CAM pairs are stabilized by coupling of actin gel patches to intracellular domains of integrin β1 chains as shown in Fig. 6a.

The glycoproteins extending by about 44 nm into the extracellular space generally act as repulsive buffers separating cells by about 50 nm. However, in the tissue they can also act as CAMs forming links with CAMs of other cells or ligands of tissue, such as collagen and fibronectin (see Fig. 6b). Similar to integrins the glycoproteins can also couple to the actin cortex to form small adhesion domains as shown in Fig. 6b. Moreover, syndecans and CD44 expose extracellular segments that can associate with integrins. These assemblies can fulfill similar functions as the adhesion domains shown in Fig. 6a.

5.1 Immunological Synapses: How Adhesion Domain Can Control Biochemical Reactions

The formation of T-Lymphocytes generating specific antibodies is stimulated by repeated adhesion of the cells on antigen-presenting cells (called dendritic cells DC). The cell–cell contacts are formed by adhesion domains consisting of clusters of links

[2]Cell surface receptors mediating adhesion by generating homophilic or heterophilic complexes are called CAMs. Segments of extracellular macromolecules such as collagen and fibronectin are called “conjugate ligands.”

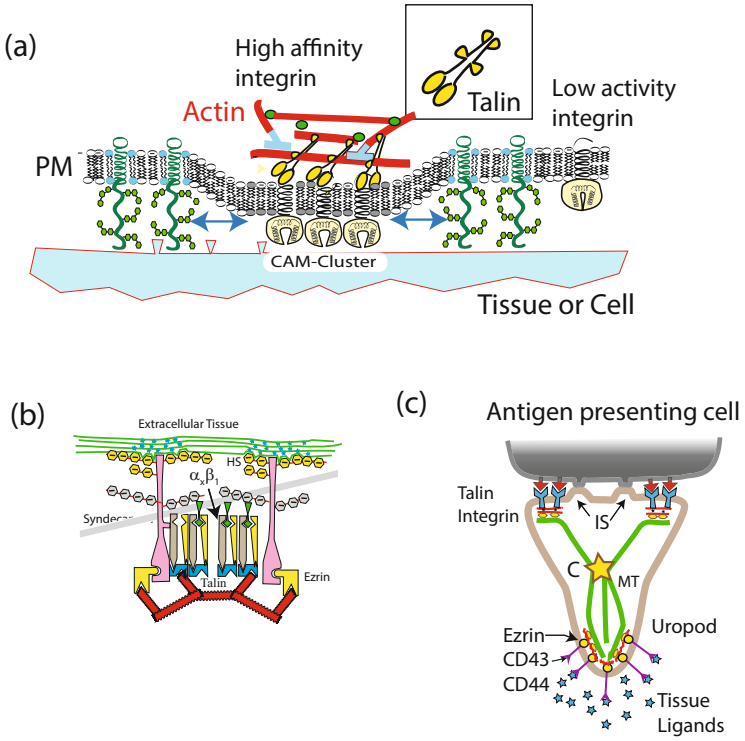

Fig. 6 Mechanisms of adhesion domain formation and adhesion-induced cell polarization. (**a**) Generation of tight adhesion domains formed by binding of integrin to ligands exposed by the tissue, such as fibronectin. A prerequisite for rapid domain formation is that the linkers are mobile in both surfaces (cells and tissue) enabling the nucleation and growth of strong links [37]. The adhesion strength is enforced by increasing the integrin affinity through binding to talin (see Fig. 3c). (**b**) Long-range adhesion of cells to tissue by proteoglycans of the syndecan family exposing heparan sulfate (HS) ligands which bind to collagen fibers. A specific feature of these adhesion domains is that the core protein of syndecans can form hetero complexes with integrins $\alpha_x b_1$. (**c**) Model of global bipolar polarization of T-cells in lymphoid tissue during brief encounters with an antigen-presenting cell (APC). While the front of the cell adheres to APCs through the formation of integrin-mediated adhesion domains forming immunological synapses IS (see Fig. 7), the posterior end, called uropod, couples to the endothelial cells of the lymphatic vessel. The glycoproteins (such as CD43) CD43 are actively displaced from the contact zone to the uropod of the cell. Whereas integrin–actin coupling at the front is mediated by talin, the CAMs at the end couple to the actin filaments and microtubules (MT) through ezrin linkers (references see [37])

between the two cells (for details, see [38, 39]). The formation of immunological synapses as the first step in the immune response of lymphocytes shows very impressively the key role that domain formation in membranes can play in biological control mechanisms.

As is common in many regulatory processes in cells, an activator (here the phosphorylating kinase Lck) and an inhibitor (here the dephosphorylating phos-

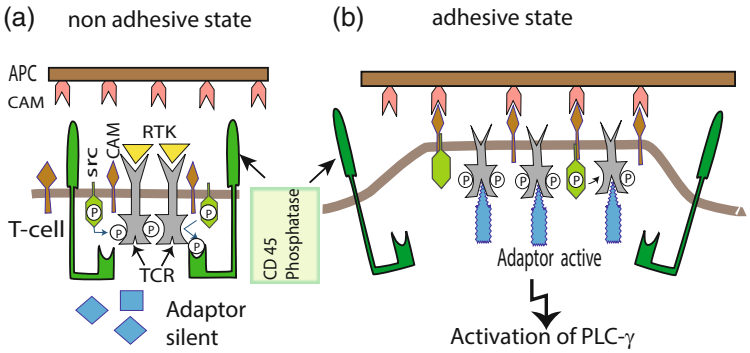

Fig. 7 Regulation of biochemical reactions at immunological synapses formed by adhesion of T cells on antigen-presenting dendritic cells (DC). (**a**) Non-adherent state. The activation of adaptor proteins by binding to phosphotyrosine groups of the cytoplasmic tail of T-cell receptors (TCR) is constitutively suppressed by the ongoing decoupling of phosphate groups (that are attached by the kinase Lck) through CD45. (**b**). Situation after formation of adhesion domains. Please note that the access of CD45 is inhibited by steric repulsion and the adaptor is activated [38]

phatase CD45) interact during the activation of functional proteins by tyrosine phosphorylation, very similar to the situation shown in Fig. 5a. While the kinase floats freely in the cytoplasm (such as the src kinase in Fig. 5a), the catalytically active phosphatase is coupled to the intracellular domain of the glycoprotein CD45, which exposes a huge extracellular domain and thus also acts as a repellent buffer molecule. In the free state of the lymphocyte, the phosphate groups on the T-cell receptors (TCR) are constantly removed by the mobile CD45 and the T-cell is not stimulated. However, as shown on Fig. 8b, after the formation of the adhesion domains CD45 is repelled from the reaction center. The T-cell can be stimulated as long as the state of adhesion prevails.

Under physiological conditions T-cells have to be stimulated a certain number of times by repeated adhesion domain formation before they divide and generate daughter cells producing the specific antibody (see [38, 42]). The situation resembles the quantal activation of nerve cells by synapses. For this reason, the T-cell activation by a minimum number of immunological synapses is called quantal law of immune response, a term first introduced by K.A. Smith [42].

An Intermediate Summary We learned how biofunctional domains in the composite cell envelope can be established by cell–cell or cell–tissue adhesion or by recruitment of adaptor proteins to sites of hormone reception. Most importantly, domains of well-defined composition can be assembled by recruiting the modules in a logistic way to the right position and at the right time, determined by the hormone receptors or the formation of adhesion domains [33]. A physiological benefit of nature's strategy of designing functional membrane domains is the regulation of biochemical reactions either by controlling the access of reactants or enzymes by generic forces or by forming synapses like connections with ER tubules according to Fig. 9d.

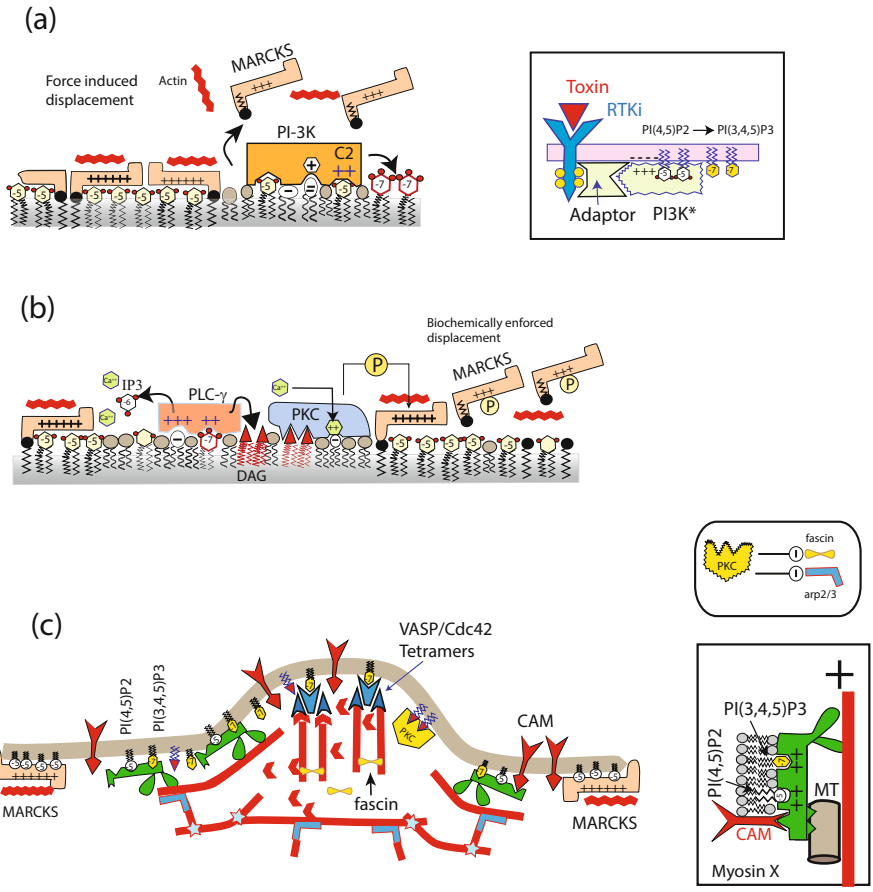

Fig. 8 Triggering of localized outgrowth such as dendritic spines or filopodia by enforced unbinding of protective MARCKS layers. (**a**) Regulation of the accessibility of swarms of PI(4,5)P2 anchors by functional polybasic proteins initiated by local unbinding of a protecting layer of MARCKS. Force-induced unbinding is initially triggered by generation of the PI(3,4,5)P3 by the very strongly binding kinase PI-3K (following Fig. 4). The inset on the right shows the triggering of the PI-3K activation by binding of bacterial toxins (such as lipopolysaccharides) to the RTK receptors. (**b**) Acceleration of MARCKS displacement by phosphorylation through PKC that binds strongly after the generation of DAG by phospholipase Cγ (PLCγ). The PI(3,4,5)P3 anchors can also recruit myosin X motors which are absolutely necessary for the generation of long filopodia [40]. Please note that the motors are activated by forming dimers after activation of the RTK by the toxin. (**c**) Model of initiation of formation of finger-like protrusions by local coupling of myosin X dimers to PI(3,4,5)P3 anchors. The anchors are generated by PI-3K, after uncoupling of MARCKS (see main text). Please note: PKC recruited to the membrane through DAG lipids simultaneously activates coronin and inactivates the bundle former fascin at the membrane surface. This step is essential to initiate the local filopodia formation [41]. The lower inset at the right shows the binding of myosin X dimers to actin and microtubules and the recruitment of cell adhesion molecules (CAMs) such as integrin. The inset at the top shows the inhibition of fascin and Arp2/3 by the membrane-anchored PKC

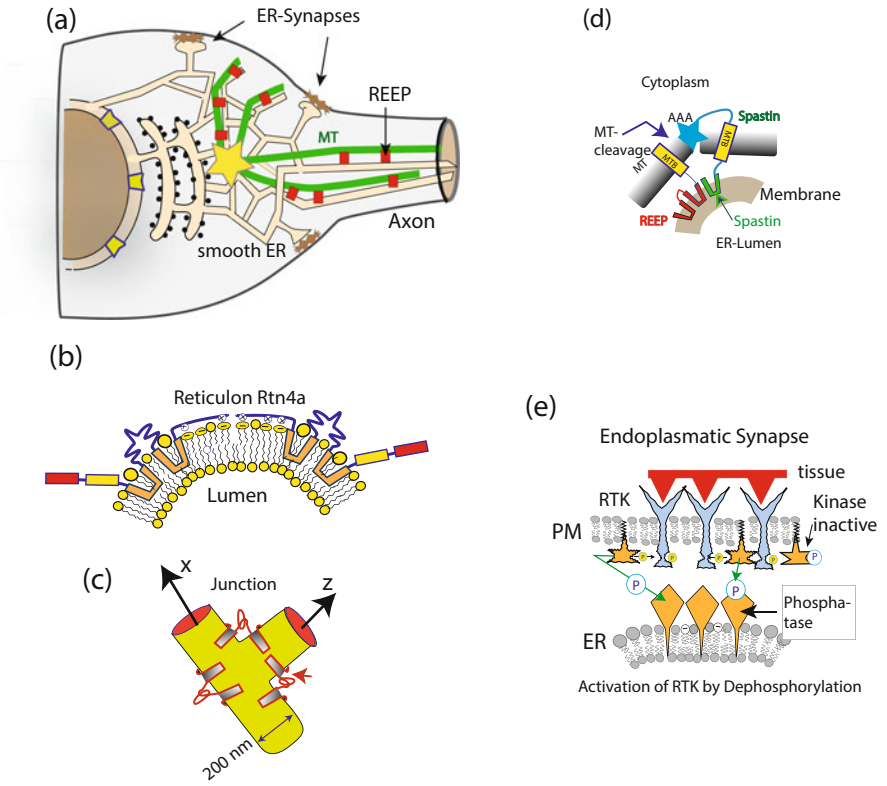

Fig. 9 (**a**) Morphology of tubular network of endoplasmic reticulum composed of disc-like cisternae studded with ribosomes (the rough ER) from which networks of tubules emanate. The tubules (exhibiting diameters of about 60 nm) are formed by ribosome-free smooth ER. They can penetrate even to the tips of axon whereby they are stabilized by coupling to microtubules through REEP and spastin. (**b**) Model of penetration of hydrophobic segment of reticulons into the lipid bilayers. Please note: due to the mismatch of the thickness of the hydrophobic region of the membrane and the length of the peptide segments of reticulons, the latter form a wedge-shaped structure [43]. (**c**) Model of stabilization of junctions of tubules by the reticulons Rtn4a/NogoA, which exhibits two twinges connected by a hydrophilic link composed of 65 hydrophilic amino acids. (**d**) Coupling of ER tubes to microtubules by the coupling protein REEP which forms complex with the MT severing protein spastin. REEP plays a key role for the abscission of two daughter cells during mitosis. (**e**) The tips of the tubules can form direct contacts with the plasma membrane (for instance, adhesion domains) where they can locally elicit specific reactions (see text). We call these signal transmitting contacts ER synapses

5.2 A Possible Role for MARCKS: Control of the Access of Proteins via Electro-hydrophobic Forces

The physiological role of MARCKS has not been extensively studied yet, despite the fact that cells (in particular brain cells) contain a large excess of this polybasic

protein (10 μM) compared to charged lipids (∼1 nM). One established role of MARCKS is the protection of PI(4,5)P2 against the uncontrolled electro-hydrophobic binding of proteins that could elicit uncontrolled membrane-mediated reactions, such as excess cell divisions causing cancer (see [30]). Examples are phospholipase Cγ (the generator of DAG anchors and Ca^{++}) and PI3K, the PI(4,5)P2-to-PI(3,4,5)P3 transformer (see Fig. 8). The DAG anchors act as strong receptors of phorbol esters. These molecules (produced by some plants) are known for their ability to exert strong carcinogenic effects [44]. A second fundamental role for MARCKS has been established recently. Together with protein kinase C, MARCKS plays a key role for the plasticity of synapses and rapid remodeling of dendritic spines. Therefore, the knock-out of MARCKS genes during the development of embryos is lethal [45, 46].

The formation of dendritic spines or displacement of MARCKS by PKC-mediated phosphorylation sheds new light on the control of membrane processes by polybasic proteins. In the resting state of cells, MARCKS exposes a peptide sequence harboring 12 basic peptides and four serine groups. This is sufficient to protect PI(4,5)P2 lipid anchors against binding of polybasic functional proteins. Thus, MARCKS has to be uncoupled to trigger a local process. One mechanism to achieve this in a controlled way is to uncouple MARCKS by phosphorylation of the four serine groups by protein kinase C (PKC). As shown by Monte Carlo simulations [31], this reduces the binding energy by a factor of three (from 15 to 5 k_BT).

An instructive example of this pathway of excitation is the formation of filopodia by macrophages, which is initiated by two processes. First, PKC enforces the uncoupling of MARCKS by phosphorylation of the serine groups (see Fig. 8b). Second, by phosphorylation of the actin binding protein coronin it abolishes the growth of branched actin gels by Arp2/3 and therefore facilitates the formation of filopodia by the growth of actin bundles (see [47, 48]). Following Breitsprecher and coworkers [41], the formation of long filopodia is mediated by pushing forces generated by the growth of parallel bundles of actin activated by the GTPase Cdc42 (see Fig. 8c). The bundles are mechanically enforced by fascin-mediated linking of parallel filaments, The Cdc42 switch is recruited to the membrane together with the actin growth promotor VASP resulting in the formation of tetramers.

The formation of the fingerlike protrusions is triggered by the membrane binding of protein kinase C (PKC) which exerts three effects. First, it accelerates the uncoupling of MARCKS from the PIP(4,5)P2 patches by phosphorylation (see Fig. 8b). Second, it activates the actin binding protein coronin, which inhibits the activity of Arp2/3. Third, by phosphorylation of fascin, it inhibits the actin bundle formation close to the membrane.

But how can the PKC-specific DAG lipid anchors be generated by phospholipase-γ while the domains are covered by MARCKS? Here the PI(3,4,5)P3 generator PI-3K comes into play. It is activated by binding of lipopolysaccharide to RTK receptors as shown in the top inset of Fig. 8a. Since, according to Fig. 4, activated PI-3K exposes very strongly binding C2 domains, it can easily displace MARCKS to generate PI(3,4,5)P3 anchors. After this triggering event, the DAG

generating phospholipase Cγ (PLC) can bind to generate swarms of DAG lipids. This results in the attraction of the kinase PKC, followed by the acceleration of the MARCKS displacement by phosphorylation. This process is called biochemically enforced displacement in Fig. 8b.

To generate long fingerlike filopodia an essential new player comes in: namely, the unconventional motor myosin X. It strongly binds to both phosphoinositide anchors [40] and moves along the actin bundle toward the tip. Most importantly, it transports the CAMs, such as integrins and the high-affinity lipid anchor PI(3,4,5)P3, to the filopodia tip where they can serve recognition of pathogens (such as bacteria and fungi).

Insight into the dynamic aspects of the triggering of filopodia formation and related electrostatically driven domain formation processes at the inner cytoplasmic membrane surfaces was provided by Monte Carlo studies. Daniel Harries and coworkers numerically calculated the kinetics of the charged lipid redistribution induced by the adsorption of polybasic proteins [49]. They showed first that for the natural lipid composition the gain in electrostatic energy by transfer of a molecule from the free membrane to the protein-covered domain is of the order 2.5 k_BT for phosphatidylserine (PS) but $\sim$12 k_BT for PI(4,5)P2, despite of the tenfold excess of PS. The entropy costs associated with the decrease in concentration of the charge component can be easily overcompensated by the gain in electric energy if the charge is increased. This estimation shows that the membrane recruitment of proteins by electrostatic forces can be finely balanced by cells through the control of the lipid composition.

Clearly, the assembly of proteins exposing polybasic proteins on PI(4,5)P2-rich membrane domains is a dynamic process with ongoing binding and unbinding of MARCKS and the functional proteins competing with these structure controlling proteins. Based on the nonlinear Poisson–Boltzmann equation developed by David Andelman and coworkers [50] the group of Daniel Harries studied the slowing down of the lateral mobility of charged lipids and proteins in the region of charged membrane domains by MC simulations [49]. They showed that the electrostatic forces alone can slow down the mobility of the acidic lipids by an order of magnitude, due to the fact that the motional jumps of the lipids are impeded by the tangential electrostatic field generated by the polybasic proteins. The situation resembles the slowing down of the ion motion in electrolytes by macroions.

A Synopsis

The triggering of filopodia formation by macrophages through binding of bacterial toxins to hormone receptors of the RTK family shows, first, how exogenic signals can initiate the formation of membrane domains by sequential recruitment of functional module to the site of action. It further demonstrates the important role of electro-hydrophobic forces.

The catching of prey by filopodia shows beautifully how cells can explore the tissue and recognize specific cells of the body or pathogens whereby lock and key force between the tip of the finger and the ligands of the hostile cells plays the role of eyes.

6 Tubular Networks of Endoplasmic Reticuli Formed by Generic Mechanisms

An impressive example of the shape diversity of membrane organelles is the formation of (branched) tubular networks by the smooth ER that extends far into the cytoplasmic space. The tubules can contact the PM at specific locations such as at the tip of axons or at adhesion domains to locally stimulate specific processes (Fig. 9a). An established example is the localized activation of src kinases shown in Fig. 9e.

A generic (topological) driving force for the formation of tubular networks and cisternae is the maximization of the area-to-volume ratio $z = A/V$ of the ER whereby perturbations of the osmotic homeostasis of cells are minimized. The area-to-volume ratios of a spherical vesicle of radius R, of a tube of radius r, and a disc of thickness δ behave as $R^{-1} : r^{-1} : \delta^{-1}$, respectively [43]. Since the thickness δ of the cisternae and the tubes are similar, both shapes would maximize the area-to-volume ratio to a similar extent. However, an advantage of the tubular network would be that it can extend far into the cytoplasmic space or into axons without impeding the intracellular transport.

Very importantly, since the lumen of the ER and the double-walled nuclear envelope form a continuous space, there is close contact between the Ca^{++}-poor cytoplasm and the Ca^{++}-rich ER lumen throughout the cell. The shape and size of the ER are determined by the cell function. The ER network of most cells consists of rough ER located close to the nucleus from which short tubules of smooth ER protrude. In contrast, liver cells and muscle cells expose extended tubular networks. The smooth ER membrane is packed with proteins serving the detoxification of our body. This task is fulfilled by the enzyme complex Cytrochrome 450/Cytochrome 450 reductase. The complex transforms lipophilic molecules (drugs or local anesthetics) into water-soluble isoforms which can be easily discharged by the body. The microfibrils of skeletal muscle cells are surrounded by a dense tubular network, the sarcoplasmic reticulum that provides the Ca^{++} which triggers the muscle contraction.

What drives the ER-network formation? The bending elasticity associated with the formation of tubules and cisternae is small ($\sim$0.05 k_BT per lipid) and the ER network formation could be generically regulated through the osmotic pressure of the cell or the spontaneous curvature of the smooth ER [43]. It has also been proposed that the formation of cisternae with pores penetrating both membranes (often called worm holes) could be formed by mixtures of lipids preferring to reside in positive and negatively curved membrane regions, respectively [51]. About 10 years ago, Tom Rapoport and coworkers solved the enigma. They discovered that the complex topology of the ER is regulated by a superfamily of proteins, called reticulons [52]. These include, first, the family of reticulons (*Rtn4a/NogoA*), which serve the branching of the tubules (see Fig. 9b), second, the related protein REEP which couples the ER tubules to microtubules, third, the microtubule severing

protein spastin (Fig. 9d), and fourth, atlastin, a GTPase that serves the homofusion of ER membranes.

A common structural feature of the reticulons is an α-helical hydrophobic sequence of peptides which can penetrate into single monolayers or bilayers. There is some evidence that the length of the helices formed by the hydrophobic peptide sequences is slightly longer then the monolayer or bilayer thickness. They are thus assumed to form wedge-like structures within the membrane (see [43] and Fig. 9b). Reticulons can thus both act as curvature-sensing and curvature-sculpturing proteins, similar to BAR domains exposing proteins, such as amphiphysin. Most importantly, the wedge-shaped peptide sequences favor the formation of complexes between two reticulons in regions of high curvature, such as at the edge of the cisternae and along the tubules. Different reticulons can thus form functional complexes which are distributed along the tubules. The situation resembles the accumulation of Gaussian curvature-sensing BAR proteins at the necks of coated pits [53].

As shown by studies of microemulsions, a particular problem is the stability of connections between tubes [54]. Tubular networks are easily formed by microemulsions but they decay rapidly. Tlusty et al. provided evidence that this is a consequence of the high entropy costs associated with the formation of branches, which restrict the degree of conformational freedom of the tubules. In the ER, the junctions of tubules are stabilized by the family of reticulons of the family Rtn4a/NogoA. They exhibit two hydrophobic wedges which are separated by a long hydrophilic sequence (comprising 64 peptides). They can form double twinges which can connect two perpendicularly oriented tubes as shown in Fig. 9c (see [43]).

An important consequence of the wedge-shaped membrane binding domains of reticulons is their capacity of curvature sensing. They can form homo- or heterocomplexes of two reticulons which preferentially accumulate at highly curved membrane areas (tubes or at the rim of cisternae) to generate machines with specific functions. Two important examples are discussed below:

- Complexes between REEP and spastin form microtubule severing machines that play a key role for the abscission of daughter cells during mitosis. REEP complexes serve the coupling of tubules to microtubules enabling their penetration into the axon tips. For that reason, mutations of spastin can lead to nerve diseases such as spastic laming [55]. The intimate coupling of ER tubes and microtubules is demonstrated by the observation that the MT decomposing Nocodazole disassembles the tubular network.
- The ER tubes extending to the cell periphery can form close contacts with functional domains of the plasma membrane (such as adhesion domains, discussed in chapter “Critical lipidomics: The consequences of lipid miscibility in biological membranes”) and serve the controlled localization of ER-bound functional proteins. A recently established example is the activation of src kinases forming loose contacts with hormone amplifying membrane domains (see Fig. 9e). The kinases are activated by the dephosphorylation of Tyr 530 through the

phosphatase PTP1B (see Fig. 9e). Since the PTP1B is an integral protein of the ER membrane, the processes are accelerated by the formation of ER-synapses (see [56]).

- The continuity and extension of the ER is controlled by the fusion of ER vesicles or tubules (called homo-fusion). In contrast to hetero-fusion (mediated by the SNARE/SNAP protein tandem), the homo-fusion is mediated by the fusion machine atlastin. The fusion process is driven by the formation of a tight complex between two atlastins anchored in two juxtaposed membranes [57]. As in the case of hetero fusion, this results in the formation of bilayer diaphragms between the membranes enabling the fusion via the pathway of hemifusion (for references, see [2]).

In summary, reticulons seem to belong to the curvature-sensing proteins similar to endophilins and amphiphysins (see [58]). The question arises whether they are needed to drive the formation of cisternae or tubular networks. The elastic energy costs associated with the formation of tube of 20 nm diameter from a membrane of bending modulus $\kappa \approx 10\ k_BT$ are about 0.02 k_BT per lipid. This small value suggests that the tubule formation of the ER can be easily established by the osmotic pressure homeostasis. The wedge-shaped hydrophobic domains of the reticulons are assumed to serve two other purposes: first, their preferred location at highly curved regions and, second, the formation of functional complexes, such as the MT severing REEP-spastin complex (see Fig. 9d).

A provoking albeit open question is whether the tubes could penetrate to the tip of axons to regulate the Ca^{++} turnover at the synapses as postulated by Park [55]. Indeed their experiments provided some evidence that local fluctuations in calcium in the dendrites can propagate through the tubules with a speed of 30 μm/s and travel from the tips of the dendrites to the nucleus within fractions of a second. They further postulated that this could even result in the Ca-triggered genetic expression. It is rather unlikely that several cm long membrane tubes are stable. More likely, the ER tubes located between the ER and the axon tip (and coupled to the MTs) are constantly fractured by fluctuating forces and re-fused again by atlastins. In this way, material could indeed be transported in a saltatory way between the ER and the axon tip in both directions.

7 Outlook, Future Perspectives, and New Directions of Membrane Research

The classical membrane physics concentrated on the control of membrane-based processes by the specific interaction between lipids and integral proteins, making use of thermodynamic properties of multicomponent lipid–protein bilayers. Thereby the lipid moiety may be considered as pseudo-binary mixture (for references, see Sackmann [2]).

During the last 10 years, it has become evident that a second, more versatile pathway of functional domain formation can be realized by the assembly of functional domains through sequential and logistically controlled recruitment of functional proteins onto intracellular leaflet of cell organelles. The site of assembly is determined by priming through master switches generating local swarms of specific high-affinity lipid anchors, such as PI(3,4,5)P3 and diacylglycerol (DAG). The high-affinity anchors recruit the functional proteins (swimming in a non-active state in the cytoplasm; see Fig. 4) to the cell membrane surface by electrostatic hydrophobic forces. The lipid anchors play the role of second messenger.

The formation and activation of functional domains are regulated by agonistically or antagonistically cooperating molecular switches. As examples we considered here the agonistic Rab4/Rab 5 tandem (controlling the rapid endocytosis and recycling of receptors) and the antagonistic pair of GTPases Rac-1 and Rho A (controlling the state of the actin cortex).

To avoid over-excitations of cells (implying the danger of tumorigenesis), the omnipresent phosphoinositide anchors are protected by layers of the structure controlling protein MACKS bound by electrostatic-hydrophobic forces,

The universality of cell control systems is exemplified by the observation that extrinsic forces and hormones can trigger the generation of very similar types of transmembrane signal transmission centers assembled around receptor tyrosine kinases (RTK).

By recruitment of scaffolding proteins exposing several active binding sites to the activated RCK receptors, several functions may be triggered by the same signal transmission center. These can include fast biochemical signals eliciting the rapid restructuring of the membranes of cellular organelles. Slow, genetically controlled processes can serve the restructuring of the tissue to adapt its mechanical impedance to that of the cell.

Membrane-based reactions can be more efficiently controlled than reactions in 3D in space. An example considered here is the activation of immune synapses.

Where should we go? Biomimetic systems can teach us basic principles of lipid protein sorting by thermomechanical forces or show how the adhesion strength is controlled by specific and generic forces. Passive and active mechanical cell model can provide insights into the mechanical control of cell shapes (see [59]). However, to gain insight into life-saving control mechanism, in vivo studies are absolutely necessary. Owing to modern techniques of genetic engineering and new microscopic and nanoscopic tools, this approach is feasible. However, to the author's judgment, a closer cooperation between physicist, biologists, and, most importantly, engineers familiar with control systems is urgently needed. Finally, it is hoped that more detailed insights in the analogy of technical and biological control mechanism may teach us how to generate new self-healing composite materials in a logistic way.

Acknowledgements Financial support by the Excellence Program of the Technical University of Munich and by the Lehrstuhl für Angewandte Physik of the Ludwig Maximilian University is gratefully acknowledged.

Appendix: Affinity Term Scheme of Bistable Molecular GTPase Switches

GTPases (such as Rac, Rho, and Cdc42) can switch between an inactive state S (with GDP bound) and an active state S* (with GTP bound). In resting cells, the GTPases form inactive complexes with "guanine dissociation inhibitor" GDI or are switched off by internal complex formation (as shown in Fig. 4b for PI-3K). The S→S* transition is induced by uncoupling of the GDI by binding of the GDP→GTP exchange proteins (called guanine nucleotide exchange factors: GEF). As shown in the left image of Fig. 10, the GTPase is generally activated by exchange of GTP for GDP, a process mediated by a GDP→GTP exchange factor (GEF).

GTPases can be recruited to the membrane in two ways. After (or together with) the GTP binding they undergo a conformational change resulting in the exposure of a polybasic peptide sequence and a fatty acid chain. In the case of logistically controlled formation of functional membrane domains, the first step consists in the membrane anchoring of the GEFs; for instance after the generation of high-affinity PI(3,4,5)P3 anchors as shown in the right image.

A second important regulation mechanism is the following. The intrinsic GTP hydrolysis activity of GTPase is very weak resulting in a long lifetime of the

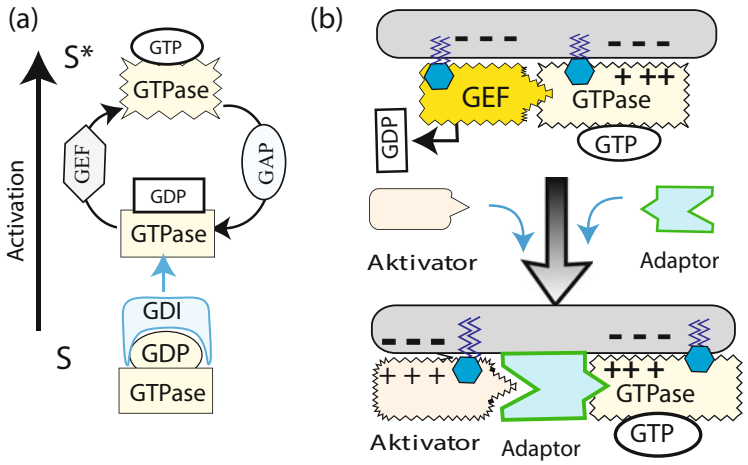

Fig. 10 Term scheme of activation and deactivation of the molecular switches of the superfamily family of Ras GTPase, such as Rac-1 and RhoA. (**a**) Mechanism of activation of the switches by the guanine exchange protein (left) and deactivation by the GTP hydrolyzing protein GAP. Please note that GAP accelerates the turnover of the switches since the (activated) GTP-binding state exhibits a very long lifetime of the order of minutes. Please note that frequently the GDP binding GTPases are stabilized by inhibitors such as GDI. (**b**) Right top image: Membrane recruitment and activation of a GTPase by the guanine exchange protein GEF mediated by electrostatic-hydrophobic forces. Bottom: the excited GTPase activates and binds an adaptor protein which is also recruited to the membrane by electrostatic-hydrophobic forces. It can attract one or several activators of control processes

activated switches. In order to accelerate this low rate of hydrolysis (which is about 0.01 min^{-1}), another regulatory protein has to come into play, namely, the "*G*TPase *a*ctivating *p*roteins" (GAP) (Fig. 10, left). They stimulate the Rho-GTPases to hydrolyze the GTP, thus deactivating the molecular switches rapidly. Taken together, GEF and GAP form a functional tandem that controls the rhythm of the transmembrane signal transmission processes.

References

1. Mouritsen OG (2011) Model answers to lipid membrane questions. Cold Spring Harb Perspect Biol 3:a004622
2. Sackmann E (2006) Thermo-elasticity and adhesion as regulators of cell membrane architecture and function. J Phys Condens Matter 18(45):R785–R825
3. Helfrich W (1973) Elastic properties of lipid bilayers: theory and possible experiments. Z Naturforsch 28c:693–703
4. Helfrich W (1978) Steric interaction of fluid membranes in multilayer systems. Z Naturforsch 33a:305–315
5. Evans EA (1974) Bending resistance and chemically induced moments in membrane bilayers. Biophys J 14:923–931
6. Seifert U, Lipowsky R (1995) Morphology of vesicles. In: Lipowsky R, Sackmann E (eds) Handbook of biological physics, vol 1A. Elsevier, Amsterdam
7. Seifert U (1997) Configurations of fluid membranes and vesicles. Adv Phys 46:13–137
8. Nelson P, Powers T, Seifert U (1995) Dynamical theory of the pearling instability in cylindrical vesicles. Phys Rev Lett 74:3384–3387
9. Kozlov M (1999) Dynamin: possible mechanism of "Pinchase" action. Biophys J 59:604–616
10. Brochard F, Lennon JF (1975) Frequency spectrum of the flicker phenomenon in erythrocytes. J Phys France 36:1035–1047
11. Millner ST, Safran S (1987) Dynamical fluctuations of droplet microemulsions and vesicles. Phys Rev A 36:4371–4382
12. Mukhopadhyay R, Lim H, Wortis M (2002) Echinocyte shapes: bending, stretching, and shear determine spicule shape and spacing. Biophys J 82:1756–1772
13. Auth T, Safran S, Gov N (2007) Fluctuations of coupled fluid and solid membranes with application to red blood cells. Phys Rev E 76:051910
14. Zilker A, Ziegler M, Sackmann E (1992) Spectral analysis of erythrocyte flickering in the 0.3-4.0 μm regime by microinterferometry combined with fast image processing. Phys Rev A 46:7998–8001
15. Döbereiner HG, Kas J, Noppl D, Sprenger I, Sackmann E (1993) Budding and fission of vesicles. Biophys J 65:1386–1403
16. Bretcher M, Munro S (1993) Cholesterol and the Golgi apparatus. Science 26:1280–1281
17. Ben-Shaul A (1995) Molecular theory of chain packing elasticity and lipid protein interaction in lipid bilayers. In: Lipowsky R, Sackmann E (eds) Handbook of biological physics, vol 1A. Elsevier, Amsterdam
18. Baumgart T, Hess ST, Webb WW (2003) Imaging coexisting fluid domains in biomembrane models coupling curvature and line tension. Nature 425:821–824
19. Schwartz SL, Cao C, Pylypenko O, Rak A, Wandinger-Ness A (2008) Rab GTPases at a glance. J Cell Sci 120:3905–3910
20. Wegener KL, Partridge AW, Han J, Pickford AR, Liddington RC, Ginsberg MH, Campbell ID (2007) Structural basis of integrin activation by talin. Cell 128:171–182
21. Rädler J, Feder TJ, Strey HH, Sackmann E (1995) Fluctuation analysis of tension controlled undulation forces between giant vesicles and solid substrates. Phys Rev E 51:4526–4536

22. Legate K, Fässler R (2009) Mechanisms that regulate adaptor binding to β-integrin cytoplasmic tails. J Cell Sci 122:187–198
23. Scott A, Antal C, Newton A (2013) Electrostatic and hydrophobic interactions differentially tune membrane binding kinetics of the C2 domain of protein kinase C. J Biol Chem 288:16905–16915
24. Galla HJ, Sackmann E (1975) Chemically induced lipid phase separation in model membranes containing containing charged lipids: a spin label study. Biochim Biophys Acta 401:509–529
25. Traeuble H, Eibl H (1974) Electrostatic effects on lipid phase transitions: membrane structure and ionic environment. Proc Natl Acad Sci USA 71:214–219
26. Cevc G (1990) Membrane electrostatics. Biochim Biophys Acta 1031:311–382
27. Andelman D (1995) Chapter12—Electrostatic properties of membranes: the Poisson-Boltzmann theory. In: Lipowsky R, Sackmann E (eds) Handbook of biological physics, vol 1. North-Holland, Amsterdam, pp 603–642
28. Netz RR (1999) Debye-Hückel theory for interfacial geometries. Phys Rev E 60:3174–3182
29. Stahelin RV, Karathanassis D, Bruzik KS, Waterfield MD, Bravo J, Williams RL, Cho W (2006) Structural and membrane binding analysis of the Phox homology domain of phosphoinositide 3-kinase-C2α. J Biol Chem 281:9845–9856
30. McLaughlin S (2002) PIP2 and proteins: interactions, organization and information flow. Annu Rev Biophys Biomol Struct 31:151–175
31. Tzlil S, Murray D, Ben Shaul A (2008) The electrostatic switch mechanism: Monte Carlo study of MARCKS-Membrane interaction. Biophys J 95:1745–1757
32. Côté JF, Vuori K (2007) GEF what? Dock180 and related proteins help Rac to polarize cells. Trends Cell Biol 17:383–393
33. Sackmann E (2015) How actin-myosin cross talks guides the adhesion, locomotion and polarization of cells. Biochim Biophys Acta 1853:3132–3142
34. Das S, Dixon J, Cho W (2003) Membrane-binding and activation mechanism of PTEN. Proc Natl Acad Sci USA 100:7491–7496
35. Landgraf KE, Pilling C, Falke JJ (2008) Molecular mechanism of an oncogenic mutation that alters membrane targeting: Glu17Lys modifies the PIP lipid specificity of the AKT1 PH domain. Biochemistry 47:12260–12269
36. Bruinsma R, Behrisch A, Sackmann E (2000) Adhesive switching of membranes: Experiment and theory. Phys Rev E 61:4253–4267
37. Sackmann E, Smith A (2014) Physics of cell adhesion: some lessons learned from cell mimetic systems. Soft Matter 10:1644–1659
38. Sackmann E (2011) Quantal concept of T-cell activation: adhesion domains as immunological synapses. New J Phys 13:065013
39. Dustin M, Allen PM, Shaw AS (2001) Environmental control of immunological synapse formation and duration. Trends Immunol 22:192–204
40. Watanabe TM, Tokuo H, Gonda K, Higuchi H, Ikebe M (2010) Myosin-X induces filopodia by multiple elongations. J Biol Chem 285:19605–19614
41. Breitsprecher D, Kiesewetter AK, Linkner J, Vinzenz M, Stradal TE, Small JV, Curth U, Dickinson RB, Faix J (2011) Molecular mechanism of Ena/VASP-mediated actin-filament elongation. EMBO J 30:456–467
42. Smith KA (2006) The quantal theory of immunity. Cell Res 16:11–19
43. Sackmann E (2014) Endoplasmatic reticulum shaping by generic mechanisms and protein-induced spontaneous curvature. Adv Colloid Interf Sci 208:153–160
44. Griner EM, Kazanietz MG (2007) Protein kinase C and other diacylglycerol effectors in cancer. Nat Rev Cancer 7:281–294
45. Haimin L, Gang C, Bing Z, Shumin D (2008) Actin filament assembly by myristoylated, alanine-rich C Kinase substrate-phosphatidylinositol-4,5-diphosphate signaling is critical for dendrite branching. Mol Biol Cell 19:4804–4813
46. Calabrese B, Wilson M, Halpain S (2006) Development and regulation of dendritic spine synapses. Physiology 21:38–47

47. Bornschlögl T, Romero S, Vestergaard C, Joanny JF, Tran Van Nhieu G, Bassereau P (2013) Filopodial retraction force is generated by cortical actin dynamics and controlled by reversible tethering at the tip. Proc Natl Acad Sci USA 110:18928–18933
48. Zidovska A, Sackmann E (2011) On the mechanical stabilization of filopodia. Biophys J 100:1428–1437
49. Khelashvili K, Weinstein H, Harries D (2008) Protein diffusion on charged membranes: a dynamic mean-field model describes time evolution and lipid reorganization. Biophys J 94:2580–2597
50. Diamant H, Andelman D (1997) Adsorption kinetic of surfactants at fluid-fluid interfaces. Progr Colloid Polym Sci 103:51–59
51. Góźdź W, Gompper G (1998) Composition-driven shape transformations of membranes of complex topology. Phys Rev Lett 80:4213–4217
52. Voeltz GK, Prinz WA, Shibata Y, Rist JM, Rapoport TA (2006) A class of membrane proteins shaping the tubular endoplasmic reticulum. Cell 124:573–586
53. Sorre B, Callan-Jones A, Manzi J, Goud B, Prost J, Bassereau P, Roux A (2012) Nature of curvature coupling of amphiphysin with membranes depends on its bound density. Proc Natl Acad Sci USA 109:173–179
54. Tlusty T, Safran S, Strey R (2000) Topology, phase instabilities, and wetting of microemulsion networks. Phys Rev Lett 84:1244
55. Park SH (2010) Hereditary spastic paraplegia proteinREEP1, spastin, and atlastin-1 coordinate microtubule interactions with the tubular ER network. J Clin Invest 120:1097–1109
56. Monteleone MC, González Wusener AE, Burdisso JE, Conde C, Cáceres A, Arregui CO (2012) ER-bound protein tyrosine phosphatase PTP1B interacts with Src at the plasma membrane/substrate interface. PLoS One 7:e38948
57. Bian X, Klemm RW, Liu TY, Zhang M, Sun S, Sui X, Liu X, Rapoport TA, Hu J (2001) Structures of the atlastin GTPase provide insight into homotypic fusion of endoplasmic reticulum membranes. Proc Natl Acad Sci USA 108:3976
58. Simunovic M, Voth GA, Callan-Jones A, Bassereau P (2015) When physics takes over: BAR proteins and membrane curvature. Trends Cell Biol 25:780–792
59. Keber F, Loiseau E, Sanchez T, DeCamp S, Giomi L, Bowick M, Marchetti M, Dogic Z, Bausch A (2014) Topology and dynamics of active nematic vesicles. Science 345:1135–1139

Part II
Membranes by the Numbers

Membranes by the Numbers

Rob Phillips

Abstract Many of the most important processes in cells take place on and across membranes. With the rise of an impressive array of powerful quantitative methods for characterizing these membranes, it is an opportune time to reflect on the structure and function of membranes from the point of view of biological numeracy. To that end, in this chapter, I review the quantitative parameters that characterize the mechanical, electrical, and transport properties of membranes and carry out a number of corresponding order-of-magnitude estimates that help us understand the values of those parameters.

Keywords Membrane properties · Fermi problems · Biological numeracy · Membrane shape

1 The Quantitative Membrane Landscape

The pace at which biology is advancing is staggering. Just as there was a short 50 year gap between the invention of manned flight by the Wright Brothers and the beginning of the space age, in the little more than a half century since the discovery of the structure of DNA and its interpretation through the genetic code, the life sciences have entered their own age, sometimes dubbed "the genome age." But there is more to living matter than genomes. While the genome age has unfolded, a second biological revolution has taken place more quietly. This other success story in the emergence of modern biology is the unprecedented and detailed microscopic view of cellular structures that have been garnered as a result of the emergence of new ways to visualize cells. Both electron and optical microscopy have afforded an incredible view of the cellular interior. In addition, the use of techniques for profiling the molecular contents of cells has provided a detailed, quantitative view of the

R. Phillips (✉)
Department of Applied Physics and Division of Biology and Biological Engineering, California Institute of Technology, Pasadena, CA, USA
e-mail: phillips@pboc.caltech.edu

P. Bassereau, P. Sens (eds.), *Physics of Biological Membranes*,
https://doi.org/10.1007/978-3-030-00630-3_3

proteomes and lipidomes of both cells and the viruses that infect them meaning that, in broad brush strokes, we know both what molecular components the cell is made of and how the cellular interior looks. A particularly fertile example that serves as the backdrop for the present chapter is given by our ever-improving understanding of the membrane organization associated with the organelles and plasma membranes of cells of many kinds [1].

The goal of this chapter is to develop a feeling for membranes in the form of biological numeracy. That is, for the many different ways we can think about membranes whether structurally, mechanically, or electrically, we will try to formulate those insights in quantitative terms. The strategy used here is to move back and forth between a data-based presentation in which key quantitative facts about membranes are examined, and a rule of thumb and simple-estimate mentality, in which we attempt to reason out why those numbers take the values they do. For those cases in which we introduce hard data, our device will be to use the so-called BioNumbers ID (BNID) [2]. Some readers will already be familiar with the PMID (Pubmed ID) that links the vast biological literature and databases. Similarly, the BioNumbers database provides a curated source of key numbers from across biology. By simply typing the relevant BNID into your favorite search engine, you will be directed to the BioNumbers website where both the value of the parameter in question will be reported and a detailed description from the primary literature of how that value was obtained. Unfortunately, my presentation is representative rather than encyclopedic. There is much more that could have (and should have) been said about the fascinating question of membrane numeracy. Nevertheless, the hope is that this gentle introduction will inspire readers to undertake a more scholarly investigation of those topics they find especially interesting, while still providing enough quantitative insights to develop intuition about membranes.

There are many conceivable organizational principles for providing biological numeracy for membranes. The strategy to be adopted here is to organize the numbers that characterize membranes along several key axes, starting with their sizes and shapes, turning then to their chemical makeup, followed in turn by some key themes such as the mechanics of membrane deformations, the transport properties of various molecular species across and within membranes, and the electrical properties of membranes. In particular, depending upon the context, there are many different ways of thinking about membranes (see Fig. 1) and each of these different pictures of a membrane has its own set of characteristic parameters. Once these parameters are in hand, we then attempt to make sense of all of these numbers in a section on membrane Fermi problems with the ambition of this section being to give an order-of-magnitude feeling for the numbers that characterize membranes [3, 4]. The notion of a Fermi problem refers to the penchant of Enrico Fermi to find his way to simple numerical estimates for complex phenomena of all kinds in short order. The chapter closes with a look to the future that lays out my views of some of the key challenges that await the next generation of scientists trying to further the cause of membrane numeracy.

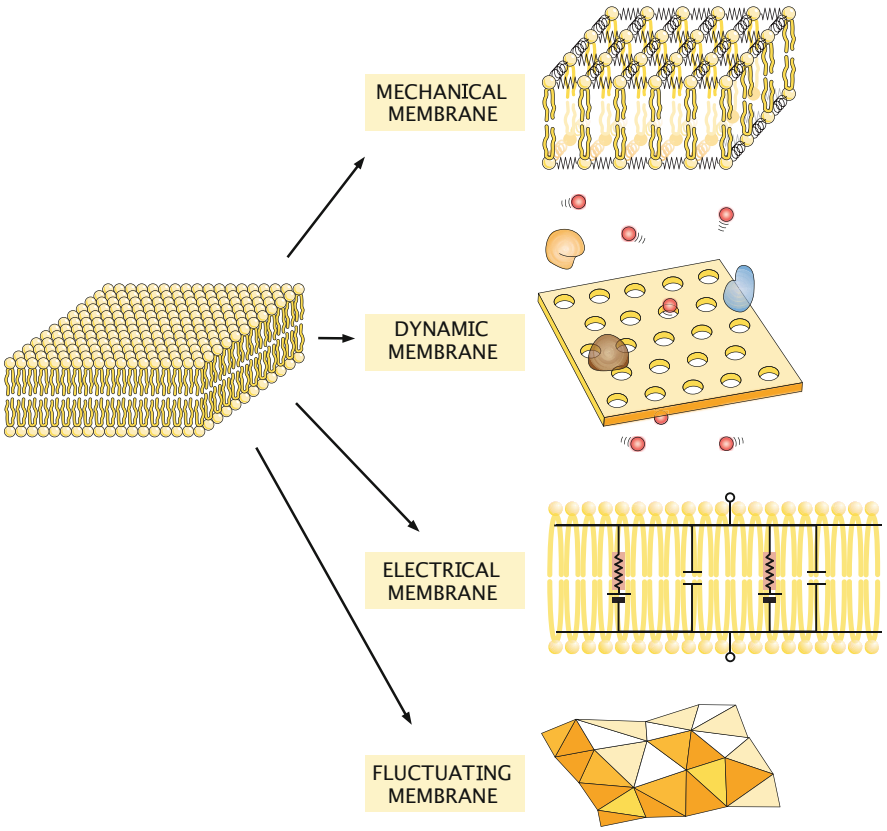

Fig. 1 The many quantitative faces of a membrane. Depending upon the experiments being done or the questions being asked, the way we characterize membranes is different. When thinking about mechanical deformations of a membrane, we will characterize it in terms of elastic constants. Mass transport across and within membranes is described by permeability and diffusion coefficients, respectively. When describing changes in the membrane potential, we characterize the membrane in terms of its conductivity and capacitance. Statistical mechanics teaches us to think about membranes from the standpoint of their fluctuations which interestingly contribute to the membrane tension. Each section of the chapter explores one of these ways of characterizing membranes from the point of view of biological numeracy

2 The Geometrical Membrane: Size and Shape

An inspiring episode from the history of modern science that relates deeply to biological numeracy was the unfolding of our understanding of lipids and the kinds of extended structures they make both in the laboratory and in living cells. In his book "Ben Franklin Stilled the Waves," Charles Tanford gives a charming and insightful tour of this development starting with the efforts of Franklin who was intrigued by the capacity of lipids when spread on water to "still the waves." Indeed,

this fascination led Franklin to a famous experiment in which a spoonful of oil was seen to cover nearly half an acre of Clapham Common near London, giving a first indication of the molecular dimensions of lipids.

Franklin's insights into the structural significance of thin films of lipids led a century later to the emergence of more formal laboratory methods for studying lipid monolayers. In a short 1890 paper on the subject, Lord Rayleigh notes "In view, however, of the great interest which attaches to the determination of molecular magnitudes, the matter seemed well worthy of investigation." To that end, he performed a table-top version of the Franklin experiment concluding that for a film of olive oil he could actually compute the thickness of a monolayer, reporting a lipid length of 1.63 nm [5]. Agnes Pockels in a letter to Lord Rayleigh published in Nature only a year later described her efforts with a trough and force measuring balance to explore surface tension of films on water surfaces [6]. But above all, the study of the "determination of molecular magnitudes" entered a new stage as a result of a tour de force investigation by Irving Langmuir that really gave a first detailed molecular view of lipid molecules and the kinds of collective structures they can form.

Langmuir walks us through his experiments and deep musings about the shape of lipids in his paper entitled "The Constitution and Fundamental Properties of Solids and Liquids. II. Liquids." Here I reproduce a lengthy but interesting series of quotes from that paper, where Langmuir says: "In order to determine the cross-sections and lengths of molecules in oil films, experiments similar to those of Marcelin were undertaken. The oil, or solid fat, was dissolved in freshly distilled benzene, and, by means of a calibrated dropping pipet, one or two drops of the solutions were placed upon a clean water surface in photographic tray. The maximum area covered by the film was measured. Dividing this area by the number of molecules of oil on the surface, the area of water covered by each molecule is readily obtained. The results are given in the first column of Table I." Langmuir's Table I is reproduced here as our own Fig. 2 and shows the impressive outcome of his work, providing not only key numbers but also a much-needed object lesson in the power of indirect experimental methods. He then goes on to tell the reader how he found the lengths of these same molecules noting, "The volume of each molecule is found by dividing the "molecular volume" of the oil (M/ρ) by the Avogadro constant N. By dividing this volume by the cross-section of each molecule, the length of the molecule in a direction perpendicular to the surface can be obtained."

Langmuir then goes on to say: "It is interesting to compare these lengths with the cross-sections. As a rough approximation we may assume that the dimensions of the molecule in directions parallel to the surface can be found by taking the square root of cross-section. This is equivalent to assuming that each molecule in the surface film occupies a volume represented by a square prism with its axis vertical. The length of the square side, which we shall refer to as the average diameter, is given in the second column of Table I, while the height of the prism (or the length of the molecule) is given in the third column." Again, the reader is encouraged to refer to Fig. 2 to see Langmuir's results. He then proceeds telling us "It is seen at once that the molecules are very much elongated. Thus the length of the palmitic

TABLE I.
Preliminary Measurements of Cross-Sections and Lengths of Molecules.

Substance	Formula	I. Cross-section. Sq. cm.	II. $\sqrt{\text{Cross. sec.}}$ Cm.	III. Length. Cm.	IV. Length per carbon atom.
Palmitic acid	$C_{15}H_{31}COOH$	21×10^{-16}	4.6×10^{-8}	24.0×10^{-8}	1.5×10^{-8}
Stearic acid	$C_{17}H_{35}COOH$	22×10^{-16}	4.7×10^{-8}	25.0×10^{-8}	1.39×10^{-8}
Cerotic acid	$C_{25}H_{51}COOH$	25×10^{-16}	5.0×10^{-8}	31.0×10^{-8}	1.20×10^{-8}
Tristearin	$(C_{18}H_{35}O_2)_3C_3H_5$	66×10^{-16}	8.1×10^{-8}	25.0×10^{-8}	1.32×10^{-8}
Oleic acid	$C_{17}H_{33}COOH$	46×10^{-16}	6.8×10^{-8}	11.2×10^{-8}	0.62×10^{-8}
Triolein	$(C_{18}H_{33}O_2)_3C_3H_5$	126×10^{-16}	11.2×10^{-8}	13.0×10^{-8}	0.69×10^{-8}
Trielaidin	$(C_{18}H_{33}O_2)_3C_3H_5$	120×10^{-16}	11.0×10^{-8}	13.6×10^{-8}	0.72×10^{-8}
Cetyl palmitate	$C_{15}H_{31}COOC_{16}H_{33}$	23×10^{-16}	4.8×10^{-8}	41.0×10^{-8}	2.56×10^{-8}
Myricyl alcohol	$C_{30}H_{61}OH$	27×10^{-16}	5.2×10^{-8}	41.0×10^{-8}	2.37×10^{-8}

Fig. 2 Lipid sizes as obtained by Langmuir [7]. This table shows that already a century ago, indirect methods had yielded a quite modern picture of lipid geometry

acid molecule is about 5.2 times the average diameter. The results prove that the molecules arrange themselves on the surface with their long dimension vertical as is required by the theory." [7]. Langmuir went much farther commenting on the significances of the different lengths and areas emboldening him even to think about the role of unsaturated bonds in determining molecular shape. Indeed, one of my favorite aspects of these experiments from Langmuir is that they led him to understand both the number of tails and their degree of saturation truly providing a detailed molecular picture of these molecules. This work went even farther in the hands of Gorter and Grendel who used similar trough experiments to hypothesize that biological membranes are lipid bilayers, a subject we will take up again in the section on "The Electrical Membrane," though I note that there are subtleties about the Gorter and Grendel approach that continue to escape me since in their analysis, they did not account in any way for the fraction of the membrane that is taken up by membrane proteins [8].

What we see from this short historical interlude is that already at the beginning of the twentieth century, long before tools such as X-ray diffraction and nuclear magnetic resonance had made their way onto the scene of modern biological science, scientists had already gleaned a detailed view of the makeup of lipids and started to synthesize a view of how they assemble in cell membranes. The same story already told by experiments using Langmuir troughs has been retold much more accurately on the basis of X-ray and electron microscopy experiments [9, 10]. Indeed, an assessment of the current state of the art for the same kinds of questions originally broached by Langmuir can be seen in Table 1.

The rules of thumb that emerge from a century of study of these molecules is that we should think of lipid masses as being in the range of many hundreds of Daltons up to thousands of Daltons for the largest lipids. The lengths of these lipids vary with tail lengths of ≈2–2.5 nm. The tail-length rule of thumb can be articulated more precisely in terms of the number of carbons in the tail (n_c) as $l_c = n_c l_{cc}$, where the length of a carbon–carbon bond is approximately $l_{cc} \approx 0.13$ nm [11]. The

Table 1 Summary of modern version of measured lipid geometric parameters to be compared to those from Langmuir shown in Fig. 2

Lipid	Area/lipid (nm^2)	Thickness (nm)
DLPE	0.51 ± 0.005	2.58
DOPS	0.65 ± 0.005	3.04
DMPC	0.61 ± 0.005	2.54
DLPC	0.63 ± 0.005	2.09
POPC	0.68 ± 0.015	2.71
diC22:1PC	0.69 ± 0.0005	3.44
DOPC	0.72 ± 0.005	2.68

All values taken from [9]

cross-sectional areas of lipids can be captured by a rule of thumb that the area per lipid is $\approx$0.25–0.75 nm^2. Note that the use of a single cross-sectional area is overly facile because lipids can have much richer shapes than the "square prism with its axis vertical" described by Langmuir. Indeed, because lipids can have shapes more like wedges, this can lead to spontaneous curvature, a topic that we will not delve into more deeply here, but that is critical to understanding the relation between membrane shape and lipid geometry. These rules of thumb are based upon a host of different measurements, with the thickness and area per molecule found here (BNID 101276, 104911, 105298, 105810, 105812). We have traveled a very long way since the days of Langmuir, since we can now order designer lipids with specific chemical properties and even with special groups attached making these lipids fluorescently labeled.

A higher-level view of the structure of cell membranes has been developing on the basis of electron cryo-microscopy which offers an unprecedented view of the very same structural features already explored a century ago using the kinds of indirect methods described above. Figure 3 provides a collage of electron cryo-microscopy images of bacterial cell membranes. We see that in most of these cases, the inner and outer membranes are easily resolved and that they have a thickness of roughly 5 nm (BNID 104911). To be more precise, we should bear in mind that in quoting numbers such as a membrane thickness of 5 nm, of course, we are talking about a characteristic dimension since the interaction of the lipids with the surrounding proteins can induce thickness variations due to the effect of hydrophobic matching of the proteins and lipids [12–14]. Since the bacteria themselves are several microns in length and a bit less than a micron in diameter, we can make a simple estimate of the overall membrane area of the inner and outer membranes by thinking of the bacterium as a spherocylinder with a characteristic volume of 1 $\mu m^3 \approx$ 1 fL and a corresponding surface area of 5–10 μm^2.

The membranes of eukaryotic organisms are typically more heterogeneous and complex than those shown in Fig. 3. Figure 4 gives several examples coming from electron microscopy to make that point. First, such cells, like their prokaryotic counterparts, have an external plasma membrane that separates them from the rest of the world. But as seen in Fig. 4a, even the cell surface can adopt extremely complex geometries as exemplified by the microvilli. One of my favorite examples in all of biology is shown in Fig. 4b where we see the outer segment of a photoreceptor

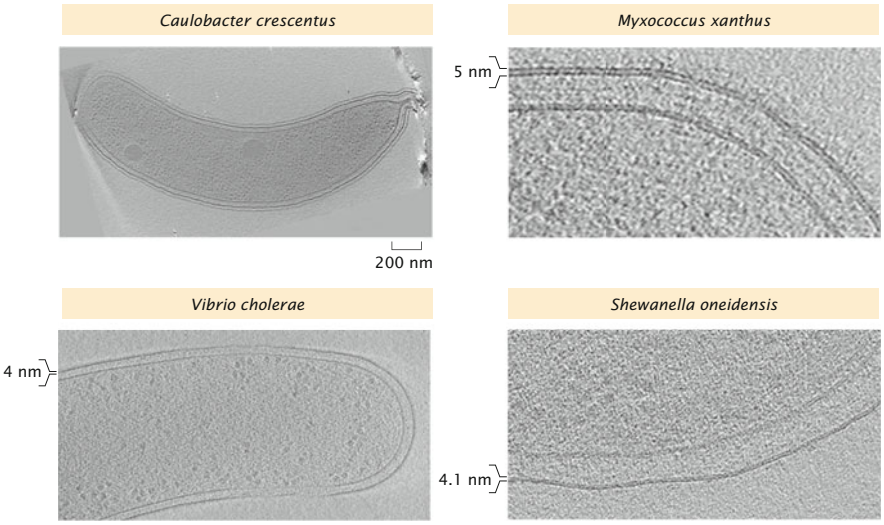

Fig. 3 Electron cryo-microscopy images of bacterial cell walls. The *Caulobacter crescentus* cell gives an impression of overall cell dimensions while the higher-resolution images of other bacteria zoom in on their membranes. Note that these are gram-negative bacteria meaning that their external membrane architecture consists of an inner membrane, a cell wall, and an outer membrane (images courtesy of Grant Jensen and his laboratory members)

with its dense and regular array of membrane stacks. However, it is perhaps the spectacular organellar membranes (see Fig. 4c) that give a sense of the great challenges that remain in understanding membrane shape in cells [15]. Structural complexity similar to that found in the mitochondria abounds in other organelles such as the endoplasmic reticulum [16, 17].

Our brief foray into the size and shape of membranes and the molecules that make them up would of course be woefully incomplete without also commenting briefly on the role proteins play in our modern view of biological membrane structures. Though early ideas about cell membranes painted a picture of a sea of lipids dotted with membrane proteins, the modern view has turned out to be altogether different. "A picture is emerging in which the membrane resembles a cobblestone pavement, with the proteins organized in patches that are surrounded by lipidic rims, rather than icebergs floating in a sea of lipids." [18]. As a rule of thumb, we can think of the protein densities in bacterial membranes as being $\sigma \approx 10^5$ proteins/μm^2. This can be used in turn to estimate the typical center-to-center protein spacing in the cell membrane as $d \approx \sigma^{-\frac{1}{2}} \approx 3\,\text{nm}$, a result that is uncomfortably tight given that typical protein sizes are themselves 3–5 nm as seen in Fig. 5. The question of mean membrane-protein spacing is also of great interest in the context of organellar membranes, with a hint at what can be expected in these cases given by a classic study on synaptic vesicles [18].

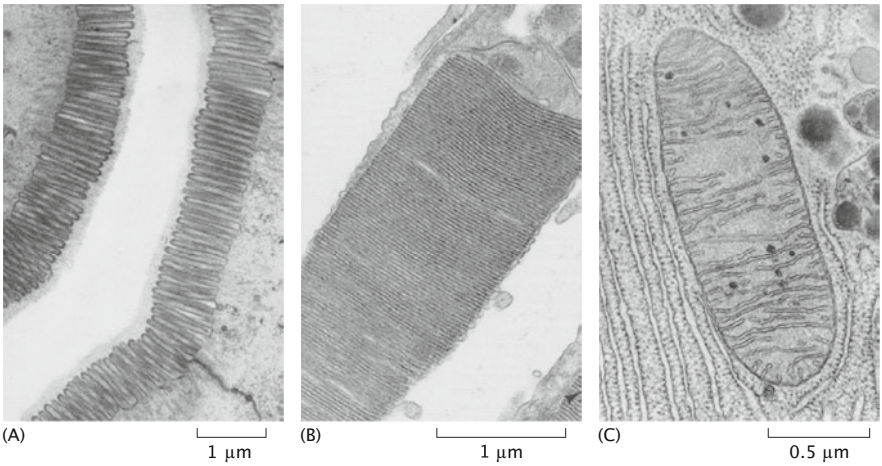

Fig. 4 Eukaryotic membrane structures. (**a**) Apical surface of intestinal epithelial cells showing the dense membrane folds around the microvilli. The sugar chains extending outwards from the surface of the membrane can also be seen as a fuzzy layer above the microvilli. (**b**) Stacks of membranes packed with photoreceptors in the outer segment of a rod cell. (**c**) Thin section of a mitochondrion surrounded by rough endoplasmic reticulum from the pancreas of a bat (all figures adapted from "Physical Biology of the Cell," Garland Press, 2012)

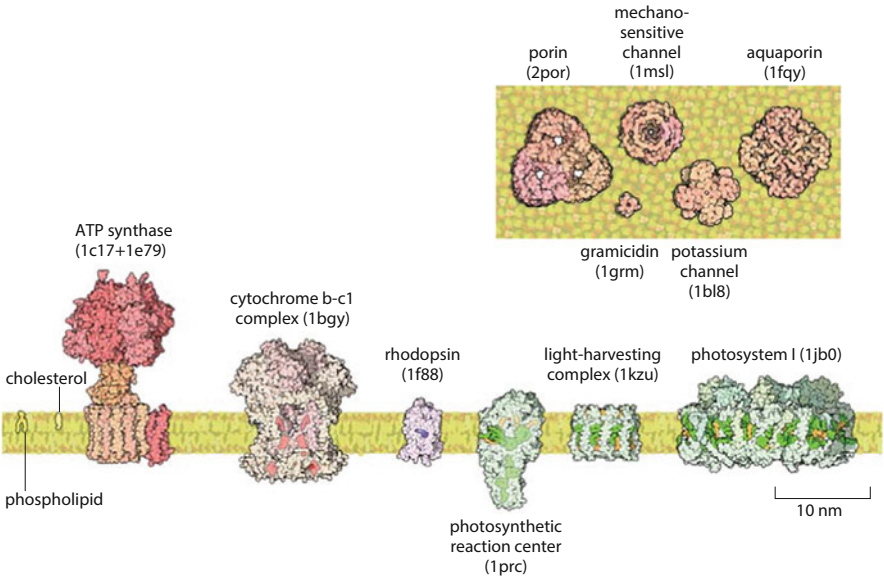

Fig. 5 Sizes and shapes of membrane proteins [19]. Top and side views of several notable membrane proteins. Note the 10 nm scale bar, though the membrane thickness can also be used as a scale marker as indicated in Fig. 3 (images courtesy of David Goodsell and adopted from "Cell Biology by the Numbers", Garland Press, 2015)

3 The Chemical Membrane

With each passing generation, our understanding of the structures of the cell is becoming more and more refined. As shown in the previous section, we have learned a huge amount about the structures of membranes and the molecules that make them up. But what about the specific chemistry of these membranes? One of the ways that our picture of the membranes of living cells has been transformed is through the ability to count up the molecules of different kinds, both the lipids making up the plasma membrane and organelles and of the many proteins that decorate these membranes. In many ways, the development of a census of lipid composition of membranes is an astonishing achievement and has revealed not only that these membranes are heterogeneous, but also that the cell "cares" about its lipid composition [18, 20–28]. Though there is still much left to be understood about precisely how cells keep track of their membrane composition and why they "care," in this section of the chapter we focus on what has been learned thus far about these chemical effects from a quantitative perspective. For a pedagogical review, see chapter 4 of Buehler's interesting book [1].

The same membrane strategy used to separate the interior of cells from the extracellular medium is also used for separating the cellular interior into a collection of membrane-bound organelles such as the nucleus, the endoplasmic reticulum, the Golgi apparatus, and mitochondria. Each of these membrane systems is host to lipids that come in different shapes, sizes, and concentrations. There are hundreds of distinct types of lipid molecules found in these membranes and, interestingly, their composition varies from one organelle to the next. This is highly intriguing since these distinct membrane systems interact directly through intracellular trafficking by vesicles. This same heterogeneity applies to the asymmetric plasma membrane, with different classes of lipids occupying the outer and cytosolic leaflets of the membrane (i.e., the two faces of the lipid bilayer).

Experimentally, the study of lipid diversity is a thorny problem. Sequencing a set of single or double bonds along a carbon backbone requires very different analytic tools than sequencing nucleotides in DNA or amino acids along proteins. Still, the omics revolution has hit the study of lipids too. The use of careful purification methods coupled with mass spectrometry has made inroads into the lipid composition of viral membranes, synaptic vesicles, and organellar and plasma membranes from a number of different cell types. Indeed, the numbers in this section owe their existence in no small measure to the maturing field of lipidomics, based in turn upon impressive advances in mass spectrometry. As noted above, we remain largely in the fact-collection stage of this endeavor since a conceptual framework that allows us to understand in detail the whys and wherefores of lipid compositions and how they change with growth conditions is quite immature.

Perhaps the simplest question we can pose about lipids at the outset is how many there are in a typical cell membrane. A naive estimate for a bacterial cell can be obtained by noting that the area of the bacterial cell membrane is roughly $5\,\mu m^2$, and recalling further that many bacteria have both an inner and outer membrane. To

effect the estimate, we take

$$N_{\text{lipids}} = \frac{4 \times \text{membrane area}}{\text{area per lipid}} \approx \frac{20 \times 10^6 \text{ nm}^2}{1/4 \text{ nm}^2} \approx 8 \times 10^7, \tag{1}$$

where the factor of 4 accounts for the fact that we have two lipid *bilayers* because of the presence of both an inner and outer membrane. This estimate is flawed, however, because we failed to account for the fraction of the membrane area that is taken up by proteins rather than lipids. As was seen in the previous section on size and shape, a useful rule of thumb is that 1/4 of the membrane area is taken up by proteins [20], so our revised estimate of the number of lipids in a cell membrane would be reduced by 25%. Further, note that we used an area per lipid on the low side and if we amended that estimate to a value of $\approx 0.5\,\text{nm}^2$ per lipid, this would also bring our estimate down by a factor of two. Literature values reported for the bacterium *E. coli* claim roughly 2×10^7 lipids per *E. coli* cell, squaring embarrassingly well with our simple estimate, and leaving us with a useful rule of thumb for the lipid density of

$$\sigma \approx \frac{2 \times 10^7 \text{ lipids}}{5\,\mu\text{m}^2 \times 4 \text{ leaflets}} \approx 10^6 \frac{\text{lipids}}{\mu\text{m}^2 \text{ leaflet}}. \tag{2}$$

Given our estimate of 2×10^7 lipids per bacterial cell, we can make a corresponding estimate of the fraction of the cell's dry mass that is lipids [29]. As a basis for comparison, we recall that the number of proteins per bacterial cell is $\approx 3 \times 10^6$ [4, 19, 29]. If these proteins have an average mass of 30,000 Da, this means the total protein mass is roughly 10^{11} Da or 0.15 pg, corresponding to roughly 1/2 of the dry mass of a bacterial cell. For our 2×10^7 lipids, each with a mass of roughly 1000 Da, this means that the lipids contribute an approximate mass of 2×10^{10} Da, corresponding to 20% of the protein mass, or 1/10 of the dry mass of the cell.

What about the composition of membranes? In broad brush strokes, what has been learned in lipidomic studies is that in most mammalian cells, phospholipids account for approximately 60% of total lipids by number and sphingolipids make up another 10%. Non-polar sterol lipids range from 0.1% to 40% depending on cell type and which subcellular compartment is under consideration. The primary tool for such measurements is the mass spectrometer. In the mass spectrometer each molecule is charged and then broken down, such that the masses of its components can be found and from that its overall structure reassembled. Such experiments make it possible to infer both the identities and the number of the different lipid molecules. Absolute quantification is based upon spiking the cellular sample with known amounts of different kinds of lipid standards. One difficulty following these kinds of experiments is the challenge of finding a way to present the data such that it is actually revealing. In particular, in each class of lipids there is wide variety of tail lengths and bond saturations. Figure 6 makes this point by showing the result of a recent detailed study of the phospholipids found in budding yeast. In Fig. 6a, we see the coarse-grained distribution of lipids over the entire class of species of lipids

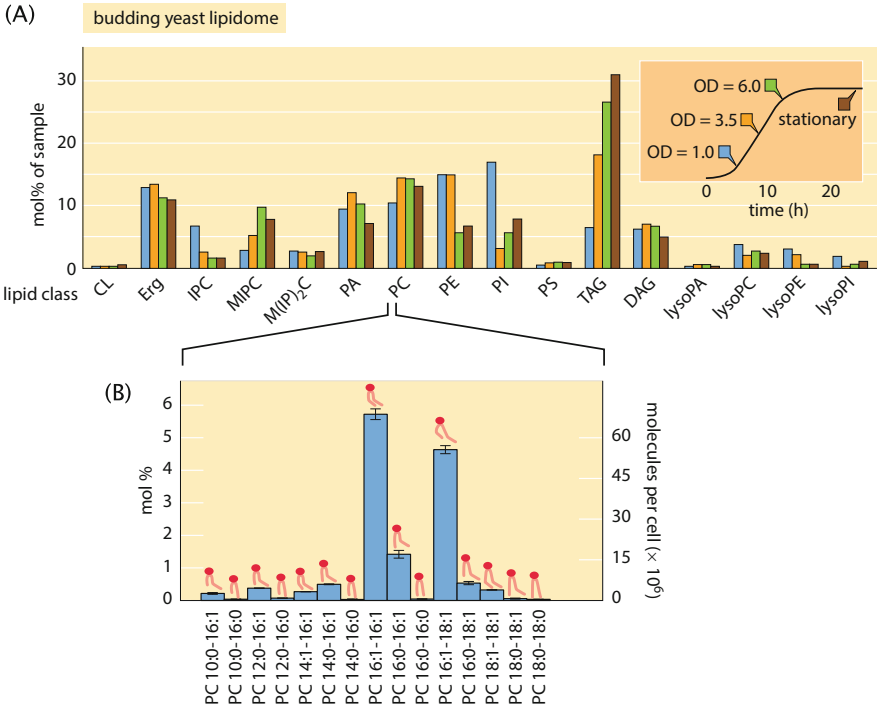

Fig. 6 Lipids in yeast. (**a**) The top panel shows the relative proportions of different types of lipid as a function of the physiological state of the cells as revealed by the inset in the upper right. That inset shows the result of cellular growth as measured by spectrophotometry and leading to the optical density (OD) as a function of time. (**b**) The lower panel shows the diversity of different phospholipids. These lipids exhibit both different tail lengths and degree of saturation as shown by the schematics of the lipids in the lower panel. The abbreviations used in the figure are: *CL* cardiolipin; *Erg* ergosterol; *IPC* inositolphosphorylceramide; *MIPC* mannosyl-inositol phosphorylceramide; *M(IP)2C* mannosyl-di-(inositolphosphoryl) ceramide; *PA* phosphatidic acid; *PC* phosphatidylcholine; *PE* phosphatidyl-ethanolamine; *PI* phosphatidylinositol; *PS* phosphatidylserine; *TAG* triacylglycerols; *DAG* diacylglycerol; *LPC* lysophosphatidylcholine. Adapted from "Cell Biology by the Numbers," Garland Press, 2015. Data in top panel adapted from [27] and data in bottom panel adapted from [22]

found while Fig. 6b gives a more detailed picture of the diversity even within one class of lipids [22]. Studies like the one presented above for yeast have also been done in other eukaryotes as shown in Fig. 7 [21, 30]. Data like this shows that the subject is even more interesting than one might first expect because we see that lipid composition is different for different organelles. As noted earlier, this is especially intriguing given the fact that these different organelles are in dynamical contact as a result of intracellular trafficking, calling for a mechanistic and quantitative description of how these composition heterogeneities are maintained. All of these measurements leave us with much left to understand since as noted at the beginning

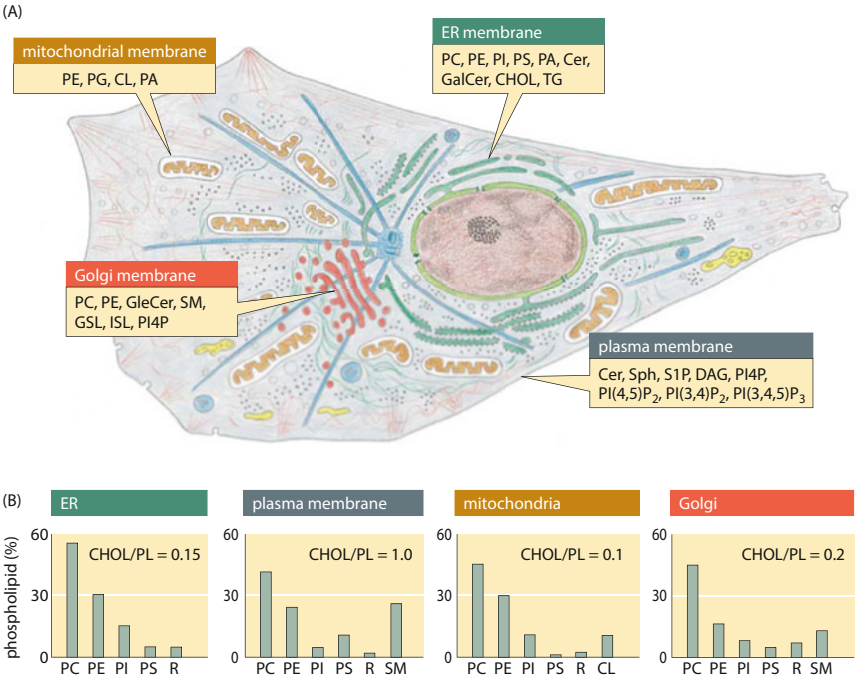

Fig. 7 Organellar lipids in mammalian cells. (**a**) Lipid production is spread across several organelles. The text associated with each organelle shows the site of synthesis for the major lipids. The main organelle for lipid biosynthesis is the endoplasmic reticulum (ER), which produces the bulk of the structural phospholipids and cholesterol. (**b**) The lipid composition of different membranes also varies throughout the cell. The graphs show the composition out of the total phospholipid for each membrane type in a mammalian cell. As a measure of sterol content, the molar ratio of cholesterol to phospholipid is indicated. *SM* sphingomyelin; *R* remaining lipids. For more detailed notation see caption of Fig. 6 (adapted from [21])

of this section, the question of how cells regulate and control their lipid composition and why they care remains unanswered.

4 The Mechanical Membrane

Electron microscopy images make it abundantly clear that whether we think of the stacked membrane discs making up the outer segment of a photoreceptor or the tortuous folds of the endoplasmic reticulum of a pancreatic cell, biological membranes are often severely deformed. But as we all know from everyday experience, changing the shape of materials usually costs energy. As a result of membrane deformations, energetic costs resulting from both membrane stretching and bending are incurred. The aim of this part of the chapter is to give a quantitative

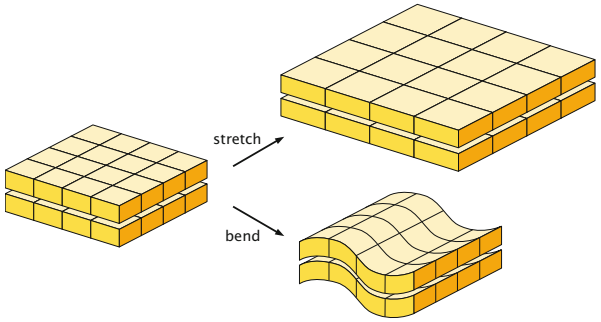

Fig. 8 The mechanics of membrane deformations. One of the deformation modes is changing the membrane area by stretching. The second mode of membrane deformation considered here is membrane bending

view of the energetic cost of these deformations [31]. These two different membrane deformation mechanisms are indicated schematically in Fig. 8.

A natural mechanical question we might imagine starting with is the energetic cost associated with bending the membrane. The free energy cost to deform a tiny patch of membrane is codified in the form of the so-called Helfrich-Canham-Evans free energy [11]. For a tiny patch of membrane with area ΔA_{patch}, the free energy cost to bend it is given by

$$\text{energy to bend a membrane patch} = \frac{\kappa_B}{2}\left(\frac{1}{R_1}+\frac{1}{R_2}\right)^2 \Delta A_{\text{patch}}, \tag{3}$$

where κ_B is the membrane bending rigidity and R_1 and R_2 are the principal radii of curvature of the patch of membrane. Note that the membrane bending rigidity has units of energy since the unit of the factor in parentheses is $1/\text{area}$ which is cancelled by ΔA_{patch} which has units of area. The values of R_1 and R_2 characterize the curvature of the surface at the point of interest. Specifically, if we visit a particular point on the surface, we can capture the curvature by using two orthogonal circles whose radii are chosen so that those two circles most closely follow the shape of the surface at that point. Given the free energy in Eq. (3), we can find the total free energy of a given deformed membrane configuration by adding up the contribution from each little patch as

$$E_{\text{bend}} = \frac{\kappa_B}{2}\int dA \left(\frac{1}{R_1(x,y)}+\frac{1}{R_2(x,y)}\right)^2, \tag{4}$$

where now we acknowledge that the curvature (as measured by R_1 and R_2) is potentially different at each point on the surface. Of course, the scale of this energy is dictated by the bending rigidity κ_B. Our discussion has neglected a second topological contribution to the membrane deformation energy related to the

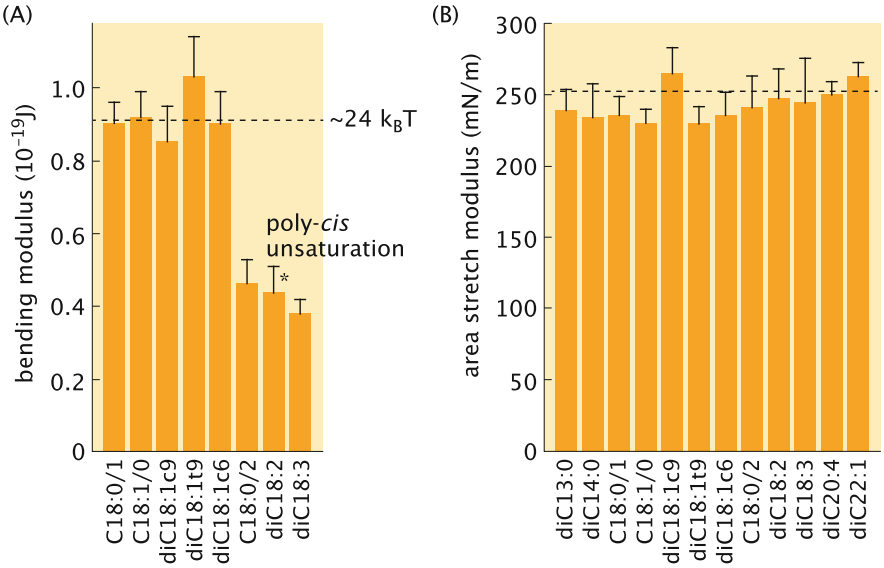

Fig. 9 Elastic moduli characterizing membrane bending and stretching. (**a**) Values for the membrane bending rigidity. Each value corresponds to a different lipid with the values showing a range of tail lengths and tail saturation. (**b**) Values for the area stretch modulus. All values obtained using pipette aspiration experiments [32]

Gaussian curvature, though clearly such terms will be of interest in the context of the topologically rich membrane structures found in cell organelles [11].

A wide range of experiments on a variety of different lipids suggest the rule of thumb that the bending modulus (κ_B) for lipid bilayers is in the range 10–25 k_BT [32, 33]. Characteristic values of the membrane bending rigidity for phospholipid bilayers are shown in Fig. 9a. We will freely use k_BT for our energy units and note the conversion factors $k_BT \approx 4.1$ pN nm $\approx 4.1 \times 10^{-21}$ J. The presence of sterols in lipid bilayers can increase those numbers to $\approx 100\, k_BT$ [34]. Interestingly, even measurements on biological membranes derived from the ER and Golgi apparatus report a membrane rigidity of $\kappa_B \approx 3 \times 10^{-19}$ J $\approx 75\, k_BT$ (BNID 110851), only a factor of three larger than the values for phospholipid bilayers reported in Fig. 9a [35, 36].

Another important question we can ask about membrane deformations is the energy cost for changing the area of the membrane as seen in Fig. 8. When we stretch a membrane away from its equilibrium area, a consequence is the development of a tension in that membrane. One way to understand the magnitude of membrane tensions is by appealing to a so-called constitutive equation which loosely speaking relates force and membrane geometry. In particular, the mechanics of membrane stretching is often described by the constitutive equation

$$\tau = K_A \frac{\Delta A}{A_0}, \tag{5}$$

where K_A is the area stretch modulus and ΔA is the area change. To figure out the tension, we compute the change in area, normalize by the total unstressed area A_0, and then multiply by the modulus K_A. In general, when we change the area of a patch of membrane by some amount ΔA, the corresponding free energy cost can be written as

$$\text{stretching energy} = \frac{K_A}{2}\left(\frac{\Delta A}{A_0}\right)^2 A_{\text{patch}}, \tag{6}$$

where note that the units of the area stretch modulus K_A are energy/area. Several examples of the values adopted by the area stretch modulus are shown in Fig. 9b, which gives the interesting insight that for a range of tail lengths and degrees of saturation, the area stretch modulus is nearly constant.

The actual magnitudes of the tensions in the membranes of both vesicles and cells can vary over a wide range and even the underlying mechanistic origins of these tensions are different depending upon what regime of tension we are considering. Interestingly, the energetics of area change is a subtle one in the same way as the energetics of stretching a polymer like DNA is. Specifically, let's remind ourselves of the subtleties associated with DNA stretching as a prelude to thinking about membrane stretching [4, 11]. In the "force free" state, DNA will be folded up and compact since such states have lower free energy in part because the entropy of the compact conformation is higher. To stretch DNA, the free energy cost can be thought of as being almost entirely entropic, meaning that with increasing stretch, there are fewer and fewer configurations available to the DNA and hence the entropy *decreases*, resulting in a net increase in free energy. It is only when the DNA is stretched to its full contour length that we enter a different regime that actually involves molecular bond stretching. Because the mechanisms in these regimes are different, it should not surprise us that they are actually characterized by different mechanical stiffnesses. Similar intuition emerges for the membrane case.

By analogy with polymer stretching, we can think of the energetic cost associated with membrane deformations in much the same way. That is, for a floppy (low tension) membrane, stretching the membrane has an associated free energy cost that results from "pulling out the wrinkles," and is effectively entropic [11]. At higher tensions, the actual bond stretching effect intervenes. Though very few systematic insights have been obtained for thinking about the membranes within cells, a series of rigorous, systematic studies in lipid bilayers have set the standard in the field [32]. At even higher tensions, lipid bilayer membranes will actually rupture with the rupture tensions occurring between 5 and 10 mN/m depending upon the type of lipids in question [37].

Though there are fewer systematic measurements for cellular membranes, some clever experiments have shed light on this topic as well. The tension measured in ER membrane networks has a value of 1.3×10^{-2} mN/m while that measured in the Golgi membrane is given by 0.5×10^{-2} mN/m [38]. These numbers are quite small as can be seen by comparing them to the membrane rupture tension which is a thousand times larger with a range of 5–10 mN/m as noted above [37]. Note

also that the subject of membrane tension is a tricky one in the cellular setting because measured tensions have many contributions including from the underlying cytoskeleton and the battery of molecular motors associated with it [39]. There is an excellent review featuring both a clear discussion of the different methods and the range of measured tensions [40]. Table 1 of that review includes an exhaustive listing of measured membrane tensions as well as the caveats associated with each such measurement.

5 The Dynamic Membrane

Perhaps the defining feature of biological membranes is that they serve as barriers between some compartment of interest (the cytoplasm, the Golgi apparatus, the nucleus, the endoplasmic reticulum, etc.) and the rest of the world. The very word "barrier" points toward underlying molecular rules that determine the rate at which molecules cross through or move within membranes, and thereby regulate how a cell distinguishes itself from the environment. In this section, we begin by exploring the permeability of biological membranes to various molecular species. After that, we then turn to the diffusive properties of molecules within the membrane.

One of the key ways we characterize membrane permeability is to ask the question of how many molecules cross a given area of membrane each second, a quantity defined as the flux, j. In particular if we have a difference in concentration of some species across the membrane given by Δc, then in the simplest model the flux is given by

$$j = -p\Delta c, \tag{7}$$

where the parameter p is the permeability of interest here. Note that a more rigorous treatment of the flux invokes the chemical potential difference across the membrane, though for our purposes this simple linearization suffices [41, 42]. The units of the permeability can be deduced by noting first that the units of j are

$$\text{units of } j = \frac{\text{number of molecules}}{L^2 T}. \tag{8}$$

Here we adopt the standard strategy when examining units of physical quantities of using the symbol L to signify units of length and T to signify the units of time [43]. Given these conventions, the units of concentration are

$$\text{units of } c = \frac{\text{number of molecules}}{L^3}. \tag{9}$$

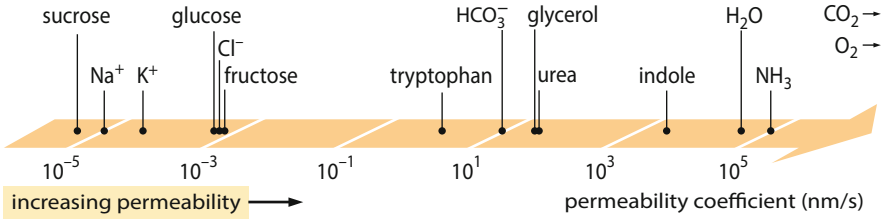

Fig. 10 Range of membrane permeabilities. Permeability coefficients for a number of different lipid species showing the huge dynamic range in permeability

The requirement that the units on the two sides of the equation balance implies that the units of the permeability itself are

$$\text{units of } p = \frac{\frac{\text{number of molecules}}{L^2 T}}{\frac{\text{number of molecules}}{L^3}} = \frac{L}{T}. \tag{10}$$

In the remainder of the paper, we will report units of permeability in nm/s, though often one finds values reported in cm/s as well.

The first and probably most important thing we should say about the numerical values adopted by membrane permeability is that there is no such thing as *the* membrane permeability. That is, the rate at which molecules pass across membranes is an extremely sensitive function of which molecules we are discussing as well as the type of molecules making up the membrane itself [10, 37, 44]. Figure 10 makes this point clear by reporting the range of values for permeability for a number of different molecular species revealing a more than 10-order-of-magnitude range of permeabilities, with the membrane being effectively impermeable to ions such as Na^+ and K^+, while for water molecules, the permeability is ten orders of magnitude larger. Though this doesn't rival the 30 order-of-magnitude range that is found for electrical conductivities of different materials, these numbers still imply a huge difference in the transport properties of different molecules across membranes.

How are such permeabilities measured? One approach to measuring these membrane permeabilities is the use of radioactive tracer molecules. By setting up a membrane separating two aqueous regions with different compositions, one can measure the accumulation of the tracer in one region as a result of flux from the other region over time [44]. A second important set of measurements for water permeability were performed using giant unilamellar vesicles using the so-called micropipette aspiration method where an osmotic pressure is applied across the membrane and the resulting flux of water across the membrane is measured. Here the idea is that a pipette with a characteristic diameter of several microns is used to grab onto a vesicle with a diameter of roughly 10 µm or larger. By applying a suction pressure, the tension of the vesicle can be monitored. Further, by using video microscopy, the volume of the vesicle can be carefully monitored, giving a sense of

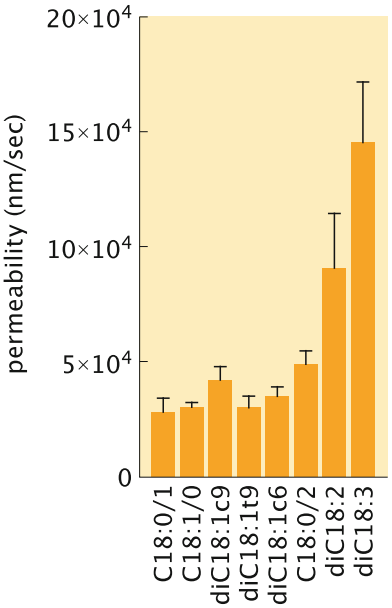

Fig. 11 Range of membrane permeabilities for water. Measurements made at 21 °C using the micropipette aspiration technique in conjunction with video microscopy to monitor vesicle size [37]

the rate at which the vesicle is inflated as a result of mass transport of water across the membrane. The results of such measurements for a set of different lipid types are shown in Fig. 11, with values entirely consistent with those shown schematically in Fig. 10.

The classic work of Hodgkin and Huxley offered many important insights. To my mind, one of the most interesting arguments that they made is a testament to the role of clear theoretical (and quantitative) thinking in biology. In particular, they argued that the membrane permeability to ions such as Na^+ and K^+ must change transiently and substantially to permit key ions across the otherwise impermeable membrane (see Fig. 10 to get a sense of the extremely low permeability of charged ions). Specifically, they introduced a highly nonlinear permeability response that suggested that there must be molecules in the membrane of the cell that could selectively change the permeability in response to changes in driving forces such as the membrane potential, effectively hypothesizing the existence of ion channels before they were known.

We now know that biological membranes are littered with batteries of different channels and pumps whose job it is to transiently alter the permeability of the membrane or to actively transport molecular species across it. These membrane proteins are responsible for many physiologically important functions including the transport of ions and sugars such as glucose and lactose that are critical to the cellular economy. Ions typically pass across ion channels at rates between 10^7 and 10^9 ions per second, though of course this rate depends upon the concentration difference across the membrane itself (BNID 103163,103164). Glucose transporters have a much lower characteristic rate of several hundred sugars per second (BNID

102931, 103160) while bacterial lactose transporters have a characteristic rate of 20–50 sugars per second (BNID 103159). Though here we report on the rates associated with several well-known membrane proteins, more generally, the rates at which the various membrane proteins that are responsible for transport operate are not that well known, with a dearth of modern data spanning the range of different membrane transporters (BNID 103160) [45].

A second kind of membrane dynamics different from the transport *across* the membrane described above is diffusion of molecules laterally within the membrane. As already noted throughout the chapter, the membrane is a highly heterogeneous composite of lipids and proteins and when thinking about the diffusive dynamics within the membrane, we need to do so on a molecule-by-molecule basis. Since we are thinking about membranes, the first class of molecules we might be interested in characterizing are the lipids themselves [46–50]. For example, in eukaryotic cell membranes, by using the clever method of fluorescence-recovery-after-photobleaching (FRAP), a lipid diffusion constant of 0.9 $\mu m^2/s$ was measured [46]. This diffusion constant is roughly tenfold lower than the values that would be found in a model lipid bilayer membrane [51]. More recent measurements confirm these classic numbers (see Figure 4 of Ref. [50], for example).

It is of great interest to characterize the in-plane diffusion not only of the lipids themselves, but also of the proteins that populate those membranes. Figure 12 gives examples of membrane diffusion constants for several different membrane

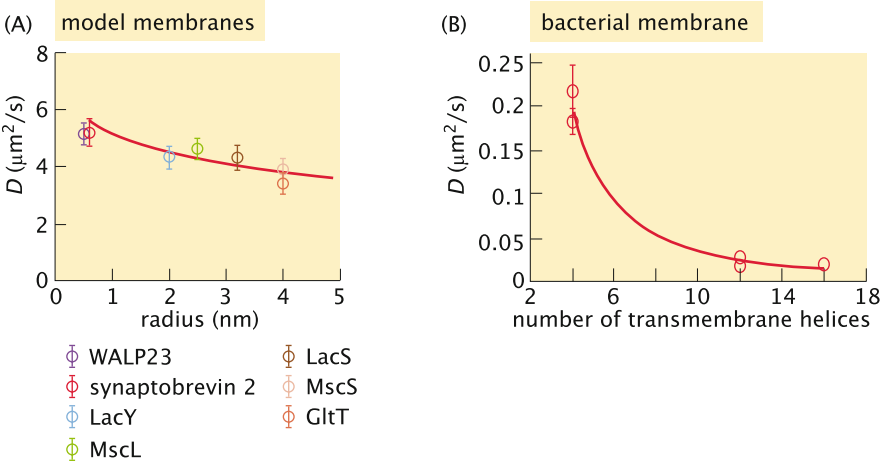

Fig. 12 Range of diffusion coefficients. (**a**) Diffusion coefficients for different membrane proteins measured using fluorescence correlation spectroscopy in giant unilamellar vesicles showing dependence on protein size. The red line is a fit using the Saffman-Delbrück model which characterizes membrane diffusion as a function of the size of the diffusing molecule [52, 53]. (**b**) Diffusion coefficients for different membrane proteins measured using fluorescence recovery after photobleaching (FRAP) in the *E. coli* cell membrane. The red line is an empirical fit as a function of the number of transmembrane helices in the protein. The names refer to particular membrane proteins used in the experiments. (**a**) adapted from [54] and (**b**) adapted from [55]

proteins. Further, we need to acknowledge the large differences in lateral diffusion coefficients between model membranes such as are found in giant unilamellar vesicles where the values of diffusion coefficients for membrane proteins are 1–10 $\mu m^2/s$ [54] and those in native membranes where membrane proteins are characterized by diffusion coefficients that are several of orders of magnitude lower with values of 0.01–0.1 $\mu m^2/s$ [50, 55–57]. However, these measurements are more nuanced than first meets the eye and the results for several membrane proteins have been shown to depend upon the timescales over which the diffusion is characterized [56]. In particular, using the FCS method which probes diffusion on short length and timescales, both the TAR receptor and TetA (a tetracycline antiporter) were found to have diffusion constants of 4.2 and 9.1 $\mu m^2/s$, respectively, to be contrasted with the values of 0.017 and 0.086 $\mu m^2/s$, respectively, found when using the FRAP measurement. Indeed, as we will note in the final section of the chapter, the question of how best to move from biological numeracy in model membranes to biological membranes with their full complexity is one of the key challenges of the coming years of membrane research.

6 The Electrical Membrane

A membrane has many different properties as shown in Fig. 1. So far, our picture of membranes has focused on their mechanical and transport properties. However, our discussion of action potentials and the pathbreaking work of Hodgkin and Huxley already hinted at the view that membranes can also be thought of as circuit elements. Specifically, part of this chapter's very business is to illustrate some of the different *abstract* ways of describing membranes and what *effective* parameters to attribute to them. We now jettison the view of a membrane as a mechanical object, instead focusing on it as a collection of resistors and capacitors as shown in one of the panels of Fig. 1.

The picture already developed under the heading of the "Electrical Membrane" in Fig. 1 tells us that in the presence of an electric potential, a lipid bilayer behaves as an array of resistors and capacitors in parallel. One way to measure the electrical conductance across a membrane patch is to form a lipid bilayer membrane across a hole separating two solutions. Then, different voltages are applied across the membrane and the current–voltage characteristics are measured, with the membrane conductance then determined by using the slope of these current–voltage curves. In our discussion of the electrical membrane we characterize electrical properties on a per unit area of membrane basis. For the conductance, a series of measurements like those described above for a number of different charged species result in a range of values for the bare membrane conductance of roughly 1–5 nS/cm^2 [58, 59]. To get a sense of how small the membrane conductance is, note that if we consider a characteristic conductance of 1 nS for an ion channel such as the mechanosensitive channels found in bacteria [60], if we normalize by the area this means that the

channel conductance is more than ten orders of magnitude larger than that of the membrane itself.

But membranes have more electrical properties than their conductance alone [4]. Capacitance is a measure of the ability of a circuit element to store charge. A local disruption of charge neutrality is permitted near surfaces. In particular, in this setting, the capacitance is defined as the ratio of the excess charge on either side of the membrane and the membrane potential, $C = q/V_{mem}$. The capacitance of a patch of the cell membrane can be approximated by thinking of it as a parallel plate capacitor. The charge on the capacitor plates is $\pm\sigma A_{\text{patch}}$, where σ is the excess charge per unit area of membrane, and A_{patch} is the area. The electric field inside a parallel plate capacitor is uniform and equal to $\sigma/(\varepsilon_0 D)$, where D is the dielectric constant of the material between the plates. Therefore the potential drop across the membrane is $V_{mem} = \sigma d/\varepsilon_0 D$, where d is the thickness of the membrane, or the distance between the plates of the parallel plate capacitor. Dividing the charge by the membrane voltage leads to the formula, $C = \varepsilon_0 D A_{\text{patch}}/d$, for the capacitance of a patch of membrane. Since the cell membrane has a thickness of $d \approx 5\,\text{nm}$ and a dielectric constant $D_{mem} = 2$, its capacitance is predicted to be $C_{\text{area}} = C/A_{\text{patch}} \approx 0.4\,\mu\text{F/cm}^2$. The typical measured value for the capacitance per unit area in cell membranes is $C_{\text{area}} = 1\,\mu\text{F/cm}^2$ [61–63].

We have already discussed the century long quest to understand the size of lipid molecules and the membranes they make up. We learned that one branch of these investigations passed through the enormously impressive work of Pockels, Rayleigh, and Langmuir. Amazingly, a completely independent line of enquiry in the hands of Fricke related to the electrical properties of membranes led to nearly the same result [61]. Using these ideas, we can recast the measured value of the membrane capacitance as a result for the membrane thickness as

$$d = \frac{\epsilon}{(C/A)} = \frac{2\epsilon_0}{(C/A)} \approx \frac{2 \times 8.8 \times 10^{-12}\,\text{F/m}}{0.4 \times 10^{-2}\,\text{F/m}^2} \approx 4\,\text{nm}, \tag{11}$$

a beautiful result astonishingly close to the value obtained using the equation of state of monolayers by Pockels, Rayleigh, and Langmuir. Note that to obtain this result, we rewrote the conventional membrane capacitance of $0.4\,\mu\text{F/cm}^2$ in the more appropriate SI units as $0.4 \times 10^{-2}\,\text{F/m}^2$. Further, whereas Frick used a relative dielectric constant of 3, the estimate used here is based upon the value of 2. In light of the measurement of the membrane capacitance, scientists such as Fricke realized that this would provide yet another sanity check on the membrane thickness [61]. In this era where many scientists seem almost to have scorn for the idea of figuring things out without seeing them directly, the determination of the thickness of lipid bilayers long before the advent of direct techniques such as electron microscopy should give readers pause before casually dismissing results that come from indirect measurements.

7 The Fermi Membrane: Thinking Up Membranes

So far, this chapter has been an ode to biological numeracy in the context of membranes, showing us the many different ways in which we can quantitatively describe our hard-earned understanding of these fascinating structures. These numbers are summarized in Table 2. But in the abstract, such numbers are often boring and sometimes useless, or worse yet, misleading. To my mind, numbers that characterize the world around us are only really interesting when put in the context of some argument or reflection. For example, we know that if we drop an object near the surface of the Earth, in the first second, it will fall roughly 5 m. So what? In the powerful hands of Newton, this innocuous number became part of his inference of the law of universal gravitation. There is a direct intellectual line from a knowledge of the radius of the Earth and the distance to the moon to Newton's estimate leading him to further trust the idea that the force of gravity falls off as the square of the distance. In that case, he realized that the distance to the moon is roughly 60 times larger than the radius of the Earth, meaning that the acceleration of the moon as it "falls" toward the center of the Earth should be $(60)^2 = 3600$ times smaller than that associated with that apocryphal apple falling from Newton's tree. To finish off his estimate, he asked the question of how far the moon falls compared to how far the apple falls when watched for the same time and found them to "answer pretty nearly," with the moon falling roughly 1/3600 as much in 1 s as the 5 m a falling

Table 2 Membranes by the numbers

Membrane parameter	Range of parameter values	BNID
Lipid length	≈2.5–3.5 nm	See Table 1
Lipid area	≈1/4–3/4 nm^2	See Table 1
Number of lipids per cell (bacterium)	$\approx 2 \times 10^7$	100071
Bending rigidity	10–25 $k_B T$	105297
Area stretch modulus	200–250 mN/m (or $\approx 50\, k_B T/\text{nm}^2$)	112590, 112659
Membrane tension	$10^{-4} - 1\, k_B T/\text{nm}^2$	110849,112509, 112519
Rupture tension	1–2 $k_B T/\text{nm}^2$	112489, 110911
Membrane permeability (water)	10–50 μm/s	112488
Membrane capacitance	≈1 $\mu\text{F/cm}^2$	110759, 109244, 110802
Membrane resistance	$0.1\text{–}1.5 \times 10^9\ \Omega\,\text{cm}^2$	110802
Membrane potential	100 mV	109775, 107759
Diffusion constant (lipid)	≈1 $\mu\text{m}^2/\text{s}$	112471, 112472
Diffusion constant (membrane protein)	≈0.02–0.2 $\mu\text{m}^2/\text{s}$	107986

A summary of the key numbers about membranes discussed throughout the chapter for easy reference. Numbers reported are "typical" values and should be used as a rule of thumb. For a more detailed description of parameter values, the reader should use the Bionumbers database through the relevant BNID. Also see Box 1 of [14]

body at the surface of the Earth falls in that same time interval. But what does this have to do with our quantitative musings on membranes? To my mind, it illustrates how powerful simple numerical arguments can sometimes be to help us see whether our way of thinking is consonant with the known facts about a system.

Inspired by the long tradition of simple estimates when faced with numerical magnitudes to describe the world around us, we now examine the ways in which the numbers presented throughout the chapter can help us to better understand membranes and the biological processes that take place at them. Indeed, we are inspired by the notion of the so-called Fermi problems introduced at the beginning of the chapter where the goal is to try to develop simple numerical estimates for various quantities of interest by pure thought. Not only does the Fermi approach allow us to estimate key magnitudes, but even more importantly, it is one of the most powerful ways I know to make sure that the stories we tell about our data actually make sense. In this section, we ask ourselves whether we can understand some of the numerical values reported throughout this chapter as well as what key scaling results we should bear in mind when thinking about membranes. We pass through each of the sections of the chapter in turn, each time taking the opportunity to reflect on the numbers we have seen.

Size and Shape Redux In the first part of the chapter, we considered different ways of characterizing the size and shapes of membranes and the molecules that make them up. This led us to the fascinating experiments of Langmuir that used the relationship between tension and area as a way of determining the size and shape of lipids. Here, our aim is to use order-of-magnitude thinking to try and put those numbers in perspective. As an example from everyday life where a simple numerical estimate of the Fermi type can help us build intuition by giving us a sense of the relative sizes of membranes and the cells they envelop, we consider the fuselage of an airplane. One of the most popular tourist destinations in Seattle is the factory of Boeing where one can see giant airplanes such as the 747, 777 and 787 in the process of assembly. As part of that tour one is treated to the view of a cross-section of a 747 fuselage which gives a sense of just how thin the skin of an airplane really is. For the perceptive flyer, this same observation can be made upon entering the plane by looking at the fuselage near the door. What one notices is that the exterior shell of the plane is less than a centimeter thick while the overall diameter of that very same fuselage is roughly 5 m, resulting in an aspect ratio of 1:500. Interestingly, the aspect ratio of cell membrane width to cell size is quite comparable to those of an airplane fuselage. For a 2 micron cell size, typical of a bacterium, the 4 nm thickness of its cell membrane implies a similar aspect ratio of 1:500.

Concentrations The section on concentrations reminded us that cell membranes are made up of molecules and that even in tiny bacterial cells, there are tens of millions of such molecules of hundreds of different types. A very simple order-of-magnitude result that emerges from these numbers is a naive estimate of the rates of lipid synthesis. Specifically, if the membrane area has to double during the cell cycle, this tells us that the number of lipids in the cell membrane has to double. For a bacterium such as *E. coli*, this means that if a typical bacterium has 2×10^7 lipids

and the cell cycle is roughly 2000 s, then the rate of lipid synthesis is roughly

$$\text{bacterial lipid synthesis rate} = \frac{\text{number of lipids}}{\text{cell cycle time}} \approx \frac{2 \times 10^7 \text{ lipids}}{2 \times 10^3 \text{ s}} \approx 10^4 \text{ lipids/s}. \tag{12}$$

It is deeply interesting to think of how the many different types of lipids are each synthesized with the correct rates to maintain the overall concentration distribution.

Another critical concern in our discussion of the chemistry of membranes was how to think about the relative abundance of lipids and proteins. One of the interesting ways to broach this question is through reference to the fraction of genomes that is devoted to membrane proteins. We can examine this question both from a genomic point of view and from a proteomic point of view. Scientists have become increasingly adept at reading genomes and as a result, by recognizing features such as transmembrane alpha helices, it is possible to estimate the fraction of proteins that are membrane proteins with a rule of thumb being that roughly 1/4 of the protein coding genes correspond to membrane proteins [64]. From a proteomic point of view, this question can be addressed by asking what are the copy numbers of these different membrane proteins. Given that a bacterium such as *E. coli* has several million proteins in total, what fraction of those proteins are in the membrane? To give a feeling for the answer to that question, we ask about the copy numbers of some key membrane proteins. Specifically, we consider membrane transporters, components of the ATP synthesis machinery, and the receptors of chemotaxis to give an idea of the molecular census for some of the most important classes of membrane proteins. Transport of sugars across the cell membrane is one of the most critical activities of growing bacteria. Recent ribosome profiling measurements and mass spectrometry measurements tell us that the number of copies of sugar transporters for glucose (ptsI proteins, a component of the phosphoenolpyruvate-dependent sugar phosphotransferase system) has a copy number of between roughly 3000 copies per cell and 15,000 copies per cell depending upon the growth conditions [65, 66]. We examine the relevance of these numbers in the context of membrane dynamics below. ATP synthase is one of the most important of membrane protein components in almost all cell types. In *E. coli* the ATP synthase complex is built up of many different subunits. For those subunits that come with a stoichiometry of one molecule per complex, their copy number ranges between 3000 and 10,000 copies per cell [65, 66]. Knowing these numbers provides a powerful sanity check on the rate of ATP production per cell since with roughly 3000 such synthases, each rotating at about 300 turns per second (BNID 104890), this means that over a cell cycle of 2000 s, on the order of 10^9 ATPs will be generated, comparable to the number needed to run the cellular economy [4, 19]. Finally, for the chemotaxis receptors such as Tar and Tsr, the copy numbers can be as low as several thousand and as high as nearly 40,000 per cell (BNID 100182) [67, 68]. These numbers give us a sense that if roughly 1000 of the 4000 or so *E. coli* proteins are membrane proteins and each comes with a copy number of roughly 1000, then a first simple

estimate is that there are a total of 10^6 membrane proteins distributed across the inner and outer membranes of these cells.

Membrane Mechanics Our section on membrane mechanics gave us a basis for thinking about many key processes that take place in cell biology. One such example that begins to shed light on the free energy demands associated with sculpting membranes into different shapes is that of membrane vesicles. From the standpoint of the energetic description given in Eq. (4), we can make a simple estimate of the free energy cost required to create spherical vesicles such as those found at synapses. Since for a sphere the two radii of curvature are equal and have a value R and the total area of each such sphere is $4\pi R^2$, Eq. (3) instructs us to sum up

$$E_{\text{vesicle}} = \frac{\kappa_B}{2}\left(\frac{1}{R} + \frac{1}{R}\right)^2 A_{\text{sphere}} = \frac{\kappa_B}{2}\frac{4}{R^2}4\pi R^2. \tag{13}$$

This implies the fascinating and for many people, counterintuitive result, that the energetic cost for vesicle formation due to membrane bending is $E_{\text{vesicle}} = 8\pi\kappa_B \approx 250\text{–}500\, k_{\text{B}}T$, completely independent of the size of the vesicle.

A second example from membrane mechanics is to try to estimate the strain suffered by a membrane at the time of rupture. To estimate this magnitude, we can use

$$\tau_{rupture} = K_A \frac{\Delta A_{rupture}}{A}, \tag{14}$$

where the subscript *rupture* indicates the value of the parameter at rupture. If we use the values provided in Table 2, we can estimate the rupture strain as

$$\frac{\Delta A_{rupture}}{A} = \frac{\tau_{rupture}}{K_A} \approx \frac{5\,\text{mN/m}}{200\,\text{mN/m}} \approx 2.5\%. \tag{15}$$

Often people are surprised by how small the rupture strains really are since we have an impression that lipid bilayers are floppy, squishy, and highly deformable materials.

Membrane Dynamics In the section on the dynamic membrane, we considered the permeability of membranes to various molecular species. One simple estimate that we can do to get a sense of the meaning of the permeability is to ask how many molecules cross the cell membrane each second given some concentration difference. Given the concept provided in Eq. (7), we can estimate

$$\frac{dN}{dt} = j \times A, \tag{16}$$

Given a typical membrane permeability for water of order $p \approx 100\,\mu\text{m/s}$ and considering a typical concentration difference of salt across the cell membrane when

cells are subjected to an osmotic shock of order 100 mM $\approx 10^8$ molecules/μm^3, [69] for example, we can make the simple estimate that

$$j \times A = p\Delta cA \approx 100\,\mu m/s \times 10^8/\mu m^3 \times 5\,\mu m^2 \approx 5 \times 10^{10}\,s^{-1}. \tag{17}$$

These numbers are interesting to contrast with the rate of transport of molecules across ion channels. Specifically, given the conductivity of a channel such as the mechanosensitive channel of large conductance (MscL), we find that the opening of a single channel yields a flow rate of several molecules per nanosecond, quite comparable to the flow rate of water across the membrane itself [60, 70].

One of the most interesting estimates concerning membrane dynamics that we can consider focuses on the mass and energy economy of a cell. To this day, I still marvel at the fact that one can take 5 mL of liquid containing some salts and sugars, inoculate that solution with a single bacterium, and 12 h later one will find as many as 10^9 cells per mL of solution. Effectively, what has happened is that the molecules in the medium have been taken up by that bacterium, used to construct building materials and energetic molecules such as ATP and then used them to construct a new cell. This process repeats over and over again every 20 or so minutes. These observations raise an obvious Fermi question: is the rate of membrane transport of sugar molecules, for example, fast enough to keep up with the needs of the cell to reproduce [19]. To approach that question, we consider the flux of sugar across the membrane using the numbers presented above, namely that there are 3000–15,000 sugar transporters per cell, each of which is able to take up sugars at a rate of several hundred sugars/sec (BNID 102931, 103160, 100736). We can get a feeling for the number of sugars taken up per cell cycle as

$$\begin{aligned}\text{flux of sugar} &= (10^4 \text{ transporters}) \times (300 \text{ sugars/transporter sec}) \times (2 \times 10^3 \text{ s}) \\ &\approx 6 \times 10^9 \text{ sugars}.\end{aligned} \tag{18}$$

This number is of the right order, though probably on the low side of what is needed to power the cellular economy and raises interesting questions about possible rate-limiting steps in cellular growth [4, 19].

Just as we did in the section of the chapter on the dynamic membrane, it is of interest to focus not only on the dynamics across the membrane, but also on the dynamics of molecules within the membrane. Specifically, one question of interest is how long does it take molecules to travel across the cell membrane given the measured diffusion constants? To answer this question, we appeal to the simple estimate that the timescale for diffusing a distance L is given by

$$t_{\text{diffusion}} \approx \frac{L^2}{D}. \tag{19}$$

For a bacterial cell with dimensions of several microns, this means that the diffusion time to explore the membrane is

$$t_{\text{diffusion}} \approx \frac{1\,\mu\text{m}^2}{1\,\mu\text{m}^2/\text{s}} \approx 1\,\text{s}, \tag{20}$$

where we have taken a diffusion coefficient for a lipid of $1\,\mu\text{m}^2/\text{s}$. This characteristic timescale is confirmed in fluorescence-recovery-after-photobleaching (FRAP) experiments (see [55], for example).

The Electrical Membrane The electric fields across biological membranes are surprisingly high as can be estimated by using

$$E \approx \frac{V}{d} \approx \frac{100\,\text{mV}}{4\,\text{nm}} \approx \frac{100 \times 10^{-3}\,\text{V}}{4 \times 10^{-9}\,\text{m}} \approx 2.5 \times 10^7\,\frac{\text{V}}{\text{m}}. \tag{21}$$

Note that this field is an order of magnitude higher than the electric fields associated with dielectric breakdown in the atmosphere. And yet, fields five times as high have been measured in membranes with no evidence for any anomalous behavior [71].

This section had as its ambition to give a sense of how the numbers summarized in Table 2 can be used to develop intuition [3, 4]. In fact, more than anything, this brief section is an invitation to others to look for meaning in the hard won outcome of the recent work to extend membrane numeracy.

8 The Missing Membrane Numbers

As a final send-off of this brief ode to biological numeracy for membranes, we reflect on the state of our art and how it can be improved. Despite a long list of truly amazing successes, there are still many things not to like about the current status of biological numeracy, not only in terms of how well we actually know the numbers, but also in terms of what those numbers might mean for a deeper understanding of biological systems. The goal in this final section is to make an attempt at critiquing both this article and the current state of the art with the aim of suggesting future directions. Though the "by the numbers" approach has become something of a cliche, my opinion remains that there is much to be gained by pushing hard with this approach on each of the many diverse and wonderful facets of biology [19, 72–77].

One of the first weaknesses of biological numeracy in the membrane setting (and beyond) is the need to establish measurements of sufficient precision that we can confidently report on measured values. For example, there is already much evidence that biological membranes "care" about their lipid composition. It would be a powerful addition to our ability to ferret out molecular mechanisms to be able to examine these membrane compositions for all organelles as a function of time

and for a variety of different environmental conditions. First steps in this direction have been made in thinking about proteomes with one of my favorites reporting on the proteome of *E. coli* in more than 20 distinct conditions [66]. Absent accurate and reproducible measurements in the membrane setting, we are handcuffed in our efforts to construct a fruitful dialogue between theory and experiment [78, 79].

A second important challenge for the future of membrane numeracy is the vast differences between model membranes and the real world of plasma and organellar membranes. Effectively each and every section of this chapter—size and shape, composition, mechanics, transport, electrical properties—is bereft of any deep understanding of how all of the heterogeneities of real membranes might alter the numbers, and what the significances of such alterations might be. The advent of mass spectrometry in conjunction with ever more sophisticated microscopies as a window onto membrane composition has left in their wake a host of mysteries and challenges. As highlighted in Figs. 6 and 7, and indicated widely in other literature,[18, 20–28] cells care about their lipid composition. What is lacking is a conceptual framework that tells us what these numbers really mean in terms of biological function, what they imply about the regulation of lipid biochemistry and perhaps most importantly, what they imply about the evolution of life.

Another example that strikes me as an exciting challenge to our current thinking broadly concerns the question of cellular shape, and the shapes of organelles, more specifically. The images shown in Fig. 4 make clear the great diversity of membrane shapes. The study of mitochondria as a concrete example presents challenges at every turn [15]. My personal favorite remains the intriguing membrane structures found in the outer segments of photoreceptors (see Fig. 4b). In the context of the ideas presented in this chapter, one of the ways that people have attacked questions of shape traditionally has been through the approach of free energy minimization [11, 80]. But there are interesting, novel alternatives that are now in play. One approach focuses on the role of dynamics where there is an interplay between differential growth and the cost of elastic deformations as characterized by the kinds of mechanical parameters reported here [81, 82].

Thus far our discussion has largely focused on the physical properties of membranes. But there is another interesting angle on membranes that is more related to their evolutionary significance. Interestingly, one of the simplest acts of biological numeracy, namely counting, can provide evolutionary insights. Specifically, the number of membranes surrounding an organelle is perhaps the best indicator of its evolutionary origins, with the argument being made that more than one such membrane means that organelle has an endosymbiotic origin and more than two such membranes might imply nested symbioses [83–85].

We are in the midst of a biological revolution. The pace of discovery in the study of living matter is dizzying in all corners of biology. The central thesis of this article is enlightenment through biological numeracy. That is, as part of our attempt to make sense of the living world, we can sharpen our questions and be more rigorous in our demands about what it means to really understand something [78, 79]. One of the ways of placing those demands is to ask for an interplay between our experimental data and our theoretical understanding of biological processes. The

study of biological membranes is one of the most important areas for future work and in many ways has not kept pace with insights into genomes and the proteins they code for because of a want of appropriate tools. It is hoped that the chapters in this book will serve as an inspiration for the development of the tools that will make membrane numeracy as sophisticated as is our understanding of nucleic acids and proteins.

Acknowledgements One of the best parts of being a member of the scientific enterprise is all the smart and interesting people we get to interact with. In preparing this chapter I sent out a survey to many experts in membrane biology and biophysics and was overwhelmed with the thoughtful responses that I received from many colleagues. I am grateful to Olaf Andersen, Patricia Bassereau, Joel Dacks, Markus Deserno, Evan Evans, Ben Freund, Jay Groves, Christoph Haselwandter, Liz Haswell, KC Huang, Ron Kaback, Heun Jin Lee, Mike Lynch, Bill Klug, Jane Kondev, Ron Milo, Uri Moran, John Nagle, Phil Nelson, Bert Poolman, Tom Powers, Doug Rees, James Saenz, Pierre Sens, Victor Sourjik, Stephanie Tristram-Nagle, and Tristan Ursell for useful discussions. I am especially grateful to Olaf Andersen, Markus Deserno, Christoph Haselwandter, James Saenz, Pierre Sens, and Tristan Ursell who have been patient and persistent in advancing my membrane education, though obviously all shortcomings in this chapter are due to my failure to absorb that education and are no fault of their own. I am privileged to be entrusted by the National Science Foundation, the National Institutes of Health, The California Institute of Technology and La Fondation Pierre Gilles de Gennes with the funds that make the kind of work described here possible. Specifically I am grateful to the NIH for support through award numbers DP1 OD000217 (Director's Pioneer Award), R01 GM085286, and 1R35 GM118043-01 (MIRA). I am also grateful to the Kavli Institute for Theoretical Physics where much of this chapter was written. More generally, this article is part of an adventure that I have undertaken with Ron Milo and Nigel Orme (our illustrator) and generously funded by the Donna and Benjamin Rosen Bioengineering Center at Caltech. Finally and sadly, since the completion of this chapter, my friend and collaborator Bill Klug was brutally murdered in his office by a former graduate student. I had asked Bill to join me in the writing of this chapter, but he was too busy during this summer and instead of having the happy presence of his name as a co-author I instead have the solemn and unhappy duty to dedicate this short piece to him, kind and intellectually deep, above all a family man, he will be deeply missed.

References

1. Buehler LK (2016) Cell membranes. Garland Press, New York
2. Milo R, Jorgensen P, Moran U, Weber G, Springer M (2010) BioNumbers—the database of key numbers in molecular and cell biology. Nucleic Acids Res 38:D750–D753
3. Mahajan S (2014) The art of insight in science and engineering: mastering complexity. The MIT Press, Cambridge
4. Phillips R, Kondev J, Theriot J, Garcia HG (2013) Physical biology of the cell, 2nd edn. Garland Science, New York. Illustrated by N. Orme
5. Tanford C (2004) Ben Franklin stilled the waves. Oxford University Press, New York
6. Pockels A (1891) Surface tension. Nature 43:437–439
7. Langmuir I (1917) The constitution and fundamental properties of solids and liquids. II. Liquids. J Am Chem Soc 39:1848–1906
8. Gorter E, Grendel F (1925) On bimolecular layers of lipoids on the chromocytes of the blood. J Exp Med 41:439–443

9. Nagle JF, Tristram-Nagle S (2000) Structure of lipid bilayers. Biochim Biophys Acta 1469:159–195
10. Nagle JF, Zeidel ML, Mathai JC, Tristram-Nagle S (2008) Structural determinants of water permeability through the lipid membrane. J Gen Physiol 131:69–76
11. Boal D (2002) Mechanics of the cell, 1st edn. Cambridge University Press, Cambridge
12. Harroun TA, Weiss TM, Yang L, Huang HW (1999) Theoretical analysis of hydrophobic matching and membrane-mediated interactions in lipid bilayers containing gramicidin. Biophys J 76(6):3176–3185
13. Nielsen C, Andersen OS (2000) Inclusion-induced bilayer deformations: effects of monolayer equilibrium curvature. Biophys J 79(5):2583–2604
14. Phillips R, Ursell T, Wiggins P, Sens P (2009) Emerging roles for lipids in shaping membrane-protein function. Nature 459(7245):379–385
15. Neupert W (2012) SnapShot: mitochondrial architecture. Cell 149(3):722–722.e1
16. Shibata Y, Voeltz GK, Rapoport TA (2006) Rough sheets and smooth tubules. Cell 126(3): 435–439
17. Shibata Y, Shemesh T, Prinz WA, Palazzo AF, Kozlov MM, Rapoport TA (2010) Mechanisms determining the morphology of the peripheral ER. Cell 143(5):774–788
18. Takamori S, Holt M, Stenius K, Lemke EA, Gronborg M, Riedel D, Urlaub H, Schenck S, Brugger B, Ringler P, Muller SA, Rammner B, Grater F, Hub JS, De Groot BL, Mieskes G, Moriyama Y, Klingauf J, Grubmuller H, Heuser J, Wieland F, Jahn R (2006) Molecular anatomy of a trafficking organelle. Cell 127(4):831–846
19. Milo R, Phillips R (2016) Cell biology by the numbers. Garland Press, New York
20. Dupuy AD, Engelman DM (2008) Protein area occupancy at the center of the red blood cell membrane. Proc Natl Acad Sci U S A 105(8):2848–2852
21. van Meer G, Voelker DR, Feigenson GW (2008) Membrane lipids: where they are and how they behave. Nat Rev Mol Cell Biol 9(2):112–124
22. Ejsing CS, Sampaio JL, Surendranath V, Duchoslav E, Ekroos K, Klemm RW, Simons K, Shevchenko A (2009) Global analysis of the yeast lipidome by quantitative shotgun mass spectrometry. Proc Natl Acad Sci U S A 106(7):2136–2141
23. Kalvodova L, Sampaio JL, Cordo S, Ejsing CS, Shevchenko A, Simons K (2009) The lipidomes of vesicular stomatitis virus, semliki forest virus, and the host plasma membrane analyzed by quantitative shotgun mass spectrometry. J Virol 83(16):7996–8003
24. Sampaio JL, Gerl MJ, Klose C, Ejsing CS, Beug H, Simons K, Shevchenko A (2011) Membrane lipidome of an epithelial cell line. Proc Natl Acad Sci U S A 108(5):1903–1907
25. Layre E, Sweet L, Hong S, Madigan CA, Desjardins D, Young DC, Cheng TY, Armand JW, Kim K, Shamputa IC, McConnell MJ, Debono CA, Behar SM, Minnaard AJ, Murray M, Barry CE, Matsunaga I, Moody DB (2011) A comparative lipidomics platform for chemotaxonomic analysis of mycobacterium tuberculosis. Chem Biol 18:1537–1549
26. Carvalho M, Sampaio JL, Palm W, Brankatschk M, Eaton S, Shevchenko A (2012) Effects of diet and development on the *Drosophila* lipidome. Mol Syst Biol 8:600
27. Klose C, Surma MA, Gerl MJ, Meyenhofer F, Shevchenko A, Simons K (2012) Flexibility of a eukaryotic lipidome–insights from yeast lipidomics. PLoS One 7(4):e35063
28. Klose C, Surma MA, Simons K (2013) Organellar lipidomics–background and perspectives. Curr Opin Cell Biol 25(4):406–413
29. Neidhardt FC, Ingraham JL, Schaechter M (1990) Physiology of the bacterial cell: a molecular approach. Sinauer Associates, Sunderland
30. Levental KR, Levental I (2015) Giant plasma membrane vesicles: models for understanding membrane organization. Curr Top Membr 75:25–57
31. Evans E, Rawicz W, Smith BA (2013) Back to the future: mechanics and thermodynamics of lipid biomembranes. Faraday Discuss 161:591–611
32. Rawicz W, Olbrich KC, McIntosh T, Needham D, Evans E (2000) Effect of chain length and unsaturation on elasticity of lipid bilayers. Biophys J 79(1):328–339
33. Nagle JF, Jablin MS, Tristram-Nagle S, Akabori A (2015) What are the true values of the bending modulus of simple lipid bilayers? Chem Phys Lipids 185:3–10

34. Song J, Waugh RE (1993) Bending rigidity of SOPC membranes containing cholesterol. Biophys J 64:1967–1970
35. Hochmuth FM, Shao JY, Dai J, Sheetz MP (1996) Deformation and flow of membrane into tethers extracted from neuronal growth cones. Biophys J 70(1):358–369
36. Dai J, Sheetz MP, Wan X, Morris CE (1998) Membrane tension in swelling and shrinking molluscan neurons. J Neurosci 18(17):6681–6692
37. Olbrich KC, Rawicz W, Needham D, Evans E (2000) Water permeability and mechanical strength of polyunsaturated lipid bilayers. Biophys J 79:321–327
38. Upadhyaya A, Sheetz MP (2004) Tension in tubulovesicular networks of Golgi and endoplasmic reticulum membranes. Biophys J 86(5):2923–2928
39. Peukes J, Betz T (2014) Direct measurement of the cortical tension during the growth of membrane blebs. Biophys J 107(8):1810–1820
40. Sens P, Plastino J (2015) Membrane tension and cytoskeleton organization in cell motility. J Phys Condens Matter 27(27):273103
41. Kedem O, Katchalsky A (1958) Thermodynamic analysis of the permeability of biological membranes to non-electrolytes. Biochim Biophys Acta 27:229–246
42. Manning GS (1968) Binary diffusion and bulk flow through a potential-energy profile: a kinetic basis for the thermodynamic equations of flow through membranes. J Chem Phys 49: 2668–2675
43. Robinett RW (2015) Dimensional analysis as the other language of physics. Am J Phys 83: 353–361
44. Finkelstein A (1976) Water and nonelectrolyte permeability of lipid bilayer membranes. J Gen Physiol 68(2):127–135
45. Stein WD (1990) Channels, carriers and pumps. An introduction to membrane transport. Academic, Cambridge
46. Schlessinger J, Axelrod D, Koppel DE, Webb WW, Elson EL (1977) Lateral transport of a lipid probe and labeled proteins on a cell membrane. Science 195(4275):307–309
47. Alecio MR, Golan DE, Veatch WR, Rando RR (1982) Use of a fluorescent cholesterol derivative to measure lateral mobility of cholesterol in membranes. Proc Natl Acad Sci U S A 79(17):5171–5174
48. Gaede HC, Gawrisch K (2003) Lateral diffusion rates of lipid, water, and a hydrophobic drug in a multilamellar liposome. Biophys J 85(3):1734–1740
49. Doeven MK, Folgering JH, Krasnikov V, Geertsma ER, van den Bogaart G, Poolman B (2005) Distribution, lateral mobility and function of membrane proteins incorporated into giant unilamellar vesicles. Biophys J 88(2):1134–1142
50. Nenninger A, Mastroianni G, Robson A, Lenn T, Xue Q, Leake MC, Mullineaux CW (2014) Independent mobility of proteins and lipids in the plasma membrane of *Escherichia coli*. Mol Microbiol 92(5):1142–1153
51. Fahey PF, Koppel DE, Barak LS, Wolf DE, Elson EL, Webb WW (1977) Lateral diffusion in planar lipid bilayers. Science 195(4275):305–306
52. Saffman PG, Delbruck M (1975) Brownian motion in biological membranes. Proc Natl Acad Sci U S A 72(8):3111–3113
53. Gambin Y, Lopez-Esparza R, Reffay M, Sierecki E, Gov NS, Genest M, Hodges RS, Urbach W (2006) Lateral mobility of proteins in liquid membranes revisited. Proc Natl Acad Sci U S A 103(7):2098–2102
54. Ramadurai S, Holt A, Krasnikov V, van den Bogaart G, Killian JA, Poolman B (2009) Lateral diffusion of membrane proteins. J Am Chem Soc 131(35):12650–12656
55. Kumar M, Mommer MS, Sourjik V (2010) Mobility of cytoplasmic, membrane, and DNA-binding proteins in *Escherichia coli*. Biophys J 98(4):552–559
56. Chow D, Guo L, Gai F, Goulian M (2012) Fluorescence correlation spectroscopy measurements of the membrane protein TetA in *Escherichia coli* suggest rapid diffusion at short length scales. PLoS One 7(10):e48600
57. Mika JT, Schavemaker PE, Krasnikov V, Poolman B (2014) Impact of osmotic stress on protein diffusion in *Lactococcus lactis*. Mol Microbiol 94(4):857–870

58. Hanai T, Haydon DA, Taylor J (1965) The variation of capacitance and conductance of bimolecular lipid membranes with area. J Theor Biol 9:433–443
59. Vorobyov I, Olson TE, Kim JH, Koeppe RE 2nd, Andersen OS, Allen TW (2014) Ion-induced defect permeation of lipid membranes. Biophys J 106(3):586–597
60. Haswell ES, Phillips R, Rees DC (2011) Mechanosensitive channels: what can they do and how do they do it? Structure 19(10):1356–1369
61. Fricke H (1925) The electric capacity of suspensions with special reference to blood. J Gen Physiol 9:137–152
62. Curtis HJ, Cole KS (1938) Transverse electric impedance of the squid giant axon. J Gen Physiol 21:757–765
63. Almers W (1978) Gating currents and charge movements in excitable membranes. Rev Physiol Biochem Pharmacol 82:97–190
64. Fagerberg L, Jonasson K, von Heijne G, Uhlen M, Berglund L (2010) Prediction of the human membrane proteome. Proteomics 10(6):1141–1149
65. Li GW, Burkhardt D, Gross C, Weissman JS (2014) Quantifying absolute protein synthesis rates reveals principles underlying allocation of cellular resources. Cell 157(3):624–635
66. Schmidt A, Kochanowski K, Vedelaar S, Ahrne E, Volkmer B, Callipo L, Knoops K, Bauer M, Aebersold R, Heinemann M (2016) The quantitative and condition-dependent *Escherichia coli* proteome. Nat Biotechnol 34(1):104–110
67. Li M, Hazelbauer GL (2004) Cellular stoichiometry of the components of the chemotaxis signaling complex. J Bacteriol 186(12):3687–3694
68. Bitbol AF, Wingreen NS (2015) Fundamental constraints on the abundances of chemotaxis proteins. Biophys J 108(5):1293–1305
69. Bialecka-Fornal M, Lee HJ, Phillips R (2015) The rate of osmotic downshock determines the survival probability of bacterial mechanosensitive channel mutants. J Bacteriol 197(1): 231–237
70. Louhivuori M, Jelger Risselada H, van der Giessen E, Marrink SJ (2010) Release of content through mechano-sensitive gates in pressurized liposomes. Proc Natl Acad Sci U S A 107: 19856–19860
71. Andersen OS (1983) Ion movement through gramicidin a channels single-channel measurements at very high potentials. Biophys J 41:119–133
72. Bintu L, Buchler NE, Garcia HG, Gerland U, Hwa T, Kondev J, Phillips R (2005) Transcriptional regulation by the numbers: models. Curr Opin Genet Dev 15(2):116–124
73. Garcia HG, Sanchez A, Kuhlman T, Kondev J, Phillips R (2010) Transcription by the numbers redux: experiments and calculations that surprise. Trends Cell Biol 20:723–733
74. Phillips R, Milo R (2009) A feeling for the numbers in biology. Proc Natl Acad Sci U S A 106(51):21465–21471
75. Moran U, Phillips R, Milo R (2010) SnapShot: key numbers in biology. Cell 141(7): 1262–1262.e1
76. Flamholz A, Phillips R, Milo R (2014) The quantified cell. Mol Biol Cell 25(22):3497–3500
77. Shamir M, Bar-On Y, Phillips R, Milo R (2016) SnapShot: timescales in cell biology. Cell 164(6):1302–1302.e1
78. Phillips R (2015) Theory in biology: Figure 1 or Figure 7? Trends Cell Biol 25(12):723–729
79. Bialek W (2015) Perspectives on theory at the interface of physics and biology. ArXiv: 1512.08954
80. Seifert U (1997) Configurations of fluid membranes and vesicles. Adv Phys 46:13
81. Savin T, Kurpios NA, Shyer AE, Florescu P, Liang H, Mahadevan L, Tabin CJ (2011) On the growth and form of the gut. Nature 476(7358):57–62
82. Shyer AE, Tallinen T, Nerurkar NL, Wei Z, Gil ES, Kaplan DL, Tabin CJ, Mahadevan L (2013) Villification: how the gut gets its villi. Science 342(6155):212–218
83. Dacks JB, Peden AA, Field MC (2009) Evolution of specificity in the eukaryotic endomembrane system. Int J Biochem Cell Biol 41(2):330–340

84. Field MC, Dacks JB (2009) First and last ancestors: reconstructing evolution of the endomembrane system with ESCRTs, vesicle coat proteins, and nuclear pore complexes. Curr Opin Cell Biol 21(1):4–13
85. Richardson E, Zerr K, Tsaousis A, Dorrell RG, Dacks JB (2015) Evolutionary cell biology: functional insight from "endless forms most beautiful". Mol Biol Cell 26:4532–4538

Part III
Spatial Heterogeneities in Biomembranes

Lipid Rafts: A Personal Account

Kai Simons

Abstract The lipid raft concept of membrane sub-compartmentalization was introduced in 1997 and originated from studies on epithelial cell surface polarity. It was the first time that membrane lipid specificity was incorporated into the mechanisms that generate cell architecture. From its epithelial origins, the raft concept was generalized to explain how cells manage to perform their full spectrum of membrane functions. The associative capability of saturated sphingolipids and phospholipids with cholesterol and their repulsion of polyunsaturated membrane lipids formed the basis of the raft concept. With the demonstration that isolated plasma membrane vesicles can separate into two phases by liquid–liquid demixing, this became the physicochemical principle underlying raft sub-compartmentalization. The compartmentalization achieved by clustering fluctuating raft assemblies in *living cells* could be called an *abortive nonequilibrium phase separation*. Moreover, recent data demonstrate that raft lipids and proteins form collective cooperatives with emerging properties that enrich their functional repertoire. Together these features provide a new perspective on cell membrane function.

Keywords Lipid rafts · Membrane domains · Phase separation · Liquid–liquid demixing · Epithelial surface polarity · Cholesterol

The lipid raft concept has a lengthy history. I am still amazed myself how durable this idea has been, considering its humble beginnings. In this chapter I will summarize my personal perspective on the evolution of this principle of membrane organization.

K. Simons (✉)
Max-Planck-Institute of Molecular Cell Biology and Genetics, Dresden, Germany
e-mail: simons@mpi-cbg.de

P. Bassereau, P. Sens (eds.), *Physics of Biological Membranes*,
https://doi.org/10.1007/978-3-030-00630-3_4

1 Early Days

At the end of the 1970s, I decided to leave my research on Semliki Forest virus. Together with Ari Helenius and Henrik Garoff we had elucidated how the virus uses endocytosis to infect the host cell and how the virus progeny assembles and exits the host cell [1]. Searching for a new theme, I finally settled on epithelial polarity. First, there was a cell line, MDCK cells that perfectly suited my goals. These cells grew as an epithelium. Each cell was polarized into an apical and basolateral plasma membrane domain, separated by tight junctions that functioned as a diffusion barrier and fence [2] (Fig. 1). Second, when influenza virus infected MDCK cells, the newly synthesized virus acquired its membrane from the apical membrane, from where it exited. Vesicular stomatitis virus, on the other hand, budded from the basolateral side [3]. Because the viral membrane glycoproteins become transported to the surface and determined where the virus exits, they provided experimental tools to find out how the asymmetric protein sorting is mechanistically organized. But third and as important for me was the fact that the lipid composition in the two surface domains was different. This was not known for MDCK cells themselves but I simply assumed that this would hold true because studies on the lipid compositions of the apical and the basolateral membranes in intestinal epithelial cells had showed that glycosphingolipids were enriched in the apical membrane (see [4]). Thus, I planned to include lipid sorting in our studies. By being able to compare the apical and the basolateral sorting pathways with each other, I was hoping to have tools at

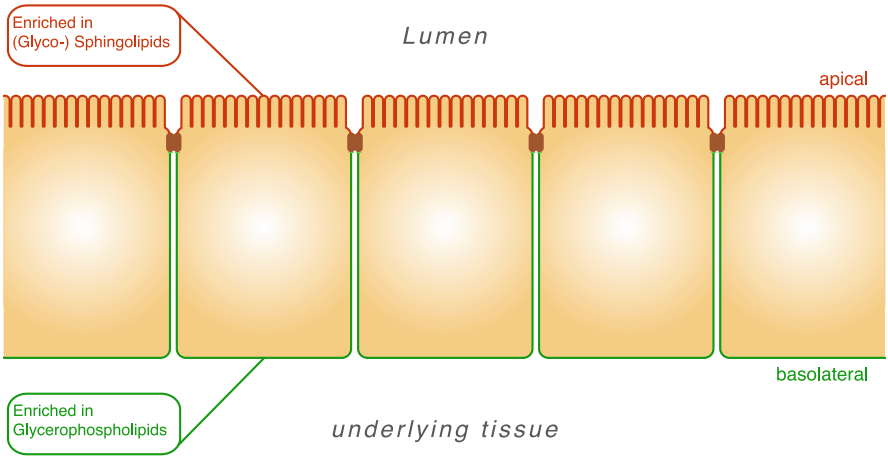

Fig. 1 Epithelial cells form a monolayer of cells, in which each cell is polarized into an apical plasma membrane domain, directed toward the lumen e.g. of the gut and a basolateral plasma membrane domain that is facing the underlying tissue and the internal milieu. The apical and basolateral surface domains have different lipid and protein compositions that serve the vectorial functions that epithelia have. The cells are connected by tight junctions (brown) that function as gates between the cells and as fences between the surface domains. Courtesy of Mathias Gerl

hand for analyzing how both lipids and proteins become sorted to the polarized cell surface.

James Rothman had already started his pioneering work on the biochemistry of vesicular transport in mammalian cells [5]. Randy Schekman had published his groundbreaking genetic screen, revealing mutants that blocked biosynthetic membrane transport to the cell surface in yeast [6]. I reasoned that my experimental system would go one step further by providing insights into how cell surface proteins and lipids are sorted to establish an asymmetric plasma membrane architecture. I would use the membrane glycoproteins of the two viruses as my apical and basolateral model proteins in the same way as we had studied the cell surface transport of the Semliki Forest membrane glycoprotein in non-polarized fibroblasts. Somewhere along the line, I hoped that I could get a handle on lipid transport as well.

2 Launching of the Raft Concept

The first real insight emerged when we demonstrated that the apical and the basolateral viral glycoproteins were sorted at the *trans*-side of the Golgi complex and exited from a new compartment that we called the *trans*-Golgi network (TGN) [7–9]. But it took until 1987 until we got a handle on the glycolipids. Gerrit van Meer used fluorescent NBD-ceramide and could show that NBD-glucosylceramide was preferentially sorted to the apical surface [10]! Based on vague clues that suggested that glycolipids weakly associated with each other [11], we postulated that apical proteins and glycolipids came together to assemble membrane "platforms" in the TGN that then vesiculated to form apical transport carriers [4]. We thought that this was an epithelial invention and was the basis for creating an asymmetric plasma membrane. The vesicular stomatitis virus membrane proteins, on the other hand, were excluded for the apical "platforms" and were thus sorted into basolateral membrane carriers.

Soon, Karl Matlin who had been my partner to set up the MDCK cell system demonstrated that hemagglutinin, the major membrane glycoprotein in influenza virus, became insoluble in Triton X-100 when it passed through the Golgi complex [12]. This was biochemical evidence that the apical protein changed its biochemical state when being prepared for exit from the Golgi complex. Debbie Brown and Jack Rose found that detergent-insoluble membrane residue was not only enriched in apical proteins but also in glycolipids [13]. This was how DRMs (detergent-insoluble membranes) came into the picture and became what was then the only method to identify proteins that potentially interacted with glycolipids. This was all quite shaky. Obviously, the insoluble residue, remaining after solubilizing cells with Triton X-100 in the cold, cannot be a very specific method for characterizing protein–lipid interactions. For me, the most important clue was the change of state of apical proteins when exiting Golgi. Since DRMs were not specific to epithelial cells, it started to dawn on us that this principle might be general. The

next step forward were experiments by Thomas Harder in my lab, who demonstrated that when detergent-insoluble influenza virus hemagglutinin and glycosylphosphatidylinositol (GPI)-anchored proteins were cross-linked with antibodies on living BHK cells and Jurkat T-lymphoma cells, these surface proteins formed patched together [14]. When the same experiment was performed with detergent-soluble plasma membrane proteins, the non-DRM proteins segregated away from the detergent-insoluble proteins. Most striking was that this patching was abrogated by cholesterol depletion. The co-patching experiments were important because they were the first to use a non-detergent approach to demonstrate specificity of DRM protein behavior.

As these observations were developing, I had been struggling to find a name for the apical "platforms" in the TGN that gave rise to the apical membrane carriers, transporting proteins, and lipids to the apical membrane. Finally, we named them "rafts" from Finnish logger movies (Fig. 2). I wanted to stress that there are cholesterol-dependent protein and lipid assemblies in the TGN and the plasma membrane, separating away from the surrounding bilayer. The rafts were partitioning devices. Having a name simplified discussions of these enigmatic membrane structures, but, in hindsight, it probably also ignited some of the controversy that emerged when we launched the raft concept in 1997 [15]. Why? Because the schematic figures displayed, gave the impression of fixed sized platforms, and missed out on the dynamic nature of these assemblies that became revealed later. Most disturbing was that many investigators did not want to accept

Fig. 2 Loggers (proteins) on a raft (lipids) in a Finnish river

that rafts in native membranes had no physical relationship with the DRMs that were aggregates of raft assemblies, allowing a crude biochemical identification of possible raft constituents. This gave rise to completely useless debates that hindered progress in the field.

Parallel to these developments, biophysicists working with model membranes had discovered that two liquid phases could coexist in the lipid bilayer: a liquid-ordered (Lo) phase and a liquid-disordered (Ld) phase [16–18]. The Lo phase was formed from saturated phosphoglycerolipids or sphingolipids, together with cholesterol. The Ld phase preferred unsaturated phosphoglycerolipids. The high melting lipids—sphingolipids and saturated phosphoglycerolipids—attract cholesterol and these are repulsed by polyunsaturated phospholipids (see [19]). The raft concept combined these insights into one generalized hypothesis to explain how cell membranes containing Lo lipids could sub-compartmentalize into dynamic domains assembled from specific proteins and lipids. At that time I was not so sure that liquid–liquid phase separation would be possible in a plasma membrane containing a complex mixture of different lipid species and proteins but hoped that future experiments would support our raft concept. Clearly, lateral plasma membrane heterogeneity had been observed before with general biophysical methods, but their chemical constituents and possible physiological functions remained enigmatic. The raft concept postulated that sphingolipids together with cholesterol formed membrane domains that incorporated specific sets of membrane proteins and functioned as membrane sub-compartmentalization devices that operated in membrane trafficking, in signal transduction, and in other membrane-associated processes [20]. The concept gave cell membranes, containing raft lipids and proteins, novel material properties, capable of dynamic compartmentalization, way beyond the passive role of just forming a boring liquid matrix. Important was also the possibility that the formation of the liquid-ordered domains could activate membrane proteins by lipid-mediated forces.

3 A Wave of DRM Papers

What followed the publication of our 1997 Nature article was a stream of papers, which for a while got published without difficulty. You only had to get your protein into DRMs and then you could publish. And this is not so difficult as we all know! One mystery that confronted researchers in this field was that lateral heterogeneity was usually not observed when cells were imaged by fluorescence microscopy. Only after crosslinking with multivalent reagents (e.g., antibodies, lectins, cholera toxin) did patches emerge [20]. Were the patches artifacts without biological meaning? What was the size of rafts in cells? Did they exist at all?

Another area of confusion was provided by studies on caveolae, 60 nm invaginations of the plasma membrane, formed by caveolins and other proteins. Caveolin was found in DRMs and for a while caveolae became identical with DRMs [21]. This made no sense but tarnished the raft concept into a state of illusiveness [22].

4 Introducing Biophysical Methods to Study Membrane Organization

The confusion was due to the crudity of the methods used to study membrane organization. Invigorating input then came from the introduction of new methodology (see [23]).

The first biophysical studies with relevance for raft organization were the studies of Satyajit Mayor using fluorescence microscopy as a measure of homo FRET to analyze the distribution of GPI-anchored proteins in the live cell plasma membrane. They suggested that these proteins were in domains of less than 70 nm in diameter and were disrupted by cholesterol depletion [24]. Their later studies came to the conclusion that GPI proteins form cholesterol-dependent nanoclusters, containing at the most four molecules. They also proposed that actin asters could play a role as raft nucleators [25].

The work of the group of Akihiro Kusumi employed single-particle tracking with high temporal resolution, using colloidal gold probes that bound to plasma membrane proteins or lipids [26]. From the trajectories, they concluded that resting state rafts are short-lived structures that bump into actin filaments, dissolve, and move onward until they encounter the next fence. Kusumi postulated a picket-fence model for the organization of the plasma membrane [27].

At EMBL we employed photonic force microscopy to measure the viscous drag of raft and non-raft proteins in the living cell. The size of the platforms was around 50 nm diameter and the rafts were rather long-lived on the timescale of minutes. Cholesterol depletion dissolved them [28].

Another method was developed in the group of Marguet, based on fluorescence correlation spectroscopy [29]. They varied the size of the laser focus to analyze whether proteins get trapped by putative raft platforms. They found transient confinement of GPI proteins that was abrogated by cholesterol and sphingolipid depletion.

Several other methods were also applied [30]. However, no consensus on the properties of lipid rafts emerged. Overall, the data obtained varied with the conditions used and the method employed. For someone outside the field, lipid rafts remained “elusive and illusive.”

5 Phase Separation in Plasma Membranes

But then came the breakthrough that shed light on the bewildering range of temporal and spatial timescales that had been reported. A series of studies demonstrated that plasma membranes can indeed phase separate on a micrometer scale into a liquid-ordered (raft) and less-ordered (non-raft) domains in the same fashion as in three-component model systems! Tobias Baumgart produced membrane blebs from cells by a harsh treatment, consisting of paraformaldehyde and dithiothreitol

[31]. By decreasing the temperature, the membrane blebs phase separated. Daniel Lingwood in my lab blew up cells into balloons, giant plasma membrane spheres, and added cholera toxin at 37 °C to induce phase separation, but he used no chemical additive [32]. The big difference between the two methods was that while GPI proteins were included in the raft phase in both the blebs and the balloons, raft transmembrane proteins were excluded from the more ordered domains in the blebs while they were included in the plasma membrane balloons. Ilya Levental in my lab worked out why and demonstrated that it had to do with the fact that dithiothreitol used to produce the blebs, de-palmitoylated proteins. When it was replaced by *N*-ethylmaleimide, then plasma membrane blebs were produced in which the transmembrane raft proteins were enriched in the raft phase after phase separation. These data suggested the protein and lipid compositions in plasma membranes must be so tightly regulated that they are positioned close to a phase boundary, making separation into 2 micrometer-sized phases possible. Both in blebs and balloons, the membrane phosphoinositides (PI (4,5)P2) were hydrolyzed, leading to actin filament dissociation. Because the cortical actin barriers do not block diffusion of the clustered and stabilized raft assemblies anymore, further coalescence into the micrometer raft domains is permitted.

Veatch et al. demonstrated critically fluctuating membrane domains in the paraformaldehyde–DTT-induced blebs [33]. Their data suggested that the composition of the plasma membrane was not only close to a phase boundary but resided near a miscibility critical point, analogous to a supercritical fluid. These results, especially the findings that plasma membrane balloons produced without any chemical additives phase separate, revealed the physico-chemistry underlying the capability of membranes to sub-compartmentalize. The fact that not only GPI proteins but also raft *trans*-membrane proteins partition preferentially into the more ordered phase implies that the membrane maintains the characteristics of the native bilayer that are required for sub-compartmentalization to work. It is important to stress that the raft phase in the blebs and the balloons is less ordered than Lo phases in three-component model membranes and that the disordered (non-raft) phase is more ordered than the Ld phases [34]. Thus, the material properties of the native phases, separating in plasma membrane, are quite different from those of simple model membrane systems.

6 Connecting the Pieces of the Puzzle

Until the discovery that plasma membranes can phase separate, despite their complex protein and lipid compositions, the foundation of the raft concept was shaky. It was of course well established that three-component model membranes consisting of sphingolipids, unsaturated phospholipids, and sterols in the right mixture could separate into Lo and Ld phases. But who could have predicted in the 1990s that complex biomembranes also could phase separate into two discrete liquid phases? Knowing that plasma membranes in living cells are positioned close

to a phase boundary provides a refreshingly new way to interpret all the differing results obtained by employing different methods under different conditions. *Nano-assemblies of raft lipids and proteins in the one phase state could, without much energy expenditure, be pushed over the boundary to separate into Lo-like domains of varying size, which could be tuned by the nature of the stimulus*. In the live cell, the cortical actin network would limit the size of the coalescing platforms [35]. The proteins and the lipids in the elusive resting state rafts would associate and dissociate on a sub-second timescale, ready to be activated by crosslinking stimuli to form larger, more stable assemblies. Depending on the experimental conditions, different degrees of clustering would result in differently sized platforms. Only glimpses of the dynamic resting-state raft assemblies would be possible with the methods available. Novel approaches are required to elucidate the length and time scales of these fluctuating nano-assemblies. However, even if the dynamics of the system in live cells complicates analysis, the fact that micrometer phase separation can be observed at equilibrium in isolated plasma membrane vesicles demonstrates the physical principles involved. I would call the sub-compartmentalization achieved by clustering fluctuating raft assemblies an *abortive nonequilibrium phase separation*.

Based on these new insights, let me briefly summarize how I now interpret the startling variety that has confused the field.

1. Starting with DRMs, addition of Triton X-100 to cells leads to incorporation of detergent molecules into the membrane bilayers, inducing a phase separation at low temperatures (e.g., 4 °C). The Lo-like raft phase is insoluble, while the Ld-like phase is solubilized. The resulting insoluble residue is a mess of DRMs from those cell membranes that contain raft lipid and proteins at high enough concentration. This remains a crude method to identify membrane proteins with raft specificity that should be complemented with other methods to ensure specificity.
2. The reason why we observed the 50 nm raft domains with photonic microscopy was probably due to clustering by the antibodies on the gold particles used to bind to raft proteins on the live cells (see [36]).

   Similar crosslinking also occurred in other studies employing biotinylated quantum dots [37] or other ligands [38] that are functionally multivalent. Especially problematic has been the use of fixation. Our own experience demonstrated that raft patches were easily induced by fixing by paraformaldehyde or glutaraldehyde and most likely explain the observations of cholesterol-dependent protein islands in the plasma membrane [39].
3. We have to assume that almost any "insult" could potentially lead to detectable raft domain formation. Even photo-oxidation alone could potentially induce phase separation [40], showing how easily one can induce raft platforms from fluctuating nanorafts in living cells.

Nevertheless, the propensity to activate nanorafts by crosslinking into more stabilized platforms is key to their capability to sub-compartmentalize cell membranes (Fig. 3). Because each physiological activating stimulus will be specific, e.g., binding to only one specific raft protein and further coalescence limited by cortical

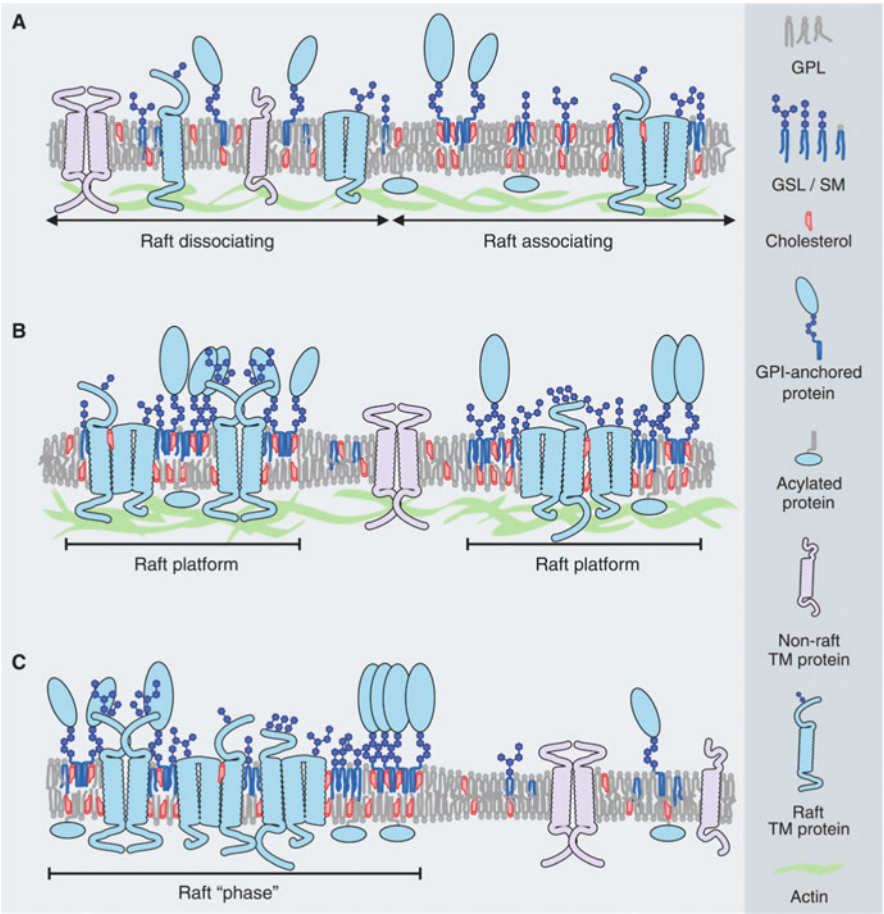

Fig. 3 Hierarchy of raft-based heterogeneity in cell membranes. (**a**) Fluctuating nanoscale assemblies of sterol- and sphingolipid-related biases in lateral composition. This sphingolipid/sterol assemblage potential can be accessed and/or modulated by GPI-anchored proteins, certain TM proteins, acylated cytosolic effectors, and cortical actin. Gray proteins do not possess the chemical or physical specificity to associate with these membrane assemblies and are considered non-raft. *GPL* glycerophospholipid, *SM* sphingomyelin. (**b**) Nanoscale heterogeneity is functionalized to larger platforms by lipid- and/or protein-mediated activation events (e.g., multivalent ligand binding, synapse formation, protein oligomerization) that trigger the coalescence of membrane order-forming lipids with their accompanying selective chemical and physical specificities for protein. This level of lateral sorting can also be buttressed by cortical actin. (**c**) The membrane basis for heterogeneity as revealed by the activation of raft phase coalescence at equilibrium in plasma-membrane spheres. Separated from the influence of cortical actin and in the absence of membrane traffic, multivalent clustering of raft lipids can amplify the functional level to a microscopic membrane phase. Membrane constituents are laterally sorted according to preferences for membrane order and chemical interactions. Taken from Science (2010) 327, 46–50

actin filaments, only one specific set of rafts will usually be activated. This feature enables parallel and independent processing in the same membrane, facilitating dynamic multitasking. Cell membranes are truly incredible 2-D liquids, which not only continue to baffle researchers by the data that they give rise to but which also possess bewildering material properties.

What is so exciting about cell membrane research is that it exemplifies the challenges that present-day biology faces. Gone are the days when we could focus on one gene or one protein. Now we have to include the entire chemical, physical, and physiological context in the analysis. In order to understand a membrane process, we need to use a battery of methods to retrieve information on the interplay between lipids and proteins that gives rise to function. Most importantly, physico-chemistry—almost extinct from biology in the wake of the DNA revolution—cannot be neglected anymore.

Two recent studies illustrate the difficulties facing researchers analyzing the dynamics of membrane organization. Schütz et al. used single-molecule tracking combined with micro-patterning to find out how GPI-anchored proteins patched by antibodies influenced the local membrane environment [41]. The antibodies were fixed to a solid support at different densities and the unexpected result was that the clustering of the monomeric GFP-GPI molecules expressed in live cells by binding to the solid support had no effect on the local membrane environment. Other raft proteins and lipids were not trapped by the micro-patterned GFP-GPI molecules as had been shown before. Even at the highest density of 10000 GFP-GPI molecules per square micron, no formation of a connective raft phase could be observed.

Pralle et al. addressed the same experimental issue [42]. By combining total internal fluorescence microscopy with fluorescence correlation microscopy, they measured protein diffusion in differently sized areas on the live cell surface simultaneously. With their method, having a time resolution of 1.7 ms, they demonstrated that one GPI protein can trap another GPI protein in sub-microscopic membrane domains. This trapping was weakened by cholesterol oxidation. They could further show that dimerization of the monomeric GFP-GPI reduced its diffusion coefficient more than expected from the effect on the viscous drag increase. This made sense in the context of data showing that dimerizing transmembrane raft proteins [43] as well as dimerizing GPI proteins associate more strongly than monomers with the cholesterol-sensitive membrane domains. Pralle et al. also analyzed how GPI-protein trapping was influenced by the cortical action network. The presence of cortical actin increased the trapping rate. Trapping was still measurable after dissociation of the actin filaments, albeit more weakly.

One reason for these opposite results could be that Schütz et al. used antibodies, spatially fixed on a solid support. Thus, the spacing between the clustered GPI-proteins in the plasma membrane also became fixed after antibody binding. In the Pralle experiments, the GPI proteins were freely diffusing. Previous work has stressed the importance of the spacing for raft coalescence to occur. The coming together of raft lipids and proteins is governed by weak interactions and these interactions are regulated by spatial proximity [44]. This would be expected if association were to occur by hydrogen bonding and van der Waal interactions as

postulated. If the interacting partners were hindered to move, then the weak binding is blocked.

7 Perspectives

To study membrane organization we have to consider the whole membrane as a system. Raft organization is neither protein-centric nor lipid-centric nor actin-focused. All of these molecules are involved. The assembly functions optimally with all the players together. We can take the membrane apart and this is indeed what we should aim for: to reconstitute membrane function to such a depth that we achieve a mechanistic understanding of how the molecules involved interact. Because of the dynamics and the interplay of weakly interacting proteins and lipids, we have to accept that our experimental means are still limited, but new methods are constantly being developed that will expand our capabilities to analyze such dynamic systems. We badly need methods that analyze collectives of molecules.

Especially challenging is the complexity that we are facing. A three-component lipid bilayer can phase separate and so can a cell membrane, which contains hundreds of different lipids and proteins. The chemistry is orders of magnitude more complex in biological membranes than in model membranes. So how can we ever hope to understand how the native mixture functions?

It is well to be reminded that "Nothing in biology makes sense except in the light of evolution" [45]. Phase-separating cell membranes probably arose early in evolution. As more proteins and lipids were added to the membrane mix, an increasing number of membrane functions were added to the cellular repertoire. In order for the system to perform, I assume that the chemistry of each newcomer in the membrane mix had to be adjusted so that the capability to modulate phase separation was conserved. To produce cholesterol, almost 30 biosynthetic steps are required and the resulting molecule is optimized not only to order the lipid bilayer and to interact with proteins but also to facilitate phase separation. When complexity increased during evolution, somewhere along the line a mechanism was introduced to limit phase separation. Mixing of all raft constituents in a membrane makes little functional sense. Cortical actin was brought into play to hinder coalescence early before different rafts mix. I argue that nature has capitalized on liquid–liquid phase separation to generate specific membrane sub-compartmentalization by limiting of coalescence in living cells. Therefore, my view is that the raft concept of membrane sub-compartmentalization is driven by an abortive nonequilibrium phase separation.

What we now need are studies, which explore how raft assemblies not only sub-compartmentalize membranes but also contribute to biological function. A recent example was the demonstration by super-resolution fluorescence localization microscopy that B-cell receptors become active after clustering by attracting key regulators into an extended ordered domain. Thus, lipid-mediated forces can impact signal transduction beyond the dominating protein–protein interaction paradigm

[46]. The length of the hydrocarbon chains, every methyl group, and double bond count and have a function [47, 48].

But how do bacterial membranes perform their function? They have no sterols [49]. Do they also need to sub-compartmentalize? What are worms (*C. elegans*) employing to order and sub-compartmentalize their membranes? They are also not using sterols for these tasks [50]. By unraveling biological innovations that different organisms have evolved to perform similar functions, we will take a leap toward understanding the principles that guide membrane organization and function. Evolution provides the framework to understand both the chemistry and the physics of biological function.

Membrane biologists have to accept that physico-chemistry after years of neglect is here to stay. Liquid phase separation is not only an important principle in membrane organization and function, but is now also invading the cytoplasm. Hyman et al. have discovered that P-granules, consisting of RNA–protein complexes, are liquid droplets that result from three-dimensional liquid–liquid phase separation [51]. Rosen et al. have demonstrated that scaffolding molecules, binding to cell surface *trans*-membrane proteins, form liquid droplets that link membrane proteins with actin filaments [52]. These discoveries open up completely new visions for cellular organization. We now know that such phase segregation into liquid droplets is a feature of many cellular processes. These insights demonstrate how approaching the crossroads of biochemistry, biophysics, and cell biology will deepen our understanding of the underlying principles of cellular organization. Cell membrane research is leading the way into this new era of individual molecules forming collective cooperatives with emerging properties that enrich their functional repertoire.

Acknowledgements Thanks to Mathias Gerl for help with references and figures.

References

1. Simons K, Garoff H, Helenius A (1982) How an animal virus gets into and out of its host cell. Sci Am 246(2):58–66
2. Cereijido M, Robbins ES, Dolan WJ, Rotunno CA, Sabatini DD (1978) Polarized monolayers formed by epithelial cells on a permeable and translucent support. J Cell Biol 77(3):853–880
3. Rodriguez Boulan E, Sabatini DD (1978) Asymmetric budding of viruses in epithelial monlayers: a model system for study of epithelial polarity. Proc Natl Acad Sci USA 75(10):5071–5075
4. Simons K, van Meer G (1988) Lipid sorting in epithelial cells. Biochemistry 27(17):6197–6202
5. Fries E, Rothman JE (1980) Transport of vesicular stomatitis virus glycoprotein in a cell-free extract. Proc Natl Acad Sci USA 77(7):3870–3874
6. Novick P, Field C, Schekman R (1980) Identification of 23 complementation groups required for post-translational events in the yeast secretory pathway. Cell 21(1):205–215
7. Griffiths G, Simons K (1986) The trans Golgi network: sorting at the exit site of the Golgi complex. Science 234(4775):438–443

8. Matlin KS, Simons K (1984) Sorting of an apical plasma membrane glycoprotein occurs before it reaches the cell surface in cultured epithelial cells. J Cell Biol 99(6):2131–2139
9. Pfeiffer S, Fuller SD, Simons K (1985) Intracellular sorting and basolateral appearance of the G protein of vesicular stomatitis virus in Madin-Darby canine kidney cells. J Cell Biol 101(2):470–476
10. van Meer G, Stelzer EH, Wijnaendts-van-Resandt RW, Simons K (1987) Sorting of sphingolipids in epithelial (Madin-Darby canine kidney) cells. J Cell Biol 105(4):1623–1635
11. Thompson TE, Tillack TW (1985) Organization of glycosphingolipids in bilayers and plasma membranes of mammalian cells. Annu Rev Biophys Biophys Chem 14:361–386
12. Skibbens JE, Roth MG, Matlin KS (1989) Differential extractability of influenza virus hemagglutinin during intracellular transport in polarized epithelial cells and nonpolar fibroblasts. J Cell Biol 108(3):821–832
13. Brown DA, Rose JK (1992) Sorting of GPI-anchored proteins to glycolipid-enriched membrane subdomains during transport to the apical cell surface. Cell 68(3):533–544
14. Harder T, Scheiffele P, Verkade P, Simons K (1998) Lipid domain structure of the plasma membrane revealed by patching of membrane components. J Cell Biol 141(4):929–942
15. Simons K, Ikonen E (1997) Functional rafts in cell membranes. Nature 387(6633):569–572
16. de Almeida RF, Fedorov A, Prieto M (2003) Sphingomyelin/phosphatidylcholine/cholesterol phase diagram: boundaries and composition of lipid rafts. Biophys J 85(4):2406–2416
17. Ipsen JH, Karlstrom G, Mouritsen OG, Wennerstrom H, Zuckermann MJ (1987) Phase equilibria in the phosphatidylcholine-cholesterol system. Biochim Biophys Acta 905(1):162–172
18. Silvius JR (1992) Cholesterol modulation of lipid intermixing in phospholipid and glycosphingolipid mixtures. Evaluation using fluorescent lipid probes and brominated lipid quenchers. Biochemistry 31(13):3398–3408
19. Wang C, Yu Y, Regen SL (2017) Lipid raft formation: key role of polyunsaturated phospholipids. Angew Chem Int Ed Engl 56(6):1639–1642
20. Simons K, Toomre D (2000) Lipid rafts and signal transduction. Nat Rev Mol Cell Biol 1(1):31–39
21. Kurzchalia TV, Hartmann E, Dupree P (1995) Guilty by insolubility—does a protein's detergent insolubility reflect a caveolar location. Trends Cell Biol 5(5):187–189
22. Munro S (2003) Lipid rafts: elusive or illusive? Cell 115(4):377–388
23. Levental I, Veatch SL (2016) The continuing mystery of lipid rafts. J Mol Biol 428(24 Pt A):4749–4764
24. Varma R, Mayor S (1998) GPI-anchored proteins are organized in submicron domains at the cell surface. Nature 394(6695):798–801
25. Raghupathy R, Anilkumar AA, Polley A, Singh PP, Yadav M, Johnson C, Suryawanshi S, Saikam V, Sawant SD, Panda A, Guo Z, Vishwakarma RA, Rao M, Mayor S (2015) Transbilayer lipid interactions mediate nanoclustering of lipid-anchored proteins. Cell 161(3):581–594
26. Kusumi A, Koyama-Honda I, Suzuki K (2004) Molecular dynamics and interactions for creation of stimulation-induced stabilized rafts from small unstable steady-state rafts. Traffic 5(4):213–230
27. Fujiwara T, Ritchie K, Murakoshi H, Jacobson K, Kusumi A (2002) Phospholipids undergo hop diffusion in compartmentalized cell membrane. J Cell Biol 157(6):1071–1081
28. Pralle A, Keller P, Florin EL, Simons K, Horber JK (2000) Sphingolipid-cholesterol rafts diffuse as small entities in the plasma membrane of mammalian cells. J Cell Biol 148(5):997–1008
29. Lenne P, Wawrezinieck L, Conchonaud F, Wurtz O, Boned A, Guo X, Rigneault H, He H, Marguet D (2006) Dynamic molecular confinement in the plasma membrane by microdomains and the cytoskeleton meshwork. EMBO J 25(14):3245–3256
30. Klotzsch E, Schutz GJ (2013) A critical survey of methods to detect plasma membrane rafts. Philos Trans R Soc Lond Ser B Biol Sci 368(1611):20120033

31. Baumgart T, Hammond AT, Sengupta P, Hess ST, Holowka DA, Baird BA, Webb WW (2007) Large-scale fluid/fluid phase separation of proteins and lipids in giant plasma membrane vesicles. Proc Natl Acad Sci USA 104(9):3165–3170
32. Lingwood D, Ries J, Schwille P, Simons K (2008) Plasma membranes are poised for activation of raft phase coalescence at physiological temperature. Proc Natl Acad Sci USA 105(29):10005–10010
33. Veatch SL, Cicuta P, Sengupta P, Honerkamp-Smith A, Holowka D, Baird B (2008) Critical fluctuations in plasma membrane vesicles. ACS Chem Biol 3(5):287–293
34. Kaiser HJ, Lingwood D, Levental I, Sampaio JL, Kalvodova L, Rajendran L, Simons K (2009) Order of lipid phases in model and plasma membranes. Proc Natl Acad Sci USA 106(39):16645–16650
35. Kusumi A, Suzuki KG, Kasai RS, Ritchie K, Fujiwara TK (2011) Hierarchical mesoscale domain organization of the plasma membrane. Trends Biochem Sci 36(11):604–615
36. Simons K, Gerl MJ (2010) Revitalizing membrane rafts: new tools and insights. Nat Rev Mol Cell Biol 11(10):688–699
37. Pinaud F, Michalet X, Iyer G, Margeat E, Moore HP, Weiss S (2009) Dynamic partitioning of a glycosyl-phosphatidylinositol-anchored protein in glycosphingolipid-rich microdomains imaged by single-quantum dot tracking. Traffic 10(6):691–712
38. van Zanten TS, Gomez J, Manzo C, Cambi A, Buceta J, Reigada R, Garcia-Parajo MF (2010) Direct mapping of nanoscale compositional connectivity on intact cell membranes. Proc Natl Acad Sci USA 107(35):15437–15442
39. Lillemeier BF, Pfeiffer JR, Surviladze Z, Wilson BS, Davis MM (2006) Plasma membrane-associated proteins are clustered into islands attached to the cytoskeleton. Proc Natl Acad Sci USA 103(50):18992–18997
40. Ayuyan AG, Cohen FS (2006) Lipid peroxides promote large rafts: effects of excitation of probes in fluorescence microscopy and electrochemical reactions during vesicle formation. Biophys J 91(6):2172–2183
41. Sevcsik E, Brameshuber M, Folser M, Weghuber J, Honigmann A, Schutz GJ (2015) GPI-anchored proteins do not reside in ordered domains in the live cell plasma membrane. Nat Commun 6:6969
42. Huang H, Simsek MF, Jin W, Pralle A (2015) Effect of receptor dimerization on membrane lipid raft structure continuously quantified on single cells by camera based fluorescence correlation spectroscopy. PLoS One 10(3):e0121777
43. Levental I, Lingwood D, Grzybek M, Coskun U, Simons K (2010) Palmitoylation regulates raft affinity for the majority of integral raft proteins. Proc Natl Acad Sci USA 107(51):22050–22054
44. Ewers H, Romer W, Smith A, Bacia K, Dmitrieff S, Chai W, Mancini R, Kartenbeck J, Chambon V, Berland L, Oppenheim A, Schwarzmann G, Feizi T, Schwille P, Sens P, Helenius A, Johannes L (2010) GM1 structure determines SV40-induced membrane invagination and infection. Nat Cell Biol 12(1):11–18
45. Dobzhansky T (1973) Nothing in biology makes sense except in the light of evolution. Am Biol Teach 35(3):125–129
46. Stone MB, Shelby SA, Nunez MF, Wisser K, Veatch SL (2017) Protein sorting by lipid phase-like domains supports emergent signaling function in B lymphocyte plasma membranes. eLife 6:e19891
47. Klemm RW, Ejsing CS, Surma MA, Kaiser HJ, Gerl MJ, Sampaio JL, de Robillard Q, Ferguson C, Proszynski TJ, Shevchenko A, Simons K (2009) Segregation of sphingolipids and sterols during formation of secretory vesicles at the trans-Golgi network. J Cell Biol 185(4):601–612
48. Proszynski TJ, Klemm RW, Gravert M, Hsu PP, Gloor Y, Wagner J, Kozak K, Grabner H, Walzer K, Bagnat M, Simons K, Walch-Solimena C (2005) A genome-wide visual screen reveals a role for sphingolipids and ergosterol in cell surface delivery in yeast. Proc Natl Acad Sci USA 102(50):17981–17986

49. Saenz JP, Grosser D, Bradley AS, Lagny TJ, Lavrynenko O, Broda M, Simons K (2015) Hopanoids as functional analogues of cholesterol in bacterial membranes. Proc Natl Acad Sci USA 112(38):11971–11976
50. Kurzchalia TV, Ward S (2003) Why do worms need cholesterol? Nat Cell Biol 5(8):684–688
51. Brangwynne CP, Eckmann CR, Courson DS, Rybarska A, Hoege C, Gharakhani J, Julicher F, Hyman AA (2009) Germline P granules are liquid droplets that localize by controlled dissolution/condensation. Science 324(5935):1729–1732
52. Li P, Banjade S, Cheng HC, Kim S, Chen B, Guo L, Llaguno M, Hollingsworth JV, King DS, Banani SF, Russo PS, Jiang QX, Nixon BT, Rosen MK (2012) Phase transitions in the assembly of multivalent signalling proteins. Nature 483(7389):336–340

Theories of Equilibrium Inhomogeneous Fluids

Michael Schick

Abstract I review two theoretical explanations for the existence of inhomogeneities in a fluid bilayer, such as the mammalian plasma membrane, which one might well expect to be homogeneous. The first is the existence of a phase separation. If biologically relevant temperatures are below the critical temperature of the separation, then these inhomogeneities are simply inclusions of one phase within the other. One has to understand, however, why macroscopic separation is not seen in the plasma membrane. If biologically relevant temperatures are above the critical temperature, then the inhomogeneities could be ascribed to critical fluctuations. There are difficulties with this interpretation which I note. The second possible interpretation is that the dynamic heterogeneities are evidence of a two-dimensional microemulsion. Several mechanisms which could give rise to it are discussed. Particular attention is paid to the coupling of membrane height fluctuations to composition differences. Such a mechanism naturally gives rise to a length scale which is of the correct order of magnitude for the domains postulated to exist in the plasma membrane.

Keywords Rafts · Phase separation · Critical phenomena · Modulated phases · Microemulsions

1 Introduction

With such great interest in the hypothesis that the mammalian plasma membrane is characterized by inhomogeneities, or "rafts," of a characteristic size on the order of 100 nm [1, 2], it is incumbent upon us to understand how such distinct regions could come about. Why should a fluid be heterogeneous; more specifically, why should a biological membrane be heterogeneous? What mechanism overcomes the entropic

M. Schick (✉)
Department of Physics, University of Washington, Seattle, WA, USA
e-mail: schick@uw.edu

P. Bassereau, P. Sens (eds.), *Physics of Biological Membranes*,
https://doi.org/10.1007/978-3-030-00630-3_5

tendency for all components to mix uniformly? There are not many candidates for such a mechanism that one can invoke, and even fewer if one assumes the membrane to be in thermal equilibrium, as I shall. Non-equilibrium processes are discussed elsewhere in this volume. Furthermore I will concentrate on a pure lipid bilayer, and ignore the possible effects that proteins could have on bringing about non-uniformity in a lipid system. I focus on the two mechanisms most often discussed. The first is simple phase separation, which has been observed recently in different membranes, those of yeast vacuoles [3].

2 Phase Separation and Associated Critical Fluctuations

Consider first a system containing only one species of lipid, say the saturated dipalmitoylphosphatidylcholine (DPPC). At high temperatures, its acyl chains explore many configurations in which the chains are not at all straight but are rather disordered, a disorder characterized by the appearance of thermally-excited kinks, i.e., gauche bonds. As a consequence, the chains do not pack well together. The system is in a liquid phase. As the temperature is lowered, the number of these thermally excited gauche bonds decreases. At the main-chain transition temperature, the number of these bonds decreases discontinuously; the chains become more ordered and pack together better. The system is in the gel phase.

The chains of a mono-unsaturated lipid, such as dioleoylphosphatidylcholine (DOPC), are characterized by a permanent kink at the site of the *cis* double bond. As a consequence, it is more difficult for these chains to pack together and they are always more disordered than saturated chains of the same length at the same temperature. Hence the temperature of their main-chain transition is lower than that of the system of saturated chains.

Now consider a two-component mixture of DPPC and DOPC. Due to the presence of DOPC with its disordered chains, it is more difficult for the DPPC to order. When the temperature is lowered sufficiently for ordering to occur, the saturated lipids expel many of the unsaturated ones resulting in the coexistence of two phases: a DPPC-rich gel phase and a DOPC-rich liquid phase. The transition is a first-order one; that is, there is a difference in the densities of DPPC and DOPC in the two phases. That chain-packing is indeed the mechanism which drives the transition is borne out by calculations on microscopic models of the lipids that describe very well the configurations of the lipid chains [4]. The results are in good agreement with experiments which observe the phase transition in such systems [5].

The addition of cholesterol to this mix changes things in an interesting way. The rather rigid cholesterol molecule does not insert itself well in between the tightly packed tails of the gel phase. Hence its presence tends to disorder it. With the addition of enough cholesterol, the DPPC-rich gel phase melts to a DPPC-rich liquid, one quite distinct from the DOPC-rich liquid which coexisted with the gel phase. So now the ternary system can exhibit two different liquid phases. Not only do they differ in composition, but they also differ in the degree of order of the acyl

chains. As noted above, the chains of the DOPC-rich liquid are rather disordered. Those of the saturated DPPC-rich liquid are more ordered. Furthermore now that the cholesterol can insert itself between the less-tightly packed chains of the DPPC-rich fluid, its rigidity tends to further order those chains. Because of the difference in the average configuration of chains in the two fluids, they are denoted liquid-ordered and liquid-disordered, respectively [6]. A typical ternary phase diagram, this one for the system of the saturated lipid, palmitoylsphingomyelin (PSM), the unsaturated lipid, palmitoyloleloylphosphatidylcholine (POPC), and cholesterol [7] is shown in Fig. 1. It exhibits all three phases: gel, denoted S_o in the figure, liquid-ordered (L_o), and liquid-disordered (L_d). There is a region in which all three phases coexist. The two liquid phases become one at a critical point. Again, the above explanation for the phase behavior is supported by a theoretical calculation [8] which embodies these ideas, treats the chains accurately, and produces a ternary phase diagram with the same general features as that in Fig. 1. Once the origin of the phase behavior is understood, it can be reproduced by simpler models which replace the many coordinates needed to specify a chain configuration by a single order parameter [9]. Even more simply, one can restrict that order parameter to only two values thereby dividing the saturated chains into just two classes: ordered, representing chains with few gauche bonds, and disordered, representing chains with more. Because one does not control the number in each class, the configurations freely interchange with one another [10]. Molecular Dynamics simulations of coarse-grained models of ternary mixtures of cholesterol, a saturated, and an unsaturated lipid, while not attempting to obtain the whole phase diagram, do find the new and interesting feature of these ternary systems, namely the coexistence of two liquid phases [11, 12].

As noted, for the particular temperature, 23 °C, for which the phase diagram in Fig. 1 was determined, there is a critical point at a particular concentration of the components. As such a point exists at nearby temperatures as well, there is a critical line in the phase diagram when temperature is included as a variable. The behavior of a system near a critical point has been studied intensely and is well understood. In particular, the one-phase fluid near the critical point is characterized

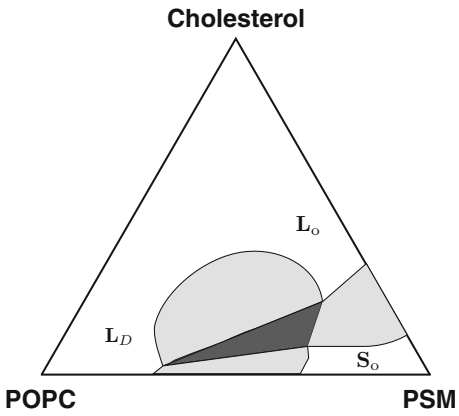

Fig. 1 Phase diagram of a ternary mixture of POPC, sphingomyelin, here labeled PSM, and cholesterol. There are two liquid phases, labeled L_o and L_d, and a gel phase, S_o. The three regions of coexistence between two phases are shown in light gray, and the triangular region of coexistence of all three phases is shown in dark gray. After reference [7]

by droplets with compositions corresponding to either the L_o or L_d phase and of a size characterized by a correlation length ξ which diverges as the critical point is approached. In particular, if the composition of the system corresponded to one on the critical line at a temperature T_c (in degrees Kelvin) then, as the temperature approached T_c, the correlation length would diverge as

$$\xi(T) = \xi_0 \left(\frac{T - T_c}{T_c} \right)^{-\nu}, \tag{1}$$

where for a lipid bilayer ξ_0 is of the order of a few nm and the critical exponent $\nu = 1$. That this should be the case for the critical point of a miscibility transition of a lipid bilayer follows from the modern theory of critical phenomena; in particular that the miscibility transition in the two-dimensional bilayer is characterized by a one-component order parameter and is therefore in the universality class of the two-dimensional Ising model of which the exact critical behavior was famously solved by Onsager [13]. Nevertheless it was nice to have this strong expectation confirmed by experiment [14].

The phenomenon of macroscopic liquid–liquid phase separation provides a plausible explanation for the origin of inhomogeneities, or "rafts," in the plasma membrane: they are droplets of one phase immersed in a background of the other. Presumably if one waited long enough, these droplets would coalesce into a macroscopic phase so that one would observe the coexistence of two phases as one does in the case of yeast vacuoles [3].

But nothing like liquid–liquid phase separation is seen in the plasma membrane. Why is this? Several answers have been proposed. One is that while the transition does occur, the macroscopic separation of phases which should accompany it is prevented by the underlying cytoskeleton which forms a network of corrals [15]. The size of these corrals was found to be of the order of 300 nm, large enough to hold a raft, so this idea explains the absence of macroscopic phase separation, but preserves the idea of a phase transition being the cause of the inhomogeneities.

A second line of argument [16] is that integral membrane proteins or attachments of the membrane to the cytoskeleton favor one of the phases over the other and, occurring randomly across the membrane, destroy the transition just as a random field is known to do in the two-dimensional Ising model [17]. This argument would seem to doom an explanation of rafts in terms of phase separation.

A third possible reason for the lack of macroscopic phase separation is that, while the biological system can undergo a miscibility phase transition, the critical temperature is below that of relevant body temperature. However if the latter is sufficiently close to a critical transition, there are large fluctuations as noted above, and these could be identified as rafts [18, 19]. The effect of a cytoskeleton-like network is to cut off fluctuations larger than the mesh size of the network, but smaller fluctuations remain and, again, could be identified as the much-sought after inhomogeneities [20]. This explanation does require that the system, at a biological temperature T, be close to the line of critical transitions. If the transition were at a

temperature $T_c = T - \Delta T$, then the correlation length $\xi(T)$ at T would be larger than the typical size of a lipid, ξ_0, by a factor

$$\frac{\xi(T)}{\xi_0} = \frac{T - \Delta T}{\Delta T}. \tag{2}$$

Note that there is no "characteristic size" of the fluctuations. Rather their size depends upon how close the system is to its critical point. If $\xi(T)$ were to be 30 nm, an order of magnitude larger than $\xi_0 \approx 3$ nm, then the system would need be about 30 °C above a critical transition. But it is more than that; the system at biological temperature would have to have *almost the same composition* as the system which is critical at the lower temperature. This is a priori unlikely and one must argue that the cell regulates its composition in order to be near the critical transition. There is no evidence that this is, or is not, the case for the plasma membrane. The evidence from giant plasma membrane vesicles [18], isolated from living cells and carrying no cytoskeleton, is reviewed in this volume by Veatch and Cicuta in chapter "Critical Lipidomics: The Consequences of Lipid Miscibility in Biological Membranes." Another problem which must be addressed if one favors criticality as the origin of rafts is that a miscibility transition seems to be characteristic only of the exoplasmic leaf of the plasma membrane. Lipid bilayers in which both leaves have a composition characteristic of the cytoplasmic leaf of the plasma membrane do not exhibit phase separation [21]. That is because the lipids in the cytoplasmic leaf are almost all unsaturated. There are too few saturated lipids to bring about a phase of their own. Therefore if phase separation were to occur in the plasma membrane, composition differences in the cytoplasmic leaf would be small. As a consequence of that, there would be little distinction between "raft" and "sea," hence no useful mechanism for conveying information from one leaf to the other. The same argument would apply to fluctuations near a critical point.

In addition to the three possible reasons given above for the lack of a macroscopic phase separation in the plasma membrane, there is also a fourth: macroscopic phase separation is not seen because the plasma membrane is not near a miscibility phase transition. As noted above, whereas the exoplasmic leaf is expected to display a tendency to undergo phase separation, the cytoplasmic leaf is not. Any coupling between the exoplasmic and cytoplasmic leaves will tend to drive the system away from phase separation temperatures characteristic of the exoplasmic leaf, an effect seen experimentally [22, 23] and understood theoretically [24, 25].

In closing this section, I can summarize by saying that nothing like the phase separation observed in yeast vacuoles is seen in the plasma membrane of mammalian cells. Large Molecular Dynamics simulations of the plasma membrane do not see such separation [26]. Whether associated critical fluctuations will prove to be the origins of rafts remains to be seen, and the case is open. Personally I remain a skeptic on this, both because the cell would have to regulate its composition to bring it near a critical transition, and because it is not clear that there would be much of an effect in the cytoplasmic leaf. That lack would defeat the purpose for which rafts were proposed.

3 Modulated Phases and Associated Microemulsions

For those of us who had worked on the theory of inhomogeneous fluids in three-dimensional systems [27], the idea that rafts could be associated with two-dimensional microemulsions was an appealing one. After all, microemulsions are characterized by regions, or droplets, which have a characteristic size and which are dynamic, fluctuating objects. In the best-known bulk system of oil, water, and amphiphile, the latter, as its name implies, loves both of the former, gaining energy by sitting between them. Because it likes the oil and water to mix, it increases the region of phase space in which they do so, driving down the miscibility transition temperature [28]. Further it reduces the surface tension between coexisting phases. If enough amphiphile is added, the energy of such interfaces is driven to zero and a modulated phase, one of lamellae or cylinders or droplets, appears in which there is an extensive amount of oil–water interface. The observation of modulated phases, or perhaps melted versions of them in lipid bilayers [29–31], and in giant plasma membrane vesicles strengthens the idea that rafts could be identified with a microemulsion.

The problem with identifying rafts with the droplets of a microemulsion is that there is no obvious amphiphile that loves both saturated and unsaturated lipids. In particular, cholesterol is certainly not. One knows this because the addition of cholesterol to a one-phase region of a mixture of saturated and unsaturated lipids brings about phase separation, i.e., raises the miscibility transition [32], a clear indicator that the cholesterol prefers one component to the other, and hence benefits if the two components separate. Safran and co-workers [33, 34] proposed that the common unsaturated lipids, those with one saturated tail and one unsaturated tail, which they called "hybrid" lipids, could be *both* a major component of the liquid-disordered phase and an amphiphile which would like to sit between that phase and the saturated-rich liquid-ordered phase. The idea is that at an $L_o - L_d$ interface, the hybrid lipid will reduce its energy if its saturated leg is oriented toward the L_o phase and its unsaturated leg toward the L_d phase. This leads naturally to a model in which the hybrid lipids are modeled by two-dimensional vectors [35]. Such models have been explored extensively [33–37] and have been reviewed recently [38, 39].

There is no doubt in my mind that the mechanism works in principle, but one must believe that the energy gain in *orienting* a hybrid lipid at a $L_o - L_d$ interface is substantial, comparable to the repulsive interaction between saturated and unsaturated lipids itself. Further, recent experimental evidence appeared that indicates that hybrid lipids do not play a unique role as an amphiphile in lipid bilayers [40].

But if there is no amphiphile in the lipid bilayer, is it possible to bring about modulated phases and microemulsions in them by some other means? The answer to this question is, yes, there is. It is well known that there are many mechanisms, several not employing an amphiphile, that can bring about modulated phases in many different kinds of systems [41]. One that is of particular interest for lipid bilayers is the coupling of lipid curvature to height fluctuations of the membrane

[42–44]. The basic idea is that in a height fluctuation, the membrane will bend outward in some places, and bend inward in others. Lipids with a large head group and small tail will move toward the former regions whereas lipids with a small head group and large tails will move to the latter. If the coupling between the fluctuations and composition is sufficiently strong, the system will form modulated phases [45]. It follows that the system can also support a microemulsion because a microemulsion can be viewed simply as a melted modulated phase [46].

In order for the coupling to be strong, it is clear that there must be a significant difference between the spontaneous curvatures of the lipids. Unfortunately this is not the case in the exoplasmic leaf. The major lipid components of this leaf are phosphatidylcholine (PC) and sphingomyelin (SM), both of which have similar, small spontaneous curvatures [47]. But in this regard the cytoplasmic leaf is quite another story. Its major components are phosphatidylserine (PS) and phosphatidylethanolamine (PE). The first, again, has a small spontaneous curvature, but that of PE is large in magnitude because of the small PE head group. Thus the difference in spontaneous curvatures of the two components is large. If there is any hope that this mechanism brings about a microemulsion in the plasma membrane, it seems that it will be due to a coupling of height fluctuations to composition differences in the cytoplasmic leaf. That there are composition differences in this leaf will be conveyed to the exoplasmic leaf by coupling between the leaves. The exoplasmic leaf will respond presumably because, as we have seen, its composition is such that it is near a phase separation which implies that the response of its lipids to perturbations in composition is large. In this way the system brings about a raft in *both* of its leaves [48]. This is in contrast to the problem I noted above, that a raft initiated by phase separation in the outer leaf is not expected to have much effect on the composition of the inner leaf.

A theoretical description of the system is readily formulated. We denote by $\phi(\mathbf{r})$ the local difference in mol fraction of PS and PE in the inner leaf, and by $\psi(\mathbf{r})$ that of SM and PC in the outer leaf. We assume equal numbers, N, of lipids in the two leaves which have equal areas A. The local, planar, free energy functional per unit area of the bilayer can be written in the usual form [45]

$$\begin{aligned} f_{plane}[\phi(\mathbf{r}), \psi(\mathbf{r})] = &-J_\phi n\phi^2 + \frac{k_B T}{2} n[(1+\phi)\ln(1+\phi) + (1-\phi)\ln(1-\phi)], \\ &-J_\psi n\psi^2 + \frac{k_B T}{2} n[(1+\psi)\ln(1+\psi) + (1-\psi)\ln(1-\psi)] \\ &-\Lambda\phi\psi, \end{aligned} \tag{3}$$

where k_B is Boltzmann's constant and T the temperature, $n \equiv N/A$ is the areal density of lipids, and Λ is an energy of coupling between the leaves. The quantities $J_\psi > J_\phi > 0$ are interaction energies, and the inequality ensures that the outer leaf

is closer, in temperature, to a phase separation than is the inner. The total free energy of the planar bilayer is then

$$F_{plane}[\phi,\psi] = \int d^2r \left[\frac{b_\phi}{2}(\nabla\phi)^2 + \frac{b_\psi}{2}(\nabla\psi)^2 + f_{plane}\right], \tag{4}$$

where b_ϕ is related to the energy per unit length between regions rich in PS and those rich in PE, and b_ψ is similarly related to the energy per unit length between regions rich in SM and those rich in PC.

The elastic free energy of the bilayer is taken to be [49]

$$F_{curv}[h] = \int d^2r \left[\frac{\kappa}{2}(\nabla^2 h)^2 + \frac{\gamma}{2}(\nabla h)^2\right] \tag{5}$$

where $h(r)$ is the height of the bilayer from some reference plane and κ and γ are the bilayer bending modulus and surface tension, respectively. The latter is the tension related to the membrane's response to normal, i.e., perpendicular to the membrane, strain [50, 51]. It is often referred to as the "frame tension." It is the quantity that can be obtained from tether-pulling experiments.

Now one couples the curvature of the bilayer to the difference in mol fractions of PS and PE in the inner leaflet:

$$F_{coupl}[\phi,h] = -\Gamma \int d^2r\ \phi(\mathbf{r})\nabla^2 h(\mathbf{r}). \tag{6}$$

The total free energy, $\tilde{F}_{tot}[\phi,\psi,h]$ is then $\tilde{F}_{tot} = F_{plane} + F_{curv} + F_{coupl}$.

It is appropriate at this point to mention related work of Friederike Schmid and collaborators [52, 53]. Suppose that one wanted to study bilayers containing PE in the laboratory. Most likely they would be symmetric bilayers. In such a case, the curvature of the bilayer would couple to composition differences in *both* leaves. One can picture PE-rich regions opposite one another bending inward on both leaves. It is essentially this situation described by Schmid. But again, this differs from the asymmetric plasma membrane in which the PE is almost completely in the inner leaf.

Returning to the total free energy above, we minimize it with respect to the height variable $h(\mathbf{r})$ for a given distribution of the membrane components, one specified by $\phi(\mathbf{r})$ and $\psi(\mathbf{r})$. After doing so, we express the resulting free energy in terms of the Fourier transforms of $\phi(\mathbf{r})$ and $\psi(\mathbf{r})$, and obtain

$$F_{tot}[\phi,\psi] = \int d^2r\ f_{plane} + \frac{A^2}{(2\pi)^2}\int d^2k \left[\frac{b_\psi}{2}k^2\psi(k)\psi(-k) + \frac{b_\phi}{2}\left\{1 - \frac{(\Gamma^2/b_\phi\gamma)}{1+\kappa k^2/\gamma}\right\}k^2\phi(k)\phi(-k)\right]. \tag{7}$$

Note that the free energy to bring about spatial variations in the order parameter $\phi(\mathbf{r})$, which had been $[b_\phi/2][\nabla\phi]^2 \propto [b_\phi/2]k^2\phi(k)\phi(-k)$, is reduced by its coupling to the height fluctuations. Of most interest to us is a disordered, fluid phase, for which the ensemble average values of all quantities are constant, independent of position. To examine the fluctuations in that phase, we expand $\phi(r)$ and $\psi(r)$ about their average values $\bar{\phi}$ and $\bar{\psi}$, and then expand the free energy, $F_{tot}[\phi, \psi]$, about that of the uniform fluid phase to second order in these deviations. The result is [54]

$$F_{tot}[\phi, \psi] = F_{tot}(\bar{\phi}, \bar{\psi}) + \frac{A^2}{(2\pi)^2}\int d^2k \left[\left\{a_\phi + \frac{b_\phi}{2}\left[1 - \frac{(\Gamma^2/b_\phi\gamma)}{(1+\kappa k^2/\gamma)}\right]k^2\right\}\phi(k)\phi(-k) + \left(a_\psi + \frac{b_\psi}{2}k^2\right)\psi(k)\psi(-k) - \Lambda\phi(k)\psi(-k)\right], \tag{8}$$

where

$$a_\phi = \frac{n}{2}\left[\frac{k_BT}{1-\bar{\phi}^2} - 2J_\phi\right]$$

$$a_\psi = \frac{n}{2}\left[\frac{k_BT}{1-\bar{\psi}^2} - 2J_\psi\right].$$

The quantity a_ψ, with the dimension of energy per unit area, measures how far the temperature T is from the critical temperature, $2J_\psi/k_B$, of a symmetric, uncoupled (i.e., $\Lambda = 0$), bilayer with equal average compositions of SM and PC ($\bar{\psi} = 0$). A similar statement applies to a_ϕ.

One can see what the fluid phase is like by examining the structure functions

$$S_{\phi\phi} \equiv \langle\phi(k)\phi(-k)\rangle,$$

$$S_{\psi\psi} \equiv \langle\psi(k)\psi(-k)\rangle,$$

$$S_{\phi\psi} \equiv \frac{\langle\phi(k)\psi(-k) + \psi(k)\phi(-k)\rangle}{2},$$

which are all measurable, in principle, by means of scattering. The brackets denote an ensemble average. The results are [37, 55]

$$S_{\phi\phi} = \frac{2g_\psi}{4g_\phi g_\psi - \Lambda^2} \tag{9}$$

$$S_{\psi\psi} = \frac{2g_\phi}{4g_\phi g_\psi - \Lambda^2} \tag{10}$$

$$S_{\phi\psi} = \frac{\Lambda}{4g_\phi g_\psi - \Lambda^2} \tag{11}$$

where

$$g_\phi(k) = \Lambda \left\{ \frac{(b_\phi/2\Lambda)(\kappa/\gamma)k^4 - (b_\phi/2\Lambda)[(\Gamma^2/b_\phi\gamma) - 1]k^2}{1 + \kappa k^2/\gamma} + \frac{a_\phi}{\Lambda} \right\} \quad (12)$$

$$g_\psi(k) = \Lambda \left\{ \frac{b_\psi}{2\Lambda} k^2 + \frac{a_\psi}{\Lambda} \right\}. \quad (13)$$

From this, one sees that there is a characteristic length in the system, $(\kappa/\gamma)^{1/2}$ which originates from the properties of the membrane. Let us pause and evaluate this length for the plasma membrane. Both the bending modulus, κ, and the surface tension, γ, of the plasma membrane have been measured several times. The values obtained vary by an order of magnitude due to the use of different cell lines and methods of measurement. Results for the bending modulus range from 1.8×10^{-19} to 1.6×10^{-18} Nm, while those for the surface tension fall between 10^{-6} and 10^{-5} N/m. I choose values from a recent measurement [56]: $\kappa = 4.1 \times 10^{-19}$ Nm and $\gamma = 0.8 \times 10^{-5}$ N/m. This yields a characteristic length of 226 nm which is certainly of the correct order of magnitude of the phenomena one is trying to explain. This does not mean that it is the correct explanation, but at least it indicates that it is not obviously wrong.

The structure functions tell us the response of the system to fluctuations in the order parameters; i.e., they are essentially susceptibilities to perturbations in the order parameter at a certain wavelength. The essence of the phase diagram can be obtained from them. There are four phases. At high temperatures and for concentration–curvature couplings Γ which are not too large, the system is in a disordered fluid phase. As the temperatures is lowered, the system undergoes a transition to two coexisting fluid phases. In one, assuming that the inter leaf coupling $\Lambda > 0$, the inner leaf is rich in PS, and the outer in SM, while in the other phase, the inner leaf is rich in PE, and the outer in PC. In the disordered phase in the vicinity of the transition, all structure functions are peaked at $k = 0$, and as the transition is approached, all structure functions diverge. If the temperature is lowered for large couplings Γ, then the system makes a transition to a modulated, striped, phase. Just above the transition, the structure functions take their maximum values at some $k^* > 0$ and diverge as the transition is approached. These two lines of continuous transitions meet at a Lifshitz point which occurs at some coupling Γ_{Lif}. At lower temperatures, the modulated phase coexists with the two fluid phases along a triple line. A phase diagram is shown in Fig. 2 as a function of the temperature-like variable $a \equiv a_\phi$ and $\tau \equiv [\Gamma_{Lif} - \Gamma]/(b_\phi\gamma)^{1/2}$.

The disordered fluid is of particular interest, and its nature can again be determined by examining the structure functions, in particular, $S_{\phi\phi}(k)$. When the coupling, Γ, between curvature and composition is small, the peak in $S_{\phi\phi}(k)$ occurs at $k = 0$, and the fluid is an ordinary one. The density–density correlation function, which is the Fourier transform of the structure function, is characterized by a single length, the correlation length, over which correlations decay. But for larger values of Γ, the peak in $S_{\phi\phi}(k)$ occurs at some non-zero value of k

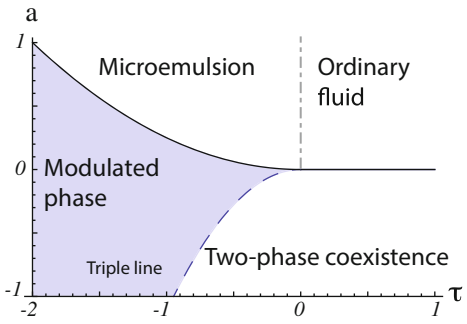

Fig. 2 Phase diagram of the model as obtained from mean-field theory which does not include effects of fluctuations. The phases are shown as a function of the temperature-like parameter, a, and the coupling, τ. Solid lines denote continuous transitions, while the dashed line denotes a triple line, i.e., three-phase coexistence. The dashed-dotted line is the Lifshitz line separating the ordinary disordered fluid from the microemulsion

indicating that the fluid is most susceptible to fluctuations which vary in space. The density–density correlation function is characterized by *two* lengths, and behaves like an exponentially-damped oscillatory function. The scale of the damping is the correlation length and the additional length is the wavelength of the oscillation in space of the fluctuations. It is the same length which characterizes the nearby modulated phase. When the modulated phase melts, the fluid to which it melts "remembers" the characteristic length scale. This is analogous to the melting of a solid to a liquid; the liquid's density–density correlation function clearly shows that the first few neighbors are at about the same distance that they were in the solid. It is this disordered fluid which clearly has structure which is denoted a *microemulsion*. There is no phase transition between the ordinary disordered fluid and the microemulsion, no singularity in the free energy. Thus the boundary in the phase diagram between these two fluids is an arbitrary one. A common, and experimentally accessible, definition is the locus of points at which the peak in a structure factor moves off of zero wave vector. That locus is called the Lifshitz line. It is denoted in Fig. 2 by the dashed-dotted line. Note that within this phase diagram, obtained via a mean-field theory, the microemulsion and the regions of two-phase coexistence are not contiguous; that is, there is no phase transition from the one to the other. It is always the ordinary fluid that undergoes phase separation.

Some of the effects of thermal fluctuations on this phase diagram have been investigated by simulations [57, 58]. The effects are seen in Fig. 3. Of interest is that the microemulsion and two-phase coexistence are now close to one another in the sense that one can go from one to the other via a first-order transition [59]. This phase diagram presents a simple explanation for the observation of the sequence of phase separation, followed by a modulated phase, followed by a disordered fluid in a four-component lipid mixture [29].

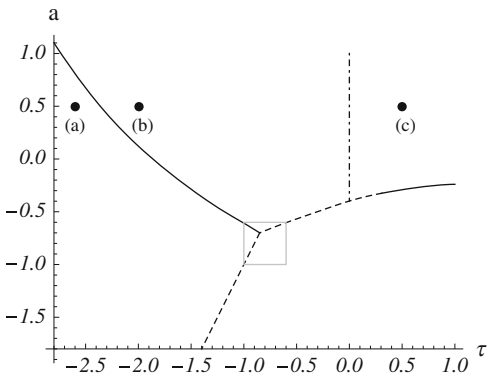

Fig. 3 Phase diagram of the model including fluctuations as a function of the two parameters a and τ. Dashed lines denote first-order transitions, solid lines continuous ones. Phase boundaries within the boxed region are extrapolations from the regions outside. The parameter b_ϕ has been set to 4.0. The dashed-dotted line is the Lifshitz line. The dots a, b, and c indicate the systems whose representative configurations are shown in Fig. 4

Representative configurations within the modulated phase, the microemulsion, and the ordinary fluid are shown in Fig. 4. That the microemulsion (b) is a melted version of the modulated phase (a) is clear. Similarly one see that as the parameters change to bring the system from (b) to the ordinary fluid (c), the amount of contrast, that is the difference in the order parameter, between neighboring droplets decreases.

4 Conclusion

Because the proposition [1, 2] that the plasma membrane is inhomogeneous, characterized by "rafts" rich in sphingomyelin and cholesterol, has attracted so much attention, one would certainly like to understand the physical basis for them. Assuming that the phenomenon is an equilibrium one, I have reviewed the two most likely explanations: (1) that they arise from a phase transition, or at least the proximity to one, or (2) that they are the manifestation of a microemulsion brought about by one of the several possible mechanisms, also reviewed. So does either apply to the mammalian plasma membrane? Many questions must be resolved and these pose experimental challenges. Are there critical fluctuations in the plasma membrane itself as opposed to those fluctuations observed in giant plasma membrane vesicles? If the plasma membrane were characterized by a microemulsion, how would one know it? One might think that a microemulsion, which has been predicted [57] to be one of the phases which has been observed in vitro [29] in micron-sized GUVs could be detected by neutron scattering experiments which are capable of determining the structure function. That of a microemulsion is characterized by a peak at a non-zero

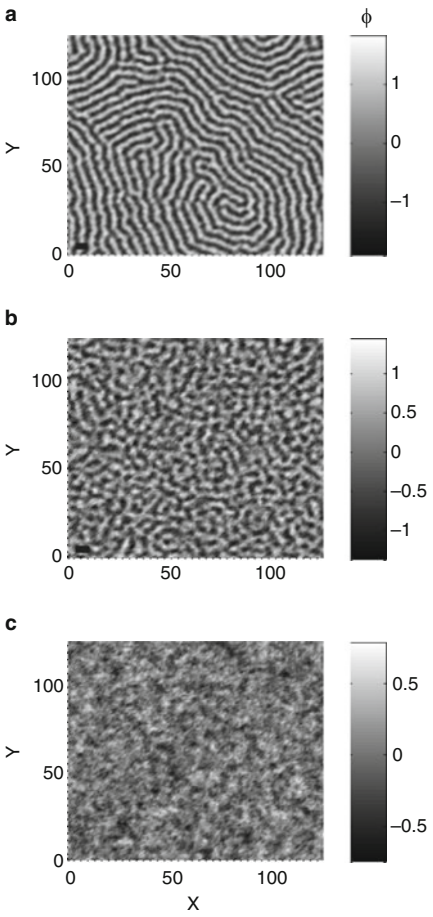

Fig. 4 Representative configurations from different phases of the system. The parameter b_ϕ is set to 4. (**a**) The location of the system is $a = 0.5$ and $\tau = -2.6$ and the system is in the stripe phase. (**b**) The location of this system is $a = 0.5$, $\tau = -2.0$. The system is a microemulsion. (**c**) At $a = 0.5$ and $\tau = 0.5$. The system is an ordinary fluid. These three systems are indicated in the phase diagram of Fig. 3

wave vector. But thus far, scattering experiments have only been carried out on small vesicles of a radius of tens of nanometers. A peak at non-zero wavevector was indeed observed in that system, but was interpreted by the authors as arising from the presence of circular domains of a system at coexistence [60]. The interpretation is not unique however.

As I have noted, a system which exhibits phase separation could be very close, in its parameters, to another which exhibits a microemulsion. This is interesting as it prods one to compare the lipid composition of a system which clearly shows phase separation, like a yeast vacuole [3], to one in which the mechanism causing inhomogeneities is not clear, like the plasma membrane. One might well hope that comparative studies of the lipid composition of these systems will resolve the very basic issue underlying the concept of rafts.

Acknowledgements I have been working in this area for many years now and have been fortunate in my colleagues. First and foremost are the "amphiphilophiles" with whom I meet weekly: Sarah Keller, Lutz Maibaum, and their students, both current and former, like Sarah Veatch, Aurelia Honerkamp Smith, and Matt Blosser, and Post-Doctoral Fellows, Marcus Collins and Thomas Portet. I thank my own Post-Doctoral Fellows, Roie Shlomovitz and Ha Giang for many hours of stimulating conversation. I have enjoyed interactions on the theory of this subject with former colleagues, Marcus Mueller and Friederike Schmid, and am grateful to the experimentalists who have shared their knowledge with me: Erwin London, Gerry Feigenson, and John Katsaras. Finally I am indebted to the National Science Foundation for their constant support. This work was supported by the NSF on Grant No. DMR-1203282.

References

1. Simons K, Ikonen E (1997) Functional rafts in cell membranes. Nature 387:569–572
2. Brown D, London E (1998) Structure and origin of ordered lipid domains in biological membranes. J Membr Biol 164:103–114
3. Toulmay A, Prinz W (2013) Direct imaging reveals stable micrometer-scale lipid domains that segregate proteins in live cells. J Cell Biol 202:35–44
4. Elliott R, Katsov K, Schick M, Szleifer I (2005) Phase separation of saturated and mono-unsaturated lipids as determined from a microscopic model. J Chem Phys 122:044904-1–044904-11
5. Shimshick E, McConnell HM (1973) Lateral phase separation in phospholipid membranes. Biochemistry 12:2351–2360
6. Ipsen JH, Karlstrom G, Mouritsen O, Wennerstrom H, Zuckermann M (1987) Phase equilibria in the phosphatidylcholine-cholesterol system. Biochim Biophys Acta 905:162–172
7. Veatch S, Keller S (2005) Miscibility phase diagrams of giant vesicles containing sphingomyelin. Phys Rev Lett 94:148101-1–148101-4
8. Elliott R, Szleifer I, Schick M (2006) Phase diagram of a ternary mixture of cholesterol and saturated and unsaturated lipids calculated from a microscopic model. Phys Rev Lett 96:098101-1–098101-4
9. Putzel GG, Schick M (2008) Phenomenological model and phase behavior of saturated and unsaturated lipids and cholesterol. Biophys J 95:4756–4762
10. Putzel G, Schick M (2011) Insights on raft behavior from minimal phenomenological models. J Phys Condens Matter 23:284101:1–284101:5
11. Risselada H, Marrink S (2008) The molecular face of lipid rafts in model membranes. Proc Natl Acad Sci U S A 105:17367–17372
12. Perlmutter JD, Sachs JN (2011) Interleaflet interaction and asymmetry in phase separated lipid bilayers: molecular dynamics simulations. J Am Chem Soc 133:6563–6577
13. Onsager L (1944) Crystal statistics. I. A two-dimensional model with and order-disorder transition. Phys Rev 65:117–149
14. Honerkamp-Smith AR, Cicuta P, Collins MD, Veatch SL, Schick M, den Nijs MPM, Keller SL (2008) Line tensions, correlation lengths, and critical exponents in lipid membranes near critical points. Biophys J 95:236–246
15. Kusumi A, Sako Y, Yamamoto M (1993) Confined lateral diffusion of membrane receptors as studied by single particle tracking (nanovid microscopy). Effects of calcium-induced differentiation in cultured epithelial cells. Biophys J 65:2021–2040
16. Yethiraj A, Weisshaar J (2007) Why are lipid rafts not observed in vivo? Biophys J 93:3113–3119
17. Grinstein G, Ma SK (1982) Roughening and lower critical dimension in the random-field ising model. Phys Rev Lett 49:685

18. Veatch SL, Sengupta P, Honerkamp-Smith A, Holowka D, Baird B (2008) Critical fluctuations in plasma membrane vesicles. ACS Chem Biol 3:287–293
19. Matcha B, Veatch S, Sethna J (2012) Critical Casimir forces in cellular membranes. Phys Rev Lett 109:138101
20. Matcha B, Papanikolaou S, Sethna J, Veatch S (2011) Minimal model of plasma membrane heterogeneity requires coupling cortical actin to criticality. Biophys J 100:1668–1677
21. Wang TY, Leventis R, Silvius JR (2000) Fluorescence-based evaluation of the partitioning of lipids and lipidated peptides into liquid-ordered microdomains: a model for molecular partitioning into 'lipid rafts'. Biophys J 79:919–933
22. Kiessling V, Crane JM, Tamm LK (2006) Transbilayer effects of raft-like lipid domains in asymmetric planar bilayers measured by single molecule tracking. Biophys J 91:3313–3326
23. Collins M, Keller S (2008) Tuning lipid mixtures to induce domains across leaflets of unsupported asymmetric bilayers. Proc Natl Acad Sci U S A 105:124–128
24. Putzel G, Schick M (2008) Phase behavior of a model bilayer membrane with coupled leaves. Biophys J 94:869–877
25. Wagner AJ, Loew S, May S (2007) Influence of monolayer-monolayer coupling on the phase behavior of a fluid lipid bilayer. Biophys J 93:4268–4277
26. Ingólfsson H, Melo M, van Eerden F, Amarez C, Lopez CA, Wassenaar TA, Periole X, de Vries AH, Tieleman DP, Marrink SJ (2014) Lipid organization of the plasma membrane. J Am Chem Soc 136:14554–14559
27. Gompper G, Schick M (1994) Self-assembling amphiphilic systems. Academic, San Diego
28. Prigogine I, Defay R (1954) Chemical thermodynamics. Longmans Green, London
29. Konyakhina T, Goh S, Amazon J, Heberle F, Wu J, Feigenson G (2011) Control of a nanoscopic-to-macroscopic transition:modulated phases in four-component DSPC/DOPC/POPC/Chol giant unilamellar vesicles. Biophys J 101:L08–L10
30. Goh SL, Amazon J, Feigenson G (2013) Toward a better raft model: modulated phases in the four-component bilayer, DSPC/DOPC/POPC/Chol. Biophys J 104:853–862
31. Stanich CA, Honerkamp-Smith AR, Putzel GG, Warth CS, Lamprecht AK, Mandal P, Mann E, Hua T-AD, Keller SL (2013) Coarsening dynamics of domains in lipid membranes. Biophys J 106:444–454
32. Veatch SL, Gawrisch K, Keller SL (2006) Closed-loop miscibility gap and quantitative tie-lines in ternary membranes containing diphytanoyl PC. Biophys J 90:4428–4436
33. Yamamoto T, Brewster R, Safran S (2010) Chain ordering of hybrid lipids can stabilize domains in saturated/hybrid/cholesterol lipid membranes. Euro Phys Lett 91:28002:1–28002:6
34. Palmieri B, Safran S (2013) Hybrid lipids increase the probability of fluctuating nanodomains in mixed membranes. Langmuir 29:5246–5261
35. Matsen M, Sullivan D (1992) Lattice model for microemulsions in two dimensions. Phys Rev A 46:1985–1991
36. Hirose Y, Komura S, Andelman DA (2009) Coupled modulated bilayers: a phenomenological model. ChemPhysChem 10:2839–2846
37. Hirose Y, Komura S, Andelman D (2012) Concentration fluctuations and phase transitions in coupled modulated bilayers. Phys Rev E 86:021916-1–021916-113
38. Palmieri B, Yamamoto T, Brewster R, Safran S (2014) Line active molecules promote inhomogeneous structures in membranes: theory, simulations and experiments. Adv Colloid Interf Sci 208:58–65
39. Komura S, Andelman D (2014) Physical aspects of heterogeneities in multi-component lipid membranes. Adv Colloid Interf Sci 208:34–46
40. Heberle F, Doctorova M, Goh S, Standaert RS, Katsaras J, Feigenson GW (2013) Hybrid and nonhybrid lipids exert common effects on membrane raft size and morphology. J Am Chem Soc 135:14932–14935
41. Seul M, Andelman D (1995) Domain shapes and patterns; the phenomenology of modulated phases. Science 267:476–483
42. Leibler S (1986) Curvature instability in membranes. J Phys 47:507–516

43. Leibler S, Andelman D (1987) Ordered and curved meso-structures in membranes and amphiphilic films. J Phys 48:2013–2018
44. Vidal IB, Rosetti CM, Pastorino C, Müller M (2014) Measuring the composition-curvature coupling in binary lipid membranes by computer simulation. J Chem Phys 141:194902
45. Kumar PBS, Gompper G, Lipowsky R (1999) Modulated phases in multicomponent fluid membranes. Phys Rev E 60:4610–4618
46. Schick M (2012) Membrane heterogeneity: manifestation of a curvature-induced microemulsion. Phys Rev E 85:031902-1–031902-4
47. Kollmitzer B, Heftberger P, Rappolt M, Pabst G (2013) Monolayer spontaneous curvature of raft-forming membrane lipids. Soft Matter 9:10877–10884
48. Shlomovitz R, Schick M (2013) Model of a raft in both leaves of an asymmetric lipid bilayer. Biophys J 105:1406–1413
49. Safran S (1994) Statistical thermodynamics of surfaces, interfaces, and membranes. Addison-Wesley, Reading
50. Diamant H (2011) Model-free thermodynamics of fluid vesicles. Phys Rev E 84:061123-1–061123-7
51. Farago O, Pincus P (2004) Statistical mechanics of bilayer membrane with a fixed projected area. J Chem Phys 120:2934–2950
52. Meinhardt S, Vink R, Schmid F (2013) Monolayer curvature stabilizes nanoscale raft domains in mixed lipid bilayers. Proc Natl Acad Sci U S A 110:4476–4481
53. Brodbek L, Schmid F (2016) Interplay of curvature-induced micro- and nanodomain structures in multicomponent lipid bilayers. Int J Adv Eng Sci Appl Math 8:111–120
54. Liu J, Qi S, Groves J, Chakraborty A (2005) Phase segregation on different length scales in a model cell membrane system. J Phys Chem 109:19960–19969
55. Gompper G, Schick M (1990) Lattice model of microemulsions. Phys Rev B 41:9148–9162
56. Pontes B, Ayala Y, Fonseca A, Romao L, Amaral R, Salgado L, Lima FR, Farina M, Viana NB, Moura-Neto V, Nussenzveig HM (2013) Membrane elastic properties and cell function. PLOS One 8:67708
57. Shlomovitz R, Maibaum L, Schick M (2014) Macroscopic phase separation, modulated phases, and microemulsions: a unified picture of rafts. Biophys J 106:1979–1985
58. Sadeghi S, Müller M, Vink RL (2014) Raft formation in lipid bilayers coupled to curvature. Biophys J 107:1591–1600
59. Gompper G, Schick M (1990) Lattice model of microemulsions: the effect of fluctuations in one and two dimensions. Phys Rev A 42:2137–2149
60. Heberle F, Petruzielo R, Pan J, Drazba P, Kucerka N, Standaert R, Feigenson GW, Katsaras J (2013) Bilayer thickness mismatch controls domain size in model membranes. J Am Chem Soc 135:6853–6859

Critical Lipidomics: The Consequences of Lipid Miscibility in Biological Membranes

Sarah L. Veatch and Pietro Cicuta

Abstract There is growing evidence that cell plasma membranes exhibit significant lateral heterogeneity in the composition of lipids and concentration of proteins. These domains have sub-micron dimensions and have been implicated in vital cell functions. Similar liquid domains are also observed, with fluorescence and non-perturbative techniques such as NMR, in model bilayer membrane mixtures that mimic cellular lipid compositions. This chapter overviews the physics, biological evidence, and consequences connected to liquid immiscibility in phospholipid membranes. The presence of phase transitions close to physiological conditions and concentrations directly implies a wide phenomenology of spontaneous lipid organization and dynamics on different length-scales. The interplay of this spontaneous lipid ordering due to the miscibility transition, with protein function and other regulatory, structural, biochemical, and mechanical membrane processes, is still an open area of investigation.

Keywords Lipid rafts · Lipidomics · Membrane proteins · Phase separation

1 Introduction

A basic aspect of cell membranes is to provide a barrier to partition volumes, and regulate the transport of charged molecules; they also act as a two dimensional substrate for membrane bound proteins, and indeed a large fraction of protein biochemistry in a cell takes place on or near membranes [1]. In infectious disease, parasites (viruses, bacteria, apicomplexans) bind and penetrate the cell through the membrane. It is crucial for all these functions that cell membranes are in a liquid

S. L. Veatch
Departments of Biophysics and Physics, University of Michigan, Ann Arbor, MI, USA
e-mail: sveatch@umich.edu

P. Cicuta (✉)
Cavendish Laboratory, University of Cambridge, Cambridge, UK
e-mail: pc245@cam.ac.uk

P. Bassereau, P. Sens (eds.), *Physics of Biological Membranes*,
https://doi.org/10.1007/978-3-030-00630-3_6

state, where proteins and lipids are able to diffuse laterally. Over the years, a better understanding of the physics of lipid mixtures has shed light on the fact that the lipid component of cell membranes plays a quite active regulatory and functional role [2–4]. Biological membranes vary significantly in topological complexity from small, highly curved single bilayer structures (e.g., synaptic vesicles) to extended highly convoluted organelles (e.g., cubic membranes in endoplasmic reticulum [5], and the Golgi apparatus), extended single bilayers (e.g., the plasma membrane), and "bulk" liquid-crystalline phases (e.g., the myelin sheath). The energy related to curvature and the intrinsic curvature of bilayers are important in defining the shape of the biological membrane [6]. Many vital cell processes involve dynamic interconversions between these different morphologies, for example, by membrane fusion, fission, or budding, on time-scales spanning milliseconds to days or longer (10^{-3}–10^{6} s). Lipid asymmetry across the bilayer, lateral organization into domains, and curvature are all known to play crucial roles in maintaining these structures and their associated functionalities [7]. Cells maintain lipid homeostasis not just globally, but within each compartment of a very dynamic environment characterized by constant flow of lipid vesicles between different membranes [7].

As well as the properties that determine structure and stability, the physical parameters linked to transport and dissipation within the membrane also play an important regulating role; in particular the membrane viscosity determines how fast objects confined to the membrane can move. Typical "objects" are the membrane proteins, and assemblies of these proteins. Their function is to allow processes both within the membrane and also in the bulk fluid inside and outside the cell [8]. For example, there are pumps that regulate the concentration of calcium, potassium, pH, etc. across the membrane. Other proteins promote the formation and budding off of small membrane vesicles, which are essential for the directed transport of molecules to particular areas of cells [9]. A very important class of membrane proteins are those that act as receptors, binding to specific chemicals, and triggering a particular downstream response; the sequence of such responses within the cell is called a signaling pathway (or transduction cascade). The molecules that relay signals from receptors on the cell surface to target molecules in the cell cytoplasm or nucleus inside the cell are called second messengers (the first messengers being the signal molecules that arrive on the cell) [8]. While many of these processes are very specific, and the biochemical details are different for each set of coupled chemical reactions, signaling pathways are themselves an area where general physical principles are important.

Many phases exist in lipid monolayers and bilayers, each characterized by differing symmetry in the lipid order (these are liquid crystal phases), and authors have used a variety of notation. The main phases we discuss here are: the disordered and highly fluid phase that occurs when pure lipids are above their chain melting temperature; the solid like gel phase below the lipid's chain melting temperature; the intermediate "liquid ordered" phase that occurs when a significant fraction cholesterol is mixed with saturated lipids, which has been postulated to occur both above and below the main transition temperature. For notation, consistent with many papers, we will use L_α to denote the disordered phase in the absence of cholesterol

(e.g., in the phase separation that can take place between saturated and unsaturated binary lipid mixtures), and L_o/L_d (ordered/disordered) to indicate the two liquid phases, of differing order and physical properties, that can occur in the presence of sterols. The subject of this chapter is the discovery, over the last few decades, that the composition of eukaryotic plasma membranes of cells is tightly regulated such that the system is close (and the proximity is seen to be changed in various cell regulatory transitions) to a thermodynamical critical point for demixing into coexisting L_o/L_d liquid phases, containing different lipid and protein components.

Physical systems in the vicinity of critical points have general behavior that depends only on the symmetry of the order parameter and the dimensionality of the system, and not on the detailed molecular interactions. In general, near a second order phase transition (such as the demixing that takes place in the ternary lipid mixtures) the susceptibility diverges, and fluctuations in the order parameter become large and long lived; this is referred to as "critical behavior." There are specific laws (common to wide classes of systems) to describe the critical behavior of thermodynamic parameters as a function of the distance to the critical point, in particular here the temperature difference [10]. Laterally separated liquid domains also spontaneously form in model bilayer membranes with certain lipid compositions, allowing the thermodynamic transitions, and organization on multiple length-scales, to be well characterized.

We argue in this chapter that the thermodynamic proximity of the critical point is biologically relevant, entailing a variety of behavior well understood from the physics of phase transitions, including spontaneous formation of transient domains. Also, the formation of more permanent domains can occur with a modest energetic cost. It is known from various communities, through experiments using a variety of methods, including recent direct observations in living cells, that saturated lipids and cholesterol in cell membranes laterally organize into domains or "rafts," affecting protein function. It is likely that phase separation is the key physical concept underlying raft formation in biological membranes, and that the related mechanisms are exploited by cells as important regulators of membrane biochemistry.

2 Lipid Phases and Structure in Biological Membranes

Three major classes of lipids are present in biological membranes: phospholipids, glycolipids, and sterols. Phospholipids are a major component of cell membranes, and are composed of a head group and phosphate group; these are covalently linked to two hydrophobic chains through either a glycerol (glycerophospholipids) or sphingosine (sphingophospholipids) backbone [1, 11, 12]. The hydrocarbon chains can each vary in length (number of carbons) and in the level of unsaturation (number of double bonds): these are the main aspects that determine the main chain transition temperature, and mixing behavior between different species. Common head groups are choline (phosphatidylcholine, PC), serine (PS), and ethanolamine (PE). Among the sphingophospholipids, sphingomyelin (SM) is commonly found in cell membranes.

Glycolipids have a sugar group (e.g., glucose) in place of the polar head, and then like phospholipids their backbone can be glycerol or sphingosine. In both phospholipids and glycolipids, the head group is exposed to the aqueous environment, and is responsible for specific chemical affinity to proteins. Sterols are present in plant and animal cells, and absent in most prokaryotes. They are also strongly amphiphilic molecules, with a very small hydrophilic region (O–H). A typical sterol is cholesterol, where the hydrophobic region is made up of a rigid, planar, ring structure, and a short hydrocarbon chain which terminates in two methyl groups. The amount of cholesterol in biological membranes of eukaryotes varies significantly, increasing concentration from the endoplasmic reticulum (ER) where lipids are synthesized, through the "secretory pathway," up to the plasma membrane [13]. Sterols generally can partition in the hydrophobic region of phospholipid bilayers, altering the physical properties, and in some cases giving rise to phase separation or formation of physically distinct phases [14].

2.1 Lipid Bilayer Phases

Membranes made of lipids with long, saturated chains tend to tightly pack and form gel (S_o) phases at room temperature (note, this classification is a simplification, considering together various possible distinct solid phases). In the S_o phase, lipid chains are ordered and extended, molecules are arranged in a hexatic lattice with a correlation length of approximately 290 nm [15], and individual lipids diffuse slowly in the plane of the membrane, with a diffusion constant of approximately $10^{-10}\,\mathrm{cm}^2/\mathrm{s}$ [16]. Above the chain melting temperature (T_m), membranes of pure phospholipids are in a liquid-crystalline (L_α) state, or, in other words, T_m is the boundary between S_o and L_α phases. The L_α phase is characterized by fast diffusion ($D \simeq 10^{-8}\,\mathrm{cm}^2/\mathrm{s}$ [16]), short lateral correlation lengths, and highly mobile hydrocarbon chains. Bilayers in the L_α phase are thinner (38 Å in L_α vs 44 Å in S_o, for DPPC [15]), and individual lipids occupy more cross-sectional area ($\simeq 70\,\text{Å}^2$ (L_α) vs. $\simeq 50\,\text{Å}^2$ (S_o) for DPPC [15]), than in S_o phase membranes of the same lipid species. Lipids with unsaturated hydrocarbon chains have low chain melting temperatures and tend to form L_α phases. The double bond restricts the mobility of the chain and prevents tight packing of the lipids into a gel state. Most lipids in cell membranes contain unsaturated bonds, contributing to the high fluidity of the membrane.

SM lipids often have high chain melting temperatures (T_m for 16:0 SM is 41 °C [17]). In cells, SM usually constitutes a large fraction of saturated lipids in the plasma membrane. Cholesterol is a ubiquitous molecule in mammalian cells, where it often makes up 20–40 mol% of the lipids in the plasma membrane. The planar ring structure of cholesterol is known to disrupt lipid packing when mixed with lipids below their chain melting temperature, while ordering the chains of lipids for $T > T_m$ [18].

A third phase of bilayer lipid membranes that will be discussed is called liquid-ordered (L_o). The L_o phase often contains saturated lipids and cholesterol. In this phase, the hydrocarbon chains of saturated lipids are more ordered and extended than in the L_α phase, though membranes remain in a liquid state where lipid diffusion constants are high ($D \simeq 5 \times 10^{-9}\,\mathrm{cm}^2/\mathrm{s}$ [16]), such that there is lateral disorder.

2.2 Lipids in Cell Membranes

In cells, lipids are found in bilayer membranes which provide a substrate for membrane bound proteins. Proteins are bound to the membrane either through hydrophobic peptide segments that span both leaflets (transmembrane protein) or are anchored to one leaflet through a few hydrophobic amino acids (e.g., cytosolic protein). Some proteins are acylated (modified with hydrocarbon chains) or directly bind to specific lipid species (e.g., GPI linked protein [19]). Some proteins are associated with the membrane through direct binding to a membrane bound protein (peripheral protein). Many lipids and proteins in the extracellular (outer) leaflet are decorated with carbohydrate moieties that contribute to an extracellular matrix. Some proteins that are exposed on the cytoplasmic face of the membrane are attached to the actin cytoskeleton (either directly or indirectly) and contribute to the structural stability of the membrane.

An added complexity is that lipids are distributed asymmetrically in the plasma membrane of living cells [7, 20]. Charged PS and PE lipids are actively pumped to the inner leaflet, while PC and SM lipids are found mainly in the outer leaflet. The loss of this asymmetry is a signal of cell death and can lead to degradation of the cell by the immune system.

2.3 Liquid-Ordered Phases and the Origin of the Raft Hypothesis

With the discovery of the liquid-ordered phase in mixtures of saturated lipids and cholesterol in the 1970s–1990s, physical scientists began to speculate that cell membranes might contain coexisting L_o and L_d phases (e.g., [21, 22]). It is more appealing to assume the existence of an L_o phase rather than an ordered S_o phase because S_o phases are rigid and would not be good substrates for membrane bound proteins. It was demonstrated that membrane lipid composition [23] and phase behavior [24] could affect protein function. Work by Simons and Van Meer [25] and Brown and Rose [26] in epithelial cells brought these ideas to the cell biology community and created a link between model and cellular systems [27]. In 1997, a landmark paper coined the words “Lipid raft” and described these biological

entities as small (<100 nm) L_o domains of saturated lipids and cholesterol in a "sea" rich of unsaturated lipid L_d phase [28]. Since then the field of lipid rafts has exploded, and many cell processes have been associated with these cholesterol and saturated lipid rich microdomains, including immune cell response, viral entry, cell polarity, protein sorting, endocytosis, cholesterol regulation, apoptosis, and many cell signaling pathways (reviewed in [29]). There is evidence for lipid rafts in a wide variety of cell types, including yeast [30], plant cells [31], and neurons [32].

The immense popularity of the raft hypothesis is due in part to the simple biochemical assay that is used to determine protein raft association. Lipid rafts are generally too small to resolve by confocal or widefield optical microscopy, but are thought to be biochemically isolated by exposing membranes to non-ionic detergents [26, 27]. The part of the membrane that remains after detergent extraction is thought to contain raft domains. This detergent resistant membrane (DRM) fraction is easy to isolate and biochemically analyze, and it has been shown that DRMs are enriched in saturated SM lipids, cholesterol, and certain membrane bound proteins [28]. While there is some evidence from model studies that DRMs contain lipids in a liquid-ordered state [33, 34], the interpretation of DRMs is strongly questioned by biologists and physicists alike. Detergent extractions are usually conducted at low temperature where more ordered phases may exist even if they are not present under physiological conditions. Also, it has been shown that the addition of detergent can promote phase separation [35]. Biologists have noticed that the composition of DRMs can vary when different detergents are used [36], or the same detergent is used in different concentrations [37]. In addition, proteins resident in internal membranes are often found in the DRM fraction, even though lipid rafts are thought to only exist in the outer plasma membrane of eukaryotic cells [38]. Other experimental methods are often combined with detergent extraction to support observations of lipid rafts, but they also have associated artifacts. For example, a protein is deemed "raft associated" if a fluorescently labeled version co-patches with known "raft markers" such as the ganglioside GM1 [39]. Unfortunately, this assay typically involves massively crosslinking both the raft markers and proteins of interest, begging the question if co-clustering is purely a consequence of this aggregation procedure and not reflective of the native state [38].

A second commonly used experimental method is cholesterol depletion. It is accepted that cholesterol is vital for raft formation, and therefore removing cholesterol should disrupt lipid rafts and their associated biochemical pathways. Cholesterol can be removed from the membrane by various molecules, disrupting protein organization and altering biochemical pathways. While it is possible to quantitatively measure the amount of cholesterol removed from the cell, in most cases it is not possible to determine the cholesterol concentration in the plasma membrane [38] because cholesterol can reside in internal membranes, and can be rapidly synthesized by the cell [40]. In addition, it has been shown that cholesterol depletion can have secondary effects that can alter protein organization. For example, a reduction in plasma membrane cholesterol can lead to disruption of the actin cytoskeleton which, in turn, alters the organization of both raft and non-raft proteins [41]. These experimental problems with raft assays led to skepticism

regarding the validity of the raft hypothesis, until better experimental methods were developed.

In its current form, lipid rafts are postulated to be small and dynamic regions of heterogeneous membrane composition, but can become larger and more stable in response to stimuli [42, 43]. This is consistent with a range of experimental data, including domains that form in immune cells after receptors are cross-linked with multivalent antigen [44]. A major criticism remains that the raft hypothesis lacks a firm mechanistic basis, as well as experimental methods to reliably probe consequences of membrane organization in cells [45].

3 Experiments on In-Vitro and Ex-Vivo Lipid Mixtures

3.1 Early Work on Binary Mixtures with Cholesterol

Much work was carried out from the 1970s on phase diagrams of binary mixtures (particularly, on phospholipid/sterol systems) [46–48], elucidating the quite complex role of cholesterol. Vist and Davis were the first to use the experimental methods of DSC and 2H NMR in concert to yield consistent results, and obtained the partial phase diagram for binary mixtures of DPPC-d62 and cholesterol shown in Fig. 1a [49]. By DSC, two peaks are detected in mixtures of saturated lipids and cholesterol. One of these peaks is sharp and corresponds to the main chain transition of the saturated lipid, while the other is broad and has been interpreted as demixing of liquid-crystalline disordered (L_d) and liquid- ordered (L_o) phases. The sharp transition remains fixed just below T_m and decreases in intensity with increasing cholesterol concentration. At the same time, the broad component increases in intensity, shifts to higher temperature, and becomes increasingly broad. The main chain transition is not observed in membranes with greater than 25% cholesterol, and the broad component can no longer be resolved when cholesterol exceeds 10–40%. Deuterium (2H) NMR directly measures anisotropic motions of the hydrocarbon chains. Distinct 2H NMR spectra can be acquired for membranes in the S_o, L_d, and L_o phases and are shown in Fig. 1b. Clear superposition of S_o and L_o spectra are observed in mixtures of DPPC and between 5 and 25% cholesterol at low temperatures ($T < T_m$). These results are in good agreement with DSC measurements which indicate an S_o–L_o coexistence region between membranes of 5–25% cholesterol. At higher temperatures ($T > T_m$), the interpretation of 2H NMR spectra is more difficult: No clear superposition of spectra are observed, instead 2H NMR spectra lose resolution in the proposed L_d–L_o coexistence region inferred by DSC. The loss of resolution is attributed to lipids exchanging between lipid environments on a time-scale comparable to the measured 2H NMR frequency differences ($\sim 10\,\mu s$). Since lipids exchange between domains via normal diffusion, this puts a limit on domain size of $<100\,nm$. At high temperatures and high cholesterol concentrations, the resolution of 2H NMR spectra is restored and

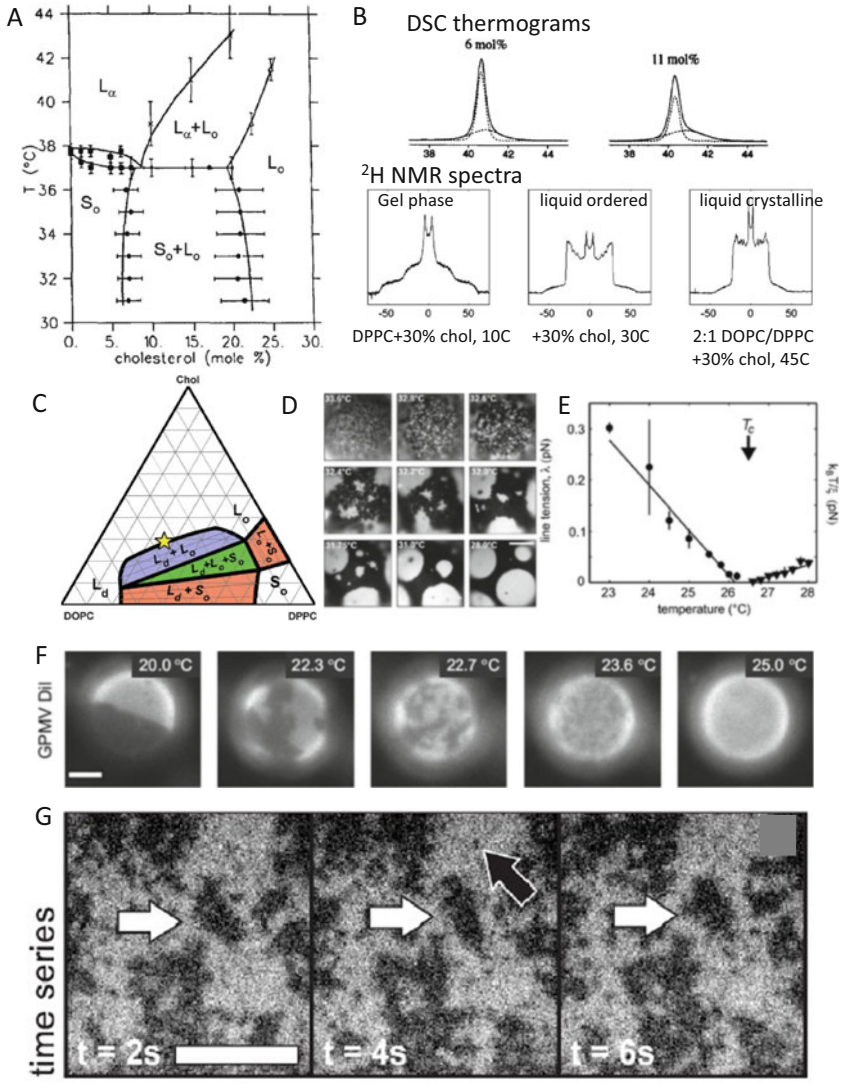

Fig. 1 Phase diagrams obtained in monolayers and membrane bilayers at concentrations mimicking the plasma membrane show phase separation and critical phenomena, and similar results are also obtained with GPMV extracted from cells. (**a**) Early work on binary mixtures of DPPC and cholesterol [49]; (**b**) DSC and NMR both allow determination of phase transition boundaries [50]; (**c**) composition phase diagram typical of a wide variety of ternary mixtures, at close to physiological temperature. Increasing T, the $L_d + L_o$ coexistence region shrinks and eventually vanishes. The yellow star marks the critical point at a particular T. (**d**, **e**) Changing T, and observing vesicles or GPMV in fluorescence microscopy, it is possible to measure the vanishing of line tension, and the growth of critical fluctuations, around the critical T [51]. (**f**) This $L_d + L_o$ coexistence and critical behavior are also observed in GPMV [52]. (**g**) The large critical fluctuations are transient, and their characteristic lifetimes (as well as their structure) depend on the proximity to the critical point in a way that is common to many other physical systems [53]

membranes are thought to be in one uniform phase. Additional evidence for the L_d–L_o phase boundaries is seen by analyzing trends in the moments of 2H NMR spectra as a function of composition and temperature. Phase diagrams like the one shown in Fig. 1a have also been evaluated by examining the lipid environment around spin probes (ESR [46]), by measuring diffusion constants of fluorescently tagged lipids (FRAP [54]), and by detecting short range interactions between fluorescent probes (FRET [55]). FRET experiments have also put a limit on domain size in the L_o–L_α coexistence region. Even though there are indications of thermodynamic transitions using experimental methods of DSC, NMR, ESR, and FRET, all phase separations detected in mixtures of saturated lipids and cholesterol are on a small length-scale [56, 57]. Fluorescence microscopy on membranes of binary mixtures of DPPC and cholesterol shows no $>1\,\mu$m arrangement of lipids, though there is evidence for $<1\,\mu$m lipid organization in membranes with $<25\%$ cholesterol below the chain melting temperature of DPPC [57]. In addition, a large change in area per molecule is detected in GUVs as temperature is scanned through T_m [58]. It is not obvious that small-scale lipid organization constitutes a true thermodynamic phase separation in mixtures of phospholipids and cholesterol. On one hand, the limits on domain size are large on the lipid length-scale (over 15,000 lipids could be contained in an 80 nm domain). On the other hand, these inhomogeneities are dynamic entities with interfacial regions that are not negligible. In addition, it is not known what governs the length-scale of <100 nm lipid domains. The nature and role of lipid domains have been addressed by the biophysical community for over 20 years [56, 59–61].

3.2 Recent Developments and Current Questions

Proximity to the critical point is a general mechanism that will lead to composition heterogeneity, but it should be noted that other mechanisms can also be at play: for example, stable nanodomains can arise in particular points of the phase diagram [4] (but perhaps not physiologically relevant to the plasma membrane concentration of sterols), and the coupling of composition with curvature can stabilize lipid heterogeneity (as well as then rapidly recruiting a variety of curvature sensing proteins) [60]. Many factors and organizing principles have been proposed and highlighted in isolation, and an interplay between these factors (lateral membrane heterogeneity, cytoskeleton pinning, clustering of lipids around proteins, and curvature) can result in very rich functional behavior. Many questions have been posed, and answered to differing degrees, out of this wide field of investigation: What types of lipids are needed to have a miscibility transition? How does composition affect transition temperature? What about phase morphology? Which lipids are found in the coexisting phases? And is one phase really liquid-ordered (L_o)? Also, are these phase separated membranes related to lipid rafts? If so, what do we learn about lipid rafts by studying miscibility? What regulatory roles can rafts play in the cell membrane? The remainder of this chapter describes the state of

work through these questions, focusing mainly on the effects that are expected from proximity to phase separation: from the determination of phase boundaries, characterization of the coexisting phases, exploration of cell membrane extracts, to the most recent experiments finding correlation (and in some cases direct links) of this phenomenology to cell biochemical protein processes.

The last two decades saw great progress in understanding liquid immiscibility in model lipid membranes, in large part made possible by the use of fluorescence microscopy to visualize phase morphologies in giant unilamellar vesicles (GUVs) [62], and the rationalization of results within the context of thermodynamic free energies of mixing. Fluorescence microscopy, coupled to suitable membrane dyes (and fluorescent antibodies and protein fusions for cell work), has become a tool of choice (validated in various ways by NMR, DSC, and AFM): it can directly highlight critical fluctuations and domain structure in GUVs (for example, artificial binary mixture vesicles [63], ternary systems [64], or cell membrane extracts [52, 65]). By this method, it has been shown that if the mixtures are allowed to phase separate then domains can grow to be large ($>1\,\mu$m), and S_o phases take on a variety of shapes that depend on lipid structure, whereas the liquid L_d and L_o phases form circular domains. Some fluorescent probes have spectral characteristics that are sensitive to the ordering of the hydrocarbon chains [63]. When these probes are used, lateral organization and chain order can be measured simultaneously.

The key initial studies were two reports of coexisting liquid domains in membranes with at least three lipid components. The first was by Dietrich and colleagues [34] where they directly observed coexisting liquid domains in giant unilamellar vesicles and supported bilayers by fluorescence microscopy. These domains differed from those observed in binary mixtures with cholesterol because domains were large ($>10\,\mu$m) and could be clearly resolved using fluorescence microscopy (e.g., see Fig. 1d, f). They characterized the phases as liquid, by quantifying diffusion constants, and showed that the more ordered phase was resistant to detergent at low temperature. A second study by Samsonov et al. [66] used black lipid membranes (a bilayer membrane spread over an aperture) and extended this work to additional lipid mixtures, varying cholesterol concentration, and making the connection between the miscibility transition and the chain melting temperature of the saturated component.

3.3 Direct Imaging Experiments Show Criticality in Model Systems

Many results on the properties of lipid mixtures near their critical point of demixing have been obtained by fluorescence microscopy, on giant unilamellar vesicles (GUVs) or on membrane extracts (giant plasma membrane vesicles, GPMVs). The resolution of fluorescence microscopy is sufficient to detect with good accuracy the miscibility transition temperature (T_{mix}) and also to extract length-scales and

fluctuation properties, so that the parameters of the criticality can be measured. Most observations to date are well described within thermodynamic models of the membrane, as reviewed in [67]. With recent advances in super-resolution imaging, it is becoming possible to investigate co-localization in vivo of lipid species and membrane proteins [44].

3.3.1 Giant Unilamellar Vesicles (GUVs)

Giant unilamellar vesicles (GUVs) of diameters 10–100 μm are most often prepared in >18 MΩ/cm water or non-ionic solutions, by the process of electroformation as described by [58, 68], with modifications to increase yield and compositional uniformity [69]. This specific method produces a high yield of compositionally uniform, single-walled bilayer vesicles when phosphatidylcholine (PC) or sphingomyelin (SM) lipids are used and when vesicles are grown at temperatures well above the chain melting temperature. It is possible to make bilayers of many lipid species, and typically a small molar fraction of one lipid species is tagged with a fluorescent marker; this trace species will in many cases partition proportionally to the compositions of the L_o/L_d phases. Other methods of making GUVs have been proposed, and have advantages in controlling size monodispersity, or enabling asymmetric compositions in the bilayers; however, they are challenging to fine tune for multicomponent mixtures, where each species differs in its amphiphilic character and adsorption dynamics.

3.3.2 Giant Plasma Membrane Vesicles (GPMVs)

Giant plasma membrane vesicles (GPMVs) can be derived from various types of mammalian cells. These GPMVs are thought to be free of cytoskeletal constraints and have been shown to display the same geometries and phase behavior of giant unilamellar vesicles (and once harvested, they can be worked on with similar methods). Fluorophores with preferential partitioning can be used to highlight fluid phases. The protocols differ slightly depending on cell type, but typically cells are grown to high density (sometimes to confluency) in tissue culture flasks, then washed and treated with formaldehyde and DTT [65, 70], causing blebs to form. With further incubation and gentle shaking GPMV detached from cells, and can be decanted. GPMVs are usually allowed to settle on ice before collection. By using this method, a single confluent 25 cm^2 flask yields sufficient GPMVs to create several dozen microscopy samples. In an alternative protocol, formaldehyde and DTT can be replaced by 2 mM N-ethylmaleimide, a reagent previously shown to cause GPMV formation [56]; all other steps are identical [71]. This alternative reagent is thought to induce less lipid/protein crosslinking, and generally to cause a milder chemical perturbation of the membrane; the resulting critical temperature in GPMVs obtained with this method is much lower, but the critical lipid phenomenology is the same. As a downside, the yield of GPMV is lower (more cells detach under these

conditions), and the mixing temperature close to freezing makes characterization of GPMVs more challenging.

3.3.3 Critical Behavior Near Liquid–Liquid Demixing

The phase diagram of ternary mixtures of saturated and unsaturated lipids, plus a sterol, has the general phases shown in Fig. 1c. On heating, the liquid–liquid region shrinks, meaning that phase separation (or more generally the proximity to the critical point), and hence the whole array of critical effects can be initiated by either changing temperature or by altering lipid composition. When lowering temperature through T_{mix}, small domains initially form in the membrane. These domains are circular, diffuse freely, and their edges fluctuate indicating that both the domain and the background phase are liquid [51, 72]. The vesicle ripens as domains collide and coalesce to form larger circular domains [73]. In most cases, vesicles completely phase separate at long times after the temperature quench (>1–30 min, depending on membrane composition, temperature, and state of tension). Alternatively, molecules can be added to the vesicle solution to initiate the miscibility transition at fixed temperature by changing lipid composition, for example, methyl-β-cyclodextrin (MBD, a carbohydrate molecule that binds cholesterol and removes it from the membrane) has proven useful.

Transition temperatures can be identified at a glance observing when recognizable domains appear (disappear) as temperature decreases (increases). More precise determinations of T_{mix}, analogously to what is done in other experiments of critical phenomena, can be obtained once the character of the phase transition is known. For example, in ternary mixtures the phase transition to L_o/L_d phases has been shown to exhibit a critical point and to be second order with Ising universality [10]; with this knowledge one can quite precisely find T_{mix} from the zero of reduced temperature by extrapolating some critical property like the domain line tension to zero (or in other cases finding their temperature of divergence, e.g., correlation lengths).

Even in the absence of protein interactions, it is possible to form metastable or even stable equilibrium phases with L_o/L_d domains of finite size. This can happen because of coupling with curvature, at low enough membrane tension [74, 75], or if the situation arises that the line tension is extremely small, akin to microemulsions [59]. Ultra small (radius < 5 nm) domains at physiological concentrations have also been reported recently, inferring their existence from FRET experiments [61].

There is biological significance in including sphingomyelin and POPC ((16:0–18:1)PC) in model vesicle systems. Phase diagrams for membranes of POPC mixed with palmitoyl SM (PSM) and cholesterol are strikingly similar to phase diagrams of mixtures that substitute DOPC for POPC (POPC/PSM/Chol), or dipalmitoyl PC (DPPC) for PSM (DOPC/DPPC/Chol) [76].

The system of diPhytanoylPC/DPPC/Chol has been studied in detail and has become a reference system, with a quantitative characterization of its properties near the critical point of demixing [51]. The choice of roughly equimolar concentrations of the three components positions the system close to its critical composition. Then,

above the critical temperature, the system is in a homogeneous phase; concentration fluctuations occur only below a characteristic size, which diverges (and domains take over the whole system) as the temperature is lowered to the critical temperature, see Fig. 1c. The divergence of this characteristic size is linear with temperature, consistent with critical behavior (Ising class universality) expected of physical systems in two dimensions [10]. As a counterpart to this behavior, it has been observed that below the demixing temperature, the circular domain shape is determined by a line tension; this tension vanishes (again, linearly) as temperature approaches mixing, from below. A subsequent study also established that the dynamics of these concentration fluctuations near their critical point is also analogous to that of simpler condensed matter systems [53]. These experiments allow the extrapolation of length- and time-scales beyond the experimentally accessible window.

Interestingly, GPMVs, which have the complex and rich composition of the plasma membrane, also exhibit liquid–liquid phase separation: the behavior appears critical-like (see Fig. 1f), and with apparently the same universality properties as in the model ternary mixtures [52, 65]. Critical fluctuations, and phase separation, are observed on cooling GPMVs below physiological temperature. Because of the invasive nature of the protocols used to produce GPMVs, one should not put too much weight on the exact temperature for phase separation; however, what is remarkable is that this temperature is robust for cells grown in identical conditions, and furthermore that consistent shifts in the phase separation temperature are observed as a consequence of perturbing the cells via drugs or signaling molecules [77–80]. This shows that the composition of the plasma membrane in cells is maintained close to the critical point, and the correlation of T_{mix} with pharmaceutical and biological stimuli is indirect proof that critical behavior is biologically relevant.

4 Cell Membrane Heterogeneity

Over the past few years, efforts from both membrane biology and biophysics communities have focused on the role lipids play in membrane organization [81–83]. In cell membranes, lipid rafts are currently thought to be localized regions that are on the order of 10–100 nm in diameter, possibly transient and rapidly dynamic over time, in which certain proteins and lipids are concentrated. Both the raft domains and the surrounding lipid matrix are liquid [83]. Lipid rafts have been associated with important biological processes such as endocytosis, adhesion, signaling, protein transport, apoptosis, and cytoskeleton organization [29, 84–86]. Since rafts in cell membranes have not been directly observed by standard microscopy, most current assays employ either indirect methods (e.g., detergent resistance), or crosslinking of rafts into larger aggregates (e.g., colocalization) [39]. Lipid-driven lateral separation of immiscible liquid phases is likely a factor in the formation of rafts in cell membranes. There is mounting evidence that the plasma membrane of many cells is inhomogeneous. Raft domains in cell membranes are thought to preferentially contain cholesterol and saturated lipids, as well

as specific lipids (e.g., sphingomyelin and the ganglioside GM1) and proteins (e.g., certain receptors and proteins with palmitoyl or glycosylphosphatidylinositol anchors) [28, 87]. The list of important physiological processes in which rafts are thought to play a role is long (see [88], and the references therein).

There is also ample evidence for biological tuning of plasma membrane lipid composition: It is well established that cells alter their lipid content in response to their environment. For example, bacteria and higher organisms change their membrane composition and physical properties when grown at different temperatures [89–93], yeasts alter their lipid content to counteract the membrane fluidizing effects of ethanol produced during fermentation [94–96], and mammalian cells adjust their lipids during the cell cycle [97–100] and differentiation [101, 102], and in response to stress or disease [103–105]. Some of these changes reflect the cells' effort to retain a robust and flexible barrier at the cell periphery.

Our current thinking, see Fig. 2, is that cells adjust their membrane composition also to maintain a functionally useful level of membrane heterogeneity, by tuning to be in close proximity to a miscibility critical point, a concept we think of as "critical lipidomics."

4.1 Lipids and Membrane Proteins

About 50% by mass of a biological membrane is composed of proteins (as little as 25% in the insulating myelin sheath, and as much as 75% in the membranes of mitochondria and chloroplasts). Some membrane proteins are transmembrane, extending across the bilayer. Others reside in the cytosol, and are anchored into a leaflet by one or more fatty acid chains, or anchored covalently to a lipid in the leaflet. Many membrane proteins are common between prokaryotes and eukaryotes. The transmembrane section of proteins is often one or more α-helix segments, which are relatively hydrophobic. The β-barrel is also a common motif, as in the porins, which are discussed below [8].

In order for a membrane protein to feel the effects of lipid heterogeneity, it must prefer to be surrounded by certain lipid types along their boundary. If these boundary conditions are specific enough, then the protein's localization and function can couple to local structure in the membrane bilayer. There are several ways that a cell might accomplish coupling to a more ordered local lipid composition. A common mechanism could be through posttranslational modification with saturated acyl groups such as palmitoylations and myristoylations. It is also hypothesized that proteins with greater hydrophobic thickness tend to prefer more ordered lipid local environments, since lipid chains in these regions tend to be more ordered and extended [107]. A third general mechanism to couple proteins to more ordered local lipids could be direct binding between proteins and specific lipids. Numerous "raft" associated proteins have proposed cholesterol binding sites, and some transmembrane proteins such as GPCRs have been shown to have preferential

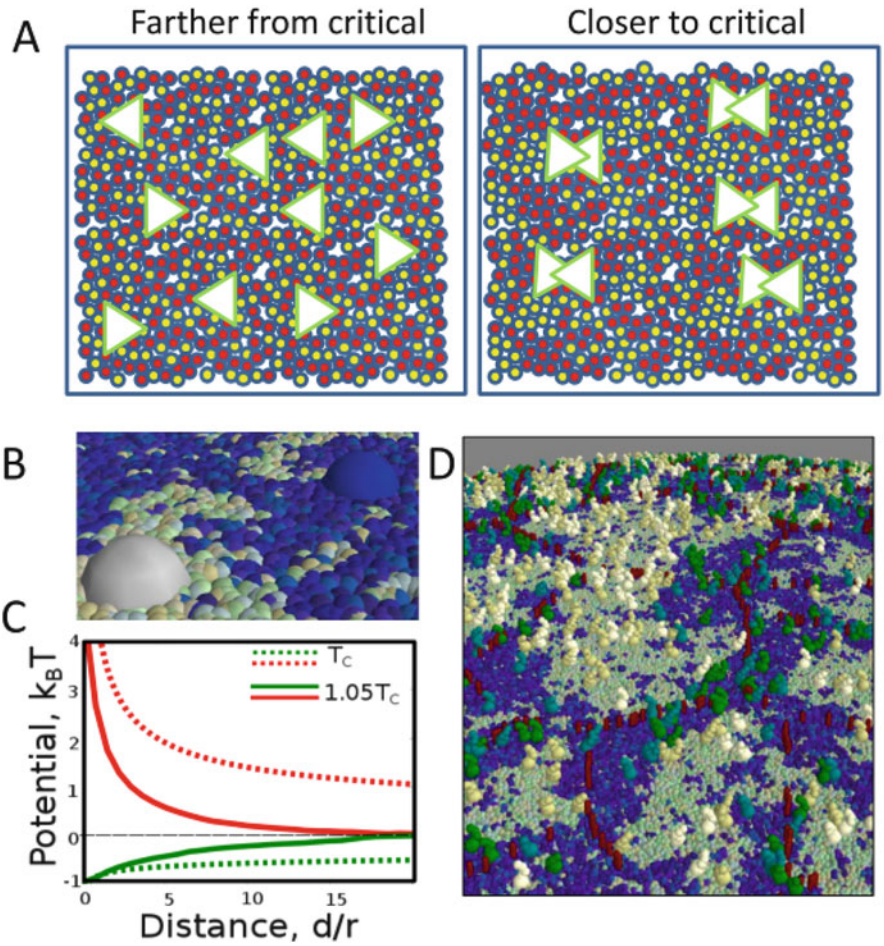

Fig. 2 Cells change membrane lipid composition, regulating the distance from the critical point. Critical lipidomics can profoundly affect cell membrane biochemistry, through a variety of mechanisms discussed in the text. One aspect is illustrated schematically in (**a**): closer to the critical point lipid domains form spontaneously, and can recruit proteins with a specific affinity, thus enhancing the local receptor protein concentration and changing the dimerized fraction. Conversely, association of proteins that require a particular lipid micro-environment is also facilitated closer to a miscibility transition. Lipid-mediated interactions between proteins can be tuned by adjusting $T - T_c$. (**b**) Schematic of two membrane inclusions (grey and blue caps) that prefer different local lipid environments feel a repulsion because they don't want to share the same local lipids. (**c**) The magnitude and range of this interaction is related to the proximity to the critical point. (**d**) Fluctuations within the membrane can couple to cortical cytoskeleton (drawn in red in the diagram), possibly also contributing to corralled diffusion [106]

interactions with polyunsaturated lipid chains [108]. Membrane proximal regions of proteins can have specific interactions with local lipids, such as through poly basic stretches on the cytoplasmic face which specifically interact with anionic lipids or glycolipid binding domains on the extracellular face. Recent studies also suggest

specific amino acid sequences within transmembrane helices can influence protein partitioning into ordered local environments [109].

Some membrane lipids are themselves directly involved in reactions: for example, binding of the protein AKT to the phospholipid PIP_3 is a signal that can trigger a range of events downstream, including the onset of cell growth and protein production [110]. PIP_3 is a minority component, accounting with PIP_2 mentioned above for around 1% of membrane phospholipids. Yet they are involved in a variety of processes [111]. The localization of PIP_3 has been studied in depth, in relation to the question of cell polarization and eukaryotic chemotaxis [112]. In response to a weak chemotactic gradient, a phase separation process is triggered, localizing PIP_3 on the plasma membrane side exposed to the highest chemoattractant concentration, and the PIP_3-degrading enzyme PTEN and its product PIP_2 to a complementary pattern [113].

A number of membrane proteins respond to the global mechanical properties of the membrane in which they are embedded; this "mechanics" (e.g., state of tension, state of curvature, flexibility to bend) can in turn be determined by composition, thus providing another mechanism coupling protein function to composition. An important example of this is represented by the mechano-sensitivity of ion channels [114, 115]. Taken together, cells have a number of different mechanisms at their disposal to regulate protein association through lipid composition.

5 Critical Lipidomics in Biomedical Scenarios

Section 3 overviewed what is known about criticality in model systems, and Sect. 4 gave a flavor of activity at the cell membrane, and how lipids, with their heterogeneity, can impact on proteins, and hence on a variety of functions. Very generic mechanisms should be at play in the membrane: the spontaneous formation of small domains, and hence tendency to recruit a higher concentration of proteins compared to a homogeneous membrane; the complementary side of the same mechanism, i.e., possibility of proteins to surround themselves in patches of specific lipid composition, see Fig. 2. Note the key importance (through mass balance kinetics) of the *local* protein concentration, for any process which (as typical of transmembrane receptors) requires a dimerization step, and even more for other processes requiring self-assembly of large protein structures (e.g., vesicle coating proteins). This is perhaps not fully or quantitatively appreciated in the literature.

Many protein processes are generic to many cell types (e.g., endocytic traffic) and represent what we can consider a basal cell activity. The lipid behavior consequent to the composition being close to a critical point is likely to be an important feature in these constitutive processes. However, in order to elucidate the importance of lipid composition, it is particularly interesting to look at some cell biology situations in which it is known that significant lipid composition changes occur. This has been observed (generally data exists from experiments involving mass spectrometry measurements on cell populations) in a variety of situations where cells differentiate,

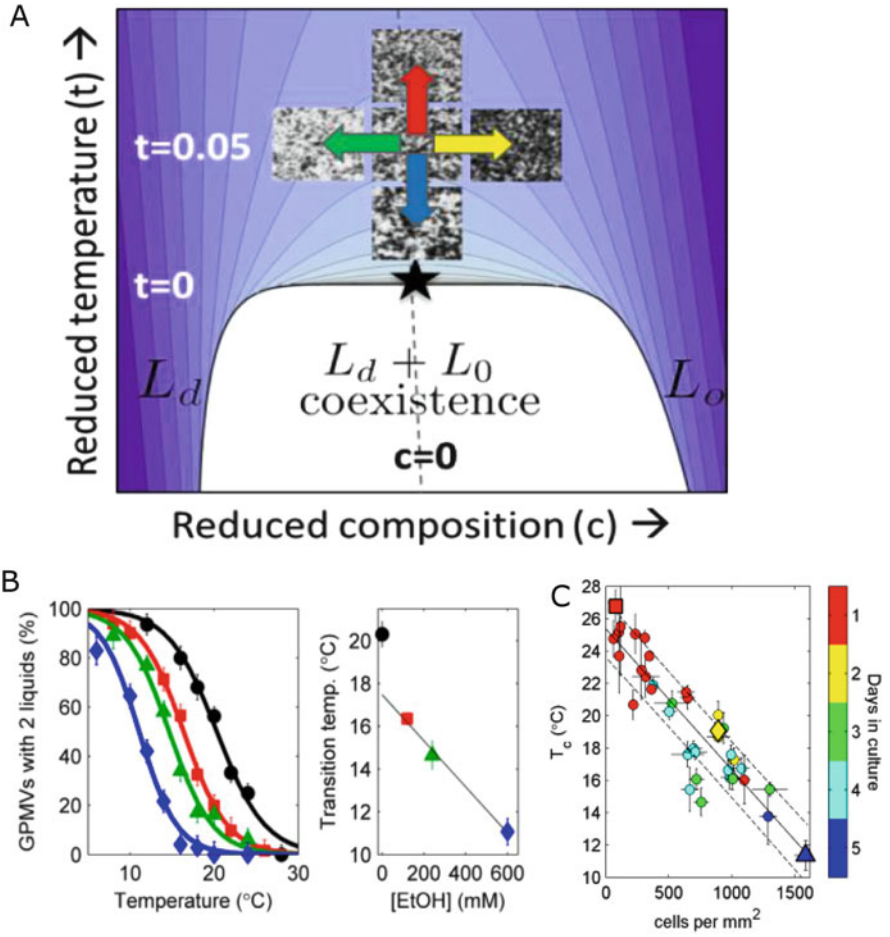

Fig. 3 There are now many cases where changes in lipidomics have been shown to correspond to varying distance to the critical point. (**a**) Schematic phase diagram of the PM, illustrating what different types of perturbations might do to lipid membrane structure. The data in (**b**) show that cell exposure to ethanol leads to composition changes that move the membrane away from criticality, as measured in isolated plasma membrane vesicles. Cells also can alter their own critical temperatures, panel (**c**) shows the case of cells grown up to different densities [77]

or enter different regulatory states, or in the context of disease [116]. We present here a few examples, and describe them in the eye of critical lipid behavior (Fig. 3).

More broadly, it is very likely that the regulatory and functional system coming from criticality underpins many "raft" dependent functional processes, ranging from immune, growth factor, and other signaling systems in other cell types to cellular processes where lipids are thought to play a role such as apoptosis, endocytosis, polarization, and cell division [112, 117–120]. Targeting biochemical modulators of membrane heterogeneity could be considered as a novel therapeutic strategy against

diseases characterized by altered lipid homeostasis, such as diabetes, inflammation, and some cancers [103, 121].

5.1 Lipid Criticality in Cancer

Cholesterol and phospholipid homeostasis is significantly altered in many cancers [103], this acts to suppress apoptotic signaling [122] and promote growth pathways [123] leading to cellular proliferation. For example, in human prostate cancer, there is an increased ratio of monosaturated to saturated fatty acids and these changes have been shown to affect the Akt pathway [124]. Frequently cholesterol levels are increased in tumors compared to normal tissues [125], and sphingolipid levels are reduced in many cancers, especially those resistant to traditional cancer therapies [126]. Interestingly, cancer cells primarily synthesize lipids directly [127], and the ABCA1 transporter is down-regulated in many cancers, resulting in decreased efflux of excess cellular cholesterol into LDL particles circulating in the blood [122]. In sum, there is a vast literature indicating that cancer cells actively alter their lipid composition while isolating themselves from regulation by other tissues. Numerous studies have implicated plasma membrane lipids in the maintenance and regulation of signaling pathways frequently disrupted in cancer. For example, modulations of growth factor signaling cascades are major hallmarks of cancer, and numerous studies have shown that the tyrosine kinase activity of these receptors is influenced by the local lipid environment. Both cholesterol and gangliosides are implicated in modulating the activity of receptors [128, 129], and have been shown to alter cellular responses to drugs that act to directly target receptor phosphorylation using kinase inhibitors [120]. Commonly mutated proteins in cancer downstream of growth factor receptors, such as Ras, are regulated in part through plasma membrane lipids [130]. In apoptosis, sphingomyelin lipids are converted to ceramides, and it is thought that this acts to cluster proteins involved in apoptosis pathways. Interestingly, cholesterol removal can initiate apoptotic signaling pathways even in the absence of ligands [131]. Alteration of plasma membrane lipids also recruits the tumor suppressor PTEN to the plasma membrane, which is vital for its roles in maintaining control of cell growth [132]. Thus, modified lipid compositions plays an important role in cellular proliferation beyond providing the additional biological material required for rapid cell growth.

Modulation of lipids and lipid metabolism provides a significant therapeutic effect in a variety of cancers, and is an emerging target of cancer therapies. For example, acute lowering of membrane cholesterol levels in cell culture can lead to apoptosis [133] or make cells more sensitive to cancer drugs [120]. Rates of cancer in the US population have been attributed in part to the wide use of cholesterol lowering drugs [134]. Exposure of cancer cells to lipid soluble small molecules can directly lead to apoptosis or can synergize with other drugs to promote cell death. Some examples include edelfosine [117] and 2-Hydroxyoleate [135] which are both in clinical trials, EGCG [136], and short chain ceramides [126].

Further, many drugs are thought to have a secondary mode of action linked to modulation of lipids. For instance, cisplatin which acts primarily by intercalating into and damaging DNA also induces apoptosis by clustering membrane receptors in a cholesterol dependent manner [137]. Also, the histone deacetylase inhibitor depsipeptide induces apoptosis in human prostate cancer cells by clustering death receptor ligands at the plasma membrane [138].

5.2 Lipid Criticality in Immunity

While the concept that lipids and lipid domains (sometimes referred to as "lipid rafts") contribute to the organization of immune receptors and downstream signaling partners has been around for decades [28, 139–142], we still lack a basic mechanistic understanding of how lipids influence the key signaling functions [143, 144]. In naive B cell lymphocytes, there are a large number of proteins known to modulate immune signaling cascades, most of which are anchored to the membrane through motifs that preferentially partition into either liquid-ordered (L_o) or liquid-disordered (L_d) phases at low temperatures (e.g., BCR, Lyn, and PAG1/CBP into L_o and CD45 and FcγRIIB into L_d) either in isolated plasma membranes or in membranes partially solubilized with detergent [145–149]. Acute changes in temperature or plasma membrane lipid composition, factors expected to impact the size and stability of membrane heterogeneities [52], also modulate signaling functions such as receptor phosphorylation, calcium mobilization, and antibody production [148, 150, 151]. It is likely that plasma membrane lipid heterogeneity modulates the detailed interactions between proteins involved in early steps of the B cell receptor (BCR) mediated signaling cascade. Confirming this would provide a novel and quantitative framework to understand how lipids influence immune signaling processes, enabling new strategies for the treatment of immune related disease through specific targeting of membrane physical state.

Many transmembrane and peripheral proteins are involved in initiating and modulating signaling responses that occur after the BCR is clustered through soluble or surface presented antigen [152–154]. The majority of these proteins interact with the BCR and other signaling partners primarily through direct binding, but it is also accepted that significant interactions likely arise from motifs that anchor these proteins or their adaptor proteins to the plasma membrane [149, 152, 155–157]. For example, Lyn kinase is thought to be primarily responsible for initial BCR phosphorylation after ligand binding. When activated, Lyn is known to bind the BCR weakly through direct interactions with the unique domain, or more strongly when at least one BCR ITAM tyrosine is phosphorylated [152]. Lyn is also anchored to the inner leaflet of the plasma membrane through palmitoyl and myristyl posttranslational modifications which favor more ordered lipid domains. This anchoring motif is shown to play important roles in localizing Lyn to sites of BCR clustering and for protecting Lyn from deactivation by phosphatases that prefer more disordered lipids [154, 158].

A large body of work exists supporting the concept that lipids play an important role in regulating signaling through the BCR [155, 157, 159]. Lowering cholesterol levels has been shown to lead to a reduction in the protein content found in detergent resistant membrane fractions, as well as decrease receptor and kinase phosphorylation. Other proteins involved in the BCR activation pathway are not affected or show increased activation in cells with reduced cholesterol content [148, 151]. This suggests that lipids also play important roles in down-regulating activated responses. However complications in singling out the role of sterols on specific processes, along with the lack of direct methods to probe the effects of membrane perturbations, have probably led the B cell signaling field to shift its focus from lipids to other key aspects of this signaling pathway, such as actin remodeling and the important roles of co-receptors [160, 161], perhaps missing an important element.

In innate immunity, there is clear evidence of large systematic changes in the "lipidomics" occurring together with "activation" (the pro-inflammatory set of changes in genetic regulation that neutrophil and macrophage cells make in response to sensing, for example, a bacterial infection) [162]. As part of this cell activation, the activity of various receptors is upregulated; one can imagine that changes in the lipid composition, such that the cell is moved close to the critical point, would automatically lead to a more heterogeneous membrane and hence directly to a higher fraction of dimerized receptors and signaling complexes [163], and hence a regulated higher activity (see schematic in Fig. 2a).

6 Progress Towards Direct Evidence of Lipid Criticality in Living Systems

Recent advances in single and super-resolution imaging are opening doors to a deeper understanding and characterization of heterogeneity in membranes [164]. But what do we expect to see using these tools if indeed the plasma membrane is a super-critical fluid? This in itself is a difficult question to answer. There are only subtle indications of criticality evident when monitoring single molecule mobility, especially when monitoring components like lipids or simple anchored peptides which only have direct interactions with a few lipid neighbors at any given instant. This is a well-known feature of critical systems, which can have slow dynamics of the average composition while maintaining fast dynamics of single molecules. As such, methods sensitive to single molecule motions such as FCS or single particle tracking are not expected to observe significant signatures of this type of membrane heterogeneity [165]. Super-resolution imaging methods may have a better chance of directly observing evidence of criticality in intact cells [166] (Fig. 4).

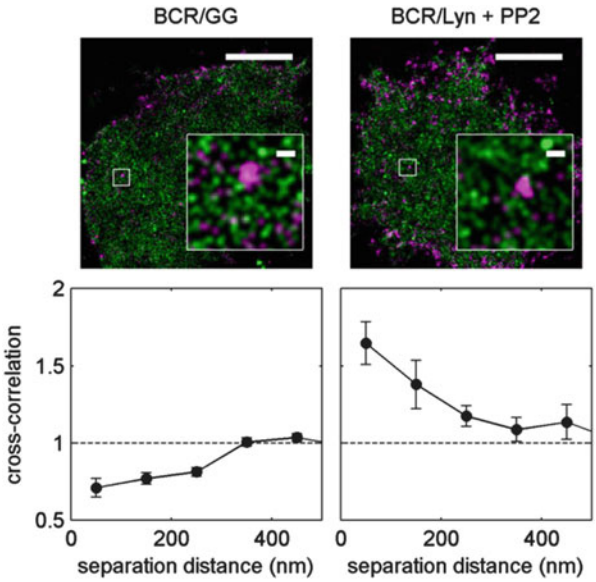

Fig. 4 Super-resolution fluorescence localization is beginning to be able to probe lipid-mediated sorting in live cells. A current challenge is to quantify the degree of lipid and protein co-localization, and then to determine the causal relation in specific situations. Imaging is likely to be an essential tool for further progress in this area. Reconstructed images show clustered B cell receptors (magenta) along with markers of disordered (GG) and ordered (Lyn) phases (green). The GG peptide is geranylgeranylated, prefers a disordered local lipid environment, and is excluded from BCR clusters. The full length Lyn protein is anchored to the plasma membrane with two saturated acyl modifications giving it a preference for more ordered lipids. This protein is recruited to BCR clusters even when cells are pre-treated with the SRC kinase inhibitor PP2 to block direct interactions between Lyn and the BCR. This is quantified using the steady state cross-correlation functions shown, where a value of 1 indicates a random distribution, less than 1 indicates exclusion, and greater than one indicates enrichment [166]

6.1 Super-Resolution Direct Imaging

One would expect various consequences in living cells based on the proximity of membrane compositions to phase separation, and specifically to critical points in the composition phase diagram:

(a) Subtle correlated densities of membrane components that partition into the same phases over short (<100 nm) length-scales .
(b) Correlated densities across-membrane leaflets, since the membrane acts as a single 2D fluid.
(c) Relatively long-lived structure in the average composition (the fundamental physics in model systems was characterized in [53]).
(d) It should be relatively easy to template changes in the average composition by coupling to structures or processes adjacent to the membrane (e.g., adhesion [167], cytoskeleton [168, 169], receptor clustering [44], etc.).

(e) Weak but long range potentials acting on components, through composition [170] or curvature effects [171], possibly coupled together (see Fig. 4).
(f) Only subtle effects on single molecule diffusion for most membrane components, as shown in [172].

Super-resolution imaging can provide direct evidence for these proposed regulatory mechanisms based on the lipid behavior. In principle, these methods have the lateral resolution and sensitivity to detect the small (<100 nm) and subtle heterogeneity expected from fluctuations. In practice, experimental details of probe over-counting, statistics, and subtle bleed-through make experiments challenging even in fixed cells. In live cells, fast single molecule mobility complicates things further [173]. Over-counting [174] and multiple observations of the same fluorophore (or antibody labeling the same protein) [175] lead to a signature in the auto-correlation of a membrane component being imaged. This is frequently much larger than the auto-correlation expected from the heterogeneity itself. Uncertainty in the magnitude of this contribution reduces the sensitivity of a single color measurement. Problems with over-counting can be addressed by co-localizing two distinct components, although problems can arise due to bleed-through between imaging channels, but can be mitigated with the use of the correct probes and imaging conditions. Even still, the predicted structures are on the edge of current resolution limits and statistics can be limiting. An easier measurement is one where one component is structured, e.g., through explicit clustering or through adhesion to a surface. In this case a second component can be probed to determine if its localization is affected by the structuring of the first component. In fixed cells there is always the concern that fixation leads to the observed heterogeneity. In live cells, single molecules diffuse orders of magnitude farther than the size of the structures being probed even when fast acquisition conditions are used.

6.2 Challenges, Controversy in Live Cells

Right now the research in this area is very active. Alongside various papers discussed and cited so far, which build on or are consistent with the idea of lipid criticality playing a significant role, it is fair to cite here a few very recent reports that challenge this view, claiming to see no evidence for "rafts" or "phase like segregation." The absence of discontinuous changes in diffusion coefficients on intact live cells, as a function of temperature, was taken as evidence that the membrane remains homogeneous [176]. We note however that crossing a second order phase transition one would not expect to observe discontinuities in the physical parameters. Also, we expect the presence of the critical point to induce effects (see section above for which effects) also in the one-fluid phase above the critical temperature. In another very recent report [177]), data is presented where live cells are grown on micropatterned substrates, whereby GPI proteins are anchored; no co-clustering of other proteins is seen in the cells, concluding against point (d) from

the list in the section above. It is very questionable however whether that experiment has the required precision to sustain this conclusion. A similar experiment, in model membranes, did observe a weak enrichment or depletion of a lipid probe at sites where a second membrane component was bound to a surface: a 20% effect [167], which is well within the error bars of [177].

7 Conclusion

Lipid composition is critical to many biochemical processes, and lipid homeostasis is important to enable cell functions in general. For example, liquid general anesthetics lower critical temperatures of the plasma membrane [77]. In particular, there is growing evidence that in living cells the lipid composition is regulated to maintain a certain distance to the critical point [65, 90], a fact that is being noted in the biological literature [178] in connection to the concept of lipid rafts. Lipid rafts represent the well-known fact that biological membranes present domains enriched with particular lipids, and that this heterogeneity couples to partitioning or adhesion of specific proteins to those regions. It is also clear that protein components of the cytoskeleton, in particular the cortical cytoskeleton, can couple to the lipid composition fluctuations [106]. The phase behavior of the lipid components seems to us a very important consideration in rationalizing complex lipidomics data, although connecting the lipidome to knowing lipid heterogeneity is itself a non-trivial task. Functional consequences upon changes in membrane organization are known for specific systems, and we have discussed various general ways in which protein function can couple to effects of lipid composition criticality (for example, some membrane receptors are known to cluster in lipid domains, affecting signaling [179]); experiments so far provide many intriguing instances of correlation, but this does not yet prove that lipidomics is acting as a regulatory mechanism: more direct evidence of causality is required. What is beyond doubt is that physiological proximity of the membrane composition and temperature to the critical point allows composition fluctuations to occur spontaneously or with very low energy cost; elucidating the biological consequences of this, and looking for general principles of membrane protein regulation by lipid composition, remain active areas of research. These questions are ripe for investigation with newly developed experimental methods capable of quantifying interactions between proteins in their native environment.

References

1. Luckey M (2008) Membrane structural biology: with biochemical and biophysical foundations. Cambridge University Press, New York
2. Nicolson GL (2014) Biochim Biophys Acta 1838:1451

3. Mouritsen OG (2004) Life - as a matter of fat: the emerging science of lipidomics. Springer, Berlin
4. Bagatolli LA, Ipsen JH, Simonsen AC, Mouritsen OG (2010) Prog Lip Res 49:378
5. Lingwood D, Schuck S, Ferguson C, Gerl MJ, Simons K (2009) J Biol Chem 284:12041
6. Voeltz GK, Prinz WA (2007) Nat Rev Mol Cell Biol 8:258
7. van Meer G, Voelker DR, Feigenson GW (2008) Nat Rev Mol Cell Biol 9:112
8. Alberts B, Bray D, Lewis J, Raff M, Roberts K, Watson JD (1994) Molecular biology of the cell. Garland Publishing, New York
9. McMahon HT, Kozlov M, Martens S (2010) Cell 140:601
10. Stanley HE (1999) Rev Mod Phys 71:358
11. Lehninger A (1975) Biochemistry. Worth Publishers, New York
12. Nelson D, Cox M (2004) Lehninger principles of biochemistry, 4th edn. W.H. Freeman, San Francisco
13. Watson H (2015) Essays Biochem 59:43
14. Kaganer VM, Möhwald H, Dutta P (1999) Rev Mod Phys 71:779
15. Nagle JF, Tristram-Nagle S (2000) Biochim Biophys Acta 1469:159
16. Alecio MR, Golan DE, Veatch WR, Rando RR (1982) Proc Natl Acad Sci USA 79:5171–5174
17. Estep TN, Mountcastle DB, Barenholz Y, Biltonen RL, Thompson TE (1979) Biochemistry 18:2112–2117
18. Ipsen JH, Karlström G, Mouritsen OG, Wennerström H, Zuckermann MJ (1987) Biochim Biophys Acta 905:162
19. Sharma P, Varma R, Sarasij RC, Ira KG, Krishnamoorthy G, Rao M, Mayor S (2004) Cell 116:577
20. Nickels JD, Smith JC, Cheng X (2015) Chem Phys Lipids. http://dx.doi.org/10.1016/j.chemphyslip.2015.07.012
21. Sperotto MM, Ipsen JH, Mouritsen OG (1989) Cell Biophys 14:79
22. Shimshick EJ, McConnell HM (1973) Biochemistry 12:2351
23. Wallace BA, Veatch WR, Blout ER (1981) Biochemistry 20:5754
24. Keller SL, Bezrukov SM, Gruner SM, Tate MW, Vodyanoy I, Parsegian VA (1993) Biophys J 65:23
25. Simons K, Van Meer G (1988) Biochemistry 27:6197
26. Brown DA, Rose JK (1992) Cell 68:533
27. Schroeder R, London E, Brown D (1994) Proc Natl Acad Sci USA 91:12130
28. Simons K, Ikonen E (1997) Nature 387:569
29. Edidin M (2003) Annu Rev Biophys Biomol Struct 32:257
30. Bagnat M, Keränen S, Shevchenko A, Shevchenko A, Simons K (2000) Proc Natl Acad Sci USA 97:3254
31. Peskan T, Westermann M, Oelmüller R (2000) Eur J Biochem 267:6989
32. Scholey JM (2002) Dev Cell 2:515
33. Ahmed SN, Brown DA, London E (1997) Biochemistry 36:10944
34. Dietrich C, Bagatolli LA, Volovyk ZN, Thompson NL, Levi M, Jacobson K, Gratton E (2001) Biophys J 47:1417–1428
35. Heerklotz H (2002) Biophys J 83:2693–2701
36. Schuck S, Honsho M, Ekroos K, Shevchenko A, Simons K (2003) Proc Natl Acad Sci USA 100:5795
37. Murphy SC, Samuel BU, Harrison T, Speicher KD, Speicher DW, Reid ME, Prohaska R, Low PS, Tanner MJ, Mohandas N, Haldar K (2004) Blood 103:1920
38. Munro S (2003) Cell 115:377
39. Thomas JL, Holowka D, Baird B, Webb WW (1994) J Cell Biol 125:795
40. Lange Y, Ye J, Steck TL (2014) PLoS One 9:e98482
41. Kwik J, Boyle S, Fooksman D, Margolis L, Sheetz MP, Edidin M (2003) Proc Natl Acad Sci USA 100:13964
42. Pike LJ (2006) J Lipid Res 47:1597

43. Simons K (2018) Lipid rafts - a personal account. In: Physics of biological membranes. Springer, Heidelberg. https://doi.org/10.1007/978-3-030-00630-3
44. Veatch S, Chiang E, Sengupta P, Holowka DA, Baird BA (2012) J Phys Chem B 116:6923
45. Kenworthy AK (2008) EMBO Rep 9:531
46. Shimshick EJ, McConnell HM (1973) Biochem Biophys Res Commun 53:446
47. Jacobs R, Oldfield E (1979) Biochemistry 18:3280
48. Lentz BR, Barrow DA, Hoechli M (1980) Biochemistry 19:1943
49. Vist MR, Davis JH (1990) Biochemistry 29:451
50. McMullen TP, McElhaney RN (1995) Biochim Biophys Acta 1234:90
51. Honerkamp-Smith AR, Cicuta P, Collins MD, Veatch SL, den Nijs M, Schick M, Keller SL (2008) Biophys J 95:236
52. Veatch SL, Cicuta P, Sengupta P, Honerkamp-Smith AR, Holowka D, Baird B (2008) ACS Chem Biol 3:287
53. Honerkamp-Smith AR, Machta BB, Keller SL (2012) Phys Rev Lett 108:265702
54. Almeida PFF, Vaz WLC, Thompson TE (1992) Biochemistry 31:6739
55. Loura L, Prieto M (2011) Front Physiol 2:1
56. Bloom M, Thewalt JL (1995) Mol Membr Biol 12:9
57. Parasassi T, Gratton E, Yu WM, Wilson P, Levi M (1997) Biophys J 72:2413–2429
58. Mathivet L, Cribier S, Devaux PF (1996) Biophys J 70:1112–1121
59. Ackerman DG, Feigenson GW (2015) Essays Biochem 57:33
60. Arumugam S, Bassereau P (2015) Essays Biochem 57:109
61. Pathak P, London E (2015) Biophys J 109:1630
62. Angelova M, Dimitrov D (1986) Faraday Discuss Chem Soc 81:303
63. Bagatolli LA, Gratton E (2000) Biophys J 78:290
64. Baumgart T, Hess S, Webb W (2003) Nature 425:821
65. Baumgart T, Hammond A, Sengupta P, Hess S, Holowka D, Baird B, Webb W (2007) Proc Natl Acad Sci USA 104:3165
66. Samsonov AV, Mihalyov I, Cohen FS (2001) Biophys J 81:1486–1500
67. Komura S, Andelman D (2014) Adv Coll Interf Sci 208:34
68. Angelova MI, Soleau S, Meleard P, Faucon JF, Bothorel P (1992) Prog Colloid Polym Sci 89:127
69. Veatch SL (2007) Methods Mol Biol 398:59
70. Levental KR, Levental I (2015) Methods Mol Biol 1232:65
71. Sezgin E, Kaiser HJ, Baumgart T, Schwille P, Simons K, Levental I (2012) Nat Protoc 7:1042–1051
72. Cicuta P, Keller SL, Veatch SL (2007) J Phys Chem B 111:3328
73. Stanich CA, Honerkamp-Smith AR, Putzel GG, Warth CS, Lamprecht AK, Mandal P, Mann E, Hua TD, Keller SL (2015) Biophys J 105:444
74. Seul M, Andelman D (1995) Science 267:476
75. Idema T, Semrau S, Storm C, Schmidt T (2010) Phys Rev Lett 104:198102
76. Veatch SL, Keller SL (2003) Biophys J 85:3074
77. Gray E, Karslake J, Machta BB, Veatch S (2013) Biophys J 105:2751
78. Zhou Y, Maxwell KN, Sezgin E, Lu M, Liang H, Hancock JF, Dial EJ, Lichtenberger LM, Levental I (2013) J Biol Chem 288:35660
79. Sezgin E, Gutmann T, Buhl T, Dirkx R, Grzybek M, Coskun U, Solimena M, Simons K, Levental I, Schwille P (2015) PLoS One 10:e0123930
80. Raghunathan K, Ahsan A, Ray D, Nyati MK, Veatch SL (2015) PLoS One 10:e0140925
81. Lingwood D, Ries J, Schwille P, Simons K (2008) Proc Natl Acad Sci USA 105:10005–10010
82. Simons K, Sampaio JL (2011) Cold Spring Harb Perspect Biol 3:a005017
83. Bernardino de la Serna J, Schütz G, Eggeling C, Cebecauer M (2016) Front Cell Dev Biol 4:106
84. Deans JP, Li H, Polyak MJ (2002) Immunology 107:176
85. Pike LJ (2003) J Lipid Res 44:655
86. Tsui-Pierchala BA, Encinas M, Milbrandt J, Johnson EMJ (2002) Trends Neurosci 25:412

87. Brown DA, London E (1998) Annu Rev Cell Dev Biol 14:111
88. McIntosh TJ, Vidal A, Simon SA (2003) Biophys J 85:1656–1666
89. Hunter K, Rose AH (1972) Biochim Biophys Acta 260:639
90. Jin A, Edidin M, Nossal R, Gershfeld NL (1999) Biochemistry 38:13275
91. Farrell J, Rose A (1967) Annu Rev Microbiol 21:101
92. Morein S, Andersson A, Rilfors L, Lindblom G (1996) J Biol Chem 271:6801
93. Kates M, Baxter RM (1962) Can J Biochem Physiol 40:1213
94. Huffer S, Clark ME, Ning JC, Blanch HW, Clark DS (2011) Appl Environ Microbiol 77:6400
95. You KM, Rosenfield CL, Knipple DC (2003) Appl Environ Microbiol 69:1499
96. Alexandre H, Rousseaux I, Charpentier C (1994) Biotechnol Appl Biochem 20:173
97. Jackowski S (1996) J Biol Chem 271:20219
98. Spiegel S, Merrill A Jr (1996) FASEB J 10:1388
99. Koeberle A, Shindou H, Koeberle SC, Laufer SA, Shimizu T, Werz O (2013) Proc Natl Acad Sci USA 110:2546
100. Atilla-Gokcumen GE, Muro E, Relat-Goberna E, Sasse S, Bedigian A, Coughlin ML, Garcia-Manyes S, Eggert US (2014) Cell 156:428
101. Ponec M, Weerheim A, Kempenaar J, Mommaas AM, Nugteren DH (1988) J Lipid Res 29:949
102. Gulaya NM, Volkov GL, Klimashevsky VM, Govseeva NN, Melnik AA (1989) Neuroscience 30:153
103. Santos CR, Schulze A (2012) FEBS J 279:2610
104. Cutler R, Kelly J, Storie K, Pedersen WA, Tammara A, Hatanpaa K, Troncoso JC, Mattson MP (2004) Proc Natl Acad Sci USA 101:2070
105. Maes M, Smith R, Christophe A, Cosyns P, Desnyder R, Meltzer H (1996) J Affect Disord 38:35
106. Machta B, Papanikolaou S, Sethna J, Veatch S (2011) Biophys J 100:1668
107. Lin Q, London E (2013) J Biol Chem 288:1340
108. Escribá PV, Wedegaertner PB, Goñi FM, Vögler O (2007) Biochim Biophys Acta Biomembr 1768:836
109. Lorent JH, Levental I (2015) Chem Phys Lipids 192:23
110. Franke T, Kaplan D, Cantley L, Toker A (1997) Science 275:665
111. Czech M (2000) Cell 100:603–606
112. Gamba A, Kolokolov V, Lebedev I, Ortenzi G (2009) J Stat Mech 2009:P02019
113. Gamba A, de Candia A, Di Talia S, Coniglio A, Bussolino F, Serini G (2005) Proc Natl Acad Sci USA 102:16927–16932
114. Ursell T, Phillips R, Kondev J, Reeves D, Wiggins P (2008) In: Kamkin A, Kiseleva I (eds) Mechanosensitivity in cells and tissues 1: mechanosensitive ion channels. Springer, Berlin, p 37
115. Phillips R, Ursell T, Wiggins P, Sens P (2009) Nature 459:379
116. Li M, Fan P, Wang Y (2015) J Glycomics Lipidomics 5:126
117. Gajate C, Gonzalez-Camacho F, Mollinedo F (2009) PLoS One 4:e5044
118. Lajoie P, Nabi IR (2010) Int Rev Cell Mol Biol 282:135
119. Gudejko HF, Alford LM, Burgess DR, Cytoskeleton (Hoboken) 69:100
120. Irwin ME, Mueller KL, Bohin N, Ge Y, Boerner JL (2011) J Cell Physiol 226:2316
121. Glass CK, Olefsky JM (2012) Cell Metab 15:635
122. Smith B, Land H (2012) Cell Rep 2:580
123. Heering J, Weis N, Holeiter M, Neugart F, Staebler A, Fehm TN, Bischoff A, Schiller J, Duss S, Schmid S, Korte T, Herrmann A, Olayioye MA (2012) Cancer Res 72:2855
124. Fritz V, Benfodda Z, Rodier G, Henriquet C, Iborra F, Avancès C, Allory Y, de la Taille A, Culine S, Blancou H, Cristol JP, Michel F, Sardet C, Fajas L (2010) Mol Cancer Ther 9:1740
125. Dessí S, Batetta B, Anchisi C, Pani P, Costelli P, Tessitore L, Baccino FM (1992) Br J Cancer 66:787793
126. Huang WC, Chen CL, Lin YS, Lin CF (2011) J Lipids 2011:565316
127. Menendez JA, Lupu R (2007) Nat Rev Cancer 7:763

128. Coskun Ü, Grzybek M, Drechsel D, Simons K (2011) Proc Natl Acad Sci USA 108:9044–9048
129. Ringerike T, Blystad FD, Levy FO, Madshus IH, Stang E (2002) J Cell Sci 115:1331
130. Schubbert S, Shannon K, Bollag G (2007) Nat Rev Cancer 7:295
131. Gniadecki R (2004) Biochem Biophys Res Commun 320:165
132. Goswami R, Singh D, Phillips G, Kilkus J, Dawson G (2005) J Neurosci Res 81:541
133. Li YC, Park MJ, Ye SK, Kim CW, Kim YN (2006) Am J Pathol 168:1404
134. Ravnskov U, Rosch PJ, McCully KS (2015) J Clin Oncol 33:810
135. Terés S, Lladó V, Higuera M, Barceló-Coblijn G, Martin ML, Noguera-Salvà MA, Marcilla-Etxenike A, García-Verdugo JM, Soriano-Navarro M, Saus C, Gómez-Pinedo U, Busquets X, Escribá PV (2012) Proc Natl Acad Sci USA 109:8489
136. Tsukamoto S, Hirotsu K, Kumazoe M, Goto Y, Sugihara K, Suda T, Tsurudome Y, Suzuki T, Yamashita S, Kim Y, Huang Y, Yamada K, Tachibana H (2012) Biochem J 443:525
137. Lacour S, Hammann A, Grazide S, Lagadic-Gossmann D, Athias A, Sergent O, Laurent G, Gambert P, Solary E, Dimanche-Boitrel MT (2004) Cancer Res 64:3593
138. Vanoosten RL, Moore JM, Ludwig AT, Griffith TS (2005) Mol Ther 11:542
139. Holowka D, Gosse JA, Hammond AT, Han X, Sengupta P, Smith NL, Wagenknecht-Wiesner A, Wu M, Young RM, Baird B (2005) Biochim Biophys Acta 1746:252
140. Dykstra M, Cherukuri A, Pierce SK (2001) J Leukoc Biol 70:699
141. Janes PW, Ley SC, Magee AI, Kabouridis PS (2000) Semin Immunol 12:23
142. Casey PJ (1995) Science 268:221
143. Kenworthy AK, Nichols BJ, Remmert CL, Hendrix GM, Kumar M, Zimmerberg J, Lippincott-Schwartz J (2004) J Cell Biol 165:735
144. Lichtenberg D, Goñi FM, Heerklotz H (2005) Trends Biochem Sci 30:430
145. Levental I, Grzybek M, Coskun Ü, Simons K (2010) Proc Natl Acad Sci USA 107:22050
146. Sengupta P, Hammond A, Holowka D, Baird B (2008) Biochim Biophys Acta 1778:20
147. Cheng PC, Dykstra ML, Mitchell RN, Pierce SK (1999) J Exp Med 190:1549
148. Petrie RJ, Schnetkamp PP, Patel KD, Awasthi-Kalia M, Deans JP (2000) J Immunol 165:1220
149. Gupta N, Wollscheid B, Watts JD, Scheer B, Aebersold R, DeFranco AL (2006) Nat Immunol 7:625
150. Katkere B, Rosa S, Caballero A, Repasky EA, Drake JR (2010) J Immunol 185:5032
151. Awasthi-Kalia M, Schnetkamp PP, Deans JP (2001) Biochem Biophys Res Commun 287:77
152. Dal Porto JM, Gauld SB, Merrell KT, Mills D, Pugh-Bernard AE, Cambier J (2004) Mol Immunol 41:599
153. Fleire SJ, Goldman JP, Carrasco YR, Weber M, Bray D, Batista FD (2006) Science 312:738
154. Pierce SK, Liu W (2010) Nat Rev Immunol 10:767
155. Gupta N, DeFranco AL (2007) Semin Cell Dev Biol 18:616–626
156. Sohn HW, Tolar P, Pierce SK (2008) J Cell Biol 182:367
157. Sohn HW, Tolar P, Jin T, Pierce SK (2006) Proc Natl Acad Sci USA 103:8143
158. Stone MB, Shelby SA, Núñez MF, Wisser K, Veatch SL (2017) eLife 6:e19891
159. Cheng PC, Cherukuri A, Dykstra M, Malapati S, Sproul T, Chen MR, Pierce SK (2001) Semin Immunol 13:107
160. Mattila PK, Feest C, Depoil D, Treanor B, Montaner B, Otipoby KL, Carter R, Justement LB, Bruckbauer A, Batista FD (2013) Immunity 38:461
161. Sohn HW, Krueger PD, Davis RS, Pierce SK (2011) Blood 118:6332
162. Norris PC, Dennis EA (2014) Adv Biol Regul 54:99
163. Gay NJ, Symmons MF, Gangloff M, Bryant CE (2014) Nat Rev Immunol 14:546
164. Garcia-Parajo MF, Cambi A, Torreno-Pina JA, Thompson N, Jacobson K (2014) J Cell Sci 127:4995
165. Manzo C, Garcia-Parajo MF (2015) Rep Prog Phys 78:124601
166. Stone MB, Veatch S (2015) Nat Commun 6:7347
167. Zhao J, Wu J, Veatch S (2013) Biophys J 104:825
168. Goswami D, Gowrishankar K, Bilgrami S, Ghosh S, Raghupathy R, Chadda R, Vishwakarma R, Rao M, Mayor S (2008) Cell 135:1085

169. Honigmann A, Sadeghi S, Keller J, Hell S, Eggeling C, Vink R (2014) Elife 3:e01671
170. Machta B, Veatch S, Sethna J (2012) Phys Rev Lett 109:138101
171. Fournier JB (2014) Phys Rev Lett 112:128101
172. McConnell H (2012) J Chem Phys 112:215104
173. Stone MB, Shelby SA, Veatch SL (2017) Chem Rev 117(11):7457–7477
174. Veatch SL, Machta BB, Shelby SA, Chiang EN, Holowka DA, Baird BA (2012) PLoS One 7:e31457
175. Sengupta P, Jovanovic-Talisman T, Skoko D, Renz M, Veatch S, Lippincott-Schwartz J (2011) Nat Methods 8:969
176. Lee IH, Saha S, Polley A, Huang H, Mayor S, Rao M, Groves JT (2015) J Phys Chem B 119:4450
177. Sevcsik E, Brameshuber M, Fölser M, Weghuber J, Honigmann A, Schütz GJ (2015) Nat Commun 6:6969
178. Simons K, Gerl MJ (2010) Nature 11:688
179. Bethani I, Skånland SS, Dikic I, Acker-Palmer A (2010) EMBO J 18:2677

Lateral Diffusion in Heterogeneous Cell Membranes

Didier Marguet and Laurence Salomé

Abstract The plasma membrane is organized at numerous levels as a result of its large variety of molecular constituents and of selective interactions between them. Lateral diffusion, a direct physical consequence of the Brownian agitation, plays a key organizational role by constantly redistributing the membrane constituents among the possible molecular associations. In this context, we will first review the physical mechanisms contributing to the creation of inhomogeneity. We will then describe the current methodological approaches allowing us to measure diffusion in living cells. The different levels of membrane organization will be discussed before illustrating the impact of the dynamic organization of the membrane on cellular functions.

Keywords Cell membrane · Lateral diffusion · Fluorescence microscopy · Nanodomains

1 Introduction

Over the past four decades, extensive experimental work has been dedicated to the exploration of membrane organization and dynamics. Taking benefit from continuous and impressive methodological and technological advances, many facets of the cell membrane's complexity and exquisite subtleties have been revealed, providing new information that has enriched our concepts in membrane biology [1–4]. Still, the present consensual, but not yet definitive, view of biological

D. Marguet (✉)
Centre d'Immunologie de Marseille-Luminy, Aix Marseille Université, Inserm, CNRS, Marseille, France
e-mail: marguet@ciml.univ-mrs.fr

L. Salomé
Institut de Pharmacologie et de Biologie Structurale, Université de Toulouse, CNRS, UPS, Toulouse, France
e-mail: laurence.salome@ipbs.fr

P. Bassereau, P. Sens (eds.), *Physics of Biological Membranes*,
https://doi.org/10.1007/978-3-030-00630-3_7

membranes amazingly recalls the ideas proposed by Singer and Nicolson in 1972 [5, 6]. While textbooks, reviews, and papers recognize the influential step forward taken with the Fluid Mosaic model, they quite generally retain only the notion of the membrane as "a sea of lipids in which proteins are randomly distributed." However, Singer and Nicolson's seminal article claiming that "*valid generalization may exist about the way proteins and lipids are organized in membranes"* already predicted the existence of nanometer-scale domains which is now a commonly accepted idea. What visionaries were these scientists who proposed that "*the absence of long-range order (over distances of the order of tenths of a micrometer and greater) should not be taken to imply the absence of short-range order in the membrane*" and, even more, added "*It is more likely that such short-range order exists*." The concept of nanometer-scale domains was thus introduced, although their importance and functional role remain under scrutiny. Diffusion and heterogeneity, which represent the focus of this chapter, were the major membrane features that guided Singer and Nicolson in the elaboration of their original model grounded in thermodynamic principles.

Prior to the development of the arsenal of techniques dedicated to the measurement of diffusion by W.W. Webb [7–9], diffusion of the membrane components had been demonstrated by the now-famous cell fusion experiments by Frye and Edidin [10]. Diffusion results from the noncovalent nature of the interactions governing the self-assembly of membranes but leads to a dynamic organization of cellular membranes due to its interplay with selective molecular interactions. Both effects are at work in biological functions; they keep plastic and efficient for instance the cellular response following the stimulation by a specific signal.

The diversity of membrane components, lipids and proteins, is tremendous, as has been recognized for a long time. As a consequence of this diversity, "*the formation of a supra-molecular aggregate like a biological membrane is expected to be "heterogeneously" organized as a result of cooperative phenomena among a large number of different molecular species*" [11].

In this chapter, we first recall the general physical mechanisms governing the formation of lateral heterogeneities and the dynamics of membrane organization. We then compare the methodological and experimental approaches available to probe this dynamic membrane organization. Subsequently, we describe the different levels of organization observed in biological membranes, as well as their impact on cellular functions. Finally, we outline the questions that should be answered by future research in this field.

2 Physical Mechanisms Governing the Formation of Lateral Heterogeneity and the Dynamics of the Membrane Organization

As recalled in the introduction, the framework initially established by Singer and Nicolson to describe the structure of the cell membrane relies on proteins being wholly or partly embedded within lipid bilayers, in which it is assumed that

particular molecular associations take place at short range. The reason why biomembranes still are fascinating study objects from a physical and biological point of view has to do with these supramolecular aggregates being built upon weak intermolecular interactions between a broad variety of lipids and proteins. Therefore, this characteristic combined with the thermal agitation occurring between molecules at physiological temperature would ultimately generate local inhomogeneity. On first thought, these two features—i.e., weak intermolecular interactions and thermal agitation—might appear to be antagonistic: the former creates selective interactions, i.e., "order," whereas the latter introduces a tendency toward mixing, i.e., "noise," within the system. But, in a counterintuitive manner, and because of the large number of different molecular species, the Brownian agitation enables through molecular random motion the existence of a number of selective interactions which contribute to create the lateral heterogeneity [12]. Therefore, creating order as a result of noisy agitation should be considered to lie at the core of the mechanism behind the organization of cellular membranes by generating the heterogeneity and plasticity required for life processes [13, 14].

Indeed, the nonrandom distribution of the membrane components directly results from the balance between the energy involved in a molecular interaction and the thermal energy within the system. In cell membranes, the energy related to interactions among the membrane components is of comparable magnitude to the thermal energy occurring at physiological temperature. As a consequence:

- The characteristic length scales of the membrane organization strongly depend on temperature.
- The lifetime of an interaction is shortened if the thermal energy is higher than the characteristic energy required for a molecular association and vice versa.

Although long considered as only providing a passive fluid matrix to the proteins, lipids are now recognized to play effective roles in cellular membranes. Their physicochemical properties provide the fundamental principles from which the lateral heterogeneity and dynamics of membrane organization arise. Indeed, the primary physical mechanism organizing the cell membrane relies on the amphiphilic nature of lipids which are divided into a hydrophobic part, the hydrocarbon chains, and a hydrophilic part, the head group. When mixed with water, the biological solvent, lipids self-assemble by an entropic effect resulting from the incapability of the hydrocarbon chains to form hydrogen bonds and, concomitantly, from the capability of the polar head groups to collectively decrease the interfacial tension between water and the lipids. Altogether, the thermodynamic laws and intermolecular forces determine the complex dynamical organization of membrane components. However, favoring a state of aggregation by minimizing the free energy does not provide a complete understanding of the classical lipid bilayer organization observed by biologists. For instance, in artificial membranes, changes in the composition of lipid mixtures or in temperature can induce a transition from a lamellar organization to a micellar one or vice versa.

One should also consider the huge lipid diversity. Although all lipids share a very similar chemical structure with a polar head and hydrophobic hydrocarbon chains,

up to a thousand different molecular species can be found within a single cell. This has direct impacts on the cell membrane organization and more specifically on:

- The membrane thickness. The trans-bilayer structure is characterized by its thickness and relies on the lateral pressure profile of the bilayer. This profile is the consequence of the balance of forces occurring between (1) the interaction between lipid head groups, (2) the interfacial tension, and (3) the flexibility of the hydrocarbon chains;
- The lateral organization. The molecular organization within the plane of the bilayer is a consequence of a cooperative phenomenon generated by a number of selective intermolecular interactions among different lipid species, which arise through thermal agitation. As a consequence, phase separations which have been described in detail for lipid mixtures of different complexity contribute to the creation of lipid domains; the size, lifetime, or shape of such domains depends on thermodynamic conditions.
- The spontaneous curvature of the membrane. This parameter is influenced by the packing parameter calculated for individual lipid species. It takes into account the surface area of the hydrophilic group, and the volume, length, and degree of unsaturation of the hydrophobic chains [11]. The so-called shape of a lipid determines its capability to fit within a given lipid aggregate. In other words, the overall structure of a bilayer will tend to minimize the curvature elastic stress energy through an asymmetric distribution of lipid species between the two membrane leaflets and within each leaflet by developing selective lipid associations or exclusions.

Membrane proteins add another level of complexity to this basic membrane organization and ultimately contribute to generate lateral heterogeneity within cellular membranes. Indeed, cellular membranes also contain a large number of different proteins, either directly embedded within the lipid bilayer or bound directly or indirectly to it. Significant efforts have been made to integrate the following features in the current description of membrane dynamics:

- The diversity of the proteins with respect to their nature, function, and size, as well as their inherent asymmetric orientation within membranes
- The quaternary structure of proteins and the interactions between such supramolecular complexes both within the membranes and at their vicinity
- The interactions between lipids and proteins, the way they pack together (i.e., favorably accommodate each other), and the way that protein conformational changes occur during biological processes

All of these features are of particular significance and govern the organization and dynamics of cellular membranes.

As a consequence of the thermal agitation of molecules at physiological temperatures, lipids and proteins are driven by Brownian motion, but their diffusion is restricted to the membrane plane. If unhindered, such lateral diffusion allows the molecules to explore the cellular membrane in a short amount of time—for instance, a membrane component diffuses through the plasma membrane of a standard cell

size in a few tens of seconds—and should create a homogeneous distribution of the membrane components in the absence of selective interactions. However, the diversity of the membrane composition generates differential molecular interactions of various strengths which ultimately nucleate local heterogeneity. Thus, this leads to a switch of the behavior of the components from a strictly free diffusion regime to a constrained one, for example confined diffusion within subdomains or oriented diffusion by direct or indirect interactions with motors linked to the cytoskeleton.

Therefore, there is no doubt that collectively lipids and membrane-associated proteins contribute to create local heterogeneity. Experimentally, such heterogeneities in membranes have to be revealed by the description of the molecular distribution of their constituents with the appropriate spatial resolution. This has been achieved by electron and fluorescence microscopies (see for example [15, 16]) although experimental limitations due to fixation and labeling procedures remain [17, 18].

Ideally, a dynamic map of the molecular distribution of the membrane components should be established. The most recently developed techniques for measuring the lateral diffusion, providing the adequate spatiotemporal resolution, indeed tend toward this objective. This should allow the identification of the mechanisms prevailing in the membrane organization.

3 Methodological Approaches to Probe the Dynamics of the Membrane Organization

After the initial observation by Frye and Edidin [10] revealing the diffusion of membrane components by rapid intermixing of membrane proteins after cell fusion, a large panel of techniques, spanning several orders of magnitude in time and length scales, has been invented to investigate the lateral diffusion of membrane lipids and proteins (Fig. 1). These methods are mainly based on fluorescence microscopy. They owe their emergence to the impressive creativity of W.W. Webb who focused his research on the observation of the dynamics of the biomolecular processes of life. Nowadays renowned for the experimental demonstration of the two-photon absorbance phenomenon and its application to multi-photon microscopy, this scientist has also invented fluorescence recovery after photobleaching (FRAP) [7] and fluorescence correlation spectroscopy (FCS) [9, 19] and performed the first single-particle tracking (SPT) experiments [8] (see Fig. 2 for the basic principles of the techniques). Since then, improvements and variants of these three major techniques have been further developed. As an example related to FCS, fluorescence cross-correlation spectroscopy (FCCS) enables the observation of co-diffusion of molecules [20]. A variety of alternative image correlation spectroscopy (ICS) methods have emerged as well [21]. During the last decade, the use of single-molecule methods has literally exploded, first thanks to the increase of the sensitivity of the detectors making possible the imaging of single fluorophores with relevant

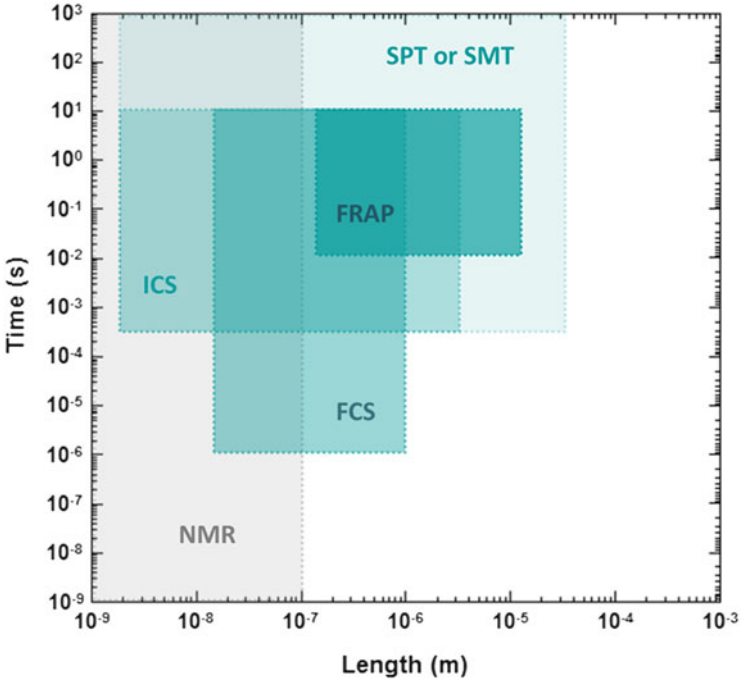

Fig. 1 Time and length scale ranges covered by the techniques dedicated to the investigation of membrane dynamics. Abbreviations: *NMR* Nuclear magnetic resonance, *FRAP* Fluorescence recovery after photobleaching, *FCS* Fluorescence correlation spectroscopy, *ICS* image correlation spectroscopy, *SMT* Single-molecule tracking, *SPT* Single-particle tracking

time resolution and more recently due to the capacity to control the fluorescence state or the illumination geometry of the probes, leading to the development of super-resolution microscopies such as PALM, STORM, etc. [22].

Our purpose in this chapter is not to discuss the general features of each of the techniques dedicated to membrane diffusion measurements. For this we invite the reader to consult recent reviews for useful information on the principles of these techniques, the proper choice of probe and instrumentation, the existing labeling strategies, and the basic analytic tools to compute the diffusion parameters from the experimental output of FRAP [23], FCS [24, 25] and SPT [21, 26]. Here, we will rather present a critical overview of the capability of these techniques to characterize heterogeneities and/or domains in membranes (Fig. 2).

First we propose to carefully delineate on which length and time scales these techniques yield information. This is of primary importance because obviously *one can find only what one is able to see* and none of the techniques covers the whole spatiotemporal range of lipid and protein diffusion. FRAP is usually considered to be a large-scale mobility assay inappropriate to go beyond a simple measurement of the diffusion coefficient of the mobile fraction of the tracer population. If a

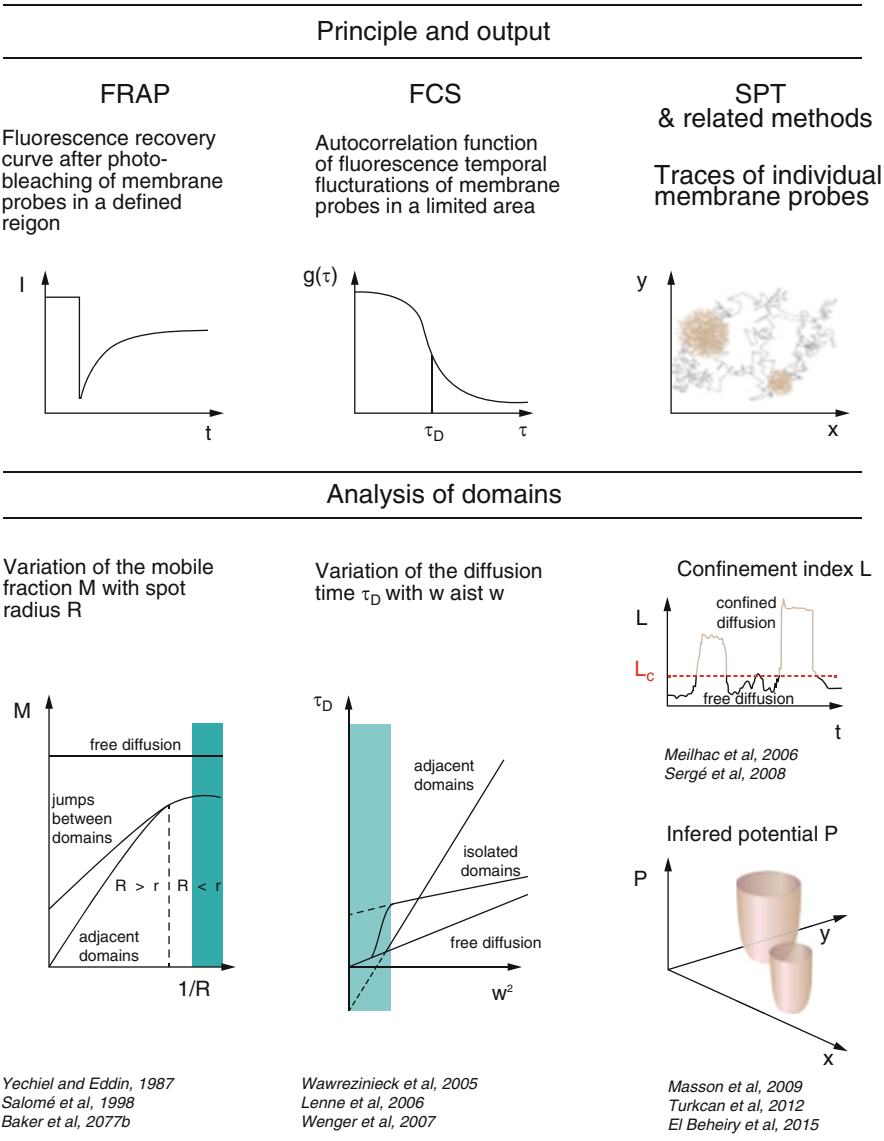

Fig. 2 Current methods for the analysis of membrane domains (of size *r*) based on diffusion measurements by FRAP, FCS, and SPT (see text for a more detailed discussion). In blue, the ranges of length scales inaccessible by conventional microscopy. In light brown, the periods of confinement and their corresponding analytical signatures

membrane is structured, this gives rise to incomplete fluorescence recovery (or an immobile fraction). The measured diffusion coefficients, which are estimated from the fit of the recovery curve assuming free diffusion within an area equal to the

bleached area, are then apparent ones. While this makes the comparison between data obtained on different cell lines problematic, it can turn out to be useful for the identification and characterization of submicrometer-sized domains by repeating measurements at variable spot size (see Fig. 2) as first demonstrated by Yechiel and Edidin [27]. Provided the microscope used can bleach areas down to about 1 μm in diameter and that the fluorescence recovery signal can be monitored without delay (these conditions are unfortunately not accessible with commercial confocal microscopes which are most often used), domain sizes as small as 200 nm can be measured together with diffusion coefficients inside these domains. A refined analysis enables to reveal whether the domains are joint and permeable or not [28–31]. The typical duration of a fluorescence recovery is of the order of a few tenths of seconds, precluding the identification of small short-lived domains by FRAP. In a similar way, FCS performed at variable beam waist gives information on spatiotemporal heterogeneities. This technique was first developed by Marguet and coworkers [32, 33] who, using nanoapertures, pushed the limit of the accessible length range down to 50 nm, well below the diffraction limit [34]. Yet another step has been taken by Eggeling and coworkers who implemented FCS on a STED microscope delivering directly a spatial resolution below 50 nm [35]. In addition to this advantage, FCS offers access to very short timescales (down to μs). Like FRAP, FCS measurements require careful and rigorous analysis to extract reliable information on the diffusion behavior based on the dependence of D (or τ) on spot size (see Fig. 2).

One would intuitively expect that it would be more straightforward to determine and characterize the deviations from free diffusion through the direct observation of the movements of individual molecules by single-particle tracking. In fact, due to intrinsic statistical fluctuations, identification of the diffusion mode from a single-molecule trajectory requires sophisticated tools from statistical physics. The identification of confined diffusion in domains usually proceeds by the search for confinement periods along the trajectories, taking care not to interpret as confinement a temporary reduction of the diffusion coefficient due to statistical fluctuations [36, 37]. Interestingly, the confinement index can also be used to detect jumps between adjacent domains in single trajectories [36], thus providing an unambiguous way to scrutinize hop diffusion [38]. An alternative method for the analysis of confined motion is Bayesian inference, particularly useful to infer diffusion coefficients and confinement potentials [39, 40] (see Fig. 2). This powerful technique has remained rather confidential but should gain notoriety in the near future with the availability of free software enabling the treatment of high-density SPT data such as those collected by, e.g., PALM [41]. Giving direct access to maps of the dynamic parameters of the molecules, this tool allows determining the physical origin of the observed motion without the intense modelization efforts needed to solve a complex inverse problem.

Nevertheless, the advent of such powerful analytical tools should not distract the experimentalist from a critical analysis of the experimental output. Although noninvasive, the techniques are not devoid of bias.

Especially for SPT techniques, the effects of time averaging of the particle's position by the detector and the influence of the probe's functionalization should be carefully considered. The former has been rigorously evaluated in the case of confined diffusion. Interestingly, corrections can be made to the apparent diffusion coefficients and domain size to recover the real values in an experimentally relevant range [42]. The latter concerns experiments making use of quantum dot (QD) nanoparticles coupled to antibodies. Monovalency, i.e., functionalizing the QD with (on average) a single antibody molecule, reduces the risk of crosslinking the targeted receptors. However, priority should be given to minimizing the friction of the particle with the membrane; hence the optimal antibody-to-particle ratio should be chosen as the one leading to the largest short-term diffusion coefficient [43].

A final and important bias, shared by all methods measuring lateral diffusion in membranes, is the topography of the cell surface which is not taken into account despite its influence. Very soon after the development of the FRAP technique, the question was raised whether invaginations or microvilli would affect the measurement of diffusion coefficients. After measuring the diffusion coefficients of lipophilic membrane probes in cells or cell regions devoid of or with a high density of microvilli, two research groups [44, 45] concluded that the presence of microvilli had no effect. Surprisingly, these authors did not question the procedure they used to analyze the FRAP recovery curves. Indeed, they computed the diffusion coefficient from the half-time of recovery without taking into account the roughness of the cell membranes and assuming that the diffusion area was equal to the bleached area. Three decades of extensive investigations of membrane dynamics neglecting the effect of membrane topology ensued, before observations by scanning ion conductance microscopy showed that the quite generally non-flat topography of the cell surface at the sub-micrometer scale compromises the interpretation of lateral diffusion measurements [46]. Curved surfaces can not only impact the diffusive timescales [47] but also lead to erroneous conclusions regarding the heterogeneities exhibited by membranes, such as apparent trapping [46]. Thus, it should be mandatory to accompany diffusion measurement by a characterization of the surface roughness [48]. As suggested by Jalink and van Rheenen [49], who even earlier pointed out the implications of membrane wrinkling in cell biology [50], one possible approach "*to control for local membrane content is by normalizing to the fluorescence of a homogeneously distributed membrane marker*." Alternatively, the identification of the existence of surface roughness and the evaluation of its extent can be obtained using an autocorrelation function approach [51]. Obviously, high-resolution 3D particle tracking provides in this respect an a priori ideal method [52, 53].

As a last advice, we recommend that experimentalists try as much as possible to confront results obtained by different techniques in parallel for a rigorous validation of their observations.

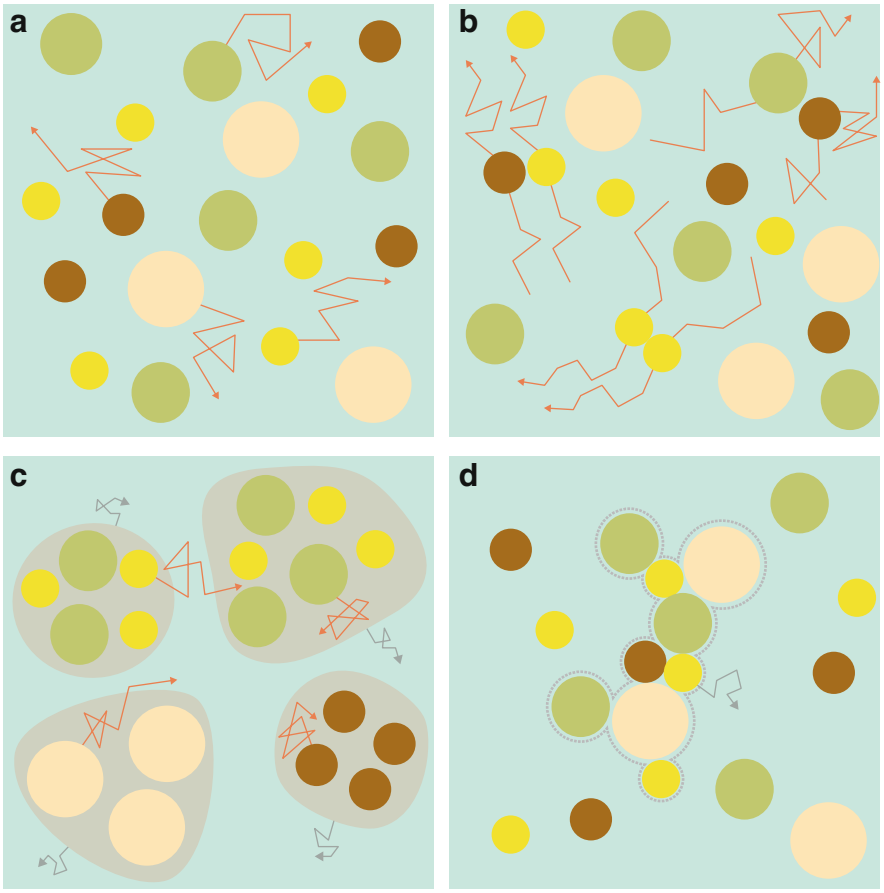

Fig. 3 Schematic representation of the different molecular organizations and their diffusional signatures. (**a**) Isolated molecules; (**b**) transient (top right and bottom) or permanent (left) oligomers; (**c**) dynamic clusters; (**d**) rigid aggregates. Orange arrows: individual movements; gray arrows: collective movements

4 The Different Levels of Molecular Organization

Nowadays, it is well accepted that different levels of molecular organization exist in living cells, leading to inhomogeneities such as submicrometer-sized entities named subdomains. Thus, the notion of *subdomain* is ill defined as it encompasses a broad range of spatiotemporal characteristics (Fig. 3). Both lipids and proteins are organized in supramolecular assemblies held together by noncovalent bonds—from the annular lipid shell to the clathrin-coated pits or caveolae, morphologically identifiable structures, and, on an intermediate scale, quaternary protein structure, lipid rafts, clusters, protein lattices, and aggregates.

Assembly of monomers into homo- or hetero-multimerized entities constitutes the first brick contributing to the organization of the membrane. FRET-related techniques are of particular interest to probe this level of organization. Note that lateral diffusion measurements can hardly inform on the formation of molecular complexes on the basis of their intrinsic mobility alone, because the diffusion coefficient of a membrane inclusion only moderately depends on its size (for a detailed discussion, see Chapter "Membrane domains under cellular recycling" by V. Démery and D. Lacoste). However, the interactions of supramolecular complexes with their environment will be different from those experienced by the monomers (Fig. 3a), and this influences the diffusion parameters beyond the diffusion coefficient. Single-molecule methods provide the possibility to count the proteins within an aggregate [54] and to evaluate the level of heterogeneity by a scrutiny of individual trajectories (Fig. 3b) [55]; FCS-related techniques provide the possibility to characterize such variations in the molecular organization by looking at the distribution of molecular brightness (Number & Brightness techniques) [56].

In the following paragraphs, we examine observations made on a well-characterized membrane receptor, the epidermal growth factor receptor (EGFR), to illustrate these different levels of membrane organization. This receptor is involved in the regulation of cellular growth and proliferation following its oligomerization through the binding of the EGF. Studies of the EGFR oligomeric state under resting and activated conditions have provided evidence that, in the resting state, the EGFR is mainly monomeric but also forms homo- and heterodimers, depending on its membrane density but not on the binding of EGF [57–60]. Further EGFR multimerization might be required for efficient signaling [61]. It is also interesting to notice that pre-assembled EGFR dimers, which have a finite lifetime, are prominent in lamellipodia but without the slow diffusion characteristic observed for ligand-bound EGFR dimers [57]. This effect is presumably due to the interactions with the signaling machinery observed in the presence of the ligand.

A higher level of membrane organization corresponds to the possible formation of subdomains from the bricks of multimeric complexes. At this point, we would like to distinguish between cluster, lattice, and aggregate. A molecular cluster relates to a dynamic assembly of membrane components, each of them individually maintaining a certain level of freedom within a cluster [62, 63]. Proteins, together with lipids, determine the diffusional properties of a cluster (Fig. 3c). Molecular aggregation corresponds more to the notion of molecules clumping together into weakly structured entities containing mainly proteins. In that case, each protein within the aggregate has the diffusional characteristics of the aggregate itself (Fig. 3d). Multimeric ligands can interact with a variety of membrane proteins, promoting their reticulation into supramolecular aggregates of undetermined size. For instance, multivalent lectins promote the formation of lattices by interacting with different membrane glycoproteins. As a consequence, the subdomains created by lectin-dependent lattices contribute to stabilizing the interactions among diverse membrane components. For instance, it has been shown that the inhibition of a specific N-glycosylation of EGFR essential for its functions results in a reduction of EGFR binding to a lattice of galectin. Moreover, the association of EGFR

with this lattice significantly reduces its diffusion in the plasma membrane and favors its association with the actin-based cytoskeleton, as demonstrated by FRAP measurements [64].

Let us now focus on specific subdomains in which lipids are critical (see also chapter "Lipid Rafts: A Personal Account" by K. Simons). Embedding a protein in a complex lipid mixture favors selective interactions that minimize hydrophobic mismatch between the length of protein's transmembrane domains and the thickness of the lipid bilayer. This is illustrated by the so-called lipid shell formed by lipids surrounding the transmembrane segment of a protein. It is assumed that such lipid shells behave like individual thermodynamically stable structures (Niemela et al. [65] and for review Anderson and Jacobson [66]).

It has also been hypothesized that lipid shells might have a certain affinity for the so-called lipid rafts. This concept had previously emerged from biochemical studies on principles governing sorting mechanisms in polarized cells through intracellular trafficking. It was initially defined as the capability of cholesterol and sphingolipids to mediate phase separation at the plasma membrane [4]. It has been postulated that the lipids within rafts are in a liquid-ordered phase. In fact, the direct translation of the thermodynamic phase observed in model membranes to cellular membranes denotes an oversimplification that neglects both the membrane's chemical heterogeneity and the nonequilibrium conditions of a biological system. Although the definition of lipid raft has evolved over time, the concept itself is still under debate, mainly due to semantic issues which make it difficult to group under a single denomination a huge diversity of molecular ensembles studied on different experimental models by methodologies that differ in terms of spatiotemporal resolution. This concept has been discussed in [67–69] and in chapter "Lipid Rafts: A Personal Account" by K. Simons.

The possible implication of lipid rafts in the organization of EGFR at the plasma membrane has been investigated by electron microscopy, demonstrating the localization of the receptor in subdomains enriched in cholesterol and sphingolipids [70]. Additional experimental evidence has been provided by depleting cholesterol from the cellular membrane; such conditions altered both the oligomeric state equilibrium of EGFR and its diffusional behavior [60, 71]. In fact, the activation of the receptor seems capable by itself of remodeling its lipid environment, allowing the formation of nanoclusters [72]. Conversely, it has been reported that EGFR can be activated in the absence of a ligand solely by disrupting the lipid-raft organization [73]. In that case, it is possible that the depletion of cholesterol by methyl-beta-cyclodextrin leads to receptor aggregation and consequently to its spontaneous activation.

So far, we have not considered the shape of the cell membrane except as a possible bias in the analysis of diffusion measurements. Recently, the potential influence of the membrane shape on cellular signaling via a modulation of the distribution of membrane components was hypothesized and the idea put forward that regions of high curvature would favor the recruitment of effectors during the activation of

receptors [74, 75]. This notion is supported by different experimental observations showing that interdependent mechanisms would be at play: (1) curvature favors the selective recruitment of specific peripheral proteins having curvature-sensitive domains [76, 77]; (2) curvature can induce a partitioning of lipids with consequences on the localization of lipid-anchored proteins [78]; (3) curvature can finely tune the activity of enzymes working at the membrane–water interface, especially the lipases [79]; and (4) curvature can result from the specific binding of a protein on planar membrane [80]. As recently exemplified for the coupling of BAR proteins with the membrane shape by Bassereau and coworkers [81], a refined understanding of the mechanisms driving these complex phenomena can be attained by a combination of numerical simulations and in vitro experiments on model membranes.

Finally, it is also important to connect the plasma membrane with its immediate molecular vicinity, both in the outer and inner cellular spaces in which selective interactions take place during biological processes. For instance, the membrane-associated actin-based cytoskeleton and the transmembrane proteins directly or indirectly associated with this cytoskeleton act as membrane organizers by corralling membrane constituents in this meshwork (see for review [3]).

Together, these different levels of organization contribute with their own dynamics to the compartmentalization of the plasma membrane in a diversity of subdomains. Presently, defining a hierarchy among these different organizing principles is still challenging and requires to refine our understanding or to create an alternative view of the cell membrane.

5 The Impact of the Dynamic Organization of the Membrane on Cellular Functions

It is commonly argued that the multiscale organization of lipids and proteins into clusters, nanodomains, or larger mesoscale domains plays a role in cellular processes [5]. Along this line, the idea is often invoked of specialized domains acting as operational platforms that concentrate specific proteins or lipids involved in a particular function. To counterbalance this ordering propensity, thermally driven motion, i.e., lateral diffusion, introduces the fluctuations "*fundamental to the function of biological systems*" and "*ubiquitous in life science*" [14]. Diffusion is obviously essential for membrane homeostasis. Diffusion promotes encounters between partners, increases the number of accessible distribution configurations, and extends the range of a perturbation, thereby boosting the reaction capability of the membrane. Confining diffusing molecules into domains in turn creates additional interesting properties. When signaling partners are sequestered in domains, this not only dramatically increases their frequency of encounters, hence improving the signaling efficiency, but it also avoids undesired interferences that could result from interactions with other proteins by keeping them spatially separated. With respect to the existence of receptor cross talk, this last feature might be the most

relevant one; see for example [82]. Combining order and disorder, i.e., clustering and diffusion, would thus facilitate the orchestration of the cellular activity at the cell surface by permitting a refined spatiotemporal regulation of the complex and manifold biological functions.

These concepts are extremely attractive due to their simplicity. They are systematically brought up in the discussion of experimental or theoretical results while clear demonstration that they are effectively at work is rarely provided. The existence of a relationship between the dynamic organization of a membrane component and the function it accomplishes is challenging to demonstrate, and understanding the underlying mechanisms of this coupling is even more difficult.

As already noted, most if not all membrane components—lipids and proteins—analyzed to date have been found to exhibit nonrandom diffusion for at least a fraction of their time and/or a fraction of their population. With the emergence of super-resolution microscopies and the improved tools for analysis, the description of membrane domains has become more precise. Thus, the confinement in nanoclusters of membrane proteins involved in extremely diverse functions, like GPI-anchored proteins [83], Ras proteins [84], and SNARE proteins [82, 85], is now firmly established. These nanoclusters are dynamic, with proteins diffusing in and out of them. Some clusters are found to be long-lived (up to minutes) [86]. Larger-scale organization of membrane proteins that tune signaling functions was also revealed. The TGF receptors, TβRI and TβRII, separate in distinct regions at focal adhesions but collapse to form a signaling complex upon release of cellular tension [87].

T cell receptors (TCR) represent another biological model on which extensive investigations have been performed to determine how the dynamics of membrane subdomains shapes the mechanism underlying the process of TCR transmembrane signaling, inducing CD3 phosphorylation, commonly called TCR triggering [88, 89]. The different mechanisms for TCR triggering proposed thus far are hotly debated, presumably because each one deals with one facet of the process [90]. In contrast, a consensus has emerged for the B cell receptor (BCR), another immune receptor. Indeed, recent work supports the notion that BCRs are organized into nanoclusters in resting B cells, whereas they dissociate during B cell activation by a mechanism whereby the Syk kinase induces an inside-out signaling [91]. In this dissociation-activation model, quiescent nanoclusters are not functional but switch to an activated state by a disassembly process.

Among membrane receptors, the superfamily of the G-protein-coupled receptors (GPCRs) deserves special interest as they constitute the largest and most diverse group. The Rhodopsin-like (or class A) GPCRs transduce extracellular signals through complex cascades of interactions with various partners starting with the heterotrimeric G-protein. To account for the rapidity and specificity of signaling, and based on indications that the receptors and G-proteins had a nonrandom diffusion and distribution, it was proposed in the 1990s that the receptors and their partners were localized in membrane compartments. The first experimental proof of the confinement of a GPCR was obtained 10 years later by the SPT analysis of hMOR, the main receptor of morphine [92]. These results were validated by different research groups [93]. Subsequent studies of other GPCRs using ad

hoc techniques found that at least an important fraction of them exhibit either a permanent dynamical confinement or transient confined diffusion [94]. So far, the integrated description and understanding of the relationship between the dynamical organization of the receptors during the signaling events that follow a ligand binding to a receptor are not yet established. In particular, the studies exploring the behavior of active receptors all report a correlation between the functional state of the receptors and their diffusion parameters. The emerging general feature is an increase of the confined population together with a constriction of the domains and a decrease of the receptor mobility [31, 95]. One exception is the serotonin receptor [96]. Interestingly, heterologous regulation by activation of other GPCRs can also change the dynamic organization of a receptor but in a different way from that induced upon homologous stimulation [97].

Constituting a specific subfamily of GPCRs, the metabotropic glutamate receptors have been the subject of intensive work, in particular using nanoscale microscopy, to unveil their trafficking pathway at neuronal synapses [98]. This study resulted in the most complete example of a tight link between function and dynamic organization with a new model of synapse organization and novel clues to potential pharmacological targets. Contrary to a historical paradigm, instead of being stably localized at the synapse, receptors are in a dynamical equilibrium between synaptic, extrasynaptic, and intracellular compartments "*governed by a tight interplay between surface diffusion and membrane recycling*" [99]. The synapse itself should be viewed as highly heterogeneous with neurotransmitter receptors distributed between stable but dynamic nanodomains and zones outside those nanodomains. Experiments have convincingly supported the idea that the rapidity of receptor exchanges between the vicinity and the interior of the postsynaptic density is a main factor of synaptic plasticity [100].

6 Concluding Remarks

Thermally driven diffusion is an essential phenomenon at the molecular scale, extremely important in membranes because of the absence of covalent links between their constituents. Manifold specific but also nonspecific interactions are nevertheless present, leading to multiscale heterogeneities in the distribution of the membrane components. Indeed, as asserted by Bigay and Antonny [76] "*collective effects arising from multiple low energy interactions have at least the same importance as biomolecular stereospecific interactions*." In this context, the lateral diffusion of proteins and lipids at the cell surface takes very complex forms. Characterization of this diffusion can ultimately reveal the underlying dynamic maps of the distribution of the various constituents and the forces between them. Such information is undoubtedly of great help to provide a mechanistic explanation of biological phenomena taking place at the membrane.

During the past decades, our understanding of the plasma membrane organization has benefited from massive technological advances, reaching unprecedented levels

of sensitivity and resolution allowing the measurement of relevant observables. The organization of the cell membrane into submicron domains has emerged as the major feature. We have presented the main techniques available to date for measuring diffusion and the associated analytic procedures dedicated to the identification and characterization of such organization. Those techniques are predominantly based on fluorescence microscopy. Particular attention has been given to the often neglected experimental and analytical pitfalls that should be considered before embarking upon such studies. Among the possible diffusion modes, we voluntarily did not discuss anomalous diffusion. The main reason is that no convincing evidence has yet been produced that such reported behavior is indeed due to an underlying self-similar structuration, as expected for genuine anomalous diffusion [101]. Most often, traces attributed to anomalous diffusion can be interpreted as a combination of a short-term confined diffusion with a longer-term and slower free diffusion [102]. As is customary in science, Occam's razor "*Pluralitas non est ponenda sine necessitate*" should also be privileged in this field. Combined with a panel of biochemical, biological, or physical techniques, diffusion measurements have succeeded in unveiling a variety of molecular organizations and influential parameters. However, we would like to point out a major difference between membrane proteins, which can be directly analyzed (ultimately native proteins can be labeled in situ), and lipids which are mainly studied through fluorescent analogs inserted in the membrane. Due to renewed interest in lipids, originating in part from the lipid-raft hypothesis, future progress can be expected in the design of novel probes or labeling schemes that more faithfully report on the lipid behavior in all its complexity.

Finally, even though the highly important notion of dynamic structure was clearly emphasized by Singer and Nicolson in their classic fluid mosaic model, it took several decades before the nonrandom distribution of membrane components at short, i.e., nanometer, length scales could be thoroughly documented through experimental investigations of the diffusion of membrane components, and accepted by the community.

In the future, efforts should continue to concentrate on a comprehensive description of membrane organization and dynamics. Progress is still needed to establish the physical laws governing specific features observed in membranes. In this respect, experiments on biomimetic systems permit to determine the minimal conditions necessary to reproduce a given behavior. In conjunction with theoretical modeling, in particular through numerical simulations which offer the possibility to bridge the gap between necessarily simplified models and highly complex cell membranes, biomimetic models constitute a promising approach to finally arrive at a functional model for the diffusion in the cell membrane.

Acknowledgments We thank our colleagues at CIML and IPBS, especially Evert Haanappel for the preparation of the figures and careful reading of this manuscript. This work was supported by the Ministère de l'Enseignement Supérieur et de la Recherche (ANR-09-PIRI-0008-03, ANR-10-BLAN-1214, ANR-10-INBS-04 France BioImaging, and ANR-11-LABX-0054 Labex INFORM), Aix-Marseille Université (ANR-11-IDEX-0001-02 A*MIDEX), and Université de Toulouse and

institutional funding from the Centre National de la Recherche Scientifique and the Institut National de la Santé et de la Recherche Médicale.

References

1. Engelman DM (2005) Membranes are more mosaic than fluid. Nature 438:578–580
2. Jacobson K, Sheets ED, Simson R (1995) Revisiting the fluid mosaic model of membranes. Science 268:1441–1442
3. Kusumi A, Suzuki KG, Kasai RS, Ritchie K, Fujiwara TK (2011) Hierarchical mesoscale domain organization of the plasma membrane. Trends Biochem Sci 36:604–615
4. Simons K, Ikonen E (1997) Functional rafts in cell membranes. Nature 387:569–572
5. Nicolson GL (2014) The Fluid-Mosaic Model of Membrane Structure: still relevant to understanding the structure, function and dynamics of biological membranes after more than 40 years. Biochim Biophys Acta 1838:1451–1466
6. Singer SJ, Nicolson GL (1972) The fluid mosaic model of the structure of cell membranes. Science 175:720–731
7. Axelrod D, Koppel DE, Schlessinger J, Elson E, Webb WW (1976) Mobility measurement by analysis of fluorescence photobleaching recovery kinetics. Biophys J 16:1055–1069
8. Barak LS, Webb WW (1982) Diffusion of low density lipoprotein-receptor complex on human fibroblasts. J Cell Biol 95:846–852
9. Koppel DE, Axelrod D, Schlessinger J, Elson EL, Webb WW (1976) Dynamics of fluorescence marker concentration as a probe of mobility. Biophys J 16:1315–1329
10. Frye LD, Edidin M (1970) The rapid intermixing of cell surface antigens after formation of mouse-human heterokaryons. J Cell Sci 7:319–335
11. Mouritsen OG, Bagatolli LA (2016) Life—as a matter of fat. Springer, Heidelberg
12. Marguet D, Lenne PF, Rigneault H, He HT (2006) Dynamics in the plasma membrane: how to combine fluidity and order. EMBO J 25:3446–3457
13. Shinbrot T, Muzzio FJ (2001) Noise to order. Nature 410:251–258
14. Yanagida T, Ueda M, Murata T, Esaki S, Ishii Y (2007) Brownian motion, fluctuation and life. Bio Systems 88:228–242
15. Prior IA, Muncke C, Parton RG, Hancock JF (2003) Direct visualization of Ras proteins in spatially distinct cell surface microdomains. J Cell Biol 160:165–170
16. Van Zanten TS, Gomez J, Manzo C, Cambi A, Buceta J, Reigada R, Garcia-Parajo MF (2010) Direct mapping of nanoscale compositional connectivity on intact cell membranes. Proc Natl Acad Sci USA 107:15437–15442
17. Takatori S, Mesman R, Fujimoto T (2014) Microscopic methods to observe the distribution of lipids in the cellular membrane. Biochemistry 53:639–653
18. Tanaka KA, Suzuki KG, Shirai YM, Shibutani ST, Miyahara MS, Tsuboi H, Yahara M, Yoshimura A, Mayor S, Fujiwara TK, Kusumi A (2010) Membrane molecules mobile even after chemical fixation. Nat Methods 7:865–866
19. Magde D, Elson EL, Webb WW (1974) Fluorescence correlation spectroscopy. II. An experimental realization. Biopolymers 13:29–61
20. Bacia K, Kim SA, Schwille P (2006) Fluorescence cross-correlation spectroscopy in living cells. Nat Methods 3:83–89
21. Arnspang EC, Schwartzentruber J, Clausen MP, Wiseman PW, Lagerholm BC (2013) Bridging the gap between single molecule and ensemble methods for measuring lateral dynamics in the plasma membrane. PLoS One 8:e78096
22. Curthoys NM, Parent M, Mlodzianoski M, Nelson AJ, Lilieholm J, Butler MB, Valles M, Hess ST (2015) Dances with membranes: breakthroughs from super-resolution imaging. Curr Top Membr 75:59–123

23. Blumenthal D, Goldstien L, Edidin M, Gheber LA (2015) Universal approach to FRAP analysis of arbitrary bleaching patterns. Sci Rep 5:11655
24. Tetin SY (2013) Methods in enzymology. Fluorescence fluctuation spectroscopy (FFS), part A. Preface. Methods Enzymol 518:xi–xii
25. Tetin SY (2013) Methods in enzymology. Fluorescence fluctuation spectroscopy (FFS), part B. Preface. Methods Enzymol 519:xiii–xxiv
26. Garcia-Parajo MF, Cambi A, Torreno-Pina JA, Thompson N, Jacobson K (2014) Nanoclustering as a dominant feature of plasma membrane organization. J Cell Sci 127:4995–5005
27. Yechiel E, Edidin M (1987) Micrometer-scale domains in fibroblast plasma membranes. J Cell Biol 105:755–760
28. Baker AM, Sauliere A, Gaibelet G, Lagane B, Mazeres S, Fourage M, Bachelerie F, Salome L, Lopez A, Dumas F (2007) CD4 interacts constitutively with multiple CCR5 at the plasma membrane of living cells. A fluorescence recovery after photobleaching at variable radii approach. J Biol Chem 282:35163–35168
29. Pucadyil TJ, Chattopadhyay A (2007) Cholesterol depletion induces dynamic confinement of the G-protein coupled serotonin(1A) receptor in the plasma membrane of living cells. Biochim Biophys Acta 1768:655–668
30. Salome L, Cazeils JL, Lopez A, Tocanne JF (1998) Characterization of membrane domains by FRAP experiments at variable observation areas. Eur Biophys J 27:391–402
31. Sauliere-Nzeh Ndong A, Millot C, Corbani M, Mazeres S, Lopez A, Salome L (2010) Agonist-selective dynamic compartmentalization of human Mu opioid receptor as revealed by resolutive FRAP analysis. J Biol Chem 285:14514–14520
32. Lenne PF, Wawrezinieck L, Conchonaud F, Wurtz O, Boned A, Guo XJ, Rigneault H, He HT, Marguet D (2006) Dynamic molecular confinement in the plasma membrane by microdomains and the cytoskeleton meshwork. EMBO J 25:3245–3256
33. Wawrezinieck L, Rigneault H, Marguet D, Lenne PF (2005) Fluorescence correlation spectroscopy diffusion laws to probe the submicron cell membrane organization. Biophys J 89:4029–4042
34. Wenger J, Conchonaud F, Dintinger J, Wawrezinieck L, Ebbesen TW, Rigneault H, Marguet D, Lenne PF (2007) Diffusion analysis within single nanometric apertures reveals the ultrafine cell membrane organization. Biophys J 92:913–919
35. Vicidomini G, Ta H, Honigmann A, Mueller V, Clausen MP, Waithe D, Galiani S, Sezgin E, Diaspro A, Hell SW, Eggeling C (2015) STED-FLCS: an advanced tool to reveal spatiotemporal heterogeneity of molecular membrane dynamics. Nano Lett 15:5912–5918
36. Meilhac N, Le Guyader L, Salome L, Destainville N (2006) Detection of confinement and jumps in single-molecule membrane trajectories. Phys Rev E Stat Nonlin Soft Matter Phys 73:011915
37. Serge A, Bertaux N, Rigneault H, Marguet D (2008) Dynamic multiple-target tracing to probe spatiotemporal cartography of cell membranes. Nat Methods 5:687–694
38. Fujiwara T, Ritchie K, Murakoshi H, Jacobson K, Kusumi A (2002) Phospholipids undergo hop diffusion in compartmentalized cell membrane. J Cell Biol 157:1071–1081
39. Masson JB, Casanova D, Turkcan S, Voisinne G, Popoff MR, Vergassola M, Alexandrou A (2009) Inferring maps of forces inside cell membrane microdomains. Phys Rev Lett 102:048103
40. Turkcan S, Alexandrou A, Masson JB (2012) A Bayesian inference scheme to extract diffusivity and potential fields from confined single-molecule trajectories. Biophys J 102:2288–2298
41. El Beheiry M, Dahan M, Masson JB (2015) InferenceMAP: mapping of single-molecule dynamics with Bayesian inference. Nat Methods 12:594–595
42. Destainville N, Salome L (2006) Quantification and correction of systematic errors due to detector time-averaging in single-molecule tracking experiments. Biophys J 90:L17–L19
43. Haanappel E, Mascalchi P, Carayon K, Mazères S, Salomé L (2012) Probing the influence of the particle in Single Particle Tracking measurements of lipid diffusion. Soft Matter 8:4462–4470

44. Dragsten P, Henkart P, Blumenthal R, Weinstein J, Schlessinger J (1979) Lateral diffusion of surface immunoglobulin, Thy-1 antigen, and a lipid probe in lymphocyte plasma membranes. Proc Natl Acad Sci USA 76:5163–5167
45. Wolf DE, Handyside AH, Edidin M (1982) Effect of microvilli on lateral diffusion measurements made by the fluorescence photobleaching recovery technique. Biophys J 38:295–297
46. Adler J, Shevchuk AI, Novak P, Korchev YE, Parmryd I (2010) Plasma membrane topography and interpretation of single-particle tracks. Nat Methods 7:170–171
47. Kusters R, Storm C (2014) Impact of morphology on diffusive dynamics on curved surfaces. Phys Rev E Stat Nonlin Soft Matter Phys 89:032723
48. Parmryd I, Onfelt B (2013) Consequences of membrane topography. FEBS J 280:2775–2784
49. Jalink K, Van Rheenen J (2010) Nano-imaging of membrane topography affects interpretations in cell biology. Nat Methods 7:486
50. van Rheenen J, Jalink K (2002) Agonist-induced PIP(2) hydrolysis inhibits cortical actin dynamics: regulation at a global but not at a micrometer scale. Mol Biol Cell 13:3257–3267
51. Hall D (2008) Analysis and interpretation of two-dimensional single-particle tracking microscopy measurements: effect of local surface roughness. Anal Biochem 377:24–32
52. Abrahamsson S, Chen J, Hajj B, Stallinga S, Katsov AY, Wisniewski J, Mizuguchi G, Soule P, Mueller F, Dugast Darzacq C, Darzacq X, WU C, Bargmann CI, Agard DA, Dahan M, Gustafsson MG (2013) Fast multicolor 3D imaging using aberration-corrected multifocus microscopy. Nat Methods 10:60–63
53. Wells NP, Lessard GA, Phipps ME, Goodwin PM, Lidke DS, Wilson BS, Werner JH (2009) Going beyond 2D: Following membrane diffusion and topography in the IgE-Fc[Epsilon]RI system using 3-dimensional tracking microscopy. Proc SPIE Int Soc Opt Eng 7185:71850Z
54. Cognet L, Tardin C, Negrier ML, Breillat C, Coussen F, Choquet D, Lounis B (2008) Robust single-molecule approach for counting autofluorescent proteins. J Biomed Opt 13:031216
55. Low-Nam ST, Lidke KA, Cutler PJ, Roovers RC, van Bergen en Henegouwen PM, Wilson BS, Lidke DS (2011) ErbB1 dimerization is promoted by domain co-confinement and stabilized by ligand binding. Nat Struct Mol Biol 18:1244–1249
56. Digman MA, Dalal R, Horwitz AF, Gratton E (2008) Mapping the number of molecules and brightness in the laser scanning microscope. Biophys J 94:2320–2332
57. Chung I, Akita R, Vandlen R, Toomre D, Schlessinger J, Mellman I (2010) Spatial control of EGF receptor activation by reversible dimerization on living cells. Nature 464:783–787
58. Moriki T, Maruyama H, Maruyama IN (2001) Activation of preformed EGF receptor dimers by ligand-induced rotation of the transmembrane domain. J Mol Biol 311:1011–1026
59. Nagy P, Claus J, Jovin TM, Arndt-Jovin DJ (2010) Distribution of resting and ligand-bound ErbB1 and ErbB2 receptor tyrosine kinases in living cells using number and brightness analysis. Proc Natl Acad Sci USA 107:16524–16529
60. Saffarian S, Li Y, Elson EL, Pike LJ (2007) Oligomerization of the EGF receptor investigated by live cell fluorescence intensity distribution analysis. Biophys J 93:1021–1031
61. Kozer N, Barua D, Henderson C, Nice EC, Burgess AW, Hlavacek WS, Clayton AH (2014) Recruitment of the adaptor protein Grb2 to EGFR tetramers. Biochemistry 53:2594–2604
62. Destainville N (2008) Cluster phases of membrane proteins. Phys Rev E Stat Nonlin Soft Matter Phys 77:011905
63. Meilhac N, Destainville N (2011) Clusters of proteins in biomembranes: insights into the roles of interaction potential shapes and of protein diversity. J Phys Chem B 115:7190–7199
64. Lajoie P, Partridge EA, Guay G, Goetz JG, Pawling J, Lagana A, Joshi B, Dennis JW, Nabi IR (2007) Plasma membrane domain organization regulates EGFR signaling in tumor cells. J Cell Biol 179:341–356
65. Niemela PS, Miettinen MS, Monticelli L, Hammaren H, Bjelkmar P, Murtola T, Lindahl E, Vattulainen I (2010) Membrane proteins diffuse as dynamic complexes with lipids. J Am Chem Soc 132:7574–7575
66. Anderson RG, Jacobson K (2002) A role for lipid shells in targeting proteins to caveolae, rafts, and other lipid domains. Science 296:1821–1825

67. Elson EL, Fried E, Dolbow JE, Genin GM (2010) Phase separation in biological membranes: integration of theory and experiment. Annu Rev Biophys 39:207–226
68. Lingwood D, Simons K (2010) Lipid rafts as a membrane-organizing principle. Science 327:46–50
69. Sevcsik E, Schutz GJ (2016) With or without rafts? Alternative views on cell membranes. Bioessays 38:129–139
70. Ringerike T, Blystad FD, Levy FO, Madshus IH, Stang E (2002) Cholesterol is important in control of EGF receptor kinase activity but EGF receptors are not concentrated in caveolae. J Cell Sci 115:1331–1340
71. Orr G, Hu D, Ozcelik S, Opresko LK, Wiley HS, Colson SD (2005) Cholesterol dictates the freedom of EGF receptors and HER2 in the plane of the membrane. Biophys J 89:1362–1373
72. Ariotti N, Liang H, Xu Y, Zhang Y, Yonekubo Y, Inder K, Du G, Parton RG, Hancock JF, Plowman SJ (2010) Epidermal growth factor receptor activation remodels the plasma membrane lipid environment to induce nanocluster formation. Mol Cell Biol 30:3795–3804
73. Lambert S, Vind-Kezunovic D, Karvinen S, Gniadecki R (2006) Ligand-independent activation of the EGFR by lipid raft disruption. J Invest Dermatol 126:954–962
74. Rangamani P, Lipshtat A, Azeloglu EU, Calizo RC, Hu M, Ghassemi S, Hone J, Scarlata S, Neves SR, Iyengar R (2013) Decoding information in cell shape. Cell 154:1356–1369
75. Schmick M, Bastiaens PI (2014) The interdependence of membrane shape and cellular signal processing. Cell 156:1132–1138
76. Bigay J, Antonny B (2012) Curvature, lipid packing, and electrostatics of membrane organelles: defining cellular territories in determining specificity. Dev Cell 23:886–895
77. Mcmahon HT, Gallop JL (2005) Membrane curvature and mechanisms of dynamic cell membrane remodelling. Nature 438:590–596
78. Larsen JB, Jensen MB, Bhatia VK, Pedersen SL, Bjornholm T, Iversen L, Uline M, Szleifer I, Jensen KJ, Hatzakis NS, Stamou D (2015) Membrane curvature enables N-Ras lipid anchor sorting to liquid-ordered membrane phases. Nat Chem Biol 11:192–194
79. Reis P, Holmberg K, Watzke H, Leser ME, Miller R (2009) Lipases at interfaces: a review. Adv Colloid Interf Sci 147-148:237–250
80. Windschiegl B, Orth A, Romer W, Berland L, Stechmann B, Bassereau P, Johannes L, Steinem C (2009) Lipid reorganization induced by Shiga toxin clustering on planar membranes. PLoS One 4:e6238
81. Simunovic M, Voth GA, Callan-Jones A, Bassereau P (2015) When physics takes over: BAR proteins and membrane curvature. Trends Cell Biol 25:780–792
82. Destainville N, Schmidt TH, Lang T (2016) Where biology meets physics-a converging view on membrane microdomain dynamics. Curr Top Membr 77:27–65
83. Saha S, Anilkumar AA, Mayor S (2016) GPI-anchored protein organization and dynamics at the cell surface. J Lipid Res 57:159–175
84. Zhou Y, Hancock JF (2015) Ras nanoclusters: Versatile lipid-based signaling platforms. Biochim Biophys Acta 1853:841–849
85. Bethani I, Skanland SS, Dikic I, Acker-Palmer A (2010) Spatial organization of transmembrane receptor signalling. EMBO J 29:2677–2688
86. Saka SK, Honigmann A, Eggeling C, Hell SW, Lang T, Rizzoli SO (2014) Multi-protein assemblies underlie the mesoscale organization of the plasma membrane. Nat Commun 5:4509
87. Rys JP, Dufort CC, Monteiro DA, Baird MA, Oses-Prieto JA, Chand S, Burlingame AL, Davidson MW, Alliston TN (2015) Discrete spatial organization of TGFbeta receptors couples receptor multimerization and signaling to cellular tension. eLife 4:e09300
88. Choudhuri K, Dustin ML (2010) Signaling microdomains in T cells. FEBS Lett 584:4823–4831
89. He HT, Marguet D (2008) T-cell antigen receptor triggering and lipid rafts: a matter of space and time scales. Talking Point on the involvement of lipid rafts in T-cell activation. EMBO Rep 9:525–530

90. Huppa JB, Davis MM (2013) The interdisciplinary science of T-cell recognition. Adv Immunol 119:1–50
91. Klasener K, Maity PC, Hobeika E, Yang J, Reth M (2014) B cell activation involves nanoscale receptor reorganizations and inside-out signaling by Syk. eLife 3:e02069
92. Daumas F, Destainville N, Millot C, Lopez A, Dean D, Salome L (2003) Confined diffusion without fences of a g-protein-coupled receptor as revealed by single particle tracking. Biophys J 84:356–366
93. Suzuki K, Ritchie K, Kajikawa E, Fujiwara T, Kusumi A (2005) Rapid hop diffusion of a G-protein-coupled receptor in the plasma membrane as revealed by single-molecule techniques. Biophys J 88:3659–3680
94. Baker A, Sauliere A, Dumas F, Millot C, Mazeres S, Lopez A, Salome L (2007) Functional membrane diffusion of G-protein coupled receptors. Eur Biophys J 36:849–860
95. Veya L, Piguet J, Vogel H (2015) Single molecule imaging deciphers the relation between mobility and signaling of a prototypical G protein-coupled receptor in living cells. J Biol Chem 290:27723–27735
96. Pucadyil TJ, Kalipatnapu S, Harikumar KG, Rangaraj N, Karnik SS, Chattopadhyay A (2004) G-protein-dependent cell surface dynamics of the human serotonin1A receptor tagged to yellow fluorescent protein. Biochemistry 43:15852–15862
97. Carayon K, Mouledous L, Combedazou A, Mazeres S, Haanappel E, Salome L, Mollereau C (2014) Heterologous regulation of Mu-opioid (MOP) receptor mobility in the membrane of SH-SY5Y cells. J Biol Chem 289:28697–28706
98. Willig KI, Barrantes FJ (2014) Recent applications of superresolution microscopy in neurobiology. Curr Opin Chem Biol 20:16–21
99. Choquet D, Triller A (2013) The dynamic synapse. Neuron 80:691–703
100. Heine M, Groc L, Frischknecht R, Beique JC, Lounis B, Rumbaugh G, Huganir RL, Cognet L, Choquet D (2008) Surface mobility of postsynaptic AMPARs tunes synaptic transmission. Science 320:201–205
101. Saxton MJ (2012) Wanted: a positive control for anomalous subdiffusion. Biophys J 103:2411–2422
102. Destainville N, Sauliere A, Salome L (2008) Comment to the article by Michael J Saxton: A biological interpretation of transient anomalous subdiffusion I qualitative model. Biophys J 95:3117–3119 author reply 3120-2

Mechanical Factors Affecting the Mobility of Membrane Proteins

Vincent Démery and David Lacoste

Abstract The mobility of membrane proteins controls many biological functions. The application of the model of Saffman and Delbrück to the diffusion of membrane proteins does not account for all the experimental measurements. These discrepancies have triggered a lot of studies on the role of the mechanical factors in the mobility. After a short review of the Saffman and Delbrück model and of some key experiments, we explore the various ways to incorporate the effects of the different mechanical factors. Our approach focuses on the coupling of the protein to the membrane, which is the central element in the modeling. We present a general, polaron-like model, its recent application to the mobility of a curvature sensitive protein, and its various extensions to other couplings that may be relevant in future experiments.

Keywords Membrane proteins · Diffusion · Protein mobility · Membrane-protein interactions

1 Introduction

Cell membranes are barriers that separate the cytoplasm from the external world. Through compartmentalization, they allow highly selective biochemical reactions to take place in their internal volume which would essentially never occur in the absence of such barriers. Far from being inert, biological membranes thus play a key role in many functions such as signaling, cell division, or energy production in cellular organelles.

Many of these biological functions involve membrane proteins, which form a vast family of essential proteins. While some of them are embedded permanently in the membrane, others transiently bind to it in order to perform a specific task and then unbind from it when the task is done. When they are inserted in the

V. Démery · D. Lacoste (✉)
Laboratoire de Physico-Chimie Théorique, UMR CNRS Gulliver 7083, ESPCI, Paris, France
e-mail: vincent.demery@espci.fr; david.lacoste@espci.fr

P. Bassereau, P. Sens (eds.), *Physics of Biological Membranes*,
https://doi.org/10.1007/978-3-030-00630-3_8

membrane, membrane proteins typically diffuse laterally in the fluid environment of the lipid membrane. This lateral diffusion is an essential aspect to their function, in the frequent case that membrane proteins must interact or form clusters with other membrane proteins. Membrane proteins typically diffuse in a crowded environment of other lipids and proteins. Modeling the various factors (mechanical or biochemical) affecting the mobility of membrane proteins is a challenging issue, but one that should be addressed in order to properly understand their biological function.

In this chapter, we review some of the experiments and theories, which have been devoted to the mobility of membrane proteins. In the next Sect. 2, we present the pioneering work of P. G. Saffman and M. Delbrück (SD) on the mobility of membrane proteins, which is followed in Sect. 3 by a discussion of the experiments which have either tested the model or pointed out its limitations. In Sect. 4, we investigate the crucial couplings between the membrane protein and the membrane. Then, in Sect. 5 we present some of the main theoretical ideas or models which have been put forward to understand the mobility of membrane proteins beyond the SD model. We end up with a discussion on future perspectives.

2 The Saffman and Delbrück Hydrodynamic Model (SD)

Brownian motion plays an essential role in biological processes. Since the work of Einstein [1] and the pioneering experiments of Perrin [2], the observation of diffusing objects has emerged as a mean to extract the rheological properties of the surrounding medium or the probe particle size. The theoretical investigation of diffusion of proteins within membranes has been studied widely going back to P. G. Saffman and M. Delbrück (SD). They investigated the hydrodynamic drag acting on a membrane inclusion of radius a_p moving in a membrane described as a two-dimensional fluid sheet of viscosity μ_m; which is itself in contact with a less viscous fluid of viscosity η [3]. The two-dimensional surface viscosity of the membrane μ_m is the product of the membrane thickness h by its three-dimensional viscosity η_m, $\mu_\mathrm{m} = h\eta_\mathrm{m}$. The velocity field inside the membrane is exactly two-dimensional but it is hydrodynamically coupled to the external fluid. Using singular perturbation techniques, which are valid when $\eta_\mathrm{m} h \gg \eta a_\mathrm{p}$, Saffman and Delbrück (SD) obtained the diffusion coefficient D_0 for the translational Brownian motion of a cylindrical inclusion of radius a_p in the membrane:

$$D_0 = \frac{k_\mathrm{B}T}{4\pi\mu_\mathrm{m}}\left[\log\left(\frac{\ell}{a_\mathrm{p}}\right) - \gamma\right], \tag{1}$$

where $k_\mathrm{B}T$ is the thermal energy, γ is Euler's constant, and $\ell = \mu_\mathrm{m}/\eta$ is the SD length. The expression (1) corresponds to the choice of a no-slip boundary condition at the surface of the inclusion; for the alternate choice of zero tangential stress boundary condition, a factor $1/2$ should be added inside the bracket. Saffman and

Delbrück also derived an expression for the rotational diffusion coefficient, which unlike the translational diffusion coefficient only depends on the viscosity of the membrane: $D_R = k_B T/4\pi h\mu_m a_p^2$.

The SD dimensionless parameter $\epsilon = \ell/a_p$ represents physically the ratio of the hydrodynamic resistances of the inclusion in the fluid membrane and in the external fluid. Indeed, the former is of the order of the lateral area of the inclusion $2\pi a_p h$ times the membrane shear stress $v\eta_m/a_p$ for a velocity v of the inclusion; while the latter is of the order of the top cylindrical area πa_p^2 times the shear stress in the fluid, $v\eta/a_p$. When $\epsilon \gg 1$, the hydrodynamic resistance due to the motion in the membrane dominates; this is the regime considered by Saffman and Delbrück, which is relevant for small inclusions (*i.e.*, for small values of the radius of the inclusion a_p, which is the only lateral length scale considered in the model). Instead, when $\epsilon \ll 1$, the resistance occurs mainly due to the motion in the external fluid; this is the regime relevant for large inclusions. In this case, since the motion mainly occurs in the bulk external fluid, it is described by the Stokes–Einstein formula, with a mobility going as $1/a_p$. We therefore expect a cross-over between both regimes, when the size of the inclusion is of the order of 500 nm, which is the estimate for ℓ for a typical ratio of viscosities $\eta_m/\eta \simeq 100$ and a membrane thickness $h \simeq 5$ nm.

3 Experimental Tests of the Saffman–Delbrück Model

Theoretically, a more complete solution of the SD hydrodynamic problem has been proposed which interpolates between the SD regime and the Stokes–Einstein regime [4]. Such expressions have been tested using simulations [5], and later improved by the group of Schwille [6] who also carried out a set of careful experiments with micron-sized solid domains in giant unilamellar vesicles, confirming the results expected in the regime $\epsilon \ll 1$ [7].

Below, we focus on some of the experiments which have tested or challenged the SD model in the regime of small inclusions $\epsilon \gg 1$ and for flat membranes, which are conditions for which the model should be applicable. In 2006, Gambin et al. [8] performed experiments with a large panel of peptides and membrane proteins with various shapes and particle sizes ranging from 5 to 30 nm; the diffusion coefficient has been measured using fringe pattern photobleaching. They reported a dependence of the diffusion coefficient on the size of the particle of the Stokes type ($D_0 \sim 1/a_p$, see Fig. 1), much stronger than the logarithmic dependence predicted by Eq. (1). In a second set of experiments, Gambin et al. tuned the membrane thickness by swelling the membrane with a hydrophobic solvent, and measured the effect on the mobility of the peptides. They found that the mobility of the inclusions is maximal when their height matches the membrane thickness. They attributed the reduced mobility of peptides with a smaller length than the bilayer thickness to the pinching of the bilayer (provided that the peptides are sufficiently long to span the bilayer). On the other hand, peptides much longer than the membrane thickness cannot fit in the upright position and must tilt with respect to the membrane

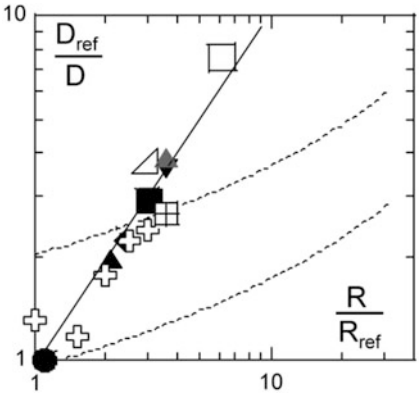

Fig. 1 Figure taken from Ref. [8]: Normalized inverse diffusion coefficient D_{ref}/D vs. object radius R/R_{ref}, with open symbols representing data gathered from the literature, and filled symbols data from Ref. [8]. Filled symbols represent peptide assemblies, with the peptide called L_{12} as reference, while for oligomers of peptides (crosses), acetylcholine receptor (AChR), bacteriorhodopsin (BR), and SR-ATPase (squares), the lipid diffusion serves as reference. The solid line is a power-law regression leading to $D_{ref}/D \sim R^{1.04}$. For comparison, the dashed line represents the prediction of the Saffman–Delbrück model (Eq. (1)) (upper line, same as in Fig. 3, and lower fit as in Fig. 2 of Ref. [8])

normal, which may cause, again, a reduction of their mobility. These experiments triggered a lot of activity on the theoretical side, which we review in the theory section.

In contrast to these experiments, one work [9] reported a weak dependence of D_0 on the protein radius a_p, using fluorescence correlation spectroscopy (FCS) in line with the predictions of the SD model from Eq. (1). The discrepancy with the data of Gambin et al. is likely to come from differences in the experimental techniques which have been used in both cases. Recently, Weiss et al. performed experiments with dual focus fluorescence correlation spectroscopy [10], which provided accurate measurements, of higher quality than with simple FCS. These more accurate measurements of diffusion coefficients for membrane proteins in black lipid membranes are in perfect agreement with the SD model. The original figure of Ref. [10] is reproduced here in Fig. 2 with courtesy of J. Enderlein. We believe that the reason for this perfect agreement may be that these experiments have been performed with black lipid membranes, which are tense membranes.

The idea that the membrane tension may affect the protein mobility has only been investigated recently in a study involving one of us [11]. In this work, the mobility of two transmembrane proteins with the same lateral size, aquaporin 0 (AQP0) and a voltage-gated potassium channel (KvAP), has been measured by attaching quantum dots to these proteins and by tracking them. One advantage of using this technique of single particle tracking is that it is free of the possible artifacts due to averaging over a population of interacting proteins (on which

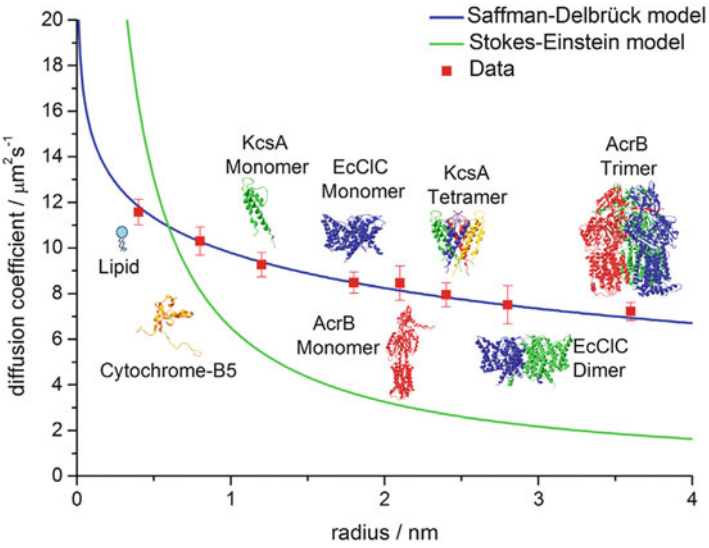

Fig. 2 Figure taken from Ref. [10]: Saffman–Delbrück versus Stokes–Einstein model. The investigated species are DPPE, cytochrome B5 (depicted without transmembrane domain), KcsA, EcClC, and AcrB. The monomeric forms of membrane proteins were directly added to the BLM. The oligomeric forms were reconstituted via SNARE-mediated vesicle fusion. DPPE was labeled with Atto655, and all proteins were labeled with Alexa647. In addition, we fitted the HPW-based model suggested by Petrov and Schwille [6], which can reproduce the classical Saffman–Delbrück model in the size range investigated. The fit parameter for all fits was the product of membrane viscosity and thickness, $\eta_m h$. The temperature was set to 295 K and the viscosity of the surrounding buffer was $\eta = 0.96$ mPa

the experiments reported in Refs. [8, 12] rely). Whereas AQP0 does not deform the bilayer, KvAP is curved and bends the membrane. These experiments have shown that the curvature-coupled protein KvAP undergoes a significant increase in mobility under tension—an effect clearly beyond the SD model, whereas the mobility of the curvature-neutral water channel AQP0 is insensitive to it and follows the prediction of the SD model, as shown in Fig. 3. Importantly, at high tension, the mobility of both proteins agrees well with the prediction of the SD model, which gives $D_0 = 2.5\ \mu m^2/s$ [8].

So far, we have only discussed proteins diffusing in flat membranes. However, the SD model has also been tested using the same technique of single particle tracking and the same protein KvAP, but in different membrane environments namely in the curved and confined space of membrane nanotubes [13]. In this work, it was found that measurements of the mobility of this protein in the tube are well described by an extension of the SD model to cylindrical geometries [14].

Finally, let us mention some applications of the SD model for microrheology. Similarly to the Einstein relation, which allows the determination of the 3D local viscosity, based on measurements of the fluctuations of one or two tracers in a bulk

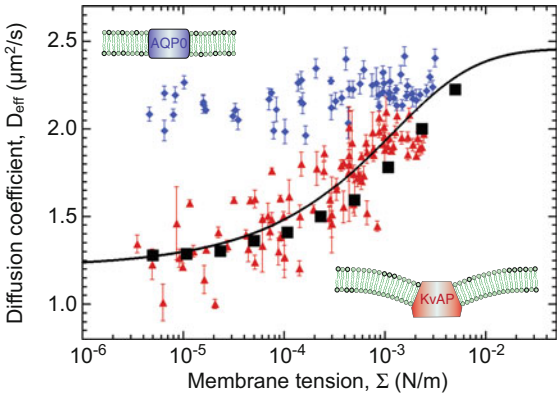

Fig. 3 Figure taken from Ref. [11]: protein lateral mobility in fluctuating membranes. Semilogarithmic plot of the diffusion coefficients (D_{eff}) as a function of the membrane tension Σ, for AQP0 (blue filled diamond) and KvAP (red filled triangle) labeled with streptavidin QDs. KvAP data adjusted by Eq. (20) (solid line) yields a protein coupling coefficient $\Theta = 3.5 \times 10^{-7}$ m considering $a = 5$ nm, $\kappa = 20\ k_B T$, and $D_0 \simeq 2.5\ \text{m}^2/\text{s}$. Simulations of the protein diffusion on a membrane subject to thermal fluctuations (filled square) agree well with the experimental data and theory. Insets: sketches of membrane deformation near proteins

fluid, the SD relation allows the determination of local membrane viscosity from measurements of the fluctuations of a tracer. This tracer can be a protein, but in that case it is crucial to properly understand the coupling between the protein and the membrane, as emphasized in the present chapter. In order to disentangle effects due to the tracer and the membrane, it is helpful if possible to combine measurements of translation or rotation diffusion as shown in Ref. [15].

4 Relevant Geometrical or Mechanical Factors and Protein–Membrane Couplings

Various geometrical or mechanical factors can affect the mobility of membrane proteins. The main factors are listed below:

- Geometrical properties of the membrane. The most basic geometrical parameter of the membrane is its thickness. For lipid membranes, this parameter is generally assumed to be constant of the order of 4–5 nm. However, biological membranes are intrinsically heterogeneous and usually composed of mixtures of several kinds of lipid domains. In such systems, the membrane thickness can vary depending on the location inside or outside the domains. Another very important local geometrical property of the membrane is its curvature. A preference of certain membrane proteins for membrane curvature means in particular that it is

possible to sort them according to the local curvature as demonstrated in Ref. [16].

- Mechanical and chemical properties of the membrane. The former ones include the elastic moduli of the membrane, such as its bending modulus and its tension, and dissipative moduli, such as the membrane viscosity and the relative friction between membrane leaflets. The latter ones include the chemical composition of the membrane, which controls many of its properties. Both parameters should be regarded as local or global depending on the level of heterogeneity.
- Geometrical parameters and mechanical properties of the membrane protein. The geometrical parameters of the protein include its size and shape [16–19]. Its shape notably defines its spontaneous curvature, which is a scalar for isotropic inclusions but becomes a tensor for anisotropic ones. Other important protein mechanical properties include its compliance, which can be split into elastic and dissipative moduli.
- The solvent in which the protein and the membrane are embedded. It is mainly characterized by its viscosity which controls the hydrodynamic part of the dissipation. In the case that the membrane and its solvent are confined by rigid walls, the solvent will be also described by its thickness, which can affect the mobility of membrane proteins via hydrodynamic screening effects [20, 21].
- Other inclusions present in the membrane modify the mobility of a given membrane protein, via direct interactions such as exclusion or indirect ones, such as membrane-mediated interactions [22, 23]. Since at the microscopic scale, biological membranes are a crowded mix of membrane proteins and lipid partners, such collective effects are expected to be important.

In order to understand the way mechanical factors affect the mobility of a given protein, it is important to focus on the mechanism by which the protein couples to the membrane. The main coupling mechanisms are:

- Hydrodynamic coupling. Since the protein evolves in the membrane which is fluid, there is a clear hydrodynamic coupling due to the fluid membrane. But since the external fluid may be dragged by the motion of the lipids induced by the protein, there is also hydrodynamic coupling with the external fluid, which is usually water. This is the coupling considered by Saffman and Delbrück [3] and in [20, 21].
- Coupling to the local membrane curvature. A mismatch between the spontaneous curvature of the protein and the curvature of the membrane deforms the lipids around the protein, leading to an energetic penalty [11, 22, 24–26]. The precise form of this coupling depends whether the protein is assumed to be hard or soft.
- Coupling to the membrane thickness. A hydrophobic mismatch between the protein and the membrane thickness stretches or compresses the lipid tails around the protein [27].
- Coupling to the membrane composition. Such an effect will be present when the protein has a special affinity for one kind of lipids while the membrane is made of a mix of various lipids [23].

- Electrostatic coupling. Various mechanisms are possible, depending on whether the protein and the lipids are charged or not. Note that even if the lipids are uncharged, such couplings may be present since the lipids may be polarized locally by the protein if the latter is charged. For membrane ion channels, there is generally a coupling of electrostatic origin in the presence of a transmembrane voltage since the field lines are deformed locally near the protein [28]. Such a coupling is involved in the mechanism of voltage gating in ion channels [29].
- Coupling due to geometrical effects. This form of coupling arises because the real trajectories of membrane proteins occur in 3D whereas these trajectories are typically recorded experimentally in a 2D space [24, 30]. This projection of real trajectories on 2D space results in an additional reduction of the protein mobility.

Naturally, a given protein may couple to the membrane via several couplings of this kind simultaneously, and more couplings are possible. In the next section, we explore non-hydrodynamic couplings, and their consequences for the mobility of the membrane protein.

5 Theoretical Models

SD theory implicitly assumes that the protein diffuses in a membrane which remains flat and unaffected by the presence of the protein. Therefore, a possible origin for the discrepancy observed by Gambin et al. [8] is the significant local membrane deformation due to the interaction between the protein and the lipid bilayer as proposed in 2007 by Naji et al. [31]. In this view, a given membrane protein should experience additional dissipation, either within the membrane or within the external fluid, due to the local deformation which it carries along as it diffuses in the membrane.

In the next subsection, we sketch the original theoretical argument put forward by Naji et al. Then, we turn to a more formal analysis of the drag coefficient for a general order parameter using the so-called polaron model. In the next subsection, this polaron model is applied to the specific membrane curvature coupling and used to analyze the experiments of Ref. [11]. We finish with other potential applications of this framework and with a list of open problems.

5.1 Heuristic Approach to the Membrane Perturbation

Naji et al. suggested that the discrepancy between the SD prediction [3] and the experimental results of Gambin et al. [8] could be attributed to the perturbation of a local order parameter $\phi(\mathbf{r})$ of the membrane that could represent its lipid composition, thickness, or height [31]. They assumed that the perturbation of the order parameter ϕ has a characteristic length ξ, and is dragged along with the

protein, dissipating energy in a boundary layer of width $\delta\xi$. The power dissipated by this process is $P_\phi \sim 2\pi(a_\mathrm{p}+\xi)\delta\xi v^2$, corresponding to a drag coefficient:

$$\lambda_\phi \sim 2\pi(a_\mathrm{p}+\xi)\delta\xi. \tag{2}$$

If the length scale of the perturbation is small with respect to the size of the protein, $\xi \ll a_\mathrm{p}$, the drag coefficient takes the form $\lambda_\phi = \Gamma a_\mathrm{p}$. This drag coefficient enters the Einstein relation for the diffusion coefficient together with the SD drag λ_SD, giving

$$D = \frac{kT}{\lambda_\mathrm{SD}+\lambda_\phi} = \frac{kT}{\lambda_\mathrm{SD}+\Gamma a_\mathrm{p}}. \tag{3}$$

If the dissipation due to the perturbation of the order parameter ϕ dominates, the diffusion coefficient scales as $D \sim 1/a_\mathrm{p}$, which is compatible with the experiments of Gambin et al. [8].

In the following subsection, we turn to a formal description of the perturbation of the order parameter ϕ, which allows to compute the drag coefficient precisely.

5.2 *A Polaron Model for the Perturbation of an Order Parameter*

The back-action on an object that modifies its environment generates a drag force known as the polaron effect, which was originally described for an electron moving in a lattice [32]. A polaron is a charge carrier which deforms a surrounding lattice and moves in it with an induced polarization field. This effect has been applied to soft matter systems by one of us [33, 34]. We recall briefly the steps that allow to compute the drag coefficient generated by the coupling between the protein and a local order parameter (or field) $\phi(\mathbf{r})$, which may represent, e.g., the membrane height, thickness, or composition.

5.2.1 Definition of the Model

There are two steps in the modeling of the coupling between the protein and the order parameter $\phi(\mathbf{r})$ of the membrane. The first is to write the Hamiltonian of the protein-order parameter system, that we assume to be of the form:

$$\mathscr{H}[\phi(\mathbf{r}),\mathbf{R}] = \frac{1}{2}\int \phi(\mathbf{r})\Delta * \phi(\mathbf{r}) d^2\mathbf{r} - K * \phi(\mathbf{R}), \tag{4}$$

where the star denotes the convolution product $A * B(\mathbf{r}) = \int A(\mathbf{r}-\mathbf{r}')B(\mathbf{r}')d^2\mathbf{r}'$.

The first term is the energy of the order parameter itself, it is quadratic in the field and determined completely by the operator $\Delta(\mathbf{r})$. The second term couples the order parameter to the position of the protein, it is linear in the field and determined by the operator $K(\mathbf{r})$. The second step is to give the dynamics of the field, that we assume to be overdamped:

$$\frac{\partial\phi}{\partial t}(\mathbf{r},t) = -R * \frac{\delta\mathscr{H}}{\delta\phi(\mathbf{r},t)} + \eta(\mathbf{r},t), \tag{5}$$

where $R(\mathbf{r})$ is a linear operator and $\eta(\mathbf{r},t)$ is a Gaussian white noise with correlation function:

$$\left\langle \eta(\mathbf{r},t)\eta(\mathbf{r}',t')\right\rangle = 2TR(\mathbf{r}-\mathbf{r}')\delta(t-t'), \tag{6}$$

and $\delta\mathscr{H}/\delta\phi(\cdot,t)$ denotes a functional derivative [35].

The presence of the operator $R(\mathbf{r})$ in the noise correlation ensures that detailed balance is satisfied. Under this form, the model is completely determined by the three linear operators $\Delta(\mathbf{r})$, $K(\mathbf{r})$, and $R(\mathbf{r})$.

5.2.2 Computation of the Drag Coefficient

The force exerted by the field on the protein is given by the gradient of the interaction energy:

$$\mathbf{f}[\phi(\mathbf{r}),\mathbf{R}] = -\nabla_{\mathbf{R}}\mathscr{H}[\phi(\mathbf{r}),\mathbf{R}] = \nabla K * \phi(\mathbf{R}). \tag{7}$$

To compute the drag coefficient, a constant velocity $\mathbf{v}$ is imposed to the protein, $\mathbf{R}(t) = \mathbf{v}t$. We introduce the average field in the reference frame of the protein, which is time-independent in the stationary regime:

$$\Phi(\mathbf{r}) = \langle\phi(\mathbf{r}-\mathbf{R}(t),t)\rangle, \tag{8}$$

The average drag force can be written as:

$$\langle\mathbf{f}[\phi(\mathbf{r},t),\mathbf{R}(t)]\rangle = \nabla K * \Phi(0). \tag{9}$$

The average field in the reference frame of the protein is obtained by averaging Eq. (5) in the moving frame:

$$-\mathbf{v}\cdot\nabla\Phi(\mathbf{r}) = -R * \Delta * \Phi(\mathbf{r}) + R * K(-\mathbf{r}), \tag{10}$$

This equation is solved in Fourier space:

$$\tilde{\Phi}(\mathbf{k}) = \int d^2\mathbf{r}\, e^{-i\mathbf{k}\cdot\mathbf{r}}\Phi(\mathbf{r}) = \frac{\tilde{R}(\mathbf{k})\tilde{K}^*(\mathbf{k})}{\tilde{R}(\mathbf{k})\tilde{\Delta}(\mathbf{k}) - i\mathbf{k}\cdot\mathbf{v}}. \tag{11}$$

The force can be deduced from this Fourier transform:

$$\langle\mathbf{f}\rangle = \int \frac{d^2\mathbf{k}}{(2\pi)^2}\, i\mathbf{k}\tilde{K}(\mathbf{k})\tilde{\Phi}(\mathbf{k}) = \int \frac{d^2\mathbf{k}}{(2\pi)^2} \frac{i\mathbf{k}\tilde{R}(\mathbf{k})\left|\tilde{K}(\mathbf{k})\right|^2}{\tilde{R}(\mathbf{k})\tilde{\Delta}(\mathbf{k}) - i\mathbf{k}\cdot\mathbf{v}} \tag{12}$$

Expanding the force at small velocity leads to

$$\langle\mathbf{f}\rangle \underset{|\mathbf{v}|\to 0}{\sim} -\frac{\mathbf{v}}{2}\int \frac{d^2\mathbf{k}}{(2\pi)^2}\frac{\mathbf{k}^2\left|\tilde{K}(\mathbf{k})\right|^2}{\tilde{R}(\mathbf{k})\tilde{\Delta}(\mathbf{k})^2}, \tag{13}$$

where we used that $\int \mathbf{k}\cdot\mathbf{v}\mathbf{k} f(|\mathbf{k}|)d^2\mathbf{k} = \frac{1}{2}\mathbf{v}\int \mathbf{k}^2 f(|\mathbf{k}|)d^2\mathbf{k}$ for any function $f(|\mathbf{k}|)$. The drag coefficient is thus

$$\lambda = \frac{1}{2}\int \frac{d^2\mathbf{k}}{(2\pi)^2}\frac{\mathbf{k}^2\left|\tilde{K}(\mathbf{k})\right|^2}{\tilde{R}(\mathbf{k})\tilde{\Delta}(\mathbf{k})^2} = \frac{1}{4\pi}\int_0^\infty dk\, \frac{k^3\left|\tilde{K}(k)\right|^2}{\tilde{R}(k)\tilde{\Delta}(k)^2}. \tag{14}$$

The second equality assumes isotropic operators.

If this integral diverges at large wavevectors k, the finite size $a_\mathrm{p} > 0$ of the protein can be used to cut off the integral at $k_\mathrm{max} = \pi/a_\mathrm{p}$ [33, 34]. This regularization introduces a dependence of the drag on the size of the protein, whose form depends on the divergence of the integral.

The formula (14) involves the three operators that determine the model. We shall see below how it applies to the coupling of the membrane curvature with a protein with spontaneous curvature.

5.2.3 Link to the Diffusion Coefficient

The Einstein relation [1] relates the diffusion coefficient D to the drag coefficient λ_f defined as the ratio between the constant force applied to the particle and its average velocity, $\mathbf{f} = \lambda_\mathrm{f}\langle\mathbf{v}\rangle$ by $D = k_\mathrm{B}T/\lambda_\mathrm{f}$. In a fluctuating field, the drag coefficient λ_f and the drag coefficient λ computed *at constant velocity* are not equal [36, 37]. However, in the adiabatic regime where the field equilibrates much faster than the particle, the field remains close to equilibrium and the two drag coefficients are equal [36, 37]. In this case, the diffusion coefficient can be written as:

$$D_\mathrm{eff} = \frac{k_\mathrm{B}T}{\lambda_\mathrm{SD} + \lambda_\phi}, \tag{15}$$

where λ_ϕ is given by Eq. (14).

5.3 Application to a Protein That Couples to the Membrane Curvature

The coupling of a protein to the membrane curvature and its effect on its diffusion coefficient has been investigated before the introduction of the general model presented above [22, 24, 26, 38, 39]. These models resemble the model above where the operators have been specified for the coupling to the membrane curvature; the differences are discussed in Sect. 5.5.

Let us consider a single protein diffusing on a membrane patch of size $L \gg a_\mathrm{p}$ described by a height function $h(\mathbf{r})$. We use the modified Helfrich Hamiltonian:

$$\mathscr{H}_0[h, \mathbf{R}] = \frac{\kappa}{2} \int d^2\mathbf{r} \left[\left(\nabla^2 h \right)^2 + \frac{\Sigma}{\kappa} (\nabla h)^2 - \Theta G(\mathbf{r} - \mathbf{R}) \nabla^2 h \right], \tag{16}$$

where the first two terms represent the energy of elastic bending of the bilayer with modulus κ and tension Σ, and the last term models the membrane curvature induced at the location of the protein $\mathbf{R}$, which is time-dependent. The strength of the induced curvature scales linearly with the protein spontaneous curvature C_p, $\Theta = 4\pi a_\mathrm{p}^2 C_p$, similarly to [26, 31]. The range of influence of the protein on the membrane is modeled by the weight function G which is normalized to one and is nonzero over a distance of the order of a_p. This Hamiltonian carries with it a cutoff length a, which corresponds to the bilayer thickness ($\sim$5 nm). This model is a particular case of the polaron model described in the previous section, where the operators are given in Fourier space by:

$$\tilde{\Delta}(k) = \kappa k^4 + \Sigma k^2, \tag{17}$$

$$\tilde{R}(k) = \frac{1}{4\eta k}, \tag{18}$$

$$\tilde{K}(\mathbf{k}) = -\frac{\kappa\Theta}{2} k^2 \tilde{G}(\mathbf{k}). \tag{19}$$

As explained in Sect. 5.2.3, the diffusion coefficient is given by Eq. (15) if the dynamics of the membrane is much faster than the diffusion of the inclusion. This adiabatic approximation has been checked using numerical simulations [26] and by an explicit evaluation of the slowest membrane relaxation times for the conditions of the experiment of Ref. [11].

The polaron approach thus provides explicit predictions for the membrane profile and for the effective friction coefficient of the protein. The effective friction coefficient is $\lambda(\sigma) = \Theta^2 \eta W_0(\sigma)/2a$ where $\sigma = \Sigma a^2/4\pi\kappa$ is a reduced tension and $W_0(\sigma)$ a function given in Eq. S27 of Ref. [11]. The diffusion coefficient D_eff is obtained from the effective drag coefficient using the Stokes–Einstein relation:

$$\frac{D_0}{D_\mathrm{eff}} = 1 + \frac{\eta D_0 \Theta^2 W_0(\sigma)}{2a k_\mathrm{B} T}, \tag{20}$$

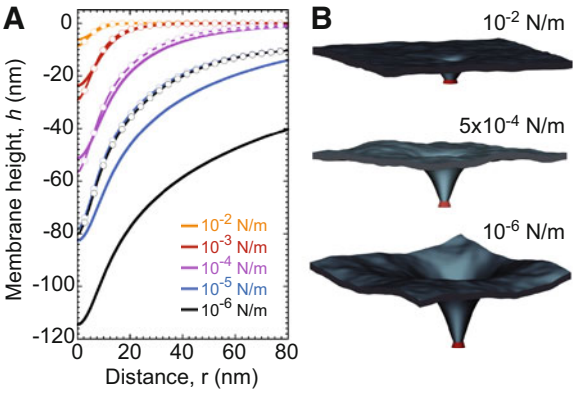

Fig. 4 Figure taken from Ref. [11]: Membrane shape as a function of the tension. (**a**) Theoretical profile with parameters $\Theta = 3.5 \times 10^{-7}$ m, $\kappa = 20\,k_BT$, $a_p = 4$ nm (solid lines). Profile calculated from the numerical energy minimum shape using simulation (dashed line). The height value far away from the inclusion is chosen to be zero. Discrepancy at low tension originates from the finite size of the membrane L^2 used in the simulations. (**b**) Three-dimensional membrane profiles obtained from numerical simulations for three different tensions

where D_0 represents the bare diffusion coefficient of the inclusion in a flat tense membrane, given by Eq. (1). The tension dependence of D_{eff} is shown in Fig. 3, together with the experimental data and the simulation data. For the simulation data, the protein diffusivity was directly computed from the MSD of stochastic trajectories, which were generated by numerically integrating the stochastic equations of motion of the inclusion and the membrane.

The membrane profile around the inclusion is obtained by the same method. The lateral characteristic width of this profile is the cross-over length between the tension and the bending regime for the fluctuations, namely $\xi = \sqrt{\kappa/\Sigma}$, while the characteristic height of the membrane deformation at zero tension scales as Θ. The geometry of the local deformation from the membrane mid-plane induced by KvAP when subjected to various tensions is shown in Fig. 4. Using the method of [26, 31, 40], we have carried out simulations, which also confirm the expected theoretical membrane profile as shown in Fig. 4.

5.3.1 Discussion of the Results of the Polaron Model

We find that theory and simulations fit very well the experimental results for the diffusion coefficient of KvAP using a coupling coefficient $\Theta = 3.5 \times 10^{-7}$ m. This proves that the mechanical coupling between the proteins and the membrane can strongly affect protein mobility. At high tension, the experimental data of AQP0 and KvAP converge to the same plateau value, consistently with the SD limit since they have about the same steric radius. As a control, the diffusion coefficient of pure lipids was measured and found to be independent of tension as for AQP0. The

corresponding constant value for D_0 agrees with the prediction of the SD model, using a lipid size $a_\mathrm{p} = 0.5\,\mathrm{nm}$. At lower tension, Fig. 3 shows that the KvAP data starts to deviate significantly from the plateau at $\Sigma \sim 5 \times 10^{-3}\,\mathrm{N/m}$, which corresponds to the point at which the lateral characteristic length ξ is of the order of the protein size.

An additional outcome of this approach concerns the dependence of D_eff with the protein radius a_p, which can be obtained from the following scaling argument. Since the protein makes a fixed angle with respect to the membrane, $C_p \sim 1/a_\mathrm{p}$. Given the relation $\Theta = 4\pi a_\mathrm{p}^2 C_p$, this implies $\Theta \sim a_\mathrm{p}$. Below the cross-over to the SD regime, the local membrane deformation is much larger than the protein size $a_\mathrm{p} \ll \xi$, and the drag is dominated by the contribution due to the membrane deformation. Therefore using Eq. (20), one finds $D_\mathrm{eff} \sim k_\mathrm{B} T a / a_\mathrm{p}^2$, in agreement with Ref. [33]. Note that such a result is also compatible with the Stokes–Einstein scaling law in $1/a_\mathrm{p}$ obtained in Ref. [31], because in this reference only one characteristic length for the protein is used thus $a \simeq a_\mathrm{p}$.

Despite a good agreement between model and data, the physical interpretation of the coupling coefficient Θ requires a more detailed discussion. Indeed, the spontaneous curvature deduced from this coupling coefficient via a fit of the data is significantly larger than that obtained from thermodynamic measurements, based on the preferential sorting at equilibrium of the proteins between GUV and highly curved membrane nanotubes [16]. One possible interpretation for this discrepancy is that in dynamic measurements, the basic relevant object, namely the association of the moving protein with the deformed membrane around it, may have a size larger than a_p. Such an enhancement of the size could in principle describe physically a layer of lipids dragged by the motion of the protein as considered in [41]. However, given the value of the coupling coefficient Θ, this translates into an effective radius of 47 nm, a rather large value with respect to the lipid and protein sizes (0.5 and 4 nm respectively). For this reason, we have proposed in Ref. [11] an alternate explanation, namely that this discrepancy reflects an additional source of internal dissipation, which for the present problem, could arise from inter-monolayer slip due to the motion of the inclusion. By considering this additional dissipative mechanism internal to the membrane, we have shown that we can still account for the dependence of D_eff versus Σ, but with a lower a coupling coefficient $\Theta = 3.4 \times 10^{-8}\,\mathrm{m}$, corresponding to a $C_p = 0.16\,\mathrm{nm}^{-1}$. This value is then much more compatible with the thermodynamic measurements previously reported in [16].

5.4 *Application to Other Order Parameters*

An important advantage of the polaron model is that it can be applied to other order parameters than the membrane height. Already in the previous subsection, we have mentioned an extension of the original polaron model, including dissipation mechanisms internal to the membrane, as a possible scenario to explain the value

of the coupling constant in Ref. [11]. In that extension, the relevant order parameter was already no longer the membrane height field, but rather the difference of lipid densities in the two leaflets of the membrane. Below, we explain how different order parameters can be described in the polaron model.

5.4.1 Coupling to the Thickness

When the hydrophobic length of the protein differs from the membrane height, the membrane is compressed or stretched close to the protein. The order parameter $\phi(\mathbf{r})$ is the difference between the local thickness of the membrane and its average thickness. If the membrane has a bending modulus κ and a compressibility χ, the energetic operators are given by [27, 42, 43]:

$$\tilde{\Delta}(k) = \kappa k^4 + \chi, \tag{21}$$

$$\tilde{K}(k) = \pi a_{\mathrm{p}} \Theta, \tag{22}$$

where the coupling constant Θ now depends on the height mismatch and the energetic cost for exposing a hydrophobic area.

To our knowledge, no dynamics has been proposed for the system. However, if we assume a simple form for the membrane friction (defined by the parameter γ in a way which conforms to model A dynamics [35]) and if we add to that the usual hydrodynamic friction due to the flow created in the solvent, we can propose an operator of the form:

$$\tilde{R}(k) = \gamma + \frac{1}{4\eta k}. \tag{23}$$

5.4.2 Coupling to the Composition

Real membranes are composed of several types of lipids, which may be mixed or separated. Proteins may couple to the composition field if they are preferentially wetted by one kind of lipids. Close to the demixing transition, which can be controlled in vitro in lipid vesicles [44, 45], this coupling to the composition induces long-range forces between the proteins [46]. Numerical simulations have shown that it may induce the aggregation of proteins [23].

In the simplest case, the relevant order parameter $\phi(\mathbf{r})$ is the difference between the local and average concentrations of a lipid specie. Its energy involves its correlation length, ξ, which diverges at the demixing transition, allowing long-range forces. The dynamics is conserved, the timescale being set by the diffusion coefficient D_0 of the lipids. The operators take the form [47]:

$$\tilde{\Delta}(k) = A\left[k^2 + \xi^{-2}\right], \tag{24}$$

$$\tilde{K}(k) = \Theta, \tag{25}$$

$$\tilde{R}(k) = D_0 k^2, \tag{26}$$

where Θ quantifies again the strength of the coupling. Similarly to what happens for the interaction between proteins, the strongest effect on the mobility is expected close to the demixing transition (see also Ref. [48] for a careful calculation of the drag coefficient of a diffusing domain in a near critical binary mixture).

In the description given above, we have not included the fact that the different lipid species may have different spontaneous curvatures. If this is the case [47, 49], the concentration field is coupled to the curvature field and there are two order parameters.

5.4.3 Coupling to Other Fields

The membrane could be coupled to other order parameters, and to several parameters at the same time. This situation has been evoked in the previous section, where the curvature is coupled to the composition. Also, a coupling of the membrane curvature to the lipid density in the two leaflets has been suggested to provide another dissipative mechanism in Ref. [11]. The polaron model needs to be extended to deal with these situations where there are several order parameters.

Another possible order parameter is the liquid crystalline order parameter of the lipids, which is expected to be distorted near small inclusions like proteins [50]. The dynamics of a liquid crystalline order parameter can be described using continuum theories of liquid crystals and there are many studies on the dynamics of topological defects in liquid crystals [35, 51]. Pre-transition (or pre-melting) effects which are well known in liquid crystals are also relevant for transmembrane proteins, which can, for instance, stabilize a microscopic order–disorder interface, when their hydrophobic thickness matches that of the disordered phase and when they are embedded in an ordered bilayer [52].

It is important to appreciate that if the protein couples to the membrane through an order parameter different from the height field, like a concentration field or a nematic order parameter field, it could happen that there will be no observable membrane deformation near the protein, while the order parameter is still perturbed.

5.5 Extension of the Polaron Model

We discuss here three ways to extend the simple polaron model presented in Sect. 5.2. First, we consider the case where several order parameters are coupled together and with the protein. Second, we discuss different ways to couple the order parameter and the protein. Finally, the coupling of the dynamics of the order parameter to the hydrodynamic flow in the membrane is evoked.

5.5.1 Coupling to Several Order Parameters

There are cases where several order parameters $\phi_\alpha(\mathbf{r})$ are coupled [11, 47]. The polaron model can be extended to handle several order parameters. The three operators become matrix operators:

$$\Delta(\mathbf{r}) \rightarrow \Delta_{\alpha\beta}(\mathbf{r}), \tag{27}$$

$$K(\mathbf{r}) \rightarrow K_\alpha(\mathbf{r}), \tag{28}$$

$$R(\mathbf{r}) \rightarrow R_{\alpha\beta}(\mathbf{r}). \tag{29}$$

In this way, the new Hamiltonian becomes

$$\mathscr{H}[\phi(\mathbf{r}), \mathbf{R}] = \frac{1}{2}\int \phi_\alpha(\mathbf{r})\Delta_{\alpha\beta} * \phi_\beta(\mathbf{r})d^2\mathbf{r} - K_\alpha * \phi_\alpha(\mathbf{R}), \tag{30}$$

where the Greek indices run over the different order parameters and a summation over repeated indices is implicit.

The extension of the computation of the drag coefficient given in Sect. 5.2.2 is straightforward, leading to:

$$\lambda = \frac{1}{2}\int \mathbf{k}^2 \tilde{K}(\mathbf{k})_\alpha \tilde{\Delta}(\mathbf{k})^{-1}_{\alpha\beta} \tilde{R}(\mathbf{k})^{-1}_{\beta\gamma} \tilde{\Delta}(\mathbf{k})^{-1}_{\gamma\delta} \tilde{K}(\mathbf{k})^*_\delta \frac{d^2\mathbf{k}}{(2\pi)^2}. \tag{31}$$

5.5.2 Other Protein Couplings to the Order Parameter

In the example of a protein coupled to the curvature of the membrane, it is clear that a linear coupling cannot be used to "impose" a given curvature to the membrane at the location of the protein. Instead, the value of the membrane curvature depends on the Hamiltonian operators $\Delta(\mathbf{r})$ and $K(\mathbf{r})$.

The more direct way to impose the membrane curvature is to set it as a boundary condition [41, 53], using a relation of the form $K * \phi(\mathbf{R}) = A$ (in this case of a coupling to the membrane curvature, A corresponds to the curvature of the membrane at the location of the protein, denoted C_p above). In this framework, the force can no longer be computed with Eq. (7), and one should instead integrate the stress tensor around the protein [54, 55].

An imposed boundary condition can be modeled in the framework of the polaron model, by introducing a parameter α in front of the coupling operator $K(\mathbf{r})$ and tuning it so that the boundary condition is satisfied. In this case, α depends on the other parameters of the model (e.g., the membrane tension and bending modulus when the protein is coupled to the curvature of the membrane). This approach has been shown to give results consistent with those obtained with an imposed boundary condition [41].

Alternatively, the polaron model can be modified by replacing the linear coupling to the order parameter by a coupling of the form:

$$\mathscr{H}_{\text{int}}[\phi(\mathbf{r}), \mathbf{R}] = \frac{\kappa_{\text{p}}}{2} \left[K * \phi(\mathbf{R}) - A\right]^2 , \tag{32}$$

where κ_{p} is the "rigidity" of the coupling (e.g., the bending rigidity of the protein). In the limit of infinite rigidity, $\kappa_{\text{p}} \to \infty$, one recovers the imposed boundary condition. This form of coupling has been used to model the coupling to curvature in Refs. [26, 39]. In the limit where $K * \phi(\mathbf{R})$ is small with respect to A, the linear coupling introduced in Eq. (4) is recovered.

In the particular case $A = 0$, the coupling does not affect the average value of the order parameter, but only its fluctuations. This Casimir-like coupling gives rise to another source of drag [56] and further reduction of the diffusion coefficient [57]. For a coupling to curvature, when both effects (average field deformation and fluctuations) compete, the fluctuations induced part is often neglected owing to the fact that the thermal fluctuations are small, i.e., $k_{\text{B}}T \ll \kappa$.

In the general case, the interaction Hamiltonian given in Eq. (32) depends on one more parameter than the linear interaction in Eq. (4). This has important implications: for example, when the coupling to membrane curvature is modeled by a linear interaction, as in Eq. (16), the rigidity of the protein and its spontaneous curvature cannot be decoupled. On the other hand, the rigidity κ_{p} and the preferred average value A have very different effects with the quadratic coupling, Eq. (32).

5.5.3 Interaction of the Order Parameter with the Hydrodynamic Flow

The polaron model is completely independent of the hydrodynamic calculation of Saffman and Delbrück, in the sense that the flow in the membrane and in the solvent are neglected, and the order parameter dynamics is not coupled to these flows. For example, if the order parameter represents the concentration difference between two lipid species, it is clear that besides diffusion, the order parameter is advected by the lipid flow in the membrane [23].

The coupling between the order parameter $\phi(\mathbf{r})$ and the hydrodynamic flow $\mathbf{u}(\mathbf{r})$ has been modeled by Camley and Brown [41]. They found that the advection of the order significantly changes the total drag on the protein. As a result, the protein is endowed with a larger effective radius, since the lipids which are closest to the protein are carried along with it. Although this effect will affect the value of the drag, this will not change the qualitative behavior, in particular the result that the drag should scale with the particle size, in a logarithmic way in the SD regime and linearly for large particles.

Recently, another very interesting hydrodynamic model [58, 59] has been proposed to account for the experimental data on the tension dependence of the mobility of KvAP discussed in this paper and first reported in Ref. [11]. Assuming a negligible contribution due to the hydrodynamics of the surrounding fluid, the

authors of this study have exploited a covariant formulation of the membrane hydrodynamics of the inclusion, which has specific features due to the Gaussian curvature induced locally by the inclusion. In this way, they could explain the experimental data on the mobility of KvAP without requiring additional mechanism of internal dissipation. Interestingly, a key ingredient of their model is the deformability of the inclusion, which is particularly important for gated membrane channels [60]. We note that the polaron model could account for the deformability of the inclusion, and could also be combined with such hydrodynamic description of the membrane.

6 Concluding Perspective

In this chapter, we have presented some simple views on the way geometrical or mechanical factors influence the mobility of membrane proteins. We have shown that one should expect generally a significant dependence of the protein mobility on its local environment.

Naturally, many molecular details affect this local environment, which makes the modeling of the protein mobility a challenging task. However, despite the complexity of this problem, there is a simple take-home message. In order to predict the way various mechanical factors that affect the mobility of membrane proteins, one should not focus on the mechanical factors themselves or on the details of the local environment of the protein, but instead on the form of coupling between the membrane and the protein. We have provided in this chapter a list of various relevant couplings, and a detailed study of one coupling, namely the tension-dependent coupling to the local membrane curvature. Clearly, it would be desirable to perform similar experimental studies in order to test more couplings and their dependence to other mechanical factors. The importance of these couplings goes beyond the specific question of the mobility of membrane proteins, since they are also relevant to understand the function of many membrane proteins, like voltage-gating channels, mechano-sensitive channels, G-protein-coupled receptors (GPCR), or light-activated rhodopsins [29]. These couplings also play a key role in the interactions between membrane proteins, and in their self-organization into complex dynamical structures, such as membrane clusters.

At the level of single membrane proteins, other directions for future research should investigate: (i) a protein diffusing in a membrane which may be driven out of equilibrium, or (ii) a protein which can be activated or can change conformation while diffusing on the membrane. For studying the former case (i), various strategies can be used to drive a membrane out of equilibrium by applying external fields on it directly or by embedding other proteins in it on which forces can be applied [61]. Measurements of the force-dependent mobility of a membrane protein could advantageously provide information on the way it couples to its environment, which as mentioned above is a crucial aspect of the problem. For case (ii), the internal dynamics of the protein can matter for the protein mobility because different internal states can couple differently to the membrane and the characteristic time of these

internal transitions (typically 10–1000 ms) can be much longer than the time of diffusion of the protein over a distance equal to its radius (typically <1 ms) [62]. For many membrane proteins, the transition rates can be tuned by changing the amount of ATP, allowing to probe different dynamical regimes for the mobility of the protein.

In cell membranes, the local environment of proteins is crowded and heterogeneous. Membrane protein crowding is of primary importance to understand the mobility of membrane proteins and membrane-mediated interactions between different proteins. Such effects are not well understood and they need to be investigated more systematically both experimentally and theoretically.

We hope that this chapter can be useful to motivate further experimental and theoretical studies on these questions.

Acknowledgements We would like to thank P. Quemeneur, J. K. Sigurdsson, M. Renner, P. J. Atzberger, and P. Bassereau for a previous collaboration, which motivated this chapter. In addition, we would like to acknowledge stimulating discussions with W. Urbach and M. S. Turner. D L would also like to thank Labex CelTisPhysBio (N ANR-10-LBX-0038) part of IDEX PSL (NANR-10-IDEX-0001-02 PSL) for financial support.

References

1. Einstein A (1905) Ann Phys 322:549
2. Perrin JB (1909) Ann Chim Phys 19:5
3. Saffman PG, Delbrück M (1975) Proc Natl Acad Sci USA 72(8):3111
4. Hughes BD, Pailthorpe BA, White LR (1981) J Fluid Mech 110:349
5. Guigas G, Weiss M (2008) Biophys J 95(3):L25
6. Petrov EP, Schwille P (2008) Biophys J 94(5):L41
7. Petrov EP, Petrosyan R, Schwille P (2012) Soft Matter 8:7552
8. Gambin Y, Lopez-Esparza R, Reffay M, Sierecki E, Gov NS, Genest M, Hodges RS, Urbach W (2006) Proc Natl Acad Sci USA 103:2098
9. Ramadurai S, Holt A, Krasnikov V, van den Bogaart G, Killian JA, Poolman B (2009) J Am Chem Soc 131(35):12650
10. Weiß K, Neef A, Van Q, Kramer S, Gregor I, Enderlein J (2013) Biophys J 105(2):455
11. Quemeneur F, Sigurdsson JK, Renner M, Atzberger PJ, Bassereau P, Lacoste D (2014) Proc Natl Acad Sci USA 111(14):5083
12. Gambin Y, Reffay M, Sierecki E, Homblé F, Hodges RS, Gov NS, Taulier N, Urbach W (2010) J Phys Chem B 114(10):3559
13. Domanov YA, Aimon S, Toombes GES, Renner M, Quemeneur F, Triller A, Turner MS, Bassereau P (2011) Proc Natl Acad Sci USA 108(31):12605
14. Daniels DR, Turner MS (2007) Langmuir 23(12):6667
15. Hormel TT, Kurihara SQ, Brennan MK, Wozniak MC, Parthasarathy R (2014) Phys Rev Lett 112:188101
16. Aimon S, Callan-Jones A, Berthaud A, Pinot M, Toombes GES, Bassereau P (2014) Dev Cell 28(2):212
17. Chang G, Spencer RH, Lee AT, Barclay MT, Rees DC (1998) Science 282(5397):2220
18. Liu Z, Gandhi CS, Rees DC (2009) Nature 461(7260):120
19. Camley BA, Brown FLH (2013) Soft Matter 9(19):4767
20. Seki K, Ramachandran S, Komura S (2011) Phys Rev E 84:021905

21. Stone HA, Ajdari A (1998) J Fluid Mech 369:151
22. Goulian M, Bruinsma R, Pincus P (1993) Europhys Lett 22(2):145
23. Reynwar B, Deserno M (2008) Biointerphases 3:FA117
24. Reister E, Seifert U (2005) Europhys Lett 71(5):859
25. Reynwar BJ, Illya G, Harmandaris VA, Muller MM, Kremer K, Deserno M (2007) Nature 447(7143):461
26. Naji A, Atzberger PJ, Brown FLH (2009) Phys Rev Lett 102(13):138102
27. Andersen OS, Koeppe RE (2007) Annu Rev Biophys Biomol Struct 36(1):107
28. Winterhalter M, Helfrich W (1987) Phys Rev A 36:5874
29. Phillips R, Ursell T, Wiggins P, Sens P (2009) Nature 459(7245):379
30. Reister-Gottfried E, Leitenberger SM, Seifert U (2007) Phys Rev E 75(1):011908
31. Naji A, Levine AJ, Pincus PA (2007) Biophys J 93(11):L49–L51
32. Landau LD (1933) Phys Z Sowjetunion 3:644
33. Démery V, Dean DS (2010) Phys Rev Lett 104(8):080601
34. Démery V, Dean DS (2010) Eur Phys J E 32:377
35. Chaikin PM, Lubensky TC (1995) Principles of condensed matter physics. Cambridge University Press, Cambridge
36. Dean DS, Démery V (2011) J Phys Condens Matter 23(23):234114
37. Démery V, Dean DS (2011) Phys Rev E 84(1):011148
38. Leitenberger SM, Reister-Gottfried E, Seifert U (2008) Langmuir 24:1254
39. Reister-Gottfried E, Leitenberger SM, Seifert U (2010) Phys Rev E 81:031903
40. Sigurdsson JK, Brown FL, Atzberger PJ (2013) J Comput Phys 252:65
41. Camley B, Brown F (2012) Phys Rev E 85(6):061921
42. Gruner SM (1985) Proc Natl Acad Sci USA 82(11):3665
43. Mouritsen OG, Bloom M (1993) Annu Rev Biophys Biomol Struct 22(1):145. PMID: 8347987
44. Veatch SL, Keller SL (2003) Biophys J 85(5):3074
45. Veatch SL, Soubias O, Keller SL, Gawrisch K (2007) Proc Natl Acad Sci USA 104(45):17650
46. Machta BB, Veatch SL, Sethna JP (2012) Phys Rev Lett 109(13):138101
47. Taniguchi T (1996) Phys Rev Lett 76(23):4444
48. Fujitani Y (2013) J Phys Soc Jpn 82(12):124601
49. Yanagisawa M, Imai M, Masui T, Komura S, Ohta T (2007) Biophys J 92(1):115
50. Bartolo D, Long D, Fournier JB (2000) Europhys Lett 49(6):729
51. de Gennes PG, Prost J (1993) The physics of liquid crystals. Oxford University Press, Oxford
52. Katira S, Mandadapu KK, Vaikuntanathan S, Smit B, Chandler D (2016) eLife 5:e13150
53. Bitbol AF, Dommersnes PG, Fournier JB (2010) Phys Rev E 81(5):050903
54. Bitbol AF, Fournier JB (2011) Phys Rev E 83(6):061107
55. Capovilla R, Guven J (2002) J Phys A Math Gen 35:6233
56. Démery V, Dean DS (2011) Phys Rev E 84(1):010103
57. Démery V (2013) Phys Rev E 87(5):052105
58. Morris RG, Turner MS (2015) Phys Rev Lett 115:198101
59. Daniels DR (2016) Eur Phys J E 39(10):96
60. Morris RG (2017) Biophys J 112(1):3
61. Lacoste D, Bassereau P (2013). In: Pabst G (ed) Liposomes, lipid bilayers and model membranes: from basic research to applications. Taylor and Francis, London, pp 271–287
62. Bouvrais H, Cornelius F, Ipsen JH, Mouritsen O (2012) Proc Natl Acad Sci USA 109(45):18442

Membrane Domains Under Cellular Recycling

S. Alex Rautu and Matthew S. Turner

Abstract Living cells are bounded by sac-like membranes that play a crucial role in almost every cellular process. These membranes are highly dynamic, two-dimensional systems, with components that are continuously exchanged with rest of the living cell by the secretion and absorption of small vesicles with sizes of the order of tens or hundreds of nanometers in diameter. This constant recycling of the cell membranes leads to a complete turnover of its constituents on the order of tens of minutes. The presence of distinct nano-scale microphase separated domains in biomembranes has been confirmed by numerous experiments. In this chapter we address recent advances in our understanding of the role of recycling in the control of membrane microdomain formation. These results relate to both the steady-state distribution of domain sizes and the transient response of this distribution following perturbation of cellular synthesis, transport, or recycling pathways. This gives a route to testing and calibrating theoretical models from experiments that measure the domain size distribution.

Keywords Endocytosis · Membrane · Microdomain · Raft · Recycling

1 Introduction

Living cells are bounded by sac-like membranes that play a crucial role in almost every cellular process [1]. Cellular function also relies on numerous membrane-bound organelles. The fundamental architecture of all biological membranes arises

S. A. Rautu
Department of Physics, University of Warwick, Coventry, UK

National Centre for Biological Sciences, UAS-GKVK Campus, Bangalore, India

M. S. Turner (✉)
Department of Physics, University of Warwick, Coventry, UK

Centre for Complexity Science, University of Warwick, Coventry, UK
e-mail: m.s.turner@warwick.ac.uk

P. Bassereau, P. Sens (eds.), *Physics of Biological Membranes*,
https://doi.org/10.1007/978-3-030-00630-3_9

from the self-assembly of lipid molecules which form thermodynamically stable bilayer structures a few nm in thickness[2]. This bilayer acts as a platform to which many other molecules either incorporate or adhere. These membranes are highly dynamic, two-dimensional systems, comprised of a myriad of different lipids and proteins. These components are continuously exchanged with rest of the living cell by the secretion and absorption of small vesicles with sizes of the order of tens or hundreds of nanometers in diameter [3]. This constant recycling of the cell membranes leads to a complete turnover of its constituents on the order of tens of minutes [4].

The presence of distinct nano-scale domains in biomembranes has been confirmed by numerous experiments [5]. However, this evidence is based on indirect measurements, such as the diffusive trajectories of labeled lipids or proteins that show a temporary confinement to a small region of the biomembrane [6–9]. Further supporting evidence is also given by the biochemical experiments on membrane samples which are dissolved in specific detergents [10]. Since a significant portion of the plasma membranes has been observed to be detergent-resistant, it has been hypothesized that this membrane fraction corresponds to these domains, sometimes called rafts [11], enriched in cholesterol and sphingolipids [12]. There is also a body of accumulated evidence that certain proteins have high affinity to these lipid rafts [13], which can be recruited to (or removed from) through the attachment (or the enzymatic cleavage) of their hydrocarbon anchors [14]. Due to this protein–raft affiliation numerous functions have been associated with the presence of lipid rafts [15]. However, the nature of these membrane domains as well as their formation remains elusive [16] and there are many unanswered questions that require further investigation [13].

2 Phase Coexistence in Lipid Mixtures

When water and lipid molecules are combined the total free-energy is minimized by shielding the hydrocarbon chains of the lipids from their aqueous environment [2]. Due to this hydrophilic effect, lipids self-assemble into super-molecular structures. One of the most common structures is a lipid bilayer, which forms the basic architecture of all biological membranes [17].

Within this simple construction principle the compositions of both the hydrophilic groups and the hydrocarbon chains display a large variation, giving raise to a “zoo” of various types of lipid species, which is on the order of several thousands [2]. Out of this plethora of lipid species, phospholipids are the most abundant type [17], and their head-group composition may include various organic compounds, such as choline, ethanolamine, serine, inositol, or glycerol [17]. There is also a large range of possible fatty acid chains, which can vary by chain length and degree of saturation [2]. The latter describes the number of double bonds between the carbon atoms that are present along the chain. Most of the hydrocarbon tails are

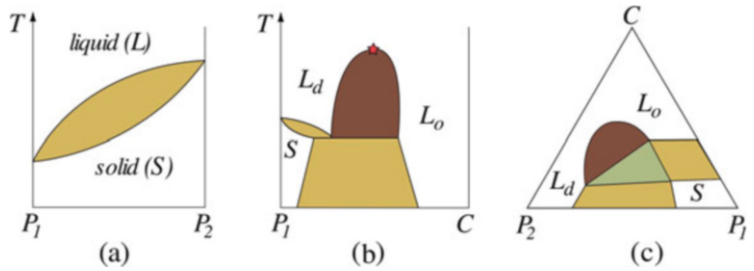

Fig. 1 Schematic phase diagrams of a lipid bilayer, depicting the solid phase (S), the liquid-ordered phase (L_o), and the disordered phases (L_d), as a function of temperature T and its membrane composition: (**a**) a two-component mixture of saturated and unsaturated phospholipids, denoted here by P_1 and P_2, respectively; (**b**) a binary mixture of phospholipid P_1 and cholesterol (C); and (**c**) a ternary mixture of P_1, P_2, and C at a physiological temperature. The region of the solid–liquid phase coexistence is shown in yellow, whereas the associated regions between two liquid phases are illustrated in brown. Moreover, the three-phase coexistence region in (**c**) is depicted by green, and the red star in (**b**) marks the critical point at which the liquid phases become the same phase. Adapted from [18]

unsaturated [2], namely they have at least one double bond. Lipid molecules that have only single bonds are known to be *saturated* [2].

An important property of model membrane systems composed of a single lipid species is that their lipid order undergoes a phase transition [5]. As the temperature is increased above a particular melting temperature, the membrane changes from a solid, or *gel* phase (S), to a *liquid disordered* phase (L_d), as illustrated in Fig. 1a. The latter is characterized by a high lateral mobility of lipids, which are randomly distributed, and all their hydrocarbon tails are disordered (or fluid-like) [2]. On the other hand, in the gel phase, the mobility of lipids is greatly reduced, and their fatty acid chains are tightly packed, displaying a regular arrangement (a two-dimensional triangular lattice) [2]. In other words, the chain conformation becomes more disordered at high temperatures, disrupting the crystalline structure of the lipid bilayer. The chain melting temperatures are higher as the length of the hydrocarbon chain is longer [2]. However, the presence of double bonds significantly decreases this melting point [2]. Thus, saturated lipids melt at considerably higher temperatures (i.e., they are easier to order) than lipids with unsaturated chains which have permanent kinks. This effect is used by a variety of organisms that adjust their membranes to function at lower or higher temperatures [14].

If a high concentration of cholesterol ($\gtrsim$ 30%) is also added to the lipid molecules, a third phase can be found, see Fig. 1b, which is commonly referred to as the *liquid-ordered* phase (L_o) [19]. The addition of cholesterol to lipid bilayers has a twofold effect: it encourages the close packing of the hydrocarbon tails in the L_d phase, while disrupting the chain conformational ordering in the S phase [12]. Thus, a membrane in the liquid-ordered phase behaves as a fluid with translational disorder and high lateral mobility. This decreases its melting temperature [2]. As a

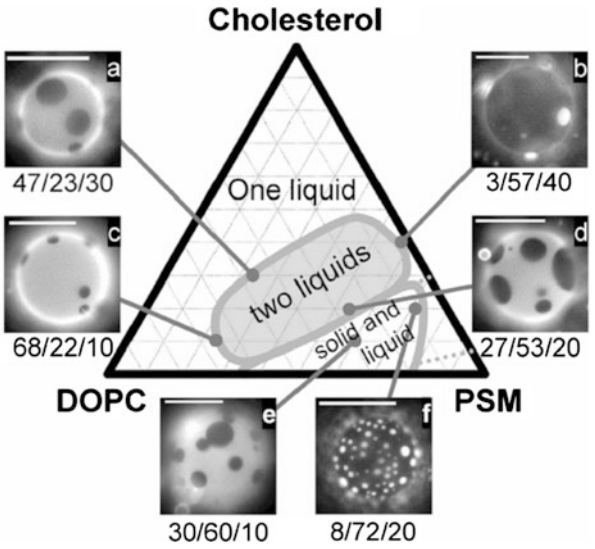

Fig. 2 Fluorescence microscopy phase diagram of a three-component system, namely an unsaturated lipid, dioleoylphosphatidylcholine (DOPC), a saturated lipid, palmitoylsphingomyelin (PSM), and cholesterol (Chol). The images a–f correspond to different DOPC/PSM/Chol concentrations, showing the domains before they fully phase separate. Scale bars are given by 20 μm. Here, the dark patches are rich in PSM and Chol, while the bright ones are rich in DOPC. Adapted from [22]

consequence, in a ternary mixture of cholesterol, saturated and unsaturated lipids, the solid phase S, and/or the two *liquid* phases L_o and L_d can co-exist, as sketched in Fig. 1c, leading to a lateral phase separation [12, 14]. In fact, the simplest way of forming lipid membrane domains is to quench the system into a two-phase coexistence region by changes in temperature, or membrane composition [18]. This lateral phase separation and demixing has been experimentally observed in model membranes of two phospholipids and cholesterol [20–22], as shown in Fig. 2.

Although there is currently no explicit definition of lipid rafts they are commonly characterized in terms of their average size, lifetime, and their broad composition [23–25]. Specifically, they are small, transient structures with a typical size in the range of 10–200 nm that are highly enriched in cholesterol and sphingolipids [23]. As sphingolipids are saturated lipids, they have a much higher melting temperature [14]. This aspect, together with the presence of a high concentration of cholesterol (which encourages the ordering of the hydrocarbon chains), leads to the hypothesis that lipid rafts might be, in their basic form, related to membrane patches in a L_o phase, which move within a background of L_d lipids [21, 26]. Mixtures of a small number of different lipid species have been widely investigated using fluorescence microscopy. These show that phase separation can occur in model membrane systems over a range of temperatures (see Fig. 2), giving rise to raft-like structures that resemble a liquid-order phase [20]. At the same time, a number of theoretical studies of three-component membranes (based on microscopic [19] and phenomenological models [27]) have been used to understand and reproduce the observed phase behavior of such lipid mixtures when they are subject to the addition of cholesterol [12]. Although the latter is pivotal to the existence of this liquid–liquid phase region, its role and mechanism in the formation of L_o phase is still elusive [5]. Nonetheless, the size of the observed domains in these in vitro

experiments is much larger than those observed in cells. This is expected as the phase separation in a two-component system manifests itself by the appearance of separated domains, which then grow until they reach the size of the system [28]. However, this separation occurs without any intermediate stable sizes, such as the nano-scale length of membrane rafts. This simple argument makes the existence of rafts somewhat surprising from a physical point of view, as they possess a characteristic size that is much smaller than the typical diameter of cells (that is, on the order of tens or hundreds of microns).

A number of explanations have been put forth to explain their relatively small size based on the assumption that the sub-micron membrane inhomogeneities are an aspect of the L_o–L_d phase coexistence. These explanations can be attributed to the effects due to cytoskeleton pinning, binding of cross-linkers, extracellular adhesion (e.g., through cell–cell junctions, or interactions with the extracellular matrix) [29], or integral proteins [25]. By favoring one of the liquid phases, these attachments can prevent the appearance of macroscopic phase separation, which limit the growth of membrane domains to sizes on the order of hundreds of nanometers [30]. Moreover, the growth of the domains may also be avoided if their diffusive motion is inhibited (e.g., membranes onto a solid support [31–33]), or if there is a repulsion as they encounter each other. The latter can be due to electrostatics [34] or membrane-mediated interactions that can be induced by a hydrophobic mismatch [35–37] or by the presence of different curvatures within each liquid phase [38–40]. As a result, the formation of nano-scale domains in biomembranes might be an upshot of the interplay between various biophysical parameters that contribute to the local demixing and control the size of the membrane domains. In the next sections, we present in more detail some of the attempts that can also give rise to sub-micron heterogeneities in membranes, which views them as: near-critical composition fluctuations [41], two-dimensional microemulsions [42], and non-equilibrium clusters driven by membrane recycling [43].

3 Critical Phenomena in Membranes

A multi-component membrane can exhibit critical-point phenomena [41] at a particular temperature that depends on the lipid composition. This is known as the critical mixing point. In a binary mixture of phospholipids and cholesterol, the two liquid phase, L_o and L_d, become the same fluid phase at a critical point [14]. In other words, as the temperature increases passed a critical temperature T_c, the system transits from a two-phase coexistence region (where the formation of domains is present) to a one-phase region, as shown in Fig. 1b. Near this critical mixing, the lipid bilayer is subjected to large fluctuations in its local membrane composition, and domains of different sizes are transiently formed, consisting of both liquid phases and displaying a characteristic structure [41].

This type of miscibility transition is found to be in the universality class of the two-dimensional Ising model, which has been widely studied in the literature [44].

As a result, the typical size of the concentration fluctuations, at a temperature T close to T_c, is characterized by a correlation length of the form $\xi \sim |T - T_c|^{-1}$ [45]. This property has been experimentally confirmed and measured for ternary mixtures of cholesterol, saturated and unsaturated lipids over a broad range of temperatures [46]. Furthermore, the same critical phenomena of a two-dimensional Ising model have been observed in the so-called *giant plasma membrane vesicles* (GPMVs), which is a model system of membranes with a composition of lipids and proteins that has been extracted from living cells [47].

These experiments have led to the hypothesis that the inhomogeneities in a biological membrane are simply the concentration fluctuations associated with a nearby critical point of a two-phase coexistence region [41]. The size of these near-critical fluctuations is described by ξ and thus depends solely of how close the system is tuned to its critical mixing. These can be large, diverging as the temperature approaches T_c [45]. The nano-scale sizes of the membrane heterogeneities observed in vivo could then be ascribed either to regulatory fine-tuning of the composition to the actual temperature so at to generate the appropriate value of $T - T_c$, leading to the observed membrane fluctuations, or to a cut-off of these large fluctuations, which might be induced by some extrinsic pinning or anchoring of the membrane, such as the finite size mesh of the cytoskeleton [48]. Nevertheless, remaining in the proximity of a critical point is a rather specific condition, which may not correspond to the physiological regime [12].

4 Two-Dimensional Microemulsions

Since lipid rafts are characterized as transient structures of some representative size [13] it has been hypothesized that these membrane domains are simply a (two-dimensional) microemulsion, caused by the presence of an *edgeactant* component, the analogue of a three-dimensional *surf*actant [49]. This is a hypothetical component that prefers to sit at the interface between the two liquid phases. This edgeactant results in a (tuneable) reduction of the line tension associated with the periphery of the membrane domains. This leads to a new characteristic length scale corresponding to the typical size of the domains that are decorated with edgeactant (roughly the total domain area divided by the total length of the edgeactant stabilized interface). This can be very different to the correlation length ξ that is associated with the system's proximity to a critical point [12].

Although there is no clear example of such an edgeactant in biological membranes, a few potential candidates have been proposed. These include certain proteins or *hybrid lipids* that consist of two motifs with different binding affinities to the surrounding lipidic environment [41]. Cholesterol is unlikely to play such a role as it is known to be enriched in the phase rich in saturated lipids (rather than at the interface) [12, 41]. Cholesterol does not act as an edgeactant but rather it promotes lipid demixing. A possible example of a membrane protein that might function as edgeactant is N-Ras, which has been lipidated entirely in a giant unilamellar vesicle of a ternary lipid mixture [50]. Although it preferentially occurs in the L_d phase, a

large fraction of N-Ras is also found to reside at the L_o–L_d phase boundary. Similarly, hybrid lipids have been also proposed as a candidate [12, 49]. These are lipid molecules with two hydrocarbon chains, where one of the tails is saturated while the other is unsaturated. For instance, 1-palmitoyl-2-oleoylphosphatidylcholine (POPC) and 1-stearoyl-2-oleoyl-sn-glycero-3-phosphocholine (SOPC) are some commonly used hybrid lipids in model systems [41]. As a result, mixtures of a hybrid lipid, a saturated lipid, and an unsaturated lipid have been characterized as a microemulsion [51–56]. This is thought to be associated with the positioning of hybrid lipids at the domain interface where they reorientate their lipid chains so that they are adjacent to lipid regions with a similar degree of saturation [51]. This re-orientation leads to a decrease of the line tension at the domain boundary [49] and, furthermore, near a critical point this may increase the lifetime of the composition fluctuations as more hybrid lipids are added [54].

However, it is still unclear whether hybrid lipids, such as POPC or SOPC, can truly function as a two-dimensional surfactant, and how this aspect reconciles with the experimental observation that macroscopic phase separation occurs in model systems where POPC or SOPC acts as the primary component of both L_d [20] and L_o phases [57]. Interestingly, there are other mechanisms that can give rise to a microemulsion-like behavior which do not explicitly involve the presence of an edgeactant [55, 56, 58]. Often, equilibrium systems display some kind of modulation in their structural properties, caused by the intricate competition of different energy terms associated with the structure [59]; e.g., the coupling between membrane composition asymmetry and its curvature [58, 60–62]. This modulation brings about a number of visually compelling patterns, such as elongated stripes or compact domains in a hexagonal arrangement [59]. In this framework, a two-dimensional microemulsion can then be interpreted as a melted configuration of a modulated phase [12].

5 Membrane Recycling

All of the research discussed above is framed under the assumption that the membrane is at thermodynamic equilibrium. However, biological membranes in living cells are active systems [63], which can be driven far from a equilibrium condition [24], possibly to a steady state. Thus, it may be dangerous to draw inferences from model systems that are at equilibrium to biomembranes [13]. Nevertheless, these equilibrium or near-the-equilibrium studies can provide us with a basic framework for understanding of the formation and maintenance of membrane rafts. For example, research on GPMVs, which are vesicles with a complex composition extracted from cells, has demonstrated that their membranes resemble those observed in model systems [13]. But, at the same time, such systems do not include cytoskeletal processes (such as the acto-myosin dynamics [64]) or the constant membrane recycling (e.g., clathrin-mediated endocytosis and caveolae pathway [65]). Both of these mechanisms are believed to play a crucial role in the stability and lifetime of the membrane heterogeneities which is observed

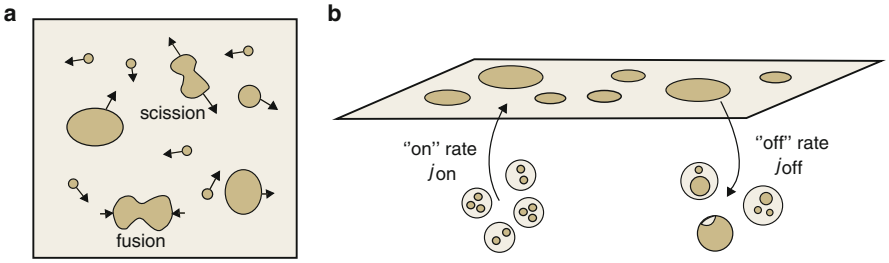

Fig. 3 Smoluchowski-type model for a two-component membrane under a continuous recycling. (**a**) In general, the intramembrane dynamics of domains involves both scission and fusion events; although the former is usually unfavorable due to the high line tension. (**b**) The membrane recycling scheme consists of a deposition of monomeric components with a flux rate j_{on}, and also a removal of membrane clusters with a rate given by j_{off}, which is independent of their size. Adapted from [43]

in the plasma membrane of cells, but also in other organelle membranes, such as the Golgi apparatus. Herein, we review the latter case, where a number of studies [43, 66–72] have proposed that raft formation in biological membranes is mediated by the non-equilibrium processes associated with the membrane recycling; in particular, the constant transport and exchange of membrane constituents between the lipid bilayer and its environment [12]. Heuristically, the main effect of this recycling is simply a decrease in the lifetime of the domains, reducing its chance to interact with other membrane components or clusters of membrane constituents [72]. Thus, the characteristic size of such clusters or aggregates is reduced as the rate of membrane recycling is amplified. This can be quantitatively studied as a Smoluchowski coagulation process with an external source term [43, 72–75], or a reaction–diffusion equations [66, 67].

Based on a discrete model previously introduced by [43], we re-examine the dynamics and steady-state distribution of the domain sizes, using a continuum description of non-equilibrium phase separation under a continuous recycling [76]. We consider an infinite flat membrane composed of two species that undergo a phase demixing (as illustrated in Fig. 3), giving rise to domains of various sizes. Furthermore, the domain scission events are assumed to be rare, corresponding to a regime of large line tension [43]. The latter characterizes the energy penalty of having a finite boundary between the different phases. Since the two components demix, the regime of interest is at large line tension. Therefore, the in-plane dynamics of the membrane domains is solely controlled by the coalescence events [43]. Then the time evolution of the domain size distribution under a continuous membrane recycling is governed by the following master equation [75]:

$$\frac{\mathrm{d}\mathcal{P}}{\mathrm{d}t} = \mathcal{R}(a,t) - \int_0^\infty \mathcal{G}\left(a,\, a'\right) \mathcal{P}\left(a,\, t\right) \mathcal{P}\left(a',\, t\right)\, \mathrm{d}a' + \frac{1}{2}\int_0^a \mathcal{G}\left(a,\, a'\right) \mathcal{P}\left(a',\, t\right)\, \mathcal{P}\left(a-a',\, t\right)\, \mathrm{d}a', \qquad (5.1)$$

where $\mathcal{P}(a,t)$ represents the density at time t for the number-per-area of domains of size a (in area units). Here, we assume that two membrane domains merge whenever they come into contact by diffusive motion, so that the function $\mathcal{G}(a,a')$ in Eq. (5.1) can be regarded as a constant proportional to the diffusion coefficient D of lipid rafts, neglecting its size-dependence on the fusion rate [77]. Since this is the only parameter that dictates the intramembrane dynamics, $\mathcal{G}$ is chosen to be identically $D \simeq 10^5 \mathrm{nm}^2/\mathrm{s}$, thus fixing the time scale in this model. Lastly, $\mathcal{R}(a,t)$ is a function that controls the recycling, i.e.,

$$\mathcal{R}(a,t) = j_{\mathrm{on}} \frac{e^{-a/a_S}}{a_S} - j_{\mathrm{off}}\, \mathcal{P}(a), \tag{5.2}$$

where single domains are brought to the membrane at random with a flux j_{on} and with a size drawn from a normalized exponential distribution. Here, $a_S \simeq 10\mathrm{nm}^2$ represents the typical size of domains that are injected into the membrane. Also, entire domain clusters are stochastically removed irrespective of their size with a rate given by j_{off}.

The differential equation given by (5.1) can be solved in the Laplace transform space [78], namely we define the following function $\hat{\mathcal{P}}(\lambda,t) = a_S \int_0^\infty \mathcal{P}(a,t)\, e^{-a\lambda/a_S}\, \mathrm{d}a$. For the sake of clarity, we also rewrite the dimensionless quantities: $\tau = t\, D/a_S$, $J_{\mathrm{on}} = j_{\mathrm{on}}\, a_S^2/D$, and $J_{\mathrm{off}} = j_{\mathrm{off}}\, a_S/D$. By expressing then Eq. (5.1) in terms of the above quantities, we obtain a nonlinear differential equation of the form:

$$\frac{\mathrm{d}\hat{\mathcal{P}}}{\mathrm{d}\tau} = \frac{J_{\mathrm{on}}}{1+\lambda} - [\rho\,(\tau) + J_{\mathrm{off}}]\, \hat{\mathcal{P}}(\lambda,\tau) + \frac{1}{2}\, \hat{\mathcal{P}}^2(\lambda,\tau)\,, \tag{5.3}$$

where $\rho(\tau) = \hat{\mathcal{P}}(\lambda=0,\tau)$ is the total number-per-area of domains (non-dimensionalized by a_S). Evaluating Eq. (5.3) at $\lambda = 0$, we find that

$$\frac{\mathrm{d}\rho}{\mathrm{d}\tau} = J_{\mathrm{on}} - J_{\mathrm{off}}\, \rho(\tau) - \frac{1}{2}\, \rho^2(\tau), \tag{5.4}$$

which can be solved by separation of variables. Using the initial condition $\rho_0 = \rho(\tau=0)$, the solution to Eq. (5.4) is given by

$$\rho(\tau) = \mathcal{Q}_\infty \frac{(\rho_0 + J_{\mathrm{off}}) + \mathcal{Q}_\infty \tanh\left[\frac{\tau \mathcal{Q}_\infty}{2}\right]}{(\rho_0 + J_{\mathrm{off}}) \tanh\left[\frac{\tau \mathcal{Q}_\infty}{2}\right] + \mathcal{Q}_\infty} - J_{\mathrm{off}}, \tag{5.5}$$

where $\mathcal{Q}_\infty = \sqrt{J_{\mathrm{off}}^2 + 2J_{\mathrm{on}}}$. To find $\hat{\mathcal{P}}(\lambda,\tau)$, we define the function $\psi(\lambda,\tau) = \rho(\tau) - \hat{\mathcal{P}}(\lambda,\tau)$, which by substitution into Eq. (5.3) gives that

$$\frac{\mathrm{d}\psi}{\mathrm{d}\tau} = \frac{\lambda\, J_{\mathrm{on}}}{1+\lambda} - J_{\mathrm{off}}\, \psi(\lambda,\tau) - \frac{1}{2}\, \psi^2(\lambda,\tau). \tag{5.6}$$

This resembles Eq. (5.4), and thus its solution takes a similar form,

$$\psi(\lambda,\tau) = \mathcal{Q}_\lambda \frac{(\psi_0(\lambda) + J_{\text{off}}) + \mathcal{Q}_\lambda \tanh\left[\frac{\tau \mathcal{Q}_\lambda}{2}\right]}{(\psi_0(\lambda) + J_{\text{off}}) \tanh\left[\frac{\tau \mathcal{Q}_\lambda}{2}\right] + \mathcal{Q}_\lambda} - J_{\text{off}}, \tag{5.7}$$

where $\psi_0(\lambda) = \psi(\lambda, \tau = 0)$ and $\mathcal{Q}_\lambda = \sqrt{J_{\text{off}}^2 + \frac{2\lambda}{1+\lambda} J_{\text{on}}}$. As a consequence, higher order moments of $\mathcal{P}$ can be found by differentiating $\hat{\mathcal{P}}(\lambda,\tau)$, or equivalently $-\psi(\lambda,\tau)$, with respect to λ and then evaluating the expression at $\lambda = 0$. For instance, the first moment of the distribution $\phi(\tau) = \int_0^\infty a\,\mathcal{P}(a,\tau)\,\mathrm{d}a = -\frac{\mathrm{d}}{\mathrm{d}\lambda}\hat{\mathcal{P}}(\lambda = 0,\ \tau)$ is found to be

$$\phi(\tau) = \frac{J_{\text{on}}}{J_{\text{off}}}\left[1 - e^{-\tau J_{\text{off}}}\left(1 - \frac{J_{\text{off}}}{J_{\text{on}}}\phi_0\right)\right], \tag{5.8}$$

which corresponds to the area-fraction of membrane domains; here, $\phi_0 = \frac{\mathrm{d}}{\mathrm{d}\lambda}\psi_0(\lambda = 0)$.

In addition, this allows us to find the time evolution of the average domain size, which is defined by $\mathcal{A}(\tau) = a_S\,\phi(\tau)/\rho(\tau)$; see Fig. 4a. In a similar way, the second moment $\sigma(\tau) = \frac{\mathrm{d}^2}{\mathrm{d}\lambda^2}\hat{\mathcal{P}}(\lambda = 0,\ \tau)$ can be exactly calculated, which yields the full dynamics of the standard deviation $\mathcal{W}(\tau)$ of the domain size distribution, shown in Fig. 4b. The solutions shown in Fig. 4 tell us how the system will relax after an initial perturbation in the recycling rates. For example, the average domain size after reduction of J_{on} (red) first increases, because there are fewer small domains, and then decreases, as the reduced overall mass leads to a smaller steady-state size. It may be possible to perform such an assay experimentally by knocking down or up-regulating key components of the synthesis or endocytic pathway. Since the characteristic relaxation times of these central moments can be on the order of tens of minutes (cf. Fig. 2), they are therefore experimentally accessible. Such

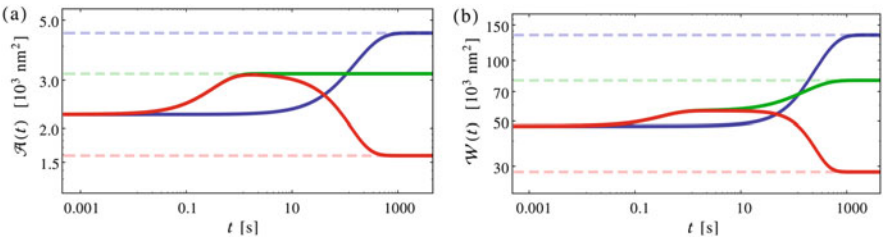

Fig. 4 Plots of (**a**) the average domain size $\mathcal{A}(t)$ and (**b**) the associated standard deviation of domain sizes $\mathcal{W}(t)$ as a function of time, for physiologically reasonable values of recycling rates $J_{\text{on}} = 10^{-7}$ and $J_{\text{off}} = 10^{-6}$. The initial boundary conditions at $\tau = 0$ are given by the following step-like changes after the system reached its steady-state configuration, namely we induce a 50% decrease in J_{off} (blue), a 50% decrease in J_{on} (red), and a 50% decrease in both J_{on} and J_{off} (green)

measurements will allow us to estimate $J_{\rm on}$ and $J_{\rm off}$. Another approach to obtaining information on the recycling rates is therefore to measure the steady-state values of both $\rho(\tau)$ and $\phi(\tau)$. These are given by their limits as time $\tau \to \infty$, namely $\rho_\infty = \mathcal{Q}_\infty - J_{\rm off}$ and $\phi_\infty = J_{\rm on}/J_{\rm off}$, respectively. These methods illustrate the predictive power of this model.

Moreover, the steady-state value of $\hat{\mathcal{P}}(\lambda, \tau)$ is given by $\hat{\mathcal{P}}_\infty(\lambda) = \mathcal{Q}_\infty - \mathcal{Q}_\lambda$. This can be inverse Laplace transformed, and a closed-form solution to the steady-state distribution can be found:

$$\mathcal{P}_\infty(a) = \frac{J_{\rm on}\, e^{-a(1-\Omega)/a_S}}{a_S^2\, \mathcal{Q}_\infty} \left[I_0\!\left(\frac{a\,\Omega}{a_S}\right) - I_1\!\left(\frac{a\,\Omega}{a_S}\right)\right], \tag{5.9}$$

where $\Omega = J_{\rm on}/\mathcal{Q}_\infty^2$, and also I_1 and I_0 are the modified Bessel functions of the first kind of order one and zero, respectively [79]. If plotted against the domain size a, the form of the distribution shows a power-law behavior with a exponential cut-off [43, 74], which can be clearly seen in the large domain size asymptotic expansion of Eq. (5.9), namely

$$\mathcal{P}_\infty(a) \simeq \frac{e^{-a/a_C}}{a^{3/2}} \sqrt{\frac{a_S J_{\rm on}}{8\pi\Omega^2}}, \tag{5.10}$$

where $a_C = a_S\left(1 + 2\,J_{\rm on}/J_{\rm off}^2\right) \simeq 4\,\mathcal{A}_\infty^2/a_S$, with $\mathcal{A}_\infty$ as the steady-state value of the mean domain size. Since the critical size $a_C \gg \mathcal{A}_\infty$, the average size of the domains will mostly be found within the power-law regime. Recently a very similar scaling has been observed in the cluster size distribution of E-cadherin [80]. This is a membrane protein that diffuses, aggregates, and is subject to recycling and therefore can be thought of as being described within the same theoretical framework. A key feature that arises from recycling is that physiologically reasonable values for the rates $J_{\rm on}$ and $J_{\rm off}$ give rise to membrane clusters or heterogeneities on the correct sub-micron length scale, this being simultaneously much larger than the molecular size and much smaller than the size of the system (Fig. 5).

6 Summary

We have here reviewed some studies of the lateral demixing of membrane constituents in model systems as well as their connection to membranes in living cells. We show how a simple two-component membrane under membrane recycling can result in clusters or domains of intermediate sizes. In contrast, similar (equilibrium) systems undergo macroscopic phase separation. In order to describe the physics of the system we discussed a simple Smoluchowski-type model with external fluxes. This can be tested against experiments and such a comparison will constrain the unknown biophysical parameters controlling recycling. Suitable targets for such a

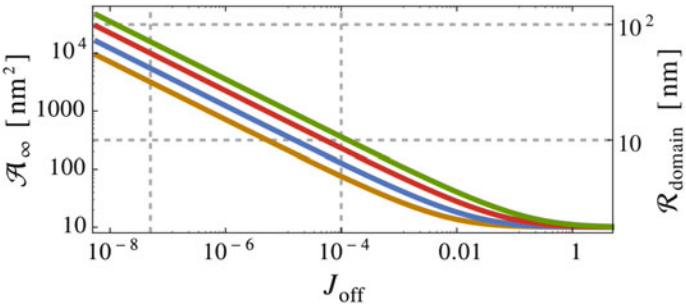

Fig. 5 Log–log plot of the steady-state value of the dimensionless mean domain size $\mathcal{A}_\infty$, and its associated average domain radius $\mathcal{R}_{\text{domain}}$ in nanometers, as a function of the recycling strength J_{off} at a fixed area coverage: 10% (blue); 20% (red); and 50% (green). Here, the dashed lines represent the upper and lower bounds of estimates of the physiological values of J_{off} and $\mathcal{R}_{\text{domain}}$, which shows that this model robustly recovers reasonable values for the average domain size over a large range of recycling rates

comparison include experimental measurements of the moments and their relaxation times. The main biophysical significance of the recycling mechanisms reviewed in this chapter may well be in that they provide mechanisms for regulation of the lateral membrane heterogeneity observed in cells. More elaborate and more biologically detailed models can be constructed by extending these models to include finite size effects [72] and/or some size-dependence of the recycling rates [76].

Acknowledgements We acknowledge longstanding collaboration with Dr. P. Sens (Paris), and funding from UK EPSRC under Grant No. EP/I005439/1 (M.S.T.) and Simons Foundation (S.A.R).

References

1. Alberts B et al (2008) Molecular biology of the cell, 5th edn. Garland Science, New York
2. Heimburg T (2007) Thermal biophysics of membranes. Wiley-VCH, Berlin,
3. Lenne P-F et al (2006) Dynamic molecular confinement in the plasma membrane by microdomains and the cytoskeleton meshwork. EMBO J 25:3245–3256
4. Hao M (2000) Characterization of rapid membrane internalization and recycling. J Biol Chem 275:15279–15286
5. Hancock JF (2006) Lipid rafts: contentious only from simplistic standpoints. Natl. Rev. Mol. Cell Biol. 7:456–62
6. Daumas F et al (2003) Confined diffusion without fences of a g-protein-coupled receptor as revealed by single particle tracking. Biophys J 84:356–66
7. Destainville N, Dumas F, Salomé L (2008) What do diffusion measurements tell us about membrane compartmentalisation? Emergence of the role of interprotein interactions. J Chem Biol 1:37–48
8. Ying W, Huerta G, Steinberg S, Zúñiga M (2009) Time series analysis of particle tracking data for molecular motion on the cell membrane. Bull Math Biol 71:1967–2024
9. Robson A, Burrage K, Leake MC (2012) Inferring diffusion in single live cells at the single-molecule level. Phil Trans R Soc B 368:20120029

10. Brown DA (2006) Lipid rafts, detergent-resistant membranes, and raft targeting signals. Physiology 21:430–439
11. Simons K, Ikonen E (1997) Functional rafts in cell membranes. Nature 387:569–572
12. Komura S, Andelman D (2014) Physical aspects of heterogeneities in multi-component lipid membranes. Adv Colloid Interface Sci 208:34–46
13. Pike LJ (2009) The challenge of lipid rafts. J Lipid Res 50:S323–S328
14. Mouritsen OG, Bagatolli LA (2016) Life – as a matter of fat: lipids in a membrane biophysics, 2nd edn. Springer, London
15. Simons K, Sampaio JL (2011) Membrane organization and lipid rafts. Cold Spring Harb Perspect Biol 3:a004697
16. Leslie M (2011) Do lipid rafts exist? Science 334:1046–1047
17. Gennis RB (1989) Biomembranes: molecular structure and function. Springer, New York
18. Lipowsky R, Dimova R (2003) Domains in membranes and vesicles. J Phys Condens Matter 15:S31–S45
19. Ipsen JH, Karlström G, Mouritsen OG, Wennerström H, Zuckermann MJ (1987) Phase equilibria in the phosphatidylcholine-cholesterol system. Biochim Biophys Acta 905:162–172
20. Veatch SL, Keller SL (2005) Seeing spots: complex phase behavior in simple membranes. Biochim Biophys Acta 1746:172–185
21. Goñi FM et al. (2008) Phase diagrams of lipid mixtures relevant to the study of membrane rafts. Biochim Biophys Acta 1781:665–684
22. Veatch SL, Keller SL (2005) Miscibility phase diagrams of giant vesicles containing sphingomyelin. Phys Rev Lett 94:148101
23. Pike LJ (2006) Rafts defined: a report on the Keystone Symposium on Lipid Rafts and Cell Function. J Lipid Res 47:1597–1598
24. Mouritsen OG, Bagatolli LA (2015) Lipid domains in model membranes: a brief historical perspective. Essays Biochem 57:1–19
25. Arumugam S, Bassereau P (2015) Membrane nanodomains: contribution of curvature and interaction with proteins and cytoskeleton. Essays Biochem 57:109–119
26. Bagatolli LA, Sunil Kumar PB (2009) Phase behavior of multicomponent membranes: Experimental and computational techniques. Soft Matter 5:3234
27. Komura S, Shirotori H, Olmsted PD, Andelman D (2004) Lateral phase separation in mixtures of lipids and cholesterol. Eur Lett 67:321–327
28. Bray A (1994) Theory of phase-ordering kinetics. Adv Phys 43:357–459
29. Lajoie P, Goetz JG, Dennis JW, Nabi IR (2009) Lattices, rafts, and scaffolds: domain regulation of receptor signaling at the plasma membrane. The Journal of Cell Biology 185:381–385. http://jcb.rupress.org/content/185/3/381.full.pdf
30. Yethiraj A, Weisshaar JC (2007) Why are lipid rafts not observed in vivo? Biophys J 93:3113–3119
31. Stottrup BL, Veatch SL, Keller SL (2004) Nonequilibrium behavior in supported lipid membranes containing cholesterol. Biophys J 86:2942–2950
32. Lipowsky R, Rouhiparkouhi T, Discher DE, Weikl TR (2013) Domain formation in cholesterolphospholipid membranes exposed to adhesive surfaces or environments. Soft Matter 9:8438
33. Stone HA, Armand A (1998) Hydrodynamics of particles embedded in a flat surfactant layer overlying a subphase of finite depth. J Fluid Mech 369:151–173
34. Liu J, Qi S, Groves JT, Chakraborty AK (2005) Phase segregation on different length scales in a model cell membrane system. J Phys Chem B 109:19960–19969
35. Wallace EJ, Hooper NM, Olmsted PD (2006) Effect of hydrophobic mismatch on phase behavior of lipid membranes. Biophys J 90:4104–4118
36. García-Sáez AJ, Chiantia S, Schwille P (2007) Effect of line tension on the lateral organization of lipid membranes. J Biol Chem 282:33537–33544
37. Lin Q, London E (2013) Altering hydrophobic sequence lengths shows that hydrophobic mismatch controls affinity for ordered lipid domains (rafts) in the multitransmembrane strand protein perfringolysin O. J Biol Chem 288:1340–1352

38. Baumgart T, Hess ST, Webb WW (2003) Imaging coexisting fluid domains in biomembrane models coupling curvature and line tension. Nature 425:821–824
39. Baumgart T, Das S, Webb WW, Jenkins JT (2005) Membrane elasticity in giant vesicles with fluid phase coexistence. Biophys J 89:1067–1080
40. Ogunyankin MO, Longo ML (2013) Metastability in pixelation patterns of coexisting fluid lipid bilayer phases imposed by e-beam patterned substrates. Soft Matter 9:2037–2046
41. Honerkamp-Smith AR, Veatch SL, Keller SL (2009) An introduction to critical points for biophysicists; observations of compositional heterogeneity in lipid membranes. Biochim Biophys Acta 1788:53–63
42. Giang H, Shlomovitz R, Schick M (2015) Microemulsions, modulated phases and macroscopic phase separation: a unified picture of rafts. Essays Biochem 57:21–32
43. Turner MS, Sens P, Socci ND (2005) Nonequilibrium raftlike membrane domains under continuous recycling. Phys Rev Lett 95:168301
44. Honerkamp-Smith AR, et al (2008) Line tensions, correlation lengths, and critical exponents in lipid membranes near critical points. Biophys J 95:236–246
45. Kardar M (2007) Statistical physics of particles. Cambridge University Press, Cambridge
46. Veatch SL, Soubias O, Keller SL, Gawrisch K (2007) Critical fluctuations in domain-forming lipid mixtures. Proc Natl Acad Sci USA 104:17650–17655
47. Veatch SL, et al (2008) Critical fluctuations in plasma membrane vesicles. ACS Chem Biol 3:287–293
48. Machta BB, Papanikolaou S, Sethna JP, Veatch SL (2011) Minimal model of plasma membrane heterogeneity requires coupling cortical actin to criticality. Biophys J 100:1668–1677
49. Palmieri B, Yamamoto T, Brewster RC, Safran SA (2014) Line active molecules promote inhomogeneous structures in membranes: theory, simulations and experiments. Adv Colloid Interface Sci 208:58–65
50. Nicolini C, et al (2006) Visualizing association of N-Ras in lipid microdomains: influence of domain structure and interfacial adsorption. J Am Chem Soc 128:192–201
51. Yamamoto T, Brewster R, Safran SA (2010) Chain ordering of hybrid lipids can stabilize domains in saturated/hybrid/cholesterol lipid membranes. Eur Lett 91:28002
52. Brewster R, Safran SA (2010) Line active hybrid lipids determine domain size in phase separation of saturated and unsaturated lipids. Biophys J 98:L21–L23
53. Palmieri B, Safran SA (2013) Hybrid lipids increase the probability of fluctuating nanodomains in mixed membranes. Langmuir 29:5246–5261
54. Palmieri B, Safran SA (2013) Hybrid lipids increase nanoscale fluctuation lifetimes in mixed membranes. Phys Rev E 88:032708
55. Hirose Y, Komura S, Andelman D (2009) Coupled modulated bilayers: a phenomenological model. ChemPhysChem 10:2839–2846
56. Hirose Y, Komura S, Andelman D (2012) Concentration fluctuations and phase transitions in coupled modulated bilayers. Phys Rev E 86:021916
57. Veatch SL, Gawrisch K, Keller SL (2006) Closed-loop miscibility gap and quantitative tie-lines in ternary membranes containing diphytanoyl PC. Biophys J 90:4428–4436
58. Schick M (2012) Membrane heterogeneity: Manifestation of a curvature-induced microemulsion. Phys Rev E 85:1–4
59. Andelman D, Rosensweig RE (2009) Modulated phases: review and recent results. J Phys Chem B 113:3785–3798
60. Leibler S, Andelman D (1987) Ordered and curved meso-structures in membranes and amphiphilic films. J Phys Fr 48:2013–2018
61. Rautu SA, Rowlands G, Turner MS (2015) Membrane Composition Variation and Underdamped Mechanics near Transmembrane Proteins and Coats. Phys Rev Lett 114:098101
62. Shlomovitz R, Schick M (2013) Model of a raft in both leaves of an asymmetric lipid bilayer. Biophys J 105:1406–1413
63. Mayor S, Rao M (2004) Rafts: scale-dependent, active lipid organization at the cell surface. Traffic 5:231–240
64. Gowrishankar K, et al (2012) Active remodeling of cortical actin regulates spatiotemporal organization of cell surface molecules. Cell 149:1353–1367

65. Tang Q, Edidin M (2001) Vesicle trafficking and cell surface membrane patchiness. Biophys J 81:196–203
66. Foret L (2005) A simple mechanism of raft formation in two-component fluid membranes. Eur Lett 71:508–514
67. Glotzer SC, Di Marzio EA, Muthukumar M (1995) Reaction-controlled morphology of phase-separating mixtures. Phys Rev Lett 74:2034–2037
68. Foret L (2012) Aggregation on a membrane of particles undergoing active exchange with a reservoir. Eur Phys J E 35:12
69. Gómez J, Sagués F, Reigada R (2008) Actively maintained lipid nanodomains in biomembranes. Phys Rev E 77:021907
70. Gómez J, Sagués F, Reigada R (2009) Nonequilibrium patterns in phase-separating ternary membranes. Phys Rev E 80:011920
71. Fan J, Sammalkorpi M, Haataja M (2010) Influence of nonequilibrium lipid transport, membrane compartmentalization, and membrane proteins on the lateral organization of the plasma membrane. Phys Rev E 81:011908
72. Vagne Q, Turner MS, Sens P (2015) Sensing Size through Clustering in Non-Equilibrium Membranes and the Control of Membrane-Bound Enzymatic Reactions. PLoS One 10:e0143470
73. Camacho J (2001) Scaling in steady-state aggregation with injection. Phys Rev E 63:046112
74. Connaughton C, Krapivsky PL (2010) Aggregation-fragmentation processes and decaying three-wave turbulence. Phys Rev E 81:035303(R)
75. Leyvraz F (2003) Scaling theory and exactly solved models in the kinetics of irreversible aggregation. Phys Rep 383:95–212
76. Rautu SA, Rowlands G, Turner MS (2018) Size-dependent recycling of membrane clusters. Europhys Lett 21:58004
77. Saffman PG, Delbruck M (1975) Brownian motion in biological membranes. Proc Natl Acad Sci USA 72:3111–3113
78. Olver FWJ, Lozier DW, Boisvert RF, Clark CW (eds) (2010) NIST handbook of mathematical functions. Cambridge University Press, New York
79. Abramowitz M, Stegun I (1965) Handbook of mathematical functions. Dover Publications Inc., New York
80. Truong Quang B-A, Mani M, Markova O, Lecuit T, Lenne P-F (2013) Principles of E-cadherin supramolecular organization in vivo. Curr Biol 23:2197–2207

Protein Pattern Formation

Erwin Frey, Jacob Halatek, Simon Kretschmer, and Petra Schwille

Abstract Protein pattern formation is essential for the spatial organisation of many intracellular processes like cell division, flagellum positioning, and chemotaxis. A prominent example of intracellular patterns are the oscillatory pole-to-pole oscillations of Min proteins in *E. coli* whose biological function is to ensure precise cell division. Cell polarisation, a prerequisite for processes such as stem cell differentiation and cell polarity in yeast, is also mediated by a diffusion–reaction process. More generally, these functional modules of cells serve as model systems for self-organisation, one of the core principles of life. Under which conditions spatio-temporal patterns emerge, and how these patterns are regulated by biochemical and geometrical factors are major aspects of current research. Here we review recent theoretical and experimental advances in the field of intracellular pattern formation, focusing on general design principles and fundamental physical mechanisms.

Keywords Pattern formation · Intracellular dynamics · Min oscillations · Cell polarity · Self-organisation · Proteins · Membranes

E. Frey (✉) · J. Halatek
Arnold-Sommerfeld-Center for Theoretical Physics and Center for NanoScience, Department of Physics, Ludwig-Maximilians-Universität München, München, Germany
e-mail: frey@lmu.de; jacob.halatek@physik.lmu.de

S. Kretschmer
Department of Cellular and Molecular Biophysics, Max-Planck-Institute of Biochemistry, Martinsried, Germany

Graduate School of Quantitative Biosciences, Ludwig-Maximilians-Universität München, München, Germany
e-mail: kretschmer@biochem.mpg.de

P. Schwille
Department of Cellular and Molecular Biophysics, Max-Planck-Institute of Biochemistry, Martinsried, Germany
e-mail: schwille@biochem.mpg.de

P. Bassereau, P. Sens (eds.), *Physics of Biological Membranes*,
https://doi.org/10.1007/978-3-030-00630-3_10

1 Introduction

From cellular structures to organisms and populations, biological systems are governed by principles of self-organisation. The intricate cycles of autocatalytic reactions that constitute cell metabolism, the highly orchestrated processes of nucleic acid transcription and translation, the replication and segregation of chromosomes, the cytoskeletal assemblies and rearrangements that mechanically drive important cellular processes like cell division and cell motility, the morphogenesis of complex tissue from a single fertilised egg—all of these processes rely on the generation of structures and gradients based on molecular self-organisation. Frequently, the assembly and maintenance of these structures is accompanied by spatial and temporal protein patterning.

What are the principles underlying self-organising processes that result in protein patterns? Though the term 'self-organisation' is frequently employed, as it is here, in the context of complex systems, it needs to be emphasised that there is no generally accepted theory of self-organisation that explains how internal molecular processes are able to coordinate the interactions between a system's components such that order and structure emerge. The field which has arguably contributed most to a deeper understanding of emergent phenomena is 'nonlinear dynamics', especially with concepts such as 'catastrophes' [1], 'Turing instabilities' [2], and 'nonlinear attractors' [3]. However, although pattern formation and its underlying concepts have found their way into textbooks [4], we are far from answering the above question in a comprehensive and convincing way. This chapter will highlight some of the recent progress in the field, but also address some of the fascinating questions that remain open.

In contrast to the conventional representation of pattern-forming systems in classical texts, our exposition will be closely tied to the analysis of quantitative models for specific biological systems. At first, this might appear to involve a loss of generality. However, as we will see, only by studying the actual physical processes that give rise to what we call self-organisation will we be able to uncover its key features in the first place. These key aspects can then be generalised again by identifying the according processes in other systems. Here, we will mainly, but not exclusively, focus on a model for Min protein dynamics, a system of self-organising proteins that is essential for precise cell division in the bacterium *Escherichia coli*. The Min system offers an ideal combination of a broad and rich phenomenology with accessibility to theoretical and experimental analyses on a quantitative level. As we will see, a major finding from the study of the Min system is the role of mass-conserved interactions and of system geometry in the understanding of self-organised pattern formation.

2 Intracellular Protein Patterns

The formation of protein patterns and the localisation of protein clusters is a fundamental prerequisite for many important processes in bacterial cells. Examples include Min oscillations that guide the positioning of the Z-ring to midcell in *Escherichia coli*, the localisation of chemotactic signalling arrays and the positioning of flagella, as well as chromosome and plasmid segregation. In all these examples, experimental evidence supports mechanisms based on reaction–diffusion dynamics. Moreover, the central elements of the biochemical reaction circuits driving these processes are P-loop NTPases. These proteins are able to switch from an NTP-bound 'active' form that preferentially binds to an intracellular interface (membrane or nucleoid) to an inactive, freely diffusing, NDP-bound form in the cytosol.

Interestingly, these types of pattern–forming mechanisms are not restricted to prokaryotic cells, but are found in eukaryotic cells as well. An important example is cell polarisation, an essential developmental process that defines symmetry axes or selects directions of growth. Signalling molecules accumulate in a restricted region of the inner surface of a cell's plasma membrane where they initiate further downstream processes. For example, in the yeast *Saccharomyces cerevisiae*, cell polarisation determines the position of a new growth or bud site. The central polarity regulator responsible for this process is Cdc42, a small GTPase of the Rho family [5]. Similarly, cell polarity plays an important role in proper stem cell division [6] and in plant growth processes such as pollen tube or root hair development [7, 8]. Another intriguing example of self-organised polarisation occurs in the *Caenorhabditis elegans* zygote through the action of mutually antagonistic, so-called partitioning-defective (PAR) proteins [9]. Moreover, the crucial role of protein pattern formation in animal cell cytokinesis is highlighted by cortical waves of Rho activity and F-actin polymerisation, recently observed in frog and starfish oocytes and embryos [10].

Yet another system where protein patterns play an important role is the transport of motor proteins along cytoskeletal filaments. We will not elaborate on this system in this review, but would like to note that pattern formation in these systems is based on similar principles as for the other systems. For instance, microtubules are highly dynamic cytoskeletal filaments, which continually assemble and disassemble through the addition and removal of tubulin heterodimers at their ends [11]. It was recently shown that traffic jams of molecular motors on microtubules play a key regulatory mechanism for the length control of microtubules [12–16].

2.1 MinCDE Oscillations in E. coli

Proteins of the Min system in the rod-shaped bacterium *E. coli* show pole-to-pole oscillations [17–20], see Fig. 1. A combination of genetic, biochemical, and cell biological studies has identified the following key features of the underlying

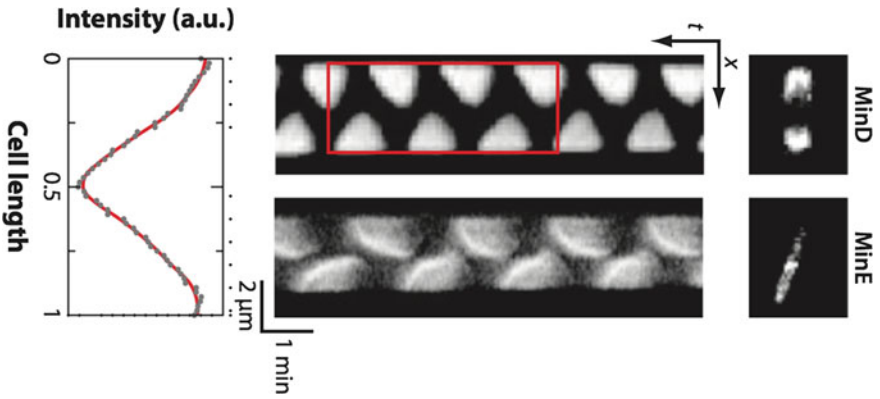

Fig. 1 Oscillatory patterns of Min proteins in vivo. *Left:* Time-averaged MinD fluorescence intensity profile along the red rectangle shown in the kymograph. *Middle:* Kymograph of pole-to-pole oscillations of MinD and MinE in cells of normal length (shorter than 5 µm). *Right:* Micrographs of GFP-MinD and MinE-GFP in vivo. Adapted from Ref. [21]

interaction network: (1) The ATPase MinD, in its ATP-bound dimeric form, cooperatively binds to the cytoplasmic membrane [22–25], and forms a complex with MinC that inhibits Z-ring formation [26]. (2) MinD then recruits its ATPase Activating Protein (AAP) MinE to the membrane, triggering MinD's ATPase activity and thereby stimulating detachment of MinD from the membrane in its monomeric form [27]. (3) Subsequently, MinD undergoes nucleotide exchange in the cytosol and rebinds to the membrane [28]. (4) Notably, MinE's interaction with MinD converts it from a latent to an active form, by exposing a sequestered MinD-interaction region as well as a cryptic membrane targeting sequence [29, 30].

All of these biochemical features give us highly valuable molecular information, but in themselves they do not suffice to explain the emergent phenomenon of Min oscillations. There are basically two unknowns. First, the detailed dynamic processes underlying, for example, cooperative membrane binding of MinD, are poorly understood on a mechanistic molecular level. At present, one can only speculate on them based on structural data. For example, Hill coefficients have been measured for MinD ATP (∼2) and ADP (∼1) [25], indicating that recruitment may be associated with dimerisation. Secondly, and perhaps even more importantly, even if all the details of the molecular processes were known, one would still not know which is responsible to what degree for any specific macroscopic property of the dynamic Min pattern. Furthermore, how these processes are affected by changing protein expression levels and cell geometry is unclear, a priori. Both of these obstacles represent major challenges for the field, and can be overcome only by a combined experimental and theoretical approach.

The main biological function of Min oscillations is to regulate formation and positioning of the Z-ring [20], comprised of curved, overlapping FtsZ filaments, which interact with a range of accessory proteins that together make up the

cytokinetic machinery [31]. The pole-to-pole oscillations of the MinD-ATP/MinC complex result in a time-averaged density profile of MinC that is highest at the cell poles and lowest at midcell. Since MinC acts as an antagonist of FtsZ assembly, Min oscillations inhibit Z-ring formation at the poles and restrict it to midcell [26]. How self-organisation into the Z-ring occurs remains unknown and is subject to extensive research [32–34].

2.2 *Cell Polarity in Yeast*

Polarity establishment in budding yeast relies on crosstalk between feedback loops, one based on the actin cytoskeleton, the other on a reaction–diffusion system [5]. Both are regulated by the Rho-type GTPase Cdc42. To fulfil its functions, it must constantly cycle between a GTP-bound (active) and a GDP-bound (inactive) state. In budding yeast, activation of Cdc42 is controlled by a single guanine nucleotide exchange factor (GEF), Cdc24, and the hydrolytic activity of Cdc42 is promoted by several GTPase-activating proteins (GAPs). In addition, Cdc42 is extracted from membranes by a single Rho-guanine nucleotide dissociation inhibitor (GDI), Rdi1 [35]; see Fig. 2 for an illustration of the biochemical network.

Initially two independent feedback loops were identified: one based on the actin cytoskeleton and one based on a reaction–diffusion system that in vivo depends on the scaffold protein Bem1 [35]. A combined experimental and theoretical study has shown that a combination of actin- and GDI-dependent recycling of the GTPase Cdc42 is required to achieve rapid, robust, and focused polarisation [36]. However, there are still many open issues on the detailed interplay between these two mechanisms.

The GDI-mediated polarisation in itself is reasonably well understood. Theoretical models differ in how they describe the recruitment of the GEF (Cdc24) towards active Cdc42 on the membrane [37, 38]. Experimental data [36] support a reaction network where recruitment of Cdc24 is mediated by Bem1 (Fig. 2):

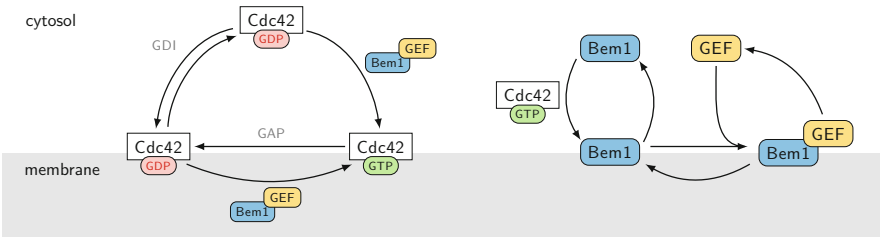

Fig. 2 Reaction network of the Cdc 42 system in yeast with a guanine nucleotide exchange factor (Cdc24) and GAPs controlling the hydrolytic activity of Cdc42. The polarisation relies on activation of Cdc42 through a Bem1-Cdc24-Cla4 complex and on extraction of Cdc42 from membranes by the GDI Rdi1

Cytosolic Bem1 is targeted to the membrane by interaction with active Cdc42 or other Cdc42-GTP-bound proteins such as Cla4 and subsequent binding of Bem1 to the membrane [39–41]. Once bound to the membrane it recruits the Cdc24 from the cytosol to the membrane [39, 40]. Membrane-bound Cdc24 then enhances both the attachment and activation of cytosolic Cdc42-GDP to the membrane and the nucleotide-exchange of membrane-bound Cdc42-GDP [36, 38]. A mathematical model [38] based on this reaction scheme accurately predicts phenotypes associated with changes in Cdc42 activity and recycling, and suggests design principles for polarity establishment through coupling of two feedback loops. Recently, there has even been evidence for a third feedback loop [42].

In a recent in vivo study the essential component Bem1 was deleted from the reaction–diffusion feedback loop [43]. Interestingly, after the mutant was allowed to evolve for about 1000 generations, a line was recovered that had regained the ability to polarise, despite the absence of Bem1. Moreover, the newly evolved network had actually lost more components, resulting in a simpler reaction–diffusion system. The structure of this minimal network has yet to be identified (F. Brauns, J. Halatek, L. Laan and E. Frey, unpublished).

2.3 Protein Pattern Formation in Animal Cell Polarisation and Cytokinesis

As we have seen for the Min system in *E. coli* and Cdc42 in budding yeast, protein patterns are an elegant way to convey intracellular positional information. Thus, it is not surprising that more complex organisms also employ protein pattern formation to control essential processes including cell polarisation, cytokinesis, embryogenesis, and development.

An animal's body plan is typically specified during embryogenesis. In this context, the establishment and stable maintenance of cell polarity is a fundamental feature of developmental programs. The so-called partitioning defective (PAR) proteins are key molecular players that promote symmetry breaking and establish intracellular polarity in diverse animal cells [44]. Here, we focus on the PAR network in the nematode worm *C. elegans*, as this system has been particularly well studied.

C. elegans PAR proteins are required for asymmetric cell division of the zygote, which they achieve by generating two distinct and complementary membrane domains with the aid of actomyosin flows [9, 45]. Several "design principles" of the PAR network have been established by a combination of experiments and theory [46]. A core feature of PAR polarity is the mutual antagonism between anterior and posterior PAR components (Fig. 3), which preferentially accumulate on the anterior and posterior halves of the membrane respectively, while being excluded from the opposite half. The maintenance of this polarity is highly dynamic and involves mobility of PAR proteins in the cytosol, their cross-inhibition via phosphorylation as well as additional feedback loops [46]. Importantly, the mutual antagonism in

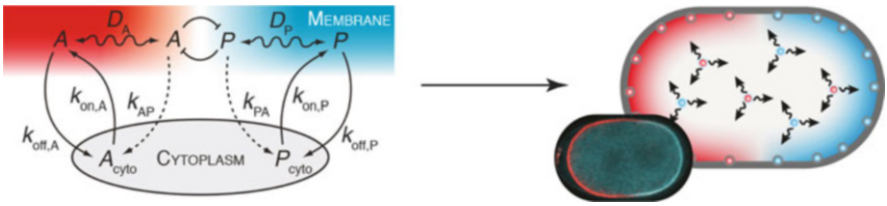

Fig. 3 Cell polarisation in the *C. elegans* embryo. A reaction–diffusion network of mutually antagonistic anterior and posterior PAR proteins, switching between "active" membrane-bound and "inactive" cytosolic states, sustains opposing membrane domains in the *C. elegans* embryo. Anterior and posterior PAR components are shown in red and blue, respectively. Adapted from Ref. [47], copyright 2012 with permission from Elsevier and Ref. [9] with permission from AAAS

the PAR network relies on reversible switching of PAR proteins between "inactive", rapidly diffusing cytosolic and "active", slowly diffusing membrane-bound states [46], one of the key features of the pattern-forming protein networks discussed in this chapter.

Another intriguing example of protein pattern formation occurs during animal cell cytokinesis. This process involves the small GTPase Rho, whose localised activation directs assembly of the cytokinetic machinery, consisting of F-actin and myosin-2, in the equatorial cortex [48]. Recently, cortical waves of Rho activity and F-actin polymerisation were discovered in frog and echinoderm oocytes and embryos [10]. These protein patterns exhibited excitable dynamics and were proposed to emerge through a reaction–diffusion mechanism involving positive feedback during Rho activation and delayed negative feedback exerted by F-actin (Fig. 4). In this view, Rho attaches to the plasma membrane in its inactive GDP-bound form. On the membrane, Rho is then converted to its GTP-bound active

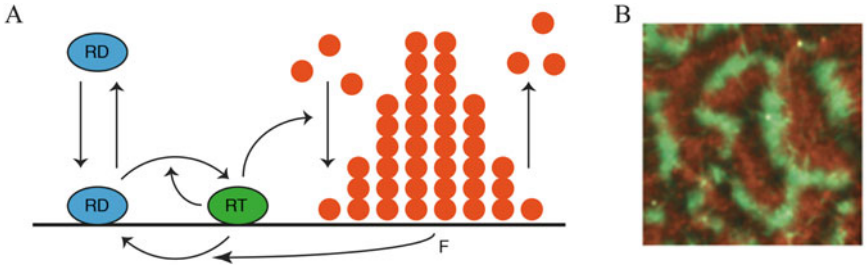

Fig. 4 Cortical waves of Rho activity and F-actin polymerisation involved in animal cell cytokinesis. (**a**) Possible scheme of interactions underlying wave formation. Inactive GDP-bound Rho (RD) binds to the membrane, where it is activated to GTP-bound Rho (RT) via nucleotide exchange in an autocatalytic, GEF-dependent manner. Subsequently, the theoretical model assumes that coupled F-actin polymerisation (F) exerts a negative feedback on Rho activity converting it back into its inactive form [10]. (**b**) Fluorescence image of cortical waves of Rho (malachite) and F-actin (copper) in an Ect2-overexpressing starfish oocyte. Adapted from Ref. [10] by permission from Macmillan Publishers Ltd: Nature Cell Biology [10], copyright 2015

form in an autocatalytic manner, dependent on the Rho GEF Ect-2. Subsequently, F-actin is assumed to mediate a negative feedback on Rho, converting it back to its inactive form [10]. Remarkably, this reaction–diffusion network shares many similarities with our previous examples, such as reversible protein attachment to a lipid membrane, switching between different NTP-bound states and coupling of feedback loops.

2.4 The Switch Paradigm

The molecular mechanisms underlying the spatio-temporal organisation of cellular components in bacteria are frequently linked to P-loop ATPases such as ParA and MinD [31, 49, 50]. ParA and MinD proteins belong to a family of proteins known as the ParA/MinD superfamily of P-loop ATPases [31]. Both are known to form self-organised dynamic patterns at cellular interfaces, ParA on the nucleoid and MinD on the cell membrane. The nucleotide state of these ATPases determines their subcellular localisation: While the ATP-bound form dimerises and binds to the appropriate surface, the ADP-bound form is usually a monomer with a significantly reduced affinity for surface binding that freely diffuses in the cell. Importantly, both ParA and MinD have a partner protein (ParB and MinE, respectively) that stimulates their ATPase activity and causes them to detach from their respective surfaces. Moreover, there is a delay due to nucleotide exchange between the release of the ADP-bound form from the surface and its subsequent rebinding in the dimeric ATP-bound form. These interactions enable proteins to cycle between surface-bound and cytosolic states, depending on the phosphorylation state of their bound nucleotide. The surface-bound state is typically associated with spatially localised function (e.g. the downstream regulation of other proteins on the surface), whereas the cytosolic state enables spatial redistribution and formation of surface bound patterns of these proteins. Despite the striking similarities on a molecular level, the biological functions of ParA and MinD differ significantly. The Min system directs the placement of the division site at midcell by inhibiting the assembly of FtsZ into a ring-like structure (Z-ring) close to the cell poles. In contrast, ParA is involved in chromosome and plasmid segregation. Several other ParA-like proteins have been identified that are also important for the correct localisation of large cellular structures at the cell poles, at midcell or along the cell length [31]. One of these is PomZ in *Myxococcus xanthus*. PomZ is part of a protein system that—like the Min system—is important for Z-ring formation. However, in contrast to the Min system, the Pom system positively regulates the formation of the FtsZ ring at midcell [51–53]. Apart from the cell division and the chromosome partitioning machineries, there are various other multiprotein complexes that are positioned by self-organising processes based on P-loop NTPases. For example, the GTPase FlhF and the ATPase FlhG constitute a regulatory circuit essential for defining the distribution of flagella in bacterial cells [50, 54].

3 Mass-Conserving Reaction–Diffusion Systems

All of the examples of intracellular pattern-forming systems discussed in the previous section share some common features. They are reaction–diffusion systems in confined intracellular space, where proteins cycle between the cytosol and the cell membrane [55]. On the time scale on which these patterns form, net change in the levels of the proteins involved is negligible and thus the *copy number within each protein species is conserved*. The reactions correspond to transitions of each protein species between a finite number of different states (membrane-bound, cytosolic, active, inactive, etc.), and these states play different functional roles in the corresponding biochemical circuit. For example, only membrane-bound MinD induces positive and negative feedback by recruiting MinD and MinE from the cytosol to the membrane. Hence, the protein dynamics can be understood as a reaction–diffusion system where diffusion takes place in different spatial domains (membrane and cytosol), and where reactions are sequences of state changes induced by protein–nucleotide, protein–protein, and protein–membrane interactions.

Mass-conserving dynamics is the generic case for intracellular dynamics. Because the production of proteins is a resource-intensive process, any mechanism that utilises production and degradation as pattern forming mechanisms would be highly inefficient and wasteful.[1] This excludes activator-inhibitor mechanisms [56], since they are based on the interplay between autocatalytic production of a (slow diffusing) activator and its degradation by a (fast diffusing) inhibitor. Though such a mechanism is frequently invoked as a paradigm in biological pattern formation [57], it is actually irreconcilable with the fundamental physical processes on which intracellular pattern formation is based on [55]. This in turn implies that the study of biological systems should reveal hitherto unknown mechanisms for pattern formation. Recent research shows that this is indeed the case [58]. In particular, explicit account for mass-conservation yields the total protein densities as system control parameters. As we will see, these are crucial for the theoretical understanding of the experimentally observed phenomena.

3.1 Cellular Geometry: Membrane and Cytosol

Figure 5 illustrates the geometry of a rod-shaped prokaryotic cell. It is comprised of three main compartments: the cell membrane, the cytosol, and the nucleoid. There are two major facts that are relevant for intracellular pattern formation. First, the diffusion constants in the cytosol and on the cell membrane are vastly different. For example, currently accepted values for Min proteins in *E. coli* are of the order

[1] Of course, such a process would also be limited by the duration of protein synthesis.

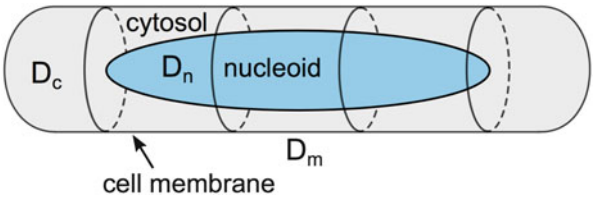

Fig. 5 Schematic representation of the geometry of a rod-shaped bacterial cell. There are three main compartments: cell membrane, cytosol, and nucleoid. The diffusion constants in these compartments will, in general, be different

of $D_c \approx 10\,\mu m^2/s$, and $D_m \approx 0.01\,\mu m^2/s$, respectively. Second, due to the rod-like shape, the ratio of cytosolic volume to membrane area differs markedly between polar and midcell regions. Beyond this local variation of volume-to-surface ratio, the overall ratio of cytosol volume to membrane area depends on the shape of the cell.

3.2 *Reaction–Diffusion Equations for the Min System*

The biochemical reactions of the Min system outlined in Sect. 2.1 are summarised in Fig. 6. In the following we will refer to this scheme as the *skeleton network*, as it accounts only for those molecular interactions that are (presently) believed to be essential for Min protein phenomenology. For a quantitative analysis, this skeleton biochemical network has to be translated into a mathematical model [59, 60].

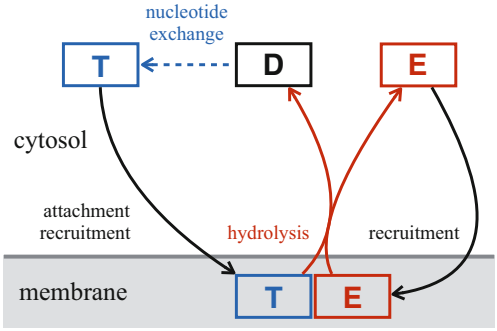

Fig. 6 Skeleton MinCDE network: Cytosolic MinD-ATP (T) attaches to the membrane, and recruits MinD-ATP and MinE (E) from the cytosol. Recruitment of MinE leads to the formation of MinDE complexes. MinE in the MinDE complexes stimulates ATP hydrolysis by MinD and thereby triggers detachment and dissociation of membrane-bound MinDE complexes into cytosolic MinD-ADP (D) and MinE

We denote the volume concentrations of MinE, MinD-ADP, and MinD-ATP in the cytosol by c_E, c_{DD}, and c_{DT}. Since the only reaction that takes place in the cytosol is reactivation of cytosolic MinD-ADP by nucleotide exchange (with rate λ) to MinD-ATP, the ensuing reaction–diffusion equations read:

$$\partial_t c_{DD} = D_c \nabla^2 c_{DD} - \lambda\, c_{DD}\,, \tag{1a}$$

$$\partial_t c_{DT} = D_c \nabla^2 c_{DT} + \lambda\, c_{DD}\,, \tag{1b}$$

$$\partial_t c_E = D_c \nabla^2 c_E\,, \tag{1c}$$

The diffusion coefficients are typically distinct for all protein configurations, for simplicity, we only distinguish between cytosolic (D_c) and membrane bound (D_m) states.

Only the active form of MinD, c_{DT}, can attach to the membrane, either spontaneously with a rate k_D or facilitated by MinD-ATP already bound to the membrane (recruitment) with a rate $k_{dD} m_d$, where m_d denotes the areal density of MinD-ATP on the membrane. Overall then, the reaction term reads $R_D^+ = (k_D + k_{dD}\, m_d)\, \tilde{c}_{DT}$, where the tilde on the cytosolic concentration of MinD-ATP indicates that the value must be taken in the immediate vicinity of the membrane. Membrane bound MinD-ATP can also recruit cytosolic MinE to the membrane and thereby form MinDE complexes. The corresponding reaction term reads $R_E^+ = k_{dE}\, m_d\, \tilde{c}_E$. Finally, MinE in the MinDE complexes stimulates ATP hydrolysis by MinD and hence facilitates detachment and decay of membrane bound MinDE complexes into cytosolic MinD-ADP and MinE, c_E, with rate k_{de}. This process is described by the reaction term $R_{DE}^- = k_{de}\, m_{de}$ where m_{de} denotes the areal density of MinDE complexes on the membrane. Taken together, the reaction–diffusion equations on the membrane read

$$\partial_t m_d = D_m \nabla_m^2 m_d + R_D^+(m_d, \tilde{c}_{DT}) - R_E^+(m_d, \tilde{c}_E), \tag{2a}$$

$$\partial_t m_{de} = D_m \nabla_m^2 m_{de} + R_E^+(m_d, \tilde{c}_E) - R_{DE}^-(m_{de})\,, \tag{2b}$$

where the index m denotes the Laplacian for membrane diffusion.

These two sets of reaction–diffusion equations, Eqs. (1) and (2), are complemented by nonlinear reactive boundary conditions at the membrane surface that guarantee local particle number conservation. In other words, the chemical reactions involving both membrane-bound and cytosolic proteins equal the diffusive flux onto (−) and off (+) the membrane (the index $\perp$ denoting the outward normal vector at the boundary):

$$D_c \nabla_\perp c_{DD}\big|_m = +R_{DE}^-(m_{de})\,, \tag{3a}$$

$$D_c \nabla_\perp c_{DT}\big|_m = -R_D^+(m_d, \tilde{c}_{DT})\,, \tag{3b}$$

$$D_c \nabla_\perp c_E\big|_m = +R_{DE}^-(m_{de}) - R_E^+(m_d, \tilde{c}_E)\,. \tag{3c}$$

For example, Eq. (3a) states that detachment of MinD-ADP following hydrolysis on the membrane is balanced by gradients of MinD-ADP in the cytosol. In general, any exchange of proteins between the membrane and the cytosol leads to diffusive fluxes and thereby to protein gradients in the cytosol since the membrane effectively acts as a sink or source of proteins. These gradients are essential for understanding the mechanisms underlying intracellular pattern formation, and preclude a naive interpretation of the cytosol as a spatially uniform particle reservoir.

For the model to be complete, one needs to know the values of all of the reaction rates. However, the estimation and choice of system parameters is a highly nontrivial problem. Nonlinear systems are generically very sensitive to parameter changes, whereas biological function has to be sufficiently robust against variations in the kinetic rates and diffusion coefficients (e.g. caused by temperature changes). In addition, only rarely are the system parameters known quantitatively from experiments. For the Min system only the diffusion coefficients have been measured and estimates for the nucleotide exchange rate λ [61] and the Min protein densities exist [62]. However, a theoretical investigation of the skeleton model by means of linear stability analysis and numerical simulations was able to identify parameter regimes where the experimentally observed patterns are formed [60].

3.3 Basic Mechanisms Underlying Min Oscillations in E. coli Cells

From the analysis of the skeleton model [60], quantified by the reaction–diffusion equations in the previous section, one can now learn how Min proteins self-organise to give rise to pole-to-pole oscillations in vivo.

The basic theme of the protein dynamics is the cycling of proteins between the membrane and the cytosol. This cycling is driven by the antagonistic roles of MinD and MinE: Membrane-bound active MinD facilitates flux of MinD and MinE from the cytosol to the membrane (recruitment). This accumulation of proteins at the membrane is counteracted by MinE's stimulation of MinD's ATPase activity, which triggers detachment of both MinD and MinE. In concert with redistribution of proteins through cytosolic diffusion, spatio-temporal patterns may emerge on the membrane.

However, the formation of pole-to-pole oscillations is by no means generic in the context of the above reaction scheme.[2] In general, there are conditions on the values of the reaction rates, as well as on the relative abundances of the proteins which

[2]In general, a given reaction–diffusion equation can generate a plethora of spatio-temporal patterns, as is well known from classical equations like the complex Ginzburg-Landau equation [63] or the Gray-Scott equation [64–68]. Conversely, a given pattern can be produced by a vast variety of mathematical equations. Hence, one must be careful to avoid falling into the trap: "Cum hoc ergo propter hoc" (correlation does not imply causation).

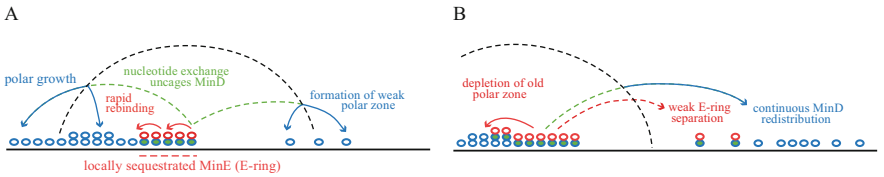

Fig. 7 Key mechanism underlying Min oscillations. (**a**) Locally sequestrated MinE constitutes the MinE ring, which moves toward the left pole through local cycling. Detaching MinD rebinds predominantly at the left pole and initiates formation of a weak polar zone at the right end. The delay in reattachment caused by the need for nucleotide exchange is indicated by dashed lines. (**b**) MinE depletes the old polar zone of MinD, until only MinDE complexes are left, then reassembles at the rim of the new polar zone, formed by redistributed MinD. Adapted from Ref. [60] under the CC-BY-NC-ND 3.0 license

have to be met. An exhaustive parameter scan for model equations (1), (2), and (3) has shown that, for spatial patterns to emerge in the skeleton model, MinE needs to be recruited faster to the membrane-bound protein layer than MinD, while being lower in total particle number [60]

$$k_{dD} < k_{dE}\,, \quad N_E < N_D\,. \tag{4}$$

These conditions give rise to the formation and separation of MinD and MinDE domains, the *polar zone* and *MinE ring*, as the two basic emergent structures of pole-to-pole oscillations. As illustrated in Fig. 7, this is (heuristically) understood as follows [60]. The higher particle number of MinD enables complete sequestration of MinE in membrane-bound MinDE complexes, while leaving a fraction of MinD available to initiate a new polar zone.[3] Given a sufficiently high MinD membrane concentration and MinE recruitment rate k_{dE}, detaching MinE rebinds immediately, forming the prominent MinE ring. Continuous MinE cycling locally depletes the membrane of MinD, leading to a slow poleward progression of the MinE ring along the gradient of membrane bound MinD, whereupon a fraction of detaching MinD initiates a weak polar zone in the opposite cell half, see Fig. 7a. The new polar zone grows due to steady redistribution of MinD, while most MinE remains sequestrated in the old polar zone until the remaining MinD molecules are converted into MinDE complexes, see Fig. 7b. Once this state is reached, the Min proteins rapidly detach, dissociate, and diffuse through the cytosol and rapidly reattach at the new polar zone, leaving behind a region of high MinDE/MinD ratio, where immediate reformation of polar zones is inhibited. Due to the faster recruitment of MinE, the MinE ring

[3]It should be noted that the condition on the particle numbers mainly serves to emphasise the sequestration mechanism. In order for MinD to accumulate in polar zones the action of MinE must be disabled, and specifying that there are fewer MinE particles permits them to be spatially confined. Outside of this zone MinD can accumulate on the membrane. Recently, it has been shown that MinE's conformational switch can transiently attenuate the action of MinE, thereby removing the requirement regarding the relative particle numbers of MinD and MinE [69].

reassembles at the rim of the new polar zone, which provides the crucial separation of MinD and MinDE maxima, i.e. a polar zone and a MinE ring.

There is one element of the above argument which needs further consideration: The sequestration of MinE is transient, and hence the system is oscillatory, only if detaching MinD gradually leaks from the old to the new polar zone. But, how is this process established and regulated? Leakage from the old polar zone is determined by the balance between two opposing factors: the ATPase cycle of MinD, and the propensity of cytosolic MinD to bind to the membrane. MinE stimulates the ATPase activity of MinD and thereby initiates detachment of ADP-bound MinD. The inactive MinD cannot reattach to the membrane until it is reactivated by nucleotide exchange. This delay implies that the zone near the membrane is depleted of active MinD, i.e. MinD has time to diffuse further away from the membrane into the cytosol before it is reactivated. Taken together, these factors effectively suppress immediate reattachment of MinD and promote its leakage from the polar zone: The slower the nucleotide exchange, the more particles leak from polar zones. This is counteracted by MinD recruitment: The stronger the recruitment, the "stickier" the membrane and hence the fewer particles leak from polar zones. Clear evidence for this reasoning comes from the slowing down of the oscillation with increasing nucleotide exchange and MinD recruitment rates, depicted in Fig. 8a.

Numerical simulation of the reaction–diffusion equations, Eqs. (1)–(3), reveals further functional characteristics of Min oscillations. For nucleotide exchange rates $\lambda = 5\,\mathrm{s}^{-1}$, close to the experimentally determined lower bound of $3\,\mathrm{s}^{-1}$, reaccumulation of the polar zone always starts in the opposite cell half, and the

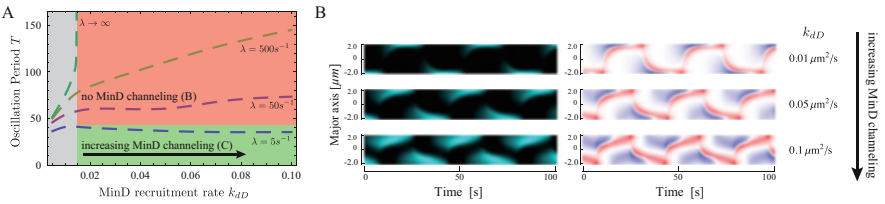

Fig. 8 Canalised MinD transfer and regulation of spatial MinD reattachment by MinD recruitment. (**a**) Temporal period of Min oscillations as a function of the MinD recruitment rate k_{dD}, and nucleotide exchange rate λ in cells of 4 µm length. With instantaneous nucleotide exchange, oscillations only exist at low MinD recruitment rates (grey). Beyond this threshold the nucleotide exchange and recruitment rates become control parameters for the spatial distribution of MinD reattachment. At high but finite nucleotide exchange rates the oscillation period increases with the MinD recruitment rate, as MinD reassembles in front of the polar zone. At low nucleotide exchange rates the oscillation period decreases with MinD recruitment, as the pole-to-pole particle transfer becomes canalised between the two cell halves. (**b**) Kymographs for $\lambda = 5\,\mathrm{s}^{-1}$ showing the total MinD membrane density, $m_d + m_{de}$, and MinD flux $J_D = D_D \nabla_\perp (c_{DT} + c_{DD})|_m$ on (blue) and off (red) the membrane, for a set of increasing MinD recruitment rates k_{dD}. MinD reaccumulates at the opposite cell pole while the old polar zone is still present. Increasing MinD recruitment accelerates the growth of new polar zones towards midcell and synchronises depletion and formation of polar zones at opposite cell ends by canalising the MinD flux from old to new polar zones. Adapted from Ref. [60] under the CC-BY-NC-ND 3.0 license

recruitment rate k_{dD} of MinD regulates how fast the new polar zone grows towards the old one (Fig. 8b). Notably, at $k_{dD} = 0.1\,\mu m^2/s$ in Fig. 8b, the redistribution of MinD from old to new polar zone is highly canalised, i.e. the total MinD flux is directed towards the opposite cell half immediately after the polar zones start to shrink (Fig. 8b). This implies that growth and depletion of polar zones are synchronised. This is also reflected in the characteristic triangular shape observed in MinD kymographs [21], where new polar zones start growing towards midcell while old polar zones shrink towards the cell pole (Fig. 8b).

Although most of the Min protein patterns (like stripe patterns) observed in filamentous mutant *E. coli* have no biological function, the theory is able to account for their occurrence. This argues strongly that they too arise from the mechanism that optimises the spatial profile of pole-to-pole oscillations for midcell localisation. In other words, the rich phenomenology in mutant cells appears to be a by-product of the evolutionary optimisation of the wild-type dynamics.

3.4 Cell Geometry and Pattern Formation

To ensure robustly symmetrical cell division, one would expect Min patterns to scale with cell size and shape, at least within the biologically relevant range. Indeed, recent experiments using 'cell-sculpting' techniques [70] have shown that longitudinal pole-to-pole oscillations are highly stable in cells with widths below 3 µm, and lengths in the range of 3–6 µm. Interestingly, however, outside of this range of cell geometries, Min proteins show diverse oscillation patterns, including longitudinal, diagonal, rotational, striped, and even transverse modes [18, 70–76]. What is the origin of the simultaneous robustness of Min oscillations inside the biologically relevant regime and the bewildering diversity of patterns and multistability outside of it? In what sense are these seemingly contradictory features two faces of the same coin?

To answer these questions one has to address how and to what extent the existence and stability of different patterns is affected by a cell's geometry, and which specific biomolecular processes in the Min reaction circuit control how the system adapts to cell geometry. This has recently been achieved by a combination of numerical studies, based on the reaction–diffusion model discussed in Sect. 3, and experimental studies, in which the geometry of *E. coli* bacteria was systematically varied [72].

There are basically two types of randomness that may affect the process of pattern selection, or transitions between patterns if multiple stable patterns are possible. First, the inherent randomness of any chemical reaction may cause stochastic transitions between patterns. Though such stochastic effects are possible in principle [77], given the large copy number of Min proteins, they are unlikely to be the major source for transitions between patterns; factors like heterogeneities and asymmetries are expected to be far more important. Second, there are many different factors which cause realistic cellular systems to be asymmetric or heterogeneous.

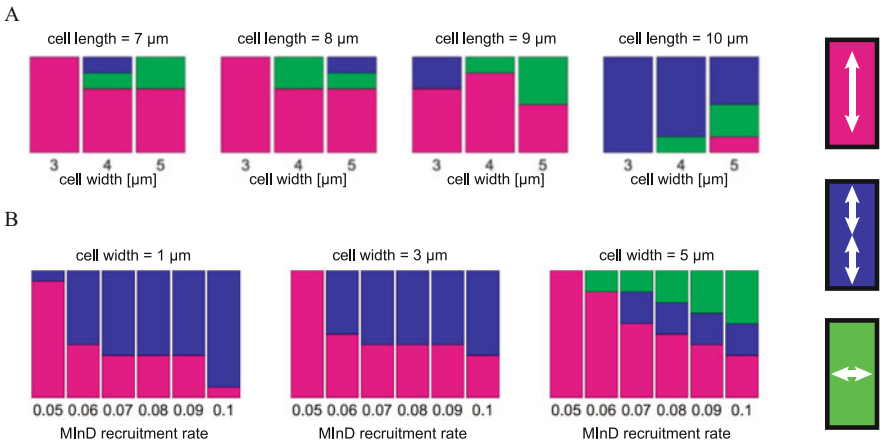

Fig. 9 Basins of attraction predicted from systematic perturbations of patterns with shallow attachment gradients. (**a**) Relative distribution of the final patterns (indicated on the right) observed after sampling all alignment angles of the MinD attachment template from 0° to 90°. The MinD recruitment rate was set to a constant value $k_{dD} = 0.1$. The data shows the increase in the incidence of multistability as the cell size is increased beyond minimal values for cell length and cell width. (**b**) Fractions of the final patterns in cells of 9- and 10-μm length after sampling all alignment angles of the MinD attachment template from 0° to 90°. The data shows that increasing the MinD recruitment rate facilitates multistability. Adapted from Ref. [72] under the CC BY 4.0 license

For example, the membrane affinity of MinD depends on the lipid composition, which in turn is sensitive to membrane curvature. Hence, small asymmetries of the cell shape translate to variations of MinD membrane attachment. While these asymmetries and heterogeneities are intrinsic to ensembles of cells, they need to be specifically emulated in numerical simulations. A natural choice are gradients in the MinD attachment rate that are inclined at all possible angles to the long axis of the cell. The magnitude of these gradients must be sufficiently large to significantly affect the pattern selection process, but at the same time small enough not to cause any asymmetry in the final stable pattern. A relative magnitude of variation in the range of 20% (well below the natural variability of MinD affinity to different lipids [25, 78]) fulfils these requirements. Figure 9 shows histograms of the final stable patterns obtained by sampling over all directions of the gradient, as a function of cell width and length, and of the MinD recruitment rate [72]. For a recruitment rate fixed to the value that facilitates canalised transfer, $k_{dD} = 0.1$, the following observations are of note. (i) As cell length is increased, striped oscillations become more frequent patterns. (ii) The fraction of oscillatory striped patterns tends to decrease in favour of transverse patterns as the cell width increases, indicating that cell width, and not cell length, is the main determinant for the onset of transverse modes. Both observations are remarkably consistent with experimental data based on random sampling of live *E. coli* cells after they have reached a defined shape [70]. Numerical simulations allow us to go beyond the analysis of cell geometry, and investigate the

effect of MinD recruitment rate, see Fig. 9b. In narrow cells with widths ranging from 1 to 3 μm, one observes that the fraction of stripes increases with the MinD recruitment rate [60, 72]. In contrast, for cells that reach a width of 5 μm, stripe patterns are absent below some threshold MinD recruitment rate. With increasing MinD recruitment rate, transverse patterns appear first and increase in frequency, while the fraction of striped patterns takes on a constant value.

There are several conclusions one can draw from these observations. The most obvious one is that multistability in Min patterns is not determined by either kinetic parameters or cell geometry alone, but originates from the interdependence between these two factors. In addition, increasing the size of a Turing-unstable system alone does not in itself facilitate the existence of multiple stable patterns.[4] This is clearly evident from the observation that the emergence of a pole-to-pole oscillation in a short cell does not generically imply the existence of a stable striped oscillation with a characteristic wavelength in a long filamentous cell [60]. Instead, the emergence of a characteristic length scale (which becomes manifest in striped oscillations) is restricted to a specific regime of kinetic parameters, where growth and depletion of spatially separated polar zones become synchronised such that multiple, spatially separated polar zones can be maintained simultaneously ("canalised transfer" regime) [60]. A key element among the prerequisites that permit this regime to be reached is that the degree of nonlinearity in the kinetics of the system (MinD cooperativity) must be particularly strong. Notably, the same mechanism that enables striped oscillations in filamentous cells also facilitates transverse oscillations in wide cells.

These findings hint at an exciting connection between multistability, the ability of patterns to sense and adapt to changes in system geometry, and the existence of an intrinsic length scale in the underlying reaction-diffusion dynamics. Remarkably—and contrary to the treatments in the classical literature—the existence of an intrinsic length scale is not generic for a Turing instability per se. One example is the aforementioned selection of pole-to-pole patterns in arbitrarily long cells where MinD recruitment is weak. In this case, irrespective of the critical wavenumber of the Turing instability, the final pattern is always a single wave traveling from pole to pole. The selection of a single polar zone is also characteristic in the context of cell polarity [38, 79], where it has been ascribed to the finite protein reservoir and a winner-takes-all mechanism. It will be an interesting task for further research to elucidate the general requirements for the emergence of an intrinsic length scale in mass-conserved reaction–diffusion systems.

[4]This is surprising, because Turing instabilities are generically associated with the existence of a *characteristic* (or intrinsic) wave length in the literature. This is evidently not the case here.

3.5 Principles of Adaptation to Geometry in Reaction–Diffusion Systems

How does the geometry of a cell affect the formation of spatio-temporal patterns? This question may be rephrased in more mathematical terms as follows: What are the inherent features of a reaction–diffusion system in confined geometry that promote or impede the adaptation of the ensuing patterns to the size and shape of that confining space?[5] In previous sections, we have seen two recurrent themes: nucleotide exchange and positive feedback through recruitment. To elucidate the role of these two factors we will in this section study a minimal pattern-forming system comprised of a single NTPase only.

As illustrated in Fig. 10, the NTPase cycles between an NDP-bound inactive (D) and an NTP-bound active state (T). Both protein species are able to bind to the membrane spontaneously; for simplicity, we take the rates to be identical and given by k_+. In addition, to direct membrane attachment, each protein species may also bind cooperatively to the membrane with corresponding recruitment rates k_{mD} for the inactive and k_{mT} for the active protein species. Detachment of the membrane-bound species is asymmetric: While the inactive species is simply released to the cytosol with *detachment rate* k_-, detachment of the active species is triggered by NTP hydrolysis which is thereby converted into cytosolic inactive D; again, for simplicity, we assume the corresponding detachment rates to be equal and given by k_-. Reactivation of cytosolic inactive D through nucleotide exchange occurs at rate λ. Both protein forms are allowed to freely diffuse in the cytosol and the membrane with diffusion constants D_c and D_m, respectively.

Denoting the concentrations of D and T in the cytosol by c_D and c_T and by m_D and m_T on the membrane, respectively, the reaction–diffusion equations read

$$\partial_t c_T = D_c \, \Delta \, c_T + \lambda \, c_D \,, \tag{5a}$$

$$\partial_t c_D = D_c \, \Delta \, c_D - \lambda \, c_D \,, \tag{5b}$$

$$\partial_t m_T = D_m \, \Delta_m \, m_T + (k_+ \, \tilde{c}_T - k_- \, m_T) + \, k_{mT} \, m_T \, \tilde{c}_T \,, \tag{5c}$$

$$\partial_t m_D = D_m \, \Delta_m \, m_D \, + (k_+ \, \tilde{c}_D \, - k_- \, m_D) + k_{mD} \, m_D \, \tilde{c}_D \,. \tag{5d}$$

[5] In 1966 Mark Kac published an article entitled "Can one hear the shape of a drum?"[80]. As the dynamics (frequency spectrum) of an elastic membrane whose boundary is clamped is described by the Helmholtz equation $\nabla^2 u + \sigma u = 0$ with Dirichlet boundaries, $\nabla u \mid_\perp = 0$, this amounts to asking how strongly the eigenvalues σ depend on the shape of the domain boundary. Here we ask a much more intricate question, as the dynamics of pattern-forming systems are nonlinear and we would like to know the nonlinear attractor for a given shape and size of a cell.

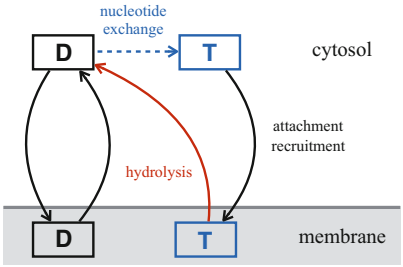

Fig. 10 The NTPase can bind to the membrane in both of its states with *attachment rate* k_+, or cooperatively with corresponding *recruitment rates* k_{mD} for D and k_{mT} for T. NTP *hydrolysis* by T triggers *detachment* with rate k_-, converting membrane-bound T into cytosolic D. Membrane-bound D is also spontaneously released to the cytosol with *detachment rate* k_-. Cytosolic D undergoes *nucleotide exchange* with a rate λ

As before, reactive and diffusive fluxes balance at the membrane-cytosol boundary

$$D_c \, \nabla_\perp c_T|_m = -(k_+ + k_{mT} \, m_T) \, \tilde{c}_T \tag{6a}$$

$$D_c \, \nabla_\perp c_D|_m = -(k_+ + k_{mD} \, m_D) \, \tilde{c}_D + k_- \, (m_D + m_T) \, . \tag{6b}$$

Solving this set of equations numerically in elliptical geometry reveals a series of striking features (Fig. 11): (i) In elongated cells the protein density on the membrane and in the cytosol is *always* inhomogeneous, and reflects the local cell geometry. (ii) There are two distinct types of patterns: membrane-bound proteins either accumulate at midcell or form a bipolar pattern with high densities at both cell poles. (iii) The protein gradients scale with the size of the cell, i.e. fully adapt to the geometry of the cell.

The type of polarity of these patterns is quantified by the ratio of the density of membrane-bound proteins located at the cell poles to that at midcell: $\mathscr{P} = m_{\text{pole}}/m_{\text{midcell}}$. Accumulation occurs either at the cell pole or at midcell depending on the value of the preferential recruitment parameter $\mathscr{R} = (k_{mD} - k_{mT})/(k_{mD} + k_{mT})$: One finds that proteins accumulate at the cell poles ($\mathscr{P} > 1$) if there is a preference for cooperative binding of D ($\mathscr{R} > 0$). Moreover, the polarity $\mathscr{P}$ of this bipolar pattern becomes more pronounced with increasing $\mathscr{R}$. In contrast, when cooperative binding favours T ($\mathscr{R} < 0$), proteins accumulate at midcell ($\mathscr{P} < 1$). Thus, the sign of the recruitment preference $\mathscr{R}$ for a protein in a particular nucleotide state controls the type, while its magnitude determines the amplitude of the pattern. With increasing eccentricity of the ellipse, the respective pattern becomes more sharply defined; for a spherical geometry, the pattern vanishes. In summary, cell geometry controls the definition of the pattern, and the preference for membrane recruitment of a certain nucleotide state determines both the location on the cell membrane where the proteins accumulate and how pronounced this accumulation becomes.

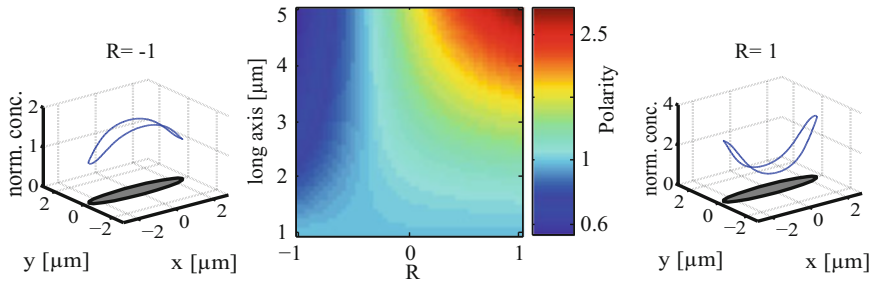

Fig. 11 Membrane-bound proteins either accumulate at midcell (left) or form a bipolar pattern with high protein densities at the cell poles (right). The left and right plots show the normalised concentration of the membrane density (blue curve) and the corresponding geometry of the cell (grey ellipse). The membrane density of the protein is divided by its minimum concentration (left: $113\,\mu m^{-1}$, right: $100\,\mu m^{-1}$) such that the minimum of the normalised density is 1. The polarity $\mathscr{P} = m_{\rm pole}/m_{\rm midcell}$ (colour bar in plot is logarithmically spaced) of the pattern strongly depends on cell geometry and preference $\mathscr{R} = (k_{mD} - k_{mT})/(k_{mD} + k_{mT})$ for the recruitment of a certain nucleotide state (middle); the length of the short axis is fixed at $l = 1\,\mu m$, and we have used $k_{mD}+k_{mT} = 0.1\,\mu m/s$. While for large $\mathscr{R}$ (preferential recruitment of D) the proteins form a bipolar pattern on the membrane, the membrane-bound proteins accumulate at midcell for small R (preferential recruitment of T). If the recruitment processes are balanced ($\mathscr{R} = 0$), the pattern is flat and polarity vanishes. The cell geometry determines how pronounced a pattern becomes: The more elongated the ellipse, the more sharply defined the pattern, which vanishes completely when the ellipse becomes a circle. Reprinted from Ref. [81] with permission from PNAS

What is the origin of these polar patterns and their features? To answer this question in the clearest possible way, it is instructive to consider the limiting case where positive feedback effects on recruitment are absent and the dynamics hence are fully linear. Then, Eqs. (5)–(6b) imply that both the total concentration of proteins on the membrane, $m = m_D + m_T$, and in the cytosol, $c = c_D + c_T$, are spatially uniform if the detailed balance condition $k_+ \tilde{c} = k_- m$ holds for the exchange of proteins between the cytosol and the membrane. This uniformity in total protein density, however, does not imply uniformity in the densities of the active and inactive protein species, either on the cell membrane or in the cytosol! The origin of this effect is purely geometrical, and it is linked to the finite time required for nucleotide exchange in the cytosol. Heuristically, this can be seen as follows (Fig. 12a). As only inactive proteins D are released from the membrane, they act as a source of cytosolic proteins. In the cytosol they are then reactivated through nucleotide exchange, which is effectively equivalent to depleting the cytoplasmic compartment of inactive proteins. This in turn implies the formation of a gradient of inactive proteins and a corresponding, oppositely oriented gradient of active proteins as one moves away from the membrane into the cytosol. As is known from standard source-degradation processes, the ensuing density profile for D in the cytosol is exponential, with the decay length being set by $\ell_\lambda = \sqrt{D_c/\lambda}$.

Due to membrane curvature these reaction volumes overlap close to the cell poles (Fig. 12b, bottom), which implies an accumulation of D at the cell poles. The

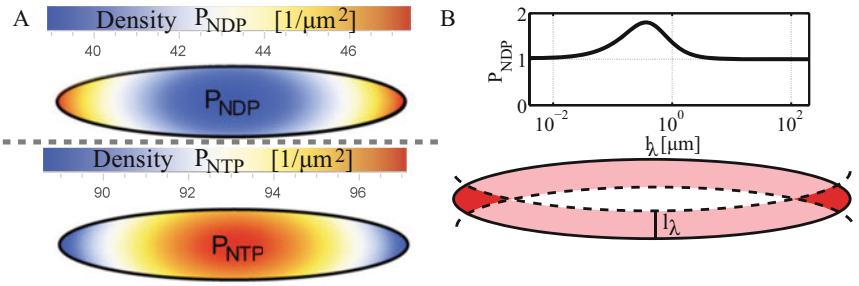

Fig. 12 Membrane affinity controls, and recruitment amplifies adaptation to geometry. The cells used for the numerical studies have a length of $L = 5\,\mu\text{m}$ and a width of $l = 1\,\mu\text{m}$. (**a**) Even when recruitment is turned off, T and D form inhomogeneous density profiles in the cytosol. D accumulates close to the poles and is depleted at midcell. In contrast, T exhibits a high concentration at midcell and a low concentration at the poles. The attachment and detachment rates are set to $1\,\mu\text{m/s}$ and 1s^{-1}, respectively, which gives a penetration depth $\ell_\lambda \approx 1.6\,\mu\text{m}$. (**b**) Illustration of the source-degradation mechanism for the spatial segregation of cytosolic D and T. All proteins that detach from the membrane are in an NDP-bound state and can undergo nucleotide exchange, the range of D in the cytosol is limited to a penetration depth ℓ_λ (dashed lines); here, $\ell_\lambda = 0.35\,\mu\text{m}$. At the poles this reaction volume receives input from opposing faces of the membrane resulting in an accumulation of cytosolic D (dark red). The magnitude of this accumulation depends on the penetration depth. The polarity $\mathscr{P}_{\text{NDP}} = m_d^{\text{pole}}/m_d^{\text{midcell}}$ of membrane-bound D plotted as a function of ℓ_λ shows a maximum at $\ell_\lambda \approx 0.35\,\mu\text{m}$ and vanishes in the limits of large as well as small penetration depths. Reprinted from Ref. [81] with permission from PNAS

effect becomes stronger with increasing membrane curvature. Moreover, there is an optimal value for the penetration depth ℓ_λ, roughly equal to a third of the length l of the short cell axis, that maximises accumulation of D at the cell poles (Fig. 12b, top). As ℓ_λ becomes larger than l, the effect weakens, because the reaction volumes from opposite membrane sites also overlap at midcell. In the limit where ℓ_λ is much smaller than the membrane curvature at the poles, the overlap vanishes, and with it the accumulation of D at the poles. More generally, these heuristic arguments imply that the local ratio of the reaction volume for nucleotide exchange to the available membrane surface is the factor that explains the dependence of the protein distribution on cell geometry.

4 In Vitro Reconstitution and Theoretical Analysis of Min Protein Pattern Formation

A key step towards understanding pattern formation mechanisms in biological systems is the identification of the essential functional modules that facilitate the formation of certain patterns. In living systems, such an identification is strongly impeded by the vast amount of potentially interacting and, therefore,

interdependent components. A common strategy for tackling the complexity of biological systems is mathematical modelling, which has been discussed in the previous section of this chapter. While mathematical analysis is able to identify possible mechanisms of pattern formation, it is also based on a priori assumptions about the biological system under consideration. However, these assumptions need to be tested by suitable experiments. Ideally, a conclusive comparison between theory and experiment requires the ability to isolate the essential players of the pattern forming dynamics and reconstitute them in a minimal system lacking any other potential interactions and allowing for precise control of parameters, such as protein concentrations or geometric boundaries.

A major breakthrough in this regard was the successful in vitro reconstitution of Min protein patterns in a lipid bilayer assay [82]. These experiments demonstrated that a flat lipid bilayer surface coupled to a cytosolic solution containing only MinD, MinE, and ATP is sufficient for the formation of membrane bound Min protein patterns. However, the patterns observed in reconstituted (in vitro) systems significantly differed from the intracellular patterns found in vivo (Fig. 13). While the majority of patterns found in vivo can be viewed as standing waves with a wavelength matching the cell length, the patterns on the flat membrane are travelling and spiral waves with wavelengths one order of magnitude greater than the typical length of *E. coli*.

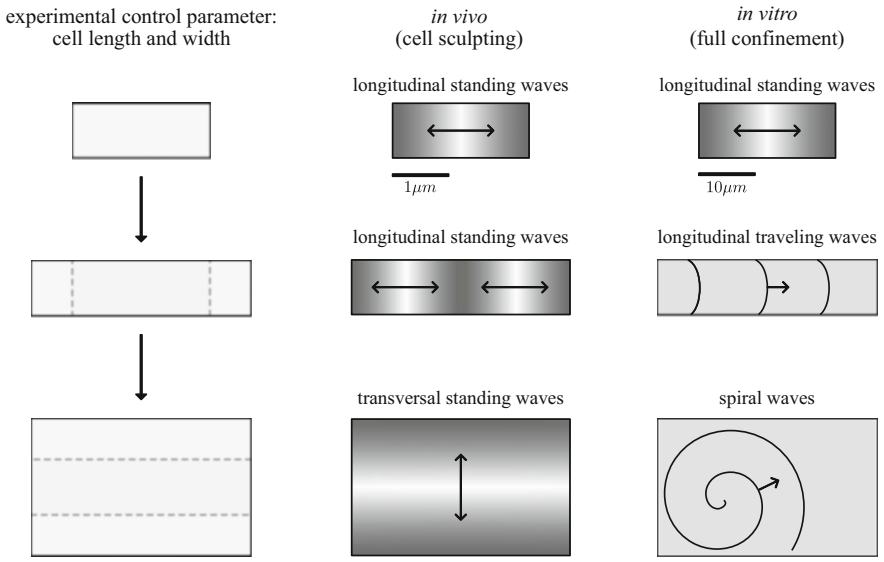

Fig. 13 Min protein patterns in vivo vs in vitro. Schematic depiction of the phenomenology observed in experiments when the system geometry is changed. For small systems the patterns in reconstituted systems [83] are similar to intracellular dynamics [70], showing pole-to-pole oscillations (with different length scales) in both cases. However, as the system length and width are increased, patterns appear that are not normally seen in vivo

4.1 A Kaleidoscope of In Vitro Patterns

The successful reconstitution of Min protein patterns on flat lipid bilayers stimulated a plethora of in vitro experiments that studied Min protein dynamics under various circumstances and revealed a true kaleidoscope of patterns (Fig. 14). On flat lipid bilayers one observed spiral and travelling wave patterns, and a varying degree of spatial coherence sometimes verging on chemical turbulence [84]. Other experiments constrained the Min protein dynamics geometrically to small membrane patches [85], semi-open PDMS grooves with varying lipid composition [86], lipid-interfaced droplets [87], and bilayer coated three-dimensional chambers of various shapes and sizes [83]. Strikingly, the observed patterns show a very broad range of characteristics and varying degrees of sensitivity to the geometry of the enclosing membrane. Other experiments were performed in large, laterally extended flow cell devices with a flat lipid bilayer of varying lipid composition attached at the bottom [88]. These experiments showed that Min protein patterns are formed even

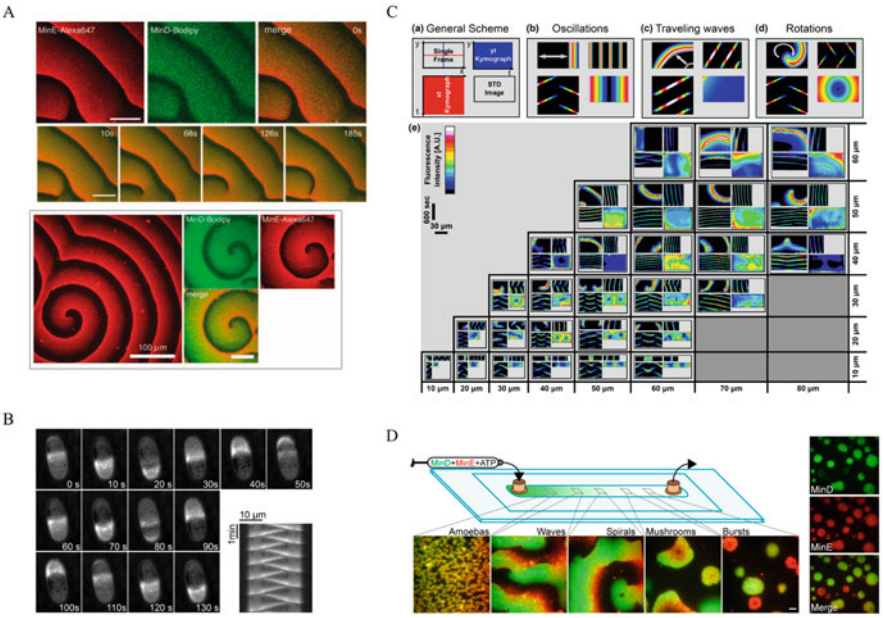

Fig. 14 Min patterns in vitro. (**a**) Spiral- and travelling-wave patterns observed on flat lipid bilayers. From Ref. [82]. Reprinted with permission from AAAS. (**b**) Pole-to-pole oscillations in semi-confined PDMS grooves. Reprinted with permission from Ref. [86], copyright 2013 Wiley-VCH Verlag GmbH and Co. KGaA, Weinheim, Germany. (**c**) Standing waves, travelling waves, and spiral waves observed in fully confined microfluidic chambers with different lateral dimensions. Adapted from Ref. [83] under the CC BY 4.0 license. (**d**) Exotic Min protein patterns on flat lipid bilayers in large laterally extended flow cells showing different phenomenology depending on the distance to the outlet and inlet of the flow cell device. Reprinted from Ref. [92] with permission from PNAS

when there is hydrodynamic flow in the cytosol. Furthermore, these experiments revealed the capability of Min protein dynamics to form exotic patterns sharing characteristics of travelling waves and stationary patterns alike [88].

Despite these intensive experimental efforts, a quantitative reconstitution of Min protein patterns observed in vivo has not been achieved. Instead a broad range of different patterns has been found, all of which exhibit wavelengths that are several times larger than that of the in vivo pattern. The pole-to-pole patterns that are observed in (semi-)confined compartments [83, 89] most closely resemble those seen in vivo. Interestingly, this resemblance is limited to geometries with dimensions below the typical wavelength of the pattern. In these systems the characteristic pole-to-pole oscillation is observed in vivo as well as in vitro. If the length and width of the confined system are increased, the reconstituted in vitro experiments [83] predominantly show traveling and spiral wave patterns, whereas in vivo experiments show longitudinal and transversal standing waves [70, 72]. This suggests that the underlying mechanisms (dynamic instabilities) are actually not the same.[6] While longitudinal and transversal standing waves have also been observed in semi-confined PDMS grooves of specific sizes [89], the patterns became chaotic in these experiments when the system size was increased [89].

Given these ambiguous results, how can we reconcile the kaleidoscope of in vitro patterns and the range of in vivo patterns? In the following, we discuss how theory can shed some light on these bewildering results. As we will see, a key problem with the interpretation of recent in vitro reconstitution experiments and their comparison to in vivo dynamics lies in the lack of the ceteris paribus condition, i.e. conditions where only one control parameter is varied while the rest are held constant. Achieving quantitative control over all parameters will be the key goal for future experiments.

4.2 The Polychotomy of Min Protein Patterns

All experimental evidence supports the assumption that the Min system can be understood as a reaction–diffusion system driven by nonlinear (cooperative) protein interactions. Therefore, we can expect that Min protein dynamics will share generic features of such nonlinear systems. In particular, as is well known in the field of nonlinear dynamics, even very simple models can produce a broad variety of patterns [64–68]. Moreover, which patterns are observed depends on the parameters

[6] We note that travelling wave patterns have also been observed in vivo [90], albeit only upon massive over-expression of MinD and MinE, leading to highly elevated intracellular protein densities and pathological phenomenology [91] relative to the wild type. While the exact protein densities in the experiments have not been measured, this observation is consistent with the observation of travelling waves in fully confined compartments, where the protein densities inside microfluidic chambers were also elevated [83]. For further discussion of the effect of protein densities, we refer the reader to Sect. 4.2.

of the system. In the classical mathematical theory these parameters are the coefficients of the (non-)linear interactions (representing the "kinetics"), as well as the diffusion coefficients.

Diffusion coefficients (in the cytosol) have been measured in vivo [61] and in vitro [82, 84], and they can be controlled experimentally by the addition of crowding agents [83, 85]. Kinetic parameters of the Min system are much more difficult to measure and to control. However, diffusion coefficients and kinetic rates are not the only control parameters. Most of the classical literature in nonlinear dynamics accounts neither for system geometry nor for the mass-conserving nature of biomolecular interactions. This might explain why the fact that system geometry as well as protein densities can be key control parameters of the system's dynamics is often overlooked. The effect of changes in these parameters is not necessarily restricted to changes in the length- and time-scales of the dynamics (e.g. wavelength, wave speed, and oscillation period), but can also induce qualitative changes and transitions between patterns.

One clear difference between the reconstituted Min system on flat lipid bilayers and the intracellular system in *E. coli* is the vastly increased ratio of cytosolic volume to membrane surface in the in vitro system, where the height of the system is of the order of milimetres, instead of μm in the living system. A recent theoretical analysis [58] has shown that increasing this volume-to-surface ratio leads to an increased wavelength of the pattern. This prediction agrees with the experimental observation of a reduced wavelength of the Min protein patterns in fully confined geometries [83] that mimic the in vivo membrane-to-cytosol ratio more closely than does the flat lipid bilayer. Strikingly, even when cytosolic diffusion was reduced to in vivo levels, these experiments still showed a 3- to 4-fold increased wavelength in confined compartments compared to the intracellular patterns—emphasising an apparent dichotomy between patterns observed in vivo and in vitro.

However, the surface-to-volume ratio is not the only difference between the intracellular and the reconstituted Min systems. Another is the particle number or effective density of MinD as well as MinE. At first glance there is no apparent difference between the protein concentrations in vivo and in vitro, since the concentrations in all reconstituted systems are adjusted to the intracellular concentrations which are about 1 μM for MinD and MinE. However, it is important to note that these are the average cytosolic densities with no proteins attached to the membrane. Since all cytosolic proteins are able to bind to the membrane,[7] the total number of cytosolic proteins determines the upper bound for the maximal membrane densities. Hence, even if the average cytosolic densities in the reconstituted system are identical to typical intracellular concentrations, the crucial control parameter is the ratio of cytosolic volume to membrane surface. In vivo, a cytosolic density of about 1 μM yields a number of proteins that can easily be absorbed by the membrane and

[7] Either directly or by complex formation as for MinDE complexes.

still remain up to two orders of magnitude below the saturation limit.[8] However, in the reconstituted system with flat lipid bilayer the volume-to-surface ratio is given by the bulk height h. For the typical bulk height on the order of millimetres, less than 1% of all proteins can bind to the membrane before saturation due to volume exclusion is reached. As a consequence, the protein densities at and on the membrane are highly increased in the reconstituted system compared to the situation in vivo, despite the average cytosolic densities being identical. Note that the densities of membrane-bound proteins are directly involved in the recruitment process which represents the only intrinsically nonlinear interaction in the Min system (cf. Sect. 3.2). As such, one can expect that changes in the average protein densities on the membrane affect the system dynamics in a significant way. Indeed, estimates of the concentration on the flat lipid bilayer show that the density across a wave profile is about two orders of magnitude higher than the typical protein densities on the intracellular membrane [84]. The same can be assumed to be the case for reconstituted Min oscillations in semi-open PDMS grooves [86, 89], since the dynamics are initialised with a high cytosolic column above the grooves which is only removed after the onset of pattern formation (and therefore membrane accumulation). Elevated protein densities were also found for the reconstituted Min patterns in confined chambers [83] since these are based on a microfluidic device. As proteins accumulate on the membrane while the flow is still active, the density at the inlet is merely a lower bound for the actual protein densities in the individual chambers. Measurements of the protein fluorescence inside the confined chambers after careful calibration show that the total densities of MinD and MinE and the MinE/MinD ratios are increased and are broadly distributed [83]. A similar result can be expected for Min protein dynamics in large, laterally extended flow cells where diverse wave patterns are observed [88, 92].

To put these findings from the in vitro reconstruction of Min protein patterns in the context of the theoretical framework, the broad variation of volume-to-surface ratios, total protein numbers, and MinE/MinD density ratios are crucial aspects to consider (cf. [93]). The theoretical analysis of the skeleton model, Eqs. (1)–(3), has shown that all these quantities are key control parameters for the system dynamics. An increase in any of these values (total density, density ratio, volume/surface ratio) can lead to a Turing- or Hopf-instability [58]. In the latter case, each point on the membrane can be considered to be an individual chemical oscillator, and the laterally extended system a field of diffusively coupled oscillators [58]. Such dynamics describe a broad class of systems well documented in the classic nonlinear dynamics literature [63]. Key characteristics of oscillatory media are spiral and travelling patterns, as well as various manifestations of chemical turbulence. All these phenomena can be observed in the reconstituted Min system [69]. From this point of view, the observed dichotomy rather appears as a polychotomy, not only between in vivo and in vitro, but also between the many different experimental

[8] Assuming a cylindrical geometry for simplicity, the volume-to-surface ratio is $\sim r/2$, i.e. well below 1 µm for typical cell radii r.

setups. Its origin lies in the broad distribution of control parameters and emphasises the diversity of Min protein dynamics on a phenomenological and mechanistic level.

5 Discussion and Outlook

As outlined in this chapter, the recent focus on the quantitative study of pattern formation in biological systems has led to conceptually new approaches in theory and experiments. Among the important milestones are the inclusion of cell geometry and an explicit distinction between cell membrane and cytosolic volume in theoretical models, as well as the identification of particle numbers and cell geometry as major control parameters of the self-organisation processes that lead to pattern formation. While these efforts enabled the quantitative study of biological pattern formation within the theoretical framework of nonlinear dynamics, experimental advances in in vitro reconstitution opened new ways to probe, study, and design protein pattern formation as well as controlled minimal systems. Due to its simplicity, the *E. coli* Min system has been the subject of intensive theoretical and experimental investigation, establishing it as a paradigm for protein pattern formation. In contrast, the eukaryotic systems discussed here remain far less well understood. In part, this is due to a higher degree of complexity and redundancy in these systems. For example, PAR networks involve several different molecular players in the anterior and posterior PAR components, respectively, and also interact with dynamic cytoskeletal structures and physical triggers [46]. Accordingly, the in vitro reconstitution of eukaryotic pattern-forming systems is typically more challenging compared to bacterial systems. Yet, efforts to experimentally reconstitute even basic aspects of such pattern-forming systems in vitro could substantially enhance our understanding of their underlying mechanisms via control and perturbation of the experimental conditions.

For the Min system, several key questions remain to be answered. Central is the experimental control over system parameters that gives rise to the multitude of observed patterns. Future research may reveal additional chemical states of MinD as well as MinE or additional chemical reactions that refine the hitherto identified skeleton network. While this will affect the number of chemical components and reaction terms one has to take into account in the mathematical model, it does not change the overall structure of the set of reaction–diffusion equations: (1) Fast cytosolic diffusion is coupled to slow membrane dynamics by chemical reactions that conserve protein number. (2) Nucleotide exchange in the cytosol implies that active MinD is spatially separated from the reactive membrane. As a consequence, the cytosol serves as a repository for active MinD. (3) MinD and MinE remain the only conserved species. The sum of individual components of each species, regardless of the number of components, will always be a conserved quantity.

Until recently, open questions relating to the molecular details of Min protein interactions concerned the roles of membrane binding and conformational state switching of MinE. A combined theoretical and experimental approach has revealed

that MinE's conformational switch makes Min patterns robust against variations in protein concentration [69]. Moreover, it has been shown that MinE's membrane interaction is not required for pattern formation per se, but its removal affects some spatio-temporal properties of Min patterns [92, 94].

In summary, protein pattern formation plays key roles in many essential biological processes from bacteria to animals, including cell polarisation and division. Combined theoretical and experimental approaches have established important principles of pattern-forming protein systems. Perhaps the most crucial feature that has emerged from these research efforts is the identification of the cytosol as a depot. This depot enables the system to store proteins and redistribute them throughout the system. Cytosolic diffusion is the key process that detects the local shape of the membrane, and it is this explicit dependence on geometry that is imprinted on membrane-bound protein patterns.

Acknowledgements We thank Fridtjof Brauns, Yaron Caspi, Cees Dekker, Jonas Denk, and Fabai Wu for helpful discussions. This research was supported by the German Excellence Initiative via the program "NanoSystems Initiative Munich" (NIM), and the Deutsche Forschungsgemeinschaft (DFG) via project A09 and B02 within the Collaborative Research Center (SFB 1032) "Nanoagents for spatio-temporal control of molecular and cellular reactions". SK was supported by a DFG fellowship through QBM.

References

1. Thom R (1983) Mathematical models of morphogenesis. Ellis Horwood, Chichester
2. Turing AM (1952) The chemical basis of morphogenesis. Philos Trans R Soc Lond Ser B Biol Sci 237(641):37–72
3. Guckenheimer J, Holmes PJ (2013) Nonlinear oscillations, dynamical systems, and bifurcations of vector fields. Springer, New York
4. Cross M, Greenside H (2009) Pattern formation and dynamics in nonequilibrium systems. Cambridge University Press, Cambridge
5. Wedlich-Soldner R, Altschuler S, Wu L, Li R (2003) Spontaneous cell polarization through actomyosin-based delivery of the Cdc42 GTPase. Science 299(5610):1231–1235
6. Florian MC, Geiger H (2010) Concise review: polarity in stem cells, disease, and aging. Stem Cells 28(9):1623–1629
7. Molendijk AJ, Bischoff F, Rajendrakumar CS, Friml J, Braun M, Gilroy S, Palme K (2001) Arabidopsis thaliana Rop GTPases are localized to tips of root hairs and control polar growth. EMBO J 20(11):2779–2788
8. Gu Y, Vernoud V, Fu Y, Yang Z (2003) Rop GTPase regulation of pollen tube growth through the dynamics of tip-localized F-actin. J Exp Bot 54(380):93–101
9. Goehring NW, Trong PK, Bois JS, Chowdhury D, Nicola EM, Hyman AA, Grill SW (2011) Polarization of PAR proteins by advective triggering of a pattern-forming system. Science (New York, NY) 334(6059):1137–1141
10. Bement WM, Leda M, Moe AM, Kita AM, Larson ME, Golding AE, Pfeuti C, Su K-C, Miller AL, Goryachev AB, von Dassow G (2015) Activator-inhibitor coupling between Rho signalling and actin assembly makes the cell cortex an excitable medium. Nat Cell Biol 17(11):1471–1483

11. Desai A, Mitchison TJ (2003) Microtubule polarization dynamics. Annu Rev Cell Dev Biol 13:83–117. https://urldefense.proofpoint.com/v2/url?u=https-3A__doi.org_10.1146_annurev.cellbio.13.1.83&d=DwIFaQ&c=vh6FgFnduejNhPPD0fl_yRaSfZy8CWbWnIf4XJhSqx8&r=9EzDtkclhbxR9XXW_9P29tltxjEeSlxA3PIkIP54CYcj_sDBrGUzapT3j7jzUnmG&m=TYcRTNDOWTawN7prfjwqOj_HGeevbSvz1umSlmoSz94&s=AWJ0fQlX53F6yqBr0qCrduJGyp3GFu5187V62GPRjxM&e=
12. Varga V, Helenius J, Tanaka K, Hyman AA, Tanaka TU, Howard J (2006) Yeast kinesin-8 depolymerizes microtubules in a length-dependent manner. Nat Cell Biol 8(9):957–962
13. Varga V, Leduc C, Bormuth V, Diez S, Howard J (2009) Kinesin-8 motors act cooperatively to mediate length-dependent microtubule depolymerization. Cell 138(6):1174–1183
14. Reese L, Melbinger A, Frey E (2011) Crowding of molecular motors determines microtubule depolymerization. Biophys J 101(9):2190–2200
15. Melbinger A, Reese L, Frey E (2012) Microtubule length regulation by molecular motors. Phys Rev Lett 108(25):258104
16. Reese L, Melbinger A, Frey E (2014) Molecular mechanisms for microtubule length regulation by kinesin-8 and xmap215 proteins. Interface Focus 4(6):20140031
17. Raskin DM, de Boer PA (1999) MinDE-dependent pole-to-pole oscillation of division inhibitor MinC in Escherichia coli. J Bacteriol 181(20):6419–6424
18. Raskin DM, de Boer PA (1999) Rapid pole-to-pole oscillation of a protein required for directing division to the middle of Escherichia coli. Proc Natl Acad Sci USA 96(9):4971–4976
19. Hu Z, Lutkenhaus J (1999) Topological regulation of cell division in Escherichia coli involves rapid pole to pole oscillation of the division inhibitor MinC under the control of MinD and MinE. Mol Microbiol 34(1):82–90
20. Lutkenhaus J (2007) Assembly dynamics of the bacterial MinCDE system and spatial regulation of the Z ring. Annu Rev Biochem 76:539–562
21. Loose M, Kruse K, Schwille P (2011) Protein self-organization: lessons from the min system. Annu Rev Biophys 40(1):315–336
22. Szeto TH, Rowland SL, Rothfield LI, King GF (2002) Membrane localization of MinD is mediated by a C-terminal motif that is conserved across eubacteria, archaea, and chloroplasts. Proc Natl Acad Sci USA 99(24):15693–15698
23. Hu Z, Lutkenhaus J (2003) A conserved sequence at the C-terminus of MinD is required for binding to the membrane and targeting MinC to the septum. Mol Microbiol 47(2):345–355
24. Lackner LL, Raskin DM, de Boer PAJ (2003) ATP-dependent interactions between Escherichia coli Min proteins and the phospholipid membrane in vitro. J Bacteriol 185(3):735–749
25. Mileykovskaya E, Fishov I, Fu X, Corbin BD, Margolin W, Dowhan W (2003) Effects of phospholipid composition on MinD-membrane interactions in vitro and in vivo. J Biol Chem 278(25):22193–22198
26. Hu Z, Mukherjee A, Pichoff S, Lutkenhaus J (1999) The MinC component of the division site selection system in Escherichia coli interacts with FtsZ to prevent polymerization. Proc Natl Acad Sci USA 96(26):14819–14824
27. Hu Z, Lutkenhaus J (2001) Topological regulation of cell division in E. coli. Spatiotemporal oscillation of MinD requires stimulation of its ATPase by MinE and phospholipid. Mol Cell 7(6):1337–1343
28. Hu Z, Gogol EP, Lutkenhaus J (2002) Dynamic assembly of MinD on phospholipid vesicles regulated by ATP and MinE. Proc Natl Acad Sci USA 99(10):6761–6766
29. Park K-T, Wu W, Battaile KP, Lovell S, Holyoak T, Lutkenhaus J (2011) The min oscillator uses MinD-dependent conformational changes in MinE to spatially regulate cytokinesis. Cell 146(3):396–407
30. Shih Y-L, Huang K-F, Lai H-M, Liao J-H, Lee C-S, Chang C-M, Mak H-M, Hsieh C-W, Lin C-C (2011) The N-terminal amphipathic helix of the topological specificity factor MinE is associated with shaping membrane curvature. PLoS ONE 6(6):e21425
31. Lutkenhaus J (2012) The ParA/MinD family puts things in their place. Trends Microbiol 20(9):411–418

32. Loose M, Mitchison TJ (2014) The bacterial cell division proteins FtsA and FtsZ self-organize into dynamic cytoskeletal patterns. Nat Cell Biol 16(1):38–46
33. Denk J, Huber L, Reithmann E, Frey E (2016) Active curved polymers form vortex patterns on membranes. Phys Rev Lett 116(17):178301
34. Ramirez-Diaz DA, García-Soriano DA, Raso A, Mücksch J, Feingold M, Rivas G, Schwille P (2018) Treadmilling analysis reveals new insights into dynamic FtsZ ring architecture. PLoS Biol 16(5):e2004845
35. Bi E, Park H-O (2012) Cell polarization and cytokinesis in budding yeast. Genetics 191(2):347–387
36. Freisinger T, Klünder B, Johnson J, Müller N, Pichler G, Beck G, Costanzo M, Boone C, Cerione RA, Frey E, Wedlich-Soldner R (2013) Establishment of a robust single axis of cell polarity by coupling multiple positive feedback loops. Nat Commun 4:1807
37. Goryachev AB, Pokhilko AV (2008) Dynamics of Cdc42 network embodies a Turing-type mechanism of yeast cell polarity. FEBS Lett 582(10):1437–1443
38. Klünder B, Freisinger T, Wedlich-Soldner R, Frey E (2013) GDI-mediated cell polarization in yeast provides precise spatial and temporal control of Cdc42 signaling. PLoS Comput Biol 9(12):e1003396
39. Bose I, Irazoqui JE, Moskow JJ, Bardes ES, Zyla TR, Lew DJ (2001) Assembly of scaffold-mediated complexes containing Cdc42p, the exchange factor Cdc24p, and the effector cla4p required for cell cycle-regulated phosphorylation of Cdc24p. J Biol Chem 276(10):7176–7186
40. Butty A-C, Perrinjaquet N, Petit A, Jaquenoud M, Segall JE, Hofmann K, Zwahlen C, Peter M (2002) A positive feedback loop stabilizes the guanine-nucleotide exchange factor Cdc24 at sites of polarization. EMBO J 21(7):1565–1576
41. Kozubowski L, Saito K, Johnson JM, Howell AS, Zyla TR, Lew DJ (2008) Symmetry-breaking polarization driven by a Cdc42p GEF-PAK complex. Curr Biol 18(22):1719–1726
42. Bendezu FO, Vincenzetti V, Vavylonis D, Wyss R, Vogel H, Martin SG (2015) Spontaneous Cdc42 polarization independent of GDI-mediated extraction and actin-based trafficking. PLoS Biol 13(4):e1002097
43. Laan L, Koschwanez JH, Murray AW (2015) Evolutionary adaptation after crippling cell polarization follows reproducible trajectories. eLife 4:e09638
44. Goldstein B, Macara IG (2007) The PAR proteins: fundamental players in animal cell polarization. Dev Cell 13(5):609–622
45. Munro E, Nance J, Priess JR (2004) Cortical flows powered by asymmetrical contraction transport PAR proteins to establish and maintain anterior-posterior polarity in the early C. elegans embryo. Dev Cell 7(3):413–424
46. Goehring NW (2014) PAR polarity: from complexity to design principles. Exp Cell Res 328(2):258–266
47. Goehring NW, Grill SW (2013) Cell polarity: mechanochemical patterning. Trends in Cell Biol 23(2):72–80
48. Green RA, Paluch E, Oegema K (2012) Cytokinesis in animal cells. Annu Rev Cell Dev Biol 28:29–58
49. Gerdes K, Howard M, Szardenings F (2010) Pushing and pulling in prokaryotic DNA segregation. Cell 141(6):927–942
50. Bange G, Sinning I (2013) SIMIBI twins in protein targeting and localization. Nat Struct Mol Biol 20(7):776–780
51. Treuner-Lange A, Søgaard-Andersen L (2014) Regulation of cell polarity in bacteria. J Cell Biol 206(1):7–17
52. Schumacher D, Bergeler S, Harms A, Vonck J, Huneke-Vogt S, Frey E, Søgaard-Andersen L (2017) The PomXYZ proteins self-organize on the bacterial nucleoid to stimulate cell division. Dev Cell 41(3):299–314
53. Bergeler S, Frey E (2018) Regulation of Pom cluster dynamics in Myxococcus xanthus. PLoS Comput Biol 14(8):e1006358
54. Schuhmacher JS, Thormann KM, Bange G, Albers S-V (2015) How bacteria maintain location and number of flagella? FEMS Microbiol Rev 39(6):812–822

55. Halatek J, Brauns F, Frey E (2018) Self-organization principles of intracellular pattern formation. Philos Trans R Soc B 373(1747):20170107
56. Segel LA, Jackson JL (1972) Dissipative structure: an explanation and an ecological example. J Theor Biol 37(3):545–559
57. Kondo S, Miura T (2010) Reaction-diffusion model as a framework for understanding biological pattern formation. Science (New York, NY) 329(5999):1616–1620
58. Halatek J, Frey E (2018) Rethinking pattern formation in reaction–diffusion systems. Nat Phys 14(5):507–514
59. Huang KC, Meir Y, Wingreen NS (2003) Dynamic structures in Escherichia coli: spontaneous formation of MinE rings and MinD polar zones. Proc Natl Acad Sci USA 100(22):12724–12728
60. Halatek J, Frey E (2012) Highly canalized MinD transfer and MinE sequestration explain the origin of robust MinCDE-protein dynamics. Cell Rep 1(6):741–752
61. Meacci G, Ries J, Fischer-Friedrich E, Kahya N, Schwille P, Kruse K (2006) Mobility of Min-proteins in Escherichia coli measured by fluorescence correlation spectroscopy. Phys Biol 3(4):255–263
62. Shih Y-L, Fu X, King GF, Le T, Rothfield L (2002) Division site placement in E.coli: mutations that prevent formation of the MinE ring lead to loss of the normal midcell arrest of growth of polar MinD membrane domains. EMBO J 21(13):3347–3357
63. Aranson IS, Kramer L (2002) The world of the complex Ginzburg-Landau equation. Rev Mod Phys 74(January):99–143
64. Gray P, Scott SK (1983) Autocatalytic reactions in the isothermal, continuous stirred tank reactor: Isolas and other forms of multistability. Chem Eng Sci 38(1):29–43
65. Gray P, Scott SK (1984) Autocatalytic reactions in the isothermal, continuous stirred tank reactor: Oscillations and instabilities in the system A + 2B $\rightarrow$ 3B; B $\rightarrow$ C. Chem Eng Sci 39(6):1087–1097
66. Gray P, Scott SK (1985) Sustained oscillations and other exotic patterns of behavior in isothermal reactions. J Phys Chem 89(1):22–32
67. Pearson JE (1993) Complex patterns in a simple system. Science (New York, NY) 261(5118):189–192
68. Lee KJ, McCormick WD, Ouyang Q, Swinney HL (1993) Pattern formation by interacting chemical fronts. Science (New York, NY) 261(5118):192–194
69. Denk J, Kretschmer S, Halatek J, Hartl C, Schwille P, Frey E (2018) MinE conformational switching confers robustness on self-organized Min protein patterns. Proc Natl Acad Sci USA 115(18):4553–4558
70. Wu F, van Schie BGC, Keymer JE, Dekker C (2015) Symmetry and scale orient Min protein patterns in shaped bacterial sculptures. Nat Nanotechnol 10(8):719–726
71. Shih Y-L, Kawagishi I, Rothfield L (2005) The MreB and Min cytoskeletal-like systems play independent roles in prokaryotic polar differentiation. Mol Microbiol 58(4):917–928
72. Wu F, Halatek J, Reiter M, Kingma E, Frey E, Dekker C (2016) Multistability and dynamic transitions of intracellular Min protein patterns. Mol Syst Biol12(6):642–653
73. Corbin BD, Yu X-C, Margolin W (2002) Exploring intracellular space: function of the Min system in round-shaped Escherichia coli. EMBO J 21(8):1998–2008
74. Touhami A, Jericho M, Rutenberg AD (2006) Temperature dependence of MinD oscillation in Escherichia coli: running hot and fast. J Bacteriol 188(21):7661–7667
75. Varma A, Huang KC, Young KD (2008) The Min system as a general cell geometry detection mechanism: branch lengths in Y-shaped Escherichia coli cells affect Min oscillation patterns and division dynamics. J Bacteriol 190(6):2106–2117
76. Männik J, Wu F, Hol FJH, Bisicchia P, Sherratt DJ, Keymer JE, Dekker C (2012) Robustness and accuracy of cell division in Escherichia coli in diverse cell shapes. Proc Natl Acad Sci USA 109(18):6957–6962
77. Fange D, Elf J (2006) Noise-induced Min phenotypes in E. coli. PLoS Comput Biol 2(6):e80
78. Renner LD, Weibel DB (2012) MinD and MinE interact with anionic phospholipids and regulate division plane formation in Escherichia coli. J Biol Chem 287(46):38835–38844

79. Otsuji M, Ishihara S, Co C, Kaibuchi K, Mochizuki A, Kuroda S (2007) A mass conserved reaction-diffusion system captures properties of cell polarity. PLoS Comput Biol 3(6):e108
80. Kac M (1966) Can one hear the shape of a drum? Am Math Mon 73(4):1
81. Thalmeier D, Halatek J, Frey E (2016) Geometry-induced protein pattern formation. Proc Natl Acad Sci USA 113(3):548–553
82. Loose M, Fischer-Friedrich E, Ries J, Kruse K, Schwille P (2008) Spatial regulators for bacterial cell division self-organize into surface waves in vitro. Science (New York, NY) 320(5877):789–792
83. Caspi Y, Dekker C (2016) Mapping out min protein patterns in fully confined fluidic chambers. eLife 5:e19271
84. Loose M, Fischer-Friedrich E, Herold C, Kruse K, Schwille P (2011) Min protein patterns emerge from rapid rebinding and membrane interaction of MinE. Nat Struct Mol Biol 18(5):577–583
85. Schweizer J, Loose M, Bonny M, Kruse K, Mönch I, Schwille P (2012) Geometry sensing by self-organized protein patterns. Proc Natl Acad Sci USA 109(38):15283–15288
86. Zieske K, Schwille P (2013) Reconstitution of pole-to-pole oscillations of min proteins in microengineered polydimethylsiloxane compartments. Angew Chem Int Ed Engl 52(1):459–462
87. Zieske K, Chwastek G, Schwille P (2016) Protein patterns and oscillations on lipid monolayers and in microdroplets. Angew Chem 128(43):13653–13657
88. Ivanov V, Mizuuchi K (2010) Multiple modes of interconverting dynamic pattern formation by bacterial cell division proteins. Proc Natl Acad Sci USA 107(18):8071–8078
89. Zieske K, Schwille P (2014) Reconstitution of self-organizing protein gradients as spatial cues in cell-free systems. eLife 3:e03949
90. Bonny M, Fischer-Friedrich E, Loose M, Schwille P, Kruse K (2013) Membrane binding of MinE allows for a comprehensive description of Min-protein pattern formation. PLoS Comput Biol 9(12):e1003347
91. Sliusarenko O, Heinritz J, Emonet T, Jacobs-Wagner C (2011) High-throughput, subpixel precision analysis of bacterial morphogenesis and intracellular spatio-temporal dynamics. Mol Microbiol 80(3):612–627
92. Vecchiarelli AG, Li M, Mizuuchi M, Hwang LC, Seol Y, Neuman KC, Mizuuchi K (2016) Membrane-bound MinDE complex acts as a toggle switch that drives Min oscillation coupled to cytoplasmic depletion of MinD. Proc Natl Acad Sci USA 113(11):E1479–E1488
93. Halatek J, Frey E (2014) Effective 2D model does not account for geometry sensing by self-organized proteins patterns. Proc Natl Acad Sci USA 111(18):E1817–E1817
94. Kretschmer S, Zieske K, Schwille P (2017) Large-scale modulation of reconstituted Min protein patterns and gradients by defined mutations in MinE's membrane targeting sequence. PLoS one 12(6):e0179582

Part IV
Biomembrane Mechanics and Consequences for Their Functions

Biomembrane Mechanical Properties Direct Diverse Cell Functions

Dennis E. Discher

Abstract The shape of any cell is defined and delimited by the shape of the outermost membrane of lipid. Whether a cell's membrane is locally flat, protrusive, or invaginated at a given instant is often the resultant of forces generated by molecules within the cell as well as those attributable to external factors. For mammalian cells, major changes in cell shape are evident in processes that include cell spreading, migration, and cell division as well as differentiation and death. Such processes are illustrated here for blood cells, starting with stem cells in bone marrow plus the many different types of circulating cells, particularly RBCs whose membranes have been more deeply studied for decades compared to other mammalian cell types. A handful of the key proteins that apply or resist forces at the membrane are described here while focusing on the cortical protein meshworks that underlie membranes and contribute to properties and processes. Engulfment of particles and cells is one particular focus, with broad relevance to disease and therapy. Equally interesting is the frequently noted observation that changes in cell shape and orientation are also evident in shape and orientation changes of the cell's nucleus—which is again delimited by a membrane. A final section focuses on the physics of a sub-membranous lamina in the nucleus, which interfaces with the genome and provides insight into mechanosensing and cell fates.

Keywords Red blood cells · Hematopoiesis · Membrane skeleton · Myosin · Mechanobiology · Nucleus · Lamins · Differentiation

A cell's shape is defined by how a cell's plasma membrane is spatially arranged in its three-dimensional microenvironment. Sculpting a cell at any instant in time are the forces within a cell—including forces actively generated through energy consumption—as well as forces from outside a cell such as extracellular pressure and fluid shear. The resistance to shape change under force is variously referred to

D. E. Discher (✉)
Molecular and Cell Biophysics Lab, University of Pennsylvania, Philadelphia, PA, USA
e-mail: discher@seas.upenn.edu

P. Bassereau, P. Sens (eds.), *Physics of Biological Membranes*,
https://doi.org/10.1007/978-3-030-00630-3_11

as stiffness, elasticity, rigidity, or plasticity; some deformations are of course fully reversible (i.e. elastic) while others are irrevesible (eg. plastic). Relatively stable cell shapes are achievable for just a few mammalian cells when isolated, and the red blood cell (RBC) with its symmetrically-dimpled "discocyte" shape is the best understood. Dynamic changes in the shapes of far more active cells are critical to cell functions that range from adhesion and migration to division, differentiation, and death. Understanding the mechanisms that underlie such essential cell processes requires clarifying the forces that locally shear, dilate, and bend membranes. This chapter seeks to introduce in broad terms a few of the basic cell biological processes that involve striking changes in cell shape, and in doing so we describe a small handful of the responsible proteins.

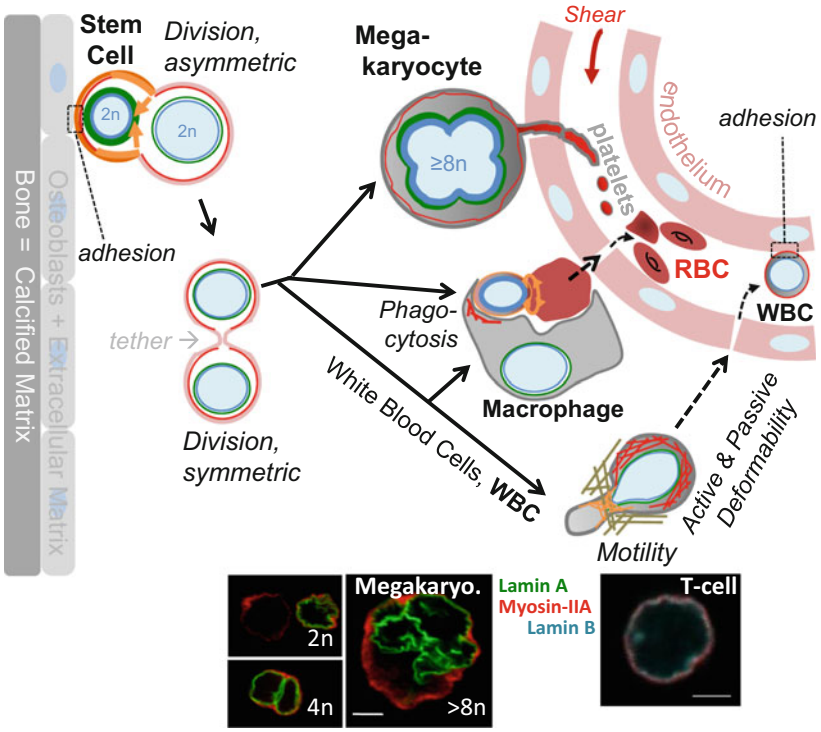

Fig. 1 Biophysical determinants of blood formation. Adhesion and contractile forces generated by MII are important in sensing matrix stiffness, which is heterogeneous in the BM microenvironment. During the cell division process, stem cells near the osteoblasts undergo asymmetric division to segregate MIIB into one daughter cell. Without MIIB, cells divide symmetrically. The other daughter cell becomes differentiated into three different lineages. Because MKs upregulate both lamin isoforms by endomitosis, they are too large to traffic through endothelial barriers. Instead, they undergo fragmentation into platelets. During erythroid differentiation, the nucleus shrinks in chromatin condensation. Condensed nuclei are too stiff to migrate through the endothelial barrier and are phagocytosed by macrophages, leading to enucleated RBCs. *RBC* red blood cell, *WBC* white blood cell, *HSC/P* hematopoietic stem cell/progenitor

An overall view of the diversity of membrane shapes and their changes within a mammalian system is perhaps best achieved by focusing on the various types of human blood cells and their ongoing development in bone marrow (Fig. 1). Human bone marrow collectively generates red blood cells, platelets, and white blood cells, each at a rate of roughly 100,000 per second. Production is matched in steady state by cell death and removal from circulation, which occurs on average after ~100 days for RBCs (red blood cells) in humans or just a few days to a week for platelets and some of the more abundant types of white blood cells. The longer life of the RBC thus explains why this is far more abundant than any other cell type in blood. The distinct multistep process by which an RBC is made and eventually destroyed provides many useful insights into biomembrane properties and forces that underlie remodeling of membrane shapes. Any terminally differentiated cell such as an RBC is derived from a less specialized cell referred to as a stem cell. Therefore, we begin by describing processes of the relevant bone marrow stem cell, focusing on the membrane and the stresses that control its shape—while. We also attempt to convey the importance of the cells and clinical motivations that every day save lives around the world.

1 Division: Fission Forces at the Membrane for Cell Differentiation

The long-term health of any tissue invariably requires that death or turnover of mature cells be balanced not only by differentiation from the relevant stem cell but also by self-renewal of the stem cell. These processes seem optimized in specialized tissue microenvironments called niches. Hematopoietic stem cells and progenitors (HSC/P) reside in bone marrow niches that are formed from extracellular matrix proteins and other cells. The latter include mesenchymal stem cells (MSCs) and MSC-derived lineages, namely, bone cells and fat cells [1]. Decades of clinical success in transplantation of HSC/Ps into patients [2] have motivated the exploration of mechanisms that underlie the balance between stem cell self-renewal, differentiation, and trafficking of mature cells from the marrow and into the blood circulation. Soluble factors and cell–cell contacts regulate these biological processes, but it is only recently appreciated that stem cells can generate and resist physical forces, while matrix stiffness and external stresses such as shear flow impact stem cell adhesion and intracellular signaling [3]. Structural proteins just below the cell membrane and even the nuclear membrane are major determinants.

Asymmetric division is one evolutionarily conserved mechanism that explains how stem cells both self-renew and differentiate [4]. A parent stem cell divides asymmetrically to give rise to one daughter cell that maintains stem cell characteristics and another that is committed to differentiation. Asymmetric segregation of proteins during division has been well documented in invertebrates [5], and in

HSC/Ps these include integral membrane proteins such as CD34 (a "surface marker" that might not be crucial to function and simply helps identify these cells) as well as proteins that contribute to asymmetric division [3]. While extrinsic adhesive cues from neighboring cells have been implicated in asymmetric division of some white blood cells [6], the requisite polarization of a cell is inextricably linked to its cytoskeleton. In blood cells, the actin-myosin cytoskeleton is just below the plasma membrane as a cortex (Fig. 1), with its forces and/or crosslinking helping to break the symmetry of the doublet of daughter cells to induce a polarized distribution of molecules. Microtubules maintain the stability of the polarization [7], but the stiffness of microtubules could also feedback and help direct the contractile activity of the actin-myosin cytoskeleton [8].

Myosin-II (MII) proteins are ATP-consuming motor proteins that assemble into bipolar filaments and apply both contractile forces to and active crosslinking of actin filaments which, in turn, link to a diverse set of membrane proteins. In comparison to the non-muscle MII in blood cell types and other non-muscle cells, cardiac MII in heart muscle striates the cytoplasm of heart cells and contracts rhythmically to pump blood out of the heart. Skeletal muscle MII likewise striates the cytoplasm of elongated muscle cells, and its neuron-triggered, voluntary contractions drives body movements. Non-muscle MII is more closely related to the most evolutionary ancient form of MII that is found even in some single-cell organisms. Among its many cellular functions in non-muscle cells, MII confers the cell-intrinsic cortical tension that both stabilizes the plasma membrane [9, 10] and drives cell division (cytokinesis). The latter is achieved through a coordination of forces in the constriction ring and at the opposite poles of the daughter cells [11]. Cortical tension is also modulated at least locally by adhesion to stiff extracellular matrix [12, 13], which provides a mechanism by which MII regulates the ability of cells to sense physical properties of the matrix such as matrix elasticity, E. A simple intuition into mechanosensing is obtained by considering that actin polymerization drives cell spreading at a near constant rate, $v_{\text{polymer}} = A$, whereas MII pulls back on the actin network at a rate $v_{\text{retract}} = B\,/\,(K + E)$ which is a hyperbolic decrease (with constants B, C) with resistance set by the extracellular load E (as with muscle, low speed at high loads). The extent of cell spreading relates to a steady state $v_{\text{polymer}} - v_{\text{retract}} = A - B\,/\,(K + E)$ that yields minimal cell spreading for $E \ll K$ and maximal spreading for $E \gg K$ as observed for spreading cells [12]. A typical value of $K \sim 5$ kPa [12], in units of stress or pressure, should be multiplied by a typical cell-generated strain of ~5% [12] and then related through the well-known law of Laplace to an effective tension ~ 0.1 mN/m in a typical protrusion curvature radius of ~1 μm. A cortical tension of ~ 0.1 mN/m has indeed been measured for HSC/Ps, and this tension decreases dramatically with MII inhibition [10].

For at least some stem cells, matrix mechanosensing can regulate cell differentiation [12, 13]; inhibition of MII also limits the proliferation of HSC/P when these cells adhere to a highly flexible or soft matrix [13]. However, in order for daughter cells to migrate away from each other, actin seems necessary while MII is not needed; such migration can help stretch and break a lipid tether or membrane nanotubule that is often the final vestige of the cytokinetic furrow [8]. Other membrane

factors in stem cells are also likely to contribute to cleavage and repair of the nano-tubule.

Cell force generators have evolved to be fine-tuned by slightly more specialized molecules, which has come to reveal how important the proper forces and dynamics need to be for cell function. In particular, humans express three myosin-II genes (MIIA, MIIB, and MIC) with different properties. MIIB appears especially key to asymmetric division of HSC/Ps [3]. MIIB motors make notably stable assemblies with actin filaments and can be seen to polarize within cells due to external stiffness or perhaps stresses such as fluid shear [3]. The latter forces could be relevant to triggering blood formation in early embryos [14]. Soft microenvironments do not sustain or transmit high stress, which limits myosin-IIB forces and polarization, and since bone marrow is very soft compared to rigid bone, polarization is more likely on the latter. External cues and spontaneous intracellular fluctuations in the cell cortex [15] could cause polarization during cell division of adult HSC/Ps, but it is very clear that MIIB segregates asymmetrically to the cortex of the one daughter cell that maintains stemness (i.e., CD34 high cells). The other nucleated daughter cell with less MIIB is thereby differentiated, and MIIB is similarly reduced per division in differentiation—at least in differentiation toward white blood cells and cells called megakaryocytes that make platelets. Asymmetric segregation of MIIB likely establishes an asymmetric cortical tension that drives differentiation, although physical differences still need to be measured.

As MIIB is downregulated in differentiating cells, MIIA is activated by dephosphorylation. This change favors MIIA assembly into filaments that again localize to the cortex. However, soft matrix favors MIIA phosphorylation. Soft microenvironments thus maintain early HSC/Ps by suppressing a switch of myosin-II's from high to low levels of MIIB and from deactivated to activated MIIA. Stiff microenvironments that resist stress have the opposite effect and initiate asymmetric division and differentiation.

RBCs have much higher levels of MIIB than platelets and white blood cells. Although myosin-II's in mature RBCs are probably vestigial in not contributing greatly to discocyte-shaped RBCs, they do contribute to the loss of nuclei during formation of RBCs. In particular, MIIB helps to polarize the nucleated RBC progenitor (called an erythroblast) and to expel the cell's nucleus in a final step of asymmetric division [16]. The expelled nucleus is rigid [3] compared to the nascent RBC, which is called a reticulocyte. As in cytokinesis, the nucleus remains tethered by a membrane nano-tubule to the reticulocyte [17]. Eventually, the tether is severed as the nucleus is engulfed by white blood cells called macrophages that reside in bone marrow as well as all other tissues [18]. Engulfment might be accompanied by macrophage-facilitated expulsion of the reticulocyte from the marrow into the blood vessels flowing through the marrow. The latter speculation is based on an absence of any data showing that reticulocytes can move or crawl. Megakaryocytes serve as a useful comparison since they actively extend pseudopods into the bloodstream via membrane-protrusive polymerization of actin and microtubules (as myosin is phospho-inhibited). The pseudopods then fragment under shear to make pre/pro-platelets [19] that are about half the size of a mature RBC. Once in the circulation,

these giant pre/pro-platelets divide to make the small and abundant platelets, and division uses MIIA that is normally activated by fluid shear unless mutations in MIIA keep it aggregated [20]. The latter mutations give rise to *MYH9*-related diseases (i.e., MIIA related diseases) that lead to "macro-thrombo-cytopenia," which refers to giant platelets that are few in number. RBCs appear relatively normal in number and shape in these patients even though a recent study of mature RBCs [21] concluded that pharmacological inhibition of myosin-II could generate a very small fraction of 'elliptocytic' RBCs. Platelet maturation thus finishes within the circulation to a much greater extent than with RBCs. What remains in the marrow from the megakaryocytes after production of many pre/pro-platelets is just a giant nucleus unable to cross the small micro-pores into the sinusoids. This nucleus that is stuck in the marrow is engulfed by macrophages. The same occurs with RBC nuclei after generation of a reticulocyte.

As with platelets, RBC maturation also finishes within the circulation: the reticulocyte sheds membrane and volume (15% and 10%, respectively [22]) within hours to become the discocyte-shaped RBC. In this final remodeling, more lipid is observed to be lost than cortical cytoskeleton, and this cytoskeleton is particularly enriched in the actin-crosslinking protein spectrin which forms a two-dimensional spectrin-actin network that attaches below the lipid bilayer. The relative loss of lipid thus increases the overall stoichiometry of 2D cytoskeleton to 2D lipid membrane. The spectrin network has been observed to dilate strongly at the tip of an RBC projection that is aspirated into a micropipette (Fig. 2) [23, 24], but in the absence of such external forces the state of stress in the "at rest" spectrin-actin network remains a matter of uncertainty. The cortical network could be under constant tension and tending to pull away from the bilayer [25], or the network could be stress free or else compressed. The cited loss of lipid relative to cytoskeleton is consistent with the network being compressed by the more limited overlying lipid bilayer, and in this case the lipid bilayer is under an equal and opposite tension which smooths and suppresses fluctuations of the lipid bilayer. Such a balance of membrane forces does not set global cell shape as the forces are too weak. Rather, the flaccid discocyte shape results from volume regulation and the relatively fixed cell area set by the near incompressibility of the lipid bilayer.

The RBC cytoplasm lacks all other organelles and is predominantly a highly concentrated fluid of hemoglobin protein (with chelated iron that makes RBCs red) plus many other macromolecules and counterions that cannot permeate the lipid bilayer. Water readily permeates the few-nanometer-thick bilayer, despite the oiliness of the core of the lipid bilayer, so that the entrapped solutes attract and retain hydrating water in strict relation to the osmotic pressure outside the cell. Thus, to first approximation, RBC volume is not regulated by membrane physical properties but could affect membrane state—such as rupture and lysis in hypo-osmotic media. Importantly, the shear resilience of an increasingly compressed spectrin-actin network would tend to resist further rapid fragmentation of the RBC, so that a cell circulates for another ~100 days after quickly shedding 15% of its initial plasma membrane and losing a smaller fraction of its cytoplasmic solutes and membrane skeleton. Old RBCs have ~3–6% less hemoglobin mass relative to

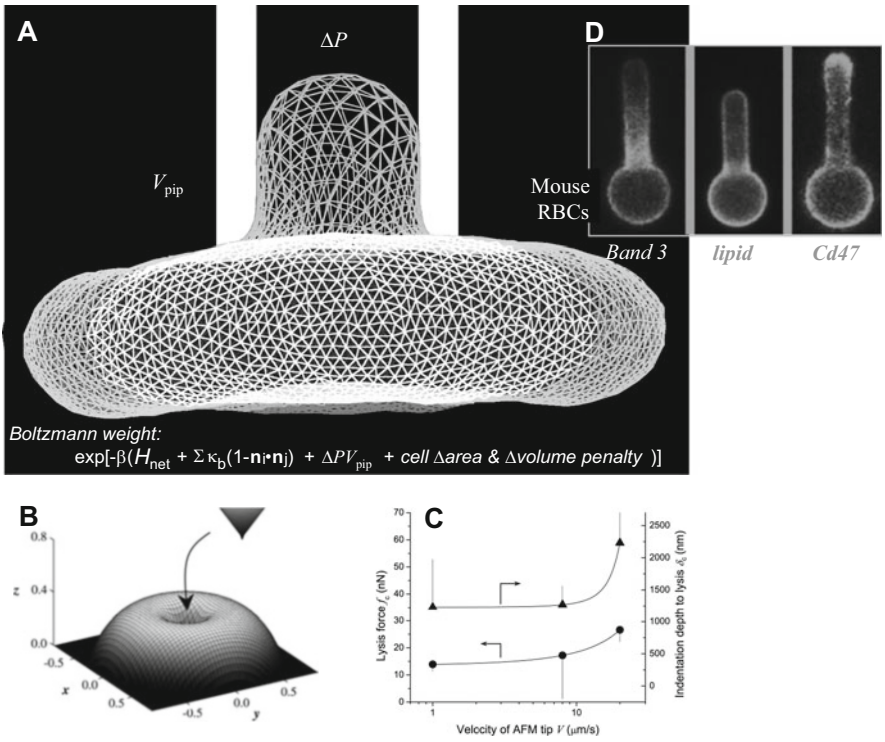

Fig. 2 (**a**) Simulation of a near full-scale RBC under aspiration. The surface of the cell is triangulated with 6110 vertex nodes that represent the spectrin-actin junction complexes of the erythrocyte cytoskeleton. Mouse RBCs have about two-thirds the surface area of human RBCs and are estimated to have about 18,000 spectrin-actin nodes, so that the simulation is about one-third scale. The volume of the cell is 0.6 times the fully inflated volume, and the snapshot is from simulation of a stress-free meshwork. (**b**) AFM indentation in a continuum calculation of an axisymmetric shape with isotropic tension and elastic dilation of the membrane, but no bending resistance. (**c**) With increasing velocity, v, of the AFM tip, the lytic force, f_c, needed to penetrate the tensed RBC membrane increases exponentially as does the indentation depth until lysis. (**d**) On mouse RBC membranes, the membrane protein Band 3 appears largely connected to the cytoskeleton, whereas another membrane protein Cd47 appears completely mobile, squeezing out to the tip of the aspirated membrane. Lipid is uniformly distributed with equal entrance and cap intensities

the bulk population [26], which indicates that the membranes of these cells rarely rupture under shear or else they rapidly reseal. Regardless, old RBCs are removed from circulation as they are engulfed or "phagocytosed" by macrophages located near slit-like blood vessels within the spleen.

Some additional physical aspects of the prototypical RBC membrane should be highlighted before proceeding to the next section on phagocytosis, with a focus on membrane-mediated interactions and cytoskeleton-driven adhesion. First, the simplicity of the RBC membrane has lent itself to a rapidly increasing number of

molecular and multiscale simulations that increasingly capture the fine structure and 2D elastic properties of the spectrin network as well as the resistance of the bilayer to both dilation and bending. One such free energy expression used in whole cell simulation (Fig. 2) has employed a "Hamiltonian" for a triangulated meshwork of spectrin chains that have both steric exclusion (as $\sim c$ / *Area* for each triangle, with c being a constant) and worm-like chain stretching energy of the spectrin chains (as fraction x of the maximum contour length):

$$H_{\text{net}} = \Sigma_{\text{triangles}} c/\text{Area} + \Sigma_{\text{bonds}} k x^2 \,(3 - 2x) \,/\, (1 - x)\,, \tag{1}$$

where k quantifies spectrin's stiffness when stretched. A change in position of a node in a triangle due to a thermal fluctuation or external force such as aspiration into a micropipette or fluid shear costs energy, which should—as a goal—reach a global minimum for the discocyte shape under stress [27]. As a function of pressure, a linear increase in length of aspirated membrane for a flaccid RBC reveals the apparent shear elastic modulus of the spectrin-actin network, which is in the range of 0.006–0.009 mN/m. This is tenfold softer than the MII-dependent cortical tension of ~0.1 mN/m typically measured for cells including HSC/Ps [10].

Membrane proteins bind to the spectrin network, so that dilation of the deformed spectrin meshwork that is evident in simulation is also seen in experiments to cause a similar density gradient of attached membrane proteins (e.g., Band 3). The steric bulk of such proteins excludes mobile membrane proteins (e.g., mouse-CD47), whereas lipid remains uniform [23]. In this way at least, the local membrane density of both mobile and immobile membrane proteins is mechanosensitive. Futhermore, unfolding of the spectrin protein when stretched has been demonstrated in intact RBC membranes [28], which provides a means for the ubiquitous spectrin network to contribute to membrane mechanosensitivity of many cell types.

Beyond the small elastic dilation limits of the bilayer, poration of RBCs with loss of hemoglobin can occur physically as well as upon addition of various chemicals that insert and disrupt the lipid membrane. Even a simple tool such as the sharpened tip of an atomic force microscope cantilever can indent adhesively attached RBCs to stress the membrane and rupture it [29, 30]. Differential geometry is useful for calculating the continuous, equilibrium shape of an indented cell up to rupture. Regardless, the rate dependence of such a process is an expected signature of stochastics in failure [31].

2 Phagocytosis and Adhesion: Microbes, Colloids, and Key Molecular Pathways for "Self" Cells

Phagocytosis was already mentioned above as important to both the removal of nuclei from the progenitor cells that make RBCs or platelets and also the clearance from circulation of old RBCs (platelets, and other cells also). Biophysical factors

and molecular factors both determine whether a macrophage engulfs an entire cell or just a nucleus. A "macro*phage*" is a large cell that *devours*, with principal "targets" for engulfment being microbes that constantly cross beach tissue barriers. The occasional serious pathogen might include malaria parasites which are notable for having a blood stage in which this microbe enters an RBC to digest hemoglobin and replicate. Additional targets of phagocytosis are now well appreciated to include all types of injected colloids, including nanoparticles, and also dying cells (or nuclei) in the same tissue, but there are also exciting efforts to make macrophages eat cancer cells. Multiple features of a target influence eating by a macrophage, including surface molecules that promote adhesion and eating, but also at least one molecule that inhibits eating as elaborated below. In addition, physical properties such as target shape and target rigidity impact phagocytosis efficiency of the target.

Phagocytosis is undoubtedly an ancient evolutionary development that provided sustenance to some of the first amoeboid cells. With soft plasma membranes rather than the rigid cell walls of bacteria, ancient amoeba (like modern amoeba typified by *Dictyostelium*) could wrap around their target to engulf it and digest it within a phagosome [32]. Fast forward eons to organisms like humans that gain nutrition through a highly differentiated and multicellular digestive tract, and we find that phagocytosis within humans is a highly efficient process used primarily by specialized white blood cells of the mononuclear phagocyte system. Microbes (in and on us) remain major targets as they not only outnumber and outproliferate our own cells but also invade through any and all compromised tissue barriers [33]. Principal cell types of the mononuclear phagocyte system are macrophages which reside in every tissue and monocytes that circulate out of the bone marrow to enter a tissue and differentiate to macrophages [34]. These cells as well as the highly phagocytic neutrophils must—for the health of the organism—choose to devour "foreign" targets rather than devour human "self" cells or extracellular matrix that generally surrounds the phagocytic cell. Phagocytosis thus evolved for engulfment and destruction of "foreign" strictly for protection of the organism.

A variety of molecular cues and sensor assemblies must be used by our phagocytic cells to distinguish and destroy "foreign" amidst "self." Many decades of work have elaborated a list of biochemical entities, soluble and/or surface bound, which activate macrophages (we will hereafter ignore the distinction from monocytes) to initiate engulfment of a target. One of the most important classes of molecules that is described below in context are immunoglobulin-G (IgG) antibodies which diffuse and bind to a target surface so that when a macrophage contacts the target, the constant fragment (Fc) of the IgG binds the macrophage membrane receptor FcγR and (for some classes of FcγR) activates the macrophage to eat the opsonized target (Fig. 3). Importantly, while it is commonly presumed that our "self" cells simply lack such surface "opsonization" by activating molecules such as IgG, it is now clear that "self" recognition is *not* simply the absence of a "foreign" signal. Instead, a dominating and passivating interaction occurs between a "Marker of Self" CD47 membrane protein on a candidate target and the macrophage membrane receptor CD172a (also known as SIRPA, signal-regulatory protein alpha). Controlling the balance of "eat me" cues (e.g., IgG-FcγR interaction) and "don't eat me" signals

(CD47-SIRPA) is currently an active area of translation to the clinic for anticancer therapy [35] and has begun to be exploited on nanoparticles in preclinical models [36]. However, the decision-making process within the macrophage remains a topic in need of deeper insight.

An explosion of efforts to make a broad range of injectable and implantable particles or devices for therapy and diagnostics has also revealed phagocytes to be a major impediment to delivery. Make a nanoparticle, inject it into the bloodstream of a mouse or man, and one invariably finds that most of the particles have been eaten by macrophages of the spleen and of the liver (the latter are called Kupffer cells). Based on several decades of work on a diversity of nanoparticles, such clearance can be delayed but never eliminated [37–40]. Studies of macrophages in conventional static culture where nanoparticle diffusion and buoyancy can dominate have questioned whether evident uptake of small nanoparticles occurs by phagocytosis [36] or not [41]. In vivo, however, blood-borne nanoparticles flow into contact with macrophages that line the spleen and liver vasculature, where these cells constantly and actively filter out dying and energy-depleted blood cells (e.g., after blood storage) to maintain blood homeostasis. A leaky vasculature at a site of injury or disease such as an infarct in the heart or a tumor can allow sufficiently small particles to permeate tissue and perhaps be retained [42]. However, when macrophages in damaged and disease sites are examined, they prove to be major consumers of permeating nanoparticles [43]. Macrophages are indeed resident if distinct in every tissue in the body [34], and at damaged and disease sites they will at least be involved in clearing dead and dying tissue. A large implant (or even a splinter) also damages tissue and causes a "foreign body response" that starts with serum protein deposition and soon recruits phagocytes to the site, but phagocytosis is frustrated for large implants and somehow triggers macrophage–macrophage fusion to a "foreign body giant cell" that encases the implant [44]. Physical size is thus a factor in macrophage function, but the focus below is on targets including cells that are cell-sized or smaller, with attention to additional properties such as target rigidity and shape as well as surface signaling (Fig. 3). Despite the decades of work on synthetics, there is nothing more biocompatible than a properly matched blood transfusion, but the reasons why continue to be elaborated.

"Eat me" signals can be weak or strong but are unavoidable. IgGs are well known for high-affinity interactions (∼nano-Molar) between epitopes and their antibody fragment (Fab) domains, but they are also large glycoproteins of ∼150,000 Daltons with considerable surface area to mediate nonspecific interactions. They are among the most abundant proteins in normal serum at ∼100 μM. Antibodies and other serum proteins physisorb in vivo to red blood cells (RBCs) [45, 46], to viruses [47], and even to particles coated with PEG (polyethylene glycol) which otherwise delays adsorption and in vivo clearance from minutes to many hours [48, 49]. Autologous IgG binding to autologous RBCs in humans and dogs in vivo increases up to sevenfold toward the end of the cell's ∼100-day life span. Aged human RBCs lack additional "eat me" signals such as exposure of the negatively charged lipid phosphatidylserine [46, 50]. IgG opsonization is increased in blood diseases including sickle cell anemia and malaria among other conditions, where

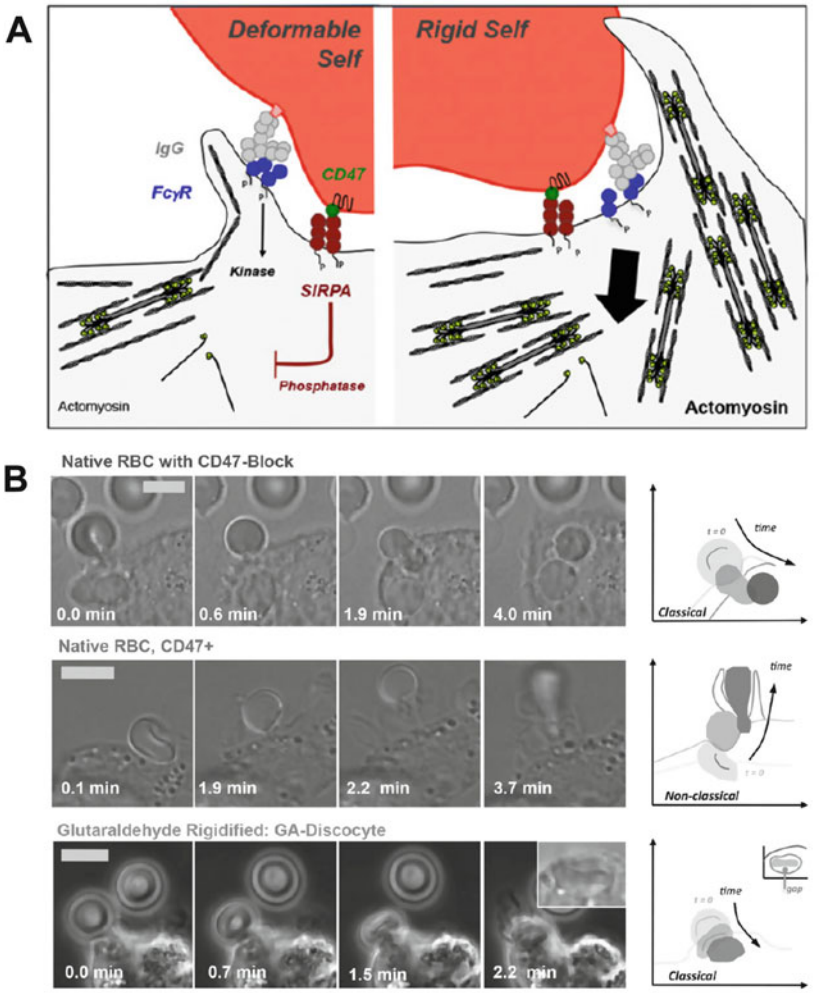

Fig. 3 (**a**) On both rigid and native flexible RBCs, SIRPA binds CD47. Downstream of FcgR binding of IgG, kinases phosphorylate multiple cytoskeletal proteins, including myosin-II, which drive assembly of the phagocytic cup and promote uptake. CD47-SIRPA signaling leads to activation of SHP-1 phosphatase that can deactivate myosin-II. Because substrate rigidity initiates assembly and polarization of myosin-II in many cell types, phagocytic target rigidity is expected to counterbalance CD47-mediated inhibition of the motor. Our working hypothesis is that with flexible self-cells (left), CD47-initiated inhibition can overcome myosin-II activation, whereas with rigid self-cells (right), the myosin-II driven cytoskeleton is not diminished by CD47-SIRPA self signals. (**b**) Phagocytic uptake of opsonized RBCs is faster with CD47 inhibition but fastest for rigid RBCs. Human-derived THP-1 macrophages were incubated with human RBCs that were opsonized with anti-hRBC antiserum and also blocked with anti-CD47, native RBCs with active CD471, or rigidified as GA discocytes. Time-lapse imaging in DIC and phase contrast begins with initial adhesion between macrophage and RBC targets and ends on complete engulfment (scale bar, 8 μm). At the right of each time-lapse series, silhouettes of the target RBC clarify the changes in RBC morphology over the course of engulfment and RBC position relative to the macrophage boundaries, as indicated by the sketched lines

phagocytosis and cell clearance are also increased (tabulated recently in [51]). When IgG-opsonized RBCs and particles are phagocytosed in vitro, uptake is hyperbolic and saturable versus IgG, which is consistent with specific activation of the FcγR phagocytosis pathway. Because macrophages and phagocytic dendritic cells can also function as antigen-presenting cells to the white blood cells of the "acquired immune system," it seems sensible that engulfment can promote immunogenicity in vivo even to foreign polymers [52].

Binding of the IgG's Fc domain to the macrophage FcγR receptor triggers phagocytic cup formation in a coordinated process of adhesion, pseudopod extension, and eventual internalization with phagosome closure. The surface interactions initiate Src family kinase phosphorylation of immunoreceptor tyrosine-based activating motifs (ITAMs) that then propagate a phosphorylation cascade [53]. Phosphopaxillin and F-actin [54, 55] accumulate in minutes or less together with other structural components at this dynamic phagocytic synapse. The process is highly analogous to adhesion formation upon integrin binding to rigid extracellular matrices, wherein the nascent adhesion matures to a focal adhesion only when the F-actin cytoskeleton is mechanically organized through pulling by non-muscle myosin-II (MII) phosphoprotein [56, 57]. At the phagocytic synapse, MIIA accumulates to greatly help with pulling targets into a macrophage, including IgG-opsonized targets as small as 100 nm nanoparticles (perhaps smaller) and at least as large as opsonized RBCs [36, 58, 59]. Engulfment of such targets is greatly decreased by inhibiting MIIA motor activity with the drug blebbistatin which also blocks MII localization without affecting F-actin or phosphopaxillin. Uptake increases linearly with MII activity based on its knockdown and overexpression [58]. At least above a low baseline level of uptake in vitro, MII makes phaogocytosis efficient for our macrophages if not for ancient amoeba like *Dictyostelium* [32].

As an IgG-opsonized target contacts a macrophage and adheres intimately via FcγR, the parallel presence on the target of an appropriate form of CD47 can lead to binding to the macrophage phagocytosis inhibitory receptor SIRPA, which accumulates in the synapse [59]. The latter complex somehow phosphorylates SIRPA's cytoplasmic immunoreceptor tyrosine-based activating motifs (ITIMs), which activates the immunomodulatory phosphatase SHP-1 (Src homology region 2 domain-containing phosphatase-1) [60] to regulate multiple proteins by dephosphorylation [61], including deactivation of MIIA [36, 58]. SIRPA-null macrophages engulf IgG-opsonized mouse RBCs more readily than wild-type macrophages [61] and show no major differences in phospho-FcγR nor the downstream effectors phospho-Syk or phosho-Cbl, which suggests that regulation of proteins even further downstream is key. Inhibition of downstream actomyosin contractility at the phagocytic synapse [36, 58] could indeed explain various observations that CD47 partially blocks engulfment of not only mouse RBCs—which started the expanding "Marker of Self" field [62] but maybe also cancer cells [63–65] and opsonized polystyrene beads (100 nm to 6 μm) that display CD47's binding domain in parallel with IgG [36, 58]. The effectiveness of CD47 with small nanobeads is surprising because pulling in *large* particles with MII forces seems more understandable

than pulling in *small* particles. Nonetheless, CD47's mechanism of inhibition is ultimately: just don't pull it in!

CD47 and SIRPA arose in evolution at the same time in amniotes and are not found even in amphibians [66]. CD47 and SIRPA are thus more recent inventions than the ancient actomyosin cytoskeleton found even in amoeba such as *Dictyostelium*. CD47 is found on all cells in man and mouse while the expression of SIRPA is more restricted. CD47 knockout mice have one-quarter to one-half the life spans of normal mice (at least for some strains) and also show evidence of anti-RBC antibodies as well as anemia [67]. This is consistent with the idea that a modest level of opsonization exists in vivo, which tilts the balance toward engulfment and possibly even an acquired immune response with antibody generation.

Saturable binding of SIRPA, CD47, and/or CD47-derived "Self" peptide to beads as well as to living cells shows that an intermediate strength interaction (sub-micro-Molar) has evolved to be largely species specific [36, 58, 68]. The molecules also differ between strains of mice. NOD-SCID strains of mice uniquely express a SIRPA variant that binds human CD47 with similar affinity as human SIRPA, which partially explains why these are the best mouse choice for engraftment of human stem cells [69]. Species specificity in vivo is a critically important issue because human-specific blocking antibodies have been injected intravenously together with opsonizing IgG to impede growth and even shrink tumors of human cancer cell lines in mice. As emphasized by others [70–72], injection of any reagent that binds human-CD47 would bind to every cell membrane in the body, even if cancer cells have severalfold more of this ubiquitous protein [73, 74]. On the other hand, CD47 is far from the most abundant protein on cells ($\sim$250 molecules/μm^2 on RBCs which is 10–20-fold less than Glycophorin-A), so that blocking CD47 even with IgG is not expected to drive strong phagocytosis unless an additional and far more abundant "eat me" cue is also bound to a candidate target. The half-max density for inhibition by CD47 on beads is independent of particle size and is $\sim$20 molecules/μm^2, which is consistent with the minimum density of CD47 on circulating RBCs from patients with anemia [36, 58]. For senescing neutrophils, CD47 is somehow downregulated from the surface and the needed cue to drive macrophage engulfment seems to be surface-exposed calreticulin (from the endoplasmic reticulum) rather than IgG [75]. Some of the above ideas are currently being put to the test in the clinic [35]. Safety is of course the first question of concern for systemic injection of any entity that limits macrophages from recognizing "self", and loss of RBCs from circulation is readily expected to be observed when patients are injected with anti-humanCD47 IgG.

Rigid cells and particles drive phagocytosis, but shape and size of a target can also frustrate engulfment. A relatively new principle in cell biology that applies to many cell types is that adhesion-induced activation of myosin-II is maximized by adhesion to a substrate that is rigid (like glass or plastic) rather than flexible like most soft tissues [12]. Bacteria such as *E. coli* and fungi such as yeast have cell walls as rigid as some plastics [76]. For the RBC precursor erythroblasts that interact with macrophages, the effective cell stiffness relative to mature RBCs has been measured by micropipette aspiration to be 50-fold higher, and senescence is

also higher in senescence and in diseases ranging from inherited anemias to malaria (tabulated in [51]). With spherical microparticles made of hydrogels and opsonized by IgG, engulfment is proportional to stiffness, which was also shown to drive focal adhesion protein assembly at the synapse [77]. Cell stiffness changes occur with cancer and with chemotherapy [78, 79]. Soft cancer cells might thus escape anticancer efforts aimed at inhibiting CD47–SIRPA interactions [63, 64]. However, a clear relation of cell or particle stiffness to CD47 signaling and to cells with more complicated shapes had been untested until recently.

With normal human RBCs, controlled stiffening could be achieved within seconds by the addition of a protein crosslinker (divalent and covalent) that does not compromise binding of CD47 to SIRPA [22]. Measurements showed that RBC Stiffness $\sim$ exp(crosslinker concentration/a). The stiffened RBCs that were highly opsonized by IgG were engulfed faster and in greater number according to "Self" Phagocytosis $\sim$exp(crosslinker concentration/b). A ratio (a/b) ~ 0.5 was determined so that we can eliminate crosslinker concentration to arrive at:

$$\text{“Self” Phagocytosis} \sim \text{Stiffness}^{0.5}, \tag{2}$$

which is a power law typical of mechanosensitive pathways dependent on myosin-II [80]. When CD47 is not on the target as is typical in past studies of polymer beads [77], estimates of bead stiffness based on the amount of crosslinker used (per [12]) suggest a stronger exponent of $\sim$1 in Eq. (2) that is generally consistent with "Self" inhibition of phagocytosis.

Rigid RBCs showed active myosin-II at the synapse [51], which suggests that CD47 cannot signal effectively even though it binds SIRPA. As expected, the MII inhibitor blebbistatin blocked MII accumulation and RBC engulfment. Injection of rigid RBC discocytes into the circulation of a mouse also confirmed equal clearance by splenic macrophages independent of whether CD47 was blocked or not with antibody. Synthetic polymer discs resembling RBCs and that lacked any CD47 or other RBC proteins were also shown to be removed from circulating blood far more rapidly when they were stiff rather than soft [81]. Mechanistically, stiff cells and particles become stuck in narrow splenic slits [82], which could facilitate probing and clearance by splenic macrophages [83].

The results which show rigid RBC *discocytes* are engulfed independent of CD47 present a paradox for the field in that rigid, *spherical* beads that display CD47 are reproducibly capable of signaling self and thereby impeding engulfment both in vitro and in vivo [36, 58]. *Shape* is an additional target factor that also modulates phagocytosis and resolves the apparent paradox. Polystyrene microbeads distorted into diverse shapes are always equally rigid but have been shown to be engulfed more readily as spheres than as non-spheres when IgG opsonized [84]. In many studies of other cell types, the topography of a substrate affects cell attachment and is sometimes referred to as "contact guidance." For macrophage engulfment, the dependence on target shape seems relevant to the diverse shapes of bacteria and fungi that are invariably rigid as noted above. Flexible PEG-based filaments also persist in the in vivo circulation many days longer than spherical particles of the

same type of polymer, with particles always eventually cleared by spleen and liver macrophages [38].

With normal human RBCs, the rapid and controlled stiffening approach [51] was used to make rounded, cup-shaped RBC "stomatocytes" that signal "self" much better than rigid RBC discocytes. The problem with a discocyte is that its rigid concavities cannot contact and signal "self" to the macrophage which builds up a high cortical tension when activated by IgG via Fc receptor. In the same studies, native and flexible human-RBC discocytes with the requisite IgG opsonization were seen in video microscopy to be greatly distended by the human macrophage, with myosin-II turned off by CD47 signaling but actin polymerization driving protrusions as if pushing the cell away in recognition of "self." Thus, since rigid but rounded cells do signal "self"—even if not as efficiently as flexible RBC—one can ultimately understand the success in delaying clearance of CD47-nanobeads that then enable better tumor imaging and drug delivery. However, it seems that a greater advantage might be achieved with flexible beads that avoid the intrinsic activation of myosin-II.

There are some important implications of phagocytic interactions for the production of RBCs within bone marrow. RBC stiffness is one among many factors including shape that changes in erythropoiesis. A plausible mechanism is that the macrophage senses both a rigid nucleus *and* a soft nascent reticulocyte, which is a cue for the macrophage to help pull the erythroblast apart provided that CD47 on the reticulocyte effectively signals "self." Target size (e.g., small nucleus versus large retic) *does not* affect uptake provided molecular densities are properly calculated [36], but additional polarized "eat me" factors might signal the macrophage to pull on a nucleus for its rapid engulfment. With mouse erythroblast nuclei, phosphatidylserine (PS) flips within minutes to the outer leaflet to promote engulfment, although PS flipped only "when cultures were subjected to weak physical stress" [85]. CD47 might be present at low levels on nuclei isolated from erythroblast cultures [86], and we had shown CD47 levels as low as ~10% of levels on RBCs still impede eating, consistent with the lowest levels of CD47 on RBCs reported in the human population [59]. Nuclear rigidity thus seems a major "eat me" cue.

3 Nuclear Membrane Properties and Mechanosensing in Brief

Although mammalian RBCs have only the outer plasma membrane, the RBC progenitor has abundant internal membrane systems, including endoplasmic reticulum which is continuous with the double bilayer of the nuclear envelope. A meshwork of proteins again forms as a sub-membranous cortical layer or lamina, and an understanding of the complex physical properties of this nuclear lamina is just emerging. Unlike the actin filaments and actin-crosslinking proteins spectrin and myosin-II that are main constituents of plasma membrane cortices discussed above

for RBCs and the other hematopoietic cells, the nuclear lamina meshwork is formed from self-assembling intermediate filament proteins, called lamins. The lamina lies just inside the nuclear envelope and interacts at least indirectly with chromatin, but the lamina also has protein linkages to nuclear membrane proteins that interact with the cytoskeleton outside the nucleus. The nucleus is thus embedded within and also linked to the stress-generating cytoskeleton, which deforms the nucleus, perhaps affecting gene expression as well as genome integrity. As suggested by the various types of differentiated cells sketched in Fig. 1, nuclear shape and orientation tend to track with cell shape and orientation—which has long been noticed in various nucleated cells (e.g. marrow derived MSCs [87]).

In humans and mice, the main forms of lamin protein are expressed from three genes: lamin-A, lamin-B1, and lamin-B2. Like other intermediate filament proteins, such as keratin in skin, fingernails, and horns, the lamins form coiled coil parallel dimers that assemble into higher-order filamentous structures that fulfill important structural roles [88]. The B-type lamins are distinct in being permanently modified by a greasy farnesyl group that promotes avid interactions of these filaments with the innermost leaflet of the nucleus' double lipid bilayer and these lamins also interact with lamin-B receptor, which is a transmembrane protein [89]. Such interactions will tend to act as effective physical crosslinks of a meshwork of lamin-B filaments, even though there no reported lamin crosslinker proteins.

Lamin-A was found in a proteomic study of diverse tissues to be almost unique among hundreds of abundant proteins of the cytoskeleton and nucleus, in that lamin-A concentration increased 30-fold as a function of increasing stiffness of tissue, E_{tissue}, from soft bone marrow and brain tissue to stiff muscle and rigid bone [80, 90]. Tissue stiffness is defined of course by how resistant the tissue is to stress and thus relates to the stress in functional tissue: bone sustains and resists high mechanical stress whereas marrow is protected by bone from stress, as is brain, and both shear very easily. Such mechanical differences between tissues are largely attributable to the amount of collagen fiber in the extracellular matrix, which is abundant in bone and minimal in marrow and brain [80]. The finding for lamin-A thus suggests that the nucleus adjusts its levels of this protein to the mean stress σ in most cells and their nuclei in a given tissue, whereas B-type lamins remain nearly constant. Importantly, the stress σ likely tracks the active (and passive) stiffness of a cell, especially contractile activity of myosin-II inside a cell that increases with matrix stiffness In terms of the tissue-type dependent stoichiometry (A:B), an experimental correlation emerges from measurements of composition and mechanics:

$$\text{lamin-A} : \text{B} \sim E_{\text{tissue}}^{0.6} \sim \sigma_{\text{tissue}}^{0.6}. \tag{3}$$

As a relevant aside given this chapter's broad focus on the sculpting of cell membrane shapes, the only other protein discovered in the same proteomic study to exhibit such a strong and clear scaling relationship across diverse tissues is a membrane-interacting protein called cavin-1. Cavin-1 is known to regulate the morphology of mechanosensitive plasma membrane invaginations called caveolae

[91, 92]. Such a scaling relationship with stress is an indicator of mechanosensing by such proteins, and since lamin-A is also a filament-forming structural protein, it should directly affect nuclear mechanics.

Micropipette aspiration has once again been used to quantify and clarify the rate-dependent deformation of nuclei under controlled pressures [93, 94]. Because of the log range in lamin-A:B stoichiometry, the characteristic contributions of A- and B-type lamins to nuclear properties have become reasonably clear, with nuclei having low lamin-A:B responding in seconds, whereas nuclei having high lamin-A:B take many minutes to deform when similarly stressed. The B-type lamin filaments that strongly associate with the nucleus' inner lipid bilayer (via lamin-B farnesylation) understandably contribute mostly to the elastic response of the nucleus, whereas lamin-A contributes most strongly to nuclear viscosity consistent with the flow physics of filamentous polymers [90, 95, 96]. Thus, when lamin-A dominates, the nucleus response is akin to a balloon filled with honey, whereas when lamin-A is very low the nucleus behaves merely as a balloon filled with water. While the importance of A-type lamins in maintaining nuclear structural integrity and cell viability has been appreciated for a long time [94, 97], the influence of lamin-A on cell motility has been more recent. A rate-limiting role for the nucleus and its lamina in migration of a given cell type through small pores is now clear for cancer cells invading nearby tissue [95] and also for hematopoietic cells that either remain within the marrow or else escape from it through small micro-pores in the endothelial lining that separates marrow from blood (Fig. 1).

4 Conclusions

In terms of future directions, a deeper understanding of the biophysical similarities and differences between a nucleus and an RBC should be pursued. Indeed, one caveat to the analyses above is that it undoubtedly applies to a flaccid nucleus in which the chromatin is highly hydrated within a relative nuclear volume that is roughly similar to that of an RBC discocyte (e.g., Fig. 2). The ~2 meters of DNA folded as chromatin inside each and every nucleus contributes most clearly to nuclear rigidity only when the genome becomes condensed with loss of water and nuclear volume [94]. Mobile nuclear proteins including DNA repair factors and transcription factors might be lost or have limited access to dense DNA [98], thereby suppressing gene expression, but the high nuclear rigidity of such a dehydrated nucleus will also tend to stimulate local contractility of myosin-II (especially MIIB) in driving an asymmetric process of "cytokinesis" or nuclear expulsion (per erythropoiesis in Fig. 1). The rigidity of an expelled nucleus will also tend to favor its phagocytosis by bone marrow macrophages regardless of whether the "Self" marker CD47 is present or not (Fig. 3), whereas the nascent RBC reticulocyte is highly flexible in being filled with a solution of hemoglobin. Severing of the lipid membrane tether between nucleus and reticulocyte and loss of lipid membrane blebs in maturation to an RBC also raise issues of limits on nuclear membrane integrity.

This is an exciting topic with increasing evidence of curvature-dependent rupture of the lamin-B meshwork that is somehow modulated by lamin-A and followed by loss of integrity of the double bilayer [99]. Within the marrow, such a stepwise process of nuclear rigidification, gene expression shutdown, nuclear expulsion, and engulfment with severing of the tether between nucleus and flexible reticulocyte are the final stages in the marrow for generating an RBC—with rich biophysics to be perturbed and more deeply understood.

Acknowledgements The author gratefully acknowledges support of the National Institutes of Health, including National Heart, Lung & Blood Institute (R01 HL124106, R21 HL128187) and National Cancer Institute under Physical Sciences Oncology Center Award U54 CA193417, a Human Frontiers Sciences Program grant RGP0024, and the US–Israel Binational Science Foundation, National Science Foundation grant agreement CMMI 15-48571.

References

1. Morrison SJ, Scadden DT (2014) The bone marrow niche for haematopoietic stem cells. Nature 505:327–334
2. Thomas ED, Lochte HL Jr, Lu WC, Ferrebee JW (1957) Intravenous infusion of bone marrow in patients receiving radiation and chemotherapy. N Engl J Med 257:491–496
3. Shin JW, Buxboim A, Spinler KR, Swift J et al (2014) Contractile forces sustain and polarize hematopoiesis from stem and progenitor cells. Cell Stem Cell 14:81–93
4. Betschinger J, Knoblich JA (2004) Dare to be different: asymmetric cell division in Drosophila, C. elegans and vertebrates. Curr Biol 14:R674–R685
5. Rhyu MS, Jan LY, Jan YN (1994) Asymmetric distribution of numb protein during division of the sensory organ precursor cell confers distinct fates to daughter cells. Cell 76:477–491
6. Chang JT, Palanivel VR, Kinjyo I, Schambach F et al (2007) Asymmetric T lymphocyte division in the initiation of adaptive immune responses. Science 315:1687–1691
7. Li R, Gundersen GG (2008) Beyond polymer polarity: how the cytoskeleton builds a polarized cell. Nat Rev Mol Cell Biol 9:860–873
8. Raab M, Discher DE (2016) Matrix rigidity regulates the microtubule network polarization in migration. Cytoskeleton (Hoboken) 74(3):114–124. https://doi.org/10.1002/cm.21349
9. Merkel R, Simson R, Simson DA, Hohenadl M et al (2000) A micromechanic study of cell polarity and plasma membrane cell body coupling in Dictyostelium. Biophys J 79:707–719
10. Shin JW, Swift J, Spinler KR, Discher DE (2011) Myosin-II inhibition and soft 2D matrix maximize multinucleation and cellular projections typical of platelet-producing megakaryocytes. Proc Natl Acad Sci 108(28):11458–11463
11. Sedzinski J, Biro M, Oswald A, Tinevez JY, Salbreux G, Paluch E (2011) Polar actomyosin contractility destabilizes the position of the cytokinetic furrow. Nature 476:462–466
12. Engler AJ, Sen S, Sweeney HL, Discher DE (2006) Matrix elasticity directs stem cell lineage specification. Cell 126:677–689
13. Holst J, Watson S, Lord MS, Eamegdool SS, Bax DV, Nivison-Smith LB, Kondyurin A, Ma L, Oberhauser AF, Weiss AS, Rasko JE (2010) Substrate elasticity provides mechanical signals for the expansion of hemopoietic stem and progenitor cells. Nat Biotechnol 28(10):1123–1128
14. Adamo L, Naveiras O, Wenzel PL, McKinney-Freeman S, Mack PJ, Gracia-Sancho J, Suchy-Dicey A, Yoshimoto M, Lensch MW, Yoder MC, García-Cardeña G, Daley GQ (2009) Biomechanical forces promote embryonic haematopoiesis. Nature 459(7250):1131–1135

15. Shin ME, He Y, Li D, Na S, Chowdhury F, Poh YC, Collin O, Su P, de Lanerolle P, Schwartz MA, Wang N, Wang F (2010) Spatiotemporal organization, regulation, and functions of tractions during neutrophil chemotaxis. Blood 116:3297–3310
16. Ubukawa K, Guo YM, Takahashi M, Hirokawa M, Michishita Y, Nara M, Tagawa H, Takahashi N, Komatsuda A, Nunomura W, Takakuwa Y, Sawada K (2012) Enucleation of human erythroblasts involves non-muscle myosin IIB. Blood 119(4):1036–1044
17. Hebiguchi M, Hirokawa M, Guo YM, Saito K, Wakui H, Komatsuda A, Fujishima N, Takahashi N, Takahashi T, Sasaki T, Nunomura W, Takakuwa Y, Sawada K (2008) Dynamics of human erythroblast enucleation. Int J Hematol 88(5):498–507
18. Chasis JA, Mohandas N (2008) Erythroblastic islands: niches for erythropoiesis. Blood 112(3):470–478
19. Junt T, Schulze H, Chen Z, Massberg S, Goerge T, Krueger A, Wagner DD, Graf T, Italiano JE Jr, Shivdasani RA, von Andrian UH (2007) Dynamic visualization of thrombopoiesis within bone marrow. Science 317:1767–1770
20. Spinler KR, Shin JW, Lambert MP, Discher DE (2015) Myosin-II repression favors pre/proplatelets but shear activation generates platelets and fails in macrothrombocytopenia. Blood 125(3):525–533
21. Smith AS, Nowak RB, Zhou S, Giannetto M, Gokhin DS, Papoin J, Ghiran IC, Blanc L, Wan J, Fowler VM (2018 May 8) Myosin IIA interacts with the spectrin-actin membrane skeleton to control red blood cell membrane curvature and deformability. Proc Natl Acad Sci USA 115(19):E4377–E4385
22. Waugh RE, McKenney JB, Bauserman RG, Brooks DM, Valeri CR, Snyder LM (1997) Surface area and volume changes during maturation of reticulocytes in the circulation of the baboon. J Lab Clin Med 129(5):527–535
23. Discher DE, Mohandas N, Evans EA (1994) Molecular maps of red cell deformation: hidden elasticity and in situ connectivity. Science 266:1032–1035
24. Subramanian S, Tsai R, Sen S, Dahl KN, Discher DE (2006) Membrane mobility and clustering of Integrin Associated Protein (IAP, CD47)—Major differences between mouse and man and implications for signaling. Blood Cells Mol Dis 36(3):364–372
25. Schmidt CF, Svoboda K, Lei N, Petsche IB, Berman LE, Safinya CR, Grest GS (1993) Existence of a flat phase in red cell membrane skeletons. Science 259(5097):952–955
26. Gifford SC, Derganc J, Shevkoplyas SS, Yoshida T, Bitensky MW (2006) A detailed study of time-dependent changes in human red blood cells: from reticulocyte maturation to erythrocyte senescence. Br J Haematol 135(3):395–404
27. Discher DE, Boal DH, Boey SK (1998) Simulations of the erythrocyte cytoskeleton at large deformation II: micropipette aspiration. Biophys J 75(3):1584–1597
28. Johnson CP, Tang HY, Carag C, Speicher DW, Discher DE (2007) Forced unfolding of proteins within cells. Science 317:663–666
29. Sen S, Subramanian S, Discher DE (2005) Indentation and adhesive probing of a cell membrane with AFM: model and experiments. Biophys J 89:3202–3213
30. Hategan A, Law R, Kahn S, Discher DE (2003) Adhesively tensed erythrocyte membrane: lysis dynamics and AFM probing. Biophys J 85:2746–2759
31. Evans E, Ritchie K (1999) Strength of a weak bond connecting flexible polymer chains. Biophys J 76(5):2439–2447
32. Shu S, Liu X, Korn ED (2005) Blebbistatin and blebbistatin-inactivated myosin II inhibit myosin II-independent processes in dictyostelium. Proc Natl Acad Sci USA 102:1472–1477
33. Skoczek DA, Walczysko P, Horn N, Parris A, Clare S, Williams MR, Sobolewski A (2014) Luminal microbes promote monocyte-stem cell interactions across a healthy colonic epithelium. J Immunol 193:439–451
34. Yonit L, Deborah W, Ronnie BG, David E, Keren SH, Merad M, Jung S, Amit I (2014) Tissue-resident macrophage enhancer landscapes are shaped by the local microenvironment. Cell 159:1312–1326
35. Alvey C, Discher DE (2017 July) Engineering macrophages to eat cancer: from “marker of self” CD47 and phagocytosis to differentiation. J Leukoc Biol 102(1):31–40

36. Rodriguez PL, Harada T, Christian DA, Pantano DA, Tsai RK, Discher DE (2013) Minimal "self" peptides that inhibit phagocytic clearance and enhance delivery of nanoparticles. Science 339:971–975
37. Hu CM, Zhang L, Aryal S, Cheung C, Fang RH, Zhang L (2011) Erythrocyte membrane-camouflaged polymeric nanoparticles as a biomimetic delivery platform. Proc Natl Acad Sci USA 108:10980–10985
38. Geng Y, Dalhaimer P, Cai S, Tsai R, Tewari M, Minko T, Discher DE (2007) Shape effects of filaments versus spherical particles in flow and drug delivery. Nat Nanotechnol 2:249–255
39. Chambers E, Mitragotri S (2007) Long circulating nanoparticles via adhesion on red blood cells: Mechanism and extended circulation. Exp Biol Med (Maywood) 232:958–966
40. Bartlett DW, Su H, Hildebrandt IJ, Weber WA, Davis ME (2007) Impact of tumor-specific targeting on the biodistribution and efficacy of siRNA nanoparticles measured by multimodality in vivo imaging. Proc Natl Acad Sci USA 104:15549
41. Swanson JA, Hoppe AD (2004) The coordination of signaling during Fc receptor-mediated phagocytosis. J Leukoc Biol 76:1093
42. Wong C, Stylianopoulos T, Cui J, Martin J, Chauhan VP, Jiang W, Popovic Z, Jain RK, Bawendi MG, Fukumura D (2011) Multistage nanoparticle delivery system for deep penetration into tumor tissue. Proc Natl Acad Sci USA 108:2426–2431
43. Turk MJ, Waters DJ, Low PS (2004) Folate-conjugated liposomes preferentially target macrophages associated with ovarian carcinoma. Cancer Lett 213:165–172
44. Rhee I, Davidson D, Souza CM, Vacher J, Veillette A (2013) Macrophage fusion is controlled by the cytoplasmic protein tyrosine phosphatase PTP-PEST/PTPN12. Mol Cell Biol 33:2458–2469
45. Turrini F, Arese P, Yuan J, Low PS (1991) Clustering of integral membrane proteins of the human erythrocyte membrane stimulates autologous IgG binding, complement deposition, and phagocytosis. J Biol Chem 266:23611–23617
46. Franco RS, Puchulu-Campanella ME, Barber LA, Palascak MB, Joiner CH, Low PS, Cohen RM (2013) Changes in the properties of normal human red blood cells during in vivo aging. Am J Hematol 88:44–51
47. Wilflingseder D, Banki Z, Garcia E, Pruenster M, Pfister G, Muellauer B, Nikolic DS, Gassner C, Ammann CG, Dierich MP, Piguet V, Stoiber H (2007) IgG opsonization of HIV impedes provirus formation in and infection of dendritic cells and subsequent long-term transfer to T cells. J Immunol 178:7840
48. Discher DE, Ortiz V, Srinivas G, Klein ML, Kim Y, Christian D, Cai S, Photos P, Ahmed F (2007) Emerging applications of polymersomes in delivery: from molecular dynamics to shrinkage of tumors. Prog Polym Sci 32:838–857
49. Lundqvist M, Stigler J, Elia G, Lynch I, Cedervall T, Dawson KA (2008) Nanoparticle size and surface properties determine the protein corona with possible implications for biological impacts. Proc Natl Acad Sci USA 105:14265
50. Rettig MP, Low PS, Gimm JA, Mohandas N, Wang J, Christian JA (1999) Evaluation of biochemical changes during in vivo erythrocyte senescence in the dog. Blood 93:376–384
51. Sosale NG, Rouhiparkouhi T, Bradshaw AM, Dimova R, Lipowsky R, Discher DE (2015) Cell rigidity and shape override CD47's "self"-signaling in phagocytosis by hyperactivating myosin-II. Blood 125:542–552
52. JK A, Hempel G, Koling S, Chan LS, Fisher T, Meiselman HJ, Garratty G (2007) Antibody against poly (ethylene glycol) adversely affects PEG-asparaginase therapy in acute lymphoblastic leukemia patients. Cancer 110:103–111
53. Cox D, Greenberg S (2001) Phagocytic signaling strategies. Fc (gamma) receptor-mediated phagocytosis as a model system. Semin Immunol 13:339–345
54. Greenberg S, Chang P, Silverstein SV (1994) Tyrosine phosphorylation of the gamma subunit of Fc gamma receptors, p72syk, and paxillin during Fc receptor-mediated phagocytosis in macrophages. J Biol Chem 269:3897–3902
55. Aderem A, Underhill BM (1999) Mechanisms of phagocytosis in macrophages. Annu Rev Immunol 17:593–623

56. Wolfenson H, Bershadsky A, Henis YI, Geiger B (2011) Actomyosin-generated tension controls the molecular kinetics of focal adhesions. J Cell Sci 124:1425–1432
57. Raab M, Swift J, Dingal D, Shah P, Shin JW, Discher DE (2012) Crawling from soft to stiff matrix polarizes the cytoskeleton and phosphoregulates myosin-II heavy chain. J Cell Biol 199:669–683
58. Tsai RK, Discher DE (2008) Inhibition of "self" engulfment through deactivation of myosin-II at the phagocytic synapse between human cells. J Cell Biol 180:989–1003
59. Tsai RK, Rodriguez PL, Discher DE (2010) Self inhibition of phagocytosis: The affinity of 'marker of self' CD47 for SIRP alpha dictates potency of inhibition but only at low expression levels. Blood Cells Mol Dis 45:67–74
60. Murata Y, Saito Y, Kaneko T, Kotani T, Kaneko Y, Ohnishi H, Matozaki T (2014) Autoimmune animal models in the analysis of the CD47-SIRP alpha signaling pathway. Methods 65:254–259
61. Okazawa H, Motegi S, Ohyama N, Ohnishi H, Tomizawa T, Kaneko Y, Oldenborg PA, Ishikawa O, Matozaki T (2005) Negative regulation of phagocytosis in macrophages by the CD47-SHPS-1 system. J Immunol 174:2004–2011
62. Oldenborg PA, Zheleznyak A, Fang YF, Lagenaur CF, Gresham HD, Lindberg FP (2000) Role of CD47 as a marker of self on red blood cells. Science 288:2051–2054
63. Willingham SB, Volkmer JP, Gentles AJ, Sahoo D, Dalerba P, Mitra SS, Wang J, Contreras-Trujillo H, Martin R, Cohen JD, Lovelace P, Scheeren FA, Chao MP, Weiskopf K, Tang C, Volkmer AK, Naik TJ, Storm TA, Mosley AR, Edris B, Schmid SM, Sun CK, Chua MS, Murillo O, Rajendran P, Cha AC, Chin RK, Kim D, Adorno M, Raveh T, Tseng D, Jaiswal S, Enger PØ, Steinberg GK, Li G, So SK, Majeti R, Harsh GR, van de Rijn M, Teng NN, Sunwoo JB, Alizadeh AA, Clarke MF, Weissman IL (2012) The CD47-signal regulatory protein alpha (SIRPa) interaction is a therapeutic target for human solid tumors. Proc Natl Acad Sci USA 109:6662
64. Horrigan SK (2017) Replication study: the CD47-signal regulatory protein alpha (SIRPa) interaction is a therapeutic target for human solid tumors. eLife 6:e18173. https://doi.org/10.7554/eLife.18173
65. Alvey CM, Spinler KR, Irianto J, Pfeifer CR, Hayes B, Xia Y, Cho S, Dingal PCPD, Hsu J, Smith L, Tewari M, Discher DE (2017 July 24) SIRPA-inhibited, marrow-derived macrophages engorge, accumulate, and differentiate in antibody-targeted regression of solid tumors. Curr Biol 27(14):2065–2077
66. Bentley AA, Adams JC (2010) The evolution of thrombospondins and their ligand-binding activities. Mol Biol Evol 9:2187–2197
67. Oldenborg P-A, Gresham HD, Chen Y, Izui S, Lindberg FP (2002) Lethal autoimmune hemolytic anemia in CD47-deficient nonobese diabetic (NOD) mice. Blood 99:3500–3504
68. Subramanian S, Parthasarathy R, Sen S, Boder ET, Discher DE (2006) Species- and cell type-specific interactions between CD47 and human SIRPalpha. Blood 107:2548–2556
69. Kwong LS, Brown MH, Barclay AN, Hatherley D (2014) Signal-regulatory protein alpha from the NOD mouse binds human CD47 with an exceptionally high affinity—implications for engraftment of human cells. Immunology 143:61–67
70. Soto-Pantoja DR, Miller TW, Frazier WA, Roberts DD (2012) Inhibitory signaling through signal regulatory protein-alpha is not sufficient to explain the antitumor activities of CD47 antibodies. Proc Natl Acad Sci USA 109:2842–2842
71. Zhao XW, Matlung HL, Kuijpers TW, van den Berg TK (2012) On the mechanism of CD47 targeting in cancer. Proc Natl Acad Sci USA 109:2843–2843
72. SB W, Volkmer JP, Gentles AJ, Sahoo D, Dalerba P, Mitra SS, Wang J, Contreras-Trujillo H, Martin R, Cohen JD, Lovelace P, Scheeren FA, Chao MP, Weiskopf K, Tang C, Volkmer AK, Naik TJ, Storm TA, Mosley AR, Edris B, Schmid SM, Sun CK, Chua MS, Murillo O, Rajendran P, Cha AC, Chin RK, Kim D, Adorno M, Raveh T, Tseng D, Jaiswal S, Enger PØ, Steinberg GK, Li G, So SK, Majeti R, Harsh GR, van de Rijn M, Teng NN, Sunwoo JB, Alizadeh AA, Clarke MF, Weissman IL (2012) The CD47-signal regulatory protein alpha

(SIRPa) interaction is a therapeutic target for human solid tumors. Proc Natl Acad Sci USA 109(17):6662–6667
73. Jaiswal S, Jamieson CH, Pang WW, Park CY, Chao MP, Majeti R, Traver D, van Rooijen N, Weissman IL (2009) CD47 is upregulated on circulating hematopoietic stem cells and leukemia cells to avoid phagocytosis. Cell 138:271–285
74. Lindberg FP, Lublin DM, Telen MJ, Veile RA, Miller YE, Donis-Keller H, Brown EJ (1994) Rh-related antigen CD47 is the signal-transducer integrin-associated protein. J Biol Chem 269:1567–1570
75. Gardai SJ, McPhillips KA, Frasch SC, Janssen WJ, Starefeldt A, Murphy-Ullrich JE, Bratton DL, Oldenborg PA, Michalak M, Henson PM (2005) Cell-surface calreticulin initiates clearance of viable or apoptotic cells through trans-activation of LRP on the phagocyte. Cell 123:321–334
76. Arfsten J, Leupold S, Bradtmoeller C, Kampen I, Kwade A (2010) Atomic force microscopy studies on the nanomechanical properties of Saccharomyces cerevisiae. Colloid Surf B 79:284–290
77. Beningo KA, Wang YL (2002) Fc-receptor-mediated phagocytosis is regulated by mechanical properties of the target. J Cell Sci 115:849–856
78. Lam WA, Rosenbluth MJ, Fletcher DA (2007) Chemotherapy exposure increases leukemia cell stiffness. Blood 109:3505–3508
79. Cross SE, Jin YS, Rao J, Gimzewski JK (2007) Nanomechanical analysis of cells from cancer patients. Nat Nanotechnol 2:780–783
80. Swift J, Ivanovska IL, Buxboim A, Harada T, Dingal PC, Pinter J, Pajerowski JD, Spinler KR, Shin JW, Tewari M, Rehfeldt F, Speicher DW, Discher DE (2013) Nuclear lamin-A scales with tissue stiffness and enhances matrix-directed differentiation. Science 341(6149):1240104
81. Merkel TJ, Jones SW, Herlihy KP, Kersey FR, Shields AR, Napier M, Luft JC, Wu H, Zamboni WC, Wang AZ, Bear JE, DeSimone JM (2011) Using mechanobiological mimicry of red blood cells to extend circulation times of hydrogel microparticles. Proc Natl Acad Sci USA 108:586–591
82. Mebius RE, Kraal G (2005) Structure and function of the spleen. Nat Rev Immunol 5:606–616
83. Deplaine G, Safeukui I, Jeddi F, Lacoste F, Brousse V, Perrot S, Biliqui S, Guillotte M, Guitton C, Dokmak S, Aussilhou B, Sauvanet A, Cazals Hatem D, Paye F, Thellier M, Mazier D, Milon G, Mohandas N, Mercereau-Puijalon O, David PH, Buffet PA (2011) The sensing of poorly deformable red blood cells by the human spleen can be mimicked in vitro. Blood 117:88–95
84. Champion JA, Mitragotri S (2006) Role of target geometry in phagocytosis. Proc Natl Acad Sci USA 103:4930–4934
85. Yoshida H, Kawane K, Koike M, Mori Y, Uchiyama Y, Nagata S (2005) Phosphatidylserine-dependent engulfment by macrophages of nuclei from erythroid precursor cells. Nature 437(7059):754–758
86. Bell AJ, Satchwell TJ, Heesom KJ, Hawley BR, Kupzig S, Hazell M, Mushens R, Herman A, Toye AM (2013) Protein distribution during human erythroblast enucleation in vitro. PLoS One 8(4):e60300
87. Buxboim A, Irianto J, Swift J, Athirasala A, Shin JW, Rehfeldt F, Discher DE (2017 Nov 7) Coordinated increase of nuclear tension and lamin-A with matrix stiffness outcompetes lamin-B receptor that favors soft tissue phenotypes. Mol Biol Cell 28(23):3333–3348
88. Herrmann H, Strelkov SV, Burkhard P, Aebi U (2009) Intermediate filaments: primary determinants of cell architecture and plasticity. J Clin Invest 119:1772–1783
89. Dechat T, Adam SA, Taimen P, Shimi T, Goldman RD (2010) Nuclear lamins. Cold Spring Harb Perspect Biol 2:a000547
90. Buxboim A, Swift J, Irianto J, Spinler KR, Dingal PC, Athirasala A, Kao YR, Cho S, Harada T, Shin JW, Discher DE (2014) Matrix elasticity regulates lamin-AC phosphorylation and turnover with feedback to actomyosin. Curr Biol 24(16):1909–1917
91. Echarri A, Del Pozo MA (2015 Aug 1) Caveolae - mechanosensitive membrane invaginations linked to actin filaments. J Cell Sci 128(15):2747–2758

92. Sinha B, Köster D, Ruez R, Gonnord P, Bastiani M, Abankwa D, Stan RV, Butler-Browne G, Vedie B, Johannes L, Morone N, Parton RG, Raposo G, Sens P, Lamaze C, Nassoy P (2011 Feb 4) Cells respond to mechanical stress by rapid disassembly of caveolae. Cell. 144(3):402–413
93. Dahl KN, Engler AJ, Pajerowski JD, Discher DE (2005) Power-law rheology of isolated nuclei with deformation mapping of nuclear substructures. Biophys J 89:2855–2864
94. Pajerowski JD, Dahl KN, Zhong FL, Sammak PJ, Discher DE (2007) Physical plasticity of the nucleus in stem cell differentiation. Proc Natl Acad Sci USA 104:15619–15624
95. Harada T, Swift J, Irianto J, Shin JW, Spinler KR, Athirasala A, Diegmiller R, Dingal PC, Ivanovska IL, Discher DE (2014) Nuclear lamin stiffness is a barrier to 3D migration, but softness can limit survival. J Cell Biol 204:669–682
96. Shin JW, Spinler KR, Swift J, Chasis JA, Mohandas N, Discher DE (2013) Lamins regulate cell trafficking and lineage maturation of adult human hematopoietic cells. Proc Natl Acad Sci USA 110(47):18892–18897
97. Broers JL, Peeters EA, Kuijpers HJ, Endert J, Bouten CV, Oomens CW, Baaijens FP, Ramaekers FC (2004) Decreased mechanical stiffness in LMNA−/− cells is caused by defective nucleo-cytoskeletal integrity: implications for the development of laminopathies. Hum Mol Genet 13:2567–2580
98. Irianto J, Pfeifer CR, Bennett RR, Xia Y, Ivanovska IL, Liu AJ, Greenberg RA, Discher DE (2016) Nuclear constriction segregates mobile nuclear proteins away from chromatin. Mol Biol Cell 27(25):4011–4020
99. Xia Y, Ivanovska IL, Zhu K, Smith L, Irianto J, Pfeifer CR, Alvey CM, Ji J, Liu D, Cho S, Bennett RR, Liu AJ, Greenberg RA, Discher DE (2018 Aug 31) Nuclear rupture at sites of high curvature compromises retention of DNA repair factors. J Cell Biol pii: jcb.201711161

Spontaneous and Intrinsic Curvature of Lipid Membranes: Back to the Origins

Michael M. Kozlov

Abstract We review the background behind the notions of spontaneous and intrinsic curvatures of lipid membranes with a goal to make clear a fundamental physical difference between them. We recall the underlying mechanical and thermodynamic models for intrinsically curved lipid monolayers, whose geometry is described by the intrinsic curvature, and for flat monolayers whose elastic stresses are captured by the spontaneous curvature. We describe the existing ideas concerning the spontaneous and intrinsic curvatures of mixed lipid membranes. We mention the conditions upon which the values of the spontaneous and intrinsic curvatures are expected to be similar and the specific systems for which each of the notions is relevant.

Keywords Membrane bending elasticity · Spontaneous curvature · Intrinsic curvature · Bending modulus

1 Introduction

Biological membranes form physical boundaries between the inner volume of a biological cell and the external medium as well as, within the cell, between the lumens of intracellular organelles and cytosol. The structural base of any biological membrane is a lipid bilayer—an about 3–4 nm thick film consisting of two monolayers of amphiphilic phospholipid molecules referred to below as the lipids. As described in more detail below, the lipid monolayer formation and coupling into bilayers in aqueous solution are driven by the hydrophobic effect [1].

Upon common physiological conditions, each monolayer has properties of a two-dimensional fluid, which is due to the ability of the lipid molecules to undergo two-dimensional diffusion in the membrane plane referred to as the lateral diffusion. Moreover, while being coupled in the direction perpendicular to the membrane

M. M. Kozlov (✉)
Sackler Faculty of Medicine, Department of Physiology and Pharmacology, Tel Aviv University, Tel Aviv, Israel
e-mail: michk@post.tau.ac.il

P. Bassereau, P. Sens (eds.), *Physics of Biological Membranes*,
https://doi.org/10.1007/978-3-030-00630-3_12

plane, the two monolayers are free to slip with respect to each other in the in-plane direction to the extent permitted by external geometrical constraints. In addition, flipping of lipid molecules between the monolayers is possible and referred to as flip-flop [2], which also contributes to an effective in-plane decoupling of the monolayers. Because of this mechanical decoupling in the lateral (in-plane) direction, a lipid monolayer represents the basic mechanical units of the membrane, whereas the mechanical properties of a bilayer can be derived from those of its constituent monolayers. Therefore, this review will be concerned, mostly, with elastic properties of lipid monolayers, which, using a loose terminology, will be also referred to as the membranes.

Since early 70th, acquiring by membranes of curved shapes and the underlying physical properties of lipid bilayers and monolayers became one of the central topics of soft matter physics. This was motivated, on the one hand, by the attempts to understand the physical mechanisms behind the shapes adopted by erythrocytes [3, 4] and, on the other hand, by X-ray investigations of three-dimensional phases formed by lipids in aqueous solutions [5]. About 30 years later, the interest to membrane curvature expanded to bona fide cell biology (see for recent review [6]), which has been motivated by the necessity to understand the intricate and strongly bent shapes of membrane-bound intracellular organelles such as endoplasmic reticulum (ER), Golgi complex, mitochondria, and transport intermediates [7, 8].

A central notion used in the curvature-related fields of membrane physics and biology is that of *spontaneous curvature*, which has been commonly meant to describe the inherently preferable membrane shapes. In parallel, although less commonly, the term of *intrinsic curvature* has been used in the membrane literature to describe, basically, the same membrane property. In some cases, the two notions appeared interchangeably in the same article. The goal of this review is to go back to the original physical contents of the concepts of spontaneous curvature, as defined by Wolfgang Helfrich [4], and of intrinsic curvature as introduced, originally, by Sol Gruner [9]. We will make clear that there is a fundamental rather than semantic difference between the two notions.

We will show that the spontaneous curvature does not have a direct meaning of a geometrical characteristic of the membrane surface but rather describes the stresses existing within a flat membrane and provides tools for computing the energy of the membrane deviation from the flat shape. In contrast, the intrinsic curvature does have a geometrical connotation describing the local membrane shape in the mechanically relaxed and, hence, energetically preferable state. We will indicate the conditions under which the spontaneous and intrinsic curvatures are expected to have approximately equal values meaning that, for practical purposes, one can be used instead of the other.

This consideration will give us a reason to come back to the "first principles" of the two alternative approaches to physics of membrane bending and discuss, specifically, the current views on the bending elastic properties and, in particular, on the spontaneous/intrinsic curvatures of membranes with mixed lipid compositions.

Although the concept of spontaneous curvature was formulated more than 10 years ahead of introduction of the intrinsic curvature, we will first overview the latter notion, which is more intuitive, and then the former, whose physical content is somewhat more involved.

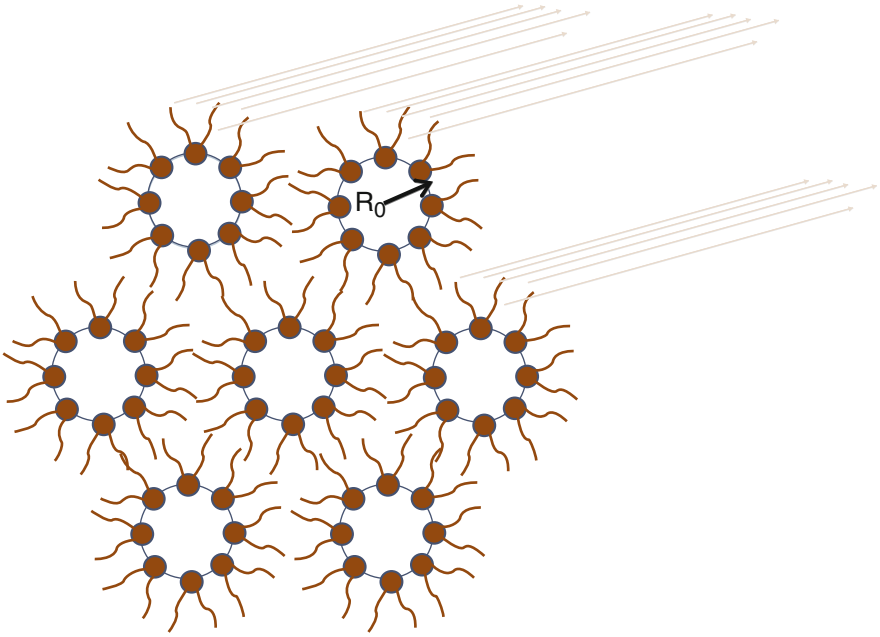

Fig. 1 Illustrations of the structure of H_{II}-phase, R_0 being the intrinsic radius of the monolayer so that the intrinsic curvature is $J_0 = 1/R_0$

2 Intrinsic Curvature

The concept of intrinsic curvature as a quantitative structural characteristic of lipid monolayers has originated from understanding the so-called lipid mesophases, which result from lipid self-assembly in aqueous surrounding [5]. Usually, mesophases are formed by continuous hydration of initially dry lipid samples up to a saturating limit. Driven by the hydrophobic forces, lipid molecules self-assemble into monolayers, which segregate in such a way that their hydrocarbon moieties are shielded from the aqueous surrounding by the layers of polar heads. Depending on the lipid composition, the monolayers adopt a plethora of shapes [10–12], the most familiar of which is the flat shape. Flat monolayers form planar bilayers, which in turn pack into stacks where they are separated by few nanometer-thick layers of water. The resulting mesophase is called the lamellar phase (see, e.g., [5, 12]).

Lipids, which do not form flat bilayers, are often called the non-bilayer lipids. The most common monolayer shape formed by such lipids is that of a narrow cylindrical tube whose internal surface of few nanometer cross-sectional diameter is covered by the lipid polar heads and engulfs a water cylinder. These lipid tubes get oriented in parallel, contact each other along the hydrophobic surfaces, and pack in such a way that their cross-sections form a two-dimensional hexagonal lattice (Fig. 1). The resulting structure is referred to as the inverted hexagonal (H_{II}) phase [11].

In addition to the H_{II}- phase, few other non-lamellar mesophases characterized by curved monolayer shape can form such as H_I- phase consisting of cylindrical micelles packed in hexagonal lattice and bicontinuous and micellar cubic phases. Here we discuss only H_{II}-phases, whereas thorough description of other phases can be found in numerous reviews (see, e.g., [10, 12]).

Essentially, a lipid monolayer within H_{II}-phase is almost free to acquire the most favorable shape dictated by the monolayer intrinsic properties. Ideally, this is possible if the inter-monolayer spatial gaps, which unavoidably form as a result of the monolayer packing within the phase, can be filled by non-lipid substances coming from external reservoirs. In a fully hydrated H_{II}-mesophase, the water cylinders inside the lipid tubes unrestrictedly exchange water molecules with the external aqueous medium. Filling of the hydrophobic gaps between the lipid tubes, which form as a result of the hexagonal packing and are referred to as the hydrophobic interstices [13], is more problematic since, usually, there are no required reservoirs of hydrophobic substances in contact with the mesophases. However, even these restrictions can be reduced or even lifted by introduction into the system of hydrophobic substances, such as tetra- or hexadecane, which redistribute into the hydrophobic interstices [9, 14–16]. As a result, the shapes adopted by lipid monolayers within H_{II}-phases can be considered as representing the intrinsically favored shapes.

The intrinsic curvature, J_0 [9], is the inverse of the radius, R_0 (Fig. 1), of a cylindrical tube formed by an unrestricted monolayer of H_{II}-phase, $J_0 = 1/R_0$. It has to be noted that the intrinsic curvature value must be related to a specific surface chosen within the monolayer as a reference plane [17]. The most convenient reference plane is the neutral surface, for which the deformations of the membrane stretching and bending are energetically decoupled [17, 18].

Due to three-dimensional long-range order of lipid packing, the structural parameters of lipid mesophases in general and of H_{II}-phases, in particular, can be measured with high precision by X-ray scattering [13]. This enables quantitative determination of the monolayer intrinsic curvatures, which needs, however, some theoretical treatment of the measured parameters [18–20].

2.1 Intrinsic Curvatures of Individual Lipids and Lipid Mixtures

A direct measurement of intrinsic curvature of a specific individual lipid requires generation of unconstrained H_{II}-phase of this lipid. In practical terms, only one such lipid, dioleoylphosphatidylethanolamine (DOPE) [13], has been found to date, which is considered to be a “king” of non-bilayer lipids [21]. The radius of water cylinder, ρ_w, within the DOPE phase is close to 2 nm so that the hydrophobic interstices, whose dimension is proportional to ρ_w, are relatively small and do not require much of the hydrophobic solvent to be introduced. The intrinsic curvature

of DOPE measured at its neutral plane located close to the level glycerol backbones of the lipid molecules [19, 20] was found to constitute $J_0^{\mathrm{DOPE}} = 1/2.75$ nm for the room temperature [22].

The H_{II}-phase of DOPE enables also determination of the intrinsic curvature values of a series of other biologically relevant lipids, such as phosphatidylcholine (PC), diacylglycerol (DAG), lysolipids, and others, which are commonly found within biological membranes but do not form H_{II}-phases by themselves. This is based on the ability of the DOPE monolayers to accommodate some amounts of these lipids. Whereas the resulting lipid mixtures keep forming the inverted hexagonal phase, the radii of the monolayer tubes deviate from that of the purely DOPE monolayer and depend on the composition of the mixed monolayer. Essentially, although not expected a priori, the dependence of the intrinsic curvature of a mixed cylinder on the mole fraction, ϕ, of the added lipid, $J_0(\phi)$, has a linear character for all investigated lipid mixtures $J_0(\phi) = J_0^{\mathrm{DOPE}} + \phi J_0^L$ [20, 23–26]. The slope of this linear dependence, J_0^L, has been defined as the intrinsic curvature of the lipid under question. The values of the intrinsic curvatures of quite a few biologically relevant lipids measured by the described method can be found in several reviews (see, e.g., [27].). It has to be emphasized that the resulting J_0^L values may not have a universal character since the conformation of a lipid molecule must depend to some extent on the surrounding lipids within the mixture, as recently confirmed by numerical simulations [28]. Therefore, strictly speaking, the intrinsic curvature values, J_0^L, obtained for individual lipids by the described method of mixed H_{II}-phases, have to be considered within the DOPE context.

2.2 *Bending Elasticity of Lipid Monolayers in the Intrinsically Curved State*

Experimentation with H_{II}-phases led to understanding the structure and mechanics of lipid monolayer in their intrinsic state beyond determination of the lipid intrinsic curvatures. The experiments consisted in application to the lipid sample of external compressing pressures and measuring the resulting deformations of H_{II}-phases. These pressures, which can have either a gravimetric (within an aqueous vapor atmosphere) (see, e.g., [13]) or osmotic (in bulk water) (see, e.g., [16]) character, change the lipid tube radii [13, 16, 19, 20] . The obtained dependence of the monolayer radius change on the applied pressure represents a stress-strain relationship, which, generally, enables determination of the system elastic constants. For weak compressions leading to small deviations of the monolayer curvature, J, from the intrinsic value, J_0, the elastic energy, F_B, accumulated with the monolayer was presented as [9]

$$F_B = \frac{1}{2} K_B (J - J_0)^2, \tag{1}$$

where K_B is the membrane bending modulus determined for the intrinsic state. While this equation captured the essential physics of the system, treatment of the experimental data required a more rigorous approach taking into account that the bending modulus must be an intensive rather than extensive thermodynamic value and that the choice of the dividing surface within the membrane becomes of primary importance for the strongly curved monolayers of H_{II}-phases. This approach was developed in a series of articles [18–20], which enabled determination of the monolayer bending moduli in the intrinsic state for pure DOPE and mixed monolayers [20, 22–26, 29]. In all cases the value of the bending modulus was close to $10k_BT \approx 4 \times 10^{-20}$ J (where k_BT is the product of Boltzmann constant and the absolute temperature).

3 Spontaneous Curvature

The concept of membrane spontaneous curvature was introduced by W. Helfrich in his seminal article establishing a model for bending elasticity of nearly flat membranes [4].

The way of reasoning, which underlies Helfrich's derivation of the energy associated with bending deformations of membrane surface, is analogous to and, possibly, inspired by the previous consideration by F.C. Frank of three-dimensional bending deformations of nematic and cholesteric liquid crystals [30]. Specifically, the notion of the membrane spontaneous curvature is parallel to that of a nematic elastic parameter defined by Frank, which can be referred to as the spontaneous splay.

The analogy between Helfrich's and Frank's approaches is based on a fundamental physical similarity existing between the two systems in spite of the fact that the nematic liquid crystal is a three-dimensional phase characterized by bulk properties (Fig. 2a), whereas a lipid membrane has been described as a surface, i.e., a two-dimensional system immersed in three-dimensional space (Fig. 2b). This similarity includes the physical variables by which the nematics and the lipid membranes can be described and the intrinsic material properties, which determine the common symmetry rules underlying the physical models of the two systems.

Specifically, the bulk of a uniaxial nematic liquid crystal, on one hand, and the membrane surface, on the other, can be described by, basically, the same physical variable, whose essence is the direction of the local orientation. (It has to be emphasized that we consider only membranes in high-temperature phase exhibiting laterally isotropic behavior and do not describe the low-temperature gel phase of lipid characterized by a collective tilting of the lipid hydrocarbon chains within the monolayer and the related lateral anisotropy of the membrane properties.) For a nematic, this variable, referred to as the director, is a unit vector, $\vec{L}$, which determines the direction of the molecular orientation in any infinitesimal volume element of the bulk (Fig. 2a) [30]. Similarly, the membrane surface can be described at every point by a unit normal vector,

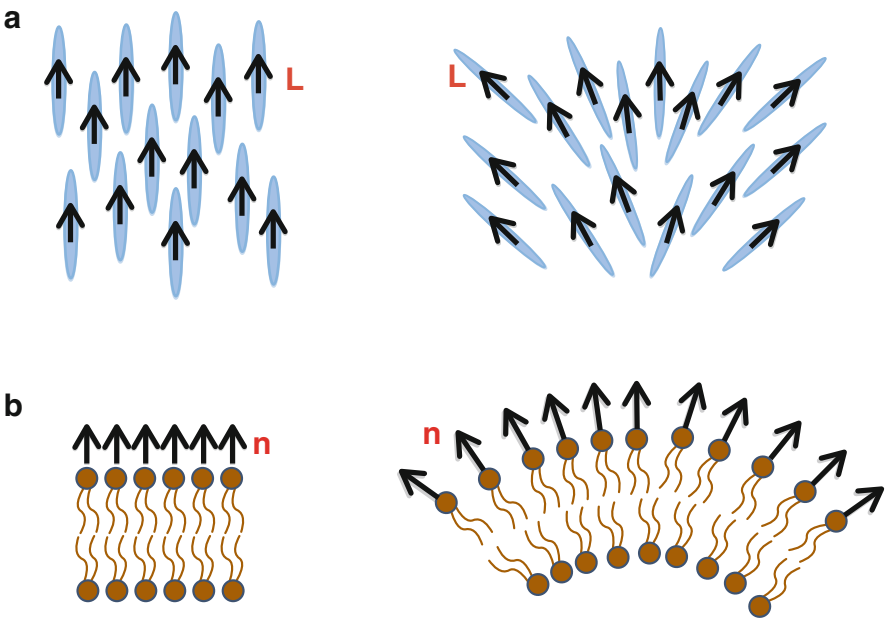

Fig. 2 Illustration of (**a**) the nematic liquid crystal characterized by the director $\vec{L}$ and (**b**) a lipid membrane described by the unit normal vector, $\vec{n}$

$\vec{n}$, characterizing the local surface orientation (Fig. 2b). Further, provided that the initial state of the liquid crystal is the state where the director, $\vec{L}$, is uniformly oriented all over the volume, the essence of the nematic bending deformation is a generation of differences in the director orientations between the adjacent volume elements throughout the system (Fig. 2a, right panel) [30]. Analogously, if the membrane is considered to be, originally, flat with the normal vector, $\vec{n}$, uniformly oriented all over the membrane surface (Fig. 2b, left panel), the membrane bending leads to deviations of $\vec{n}$ belonging to every pair of adjacent membrane elements from the initial parallel orientation (Fig. 2b, right panel).

In terms of the material properties, both nematic liquid crystals and lipid membranes in high-temperature phase exhibit a liquid-like behavior. The molecules constituting a nematic phase can switch their positions within the available volume, which is not accompanied by any stress generation. The same is true for swapping of the lipid molecule positions in the membrane plane within the given membrane area. As a result, neither nematics nor lipid membranes resist the shear deformations. A nematic phase does not develop any stress against three-dimensional shear, whereas a lipid membrane behaves as a two-dimensional liquid complying without resistance with in-plane shear.

Our goal here is to thoroughly describe the physics behind the notion of membrane spontaneous curvature. Therefore, we start with the elements of Frank's analysis of nematics [30] and then present the essence of Helfrich's consideration of the membrane elastic parameters [4, 31] by mentioning the analogy and the differences between the two systems.

3.1 Spontaneous Splay and Twist of Nematic Liquid Crystal

As already mentioned, the initial state of a nematic bulk is considered to exhibit a uniform orientation of the director, $\vec{L}$, throughout the whole system (Fig. 2a, left panel). Generally, any deformation imposed on a three-dimensional elastic phase by external forces acting on its boundaries leads to development at any point of the phase of the internal stresses, σ_{ik}, and strains, u_{ik}, so that the volumetric density of the deformation energy can be presented as [32]

$$f = \int \sigma_{ik} du_{ik}, \tag{2}$$

where the integration is performed from zero to a final strain. The total energy, F, is given by integration of the energy density, f, over the whole volume of the system $F = \oint dV(\int \sigma_{ik} du_{ik})$. Here and below we use the conventions of summation over the repeated indices.

To proceed, based on Eq. (1), one needs to specify the types of the strains, u_{ik}, and stresses, σ_{ik}, developing in the system and establish the explicit stress-strain relationships, $\sigma_{ik}(u_{ik})$.

Since the essence of the nematic bending deformations is the deviation of the director, $\vec{L}$, from the initial uniform orientation (Fig. 2a, right panel), the resulting strains, e_i, can be represented by the local gradients of $\vec{L}$. The only stresses emerging as a result of generation of the director gradients are the local torques, τ_i, counteracting the local rotation of the director, $\vec{L}$ [30]. In general, the three-dimensional bending of the nematic phase leads also to the shear stresses, but, due to the liquid nature of the system, the corresponding stresses must relax due to a rearrangement of the constituent molecules.

To express the strain components explicitly, we introduce at any point of the nematic phase a local Cartesian coordinate system, $\{z, x, y\}$, with z-axis parallel to $\vec{L}$ in the origin, $x = 0$, $y = 0$. Since our goal here is to follow the similarity between the nematics and the membranes, we consider only the deformations for which the director does not change in z-direction so that $\frac{\partial L_x}{\partial z} = \frac{\partial L_y}{\partial z} = 0$. Therefore, the

relevant for our consideration strain components are the two "splay",

$$e_{sx} = \frac{\partial L_x}{\partial x},$$
$$e_{sy} = \frac{\partial L_y}{\partial y}, \tag{3}$$

and two "twist",

$$e_{tx} = -\frac{\partial L_y}{\partial x},$$
$$e_{ty} = \frac{\partial L_x}{\partial y}, \tag{4}$$

components [30]. In the initial state of uniform director, $\vec{L}$, both splay and twist components vanish, $e^0_{sx} = e^0_{sy} = e^0_{tx} = e^0_{ty} = 0$.

The stress-strain relationships, $\tau_i(e_j)$, which have to be used for computation of the energy density according to Eq. (2), are set by the molecular interaction within the system and have, generally, a nonlinear character. However, they can be presented in a simple form for small strains. The smallness of the strains means, specifically, that the dimensionless parameters equal to the products of the absolute values of the strain components, $|e_j|$, and the internal molecular scale of the system, δ, whose essence in the effective size of molecules constituting the nematic phase remain much smaller than one,

$$\left|e_j\right| \cdot \delta \ll 1, \tag{5}$$

which means that the angles, θ_i, by which the directors deviate from the initial orientations remain small, $\theta_i \ll 1$. In this case, it is possible to use the approximate stress-strain relationships, accounting only for the contributions up to the first order in the small parameters, $|e_j| \cdot \delta$, and neglecting the higher-order terms,

$$\tau_i = \tau_i^0 + \epsilon_{ij} \cdot \delta \cdot e_j. \tag{6}$$

This expression [Eq. (6)] represents the Hooke's approximation for the relationships between the torque and the strain components.

In Eq. (6) the first contributions, τ_i^0, are the torques existing within the nematic phase in the initial state of the uniform orientation of the director, $\vec{L}$, before the onset of the bending deformations. The values of the initial torques, τ_i^0, depend on the intermolecular interactions of the specific liquid crystal. In case of vanishing initial torques, $\tau_i^0 = 0$, the uniform state is free of the torque stresses, meaning that there is no intrinsic tendency of the director, $\vec{L}$, to splay and/or twist. In

the case of nonvanishing initial torques, $\tau_i^0 \neq 0$, the inter-molecular interactions favor a deviations of the liquid crystal from the initial state of uniformly oriented director, $\vec{L}$.

The coefficients, ϵ_{ij}, in Eq. (6) represent the elastic parameters of the system. Commonly, the molecular length, δ, is included into the definition of the system elastic parameters so that one uses $\kappa_{ij} = \epsilon_{ij} \cdot \delta$, instead of ϵ_{ij}, and the torque-curvature relationships are introduced in the form

$$\tau_i = \tau_i^0 + \kappa_{ij} \cdot e_j . \tag{7}$$

Symmetry considerations taking into account the liquid-like properties of the system reduce the number of the independent initial torques to two, τ_s^0 and τ_t^0, associated with the splay and twist, respectively [30]. The number of the independent and nonvanishing elastic parameters, κ_{ij}, is reduced to four associated with the splay-only, twist-only, and mixed splay-twist deformations [30]. Using these conclusions and [Eq. (7)], the integration [Eq. (2)] from zero to the final values of the splay and twist components of the strains results in the explicit expression for the energy density, f, which can be presented in the form

$$f = \tau_s^0 \left(e_{sx} + e_{sy}\right) + \tau_t^0 \left(e_{tx} + e_{ty}\right) + \tfrac{1}{2}\kappa_{ss}\left(e_{sx} + e_{sy}\right)^2 + \tfrac{1}{2}\kappa_{tt}\left(e_{tx} + e_{ty}\right)^2 + \kappa_{st}\left(e_{sx} + e_{sy}\right)\left(e_{tx} + e_{ty}\right) + \overline{\kappa}\left(e_{sx}e_{sy} + e_{tx}e_{ty}\right). \tag{8}$$

The first two terms of [Eq. (8)] correspond, respectively, to the thermodynamic work performed against the initial splaying torque, τ_s^0, on generation of the total splay strain, $e_s = e_{sx} + e_{sy}$, and against the initial twisting torque, τ_t^0, on producing the total twist strain, $e_t = e_{tx} + e_{ty}$. The third and fourth terms are quadratic in the total splay, e_s, and twist, e_t, meaning that they represent the elastic contributions to the energy with the corresponding elastic moduli of the pure splay, κ_{ss}, and the pure twist, κ_{tt}. Fundamentally, these two elastic moduli must be positive, $\kappa_{ss} > 0$, $\kappa_{tt} > 0$, to guarantee the thermodynamic stability of the system. The fifth contribution to Eq. (8) is determined by the interplay between the splay and twist deformations, the coefficient, κ_{st}, setting the extent to which the splaying torque, τ_s, is influenced by the total twist strain, e_t, and vice versa, how the twist stress, τ_t, depends on the total splay strain, e_s. Finally, the sixth contribution has a more complicated geometrical origin depending on the product of the splay components, $e_{sx}e_{sy}$, and the twist components, $e_{tx}e_{ty}$. This energy contribution does not vanish only if the deformation occurs simultaneously in x- and y-directions so that both the x- and y-components of the splay and twist strains differ from zero. If the deformation is unidirectional, the last term in Eq. (8), which can be referred to as the saddle-splay energy, does not contribute. The coefficients, κ_{st} and $\overline{\kappa}$, may adopt positive as well as negative values, which do not violate the requirement of the thermodynamic stability of the system.

The expression [Eq. (8)] can be presented in a more compact form by introducing the parameter combinations

$$e_{s0} = -\frac{\tau_s^0}{\kappa_{ss}} \tag{9}$$

and

$$e_{t0} = -\frac{\tau_t^0}{\kappa_{tt}}$$

and changing the energy of the reference state by a constant value, $-\frac{1}{2}\kappa_{ss}{e_{s0}}^2 - \frac{1}{2}\kappa_{tt}{e_{t0}}^2$. The energy density is then presented as

$$f = \frac{1}{2}\kappa_{ss}(e_s - e_{s0})^2 + \frac{1}{2}\kappa_{tt}(e_t - e_{t0})^2 + \kappa_{st}e_s e_t + \overline{\kappa}\left(e_{sx}e_{sy} + e_{tx}e_{ty}\right). \tag{10}$$

The first two terms of Eq. (10) have a familiar form of Hooke's law for the total splay, e_s, and the total twist, e_t, respectively. The parameters e_{s0} and e_{t0} play the roles of apparent equilibrium values of the local total splay and twist for which Hooke's splay and twist stresses would vanish. Therefore, e_{s0} and e_{t0} can be, formally, considered as structural parameters determining the stress-free state of the nematic and referred to as the spontaneous splay and twist, respectively.

It is important to emphasize, however, that the real meaning of e_{s0} and e_{t0} is directly related to the stresses existing in the uniform state of the nematic, as it follows from the derivation above and the expressions [Eq. (9)]. In other words, the spontaneous splay and twist do not really describe the structure of the stress-free state of the system but rather quantify, together with the elastic moduli, κ_{ss} and κ_{tt}, the internal stresses existing within the liquid crystal in the uniform state.

This point has not just a semantic meaning but rather an important physical content. To illustrate that, let us consider, for simplicity, a nematic with vanishing elastic moduli, corresponding to the third and fourth contributions to Eq. (10), $\kappa_{st} = 0$, $\overline{\kappa} = 0$. The energy density, f, is determined in this case by Hooke's law only. Assume that a sample of such liquid crystal is not subjected to any constraints imposed on its boundaries and there are no external forces acting on the system. A practical question would be: is such liquid crystal expected to adopt the state with total splay and twist having the spontaneous values e_{s0} and e_{t0}? The answer is that, generally, this is not the case. Indeed, our consideration above was not limited to small values of the initial torques, τ_s^0 and τ_t^0. Therefore, the spontaneous splay and twist, e_{s0} and e_{t0}, do not have to be small in the sense that their products with the inverse molecular dimension, $|e_{s0}|\delta$ and $|e_{t0}|\delta$, can be comparable to or even larger than one. In such cases, adopting by the system a state characterized by e_{s0} and e_{t0} would mean a strong deviation from the initial uniform state so that the

resulting strains do not satisfy the condition of smallness [Eq. (5)], and, hence, the quadratic formula for the energy [Eq. (9)] is invalid a priori. Specifically, in the case of large initial torques, τ_s^0 and τ_t^0, the relaxation of the system from the state of uniform director, $\vec{L}$, generates large strains for which the nonlinear contributions to the stress-strain relationships [Eq. (6)] are, generally, expected to become essential. This will lead to the additional substantial contributions to the energy density [Eq. (10)] of higher than quadratic orders in splay and twist resulting in an equilibrium state different from that characterized by e_{s0} and e_{t0}.

3.2 Spontaneous Curvature of Lipid Membranes

The physical meaning of the membrane spontaneous curvature, as defined by Helfrich [4], is, basically, analogous to that of the spontaneous splay of a nematic liquid crystal described above. We present here the major steps of introduction of Helfrich model of membrane bending elasticity, which includes definition of the membrane spontaneous curvature [4]. We use, explicitly, the analogy between the physical ideas behind modeling the elastic properties of a membrane with those presented above for description of bending of a nematic liquid crystal.

The membrane is described by a surface whose infinitesimal elements are characterized by the area, da, and the orientation of the unit normal vector, $\vec{n}$, playing a role of the director (Fig. 2b). Since we are interested only in the curvature effects, we do not address here the deformations of area stretching-compression.

In the initial state, the membrane is considered to be flat so that the normal vector, $\vec{n}$, is uniformly oriented throughout the whole membrane surface (Fig. 2b, left panel). Bending of the membrane surface results in two kinds of local deformations. First, the surface elements change their shapes in the membrane plane without changing their areas, which constitutes the lateral shear deformations. Second, the normal vector, $\vec{n}$, deviates from the uniform orientation (Fig. 2b, right panel). Since, as mentioned above, the membrane has properties of a two-dimensional fluid, no in-plane shear stresses develop in the system. Therefore, the lateral shear strains do not contribute to the membrane energy. By contrast, generation of inhomogeneity in $\vec{n}$ orientation resulting in a reciprocal rotation of the normal vectors, $\vec{n}$, of neighboring membrane elements (Fig. 2b) does cost energy. The corresponding strains are represented by the components of the gradient of $\vec{n}$ determined along the surface plane. The stresses associated with these strains are the torques, τ_i, opposing the mutual turning of the adjacent surface elements.

To express, explicitly, the strains we choose at every point of the membrane surface a local Cartesian system of coordinates, $\{z, x, y\}$, with z-axis parallel to the normal vector, $\vec{n}$, in the origin ($x = 0$, $y = 0$). The membrane shape in the vicinity of the chosen point is determined by a function $z(x, y)$. Analogously to the liquid

crystal model, the membrane strain, e_j, can be presented as having two "splay",

$$e_{sx} = \frac{\partial n_x}{\partial x} \text{ and } e_{sy} = \frac{\partial n_y}{\partial y},$$

and two "twist",

$$e_{tx} = -\frac{\partial n_y}{\partial x} \text{ and } e_{ty} = \frac{\partial n_s}{\partial y}, \tag{11}$$

components.

The definition of the strain components [Eq. (11)] relates them directly to the central geometrical characteristics of the membrane surface, the covariant components of the shape tensor (second fundamental form), $b_{\alpha\beta}$ [33],

$$b_{xx} = \frac{\partial n_x}{\partial x}, b_{yy} = \frac{\partial n_y}{\partial y}, b_{yx} = \frac{\partial n_y}{\partial x}, \text{ and } b_{xy} = \frac{\partial n_x}{\partial y}. \tag{12}$$

It can be demonstrated that at the origin of the local Cartesian coordinate system, ($x = 0$, $y = 0$), where $\partial z/\partial x = 0$ and $\partial z/\partial y = 0$, the covariant, contravariant, and mixed components of the shape tensor are equal, so that $b_{xx} = b_x^x$, $b_{yy} = b_y^y$, $b_{xy} = b_x^y$, and $b_{yx} = b_y^x$.

As a result, the splay [Eq. (11)] can be represented by the diagonal,

$$e_{sx} = b_x^x, e_{sy} = b_y^y, \tag{13}$$

and the twist is given by the non-diagonal,

$$e_{t1} = -b_y^x, e_{t2} = b_x^y, \tag{14}$$

components of the mixed shape tensor, b_α^β.

Analogously to the above consideration of the bending energy of liquid crystals, the membrane bending energy can be computed by integration of the torques over the strains. In the membrane case however, this integration results in the energy per unit area of the membrane surface rather than the volumetric energy density. Since the torque-strain relationships, $\tau_k(e_i)$, are, generally, nonlinear and unknown, to proceed in the energy determination, we have to make an assumption of smallness of the strains and use the approximate linear relationships between the torques and the strains [Eq. (6) or (7)]. In the case of membrane bending, the role of the characteristic length setting the scale in the system is played by the membrane thickness, d. The smallness of the strains means that the absolute values of the shape tensor components are much smaller than the inverse membrane thickness,

$$\left|b_x^x\right| d \ll 1, \quad \left|b_y^y\right| d \ll 1, \quad \text{and} \quad \left|b_x^y\right| d = \left|b_y^x\right| d \ll 1. \tag{15}$$

Taking into account the relationships [Eq. (12)], smallness of the strains [Eq. (15)] means that the angles, $\theta_i = n_i$, generated as a result of membrane bending between the normal vectors, $\vec{n}$, in the adjacent membrane points, remain much smaller than one, $\theta_i \ll 1$.

The number of the nonvanishing elastic moduli relating the torques and the strains in the linear approximation [Eqs. (6) and (7)] is determined based on the same symmetry consideration as in the case of liquid crystals [30].

Integration of the torques over the strains accounting for [Eq. (7)], the condition [Eq. (15)], and the relationships [Eqs. (13) and (14)] results in the expression analogous to [Eq. (8)] relating the energy density to the total splay, $e_s = e_{sx} + e_{sy}$, the total twist, $e_t = e_{tx} + e_{ty}$, and the products of the strain components, $e_{sx}e_{sy}$ and $e_{tx}e_{ty}$.

It has to be taken into account that the shape tensor, by definition, statisfies, $b_x^y = b_y^x$ [33]. Therefore, the total twist, $e_t = e_{tx} + e_{tx}$, which is equal, according to Eq. (14), to the difference between the non-diagonal components of the shape tensor, vanishes,

$$e_t = b_x^y - b_x^y = 0, \tag{16}$$

which is not necessarily the case for nematics [30].

As a result, the expression for the density of the membrane energy simplifies to

$$f = \tau_s^0 \left(b_x^x + b_y^y\right) + \frac{1}{2}\kappa_{ss}\left(b_x^x + b_y^y\right)^2 + \overline{\kappa}\left(b_x^x b_y^y - b_y^x b_x^y\right), \tag{17}$$

where τ_s^0 is the splaying torque existing in the initial flat state of the membrane and κ_s and $\overline{\kappa}$ are the remaining elastic parameters relating the torque components to the strains in the linear approximation.

The first and second contributions to the density of the membrane bending energy [Eq. (17)] depend only on the total splay, $e_s = e_{sx} + e_{sy} = b_x^x + b_y^y$, which can be presented as the trace of the shape tensor, $e_s = Tr\left(b_\alpha^\beta\right)$, referred to as the total curvature of the surface, $J = Tr\left(b_\alpha^\beta\right)$ [33]. The third contribution depending on the products of the shape tensor components is proportional to the determinant of the shape tensor, $\det\left(b_\alpha^\beta\right) = b_x^x b_y^y - b_y^x b_x^y$, referred to as the Gaussian curvature of the surface, $\mathrm{K} = \det\left(b_\alpha^\beta\right)$ [33]. It has to be noted that in the mathematical literature, the notion of the mean curvature, $H = -\frac{1}{2}J$, is more common than that of the total curvature, J. According to their definitions, the total and Gaussian curvatures are surface scalars, meaning that their values do not depend on the orientation of the local x , y axes in the membrane plane. For the special local coordinate system, where x , y-orientation is such that the shape tensor has a diagonal form, $b_y^x = b_x^y = 0$, the diagonal components of the shape tensor are called the principal curvatures of the surface, $c_x = b_x^x$, $c_y = b_y^y$. The corresponding x- and

y-directions are called the principle directions [33]. The principle curvatures have a straightforward geometrical meaning of curvatures of the lines formed by crossing the membrane surface by perpendicular planes in the principle directions. Therefore, a frequent presentation of the total and Gaussian curvatures in the literature is as a sum, $J = c_x + c_y$, and a product, $K = c_x \cdot c_y$, of the principal curvatures, respectively.

Using the introduced definitions, the energy density [Eq. (17)] can be expressed through the mean and Gaussian curvatures as

$$f = \tau_s^0 J + \frac{1}{2}\kappa_{ss} J^2 + \overline{\kappa} K. \tag{18}$$

The total bending energy of the membrane, F_B, is given by integration of the energy density [Eq. (18)] over the whole membrane surface,

$$F_B = \oint f dA. \tag{19}$$

Analogously to the above consideration of the elastic model of liquid crystals [Eqs. (8) and (10)], the elastic coefficient, κ_{ss}, coupled to the total curvature square, J^2, has a meaning of an elastic modulus or, equivalently, the membrane susceptibility with respect to the total curvature, J. In the literature, this elastic modulus is referred to as the membrane bending modulus and denoted by κ_B instead of κ_{ss} [4, 31]. The bending modulus must be positive to guarantee the stability of the membrane with respect to bending deformations. The bending modulus, κ_B, has been measured by different methods for lipid bilayers and monolayers of various compositions. The characteristic value of this modulus constitutes 10 k_BT and 20 k_BT for a monolayer and a bilayer, respectively, $k_BT \approx 0.6$ kcal/mole being the product of the Boltzmann constant and the absolute temperature (see for recent review [34]). The elastic coefficient, $\overline{\kappa}$, related to the Gaussian curvature, K, is referred to as the modulus of Gaussian curvature or the saddle-splay modulus. This elastic coefficient determines the dependence of the energy density on the first power of the Gaussian curvature, K, and, therefore, does not have a meaning of susceptibility with respect to K. Hence, the membrane mechanical stability does not require $\overline{\kappa}$ to be positive, and, in fact, this modulus was shown to be negative in a few cases where it was accessible for the experimental determinations [35–37]. It has to be noted that as long as the modulus of Gaussian curvature, $\overline{\kappa}$, has a constant value all over the membrane, it becomes relevant only for membrane processes, which include topological remodeling of the membrane by fission, self-fusion, fusion with other membranes, and/or formations of holes in the membrane surface accompanied by deformation of surface regions bound by the hole rims. The reason for that is Gauss-Bonnet theorem according to which integral of Gaussian curvature, K, which has to be computed for determination of the total bending energy [Eq. (19)], is independent of the surface shape as long as the surface remains closed and varies only upon changes of the surface connectivity through topological rearrangements [33]. Importantly, in the cases where the value of the modulus of

Gaussian curvature, $\overline{\kappa}$, changes along the membrane surface, which may be the case in biological membranes, the energy contribution of the Gaussian curvature affects the membrane shapes also in the absence of topological transformations (see, e.g., [38]).

The spontaneous curvature of the surface, J_s, is defined through the initial splaying torque, τ_s^0, and the bending modulus, κ_B, by

$$J_s = -\frac{\tau_s^0}{\kappa_B}. \tag{20}$$

Using this definitions [Eq. (20)] and changing the energy of the reference flat state by a constant, $-\frac{1}{2}\kappa_B {c_0}^2$, we obtain the familiar Helfrich form for the area density of the membrane bending energy,

$$f = \frac{1}{2}\kappa_B (J - J_s)^2 + \overline{\kappa} K. \tag{21}$$

Importantly, the dependence of Helfrich bending energy [Eqs. (18) and (21)] on the total, J, and Gaussian, K, curvatures rather than, separately, on each of the principle curvatures of the surface, c_x and c_y, or on different components of the shape tensor, b_α^β, has a fundamental physical meaning. As mentioned above, according to their definitions through, respectively, the trace and the determinant of the shape tensor, the total and Gaussian curvatures are the surface scalars. The energy dependence only on the surface scalars is the consequence of the membrane properties of an isotropic two-dimensional fluid with no designated structural direction in the membrane plane.

In this context and to conclude this section, we mention the relationship between the Helfrich model of membrane bending elasticity given by Eq. (21) and that suggested by Canham [3] for explanation of red blood cell shapes [3]. The reason for this discussion is a frequent reference in the literature to the energy [Eq. (21)] as the Canham-Helfrich Hamiltonian. Canham [3] considered the membrane as a homogeneous isotropic solid sheet having no elastic stresses in the flat state rather than a two-dimensional fluid layer subject to torques while being flat. For derivation of the membrane bending energy, Canham used the common methods of the thin-shell mechanics (see, e.g., [32]). As a result, the Canham energy accounts neither for the membrane spontaneous curvature nor for the contribution of the Gaussian curvature determined by a separate elastic constant. Canham's approach can be extended to include the missing contributions, but in that case the analog of Helfrich's modulus of Gaussian curvature turns out to be proportional to the lateral shear modulus, which must vanish for fluid membranes. Summarizing, because of the substantial differences in the physical properties of membranes assumed by Helfrich and Canham's approaches and due to the crucial factors, the spontaneous curvature and the modulus of Gaussian curvature, accounted by Helfrich's but not Canham's formula, we find unjustified the association of the model [Eq. (21)] with Canham's name.

3.3 Meaning of Spontaneous Curvature

There is a substantial difference between the notion of the spontaneous curvature, as set by its definition [Eq. (20)], and the concept of the intrinsic curvature, J_0, described in the previous section. The analogous issue related to the spontaneous splay and twist of nematic liquid crystals was already addressed above. Nevertheless, because of its importance and frequent misinterpretation in the literature, we are going to discuss that matter again in a specific relation to the membrane spontaneous curvature, J_s.

The first contribution to the density of the membrane bending energy, f, presented by Helfrich's formula [Eq. (21)], has a form of Hooke's law with the spontaneous curvature, J_s, playing a role of a geometrical characteristic of the relaxed membrane state. Therefore, commonly, the spontaneous curvature, J_s, would be associated with the total curvature the membrane tended to adopt spontaneously in case there were no external forces acting on the membrane surface and the membrane did not undergo topological transformations by fusion, fission, and rupture. In other words, the spontaneous curvature, J_s, is often identified with the intrinsic curvature, J_0, defined above. Such equating of the two concepts is, generally, misleading since they have a priori different physical contents. The spontaneous curvature is merely a measure of the stress, τ_s^0, existing within the membrane in the initial flat state rather than a direct characteristic of the membrane geometry. In contrary, the intrinsic curvature, J_0, is a geometrical feature of a relaxed membrane, which does not carry any information about the membrane stresses.

At the same time, for applications, it is important to know, whether and under which conditions, in spite of the difference in the physical meaning, the value of the spontaneous curvature, J_s, can become similar to that of the intrinsic curvature, J_0. A short answer is that such concurrence can be expected in two situations: either the spontaneous and intrinsic curvatures are both much smaller than the inverse membrane thickness, $|J_s|d \ll 1$, $|J_0|d \ll 1$, or the torque-strain relationship of the membrane, $\tau_i(e_i)$, remains linear [Eqs. (6) and (7)] not only for small but also for large membrane curvatures comparable to the inverse membrane thickness.

In general case, however, the spontaneous and intrinsic curvatures are not expected to have equal or even close values. Indeed, depending on the membrane lipid composition, the initial stress, τ_s^0, can be arbitrarily large so that the spontaneous curvature determined according to Eq. (20) can adopt values comparable with or larger than the inverse membrane thickness, $|J_s|d \geq 1$. This means that, in order to reach a shape with the total curvature equal to J_s, the membrane has to deviate from the initial flat state by the extent violating the requirement of smallness of membrane strains [Eq. (16)]. In that case the Helfrich's expression for the membrane energy [Eq. (21)] has to be complemented by the terms of higher orders in the product of the curvature and the membrane [39]. Because of these additional energy contributions, the intrinsic curvature, J_0, resulting from the complete energy minimization and describing the equilibrium membrane shape, is not expected to equal the spontaneous curvature, J_s, determined by Eq. (20).

It has to be kept in mind, however, that some membranes or, more precisely, lipid monolayers of, at least, certain lipid compositions appear to demonstrate an unexpectedly long-reaching linearity in the torque-strain relationship, which, as mentioned above, can lead to the value similarity between the spontaneous, J_s, and intrinsic, J_0, curvatures. This conclusion is based on the addressed above measurements of the bending moduli of monolayers forming the strongly curved tubes of H_{II}-phases [20, 23–26]. The intrinsic curvatures of these monolayers are, practically, equal to the inverse monolayer thicknesses, $1/d \approx 1/2\text{nm}$. Deformation of these monolayers in the vicinity of their strongly curved intrinsic shapes revealed the values of the bending moduli of about $10\,k_BT$, which is very close to the bending moduli determined for nearly flat monolayers, albeit of different lipid compositions [34]. This consistency of the bending modulus values determined experimentally over a very broad range of membrane curvatures indicates, although does not prove, that the bending energy of lipid monolayers is quadratic in the total curvature in an extremely wide range of the bending deformations including those for which the curvature radii are comparable to the monolayer thickness. In other words, this means that the dependence of the monolayer torque on the total curvature may remain linear up to very large deformations. In this case, the numbers obtained experimentally for the intrinsic curvatures can be used as substitutions for the spontaneous curvature in spite of the difference between the physical meanings of the two notions.

3.4 Spontaneous Curvature of Mixed Lipid Monolayers

As, in contrast to the membrane intrinsic curvature, J_0, the spontaneous curvature, J_s, does not have a direct geometrical meaning but is rather related to the torque in the flat membrane state, τ_0, understanding how J_s depends on the membrane lipid composition requires a thermodynamic analysis rather than a purely geometrical consideration. Since, as already mentioned, the elastic properties of a lipid bilayer are determined by the properties of its constituent monolayers, we present here the thermodynamic description of mixed, weakly, and homogeneously curved lipid monolayers [40]. For constant temperature, the variation of the monolayer free energy can be written as [41, 42]

$$dF = \gamma dA + A\tau\, dJ + A\overline{\kappa} dK + \Sigma \mu_i\, dN_i, \tag{22}$$

where γ is the Gibbs tension; A is the monolayer area; N_i is the number of lipid molecules of i-th type; μ_i is the chemical potential of i-th lipid type; J and K are, respectively, the total and Gaussian curvatures of the monolayer surface; τ is the torque; and $\overline{\kappa}$ is the modulus of Gaussian curvature of the monolayer. The summation in the last term of Eq. (22) is taken over all types of the membrane lipid components. Eq. (22) provides a thermodynamic definition for the membrane torque, τ, and modulus of Gaussian curvature, $\overline{\kappa}$, through the derivatives of the free

energy with respect to the total, J, and Gaussian, K, curvatures, respectively. These thermodynamic definitions of τ and $\overline{\kappa}$ are complementary to the discussed above definitions by Helfrich [4].

All the thermodynamic functions and variables related to the curvatures depend on the choice within the membrane of Gibbs dividing surface (reference plane) [17, 18]. Generally, one can choose any arbitrary plane parallel to the membrane-bulk interface as the dividing surface. The thermodynamic description simplifies for several special dividing surfaces such as Gibbs' surface of tension [41] or the neutral surface [17, 18]. For our purposes, the most convenient is the neutral surface, for which the deformation of membrane area stretching-compression and the deformation of changing the total curvature, J, are energetically decoupled. The position of the neutral surface has been determined for a series of monolayers of different compositions and appears to be located near the interface between the polar heads and the hydrophobic moieties of the constituent lipid molecules [20].

The free energy, F, must be a first-order homogeneous function of its extensive thermodynamic variables, A and N_i. It can be, therefore presented, according to Euler's theorem, as

$$F = \gamma A + \Sigma \mu_i \, N_i, \tag{23}$$

where the tension, γ, and the chemical potentials, μ_i, are functions of the curvatures. The Gibbs-Duhem-type equations resulting from Eqs. (22) and (23)] relate the differentials of the chemical potentials, the tension, and the curvatures,

$$\Sigma \, N_i d\mu_i = -Ad\gamma + A\tau \, dJ + A\overline{\kappa} \, dK. \tag{24}$$

From Eq. (24) we can derive a general relationship between the torque and the chemical potentials of the membrane components,

$$\tau = \left(\frac{\partial \gamma}{\partial J}\right)_{A,N_i} + \frac{1}{A}\Sigma \, N_i \left(\frac{\partial \mu_i}{\partial J}\right)_{A,N_i}, \tag{25}$$

where the subscripts indicate the values, which are kept constant through the differentiation. In the following we skip this explicit indication. To present Eq. (25) in a more useful form, we apply Maxwell relationships between the derivatives of the intensive thermodynamic functions, which follow from the independence of the mixed derivatives of the energy [Eq. (22)] of the order of differentiation. The Maxwell relations we substitute in Eq. (25) are

$$A\frac{\partial \tau}{\partial N_i} = \frac{\partial \mu_i}{\partial J}. \tag{26}$$

Moreover, since we describe the lipid monolayer by its neutral surface, the derivative of the tension with respect to the total curvature vanishes, $\frac{\partial \gamma}{\partial J} = 0$. Taking

this and Eq. (26) into account, we obtain from Eq. (25) for the case of constant area

$$\tau A = \Sigma\, N_i A \frac{\partial \tau}{\partial N_i}. \tag{27}$$

It follows from Eq. (27) that for fixed monolayer area, A, the product of the torque and the area, τA, is a first-degree homogeneous function of the molecular numbers of the components, N_i, and, hence, can be presented in the form

$$\tau A = (\Sigma\, N_i) \cdot \Phi\left(\frac{N_2}{N_1}, \frac{N_3}{N_1}, \ldots, \frac{N_n}{N_1}\right). \tag{28}$$

It has to be emphasized that Eqs. (27) and (28) are general thermodynamic relationships, which must be satisfied by any specific model of the elastic parameters of mixed monolayers.

Importantly, the relationships [Eqs. (27) and (28)] impose constraints on the models for the torques, $\tau = -J_s\kappa$, rather than, separately, for the spontaneous curvature, J_s, and bending modulus, κ. In the literature, however, specific models for J_s and κ have been suggested. These models operated with the notions of spontaneous curvatures, J_s^i, and bending moduli, κ_B^i, of individual components, whose meanings were the elastic characteristics of monolayer with uniform composition consisting only of the i-th lipid. Namely, the spontaneous curvature of a mixed monolayer containing N_i molecules of i-th type has been suggested to be equal to a sum of spontaneous curvatures of the individual components, J_s^i, weighted with their molar ratios within the membrane, $\phi_i = \frac{N_i}{\Sigma N_i}$, so that $J_s = \Sigma\phi_i J_s^i$. The same assumption was made concerning the inverse bending modulus, $\frac{1}{\kappa_B} = \Sigma\frac{\phi_i}{\kappa_B^i}$ [43]. A slight development of this model taking into account a possibility of differences between the in-plane molecular areas of the components, a_i, presents the spontaneous curvature and the inverse bending modulus as sums of the characteristics of individual components weighted with their relative areas, $J_s = \frac{1}{\Sigma N_i a_i}\Sigma N_i \cdot a_i \cdot J_s^i$, $\frac{1}{\kappa_B} = \frac{1}{\Sigma N_i a_i}\Sigma N_i \cdot a_i \cdot \frac{1}{\kappa_B^i}$ [40]. The background for these models was a reasoning based on a mechanical meaning of the intrinsic rather than spontaneous curvature and ignoring a fundamental difference between the physical contents of the two notions. It is easy to see that both versions of the model do not satisfy the thermodynamic constraints [Eqs. (27) and (28)]. For example, in the latter version of the model, the torque in the flat membrane state equals $\tau_s^0 = -J_s\kappa_B = -\frac{\Sigma J_s^i N_i a_i}{\Sigma\frac{1}{\kappa_B^i} N_i a_i}$, which does not fulfill [Eq. (28)].

A thermodynamically correct model for the spontaneous curvature and bending modulus of a mixed monolayer, where the contributions of the individual

components are assumed to be additive, has to propose that J_s and κ_B satisfy [40],

$$J_s = \frac{1}{A}\Sigma N_i \cdot a_i \cdot J_s^i \tag{29}$$

$$\frac{1}{\kappa_B} = \frac{1}{\Sigma N_i a_i}\Sigma N_i \cdot a_i \cdot \frac{1}{\kappa_B^i}. \tag{30}$$

The difference between the model presented by Eqs. (29) and (30) and the previous ones consists in an assumption that the change of the monolayer area, A, upon a condition of constant number of all components, leads to variation of the spontaneous curvature [Eq. (29)] but not of the bending modulus [Eq. (30)]. The resulting expression for the bending moment in the flat membrane state,

$$\tau_s^0 = -J_s\kappa_B = -\frac{\Sigma N_i a_i}{A} \cdot \frac{\Sigma J_s^i N_i a_i}{\Sigma \frac{1}{\kappa_B^i} N_i a_i}, \tag{31}$$

fulfills (Eqs. (27) and (28)]. Obviously, also more complex relationships accounting for nonadditive contributions of different components to the monolayer elastic characteristics, J_s and κ_B [28], are allowed by the thermodynamic relationships [Eqs. (27) and (28)].

4 Conclusions

The goal of this review was to recall the physical background behind the notion of the membrane spontaneous curvature introduced by Helfrich [4], which has been ubiquitously used in the membrane literature over the last few decades, and to illustrate its essential difference from the intrinsic curvature defined by Gruner [9] for lipid monolayers. We emphasized that, while the intrinsic curvature is a geometrical characteristic of a lipid monolayer determined by X-ray studies of the inverted hexagonal phase, the spontaneous curvature characterizes the stress existing in a flat membrane and does not have a direct geometrical meaning. The spontaneous and intrinsic curvatures may have similar values, if both of them are much smaller than the inverse membrane thickness.

Which notion is more useful for the practical characterization of the membrane elastic behavior? Obviously, the answer depends on the specific membrane system. In a lipid bilayer constituting the matrix of any biological membrane, the two monolayers are coupled in the transverse direction so that acquisition of curvature by one of them leads to acquirement of an opposite curvature by the other. In case the lipid compositions of the two membrane monolayers are similar, the bilayer and, hence, the monolayers acquire a flat shape independent of the monolayer intrinsic curvatures. In this situation, each monolayer is elastically frustrated and

is characterized by a bending stress described by the spontaneous curvature. Thus, the latter is the relevant monolayer characteristic. Within the membrane structures, where the two monolayers, locally, deviate from the mutually parallel orientation, the appropriate value determining the membrane behavior may be the intrinsic rather than the spontaneous curvature. Examples are the intermediate structures formed in the course of membrane fusion and fission, the most common of which is membrane stalk [44].

While the present article discussed the spontaneous and intrinsic curvatures of purely lipid monolayers, similar ideas have been used to describe the effects of proteins on the membrane curvature and elastic behavior.

References

1. Tanford C (1973) The hydrophobic effect: formation of micelles and biological membranes. Wiley, New York
2. McConnell HM, Kornberg RD (1971) Inside-outside transitions of phospholipids in vesicle membranes. Biochemistry 10:1111–1120
3. Canham PB (1970) The minimum energy of bending as a possible explanation of the biconcave shape of the human red blood cell. J Theor Biol 26:61–81
4. Helfrich W (1973) Elastic properties of lipid bilayers: theory and possible experiments. Z Naturforsch 28c:693–703
5. Luzzati V (1968) X-ray diffraction studies of lipid-water systems. In: Chapman D (ed) Biological membranes. Academic, New York, pp 71–123
6. McMahon HT, Boucrot E (2015) Membrane curvature at a glance. J Cell Sci 128:1065–1070
7. Alberts B, Bray D, Lewis J, Raff M, Roberts K, Watson JD (2002) Molecualr biology of the cell. Garland, New York
8. Shibata Y, Hu J, Kozlov MM, Rapoport TA (2009) Mechanisms shaping the membranes of cellular organelles. Annu Rev Cell Dev Biol 25:329–354
9. Gruner SM (1985) Intrinsic curvature hypothesis for biomembrane lipid composition: a role for nonbilayer lipids. Proc Natl Acad Sci USA 82:3665–3669
10. Seddon J, Templer R (1993) Cubic phases of self-assembled amphiphilic aggregates. Philos Trans R Soc Lond A 344:377–401
11. Seddon JM (1990) Structure of the inverted hexagonal (HII) phase, and non-lamellar phase transitions of lipids. Biochim Biophys Acta 1031:1–69
12. Seddon JM, Templer RH (1995) Polymorphism of lipid-water systems. In: Lipowsky R, Sackmann E (eds) Structure and dynamics of membranes. Elsevier, Amsterdam, pp 97–160
13. Rand RP, Fuller NL (1994) Structural dimensions and their changes in a reentrant hexagonal-lamellar transition of phospholipids. Biophys J 66:2127–2138
14. Gruner SM, Parsegian VA, Rand RP (1986) Directly measured deformation energy of phospholipid HII hexagonal phases. Faraday Discuss Chem Soc:29–37
15. Gruner SM (1989) Stability of lyotropic phases with curved interfases. J Phys Chem 93:7562–7570
16. Rand RP, Fuller NL, Gruner SM, Parsegian VA (1990) Membrane curvature, lipid segregation, and structural transitions for phospholipids under dual-solvent stress. Biochemistry 29:76–87
17. Kozlov MM, Leikin SL, Markin VS (1989) Elastic properties of interfaces. Elasticity moduli and spontaneous geometrical characteristics. J Chem Soc Faraday Trans 2(85):277–292
18. Kozlov MM, Winterhalter M (1991) Elastic moduli for strongly curved monolayers. Position of the neutral surface. J Phys II France 1:1077–1084

19. Kozlov MM, Winterhalter M (1991) Elastic moduli and neutral surface for strongly curved monolayers. Analysis of experimental results. J Phys II France 1:1085–1100
20. Leikin S, Kozlov MM, Fuller NL, Rand RP (1996) Measured effects of diacylglycerol on structural and elastic properties of phospholipid membranes. Biophys J 71:2623–2632
21. Hafez IM, Cullis PR (2001) Roles of lipid polymorphism in intracellular delivery. Adv Drug Deliver Rev 47:139–148
22. Kozlov MM, Leikin S, Rand RP (1994) Bending, hydration and void energies quantitatively account for the hexagonal-lamellar-hexagonal reentrant phase transition in dioleoylphosphatidylethanolamine. Biophys J 67:1603–1611
23. Chen Z, Rand RP (1997) The influence of cholesterol on phospholipid membrane curvature and bending elasticity. Biophys J 73:267–276
24. Chen Z, Rand RP (1998) Comparative study of the effects of several n-alkanes on phospholipid hexagonal phases. Biophys J 74:944–952
25. Fuller N, Benatti CR, Rand RP (2003) Curvature and bending constants for phosphatidylserine-containing membranes. Biophys J 85:1667–1674
26. Fuller N, Rand RP (2001) The influence of lysolipids on the spontaneous curvature and bending elasticity of phospholipid membranes. Biophys J 81:243–254
27. Zimmerberg J, Kozlov MM (2006) How proteins produce cellular membrane curvature. Nat Rev Mol Cell Biol 7:9–19
28. Sodt AJ, Venable RM, Lyman E, Pastor RW (2016) Nonadditive compositional curvature energetics of lipid bilayers. Phys Rev Lett 117:138104
29. Kooijman EE, Chupin V, Fuller NL, Kozlov MM, de Kruijff B, Burger KN, Rand PR (2005) Spontaneous curvature of Phosphatidic acid and Lysophosphatidic acid. Biochemistry 44:2097–2102
30. Frank FC (1958) On the theory of liquid crystals. Discuss Faraday Soc 25:19–28
31. Helfrich W (1990) Elasticity and thermal undulations of fluid films of amphiphiles. In: Charvolin J, Joanny J-F, Zinn-Justin J (eds) Les Houches, 1988—liquids and interfaces. North-Holland, Amsterdam, pp 212–237
32. Landau LD, Lifshitz EM (1970) Theory of elasticity. Pergamon Press, London
33. Spivak M (1970) A comprehensive introduction to differential geometry. Brandeis University, Waltham
34. Dimova R (2014) Recent developments in the field of bending rigidity measurements on membranes. Adv Colloid Interf Sci 208:225–234
35. Lorenzen S, Servuss RM, Helfrich W (1986) Elastic torques about membrane edges—a study of pierced egg lecithin vesicles. Biophys J 50:565–572
36. Templer RH, Khoo BJ, Seddon JM (1998) Gaussian curvature modulus of an amphiphilic monolayer. Langmuir 14:7427–7434
37. Siegel DP, Kozlov MM (2004) The Gaussian curvature elastic modulus of N-monomethylated dioleoylphosphatidylethanolamine: relevance to membrane fusion and lipid phase behavior. Biophys J 87:366–374
38. Shemesh T, Luini A, Malhotra V, Burger KN, Kozlov MM (2003) Prefission constriction of Golgi tubular carriers driven by local lipid metabolism: a theoretical model. Biophys J 85:3813–3827
39. Mitov MD (1978) Third and fourth order curvature elasticity of lipid bilayers. Comptes Rendus de l Academie bulgare des Sciences 31:513–515
40. Kozlov MM, Helfrich W (1992) Effects of a cosurfactant on the stretching and bending elasticities of a surfactant monolayer. Langmuir 8:2792–2797
41. Gibbs JW (1961) The scientific papers. Dover, New York
42. Murphy CL (1966) Thermodynamics of low tension and highly curved interfaces. University of Minnesota, Department of Chemical Engineering
43. Markin VS (1981) Lateral organization of membranes and cell shapes. Biophys J 36:1–19
44. Kozlov MM, Markin VS (1983) Possible mechanism of membrane fusion. Biofizika 28:255–261

Membrane-Mediated Interactions

Anne-Florence Bitbol, Doru Constantin, and Jean-Baptiste Fournier

Abstract Interactions mediated by the cell membrane between inclusions, such as membrane proteins or antimicrobial peptides, play important roles in their biological activity. They also constitute a fascinating challenge for physicists, since they test the boundaries of our understanding of self-assembled lipid membranes, which are remarkable examples of two-dimensional complex fluids. Inclusions can couple to various degrees of freedom of the membrane, resulting in different types of interactions. In this chapter, we review the membrane-mediated interactions that arise from direct constraints imposed by inclusions on the shape of the membrane. These effects are generic and do not depend on specific chemical interactions. Hence, they can be studied using coarse-grained soft matter descriptions. We deal with long-range membrane-mediated interactions due to the constraints imposed by inclusions on membrane curvature and on its fluctuations. We also discuss the shorter-range interactions that arise from the constraints on membrane thickness imposed by inclusions presenting a hydrophobic mismatch with the membrane.

Keywords Lipid bilayer · Continuum elasticity · Membrane inclusion · Hydrophobic matching · Membrane-mediated interactions · Fluctuation-induced interactions

A.-F. Bitbol (✉)
Sorbonne Université, CNRS, Laboratoire Jean Perrin (UMR 8237), Paris, France

Lewis-Sigler Institute for Integrative Genomics and Department of Physics, Princeton University, Princeton, NJ, USA
e-mail: anne-florence.bitbol@sorbonne-universite.fr

D. Constantin
Laboratoire de Physique des Solides, CNRS, Univ. Paris-Sud, Université Paris-Saclay, Orsay, France
e-mail: doru.constantin@u-psud.fr

J.-B. Fournier
Laboratoire "Matière et Systèmes Complexes" (MSC), UMR 7057 CNRS, Université Paris 7 Diderot, Paris Cedex 13, France
e-mail: jean-baptiste.fournier@univ-paris-diderot.fr

P. Bassereau, P. Sens (eds.), *Physics of Biological Membranes*,
https://doi.org/10.1007/978-3-030-00630-3_13

1 Introduction

Although membrane proteins were traditionally described as free to diffuse in the cell membrane [1], it was soon acknowledged that the lipid bilayer can influence their organization and thus have an impact on many aspects of their activity [2]. Hence, interactions between proteins and the host membrane, as well as the resulting protein–protein interactions, have become fundamental topics in biophysics.

Membrane inclusions such as proteins can couple to various degrees of freedom of the membrane (curvature, thickness, composition, tilt, etc.), thus giving rise to several types of membrane-mediated interactions. It is noteworthy that these interactions are often nonspecific, i.e., they do not involve the formation of chemical bonds between the various components. Thus, understanding these interactions calls for a description of the membrane as a self-assembled system whose properties are collectively determined, and not merely given by the chemical properties of the molecules involved [3]. Over the last few decades, it has become clear that the concepts developed in soft matter physics to describe self-organized systems are extremely useful in this context, and that coarse-grained effective models such as the Helfrich model of membrane elasticity [4] can yield valuable insight.

In this chapter, we review the membrane-mediated interactions between inclusions such as membrane proteins that arise from direct constraints imposed by these inclusions on the shape of the membrane. Our point of view is mostly theoretical, in agreement with the history of this research field, but we also discuss the numerical and experimental results that are available. For clarity, we treat separately the effects that result from the coupling of the inclusions with membrane curvature and those that arise from their coupling with membrane thickness. Note however that a given inclusion can couple to both of these degrees of freedom. The first case, presented in Sect. 2, leads to interactions with a much larger range than the characteristic size of the inclusions, which will be referred to as "long-range interactions." Such effects can be described starting from the coarse-grained Helfrich model [4]. The second case, discussed in Sect. 3, yields a much shorter-range interaction and requires more detailed effective models of the membrane.

Other types of membrane-mediated interactions, arising from other underlying membrane degrees of freedom such as lipid composition and tilt, will not be discussed in detail. Besides, important applications such as the crystallization of membrane proteins and the interaction between constituents of such crystals are outside of the scope of this chapter.

2 Long-Range Membrane-Mediated Interactions

Inclusions such as proteins are generally more rigid than the membrane. Therefore, they effectively impose constraints on the shape of the membrane, especially on its curvature, which plays a crucial part in membrane elasticity. These constraints in

turn yield long-range membrane-mediated interactions between inclusions. While our focus is on inclusions, we note that similar interactions have been predicted between objects adsorbed on the membrane, e.g., grafted polymers [5], which can be described as imposing a force distribution (with zero mean) rather than a shape constraint.

We will review the first theoretical predictions of these interactions, before moving on to further results in the analytically tractable regime of distant inclusions embedded in almost-flat membranes, including anisotropy, multi-body effects, and dynamics. Extensions to other geometries will then be discussed, including the compelling but tricky regime of large deformations, where numerical simulations provide useful insight. Finally, we will examine the available experimental results.

2.1 First Predictions

2.1.1 Seminal Paper

The existence of long-range membrane-mediated forces between inclusions in lipid membranes was first predicted in Ref. [6]. (Note that a related collective effect of curvature instability induced by inclusions imposing a spontaneous curvature had been discussed previously [7].) In Ref. [6], the curvature elasticity of the membrane was described by the tensionless Helfrich Hamiltonian [4]. For an up-down symmetric membrane, it reads

$$H = \int dA \left[\frac{\kappa}{2} (c_1 + c_2)^2 + \bar{\kappa}\, c_1 c_2 \right] , \tag{1}$$

where κ is the bending rigidity of the membrane and $\bar{\kappa}$ is its Gaussian bending rigidity, while c_1 and c_2 denote the local principal curvatures of the membrane, and A its area. This elastic energy penalizes curvature. For small deformations of the membrane around a planar shape, Eq. (1) can be approximated by:

$$H[h] = \int d\boldsymbol{r} \left\{ \frac{\kappa}{2} \left[\nabla^2 h(\boldsymbol{r}) \right]^2 + \bar{\kappa}\ \det[\partial_i \partial_j h(\boldsymbol{r})] \right\} , \tag{2}$$

where $h(\boldsymbol{r})$ is the height of the membrane at position $\boldsymbol{r} = (x, y) \in \mathbb{R}^2$ with respect to a reference plane, and $(i, j) \in \{x, y\}^2$. The Hamiltonian in Eq. (2) is massless and features a translation symmetry ($h \to h + C$ where C is independent of position), yielding Goldstone modes. The associated long-range correlations give rise to long-range membrane-mediated interactions. Neglecting the effect of the membrane tension σ, as in Eqs. (1) and (2), is legitimate below the length scale $\sqrt{\kappa/\sigma}$. Note that the simplified Hamiltonian in Eq. (2) is quadratic in the field h, i.e., the field theory is Gaussian.

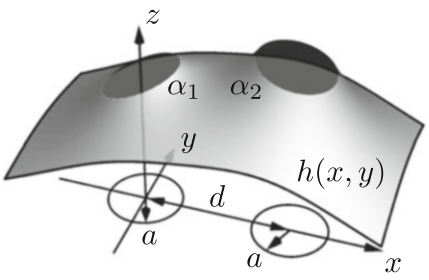

Fig. 1 Ground-state shape of a membrane containing two rigid disk-shaped inclusions that impose the contact angles α_1 and α_2, obtained by solving the Euler–Lagrange equation (see Ref. [8]). The membrane shape is described by its height h with respect to the plane $z = 0$. The radius of the inclusions is denoted by a, and the center-to-center distance by d

In Ref. [6], inclusions are characterized by bending rigidities different from those of the membrane bulk. A zone with slightly different rigidities ("perturbative regime") can represent a phase-separated lipid domain, while a very rigid zone ("strong-coupling regime") can represent a protein. Both regimes are discussed, in the geometry of two identical circular domains of radius a at large separation $d \gg a$ (see Fig. 1). An interaction potential proportional to $1/d^4$ is obtained in both regimes.

Besides, a low-temperature interaction is obtained for rigid inclusions that impose a contact angle with the membrane, e.g., cone-shaped inclusions [6, 9]:

$$U_1(d) = 4\pi\kappa(\alpha_1^2 + \alpha_2^2)\,\frac{a^4}{d^4}\,, \tag{3}$$

where α_1 and α_2 are the contact angles imposed by inclusion 1 and inclusion 2 (see Fig. 1). This interaction is obtained by calculating the membrane shape that minimizes the membrane curvature energy in Eq. (2) in the presence of the inclusions. It arises from the ground-state membrane deformation due to the inclusions and vanishes for up-down symmetric inclusions. It is repulsive. Note that this interaction does not depend on the Gaussian bending rigidity of the membrane [9], as the Gaussian curvature energy term only depends on the topology of the membrane and on boundary conditions. Hence, in most subsequent studies of the membrane-mediated forces between rigid membrane inclusions, the Gaussian curvature term in Eq. (2) is discarded. In the perturbative regime, however, the interaction depends on the perturbation of the Gaussian bending rigidity [6].

Another interaction, which is attractive and originates from the thermal fluctuations of the membrane shape, was predicted as well, and its expression for rigid inclusions reads [6, 10]:

$$U_2(d) = -6\,k_\mathrm{B}T\,\frac{a^4}{d^4}\,. \tag{4}$$

Importantly, this fluctuation-induced interaction is independent of elastic constants and of contact angles. It exists even for up-down symmetric inclusions (imposing $\alpha_1 = 0$ and $\alpha_2 = 0$) that do not deform the ground-state membrane shape.

Multipole expansions valid for $a \ll d$ were used to calculate these interactions for rigid inclusions. Details on these expansions are presented in Refs. [8, 10]. Only the leading-order terms in a/d were obtained in Ref. [6]. This method was recently pushed further, yielding higher-order terms in a/d [8].

In the perturbative regime, the interaction depends on the perturbations of κ and $\bar{\kappa}$ in the inclusions and on the value of κ in the membrane as well as on $k_B T$ [6].

2.1.2 Point-Like Approach

Reference [11] extended the study of Ref. [6]. Membrane elasticity was described by Eq. (2) as in Ref. [6], but different membrane-inclusion couplings were considered. Rigid inclusions were treated through a coupling Hamiltonian favoring a relative orientation of their main axis and of the normal of the membrane. The membrane-mediated interaction was calculated in the limit of very small inclusions, where the ultraviolet cutoff of the theory Λ appears. The radius a of the inclusions was related to Λ through $\Lambda = 2/a$ [11], yielding agreement with the results of [6]: the total interaction energy obtained is the sum of U_1 and U_2 (Eqs. (3) and (4)).

This opened the way to direct point-like descriptions of membrane inclusions. In Ref. [12], a perturbative approach was taken, where the coupling with the membrane and the inclusions was assumed to be linear or quadratic in the local mean curvature at the point location of the inclusion. In Ref. [13], the insertion energy of a protein in the membrane was approximated by a term proportional to the Gaussian curvature of the membrane at the insertion point. Then, in Refs. [14, 15], inclusions were modeled as more general local constraints on the membrane curvature tensor. Considering inclusions as point-like is justified in the case of membrane proteins, since their typical radius is comparable to membrane thickness, which is neglected when the membrane is considered as a surface, as in Eq. (2). This description simplifies the calculation of membrane-mediated interactions, by eliminating the need for a multipole expansion. In practice, one writes the partition function of the membrane described by the elastic energy in Eq. (2) (discarding Gaussian curvature), modeling inclusions as point curvature constraints [14, 15]. For one inclusion imposing a local isotropic curvature c in $\boldsymbol{r}_0$, these constraints read $\partial_x^2 h(\boldsymbol{r}_0) = \partial_y^2 h(\boldsymbol{r}_0) = c$ and $\partial_x \partial_y h(\boldsymbol{r}_0) = 0$. Then, the part of the free energy that depends on the distance d between the inclusions is the sum of U_1 and U_2 (Eqs. (3) and (4)), where the effective radius a of the point-like inclusions appears through the cutoff $\Lambda = 2/a$, and the effective contact angle is $\alpha = ac$.

References [16, 17] formalized the connection between the original description of inclusions as rigid objects [6] and the more convenient point-like description. The effective field theory formalism developed in Refs. [16, 17] for membranes (see also Ref. [18] for fluid interfaces, and Ref. [19] for a review) considers inclusions as point-like particles and captures their structure and the boundary conditions they

impose via localized coupling terms. In practice, a series of generic scalar localized terms consistent with the symmetries of the system is added to the curvature energy describing the bare membrane. Each term in the series is polynomial in the derivatives of the membrane height h, taken at the point position of the inclusion. The coefficients of each term of the series are then obtained by matching observables, such as the ground-state membrane shape responding to an imposed background, between the full model with extended inclusions and the effective field theory [17]. These Wilson coefficients are analogous to charges, polarizabilities, etc. of the inclusions and describe the interplay between the membrane and the inclusions, by encoding the long-range effects of short-range coupling [19]. Membrane-mediated interactions can be obtained from this effective field theory. It gives back the leading terms in a/d obtained previously, with a generalization to inclusions with different radii, and yields higher-order corrections [16, 17]. This general and powerful method could be extended to complex inclusions with specific Wilson coefficients, and also enables general derivation of scaling laws through power counting. However, one should bear in mind that its existing application to rigid disk-shaped inclusions a priori yields results specific to this particular model of the inclusions. In particular, the discrepancy obtained with previous point-like approaches on certain higher-order terms [17] should be regarded as a different result obtained for a different model, since previous point-like approaches did not aim to fully mimic rigid disk-shaped inclusions. Note that higher-order terms were recently calculated in the framework of extended disks [8], showing agreement with [17] and pushing the expansion further.

2.1.3 Two Types of Interactions

The long-range membrane-mediated interaction between rigid inclusions comprises two leading-order terms that both depend on the fourth power of a/d (Eqs. (3) and (4)) [6]. Subsequent works [11, 14–17] demonstrated that the total interaction is the sum of these two terms, one coming from the ground-state deformation of the membrane by the inclusions (Eq. (3)) and the second one arising from entropic effects (Eq. (4)). However, it should be noted that the separation of these two terms is mostly of formal interest, since the ground-state shape, which is obtained by minimizing the Hamiltonian of the system, may not be of much practical relevance. In practice, one may be able to measure experimentally the average shape of a membrane, but in general it would not coincide with the ground-state one, except in the Gaussian regime of small deformations (for an anharmonic potential, the mean value, and the most likely value are not necessarily the same). In this regime, which has been the focus of most theoretical work, the membrane Hamiltonian is quadratic (Eq. (2)): then, the separation of the two terms makes sense. Let us now discuss each of these two terms.

The first term, U_1 (Eq. (3)), arises from the overlap of the ground-state deformations of the membrane due to the presence of each individual inclusion, and it was first obtained in Ref. [6] by taking the (fictitious) zero-temperature

limit. It also corresponds to the membrane-mediated interaction within a mean-field approximation.

The second term, U_2 (Eq. (4)), is a fluctuation-induced or entropic effect, which exists even if both inclusions impose vanishing contact angles. Remarkably, in the case of rigid inclusions, the only energy scale involved is $k_B T$: this interaction is universal. It arises from the constraints imposed by the inclusions on the thermal fluctuations of the shape of the membrane, which is a field with long-range correlations. It is analogous to the Casimir force in quantum electrodynamics (see, e.g., [10, 11, 14, 15, 20]), which arises from the constraints imposed by non-charged objects (e.g., metal plates) on the quantum fluctuations of the electromagnetic field [21, 22]. This fluctuation-induced interaction is thus often termed "Casimir" or "Casimir-like." In Ref. [23], the fluctuation-induced force between membrane inclusions was recovered from the entropy loss associated to the suppression of fluctuation modes, thus reinforcing the formal analogy with the Casimir force. Fluctuation-induced forces analogous to the Casimir force exist in several other soft matter systems, where thermal fluctuations play an important part [24, 25]. They were first discussed by Fisher and de Gennes in the context of critical binary mixtures [26]. This "critical Casimir" force has been measured experimentally between a colloid and a surface immersed in a critical binary mixture [27]. Interestingly, such critical Casimir forces have been predicted to exist in membranes close to a critical point in lipid composition, and they are very long range, with power laws up to $(a/d)^{1/4}$ [28]. Their sign depends on the boundary conditions imposed by the inclusions [28], as in the three-dimensional critical case [25].

Let us now compare the magnitude of these two types of interactions. For two identical inclusions imposing the same contact angle α, the interactions in Eqs. (3) and (4) have the same modulus if

$$|\alpha| = \sqrt{\frac{3}{4\pi}\frac{k_B T}{\kappa}}\,. \tag{5}$$

Using the typical value $\kappa \approx 25\, k_B T$ gives $|\alpha| \approx 6°$: for larger contact angles, the mean-field repulsion dominates over the fluctuation-induced attraction.

2.2 *Further Developments on Distant Inclusions Embedded in Almost-Flat Membranes*

2.2.1 In-Plane Anisotropy

Until now, we discussed the simple case of two inclusions with isotropic (i.e., disk-shaped) in-plane cross-section, which was the first case investigated [6]. However, real membrane inclusions, such as proteins, have various shapes. Figure 2 shows a schematic of the different cases at stake: those in panels a and b were discussed above, and those in panels c and d will be discussed here.

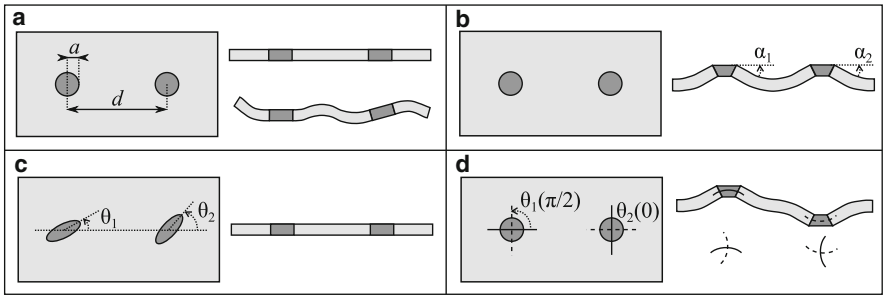

Fig. 2 Schematic representation of the different cases for inclusions with separation d much larger than their characteristic size a, embedded in a membrane with small deformations around the flat shape. In each case, a view from above and a longitudinal cut are presented. Thermal fluctuations of the shape of the membrane are only represented in the bottom right cut of panel **a**. (**a**) Isotropic, up-down symmetric. (**b**) Isotropic, not up-down symmetric. (**c**) Anisotropic, up-down symmetric. (**d**) Anisotropic, not up-down symmetric

In Ref. [11], the case of anisotropic cross-sections was treated through a coupling between membrane curvature and symmetric traceless tensor order parameters constructed from the main direction of the inclusion cross-section, integrated over the surface of the inclusion cross-section. The interaction energies obtained are anisotropic, and depend on d as $1/d^4$ for up-down symmetric inclusions that interact only through the fluctuation-induced interaction (see Fig. 2c), just as in the case of isotropic cross-sections. However, inclusions that break the up-down symmetry of the membrane feature an anisotropic interaction with a stronger $1/d^2$ power law. Its angle dependence is $\cos(2(\theta_1 + \theta_2))$, where θ_i is the angle between the main in-plane axis of inclusion i and the line joining the two inclusion centers (Fig. 2c). This orientation dependence is that of a quadrupole–quadrupole interaction [29, 30], and the interaction energy is minimized whenever $\theta_1 + \theta_2 = 0$ (or equivalently $\theta_1 + \theta_2 = \pi$). This interaction is attractive for a wide range of relative orientations, while the analogous interaction between inclusions with an isotropic cross-section is always repulsive (see Eq. (3)).

The in-plane anisotropic case of rigid up-down symmetric rods imposing vanishing contact angles to the membrane on their edges was treated in Refs. [10, 29]. Only the fluctuation-induced interaction is then at play (as in Fig. 2c). In this study, thin rods were considered in the limit of vanishing width, and in the "distant" regime where their length L is much smaller than their separation d. The opposite case $d \ll L$ will be discussed in Sect. 2.4.2. The power law obtained is in $1/d^4$, as in the case of isotropic cross-sections (Eq. (4)), and the only energetic scale involved in this fluctuation-induced force is $k_B T$. The angular dependence of the interaction is $\cos^2[2(\theta_1 + \theta_2)]$, yielding energy minima for $\theta_1 + \theta_2 = 0$ and $\pi/2$.

Anisotropic cross-sections were revisited within the point-like approach in Refs. [14, 31]. In this model, inclusions couple to the membrane by locally imposing a generic curvature tensor, with eigenvalues (principal curvatures) denoted by $K + J$ and $K - J$. The interaction between two such identical inclusions then reads, to

leading order in a/d [14, 31]:

$$U_3(d) = -8\pi\kappa\frac{a^4}{d^2}\left\{2J^2\cos(2(\theta_1+\theta_2)) + JK\left[\cos(2\theta_1)+\cos(2\theta_2)\right]\right\}, \quad (6)$$

where θ_i are angles between the line joining the inclusion centers and their axis of smallest principal curvature (see Fig. 2d). This term $\propto 1/d^2$ vanishes for isotropic inclusions ($J = 0$), consistently with Refs. [6, 11]. Furthermore, in the fully anisotropic case $K = 0$, corresponding to a saddle, the power law and the angular dependence both agree with the up-down symmetry-breaking and anisotropic cross-section case of Ref. [11]. Equation 6 shows that in the generic case where J and K are nonzero, the angular degeneracy of the lowest-energy state is lifted, and (assuming without loss of generality that K and J have the same sign) the inclusions tend to align their axis of smallest principal curvature along the line joining their centers. Their interaction is then attractive [14]. This interaction (Eq. (6)) was recovered in Ref. [16] (with different angle notations), and generalized to inclusions with different radii.

Subleading terms in $1/d^4$ were also calculated in Refs. [14] and [16], featuring different results (as for the subleading terms in the isotropic case). One should keep in mind that the models at stake are different, since Ref. [14] considers fully point-like inclusions while Ref. [16] models disk-shaped ones with finite radius through the effective field theory. While the agreement of these models on the leading-order term is a nice sign of robustness, there is no reason to expect an exact agreement at all orders.

Reference [14] also investigated the fluctuation-induced interaction, but its leading-order term was found not to be modified with respect to the isotropic case (Eq. (4)). This is at variance with the anisotropy obtained in Refs. [10, 29] for the flat rods, but one should keep in mind that the point-like saddles do not correspond to the limit of the distant flat rods.

2.2.2 Multi-Body Effects and Aggregation

A crucial and biologically relevant question is how long-range membrane-mediated interactions drive the collective behavior of inclusions, in particular aggregation. One would be tempted to start by summing the pairwise potentials discussed above, but these long-range membrane-mediated interactions are not pairwise additive. Non-pairwise additivity is a general feature of fluctuation-induced interactions. For instance, the existence of a three-body effect in the van der Waals–London interaction was demonstrated in Ref. [32]. The interaction due to the ground-state membrane deformation is not additive either. Indeed, if one considers inclusions that impose boundary conditions to the membrane on their edges, a shape minimizing the energy in the presence of one inclusions will generically not satisfy the boundary conditions imposed by the other one, yielding nonadditivity [19].

Three-body and four-body long-range membrane-mediated interactions were first calculated within a perturbative height-displacement model, breaking up-down symmetry but retaining in-plane isotropy, in Ref. [11]. The distance dependence of the three-body term involves terms in $1/(d_{12}^2 d_{23}^2)$ where d_{ij} is the distance between particles i and j. These interactions were also investigated in Ref. [12], in a different perturbative approach, considering in particular inclusions that favor a given average curvature, and then in Ref. [13] in a point-like framework, but this particular calculation was recently shown to miss some contributions [16].

In Ref. [14], the multi-body interactions and the aggregation of point-like inclusions locally imposing a curvature tensor were investigated. This generic model can include both up-down symmetry-breaking and in-plane anisotropy depending on the curvature tensor imposed. The leading three-body interaction was found to involve terms in $1/(d_{12}^2 d_{23}^2)$, as in Ref. [11], and to vanish for inclusions imposing a zero curvature tensor [14]. Monte Carlo simulations including the full multi-body interactions were performed, allowing to study the phase diagram of the system (see Fig. 3). Polymer-like linear aggregates were obtained for sufficient values of K and J, as predicted from the leading pairwise term (Eq. (6)). A gas phase was found for small J, consistent with the fact that for isotropic inclusions ($J = 0$) that break the up-down symmetry ($K \neq 0$), the leading pairwise interaction is repulsive (Eq. (3)). Finally, for small K and large J, aggregates were obtained, some of which had an "egg-carton" structure. This is made possible by the angular degeneracy of the lowest-energy state for $K = 0$ in the leading pairwise term (Eq. (6)). Multi-body interactions were shown to be quantitatively important, but the effect of the fluctuation-induced interaction (Eq. (4)) was found to be negligible [14]. The analytical calculation of multi-body effects was performed in this framework in Ref. [31], where the "egg-carton" aggregates were also further studied and related to experimentally observed structures.

Coarse-grained molecular-dynamics simulations of the highly anisotropic curvature-inducing N-BAR domain proteins adhering on membranes have demonstrated linear aggregation of these proteins on the membrane. This is a first self-assembly step, which then yields the formation of meshes enabling budding [33]. This is qualitatively in good agreement with the predictions of Ref. [14].

The influence of the long-range elastic repulsion between isotropic inclusions that break the up-down symmetry of the membrane on their aggregation was also discussed in Ref. [34], but within a less specific framework including other types of interactions. In this work, this repulsive interaction (Eq. (3)) plays the role of an energetic barrier to aggregation.

In Ref. [35], the collective behavior of inclusions locally penalizing local curvature (either only mean curvature or also Gaussian curvature) was studied using a mean-field theory for the inclusion concentration and Monte Carlo simulations. Since the inclusions considered retain both up-down symmetry and in-plane isotropy, the only membrane-mediated interaction at play is an attractive fluctuation-induced one similar to that in Eq. (4). Direct interactions were also included. Aggregation was found to occur even for vanishing direct interactions, provided

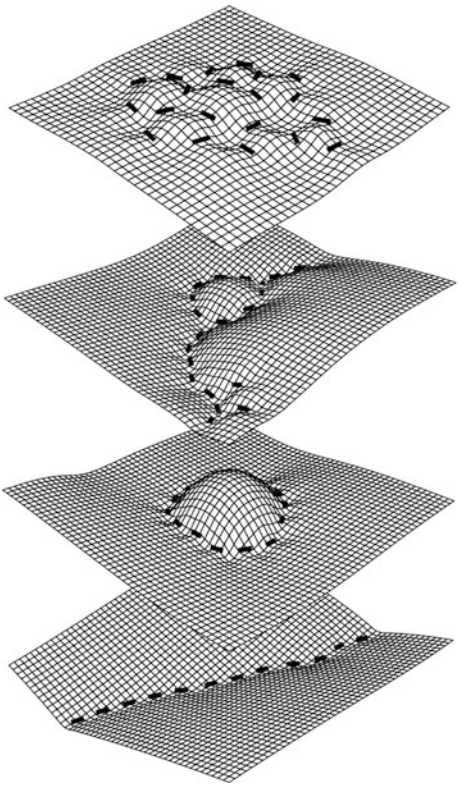

Fig. 3 Typical equilibrium aggregates obtained from Monte Carlo simulation of 20 identical point-like anisotropic curvature-inducing inclusions. Each panel represents a different set of (J, K) values. Reproduced from P.G. Dommersnes and J.-B. Fournier. N-body study of anisotropic membrane inclusions: Membrane mediated interactions and ordered aggregation. Dommersnes and Fournier [14], with kind permission of the European Physical Journal (EPJ), Copyright EDP Sciences, Società Italiana di Fisica and Springer-Verlag (1999)

that the rigidity of the inclusions was sufficient [35]. Hence, fluctuation-induced interactions may be relevant for aggregation, at least in the absence of other, stronger, interactions. Note that Eq. (4) shows that the amplitude of fluctuation-induced interactions is quite small. For instance, $d = 4a$ yields $U_2 \approx 0.02\, k_{\mathrm{B}}T$ (all the results discussed so far are strictly relevant only for $d \gg a$).

In Ref. [16], the general effective field theory framework was used in the case of in-plane isotropic inclusions. The leading-order and next-order three-body interaction terms due to the ground-state membrane deformation between up-down symmetry-breaking inclusions were obtained, as well as the leading three-body and four-body fluctuation-induced interactions.

2.2.3 Membrane Tension

Until now, we have focused on the regime where bending rigidity dominates over membrane tension. This is appropriate for length scales below $\sqrt{\kappa/\sigma}$. As σ is in the range $10^{-6} - 10^{-8}$ N/m for floppy membranes, while $\kappa \simeq 10^{-19}$ J, this length scale is then of order 1 μm. However, membrane tensions can span several orders of magnitude [36] depending on external conditions (e.g., osmotic pressure), so it is relevant to go beyond $\sqrt{\kappa/\sigma}$. For small deformations around a planar shape, the quadratic Hamiltonian of a membrane including tension reads

$$H[h] = \int d\boldsymbol{r} \left\{ \frac{\kappa}{2} \left[\nabla^2 h(\boldsymbol{r}) \right]^2 + \frac{\sigma}{2} \left[\nabla h(\boldsymbol{r}) \right]^2 \right\} , \tag{7}$$

where notations are the same as in Eq. (2), and where the Gaussian curvature term has been discarded. Note that, in a self-assembled membrane not submitted to external actions, each lipid adopts an equilibrium area. Hence, a membrane has no intrinsic surface tension (contrary to a liquid–gas interface), and stretching the membrane has an energy cost quadratic in the area variation. However, one usually considers a patch of membrane in contact with a reservoir made up by the rest of the membrane, so the tension term in Eq. (7) can be interpreted as arising from the chemical potential of this reservoir.

For length scales much larger than $\sqrt{\kappa/\sigma}$, tension dominates and Eq. (7) can be simplified into:

$$H[h] = \frac{\sigma}{2} \int d\boldsymbol{r} \left[\nabla h(\boldsymbol{r}) \right]^2 . \tag{8}$$

This case applies to a tense membrane at large scales, but also to a liquid interface (neglecting gravity). From a formal point of view, techniques similar to those employed in the bending-dominated case can be used, since the Hamiltonian is also quadratic with a single term.

Let us first focus on inclusions that do not break the up-down symmetry of the membrane. In Refs. [10, 29], the fluctuation-induced interaction between two distant up-down symmetric rigid thin rods embedded in such a surface was calculated. It was found to be similar to the analogous bending-dominated case (see above), with the same $1/d^4$ power law, but with a different angular dependence.

References [37, 38] considered the tension-dominated case of ellipsoidal colloids trapped at a fluid interface. In the case where the colloid height fluctuations are included but their contact line with the fluid is pinned, long-range fluctuation-induced interactions were obtained. This case is analogous to that of rigid in-plane anisotropic membrane inclusions preserving the up-down symmetry. Interestingly, the power law obtained was found to depend on whether or not in-plane orientational fluctuations of the colloids were allowed. If they are not allowed, the result of Refs. [10, 29] with the $1/d^4$ power law is recovered in the limit of full anisotropy. If they are allowed, a weaker anisotropic interaction with $1/d^8$ power law is

obtained [38]. This strong dependence of the power law of fluctuation-induced forces on boundary conditions was confirmed in Ref. [18] through the effective field theory method, in the specific case of in-plane isotropic (disk-shaped) rigid inclusions [16, 19]. In the case of membranes, the physical case should allow orientational fluctuations of the inclusions, and hence the $1/d^8$ power law should be considered. It is attractive and reads

$$U_4(d) = -9k_{\mathrm{B}}T\frac{a^8}{d^8}\,. \tag{9}$$

Hence, we expect a crossover between a $1/d^4$ power law (Eq. (4)) and a $1/d^8$ power law (Eq. (9)) as the tension becomes more important.

In Ref. [39], a scattering-matrix approach analogous to the one developed for the study of Casimir forces [40–42] was developed, and applied to the full Hamiltonian in Eq. (7) including both tension and bending. The focus was on disk-shaped elastic inclusions preserving the up-down symmetry, and on their fluctuation-induced interaction. The results obtained in the case of rigid inclusions were consistent with Eq. (4) in the bending-rigidity–dominated regime, and with Eq. (9) in the tension-dominated regime. Moreover, the crossover between these two regimes was studied numerically. The method developed in Ref. [39] can potentially deal with more general cases, involving multiple complex inclusions. It appears to be complementary to the effective field theory method of Refs. [16, 19], and was more straightforward in the transition regime where both tension and bending are relevant [39].

Let us now focus on the interaction due to the ground-state deformation of the membrane. Reference [43] studied the case of conical inclusions breaking up-down symmetry but retaining in-plane isotropy, and considered the full Hamiltonian in Eq. (7). They showed that for nonvanishing tension, this interaction has a sign that depends on the relative orientation of the cones with respect to the membrane plane (i.e., on the signs of the angles they impose), contrary to the vanishing-tension case (see Eq. (3)). Furthermore, at long distances between inclusions, the interaction is exponentially cut off with a decay length $\sqrt{\kappa/\sigma}$ (it involves Bessel K functions). This property was confirmed in Ref. [44]. Hence, at long distances, the fluctuation-induced force in Eq. (9) should dominate over the force due to the ground-state deformation. Conversely, in the case of colloids or inclusions with anisotropic cross-sections, Refs. [30] and [18] demonstrated the existence of a long-range interaction due to the ground-state deformation of the membrane. The leading term of this interaction is anisotropic and decays as $1/d^4$.

In Ref. [45], the effect of tension on the aggregation of the highly anisotropic curvature-inducing N-BAR domain proteins adhering on membranes was investigated through coarse-grained molecular-dynamics simulations. Increasing tension was shown to weaken the tendency of these proteins to linear aggregation, in agreement with the predicted weakening of the ground-state membrane-mediated interaction.

2.2.4 Summary of the Interaction Laws

Table 1 presents a summary of the power laws of the leading-order term of the membrane-mediated interactions in the various situations discussed until now.

2.2.5 External Forces and Torques

Until now, we have only discussed cases where inclusions couple to the membrane shape through its curvature, either explicitly or implicitly (e.g., through rigidity). This is the relevant case in the absence of external forces or torques. External forces can yield local constraints directly on the height of the membrane, e.g., quadratic ones in the case of local trapping or linear ones in the case of local pulling [12]. More specifically, inclusions may experience direct mechanical constraints if they are attached to the cytoskeleton, and torques in the presence of electrical fields because of their dipole moments [15]. In these cases, one expects membrane-mediated interactions to be enhanced, because the ground-state deformations will generically be stronger than in the case where inclusions can freely reorient to minimize them, and because the constraints imposed on fluctuations will be stronger too.

The case of inclusions subjected to external torques was studied in Ref. [15], for point-like inclusions setting a curvature tensor, in the in-plane isotropic case. Both external fields strong enough to effectively pin the orientations of the inclusions, and finite external fields that set a preferred orientation, were considered. In both cases, membrane-mediated forces are strongly enhanced, even more in the strong-field case. A logarithmic fluctuation-induced interaction was obtained, as well as an interaction due to the ground-state deformation which either scales as $1/d^2$ if the

Table 1 Summary of the power laws obtained for the leading-order terms of the two types of membrane-mediated interactions, as a function of the separation d between the inclusions, in the regime of small deformations of a flat membrane and distant inclusions

Dominant term in the Hamiltonian in Eq. (7)	Geometry	Fluctuation-induced interaction	Interaction due to the ground-state deformation—vanishes if up-down symmetric
Bending rigidity κ	Disks	$1/d^4$ [6, 11, 14]	$1/d^4$ [6, 11, 14]
	Disks + anisotropy	$1/d^4$ [11, 14]	$1/d^2$ [11, 14]
	Distant rods	$1/d^4$ [10, 29]	
Tension σ	Disks	$1/d^8$ [38, 39]	Exponentially suppressed
	Disks + anisotropy	$1/d^8$ [38, 39]	$1/d^4$ [18, 30]
	Distant rods	$1/d^4$ [10, 29]	

Different inclusion geometries are considered. In the case labeled "disks + anisotropy," the anisotropy can be either in the inclusion shape (e.g., ellipsoidal [11]) or in the constraint it imposes (e.g., an anisotropic local curvature [14])

preferred orientations are the same for both inclusions, or logarithmically if they are different. Interestingly, these interactions depend on the relative orientation of the preferred curvatures set by the inclusions, while in the torque-free case, the interaction only depends on their absolute values (see Eq. (3)) [15].

In Ref. [37], colloids at a fluid interface were considered, with different types of boundary conditions. In the case where the position of the colloids is considered to be frozen (both in height and in orientation), strong logarithmic fluctuation-induced interactions are obtained.

2.2.6 Fluctuations of the Interactions

Until now, we have discussed the average values at thermal equilibrium of membrane-mediated forces. Thermal fluctuations already play an important part since they are the physical origin of fluctuation-induced forces. But, membrane-mediated forces themselves fluctuate as the shape of the membrane fluctuates. The fluctuations of these forces have been studied in Ref. [46], using the stress tensor of the membrane [47, 48]. This approach is inspired from those used previously for the fluctuations of Casimir forces [49], and of Casimir-like forces between parallel plates imposing Dirichlet boundary conditions on a thermally fluctuating scalar field [50].

The case of two point-like membrane inclusions that locally impose a curvature tensor was studied in Ref. [46], for in-plane isotropic inclusions but including the up-down symmetry-breaking case. Integrating the stress tensor on a contour surrounding one of the two inclusions allowed to calculate the force exerted on an inclusion by the rest of the system, in any shape of the membrane [51]. The average of the force obtained gives back the known results Eqs. (3) and (4) that were obtained from the free energy in previous works. The variance of the force was also calculated, showing that the membrane-mediated force is dominated by its fluctuations. The distance dependence of the fluctuations, present in the sub-leading term of the variance, was also discussed. Interestingly, it shares a common physical origin with the fluctuation-induced (Casimir-like) force [46].

2.3 Dynamics

Fundamental interactions, e.g., electrostatic ones, are usually considered as instantaneous, in the sense that they propagate at a velocity much higher than that of the particles experiencing them. This is not the case for membrane-mediated interactions, as the spreading of membrane deformations involves slow dissipative phenomena. The dynamics of membrane-mediated interactions is a promising subject for future research. Studying out-of-equilibrium membrane-mediated interactions intrinsically requires taking into account the dynamics of the membrane. Taking care both of the motion of the membrane and of that of the inclusions is very difficult.

Hence, the first theoretical study in this direction to our knowledge, Ref. [52], considered two immobile inclusions that simultaneously change conformation, i.e., that simultaneously create a source of deformation, and therefore trigger a time-dependent interaction as the membrane deformation spreads dissipatively.

In Ref. [52], inclusions were modeled as simple point-like sources of mean curvature that are triggered simultaneously at $t = 0$. One could imagine cylindrical integral proteins such as ion channels transforming into conical ones upon receiving a chemical signal. The time-dependent Hamiltonian of these inclusions is $\mathscr{H}_{\rm inc}(t) = \theta(t) \sum_i B_i \nabla^2 h(\boldsymbol{r}_i)$, with $\theta(t)$ the Heaviside step function, B_i the curving strength, and $\boldsymbol{r}_i$ the position of inclusion i. The dynamical reaction of the membrane to such a perturbation was studied in Ref. [52].

As shown in the pioneering works of Refs. [53, 54], the dominant dissipation mechanism at short length scales is the friction between the two monolayers of the membrane. The corresponding dissipated power per unit area is $b(\boldsymbol{v}^+ - \boldsymbol{v}^-)^2$, where $\boldsymbol{v}^\pm$ are the velocities of the two lipid monolayers (the monolayers are denoted by $+$ and $-$) and $b \approx 10^9$ J s/m^4 is the intermonolayer friction coefficient. In addition, the membrane is subjected to viscous forces from the bulk solvent, of viscosity $\eta \approx 10^{-3}$ J s/m^3, and each monolayer behaves as a compressible fluid with elastic energy density $\frac{1}{2}k(\rho^\pm \pm e\nabla^2 h)^2$. In this expression, $\rho^\pm$ are the monolayer relative excess densities (normalized by their equilibrium density), measured on the membrane mid-surface, $e \approx 1$ nm is the distance between this surface and the neutral surface of the monolayers (where density and curvature effects are decoupled), and $k \approx 0.1$ J/m^2. For most practical purposes, the two-dimensional viscosities of the monolayers can be neglected [55].

Taking into account all these effects, Ref. [52] showed that the relaxation dynamics of a Fourier mode $\{h(q,t), \rho^\pm(q,t)\}$ in the membrane with two identical triggered inclusions is given, to linear order, by a set of two first-order dynamical equations:

$$2b\,\frac{\partial(\rho^+ - \rho^-)}{\partial t} = -kq^2(\rho^+ - \rho^-) + 2keq^4 h, \tag{10}$$

$$4\eta q\,\frac{\partial h}{\partial t} = -(\sigma q^2 + \tilde{\kappa} q^4)h + keq^2(\rho^+ - \rho^-) + F(\boldsymbol{q}, t), \tag{11}$$

where $F(\boldsymbol{q}, t)$ is the Fourier transform of $-\delta\mathscr{H}_{\rm inc}/\delta h(\boldsymbol{r}, t)$, σ is the membrane tension, and $\tilde{\kappa} = \kappa + 2ke^2$ the bending rigidity at frozen lipid density [53]. Solving these linear differential equations for time evolution and integrating over the Fourier modes $\boldsymbol{q}$ yields the time-dependent membrane deformation produced by one or more inclusions. Then, the force $f(t)$ exerted by one inclusion on the other can be obtained by integrating the membrane stress tensor [47, 48, 56] around one inclusion.

Two striking behaviors were observed in Ref. [52] (see Fig. 4): (1) the force $f(t)$ reaches a maximum $f_{\rm m}$ and then decreases to the equilibrium force $f_{\rm eq}$. (2) While $f_{\rm eq}$ decreases exponentially with the separation d between the inclusions, the

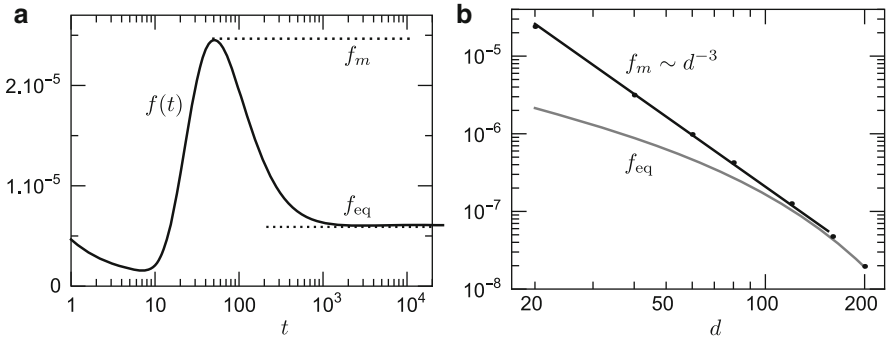

Fig. 4 (**a**) Force $f(t)$ normalized by $B^2/(\kappa e^3)$ exchanged by two inclusions separated by d versus time t after the triggering of the inclusions, normalized by $4\eta e^3/\kappa \times 10^3 \sim 40$ ns. The parameters are $d = 20e$, $\sigma = 10^{-3}\kappa/e^2$, $ke^2/\kappa = 1$, and $be^2/\eta = 1000$. (**b**) Dependence of the equilibrium force, $f_{\rm eq}$, and of the maximum of the dynamical force, $f_{\rm m}$, as a function of d normalized by e

maximum force $f_{\rm m}$ decreases as a power law $\sim d^{-3}$ until it reaches $f_{\rm eq}$. Hence, $f_{\rm m}$ is long-ranged. Although these results were obtained with a simplified Hamiltonian for the inclusions, it is likely that the general trends observed will also apply to more realistic cases. It should be straightforward to extend the model of Ref. [52] to inclusions that trigger at different times, but considering the movement of the inclusions at the same time as the movement of the membrane would be more challenging.

2.4 Other Geometries

Until now, we focused on the case of inclusions with separation d larger than their characteristic size, embedded in a membrane with small deformations around the flat shape. This is the case that has attracted the most attention in the literature, because of its relevance for proteins embedded in the membrane, and because of its technical tractability. We now move on to other geometries.

2.4.1 Spherical Vesicle

Reference [57] focused on the membrane-mediated interaction arising from the ground-state deformation between two disk-shaped inclusions embedded in the membrane of a spherical vesicle, and imposing contact angles. The case of the spherical vesicle is practically relevant both in biology and in in vitro experiments. The energy of the membrane was considered to be dominated by bending rigidity, which requires the length scales at play (in particular the vesicle radius) to be small with respect to $\sqrt{\kappa/\sigma}$. The covariant Helfrich Hamiltonian (Eq. (1) with

no Gaussian curvature term) was adapted to small deformations with respect to a sphere.

The interaction was evaluated thanks to an expansion of the energy-minimizing profile of the membrane, and it was found to be strongly enhanced with respect to the flat-geometry interaction (Eq. (3)) at length scales where the spherical shape of the vesicle is relevant. At sufficient angular separation, the effective power law of the interaction is $\sim 1/d^{1/3}$ [57]. This sheds light on the strong impact of the underlying geometry of the membrane on membrane-mediated forces. Qualitatively, in a flat membrane, the interaction is weaker because the curvature energy in Eq. (1) can be minimized quite well between the inclusions (with an almost perfect saddle that has very little curvature energy), which is not possible in the spherical geometry. Similarly, in the case of external torques (Sect. 2.2.5), the imposed orientations did not allow for this low-energy saddle, thus enhancing the interaction.

2.4.2 Close Parallel Rods

We already discussed the case of rigid rods of length L, at a distance $d \gg L$ [10, 29], which is close to the point-like case. The opposite regime $d \ll L$ is also relevant biologically, since it can model semiflexible polymers adsorbed on the membrane. In Ref. [58], the effect of the reduction of the membrane fluctuations by the presence of a semiflexible (wormlike) polymer was discussed. An effective nematic interaction was found between different segments of the polymer, and it was shown that this interaction can yield an orientational ordering transition.

Let us first consider rods that do not break the up-down symmetry of the membrane. The case of such stiff parallel rods in the limit $d \ll L$ (see Fig. 5a) embedded in a membrane with energy dominated either by bending rigidity (Eq. (2)) or by tension (Eq. (8)) was studied in Ref. [20]. A constant scale-free Casimir-like interaction per unit length is then expected [59], and indeed the Casimir-like interaction potential is then proportional to $-k_{\mathrm{B}}T\, L/d$ [20]. This interaction is much stronger than the one between point-like objects (Eq. (4)), because the constraints imposed on fluctuation modes are much stronger in the geometry of parallel close rods. Reference [20] further showed that such rods tend to bend toward one another below a certain critical distance, and that their interaction is screened by out-of-plane fluctuations if the rigidity of the polymer is finite.

This situation was further studied in Ref. [60]. Rods were modeled as constraints imposed on the membrane curvature along a straight line, allowing to define four types of rods, according to whether the membrane can twist along the rod and/or curve across it (see Fig. 5b, c for two examples of these rod types). The numerical prefactors of the potential in L/d were obtained for interactions between the different types of rods, and they were all found to be attractive, provided that the rods are rigid, i.e., that they impose $\partial_y \partial_y h = 0$ along them, with the notations of Fig. 5. However, repulsion was obtained between objects imposing completely antagonistic conditions (i.e., a rigid rod only imposing $\partial_y \partial_y h = 0$ along it, see Fig. 5b, and a nonrigid "ribbon" only imposing $\partial_x \partial_x h = 0$ along it), which is reminiscent of

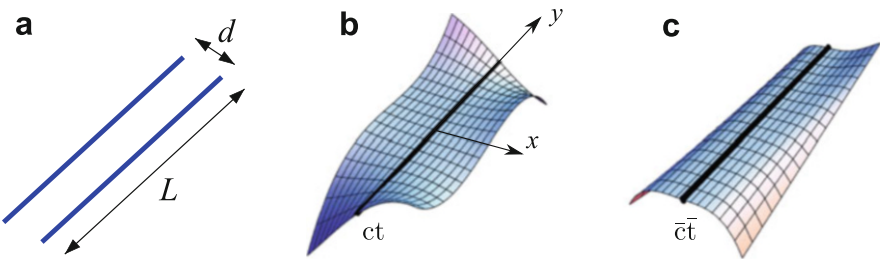

Fig. 5 Rods embedded in membranes. (**a**) Geometry: two parallel rods of length L at separation $d \ll L$. (**b**) and (**c**) Two examples of rod types. All rigid rods impose a vanishing curvature along them: $\partial_y \partial_y h = 0$ on the rod. (**b**) Rod that allows curving ("c") and twisting ("t") across it. (**c**) Rod that does not allow curving or twisting across it: it imposes $\partial_x \partial_x h = 0$ and $\partial_x \partial_y h = 0$ as well as $\partial_y \partial_y h = 0$ (see Ref. [60])

the results obtained in critical binary mixtures [25]. In addition, the interaction energy was studied numerically versus d/L, thanks to a discretization scheme [61], showing the transition between the asymptotic behaviors at large d/L [29] and at small d/L [60] were recovered. Finally, the bending and coming into contact of the rods due to the fluctuation-induced interaction was discussed: it was predicted to occur below a certain value of d [60].

The $L \gg d$ geometry gives insight into what happens between two generic inclusions that are very close to one another, through the proximity force approximation [62]. This approximation was used in the case of disk-shaped inclusions in Refs. [39, 60], showing that the fluctuation-induced interaction potential then scales as $1/d^{1/2}$.

In Ref. [63], the interaction due to the ground-state deformation between parallel rigid cylinders adsorbed on a membrane and interacting with it through an adhesion energy was studied. The membrane was assumed to be in the regime of small deformations, but both tension and bending were accounted for (see Eq. (7)), and the geometry where $d \ll L$ was considered. The interaction due to the ground-state deformation was calculated explicitly in this effectively one-dimensional case. It was found to be repulsive for a pair of cylinders adhering to the same side of the membrane, and attractive for cylinders adhering to opposite sides (and hence imposing an opposite curvature). This is at variance with the point-like case, where the interaction only depends on the modulus of the curvatures imposed (see Eq. (3)). The dependence in d is in $\tanh(d/\sqrt{\kappa/\sigma})$ in the first case, and in $\coth(d/\sqrt{\kappa/\sigma})$ in the second one [63].

2.4.3 Large-Deformation Regime

All cases discussed until now focused on small deformations. Then, the Hamiltonian of the membrane is quadratic, and the field theory is Gaussian. This provides tractability, both to solve the Euler–Lagrange equations that give the ground-state

shape, which are then linear, and to compute thermodynamical quantities such as the free energy. Here, we will discuss the biologically relevant but much trickier regime of large deformations.

In Ref. [64, 65], the covariant membrane stress and torque tensors associated to the full Helfrich Hamiltonian [47] were used to determine formal expressions of the forces between objects adsorbed on fluid membranes that are due to the ground-state deformation of the membrane. These expressions are valid without assuming small deformations, but the ground-state shape needs to be determined in order to obtain a more explicit expression. This is not an easy task in the large-deformation regime. Equilibrium shapes in the large-deformation regime were further investigated in Ref. [66], allowing to plot the force between cylinders, in the case of a fixed adhesion area between them and the membrane. The direction of the force and its asymptotic exponential decay at large $d/\sqrt{\kappa/\sigma}$ were found to remain the same as in the small-deformation regime [63]. This situation was also investigated numerically in Ref. [67] in the case of cylinders interacting with the membrane through an adhesion energy, yielding phase diagrams of the system.

In Ref. [68], the entropic contribution to the membrane-mediated interaction between two long cylinders adsorbed on the same side of a membrane was studied in the regime of large deformations, in the case of a fixed adhesion area between the cylinders and the membrane. The free energy of the system was calculated by assuming Gaussian fluctuations around the ground-state shape. Interestingly, this entropic contribution enhances the ground-state repulsion between the two cylinders [68], while the fluctuation-induced interaction between identical rods in the small-deformation regime is attractive [20, 60]. This is presumably a nontrivial effect coming from the nonlinearities at play in the large deformations. It would be interesting to go beyond the approximation of Gaussian fluctuations around the ground-state shape.

Solving the shape/Euler–Lagrange equation for membranes beyond the domain of small deformations is technically very hard for most geometries, and incorporating fluctuations too, but numerical simulations can provide further insight. The coarse-grained molecular-dynamics membrane simulations without explicit solvent description of Ref. [69] showed that the elastic interaction between two isotropic curvature-inducing membrane inclusions (quasi-spherical caps) can become attractive at short separations, provided that the inclusions induce a strong enough curvature. Recall that the interaction due to the ground-state deformation, which is dominant with respect to the fluctuation-induced one for large enough curvatures imposed by inclusions, is always repulsive in the regime of small deformations (see Eq. (3)). This hints at highly nontrivial effects of the large-deformation regime. The attractive membrane-mediated interaction was found to be able to yield aggregation of the caps and vesiculation of the membrane [69] (see Fig. 6). The case of curved phase-separated lipid domains was explored in Ref. [70] through coarse-grained molecular-dynamics simulations. The interaction between domains was found to be attractive, but the angles imposed by the domains were smaller than those yielding attraction in Ref. [69].

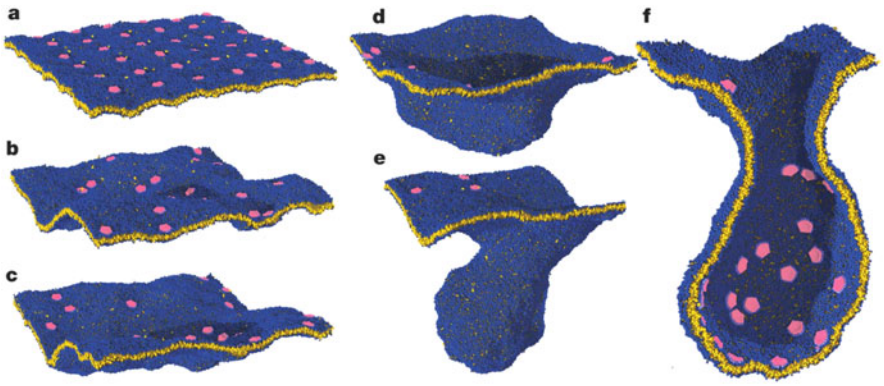

Fig. 6 Successive snapshots (**a**–**f**) of a coarse-grained simulation of a membrane with several curvature-inducing inclusions. A process of vesiculation is induced by the elastic interaction between inclusions, which becomes attractive at short separations. Reprinted by permission from Macmillan Publishers Ltd: Reynwar et al. [69], Copyright (2007)

A numerical minimization via Surface Evolver of the Helfrich Hamiltonian Eq. (1) for a membrane with two in-plane isotropic curvature-inducing inclusions was presented in Ref. [71], and forces were calculated by studying infinitesimal displacements. A change of sign of the membrane-mediated interaction due to the ground-state deformation of the membrane was obtained, consistently with Ref. [69]. The repulsive interaction, agreeing quantitatively with Eq. (3) at large d/a and for small deformations, turned attractive for d/a of order one, provided that the curvature imposed by the inclusions (and hence the membrane deformation) was large enough. The separation d is defined as the center-to-center distance projected on a reference plane, while a is the real radius of the inclusions, so that in the large-deformation regime where inclusions are very tilted, it is possible to have $d < 2a$. Attraction occurs in this regime, which is inaccessible to the small-deformation approach. Recently, Ref. [72] studied anisotropic protein scaffolds, modeling, e.g., BAR proteins, in the large-deformation regime, through similar numerical minimization methods: strongly anisotropic attractive interactions were obtained.

Reference [73] presented a Monte Carlo simulation of spherical nanoparticles adsorbed on a spherical vesicle modeled as a triangulated surface. Aggregation of the nanoparticles and inward tubulation of the vesicle were observed, implying strong attractive interactions. Note however that adhesion might have a strong impact on these structures [74]. A similar coarse-grained description of a membrane vesicle was used in Ref. [75] to investigate the collective effects of anisotropic curvature-inducing inclusions, modeling, e.g., BAR proteins. Vesicles were strongly deformed by the numerous inclusions, with sheet-like shapes or tubulation depending on inclusion concentration, and aggregation and nematic ordering of these inclusions were observed.

2.5 Experimental Studies

While membrane-mediated interactions have been the object of significant theoretical and numerical attention, quantitative experimental tests of the theoretical predictions remain scarce to this day. A very active research area in biophysics deals with the morphological changes of the cell (invagination [76], vesiculation [69], etc.) under the action of various proteins (see [77] for a recent review). However, many ingredients other than membranes and inclusions are at play in these biological systems, for instance the cytoskeleton, out-of-equilibrium events, etc., which makes it hard to isolate membrane-mediated interactions. Biomimetic lipid membranes such as giant unilamellar vesicles [78] are a good model system to study such effects. In principle, the inclusions could be real proteins, but these molecules have complex shapes, which makes it difficult to test predictions of models developed for simple geometries. Many studies have focused on the simpler and more easily controlled system of colloids adhering to membranes (see Ref. [74] for a review), and some have investigated interactions between phase-separated membrane domains [79]. However, even in these simpler cases, membrane-mediated interactions may involve other effects, such as adhesion of the colloids, variability of contact angles imposed by domains, etc.

An experimental study of the aggregation of spherical colloidal particles adhering to biomimetic lipid membranes was presented in Ref. [80]. The observed aggregation of two particles was deemed consistent with a short-range (e.g., exponential) attractive force, and no signature of a longer-range force was obtained. Note that theoretical studies predict a mostly repulsive membrane-mediated force in this geometry, except at very high deformations and small distances. Surprisingly, triplets were observed to form chains, and a linear ring-like aggregate was observed around the waist of a vesicle. Linear chain-like arrangements were also obtained in simulations of a very similar situation in Refs. [81, 82], for certain sizes of particles and adhesion regimes. Reference [82] used a scaling argument to show that this was not due to membrane-mediated interactions, but to the adhesion of the particles to the membrane, as a linear aggregate yields a higher adhesion area than a compact one. Such a phenomenon would thus not arise in the case of inclusions [74]. Attraction and aggregation of particles adhered to lipid vesicles were also reported more recently in Ref. [83].

Apart from proteins and colloids, another source of membrane deformation is the presence of phase-separated (liquid-ordered/liquid-disordered) domains, which can be partially budded. Contrast between the domains is obtained in fluorescence microscopy by adding a dye which partitions into one phase [84] or by selectively labeling one lipid species [85]. Selective deuteration can also be used to induce contrast in small-angle nuclear scattering [86]. In Ref. [79], the stability of partially budded domains was interpreted as a signature of repulsive interactions, since flat ones rapidly fused. The strength of this interaction was evaluated by measuring the distribution of inter-domain distance, and then by evaluating the effective spring constant of the confining potential. It was found to be consistent with

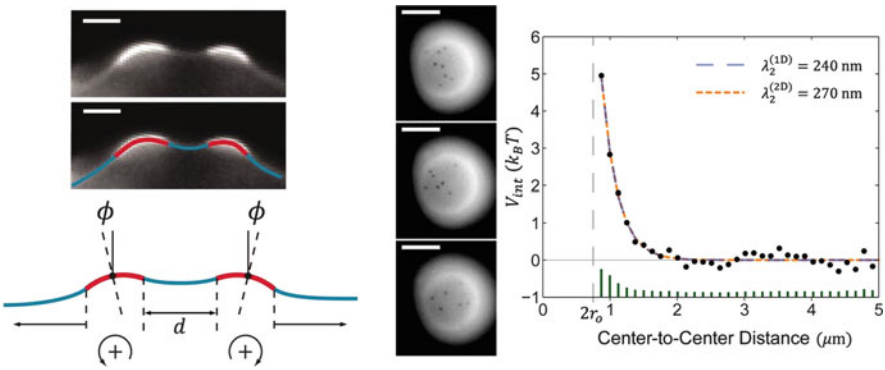

Fig. 7 Shape of the dimpled domains (left), interacting domains on the surface of the same vesicle (center), and repulsive interaction potential, with a fit to theoretical predictions from Ref. [43] (right). Adapted from Figures 3 and 4 of Ursell et al. [85], with kind permission of the National Academy of Sciences

the membrane-mediated interaction arising from the ground-state deformation of a tension-free membrane in the small-deformation and large-separation regime (Eq. (3)). In Ref. [85], a good agreement was obtained between the observed in-plane distribution of the domains and the predictions of the elastic theory in the presence of tension [43] (see Fig. 7).

3 Short-Range Membrane-Mediated Interactions

In Sect. 2, we dealt with long-range membrane-mediated interactions between inclusions, which arise from the curvature constraints imposed by rigid inclusions. There exist several other ways in which inclusions can couple to the surrounding membrane and thus interact with other inclusions through the membrane, but these effects are generally short-ranged. The study of these interactions was in fact initiated before that of their long-range counterparts [6]. Membrane proteins were shown experimentally to tend to immobilize neighboring lipids [87]. A membrane-mediated attraction between proteins was predicted to arise due to this local ordering [88], and to decay exponentially beyond the correlation length of the membrane order parameter [89]. Proteins can locally perturb the thickness of the membrane due to this local ordering, but they may also couple preferentially to one component of a lipid mixture [90].

Here, we are going to focus on the coupling of proteins to membrane thickness. Intrinsic membrane proteins can have a *hydrophobic mismatch* with the membrane: their hydrophobic thickness is slightly different from that of the unperturbed membrane. Hydrophobic mismatch is ubiquitous, and has important biological consequences, since the activity of many membrane proteins has been shown to

depend on membrane thickness [91]. As proteins are more rigid than membranes, the membrane generically deforms in the vicinity of the protein, in order to match its thickness and avoid exposing part of the hydrophobic chains of lipids to water. This local deformation of the membrane thickness yields a membrane-mediated interaction between two such proteins.

Membrane thickness deformations are not included in the traditional Helfrich description of the membrane [4]. Describing them is tricky since they occur on the nanometer scale, which corresponds to the limit of validity of usual continuum theories where only long-distance terms are kept. Let us focus on these models before moving on to the actual interactions.

3.1 Models for Local Membrane Thickness Deformations

3.1.1 Early Models

The idea that the membrane hydrophobic thickness must locally match that of an intrinsic protein was first used in theoretical descriptions of lipid–protein interactions that focused on the thermodynamic phase behavior of the lipid–protein system and on protein aggregation. In Ref. [92], a thermodynamic model called the "mattress model" was proposed in order to describe the phase diagrams of lipid bilayers containing proteins with a hydrophobic mismatch.

More detailed theoretical investigations of local membrane thickness deformations and of resulting membrane-mediated interactions were motivated by experimental results on the antimicrobial peptide gramicidin. In lipid membranes, two gramicidin monomers, one on each side of the bilayer, can associate to form a dimer, which acts as an ion channel. While isolated monomers do not deform the membrane, the dimeric channel generically possesses a hydrophobic mismatch with the membrane [93]. Conductivity measurements yield the formation rate and lifetime of the channel, which are directly influenced by membrane properties [94–96]. Hence, gramicidin constitutes a very convenient experimental system to probe the effects of local membrane thickness deformations.

The first attempt to explain the dependence of gramicidin channel lifetime on the membrane thickness was provided by Ref. [95]. It is based on the idea that the relevant membrane energy variation upon dimer breaking is mostly due to membrane tension, which pulls apart the monomers in a membrane with hydrophobic thickness larger than that of the dimer. The resulting estimate of the gap between the two monomers in the transition state is $\delta \simeq 1.8$ nm [95]. However, this is far larger than the separation required for the breaking of the hydrogen bonds that stabilize the dimer [93], which is of order 1 Å. Hence, this first model was not complete.

3.1.2 Huang's Model

The first full continuum model describing membrane thickness deformations was proposed in Ref. [97]. The Hamiltonian per unit area of the membrane was written by analogy with a smectic A liquid crystal, in which the elongated molecules organize in layers with the molecules oriented along the layers' normal. These two systems present similar symmetries. The most important energetic terms in smectic A liquid crystals correspond to compression of the layers, and to splay distortion, i.e., curvature orthogonal to the layers [98]. In addition, the contribution of the "surface tension" of the membrane was included [97]. Restricting to symmetric deformations of the two monolayers, the effective Hamiltonian H of the membrane reads [97]

$$H = \int dxdy \left[\frac{K_a}{2\,d_0^2}\, u^2 + \frac{\gamma}{4} \left(\boldsymbol{\nabla} u\right)^2 + \frac{\kappa}{8} \left(\nabla^2 u\right)^2 \right]. \tag{12}$$

In this expression, u denotes the thickness excess of the membrane relative to its equilibrium thickness d_0 (see Fig. 8), K_a is the stretching modulus of the membrane, γ its "surface tension," and κ an elastic constant associated to splay. Finally, x and y denote Cartesian coordinates on the midplane of the membrane.

Reference [97] assimilated γ to the tension of a Plateau border and κ to the Helfrich bending modulus, which may be questioned (see below). The corresponding typical values allowed to neglect the contribution of the "tension" term. By minimizing the resulting membrane Hamiltonian, analytical expressions were obtained for the membrane deformation profiles close to a mismatched protein such as the gramicidin channel, obtaining a decay length of a few nanometers. This model yields a satisfactory agreement with the experimental results of Ref. [95].

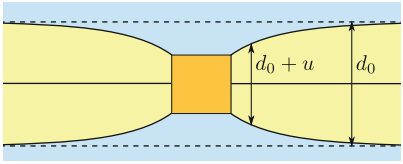

Fig. 8 Cut of a bilayer membrane (yellow) containing a protein with a hydrophobic mismatch, represented as a square (orange). The equilibrium thickness of the bilayer is d_0, while the actual thickness is denoted by $d_0 + u$

3.1.3 Models Based on the Work of Dan, Pincus, and Safran

References [99, 100] proposed another construction of the membrane Hamiltonian associated to thickness deformations. The energy per lipid molecule in each monolayer of the membrane was written for small deformations as a generic second-order expansion in the variation of area per lipid and in the local "curvature" of the monolayer thickness (different from the curvature of the shape of the membrane involved in the Helfrich model, which disregards thickness). Incompressibility of the lipids was used to relate the monolayer thickness and the area per lipid. Using the same notations as in Eq. (12), and restricting again to up-down symmetric deformations of the membrane, the membrane Hamiltonian of Ref. [100] reads

$$H = \int dxdy \left[\frac{K_a}{2\,d_0^2} u^2 + \frac{\kappa\, c_0}{2} \nabla^2 u + \frac{\kappa}{2\,d_0} \left(c_0 - c_0' \Sigma_0\right) u\, \nabla^2 u + \frac{\kappa}{8} \left(\nabla^2 u\right)^2 \right], \tag{13}$$

where c_0 is the spontaneous curvature of a monolayer, while c_0' denotes its derivative with respect to the area per molecule, and Σ_0 the equilibrium area per lipid.

The main difference between this model and that of Ref. [97] is that the effect of monolayer spontaneous curvature is included in Eq. (13). It was shown in Refs. [99, 100] that this ingredient can yield oscillations in the membrane deformation profile, and in the resulting interaction potential between two mismatched proteins. Note that no "tension" term is included in Eq. (13), but the "tension" term in Eq. (12) was neglected in all the calculations of Ref. [97] too.

The model of Refs. [99, 100] was generalized in Refs. [101, 102], where results of coarse-grained molecular-dynamics simulations for mismatched proteins in lipid membranes were also presented. The deformations of the average shape of the membrane (i.e., those usually described by the Helfrich model), and the small-scale protrusions were accounted for, as well as the symmetric thickness deformations [101, 102]. The effect of Gaussian curvature was also included in Ref. [102], and Ref. [103] added the effect of tilt.

The model of Refs. [99–102] was further generalized in Ref. [104], where an additional term, proportional to the squared gradient of thickness, was included in the initial expression of the energy per lipid molecule in each monolayer of the membrane. Physically, this term should involve a microscopic interfacial tension contribution, associated to variations of the area per lipid. Note that this is different from the Plateau border tension discussed and discarded in Ref. [97], since in a Plateau border, molecules can move along the surface and exchange with the bulk, yielding a smaller tension. Macroscopic membrane tension was also incorporated explicitly in Ref. [104], through a chemical potential μ set by the rest of the membrane on the patch considered: $\sigma = -2\mu/\Sigma_0$ then plays the part of an externally applied tension. The Helfrich Hamiltonian with tension Eq. (7) was recovered from this model for average height deformations. In the case where the average shape of the membrane is flat, and integrating out antisymmetric thickness

deformations to focus on symmetric ones, the Hamiltonian reads

$$H = \int dxdy \left[\frac{\sigma}{d_0} u + \frac{K_a}{2\, d_0^2} u^2 + \frac{K_a'}{2} (\nabla u)^2 + \frac{K_a''}{2} (\nabla^2 u)^2 \right], \tag{14}$$

plus omitted boundary terms (see Ref. [104]), with

$$K_a' = -\frac{\kappa_0}{d_0}(c_0 - c_0' \Sigma_0) + k_a', \tag{15}$$

$$K_a'' = \frac{\kappa_0}{4}, \tag{16}$$

and the same notations as in Eqs. (12) and (13), and where the new contribution k_a' with respect to Eq. (13) arises from the term proportional to the squared gradient of the thickness u. (The definition of u in Ref. [104] is slightly different from that of Refs. [99–102], but it does not affect the present discussion.)

The predictions of the model of Ref. [104] were compared with numerical profiles of membrane thickness close to a mismatched protein [101, 102, 105], and with experimental data regarding gramicidin lifetime [95] and formation rate [96]. This analysis yielded consistent results for the term stemming from the gradient of the area per molecule, and its order of magnitude was found to be of order of the contribution of the interfacial tension between water and the hydrophobic part of the membrane. In addition, the presence of this new term allowed to explain for the first time a systematic trend observed in previous numerical data.

3.1.4 Inclusions with Isotropic Cross-Section

The first models of short-range interactions between transmembrane proteins assumed that the proteins are coupled to a local order parameter describing the internal state of the membrane, either the conformational/chain-packing properties of the lipids, or the bilayer thickness u [88, 89]. Both are equivalent for a fully incompressible membrane hydrophobic core. In Refs. [90, 106], a generic Landau–Ginzburg expansion of the free energy density in terms of u and its first gradient was used to investigate the energy of a hexagonal lattice of embedded proteins imposing a value u_0 of the order parameter, i.e., a fixed hydrophobic mismatch, on their edge. Approximating the Wigner–Seitz cell of the lattice by a circle, which yields cylindrical symmetry, the authors derived a monotonically attractive short-range interaction caused by the overlap of the membrane regions deformed by the inclusions.

As discussed in Sect. 3.1, several models based on the thickness order parameter u have been developed. They have been used to study membrane-mediated interactions. These models essentially introduced terms involving the second-order derivative of u, based on the (recently questioned [104]) expectation that the term

proportional to $(\nabla u)^2$ was negligible. In particular, Ref. [97] introduced a term proportional to $(\nabla^2 u)^2$, by analogy with the splay term for smectic liquid crystals. Later, Ref. [99] introduced additional terms, linear in $\nabla^2 u$ and in $u\nabla^2 u$, which arise from the spontaneous curvature of the monolayers and its dependence on the area per lipid. This initiated a series of works [99, 100, 107] aiming to estimate the elastic energy of a hexagonal lattice of proteins with hydrophobic mismatch. These works showed that the interaction potential can be non-monotonic, with short-distance repulsion and a minimum energy at finite separation. These effects can arise from the spontaneous curvature term, but also from a fixed contact angle between the membrane hydrophobic–hydrophilic interface and the inclusion, thereafter referred to as "slope." The associated multi-body effects were investigated in Ref. [108] through a Monte Carlo simulation of inclusions fixing both the membrane thickness and its slope, in a membrane described by the elastic energy in Eq. (12). This study also demonstrated the interest of the structure factor to test the models. Another term involving second-order derivatives of the thickness profile u, proportional to its Gaussian curvature, was included in Ref. [102], improving the agreement with coarse-grained molecular-dynamics numerical simulations. Note that oscillations in the interaction potential were observed in the coarse-grained molecular-dynamics simulations of Ref. [109].

The term proportional to $(\nabla u)^2$ in the elastic energy density was originally discarded on the grounds that it originates from a negligible microscopic surface tension assimilated to that of a Plateau border [97]. However, it was recently shown by us to also originate from gradients of lipid density, and therefore to contribute significantly to the elastic Hamiltonian [104]. Note in addition that the term in $u\nabla^2 u$ introduced in Refs. [99, 100] contributes to the $(\nabla u)^2$ term once integrated by parts.

In the end, these models converge toward the most general quadratic expansion in terms of u and its first- and second-order derivatives [104, 110]. In standard statistical field theory, it is justified to neglect higher-order gradients, because the focus is on large-scale physics and the coarse-graining length is much larger than the range of the microscopic interactions [111]. However, here, such arguments do not hold since the distortions around proteins relax on a length comparable with the bilayer thickness. Therefore, in practice, one should rather rely on comparison with experiments and simulations to determine how many terms to include in the expansion. Our current understanding is that all linear and quadratic terms involving derivatives of u up to second order should contribute, and that the best strategy is to try to fit the parameters of the elastic Hamiltonian and of the protein–membrane coupling using experimental or numerical data [110].

The focus of this chapter is on membrane-mediated interactions arising from direct constraints on the membrane shape (mean shape and thickness). Hence, we will not discuss in detail the role of the underlying lipid tilt degree of freedom [103] in membrane-mediated interactions [112–117]. However, tilt certainly plays a part in these interactions. For instance, proteins with no hydrophobic mismatch but with an hourglass shape [112, 113] may induce a membrane deformation due to the boundary conditions they impose on lipid tilt. A legitimate question, though, is

how necessary it is to include this degree of freedom. Statistical physics allows integrating out virtually any degree of freedom [111]. The resulting effective elasticity for the remaining degrees of freedom takes into account the underlying distortion energy of the removed ones. For instance, integrating out the tilt degree of freedom in the presence of an hourglass-shaped inclusion would produce an effective boundary energy depending on the inclusion thickness and on its angle with the membrane. What is not clear is how many orders in the derivatives of u, both in the bulk and in the boundary energy, one would have to introduce in order to properly account for the removed degrees of freedom. Future works in this direction could be interesting.

3.1.5 Inclusions with Anisotropic Cross-Section

While most theoretical studies of short-range membrane-mediated interactions have considered cylinder-shaped inclusions, actual membrane proteins have various shapes. As in the case of long-range interactions, in-plane anisotropy may result in directional membrane-mediated interactions, which may impact the formation of multi-protein complexes.

In Ref. [118], an analytical method was developed to study membrane-mediated interactions between in-plane anisotropic mismatched inclusions. The effective Hamiltonian H associated to membrane thickness deformations was expressed as:

$$H = \int dxdy \left\{ \frac{K_a}{2d_0^2} u^2 + \gamma \left[\frac{u}{d_0} + \frac{(\nabla u)^2}{8} \right] + \frac{\kappa}{8} \left(\nabla^2 u \right)^2 \right\}, \tag{17}$$

where we have used the notations defined in Eq. (12). This model is based on that of Ref. [97] (see Eq. (12)), but includes an additional "tension" term in u/d_0. Such a term is also included in Ref. [104] (see Eq. (14)), but without the assumption that its prefactor is related to that of the squared thickness gradient term. This assumption should be viewed as a simplifying hypothesis, given the contribution of monolayer curvature to the squared thickness gradient term [99–102] and the difference between externally applied tension and interfacial tension [104] (see Sect. 3.1.3).

In Ref. [118], the solution of the Euler–Lagrange equation associated with Eq. (17) in the case of a single cylinder-shaped inclusion was expressed using Fourier–Bessel series. Then, using an ansatz introduced in Ref. [43] in the context of long-range membrane-mediated interactions, the ground-state shape of the membrane in the presence of two inclusions was written as a sum of two such series. The coefficients of the successive terms of these series can be chosen in order to match the boundary conditions imposed by both inclusions, using expansions in $a/d < 1$.

This method was extended to weakly anisotropic inclusions, modeling mechanosensitive channels of large conductance (MscL) in Ref. [118]. The in-plane cross-section of these pentameric proteins was described as a circle perturbed by a small-amplitude sinusoid, with fifth-order symmetry. Boundary conditions along the edge of these proteins were expressed perturbatively in the amplitude of the sinusoid, allowing to use the method described above. The resulting anisotropic membrane-mediated interaction features an energy barrier to dimerization and demonstrates that the tip-on orientation is more favorable than the face-on one, except at very short distances. Gating of the MscL channel was also studied in Ref. [118], by modeling open and closed channels as having different diameters and hydrophobic thicknesses [119]. The impact of having different oligomeric states of MscL on these interactions and on gating by tension (see Ref. [120]) was studied in Ref. [121].

The method developed in Ref. [118] was used in Ref. [122] to study the effect of membrane-mediated interactions on the self-assembly and architecture of bacterial chemoreceptor lattices. Chemotaxis enables bacteria to perform directed motion in gradients of chemicals. The chemoreceptors that bind to these chemicals are transmembrane proteins that organize into large honeycomb lattices of trimers of dimers at the poles of bacteria [123]. In Ref. [122], it was shown that membrane-mediated interactions between chemoreceptor trimers of dimers, modeled as inclusions with threefold symmetry, correctly predict the structure of the arrays observed in experiments. Indeed, at short distances, the face-on relative orientation of the trimers is favored by these anisotropic interactions. In addition, the collective structure of the honeycomb lattice, studied approximately through the pairwise nearest-neighbor interactions, was shown to be more favorable than other types of aggregates at realistic densities of proteins. Gateway states to this lattice were also predicted, and it was shown that membrane-mediated interactions may contribute to the cooperativity of chemotactic signaling.

3.2 Numerical Studies at the Microscopic Scale

Continuum models account for the microscopic degrees of freedom (i.e., the positions and conformations of all molecules involved) in a coarse-grained way, via effective terms in the elastic energy and the associated prefactors. However, even in the absence of a mesoscopic deformation due to hydrophobic mismatch, the presence of an inclusion constrains the configurations accessible to the lipid chains that surround it [88, 114, 124, 125]. Further insight can thus be gained by treating such microscopic degrees of freedom explicitly, in particular those describing the conformation of the lipid chains. Recent advances in numerical simulations have made such approaches possible. Here, we give a brief overview of such studies. Note that numerical studies focusing on larger-scale features were mentioned above.

References [125, 126] used the lateral density–density response function of the alkyl chains, obtained by molecular-dynamics simulations of lipid bilayers, to determine the interaction between "smooth" (no anchoring) hard cylinders inserted into the bilayer. Three values were considered for the cylinder radius. For the largest one (9 Å, comparable to that of the gramicidin pore, for instance), the long-range interaction is repulsive for all the lipids studied (DMPC, DPPC, POPC, and DOPC), with an additional short-range attraction for DMPC. This study does not discuss how the interaction might vary with the concentration of inclusions. Other studies followed suit [127–130].

A complete description should in principle combine the effects of hydrophobic mismatch and of these changes in chain order [116, 131]. Such a complete model is currently lacking, due to the theoretical difficulties but also due to the dearth of experimental data that could be used to test and validate it. As in the case of lipid tilt (see Sect. 3.1.4), one can wonder how integrating out these underlying degrees of freedom would affect an effective model written in terms of u, what effective boundary conditions non-mismatched inclusions would then impose, and whether such a model would be sufficient.

3.3 Experimental Studies

It has proven very difficult to directly measure the interactions between membrane inclusions.

3.3.1 Electron Microscopy

First among such attempts were freeze-fracture electron microscopy (FFEM) studies [132–135] that analyzed the spatial distribution of inclusions to determine their radial distribution function $g(r)$. The data was then described using liquid state theories [136–138] in terms of a hard-core model with an additional interaction, either repulsive or attractive depending on the system.

These pioneering results were not followed by more systematic investigations, probably due to the intrinsic difficulty of the technique. It is also very difficult to check whether the distribution function observed in the sample after freezing still corresponds to that at thermal equilibrium.

3.3.2 Atomic Force Microscopy

It has been known for a long time that atomic force microscopy (AFM) can resolve lateral structures down to the nanometer scale [139], but data acquisition used to be relatively slow. This changed with the introduction of high-speed AFM [140], which

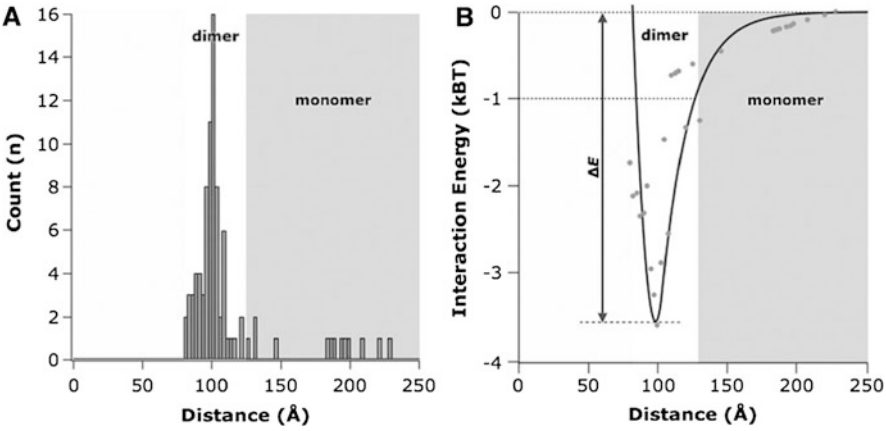

Fig. 9 Interaction between ATP synthase c-rings. (**a**) Histogram of the center-to-center distance of c-rings. (**b**) Membrane-mediated two-protein interaction energy landscape. Reprinted from Figure 2 of Casuso et al. [141], with kind permission of Elsevier, Copyright Biophysical Society (2010)

allows taking "snapshots" of the system and determining the radial distribution function. The latter gives access to the interaction potential between inclusions, as illustrated by Ref. [141] for ATP-synthase c-rings in purple membranes (see Fig. 9).

3.3.3 Small-Angle Scattering

A promising way of studying membrane-mediated interactions is through small-angle radiation (X-ray or neutrons) scattering from oriented samples, as demonstrated by Refs. [142–144]. This noninvasive technique is very well adapted to measurements of membrane-mediated interactions since the wavelength used is of the same order of magnitude as the typical length scales over which one must probe the system (nanometers). One can thus measure the structure factor of the two-dimensional system formed by the inclusions in the membrane and obtain the interaction potential between them.

This strategy was recently used to study alamethicin pores in DMPC membranes [145], inorganic particles contained in bilayers of a synthetic surfactant [146, 147] (Fig. 10), and gramicidin pores in several types of membranes [148].

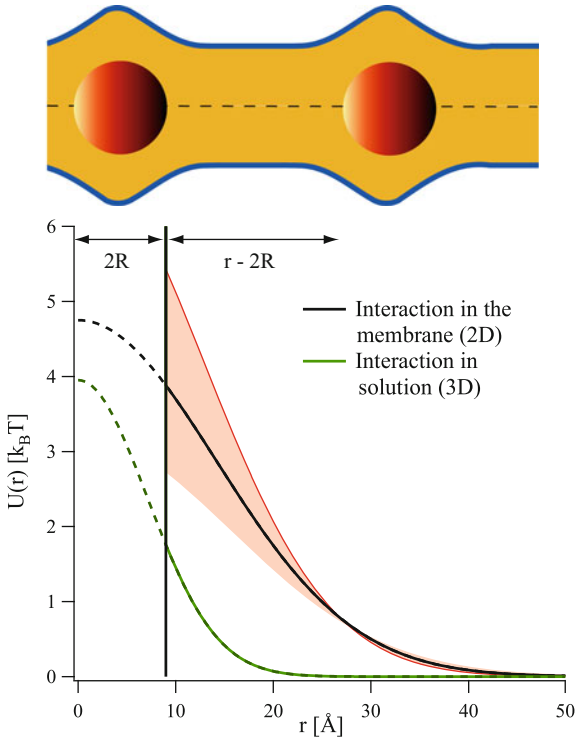

Fig. 10 Interaction potential $U(r)$ of BuSn12 particles within DDAO bilayers. The lower curve is the interaction potential of the particles in ethanol. The solid vertical line marks the hard-core interaction with radius 4.5 Å. Reprinted from Figure 3 of Constantin et al. [146], with kind permission of the American Physical Society, Copyright APS (2008)

4 Conclusion

Membrane-mediated interactions between inclusions constitute a very rich topic. Their study gives insight into the behavior of complex two-dimensional biological membranes. In particular, these interactions may have important impacts on membrane protein aggregation, and on the formation of specific biologically functional assemblies. Interestingly, inclusions can also serve as membrane probes, since membrane-mediated interactions are in part determined by the properties of the host membrane.

The field of long-range membrane-mediated interactions has been dominated by theory, yielding interesting theoretical developments such as the fluctuation-induced interaction, the general effective field theory and scattering approaches, and the questions currently raised by the dynamics of these interactions. Some experimental and numerical studies have enriched this field, and we hope for further progress allowing for more quantitative comparison with theory.

The study of short-range membrane thickness deformations was motivated by quantitative experiments on gramicidin. Work on these deformations and on the associated membrane-mediated interactions has led to several developments of the theoretical description of membrane elasticity at the nanoscale. Importantly,

the small-scale deformations involved are at the limit of the domain of validity of standard coarse-grained continuum theories, making comparison to precise experimental and numerical data even more crucially important.

An interesting fundamental feature of membrane-mediated interactions is the existence of many-body effects, arising from the interplay of the deformations caused by each of the inclusions. It would thus be particularly interesting to vary the concentration of inclusions in experiments.

Acknowledgements A.-F. B. acknowledges support from the Human Frontier Science Program. D. C. and J.-B. F. acknowledge support by ANR Grant MEMINT (2012-BS04-0023).

References

1. Singer SJ, Nicolson GL (1972) The fluid mosaic model of the structure of cell membranes. Science 175:720–731
2. Sackmann E (1984) Physical basis for trigger processes and membrane structures. In: Chapman D (ed) Biological membranes, vol 5. Academic, London, pp 105–143
3. Jensen MØ, Mouritsen OG (2004) Lipids do influence protein function–the hydrophobic matching hypothesis revisited. Biochim Biophys Acta: Biomembr 1666:205–226
4. Helfrich W (1973) Elastic properties of lipid bilayers – theory and possible experiments. Z Naturforsch C J Biosci 28:693–703
5. Bickel T, Marques C, Jeppesen C (2000) Pressure patches for membranes: the induced pinch of a grafted polymer. Phys Rev E 62(1):1124–1127
6. Goulian M, Bruinsma R, Pincus P (1993) Long-range forces in heterogeneous fluid membranes. Europhys Lett 22(2):145–150. Erratum: Europhys Lett 23(2):155 (1993). Comment: Ref. [9]. A factor 2 in the fluctuation-induced force was corrected in Ref. [10].
7. Leibler S (1986) Curvature instability in membranes. J. Physique 47:507–516
8. Fournier J-B, Galatola P (2015) High-order power series expansion of the elastic interaction between conical membrane inclusions. Eur Phys J E 38:86
9. Fournier J-B, Dommersnes PG (1997) Comment on "Long-range forces in heterogeneous fluid membranes". Europhys Lett 39(6):681–682
10. Golestanian R, Goulian M, Kardar M (1996) Fluctuation-induced interactions between rods on a membrane. Phys Rev E 54(6):6725–6734
11. Park JM, Lubensky TC (1996) Interactions between membrane inclusions on fluctuating membranes. J Phys I 6(9):1217–1235
12. Netz RR (1997) Inclusions in fluctuating membranes: exact results. J Physique I – France 7:833–852
13. Kim KS, Neu J, Oster G (1998) Curvature-mediated interactions between membrane proteins. Biophys J 75(5):2274–2291
14. Dommersnes PG, Fournier J-B (1999) N-body study of anisotropic membrane inclusions: membrane mediated interactions and ordered aggregation. Eur Phys J B 12(1):9–12
15. Dommersnes PG, Fournier J-B (1999) Casimir and mean-field interactions between membrane inclusions subject to external torques. Europhys Lett 46(2):256–261
16. Yolcu C, Rothstein IZ, Deserno M (2011) Effective field theory approach to Casimir interactions on soft matter surfaces. Europhys Lett 96:20003
17. Yolcu C, Deserno M (2012) Membrane-mediated interactions between rigid inclusions: an effective field theory. Phys Rev E 86:031906
18. Yolcu C, Rothstein IZ, Deserno M (2012) Effective field theory approach to fluctuation-induced forces between colloids at an interface. Phys Rev E 85:011140

19. Yolcu C, Deserno M (2014) The Effective Field Theory approach towards membrane-mediated interactions between particles. Adv Colloid Interface Sci 208:89–109
20. Golestanian R (1996) Reduced persistence length and fluctuation-induced interactions of directed semiflexible polymers on fluctuating surfaces. Europhys Lett 36:557–561
21. Casimir HBG (1948) On the attraction between two perfectly conducting plates. Proc K Ned Akad Wet 51(7):793–796
22. Milonni PW (1994) The quantum vacuum – an introduction to quantum electrodynamics. Academic, New York
23. Helfrich W, Weikl TR (2001) Two direct methods to calculate fluctuation forces between rigid objects embedded in fluid membranes. Eur Phys J E 5:423–439
24. Kardar M, Golestanian R (1999) The "friction" of vacuum, and other fluctuation-induced forces. Rev Mod Phys 71(4):1233–1245
25. Gambassi A (2009) The Casimir effect: from quantum to critical fluctuations. JPCS 161:012037
26. Fisher ME, de Gennes PG (1978) Wall phenomena in a critical binary mixture. C R Séances Acad Sci Ser B 287(8):207–209
27. Hertlein C, Helden L, Gambassi A, Dietrich S, Bechinger C (2008) Direct measurement of critical Casimir forces. Nature 451(7175):172–175
28. Machta BB, Veatch SL, Sethna JP (2012) Critical Casimir forces in cellular membranes. Phys Rev Lett 109:138101
29. Golestanian R, Goulian M, Kardar M (1996) Fluctuation-induced interactions between rods on membranes and interfaces. Europhys Lett 33(3):241–245
30. Stamou D, Duschl C, Johannsmann D (2000) Long-range attraction between colloidal spheres at the air-water interface: the consequence of an irregular meniscus. Phys Rev E 62(4, B):5263–5272
31. Dommersnes PG, Fournier J-B (2002) The many-body problem for anisotropic membrane inclusions and the self-assembly of "saddle" defects into an "egg carton". Biophys J 83:2898–2905
32. Axilrod BM, Teller E (1943) Interaction of the van der Waals type between three atoms. J Chem Phys 11(6):299–300
33. Simunovic M, Srivastava A, Voth GA (2013) Linear aggregation of proteins on the membrane as a prelude to membrane remodeling. Proc Natl Acad Sci U S A 110(51):20396–20401
34. Destainville N (1998) Cluster phases of membrane proteins. Phys Rev E 77:011905
35. Weikl TR (2001) Fluctuation-induced aggregation of rigid membrane inclusions. Europhys Lett 54:547–553
36. Rawicz W, Olbrich KC, McIntosh T, Needham D, Evans E (2000) Effect of chain length and unsaturation on elasticity of lipid bilayers. Biophys J 79:328–339
37. Lehle H, Oettel M (2007) Importance of boundary conditions for fluctuation-induced forces between colloids at interfaces. Phys Rev E 75:011602
38. Noruzifar E, Oettel M (2009) Anisotropies in thermal Casimir interactions: ellipsoidal colloids trapped at a fluid interface. Phys Rev E 79(5):051401
39. Lin H-K, Zandi R, Mohideen U, Pryadko LP (2011) Fluctuation-induced forces between inclusions in a fluid membrane under tension. Phys Rev Lett 107:228104
40. Genet C, Lambrecht A, Reynaud S (2003) Casimir force and the quantum theory of lossy optical cavities. Phys Rev A 67(4):043811
41. Emig T, Graham N, Jaffe RL, Kardar M (2008) Casimir forces between compact objects: the scalar case. Phys Rev D 77(2):025005
42. Rahi SJ, Emig T, Graham N, Jaffe RL, Kardar M (2009) Scattering theory approach to electrodynamic Casimir forces. Phys Rev D 80:085021
43. Weikl TR, Kozlov MM, Helfrich W (1998) Interaction of conical membrane inclusions: effect of lateral tension. Phys Rev E 57:6988–6995
44. Evans AR, Turner MS, Sens P (2003) Interactions between proteins bound to biomembranes. Phys Rev E 67:041907

45. Simunovic M, Voth GA (2015) Membrane tension controls the assembly of curvature-generating proteins. Nat Commun 6:7219
46. Bitbol A-F, Dommersnes PG, Fournier J-B (2010) Fluctuations of the Casimir-like force between two membrane inclusions. Phys Rev E 81:050903(R)
47. Capovilla R, Guven J (2002) Stresses in lipid membranes. J Phys A 35(30):6233–6247
48. Fournier J-B (2007) On the stress and torque tensors in fluid membranes. Soft Matter 3(7):883–888
49. Barton G (1991) On the fluctuations of the Casimir force. J Phys A 24(5):991–1005
50. Bartolo D, Ajdari A, Fournier J-B, Golestanian R (2002) Fluctuations of fluctuation-induced Casimir-like forces. Phys Rev Lett 89(23):230601
51. Bitbol A-F, Fournier J-B (2011) Forces exerted by a correlated fluid on embedded inclusions. Phys Rev E 83:061107
52. Fournier J-B (2014) Dynamics of the force exchanged between membrane inclusions. Phys Rev Lett 112:128101. Erratum: Phys Rev Lett 114:219901 (2015)
53. Seifert U, Langer SA (1993) Viscous modes of fluid bilayer membranes. Europhys Lett 23:71–76
54. Evans E, Yeung A (1994) Hidden dynamics in rapid changes of bilayer shape. Chem Phys Lipids 73:39–56
55. Fournier J-B (2015) On the hydrodynamics of bilayer membranes. Int J Nonlinear Mech 75:67–76
56. Bitbol A-F, Peliti L, Fournier J-B (2011) Membrane stress tensor in the presence of lipid density and composition inhomogeneities. Eur Phys J E 34:53
57. Dommersnes PG, Fournier J-B, Galatola P (1998) Long-range elastic forces between membrane inclusions in spherical vesicles. Europhys Lett 42:233–238
58. Podgornik R (1995) Orientational ordering of polymers on a fluctuating flexible surface. Phys Rev E 52:5170–5177
59. Li H, Kardar M (1992) Fluctuation-induced forces between manifolds immersed in correlated fluids. Phys Rev A 46(10):6490–6500
60. Bitbol A-F, Sin Ronia K, Fournier J-B (2011) Universal amplitudes of the Casimir-like interactions between four types of rods in fluid membranes. Europhys Lett 96:40013
61. Sin Ronia K, Fournier J-B (2012) Universality in the point discretization method for calculating Casimir interactions with classical Gaussian fields. Europhys Lett 100(3):30008
62. Derjaguin BV (1934) Analysis of friction and adhesion – IV. The theory of the adhesion of small particles. Kolloid Zeitschrift 69:155–164
63. Weikl TR (2003) Indirect interactions of membrane-adsorbed cylinders. Eur Phys J E 12:265–273
64. Müller MM, Deserno M, Guven J (2005) Interface-mediated interactions between particles: a geometrical approach. Phys Rev E 72:061407
65. Müller MM, Deserno M, Guven J (2005) Geometry of surface-mediated interactions. Europhys Lett 69:482–488
66. Müller MM, Deserno M (2007) Balancing torques in membrane-mediated interactions: exact results and numerical illustrations. Phys Rev E 76:011921
67. Mkrtchyan S, Ing C, Chen JZY (2010) Adhesion of cylindrical colloids to the surface of a membrane. Phys Rev E 81:011904
68. Gosselin P, Mohrbach H, Müller MM (2011) Interface-mediated interactions: entropic forces of curved membranes. Phys Rev E 83:051921
69. Reynwar BJ, Illya G, Harmandaris VA, Mueller MM, Kremer K, Deserno M (2007) Aggregation and vesiculation of membrane proteins by curvature-mediated interactions. Nature 447:461–464
70. Yuan H, Huang C, Zhang S (2011) Membrane-mediated inter-domain interactions. Bio-NanoScience 1:97–102
71. Reynwar BJ, Deserno M (2011) Membrane-mediated interactions between circular particles in the strongly curved regime. Soft Matter 7:8567–8575

72. Schweitzer Y, Kozlov MM (2015) Membrane-mediated interaction between strongly anisotropic protein scaffolds. PLOS Comp Biol 11(2):e1004054
73. Bahrami AH, Lipowsky R, Weikl TR (2012) Tubulation and aggregation of spherical nanoparticles adsorbed on vesicles. Phys Rev Lett 109(18):188102
74. Šarić A, Cacciuto A (2013) Self-assembly of nanoparticles adsorbed on fluid and elastic membranes. Soft Matter 9:6677–6695
75. Ramakrishnan N, Sunil Kumar PB, Ipsen JH (2013) Membrane-mediated aggregation of curvature-inducing nematogens and membrane tubulation. Biophys J 104(5):1018–1028
76. Römer W, Berland L, Chambon V, Gaus K, Windschiegl B, Tenza D, Aly MRE, Fraisier V, Florent J-C, Perrais D, Lamaze C, Raposo G, Steinem C, Sens P, Bassereau P, Johannes L (2007) Shiga toxin induces tubular membrane invaginations for its uptake into cells. Nature 450:670–675
77. McMahon HT, Gallop JL (2005) Membrane curvature and mechanisms of dynamic cell membrane remodelling. Nature 438:590–596
78. Angelova MI, Dimitrov DS (1986) Liposome electroformation. Faraday Discuss Chem Soc 81:303–311
79. Semrau S, Idema T, Schmidt T, Storm C (2009) Membrane-mediated interactions measured using membrane domains. Biophys J 96(12):4906–4915
80. Koltover I, Rädler JO, Safinya CR (1999) Membrane mediated attraction and ordered aggregation of colloidal particles bound to giant phospholipid vesicles. Phys Rev Lett 82:1991–1994
81. Yue T, Zhang X (2012) Cooperative effect in receptor-mediated endocytosis of multiple nanoparticles. ACS Nano 6(4):3196–3205
82. Šarić A, Cacciuto A (2012) Fluid membranes can drive linear aggregation of adsorbed spherical nanoparticles. Phys Rev Lett 108(11):118101
83. Sarfati R, Dufresne ER (2016) Long-range attraction of particles adhered to lipid vesicles. Phys Rev E 94(1):012604
84. Rozovsky S, Kaizuka Y, Groves JT (2005) Formation and spatio-temporal evolution of periodic structures in lipid bilayers. J Am Chem Soc 127(1):36–37
85. Ursell TS, Klug WS, Phillips R (2009) Morphology and interaction between lipid domains. Proc Natl Acad Sci U S A 106(32):13301–13306
86. Heberle FA, Petruzielo RS, Pan J, Drazba P, Kučerka N, Standaert RF, Feigenson GW, Katsaras J (2013) Bilayer thickness mismatch controls domain size in model membranes. J Am Chem Soc 135(18):6853–6859
87. Jost PC, Griffiths OH, Capaldi RA, Vanderkooi G (1973) Evidence for boundary lipid in membranes. Proc Natl Acad Sci U S A 70:480–484
88. Marčelja S (1976) Lipid-mediated protein interaction in membranes. Biochim Biophys Acta: Biomembr 455:1–7
89. Schröder H (1977) Aggregation of proteins in membranes. An example of fluctuation induced interactions in liquid crystals. J Chem Phys 67:1617–1619
90. Owicki JC, Springgate MW, McConnell H (1978) Theoretical study of protein-lipid interactions in bilayer membranes. Proc Natl Acad Sci U S A 75:1616–1619
91. Killian JA (1998) Hydrophobic mismatch between proteins and lipids in membranes. Biochim Biophys Acta: Biomembr 1376:401–416
92. Mouritsen OG, Bloom M (1984) Mattress model of lipid-protein interactions in membranes. Biophys J 46:141–153
93. Kelkar DA, Chattopadhyay A (2007) The gramicidin ion channel: a model membrane protein. Biochim Biophys Acta: Biomembr 1768:2011–2025
94. Kolb HA, Bamberg E (1977) Influence of membrane thickness and ion concentration on the properties of the gramicidin A channel: autocorrelation, spectral power density, relaxation and single-channel studies. Biochim Biophys Acta: Biomembr 464:127–141
95. Elliott JR, Needham D, Dilger JP, Haydon DA (1983) The effects of bilayer thickness and tension on gramicidin single-channel lifetime. Biochim Biophys Acta: Biomembr 735:95–103

96. Goulian M, Mesquita ON, Fygenson DK, Nielsen C, Andersen OS, Libchaber A (1998) Gramicidin channel kinetics under tension. Biophys J 74:328–337
97. Huang HW (1986) Deformation free energy of bilayer membrane and its effect on gramicidin channel lifetime. Biophys J 50:1061–1070
98. de Gennes PG (1974) The physics of liquid crystals. Clarendon Press, Oxford
99. Dan N, Pincus P, Safran SA (1993) Membrane-induced interactions between inclusions. Langmuir 9:2768–2771
100. Aranda-Espinoza H, Berman A, Dan N, Pincus P, Safran S (1996) Interaction between inclusions embedded in membranes. Biophys J 71:648–656
101. Brannigan G, Brown FLH (2006) A consistent model for thermal fluctuations and protein-induced deformations in lipid bilayers. Biophys J 90(5):1501–1520
102. Brannigan G, Brown FLH (2007) Contributions of gaussian curvature and nonconstant lipid volume to protein deformation of lipid bilayers. Biophys J 92(3):864–876
103. Watson MC, Penev ES, Welch PM, Brown FLH (2011) Thermal fluctuations in shape, thickness, and molecular orientation in lipid bilayers. J Chem Phys 135:244701
104. Bitbol A-F, Constantin D, Fournier J-B (2012) Bilayer elasticity at the nanoscale: the need for new terms. PLoS One 7(11):e48306
105. West B, Brown FLH, Schmid F (2009) Membrane-protein interactions in a generic coarse-grained model for lipid bilayers. Biophys J 96(1):101–115
106. Owicki JC, McConnell H (1979) Theory of protein-lipid and protein-protein interactions in bilayer membranes. Proc Natl Acad Sci U S A 76:4750–4754
107. Dan N, Berman A, Pincus P, Safran SA (1994) Membrane-induced interactions between inclusions. J Phys II France 4:1713–1725
108. Harroun TA, Heller WT, Weiss TM, Yang L, Huang HW (1999) Theoretical analysis of hydrophobic matching and membrane-mediated interactions in lipid bilayers containing gramicidin. Biophys J 76(6):3176–3185
109. Neder J, West B, Nielaba P, Schmid F (2011) Membrane-mediated protein-protein interaction: a Monte Carlo study. Curr Nanosci 7(5):656–666
110. Bories F, Constantin D, Galatola P, Fournier J-B (2018) Coupling between inclusions and membranes at the nanoscale. Phys Rev Lett 120:128104
111. Chaikin PM, Lubensky TC (1995) Principles of condensed matter physics. Cambridge University Press, Cambridge
112. Fournier J-B (1998) Coupling between membrane tilt-difference and dilation: a new "ripple" instability and multiple crystalline inclusions phases. Europhys Lett 43(6):725–730
113. May S, Ben-Shaul A (1999) Molecular theory of lipid-protein interaction and the L_α-$H_{||}$ transition. Biophys J 76:751–767
114. May S, Ben-Shaul A (2000) A molecular model for lipid-mediated interaction between proteins in membranes. Phys Chem Chem Phys 2:4494–4502
115. May S (2002) Membrane perturbations induced by integral proteins: role of conformational restrictions of the lipid chains. Langmuir 18:6356–6364
116. Bohinc K, Kralj-Iglič V, May S (2003) Interaction between two cylindrical inclusions in a symmetric lipid bilayer. J Chem Phys 119:7435–7444
117. Kozlovsky Y, Zimmerberg J, Kozlov MM (2004) Orientation and interaction of oblique cylindrical inclusions embedded in a lipid monolayer: a theoretical model for viral fusion peptides. Biophys J 87:999–1012
118. Haselwandter CA, Phillips R (2013) Directional interactions and cooperativity between mechanosensitive membrane proteins. Europhys Lett 101(6):68002
119. Ursell T, Huang KC, Peterson E, Phillips R (2007) Cooperative gating and spatial organization of membrane proteins through elastic interactions. PLoS Comput Biol 3(5):803–812
120. Phillips R, Ursell T, Wiggins P, Sens P (2009) Emerging roles for lipids in shaping membrane-protein function. Nature 459(7245):379–385
121. Kahraman O, Klug WS, Haselwandter CA (2014) Signatures of protein structure in the cooperative gating of mechanosensitive ion channels. Europhys Lett 107(4):48004

122. Haselwandter CA, Wingreen NS (2014) The role of membrane-mediated interactions in the assembly and architecture of chemoreceptor lattices. PLoS Comput Biol 10(12):e1003932
123. Briegel A, Li X, Bilwes AM, Hughes KT, Jensen GJ, Crane BR (2012) Bacterial chemoreceptor arrays are hexagonally packed trimers of receptor dimers networked by rings of kinase and coupling proteins. Proc Natl Acad Sci U S A 109(10):3766–3771
124. Sintes T, Baumgärtner A (1997) Protein attraction in membranes induced by lipid fluctuations. Biophys J 73:2251–2259
125. Lagüe P, Zuckermann MJ, Roux B (2000) Lipid-mediated interactions between intrinsic membrane proteins: a theoretical study based on integral equations. Biophys J 79:2867–2879
126. Lagüe P, Zuckermann MJ, Roux B (2001) Lipid-mediated interactions between intrinsic membrane proteins: dependence on protein size and lipid composition. Biophys J 81:276–284
127. Janosi L, Prakash A, Doxastakis M (2010) Lipid-modulated sequence-specific association of glycophorin A in membranes. Biophys J 99(1):284–292
128. Kik RA, Leermakers FAM, Kleijn JM (2010) Molecular modeling of proteinlike inclusions in lipid bilayers: lipid-mediated interactions. Phys Rev E 81(2):021915
129. Yoo J, Cui Q (2013) Membrane-mediated protein-protein interactions and connection to elastic models: a coarse-grained simulation analysis of gramicidin A association. Biophys J 104:128–138
130. Dunton TA, Goose JE, Gavaghan DJ, Sansom MSP, Osborne JM (2014) The free energy landscape of dimerization of a membrane protein, NanC. PLoS Comput Biol 10(1):e1003417
131. Marčelja S (1999) Toward a realistic theory of the interaction of membrane inclusions. Biophys J 76:593–594
132. Lewis BA, Engelman DM (1983) Bacteriorhodopsin remains dispersed in fluid phospholipid bilayers over a wide range of bilayer thicknesses. J Mol Biol 166:203–210
133. Chen YS, Hubbell WL (1973) Temperature- and light-dependent structural changes in rhodopsin-lipid membranes. Exp Eye Res 17:517–532
134. James R, Branton D (1973) Lipid- and temperature-dependent structural changes in *Acholeplasma laidlawii* cell membranes. Biochim Biophys Acta 323:378–390
135. Abney JR, Braun J, Owicki JC (1987) Lateral interactions among membrane proteins: implications for the organization of gap junctions. Biophys J 52:441–454
136. Pearson LT, Lewis BA, Engelman DM, Chan SI (1983) Pair distribution functions of bacteriorhodopsin and rhodopsin in model bilayers. Biophys J 43:167–174
137. Pearson LT, Edelman J, Chan SI (1984) Statistical mechanics of lipid membranes, protein correlation functions and lipid ordering. Biophys J 45:863–871
138. Braun J, Abney JR, Owicki JC (1987) Lateral interactions among membrane proteins: valid estimates based on freeze-fracture electron microscopy. Biophys J 52:427–439
139. Oesterhelt F, Oesterhelt D, Pfeiffer M, Engel A, Gaub HE, Muller DJ (2000) Unfolding pathways of individual bacteriorhodopsins. Science 288:143–146
140. Ando T, Kodera N, Takai E, Maruyama D, Saito K, Toda A (2001) A high-speed atomic force microscope for studying biological macromolecules. Proc Natl Acad Sci U S A 98(22):12468–12472
141. Casuso I, Sens P, Rico F, Scheuring S (2010) Experimental evidence for membrane-mediated protein-protein interaction. Biophys J 99(7):L47–L49
142. He K, Ludtke SJ, Huang HW, Worcester DL (1995) Antimicrobial peptide pores in membranes detected by neutron in-plane scattering. Biochemistry 34:15614–15618
143. He K, Ludtke SJ, Worcester DL, Huang HW (1996) Neutron scattering in the plane of the membranes: structure of alamethicin pores. Biophys J 70:2659–2666
144. Yang L, Weiss TM, Harroun TA, Heller WT, Huang HW (1999) Supramolecular structures of peptide assemblies in membranes by neutron off-plane scattering: method of analysis. Biophys J 77:2648–2656
145. Constantin D, Brotons G, Jarre A, Li C, Salditt T (2007) Interaction of alamethicin pores in DMPC bilayers. Biophys J 92:3978–3987

146. Constantin D, Pansu B, Impéror M, Davidson P, Ribot F (2008) Repulsion between inorganic particles inserted within surfactant bilayers. Phys Rev Lett 101:098101
147. Constantin D (2010) The interaction of hybrid nanoparticles inserted within surfactant bilayers. J Chem Phys 133:144901
148. Constantin D (2009) Membrane-mediated repulsion between gramicidin pores. Biochim Biophys Acta: Biomembr 1788:1782–1789

Simulating Protein-Mediated Membrane Remodeling at Multiple Scales

Mijo Simunovic and Gregory A. Voth

Abstract The reshaping of the cell membrane is integral in many important cellular pathways, such as division, immune response, infection, trafficking, and communication. This process is generally modeled by considering lipid membranes to be thin elastic sheets that resist bending and stretching deformations. However, biological membranes are much more complex, as the macroscopically observed behavior of the membrane is deeply connected to the underlying atomic-level interactions between proteins and lipids. Computational methods can be developed to tackle this complex and innately multiscale phenomenon, as they can model the behavior at both the molecular and the macroscopic levels. In this chapter, we discuss the general mechanisms of membrane curvature generation and computational tools developed and applied to study this problem. We focus especially on finite-temperature simulation methods that are designed to model the complex behavior of the system. We review recent efforts in multiscale simulation designed to study the large-scale membrane reshaping by proteins.

Keywords BAR proteins · Multiscale simulations · Coarse-grained simulations · Mesoscopic simulations · Membrane curvature · Lipid model · Computational modeling

1 The Multiscale Nature of Lipid Membranes

Structural features of lipid membranes are observable at multiple scales. In other words, to understand how lipids form membranes of various shapes, we need to approach the problem from molecular, mesoscopic, and macroscopic points of view. Let us first consider the molecular perspective. The key ingredients of biological membranes are the phospholipids. Chemically speaking, they are considered to be

M. Simunovic (✉) · G. A. Voth
Department of Chemistry, Institute for Biophysical Dynamics, and James Franck Institute, The University of Chicago, Chicago, IL, USA
e-mail: mijo@uchicago.edu; gavoth@uchicago.edu

P. Bassereau, P. Sens (eds.), *Physics of Biological Membranes*,
https://doi.org/10.1007/978-3-030-00630-3_14

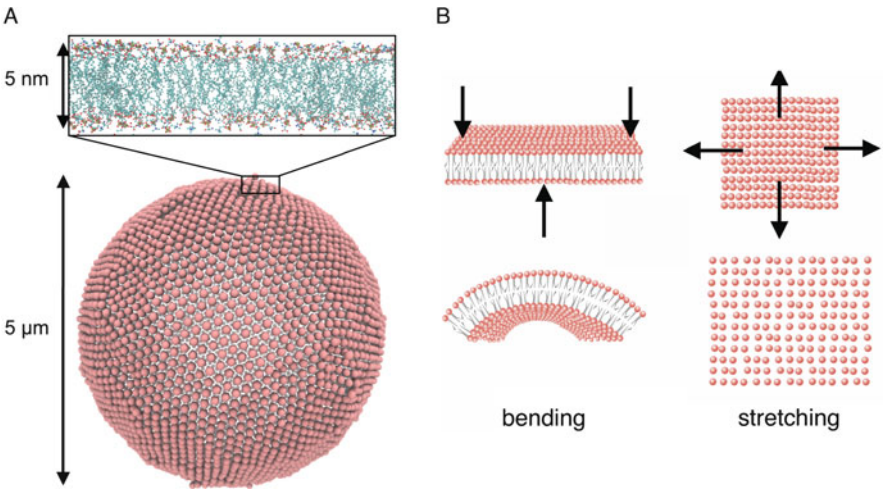

Fig. 1 The multiscale nature of lipid membranes. (**a**) Separation of scales: a bilayer spans microns in length and width where it is governed by macroscopic mechanics, while at the level of its thickness (inset), it only spans two molecules where it is governed by hydrophobic and polar interactions. (**b**) A membrane is modeled as a thin elastic sheet that resists bending and stretching deformations

amphipathic molecules, because their phosphate head group is polar, i.e., it attracts water, whereas their lipid tails are hydrophobic, i.e., they attract apolar molecules [1]. The consequences of such interactions are that when phospholipids are mixed with water, lipid tails stick to one another and the hydrophilic moieties are solvated by water. Various geometries can accommodate such interactions, but the most relevant to biology is a lipid bilayer (Fig. 1) [2].

Although the thickness of the bilayer only spans two molecules, lipids form macroscopic assemblies in lateral dimensions, and understanding their behavior at this level demands a macroscopic point of view (Fig. 1a). At larger scales, the membrane behaves like an elastic sheet, resisting bending and stretching deformations (Fig. 1b). Its long-wavelength dynamics is seemingly unconnected to its molecular nature; however, the two scales actually strongly couple [3]. How is this so? Imagine immersing a bilayer patch in water. The hydrophobic repulsion at the interface of water and lipid tails gives rise to line tension that works to minimize the edge of a bilayer. This molecular interaction has a macroscopic impact as it forces the membrane into a closed surface. The interactions among lipid molecules set the preferred area they occupy, giving rise to surface tension, i.e., the membrane's elastic resistance to stretching. Furthermore, line and surface tension compete with the elastic energy associated with the cost of bending the membrane. Finally, a result of these opposing forces—that operate at different scales—gives biological membranes a wide range of geometries [3].

The elastic description of the cell membrane has been remarkably successful in explaining the physical basis of large-scale membrane behavior, and it has

provided a very useful analytical framework for analyzing and understanding the experimental data. However, biological membranes are far more complex than thin elastic sheets. First, they are fluid, which means that they do not resist shearing—sliding of layers past each other—and they cannot tear or form sharp corners, unlike solid bendable materials. Second, membranes can contain hundreds of different components that are likely not homogenously mixed along the length of the cell membrane. Therefore, predicting its actual phase behavior seems nearly impossible. Lastly, the cell membrane is not at equilibrium, making the thermodynamic treatment all the more difficult.

Accounting for all the complexities and the innate multiscale character of a cell membrane in modeling its behavior is a daunting task. An approach uniting molecular, mesoscopic, and macroscopic scales is essential in accessing a fuller scope of membrane phenomena in biology. In this chapter, we describe computational methodologies used to study lipid membranes, specifically focusing on methods applied to investigate how proteins can change membrane shape.

2 The Reshaping of Biological Membranes

It has been widely accepted that membrane curvature plays significant roles in the cell. On the one hand, cells use curvature on larger scales to form complex intracellular structures or for motility of the whole cell. For example, the high curvature of the inner mitochondrial membrane significantly adds to the total membrane area (compared to a flat membrane enveloping the same volume), which is why the mitochondrion can host an enzymatic power source of the cell. On the other hand, membranes can be temporarily curved—usually on sub-μm scales—enabling dynamic processes, such as communication and trafficking [4].

How is membrane curvature generated in the cell? Thermal fluctuations give rise to membrane curvature, however only transiently, as the energy associated with random fluctuations is an order of magnitude lower than the bending stiffness of biological membranes [5–7]. The most commonly understood mechanism of generating curvature is by imposing an asymmetry into the bilayer, either by lipid composition or by protein binding. Consider enriching one membrane layer with a non-cylindrically shaped lipid, such as sphingomyelin or phosphatidylethanolamine. The bulky head of sphingomyelin will force one layer to expand and hence generate curvature (the first cartoon in the upper left of Fig. 2). Another way lipids may induce curvature is by phase separation. The energy resulting from the formation of edges between domains will tend to minimize, which is achieved either (a) by coalescence of like phases or (b) by squeezing the domain boundary, which results in budding [8]. Numerical calculations have been carried out to understand the morphological consequences of phase-separated vesicles, and they have resulted in a very rich shape diagram of such systems. The ultimate shape of the membrane depends on the size of domains, the elastic properties of the membrane, as well as surface and line tensions [9–17].

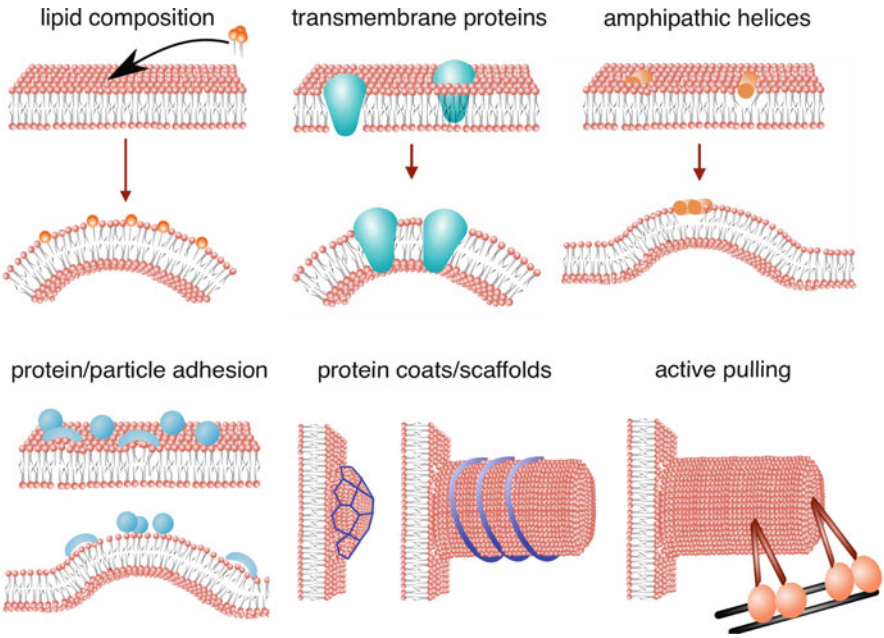

Fig. 2 Mechanisms of generating membrane curvature

Although lipids can affect the shape of membranes, the main role of curvature generators in cells belongs to proteins. It has been shown that conically shaped proteins spontaneously redistribute into membrane tubules, likely because their packing is more efficient in curved membranes [18]. In light of this discovery, the accumulation of conically shaped proteins, such as the nicotinic acetyl receptor [19] and the voltage-gated potassium channel [20], in principle could induce membrane curvature (Fig. 2).

Another way proteins may induce curvature is by inserting their amphipathic domains into the membrane [21]; however, this process is more complicated to understand with simple shape arguments (Fig. 2). Theoretical calculations have demonstrated that the magnitude of spontaneous curvature depends on the insertion depth in a non-monotonous way, which means that a deeper insertion does not lead to more curvature. Instead, there is a maximum, achieved at the insertion depth at approximately one-third of one layer [22, 23]. Many cytosolic and peripherally binding proteins contain amphipathic helices. Apolipoproteins, for example, solubilize lipids, including cholesterol, for their transport through the blood [24, 25]. Many proteins involved in endocytosis contain amphipathic helices, such as epsins and Bin/amphiphysin/Rvs (BAR) proteins, implicated in various forms of membrane remodeling [26, 27].

The peripheral binding or adhesion of proteins and particles can also lead to membrane curvature (Fig. 2). The mechanisms of curvature generation by such

proteins are even more complex and seem to tightly depend on the shape of the proteins, their surface density, and the material and morphological properties of the membrane [27, 28]. Several simplified mechanisms have been proposed: (1) each bound protein or particle alters the underlying lipid organization [29, 30], (2) proteins form a three-dimensional network that imposes a shape as a mold or a scaffold (e.g., clathrin or dynamin; see Fig. 2) [31, 32], and (3) crowding of bound particles forces membrane bending to maximize the distance between particles. An entropy-driven mechanism has also been proposed, based on a computational study showing that polymers grafted on the membrane may induce curvature [33, 34]. In this case, the loss of conformational entropy is compensated by pushing away the underlying surface from the polymers. The calculations were later experimentally demonstrated by tethering DNA and proteins on the membrane [35, 36].

Finally, membrane can be actively reshaped by an external pulling force (Fig. 2), such as with the cytoskeleton machinery and molecular motors [32]. For example, the polymerization of actin filaments gives rise to many curved cellular geometries, such as filopodia, pseudopodia, and axonal growth cones [37]. In vitro reconstitution has demonstrated that molecular motors, such as kinesins and myosins, can attach to the membrane and, walking along cytoskeletal filaments, they can extrude a tubule from a vesicle [38, 39].

Let us briefly focus on the superfamily of BAR domain proteins, key regulators of cell membrane curvature [40]. They have been implicated in many important cellular tasks, from generating membrane curvature and maintaining complex membranous geometries to helping assemble multiprotein machineries in a number of membrane-remodeling phenomena [26]. Numerous experiments have isolated the effects of BAR proteins, e.g., with overexpression in the cell, chemical targeting of BAR proteins to specific organelles, or in vitro reconstitution, all demonstrating that BAR proteins are powerful membrane remodelers [41–45]. Although BAR proteins are structurally quite diverse, they all contain a banana-shaped BAR domain [42]. To make matters even more complicated, the BAR domain itself varies in size, charge, and the magnitude of intrinsic curvature from member to member (Fig. 3). The membrane-binding region of this domain is lined with positively charged residues, so they are highly reliant on negatively charged lipids, such as phosphatidylserine and phosphatidylinositol 4,5-bisphosphate (PIP_2). Most BAR proteins also contain an N-terminal amphipathic helix, thus termed N-BAR proteins, which enhance their curvature-sensing and curvature-generating capabilities (Fig. 3, first structure on the left).

The way N-BAR proteins interact with the membrane is a combination of adhesion of an anisotropic BAR domain, the shallow insertion of amphipathic helices, and under some conditions, the scaffolding by a BAR oligomer [27, 28, 31, 46, 47]. BAR proteins often interact with other proteins, such as with molecular motors in scission of membrane nanotubes [48], making this problem very challenging. Many of these phenomena have been addressed by multiscale computer simulations, and we will outline these results below.

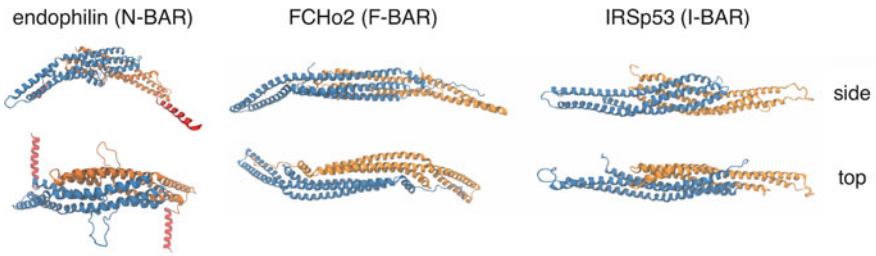

Fig. 3 Ribbon structures of various BAR protein dimers—the functional protein unit—each monomer colored differently. The N-terminal helices in endophilin (colored red) are added by hand, as they were not resolved in X-ray structural imaging. Top views along the bottom line of images represent viewing from above the bilayer surface

3 Computational Simulations of Biomembranes

Theoretical and computational approaches to studying biological phenomena have seen appreciable advancements in the past decade, allowing detailed structural and thermodynamic descriptions of fundamental cellular processes, such as protein folding, lipid vesicle formation, and large-scale structural rearrangements of macromolecules. Computational simulations are particularly attractive as they provide direct visualization of the complex evolution of the system, along with a wealth of thermodynamic and high-resolution structural data. In addition, simulations give insights into the distribution and time-dependent properties of the system and not just their average as in most experimental techniques [49].

The basic steps in computational modeling of a biomolecular system are (1) choosing the resolution of the model and the number of degrees of freedom (the so-called level of theory), (2) calculating the forces between particles (the so-called force field), and (3) simulating the movement of particles (i.e., generating a trajectory).

The choice of level of theory depends on the resolution of the system and the number of degrees of freedom we wish to simulate. For example, if we are interested in the submolecular details of the structure of a protein, we will opt for an atomic-level simulation. On the other hand, if we wish to understand processes that do not rely on specific atomic interactions, such as the large-scale remodeling of lipid membranes, we will prefer mesoscopic models. When considering the level of theory, we also need to be aware that simulating systems with many degrees of freedom is computationally very costly. Most biological problems involve many atoms so we are often forced to compromise resolution for computational feasibility. In this chapter, we will focus on three levels of theory relevant to biological membranes: (1) atomic, (2) coarse-grained (CG), and (3) continuum or mesoscopic. The scheme in Fig. 4 depicts scales associated with these three levels of theory. It also shows the flow of information from atomic to continuum descriptions, and back, in the context of N-BAR-mediated remodeling (The reader should not focus

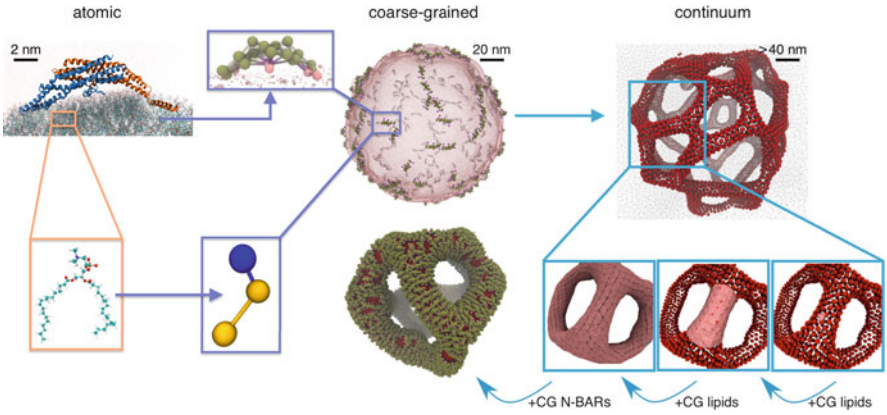

Fig. 4 A scheme of multiscale simulations of membrane remodeling by N-BAR proteins. Arrows pointing to the right represent coarse-graining (from atomic, to CG, to mesoscopic). Arrows pointing to the left depict the reverse approach—fine-graining—in which information at low resolution is used to build a model of higher resolution (see text)

on the meaning of the particular membrane phenomena shown in the figure at this point; we will refer to this scheme later in the chapter).

The dynamics of particles can be simulated in multiple ways. Molecular dynamics (MD) is the most commonly used method in biological simulations. In MD, the movement of particles is simulated by numerically integrating Newton's equations of motion, wherein the force on each atom is calculated based on the interactions defined by the force field. MD is particularly attractive because it is computationally feasible and it gives, in principle, both the static and the time-dependent properties of the system [50]. In Monte Carlo (MC) simulations, new configurations are generated by a random movement of particles, in a way that ensures the Boltzmann distribution. The strength of MC is that it does not require smooth derivatives of the potential and, considering that it permits unphysical random moves, it helps the system sample more space than allowed by MD for the same computational effort. However, it cannot be used to study the time-dependent dynamics of the system [50].

Smoothed particle hydrodynamics (SPH) is a method used for simulating continuum models based on Newtonian hydrodynamics, although originally designed to study astrophysical problems [51, 52]. SPH is particularly attractive because it discretizes continuum equations, which allows simulating complicated morphologies at the mesoscopic scale [53]. A similar method, called dissipative particle dynamics (DPD), supplements Newton's equation of motion with a dissipative and a random force [54, 55]. The combination of forces helps to conserve the momentum and the temperature of the system. Unlike MD and MC methods, SPH and DPD are by nature approximate. They are not necessarily designed to yield correct equilibrium properties; however, they reproduce the hydrodynamic behavior at large scales,

sufficient for understanding the long-wavelength behavior of the membrane [50, 56, 57].

Each modeling method comes with its own advantages and challenges. Combining different levels of theory—in what can be called the multiscale approach—can significantly extend the simulation timescale, while keeping the resolution as high as possible. A notable example is combining the quantum mechanics with the molecular mechanics (QM/MM) applied to modeling chemical reactions in the enzyme's active site [58]. QM/MM modeling elucidates how electron-level processes (i.e., the change in chemical bonding) couple with the atomic-level dynamics of the protein. Another approach in multiscale modeling is using the calculations from atomic-level simulations to estimate forces in lower resolution models, such as in CG or continuum models [59]. This approach is especially appropriate in studying membrane-remodeling phenomena where the interactions at the molecular scale communicate with much larger scales.

The use of multiscale simulations has exploded in the past decade, and it has seen tremendous success in modeling complex systems in biology and materials science. The development of multiscale models has had such an important impact on modern research that Martin Karplus, Michael Levitt, and Arieh Warshel—pioneers in certain early aspects of multiscale simulation development—received the Nobel Prize in Chemistry in 2013 [60–63].

4 Atomic Modeling

In the atomic-level (also called atomistic or all-atom) models, each atom (or in some cases a small united subset of atoms) is represented with a sphere of defined volume, mass, charge, and other physical properties (note the atomic representations of a lipid and a BAR domain in Fig. 4, left). The interactions between atoms are derived from quantum mechanical calculations or empirically fit from experimental measurements. One typically casts these interactions in a simple analytical form and divides them into (a) bonded and (b) nonbonded terms. Bonded interactions maintain the equilibrium bond length, the angle between neighboring bonds, and, often, a dihedral angle between four atoms, all modeled as a harmonic potential. Nonbonded interactions describe electrostatic, polar, and van der Waals interactions, usually modeled respectively with a Coulomb and a Lennard-Jones potential [49].

A major limitation of all-atom MD simulations is that they become computationally very expensive if the system exceeds a million atoms, roughly corresponding to a large protein surrounded by a box of water. With a recent development of high-power computing and efficient parallelization of MD computer codes, it has become possible to access microsecond dynamics of large biomolecular complexes with a computer. Notable examples include simulating entire viruses, namely, the tobacco mosaic virus [64] and the HIV-1 capsid [65]. These simulations have shown to be complements to experimental biology, as they have provided a more detailed insight into the structural properties of viral particles than cryo-electron microscopy, X-ray

crystallography, or NMR. Additionally, atomic-level MD simulations can elucidate the electrostatic environment of proteins and show the short-scale conformational dynamics of its subdomains. However, the range of time and length scales that such simulations sample is very small compared to the relevant scales in the cell and in many in vitro experiments.

Simulating membranes embedded with proteins thus tends to be more challenging. The interactions and the initial configuration in protein-membrane systems can be more complicated to model. Moreover, lipid molecules comprise a higher number of interactions for the same volume than the water-solvated protein, which makes these simulations more costly. For these reasons, simulating membrane-related phenomena at atomic resolution demands significant computational power or clever tricks that artificially enhance the sampling. For example, researchers have developed a computer architecture solely purposed for generating milliseconds-long trajectories of all-atom MD simulations [66]. They have demonstrated conformational dynamics of a transmembrane protein receptor stimulated by ligand binding [67, 68]. In addition, noteworthy efforts have been made to elucidate the way ion channels interact with the membrane and how they respond to chemical, electrical, and mechanical signals [69–73]. Even though these studies typically access much shorter timescales than in experiments, they have proven to be valuable to structural biology, helping to reveal the interactions of transmembrane proteins with the membrane and the mechanism by which they operate at the atomic level, which is in turn a difficult task for experiment alone.

In the aforementioned studies, atomic simulations mostly addressed the dynamics of the protein. The focus of this chapter is discussing the dynamics of the membrane. Several studies have used atomic-level MD simulations to study how BAR proteins deform membranes. Recall that BAR proteins couple with membrane curvature in the course of trafficking events such as endocytosis [27, 40, 47]. Simulations of the representative members of the N-BAR and F-BAR subfamilies have shown that these proteins can bend membranes, generating 20–35 nm in radius of curvature in only 25–100 ns of the simulated time (Fig. 5) [74–76]. According to subsequent simulations, however, crucial for bending the membrane are the ionic interactions between positively charged residues of the protein and the negatively charged lipids in the bilayer, as well as the screening of those interactions by the solvent [77]. In other words, these proteins are reliant on general ionic interactions, as opposed to, for instance, some specific stereochemistry [75, 78].

These works have also demonstrated that amphipathic helices of N-BAR proteins play an important role in membrane remodeling at the atomic scale. If the helices are not partially inserted (or wedged) into the bilayer, the binding of the N-BAR domain is significantly reduced, often leading to its dissociation from the surface. The loss of binding affinity may be compensated by a higher concentration of highly charged PIP_2 lipids, although PIP_2 does not fully recover the membrane-bending power of the N-BAR protein, at least not at a nanosecond timescale. With this result, we are tempted to conclude that helices are key factors for bending the membrane. However, isolated helices could only bend the membrane if their surface density was significantly increased (Fig. 5) [78]. Interestingly, in addition to surface density,

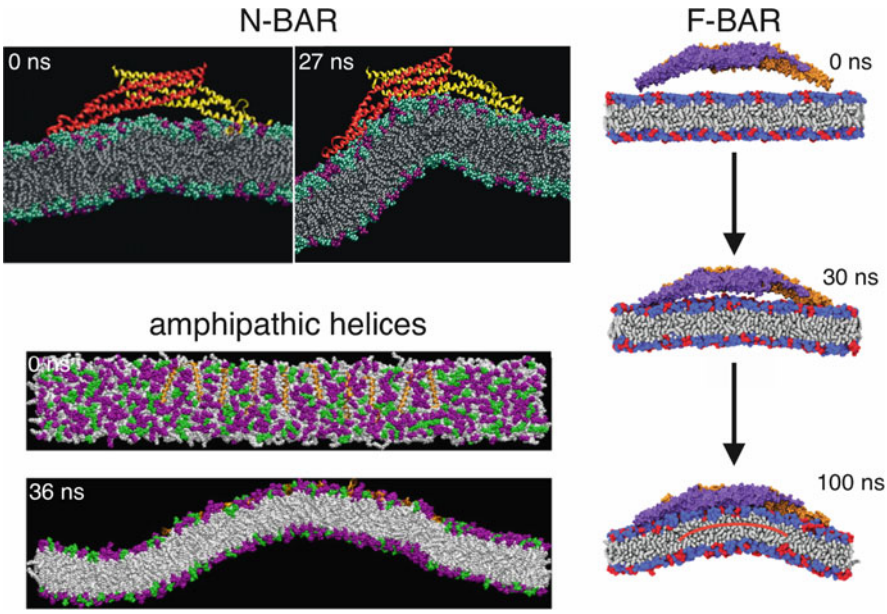

Fig. 5 Membrane remodeling by proteins modeled by all-atom simulations. Shown are initial and final snapshots of all-atom simulations of lipid bilayers embedded with N-BAR, F-BAR domains, or isolated amphipathic helices of an N-BAR domain protein. Approximate lipid-to-protein ratio for systems with N-BAR, F-BAR, and amphipathic helices, respectively: 70, 30, and 150. Note that a higher concentration of proteins is required to remodel a membrane with amphipathic helices (see text). Membrane composition in all: 30% DOPS, 70% DOPC. Figures adapted from (N-BAR) [75] copyright (2006) National Academy of Sciences; (F-BAR) [76] licensed under CC BY; (amphipathic helices) reprinted from [78] with permission from Elsevier

the orientation of the additional small helices at the dimerization interface (termed insert helices) with respect to the axis of the BAR domain also determines the magnitude of curvature [79]. The combined result indicates that both modules in N-BAR proteins—the BAR domain and the helices—are key for efficient remodeling of the membrane.

Despite the growth in computer power and parallel MD algorithms over the past 10 years, simulating large-scale membrane-remodeling phenomena at atomic resolution is still beyond reach. In fact, since the original simulation of membrane curvature induced by an N-BAR protein in 2006 [75], larger-scale all-atom MD simulations of this problem have not been reported. This comes as no surprise as membrane-remodeling phenomena involve many proteins at the mesoscopic scale and they typically comprise billions of atoms [32]. To understand these processes by a computational simulation, we need to significantly decrease the simulated number of degrees of freedom.

5 Coarse-Grained Modeling

The sheer size of membrane-remodeling events makes it too difficult a challenge to simulate at atomic resolution. Even if the system size is computationally tractable, timescales accessible by all-atom MD simulations are often insufficient to provide useful thermodynamic information at the mesoscopic level. More importantly, processes such as endocytosis invoke certain long-wavelength aspects of the membrane whose description does not even require modeling the atomic-level interactions.

Coarse-graining is a process of reducing the number of degrees of freedom by representing many atoms with a single CG particle [80]. Note on the left side in Fig. 4 the depiction of coarse-graining of lipid and N-BAR domain molecules. The first choice in coarse-graining is determining the level of resolution, i.e., how many CG particles to use to describe a molecule, such as a lipid. Figure 6 illustrates a lipid molecule (or a membrane patch) at different levels of resolution, each further discussed below. Clearly, low-resolution models will give access to much larger systems due to their computational efficiency, although deriving their effective

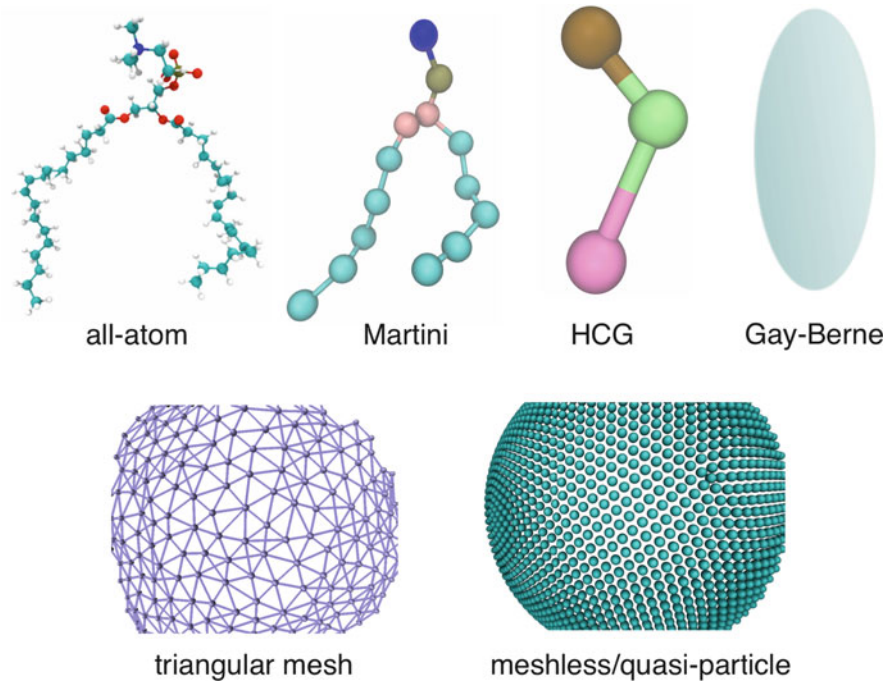

Fig. 6 Various lipid models. Top panel represents one lipid molecule in different degrees of resolution or coarseness (left to right—from finest to coarsest). Bottom panel shows a cutout of a triangular mesh and meshless membrane models (the latter may also represent a quasi-particle continuum model). Each model is described in the text. Image of the triangular mesh courtesy of Andela Saric

potentials in a systematic fashion can be more difficult. Eliminating the water molecules by making their contribution implicit, both in the potential itself and by adding stochastic terms into the dynamics (e.g., Langevin dynamics), can appreciably decrease the computational cost. No matter the approach, a good lipid CG model should as best as possible reproduce the molecular, the mesoscopic, and the macroscopic properties of the membrane, namely, (a) fluidity, (b) phase behavior, (c) structural factors (e.g., radial distribution functions), (d) material properties (e.g., bending stiffness and area compression modulus), and (e) fluctuation spectrum. However, the lateral diffusion rate of lipids is never reproduced in CG modeling, because the averaging of high-frequency motions leads to an artificially accelerated timescale, a drawback of all coarse-graining techniques, unless the effects of the missing degrees of freedom in the CG model are explicitly accounted for in the dynamics [81]. Therefore, it is important to note that most CG MD simulations—albeit providing an apparent time-dependent dynamics of the system—cannot easily be used to predict the actual timescale of molecular processes [82].

5.1 CG Lipid Models

The most difficult task of coarse-graining is accurately mapping the underlying atomic interactions onto their CG representation. There are two contrasting ways of generating a CG force field: (1) a bottom-up approach in which the forces are somehow derived from all-atom simulations and (2) a top-down approach in which the interactions are approximated by matching with experimental measurements [80]. Let us consider some CG lipid models before discussing important computational studies of membrane remodeling. First, we focus on the bottom-up models. Multiscale coarse-graining (MS-CG) methodology is a bottom-up approach that uses a rigorous statistical mechanical framework in designing a CG force field [59]. As it uses a variational calculation, in principle, MS-CG yields the optimum CG force field relative to the exact many-body potential of mean force in the CG variables [83, 84]. Important caveats of the model are that (a) it can be numerically challenging to solve the equations for complex systems, (b) it requires a reasonable sampling of the configurational space by an atomic-level MD simulation, and (c) the resulting interactions may be too complex for seamless transferability to other physical systems because, in fact, the concept of transferability of rigorously derived CG interactions from one system to another is not yet founded on clear physical principles. The MS-CG method has been used, e.g., to develop explicit solvent [85] and solvent-free models [86, 87] of phospholipids and cholesterol, in which the lipids were reduced to ten CG sites. Simulations of a binary mixed bilayer using these models have reproduced the fluidity and the structural parameters of the membrane; however, they have not yet been used to study membrane remodeling (Fig. 6).

Simulating large-scale shape changes requires more aggressively coarse-grained lipid models due to the large length and time scales involved. Bottom-up development of highly coarse models is often compromised by insufficient sampling in atomic-level simulations, especially in the short-range interactions. A way to overcome this problem is by supplementing the MS-CG forces, derived from well-sampled atomic-level simulations, with analytical functions that can be based on some known physical behavior at short range. This hybrid approach has been used to develop a solvent-free single-site lipid model [88] in which a lipid molecule was mapped onto an ellipsoidal particle, whose interactions were modeled using an anisotropic Gay-Berne potential (Fig. 6) [89]. A similar approach has been applied to develop a more flexible and physically accurate three-site hybrid CG lipid model (called HCG) using more traditional spherical CG sites [90]. Both models successfully reproduced the structural properties of bilayers at the molecular level and all of the elastic properties of the membrane at the mesoscopic level. Importantly, both models have been used in studying membrane remodeling (see more below). The HCG model has recently been expanded to model the effects of charged lipids separately from the van der Waals interactions [91]. This improvement will allow for quantitative insights into the electrostatic properties in protein-membrane systems.

A number of bottom-up methods, which are similar in spirit, derive the CG force field not by calculating a multi-body potential of mean force for the CG sites, but instead by relying on one reduced statistical distribution of the system, such as the radial distribution function, the distribution of intramolecular distances, or, say, the stress profile (e.g., [92, 93]). The effective CG potential is computed numerically, using the inverse Boltzmann [94] or inverse MC methods [95]. The inverse MC approach was used to derive CG lipid models, comprising one to ten sites, which reproduced correct structural and phase behavior at the 100-nm length scale [96–98]. However, in making of some of these models, external constraints were applied to reproduce the experimentally measured elastic parameters. By adding an effective cohesion term mimicking the hydrophobic effect, a lipid model was developed that can reproduce both the correct structural and the elastic membrane parameters [99]. The underlying modeling method was the iterative Boltzmann inversion used to match to atomic-level parameters. Its relatively high resolution (16 sites per lipid) makes it less suitable for studying long-wavelength phenomena, but it is useful when the chemical specificity of lipids is essential. Of note, a poor choice of the underlying atomic-level configuration (such as starting from an unphysical or biologically irrelevant phase of a bilayer) can adversely affect the bottom-up CG modeling [100].

The basic philosophy of a top-down coarse-graining approach is to fit the CG interactions so as to reproduce certain experimental observations, usually the self-assembly into a bilayer, and such membrane models date almost three decades [101]. A top-down model that has become popular in recent years is the MARTINI model (Fig. 6) [102]. Here, CG interactions—cast in the form of analytical functions—are fit to some bulk thermodynamic data, namely, the oil/water partitioning free energy. Due to the empirical nature of MARTINI models, they do not have a connection to the real atomistic forces that underlie each CG particle; however, they provide a

flexible framework for qualitative modeling of large-scale biomolecular processes. As the MARTINI model is built upon the amphipathic affinities, it seems suited to studying lipid systems. Indeed, MARTINI lipids have been shown to spontaneously form bilayers [103]. However, the downside of such models are that (a) not all physical interactions can be used in their parameterization and (b) the model could unintentionally bias the experimental observation that it tries to reproduce.

Some CG models use more sophisticated functional forms to describe the interactions among particles [104–106], and, although these CG lipids readily assemble into membranes, their elastic parameters are not necessarily in the experimental range. Driven by this issue, other methods are designed ensuring that the bending stiffness of the membrane is correctly reproduced, usually via tunable parameters [107–109].

Finally, there are CG models wherein each particle represents more than one lipid molecule (see bottom panel in Fig. 6). In one realization of such models, the membrane is described as a thin elastic sheet composed of a mesh of interconnected particles. Triangulating the mesh provides a computationally simple and rapid way of calculating elastic energies associated with bending and stretching deformations [110–114]. Typically, the forces are calculated using a form of a Helfrich–Canham Hamiltonian [6, 115]. Mesh-free models provide a more flexible membrane surface, and they can simulate deformations inaccessible by imposing an unbreakable meshwork (e.g., pore formation). The abovementioned self-assembly model from 1991 is an example of such a model [101], but there are many other more recent examples, which employ a combination of attractive and repulsive potentials [116–120]. These models rarely provide the correct phase behavior of the membrane, and they are devoid of molecular-level information (e.g., lipid diffusion). However, they are suited for simulating the very long-wavelength behavior, owing to their adjustable resolution and the well-reproduced mechanical parameters.

It is difficult to argue whether the bottom-up or the top-down approach is superior in practice, as each comes with its own challenges. What is important is that a CG model needs to be predictive—at least in a semi-quantitative manner—and in order to do so, it would seem to need connections to real physics. Otherwise, CG simulations run the risk of becoming solely an animation, or worse, a visualization tool for biomolecular behavior.

5.2 CG Simulations of Membrane Remodeling

Let us first consider some studies that used CG models to simulate biological membranes. Simulations employing the relatively high-resolution MARTINI or derivatives of the MARTINI model have revealed large-scale dynamics at the level of a single protein molecule, such as the conformational change of proteins and the local membrane deformation. For example, CG MD simulations have shed light on the behavior of voltage- and tension-gating of ionic channels [121–125] and the way in which embedding of small peptides couples with the local membrane

curvature [126, 127]. Furthermore, simulations of large lipid bilayers with a complex composition have revealed a transient formation of lipid nanodomains [128]. Interestingly, according to MARTINI simulations, certain lipids become enriched in regions of higher curvature [129], a phenomenon called lipid sorting [28]. The resolution of the MARTINI model is suitable for addressing questions that require the knowledge of lipid specificity, and for processes that involve a few protein molecules, such as the protein-mediated fusion [127, 130, 131]. They are still too finely grained (i.e., their resolution is too high) to address the many-protein behavior on the membrane leading to large-scale remodeling.

Three-site and lower resolution CG lipid models, on the other hand, are better suited for simulating long-wavelength phenomena while retaining a quasi-molecular level of detail. A simulation employing a tunable CG lipid model demonstrated that membrane curvature can give rise to strong attractions among particles adhered to the membrane—in their case, circular caps and capsids. The consequence of these interactions is the initial clustering of particles, followed by their engulfment and transport through the membrane [132]. This study implies that the attraction of membrane-bound objects, such as viruses and nanoparticles, may be a very general mechanism. The only requirement is that the object strongly curves the membrane locally [133]. The assembly of the capsid itself—albeit partially promoted by membrane curvature—can actually be impeded by diffusion barriers formed by very strong membrane deformations, as revealed by CG simulations [134, 135]. Interestingly, the formation of microdomains assuages these obstacles, helping the capsid fully assemble and generate a membrane bud [135].

Let us now return our focus to BAR proteins. As was discussed in the previous section, atomic-level MD simulations have shed light on the detailed interactions that give rise to the nanometer-scale membrane curvature. Since BAR proteins couple with much larger scales associated with membrane reshaping in the cell, there is high motivation to simulate their behavior with CG simulations. It should be kept in mind that modeling proteins as particles of arbitrary shape may not be adequate to capture the relevant phenomena, not even in low-resolution models. Proteins are more complex than particles: (1) because they are comparable in size to membrane thickness, (2) their shape is not simple, (3) the way they interact with the membrane is typically multimodular, and (4) proteins may undergo conformational changes. BAR proteins are especially challenging to theorists, as they often have both the shallow insertion domain and the adhesive component; therefore, it is difficult to correctly account for all these interactions.

Several studies have employed a three-site bottom-up CG lipid model to study the interaction of N-BAR proteins with the membrane. The internal conformations of the N-BAR domains were described using an elastic-network approach, which approximates the vibrational fluctuations of biomolecules using a network of elastic bonds between CG sites, often based on fluctuations derived from atomic-level simulations [136–138]. This approximation works very well for proteins that mostly exist in one conformation, such as BAR proteins. The simulations started with N-BARs randomly placed on a planar bilayer or on a lipid vesicle of optically resolvable size. The work showed that N-BAR proteins undergo a specific

self-assembly mechanism, marked by a rapid formation of long strings of protein aggregates [139]. Similar to the aforementioned study of capsid aggregation, local membrane curvature was also the primary driving force in the association of N-BAR proteins. However, the protein does not induce as high local curvature as in the capsid model, where it was shown that very high curvature is crucial in inducing effective attractions [133]. Rather, the anisotropic curvature interactions with the membrane give rise to long-range quasi-one-dimensional ordering of proteins on the membrane. This general phenomenon was first predicted with MC simulations using an analytical N-body potential, which also showed linear and circular assemblies of nonspecific anisotropic inclusions [140]. Curiously, MC simulations, using a triangular-mesh membrane model, have shown that spherical particles adhered to the membrane also undergo linear aggregation [141]. This work has implicated particle-membrane binding force—a term typically absent in analytical modeling of membrane inclusions—as the driving force that overcomes the cost of local deformations. Local deformations then mediate the effective inter-particle attractions, although, hypothetically, the anisotropic interactions that form upon the initial particle pairing might also strongly contribute to the formation of lines.

What is striking is that three very different membrane models demonstrated the same association behavior of objects interacting with the membrane (Fig. 7). The important implication for biology is that proteins that form anisotropic curvature interactions—and BAR proteins are an excellent example—may rapidly form long-range anisotropic assemblies on the membrane, even when they are present at low densities. The linear aggregation phenomenon of particles on membranes has been shown by experiments using giant vesicles decorated with nanoparticles [142]. Strikingly, a very recent study employing electron and fluorescence microscopy has confirmed the theoretical prediction that BAR proteins form linear oligomers on the surface of the membrane [143, 144].

In order to generate global membrane curvature, N-BAR proteins need to be bound at sufficiently high densities. According to CG MD simulations, at 20% surface density, proteins form a percolating meshwork on the surface, giving rise to budding instabilities at the center of protein meshes (see Fig. 7, right) [139]. Interestingly, the sign of curvature of emerging buds is positive, i.e., the membrane bends toward the proteins. Such geometry is the same as in endocytosis, where the endocytic vesicle forms on the side where the membrane-remodeling proteins are bound [31]. The association of spherical particles, on the other hand, leads to tubulation in the opposite direction, especially at high binding force (Fig. 8) [145, 146]. According to these observations, even though membrane-bound objects start from the same association geometry, the anisotropy and particle size determine the ultimate membrane shape (i.e., positive versus negative curvature).

The association of bound particles also couples with membrane's mechanical parameters, namely, membrane tension. Increasing surface tension changes the way N-BARs interact with one another: from changing the geometry of dimerization and breaking the meshwork topology to, at highest tension, inhibiting association altogether [147]. Therefore, the anisotropic shape of N-BAR proteins enriches the

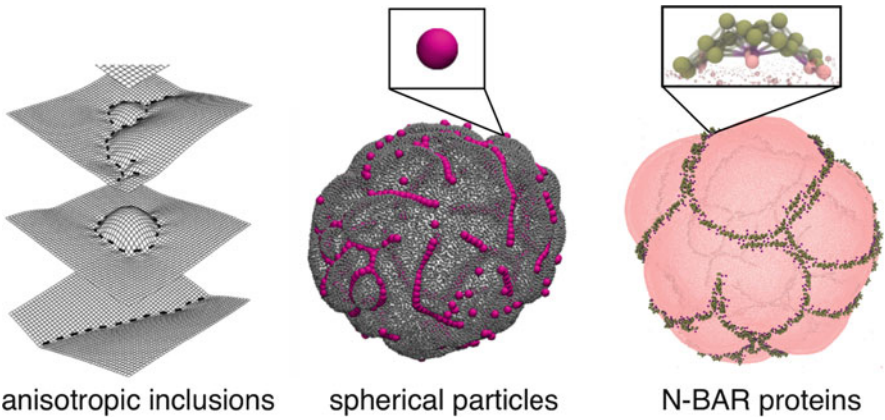

Fig. 7 Linear aggregation of membrane-bound objects [from left to right: (1) analytically modeled inclusions, (2) spherical particles, and (3) N-BAR proteins] simulated by three very different models. Left: reprinted from [140] with permission from Springer; center: courtesy of Andela Saric, based on [141]; right: based on [139]

range of geometries into which they assemble at different conditions. Moreover, these observations and a recent experimental study [148] implicate membrane tension as an important effector of membrane remodeling by proteins. Understanding this mechanism may be key to understanding how BAR proteins assemble in the course of endocytic events that involve actin, an important tension modulator [149].

When overexpressing BAR proteins in the cell, the typical phenotype is a massive tubulation of the membrane [42]. Has such remodeling been captured with CG MD simulations? A recent study using a highly CG meshless model, in which the rigidity and the spontaneous curvature of the membrane are tuned, has shown that curved rods, representing BAR proteins, could generate very long tubules from the membrane (Fig. 8). The study has also shown that the proteins initially go through stages of linear aggregation and meshing, in line with the aforementioned simulation studies, although, interestingly, the meshwork forms only if the spontaneous curvature term is positive in one direction and negative in the other [150]. In fact, the aforementioned CG study of N-BARs aggregating on vesicles, where no assumption on local curvature has been made a priori, has shown that N-BARs imprint this type of curvature on the surface [139]. When local curvature deformations by the protein have equal sign in both directions, bent particles (or in one study nematogenic inclusions) do not form a meshwork, but they still remodel the membrane into tubular and disk-like instabilities, as shown by a meshless and a triangular membrane model [150–152]. Again, subtle changes in the way proteins interact locally with the bilayer have a global impact on the shape of the membrane.

In these three studies, protein-covered membrane tubules grew continuously from the membrane surface. CG MD simulations, using a bottom-up three-site lipid model and an internal elastic network N-BAR model interacting with the membrane,

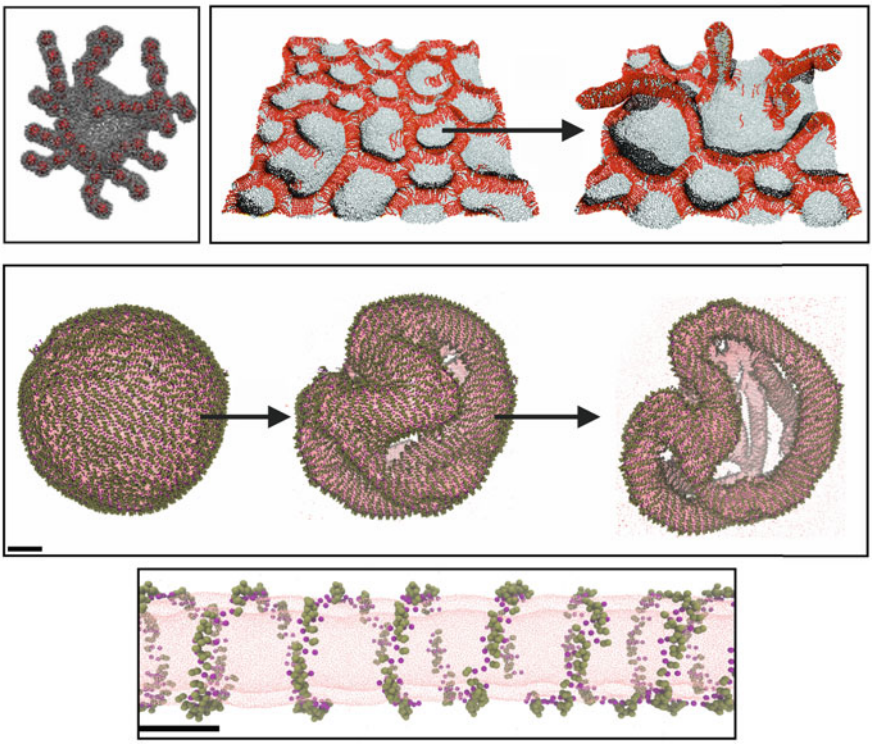

Fig. 8 Top: forming membrane tubules by spherical particles (left) and by bent rods (right). Left, courtesy of Andela Saric and based on work from [146]; right, courtesy of Hiroshi Noguchi and based on work from [150]. Center: Forming reticular membranes by breaking the bilayer topology by N-BAR proteins. Scale bar, 20 nm. Based on the work in [151]. Bottom: CG MD simulation snapshot of a membrane tube coated by an N-BAR domain scaffold. Scale bar, 20 nm. Adapted from [43], copyright (2016) National Academy of Sciences

have revealed another mechanism of forming membrane tubules. Here, the bilayer topology breaks due to high in-plane stresses imposed by many protein molecules. The prerequisites for this pathway are a rapid and a high-density binding of N-BAR proteins that essentially fold the membrane into a tubule. When they bind to a vesicle, this process leads to a transformation into a tubular network (Fig. 8), a structure which has been confirmed by cryo-electron microscopy under the same conditions [153]. According to simulations, the N-BAR proteins spontaneously form a nematic arrangement which dictates an average tubule radius of 10 nm, in remarkable agreement with experimental observations [44, 153]. Apparently, the radius of the folded tubule is also affected by the way individual proteins are arranged in this coat, as shown by MARTINI-like simulations of N-BAR and F-BAR protein lattices on membrane patches with exposed edges [76, 154]. Finally, a different CG MD study, using an internal elastic network N-BAR model

interacting with a Gay-Berne CG potential to model lipids, addressed the influence of amphipathic helices on the protein coat dynamics. They found that the presence of N-terminal helices and their antiparallel orientation (i.e., each helix oriented on the opposite side of the BAR domain) are important in stabilizing the lattice organization of the protein and the tubule rigidity [41, 155].

Less is known at the molecular level on how BAR proteins assemble on already formed tubules, an intermediate step in many endocytic pathways, e.g., in endocytosis driven by an N-BAR protein endophilin [149]. One simulation study has shown that curved rods undergo a phase separation on membrane tubules, modeled with a meshless lipid model. More precisely, the proteins get enriched in one region of the tubule, squeezing it into an hourglass shape [151]. The formation of high-density regions could explain the initial constriction of membrane tubules by BAR proteins, as observed in experiments [156]. A study combining in vitro reconstitution, CG MD simulations, and mathematical modeling shed light on the molecular details and the mechanism by which BAR proteins assemble on membrane nanotubes to form a protein scaffold. Apparently, the strength by which BAR proteins constrict the underlying tube determines where the protein nucleation takes place. Proteins that strongly constrict the membrane, such as endophilin, which creates very thin scaffolds, only 10 nm in diameter, initiate the scaffold at the base of the nanotube. By contrast, weakly constricting BAR proteins, such as β2 centaurin, which creates 40-nm-wide nanotubes, uniformly bind along the tube while making the scaffold [43]. CG MD simulations, employing a three-site lipid model, have revealed that N-BARs polymerize into a highly ordered helical structure on the tube, likely contributing to the very strong mechanical properties of the protein scaffold [43].

Simulating other proteins involved in endocytosis presents even bigger challenges, because of their more complicated structure or because their activity couples with an active, energy-driven process. For instance, clathrin is a protein that drives one of the most prominent pathways to enter cells [157]. The basic unit of clathrin is shaped like a triskelion, which polymerizes into a fullerene-like basket [158, 159]. This basket is believed to mold the membrane into a vesicle, engulfing the cargo bound on the opposite side of the bilayer (recall the coating mechanism of inducing curvature depicted in Fig. 2). Considering that clathrin (a) forms a complex polymeric structure and (b) it interacts with the membrane via adaptor proteins, it will be a great challenge to design a bottom-up CG model. Patchy particles—particles with sticky domains on the surface—have therefore been used to design shape-based models of clathrin, with interactions motivated from structural biology. These studies—albeit semi-quantitative—have fleshed out some key interactions that drive clathrin-like objects to assemble into a basket in the solution [160, 161]. They have also shown how the remodeling of the membrane by a clathrin-like basket depends on membrane's flexibility and stiffness [162]. A more flexible CG model, wherein the interactions have been derived with a parameterization scheme, has been shown to assemble into a basket both in the solution and on the membrane, identifying new intermediates in the budding pathway (Fig. 9) [163].

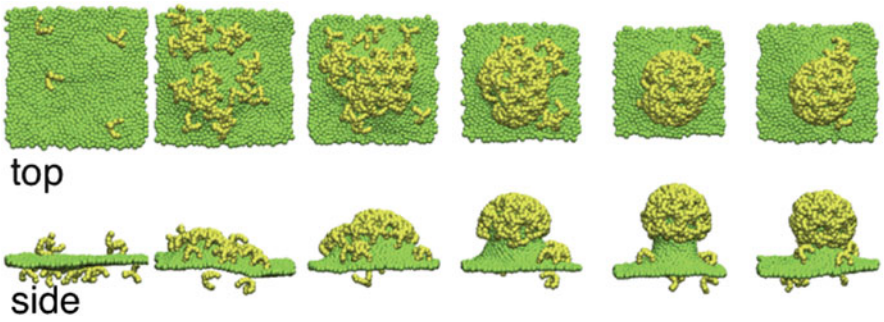

Fig. 9 The assembly of clathrin from triskelia into a basket-like structure and subsequent membrane remodeling into a vesicle. Shown are snapshots taken at regular time intervals in the simulation, viewed from the top of the membrane and from the side. Reproduced from [163] with permission from The Royal Society of Chemistry

In light of the demonstrated power of CG simulations, one may ask, "Do we then need atomic-level simulations to study membrane remodeling?" Returning to our initial discussion on multiscale nature of membranes, we immediately recognize the importance of understanding the molecular organization at the atomic scale. Although the collective action of proteins couples with the long-length scale phenomena, the small-scale interactions of individual proteins with the membrane and, in cases such as clathrin, the specific protein–protein attractions need to be studied in detail. Furthermore, CG models at present cannot account for the conformational changes of proteins that normally alter the way they interact with one another and with the membrane. Finally, the chemical reactions, such as the conversion between certain types of lipids and the hydrolysis of GTP or ATP, play key roles in membrane remodeling and will need to be addressed with atomic-level or mixed-resolution simulation techniques.

6 Continuum Modeling

Continuum modeling tackles the behavior at the mesoscopic level. The term mesoscopic in membrane physics encompasses a fairly wide range of scales, generally much larger than the membrane thickness but much smaller than the cell membrane. Scales of many CG simulations discussed in the previous section can surely be described as mesoscopic, such as the CG simulations of vesicles coated with N-BAR proteins [139]. Continuum models ignore individual molecules and describe them using collective or field variables, whose dynamics then gives only the collective properties of the system [164]. The triangular-mesh and the meshless models described in the previous section are similar to continuum models, as they do not resolve individual molecules; however, the use of discrete particles and MC or MD to integrate their motion makes them more similar to CG methods.

The premise of most continuum models is the assumption that the membrane can be described as a fluid thin elastic sheet, modeled by the Helfrich–Canham Hamiltonian [6, 115]. Minimizing the free energy functional, usually with numerical simulations, provides insight into the shape and the statistical properties of the membrane. Curvature can be modeled in multiple ways, such as by varying the value of preferred curvature [6, 115] or by imposing various constraints, such as on the area difference between the two leaflets upon asymmetric inclusion of particles [165–168]. Historically, these approaches have been used to explain the shapes of the red blood cell or vesicles embedded with inclusions, for example [169–174] and many other studies.

In the present discussion, we are more interested in continuum studies focused on the process of membrane remodeling. For studying membrane reshaping, such an approach would comprise simulating the finite-temperature dynamics, compositional variations, membrane fluctuations, and hydrodynamic effects. The so-called elastic membrane version 2 (EM2) model embodies all of these aspects of the membrane, and it has been used to study the remodeling of large lipid vesicles by BAR proteins. Given the complexity of calculating the radii of curvature for complex surfaces, such as a liposome, the free energy of the continuum membrane is discretized into quasi-particles immersed into a mesoscopic quasi-particle solvent, in the spirit of SPH techniques. The discretization allows for large-scale membrane restructuring, thermal fluctuations, and a more flexible and efficient computational approach that resembles MD simulations [175]. Equivalent to triangular-mesh models, bending and stretching energies are explicitly calculated as a pair-wise potential between two particles. However, an important advance is that each quasi-particle also has superimposed field variables, namely, lipid and protein compositions, cast in the form of a phenomenological Landau free energy functional [176]. The morphological effect on the membrane is modeled by coupling protein and lipid area fractions with the spontaneous curvature of the membrane, bending stiffness, and other parameters [175]. Other terms can be easily incorporated, for instance protein–protein interactions in the form of oligomerization energy. Finally, the composition field variable evolves according to the Landau–Ginzburg equation by using the smooth particle applied mechanics [177], which is similar to SPH.

EM2 simulations of large vesicles under the influence of a protein field variable have given insights into an unexpected molecular mechanism of forming tubules and a range of membrane morphologies. First, rapid protein binding at high surface densities transformed a vesicle into a tubular (reticulated) network, in the same way as in the CG simulations discussed in the previous section (Fig. 10). As expected, increasing the effective spontaneous curvature term in the Hamiltonian increased the propensity of the membrane to change shape. Keeping in mind that in continuum simulations the protein is only represented as a field variable, one therefore does not have knowledge of its molecular scale assembly. However, one can study how the membrane changes shape depending on how the protein couples with curvature. It turns out that the ultimate fate of the membrane depends whether the curvature field of the protein is isotropic or anisotropic [178]. In the case of the anisotropic curvature field, the vesicle transforms into a tubular network (Fig. 10). This result

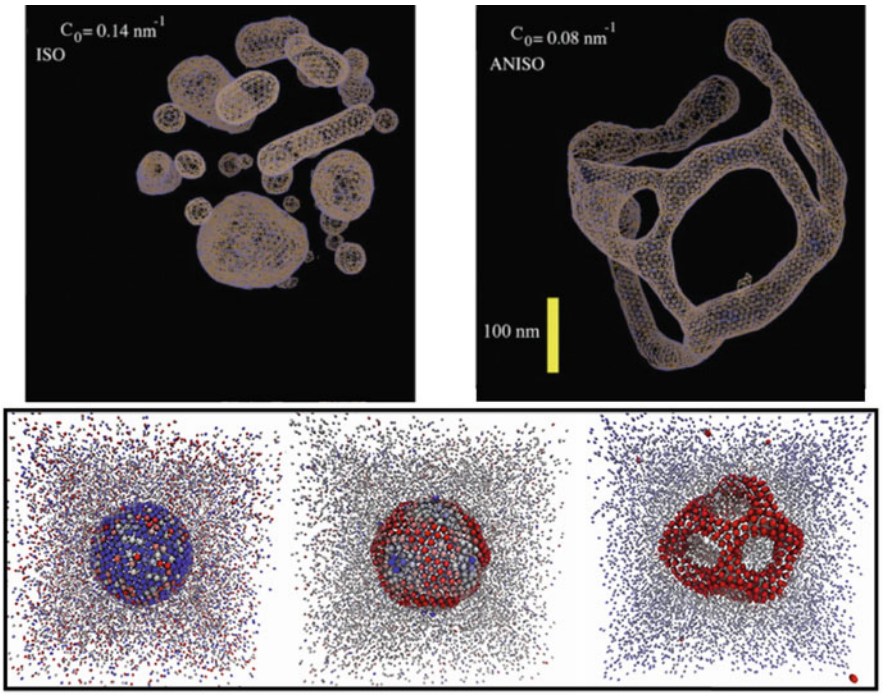

Fig. 10 Formation of tubular networks by N-BAR proteins in continuum mechanics simulations. Top: the influence of the isotropic (left) versus the anisotropic (right) spontaneous curvature. Adapted from [178] with permission from Elsevier. Bottom: time lapse of vesicle transformation, depicting the rapid recruitment of N-BARs from the mesoscopic solvent to the membrane surface. Color coding: protein concentration (red—high; white—intermediate; blue—low). Reprinted from [153] with permission from Elsevier

indicates that the proteins initially assemble on the membrane with a preferred direction, caused by interactions with other proteins. Indeed, recall that N-BAR proteins simulated at the CG level form linear aggregates when bound on a flat membrane surface [139]. In the case of an isotropic curvature field, the vesicle fragments into smaller vesicles [178]. This vesiculation phenomenon has indeed been experimentally reported when incubating curvature-coupling proteins that have amphipathic helices (such as N-BAR proteins) with 200-nm-wide liposomes [179]. It is not clear what process may disrupt the anisotropic alignment of proteins, but we can speculate that the embedding of amphipathic helices, perhaps in a different way on small liposomes than on quasi-flat membranes, introduces an additional radius of curvature. Moreover, it is possible that the high spherical curvature prevents the anisotropic ordering of BAR proteins.

It has also been shown that the formation of tubular networks takes place in a narrow configurational space, favoring membranes with a lower bending stiffness ($<15\ k_BT$) and for a range of spontaneous curvatures characteristic of N-BAR

proteins [153]. In the same simulation, if the applied spontaneous curvature is more characteristic of F-BAR proteins—which typically induce tubules of larger diameter—the EM2 model requires an additional oligomerization term in order to bend the membrane (Fig. 10) [180]. This result indicates that F-BAR proteins require explicit protein–protein interactions to reshape the membrane into a tubule, whereas for stronger curvature generators such as N-BARs, the protein–protein attractions are mostly driven by the underlying membrane.

Another notable continuous model of a fluctuating membrane that integrates the motion over time and carefully treats the hydrodynamic effects is the Fourier space Brownian dynamics [181, 182]. The method received its name because the shape of the membrane is calculated in the Fourier space, although the forces are calculated in the real space. The model is designed such that the membrane can couple with an arbitrary external force and so it can be expanded to study protein-mediated remodeling; however, it has yet not been used to address this biological question. One example using this model is a study of a membrane interacting with the cytoskeleton. The simulations have indicated that thermal fluctuations contribute to the macroscopic diffusion of proteins on the surface of a red blood cell [182].

7 Outlook: Mixed-Resolution Models

From the present discussion, it is evident that membrane remodeling by proteins is a complex process that challenges experimentalists and theorists alike. Let us briefly summarize the advantages and problems of each level of theory applied to simulating membrane reshaping by proteins. Atomic-level simulations are key in revealing the detailed interactions at the interface of the protein and the membrane. For instance, they can show the local orientation of lipids or measure the thermodynamics of binding. However, the atomic model is unable to access the mesoscopic scales of membrane remodeling. Fortunately, studying these long-length and time scale processes does not require knowing the position and the state of each individual atom in the system. CG simulations, on the other hand, access much larger scales and provide information on the collective behavior of proteins on the surface. These models also give the detailed shape of the membrane embedded by proteins, which is crucial in explaining its macroscopic morphological consequences. CG models are still limited by the challenges in obtaining an accurate CG effective force field that will not bias specific protein assembly or membrane geometry and, similar to atomic-level simulations, they can suffer from rising computational cost when simulating very large systems. Finally, continuum methods are crucial in investigating cell-sized membrane phenomena. However, application of continuum method to study protein-mediated membrane reshaping has been sparse, likely as these processes rely on thermal fluctuations, hydrodynamics, bending and stretching mechanics, but also on the lateral distribution of lipids and proteins, which are very difficult to take into account in a single model.

How can we overcome the discrepancy in scales? Let us revisit the idea behind a multiscale approach. One strategy is to connect the information between different scales in separate simulations, which is essentially the philosophy behind bottom-up coarse-graining [183]. Recall that this approach is challenging conceptually and mathematically. We can also choose some averaged properties from one resolution and take those values as a parameter in a different resolution model. In one example applied to membranes, the continuum and the atomistic descriptions were coupled. The approach used material properties of the bilayer obtained in atomic-level simulations as fixed parameters in solving the elastic free energy in the continuum model. In the opposite direction, the lateral stress profile extracted from a mesoscopic undulating surface was applied to the atomic-level simulation [184].

Another strategy is to first use the computationally less expensive simulation to generate a configuration and then to use it to make a higher-resolution model. One example employing this strategy is a study of N-BAR proteins on a reticular membrane. The formation of a reticular membrane was simulated using the mesoscopic continuum EM2 model (see the previous section). Then, the continuum membrane was fine-grained by mapping CG membrane patches atop of a triangulated mesh of EM2 quasi-particles [185]. Subsequent CG MD simulations have revealed important molecular information, such as the strongly hindered lipid mobility underneath a protein scaffold and especially in tubular junctions. This kind of information cannot be obtained from continuum models alone [153]. To visualize this fine-graining procedure, the reader is directed back to Fig. 4, where arrows from the continuum to the CG model illustrate how the mapping was accomplished. A more sophisticated approach for the future would include using field variables to accurately map the protein and lipid distribution in a CG representation.

An alternative strategy—often termed the mixed-resolution approach—consists of modeling different scales in the same simulation system. As mentioned earlier, integrating quantum mechanics with atomic-level force fields has proven very useful in modeling enzymatic reactions [58]. Similar hybrid approaches can be envisioned (1) between atomic and CG levels, (2) between CG and continuum levels, and (3) even between atomic and continuum levels [186].

Although various approaches have been developed to study proteins in solution at mixed resolution, let us focus on membrane models. One way to split a membrane system between two resolutions is by having some particle types (e.g., lipids) at one resolution and the rest (e.g., proteins or solvent) at a different resolution. For instance, one approach treated the membrane using a continuum model while it described the proteins as particles. The very low resolution of the membrane significantly accelerated the dynamics, allowing, at the same time, us to study the diffusion of proteins [187]. An alternative resolution-splitting scheme is to have one region of the space (typically smaller) at high resolution, and the rest of the system at low resolution, in the spirit of QM/MM simulations. A recent model employing a similar strategy combined CG with continuum mechanics in a way to calculate the intramolecular forces using a CG model (MARTINI in that case), whereas the computationally expensive nonbonded interactions are averaged out in the style of the mean field theory [188]. In other words, individual molecules were resolved, but

instead of interacting with many neighbors, they interacted with a field. The model has been used to simulate membrane self-assembly [189] and the insertion of carbon nanotubes into the bilayer [190].

Mixed-resolution models are yet to be used to study membrane remodeling by proteins; however, they may provide a very promising approach that deserves attention in the coming years. Future challenges will involve correctly modeling the collective behavior of proteins on the membrane, so as to permit different protein orientations at the molecular level and, even further, the interactions between different types of proteins to simulate their cooperative assembly in the course of complex membrane-remodeling processes.

References

1. Atkins P, de Paula J (2010) Atkins' physical chemistry. Oxford University Press, Oxford
2. Ashrafuzzaman M, Tuszynski JA (2012) Membrane biophysics. Springer, New York
3. Lipowsky R (1991) The conformation of membranes. Nature 349(6309):475–481. https://doi.org/10.1038/349475a0
4. Alberts B, Johnson A, Lewis J, Morgan D, Raff M, Roberts K, Walter P (2014) Molecular biology of the cell. Taylor & Francis, New York
5. Evans EA (1983) Bending elastic modulus of red blood cell membrane derived from buckling instability in micropipet aspiration tests. Biophys J 43(1):27–30. https://doi.org/10.1016/S0006-3495(83)84319-7
6. Helfrich W (1973) Elastic properties of lipid bilayers: theory and possible experiments. Z Naturforsch C 28(11):693–703
7. Kwok R, Evans E (1981) Thermoelasticity of large lecithin bilayer vesicles. Biophys J 35(3):637–652. https://doi.org/10.1016/S0006-3495(81)84817-5
8. Baumgart T, Hess ST, Webb WW (2003) Imaging coexisting fluid domains in biomembrane models coupling curvature and line tension. Nature 425(6960):821–824. https://doi.org/10.1038/nature02013
9. Funkhouser CM, Solis FJ, Thornton K (2010) Dynamics of two-phase lipid vesicles: effects of mechanical properties on morphology evolution. Soft Matter 6(15):3462–3466
10. Hu JL, Weikl TR, Lipowsky R (2011) Vesicles with multiple membrane domains. Soft Matter 7(13):6092–6102
11. Li J, Zhang H, Qiu F (2013) Budding behavior of multi-component vesicles. J Phys Chem B 117(3):843–849. https://doi.org/10.1021/jp308043y
12. Rim JE, Ursell TS, Phillips R, Klug WS (2011) Morphological phase diagram for lipid membrane domains with entropic tension. Phys Rev Lett 106(5):057801
13. Semrau S, Idema T, Holtzer L, Schmidt T, Storm C (2008) Accurate determination of elastic parameters for multicomponent membranes. Phys Rev Lett 100(8):088101
14. Sens P, Turner MS (2006) Budded membrane microdomains as tension regulators. Phys Rev E 73(3):Artn 031918. https://doi.org/10.1103/Physreve.73.031918
15. Taniguchi T (1996) Shape deformation and phase separation dynamics of two-component vesicles. Phys Rev Lett 76(23):4444–4447
16. Taniguchi T, Yanagisawa M, Imai M (2011) Numerical investigations of the dynamics of two-component vesicles. J Phys Condens Matter 23(28):284103
17. Ursell TS, Klug WS, Phillips R (2009) Morphology and interaction between lipid domains. Proc Natl Acad Sci USA 106(32):13301–13306. https://doi.org/10.1073/Pnas.0903825106
18. Aimon S, Callan-Jones A, Berthaud A, Pinot M, Toombes GE, Bassereau P (2014) Membrane shape modulates transmembrane protein distribution. Dev Cell 28(2):212–218. https://doi.org/10.1016/j.devcel.2013.12.012

19. Unwin N (2005) Refined structure of the nicotinic acetylcholine receptor at 4A resolution. J Mol Biol 346(4):967–989. https://doi.org/10.1016/j.jmb.2004.12.031
20. Mackinnon R (2004) Structural biology. Voltage sensor meets lipid membrane. Science 306(5700):1304–1305. https://doi.org/10.1126/science.1105528
21. Drin G, Antonny B (2010) Amphipathic helices and membrane curvature. FEBS Lett 584:1840–1847
22. Campelo F, McMahon HT, Kozlov MM (2008) The hydrophobic insertion mechanism of membrane curvature generation by proteins. Biophys J 95(5):2325–2339. https://doi.org/10.1529/biophysj.108.133173
23. Zemel A, Ben-Shaul A, May S (2008) Modulation of the spontaneous curvature and bending rigidity of lipid membranes by interfacially adsorbed amphipathic peptides. J Phys Chem B 112(23):6988–6996. https://doi.org/10.1021/jp711107y
24. Walther TC, Farese RV Jr (2009) The life of lipid droplets. Biochim Biophys Acta 1791(6):459–466. https://doi.org/10.1016/j.bbalip.2008.10.009
25. Wilson C, Wardell MR, Weisgraber KH, Mahley RW, Agard DA (1991) Three-dimensional structure of the LDL receptor-binding domain of human apolipoprotein E. Science 252(5014):1817–1822
26. Mim C, Unger VM (2012) Membrane curvature and its generation by BAR proteins. Trends Biochem Sci 37(12):526–533. https://doi.org/10.1016/j.tibs.2012.09.001
27. Simunovic M, Voth GA, Callan-Jones A, Bassereau P (2015) When physics takes over: BAR proteins and membrane curvature. Trends Cell Biol 25(12):780–792. https://doi.org/10.1016/j.tcb.2015.09.005
28. Callan-Jones A, Bassereau P (2013) Curvature-driven membrane lipid and protein distribution. Curr Opin Solid State Mater Sci 17(4):143–150
29. Lipowsky R (2013) Spontaneous tubulation of membranes and vesicles reveals membrane tension generated by spontaneous curvature. Faraday Discuss 161:305–331. https://doi.org/10.1039/C2fd20105d
30. Lipowsky R, Dobereiner HG (1998) Vesicles in contact with nanoparticles and colloids. Europhys Lett 43(2):219–225
31. Johannes L, Wunder C, Bassereau P (2014) Bending "on the rocks"—a cocktail of biophysical modules to build endocytic pathways. Cold Spring Harb Perspect Biol 6(1):a016741. https://doi.org/10.1101/cshperspect.a016741
32. McMahon HT, Gallop JL (2005) Membrane curvature and mechanisms of dynamic cell membrane remodelling. Nature 438(7068):590–596. https://doi.org/10.1038/nature04396
33. Bickel T, Jeppesen C, Marques CM (2001) Local entropic effects of polymers grafted to soft interfaces. Eur Phys J E 4(1):33–43
34. Breidenich M, Netz RR, Lipowsky R (2000) The shape of polymer-decorated membranes. Europhys Lett 49(4):431–437
35. Nikolov V, Lipowsky R, Dimova R (2007) Behavior of giant vesicles with anchored DNA molecules. Biophys J 92(12):4356–4368. https://doi.org/10.1529/biophysj.106.100032
36. Stachowiak JC, Schmid EM, Ryan CJ, Ann HS, Sasaki DY, Sherman MB, Geissler PL, Fletcher DA, Hayden CC (2012) Membrane bending by protein-protein crowding. Nat Cell Biol 14(9):944–949. https://doi.org/10.1038/ncb2561
37. Sheetz MP (2001) Cell control by membrane-cytoskeleton adhesion. Nat Rev Mol Cell Biol 2(5):392–396. https://doi.org/10.1038/35073095
38. Koster G, VanDuijn M, Hofs B, Dogterom M (2003) Membrane tube formation from giant vesicles by dynamic association of motor proteins. Proc Natl Acad Sci USA 100(26):15583–15588. https://doi.org/10.1073/pnas.2531786100
39. Roux A, Cappello G, Cartaud J, Prost J, Goud B, Bassereau P (2002) A minimal system allowing tubulation with molecular motors pulling on giant liposomes. Proc Natl Acad Sci USA 99(8):5394–5399. https://doi.org/10.1073/pnas.082107299
40. Qualmann B, Koch D, Kessels MM (2011) Let's go bananas: revisiting the endocytic BAR code. EMBO J 30(17):3501–3515. https://doi.org/10.1038/emboj.2011.266

41. Mim C, Cui H, Gawronski-Salerno JA, Frost A, Lyman E, Voth GA, Unger VM (2012) Structural basis of membrane bending by the N-BAR protein endophilin. Cell 149(1):137–145. https://doi.org/10.1016/j.cell.2012.01.048
42. Peter BJ, Kent HM, Mills IG, Vallis Y, Butler PJ, Evans PR, McMahon HT (2004) BAR domains as sensors of membrane curvature: the amphiphysin BAR structure. Science 303(5657):495–499. https://doi.org/10.1126/science.1092586
43. Simunovic M, Evergren E, Golushko I, Prevost C, Renard HF, Johannes L, McMahon HT, Lorman V, Voth GA, Bassereau P (2016) How curvature-generating proteins build scaffolds on membrane nanotubes. Proc Natl Acad Sci USA 113(40):11226–11231. https://doi.org/10.1073/pnas.1606943113
44. Sorre B, Callan-Jones A, Manzi J, Goud B, Prost J, Bassereau P, Roux A (2012) Nature of curvature coupling of amphiphysin with membranes depends on its bound density. Proc Natl Acad Sci USA 109(1):173–178. https://doi.org/10.1073/pnas.1103594108
45. Suarez A, Ueno T, Huebner R, McCaffery JM, Inoue T (2014) Bin/Amphiphysin/Rvs (BAR) family members bend membranes in cells. Sci Rep 4:4693. https://doi.org/10.1038/srep04693
46. Ambroso MR, Hegde BG, Langen R (2014) Endophilin A1 induces different membrane shapes using a conformational switch that is regulated by phosphorylation. Proc Natl Acad Sci USA 111(19):6982–6987. https://doi.org/10.1073/pnas.1402233111
47. Simunovic M, Bassereau P (2014) Reshaping biological membranes in endocytosis: crossing the configurational space of membrane-protein interactions. Biol Chem 395(3):275–283. https://doi.org/10.1515/hsz-2013-0242
48. Simunovic M, Manneville JB, Renard HF, Evergren E, Raghunathan K, Bhatia D, Kenworthy AK, Voth GA, Prost J, McMahon HT, Johannes L, Bassereau P, Callan-Jones A (2017) Friction mediates scission of tubular membranes scaffolded by BAR proteins. Cell 170(1):172–184.e11
49. van Gunsteren WF, Bakowies D, Baron R, Chandrasekhar I, Christen M, Daura X, Gee P, Geerke DP, Glattli A, Hunenberger PH, Kastenholz MA, Oostenbrink C, Schenk M, Trzesniak D, van der Vegt NF, Yu HB (2006) Biomolecular modeling: goals, problems, perspectives. Angew Chem 45(25):4064–4092. https://doi.org/10.1002/anie.200502655
50. Frenkel D, Smit B (2001) Understanding molecular simulation: from Algorithms to applications. Elsevier Science, San Diego
51. Gingold RA, Monaghan JJ (1977) Smoothed particle hydrodynamics: theory and application to non-spherical stars. Mon Not R Astron Soc 181(2):375–389
52. Lucy LB (1977) A numerical approach to the testing of the fission hypothesis. Astron J 82:1013–1024
53. Liu MB, Liu GR (2010) Smoothed Particle Hydrodynamics (SPH): an overview and recent developments. Arch Comput Meth Eng 17(1):25–76. https://doi.org/10.1007/S11831-010-9040-7
54. Hoogerbrugge PJ, Koelman JMVA (1992) Simulating microscopic hydrodynamic phenomena with dissipative particle dynamics. Europhys Lett 19(3):155–160. https://doi.org/10.1209/0295-5075/19/3/001
55. Koelman JMVA, Hoogerbrugge PJ (1993) Dynamic simulations of hard-sphere suspensions under steady shear. Europhys Lett 21(3):363–368. https://doi.org/10.1209/0295-5075/21/3/018
56. Shillcock JC, Lipowsky R (2002) Equilibrium structure and lateral stress distribution of amphiphilic bilayers from dissipative particle dynamics simulations. J Chem Phys 117(10):5048–5061. https://doi.org/10.1063/1.1498463
57. Yamamoto S, Maruyama Y, Hyodo S (2002) Dissipative particle dynamics study of spontaneous vesicle formation of amphiphilic molecules (vol 116, pg 5842). J Chem Phys 117(6):2990. https://doi.org/10.1063/1.1494416
58. Warshel A, Levitt M (1976) Theoretical studies of enzymic reactions: dielectric, electrostatic and steric stabilization of the carbonium ion in the reaction of lysozyme. J Mol Biol 103(2):227–249

59. Izvekov S, Voth GA (2005) A multiscale coarse-graining method for biomolecular systems. J Phys Chem B 109(7):2469–2473
60. Hodak H (2014) The Nobel Prize in chemistry 2013 for the development of multiscale models of complex chemical systems: a tribute to Martin Karplus, Michael Levitt and Arieh Warshel. J Mol Biol 426(1):1–3. https://doi.org/10.1016/j.jmb.2013.10.037
61. Karplus M (2014) Development of multiscale models for complex chemical systems: from H+H(2) to biomolecules (Nobel Lecture). Angew Chem 53(38):9992–10005. https://doi.org/10.1002/anie.201403924
62. Levitt M (2014) Birth and future of multiscale modeling for macromolecular systems (Nobel Lecture). Angew Chem 53(38):10006–10018. https://doi.org/10.1002/anie.201403691
63. Warshel A (2014) Multiscale modeling of biological functions: from enzymes to molecular machines (Nobel Lecture). Angew Chem 53(38):10020–10031. https://doi.org/10.1002/anie.201403689
64. Freddolino PL, Arkhipov AS, Larson SB, McPherson A, Schulten K (2006) Molecular dynamics simulations of the complete satellite tobacco mosaic virus. Structure 14(3):437–449. https://doi.org/10.1016/j.str.2005.11.014
65. Zhao G, Perilla JR, Yufenyuy EL, Meng X, Chen B, Ning J, Ahn J, Gronenborn AM, Schulten K, Aiken C, Zhang P (2013) Mature HIV-1 capsid structure by cryo-electron microscopy and all-atom molecular dynamics. Nature 497(7451):643–646. https://doi.org/10.1038/nature12162
66. Shaw DE, Grossman JP, Bank JA, Batson B, Butts JA, Chao JC, Deneroff MM, Dror RO, Even A, Fenton CH (2014) Anton 2: raising the bar for performance and programmability in a special-purpose molecular dynamics supercomputer. In: Proceedings of the international conference for high performance computing, networking, storage and analysis. IEEE Press, Salt Lake City, pp 41–53
67. Arkhipov A, Shan Y, Das R, Endres NF, Eastwood MP, Wemmer DE, Kuriyan J, Shaw DE (2013) Architecture and membrane interactions of the EGF receptor. Cell 152(3):557–569. https://doi.org/10.1016/j.cell.2012.12.030
68. Dror RO, Green HF, Valant C, Borhani DW, Valcourt JR, Pan AC, Arlow DH, Canals M, Lane JR, Rahmani R, Baell JB, Sexton PM, Christopoulos A, Shaw DE (2013) Structural basis for modulation of a G-protein-coupled receptor by allosteric drugs. Nature 503(7475):295–299. https://doi.org/10.1038/nature12595
69. Akitake B, Anishkin A, Liu N, Sukharev S (2007) Straightening and sequential buckling of the pore-lining helices define the gating cycle of MscS. Nat Struct Mol Biol 14(12):1141–1149. https://doi.org/10.1038/nsmb1341
70. Bjelkmar P, Niemela PS, Vattulainen I, Lindahl E (2009) Conformational changes and slow dynamics through microsecond polarized atomistic molecular simulation of an integral Kv1.2 ion channel. PLoS Comput Biol 5(2):e1000289
71. Cuello LG, Jogini V, Cortes DM, Pan AC, Gagnon DG, Dalmas O, Cordero-Morales JF, Chakrapani S, Roux B, Perozo E (2010) Structural basis for the coupling between activation and inactivation gates in K+ channels. Nature 466(7303):272–U154. https://doi.org/10.1038/Nature09136
72. Jeon J, Voth GA (2008) Gating of the mechanosensitive channel protein MscL: the interplay of membrane and protein. Biophys J 94(9):3497–3511. https://doi.org/10.1529/biophysj.107.109850
73. Jogini V, Roux B (2007) Dynamics of the Kv1.2 voltage-gated K+ channel in a membrane environment. Biophys J 93(9):3070–3082. https://doi.org/10.1529/biophysj.107.112540
74. Arkhipov A, Yin Y, Schulten K (2008) Four-scale description of membrane sculpting by BAR domains. Biophys J 95(6):2806–2821. https://doi.org/10.1529/biophysj.108.132563
75. Blood PD, Voth GA (2006) Direct observation of Bin/amphiphysin/Rvs (BAR) domain-induced membrane curvature by means of molecular dynamics simulations. Proc Natl Acad Sci USA 103(41):15068–15072. https://doi.org/10.1073/pnas.0603917103

76. Yu H, Schulten K (2013) Membrane sculpting by F-BAR domains studied by molecular dynamics simulations. PLoS Comput Biol 9(1):e1002892. https://doi.org/10.1371/journal.pcbi.1002892
77. Lyman E, Cui H, Voth GA (2010) Water under the BAR. Biophys J 99(6):1783–1790. https://doi.org/10.1016/j.bpj.2010.06.074
78. Blood PD, Swenson RD, Voth GA (2008) Factors influencing local membrane curvature induction by N-BAR domains as revealed by molecular dynamics simulations. Biophys J 95(4):1866–1876. https://doi.org/10.1529/biophysj.107.121160
79. Cui H, Ayton GS, Voth GA (2009) Membrane binding by the endophilin N-BAR domain. Biophys J 97(10):2746–2753. https://doi.org/10.1016/j.bpj.2009.08.043
80. Saunders MG, Voth GA (2013) Coarse-graining methods for computational biology. Annu Rev Biophys 42:73–93. https://doi.org/10.1146/annurev-biophys-083012-130348
81. Izvekov S, Voth GA (2006) Modeling real dynamics in the coarse-grained representation of condensed phase systems. J Chem Phys 125(15):151101. https://doi.org/10.1063/1.2360580
82. Sundararajan V, Simon SA, Benos DJ, Feller SE (2011) Computational modeling of membrane bilayers. Elsevier Science, San Diego
83. Noid WG, Chu JW, Ayton GS, Krishna V, Izvekov S, Voth GA, Das A, Andersen HC (2008) The multiscale coarse-graining method. I. A rigorous bridge between atomistic and coarse-grained models. J Chem Phys 128(24):244114
84. Noid WG, Liu P, Wang Y, Chu JW, Ayton GS, Izvekov S, Andersen HC, Voth GA (2008) The multiscale coarse-graining method. II. Numerical implementation for coarse-grained molecular models. J Chem Phys 128(24):244115
85. Izvekov S, Voth GA (2006) Multiscale coarse-graining of mixed phospholipid/cholesterol bilayers. J Chem Theory Comput 2(3):637–648
86. Izvekov S, Voth GA (2009) Solvent-free lipid bilayer model using multiscale coarse-graining. J Phys Chem B 113(13):4443–4455
87. Lu LY, Voth GA (2009) Systematic coarse-graining of a multicomponent lipid bilayer. J Phys Chem B 113(5):1501–1510
88. Ayton GS, Voth GA (2009) Hybrid coarse-graining approach for lipid bilayers at large length and time scales. J Phys Chem B 113(13):4413–4424
89. Gay JG, Berne BJ (1981) Modification of the overlap potential to mimic a linear site-site potential. J Chem Phys 74(6):3316–3319
90. Srivastava A, Voth GA (2013) A hybrid approach for highly coarse-grained lipid bilayer models. J Chem Theory Comput 9(1):750–765. https://doi.org/10.1021/ct300751h
91. Srivastava A, Voth GA (2014) Solvent-free, highly coarse-grained models for charged lipid systems. J Chem Theory Comput 10(10):4730–4744. https://doi.org/10.1021/ct500474a
92. Shelley JC, Shelley MY, Reeder RC, Bandyopadhyay S, Klein ML (2001) A coarse grain model for phospholipid simulations. J Phys Chem B 105(19):4464–4470
93. Sodt AJ, Head-Gordon T (2010) An implicit solvent coarse-grained lipid model with correct stress profile. J Chem Phys 132(20):205103. https://doi.org/10.1063/1.3408285
94. Reith D, Putz M, Muller-Plathe F (2003) Deriving effective mesoscale potentials from atomistic simulations. J Comput Chem 24(13):1624–1636. https://doi.org/10.1002/jcc.10307
95. Lyubartsev AP, Laaksonen A (1995) Calculation of effective interaction potentials from radial-distribution functions—a reverse Monte-Carlo approach. Phys Rev E 52(4):3730–3737
96. Lyubartsev AP (2005) Multiscale modeling of lipids and lipid bilayers. Eur Biophys J 35(1):53–61
97. Murtola T, Falck E, Karttunen M, Vattulainen I (2007) Coarse-grained model for phospholipid/cholesterol bilayer employing inverse Monte Carlo with thermodynamic constraints. J Chem Phys 126(7):075101. https://doi.org/10.1063/1.2646614
98. Murtola T, Falck E, Patra M, Karttunen M, Vattulainen I (2004) Coarse-grained model for phospholipid/cholesterol bilayer. J Chem Phys 121(18):9156–9165. https://doi.org/10.1063/1.1803537

99. Wang ZJ, Deserno M (2010) A systematically coarse-grained solvent-free model for quantitative phospholipid bilayer simulations. J Phys Chem B 114(34):11207–11220. https://doi.org/10.1021/jp102543j
100. Mirzoev A, Lyubartsev AP (2014) Systematic implicit solvent coarse graining of dimyristoylphosphatidylcholine lipids. J Comput Chem 35(16):1208–1218. https://doi.org/10.1002/jcc.23610
101. Drouffe JM, Maggs AC, Leibler S (1991) Computer simulations of self-assembled membranes. Science 254(5036):1353–1356
102. Marrink SJ, Risselada HJ, Yefimov S, Tieleman DP, de Vries AH (2007) The MARTINI force field: coarse grained model for biomolecular simulations. J Phys Chem B 111(27):7812–7824
103. Marrink SJ, de Vries AH, Mark AE (2004) Coarse grained model for semiquantitative lipid simulations. J Phys Chem B 108(2):750–760
104. Brannigan G, Brown FL (2004) Solvent-free simulations of fluid membrane bilayers. J Chem Phys 120(2):1059–1071. https://doi.org/10.1063/1.1625913
105. Farago O (2003) "Water-free" computer model for fluid bilayer membranes. J Chem Phys 119(1):596–605
106. Noguchi H, Takasu M (2001) Fusion pathways of vesicles: a Brownian dynamics simulation. J Chem Phys 115(20):9547–9551
107. Cooke IR, Kremer K, Deserno M (2005) Tunable generic model for fluid bilayer membranes. Phys Rev E Stat Nonlin Soft Matter Phys 72(1 Pt 1):011506
108. Noguchi H (2011) Solvent-free coarse-grained lipid model for large-scale simulations. J Chem Phys 134(5):055101
109. Wang ZJ, Frenkel D (2005) Modeling flexible amphiphilic bilayers: a solvent-free off-lattice Monte Carlo study. J Chem Phys 122(23):234711
110. Baumgartner A, Ho JS (1990) Crumpling of fluid vesicles. Phys Rev A 41(10):5747–5750
111. Ho JS, Baumgartner A (1990) Simulations of fluid self-avoiding membranes. Europhys Lett 12(4):295–300
112. Kantor Y, Kardar M, Nelson DR (1986) Statistical mechanics of tethered surfaces. Phys Rev Lett 57(7):791–794
113. Ramakrishnan N, Kumar PBS, Ipsen JH (2010) Monte Carlo simulations of fluid vesicles with in-plane orientational ordering. Phys Rev E Stat Nonlin Soft Matter Phys 81(4):041922
114. Sreeja K, Ipsen JH, Kumar PS (2015) Monte Carlo simulations of fluid vesicles. J Phys Condens Matter 27(27):273104
115. Canham PB (1970) The minimum energy of bending as a possible explanation of the biconcave shape of the human red blood cell. J Theor Biol 26(1):61–81
116. Del Popolo MG, Ballone P (2008) Melting behavior of an idealized membrane model. J Chem Phys 128(2):024705. https://doi.org/10.1063/1.2804423
117. Kohyama T (2009) Simulations of flexible membranes using a coarse-grained particle-based model with spontaneous curvature variables. Physica A 388(17):3334–3344
118. Noguchi H, Gompper G (2006) Meshless membrane model based on the moving least-squares method. Phys Rev E Stat Nonlin Soft Matter Phys 73(2):021903
119. Pasqua A, Maibaum L, Oster G, Fletcher DA, Geissler PL (2010) Large-scale simulations of fluctuating biological membranes. J Chem Phys 132(15):154107. https://doi.org/10.1063/1.3382349
120. Shiba H, Noguchi H (2011) Estimation of the bending rigidity and spontaneous curvature of fluid membranes in simulations. Phys Rev E Stat Nonlin soft Matter Phys 84(3 Pt 1):031926
121. Bond PJ, Sansom MS (2007) Bilayer deformation by the Kv channel voltage sensor domain revealed by self-assembly simulations. Proc Natl Acad Sci USA 104(8):2631–2636. https://doi.org/10.1073/pnas.0606822104
122. Delemotte L, Klein ML, Tarek M (2012) Molecular dynamics simulations of voltage-gated cation channels: insights on voltage-sensor domain function and modulation. Front Pharmacol 3:97. https://doi.org/10.3389/fphar.2012.00097
123. Maffeo C, Bhattacharya S, Yoo J, Wells D, Aksimentiev A (2012) Modeling and simulation of ion channels. Chem Rev 112(12):6250–6284. https://doi.org/10.1021/cr3002609

124. Treptow W, Marrink SJ, Tarek M (2008) Gating motions in voltage-gated potassium channels revealed by coarse-grained molecular dynamics simulations. J Phys Chem B 112(11):3277–3282. https://doi.org/10.1021/jp709675e
125. Yefimov S, van der Giessen E, Onck PR, Marrink SJ (2008) Mechanosensitive membrane channels in action. Biophys J 94(8):2994–3002. https://doi.org/10.1529/biophysj.107.119966
126. Braun AR, Lacy MM, Ducas VC, Rhoades E, Sachs JN (2014) Alpha-synuclein-induced membrane remodeling is driven by binding affinity, partition depth, and interleaflet order asymmetry. J Am Chem Soc 136(28):9962–9972
127. Fuhrmans M, Marrink SJ (2012) Molecular view of the role of fusion peptides in promoting positive membrane curvature. J Am Chem Soc 134(3):1543–1552. https://doi.org/10.1021/ja207290b
128. Ingolfsson HI, Melo MN, van Eerden FJ, Arnarez C, Lopez CA, Wassenaar TA, Periole X, de Vries AH, Tieleman DP, Marrink SJ (2014) Lipid organization of the plasma membrane. J Am Chem Soc 136(41):14554–14559. https://doi.org/10.1021/ja507832e
129. Koldso H, Shorthouse D, Helie J, Sansom MSP (2014) Lipid clustering correlates with membrane curvature as revealed by molecular simulations of complex lipid bilayers. PLoS Comput Biol 10(10):e1003911
130. Lindau M, Hall BA, Chetwynd A, Beckstein O, Sansom MS (2012) Coarse-grain simulations reveal movement of the synaptobrevin C-terminus in response to piconewton forces. Biophys J 103(5):959–969. https://doi.org/10.1016/j.bpj.2012.08.007
131. Risselada HJ, Kutzner C, Grubmuller H (2011) Caught in the act: visualization of SNARE-mediated fusion events in molecular detail. Chembiochem 12(7):1049–1055. https://doi.org/10.1002/cbic.201100020
132. Reynwar BJ, Illya G, Harmandaris VA, Muller MM, Kremer K, Deserno M (2007) Aggregation and vesiculation of membrane proteins by curvature-mediated interactions. Nature 447(7143):461–464. https://doi.org/10.1038/nature05840
133. Reynwar BJ, Deserno M (2011) Membrane-mediated interactions between circular particles in the strongly curved regime. Soft Matter 7(18):8567–8575
134. Matthews R, Likos CN (2013) Dynamics of self-assembly of model viral capsids in the presence of a fluctuating membrane. J Phys Chem B 117(27):8283–8292. https://doi.org/10.1021/jp4037099
135. Ruiz-Herrero T, Hagan MF (2015) Simulations show that virus assembly and budding are facilitated by membrane microdomains. Biophys J 108(3):585–595
136. Lyman E, Pfaendtner J, Voth GA (2008) Systematic multiscale parameterization of heterogeneous elastic network models of proteins. Biophys J 95(9):4183–4192
137. Sinitskiy AV, Voth GA (2013) Coarse-graining of proteins based on elastic network models. Chem Phys 422:165–174
138. Tirion MM (1996) Large amplitude elastic motions in proteins from a single-parameter, atomic analysis. Phys Rev Lett 77(9):1905–1908
139. Simunovic M, Srivastava A, Voth GA (2013) Linear aggregation of proteins on the membrane as a prelude to membrane remodeling. Proc Natl Acad Sci USA 110(51):20396–20401. https://doi.org/10.1073/pnas.1309819110
140. Dommersnes PG, Fournier JB (1999) N-body study of anisotropic membrane inclusions: Membrane mediated interactions and ordered aggregation. Eur Phys J B 12(1):9–12
141. Saric A, Cacciuto A (2012) Fluid membranes can drive linear aggregation of adsorbed spherical nanoparticles. Phys Rev Lett 108(11):118101
142. Koltover I, Radler JO, Safinya CR (1999) Membrane mediated attraction and ordered aggregation of colloidal particles bound to giant phospholipid vesicles. Phys Rev Lett 82(9):1991–1994. https://doi.org/10.1103/Physrevlett.82.1991
143. McDonald NA, Vander Kooi CW, Ohi MD, Gould KL (2015) Oligomerization but not membrane bending underlies the function of certain F-BAR proteins in cell motility and cytokinesis. Dev Cell 35(6):725–736. https://doi.org/10.1016/j.devcel.2015.11.023
144. Traub LM (2015) F-BAR/EFC domain proteins: some assembly required. Dev Cell 35(6):664–666. https://doi.org/10.1016/j.devcel.2015.12.003

145. Bahrami AH, Lipowsky R, Weikl TR (2012) Tubulation and aggregation of spherical nanoparticles adsorbed on vesicles. Phys Rev Lett 109(18):188102
146. Saric A, Cacciuto A (2012) Mechanism of membrane tube formation induced by adhesive nanocomponents. Phys Rev Lett 109(18):188101
147. Simunovic M, Voth GA (2015) Membrane tension controls the assembly of curvature-generating proteins. Nat Commun 6:7219. https://doi.org/10.1038/ncomms8219
148. Shi Z, Baumgart T (2015) Membrane tension and peripheral protein density mediate membrane shape transitions. Nat Commun 6:5974. https://doi.org/10.1038/ncomms6974
149. Renard HF, Simunovic M, Lemiere J, Boucrot E, Garcia-Castillo MD, Arumugam S, Chambon V, Lamaze C, Wunder C, Kenworthy AK, Schmidt AA, McMahon HT, Sykes C, Bassereau P, Johannes L (2015) Endophilin-A2 functions in membrane scission in clathrin-independent endocytosis. Nature 517(7535):493–496. https://doi.org/10.1038/nature14064
150. Noguchi H (2015) Membrane tubule formation by banana-shaped proteins with or without intermediate network structure. Sci Rep 6:20935
151. Noguchi H (2014) Two- or three-step assembly of banana-shaped proteins coupled with shape transformation of lipid membranes. EPL 108(4):48001
152. Ramakrishnan N, Sunil Kumar PB, Ipsen JH (2013) Membrane-mediated aggregation of curvature-inducing nematogens and membrane tubulation. Biophys J 104(5):1018–1028. https://doi.org/10.1016/j.bpj.2012.12.045
153. Simunovic M, Mim C, Marlovits TC, Resch G, Unger VM, Voth GA (2013) Protein-mediated transformation of lipid vesicles into tubular networks. Biophys J 105(3):711–719. https://doi.org/10.1016/j.bpj.2013.06.039
154. Yin Y, Arkhipov A, Schulten K (2009) Simulations of membrane tubulation by lattices of amphiphysin N-BAR domains. Structure 17(6):882–892. https://doi.org/10.1016/j.str.2009.03.016
155. Cui H, Mim C, Vazquez FX, Lyman E, Unger VM, Voth GA (2013) Understanding the role of amphipathic helices in N-BAR domain driven membrane remodeling. Biophys J 104(2):404–411. https://doi.org/10.1016/j.bpj.2012.12.006
156. Prevost C, Zhao H, Manzi J, Lemichez E, Lappalainen P, Callan-Jones A, Bassereau P (2015) IRSp53 senses negative membrane curvature and phase separates along membrane tubules. Nat Commun 6:8529. https://doi.org/10.1038/ncomms9529
157. McMahon HT, Boucrot E (2011) Molecular mechanism and physiological functions of clathrin-mediated endocytosis. Nat Rev Mol Cell Biol 12(8):517–533. https://doi.org/10.1038/nrm3151
158. Fotin A, Cheng Y, Sliz P, Grigorieff N, Harrison SC, Kirchhausen T, Walz T (2004) Molecular model for a complete clathrin lattice from electron cryomicroscopy. Nature 432(7017):573–579. https://doi.org/10.1038/nature03079
159. Kirchhausen T (2000) Clathrin. Annu Rev Biochem 69:699–727. https://doi.org/10.1146/annurev.biochem.69.1.699
160. den Otter WK, Renes MR, Briels WJ (2010) Asymmetry as the key to clathrin cage assembly. Biophys J 99(4):1231–1238. https://doi.org/10.1016/j.bpj.2010.06.011
161. den Otter WK, Renes MR, Briels WJ (2010) Self-assembly of three-legged patchy particles into polyhedral cages. J Phys Condens Matter 22(10):104103
162. Matthews R, Likos CN (2012) Influence of fluctuating membranes on self-assembly of patchy colloids. Phys Rev Lett 109(17):178302
163. Matthews R, Likos CN (2013) Structures and pathways for clathrin self-assembly in the bulk and on membranes. Soft Matter 9(24):5794–5806
164. Ramakrishnan N, Sunil Kumar PB, Radhakrishnan R (2014) Mesoscale computational studies of membrane bilayer remodeling by curvature-inducing proteins. Phys Rep 543(1):1–60. https://doi.org/10.1016/j.physrep.2014.05.001
165. Heinrich V, Svetina S, Zeks B (1993) Nonaxisymmetric vesicle shapes in a generalized bilayer-couple model and the transition between oblate and prolate axisymmetrical shapes. Phys Rev E 48(4):3112–3123. https://doi.org/10.1103/Physreve.48.3112

166. Iglic A, Kralj-Iglic V, Bozic B, Bobrowska-Hagerstrand M, Isomaa B, Hagerstrand H (2000) Torocyte shapes of red blood cell daughter vesicles. Bioelectrochemistry 52(2):203–211
167. Miao L, Seifert U, Wortis M, Dobereiner HG (1994) Budding transitions of fluid-bilayer vesicles: the effect of area-difference elasticity. Phys Rev E Stat Phys Plasmas Fluids Relat Interdiscip Top 49(6):5389–5407
168. Svetina S, Zeks B (1989) Membrane bending energy and shape determination of phospholipid-vesicles and red blood-cells. Eur Biophys J 17(2):101–111
169. Auth T, Gompper G (2009) Budding and vesiculation induced by conical membrane inclusions. Phys Rev E 80(3):031901
170. Bozic B, Kralj-Iglic V, Svetina S (2006) Coupling between vesicle shape and lateral distribution of mobile membrane inclusions. Phys Rev E 73(4):041915
171. Kabaso D, Bobrovska N, Gozdz W, Gov N, Kralj-Iglic V, Veranic P, Iglic A (2012) On the role of membrane anisotropy and BAR proteins in the stability of tubular membrane structures. J Biomech 45(2):231–238. https://doi.org/10.1016/j.jbiomech.2011.10.039
172. Kralj-Iglic V, Hagerstrand H, Veranic P, Jezernik K, Babnik B, Gauger DR, Iglic A (2005) Amphiphile-induced tubular budding of the bilayer membrane. Eur Biophys J 34(8):1066–1070. https://doi.org/10.1007/s00249-005-0481-0
173. Mukhopadhyay R, Lim HWG, Wortis M (2002) Echinocyte shapes: bending, stretching, and shear determine spicule shape and spacing. Biophys J 82(4):1756–1772
174. Su YC, Chen JZ (2015) A model of vesicle tubulation and pearling induced by adsorbing particles. Soft Matter 11(20):4054–4060. https://doi.org/10.1039/c5sm00565e
175. Ayton GS, McWhirter JL, Voth GA (2006) A second generation mesoscopic lipid bilayer model: connections to field-theory descriptions of membranes and nonlocal hydrodynamics. J Chem Phys 124(6):64906. https://doi.org/10.1063/1.2165194
176. Ayton GS, McWhirter JL, McMurtry P, Voth GA (2005) Coupling field theory with continuum mechanics: a simulation of domain formation in giant unilamellar vesicles. Biophys J 88(6):3855–3869. https://doi.org/10.1529/biophysj.105.059436
177. Hoover WG, Hoover CG (2003) Links between microscopic and macroscopic fluid mechanics. Mol Phys 101(11):1559–1573. https://doi.org/10.1080/0026897021000026647
178. Ayton GS, Blood PD, Voth GA (2007) Membrane remodeling from N-BAR domain interactions: insights from multi-scale simulation. Biophys J 92(10):3595–3602. https://doi.org/10.1529/biophysj.106.101709
179. Boucrot E, Pick A, Camdere G, Liska N, Evergren E, McMahon HT, Kozlov MM (2012) Membrane fission is promoted by insertion of amphipathic helices and is restricted by crescent BAR domains. Cell 149(1):124–136. https://doi.org/10.1016/j.cell.2012.01.047
180. Ayton GS, Lyman E, Krishna V, Swenson RD, Mim C, Unger VM, Voth GA (2009) New insights into BAR domain-induced membrane remodeling. Biophys J 97(6):1616–1625. https://doi.org/10.1016/j.bpj.2009.06.036
181. Lin LC, Brown FL (2004) Brownian dynamics in Fourier space: membrane simulations over long length and time scales. Phys Rev Lett 93(25):256001
182. Lin LCL, Brown FLH (2005) Dynamic simulations of membranes with cytoskeletal interactions. Phys Rev E 72(1):Artn 011910. https://doi.org/10.1103/Physreve.72.011910
183. Ayton GS, Voth GA (2010) Multiscale simulation of protein mediated membrane remodeling. Semin Cell Dev Biol 21(4):357–362. https://doi.org/10.1016/j.semcdb.2009.11.011
184. Chang R, Ayton GS, Voth GA (2005) Multiscale coupling of mesoscopic- and atomistic-level lipid bilayer simulations. J Chem Phys 122(24):244716. https://doi.org/10.1063/1.1931651
185. Lyman E, Cui H, Voth GA (2011) Reconstructing protein remodeled membranes in molecular detail from mesoscopic models. Phys Chem Chem Phys 13(22):10430–10436. https://doi.org/10.1039/c0cp02978e
186. Liu P, Voth GA (2007) Smart resolution replica exchange: an efficient algorithm for exploring complex energy landscapes. J Chem Phys 126(4):045106. https://doi.org/10.1063/1.2408415
187. Sigurdsson JK, Brown FLH, Atzberger PJ (2013) Hybrid continuum-particle method for fluctuating lipid bilayer membranes with diffusing protein inclusions. J Comput Phys 252:65–85

188. De Nicola A, Zhao Y, Kawakatsu T, Roccatano D, Milano G (2011) Hybrid particle-field coarse-grained models for biological phospholipids. J Chem Theory Comput 7(9):2947–2962. https://doi.org/10.1021/Ct200132n
189. De Nicola A, Zhao Y, Kawakatsu T, Roccatano D, Milano G (2012) Validation of a hybrid MD-SCF coarse-grained model for DPPC in non-lamellar phases. Theor Chem Accounts 131(3):Artn 1167. https://doi.org/10.1007/S00214-012-1167-1
190. Sarukhanyan E, De Nicola A, Roccatano D, Kawakatsu T, Milano G (2014) Spontaneous insertion of carbon nanotube bundles inside biomembranes: a hybrid particle-field coarse-grained molecular dynamics study. Chem Phys Lett 595:156–166. https://doi.org/10.1016/J.Cplett.2014.01.057

Mechanosensitivity of Membrane Budding and Trafficking

Lionel Foret

Abstract Intracellular compartments continually exchange material transported by small vesicles or tubules, which are formed in the membrane of the donor compartments and eventually fuse with the membrane of the receptor compartments. The formation and fission of a membrane bud giving rise to a new object and the fusion are controlled to some extent by the mechanical properties of the membranes, in particular their tension. In this chapter, we review the different mechanisms of vesicle and tubule budding and analyze the influence of the membrane tension on these processes using basic considerations of thermodynamics and mechanics. In any case, vesicle and tubule production can be impaired at high enough tension. Next, we discuss the influence of tension on membrane fusion, which is a less understood problem. Finally, since the release/absorption of vesicles or tubules should affect the tension of the donor/receptor, we speculate about the possible regulatory role of the membrane tension on intracellular trafficking and compartments stability.

Keywords Intracellular trafficking · Biological membrane · Budding · Fusion · Tension

1 Introduction

Eukaryotic cells comprise several intracellular compartments, also named organelles, bound by a fluid membrane made of lipids and proteins. The biochemical composition of the membrane defines the nature and the functions of the compartment. Examples of organelles are the endoplasmic reticulum, the Golgi apparatus, the different types of endosomes, and the lysosomes. These compartments continually exchange material with each other and with the plasma

L. Foret (✉)
Ecole Normale Supérieure, CNRS, UPMC Univ Paris 06, Laboratoire de Physique Statistique, Paris, France
e-mail: lforet@lps.ens.fr

P. Bassereau, P. Sens (eds.), *Physics of Biological Membranes*,
https://doi.org/10.1007/978-3-030-00630-3_15

membrane. The material is carried from one compartment to another by very small membrane-bound objects: transport vesicles and tubules. The genesis of a transport vesicle or tubule takes place in the membrane of the donor compartment. A local membrane deformation emerges, a process called "budding," and eventually undergoes fission giving rise to a new membrane-bound object. The vesicle or tubule released by this mean moves in the cell, pulled by molecular motors along filaments, and eventually fuses with the membrane of the target compartment where the transported material should be delivered [2, 6, 9]. All these processes, such as budding, fission, motion, and fusion are mediated by energy consuming protein machineries. The diameter of transport vesicles is of the order of 100 nm or smaller. Tubules diameter is of the order of few tens of nm and their length up to several hundred nm.

Membrane budding, fission, and fusion involve significant modifications of the membrane shape. These processes should thus be sensitive on the mechanical properties of the membrane. Depending on the membrane elasticity and tension, budding, fusion, and fission can be either facilitated or prevented. The morphology of the budding structures and released objects depends also on the mechanical parameters characterizing the donor membrane. Living cells might use this mechanosensitivity to mechanically regulate the intracellular traffic.

For large-scale deformations with respect to membrane thickness, a membrane can be described as an unstretchable bi-dimensional fluid, which elastically opposes bending [85]. The elastic modulus, or bending rigidity κ, of a biological membrane is of the order of 10^{-19} J. The membranes of the cell and of the intracellular compartments are under tension, with σ of the order of 10^{-5} N/m. This parameter in particular can play an important role in traffic regulation by its influence on budding and fusion processes.

The outline of this chapter is as follows. Section 2 presents some generality on the membrane budding process. Sections 3 and 4 are devoted to the mechanics of vesicle budding and tubule budding, respectively. The two main questions that are addressed are "how tension and rigidity affects the shape of the budding protrusions" and "under which conditions on tension and rigidity is budding possible." The theoretical predictions are compared with experimental observations. In particular, in vitro experiments on reconstituted systems, in which the mechanical parameters can be measured and sometime tuned, have provided much insights on these questions. In Sect. 5, the influence of the membrane tension on fusion is discussed. The first question that is addressed is the dependence of the fusion barrier on the tension. Despite the insights provided by molecular simulations this last decade, this question remains not well understood. The second question is the effect of tension gradient for the transport between fusing objects. Section 6 is a more speculative discussion on the possible regulatory role of membrane tension on intracellular trafficking. Tension affects budding, fission, and fusion but on the other hand, all these processes can potentially affect compartments tension by adding and removing membrane area. This mutual interaction could allow to coordinate the entry and secretion of vesicles and tubules in a compartment.

2 Membrane Budding: Generality

The first step in the genesis of a tubule or a vesicle is the gradual deformation of an initially nearly flat membrane. This is the budding process that precedes the eventual fission of the narrow membrane tubes that connects the vesicular or tubular protrusion to the rest of the membrane. The rigidity of the membrane against bending and the membrane tension oppose to membrane deformation and thus oppose to budding. Using the thin elastic fluid membrane model, the free energy of a membrane is

$$\mathcal{F}_{\mathrm{m}} = \int_A \left[\frac{\kappa}{2} (C_1 + C_2 - C_0)^2 + \kappa_{\mathrm{G}} C_1 C_2 + \sigma \right] dA \tag{1}$$

where A is the membrane area, C_1 and C_2 are the principal local curvatures, κ the bending rigidity, κ_{G} the Gaussian bending rigidity, σ the tension, and C_0 the spontaneous curvature. The integral over the Gaussian curvature $C_1 C_2$ is constant in budding processes [90]. The Gaussian bending rigidity κ_{G} thus plays no role in membrane budding and this term is omitted in the following. The energetic cost associated with the formation of a vesicle is roughly, $\mathcal{F}_{\mathrm{m}} = 8\pi\kappa + 4\pi R^2\sigma \sim 1000\ k_{\mathrm{B}}T$ for a vesicle radius $R = 50\,\mathrm{nm}$. Therefore, budding cannot occur spontaneously. It requires the action of proteins able to shape the membrane. A short review of the different mechanisms used by the cell to bend membrane and generate transport carriers is provided in the following Sect. 2.1. Whether vesicle or tubule can or cannot bud from a flat membrane, and the morphology of the budding structure, results from the competition between, on one hand the action of the proteins inducing membrane deformation, and on the other hand the membrane tension and rigidity, which oppose deformation. This issue is addressed in Sects. 3 and 4, in the case of vesicle and tubule, respectively, using simple mechanical and thermodynamical considerations. Section 2.2 presents the basics of elasticity for axisymmetrical membrane that are used to compute membrane bud shape and energy.

2.1 Mechanisms of Membrane Curvature Generation

Several reviews on this topic have been written, see [46, 52, 69, 93, 101, 125]. Here, only a brief overview of the different mechanisms is given.

- **Rigid coat formation**. Specialized peripheral proteins polymerize to form a rigid structure, which imposes its own curved shape to the membrane on which it adheres. The word coat is usually restricted to spherical protein assembly responsible for vesicle budding. Here we shall use it in a more general way, including rigid tubular structures formed by Dynamin or F-BAR proteins, for example.

- **Protein crowding**. The lateral pressure arising from the steric repulsion between peripheral proteins bound on one side of the membrane promotes membrane bending. Curvature increases the area accessible to the proteins, which is entropically favorable [99, 100].
- **Curved shape proteins**. Peripheral proteins with a curved membrane-binding side, such as those with a BAR (Bin-Amphiphysin-Rvs) domain [34], impose locally their curved shape, driving membrane deformation. Integral proteins with an asymmetrical shape should behave in an analogous way.
- **Wedge effect**. Peripheral proteins with amphipathic helices, such as ENTH (Epsin N-Terminal Homology) domain, or loop, inserted in the lipid bilayer act as wedge able to locally bend the membrane [10, 54].
- **External force**. Membrane deformation can also be driven by normal forces produced by actin filaments and molecular motors pushing or pulling the membrane [58].
- **Lipid asymmetry**. Finally, curvature can be induced by composition asymmetry between the two lipid layers, generated and maintained by enzymes that modify lipid tail or head [69, 125].

2.2 *Elasticity of Axisymmetrical Membrane*

Vesicle or tubule budding driven by protein machineries is a slow process (typically few tens of second for spherical coat assembling) as compared to membrane shape relaxation. The membrane is always at mechanical equilibrium and its shape minimizes the energy (1).

Tubular and vesicular are axisymmetrical structures. The membrane shape can be parametrized by the cylindrical coordinates $r(s)$ and $z(s)$, where s is the arc length along the shape contour, and by the angle $\psi(s)$, Fig. 1. These three quantities are not independent but obey,

$$\dot{r} = \cos\psi \ , \quad \dot{z} = -\sin\psi \ , \tag{2}$$

where the dot denotes the derivative with respect to s. The two principal curvatures of the membrane are $C_1 = \dot{\psi}$ and $C_2 = \sin\psi/r$, and the area differential

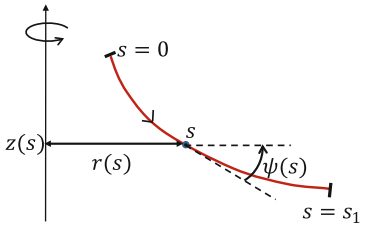

Fig. 1 Shape parametrization for an axisymmetric membrane. The red line is the contour of the membrane shape

$dA = 2\pi r ds$. The membrane free energy (1) then reads,

$$\mathcal{F}_{\rm m} = 2\pi \int_0^{s_1} \left[\frac{\kappa}{2} \left(\dot{\psi} + \frac{\sin\psi}{r} - C_0 \right)^2 + \sigma \right] r \, ds \, . \tag{3}$$

The equations satisfied by $r(s)$, $z(s)$, and $\psi(s)$ at equilibrium are obtained by minimizing (3). Inserting the equilibrium $r(s)$, $z(s)$, and $\psi(s)$ in (3) then gives the energy of the membrane deformation. The minimization procedure is detailed in [49, 90] and summarized in Appendix 1. Accounting for the possible pressure difference p across the membrane and punctual normal force f applied at the membrane center $r = 0$, the equation derived from energy minimization reads,

$$\begin{aligned} &\ddot{\psi}\cos\psi + \frac{\dot{\psi}\cos^2\psi}{r} + \frac{\dot{\psi}^2\sin\psi}{2} - \frac{\sin\psi}{2r^2}\left(2\cos^2\psi + (\sin\psi - C_0 r)^2\right) \\ &\quad - \frac{\sigma}{\kappa}\sin\psi + \frac{p}{2\kappa} r + \frac{f}{2\pi\kappa r} = 0 \, , \end{aligned} \tag{4}$$

which together with Eq. (2) form a complete set of equations satisfied by $r(s)$, $z(s)$, and $\psi(s)$ at equilibrium.

3 Vesicle Budding Driven by Rigid Coat Assembling

In living cell, rigid coat assembling on membrane is the main mechanism driving vesicle budding. Various proteins polymerize on the membrane, forming a rigid shell, or "coat," with spherical cap shape that covers the membrane. The coat grows until the formation of a nearly complete sphere [51]. The three main types of coat, clathrin coat [68], COPI [5, 44], and COPII [122] are made of different components and assemble on the membrane of different organelles (plasma membrane and endosome, Golgi apparatus, endoplasmic reticulum, respectively) but they share strong similarities regarding their structure and function [24, 70]. Coat assembling is passive, only driven by the free energy gain associated with components polymerization, and can be reconstituted in vitro with minimal sets of proteins. Vesicle formation results from the competition between the energy gain due to coat polymerization and the cost due to membrane deformation.

In the simplest model, a protein coat is a continuous spherical cap with curvature radius R. The degree of completion is characterized either by the angle $0 \leq \alpha \leq \pi$ defined on Fig. 2, or by the ratio $0 \leq x \leq 1$ of the coat area to the complete sphere area,

$$x = \frac{A_{\rm c}}{4\pi R^2} = \frac{1}{2}(1 - \cos\alpha), \tag{5}$$

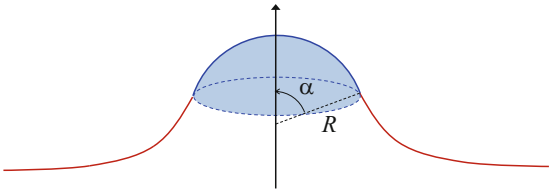

Fig. 2 The spherical cap model. The blue line is the membrane area covered by a coat. The red line is the membrane neck

A coat imposes its spherical cap shape on the membrane in the area where it adheres. The deformation propagates around the coat in a region that we call membrane *neck*, Fig. 2.

The spherical cap assumption for the coat shape is used in the following to study theoretically the shape of the membrane neck (Sect. 3.1) and its energy (Sect. 3.2) at different stages of vesicle budding and for different tension and rigidity. Then, using energetic considerations, the conditions required for vesicle budding to occur are analyzed in Sects. 3.3 and 3.4.

3.1 Shape of the Membrane Neck

The shape of the membrane around the coat might play an important role in the coordination of the budding and fission machinery [3, 84]. Several proteins involved in vesicle formation are curvature sensor, they bind and concentrate preferentially in regions with particular curvature [74, 98].

Under the spherical cap approximation, the neck is axisymmetric and its shape can be calculated using Eqs. (2), (4). We assume that the pressure difference across the membrane, the spontaneous curvature of the membrane, and the pulling force are zero ($C_0 = p = f = 0$). The deformation is imposed by the rigid coat through the boundary conditions. Equations (2), (4) contain a single parameter, the length

$$\lambda = \sqrt{\frac{\kappa}{\sigma}}\,, \tag{6}$$

which sets the typical extension of the membrane deformation around the coat. At the coat boundary, the radius and the angle are fixed and depend on the completion level of the coat, $r(0) = R\sin\alpha$ and $\psi(0) = \alpha$. Far from the coat, the membrane should recover its planar shape, $\psi(\infty) = \dot{\psi}(\infty) = z(\infty) = 0$. The shape of the membrane neck then depends on two dimensionless parameters: α and $(R\sin\alpha)/\lambda$.

Figure 3 shows the membrane contour, computed numerically, at different stages of the coat growth, i.e., for different values of α, and for different values of R/λ. The morphology strongly depends on the tension. At high tension, the deformation is concentrated in a very narrow and highly curved region near the coat. At low tension, the curvature is low and the deformation propagates far from the coat. Approximate analytical expressions for the membrane shape can be derived in different limit cases [28].

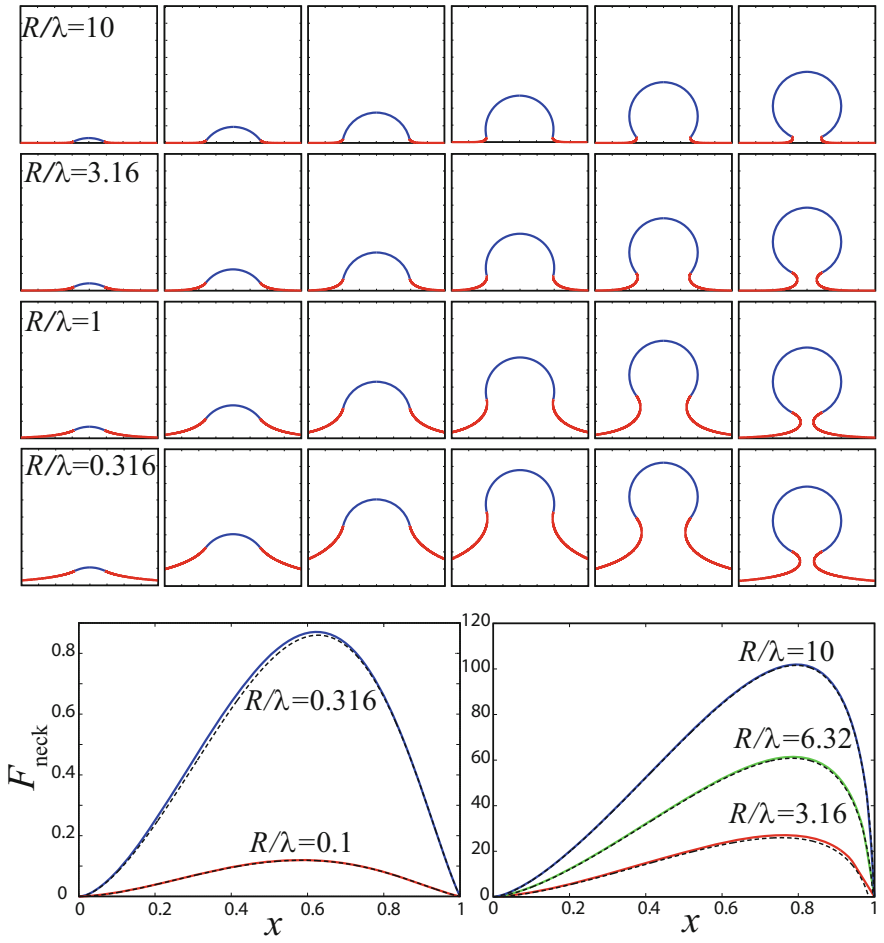

Fig. 3 Top panels: shape of the membrane neck during coat growth, i.e., for different values of α: $0.15\pi, 0.28\pi, 0.42\pi, 0.57\pi, 0.71\pi, 0.85\pi$ from the left to the right, and different values of $R/\lambda = R\sqrt{\sigma/\kappa}$, see the values on the graph. The unit length in the graphs is $\lambda/2$. Bottom panels: energy of the membrane neck $\mathcal{F}_{\rm neck}$ outside the coat as a function of x, the coat completion parameter, for different values of R/λ (see graph). The dash black line corresponds to the approximations, Eq. (16), in the low tension limit (left) and large tension limit (right)

3.1.1 Weak Deformation

When α is small, or far from the coat, the membrane deformation is weak, $\psi \ll 1$. In this limit, the shape equations (4), (2) can be linearized,

$$\ddot{\psi} r^2 + \dot{\psi} r - (1 + (\sigma/\kappa) r^2)\psi = 0\,, \quad \dot{r} = 1\,, \quad \dot{z} = -\psi \tag{7}$$

and solved analytically,

$$r = s + a, \quad \psi = \beta K_1(r/\lambda), \quad z = \beta\lambda K_0(r/\lambda)\ . \tag{8}$$

The Bessel functions K_0 and K_1 decrease exponentially at $s \gg \lambda$. The tension imposes a flat shape at a distance larger than λ. When α is small, the integration constants a and β are given by the boundary conditions at the coat border, $a = R\sin\alpha$ and $\beta = \alpha/K_1(R\sin\alpha/\lambda)$; when α is not small, the solution of the linearized equation is valid only at large enough distance from the coat, a and β depend on the shape near the coat.

3.1.2 Low Tension or Near Full Completion

In the limit $R\sin\alpha \ll \lambda$, the tension has a negligible effect near the coat at $r \ll \lambda$. At zero tension, the free energy (1) is minimum when the mean curvature is zero at each point of the membrane, $C_1 + C_2 = 0$ or using Eq. (3),

$$\dot{\psi} + \frac{\sin\psi}{r} = 0\ . \tag{9}$$

The solution of this equation combined with Eq. (2) is the catenoid,

$$r = \sqrt{(s - s_0)^2 + r_0^2}, \quad \psi = \arcsin\left(\pm\, r_0/r\right), \quad z = \mp\, r_0\ \mathrm{arcosh}(r_0/r) + z_0\ ,$$
$$\text{with}\ \ s_0 = R\cos\alpha\sin\alpha\ \ \text{and}\ \ r_0 = R\sin^2\alpha\ . \tag{10}$$

The sign in the second equation (resp. third equation) is $+$ if $s > s_0$ (resp. $-$), and reciprocally if $s < s_0$. The integration constants s_0 and r_0 are determined using the boundary conditions; r_0 is the neck radius at the narrowest position when $\alpha > \pi/2$. The principal curvatures are in general $C_1 = -C_2 = r_0/r^2$ and take their maximum absolute value $1/r_0$ where the neck is the narrowest.

Equation (10) provides a good approximation of the membrane shape near the coat, for $r \ll \lambda$. On the other hand, at large distance from the coat, the deformation is weak and the shape obeys (8). According to (10), the weak deformation condition holds for $r \ll r_0$. Thus, the ranges of validity of the two approximations, weak deformation at $r \gg r_0$ and catenoid at $r \ll \lambda$, overlap. Matching the two approximations gives the integration constants: $\beta = r_0/\lambda$ in (8) and, $z_0/r_0 = -\gamma_e + \ln(4\lambda/r_0)$ in (10) with $\gamma_e \simeq 5.77$ the Euler constant.

3.1.3 Large Tension

In the limit $(R/\lambda)\sin\alpha \gg 1$, the deformation is localized close to the coat boundary, in a region of width λ much thinner than the radius of the coat border $R\sin\alpha$. The

curvature of the coat periphery has a negligible influence on the membrane shape. Keeping only the higher order terms in r, Eq. (4) reduces to,

$$\ddot{\psi}\cos\psi + \frac{\dot{\psi}}{2}\sin\psi - \frac{\sigma}{\kappa}\sin\psi = 0\,. \tag{11}$$

Integrating this equation gives $\dot{\psi} = -2\sqrt{\sigma/\kappa}\,\sin(\psi/2)$ and then,

$$\begin{aligned}
\psi &= 4\arctan\left[\exp\left(\frac{s_0 - s}{\lambda}\right)\right],\\
r &= R\sin\alpha + s + 2\lambda\left[\cos\left(\frac{\alpha}{2}\right) - \tanh\left(\frac{s - s_0}{\lambda}\right)\right],\\
z &= \frac{2\lambda}{\cosh\left(\frac{s-s_0}{\lambda}\right)}\,, \quad \text{with} \;\; s_0 = \lambda\ln(\tan(\alpha/4))\,.
\end{aligned} \tag{12}$$

The second and third relations are obtained from Eq. (2) and s_0 is deduced from the boundary conditions. The membrane curvature $C_1 = \dot{\psi}$ ($C_2 \ll C_1$) is maximum (in absolute value) at the coat boundary, $C_1 = (\sin\alpha/2)/\lambda$.

3.2 Energy of the Membrane Bud

The membrane energy associated with the formation of a single protrusion from a flat membrane is obtained by subtracting the energy of the flat membrane to the energy of the deformed membrane,

$$\mathcal{F}_{\text{bud}} = \mathcal{F}_{\text{m}} - \sigma A_0\,, \tag{13}$$

where $\mathcal{F}_{\text{m}}$ is given by (1) and A_0 is the area of the initially flat membrane. The bud energy can be split into two contributions, the contribution from the membrane area under the coat and the contribution from the rest of the membrane (the neck),

$$\mathcal{F}_{\text{bud}} = \mathcal{F}_{\text{cap}} + \mathcal{F}_{\text{neck}}\,. \tag{14}$$

In the coat region, using the spherical cap approximation, the principal curvatures are $C_1 = C_2 = 1/R$. The spontaneous curvature of the membrane is assumed to be zero $C_0 = 0$. Characterizing the coat assembling state by x, the ratio of the cap area to the complete sphere (5), the cap area is $A = 4\pi R^2 x$ and $A_0 = \pi(R\sin\alpha^2) = 4\pi R^2 x(1-x)$. The energy of the membrane bound to the coat is,

$$\mathcal{F}_{\text{cap}} = 8\pi\kappa x + 4\pi\sigma R^2 x^2\,. \tag{15}$$

The energy of the neck is obtained by inserting the solution of the shape equations (4), (2) in the free energy (3) and by using $A_0 = 2\pi \int_0^{s_1} r \cos\psi$. Using the approximate expressions for the shape derived in the preceding section, one obtains (see [28] for detailed calculations),

$$\mathcal{F}_{\text{neck}} \simeq \begin{cases} 16\pi\sigma R^2 x^2 (1-x)^2 \big(-\gamma_e + \frac{x}{2(1-x)} - \ln\big(R\sqrt{\sigma/\kappa}\sqrt{x}(1-x)^{3/2}\big)\big) \\ 16\pi\sqrt{\kappa\sigma}R\sqrt{x(1-x)}\left(1-\sqrt{1-x}\right) \\ \quad +4\pi\kappa\left(x-4+4\sqrt{1-x}-2\ln\left(\frac{1+\sqrt{1-x}}{2}\right)\right). \end{cases} \tag{16}$$

The first line is the limit of low tension ($R\sin\alpha \ll \lambda$) with $\gamma_e \simeq 5.77$ the Euler constant, and the second line is the limit of large tension ($R\sin\alpha \gg \lambda$). Figure 3 shows the energy obtained numerically as a function of x in the large and low tension limits. It shows the good accuracy of the above approximate expressions.

3.3 *Budding or Not Budding? Influence of the Tension and Rigidity*

Vesicle budding is driven by the free energy gained by polymerizing proteins. The polymerization energy per unit of coat area μ accounts for protein–protein binding energy, for membrane–protein binding energy, and for the loss of entropy of the proteins initially dispersed in the cytosol. In the case of clathrin coat, the polymerization energy has been estimated to be $\sim 20\ k_{\text{B}}T$ per clathrin molecules or $\mu \sim 3\ k_{\text{B}}T/\text{nm}^2$ [19, 86]. For coat assembling to occur, the polymerization energy gain must counter-balance the cost associated with membrane deformation. Depending on the tension σ, the rigidity κ, and the polymerization energy μ, vesicle budding may or may not be possible.

The energy required to form a coat of spherical cap shape with the completion degree x reads,

$$\mathcal{F} = 4\pi\tau R\sqrt{x(1-x)} - 4\pi\mu R^2 x + \mathcal{F}_{\text{bud}}(x) \tag{17}$$

The last term $\mathcal{F}_{\text{bud}}$, the energy cost of the membrane deformation, is discussed in the preceding section. The second term is the energy gain due to coat polymerization $\mu \times A_c$. The first term accounts for the loss of binding energy of the coat components located at the coat edge. It is proportional to the line tension $\tau \sim k_{\text{B}}T/\text{nm}$ and to the coat perimeter $2\pi R\sin\alpha = 4\pi R\sqrt{x(1-x)}$.

Figure 4 shows a phase diagram obtained by minimizing the free energy (17). Depending on the value of $\sigma R^2/\kappa$ and $\mu R^2/\kappa$, the minimum is found at $x = 0$ (no coat assembling/no budding), or at $x = 1$ (complete vesicle budding), or at an intermediate value $0 < x^* < 1$ corresponding to a state where coat formation is

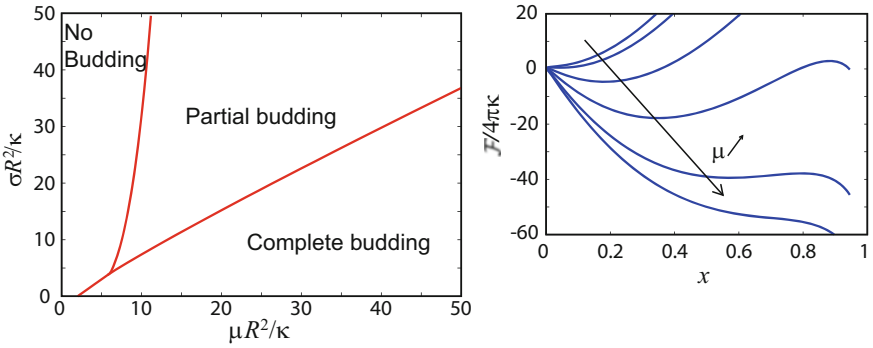

Fig. 4 Right: phase diagram obtained by minimizing $\mathcal{F}(x)$ given by (17). The minimum is either at $x = 0$ (no budding), $x = 1$ (complete budding), or $0 < x^* < 1$ (incomplete budding). Left: profile of $\mathcal{F}(x)$ for different values of μ at fixed $\sigma R^2/\kappa$ (in the large tension regime)

incomplete. The line separating the complete budding regime from the other regions of the phase diagram indicates the polymerization energy μ required to make a complete coat as a function of the tension.

At small tension, $\mathcal{F}_{\rm bud} \simeq 8\pi\kappa x$ at the lowest order in $\sigma R^2/\kappa$. The function $\mathcal{F}(x)$ has a bell shape and the two minimum are at $x = 0$ and $x = 1$. The complete budding state $x = 1$ is the most energetically favorable if

$$\mu > \sigma + \frac{2\kappa}{R^2} \,. \tag{18}$$

At large tension, the energy landscape $\mathcal{F}(x)$ is shown in Fig. 4 for different values of μ. The membrane energy is approximately $\mathcal{F}_{\rm bud} \simeq \sigma R^2 x^2$ at the lowest order in $\kappa/(\sigma R^2)$. The balance with the polymerization energy induces an energy well at

$$x^* \simeq \mu/2\sigma \,. \tag{19}$$

At large μ, the well disappears and the energy is minimum at $x = 1$. At small μ, the line tension prevents the appearance of the well, $\mathcal{F}(x)$ is monotonically increasing and is thus minimum at $x = 0$. The range where the intermediate minimum x^* exists is approximately,

$$(3/2)\tau^{2/3}\sigma^{1/3}R^{4/3} < \mu < 2\sigma \,. \tag{20}$$

The left side inequality is obtained by calculating the value of μ where the $\mathcal{F}(x)$ as an inflexion point using the approximation $\mathcal{F}_{\rm bud} = \sigma R^2 x^2$ and $x \ll 1$. The right side inequality is deduced from the condition $x^* > 1$ using the approximation (19).

The main prediction of this simple model is that tension and rigidity can either prevent coat assembling, or arrest coat assembling in an incomplete state. How does it compare to experimental observations? In vitro reconstitution of COPI

coat assembling on liposomes, on GUV [64], and on lipid droplets [107, 108] demonstrates that budding is much favored at low tension and almost inhibited at large tension. On lipid droplets, the threshold tension was found to be $\simeq 2 \times 10^{-3}$ N/m, which is located in the high tension regime of the phase diagram ($\sigma R^2/\kappa \simeq 900$ using $R = 60$ nm for COPI vesicles and $\kappa = 2\ k_B T$ for the monolayer bounding lipid droplets). Reconstitution of clathrin coat assembling on GUV [86] leads to similar results. Increasing tension and rigidity can impair clathrin assembling and even more striking, electron microscopy images showed the existence of stable shallow buds for an intermediate range of tension in agreement with theoretical predictions.

In living cell, the influence of tension on coat assembling has first been observed indirectly. Raucher and Sheetz [79] have shown strong correlation between the tension of the plasma membrane and the endocytosis rate, and thus indirectly on the rate of clathrin coated vesicle production. They suggested that tension could be an important regulator of endocytosis, its increase being responsible for the dramatic inhibition of endocytosis during mitosis. As a second example, a drug responsible for Golgi swelling, and presumably inducing the increase of its tension, is known to block COPI assembling, dramatically modifying the Golgi morphology [106].

More recently, Boulant et al. [7] have shown that actin is required for clathrin coated vesicle formation when the membrane tension is high. Disrupting actin polymerization, they observed that in membrane with high tension, clathrin coats remain arrested in an incomplete state, as predicted by the model. By pulling or pushing on the membrane bud, actin may provide the energy required to counterbalance the surface energy cost associated with coat growth. The force exerted by actin has been included in a continuous mechanical model of vesicle budding by Walani et al. [116]. They showed that this force applied to a partially coated bud leads to complete vesicle formation. The role of the tension in this actin-assisted budding case is also investigated.

Note finally that the spherical cap model studied in this section may also apply to caveola. Caveola are plasma membrane invaginations induced by oligomerization of caveolin proteins. Stretching the plasma membrane to increase the tension has been shown to lead to caveola disappearance [95].

3.4 Coat with Finite Rigidity

The vesicles produced by coat assembling can have different radius, allowing to incorporate cargo of different size [47, 68]. Clathrin coats can even form flat structures sometime named “plaques” [50]. One may wonder whether membrane tension or rigidity could influence the size and morphology of the coat. It has been proposed, for example, that high tension could lead to caveola flattening [91].

To address this issue, the spherical cap model can be generalized by assuming that the coat is an elastic layer with bending rigidity κ_c and preferential curvature radius R_c. For clathrin coat, the rigidity has been measured and is $\simeq 300\ k_B T$

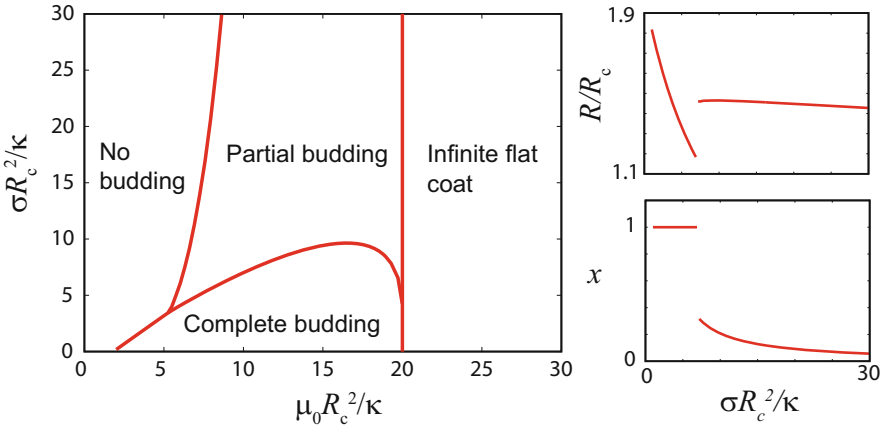

Fig. 5 Left: phase diagram for coat with finite rigidity $\kappa_c = 10\kappa$. Right: equilibrium value of R (top) and x (down) function of $\sigma R_c^2/\kappa$ for $\mu_0 R_c^2 \kappa = 10$

[48]. The morphology of the coat should then be calculated by solving the shape equation (4) in the coat and in the neck regions, as in [1, 116]. For simplicity here, let's assume that the coat shape is still a spherical cap with a radius R, which is now a free variable. The polymerization energy per area unit reads,

$$\mu(R) = \mu_0 - 2\kappa_c \left(\frac{1}{R_c} - \frac{1}{R} \right)^2 . \tag{21}$$

In a thermodynamic approach, the preferential state of a coat is obtained by minimizing $\mathcal{F}(x, R)$ (17), in which μ is given by (21), with respect to the two free variables x and R (or R and A_c, the coat area (5)). The new phase diagram is shown in Fig. 5. The three states $x = 1$, $x = 0$, and $0 < x < 1$ are still present. The most striking difference as compare to the case with infinite coat rigidity, shown in Fig. 4, is the vertical line delimiting a new state at high μ_0. In this region of the phase diagram, a coat assembles into a flat structure, which grows without bound. This prediction can be easily understood by considering the energy of a flat coat expressed as a function of the coat area A_c,

$$\mathcal{F} = \tau \sqrt{4\pi A_c} - (\mu_0 - 2\kappa_c / R_c^2) A_c . \tag{22}$$

It appears that if,

$$\mu_0 R_c^2 > 2\kappa_c , \tag{23}$$

a flat infinite coat is necessarily the energetically most favorable state. At the opposite, when this condition is not fulfilled, a flat coat cannot exist. Interestingly,

this analysis reveals that the transition toward the flat coat state is not controlled by tension.

The influence of the tension on the coat state is shown on the curves on the left of Fig. 5. At low tension, in the complete budding phase ($x = 1$), when increasing the tension, the radius decreases as

$$R = \frac{2\kappa_c R_c}{(\sigma - \mu_0)R_c + 2\kappa_c}, \tag{24}$$

which is derived from the condition, $\partial\mathcal{F}/\partial R(x = 1, R) = 0$. Once the boundary with the partial budding phase is crossed, increasing the tension has almost no effect on the radius R, while x decreases. As a conclusion, this model predicts that tension induces coat disassembling rather than flattening.

The elastic sheet model for the coat, Eq. (21), is certainly too simple to accurately describe important morphology change, which involves modifications of the internal molecular structure of the coat. Coat proteins can indeed adopt different arrangements to which correspond different radii [12, 23, 24, 40, 102, 123]. The polymerization energy $\mu(R)$ should thus have a discrete number of maximum, corresponding to allowed structures. Moreover, to go further on the study of the influence of the mechanical properties of the membrane on morphology selection, a kinetic description of coat growth is required [29]. The coat might be unable to reach the absolute free energy minimum, being kinetically trapped in some regions of the phase space. The membrane tension could not only affect the free energy of the different structures but also the height of the energy barriers separating them, allowing or not the coat to evolve toward a given structure.

4 Tubule Budding

Membrane tubules, with a radius of a few tens of nanometers and of several hundred nanometers long, are the second major type of transport carriers between the different cell compartments. Tubule budding is observed in the endoplasmic reticulum for transport toward the Golgi apparatus, in the Golgi for transport between the stacks of the Golgi and toward the endosomes or the plasma membrane, and in early and late endosomes for transport toward the plasma membrane or the Golgi, for a review see [75]. Three mechanisms can lead to tubule nucleation and growth from an initially flat membrane.

1. Application of a localized force normal to the membrane. This force can be generated by molecular motors bound to the membrane and walking along a microtubule, or by filaments pushing the membrane [21].
2. Polymerization on the membrane of proteins into a cylindrical rigid coat. Several proteins such as Dynamin, ESCRT III, Amphiphysin 1, and F-BAR domain have been found to form such cylindrical coats able to drive tubule formation [33,

41, 84, 98, 105]. The vesicle-generating coats COPI and COPII are also able to assemble into tubes [121, 123]. In vivo this mechanism could be involved for tubule formation in endosomes [16, 17] and for endoplasmic reticulum tubules stabilization [45].

3. High concentration of proteins inducing spontaneous curvature. Proteins that favor membrane bending, either by insertion of amphipathic helix [25, 57, 60], or by the binding of curved shape domains [11, 98], or by steric repulsion [99, 100], have all been observed to generate tubules.

In vivo several of the aforementioned basic mechanisms may come into play at the same time.

For the three mechanisms, the conditions required for the nucleation and growth of a single membrane tubule connected to a membrane of fixed tension are analyzed in the following. The shape of a tubule comprises a nearly cylindrical tube, the tip closing the tubule, and the neck connecting the tube to the rest of the membrane. The force acting at the tubule tip (defined positive when it opposes elongation) is,

$$f = \frac{\partial \mathcal{F}}{\partial L} \tag{25}$$

where L is the tubule length and $\mathcal{F}$ its free energy. A tubule elongates if $f \leq f_{\text{ext}}$, where f_{ext} is an externally applied force generated by molecular motors or active rigid filaments, for example, and shrinks and disappears in the opposite case. In the absence of external force, the stability of a tubule is determined by the sign of f. For long tubule, the free energy contributions from the tip and from the neck are independent of the tubule length, and hence do not contribute to the force f. Long tubule can hence be modeled in a first approximation as cylindrical membrane connected to a membrane reservoir. Note that in the following the effect of a pressure difference on each side of the membrane is neglected.

4.1 Tubule Pulled by an External Force

Pulling on a small area of a large membrane leads, at large displacement, to tubule formation [20, 42, 43, 76, 78]. The free energy of a tubule pulled from a membrane with no spontaneous curvature ($C_0 = 0$) and connected to a membrane reservoir of tension σ can be obtained from Eq. (1) by approximating the tubule shape as a cylinder of length L and radius R (the principal curvatures are thus $C_1 = 0$ and $C_2 = 1/R$),

$$\mathcal{F} = \left(\frac{\kappa}{2R^2} + \sigma \right) 2\pi RL \ . \tag{26}$$

The radius is not fixed a priori but minimizes $\mathcal{F}$,

$$R = \sqrt{\frac{\kappa}{2\sigma}} \,. \tag{27}$$

The force opposing tube elongation, defined by (25), is then,

$$f = 2\pi\sqrt{2\kappa\sigma} \,. \tag{28}$$

This is the force that has to be applied at the tip to stabilize the tubule. When the externally applied force is larger, $f_{\text{ext}} > 2\pi\sqrt{2\sigma\kappa}$, the tube elongates; for smaller force the tubule shrinks and collapses. The larger the tension, the thinner is the tubule and the larger is f. Taking $\kappa = 10^{-19}$ J and $10^{-6} < \sigma < 10^{-3}$ N/m, the radius and force are in the range $8 < R < 200$ nm and $5 < f < 100$ pN.

Under the cylindrical tube approximation and assuming a constant membrane tension independent of the tube length, the force f is independent of the length. This prediction is certainly valid at large L but should fail at early stage of tubule formation. To get more insight on the tubule shape and nucleation process, one has to solve Eqs. (2), (4) governing the shape of the membrane. The tubule shape computed numerically for different pulling forces f is shown in Fig. 6. In the neck region, far from the tube $r \gg R$, the rigidity has a negligible influence. The shape equation (4) reduces to $\sigma \sin\psi + f/2\pi r = 0$ and the shape is thus approximately a catenoid [76],

$$\psi = \arcsin\left(-\frac{f}{2\pi\sigma r}\right) \quad \text{for } r \gg R \,. \tag{29}$$

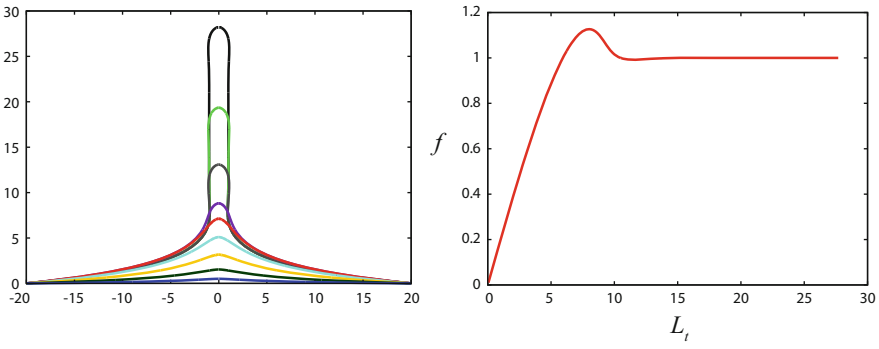

Fig. 6 Left: Tubules formed by applying punctual forces of different magnitudes at the center of a membrane disk connected to a reservoir, $f/2\pi\sqrt{2\kappa\sigma} = 0.1$ (blue), 0.3 (dark green), 0.6 (orange), 0.9 (sky blue), 1.1 (red), 1.1 (purple), 0.9965 (grey), 1 (green), 1 (black). The unit length is $\sqrt{\kappa/2\sigma}$. Right: force f (in $2\pi\sqrt{2\kappa\sigma}$ unit) at the tubule tip as a function of the total tubule length (from the disk edge to the tip)

(We remind that ψ and r characterizing the membrane shape are defined in Fig. 1.) When f is large enough, a tubular shape emerges. The tube is not perfectly cylindrical but shows small amplitude oscillations of the radius near the tip and neck. The force required to sustain the tubule as a function of the total tubule length, shown in Fig. 6, is non-monotonous. The force reaches a plateau $f = 2\pi\sqrt{2\kappa\sigma}$ at large length as predicted, but in order to nucleate the tube, a force larger by 13% has to be applied. See [20] for a more detailed analysis.

In vivo the force can be generated by molecular motors bound to the membrane and to microtubules or to actin filaments. Formation of tubules at the endoplasmic reticulum and the Golgi in particular requires molecular motors and microtubules [18, 26, 114, 117]. Membrane tubules can be produced in minimal artificial system with GUV containing motors in contact with a microtubule or actin network [53, 58, 83, 120].

Motors are able to pull-out membrane tubules only if the retracting force f due to tension and rigidity (28) is lower than the maximum force f_c that the motors can exert. The cooperation of several motors is necessary when f exceeds the stall force of an individual motor. In this case, f_c not only depends on the motor stall force, but also on the density of motors bound to the membrane and on kinetic parameters characterizing the motor [53, 58, 83, 92, 120]. For example, kinesin motors form a dynamical cluster at the tubule tip, pulling together the tubule by moving along microtubule [53, 58]. The form of f_c in this case is discussed in Appendix 2. In the case of myosin 1b, a non-processive motor that binds actin with catch-bond property (the unbinding rate increases with tension), the behavior is more complex [120]. At low density of motors, tubule formation is prevented at large f and, more surprisingly because of the catch-bond effect, also prevented at low f.

4.2 Tubule Formation Driven by Rigid Coat Polymerization

Tubule can be generated by the polymerization of proteins into a cylindrical rigid coat, which imposes its shape to the membrane. As for spherical coats discussed in Sect. 3, tubule formation results in this case from the competition between the polymerization energy driving tubule growth and, tension and rigidity opposing growth. The free energy of tubule formation reads in this case,

$$\mathcal{F} = \left(\frac{\kappa}{2R^2} + \sigma - \mu\right) 2\pi RL + \mathcal{F}_0 \,, \tag{30}$$

The first term is the energy of the coated tube, which comprises the membrane deformation cost and the polymerization energy with μ the free energy gained (per unit area) by the polymerizing proteins. The second term, $\mathcal{F}_0$, accounts for various energy contributions independent of L due to the coat boundary and to the membrane deformation outside the coated tube. The radius R is imposed by the

coat. The force opposing tube elongation (25) reads,

$$f = -2\pi R\mu + 2\pi R\sigma + \frac{\pi\kappa}{R} \; ; \tag{31}$$

In the absence of an external force, the tubule elongates if f is negative, i.e., if,

$$\mu > \sigma + \frac{\kappa}{2R^2} \; , \tag{32}$$

and collapses in the opposite case. For a tubule of 20 nm radius, $\pi\kappa/R \simeq 10\,\mathrm{pN}$ and $2\pi\sigma R$ can vary in between 0.1 and 100 pN for plausible biological membrane tension. The polymerization energy depends on the coat protein interactions and on the concentration of proteins in the reservoir. For the protein dynamin, which assembles into tubes, the polymerization force has been measured in vitro, $2\pi R\mu \simeq 18\,\mathrm{pN}$ at a dynamin concentration of 12 µM [84]. Large tension can thus prevent dynamin tube growth. In vitro experiments with dynamin also confirmed the linear dependency of the tubule force f with the tension σ, and that at low dynamin concentration (i.e., low μ) the coat is not able to sustain the tubule.

In the presence of an external force, produced, for example, by motors, the growth condition is $f < f_{\mathrm{ext}}$. Even if the external force opposes growth ($f_{\mathrm{ext}} < 0$), a tubule can grow provided that the polymerization energy is large enough.

The constant energy term $\mathcal{F}_0$ in (30) generates a nucleation barrier: even if the condition (32) is fulfilled, the initial formation of a short tubule may be energetically unfavored ($\mathcal{F} > 0$). The nucleation of a coat with short length ℓ (of the order of the size of the assembling proteins) occurs only if the polymerization energy is large enough so that the energy $f\ell + \mathcal{F}_0$ is negative or not much larger than $k_{\mathrm{B}}T$. The free energy $\mathcal{F}_0$ includes different contributions,

$$\mathcal{F}_0 = \mathcal{F}_{\mathrm{b}} + \mathcal{F}_{\mathrm{tip}} + \mathcal{F}_{\mathrm{neck}} \; . \tag{33}$$

The first term is the loss of binding energy of the proteins at the coat boundaries. The second and third terms arise from the membrane deformation induced by the coat in the tip and neck region, respectively. In these regions, the membrane shape is obtained by solving Eqs. (2), (4), with the angle $\psi = \pi/2$ imposed by the coat at its border. For a tubule emerging from an initially flat membrane, $\mathcal{F}_{\mathrm{tip}}$ and $\mathcal{F}_{\mathrm{neck}}$ can be estimated, in the small and large tension limits, using the results of Sect. 3.1,

$$\mathcal{F}_{\mathrm{tip}} \simeq \begin{cases} 4\pi\kappa \\ 4\pi R\sqrt{2\kappa\sigma} \end{cases}, \mathcal{F}_{\mathrm{neck}} \simeq \begin{cases} \pi\sigma R^2\left(-\gamma_e + \frac{1}{2} - \ln(4R\sqrt{\sigma/\kappa})\right) & R^2\sigma/\kappa \ll 1 \\ 4\pi R\sqrt{2\kappa\sigma} & R^2\sigma/\kappa \gg 1 \end{cases} \tag{34}$$

For the neck, the shape and energy are the same as those reported in Sect. 3.1 and 3.2 in the case $x = 1/2$ or $\alpha = \pi/2$. For the tip, neglecting the tension, the equilibrium membrane shape is a hemisphere of radius R. Its bending energy is thus $4\pi\kappa$. At

large tension ($R^2\sigma/\kappa \gg 1$), the membrane is highly curved very near the coat edges and flat elsewhere. As discussed in Sect. 3.1.3, the deformation is almost unidimensional and the energy should be approximately same in the tip and in the neck.

The nucleation energy is much reduced if the coat nucleates in already deformed membrane with nearly tubular shape, in particular on the membrane neck connecting a budding vesicle to the rest of the membrane. If the neck radius matches the coat radius, $\mathcal{F}_{\text{neck}}$ and $\mathcal{F}_{\text{tip}}$ vanish. This could explain why, in cell, dynamin or ESCRT proteins assemble only at the neck of budding vesicles. In other membrane regions, the nucleation barrier might be too large to be counter-balanced by the polymerization energy. To support this hypothesis, it has been observed that at physiological concentration, dynamin tube does not nucleate on flat membrane but can nucleate on already existing tubular membrane with appropriate radius [84].

4.3 Influence of Curvature-Inducing Proteins on Tubule Formation

We discuss finally the emergence of tubules on a membrane containing proteins able to bend the membrane. In the simplest approach, the effect of the proteins is to give rise to a spontaneous curvature C_0 of the membrane. Campelo et al. [10, 54] have shown theoretically that the spontaneous curvature induced by amphipathic helix insertion is proportional to the surface fraction ϕ of proteins bearing such helix, $C_0 = c\phi$ with $c \simeq 1\,\text{nm}^{-1}$, in a wide range of density. At low density, proteins with curved domains adhering on the membrane have the same effect [63] with $c = 0.15\text{nm}^{-1}$ for N-BAR domain [4]. When the spontaneous curvature is induced by the lateral pressure arising from the steric repulsion between the membrane-bound proteins, a simple calculation [99] gives $C_0 = -ph/\kappa$ where p is the lateral pressure and h the membrane half-thickness.

4.3.1 Tubule Formation on a Membrane with Spontaneous Curvature

Let's consider first that the membrane is homogeneously covered with a fixed surface fraction of curvature-inducing proteins that provide a spontaneous curvature to the membrane. The free energy associated with the formation of cylindrical membrane tube with curvatures $C_1 = 0$ and $C_2 = 1/R$ and length L, budding on (and connected to) a flat membrane with tension σ, is obtained from (1) [21, 125],

$$\mathcal{F} = \left(\frac{\kappa}{2R^2} - \frac{\kappa C_0}{R} + \sigma\right) 2\pi RL \tag{35}$$

The equilibrium radius and the retracting force (25) are then,

$$R = \sqrt{\frac{\kappa}{2\sigma}}\,, \quad f = 2\pi\kappa\left(\frac{1}{R} - C_0\right)\,. \tag{36}$$

Proteins inducing positive spontaneous curvature favor tubule budding. The larger the spontaneous curvature, the smaller the force f required to sustain the tube. The force vanishes when RC_0 approaches one.

Equation (36) suggests that a tube could spontaneously grow in the absence of external force if $1/R < C_0$, i.e., if $\sigma < \kappa C_0^2/2$. However, in this case a membrane tube is no longer stable (in the absence of pressure difference on each side of the membrane). The shape in this case should rather be a necklace of spheres [8, 21, 63, 89, 111, 112, 124] connected each other by a very thin neck. A cylindrical tube cannot spontaneously emerge in a membrane with (isotropic) spontaneous curvature without external force. Yet, the spontaneous curvature can strongly reduce the intensity of the required force.

4.3.2 Curvature–Concentration Coupling

In general, the density of proteins is not fixed and can be heterogeneous. Curvature-inducing proteins should concentrate in membrane regions with a curvature matching their preferential curvature, enhancing the local curvature.

The free energy functional of the local mean curvature $2H = C_1 + C_2$ and local surface concentration of proteins, ϕ, of a membrane piece of tension σ in contact with a reservoir of proteins is,

$$\mathcal{F}_\mathrm{m} = \int_A \left[\frac{\kappa(\phi)}{2}\big(2H - C_0(\phi)\big)^2 + g(\phi) + \sigma\right] dA\,, \tag{37}$$

where $g(\phi)$ is the free energy per unit area of the proteins on a flat membrane. Neglecting protein–protein interaction, this term reads,

$$g(\phi) = k_\mathrm{B}T\rho\big[\phi\ln\phi + (1-\phi)\ln(1-\phi)\big] - \mu_0\rho\phi\,, \tag{38}$$

where the first term is the mixing entropy with ρ, the inverse of the area of a molecule, and μ_0 is the difference between the chemical potential of the protein reservoir and the binding energy of a protein. At equilibrium, the local fraction of proteins minimizes the free energy, $\delta\mathcal{F}_\mathrm{m}/\delta\phi = 0$. The ϕ-dependence of C_0 and κ couples the equilibrium density to the equilibrium curvature. The density of proteins depends on the local curvature. In the case of a tubule connected to flat membrane reservoir, the density on the tube and on the flat membrane is different.

The free energy associated with the formation of a cylindrical membrane tube with surface fraction ϕ of proteins, radius R, and length L from a flat membrane

with surface fraction ϕ_0 of proteins is,

$$\mathcal{F} = \left(\frac{\kappa(\phi)}{2R^2} - \frac{\kappa(\phi) C_0(\phi)}{R} + \bar{g}(\phi) + \sigma \right) 2\pi R L \,, \tag{39}$$

where $\bar{g}(\phi) = g(\phi) - g(\phi_0) + \kappa(\phi) C_0(\phi)^2/2 - \kappa(\phi_0) C_0(\phi_0)^2/2$. The surface fraction in the flat membrane reservoir satisfies $\bar{g}'(\phi_0) = 0$, where the prime denotes the derivative respect to ϕ.

If the case of a weak density-curvature coupling, the free energy density in (37) can be expanded at the quadratic order in H and ϕ by assuming,

$$\kappa(\phi) = \kappa \,, \quad \bar{g}(\phi) = \frac{\chi}{2}(\phi - \phi_0)^2 \,, \quad C_0(\phi) = C_0(\phi_0) + c(\phi - \phi_0) \,, \tag{40}$$

where according to (38), $\chi = \frac{k_B T \rho}{\phi_0(1-\phi_0)} + \kappa c^2$. One then recovers Leibler's model [61, 62], which yields, using $\delta \mathcal{F}_m / \delta \phi = 0$, a linear relation between the deviation of the protein surface fraction and the curvature,

$$\phi - \phi_0 = \frac{2\kappa c}{\chi} H \,. \tag{41}$$

Inserting (40) and (41) with $2H = 1/R$ in (39), the free energy of tube formation is the same as (35) replacing C_0 by $C_0(\phi_0)$ and κ by an effective rigidity $\tilde{\kappa} = \kappa \left(1 - \kappa c^2/\chi\right)$. Doing the same replacements in (36), one obtains the equilibrium radius R and force f. The radius scales as $\sim \sigma^{-1/2}$ as in the absence of proteins. The force is an affine function of $\sqrt{\sigma}$ vanishing at a finite tension. All these features have been observed experimentally in vitro on membrane tubules pulled from GUV and covered by amphiphysin proteins [98]. The authors obtained $1/c$ of the order of 1–5 nm.

Figure 7 shows the tubule shape computed numerically, in the weak coupling approximation (40) for two different values of $RC_0(\phi_0)$. When $RC_0(\phi_0)$ approaches 1 (right panels), the tube resembles a sphere necklace at small length. At larger L, the tube is nearly cylindrical at the center but keeps an undulating shape at the extremities. The force f needed to pull the tube drops when $RC_0(\phi_0) \to 1$, as predicted. As already discussed, for $RC_0(\phi_0) < 1$ a tube is no longer stable. Figure 7 shows also the protein density along the tube: $\phi = \phi_0$ at the basis and $\phi \simeq \phi_0 + \kappa c/\chi R$ in the tube.

4.3.3 Anisotropic Spontaneous Curvature

Proteins with crescent shape, such as those with a BAR domain, induce anisotropic deformation of the membrane in their vicinity and their orientation is coupled to the local curvature of the membrane. For strong coupling, an orientational order should appear favoring anisotropic bending of the membrane [31, 56]. Simulations of membrane containing anisotropic curvature-inducing proteins [4, 73, 77] show

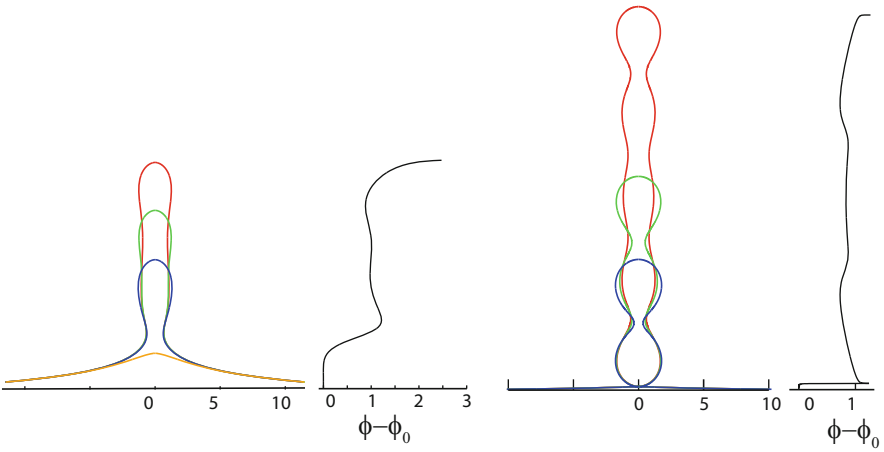

Fig. 7 The color curves show the contour of a tubule at different elongations L obtained by applying a normal punctual force f to a flat membrane containing curvature-inducing proteins. The black curves show $\phi - \phi_0$ function of z. Two sets of parameters have been used. Left: $(\kappa/\tilde{\kappa})RC_0(\phi_0) = 0.5$ and $f/2\pi\sqrt{\sigma\tilde{\kappa}} = 0.5$. Right: $(\kappa/\tilde{\kappa})RC_0(\phi_0) = 0.95$ and $f/2\pi\sqrt{\sigma\tilde{\kappa}} = 0.05$. The unit of length is R given by (36) and the unit of ϕ is $\kappa c/\chi R$

that the proteins aggregate because of curvature-mediated interactions, forming dense nematic phase domains. In these domains, the membrane is strongly curved and often adopts a tubular shape. Thus, unlike proteins inducing isotropic curvature, proteins inducing anisotropic curvature are able to drive stable tubule formation in the absence of external force.

In a nematic ordered phase the elastic free energy of the membrane with the proteins comprises additional terms, as compared with (1), favoring anisotropic bending [31, 56]. Different equivalent formulations can be found in the literature [32, 77, 115]. Using the expression of [77] it reads,

$$\mathcal{F}_{\rm m} = \int_A \left[\frac{\kappa}{2}(2H)^2 + \frac{\kappa_\parallel}{2}(C_\parallel - C_{0\parallel})^2 + \frac{\kappa_\perp}{2}(C_\perp - C_{0\perp})^2 + \sigma\right] dA + \mathcal{F}_{\rm nematic}\,, \quad (42)$$

where $2H = C_1 + C_2$, $C_\parallel$ and $C_{0\parallel}$ are the curvature and spontaneous curvature in the direction of the nematic director $\mathbf{n}$, $C_\perp$ and $C_{0\perp}$ are the curvature and spontaneous curvature in the direction normal to $\mathbf{n}$, and $\kappa_\parallel$ and $\kappa_\perp$ are bending moduli. The last term $\mathcal{F}_{\rm nematic}$ accounts for the heterogeneity of the nematic orientation.

The free energy of a cylindrical membrane tube with homogeneous nematic director orientation characterized by the angle θ with the orthoradial direction budding from a flat membrane with nematic order is,

$$\mathcal{F} = \left[\frac{\kappa}{2R^2} + \frac{\kappa_\parallel \cos^4\theta}{2R^2} - \frac{\kappa_\parallel C_{0\parallel}\cos^2\theta}{R} + \frac{\kappa_\perp \sin^4\theta}{2R^2} - \frac{\kappa_\perp C_{0\perp}\sin^2\theta}{R} + \sigma\right] 2\pi RL\,. \quad (43)$$

The analysis of the tube properties can be found in [77]. Here for simplicity, only the simple case with $\kappa_\perp = 0$ is analyzed. Minimizing the energy (43) with respect to θ and R, and computing the force (25), one obtains,

$$\cos^2\theta = C_{0\parallel} R\ , \quad R = \sqrt{\frac{\kappa}{2\sigma - \kappa_\parallel C_{0\parallel}^2}}, \quad f = \frac{2\pi\kappa}{R}\ , \quad \text{for } RC_{0\parallel} \leq 1\ ,$$
$$\cos^2\theta = 1\ , \quad R = \sqrt{\frac{\kappa + \kappa_\parallel}{2\sigma}}, \quad f = 2\pi(\kappa + \kappa_\parallel)\left(\frac{1}{R} - \frac{\kappa_\parallel}{\kappa + \kappa_\parallel} C_{0\parallel}\right), \quad \text{for } RC_{0\parallel} \geq 1\ , \tag{44}$$

At large tension (first line), the tube principal curvature is larger than the spontaneous curvature, the proteins can orientate so that the curvature along their direction matches the spontaneous curvature. Thus interestingly, the orientation depends on the tension at large tension. When $R = 1/C_{0\parallel}$, the proteins orientate perpendicular to the tube direction. The proteins keep this orientation at lower tension (second line), when the radius is too large for $C_\parallel$ to match $C_{0\parallel}$. The force vanishes at finite tension $2\sigma = \kappa_\parallel^2 C_{0\parallel}^2/(\kappa_\parallel + \kappa)$, implying the spontaneous growth of tubule at lower tension. To go further in the study of the shape and stability of tubes formed in membrane with anisotropic spontaneous curvature requires the analysis of the shape equations, which have been derived in [115].

5 Membrane Fusion in Intracellular Trafficking

After budding from a donor compartment, transport vesicles and tubules travel in the cell and eventually fuse with the membrane of the target compartment. The fusion process is discussed in more detail in chapter "Common Energetic and Mechanical Features of Membrane Fusion and Fission Machineries." In this section, we focus on the influence of the membrane tension in the fusion of intracellular vesicles.

Lipid bilayers are very stable objects that do not fuse spontaneously in general. Unlike the budding process described before, the fusion of two membranes requires major rearrangements of the molecules with the formation of several intermediate structures during the fusion process. These metastable structures are separated by energetic barriers that have to be overcome for fusion to succeed (a schematic view of the different barriers deduced from molecular simulations works is proposed in [65]). In vivo the fusion of intracellular vesicles is ensured by an energy consuming protein machinery, the SNARE complex, which can alone trigger fusion [118], possibly assisted by other proteins [13, 71]. Though the exact way by which SNAREs mediate fusion is still under debate, it is believed that the main role of the SNARE complex is to act as a pin that pulls on the two membranes to put them in very close proximity.

Because fusion involves processes taking place at the molecular level, its study is rather challenging both theoretically and experimentally. On the theoretical side, continuum media approaches such as those used in Sects. 3 and 4 to study budding are of more limited predictive power [55]. Much insights have been gained this last decade by the use of molecular simulations, see [65] for a review, and see [81, 82] for discussions, based on simulation results, on the role of SNARE. The current understanding of the fusion pathways that emerges from simulation studies is summarized in [87].

5.1 Influence of Membrane Tension on Fusion Barriers

Experimental and numerical studies show that membrane tension facilitates membrane fusion. This was first observed in experiments in which the fusion of protein-free membranes was induced by rising the membrane tension by the osmotic swelling of the fusing vesicles [15, 27]. More recently, it has been shown that vesicles stably adhering on a flat lipid bilayer fuse with the bilayer when an extensile strain is applied to the bilayer [103]. The spontaneous fusion of lipid bilayers triggered by high tension has been reproduced in molecular simulations [94]. Simulations, using dissipative particles dynamics, also showed that the average duration of the fusion process decreases exponentially with the tension [38, 39]. Some energy barriers encountered in the fusion process are thus lowered when tension increases.

Tension most probably facilitates the early stage of fusion, from the unfused membranes to the formation of the metastable intermediate structure named "the stalk" [39, 81]. In the first step of fusion, the two membranes have to come in close proximity (a few nm), which is prevented by entropic and hydration repulsion. According to [59], the energy cost of stalk formation rapidly increases when the distance between the membrane increases. Increasing the tension by stretching the membrane and lowering the lipid density should increase the hydrophobicity of the membranes and then decrease the repulsion between the two membranes, thereby helping to cross the first barrier. In the next step identified in simulations prior to stalk formation, few lipids establish bridges between the two facing monolayers by adopting a splayed conformation with each of their tail inserted in a different leaflet, [82, 96, 104]. This prestalk configuration involves the transient exposure of lipid tails to the aqueous solvent and thus the crossing of an energetic barrier. This barrier should also be lower for membrane with higher tension where the area per lipid is larger. Dissipative particle simulations confirm this statement and show that the energy barrier for prestalk formation decreases linearly with tension [38, 39].

Though high tension reduces the height of the fusion barrier, it is still not known whether tension significantly affects the fusion kinetic in the presence of the SNARE machinery. Experimental studies in this direction using simple biomimetic systems would be interesting. In living cells different studies showed that exocytosis (the fusion of intracellular vesicles with the plasma membrane) is stimulated by high

tension [35, 72]. For example, during the growth of plant cells the increase of tension due to cell expansion is believed to trigger the fusion of vesicles in order to incorporate membrane material [72]. The increase of exocytosis activity may be linked to the fact that tension facilitates membrane fusion.

5.2 Transport Driven by Tension Gradient

In analogy with fluid flowing from high pressure to low pressure regions, tension gradients can induce flow inside fluid membranes from low tension toward high tension regions. Such gradients can appear after the fusion of two membranes with different tensions, leading to a flow of membrane molecules in the fusion pore region. The area flux is obtained from the balance of the work produced by the tension difference $\Delta\sigma$ per time unit and the dissipated energy. It has been calculated in [14] for a toroidal pore and in [22] for a long tubular pore,

$$J = \frac{2\pi R^2 \Delta\sigma}{\tilde{\eta}} \tag{45}$$

where R is the pore radius and $\tilde{\eta}$ a 2D viscosity which comprises the different sources of dissipation. For the toroidal pore the dissipation is dominated by the membrane intrinsic viscosity η_s and the friction between the two monolayers μ,

$$\tilde{\eta} = \eta_s a + \eta_r b \,, \tag{46}$$

where a and b are dimensionless geometrical factors, and $\eta_r = \mu h^2$ with h the membrane thickness. The typical values of biological membrane viscosity are in the range $\eta_s \sim 10^{-8}$–10^{-9} kg/s. The viscosity due to inter-layer friction η_r is less well characterized and usually smaller than η_s. For $R = 10\,\text{nm}$ and a realistic tension difference $\Delta\sigma \sim 10^{-5}$ N/m [113], one obtains a flux of the order $J \sim 0.1$–$1\,\mu\text{m}^2/\text{s}$, i.e., a velocity in the pore $v \sim 10\,\mu\text{m}^2/\text{s}$. For a long cylindrical tubule with length L, the dissipation is mainly due to the viscosity of the surrounding fluid η, and thus,

$$\tilde{\eta} = \frac{4\eta L}{\ln(L/R) - 1/2} \,. \tag{47}$$

The flow of membrane drags the fluid in the membrane vicinity leading to a flow of fluid through the pore. Note that the tension gradient also generates a pressure gradient because of the Laplace law, leading to a (smaller) counter-flow. The detailed calculation for a long tubule has been done in [22]. It shows that the net flux of fluid in the tubule is oriented in the same direction as the membrane flux: toward the high tension region. This mechanism allows membrane molecules of the lumen to be pumped from one organelle at low tension toward another at higher tension.

Tension-induced flow might be a powerful way to transport material between two organelles, for instance, through tubules bridging the two membranes. It is faster than diffusion and provides a directionality, crucial in intracellular trafficking. This phenomenon has first been invoked in living cell to explain the absorption of the Golgi apparatus by the ER in cells treated with Brefeldin A [88]. The measure of the difference of the membrane tension between the Golgi and the ER strengthens this hypothesis and more generally the relevance of the mechanism in intracellular trafficking [113]. It might be at work in particular for the transport inside the Golgi [37], where tubular connections between *cisterna* have been observed [66, 110].

6 Intracellular Traffic Regulation by Tension

The mechanical properties of the membrane and in particular the tension affect the elementary processes of intracellular trafficking. Vesicle and tubule budding is prevented at high tension and high tension favors membrane fusion. On the other hand, tension is directly related to membrane area change. Fusion of vesicles brings area to the membrane of the receptor compartment, which should lead to the decrease of its tension. Reversely, vesicle budding and fission by removing area from the donor compartment should increase its tension. The influence of fusion and budding on membrane tension has been observed in in vitro experiments. The tension of GUV fusing with small vesicles drops eventually leading to the membrane destabilization [97]. In lipid droplets the secretion of small vesicles (produced by COPI coat) increases the tension of the droplet until vesicle budding is no longer possible [108]. In the same manner, the unexpected relationship observed in [99] between the length and radius of tubules budding on GUV and the initial volume of GUV revealed that GUV tension increases during tubule growth until the threshold tension of tubule growth is reached.

The mutual influence between the fusion and production of transport vesicles and tubules, and the value of the tension of the donor/target compartment suggests that tension could be a major regulator of intracellular trafficking. It could coordinate the release and entry of transport vesicles and tubules in a compartment. Successive fusions by lowering the tension could trigger tubules or vesicle production [97]. At the opposite, successive vesicle or tubule budding could increase the tension enough to stop further secretion and favor fusion. Such feedback would ensure the compartment stability.

The coordination of material absorption and release is crucial for the intracellular compartments named endosomes. They are sorting platforms that collect, sort, and then send to the proper location of the endocytosed material. For this purpose, they fuse with small vesicles internalized by the cell and release the sorted molecules in different tubules and vesicles. Endosomes work in a collective manner frequently fusing each other [30, 80]. Tension could partly coordinate their activity, allowing vesicle and tubule release only when enough fusion processes have taken place (lowering the tension below the budding threshold) and brought material to be sorted

and released. In order to meet and fuse, endosomes move inside the cell, pulled by molecular motors along cell filaments. Depending on the endosome membrane tension, motor pulling on membrane could either induce tubule budding at low tension, or induce motion when the membrane is stiffer at high tension. It is thus possible that the succession of motion–fusion–tubule release–motion realized by endosomes is regulated to some extent by the endosome tension. High tension would lead to endosome motion until its fusion with another endosome. The resulting drop of the tension would then favor tubule release until the tension has increased again.

Lipid droplets provide another example of cell compartment where tension may have a regulatory role. Lipid droplets are in charge of the storage and on-demand delivery of neutral lipids [67, 109]. COPI coats assemble on their membrane (a monolayer in this case) leading to vesicle release. It has been proposed that the goal of this vesicle secretion is to increase the droplet tension in order to put the droplet in a highly fusogenic state [108, 119]. The membrane of the droplet would then be able to spontaneously fuse with that of the endoplasmic reticulum and create the observed bridges between the two organelles. Such bridge could permit the transfer of enzymes from the endoplasmic reticulum to the lipid droplets, possibly assisted by the tension gradient.

Tension may also be an important physical regulator of the plasma membrane dynamics [36]. Exocytosis (fusion of the plasma membrane with intracellular vesicles) and endocytosis (production of intracellular vesicles by the plasma membrane) are known to be influenced by the membrane tension [35, 72, 79]. They also participate to membrane area regulation, and thus tension regulation, even if in the case of the plasma membrane, tension is also controlled to a large extent by the cytoskeleton and area reservoirs such as caveolae [95]. Tension may also correlate trafficking to other mechanosensitive processes such as cell adhesion and motility [36].

Appendix 1: Shape Equations for Axisymmetric Membrane

The shape of a membrane with cylindrical symmetry can be characterized by the functions $r(s)$, $z(s)$, and $\psi(s)$, where s is the arc length along the shape contour in a plane at a fixed azimuthal angle. r and z are the usual cylindrical coordinates and ψ is the angle between the radial and the tangent vectors, see Fig. 2.

In the most general case in which the membrane undergoes a pressure difference between each side and a force pulling along the z-axis at the contour boundaries, the shape of the membrane minimizes the free energy,

$$\mathcal{G} = \mathcal{F}_{\mathrm{m}} - pV - fL\,, \tag{48}$$

The second term is the energy cost associated with the volume change with $V = \pi \int_0^{s_1} r^2 \sin\psi ds$ the volume enclosed by the membrane and p the pressure difference across the membrane. The last term is included when $L = z(0) - z(s_1) =$

$\int_0^{s_1} \sin\psi ds$ is fixed; f is then the force exerted by the membrane at $s = 0$ and $s = s_1$ in the z direction.

In order to minimize $\mathcal{G}$ with respect to $r(s)$ and $\psi(s)$ accounting for the constrain (2), one has to introduce a Lagrange multiplier $\gamma(s)$ and minimize the functional,

$$S[r(s), \psi(s)] = \frac{\mathcal{G}}{2\pi\kappa} + \int_0^{s_1} \gamma(s)(\dot{r} - \cos\psi)ds = \int_0^{s_1} \mathcal{L}(\psi, \dot{\psi}, r, \dot{r})ds \quad (49)$$

with,

$$\mathcal{L} = \frac{1}{2}\left(\dot{\psi} + \frac{\sin\psi}{r} - C_0\right)^2 r + \frac{\sigma}{\kappa}r - \frac{p}{2\kappa}r^2\sin\psi - \frac{f}{2\pi\kappa}\sin\psi + \gamma(\dot{r} - \cos\psi) \quad (50)$$

The condition $\delta S = 0$ leads to the Euler–Lagrange equations $\frac{\partial\mathcal{L}}{\partial r} - \frac{d}{ds}\frac{\partial\mathcal{L}}{\partial\dot{r}} = 0$ and $\frac{\partial\mathcal{L}}{\partial\psi} - \frac{d}{ds}\frac{\partial\mathcal{L}}{\partial\dot{\psi}} = 0$,

$$\begin{aligned}
\ddot{\psi} &= -\frac{\dot{\psi}\cos\psi}{r} + \frac{\cos\psi\sin\psi}{r^2} - \frac{p}{2\kappa}r\cos\psi + \frac{\gamma\sin\psi}{r} - \frac{f}{2\pi\kappa}\frac{\cos\psi}{r}\,, \\
\dot{\gamma} &= \frac{1}{2}\left(\dot{\psi} - C_0\right)^2 - \frac{1}{2}\frac{\sin^2\psi}{r^2} + \frac{\sigma}{\kappa} - \frac{p}{\kappa}r\sin\psi\,,
\end{aligned} \quad (51)$$

and to the boundary conditions at $s = 0$ and $s = s_1$,

$$\begin{aligned}
&\psi \text{ fixed or } \frac{\partial\mathcal{L}}{\partial\dot{\psi}} = \dot{\psi} + \frac{\sin\psi}{r} - C_0 = 0\,, \\
&r \text{ fixed or } \frac{\partial\mathcal{L}}{\partial\dot{r}} = \gamma = 0.
\end{aligned} \quad (52)$$

Equation (51) together with Eq. (2) forms a close set of differential equations of 4th order complemented by four boundary conditions (52).

In the usual case where the contour length s_1 is not fixed, then $H = \dot{r}\partial_{\dot{r}}\mathcal{L} + \dot{\psi}\partial_{\dot{\psi}}\mathcal{L} - \mathcal{L} = 0$, which gives,

$$\frac{r\dot{\psi}^2}{2} - \frac{r}{2}\left(\frac{\sin\psi}{r} - C_0\right)^2 - \frac{\sigma}{\kappa}r + \frac{p}{2\kappa}r^2\sin\psi + \gamma\cos\psi + \frac{f}{2\pi\kappa}\sin\psi = 0\,. \quad (53)$$

This equation can be combined with (51) to eliminate γ and obtain a lowest order equation in ψ and r, Eq. (4).

Appendix 2: Model for Dynamical Cluster of Kinesin at Tubule Tip

The force f required to pull a tubule is usually larger than the stall force $f_s \sim 10\,\mathrm{pN}$ of a single motor. Several motors, localized at the tip of the tubule, then work cooperatively to extract a tube [53, 58]. Tubule formation then relies on two conditions: (1) the formation of a stable cluster of N motors at the tip, and (2) the load on each motor (f/N assuming that the force created by the membrane is equally distributed among the motors) should be smaller than the stall force. Let's consider the first condition. A cluster of motors at the tubule tip is sustained by an influx J_b of motors moving along the tube, and looses motors that unbind the microtubule at a rate dependent of their load, $k_u \exp\left(\frac{fa}{Nk_BT}\right)$, where k_u is the unbinding rate at zero load and a is the typical distance of the motor–microtubule interaction. The influx J_b depends on the density of motors on the membrane, and kinetic parameters such as the motor velocity, the binding and unbinding rates [53, 58]. The flux balance,

$$k_u N \exp\left(\frac{fa}{Nk_BT}\right) = J_b\,, \tag{54}$$

determines N, the number of motors in the cluster. A stable cluster can exist only if $\frac{J_b k_B T}{k_u} fa > e$ where $e \simeq 2.71$ is the base of natural logarithm. In this case, N is in the range $\frac{J_b}{k_u} < N < \frac{J_b}{k_u} e$. Then accounting for the second condition, $f/N < f_s$, tubule extraction by the collective action of molecular motors is possible if the force f (28) exerted by the membrane is lower than a critical value,

$$f < f_c \quad \text{with}\,, \quad f_c = \begin{cases} \frac{k_B T}{a} \frac{J_b}{k_u} \frac{1}{e} & \text{if } f_s a > k_B T \\ f_s \frac{J_b}{k_u} \exp\left(-\frac{f_s a}{k_B T}\right) & \text{if } f_s a < k_B T \end{cases} \tag{55}$$

References

1. Agrawal NJ, Nukpezah J, Radhakrishnan R (2010) Minimal mesoscale model for protein-mediated vesiculation in clathrin-dependent endocytosis. PLoS Comput Biol 6(9):e1000926
2. Alberts B, Johnson A, Lewis J, Morgan D, Raff M, Roberts K, Walter P (2014) Molecular biology of the cell, 6th edn. Garland, New York
3. Antonny B (2006) Membrane deformation by protein coats. Curr Opin Cell Biol 18(4):386–394
4. Ayton GS, Blood PD, Voth GA (2007) Membrane remodeling from n-bar domain interactions: insights from multi-scale simulation. Biophys J 92(10):3595–3602
5. Beck R, Ravet M, Wieland FT, Cassel D (2009) The COPI system: molecular mechanisms and function. FEBS Lett 583(17):2701–2709
6. Bonifacino JS, Glick BS (2004) The mechanisms of vesicle budding and fusion. Cell 116(2):153–166

7. Boulant S, Kural C, Zeeh J-C, Ubelmann F, Kirchhausen T (2011) Actin dynamics counteract membrane tension during clathrin-mediated endocytosis. Nat Cell Biol 13(9):1124–1131
8. Bukman DJ, Yao JH, Wortis M (1996) Stability of cylindrical vesicles under axial tension. Phys Rev E 54(5):5463
9. Cai H, Reinisch K, Ferro-Novick S (2007) Coats, tethers, Rabs, and SNAREs work together to mediate the intracellular destination of a transport vesicle. Dev Cell 12(5):671–682
10. Campelo F, McMahon HT, Kozlov MM (2008) The hydrophobic insertion mechanism of membrane curvature generation by proteins. Biophys J 95(5):2325–2339
11. Carlton J, Bujny M, Peter BJ, Oorschot VMJ, Rutherford A, Mellor H, Klumperman J, McMahon HT, Cullen PJ (2004) Sorting nexin-1 mediates tubular endosome-to-TGN transport through coincidence sensing of high-curvature membranes and 3-phosphoinositides. Curr Biol 14(20):1791–1800
12. Cheng Y, Boll W, Kirchhausen T, Harrison SC, Walz T (2007) Cryo-electron tomography of clathrin-coated vesicles: structural implications for coat assembly. J Mol Biol 365(3):892–899
13. Chernomordik LV, Kozlov MM Mechanics of membrane fusion. Nat Struct Mol Biol 15(7):675–683 (2008)
14. Chizmadzhev YA, Kumenko DA, Kuzmin PI, Chernomordik LV, Zimmerberg J, Cohen FS (1999) Lipid flow through fusion pores connecting membranes of different tensions. Biophys J 76(6):2951–2965
15. Cohen FS, Akabas MH, Finkelstein A (1982) Osmotic swelling of phospholipid vesicles causes them to fuse with a planar phospholipid bilayer membrane. Science 217(4558):458–460
16. Cullen PJ (2008) Endosomal sorting and signalling: an emerging role for sorting nexins. Nat Rev Mol Cell Biol 9(7):574–582
17. Cullen PJ, Korswagen HC (2012) Sorting nexins provide diversity for retromer-dependent trafficking events. Nat Cell Biol 14(1):29–37
18. Dabora SL, Sheetz MF (1988) The microtubule-dependent formation of a tubulovesicular network with characteristics of the ER from cultured cell extracts. Cell 54(1):27–35
19. den Otter WK, Briels WJ (2011) The generation of curved clathrin coats from flat plaques. Traffic 12(10):1407–1416
20. Derényi I, Jülicher F, Prost J (2002) Formation and interaction of membrane tubes. Phys Rev Lett 88(23):238101
21. Derényi I, Koster G, Van Duijn MM, Czövek A, Dogterom M, Prost J (2007) Membrane nanotubes. In: Controlled nanoscale motion. Springer, Berlin, pp 141–159
22. Dommersnes PG, Orwar O, Brochard-Wyart F, Joanny JF (2005) Marangoni transport in lipid nanotubes. Europhys Lett 70(2):271
23. Faini M, Prinz S, Beck R, Schorb M, Riches JD, Bacia K, Brügger B, Wieland FT, Briggs JAG (2012) The structures of COPI-coated vesicles reveal alternate coatomer conformations and interactions. Science 336(6087):1451–1454
24. Faini M, Beck R, Wieland FT, Briggs JAG (2013) Vesicle coats: structure, function, and general principles of assembly. Trends Cell Biol 23(6):279–288
25. Farsad K, Ringstad N, Takei K, Floyd SR, Rose K, De Camilli P (2001) Generation of high curvature membranes mediated by direct endophilin bilayer interactions. J Cell Biol 155(2):193–200
26. Feiguin F, Ferreira A, Kosik KS, Caceres A (1994) Kinesin-mediated organelle translocation revealed by specific cellular manipulations. J Cell Biol 127(4):1021–1039
27. Finkelstein A, Zimmerberg J, Cohen FS (1986) Osmotic swelling of vesicles: its role in the fusion of vesicles with planar phospholipid bilayer membranes and its possible role in exocytosis. Annu Rev Physiol 48(1):163–174
28. Foret L (2014) Shape and energy of a membrane bud induced by protein coats or viral protein assembly. Eur Phys J E 37(5):1–13
29. Foret L, Sens P (2008) Kinetic regulation of coated vesicle secretion. Proc Natl Acad Sci 105(39):14763–14768

30. Foret L, Dawson JE, Villaseñor R, Collinet C, Deutsch A, Brusch L, Zerial M, Kalaidzidis Y, Jülicher F (2012) A general theoretical framework to infer endosomal network dynamics from quantitative image analysis. Curr Biol 22(15):1381–1390
31. Fournier JB (1996) Nontopological saddle-splay and curvature instabilities from anisotropic membrane inclusions. Phys Rev Lett 76(23):4436
32. Frank JR, Kardar M (2008) Defects in nematic membranes can buckle into pseudospheres. Phys Rev E 77(4):041705
33. Frost A, Perera R, Roux A, Spasov K, Destaing O, Egelman EH, De Camilli P, Unger VM (2008) Structural basis of membrane invagination by f-bar domains. Cell 132(5):807–817
34. Frost A, Unger VM, De Camilli P (2009) The bar domain superfamily: membrane-molding macromolecules. Cell 137(2):191–196
35. Gauthier NC, Fardin MA, Roca-Cusachs P, Sheetz MP (2011) Temporary increase in plasma membrane tension coordinates the activation of exocytosis and contraction during cell spreading. Proc Natl Acad Sci 108(35):14467–14472
36. Gauthier NC, Masters TA, Sheetz MP (2012) Mechanical feedback between membrane tension and dynamics. Trends Cell Biol 22(10):527–535
37. Glick BS, Nakano A (2009) Membrane traffic within the Golgi apparatus. Annu Rev Cell Dev Biol 25:113
38. Grafmüller A, Shillcock J, Lipowsky R (2007) Pathway of membrane fusion with two tension-dependent energy barriers. Phys Rev Lett 98(21):218101
39. Grafmüller A, Shillcock J, Lipowsky R (2009) The fusion of membranes and vesicles: pathway and energy barriers from dissipative particle dynamics. Biophys J 96(7):2658–2675
40. Gürkan C, Stagg SM, LaPointe P, Balch WE (2006) The COPII cage: unifying principles of vesicle coat assembly. Nat Rev Mol Cell Biol 7(10):727–738
41. Hanson PI, Roth R, Lin Y, Heuser JE (2008) Plasma membrane deformation by circular arrays of ESCRT-iii protein filaments. J Cell Biol 180(2):389–402
42. Heinrich V, Božič B, Svetina S, Žekš B (1999) Vesicle deformation by an axial load: from elongated shapes to tethered vesicles. Biophys J 76(4):2056–2071
43. Hochmuth RM, Wiles HC, Evans EA, McCown JT (1982) Extensional flow of erythrocyte membrane from cell body to elastic tether. II. experiment. Biophys J 39(1):83
44. Hsu VW, Lee SY, Yang J-S (2009) The evolving understanding of COPI vesicle formation. Nat Rev Mol Cell Biol 10(5):360–364
45. Hu J, Shibata Y, Voss C, Shemesh T, Li Z, Coughlin M, Kozlov MM, Rapoport TA, Prinz WA (2008) Membrane proteins of the endoplasmic reticulum induce high-curvature tubules. Science 319(5867):1247–1250
46. Hurley JH, Boura E, Carlson L-A, Różycki B (2010) Membrane budding. Cell 143(6):875–887
47. Jackson LP (2014) Structure and mechanism of COPI vesicle biogenesis. Curr Opin Cell Biol 29:67–73
48. Jin AJ, Prasad K, Smith PD, Lafer EM, Nossal R (2006) Measuring the elasticity of clathrin-coated vesicles via atomic force microscopy. Biophys J 90(9):3333–3344
49. Jülicher F, Seifert U (1994) Shape equations for axisymmetric vesicles: a clarification. Phys Rev E 49(5):4728
50. Kirchhausen T (2009) Imaging endocytic clathrin structures in living cells. Trends Cell Biol 19(11):596–605
51. Kirchhausen T (2000) Three ways to make a vesicle. Nat Rev Mol Cell Biol 1(3):187–198
52. Kirchhausen T (2012) Bending membranes. Nat Cell Biol 14(9):906–908
53. Koster G, VanDuijn M, Hofs B, Dogterom M (2003) Membrane tube formation from giant vesicles by dynamic association of motor proteins. Proc Natl Acad Sci 100(26):15583–15588
54. Kozlov MM, Campelo F, Liska N, Chernomordik LV, Marrink SJ, McMahon HT (2014) Mechanisms shaping cell membranes. Curr Opin Cell Biol 29:53–60
55. Kozlovsky Y, Kozlov MM (2002) Stalk model of membrane fusion: solution of energy crisis. Biophys J 82(2):882–895

56. Kralj-Iglič V, Heinrich V, Svetina S, Žekš B (1999) Free energy of closed membrane with anisotropic inclusions. Eur Phys J B 10(1):5–8
57. Krauss M, Jia J-Y, Roux A, Beck R, Wieland FT, De Camilli P, Haucke P (2008) Arf1-GTP-induced tubule formation suggests a function of Arf family proteins in curvature acquisition at sites of vesicle budding. J Biol Chem 283(41):27717–27723
58. Leduc C, Campàs O, Zeldovich KB, Roux A, Jolimaitre P, Bourel-Bonnet L, Goud B, Joanny J-F, Bassereau P, Prost J (2004) Cooperative extraction of membrane nanotubes by molecular motors. Proc Natl Acad Sci USA 101(49):17096–17101
59. Lee JY, Schick M (2007) Dependence of the energies of fusion on the intermembrane separation: optimal and constrained. J Chem Phys 127(7):075102
60. Lee MCS, Orci L, Hamamoto S, Futai E, Ravazzola M, Schekman R (2005) Sar1p N-terminal helix initiates membrane curvature and completes the fission of a COPII vesicle. Cell 122(4):605–617
61. Leibler S (1986) Curvature instability in membranes. J Phys 47(3):507–516
62. Leibler S, Andelman D (1987) Ordered and curved meso-structures in membranes and amphiphilic films. J Phys 48(11):2013–2018
63. Lipowsky R (2013) Spontaneous tubulation of membranes and vesicles reveals membrane tension generated by spontaneous curvature. Faraday Discuss 161:305–331
64. Manneville J-B, Casella J-F, Ambroggio E, Gounon P, Bertherat J, Bassereau P, Cartaud J, Antonny B, Goud B (2008) COPI coat assembly occurs on liquid-disordered domains and the associated membrane deformations are limited by membrane tension. Proc Natl Acad Sci 105(44):16946–16951
65. Markvoort AJ, Marrink SJ (2011) Lipid acrobatics in the membrane fusion arena. Curr Top Membr 68:259–294
66. Marsh BJ, Volkmann N, McIntosh JR, Howell KE (2004) Direct continuities between cisternae at different levels of the Golgi complex in glucose-stimulated mouse islet beta cells. Proc Natl Acad Sci USA 101(15):5565–5570
67. Martin S, Parton RG (2006) Lipid droplets: a unified view of a dynamic organelle. Nat Rev Mol Cell Biol 7(5):373–378
68. McMahon HT, Boucrot E (2011) Molecular mechanism and physiological functions of clathrin-mediated endocytosis. Nat Rev Mol Cell Biol 12(8):517–533
69. McMahon HT, Gallop JL (2005) Membrane curvature and mechanisms of dynamic cell membrane remodelling. Nature 438(7068):590–596
70. McMahon HT, Mills IG (2004) COP and clathrin-coated vesicle budding: different pathways, common approaches. Curr Opin Cell Biol 16(4):379–391
71. McMahon HT, Kozlov MM, Martens S (2010) Membrane curvature in synaptic vesicle fusion and beyond. Cell 140(5):601–605
72. Morris CE, Homann U (2001) Cell surface area regulation and membrane tension. J Membr Biol 179(2):79–102
73. Noguchi H (2016) Membrane remodeling from n-bar domain interactions: insights from multi-scale simulation. Sci Rep 6:20935
74. Peter BJ, Kent HM, Mills IG, Vallis Y, Butler PJG, Evans PR, McMahon HT (2004) BAR domains as sensors of membrane curvature: the amphiphysin bar structure. Science 303(5657):495–499
75. Polishchuk RS, Capestrano M, Polishchuk EV (2009) Shaping tubular carriers for intracellular membrane transport. FEBS Lett 583(23):3847–3856
76. Powers TR, Huber G, Goldstein RE (2002) Fluid-membrane tethers: minimal surfaces and elastic boundary layers. Phys Rev E 65(4):041901
77. Ramakrishnan N, Sunil Kumar PB, Ipsen JH (2013) Membrane-mediated aggregation of curvature-inducing nematogens and membrane tubulation. Biophys J 104(5):1018–1028
78. Raucher D, Sheetz MP (1999) Characteristics of a membrane reservoir buffering membrane tension. Biophys J 77(4):1992–2002
79. Raucher D, Sheetz MP (1999) Membrane expansion increases endocytosis rate during mitosis. J Cell Biol 144(3):497–506

80. Rink J, Ghigo E, Kalaidzidis Y, Zerial M (2005) Rab conversion as a mechanism of progression from early to late endosomes. Cell 122(5):735–749
81. Risselada HJ, Grubmüller H (2012) How snare molecules mediate membrane fusion: recent insights from molecular simulations. Curr Opin Struct Biol 22(2):187–196
82. Risselada HJ, Kutzner C, Grubmüller H (2011) Caught in the act: visualization of snare-mediated fusion events in molecular detail. ChemBioChem 12(7):1049–1055
83. Roux A, Cappello G, Cartaud J, Prost J, Goud B, Bassereau P (2002) A minimal system allowing tubulation with molecular motors pulling on giant liposomes. Proc Natl Acad Sci 99(8):5394–5399
84. Roux A, Koster G, Lenz M, Sorre B, Manneville J-B, Nassoy P, Bassereau P (2010) Membrane curvature controls dynamin polymerization. Proc Natl Acad Sci 107(9):4141–4146
85. Safran SA (1994) Statistical thermodynamics of surfaces, interfaces, and membranes. Addison-Wesley, Reading
86. Saleem M, Morlot S, Hohendahl A, Manzi J, Lenz M, Roux A (2015) A balance between membrane elasticity and polymerization energy sets the shape of spherical clathrin coats. Nat Commun 6(6249)
87. Schick M (2011) Membrane fusion: the emergence of a new paradigm. J Stat Phys 142(6):1317–1323
88. Sciaky N, Presley J, Smith C, Zaal KJM, Cole N, Moreira JE, Terasaki M, Siggia E, Lippincott-Schwartz J (1997) Golgi tubule traffic and the effects of Brefeldin A visualized in living cells. J Cell Biol 139(5):1137–1155
89. Seifert U (1997) Configurations of fluid membranes and vesicles. Adv Phys 46(1):13–137
90. Seifert U, Berndl K, Lipowsky R (1991) Shape transformations of vesicles: phase diagram for spontaneous-curvature and bilayer-coupling models. Phys Rev A 44(2):1182
91. Sens P, Turner MS (2006) Budded membrane microdomains as tension regulators. Phys Rev E 73:031918
92. Shaklee PM, Idema T, Koster G, Storm C, Schmidt T, Dogterom M (2008) Bidirectional membrane tube dynamics driven by nonprocessive motors. Proc Natl Acad Sci 105(23):7993–7997
93. Shen H, Pirruccello M, De Camilli P (2012) Snapshot: membrane curvature sensors and generators. Cell 150(6):1300–1300
94. Shillcock JC, Lipowsky R (2005) Tension-induced fusion of bilayer membranes and vesicles. Nat Mater 4(3):225–228
95. Sinha B, Köster D, Ruez R, Gonnord P, Bastiani M, Abankwa D, Stan RV, Butler-Browne G, Vedie B, Johannes L et al (2011) Cells respond to mechanical stress by rapid disassembly of caveolae. Cell 144(3):402–413
96. Smirnova YG, Marrink S-J, Lipowsky R, Knecht V (2010) Solvent-exposed tails as prestalk transition states for membrane fusion at low hydration. J Am Chem Soc 132(19):6710–6718
97. Solon J, Pécréaux J, Girard P, Fauré M-C, Prost J, Bassereau P (2006) Negative tension induced by lipid uptake. Phys Rev Lett 97(9):098103
98. Sorre B, Callan-Jones A, Manzi J, Goud B, Prost J, Bassereau P, Roux A (2012) Nature of curvature coupling of amphiphysin with membranes depends on its bound density. Proc Natl Acad Sci 109(1):173–178
99. Stachowiak JC, Hayden CC, Sasaki DY (2010) Steric confinement of proteins on lipid membranes can drive curvature and tubulation. Proc Natl Acad Sci 107(17):7781–7786
100. Stachowiak JC, Schmid EM, Ryan CJ, Ann HS, Sasaki DY, Sherman MB, Geissler PL, Fletcher DA, Hayden CC (2012) Membrane bending by protein–protein crowding. Nat Cell Biol 14(9):944–949
101. Stachowiak JC, Brodsky FM, Miller EA (2013) A cost-benefit analysis of the physical mechanisms of membrane curvature. Nat Cell Biol 15(9):1019–1027
102. Stagg SM, LaPointe P, Razvi A, Gürkan C, Potter CS, Carragher B, Balch WE (2008) Structural basis for cargo regulation of COPII coat assembly. Cell 134(3):474–484

103. Staykova M, Holmes DP, Read C, Stone HA (2011) Mechanics of surface area regulation in cells examined with confined lipid membranes. Proc Natl Acad Sci 108(22):9084–9088
104. Stevens MJ, Hoh JH, Woolf TB (2003) Insights into the molecular mechanism of membrane fusion from simulation: evidence for the association of splayed tails. Phys Rev Lett 91(18):188102
105. Takei K, Slepnev VI, Haucke V, De Camilli P (1999) Functional partnership between amphiphysin and dynamin in clathrin-mediated endocytosis. Nat Cell Biol 1(1):33–39
106. Takizawa PA, Yucel JK, Veit B, John Faulkner D, Deerinck T, Soto G, Ellisman M, Malhotra V (1993) Complete vesiculation of Golgi membranes and inhibition of protein transport by a novel sea sponge metabolite, ilimaquinone. Cell 73(6):1079–1090
107. Thiam AR, Pincet F (2015) The energy of COPI for budding membranes. PLoS One 10(7):e0133757
108. Thiam AR, Antonny B, Wang J, Delacotte J, Wilfling F, Walther TC, Beck R, Rothman JE, Pincet F (2013) Copi buds 60-nm lipid droplets from reconstituted water–phospholipid–triacylglyceride interfaces, suggesting a tension clamp function. Proc Natl Acad Sci 110(33):13244–13249
109. Thiam AR, Farese RV Jr, Walther TC (2013) The biophysics and cell biology of lipid droplets. Nat Rev Mol Cell Biol 14(12):775–786
110. Trucco A, Polishchuk RS, Martella O, Di Pentima A, Fusella A, Di Giandomenico D, San Pietro E, Beznoussenko GV, Polishchuk EV, Baldassarre M et al (2004) Secretory traffic triggers the formation of tubular continuities across golgi sub-compartments. Nat Cell Biol 6(11):1071–1081
111. Tsafrir I, Sagi D, Arzi T, Guedeau-Boudeville M-A, Frette V, Kandel D, Stavans J (2001) Pearling instabilities of membrane tubes with anchored polymers. Phys Rev Lett 86(6):1138
112. Tsafrir I, Caspi Y, Guedeau-Boudeville M-A, Arzi T, Stavans J (2003) Budding and tubulation in highly oblate vesicles by anchored amphiphilic molecules. Phys Rev Lett 91(13):138102
113. Upadhyaya A, Sheetz MP (2004) Tension in tubulovesicular networks of golgi and endoplasmic reticulum membranes. Biophys J 86(5):2923–2928
114. Vale RD, Hotani H (1988) Formation of membrane networks in vitro by Kinesin-driven microtubule movement. J Cell Biol 107(6):2233–2241
115. Walani N, Torres J, Agrawal A (2014) Anisotropic spontaneous curvatures in lipid membranes. Phys Rev E 89(6):062715
116. Walani N, Torres J, Agrawal A (2015) Endocytic proteins drive vesicle growth via instability in high membrane tension environment. Proc Natl Acad Sci 112(12):E1423–E1432
117. Waterman-Storer CM, Salmon ED (1998) Endoplasmic reticulum membrane tubules are distributed by microtubules in living cells using three distinct mechanisms. Curr Biol 8(14):798–807
118. Weber T, Zemelman BV, McNew JA, Westermann B, Gmachl M, Parlati F, Söllner TH, Rothman JE (1998) SNAREpins: minimal machinery for membrane fusion. Cell 92(6):759–772
119. Wilfling F, Thiam AR, Olarte M-J, Wang J, Beck R, Gould TJ, Allgeyer ES, Pincet F, Bewersdorf J, Farese RV et al (2014) Arf1/COPI machinery acts directly on lipid droplets and enables their connection to the ER for protein targeting. Elife 3:e01607
120. Yamada A, Mamane A, Lee-Tin-Wah J, Di Cicco A, Prévost C, Lévy D, Joanny J-F, Coudrier E, Bassereau P (2014) Catch-bond behaviour facilitates membrane tubulation by non-processive myosin 1b. Nat Commun 5:3624
121. Yang J-S, Valente C, Polishchuk RS, Turacchio G, Layre E, Moody DB, Leslie CC, Gelb MH, Brown WJ, Corda D et al (2011) COPI acts in both vesicular and tubular transport. Nat Cell Biol 13(8):996–1003
122. Zanetti G, Pahuja KB, Studer S, Shim S, Schekman R (2012) COPII and the regulation of protein sorting in mammals. Nat Cell Biol 14(1):20–28
123. Zanetti G, Prinz S, Daum S, Meister A, Schekman R, Bacia K, Briggs JAG (2013) The structure of the COPII transport-vesicle coat assembled on membranes. Elife 2:e00951

124. Zhong-Can O-Y, Helfrich W (1989) Bending energy of vesicle membranes: General expressions for the first, second, and third variation of the shape energy and applications to spheres and cylinders. Phys Rev A 39(10):5280
125. Zimmerberg J, Kozlov MM (2006) How proteins produce cellular membrane curvature. Nat Rev Mol Cell Biol 7(1):9–19

Common Energetic and Mechanical Features of Membrane Fusion and Fission Machineries

David Tareste and Aurélien Roux

Abstract Membrane fusion and fission reactions are two antagonistic processes involved in several important biological functions, including intracellular and intercellular communication, viral infection, and the maintenance of shape and function of the mitochondrial and endoplasmic reticulum networks. Both reactions imply transient membrane remodeling events requiring a high energy input to overcome the intrinsic stability of the membrane lipid bilayer structure. This energy is provided by specialized proteins that accompany membranes on their path to fusion/fission. In this chapter, we present the physical principles of membrane fusion and fission reactions, review the several mechanisms used by specific proteins to mediate membrane fusion and fission, and emphasize the common strategies employed by these proteins to manipulate lipid bilayers during fusion/fission events.

Keywords Membrane · Fusion · Fission · SNARE · Dynamin · Energy

1 Introduction

Biological membranes are constantly remodeled through the opposite reactions of membrane fusion and fission, which, respectively, lead to the merging of two membranes into one and the splitting of one membrane into two (Fig. 1). Membrane fusion and fission reactions are crucial for cell physiology and orchestrate many fundamental processes such as cellular communication, organelle biogenesis,

D. Tareste (✉)
Institute of Psychiatry and Neuroscience, UMR S-894 INSERM-Paris Descartes University, Paris, France
e-mail: david.tareste@inserm.fr

A. Roux
Biochemistry Department, Geneva University, Geneva, Switzerland
e-mail: Aurelien.Roux@unige.ch

P. Bassereau, P. Sens (eds.), *Physics of Biological Membranes*,
https://doi.org/10.1007/978-3-030-00630-3_16

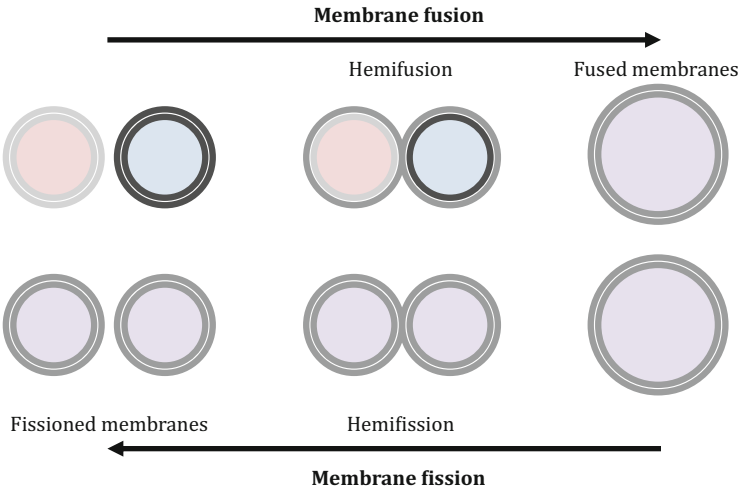

Fig. 1 Opposite reactions of membrane fusion and fission. During membrane fusion, two membrane-bound compartments mix their lipid content (light gray and dark gray) and their soluble content (red and blue), passing through an intermediate state (hemifusion), where lipids of the outer monolayers are mixed (medium gray), while lipids of the inner monolayers and soluble contents are still separated. During membrane fission, a single membrane-bound compartment generates two compartments with identical lipid and soluble contents, going through a similar intermediate state (hemi-fission), where the outer monolayers are still merged

and enveloped virus infection. Membrane-bound intracellular compartments communicate with each other through cargo-containing transport vesicles that are produced by budding and fission from a donor compartment, move to an acceptor compartment, and fuse with the acceptor membrane to deliver their cargo [1]. Within cells, the mitochondria undergo continuous cycles of membrane fusion and fission events, which define their overall morphology and maintain their normal function [2]. Infection of cells by enveloped viruses occurs when the viral membrane fuses with the cell plasma membrane to deliver the viral genome directly into the cell cytosol, or alternatively, when the virus is first endocytosed (via an endosome generated by fission of the cell plasma membrane) and then fuses its membrane with the endosomal membrane to release its genome into the cytosol [3].

Membrane fusion and fission reactions involve important membrane bending at the site of fusion/fission and require significant perturbation of the membrane structure [4]. The core structural element of all biological membranes is a lipid bilayer assembly, whose structural integrity is notably maintained by strong hydrophobic interactions between the aliphatic chains of lipid molecules. These powerful hydrophobic forces offer resistance to any attempt at bending and remodeling membranes. Energy must therefore be provided to membranes in order to allow their deformation and fusion/fission. Membrane fusion and fission processes are made possible thanks to specialized proteins that have the capacity to manipulate lipid bilayer structures and help membranes to overcome the several

energetic barriers of the fusion/fission pathways [5]. These core fusion/fission proteins often collaborate with regulatory factors, lipids, or other proteins, which facilitate membrane remodeling events and allow fusion/fission to occur at the right time and place.

Here, we first describe the biophysical mechanisms of membrane fusion and fission reactions deduced from in vitro experimental studies and in silico modeling approaches with protein-free lipid bilayers. Then, we present the various strategies employed by fusion/fission proteins to remodel biological membranes. Finally, we conclude by identifying common mechanisms, protein families, and protein domains involved in both membrane fusion and fission processes.

2 Protein-Free Fusion and Fission of Model Membranes In Vitro

2.1 Protein-Free Fusion in Model Systems

Membrane fusion proceeds through a series of successive intermediate stages that include membrane approach and contact, membrane disruption and merging, and culminate in the formation and expansion of a fusion pore allowing the communication between the aqueous volumes initially delimited by the two membranes

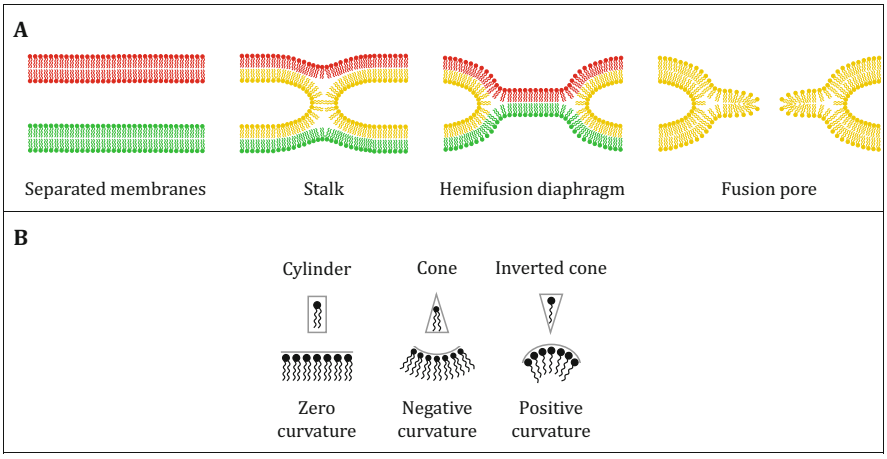

Fig. 2 Intermediates of membrane fusion. (**a**) The fusion of two membranes begins with the deformation and the connection of their respective outer monolayer to form a stalk-like structure, where the outer monolayers have merged, while the inner monolayers are not yet in contact with each other. Radial expansion of the stalk drives inner monolayer apposition and formation of a hemifusion diaphragm. Rupture of the hemifusion diaphragm leads to inner monolayer merging and formation of a fusion pore allowing the passage of soluble contents across the fused membranes. (**b**) Lipid geometry plays a key role in fusion by inducing membrane curvature facilitating stalk/hemifusion development (e.g., cone-shaped lipids residing in the outer monolayers) or fusion pore formation (e.g., inverted cone-shaped lipids residing in the inner monolayers)

(Fig. 2a). Theoretical predictions as well as in vitro and in vivo observations of protein-free and protein-driven membrane fusion reactions all converge on the idea that membrane fusion begins with the development of an intermediate stalk structure, where the outer monolayers of the membranes are mixed while their inner monolayers remain separated [6] (Fig. 2a). Progress in identifying the intermediate lipidic structures on the path to fusion and to characterize their associated energy first came from studies on protein-free membrane fusion processes using in vitro experimental assays and in silico modeling approaches.

2.1.1 Membrane Fusion Induced by Calcium Ions

In vitro, protein-free membrane fusion can be induced with molecules mediating close contact and dehydration of lipid bilayer surfaces. Seminal studies used multivalent cations to trigger the fusion between negatively charged lipid bilayers. The most widely used model system of multivalent cation-induced membrane fusion is the Ca^{2+}-mediated fusion of liposomes containing high concentrations (>25% mol/mol) of phosphatidylserine (PS) lipids [7]. When Ca^{2+} ions bind to negatively charged PS-containing liposomes, they reduce the electrostatic repulsion between the bilayer surfaces, which lowers the energy barrier for membrane approach and thus leads to liposome aggregation. Aggregation of negatively charged liposomes in the presence of Ca^{2+} was shown to be much faster than that observed between neutral liposomes solely composed of phosphatidylcholine (PC) lipids (time scale of seconds to minutes for PS-containing liposomes versus order of hours to days for PC liposomes) [8]. But membrane approach is not sufficient for fusion; another energy barrier must be overcome to destabilize the lipid bilayer structure and notably to remove the hydration layer from the two approaching bilayer surfaces. Ca^{2+} ions can engage in trans complexes involving negative lipids from opposing bilayers, thus contributing to water displacement and leading to close membrane apposition. Additional perturbation of the lipid bilayer structure can occur through the formation of cis complexes between Ca^{2+} ions and negative lipids from the same bilayer. Such cis complexes induce a phase separation and the formation of membrane domains composed of tightly packed negative lipids, leading to zones of the outer monolayer, at the boundaries of these condensed domains, which have a lower lipid density and thus expose hydrophobic chains from the inner monolayer. Such hydrophobic defects reduce membrane stability and induce lipid bilayer fusion through attractive hydrophobic interactions [9].

These early studies using multivalent ion-induced fusion of negatively charged liposomes led to the identification of several fundamental factors affecting membrane fusion [8]. Most notably, fusion was shown to depend on the size and lipid composition of the liposomes. Small liposomes (∼30 nm diameter) have a much greater capacity to fuse than larger liposomes (∼100 nm diameter); this is attributed to their high membrane curvature which imposes a strain on the bilayers and facilitates their destabilization and fusion into larger, more relaxed, structures [10]. Membrane curvature and fusion can also be modulated by lipid composition. Fusion

is facilitated when the membrane of liposomes contains phosphatidylethanolamine (PE) lipids [7]. PE lipids have a small head group area as compared to the cross-sectional area of their hydrophobic chains; this cone-like molecular shape allows PE lipids to induce negative (concave) spontaneous curvature and facilitates bilayer to non-bilayer (hexagonal) transition, which is a key event in membrane fusion.

2.1.2 Membrane Fusion Induced by Polyethylene Glycol

Membrane fusion can also be artificially triggered in vitro with highly hydrophilic and non-adsorbing polymers such as polyethylene glycol (PEG). PEG has been widely used to induce cell hybridization through cell–cell fusion [11, 12] and to deliver macromolecules into cells through the fusion of cargo-containing red blood cells or liposomes [13, 14]. The capacity of PEG to mediate the fusion between model membranes such as liposomes has been largely employed to gain insight into the mechanisms of membrane fusion [15, 16]. PEG produces its main fusogenic effect by bringing lipid bilayers into very close proximity, leaving only a gap of about 0.5 nm between the membrane surfaces [17, 18]. Membrane aggregation by PEG is produced via an attractive depletion force resulting from the exclusion of the polymer from the contact region between two approaching membranes [19]. This inter-bilayer attractive force comes from the increase of the osmotic pressure of PEG in the bulk region surrounding two approaching membranes compared to the gap region between their lipid bilayer surface [20]. PEG might also have a destabilizing effect on lipid bilayers. In fact, PEG was shown to produce structural defects in lipid bilayers and to generate non-bilayer phases, which could correspond to an intermediate stage of the fusion process [21]. PEG was also shown to cause lipid condensation, probably through dehydration of the lipid head groups [22]. Because lipids outside the contact region between two apposed membranes are exposed to higher PEG concentrations, it was proposed that this could lead to lipid depletion within the outer monolayers in the contact region. The resulting exposure of hydrophobic chains from inner monolayers would thus promote hydrophobic-driven membrane attraction, destabilization, and fusion [19].

Studies on PEG-mediated liposome fusion have confirmed that membrane fusion is promoted by high membrane curvature [23, 24] and have highlighted fundamental physical properties of lipids in fusion. PE lipids were shown to stimulate PEG-mediated fusion of both small (∼30 nm diameter) and large (∼100–200 nm diameter) liposomes [17, 18, 25]. This effect was not due to a reduction of the inter-bilayer distance—originating from the weak repulsive hydration forces between PE headgroups [26]—since lipid bilayers with or without PE displayed the same separation distance in the presence of PEG [17, 18]. Instead, PE most likely favors PEG-mediated fusion because its cone-shaped geometry induces negative membrane curvature and thus promotes formation of the intermediate stalk/hemifused structure. Cholesterol (CHOL) also increases PEG-mediated fusion (probably because of its intrinsic negative curvature) but at the same time induces liposome instability (membrane rupture and leakage),

whereas sphingomyelin (SM) reduces both membrane fusion and rupture. An optimal SM/CHOL molar ratio of 3/4 was found to minimize membrane rupture and to maximize membrane fusion [18]. Importantly, PEG-mediated fusion was optimized when liposomes consisted of PC/PE/SM/CHOL at a 35:30:15:20 molar ratio, which is close to the lipid composition of the synaptic vesicle membrane [27]. Finally, lipids with long hydrophobic chains were shown to further increase PEG-mediated fusion of liposomes with this optimal synaptic-like lipid composition, which can be accounted for by their capacity to fill the hydrophobic voids that are created between the outer and inner monolayers in the stalk structure (Fig. 2a), thus reducing the energy of stalk formation [28].

2.1.3 Experimental Observations of Membrane Fusion Intermediates

Experimental investigations of protein-free membrane fusion processes allowed the identification of two important intermediates of the fusion reaction: hemifusion and fusion pore formation (Fig. 2a). In the hemifused state, the outer monolayers of the opposing membranes have fused, while the inner monolayers remain separated. Fusion pore formation leads to the merging of the inner monolayers and to the connection between the aqueous compartments initially delimited by the two membranes. Experimentally, hemifusion is thus characterized by lipid mixing in the absence of content mixing and fusion pore formation by mixing of lipids from the inner monolayers accompanied by mixing of aqueous contents. Hemifusion and fusion pore intermediates were directly observed in vitro using small liposomes fused by divalent cations or PEG [29, 30] but also in assays following the fusion between two planar lipid bilayers [9, 19, 31], between two giant liposomes [32, 33] or between giant liposomes and planar lipid bilayers [34]. Kinetic analysis of PEG-mediated fusion of small liposomes provided the characteristic times and the activation energies associated with the intermediate stages leading to fusion [30, 35]. Once liposome docking was established by PEG, mixing of the outer monolayers occurred on a time scale of 10 s, followed by mixing of the inner monolayers concomitant with mixing of the aqueous contents, which both occurred with a characteristic time of 150 s but with lipid mixing that ended before content mixing. The activation energy of PEG-mediated outer monolayer mixing (corresponding to stalk formation) was estimated to be about 60 k_BT and that of content mixing (corresponding to fusion pore formation) about 40 k_BT. In experiments, monitoring PEG-mediated fusion of supported lipid bilayers with the surface forces apparatus (SFA), the stalk was observed 3 min after the bilayers were put in contact [19]. Faster kinetics were observed between lipid-depleted supported bilayers, where the stalk appeared 1 s after bilayer contact [9].

Hemifusion and fusion pore structures depend differently on the geometrical properties of lipids present in the outer and inner monolayers of the fusing membranes [4, 29, 36]. Lipids with a cone-shaped geometry such as PE favor negative membrane curvature (bending toward the side of the hydrophobic chains) and thus promote hemifusion when they are present in the outer monolayers

(Fig. 2b). In contrast, lipids with an inverted cone-shaped geometry such as lysophosphatidylcholine (LPC) induce positive membrane curvature (bending in the direction of the headgroups) and therefore facilitate fusion pore formation when they are present in the inner monolayers (Fig. 2b). Membrane tension also plays a role in driving membrane fusion. For example, osmotic swelling of giant liposomes was shown to induce their fusion with planar membranes and to promote opening of the fusion pore [34, 37]. Several attempts were made at imaging the intermediate lipidic structures of protein-free membrane fusion reactions, including inspection by freeze-fracture electron microscopy, cryoelectron microscopy, or X-ray diffraction [38–41]. The most convincing study is probably the observation by X-ray diffraction of a rhombohedral lipidic phase consisting of regularly spaced stalk/hemifused structures, which was first obtained upon dehydration of a stack of parallel bilayers of diphytanoyl phosphatidylcholine (DPhPC) lipids [41]. More recent X-ray experiments have observed a similar rhombohedral phase with physiological lipids, including mixtures of PC, PE, and CHOL, and have shown that the stalk structure and the critical inter-bilayer distance at which the stalk forms ($d \sim 0.9$ nm) were both independent on the lipid composition of the bilayers [42] (Fig. 3a).

2.1.4 Theoretical Descriptions of Membrane Fusion Intermediates

To complement experimental investigations of protein-free membrane fusion reactions, different modeling approaches have been used to predict the propensity of two membranes to fuse and to describe the intermediate lipidic structures leading to membrane merging [45, 46]. These approaches range from the macroscopic study of lipid bilayers as two-dimensional sheets whose physical properties can be described by the elastic theory of lipid membranes (elastic models) to the microscopic description, through molecular simulations, of the dynamics and structural rearrangements of lipid assemblies during fusion (simulation approaches). Elastic models present the advantage of relying on a minimal set of physical parameters to predict membrane fusion pathways; these parameters are the bending moduli of lipid monolayers and the stretching and tilting moduli of lipid molecules. However, because these models consider average properties of lipid membranes and assume axially symmetric fusion intermediates, they only allow a limited number of possible membrane conformations. Simulation approaches, on the other hand, account for the molecular details of lipid bilayers and do not impose any constraints on the possible intermediate structures adopted by the lipid assemblies in the course of fusion. These approaches use complex force fields to describe the dynamics and the interactions of lipid molecules within membranes. Given the current speed limit of computer experiments, simulated fusing membranes can only include a restricted number of lipid molecules, typically 7000 lipids, which corresponds to liposomes of ~30 nm diameter.

Elastic models have been very successful in predicting the sequence of events leading to membrane fusion and in estimating the successive energy barriers that

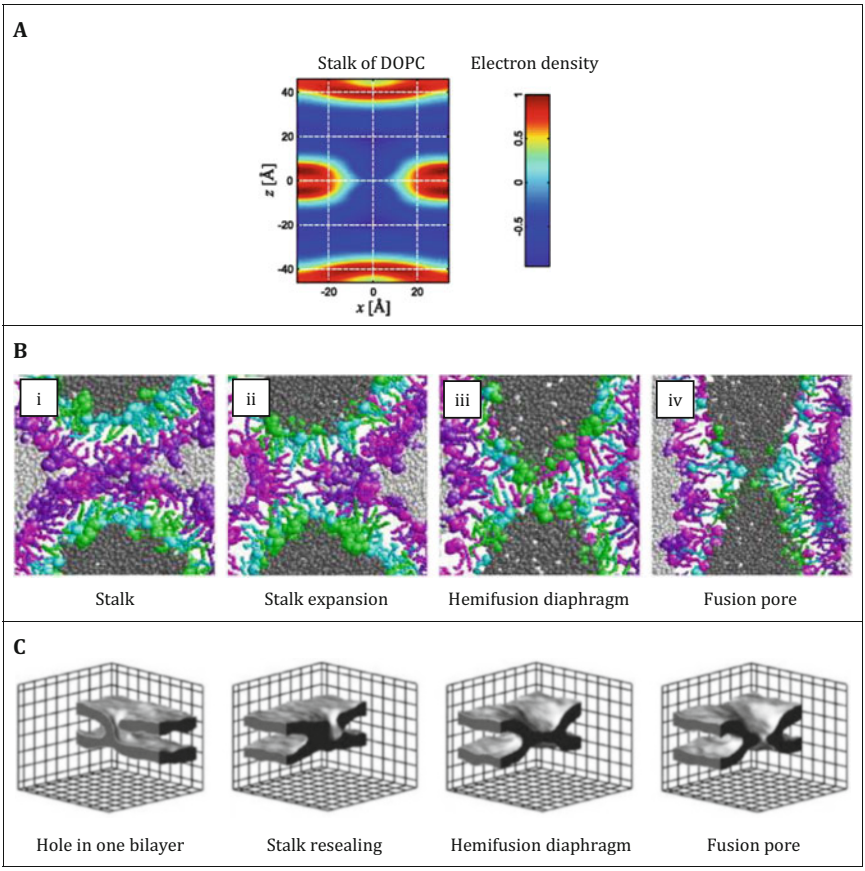

Fig. 3 Observation of fusion intermediates. (**a**) Experimental observation of the stalk intermediate. 2D electron density map of a stalk of dioleoylphosphatidylcholine (DOPC) obtained by X-ray diffraction. Regions of higher electron density (red) correspond to lipid headgroups, and regions of lower electron density (blue) correspond to acyl chains or residual water. This figure is adapted from reference [42]. (**b**) All-atom molecular dynamic simulation of the fusion between two 14-nm-diameter liposomes composed of 33 mol% dipalmitoylphosphatidylcholine (DPPC) and 67 mol% palmitic acid (PA). The simulation starts from a preformed stalk (i) which expands radially (ii) to form a hemifusion diaphragm (iii) and culminates in the formation of a fusion pore. This figure is adapted from reference [43]. (**c**) Coarse-grained Monte Carlo simulation of the fusion between two planar bilayers under tension. The hydrophobic portion of the bilayers is shown in dark gray, and their hydrophobic–hydrophilic interface is shown in light gray (for clarity, the hydrophilic portion of the bilayers is not displayed). Here, the stalk does not expand radially but induces the formation of a hole in one of the two bilayers in its vicinity. The stalk then encircles this hole to generate a hemifusion diaphragm composed of the bilayer that did not rupture. A fusion pore finally forms in this bilayer. This figure is adapted from reference [44]

the two membranes must overcome during the fusion process [47–50]. Based on this series of theoretical works, membrane fusion is believed to start from the development of a point-like protrusion initiating the contact between the apposed membranes at minimal energetic cost. The lipid assembly then reorganizes into an hourglass-shaped stalk structure. Radial expansion of this stalk structure brings the inner monolayers into contact and induces formation of a circular hemifusion diaphragm. Disruption of the hemifusion diaphragm finally leads to the opening of a fusion pore either at the center or at the periphery of the diaphragm. An alternative route was proposed, whereby the fusion pore forms directly from the stalk structure, therefore bypassing the stage of radial stalk expansion [49, 51]. The energy required to form the stalk intermediate was first obtained by elastic models, taking into account the energetic costs associated with lipid monolayers bending and the presence of hydrophobic voids within the stalk structure [51]. This first estimate resulted in unrealistically large energies ($\sim$200 k_BT) for monolayers with zero spontaneous curvature such as those of PC lipids, suggesting that stalk formation was a very unlikely event on biological timescales. Refined elastic models included tilting and stretching of the hydrophobic chains of lipids as additional processes to deform membranes. These modifications allowed for filling the hydrophobic voids of the stalk structure and reduced significantly the energetic cost of stalk formation, which became about 40 k_BT for PC membranes [48]. Elastic models were also used to estimate the energy of fusion pore formation either directly from the stalk structure [49] or after expansion of the stalk into a hemifusion diaphragm [52, 53]. In both pathways, the energy required to form a fusion pore of $\sim$0.5 nm was found to be about 40–60 k_BT for PC membranes. Stalk expansion into a hemifusion diaphragm of $\sim$5 nm diameter was shown to require an additional $\sim$50 k_BT [50]. Altogether, elastic models therefore suggest that the total energy required to go from two separate lipid bilayers with zero spontaneous curvature (such as PC membranes) to the opening of a fusion pore between two fused bilayers is about 100–150 k_BT.

Almost all simulation approaches have confirmed that membrane fusion is initiated by formation of a stalk structure between the apposed bilayers [43, 44, 54] (Fig. 3b, c). However, in one study simulating the fusion between membranes under high tension, the fusion pathway was proposed to start with the inter-bilayer flipping of lipid hydrophobic chains, leading to a disordered hydrophobic contact zone between the apposed bilayers; this region then evolved into a small hemifusion diaphragm, which ruptured at its periphery to form a fusion pore [55]. In addition, although the stalk intermediate has been consistently described by theoretical models and directly observed in experimental systems, results obtained from the different available simulation approaches sometimes diverge in the proposed sequence of events following stalk formation. Most notably, three independent simulation models described stalk elongation and rupture in addition to the radial stalk expansion pathway predicted by the elastic models [44, 54, 56]. In this alternative pathway, a hole forms very close to the stalk in one of the two membranes; a quick rearrangement of the stalk structure follows, creating a hemifusion diaphragm composed of the two monolayers from the membrane that do not rupture; a pore finally opens in this hemifusion diaphragm to complete

fusion (Fig. 3c). As a consequence of this alternative scenario, lipids from the inner and outer monolayers of the membrane that ruptured mix with each other as well as with lipids from the outer monolayer of the other membrane. In addition, this process is expected to be transiently leaky, leading to the loss of aqueous contents in the surrounding medium. Interestingly, both phenomena (mixing of lipids between inner and outer monolayers and leakage of aqueous content) have been observed in PEG-mediated fusion experiments between protein-free membranes [57, 58].

Modeling approaches also helped in identifying physical factors that can facilitate or inhibit membrane fusion. The effect of lipid composition and notably the role of lipid shape on membrane curvature and fusion, already observed in experimental systems, has been confirmed and expanded by elastic models [59] and computer simulations [54, 60]. PE lipids were shown to accelerate both stalk and hemifusion diaphragm formation in simulations of fusion between PC/PE membranes. Importantly, this effect depended exclusively on the amount of PE lipids in the outer monolayer of the fusing membranes, pointing to the importance of asymmetric *trans*-bilayer lipid distribution on fusion mechanism [60, 61]. Accordingly, elastic models have shown that the energies required to form the stalk and the hemifusion diaphragm structures decrease rapidly when the concentration of PE lipids in the outer monolayer increases and that stalk and hemifusion diaphragm formation even become energetically favorable at roughly equimolar concentrations of PC and PE lipids [48, 50]. Theoretical models also highlighted the importance of membrane tension in fusion [44, 55] and revealed the role of tension in hemifusion diaphragm formation and fusion pore expansion. Modeling of PEG-mediated fusion between planar bilayers predicted that radial stalk expansion is facilitated by membrane tension in the outer lipid monolayers at distance from the stalk region [62]. Modeling of fusion pore growth using a physical approach developed for nucleation phenomena demonstrated that membrane tension promotes fusion pore expansion [63]. Like for the stalk, experimental and modeling approaches thus give concordant results regarding the role of lipid composition, membrane curvature, and membrane tension in fusion. But modeling approaches are not only consistent with most experimental approaches; they also provide additional structural details of fusion intermediates at the scale of lipid molecules that are difficult to obtain experimentally.

2.2 Protein-Free Fission in Model Systems

Protein-free fission in model systems has been less studied than fusion, mainly because it is thought that fission and fusion pathways are symmetrical to one another and thus that fission can be described following the same theoretical framework as fusion: an energy barrier that must be overcome to reach a stalk intermediate called hemi-fission in this case (Fig. 1). However, there is one essential difference between fusion and fission: the membrane connecting the two compartments to be separated has to be constricted in order to proceed to fission. Because of this constriction step,

the mechanical properties of the membrane are thus expected to greatly influence the energy barrier for fission and thus to control the kinetics of membrane fission. In particular, the shape of the membrane, which depends on membrane bending rigidity κ, membrane tension σ, and Gaussian bending rigidity κ_G, is expected to play an important role. Moreover, lipid phase separation, which creates a line tension, can participate in membrane deformation and constriction of the membrane neck, facilitating fission.

These two essential effects (constriction and line tension) have been studied theoretically and experimentally. In the following, we will briefly describe the main experiments performed that led to these findings.

2.2.1 Energy Barrier to Reach the Hemi-fission Intermediate

The first theoretical study of fission addressed the energetics of constriction to reach the hemi-fission intermediate [64]. The authors compared the equilibrium energy of a constricted neck to the energy of a stalk (hemi-fissioned state) both connecting a spherical bud and a flat membrane. They calculated the energy difference as a function of the radius of the neck, using the Canham–Helfrich model. The energy needed to constrict the neck was modeled by a protein coat force that fixed the radius of the bud and would put sufficient force on the neck to reach the desired neck radius. Surprisingly, the authors found that for an outer radius of approximately 3 nm (1 nm radius for the lumen), the energy of the constricted state was the same as that of the hemi-fission intermediate. Thus, the inner monolayer of the membrane neck could spontaneously merge to form the hemi-fission intermediate when the neck was constricted down to 3 nm radius.

Interestingly, the shape of the connection and thus the energy barrier to fission depend on the global geometry of the membrane bud and of the flat membrane "reservoir." In the case of spherical buds formed by coat proteins, those have to provide the energy to both form the bud and restrict the diameter of the neck [64]. In the case of continuous, infinite membrane tubes, local constriction necks generate a local elastic energy increase linked to a local "bump" in the membrane [65]. Simulations show that this local increase is almost linear with the ratio between the neck radius and the tube radius, which in this case predicts that membrane tension would facilitate fission by lowering the energy barrier, whereas increase of bending rigidity would hinder fission by increasing its energy barrier [66]. If one considers the case of a tube connected to a flat membrane that is constricted at its basis—an intermediate case between the fission of a spherical bud and the fission of continuous tubes—similar predictions are made than for continuous tubes, but with overall smaller energy barriers [66].

In conclusion, mechanical properties of the membrane are thus expected to control the energy barrier for fission, as well as the overall shape of the connecting membrane neck and of the flat membrane reservoirs. However, the effect of κ and σ may vary depending on the overall geometry of the system.

2.2.2 Lipid Phase Separation

Lipid phase separation has been described since the 1970s and was proposed to have strong implications in cellular membrane traffic as this phenomenon could participate in lipid and protein segregation in the form of "rafts" [67] (see Chapter "Lipid Rafts: A Personal Account"). Lipid phase separation creates a line tension τ which itself could participate in membrane remodeling (see Chapter "Membrane Domains Under Cellular Recycling" for a more extensive description), i.e., membrane deformation and fission. The earliest theoretical work on this has been proposed by Jülicher and Lipowsky [68, 69].

The formation of a lipid domain with a line tension can cause membrane deformation by forming a bud (Fig. 4a). For a given size of the domain (of radius R), the energy gain of reducing the line tension energy by budding (thus, reducing the perimeter of the interface) is balanced by the energy cost of budding that depends on κ and σ. The simplest calculation of this competition has been proposed by Pierre Sens [72, 73], but all calculations predict that for $\sigma = 0$, there is a minimal domain size for budding, typically 1 μm radius for standard values of κ, and that above this size, there is a threshold tension below which spontaneous budding occurs. The bud neck constriction is expected to increase with the line tension τ. From

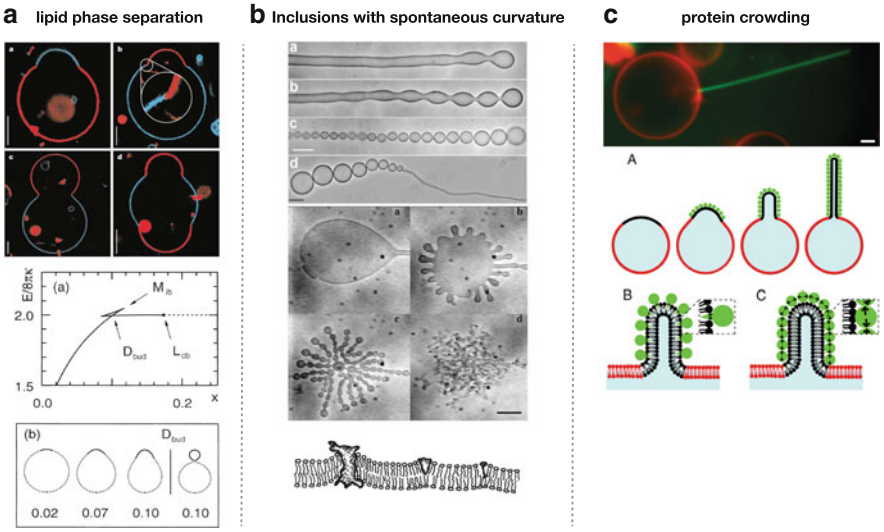

Fig. 4 Membrane remodeling mechanisms involved in fission. (**a**) Lipid phase separation. Vesicles made of DPPC, DOPC, and cholesterol exhibit phase-separated domains, which can bud under the action of line tension, from reference [70]. Theoretical prediction shows a discontinuity in the free energy (middle diagram), corresponding to a shape transition from dome to fully budded membrane (lower panel), from reference [69]. (**b**) Induction of spontaneous curvature by asymmetric insertion of amphipathic copolymers; lower and upper panels are from references [78, 79], respectively. (**c**) Induction of curvature by local concentration of proteins onto the membrane, called the crowding effect; from reference [71]

theoretical estimates, based on standard values of κ and σ, domain budding should be observed for 0.1 pN $< \tau <$ 1 pN. Budding events have been reported in many different types of reconstituted lipid membranes; moreover, quantitative bud shape analysis validated this theory and gave estimates of line tensions that fell within the theoretically predicted values [70]. But, for very high values of τ (above 10 pN), constriction is expected to be enough to lead to fission of spherical buds [69, 74] or tubes with coexisting domains [69, 74].

Phase-separated membrane tubes break at the boundaries between lipid phases [75, 76], which supports that fission in model systems is mostly triggered by a strong line tension. Membrane tension promotes this constriction, by first reducing the overall radius of the tube, and second, by increasing the curvature gradient at the site of constriction. Both effects reduce the energy barrier to fission, which is consistent with the observation that at high membrane tension, fission occurs within 1 s, whereas it takes a few tens of seconds at low tension [75]. But interestingly, as predicted from the dependence of membrane fission with the global geometry of the membrane bud, membrane fission induced by lipid phase separation is facilitated in membrane tubules as compared to spherical budding [76]. An opposite effect of membrane tension is expected for spherical budding: as discussed above, increased membrane tension is expected to widen the constricted neck in this geometry [77] and to inhibit fission. Thus, the overall geometry of the membrane system is expected to strongly affect how tension and rigidity regulate fission kinetics.

2.2.3 Induction of Spontaneous Curvature by Freely Diffusive Membrane Inclusions

Induction of spontaneous curvature can lead to constriction, which in turn drives fission. In Helfrich's early model, spontaneous curvature is a local term in the Hamiltonian and can thus describe local differences of membrane curvature induced by local differences of spontaneous curvature. For example, the effect of freely diffusing membrane inclusions with an intrinsic spontaneous curvature different from that of the membrane has been calculated in the 1980s by Stanislas Leibler [78]. He predicted that dramatic curvature instabilities could occur: if the intrinsic spontaneous curvature of inclusions is higher than that of the membrane, they can diffuse to reach areas of the membrane that have a curvature energetically more favorable for them and concentrate locally. This local increase of inclusion density increases the local effective spontaneous curvature of the membrane, implying that the curved parts of the membrane become even more curved, potentially leading to membrane instabilities. Thus, at equilibrium, theory predicts apparition of highly curved domains containing high densities of inclusions and other regions with low curvature and almost no inclusions.

This theory has been verified many times experimentally, and we will focus here on the most striking results. Amphipathic copolymers, when mixed to flat disks

of membrane with a very low tension, induce the formation of membrane tubules [79] (Fig. 4b). This effect is due to the insertion of the hydrophobic part of the copolymers into the membrane. The formation of tubules is highly dynamic, and while they grow, they undergo a striking pearling instability similar to the Rayleigh instability [80]. At equilibrium, tubules are usually segregated in two parts: one part with very low density of copolymers and large pearls and another part with very high density of copolymers and very small pearls [80]. However, even if theory predicts sufficient curvature induction by this mechanism to reach fission in between the pearls, fission is usually not observed. This is because two physical effects can counteract this instability. First, tension can flatten spontaneous fluctuations of the membrane, and also highly curved domains formed by segregated inclusions, and will thus oppose the instability. This effect is sufficient to block fission even at low membrane tension. Second, entropic forces arise from the segregation of inclusions in highly dense domains of the membrane and thus counteract this segregation. Entropic forces can however induce curvature if the inclusions are all oriented in the same way in the membrane. In this case, entropic forces arise only on one side of the membrane and lead to surface expansion of this side, which causes spontaneous curvature. This effect is called "crowding" (Fig. 4c) and can lead to the formation of tubules and spherical buds at very high density of inclusions [71, 81]. More recently, crowding was even shown to be sufficient to cause membrane fission in vitro [82]. It is still debated whether this mechanism is energetically efficient [83], because it requires extremely high densities of insertions to generate sufficient force to curve membranes [84].

2.2.4 Fission by Membrane Shearing

Breaking a membrane can also be achieved by tearing it. This effect results from shearing forces within the leaflets or between the leaflets, which drives membrane thinning and breakage. It is probably the most difficult way to break membranes, as lipid membranes are usually considered—at least in the case of protein-free lipid membranes—to be highly fluid. Thus, it usually requires extreme flows to sufficiently counteract diffusion so that shearing forces can arise. Rare studies have tackled this effect: Evan Evans showed, for example, that membrane tubules could be broken by swift extraction from giant unilamellar vesicles [85]. Pulling rates higher than 100 μm per second created sufficient flow difference between the two leaflets to tear the membrane while lipids were flowing within the neck connecting the tube to the vesicle. Such flow rates are unrealistic in living cells, but cells have found a clever way to increase this effect by limiting lipid mobility at the neck of membranes to be separated (see Sect. 3.2).

3 Protein Machineries of Biological Membrane Fusion

3.1 The Main Machinery for Intracellular Membrane Fusion: The SNARE Complex

All intracellular fusion reactions—except the homotypic fusion events involving mitochondrial or endoplasmic reticulum (ER) membranes—are mediated by proteins from the soluble *N*-ethylmaleimide-sensitive factor attachment protein receptor (SNARE) family. Current knowledge on the molecular mechanisms underlying the function of SNARE proteins stems from the large body of genetic and biochemical data obtained with SNARE proteins involved in synaptic vesicle fusion. Neuronal communication relies on the liberation of neurotransmitters and hormones in the presynaptic cleft through the fusion of cargo-containing synaptic vesicles with the presynaptic plasma membrane. Synaptic vesicle fusion involves the pairing between the vesicular (v-) SNARE protein VAMP2 (residing in the synaptic vesicle membrane) and the target (t-) SNARE proteins Syntaxin1 and SNAP25 (residing in the presynaptic plasma membrane) to form a membrane-bridging trans-SNARE complex (or SNAREpin) that allows the synaptic vesicle to dock and fuse with its target membrane [86] (Fig. 5). Deletion of an individual SNARE strongly impairs neurotransmission in various model organisms such as worm, fly, and mouse [87–90]. In addition, botulinum and tetanus neurotoxins inhibit synaptic

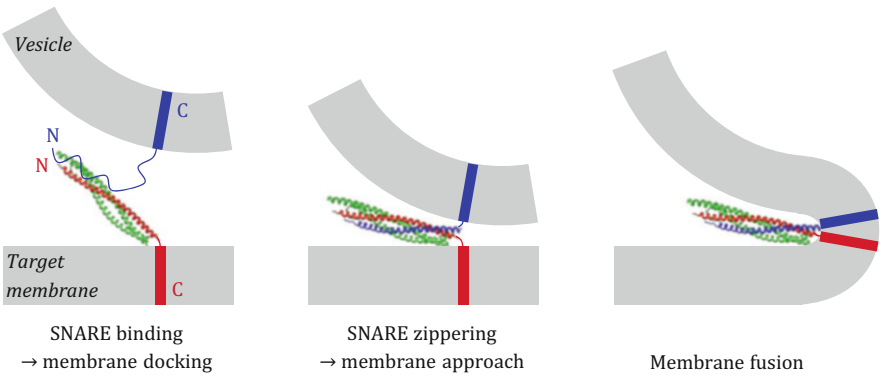

Fig. 5 The SNARE fusion machinery. SNARE-mediated membrane fusion involves the interaction between a v-SNARE protein (blue) on the vesicle membrane and a t-SNARE protein (red and green) on the target membrane. These cognate v- and t-SNARE proteins bind to each other to form a membrane-bridging trans-SNARE complex (or SNAREpin) that assembles like a zipper from its membrane distal (N-terminal) region toward its membrane proximal (C-terminal) region, bringing the membranes in very close apposition until they fuse. The model was generated using the structure of the synaptic SNARE complex composed of VAMP2 (blue), Syntaxin1 (red), and SNAP25 (green) [Protein Data Bank entry 1SFC]

transmission through proteolytic cleavage of VAMP2, SNAP25, or Syntaxin1 [91–93]. In vitro, when recombinant versions of the v-SNARE protein VAMP2 and the t-SNARE dimer Syntaxin1/SNAP25 are reconstituted into two separate populations of artificial vesicles (liposomes), they induce liposome docking and fusion through the formation of membrane-bridging SNAREpin complexes [94]. Synaptic SNARE proteins can also mediate fusion between two populations of cognate cells that have been engineered to express either the v-SNARE protein VAMP2 or the t-SNARE proteins Syntaxin1 and SNAP25 on their surface [95]. Together these data unambiguously demonstrate that the SNARE complex constitutes the core machinery for intracellular membrane fusion but leave open the question of how they exactly operate at the molecular level.

Protein-free membrane fusion can be triggered in vitro by molecules such as divalent cations and polyethylene glycol (PEG) that mediate close membrane apposition and membrane dehydration/perturbation (§ I-A). So, does the SNARE complex induce membrane fusion using the same mechanism? SNARE proteins display a relatively simple molecular architecture. They are characterized by an evolutionary conserved cytoplasmic region of 60–70 residues called the SNARE motif. VAMP2 and Syntaxin1 both have a single SNARE motif and a C-terminal transmembrane domain (TMD) connected to each other by a short linker rich in positively charged residues. SNAP25 contains two SNARE motifs connected by a flexible loop, which targets them to membranes via palmitoylation. Many SNAREs, like Syntaxin1, also possess an autonomously folded N-terminal extension with important regulatory functions [96, 97]. The X-ray crystal structure of the synaptic SNARE complex revealed that v-SNARE and t-SNARE proteins can assemble as a highly stable four-helix bundle, with the SNARE motifs of VAMP2 and Syntaxin1 each contributing one helix and the SNARE motifs of SNAP25 contributing two helices. In this structure, the SNARE motifs are oriented in parallel, i.e., with their N-termini located at one end of the bundle and their C-termini at the other end [98] (Fig. 5). In vitro and in vivo studies, in which N- or C-terminal folding of the SNARE bundle was specifically inhibited, then showed that v-SNARE and t-SNARE proteins assemble like a zipper from their N-terminal (membrane distal) domains to their C-terminal (membrane proximal) domains, suggesting that they bring the membranes close together in the course of this zipper-like assembly [99, 100] (Fig. 5). A more recent X-ray structural analysis of the synaptic SNARE complex including the linkers and TMD domains of VAMP2 and Syntaxin1 further revealed that SNARE zippering extends all the way into the membrane, suggesting that C-terminal assembly of the v-SNARE and t-SNARE proteins is functionally coupled to membrane merging [101] (Fig. 5). Following fusion, all SNARE proteins reside in the single fused membrane in the form of a highly stable cis-SNARE complex that resists a temperature as high as 80 °C [102, 103]. Disassembly of the cis-SNARE complex thus requires a very high amount of energy. This energy is provided by the hexameric ATPase NSF that binds to the SNAREs via the adaptor proteins α-SNAP and invests energy of an ATP/ADP conformational switch to unfold the SNARE bundle, therefore allowing the individual SNAREs to be reused in subsequent fusion reactions [86, 104].

The energy versus distance profile of zippering SNAREpins was elucidated using surface forces apparatus (SFA) measurements between two bilayers decorated with t-SNARE or v-SNARE proteins [105]. In this system, the SNARE motifs started to interact when the bilayers were ~10 nm apart and culminated in the form of a highly energetic, partially assembled, membrane-bridging SNAREpin releasing 35 k_BT of energy and remaining 30% unstructured in its membrane-proximal end. Single-molecule atomic force microscopy (AFM) measurements between SNARE proteins affixed to solid supports also predicted a SNARE adhesion energy of about 30 k_BT [106]. Recent force measurements performed at the single molecule level using optical or magnetic tweezers confirmed the existence of the partially assembled SNAREpin and further observed membrane-proximal assembly upon reduction of the applied pulling force that mimicked the repulsion between two approaching bilayers during fusion [107, 108]. The total amount of energy released in the course of this two-step (N-terminal then C-terminal) SNAREpin zippering was estimated to be 65 k_BT [108]. Because the energy required to fuse two lipid bilayers was predicted to be 100–150 k_BT [109, 110], these results suggest that the assembly of few SNAREpins can provide enough energy for membrane fusion. The minimal number of SNARE complexes that are needed for membrane fusion is however still strongly debated. In vitro liposome fusion experiments suggested that one SNARE complex is sufficient [111], while in vivo vesicle exocytosis assays estimated that between two and eight complexes are required [112–115]. A novel in vitro fusion system between liposomes and lipid bilayer nanodiscs may reconcile these seemingly contradictory results by showing that one SNARE complex is enough to trigger lipid bilayer mixing, while at least three SNARE complexes are needed to mediate efficient content mixing [116].

SNARE-mediated membrane fusion was shown to include an intermediate hemifusion state in various experimental systems, including in vitro liposome-liposome and liposome-planar bilayer fusion assays [117–119], as well as in situ electron tomography imaging of synaptic vesicles docked to the active zone of synapses [120] and in vivo fluorescence imaging of sea urchin cortical granules attached to the plasma membrane [121]. Consistent with these various experimental observations, molecular dynamic simulations of SNARE-mediated fusion also identified a hemifused intermediate, which was preceded by stalk formation and required only a single SNARE complex [122]. In these simulations, transition from hemifusion to fusion pore opening was facilitated by the cooperative action of at least two SNARE complexes. In addition, at the end of the simulation, SNARE proteins were zippered all the way into their membrane region, in good agreement with the most recent X-ray crystal structure of the SNARE complex [101].

3.2 Viral Fusion

Many viruses possess a lipid bilayer envelope which surrounds their genetic material. Such enveloped viruses enter the cells they infect either by endocytosis

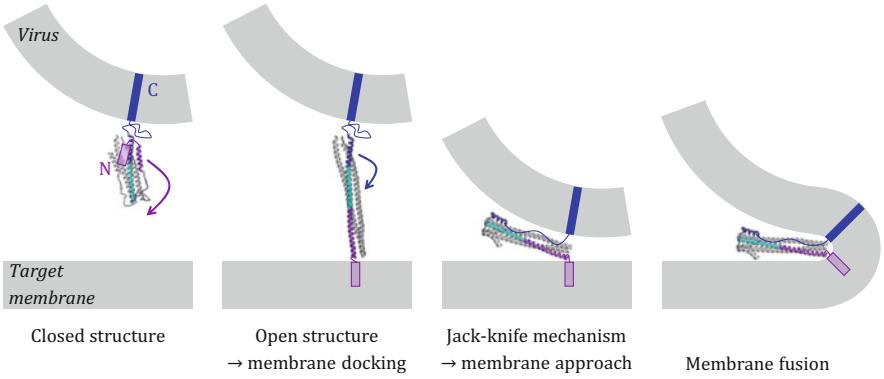

Fig. 6 Mechanisms of fusion by viral proteins. Before fusion, the viral fusion protein is anchored to the viral membrane via its transmembrane domain (TMD, dark blue) and displays a closed and inactive conformation, in which a fusion peptide (purple) is sequestered. During fusion, the viral protein first opens up in response to a triggering signal (e.g., low pH or binding to a cellular receptor), which leads to exposure of the fusion peptide that inserts into the target membrane and thus establishes a molecular bridge between viral and target membranes. Next, the viral fusion protein folds back on itself in a jackknife mechanism, so that the fusion peptide and the TMD come together, bringing the viral and target membranes in close proximity. Viral membrane fusion proceeds as a result of this close membrane apposition and lipid bilayer perturbation produced by membrane-insertion of the fusion peptide. The model was generated using the structure of the influenza virus HA protein [Protein Data Bank entries 2YPG and 1QU1]

(e.g., the influenza virus) or by direct fusion between the viral membrane and the host cell plasma membrane (e.g., the human immunodeficiency virus). Viruses that enter via endocytosis fuse their membrane with the endosomal membrane to release their genetic material into the host cell cytosol. Viral fusion events are controlled by specialized membrane proteins that reside on the viral envelope and undergo large conformational rearrangements allowing lipid bilayer approach and merging in response to specific triggering signals (e.g., low pH in the case of fusion with endosomes or interaction with receptors on the cell surface in the case of infection by direct fusion with the cell membrane). Our current understanding of the mechanisms of viral membrane fusion mainly comes from the large number of available structural data on viral fusion proteins in their pre-fusion or post-fusion conformations [123, 124]. Based on these structural data, viral fusion proteins can be subdivided into three main categories. Class I viral fusion proteins, such as the influenza virus hemagglutinin protein (HA) and the human immunodeficiency virus (HIV) gp41 protein, display mostly α-helical content; class II viral fusion proteins (e.g., the dengue virus E protein) are essentially composed of β-sheets; and class III viral fusion proteins, such as the herpes virus gB protein, have a mixture of α-helical and β-sheet contents. Despite this great diversity of molecular architectures, viral fusion proteins all seem to operate following the same fundamental principles, exemplified by the mode of action of the influenza virus HA protein (Fig. 6).

3.2.1 Influenza Virus Hemagglutinin Protein (HA)

The best characterized viral fusion machinery is certainly the influenza virus HA protein, which has been the subject of many structural and functional studies [123, 125, 126]. The pre-fusion structure of HA consists of a trimeric coiled coil structure anchored to the viral membrane by a C-terminal TMD, where each monomer consists of a long central α-helix and a short N-terminal α-helix that are packed antiparallel and connected to each other by a flexible loop (Fig. 6). A 23-residue fusion peptide found at the N-terminus of each monomer is initially buried in the cavity formed by the three central α-helices. Following exposure to low pH of the endosome, the loop between the two α-helices of each monomer becomes helical, which opens up the HA protein and releases the fusion peptide (Fig. 6). The resulting conformation is an extended three-helix coiled coil structure relocating the fusion peptide into the target membrane. This structure then collapses onto itself in the form of a six-helix coiled coil, bringing together the fusion peptide and the TMD, along with the respective membranes in which they reside (Fig. 6). The fusion peptide of HA is an amphipathic α-helix with a V-shaped structure that can penetrate into the outer lipid monolayer of membranes [127, 128]. Such an insertion was proposed to perturb lipid packing within the target membrane and to induce local membrane bending toward the viral membrane by a wedge effect. Accordingly, HA was shown to induce small membrane protrusions of ∼20 nm diameter on the surface of liposomes or cells [129, 130]. Thus, like SNARE proteins, HA proteins use the folding energy of coiled coil structures to bring the fusing membranes into close proximity. Energy for fusion is provided by a "jackknife" self-folding mechanism in the case of HA, instead of a "zipper-like" assembly mechanism between cognate proteins in the case of SNAREs. Differential scanning calorimetry and circular dichroism measurements on a soluble recombinant fragment of the HIV gp41 protein indicated that the free energy of formation of a six-helix coiled coil structure is about 30 k_BT [131]. In addition to their membrane apposition activity, HA proteins may lower the energy barrier of membrane fusion by using the lipid bilayer perturbation effect of their amphipathic fusion peptide. The free energy released during insertion of the HA fusion peptide into lipid bilayers was estimated to be about 13 k_BT by isothermal titration calorimetry [132]. This energy could be used to manipulate and perturb lipid bilayer structures during fusion.

The first experimental evidence of hemifusion as an intermediate state of biological membrane fusion came from seminal works that assessed the capacity of cells expressing HA proteins on their surface to fuse with red blood cells or with supported lipid bilayers [133, 134]. In these studies, the occurrence of HA-mediated hemifusion was unambiguously proven by combining lipid and content mixing measurements by fluorescence microscopy, with ion flux measurements (to detect fusion pores) by electrophysiological recordings. HA proteins whose 27-residue TMD was replaced by a glycophosphatidylinositol (GPI) lipid anchor or in which more than 10 residues were deleted could only mediate hemifusion, suggesting that an intact TMD spanning both lipid monolayers of membranes is required to mediate transition from hemifusion to full fusion, i.e., fusion pore opening [133,

135]. Decreasing the surface density of TMD-anchored HA proteins also impaired full fusion and arrested the process at the hemifusion stage, suggesting that the cooperativity of several HA trimers is necessary for full fusion. Oligomerization of HA trimers was first evidenced by the decrease of their lateral mobility following exposure to low pH [136]. Accordingly, more recent studies monitoring in real time the fusion of single influenza virus particles with supported lipid bilayers by fluorescence microscopy showed that three HA trimers were required to trigger membrane merger [137, 138]. In hemifusion-arrested systems, the transition from hemifusion to fusion pore opening could be induced upon perturbation of the hemifusion diaphragm, either by applying an osmotic chock, consistent with a role of membrane tension in fusion, or by manipulating the lipid composition, typically by adding lipids with an inverted cone-shaped geometry to the inner monolayers of the fusing membranes [139]. Along these lines, HA proteins residing outside of the contact zone between two fusing membranes were suggested to form a molecular coat with the capacity to induce bending stress, promoting formation and radial expansion of the fusion stalk, as well as lateral tension stress, facilitating fusion pore opening. This echoes the role of protein coats in membrane budding and fission events and raises the interesting hypothesis that membrane fusion and fission reactions could be driven by the same fundamental forces acting in the opposite directions [140].

3.3 Homotypic Membrane Fusion Machineries

The molecular mechanisms of the protein machineries that mediate homotypic membrane fusion, i.e., the fusion between membranes of the same type, only begin to emerge. Homotypic fusion occurs between intracellular organelles, such as the endoplasmic reticulum (ER) and mitochondria, and is crucial for the morphological and functional maintenance of these organelles. ER and mitochondrial fusion are controlled by large membrane-anchored GTPase proteins from the dynamin superfamily [141]. Homotypic fusion also occurs between cells and plays, for example, a key role in the development and homeostasis of various organs, such as the eyes, muscles, bones, and placenta [124]. The proteins involved in cell–cell fusion events are much less described, and there seems to be no consensus about their molecular architecture and mode of operation, although immunoglobulin (Ig)-like domains are found in several cell–cell fusion proteins [142].

3.3.1 ER Fusion

The ER consists of a network of interconnected sheets and tubules. In eukaryotic cells, new tubular ER connections are constantly formed by membrane fusion, and these structures likely constitute regions of the ER membrane where lipid synthesis and contact with other organelles for non-vesicular lipid transfer might

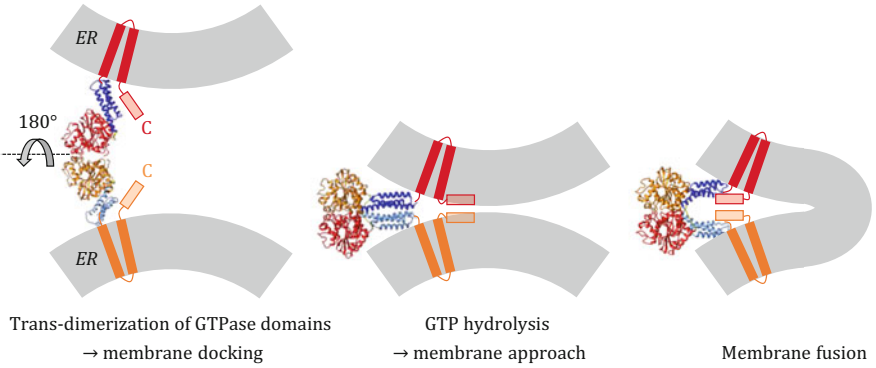

Fig. 7 Atlastin-mediated ER fusion. The fusion of ER membranes is believed to begin with the homotypic interaction between the N-terminal GTPase domains of two Atlastin molecules (red and orange) residing in opposing ER membranes to form a loosely docked state. GTP hydrolysis would then induce a 180° twist of the GTPase domains leading to membrane approach and the development of a tightly docked state involving contacts between the middle domains (dark blue and light blue). This new conformation would release the C-terminal amphipathic helices (light red and light orange) and allow them to bind and perturb the lipid bilayer structure, thus triggering ER membrane fusion. The model was generated using the structure of the cytosolic domain of atlastin1 protein [Protein Data Bank entries 3QOF, 4IDQ and 3QNU]

occur [141, 143]. Homotypic ER fusion is mediated by the large transmembrane-anchored GTPase protein Atlastin of the ER membrane. Atlastin possesses an N-terminal GTPase domain, a three-helix bundle middle domain, two TMDs, and a C-terminal cytoplasmic tail (Fig. 7). The structure function of Atlastin was recently elucidated thanks to a combination of structural biology, biochemistry, and cell biology approaches. The X-ray crystal structure of N-terminal cytosolic fragments of Atlastin bound to GDP or to non-hydrolyzable forms of GTP revealed two dimeric conformations: a first one that is stabilized by interactions between the GTPase domains and a second one that also involves interactions between the middle domains [144–146]. In a configuration where two Atlastin partners initially reside on opposing membranes, the first conformation would thus correspond to a loosely docked state and the second conformation to a tightly docked state bringing the membrane into closer proximity (Fig. 7). In vitro liposome fusion experiments revealed that Atlastin induces fusion using GTP-dependent trans-dimerization through the middle domain; fusion also required intact TMDs and the C-terminal cytoplasmic tail of Atlastin [147–149]. The TMDs were proposed to be involved in Atlastin oligomerization within the plane of each opposing membrane before GTP hydrolysis and membrane fusion, therefore constituting a pool of molecules that could assemble synergistically across membranes upon GTP hydrolysis [149, 150]. The C-terminal cytoplasmic tail was shown to form a conserved amphipathic helix that interacts with membranes and perturbs their lipid bilayer structure [149, 151]. Based on these recent observations, Atlastin-mediated fusion would thus proceed as

follows: ER membranes would be first brought into molecular contact through the cooperative GTP-dependent assembly of several trans-Atlastin complexes and then destabilized by the C-terminal amphipathic helix of Atlastin that renders the lipid bilayers prone to fusion [141] (Fig. 7).

3.3.2 Mitochondrial Fusion

Mitochondria form a network of highly dynamic organelles that constantly move, fuse, and divide within cells [2]. Mitochondrial fusion involves the merging of four membranes: an inner and an outer membrane on each fusing partner. Inner and outer membrane fusion events are coordinated but can be mechanically uncoupled and use two distinct protein machineries. Inner membrane fusion depends on two isoforms of the large GTPase optic atrophy protein 1 (OPA1): a long isoform (l-OPA1) that is anchored to the inner membrane and a short soluble isoform (s-OPA1) that resides in the space between inner and outer membranes (Fig. 8a). The long isoform contains an N-terminal TMD, a first heptad repeat domain (HR1), a GTPase domain, a middle domain, and a second heptad repeat domain (HR2), which is believed to be the GTPase effector domain (Fig. 8a). The short isoform is produced upon proteolytic cleavage between the TMD and HR1 (Fig. 8a). Long and short isoforms of OPA1 are both required for inner mitochondrial membrane fusion, but their mechanism of action remains largely unknown, notably because we still await their 3D structure determination. The current working model proposes that l-OPA1 mediates the docking of inner membranes, whereas s-OPA1 induces their merging by locally deforming lipid bilayers in a GTP-dependent manner [152–154]. Outer mitochondrial membrane fusion requires the Mitofusin proteins, Mfn1 and Mfn2, two large transmembrane-anchored GTPases of the outer membrane. Mitofusins possess an N-terminal GTPase domain, a first heptad repeat domain (HR1), two C-terminal TMDs, and a second heptad repeat domain (HR2) (Fig. 8a). All four functional domains are crucial for Mitofusin function, but their exact role in mitochondrial fusion remains unclear. The X-ray crystal structure of the HR2 domain identified an antiparallel coiled coil dimer of $\sim$10 nm with the potential to mediate mitochondrial docking before fusion [155]. In vitro reconstitution experiments showed that the HR1 domain could induce liposome fusion and identified a conserved amphipathic helix within the HR1 sequence, having the capacity to perturb lipid bilayer structures, notably in membrane regions of high curvature [156]. GTP binding and hydrolysis were shown to be essential for mitochondrial fusion [11, 157, 158], but the underlying function of the GTPase domain in fusion is still unknown. The GTPase domain could generate high membrane curvatures and thus act in synergy with the membrane destabilization property of the amphipathic HR1 domain. The recent X-ray structure determination of Mfn1 GTPase domain linked to the HR2 domain via an artificial flexible linker suggests an interesting alternative scenario for Mitofusin-mediated mitochondrial docking [159, 160]. This GTPase-HR2 construct was shown to form a closed dimeric conformation resembling that of the bacterial dynamin-like protein

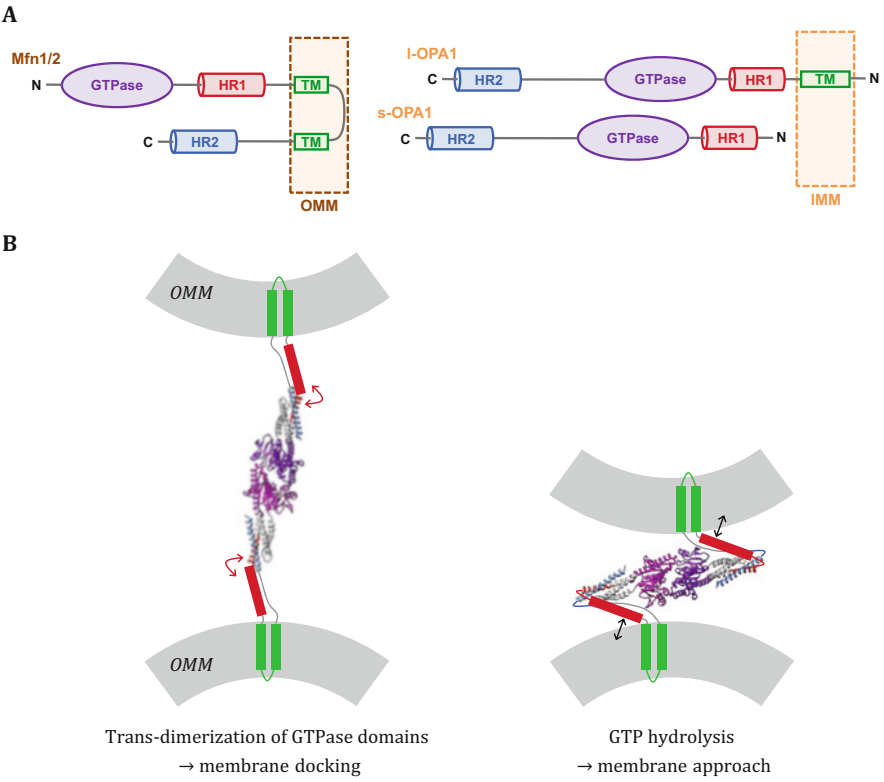

Fig. 8 Mechanisms of mitochondrial fusion. (**a**) Molecular architecture of mitochondrial fusion proteins: OPA1 proteins (l-OPA1 and s-OPA1) for fusion of the inner mitochondrial membrane (IMM) and Mitofusin proteins (Mfn1 and Mfn2) for fusion of the outer mitochondrial membrane (OMM). (**b**) Possible mode of action of Mitofusin in outer mitochondrial membrane fusion. Mitofusin may mediate long-distance docking through trans-dimerization of its GTPase domain (purple) and bring outer mitochondrial membranes in close apposition through GTP-hydrolysis-driven open/closed conformational transition. In the closed form, the HR1 domain (red) lies close to the membrane surface and may trigger fusion by destabilizing the lipid bilayer structure. An alternative/additional docking step (not shown here) may involve the formation of an antiparallel dimer of HR2 (blue) across mitochondria. The model was generated using the structure of the GTPase-HR2 fragment of Mfn1 protein [Protein Data Bank entry 5GOM]

(BDLP). By analogy with BDLP, which can switch from an open to a closed conformation upon GTP hydrolysis, Mitofusin could thus dock membranes through trans-dimerization of its GTPase domain and bring membranes close together by folding back on itself (Fig. 8b). In the resulting closed conformation, the HR1 domain would be perfectly placed to interact with the lipid bilayer surface and could thus constitute the molecular trigger of mitochondrial fusion (Fig. 8b).

3.3.3 Cell–Cell Fusion

Cell–cell fusion machineries are much less understood than the protein machineries mediating viral fusion or intracellular membrane fusion events. Very few proteins of the cell surface with the capacity to directly mediate cell–cell fusion have been identified so far [161]. Here, we only present the example of the best characterized cell–cell fusion protein, the *Caenorhabditis elegans* protein epithelial fusion failure 1 (EFF-1). Cell–cell fusion is fundamental to the development and shaping of various organs in *Caenorhabditis elegans* by allowing the generation of multinucleated syncytial cells that constitute the building blocks of, for example, the pharynx, the vulva, and the skin. EFF-1 was initially identified by using genetic screens for mutants with fusion failure phenotypes [162] and shortly after unambiguously characterized as a true homotypic cell–cell fusion protein. Expression of EFF-1 on the surface of cells that do not normally fuse was shown to be sufficient to induce their fusion [163]. In addition, EFF-1-mediated fusion required the protein to be present on the two cells destined to fuse and included the passage through a hemifused intermediate [164]. EFF-1 is anchored to the cell surface via a single C-terminal TMD and displays a bulky extracellular N-terminal domain and an unstructured cytosolic C-terminal tail. The X-ray crystal structure of the extracellular domain of EFF-1 identified a trimer in which each monomeric subunit consists of three β-sandwich domains (I, II, and III) organized as in the post-fusion hairpin conformation of viral class II fusion proteins, notably with the C-terminal domain III folding back onto the N-terminal domains I and II [165]. However, in this structure, the usual N-terminal hydrophobic fusion peptide of domain II, which allows target membrane insertion and perturbation in the case of viral fusion, is replaced by a highly hydrophilic peptide, indicating a different fusion mechanism. Cell–cell fusion was shown to be inhibited by trimerization-defective EFF-1 mutants and upon the addition of soluble EFF-1 monomers or EFF-1 domain III, suggesting that fusion is triggered by trans-trimerization (e.g., interaction between monomers and dimers across opposing membranes) followed by domain III folding back to adopt the hairpin configuration. Formation of the hairpin structure would bring the membranes in close proximity and allow the TMDs of the monomers and dimers to interact with each other and trigger lipid bilayer merger. EFF-1 proteins would thus drive cell–cell fusion by using the conformational change properties of viral proteins and the trans-oligomerization properties of SNARE and Atlastin proteins. The actin cytoskeleton was also shown to play a role in EFF-1-mediated fusion. Actin polymerization at the site of fusion stimulated EFF-1-mediated fusion through the generation of highly curved finger-like protrusions on the cell membrane [166]. Therefore, localized actin-driven membrane deformations could compensate for the absence of hydrophobic fusion peptides to perturb membranes in cell–cell fusion events.

4 Protein Machineries of Biological Membrane Fission

Compared to proteins driving fusion reactions, those involved in fission have been discovered later, and their characterization took longer. This is partly because there is no general fission machinery and because different mechanisms are involved whether fission proteins are located outside or inside the membrane neck. In contrast to SNARE proteins that mediate most intracellular fusion reactions, dynamin—despite being the most characterized fission machinery—is specific to endocytic routes at the plasma membrane and has a probable role at the trans-Golgi network. Thus, for many fission reactions occurring in vivo, in particular at the Golgi, endoplasmic reticulum, or endosomes, we are still lacking many of the essential players.

Scientists have isolated two fission machineries and started unraveling the common aspects of all fission reactions: dynamin and endosomal sorting complex for retrograde transport complex III (ESCRT-III). Both machineries work at narrow necks of membranes to break them, but dynamin is located outside the neck, whereas ESCRT-III is located inside the neck. We first discuss dynamin and ESCRT and then other factors identified in other fission reactions.

4.1 The Constrictase Dynamin

Dynamin is a fairly big enzyme (100 kDa) that hydrolyzes GTP. Its ubiquitous form is Dynamin2 in mammals [167]. Dynamin1 is neuronal specific, and Dynamin3 is expressed only in a small number of cell types, like the nurse cells in the testis [168]. Most of invertebrates have only one gene encoding dynamin. Dynamin was initially found in the microtubule-associated protein fraction during tubulin purification and was thus thought to be a microtubule bundling factor [169]. However, the drosophila thermo-sensitive mutant called *shibire* ("paralyzed" in Japanese) was found to encode for dynamin [170]. This discovery revealed the role of dynamin in the formation of synaptic vesicles. The temperature-induced paralytic phenotype of these flies arises from the fact that clathrin-coated pits at the synapses cannot be released from the plasma membrane [171]. This process is essential for synaptic vesicle formation and thus neuronal communication. These results indicated that dynamin was probably involved in the fission reaction that separates clathrin buds from the plasma membrane. Similar results were found with GTPase defective mutants in mammalian cells [172, 173]. At the time, it was the first protein/gene to be described with a clear phenotype in lipid membrane fission.

Structural and biochemical studies of dynamin allowed the formulation of its hypothetical mechanism of action. Purified dynamin was found to oligomerize into cylindrical helices of approximately 10 nm internal radius [174] independently of GTP. These helices were found to wrap around the neck of clathrin-coated pits in vivo [175]. It was thus proposed that dynamin would spontaneously associate as a

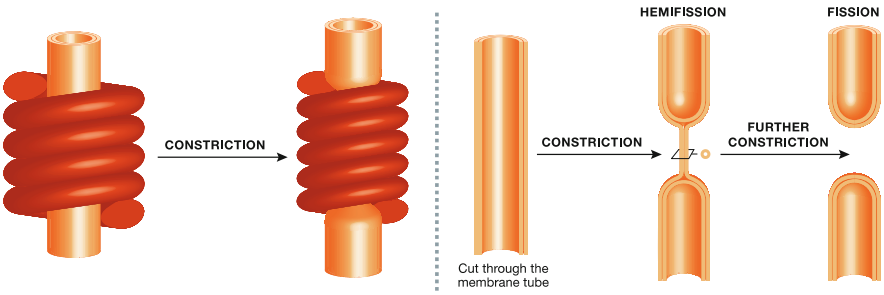

Fig. 9 Fission of a membrane neck by constriction. A protein coat (typically dynamin) can constrict a membrane neck, until it reaches hemi-fission (equivalent to hemifusion). Such constricted neck can then break spontaneously or by further constriction [176]

ring at the neck of membrane buds and that this dynamin ring would constrict upon GTP hydrolysis to break the membrane [174, 175]. The constriction was thought to first lead to hemi-fission of the membrane neck and then spontaneously resolve into full fission (Fig. 9).

Electron microscopy experiments rapidly supported this hypothesis, as dynamin mixed with liposomes formed membrane tubules circled by the dynamin helix that underwent constriction and fission upon GTP addition [177]. However, when these tubules were treated with GTP in solution instead of being attached to the EM grid, they would still constrict, but would not undergo fission [178]. Thus, dynamin can constrict membrane upon GTP hydrolysis, but constriction is not sufficient for fission. Structural studies have reached the same conclusions. A 3D structure of the polymer formed by dynamin around a membrane tube was obtained by cryo-EM [179, 180]. The most constricted state of dynamin [181] reduced the lumen of the tube down to 1.9 nm, but there was still a lumen. Thus, by constriction, dynamin does not reach hemi-fission, which explains why constriction is not sufficient for fission. In the following, we will describe how dynamin constricts and why its constriction needs other factors to mediate fission.

4.1.1 Structure of the Dynamin Helix and Mechanism of Constriction

The crystal structure of dynamin has been resolved in the absence of nucleotides [182, 183]. It is composed of four parts: the GTPase domain, the bundle signaling element (BSE), the stalk, and the Pleckstrin homology (PH) domain that binds the lipid phosphoinositides-(4,5)bisphosphate (PIP_2). The stalk is an elongated bundle of α-helices, which corresponds to the core of the protein and mediates self-assembly. It associates into a cross-like structure, forming antiparallel dimers [182, 183] that can further polymerize into a tetramer [184] and further into a polymer (Fig. 10a). The GTPase domain is connected to one end of the stalk through a flexible hinge, the BSE [185, 186]. The PH domain is linked to the other end of

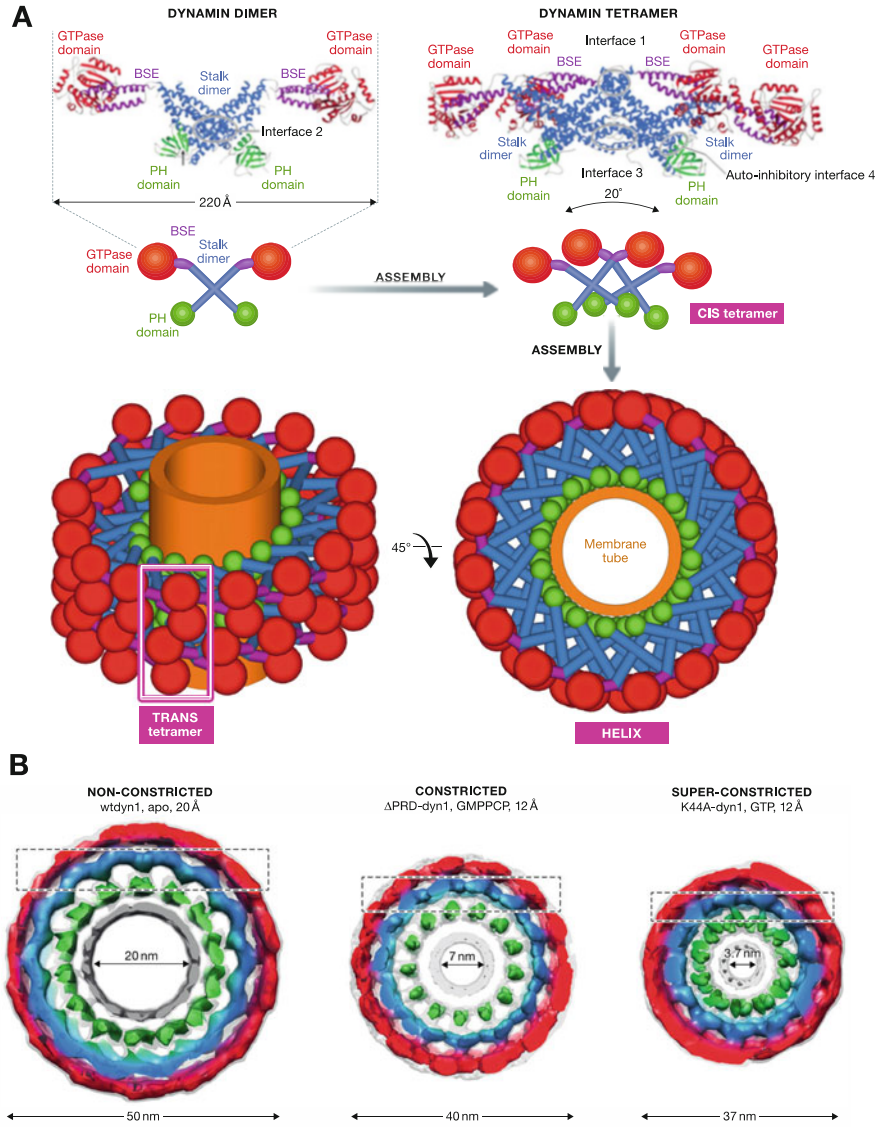

Fig. 10 (**a**) Structure of the dynamin helix during constriction. Structure of the dynamin dimer, dynamin tetramer, and proposed assembly process with domain names and dimensions; from reference [176]. (**b**) Cryo-EM images of the three states of dynamin-coated membrane tubules, with dimension and same color code as in A; from reference [176]

the stalk and found itself in the inner side of the helical cylinder, consistent with its binding to the membrane. Thus, the GTPase domain is found on the outer layer of the dynamin helix, as shown by fitting crystal structures within the cryo-EM maps (Fig. 10b).

A truncated dynamin that contains only the GTPase domain and part of the BSE [186] was crystalized with GDP.Alf4-, a nucleotide analog that is proposed to mimic the intermediate state of GTP hydrolysis. In this structure, the BSE changes dramatically its orientation toward the GTPase domain. Also, in the presence of GDP.Alf4-, GTPase domains are found in the crystal as very strong dimers, interacting through a specific interface. This so-called G–G interaction is not seen in the absence of nucleotide and is thus absent from the full-length structures [182–184]. This conformational change is proposed to explain the constriction of the entire polymer, as seen by cryo-EM (Fig. 10b).

The electron density maps of the super-constricted, constricted, and non-constricted helix of dynamin (Fig. 10b) have been used to fit in the crystal structure of dynamin [179, 180, 187, 188]. In these maps, GTPase domains of the antiparallel dimers are positioned in a way that allows for direct G–G interactions between GTPase domains of adjacent helical turns (Fig. 10a). In the non-constricted state, there are 14 dimers per helical turn. The constricted state is obtained in the presence of a non-hydrolysable analog of GTP (GMP-PCP [179]) and corresponds to 13 dimers per helical turn. The super-constricted state, which is believed to be the most constricted state of dynamin, corresponds to 11 dimers and is obtained with the GTP-loaded K44A mutant [181]. Some evidence exists that dynamin wild type in the presence of GTP would reach a similar constriction to that seen in the super-constricted state [189]. These data strongly support a mechanism in which adjacent turns could slide relatively to one another during GTP hydrolysis. In this case, GTPase domains would transiently interact and perform their BSE conformational changes to actively promote the sliding of the helical turns. This mechanism is fairly similar to myosin walking on an actin filament, with the notable difference that dynamin plays the role of both actin and myosin in this case.

The sliding movement between the dynamin turns is best evidenced by the rotation of beads attached to the dynamin-coated tubes and treated with GTP [190]. The displacement of adjacent helical turns generates torsion of the helix, thus inducing bead rotation. Dynamin is a right-handed helix and undergoes a right-handed twist, consistent with its constriction. The number of bead rotations is proportional to the number of helical turns present in the polymer (thus to its length), and in long polymers, the friction of the dynamin polymer onto the membrane hinders the constriction [191]. Indeed, the constriction of long polymeric helices is far from being a simple problem, as both the membrane and the liquid have to be expulsed from the tube while the helix is constricting [192]. However, the friction is not sufficient to shear the membrane enough to tear it.

An interesting aspect of this mechanism is that each GTPase domain (with the BSE) can be seen as a single molecular motor. However, while constricting, the load on each motor dramatically increases, for two reasons [192]. First, to constrict the membrane from 10 nm radius (initial, non-constricted state of the dynamin polymer)

to 5 nm, the dynamin coat has to apply a 500 pN nm constriction torque [191]. Second, it is most probable that the constriction leads to internal stresses within the polymeric structure of the dynamin helix, which will apply counteracting forces on the moving GTPase heads [192]. Thus, the constriction may stall at 11 dimers per helical turn because of the pressure of the membrane circled by the dynamin coat or because of the stresses rising with in the coat. However, the torque generated by dynamin onto rotating beads has been measured in the range of 1 nN nm, above the required value for efficient constriction, and the mechanical work provided in constriction matches the energy delivered by the GTP hydrolysis [66]. Thus, dynamin is a constrictase, which uses GTP energy to apply a constricting torque to the membrane and hold it tight.

However, this constriction, as powerful as it is, is not sufficient for fission. What are the requirements for dynamin-mediated fission? It turns out that the peculiar mechanical properties of the membrane are essential features of dynamin-mediated membrane fission.

4.1.2 Dynamin-Mediated Fission Depends on Membrane Mechanics

A striking observation was made when preparing samples for electron microscopy: when dynamin-coated tubules were attached to EM grids for negative stain [178] and then treated with GTP, they all broke, but when they were treated in solution with GTP and then frozen for cryo-EM, only constriction occurred, suggesting that attachment points to the substrate were essential in mediating fission [178]. Indeed, live-time imaging in an in vitro reconstitution assay of dynamin-mediated membrane fission showed that free dynamin-coated tubules would form supercoils and collapse without breaking, whereas those attached to the glass surface would get tense and undergo fission [190]. In this assay, the tension and the supercoils were resulting from the torsion activity resulting from constriction (see above). Thus, it was proposed that membrane tension was necessary for fission.

But why constriction and tension would be required for fission? The answer came from theoretical calculation [64]. Through the Canham–Helfrich model, as reported in the first part of this chapter, it was found that the elastic energy of a highly constricted neck, with a lumen of 1 nm radius, was the same as that of a hemi-fission intermediate [64]. When the lumen is constricted down to 2–3 nm by dynamin, the energy barrier for fission could thus be low enough for the neck to fission spontaneously through thermal fluctuations of the membrane [66].

This theoretical work has two main implications: first, if the fission reaction is happening spontaneously through thermal fluctuations, it should be stochastic, and its rate should depend on the energy barrier left to reach hemi-fission; second, this model postulates that the elastic energy of the membrane is a good approximation of the hemi-fission intermediate. This is far from being intuitive, as the stalk intermediate is a complex structure, where the energy depends certainly on the shape of the membrane but, as well, on the exact position and conformation of the lipids at the place where leaflets are merging. Hundreds to thousands of lipids are

involved in this structure, and it is thus fairly difficult to estimate the energy of such an intermediate through molecular dynamic approaches.

However, this relatively simple theoretical framework has the advantage of making the non-intuitive prediction that the membrane does not need to be constricted to hemi-fission in order to be broken, which seems to agree with the current structural knowledge of dynamin. Another consequence of this model is that, since the elastic energy of the membrane depends on its tension and rigidity, the energy of the fission intermediate also depends on these two parameters. In this case, it should also be the case for the rate of fission, which may explain the requirement for tension observed in reconstitution assays.

In vitro, the fission reaction mediated by dynamin is stochastic, following an exponential distribution with a typical time of 5–10 s [66]. Importantly, fission occurs right at the edge of the dynamin-constricted part, in the neck connecting the membrane constricted by dynamin and the rest of the membrane [66]. Numerical estimates of the elastic energy of the neck region give values between 30 and 70 k_BT, which should be rough estimates of the energy barrier to fission, and shows that it strongly depends on membrane tension and rigidity.

Experimental results confirmed that membrane rigidity hinders fission, while tension facilitates it in a roughly quantitative agreement with theory [66]. These results explained why dynamin constriction was not sufficient for fission and why tension was required. Surprisingly enough, both the time distribution and characteristic time of fission in vivo (with the notable exception of membrane fission at synapses) are very similar to those measured in vitro [66], i.e., typically 5–10 s [193]. This is different from SNARE-mediated fusion, where in vitro times are usually longer than in vivo ones, and only regulatory proteins can help to reach similar time values in vitro. But in vivo membrane fission is regulated in a similar way than in vitro. For example, osmotic shocks that decrease membrane tension in vitro were also shown to block dynamin-induced scission of the clathrin-coated pits in vivo [66].

4.2 The ESCRT Complex

The second best described fission machinery is called ESCRT-III, the fourth of a group of membrane-bound protein complexes involved in retrograde transport within the cell (ESCRT stands for endosomal sorting complex in retrograde transport). It was found through a genetic screen in yeast to isolate genes involved in retrograde transport [194, 195]. These genes, when mutated, were causing a dramatic morphological change of the yeast vacuole, the organelle in which cell components are degraded and recycled (functionally similar to the mammalian lysosome). Most of these genes are thus called VPS for vacuolar protein sorting. The three first complexes, ESCRT-0, ESCRT-I, and ESCRT-II are proposed to be involved in gathering all membrane proteins that are ubiquitinylated (ubiquitin is a small protein that is used to tag proteins that need to be degraded). They have

molecular interactions between them, which triggered the hypothesis that they operate sequentially, ESCRT-0 recruiting ESCRT-I and so on. The last complex to act is proposed to be ESCRT-III, which is involved in the formation—which means both membrane deformation and fission—of intraluminal vesicles (ILVs) that are budding inward from the endosome membrane, leading to the formation of multivesicular bodies (MVBs). These ILVs contain ubiquitinylated transmembrane proteins that are degraded when the MVBs fuse with the lysosome/vacuole [196].

The role of ESCRT-III in membrane fission has gained a lot of attention for several reasons. First, it is the second large protein complex after dynamin to exhibit a clear fission activity. Second, ESCRT-III polymerizes inside the membrane neck, instead of acting from the outside like dynamin [197]. Third, it was found to be a fission machinery with a broad spectrum of action. Dynamin is essentially acting at the plasma membrane, in a limited set of endocytic events, and maybe at the endosomal level. In contrast, the ESCRT-III complex, besides its role in MVBs biogenesis, is also implicated in many other cellular processes that require the same fission orientation.

ESCRT-III is involved in the last step of cytokinesis, the final phase of cell division, to break the membrane neck connecting the two daughter cells. This process, similar to membrane fission, is called abscission [198]. In abscission, ESCRT-III assembles within the cellular bridge connecting the two cells, onto a remnant structure of the constricted mitotic spindle called the midbody. ESCRT-III is also involved in viral budding, and in particular in HIV budding [199]. ESCRT-III, in this case, is hijacked by the viral capsid, which triggers the assembly of ESCRT-III within the neck connecting the virion to the plasma membrane [168]. More recently, ESCRT-III has been involved in the resolution of pores appearing during the formation of double-membrane organelles. A first example is the reformation of the nuclear envelope from vesicles dispersed in the cytoplasm at the end of the cell division [200, 201]. These vesicles fuse together in a double-membrane envelope. But many microtubules of the mitotic spindle stay trapped in holes through this envelope. These holes are closed by the polymerization of ESCRT-III proteins, triggered by the microtubules, in a process similar to abscission [201, 202]. A second example is the closure of the autophagosome, a double-membrane structure that also forms from vesicular fusion [202]. The autophagosome encloses parts of the cytoplasm that is digested to provide the cell with energy and molecules in case of starvation. The autophagosome is thought to grow from the rim of the cup formed by the double membrane, where vesicles are proposed to fuse. But the final closure, when a tiny neck is left, is mediated by ESCRT-III [203, 204]. Then the autophagosome fuses with lysosomes to digest the isolated material.

Because of these many roles in cell life, ESCRT-III became a major focus of interest for many scientists since 2000 [205]. However, even if its structure and its assembly dynamics start to be deciphered, because of its intrinsic complexity, how ESCRT-III promotes membrane fission is still not understood. In the following, we will describe the current models proposed for ESCRT-III-mediated fission, revealing unique mechanical properties of the entire complex.

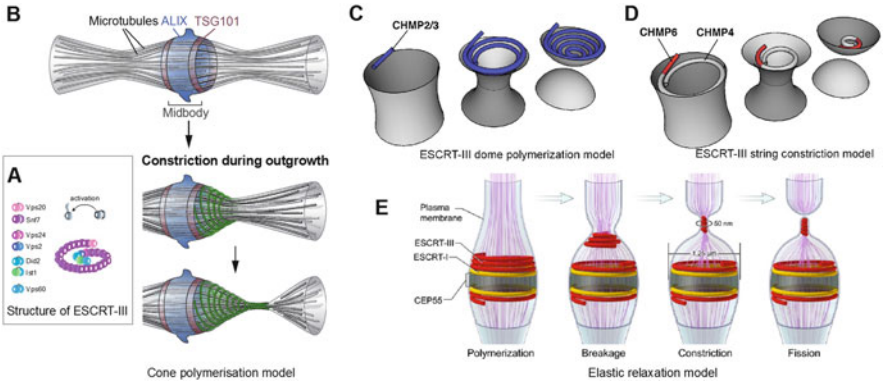

Fig. 11 Hypothetical mechanisms of ESCRT-III-mediated membrane fission. (**a**) Simple structure of the core complex of ESCRT-III [207]. (**b**) The cone polymerization model [208], (**c**) the dome polymerization model, (**d**) the constriction model, and (**e**) the elastic relaxation model [209]

4.2.1 Structure of the ESCRT-III Complex

Unlike dynamin, the core machinery of the ESCRT-III complex is composed of five components, with different names depending on the species considered (we will mostly use names from yeast and mammals) and different roles in the assembly of the complex [206]. The first protein is the nucleator of the ESCRT-III complex, called Vps20 in yeast and chmp6 in mammals (Fig. 11a). It binds the ESCRT-II complex and nucleates the polymerization of the second protein of ESCRT-III called Vps32/Snf7 in yeast and chmp4 in mammals [210]. Vps32/Snf7/chmp4 is the main component of the ESCRT-III complex and forms filaments with various shapes (see below). The third and fourth proteins are acting in tandem, Vps2 and Vps24 in yeast and chmp2 and chmp3 in mammals. They are thought to stop the polymerization of the Snf7/chmp4 filament [210] and to recruit the last and fifth protein, Vps4 [211, 212]. Vps4 is a homohexamer belonging to the AAA ATPases, a class of proteins involved in protein folding and filament disassembly [213]. Indeed, Vps4 is proposed to disassemble the entire complex. In vitro, it disassembles the complex only in the absence of free Snf7 molecules but promotes turnover and assembly when the filaments are in equilibrium with a pool of soluble ESCRT-III proteins [214]. Importantly, the various functions of the different core subunits of the ESCRT-III complex suggest that they are recruited to the complex in a sequential manner [206]. However, these subunits have been found to assemble all together both in vitro and in vivo [214]. Also, besides the five core proteins present in all ESCRT-III complexes, associated subunits may play additional roles in specific functions of the ESCRT-III complex. For example, even though there is only one isoform of Snf7 in yeast and in drosophila (called *shrub*), there are three isoforms in mammals (chmp4 A, B, and C) thought to play specific roles in abscission. Chmp4C is specifically involved in delaying abscission as a response to a specific checkpoint. As well, Did2/chmp1B and Ist1 are proposed to play regulatory roles in

specific subsets of reactions [215]. For example, chmp1b is involved in recruiting Spastin, the AAA ATPase that cuts the microtubule bundle at the midbody to allow for constriction of the membrane by the ESCRT-III complex [216].

Another important partner of the ESCRT-III complex is Bro1/Alix, a multivalent protein that binds ESCRT-II, ESCRT-III (through Snf7/chmp4 [217]), and the lipid membrane through Lyso-BisPhosphatic Acid (LBPA) [218], a lipid found only in the outer membrane of MVBs, which plays a role in ILV formation [219]. A notable difference between yeast and mammals is that the yeast Bro1 does not interact with LBPA and that LBPA itself has not yet been identified in yeast. Nevertheless, Bro1/Alix has been proposed to recruit ESCRT-III proteins to many sites where it performs fission, from abscission [220] to HIV budding [221–224], where it interacts directly with the Gag proteins of the viral capsid, and of course MVBs.

Apart from this large subunit family, and many modular partners, all ESCRT-III core proteins are structurally extremely similar, consisting of a four-helix bundle and a MIM (mutated in metastasis) domain that allows for direct interaction with partners, in particular with Vps4 [212]. Interestingly, these proteins have been recently shown to have two conformations, a closed one, where the four helices form a tight bundle, and an open one, where helix 2 and helix 3 align to form an extended helix that participates in a helix-swapping mechanism forming a tight interaction between monomers [225–227]. This interaction is at the basis of the oligomerization mechanism of ESCRT-III proteins, as it promotes their linear association.

Because of this common structure and close/open conformational switch, many ESCRT-III proteins have been shown to form oligomers in vitro [217, 225, 228, 229]. However, the shape of these oligomers is very variable, depending on the protein considered and on the conditions of assembly. Snf7 assembles into long filaments with curly ends [229] and spirals in solution or at the surface of lipid membranes [230]. Chmp2 and chmp3 co-assemble in tubular helices with closed dome-like structure at their tips when membrane is added. More strikingly, the accessory proteins Ist1 and chmp1b co-assemble in a two-layered helical tube, chmp1b in the opened, polymerized conformation, Ist1 keeping its closed conformation [225]. In some cases, conical spirals have been observed, which resemble dramatically the ESCRT-III structures seen at the midbody [231] or at the basis of ESCRT-III-induced membrane invaginations when chmp4b is overexpressed in HeLa cells [225, 232, 233]. Moreover, adding Vps2 and Vps24 to Snf7 oligomers also transform the flat spirals into helical cylinders [229].

These findings are very interesting for two reasons: first, it strongly suggests that the oligomer is itself curved, with a preferred radius of curvature. Indeed, the helix-swapping polymerization process creates an angle between monomers, defining a curved oligomer; second, the variability of the structures observed by assembly of single or multiple ESCRT-III proteins suggests that membrane remodeling occurs by a different mechanism than scaffolding. Like it happens for clathrin-mediated membrane deformation, scaffolding occurs when a protein polymerizes at the surface of a lipid membrane into a specific shape that "molds" the lipid membrane. A corollary of this definition is that the protein assembly must adopt a given shape or structure, with little flexibility.

In the following, we describe how membrane remodeling is proposed to occur when mediated by ESCRT-III proteins. Some of the hypothetical mechanisms are relying on new mechanical and physical principles, previously unknown in the field of membrane fission.

4.2.2 Constriction of Necks by ESCRT-III

Since fission of membranes requires constriction of membrane necks to a size that allow them to spontaneously break, and since the characterization of the ESCRT-III complex is too limited to yet have a clear mechanism, several hypotheses have been proposed to explain how the ESCRT-III complex could constrict membranes. A first hypothesis is constriction by polymerization, a second one is constriction by depolymerization, and a third one is constriction by elastic relaxation. In the following, we briefly describe the possible mechanisms by which ESCRT-III could constrict and fission membranes. However, these mechanisms are highly hypothetical, and not yet strongly supported by experimental facts.

Constriction by Conical Polymerization of the ESCRT-III Complex (Fig. 11b)
This hypothetical mechanism is based on several observations. At the midbody, during abscission, ESCRT-III proteins assemble into a conical lattice, whose basis is connected to the midbody and further grows from the midbody into the membrane neck [231, 234]. Because of its conical shape, the more it grows, the more it constricts. Such conical shapes have been observed in vitro and in vivo in the neck of virion-like particles formed at the plasma membrane [232]. Thus, it has been proposed that this particular conical shape could be a determinant of constriction by assembly, the membrane strongly adhering onto the outer surface of the cone. But since in vitro, as well as in vivo, many different shapes of the ESCRT-III polymer are observed, it is difficult to know if the conical shape is the result of a specific sequence or stoichiometry of assembly in vivo [235] or whether it is the result of another constriction mechanism which forces ESCRT-III to adopt a conical shape. Moreover, the tip of the cone, which is the most constricted part, has never been observed with a radius lower than 15 nm, which is still very far from what is required for fission (2–3 nm).

Fission by Adhesion: The Dome Model (Fig. 11c)
Another mechanism, still utilizing polymerization of the ESCRT-III proteins, was proposed to force membrane constriction. Chmp2 and chmp3 have been shown to co-assemble in cylindrical tubules [228], with blunt ends in the absence of membrane. But when liposomes are added to the mixture, they strongly adhere to the outer layer of the polymer. In this case, the tips of the cylinder are assembled into a dome-like structure coated with membranes, and the tubules are shorter than in the absence of liposomes, suggesting that the presence of the membrane induces the polymerization of chmp2/3 into a dome-like structure. Based on these results, the authors proposed that the dome-like structure could promote scaffolding of the membrane and constriction at the tip of the dome to radius compatible with

fission. In this mechanism, the critical energy parameter is the adhesion energy of the membrane onto the dome, which competes with the elastic energy of the membrane required for constriction. Depending on how strong the adhesion of the membrane onto the polymer is, the constriction may be spontaneous, reaching a radius sufficient for fission, or stalls at a larger radius [236]. Values of the chmp2/3 affinity for lipid membranes seem to agree with the adhesion energy being sufficient for constriction and fission.

Constriction and Fission by Depolymerization of the ESCRT-III Complex (Fig. 11d)

The requirement of Vps4 for membrane fission has suggested a mechanism by which depolymerization of ESCRT-III could trigger constriction [210]. This mechanism is called the "lasso." In this case, the process also starts with Vps20/chmp6 nucleating the assembly of Vps32/Snf7/chmp4. The Snf7 polymer grows into a loop, connecting back onto the Vps20/chmp6 nuclei. Once closed, the loop recruits Vps2/chmp2 and Vps24/chmp3 and further Vps4 to start depolymerizing the loop from one end, reducing its radius with time. If the complex is within a tubular membrane, reduction of its radius would cause constriction of the membrane tube. A limit of this model is that the constriction occurs at the site of the polymer, which means, since the proteins are 3 nm thick at least that they all have to be removed in order to allow for fission. Another limit is the geometry of the neck. If the polymerization of Vps32/Snf7/chmp4 happens within the tubular part of the neck, constriction can occur by depolymerization. But, it does not explain how ESCRT-III could deform the membrane into a bud. It was proposed that transmembrane cargoes, which should be trapped into the ESCRT-III loop, could be the handle onto which the constriction of the loop could apply forces. In this case, the cargoes would get concentrated while the loop is shrinking through depolymerization, and because of this crowding of proteins onto the membrane, the membrane could bud off, by creating an asymmetric repulsion force on one side of the lipid bilayer, that will be compensated by curvature [81, 83]. However, this scenario remains highly speculative.

Constriction and Fission by Elastic Relaxation of the ESCRT-III Complex (Fig. 11e)

A striking observation was made during abscission. Right before the membrane breaks, the ESCRT-III conical structure splits into two rings, a large one, still connected to the midbody, and a constricted one, a few microns from the midbody [234]. Abscission, membrane fission, occurs right next to the second one. It was thus proposed that Vps4 would be involved in splitting the ring and that constriction and fission would occur by elastic relaxation of the free ring [209]. In this mechanism, the ESCRT-III conical structure would grow around solid structures, the midbody and the microtubule bundle, which force it to grow at a large radius of curvature. Once these constraints have been removed, by breaking the ESCRT-III cone into two parts freeing it from the midbody, and by cleavage of the microtubules at the tip of the cone by Spastin [216, 237], the ESCRT-III ring could relax to its preferred radius of curvature.

In this mechanism, the mechanical properties of the Vps32/Snf7/chmp4 filament are essential: the filament must have a fairly small spontaneous radius of curvature; it also has to be flexible, meaning it can grow at wider radii than its preferred radius; once grown, it has to be able to relax to its preferred radius of curvature. Interestingly, some of the hypotheses at the basis of this mechanism have been verified in vitro [238]. The filaments have a preferred radius of curvature of 25 nm and a persistence length of 300 nm, explaining the high flexibility of the ESCRT-III polymer. Polymerization energy per unit area was measured to be sufficient to deform filaments, with a value of 10^{-4} N/m.

These properties could also explain the striking membrane deformation observed in mammalian cells overexpressing chmp4 [233]. In these cells, the cytoplasmic leaflet of the membrane is covered with flat spirals of chmp4. But if Vps4 ATPase dead mutant is co-expressed, the spirals become tubules protruding from the cells and filled with chmp4 filaments. A buckling mechanism has been proposed to generate these structures [239] that depend on a competition between the elastic stress accumulated in growing flat spirals and the energy required to deform the membrane [239]. If the membrane is too rigid, the spiral grows flat. If the filament is too rigid, it grows into a helical tube from the beginning, to better accommodate the preferred curvature of all ESCRT-III turns. For intermediate conditions, however, the spiral starts to grow flat and buckles into a helix above a threshold size.

4.3 Other Fission Machineries

Another class of proteins that has been proposed to directly participate in fission is the BAR protein family. These proteins all contain a Bin-Amphiphysin-Rvs (BAR) domain, which is a dimer with a crescent shape [240]. Positively charged residues are essentially found on the internal side of the crescent, mediating electrostatic interactions with the negatively charged lipids of the membrane. Strikingly, different BAR domains have different curvatures, from very shallow (radius of 50–70 nm) for the F-BAR domains (found, e.g., in syndapin) to very narrow (10 nm radius) like the N-BAR domains of endophilin and amphiphysin. These different curvatures match the size of membrane tubes generated by BAR proteins when mixed with negatively charged liposomes [241].

The BAR domain proteins have thus been thought to either induce curvature or sense curvature of growing buds. Seen as inclusions in the membrane that have a specific spontaneous curvature, the balance between curvature-sensing and curvature-inducing properties was shown to depend on BAR domain membrane densities [242]. However, even if the curvature-inducing function of the BAR domains may help membrane fission, the overall function of BAR domain proteins in membrane fission is not clear yet.

Several studies report apparently contradictory properties on fission induction or fission inhibition by BAR domain proteins. On the one hand, the amphipathic helices of the N-BAR domain can induce high curvature and membrane fission both

in vitro and in vivo [243]. On the other hand, the crescent shape of the BAR domain can fix the curvature to a value above the threshold for spontaneous fission, thus blocking fission [243]. Specifically, in the case of dynamin-mediated membrane fission, the BAR proteins binding to dynamin are proposed to either block or activate fission: amphiphysin was found to promote fission, while endophilin, although bearing two additional amphipathic helices, was found to block it [244]. However, both proteins reduced the GTPase activity of dynamin, an effect found later to depend on membrane curvature [245]. The reduction of both the GTPase and fission activities of dynamin by endophilin is consistent with the recently observed insertion of the BAR domain in between helical turns of dynamin [246].

BAR domains however unambiguously promote fission in newly discovered endocytic routes. Notably, endophilin A2 clearly plays a direct role in fission of both Shiga toxin-induced endocytic carriers [247–249] and hormone receptor-specific carriers [250]. Surprisingly, endophilin A2 formed a rigid scaffold on pre-formed membrane tubes [251], growing very much like dynamin scaffolds [252]. However, when pulling forces were applied to endophilin A2-coated membrane tubes, the tubes underwent fission [249]. It was later found that lipid diffusion below the endophilin A2 coat was highly limited, which led to the thinning of the uncoated part of the tube when active forces were extending the tube [253]. As the thinning of the tube depended both on the length of the endophilin A2 coat and the pulling rate, conditions in which the thinning of the tube was sufficient to reach spontaneous fission corresponded to a large area of the phase diagram in vitro. Interestingly, these findings show how fission by membrane shearing, which occurred only at very high extrusion rates with pure lipid membranes [85], can occur when proteins limit lipid diffusion. While this effect was initially thought to be irrelevant to physiological conditions because of the high pulling rates it required, endophilin A2 action reduced the required pulling rates to those observed in vivo for actin and molecular motors. It also explains the general requirement of actin polymerization for all membrane fission reactions in the cell.

5 Conclusion: Comparison Between Fusion and Fission Machineries

Membrane fusion and fission reactions both strongly depend upon reaching a critical distance between two membrane monolayer surfaces (outer monolayers during fusion and inner monolayers during fission) and upon inducing significant perturbation of the membrane bilayer structure to render the fusion/fission process energetically favorable. The protein machineries of membrane fusion and fission employ various strategies to achieve these fundamental tasks. Membrane approach in fusion is mediated by large conformational changes of fusion proteins across membranes to form specific tertiary structures with the capacity to dock membranes and bring their outer monolayers into close proximity. SNARE and viral fusion

proteins assemble into membrane-bridging coiled coil structures using, respectively, a zippering and a jackknife mechanism (Figs. 5 and 6). Membrane approach in fission is induced by scaffolding effects to narrow the fission neck. ESCRT proteins may form a dome-like structure onto which the membrane adheres and spreads radially, reducing the neck diameter above the dome, whereas dynamin proteins polymerize around the membrane neck in the form of a spiral that constricts upon GTP hydrolysis (Figs. 10 and 11). Membrane perturbations by fusion and fission proteins are strongly dependent on the intrinsic mechanical properties of membranes, notably membrane tension and curvature. Perturbation by membrane bending is a common principle used by membrane fusion and fission proteins, which often insert an amphipathic domain into lipid bilayers to induce strong local curvature at the sites of fusion/fission. The fission proteins epsin, endophilin, and amphiphysin, as well as the viral fusion protein hemagglutinin, all use N-terminal amphipathic helices, which bind to outer lipid monolayers and cause membrane bending by a wedge effect. Membrane insertion of amphipathic helices can also generate other types of structural perturbations such as lipid bilayer thinning and lipid aliphatic chain disorder, as observed with the C-terminal amphipathic helix of the fusion protein Atlastin. The local lipid composition at sites of fusion/fission can also affect the intrinsic curvature and stability of membranes. Lipids with curvature-inducing molecular shapes were shown to activate both fusion and fission processes. Fusion and fission reactions also share common intermediate lipidic structures and energies. They both proceed through a hemifusion/hemi-fission stalk, which corresponds to self-merging of the inner monolayers of the neck membrane in the case of fission and to the merging of the approaching outer monolayers in the case of fusion. The energy barriers of fusion and fission were estimated to be of the order of 50 k_BT, which is in line with the energy generated by SNARE zippering during membrane fusion and by dynamin constriction during membrane fission. Given these similarities between fusion and fission reactions, it is not surprising to find proteins from the same family being involved in both fusion and fission processes. Large GTPase proteins from the dynamin superfamily, which were initially described for their role in membrane fission, are also involved in cellular homotypic fusion events. Mitochondrial fusion and fission events are both mediated by dynamin-related proteins. In mammals, DRP1 controls mitochondrial fission, whereas Mitofusins and OPA1 induce the fusion of outer and inner mitochondrial membranes, respectively. Fusion between ER tubules is controlled by the large membrane-anchored GTPase Atlastin. Interestingly, fusion and fission reactions, respectively, mediated by SNARE and dynamin proteins were recently found to compete at the level of the hemifusion/hemi-fission intermediate state in live cells to determine the transition to fusion or fission [254], further confirming the tight interplay and complementarity between fusion and fission mechanisms.

References

1. Söllner TH, Rothman JE (1996) Molecular machinery mediating vesicle budding, docking and fusion. Cell Struct Funct 21:407–412
2. Chan DC (2006) Mitochondrial fusion and fission in mammals. Annu Rev Cell Dev Biol 22:79–99
3. Weissenhorn W, Hinz A, Gaudin Y (2007) Virus membrane fusion. FEBS Lett 581:2150–2155
4. Chernomordik LV, Kozlov MM (2003) Protein-lipid interplay in fusion and fission of biological membranes. Annu Rev Biochem 72:175–207
5. Kozlov MM, McMahon HT, Chernomordik LV (2010) Protein-driven membrane stresses in fusion and fission. Trends Biochem Sci 35:699–706
6. Chernomordik LV, Kozlov MM (2005) Membrane hemifusion: crossing a chasm in two leaps. Cell 123:375–382
7. Düzgüneş N, Wilschut J, Fraley R, Papahadjopoulos D (1981) Studies on the mechanism of membrane fusion. Role of head-group composition in calcium- and magnesium-induced fusion of mixed phospholipid vesicles. Biochim Biophys Acta 642:182–195
8. Nir S, Bentz J, Wilschut J, Duzgunes N (1983) Aggregation and fusion of phospholipid vesicles. Prog Surf Sci 13:1–124
9. Helm CA, Israelachvili JN, McGuiggan PM (1989) Molecular mechanisms and forces involved in the adhesion and fusion of amphiphilic bilayers. Science 246:919–922
10. Nir S, Wilschut J, Bentz J (1982) The rate of fusion of phospholipid vesicles and the role of bilayer curvature. Biochim Biophys Acta 688:275–278
11. Chen H et al (2003) Mitofusins Mfn1 and Mfn2 coordinately regulate mitochondrial fusion and are essential for embryonic development. J Cell Biol 160:189–200
12. Davidson RL, Gerald PS (1976) Improved techniques for the induction of mammalian cell hybridization by polyethylene glycol. Somatic Cell Genet 2:165–176
13. Schlegel R, McEvoy L (1987) Red cell-mediated microinjection. Methods Enzymol 149:293–300
14. Szoka F et al (1981) Use of lectins and polyethylene glycol for fusion of glycolipid-containing liposomes with eukaryotic cells. Proc Natl Acad Sci USA 78:1685–1689
15. Lentz BR (1994) Polymer-induced membrane fusion: potential mechanism and relation to cell fusion events. Chem Phys Lipids 73:91–106
16. Lentz BR (2007) PEG as a tool to gain insight into membrane fusion. Eur Biophys J 36:315–326
17. Burgess SW, McIntosh TJ, Lentz BR (1992) Poly(ethylene glycol)-induced fusion by membrane hydration: importance of interbilayer separation. Biochemistry 31:2653–2661
18. Haque E, McIntosh TJ, Lentz BR (2001) Influence of lipid composition on physical properties and PEG-mediated fusion of curved and uncurved model membrane vesicles: " nature's own " fusogenic. Biochemistry 40:4340–4348
19. Kuhl T et al (1996) Direct measurement of polyethylene glycol induced depletion attraction between lipid bilayers. Langmuir 12:3003–3014
20. Evans E, Needham D (1988) Attraction between lipid bilayer membranes in concentrated solutions of nonadsorbing polymers: comparison of mean-field theory with measurements of adhesion energy. Macromolecules 21:1822–1831
21. Boni LT, Stewart TP, Alderfer JL, Hui SW (1981) Lipid-polyethylene glycol interactions: II. Formation of defects in bilayers. J Membr Biol 62:71–77
22. Tilcock CPS, Fisher D (1979) Interaction of phospholipid membranes with poly(ethylene glycol)s. Biochim Biophys Acta 577:53–61
23. Lentz BR, McIntyre GF, Parks DJ, Yates JC, Massenburg D (1992) Bilayer curvature and certain amphipaths promote poly(ethylene glycol)-induced fusion of dipalmitoylphosphatidylcholine unilamellar vesicles. Biochemistry 31:2643–2653

24. Talbot WA, Zheng LX, Lentz BR (1997) Acyl chain unsaturation and vesicle curvature alter outer leaflet packing and promote poly(ethylene glycol)-mediated membrane fusion. Biochemistry 36:5827–5836
25. Yang Q, Guo Y, Li L, Hui SW (1997) Effects of lipid headgroup and packing stress on poly(ethylene glycol)-induced phospholipid vesicle aggregation and fusion. Biophys J 73:277–282
26. Marra J, Israelachvili J (1985) Direct measurements of forces between phosphatidylcholine and phosphatidylethanolamine bilayers in aqueous electrolyte solutions. Biochemistry 24:4608–4618
27. Takamori S et al (2006) Molecular anatomy of a trafficking organelle. Cell 127:831–846
28. Haque ME, Lentz BR (2004) Roles of curvature and hydrophobic interstice energy in fusion: studies of lipid perturbant effects. Biochemistry 43:3507–3517
29. Meers P, Ali S, Erukulla R, Janoff AS (2000) Novel inner monolayer fusion assays reveal differential monolayer mixing associated with cation-dependent membrane fusion. Biochim Biophys Acta 1467:227–243
30. Lee J, Lentz BR (1997) Evolution of lipidic structures during model membrane fusion and the relation of this process to cell membrane fusion. Biochemistry 36:6251–6259
31. Chernomordik LV, Melikyan GB, Chizmadzhev YA (1987) Biomembrane fusion: a new concept derived from model studies using two interacting planar lipid bilayers. Biochim Biophys Acta Rev Biomembr 906:309–352
32. Lei G, MacDonald RC (2003) Lipid bilayer vesicle fusion: intermediates captured by high-speed microfluorescence spectroscopy. Biophys J 85:1585–1599
33. Heuvingh J, Pincet F, Cribier S (2004) Hemifusion and fusion of giant vesicles induced by reduction of inter-membrane distance. Eur Phys J E Soft Matter 14:269–276
34. Chanturiya A, Chernomordik LV, Zimmerberg J (1997) Flickering fusion pores comparable with initial exocytotic pores occur in protein-free phospholipid bilayers. Proc Natl Acad Sci USA 94:14423–14428
35. Lee J, Lentz BR (1998) Secretory and viral fusion may share mechanistic events with fusion between curved lipid bilayers. Proc Natl Acad Sci USA 95:9274–9279
36. Chernomordik L, Chanturiya A, Green J, Zimmerberg J (1995) The hemifusion intermediate and its conversion to complete fusion: regulation by membrane composition. Biophys J 69:922–929
37. Cohen FS, Zimmerberg J, Finkelstein A (1980) Fusion of phospholipid vesicles with planar phospholipid bilayer membranes. II. Incorporation of a vesicular membrane marker into the planar membrane. J Gen Physiol 75:251–270
38. Verkleij AJ, Mombers C, Gerritsen WJ, Leunissen-Bijvelt L, Cullis PR (1979) Fusion of phospholipid vesicles in association with the appearance of lipidic particles as visualized by freeze fracturing. Biochim Biophys Acta 555:358–361
39. Siegel DP, Burns JL, Chestnut MH, Talmon Y (1989) Intermediates in membrane fusion and bilayer/nonbilayer phase transitions imaged by time-resolved cryo-transmission electron microscopy. Biophys J 56:161–169
40. Siegel DP, Epand RM (1997) The mechanism of lamellar-to-inverted hexagonal phase transitions in phosphatidylethanolamine: implications for membrane fusion mechanisms. Biophys J 73:3089–3111
41. Yang L, Huang HW (2002) Observation of a membrane fusion intermediate structure. Science 297:1877–1879
42. Aeffner S, Reusch T, Weinhausen B, Salditt T (2012) Energetics of stalk intermediates in membrane fusion are controlled by lipid composition. Proc Natl Acad Sci USA 109:E1609–E1618
43. Knecht V, Marrink SJ (2007) Molecular dynamics simulations of lipid vesicle fusion in atomic detail. Biophys J 92:4254–4261
44. Müller M, Katsov K, Schick M (2003) A new mechanism of model membrane fusion determined from Monte Carlo simulation. Biophys J 85:1611–1623
45. Jahn R, Grubmüller H (2002) Membrane fusion. Curr Opin Cell Biol 14:488–495

46. Chernomordik LV, Kozlov MM (2008) Mechanics of membrane fusion. Nat Struct Mol Biol 15:675–683
47. Efrat A, Chernomordik LV, Kozlov MM (2007) Point-like protrusion as a prestalk intermediate in membrane fusion pathway. Biophys J 92:L61–L63
48. Kozlovsky Y, Kozlov MM (2002) Stalk model of membrane fusion: solution of energy crisis. Biophys J 82:882–895
49. Kuzmin PI, Zimmerberg J, Chizmadzhev YA, Cohen FS (2001) A quantitative model for membrane fusion based on low-energy intermediates. Proc Natl Acad Sci USA 98:7235–7240
50. Kozlovsky Y, Chernomordik LV, Kozlov MM (2002) Lipid intermediates in membrane fusion: formation, structure, and decay of hemifusion diaphragm. Biophys J 83:2634–2651
51. Siegel DP (1993) Energetics of intermediates in membrane fusion: comparison of stalk and inverted micellar intermediate mechanisms. Biophys J 65:2124–2140
52. Markin VS, Albanesi JP (2002) Membrane fusion: stalk model revisited. Biophys J 82:693–712
53. Jackson MB (2009) Minimum membrane bending energies of fusion pores. J Membr Biol 231:101–115
54. Marrink SJ, Mark AE (2003) The mechanism of vesicle fusion as revealed by molecular dynamics simulations. J Am Chem Soc 125:11144–11145
55. Grafmüller A, Shillcock J, Lipowsky R (2009) The fusion of membranes and vesicles: pathway and energy barriers from dissipative particle dynamics. Biophys J 96:2658–2675
56. Noguchi H, Takasu M (2001) Fusion pathways of vesicles: a Brownian dynamics simulation. J Chem Phys 115:9547
57. Lentz BR, Talbot W, Lee J, Zheng LX (1997) Transbilayer lipid redistribution accompanies poly(ethylene glycol) treatment of model membranes but is not induced by fusion. Biochemistry 36:2076–2083
58. Evans KO, Lentz BR (2002) Kinetics of lipid rearrangements during poly(ethylene glycol)-mediated fusion of highly curved unilamellar vesicles. Biochemistry 41:1241–1249
59. Chernomordik LV et al (1985) The shape of lipid molecules and monolayer membrane fusion. Biochim Biophys Acta Biomembr 812:643–655
60. Kasson PM, Pande VS (2007) Control of membrane fusion mechanism by lipid composition: predictions from ensemble molecular dynamics. PLoS Comput Biol 3:e220
61. Lee JY, Schick M (2007) Field theoretic study of bilayer membrane fusion III: membranes with leaves of different composition. Biophys J 92:3938–3948
62. Hed G, Safran SA (2003) Initiation and dynamics of hemifusion in lipid bilayers. Biophys J 85:381–389
63. Chizmadzhev YA, Kuzmin PI, Kumenko DA, Zimmerberg J, Cohen FS (2000) Dynamics of fusion pores connecting membranes of different tensions. Biophys J 78:2241–2256
64. Kozlovsky Y, Kozlov MM (2003) Membrane fission: model for intermediate structures. Biophys J 85:85–96
65. Shlomovitz R, Gov NS (2009) Membrane-mediated interactions drive the condensation and coalescence of FtsZ rings. Phys Biol 6:046017
66. Morlot S et al (2012) Membrane shape at the edge of the dynamin helix sets location and duration of the fission reaction. Cell 151:619–629
67. Lingwood D, Simons K (2010) Lipid rafts as a membrane-organizing principle. Science 327:46–50
68. Jülicher F, Lipowsky R (1996) Shape transformations of vesicles with intramembrane domains. Phys Rev E Stat Phys Plasmas Fluids Relat Interdiscip Topics 53:2670–2683
69. Jülicher F, Lipowsky R (1993) Domain-induced budding of vesicles. Phys Rev Lett 70:2964–2967
70. Baumgart T, Hess ST, Webb WW (2003) Imaging coexisting fluid domains in biomembrane models coupling curvature and line tension. Nature 425:821–824
71. Stachowiak JC, Hayden CC, Sasaki DY (2010) Steric confinement of proteins on lipid membranes can drive curvature and tubulation. Proc Natl Acad Sci USA 107:7781–7786

72. Sens P, Turner MS (2006) Budded membrane microdomains as tension regulators. Phys Rev E Stat Nonlinear Soft Matter Phys 73:031918
73. Sens P (2004) Dynamics of nonequilibrium membrane bud formation. Phys Rev Lett 93:108103
74. Allain JM, Ben Amar M (2006) Budding and fission of a multiphase vesicle. Eur Phys J E Soft Matter 20:409–420
75. Allain JM, Storm C, Roux A, Ben Amar M, Joanny JF (2004) Fission of a multiphase membrane tube. Phys Rev Lett 93:158104
76. Roux A et al (2005) Role of curvature and phase transition in lipid sorting and fission of membrane tubules. EMBO J 24:1537–1545
77. Lenz M, Morlot S, Roux A (2009) Mechanical requirements for membrane fission: common facts from various examples. FEBS Lett 583:3839–3846
78. Leibler S (1986) Curvature instability in membranes. J Phys 47:507–516
79. Tsafrir I, Caspi Y, Guedeau-Boudeville MA, Arzi T, Stavans J (2003) Budding and tubulation in highly oblate vesicles by anchored amphiphilic molecules. Phys Rev Lett 91:138102
80. Tsafrir I et al (2001) Pearling instabilities of membrane tubes with anchored polymers. Phys Rev Lett 86:1138–1141
81. Stachowiak JC et al (2012) Membrane bending by protein-protein crowding. Nat Cell Biol 14:944–949
82. Snead WT et al (2017) Membrane fission by protein crowding. Proc Natl Acad Sci USA 114:E3258–E3267
83. Kozlov MM et al (2014) Mechanisms shaping cell membranes. Curr Opin Cell Biol 29:53–60
84. Stachowiak JC, Brodsky FM, Miller EA (2013) A cost-benefit analysis of the physical mechanisms of membrane curvature. Nat Cell Biol 15:1019–1027
85. Evans E, Yeung A (1994) Hidden dynamics in rapid changes of bilayer shape. Chem Phys Lipids 73:39–56
86. Söllner T, Bennett MK, Whiteheart SW, Scheller RH, Rothman JE (1993) A protein assembly-disassembly pathway in vitro that may correspond to sequential steps of synaptic vesicle docking, activation, and fusion. Cell 75:409–418
87. Nonet ML, Saifee O, Zhao H, Rand JB, Wei L (1998) Synaptic transmission deficits in Caenorhabditis elegans synaptobrevin mutants. J Neurosci 18:70–80
88. Deitcher DL et al (1998) Distinct requirements for evoked and spontaneous release of neurotransmitter are revealed by mutations in the Drosophila gene neuronal-synaptobrevin. J Neurosci 18:2028–2039
89. Schoch S et al (2001) SNARE function analyzed in synaptobrevin/VAMP knockout mice. Science 294:1117–1122
90. Washbourne P et al (2002) Genetic ablation of the t-SNARE SNAP-25 distinguishes mechanisms of neuroexocytosis. Nat Neurosci 5:19–26
91. Schiavo G et al (1992) Tetanus and botulinum-B neurotoxins block neurotransmitter release by proteolytic cleavage of synaptobrevin. Nature 359:832–835
92. Blasi J et al (1993) Botulinum neurotoxin A selectively cleaves the synaptic protein SNAP-25. Nature 365:160–163
93. Blasi J et al (1993) Botulinum neurotoxin C1 blocks neurotransmitter release by means of cleaving HPC-1/syntaxin. EMBO J 12:4821–4828
94. Weber T et al (1998) SNAREpins: minimal machinery for membrane fusion. Cell 92:759–772
95. Hu C et al (2003) Fusion of cells by flipped SNAREs. Science 300:1745–1749
96. Dietrich LE, Boeddinghaus C, LaGrassa TJ, Ungermann C (2003) Control of eukaryotic membrane fusion by N-terminal domains of SNARE proteins. Biochim Biophys Acta 1641:111–119
97. Daste F, Galli T, Tareste D (2015) Structure and function of longin SNAREs. J Cell Sci 128:4263–4272
98. Sutton RB, Fasshauer D, Jahn R, Brunger AT (1998) Crystal structure of a SNARE complex involved in synaptic exocytosis at 2.4 A resolution. Nature 395:347–353

99. Melia TJ et al (2002) Regulation of membrane fusion by the membrane-proximal coil of the t-SNARE during zippering of SNAREpins. J Cell Biol 158:929–940
100. Sørensen JB et al (2006) Sequential N- to C-terminal SNARE complex assembly drives priming and fusion of secretory vesicles. EMBO J 25:955–966
101. Stein A, Weber G, Wahl MC, Jahn R (2009) Helical extension of the neuronal SNARE complex into the membrane. Nature 460:525–528
102. Fasshauer D, Antonin W, Subramaniam V, Jahn R (2002) SNARE assembly and disassembly exhibit a pronounced hysteresis. Nat Struct Biol 9:144–151
103. Hayashi T et al (1994) Synaptic vesicle membrane fusion complex: action of clostridial neurotoxins on assembly. EMBO J 13:5051–5061
104. May AP, Whiteheart SW, Weis WI (2001) Unraveling the mechanism of the vesicle transport ATPase NSF, the N-ethylmaleimide-sensitive factor. J Biol Chem 276:21991–21994
105. Li F et al (2007) Energetics and dynamics of SNAREpin folding across lipid bilayers. Nat Struct Mol Biol 14:890–896
106. Liu W, Montana V, Parpura V, Mohideen U (2009) Single Molecule Measurements of Interaction Free Energies Between the Proteins Within Binary and Ternary SNARE Complexes. J Nanoneurosci 1:120–129
107. Min D et al (2013) Mechanical unzipping and rezipping of a single SNARE complex reveals hysteresis as a force-generating mechanism. Nat Commun 4:1705
108. Gao Y et al (2012) Single reconstituted neuronal SNARE complexes zipper in three distinct stages. Science 337:1340–1343
109. Cohen FS, Melikyan GB (2004) The energetics of membrane fusion from binding, through hemifusion, pore formation, and pore enlargement. J Membr Biol 199:1–14
110. Ryham RJ, Klotz TS, Yao L, Cohen FS (2016) Calculating transition energy barriers and characterizing activation states for steps of fusion. Biophys J 110:1110–1124
111. Van den Bogaart G et al (2010) One SNARE complex is sufficient for membrane fusion. Nat Struct Mol Biol 17:358–364
112. Hua Y, Scheller RH (2001) Three SNARE complexes cooperate to mediate membrane fusion. Proc Natl Acad Sci USA 98:8065–8070
113. Han X, Wang CT, Bai J, Chapman ER, Jackson MB (2004) Transmembrane segments of syntaxin line the fusion pore of Ca2+-triggered exocytosis. Science 304:289–292
114. Mohrmann R, de Wit H, Verhage M, Neher E, Sørensen JB (2010) Fast vesicle fusion in living cells requires at least three SNARE complexes. Science 330:502–505
115. Sinha R, Ahmed S, Jahn R, Klingauf J (2011) Two synaptobrevin molecules are sufficient for vesicle fusion in central nervous system synapses. Proc Natl Acad Sci USA 108:14318–14323
116. Shi L et al (2012) SNARE proteins: one to fuse and three to keep the nascent fusion pore open. Science 335:1355–1359
117. Lu X, Zhang F, McNew JA, Shin YK (2005) Membrane fusion induced by neuronal SNAREs transits through hemifusion. J Biol Chem 280:30538–30541
118. Yoon TY, Okumus B, Zhang F, Shin YK, Ha T (2006) Multiple intermediates in SNARE-induced membrane fusion. Proc Natl Acad Sci USA 103:19731–19736
119. Liu T, Wang T, Chapman ER, Weisshaar JC (2008) Productive hemifusion intermediates in fast vesicle fusion driven by neuronal SNAREs. Biophys J 94:1303–1314
120. Zampighi GA et al (2006) Conical electron tomography of a chemical synapse: vesicles docked to the active zone are hemi-fused. Biophys J 91:2910–2918
121. Wong JL, Koppel DE, Cowan AE, Wessel GM (2007) Membrane hemifusion is a stable intermediate of exocytosis. Dev Cell 12:653–659
122. Risselada HJ, Kutzner C, Grubmüller H (2011) Caught in the act: visualization of SNARE-mediated fusion events in molecular detail. Chembiochem 12:1049–1055
123. Harrison SC (2008) Viral membrane fusion. Nat Struct Mol Biol 15:690–698
124. Podbilewicz B (2014) Virus and cell fusion mechanisms. Annu Rev Cell Dev Biol 30:111–139

125. Tamm LK, Crane J, Kiessling V (2003) Membrane fusion: a structural perspective on the interplay of lipids and proteins. Curr Opin Struct Biol 13:453–466
126. Hamilton BS, Whittaker GR, Daniel S (2012) Influenza virus-mediated membrane fusion: determinants of hemagglutinin fusogenic activity and experimental approaches for assessing virus fusion. Viruses 4:1144–1168
127. Han X, Bushweller JH, Cafiso DS, Tamm LK (2001) Membrane structure and fusion-triggering conformational change of the fusion domain from influenza hemagglutinin. Nat Struct Biol 8:715–720
128. Lorieau JL, Louis JM, Bax A (2010) The complete influenza hemagglutinin fusion domain adopts a tight helical hairpin arrangement at the lipid:water interface. Proc Natl Acad Sci USA 107:11341–11346
129. Kanaseki T, Kawasaki K, Murata M, Ikeuchi Y, Ohnishi S (1997) Structural features of membrane fusion between influenza virus and liposome as revealed by quick-freezing electron microscopy. J Cell Biol 137:1041–1056
130. Frolov VA, Cho MS, Bronk P, Reese TS, Zimmerberg J (2000) Multiple local contact sites are induced by GPI-linked influenza hemagglutinin during hemifusion and flickering pore formation. Traffic 1:622–630
131. Jelesarov I, Lu M (2001) Thermodynamics of trimer-of-hairpins formation by the SIV gp41 envelope protein. J Mol Biol 307:637–656
132. Li Y, Han X, Tamm LK (2003) Thermodynamics of fusion peptide-membrane interactions. Biochemistry 42:7245–7251
133. Kemble GW, Danieli T, White JM (1994) Lipid-anchored influenza hemagglutinin promotes hemifusion, not complete fusion. Cell 76:383–391
134. Melikyan GB, White JM, Cohen FS (1995) GPI-anchored influenza hemagglutinin induces hemifusion to both red blood cell and planar bilayer membranes. J Cell Biol 131:679–691
135. Armstrong RT, Kushnir AS, White JM (2000) The transmembrane domain of influenza hemagglutinin exhibits a stringent length requirement to support the hemifusion to fusion transition. J Cell Biol 151:425–437
136. Gutman O, Danieli T, White JM, Henis YI (1993) Effects of exposure to low pH on the lateral mobility of influenza hemagglutinin expressed at the cell surface: correlation between mobility inhibition and inactivation. Biochemistry 32:101–106
137. Floyd DL, Ragains JR, Skehel JJ, Harrison SC, van Oijen AM (2008) Single-particle kinetics of influenza virus membrane fusion. Proc Natl Acad Sci USA 105:15382–15387
138. Ivanovic T, Choi JL, Whelan SP, van Oijen AM, Harrison SC (2013) Influenza-virus membrane fusion by cooperative fold-back of stochastically induced hemagglutinin intermediates. eLife 2:e00333
139. Chernomordik LV, Frolov VA, Leikina E, Bronk P, Zimmerberg J (1998) The pathway of membrane fusion catalyzed by influenza hemagglutinin: restriction of lipids, hemifusion, and lipidic fusion pore formation. J Cell Biol 140:1369–1382
140. Kozlov MM, Chernomordik LV (2002) The protein coat in membrane fusion: lessons from fission. Traffic 3:256–267
141. McNew JA, Sondermann H, Lee T, Stern M, Brandizzi F (2013) GTP-dependent membrane fusion. Annu Rev Cell Dev Biol 29:529–550
142. Martens S, McMahon HT (2008) Mechanisms of membrane fusion: disparate players and common principles. Nat Rev Mol Cell Biol 9:543–556
143. Hu J, Prinz WA, Rapoport TA (2011) Weaving the web of ER tubules. Cell 147:1226–1231
144. Bian X et al (2011) Structures of the atlastin GTPase provide insight into homotypic fusion of endoplasmic reticulum membranes. Proc Natl Acad Sci USA 108:3976–3981
145. Byrnes LJ, Sondermann H (2011) Structural basis for the nucleotide-dependent dimerization of the large G protein atlastin-1/SPG3A. Proc Natl Acad Sci USA 108:2216–2221
146. Byrnes LJ et al (2013) Structural basis for conformational switching and GTP loading of the large G protein atlastin. EMBO J 32:369–384
147. Orso G et al (2009) Homotypic fusion of ER membranes requires the dynamin-like GTPase atlastin. Nature 460:978–983

148. Moss TJ, Andreazza C, Verma A, Daga A, McNew JA (2011) Membrane fusion by the GTPase atlastin requires a conserved C-terminal cytoplasmic tail and dimerization through the middle domain. Proc Natl Acad Sci USA 108:11133–11138
149. Liu TY et al (2012) Lipid interaction of the C terminus and association of the transmembrane segments facilitate atlastin-mediated homotypic endoplasmic reticulum fusion. Proc Natl Acad Sci USA 109:E2146–E2154
150. Liu TY et al (2015) Cis and trans interactions between atlastin molecules during membrane fusion. Proc Natl Acad Sci USA 112:E1851–E1860
151. Faust JE et al (2015) The Atlastin C-terminal tail is an amphipathic helix that perturbs the bilayer structure during endoplasmic reticulum homotypic fusion. J Biol Chem 290:4772–4783
152. Zick M et al (2009) Distinct roles of the two isoforms of the dynamin-like GTPase Mgm1 in mitochondrial fusion. FEBS Lett 583:2237–2243
153. DeVay RM et al (2009) Coassembly of Mgm1 isoforms requires cardiolipin and mediates mitochondrial inner membrane fusion. J Cell Biol 186:793–803
154. Ban T, Heymann JA, Song Z, Hinshaw JE, Chan DC (2010) OPA1 disease alleles causing dominant optic atrophy have defects in cardiolipin-stimulated GTP hydrolysis and membrane tubulation. Hum Mol Genet 19:2113–2122
155. Koshiba T et al (2004) Structural basis of mitochondrial tethering by mitofusin complexes. Science 305:858–862
156. Daste F et al (2018) The heptad repeat domain 1 of Mitofusin has membrane destabilization function in mitochondrial fusion. EMBO Rep 19:e43637
157. Meeusen S, McCaffery JM, Nunnari J (2004) Mitochondrial fusion intermediates revealed in vitro. Science 305:1747–1752
158. Brandt T, Cavellini L, Kühlbrandt W, Cohen MM (2016) A mitofusin-dependent docking ring complex triggers mitochondrial fusion in vitro. eLife 5:e14618
159. Qi Y et al (2016) Structures of human mitofusin 1 provide insight into mitochondrial tethering. J Cell Biol 215:621–629
160. Cao YL et al (2017) MFN1 structures reveal nucleotide-triggered dimerization critical for mitochondrial fusion. Nature 542:372–376
161. Aguilar PS et al (2013) Genetic basis of cell-cell fusion mechanisms. Trends Genet 29:427–437
162. Mohler WA et al (2002) The type I membrane protein EFF-1 is essential for developmental cell fusion. Dev Cell 2:355–362
163. Shemer G et al (2004) EFF-1 is sufficient to initiate and execute tissue-specific cell fusion in C. elegans. Curr Biol 14:1587–1591
164. Podbilewicz B et al (2006) The C. elegans developmental fusogen EFF-1 mediates homotypic fusion in heterologous cells and in vivo. Dev Cell 11:471–481
165. Pérez-Vargas J et al (2014) Structural basis of eukaryotic cell-cell fusion. Cell 157:407–419
166. Shilagardi K et al (2013) Actin-propelled invasive membrane protrusions promote fusogenic protein engagement during cell-cell fusion. Science 340:359–363
167. Morlot S, Roux A (2013) Mechanics of dynamin-mediated membrane fission. Annu Rev Biophys 42:629–649
168. Van Engelenburg SB et al (2014) Distribution of ESCRT machinery at HIV assembly sites reveals virus scaffolding of ESCRT subunits. Science 343:653–656
169. Shpetner HS, Vallee RB (1989) Identification of dynamin, a novel mechanochemical enzyme that mediates interactions between microtubules. Cell 59:421–432
170. Chen MS et al (1991) Multiple forms of dynamin are encoded by shibire, a Drosophila gene involved in endocytosis. Nature 351:583–586
171. Koenig JH, Ikeda K (1989) Disappearance and reformation of synaptic vesicle membrane upon transmitter release observed under reversible blockage of membrane retrieval. J Neurosci 9:3844–3860
172. Damke H, Baba T, Warnock DE, Schmid SL (1994) Induction of mutant dynamin specifically blocks endocytic coated vesicle formation. J Cell Biol 127:915–934

173. Damke H, Baba T, van der Bliek AM, Schmid SL (1995) Clathrin-independent pinocytosis is induced in cells overexpressing a temperature-sensitive mutant of dynamin. J Cell Biol 131:69–80
174. Hinshaw JE, Schmid SL (1995) Dynamin self-assembles into rings suggesting a mechanism for coated vesicle budding. Nature 374:190–192
175. Takei K, McPherson PS, Schmid SL, De Camilli P (1995) Tubular membrane invaginations coated by dynamin rings are induced by GTP-gamma S in nerve terminals. Nature 374:186–190
176. Antonny B et al (2016) Membrane fission by dynamin: what we know and what we need to know. EMBO J 35:2270–2284
177. Sweitzer SM, Hinshaw JE (1998) Dynamin undergoes a GTP-dependent conformational change causing vesiculation. Cell 93:1021–1029
178. Danino D, Moon KH, Hinshaw JE (2004) Rapid constriction of lipid bilayers by the mechanochemical enzyme dynamin. J Struct Biol 147:259–267
179. Zhang P, Hinshaw JE (2001) Three-dimensional reconstruction of dynamin in the constricted state. Nat Cell Biol 3:922–926
180. Chen YJ, Zhang P, Egelman EH, Hinshaw JE (2004) The stalk region of dynamin drives the constriction of dynamin tubes. Nat Struct Mol Biol 11:574–575
181. Sundborger AC et al (2014) A dynamin mutant defines a superconstricted prefission state. Cell Rep 8:734–742
182. Ford MG, Jenni S, Nunnari J (2011) The crystal structure of dynamin. Nature 477:561–566
183. Faelber K et al (2011) Crystal structure of nucleotide-free dynamin. Nature 477:556–560
184. Reubold TF et al (2015) Crystal structure of the dynamin tetramer. Nature 525:404–408
185. Chappie JS et al (2009) An intramolecular signaling element that modulates dynamin function in vitro and in vivo. Mol Biol Cell 20:3561–3571
186. Chappie JS, Acharya S, Leonard M, Schmid SL, Dyda F (2010) G domain dimerization controls dynamin's assembly-stimulated GTPase activity. Nature 465:435–440
187. Mears JA, Ray P, Hinshaw JE (2007) A corkscrew model for dynamin constriction. Structure 15:1190–1202
188. Chappie JS et al (2011) A pseudoatomic model of the dynamin polymer identifies a hydrolysis-dependent powerstroke. Cell 147:209–222
189. Mattila JP et al (2015) A hemi-fission intermediate links two mechanistically distinct stages of membrane fission. Nature 524:109–113
190. Roux A, Uyhazi K, Frost A, De Camilli P (2006) GTP-dependent twisting of dynamin implicates constriction and tension in membrane fission. Nature 441:528–531
191. Morlot S, Lenz M, Prost J, Joanny JF, Roux A (2010) Deformation of dynamin helices damped by membrane friction. Biophys J 99:3580–3588
192. Lenz M, Prost J, Joanny JF (2008) Mechanochemical action of the dynamin protein. Phys Rev E Stat Nonlinear Soft Matter Phys 78:011911
193. Perrais D, Merrifield CJ (2005) Dynamics of endocytic vesicle creation. Dev Cell 9:581–592
194. Babst M, Katzmann DJ, Estepa-Sabal EJ, Meerloo T, Emr SD (2002) Escrt-III: an endosome-associated heterooligomeric protein complex required for mvb sorting. Dev Cell 3:271–282
195. Babst M, Wendland B, Estepa EJ, Emr SD (1998) The Vps4p AAA ATPase regulates membrane association of a Vps protein complex required for normal endosome function. EMBO J 17:2982–2993
196. McCullough J, Colf LA, Sundquist WI (2013) Membrane fission reactions of the mammalian ESCRT pathway. Annu Rev Biochem 82:663–692
197. Hurley JH, Hanson PI (2010) Membrane budding and scission by the ESCRT machinery: it's all in the neck. Nat Rev Mol Cell Biol 11:556–566
198. Carlton JG, Martin-Serrano J (2007) Parallels between cytokinesis and retroviral budding: a role for the ESCRT machinery. Science 316:1908–1912
199. Garrus JE et al (2001) Tsg101 and the vacuolar protein sorting pathway are essential for HIV-1 budding. Cell 107:55–65

200. Olmos Y, Hodgson L, Mantell J, Verkade P, Carlton JG (2015) ESCRT-III controls nuclear envelope reformation. Nature 522:236–239
201. Vietri M et al (2015) Spastin and ESCRT-III coordinate mitotic spindle disassembly and nuclear envelope sealing. Nature 522:231–235
202. Bruns C, McCaffery JM, Curwin AJ, Duran JM, Malhotra V (2011) Biogenesis of a novel compartment for autophagosome-mediated unconventional protein secretion. J Cell Biol 195:979–992
203. Spitzer C et al (2015) The endosomal protein CHARGED MULTIVESICULAR BODY PROTEIN1 regulates the autophagic turnover of plastids in Arabidopsis. Plant Cell 27:391–402
204. Gao C et al (2015) Dual roles of an Arabidopsis ESCRT component FREE1 in regulating vacuolar protein transport and autophagic degradation. Proc Natl Acad Sci USA 112:1886–1891
205. Hurley JH (2015) ESCRTs are everywhere. EMBO J 34:2398–2407
206. Teis D, Saksena S, Emr SD (2008) Ordered assembly of the ESCRT-III complex on endosomes is required to sequester cargo during MVB formation. Dev Cell 15:578–589
207. Hurley JH (2010) The ESCRT complexes. Crit Rev Biochem Mol Biol 45:463–487
208. Mierzwa B, Gerlich DW (2014) Cytokinetic abscission: molecular mechanisms and temporal control. Dev Cell 31:525–538
209. Elia N, Fabrikant G, Kozlov MM, Lippincott-Schwartz J (2012) Computational model of cytokinetic abscission driven by ESCRT-III polymerization and remodeling. Biophys J 102:2309–2320
210. Saksena S, Wahlman J, Teis D, Johnson AE, Emr SD (2009) Functional reconstitution of ESCRT-III assembly and disassembly. Cell 136:97–109
211. Obita T et al (2007) Structural basis for selective recognition of ESCRT-III by the AAA ATPase Vps4. Nature 449:735–739
212. Adell MA et al (2014) Coordinated binding of Vps4 to ESCRT-III drives membrane neck constriction during MVB vesicle formation. J Cell Biol 205:33–49
213. Yang B, Stjepanovic G, Shen Q, Martin A, Hurley JH (2015) Vps4 disassembles an ESCRT-III filament by global unfolding and processive translocation. Nat Struct Mol Biol 22:492–498
214. Mierzwa BE et al (2017) Dynamic subunit turnover in ESCRT-III assemblies is regulated by Vps4 to mediate membrane remodelling during cytokinesis. Nat Cell Biol 19:787–798
215. Campsteijn C, Vietri M, Stenmark H (2016) Novel ESCRT functions in cell biology: spiraling out of control? Curr Opin Cell Biol 41:1–8
216. Yang D et al (2008) Structural basis for midbody targeting of spastin by the ESCRT-III protein CHMP1B. Nat Struct Mol Biol 15:1278–1286
217. Pires R et al (2009) A crescent-shaped ALIX dimer targets ESCRT-III CHMP4 filaments. Structure 17:843–856
218. Bissig C et al (2013) Viral infection controlled by a calcium-dependent lipid-binding module in ALIX. Dev Cell 25:364–373
219. Bissig C, Gruenberg J (2014) ALIX and the multivesicular endosome: ALIX in Wonderland. Trends Cell Biol 24:19–25
220. Christ L et al (2016) ALIX and ESCRT-I/II function as parallel ESCRT-III recruiters in cytokinetic abscission. J Cell Biol 212:499–513
221. Prescher J et al (2015) Super-resolution imaging of ESCRT-proteins at HIV-1 assembly sites. PLoS Pathog 11:e1004677
222. Carlson LA, Hurley JH (2012) In vitro reconstitution of the ordered assembly of the endosomal sorting complex required for transport at membrane-bound HIV-1 Gag clusters. Proc Natl Acad Sci USA 109:16928–16933
223. Bleck M et al (2014) Temporal and spatial organization of ESCRT protein recruitment during HIV-1 budding. Proc Natl Acad Sci USA 111:12211–12216
224. Sette P et al (2016) HIV-1 nucleocapsid mimics the membrane adaptor syntenin PDZ to gain access to ESCRTs and promote virus budding. Cell Host Microbe 19:336–348

225. McCullough J et al (2015) Structure and membrane remodeling activity of ESCRT-III helical polymers. Science 350:1548–1551
226. Tang S et al (2015) Structural basis for activation, assembly and membrane binding of ESCRT-III Snf7 filaments. eLife 4:e12548
227. Tang S et al (2016) ESCRT-III activation by parallel action of ESCRT-I/II and ESCRT-0/Bro1 during MVB biogenesis. eLife 5:e15507
228. Lata S et al (2008) Helical structures of ESCRT-III are disassembled by VPS4. Science 321:1354–1357
229. Henne WM, Buchkovich NJ, Zhao Y, Emr SD (2012) The endosomal sorting complex ESCRT-II mediates the assembly and architecture of ESCRT-III helices. Cell 151:356–371
230. Shen QT et al (2014) Structural analysis and modeling reveals new mechanisms governing ESCRT-III spiral filament assembly. J Cell Biol 206:763–777
231. Guizetti J et al (2011) Cortical constriction during abscission involves helices of ESCRT-III-dependent filaments. Science 331:1616–1620
232. Cashikar AG et al (2014) Structure of cellular ESCRT-III spirals and their relationship to HIV budding. eLife 3:e02184
233. Hanson PI, Roth R, Lin Y, Heuser JE (2008) Plasma membrane deformation by circular arrays of ESCRT-III protein filaments. J Cell Biol 180:389–402
234. Elia N, Sougrat R, Spurlin TA, Hurley JH, Lippincott-Schwartz J (2011) Dynamics of endosomal sorting complex required for transport (ESCRT) machinery during cytokinesis and its role in abscission. Proc Natl Acad Sci USA 108:4846–4851
235. Chiaruttini N, Roux A (2017) Dynamic and elastic shape transitions in curved ESCRT-III filaments. Curr Opin Cell Biol 47:126–135
236. Fabrikant G et al (2009) Computational model of membrane fission catalyzed by ESCRT-III. PLoS Comput Biol 5:e1000575
237. Reid E et al (2005) The hereditary spastic paraplegia protein spastin interacts with the ESCRT-III complex-associated endosomal protein CHMP1B. Hum Mol Genet 14:19–38
238. Chiaruttini N et al (2015) Relaxation of loaded ESCRT-III spiral springs drives membrane deformation. Cell 163:866–879
239. Lenz M, Crow DJ, Joanny JF (2009) Membrane buckling induced by curved filaments. Phys Rev Lett 103:038101
240. Peter BJ et al (2004) BAR domains as sensors of membrane curvature: the amphiphysin BAR structure. Science 303:495–499
241. Daumke O, Roux A, Haucke V (2014) BAR domain scaffolds in dynamin-mediated membrane fission. Cell 156:882–892
242. Sorre B et al (2012) Nature of curvature coupling of amphiphysin with membranes depends on its bound density. Proc Natl Acad Sci USA 109:173–178
243. Boucrot E et al (2012) Membrane fission is promoted by insertion of amphipathic helices and is restricted by crescent BAR domains. Cell 149:124–136
244. Farsad K et al (2001) Generation of high curvature membranes mediated by direct endophilin bilayer interactions. J Cell Biol 155:193–200
245. Yoshida Y et al (2004) The stimulatory action of amphiphysin on dynamin function is dependent on lipid bilayer curvature. EMBO J 23:3483–3491
246. Hohendahl A et al (2017) Structural inhibition of dynamin-mediated membrane fission by endophilin. eLife 6:e26856
247. Römer W et al (2007) Shiga toxin induces tubular membrane invaginations for its uptake into cells. Nature 450:670–675
248. Römer W et al (2010) Actin dynamics drive membrane reorganization and scission in clathrin-independent endocytosis. Cell 140:540–553
249. Renard HF et al (2015) Endophilin-A2 functions in membrane scission in clathrin-independent endocytosis. Nature 517:493–496
250. Boucrot E et al (2015) Endophilin marks and controls a clathrin-independent endocytic pathway. Nature 517:460–465

251. Simunovic M et al (2016) How curvature-generating proteins build scaffolds on membrane nanotubes. Proc Natl Acad Sci USA 113:11226–11231
252. Roux A et al (2010) Membrane curvature controls dynamin polymerization. Proc Natl Acad Sci USA 107:4141–4146
253. Simunovic M et al (2017) Friction mediates scission of tubular membranes scaffolded by BAR proteins. Cell 170:172–184.e11
254. Zhao WD et al (2016) Hemi-fused structure mediates and controls fusion and fission in live cells. Nature 534:548–552

Interaction of Particles and Pathogens with Biological Membranes

Thorsten Auth, Sabyasachi Dasgupta, and Gerhard Gompper

Abstract Biological membranes are both barriers and communication interfaces of cells. Transport across membranes is therefore essential for life. It encompasses both endocytotic and exocytotic processes important for cell function, but also the invasion of cells by parasites and viruses, and targeted drug delivery. Whereas interactions on the molecular scale are important for particles with sizes comparable with the thickness of the membrane, the mechanical properties of the entire membrane determine its interaction with larger particles. We focus here on large particles and parasites and discuss wrapping of single particles by homogeneous and complex membranes. Both solid particles with various shapes as well as soft particles are considered. Membrane-mediated interactions of many particles lead to aggregation and tubulation. Finally, active biological mechanisms are shown to support the invasion of parasites, such as the malaria parasite, and to drive phagocytosis.

Keywords Nanoparticles · Helfrich Hamiltonian · Endocytosis · Pathogens · Malaria · Phagocytosis

1 Introduction

Membranes are ubiquitous in biological cells. While the plasma membrane encloses the entire cell, membranes also compartmentalize cells and thereby define organelles. Transmembrane transport is essential for both the intracellular communication and the communication of cells with their environment [16, 60]. The interaction of particles and pathogens with biological membranes—and therefore

T. Auth (✉) · G. Gompper
Forschungzentrum Jülich, Theoretical Soft Matter and Biophysics, Institute of Complex Systems and Institute for Advanced Simulation, Jülich, Germany
e-mail: t.auth@fz-juelich.de; g.gompper@fz-juelich.de

S. Dasgupta
National University of Singapore, Mechanobiology Institute, Singapore, Singapore

P. Bassereau, P. Sens (eds.), *Physics of Biological Membranes*,
https://doi.org/10.1007/978-3-030-00630-3_17

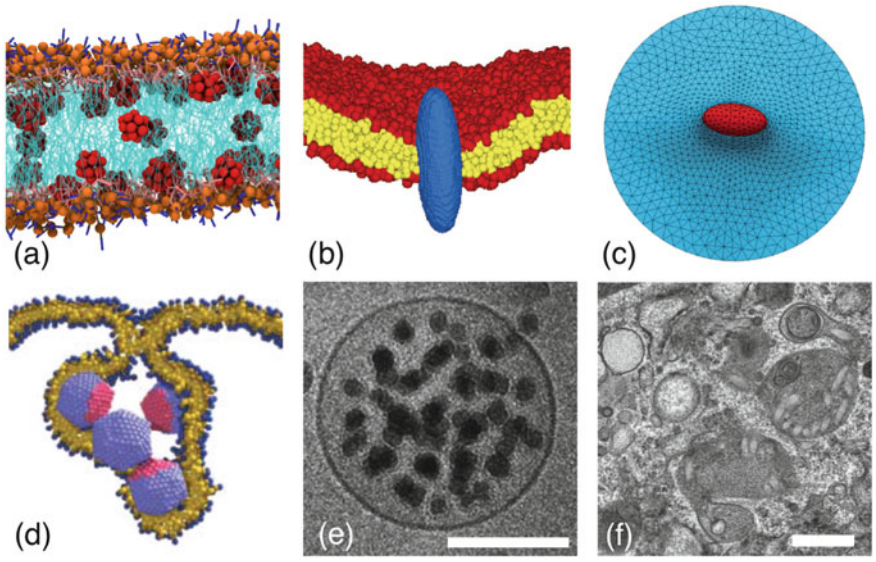

Fig. 1 Interaction of nanoparticles with membranes. (**a**) Incorporation. Fullerenes in a POPC membrane. Reprinted with permission from [10]. Copyright 2014 by the American Physical Society. (**b**) Penetration. An ellipsoidal nanoparticle passes through a lipid bilayer. Adapted by permission from Macmillan Publishers Ltd: Nat. Nanotechnol., [116], Copyright © 2010. (**c**) Wrapping. An ellipsoidal nanoparticle gets wrapped by a lipid bilayer membrane. Reproduced from [31] with permission from The Royal Society of Chemistry. (**d**) Cooperative wrapping. Capsids bud cooperatively. Adapted by permission from Macmillan Publishers Ltd: Nature, [87], Copyright © 2007. (**e**) Cryo-TEM micrographs of nanoparticles incorporated into a vesicle. The length of the scale bar corresponds to 100 nm. Reprinted from [72] with permission from The Royal Society of Chemistry. (**f**) TEM micrographs of nanoparticles internalized in human mesenchymal stem cells. The length of the scale bar corresponds to 500 nm. Adapted with permission from [45]. Copyright © 2012 Wiley-VCH Verlag GmbH & Co. KGaA, Weinheim

also their transport across membranes—crucially depends on the particle size, shape, softness, and surface functionalization. A zoo of engineered nanoparticles can nowadays be fabricated, with sizes from nanometers to micrometers and various shapes, such as spherical, ellipsoidal, cuboidal, dumbbell-shaped, and bullet-shaped [18, 22, 82]. Pathogens are nanometer-sized viruses, such as the filamentous Marburg and Ebola viruses [78, 113], and micrometer-sized parasites, such as the egg-shaped malaria parasite [25, 30]. Figure 1 shows an overview over particle–membrane interactions.

For particles with diameters that are large compared to the thickness of the membrane, the membrane can be modeled using a mathematical surface with curvature-elastic properties. The deformation energy is calculated using the Helfrich Hamiltonian [55], and the attractive interaction between particle and membrane can

be taken into account using a contact energy:

$$\mathscr{H} = \int_S dS \left[\gamma + 2\kappa (H - c_0)^2 + \bar{\kappa} K\right] + w \int_{S_{\mathrm{ad}}} dS\,. \tag{1}$$

The membrane conformation is characterized by the two principal curvatures at each point of the membrane, c_1 and c_2, that enter the Hamiltonian via the mean curvature $H = (c_1 + c_2)/2$ and the Gaussian curvature $K = c_1 c_2$. The total deformation energy is obtained by integration over the entire membrane area S, the adhesion energy by integration over the adhered membrane area S_{ad}. Membrane tension γ, bending rigidity κ, Gaussian saddle-splay modulus $\bar{\kappa}$, and spontaneous curvature c_0 describe the mechanical properties of the membrane; the adhesion strength w characterizes the contact interaction. If we assume a homogeneous membrane and disregard topology changes, i.e., the last step of detachment of a wrapped particle that is still connected via a small neck to the lipid bilayer membrane, the contribution of the Gaussian curvature is constant and given by the Euler characteristic of the surface [1]. Typical values for the bending rigidity are $20\,k_{\mathrm{B}}T < \kappa < 100\,k_{\mathrm{B}}T$, for the membrane tension $10^{-5}\,k_{\mathrm{B}}T/\mathrm{nm}^2 < \gamma < 1\,k_{\mathrm{B}}T/\mathrm{nm}^2$ [103], and for the adhesion strength $2 \times 10^{-6}\,k_{\mathrm{B}}T/\mathrm{nm}^2 < w < 0.2\,k_{\mathrm{B}}T/\mathrm{nm}^2$ [2].

In Sect. 2, wrapping of single spherical and nonspherical particles by homogeneous model membranes is discussed. For tensionless membranes, spherical particles are either not wrapped or completely wrapped by the membrane at low and high adhesion strength, respectively. The transition between these two states is discontinuous. Nonspherical particles show a much more complex wrapping behavior and an increased stability of partial-wrapped states [29]. Soft particles deform while adhering to the membrane, which further increases the stability of partial-wrapped states. We also briefly address dynamical aspects of particle wrapping. For partial wrapping of spherical particles, not only the attached membrane, but also the free membrane around particles and the particle itself gets deformed. Both contribute to the deformation energy.

In Sect. 3, the complexity of the single-particle wrapping scenario is extended to multicomponent biomembranes. Biomembranes can show strong and weak segregation, domain formation and aggregation of lipid and protein components within the membranes, respectively. In Sect. 4, examples for membrane deformation-mediated interaction between particles and for particle self-assembly are presented. In Sect. 5, systems with biological activity are discussed, such as the invasion of the malarial parasite and phagocytosis.

Interaction of Small Particles with Biological Membranes Particles that are comparable with molecular sizes of lipids interact similarly with biological membranes as proteins. Particles with suitable hydrophobicity may penetrate the lipid bilayer [84], which is also observed for cell-penetrating peptides [24] and which has been proposed for amphiphilic polymers [114].

(continued)

Hydrophobic nanoparticles assemble within the tail region of the lipid bilayer [90, 100] and aggregate, probably similar to integral proteins that deform the headgroup layers of the bilayer [27, 64, 96, 107]. Small nanoparticles distort the lipid structure and may affect the integrity of lipid bilayer membranes [68, 69, 105, 106, 122]. Besides surface properties, also particle shape has been found to strongly affect the interaction of small particles with membranes [104]. The formation of a protein corona on the surface of a nanoparticle considerably affects both size and surface properties of the particles [23, 67, 75]. Small polymeric nanoparticles may be unstable and dissolve [90]. The interaction of small nanoparticles with membranes is studied experimentally using optical microscopy [112], electron microscopy [98, 111], and scattering techniques [58, 99]. Atomistic and coarse-grained models can be used to study the interaction of small nanoparticles with membranes using computer simulations [41, 76, 84, 114, 116].

Interaction of Large Particles with Biological Membranes Particles with sizes significantly larger than lipids interact with membranes via wrapping. This encompasses engineered nanoparticles [7, 8, 28, 29, 31, 37–40, 51, 73, 93–95, 119], but also viruses and parasites [26, 30, 78, 113]. Size, shape, surface functionalization, and particle orientation determine the interaction of particles and membranes [21, 29, 45, 89, 115, 118, 124]. An energy gain due to adhesion is opposed by a deformation energy cost for wrapping the membrane around the particle [39]. The adhesion can be mediated by van der Waals interaction or by receptor–ligand bonds [48, 123]. Membrane-mediated and direct interactions may lead to clustering of particles [7, 61, 93, 94]. A passive cytoskeleton below the membrane contributes shear elasticity to the membrane deformation energy [6, 92] and can hinder particle wrapping by the bilayer that it attaches to [54], while an active cytoskeleton can assist particle wrapping [88, 101]. The interaction of large particles with membranes is studied experimentally using optical microscopy [45, 47], electron microscopy [62, 66, 72], atomic force microscopy [83, 110], and scattering techniques [62, 63, 109]. Computer simulations and analytical calculations using coarse-grained and continuum models have been used to study the interaction of large particles with membranes [28, 29, 31, 39, 59, 104].

2 Wrapping by Homogeneous Membranes

Particles that interact with lipid bilayer membranes force the membranes to deform upon particle wrapping (Fig. 2a), which results in deformation energy costs. The adhesion energy gain upon direct contact of the particle with the membrane drives the wrapping process.

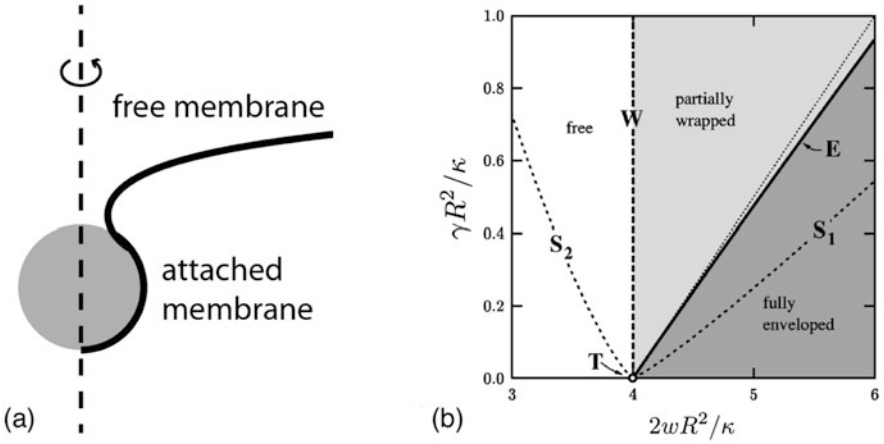

Fig. 2 Wrapping of a spherical nanoparticle of radius R by a membrane with bending rigidity κ and tension γ. The adhesion strength between particle and membrane is w. (**a**) The membrane deforms in a cylindrically symmetric way around the symmetry axis, and the shape can be described by a radial deformation profile. For an infinitely large tensionless membrane, the shape of the free membranes is catenoidal. Reprinted with permission from [32]. CC BY 3.0. (**b**) Wrapping phase diagram for membrane tension and adhesion strength. Nanoparticles are unwrapped for adhesion strengths below $2wR^2/\kappa = 4$, indicated by the thick dashed line (W). They are completely enveloped for adhesion strengths beyond the thick solid line (E). The thin dotted line is the envelopment transition calculated neglecting the deformation energy of the free membrane. The thin dashed lines (S1, S2) describe the spinodals for spontaneous unwrapping (directly to the free state) and for spontaneous envelopment. T indicates the triple point. Reprinted with permission from [37]. Copyright 2004 by the American Physical Society

2.1 Spherical Particles

When particles interact with membranes, both the membrane attached to the particle and the free membrane surrounding the particle get deformed, see Fig. 2a. For spherical particles that attach to an infinitely large tensionless membrane, the free membrane forms a catenoid without deformation energy costs. Spherical particles have the same curvature everywhere on their surface, therefore the deformation energy cost increases linearly with the attached area. The deformation energy cost for wrapping an entire particle with radius R by a membrane with bending rigidity κ and tension γ is $E_{\text{def.}} = 8\pi\kappa + 4\pi R^2\gamma$, and the adhesion energy gain is $E_{\text{adh.}} = -4\pi R^2 w$. The contribution of bending to the deformation energy dominates for particle radii below $R^* = \sqrt{2\kappa/\gamma}$, the contribution of tension for larger particle radii. For values of bending rigidity and tension in the range reported above, $6\,\text{nm} < R^* < 4.5\,\mu\text{m}$.

Particles get wrapped by membranes if the adhesion energy gain exceeds the deformation energy cost, $E_{\text{def.}} + E_{\text{adh.}} \leq 0$. For initially planar membranes, this determines a minimal radius for complete envelopment, $R_{\text{env.}} = \sqrt{2\kappa/(w-\gamma)}$. The minimal radius for binding, $R_{\text{bind.}} = \sqrt{2\kappa/w}$, is independent of the membrane tension [37]. Binding and envelopment transition obtained by these estimates are indicated by the thick dashed line and the thin dotted line in the wrapping phase diagram in Fig. 2b, respectively. While the bending energy is scale invariant, both tension and adhesion contributions to the total energy increase with the surface area of the particle. In the bending-dominated regime, a larger particle therefore gets wrapped easier than a smaller particle. Dimensionless quantities for energies, membrane tension, and adhesion strength,

$$\tilde{E} = E/(\pi\kappa) \qquad \tilde{\gamma} = \gamma R^2/\kappa \qquad \tilde{w} = 2wR^2/\kappa\,, \tag{2}$$

make results universally applicable for various particle sizes. It is obvious from these definitions that for $\gamma = 0$ increasing w is equivalent to increasing R^2.

Figure 2b indicates the wrapping states of particles obtained from energy minimization for various values of w and γ. Below a threshold adhesion strength, particles remain free. The transition from free to partial-wrapped and complete-wrapped states is continuous, and the transition from partial-wrapped to complete-wrapped states is discontinuous. The latter transition is shifted to slightly higher adhesion strengths than those estimated above, because of a local energy minimum for stable partial-wrapped states. The energy barrier between partial-wrapped and complete-wrapped states results in spinodals that delimit the regimes where particles spontaneously wrap and unwrap. While wrapping occurs via stable partial-wrapped states, spontaneous unwrapping occurs directly to the free state.

2.2 *Nonspherical Particles*

Particle shape is a critical parameter for drug delivery [44]; for example, higher specificity has been reported for nonspherical antibody-displaying nanoparticles compared with spherical particles [11]. Engineered nanoparticles with a variety of shapes can be fabricated, see Fig. 3. Furthermore, viruses can have very different shapes, e.g., elongated filoviruses and bullet-shaped rhabdoviruses [49, 113], and, for example, the malaria parasite is egg-shaped [30]. Nonspherical particles at homogeneous membranes show a much richer wrapping behavior compared with spherical particles, because the curvature of their surface is not homogeneous. The local bending energy cost is proportional to the squared mean curvature of the membrane, while the adhesion energy gain is independent of the shape of the membrane. Thus, energy barriers for wrapping are associated with highly curved regions on the particle surface, which stabilizes partial-wrapped states. For example, for wrapping fractions below 50 %, ellipsoidal particles have partial-wrapped states with their long axis parallel to the membrane that avoid the strong membrane

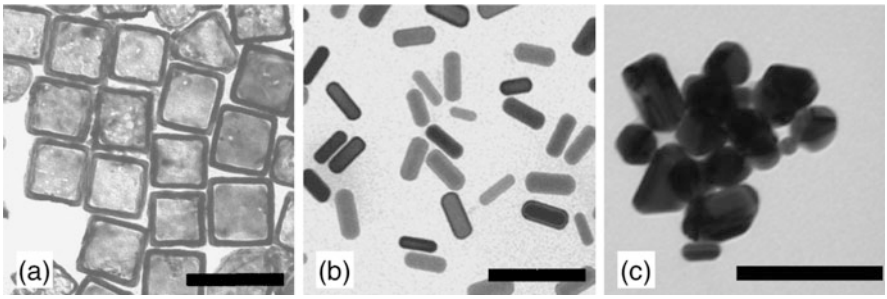

Fig. 3 Examples for engineered nanoparticles: (**a**) Cube-like and (**b**) rod-like gold nanoparticles. Reprinted by permission from Macmillan Publishers Ltd: Nat. Nanotech., [22], Copyright © 2011. (**c**) Silver nanoparticles with irregular shapes. Reprinted with permission from [61]. OA CC BY 4.0. The length of the scale bars corresponds to 100 nm

deformations at the highly curved tips of the particle [31]. Similarly, for cube-like and rod-like particles highly curved ridges constitute energy barriers [29]. In contrast, locally planar parts of the particle surface, such as the faces of a cube, readily attach to a planar membrane at infinitely small adhesion strengths.

Nonspherical particle shapes can be described analytically using $(x/a)^n + (y/a)^n + (z/b)^n = 1$ for cube-like particles and $[(x^2 + y^2)/a^2]^{n/2} + (z/b)^n = 1$ for rod-like, "superegg" particles. In both expressions, $a = b$ and $n = 2$ gives a sphere; a superegg with $a \neq b$ and $n = 2$ is an ellipsoid. The deformation energy can be calculated numerically using triangulated membranes [14, 50], where the surface is constructed by small triangles. The dihedral angle between adjacent triangles is used to calculate the bending energy; the total area of all triangles couples to the membrane tension. Figure 4a–c shows a wrapping diagram and snapshots for stable, partial-wrapped states for a Hauser's cube-shaped particle, described by $(x/a)^6 + (y/a)^6 + (z/a)^6 = 1$. We use dimensionless parameters $\tilde{\gamma} = \gamma a^2/\kappa$ and $\bar{w} = wA/(2\pi\kappa)$, where A is the particle surface area. The particle attaches at vanishing adhesion strength to one of the flat faces. In this shallow-wrapped state, the membrane binds to approximately $1/6$ of the particle's surface area. In order to transit to the deep-wrapped state with a wrapping fraction of $5/6$, an energy barrier because of the highly bent edges of the particle has to be overcome; the same applies for the transition from the deep-wrapped state to the complete wrapped state. Because of the energy barriers, these transitions are discontinuous already for tensionless membranes. In addition to a globally stable state with the lowest energy, the system may therefore also be found in a metastable state. Qualitatively similar wrapping behavior is observed for other nonspherical particles. In general, a nonspherical particle shape stabilizes partial-wrapped states.

While the binding transition of the particle is always continuous, the other transitions between wrapping states are often associated with energy barriers and are thus discontinuous. For elongated particles, also the orientation of the particle with respect to the membrane varies with the wrapping state. For shallow-wrapped

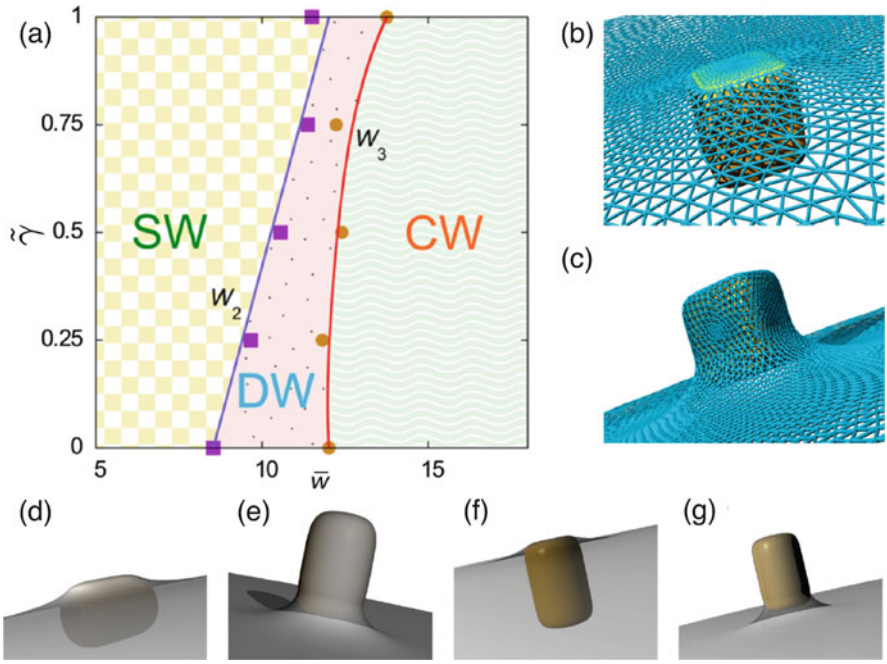

Fig. 4 Wrapping of cube-like and rod-like nanoparticles. (**a**) Phase diagram for wrapping of Hauser's cube for membrane tension $\tilde{\gamma}$ and adhesion strength $\bar{w}$; the parameters are given in dimensionless form. We find a shallow-wrapped (SW), a deep-wrapped (DW), and a complete-wrapped (CW) state, separated by two discontinuous wrapping transitions, W_2 and W_3. (**b**), (**c**): Membrane deformation for wrapping of Hauser's cube. The network of edges and triangles describes the membrane shape and is used for the numerical calculation of the curvature energy. Membrane conformations are shown at fixed tension $\tilde{\gamma} = 0.50$ for two corresponding states at the W_2 phase boundary: (**b**) a shallow-wrapped state with approximately 10% of particle wrapped, and (**c**) a deep-wrapped state with a wrapping fraction of approximately 80%. (**d**)–(**g**) Membrane-particle conformations for rod-like nanoparticles with (**d**) $n = 4$ and $b/a = 1.5$ (SW), (**e**) $n = 4$ and $b/a = 1.5$ (DW), (**f**) $n = 6$ and $b/a = 1.5$ (SW), and (**g**) $n = 6$ and $b/a = 1.5$ (DW). Adapted with permission from [29]. Copyright (2014) American Chemical Society

states, particles are mostly oriented with their long axis parallel to the membrane, the so-called submarine orientation, while for deep-wrapped states particles are oriented with their long axis perpendicular to the membrane, the so-called rocket orientation. This behavior can again be rationalized by the requirement to maximize the adhered membrane area while avoiding highly curved regions of the particle. A point of caveat for comparing the wrapping behavior of particles with different shapes quantitatively is that particle size also has to be taken into account. Although the bending energy is scale-independent, the tension and adhesion contributions to the total energy are not. Therefore, when comparing, for instance, two rod-like particles with different aspect ratios, it is essential to specify whether particle volume, surface area, or the length of the small axis is fixed [29]. Table 1 qualitatively summarizes

Table 1 Shape dependence of particle wrapping, based on [28, 31, 37] and this work

Particle shape	Membrane	Binding transition	Shallow-wrapped state	Deep-wrapping transition	Deep-wrapped state	Envelopment transition
Spherical	κ	Cont., for $w = 2\kappa/R^2$	–	–	–	$\equiv$ binding
Spherical	κ and γ	Cont., for $w = 2\kappa/R^2$	Yes	–	–	Discont.
Ellipsoidal	κ, κ and γ	Cont., indep. of γ	Yes, submarine	Discont., reorient.	Yes, rocket	Cont.
Ellipsoidal[a]	κ, κ and γ	Cont., indep. of γ	Yes, submarine	–	–	Discont.
Cube-like	κ, κ and γ	At vanishing w	Yes	Discont.	Yes	Discont.
Sphero-cylinder	κ, κ and γ	At vanishing w, rocket	Yes, submarine	Discont., reorient.	Yes, rocket	Discont.
Rod-like	κ, κ and γ	At vanishing w, rocket	Yes, submarine	Discont., reorient.	Yes, rocket	Discont.
Rod-like[a]	κ, κ and γ	At vanishing w, rocket	Yes, submarine	–	–	Discont.
Rod-like[b]	κ, κ and γ	At vanishing w, rocket	Yes, rocket	Discont.	Yes, rocket	Discont.

The membrane can be characterized by bending rigidity only, "κ", or by bending rigidity and membrane tension, "κ and γ"; the binding transition can occur at finite or vanishing adhesion strength w; the particle can be in submarine or rocket orientation; transitions can be continuous (cont.) or discontinuous (discont.) and may involve reorientation (reorient.). The binding transition for ellipsoids is independent of the membrane tension and is given in [28, 31]. Reprinted with permission from [29]. Copyright (2014) American Chemical Society

[a]Fast wrapping at high adhesion strength, such that a bound ellipsoid cannot reorient to rocket orientation

[b]Rocket mode for supereggs with blunt tips and small aspect ratio (e.g., $n = 4$ and $b/a = 1.5$)

the wrapping behavior for various shapes of the particle and curvature-elastic properties of the membrane.

The role of edge curvature for wrapping nonspherical particles is illustrated in Fig. 5. A spherical particle at a tensionless membrane directly transits from the free to the complete-wrapped state. Ellipsoidal particles experience an energy barrier between the shallow-wrapped state in submarine orientation and the deep-wrapped/complete-wrapped state that depends on the curvature of the tips and therefore on the aspect ratio. For a rod-like particle, aspect ratio and edge curvature are independent of each other. In the shallow-wrapped state, a particle is found in rocket ($b/a = 1$) or submarine ($b/a = 2$) orientation. The extent of the partial-wrapped regime increases with edge curvature, and the transitions to the deep-wrapped state and to the complete-wrapped state both shift to higher values of the adhesion strength. Therefore, not only size and aspect ratio of a particle, but also local curvature distribution and, e.g., surface roughness crucially influence the wrapping behavior.

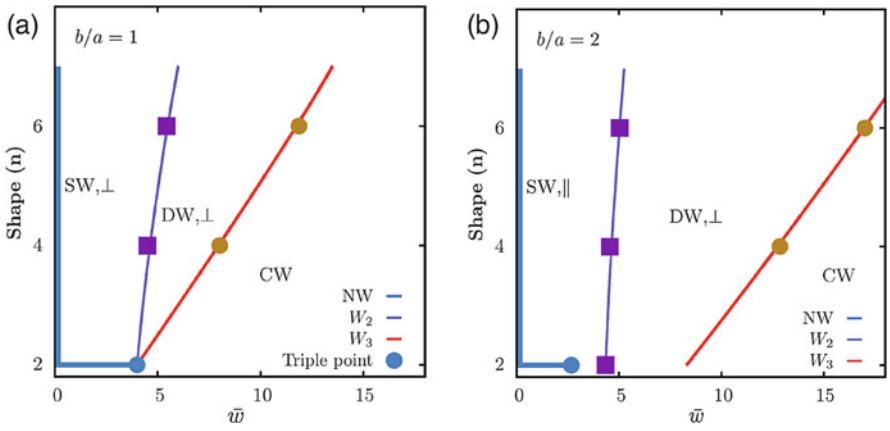

Fig. 5 Role of edge curvature (characterized by n) on the wrapping behavior of a tensionless membrane for rod-like nanoparticles with fixed aspect ratios, (**a**) $b/a = 1$ and (**b**) $b/a = 2$. The particle orientation in the shallow-wrapped (SW) and the deep-wrapped (DW) states is indicated by the symbols $\perp$ and $\parallel$, corresponding to rocket and submarine orientation, respectively. Non-wrapped (NW) states are marked by light-blue lines, and W_1 and W_2 indicate the transitions between shallow-wrapped and deep-wrapped states, and between deep-wrapped and complete-wrapped states, respectively. Reprinted with permission from [29]. Copyright (2014) American Chemical Society

2.3 *Deformable Particles*

Macrophages preferentially engulf rigid objects [13]. Soft microgel particles in the hydrophilic swollen state have been shown to adsorb densely on giant unilamellar vesicles; the same particles in the more hydrophobic collapsed state remain attached, but partially desorb from the membrane and self-organize in domains [73]. Both observations indicate that particle wrapping is also affected by particle deformability. When soft particles get wrapped by lipid bilayer membranes, for partial-wrapped states not only the membrane but also the particle deforms, see Fig. 6a, b. Therefore in a passive system, a soft particle that attaches to a planar membrane assumes an oblate shape, and the deformation of the planar membrane is reduced compared to a hard particle of the same size. Wrapping of a lipid vesicle or a thin elastic capsule with initial radius R by a lipid membrane can serve as model system for wrapping of a soft particle [117, 119, 121]. The total energy for a vesicle wrapped by an initially flat membrane is [119]

$$\mathscr{H} = \sum_{i=1,2,3} \int_{S_i} dS_i \left[2\kappa_i H^2 + \bar{\kappa}_i K \right] + pV_\mathrm{v} + \Gamma A_\mathrm{v} + \gamma A_\mathrm{f} - wA_\mathrm{ad}\,, \qquad (3)$$

where $i = 1$ denotes the vesicle membrane, $i = 2$ the initially planar membrane, and $i = 3$ the double bilayer formed by vesicle and planar membrane. Thus, $\kappa_3 = \kappa_1 + \kappa_2$ and $\bar{\kappa}_3 = \bar{\kappa}_1 + \bar{\kappa}_2$. In addition, p, Γ, γ, and w characterize the energy change

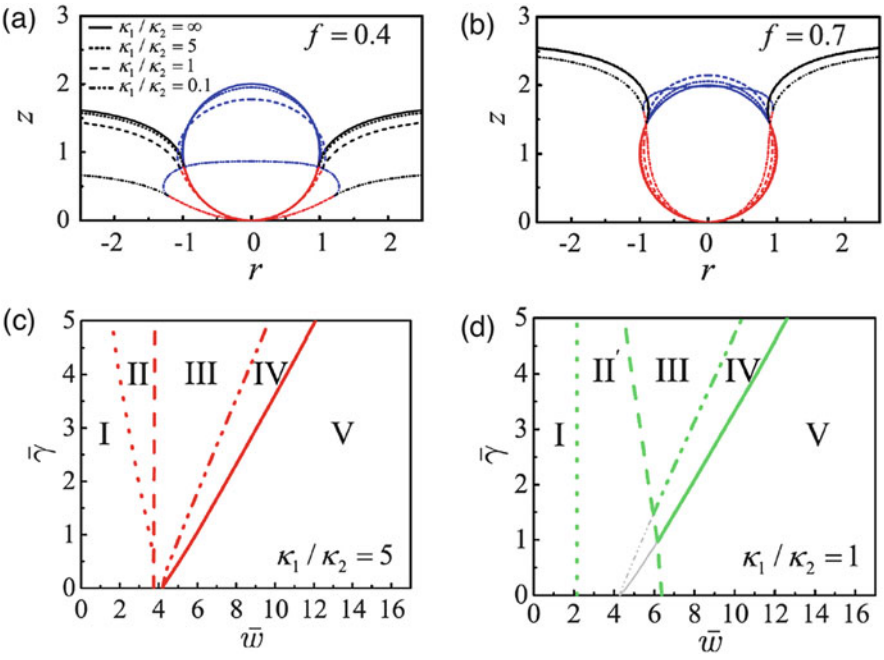

Fig. 6 Wrapping of vesicles by initially flat membranes. (**a**)–(**b**) Vesicle shapes for partial-wrapped states with wrapping fractions $f = 0.4$ and $f = 0.7$ for various ratios of the bending rigidity of vesicle and initially flat membrane, κ_1/κ_2. (**c**)–(**d**) Wrapping phase diagrams for pressure $p = 0$ with respect to the dimensionless adhesion strengths $\bar{w} = 2wR^2/\kappa_2$ and surface tension $\bar{\gamma} = 2\gamma R^2/\kappa_2$ at different values of the rigidity ratio κ_1/κ_2: (I) stable non-wrapped state, (II) stable non-wrapped and metastable partial-wrapped state, (II') stable partial-wrapped and unstable non-wrapped state, (III) stable partial-wrapped state and metastable complete-wrapped state, (IV) stable complete-wrapped state and metastable partial-wrapped state, and (V) stable complete-wrapped state. Reprinted with permission from [119]. Copyright 2011 by the American Physical Society

upon changes of volume V_v and area A_v of the vesicle, area A_f of the initially flat membrane, and the contact area A_{ad} between vesicle and membrane, respectively.

Phase diagrams for wrapping of soft nanoparticles with different ratios between the stiffnesses of the vesicle membrane and the membrane that wraps the vesicle, κ_1/κ_2, are shown in Fig. 6c, d. For stiff vesicles, the wrapping phase diagram in Fig. 6c is very similar to the wrapping phase diagram for hard spherical nanoparticles in Fig. 2b. For soft vesicles, the phase boundary between non-wrapped and partial-wrapped states is shifted to smaller adhesion strengths, see Fig. 6d. The regime with stable non-wrapped states and metastable partial-wrapped states is replaced by a regime with stable partial-wrapped and unstable non-wrapped states, which also partially extends into the regime of stable complete-wrapped states for hard particles. Soft nanoparticles therefore attach much more readily to membranes, while at the same time the transition to the complete-wrapped state shifts to higher adhesion strengths.

2.4 Dynamics

The dynamics of particle wrapping is determined by the typical timescales of the relevant processes, such as membrane deformation and—for complex membranes—receptor diffusion and potentially deformation or remodeling of the cytoskeleton. Molecular dynamics simulations for nanoparticles that interact with initially flat lipid bilayer membranes allow to follow a typical wrapping process in time [59, 104]. After the initial contact between nanoparticle and membrane, the size of the deformed membrane patch around the particles increases; it is largest for about half-wrapped nanoparticles. Towards the end of the wrapping process, the bent membrane attached to the particle is connected to the flat region surrounding the particle only by a small neck. Formation of a defect in the neck leads to separation of bent and flat membrane and completes the wrapping process.

Dynamics is particularly interesting for nonspherical particles that attach to lipid bilayer membranes. While the stable orientation for elongated particles at small wrapping fraction is (usually) the submarine orientation with the long axis parallel to the membrane, for high wrapping fraction the rocket orientation with the long axis perpendicular to the membrane corresponds to the lowest energy [29]. Coarse-grained molecular dynamics simulations allow to follow the orientational changes that elongated nanoparticles undergo during wrapping [59, 104]. A local free energy analysis and incremental changes of the nanoparticle orientation in the direction of lowest energy allow to predict a wrapping pathway, see Fig. 7. The corresponding curvature energy landscapes are plotted using color density plots. A sphero-cylindrical nanoparticle that is initially in the unfavorable rocket orientation first reorients towards submarine orientation. Although energetically most favorable until half-wrapping, the particle may never actually reach submarine orientation. Beyond half-wrapping, the particle turns back to the then favorable

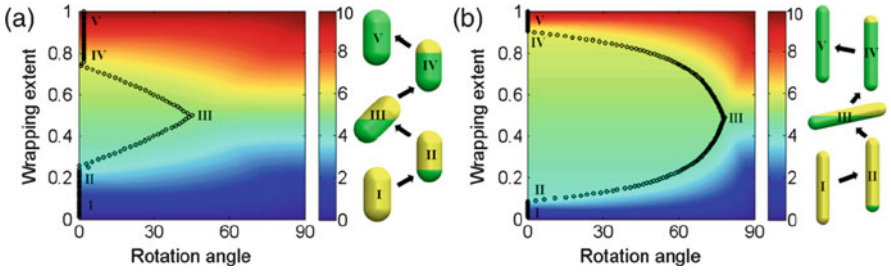

Fig. 7 Endocytic pathways for nanoparticles with aspect ratios (**a**) 2 and (**b**) 5.5 predicted by local energetics. The sphero-cylindrical nanoparticles take a general laying-down-then-standing-up sequence during endocytosis. The contour maps plot the curvature energy level in the plane of rotation angle and wrapping extent. The turning points (I–V) along the endocytic pathways predicted by local free-energy analysis are schematically shown in each subfigure, where the green-shaded areas are wrapped, while yellow-shaded areas are naked. Reprinted with permission from [59]. Copyright (2013) American Chemical Society

rocket orientation, in agreement with the energetics discussed in Sect. 2.2. For very fast uptake, reorientation may be suppressed and an ellipsoidal particle may, for example, be taken up completely in submarine orientation [31].

3 Wrapping by Complex Membranes

Many biological membranes contain a variety of lipids and proteins and are much more complex than the model membranes that have been discussed so far [91]. These different components can interact with particles and pathogens and may either be randomly distributed as suggested by the fluid mosaic model or aggregated already before the interaction with particles in lipid rafts [77]. Furthermore, a cortical cytoskeleton may rigidify the membrane by adding shear elasticity [6, 53], slow down diffusion within the membrane [5], and alter distribution of lipids and proteins [42].

3.1 Two-Component Membranes with Domains

Particle adhesion has been found experimentally to depend on lipid composition and membrane structure: small particles with $R < 100\,\mathrm{nm}$ have been observed to attach to the liquid-ordered phase, larger particles attach to the liquid-disordered phase [52]. Computer simulations for a particle that is attached to a lipid raft show that the presence of the domain boundary facilitates particle detachment from the membrane after complete wrapping [97]. Membranes where two or more phases with different lipid compositions coexist can be described by a set of elastic parameters for each domain and a line tension at the domain boundary. Domain formation alone can induce budding [12, 70], therefore domains can assist particle wrapping. The effect of lipid phase segregation on the interaction of particles with membranes can be investigated using the Hamiltonian:

$$\mathscr{H} = \sum_{i=1,2} \left\{ \int_{S_i} dS_i \left[\gamma_i + 2\kappa_i (H - c_{0,i})^2 + \bar{\kappa}_i K \right] + \gamma_\ell \int_{\ell_c} d\ell - w_i \int_{S_{\mathrm{ad,i}}} dS_i \right\}, \tag{4}$$

where the sum adds the integrals over a domain and its surrounding, see Fig. 8a. The line tension γ_ℓ arises at the boundary where the phases are in contact, and it might be very small if hybrid lipids with one saturated and one partially unsaturated chain act as line-active component [15]. The value of $\bar{\kappa}$ is not well known in many cases, because the Gaussian saddle-splay modulus only contributes to the energy of the membrane if it is inhomogeneous or if topology changes of the membrane are observed. We neglect this contribution in the following discussion, the contribution at the domain boundary might be thought of as redefined line tension.

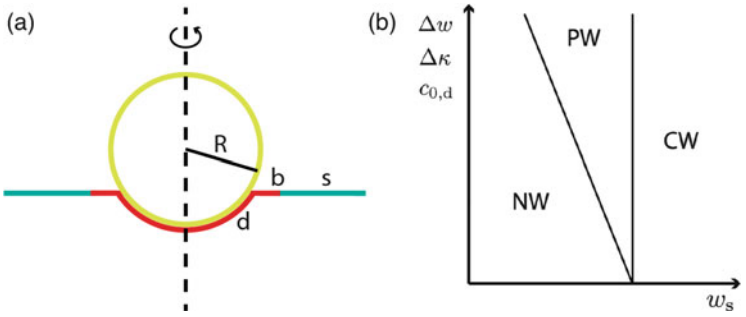

Fig. 8 Particle wrapping by multicomponent membranes with strong segregation. (**a**) Membrane with domain size smaller than the particle surface area partially wrapped around the particle (d: domain area, s: surrounding membrane, and b: domain boundary). (**b**) Wrapping phase diagrams for a particle that preferentially adheres to a domain that is smaller than the surface area of the particle (NW: non-wrapped particle, PW: partial-wrapped particle, and CW: complete-wrapped particle). The phases are sketched for the adhesion strength of the surrounding membrane w_s and either the difference of the adhesion strengths Δw, the difference of the bending rigidities $\Delta\kappa$, or the spontaneous curvature $c_{0,\mathrm{d}}$ of the membrane that forms the domain. All other parameters are kept constant. Calculated using the model in (**a**)

Figure 8b shows a phase diagram for particles that interact with a domain in a tensionless, phase-separated membrane with vanishing line tension at the domain boundary. If the domain is larger than the surface area of the particle, the wrapping behavior is expected to be similar to a homogeneous membrane. If the domain is too small to cover the entire surface area of the particle, the change of curvature-elastic constants and adhesion strength is reflected in the wrapping phase diagrams. The diagram shows wrapping phases for particles that adhere to a domain with adhesion strength $w_\mathrm{d} \geq w_\mathrm{s}$, where w_s is the adhesion strength between the particle and the surrounding membrane. Stable partial-wrapped states occur when the w_d is large enough for wrapping, but w_s is too small. The phases are plotted for w_s and $\Delta w = w_\mathrm{d} - w_\mathrm{s}$. Analogous to an increased adhesion strength, stable partial-wrapped states are found if the bending rigidity of the membrane that forms the domain is smaller than the bending rigidity of the surrounding membrane, $\Delta\kappa = \kappa_\mathrm{s} - \kappa_\mathrm{d} > 0$, and if the membrane of the domain has a preferable spontaneous curvature $c_{0,\mathrm{d}}$. A finite line tension for the boundary of a preexisting domain also assists wrapping, because the length of the domain boundary decreases with increasing wrapping fraction of the particle.

3.2 Receptor–Ligand Bond-Mediated Wrapping

The interaction of particles with multicomponent membranes in a single phase cannot be described by domains with different curvature-elastic parameters and adhesion strengths as discussed in Sect. 3.1. Here, the presence of the nanoparticle

can induce segregation of the components, such as aggregation of receptors in the adhered region. Experimental data indicates the importance of receptor-mediated nanoparticle wrapping. For example, particles that are half-coated with ligands are endocytosed in steps [47]. In a first step, a membrane cup forms on the ligand-coated surface and afterwards the endocytic process stalls. Only in a second step, the ligand-absent hemisphere is wrapped. Furthermore, experiments for nanoparticle uptake by cells reveal a preferred particle radius of about 25 nm [20, 21, 81], while calculations with a homogeneous adhesion strength between particle and membrane predict that the larger the nanoparticle the easier it gets wrapped. This has triggered theoretical studies on receptor-mediated endocytosis using kinetic [9, 34, 35, 48] and free-energy approaches [33, 120] that both predict an optimal radius for uptake close to the experimentally observed radius.

Receptor-mediated adhesion is a natural choice to model the adhesive interaction in computer simulations, because nanoparticles are often modeled by an assembly of beads [59, 104]. Figure 9a shows wrapping for a nanoparticle with ligand coverages of 20% and 80% and receptor–ligand bond energies $\epsilon = 2\,k_{\mathrm{B}}T$ and $\epsilon = 8\,k_{\mathrm{B}}T$. A bound nanoparticle is observed for small bond energy and small ligand coverage, a partial-wrapped nanoparticle is observed for small bond energy and high ligand coverage or for high bond energy and low ligand coverage, and a complete-wrapped nanoparticle is observed for high ligand coverage and high bond energy. Analogous to the competition of adhesion energy and bond energy, for homogeneous adhesion strength the nanoparticles get wrapped only if the adhesion energy gain exceeds the deformation energy cost (this estimation neglects an energy minimum for partial-

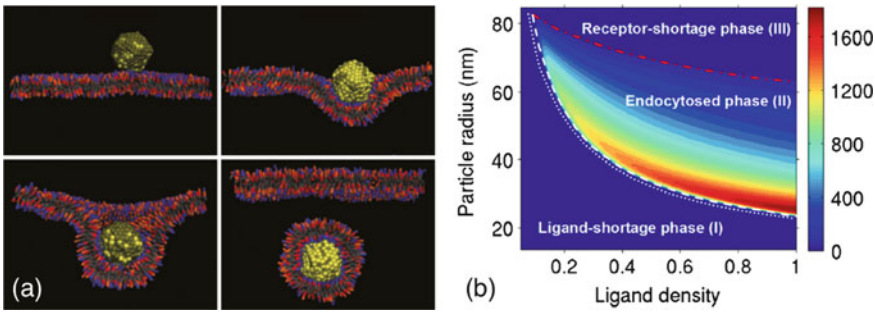

Fig. 9 Particle wrapping by multicomponent membranes with weak segregation. (**a**) Receptor-mediated wrapping for a spherical nanoparticle interacting with a membrane. Binding, partial, and complete wrapping are observed depending on ligand coverage and receptor–ligand bond energy. Color coding: nanoparticle, yellow beads are ligands and gray beads are purely repulsive; membrane, blue beads are membrane receptors, orange are headgroups, and gray and orange are tail beads. Adapted with permission from [104]. Copyright (2011) American Chemical Society. (**b**) The phase diagram shows the cellular uptake for various particle sizes and ligand densities. The dotted line represents the theoretical lower bound $R = \sqrt{2\kappa/\epsilon}a_{\mathrm{r}}$. The color bar indicates the level of cellular uptake. The endocytosed phase (II) is separated from the ligand-shortage phase (I) and the receptor-shortage phase (III) by the dashed and the dashed-dotted line. Reprinted with permission from [120]. Copyright 2010 by the American Physical Society

wrapped states). A minimal particle radius is given by $\epsilon/a_r^2 > 2\kappa/R^2$, where a_r is the area per receptor.

For a given wrapping fraction of the nanoparticle, the free energy for the receptors on the membrane is

$$F = -N_b\epsilon - k_B T \ln\left[\binom{S_b}{N_b}\binom{S_f}{N_f}\right]. \tag{5}$$

Here, we assume the ligands to be regularly distributed and fixed on the particle. The receptor entropy is calculated for a membrane that is discretized into sites. S_b and S_f are the numbers of available sites on the bound and unbound region of the membrane, and N_b and N_f the numbers of bound and free receptors. The first term represents the total bond energy and the second term represents the contribution of the receptor entropy to the free energy. This is a simplified model that highlights the interplay of bond energy and entropy of the receptors. A more complete model for receptor-mediated adhesion accounts in addition for the entropy of the differently wrapped nanoparticles, the enthalpy change by taking nanoparticles out of the solution, and the membrane deformation energy [120]. Figure 9b quantifies cellular uptake for a membrane with bending rigidity and tension. Three different wrapping regimes are found: (1) a ligand-shortage phase where $\epsilon/a_r^2 < 2\kappa/R^2$, (2) an endocytosed phase where the nanoparticle gets wrapped, and (3) a receptor-shortage phase where both membrane tension and receptor entropy prevent wrapping.

Extensions of the basic model for receptor-mediated adhesion of single particles allow to study of further aspects of related systems. For example, taking into account mutual attraction of nanoparticles during cellular uptake leads to distributions for uptake as function of nanoparticle size that agree better with the experimental data than single-particle calculations [19]. In biological systems with high salt concentrations and strong electrostatic screening, charged membranes that interact with charges on the nanoparticle show a similar dependence of the energy of the system on the wrapping fraction as found for receptor-mediated wrapping [46]. In particular, frustrated endocytosis with partial-wrapped states is observed for lack of charges on the membrane. Receptor-like models can also be used to understand the role of curved proteins for wrapping, where the energy gain for the proteins in the membrane adhered to the particle with favorable curvature competes with the loss of entropy for protein aggregation [2, 79]. Finally, viral budding from and entry into host cells is a receptor-mediated process [80, 102].

4 Many-Particle Interactions

Many-particle interactions significantly alter the interaction of nanoparticles with membranes. For example, single nanoparticles are too small to be phagocytosed, but aggregates may enter the cell via this pathway [16]. For dosage-dependent effects, also membrane-mediated interaction is an important player in addition to

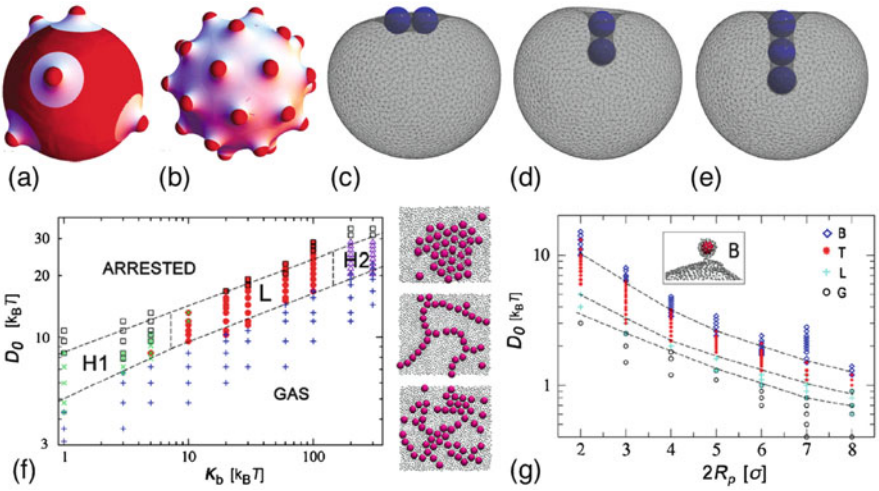

Fig. 10 Membrane-mediated interaction. (**a**)–(**b**) Inclusions, indicated by small red caps, on a vesicle. White catenoidal deformations with vanishing bending energy form around the inclusions. An inclusion-decorated vesicle with vanishing bending energy cost at optimal inclusion density. Reprinted with permission from [4]. Copyright 2009 by the American Physical Society. (**c**)–(**e**) Nanoparticles attached to a vesicle aggregate, tubes form for sufficiently small reduced volume of the vesicle, such that enough area is available to allow for this deformation. Reprinted with permission from [7]. Copyright 2012 by the American Physical Society. (**f**) Phase diagram for nanoparticle self-assembly in terms of membrane bending rigidity $K_b = 2\sqrt{3}\kappa$ [50] and particle binding strength D_0 that is proportional to the adhesion strength w. The snapshots show typical aggregates in H1, L, and H2 phase (top to bottom). Reprinted with permission from [93]. Copyright 2012 by the American Physical Society. (**g**) Phase diagram in terms of nanoparticle radius R_p (in units of the radius of the beads that are used to represent the membrane in the simulations) and D_0: gaseous phase G, linear aggregation L, tube formation (T), and single-particle bud formation B. Reprinted with permission from [94]. Copyright 2012 by the American Physical Society

direct interaction between nanoparticles. We first discuss the interaction of curved inclusions: while two small spherical-cap inclusions—where the cap is only a small part of the entire sphere—interact repulsively, for large spherical caps attraction is observed [86, 87]; furthermore, many inclusions aggregate and induce bud formation [3, 4, 87]. Figure 10a, b shows catenoidal membrane deformations around inclusions that reduce the total bending energy of an inclusion-decorated vesicle compared with a bare vesicle. The bending energy of the inclusion-decorated vesicle vanishes at optimal inclusion density, while an energetic cost arises from the same number of inclusions at maximal mutual distance on a planar membrane of finite size. Thus, vesicle curvature screens the membrane-mediated repulsion between inclusions.

The membrane-mediated many-particle interactions that have been studied so far are always attractive. For instance, two particles form a dimer that switches from a linear aggregate on the membrane to a tubule for increasing wrapping fraction [7, 94], see also the discussion on submarine and rocket orientation of elongated

particles in Sect. 2.2. The wrapping fraction of the particle can be tuned by adjusting the reduced volume of the vesicle, $v = V/V_{\mathrm{sph}}$, where V is its actual volume and V_{sph} is the volume of a spherical vesicle with the same membrane area. Small reduced volumes allow more than two particles to join a tube. The energetic gain of tubular assemblies compared with single, complete-wrapped particles strongly depends on the range of the particle–membrane interaction potential ρ; for example, the energy gain is about 5κ for $\rho/R = 0.2$ [85], because the curvature energy decreases for a tube-like arrangement of nanoparticles, but the adhesion energy hardly increases due to the finite potential range.

Figure 10f shows a phase diagram for many nanoparticles on a membrane for different values of κ and particle binding strength D_0 [93]. For small bending rigidities, partial-wrapped particles form a hexagonal cluster phase where the membrane penetrates inbetween the particles. For high bending rigidities, partial-wrapped particles are barely attached to the membrane; they deform the membrane only weakly and therefore also interact only weakly. Linear aggregates are observed inbetween both phases for biologically relevant bending rigidities $10\,k_{\mathrm{B}}T < \kappa < 100\,k_{\mathrm{B}}T$. Whereas the deformation energy cost prefers a hexagonal cluster, the higher adhesion energy gain leads to formation of linear clusters [93]. Linear aggregates have also been observed in experiments where colloidal particles were bound to giant unilamellar vesicles (GUVs) [65]. In computer simulations at high adhesion strengths, the particles are found in an arrested phase; this can either be single-particle buds or tubular aggregates [94], see Fig. 10g. Tubule formation has been observed experimentally, for instance, for the interaction of viruses with cells and GUVs [43].

5 Pathogens and Other Active Biological Systems

Phagocytosis—a feeding mechanism or an immune response to foreign objects of cells—and entry or exit of parasites involve active biological processes. For example, mammalian cells form actin protrusions to interact with their immediate environment; membrane reservoirs and clustering of receptors and signaling molecules can help to sculpture the plasma membrane into different shapes. The malaria parasite is equipped with motor complexes that can assist invasion into red blood cells.

5.1 Invasion of the Malaria Parasite into Erythrocytes

Malaria is a deadly disease that affects several hundred million people every year around the world. One of the crucial stages of infection is the blood stage, where the merozoites invade red blood cells [25]. A merozoite has an asymmetric egg-like shape with a total surface area of $8\,\mu\mathrm{m}^2$ and a width/length ratio of 0.71. Merozoites

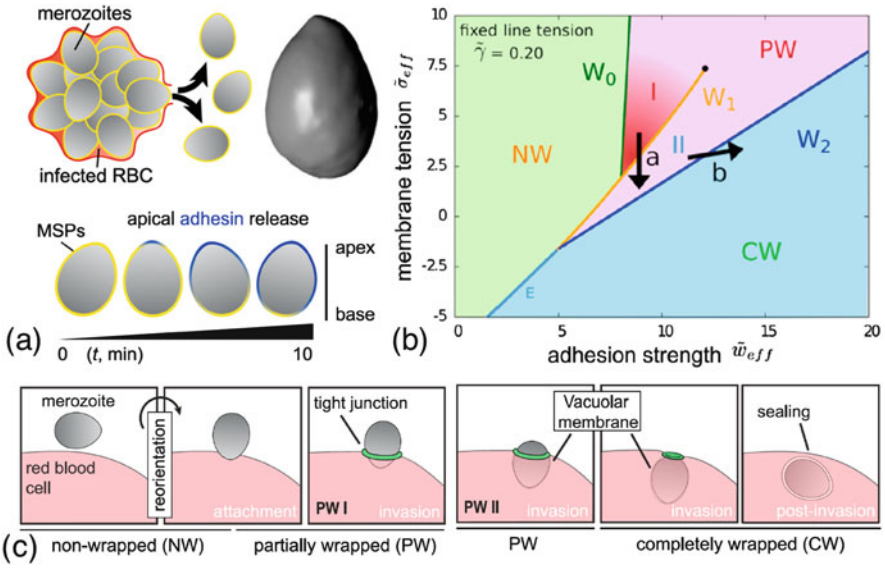

Fig. 11 Membrane-wrapping contributions to malaria parasite invasion of the human erythrocyte. (**a**) Malaria egress from an infected erythrocyte and an isosurface of a merozoite obtained from cryo X-ray imaging. Merozoites are infectious for about 10 min, during which an adhesin gradient may develop. (**b**) Wrapping phase diagram for a tip-first-oriented merozoite for adhesion strength and membrane tension at fixed reduced line tension $\tilde{\gamma} = 0.2$: (**c**) Schematic representation depicting different wrapping phases of the merozoite from reorientation through to invasion and post-invasion. Reprinted with permission from [30]. CC BY 4.0

approach the erythrocyte surface in a random orientation and then quickly undergo reorientation with the pointed apical end towards the membrane. This reorientation can be triggered by an adhesive gradient on the merozoite surface, see Fig. 11a. Next, the merozoite invades the erythrocyte within several minutes by traversing through the partial-wrapped states PW I and PW II, see Fig. 11b.

Phase diagrams for wrapping the parasite with erythrocyte membrane highlight the interplay of membrane curvature elasticity and tension, parasite shape and adhesion energy, and line tension where the membrane detaches from the parasite (that possibly originates from the cytoskeleton of the erythrocyte) [30]. Wrapping phase diagrams can be calculated along the same lines as described in Sect. 2. The states in the phase diagram for a tip-first-oriented merozoite and a fixed line tension in Fig. 11b correspond to the sketches in Fig. 11c: non-wrapped (NW), partial-wrapped with small wrapping fraction (PW I), partial-wrapped with high wrapping fraction (PW II), and complete-wrapped (CW). The transition W_0 between the non-wrapped and the partial-wrapped state is continuous, whereas the transitions W_1, W_2, and E are discontinuous. At a critical membrane tension, the energy barrier between the two partial-wrapped states vanishes and W_1 ends at a critical point. The arrows in Fig. 11b indicate active biological processes during invasion: **a** secretion

of unstructured membrane by the merozoite, and **b** aggregation or secretion of membrane components with favorable spontaneous curvature.

Wrapping-energy calculations provide a systematic understanding for passive energetic contributions to the invasion process and can help to quantify the effect of various active biological processes. (1) A gradient of adhesive strength can lead to tip-first orientation of the parasite, the crucial first step of the invasion process. (2) Parasite-stimulated reorganization of the erythrocyte cytoskeleton and release of parasite-derived membrane area may affect elastic properties of the host-cell membrane, such as tension and spontaneous curvature and thereby facilitate wrapping. (3) Parasite actomyosin motor contributions can help to overcome energetic barriers and to transition from metastable partial-wrapped to stable complete-wrapped states. Combining these biophysical insights with a parasitological framework, drawing on a broad foundation of molecular and cellular evidence, it is proposed that invasion is achieved via a balance between parasite and host cell contributions. These findings lay the foundations for identifying mechanisms related to the host cell membrane that might be targeted in malaria treatment.

5.2 Active Invasion Mechanisms During Phagocytosis

Phagocytosis involves complex physiological mechanisms by which eukaryotic cells ingest nutrients and immune cells eliminate pathogenic particles or dead biological material. While particles with sizes below 500 nm are internalized via receptor-mediated endocytosis, particles with sizes larger than 1 μm are internalized through a phagocytic process [36]. Here, cells employ active mechanochemical processes, such as cytoskeletal reorganization. Actin–myosin rings or phagocytic cups, specific or unspecific adhesion mediated via receptor–ligand bonds, and dynamical regulation of membrane tension assist to sculpture the plasma membrane into a phagosome. Experiments demonstrate that local particle shape, not overall particle size, plays a decisive role in initiating phagocytosis [17, 74]. For instance, macrophages that attach to a flat side of an oblate ellipsoidal particle spread on one side of the particle, but no formation of an actin ring and no phagocytosis are observed. Figure 12a shows representative scanning electron micrographs and fluorescent micrographs with actin staining for cells that interact with polystyrene particles of different shapes. The fluorescent micrographs reveal remodeling of the cytoskeleton to form ring-like and cup-like structures. The experiments suggest that cells are not able to detect macroscopic properties, such as volume, until phagocytosis is complete. However, the size of the particle could prevent the cell from successfully completing internalization.

Cellular uptake of large spherical particles by phagocytosis occurs in two distinct phases, see Fig. 12b. During a first, slow engulfment phase, wrapping is achieved by actin-rich protrusions. Receptor-mediated interactions drive the wrapping process, such that for specific adhesion the efficiency can be increased by higher receptor densities [17, 47]. During a second, fast envelopment phase,

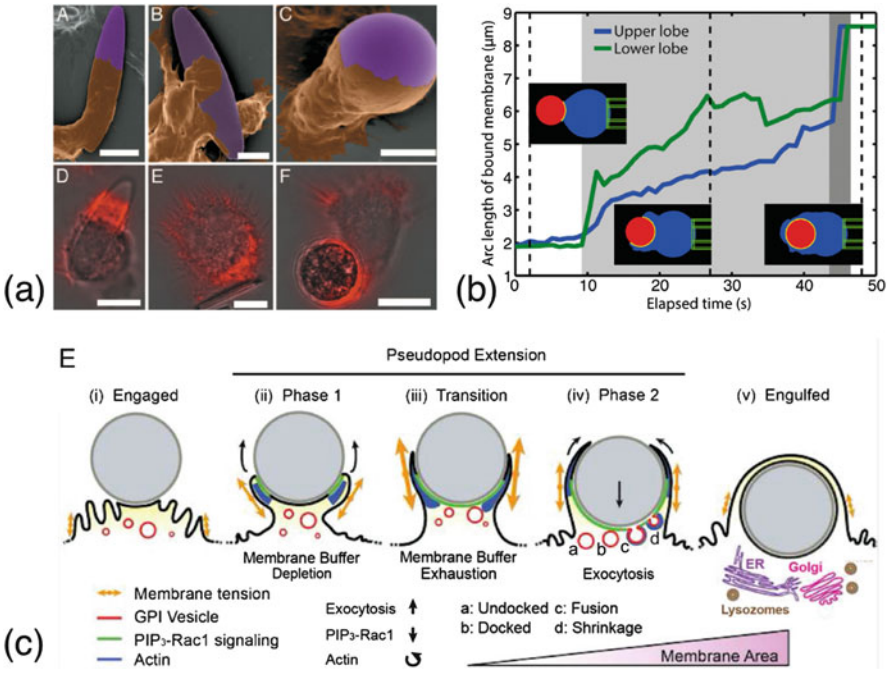

Fig. 12 Phagocytosis. (**a**) Micrographs of cells and opsonized particles, colored brown and purple, respectively, and overlays of bright-field and fluorescent images after fixing the cells and staining for polymerized actin with rhodamine phalloidin. A: Cell body at an end of a half-wrapped elliptical disk. (Scale bar: 10 μm.) B: Cell attached to flat side of an elliptical disk. (Scale bar: 5 μm.) C: Spherical particle attached to top of a cell. (Scale bar: 5 μm.) D–F: Actin reorganization–ring formation, polymerization at site of attachment, and start of internalization. (Scale bars in D-F: 10 μm). Reprinted with permission from [17]. Copyright (2006) National Academy of Sciences, USA. (**b**) Analysis of the wrapping fraction for phagocytosis for a spherical bead with $R = 2.3\,\mu\text{m}$. Initially, slow engulfment (light gray) is followed by a much quicker engulfment (dark gray). Insets show snapshots of the data that has been analyzed (blue: cell, red: bead, green: outline of pipette, and yellow: attached membrane). Reprinted with permission from [88], Copyright (2014), with permission from Elsevier. (**c**) Dynamical regulation of membrane tension during phagocytosis. After bead engagement (1), signaling is activated and actin polymerization pushes the membrane forward around the particle (2). Membrane tension increases because of protrusion, leading to membrane buffer (folds) depletion. High membrane tension leads to deactivation of signaling, actin reorganization, and activation of exocytosis (3). Increase of membrane area by actin-associated exocytosis (4) and complete engulfment (5). Reprinted with permission from [71]

the particle is completely engulfed via a zipper-like mechanism. Fast wrapping is also observed in the absence of receptors on half of the particle [47]. For elongated particles, such as prolate ellipsoidal particles, internalization is most efficient when the particles are wrapped tip-first; this is also predicted by calculations [88, 108]. These results suggest that phagocytic uptake is a combination of passive wrapping with a competition of adhesion and deformation energy and active, regulated cellular processes, such as cytoskeletal reorganization and formation of a phagocytic cup.

Despite longstanding efforts to unravel phagocytosis, the current understanding of the governing biophysical processes is limited. Therefore, efforts that interpret experimental data using theoretical models for active engulfment scenarios in biological cells are required to identify mechanisms. We discuss below some of these modeling approaches for active uptake.

In [108], a set of reaction–diffusion equations is used to model the dynamics of the signaling pathway. These equations are combined with an equation for the dynamics of the phagocytic cup and the deformation energy of the membrane. In agreement with experiments, this model predicts a mechanical bottleneck at half-wrapping as well as high uptake for spherical and prolate ellipsoidal particles and stalled phagocytosis for oblate ellipsoidal particles.

An alternative mechanism is described in [71] that suggests that the biphasic process for pseudopod formation during phagocytosis is regulated by plasma membrane tension. In the first phase of phagocytosis, a particle is wrapped until a buffer for membrane area that is stored in folds and ruffles is depleted after about half-wrapping. Hereafter, phagocytosis can only proceed if the tension of the plasma membrane is again lowered. This occurs during the second phase of phagocytosis by fusion of exocytic vesicles with the plasma membrane that enlarge its area and decrease its tension. Figure 12c illustrates this process.

A zipper mechanism for phagocytic uptake is proposed and investigated in [101]. Monte Carlo simulations for a fluctuating membrane are combined with adhesive particles of different shapes. The deformation energy is modeled using a triangulated membrane with the bending energy given by the Helfrich Hamiltonian. For the adhesive interaction, the vertices of the membrane close to the particle either gain a finite adhesion energy and attach reversibly or stick irreversibly. These two interactions model passive adhesion and an active zipper mechanism, respectively. The model suggests an increased importance of active wrapping with increasing particle size and also predicts the mechanical bottleneck where cups get stalled at or before half-wrapping. Furthermore, it reproduces the dependence of uptake on the orientation for prolate ellipsoidal particles, tip-first uptake is faster than side-first uptake.

Finite-element calculations for the membrane include the adhesive interaction between cell surface and target, mimic actin cytoskeletal polymerization at the leading edge, and invoke contractility at the cell–bead interface [56, 57]. Using this model, shapes for the phagocytic cups can be obtained that are similar to those observed experimentally during uptake.

A two-stage model assumes passive adhesion by receptor-mediated interaction that is limited by receptor diffusion in the first phase, and active mechanisms with directed motion of the receptors and signaling in the second phase [88]. This model is consistent with slow wrapping in the first phase and fast wrapping in the second phase, as observed in experiments. It also reproduces the observed quicker uptake when prolate ellipsoidal particles enter tip-first.

6 Conclusions and Outlook

With the advancement of technology, novel techniques to engineer nanoparticles of various shapes and sizes are now available. Such particles are obvious candidates for novel applications, therefore knowledge about their interaction in particular with plasma membranes as first step of their interaction with biological cells is required. A better understanding of the interaction of particles with biomembranes can facilitate development of drug and gene-delivery systems, advance the research on diseases by illuminating parasite and virus invasion, and may also help to develop strategies to engineer nanostructured surfaces for optimal cell adhesion to, e.g., biosensors. Soft particles, complex particle shapes, complex membrane compositions, more realistic calculations for dynamics of particle wrapping, and various active mechanisms, for example for phagocytic uptake, await further research both using theoretical and experimental techniques.

Acknowledgements Our research on the interaction of particles with biological membranes has been supported by the EU FP7 NMP collaborative project PreNanoTox (309666).

References

1. Abbena E, Salamon S, Gray A (2006) Modern differential geometry of curves and surfaces with Mathematica. Chapman and Hall/CRC, Boca Raton
2. Agudo-Canalejo J, Lipowsky R (2015) Critical particle sizes for the engulfment of nanoparticles by membranes and vesicles with bilayer asymmetry. ACS Nano 9(4):3704–3720
3. Atilgan E, Sun SX (2007) Shape transitions in lipid membranes and protein mediated vesicle fusion and fission. J Chem Phys 126(9):095102
4. Auth T, Gompper G (2009) Budding and vesiculation induced by conical membrane inclusions. Phys Rev E 80(3):031901
5. Auth T, Gov NS (2009) Diffusion in a fluid membrane with a flexible cortical cytoskeleton. Biophys J 96(3):818–830
6. Auth T, Safran SA, Gov NS (2007) Fluctuations of coupled fluid and solid membranes with application to red blood cells. Phys Rev E 76(5):051910
7. Bahrami AH, Lipowsky R, Weikl TR (2012) Tubulation and aggregation of spherical nanoparticles adsorbed on vesicles. Phys Rev Lett 109(18):188102
8. Bahrami AH et al (2014) Wrapping of nanoparticles by membranes. Adv Colloid Interf Sci 208:214–224
9. Bao G, Bao XR (2005) Shedding light on the dynamics of endocytosis and viral budding. Proc Natl Acad Sci USA 102(29):9997–9998
10. Barnoud J, Rossi G, Monticelli L (2014) Lipid membranes as solvents for carbon nanoparticles. Phys Rev Lett 112(6):068102
11. Barua S et al (2013) Particle shape enhances specificity of antibody-displaying nanoparticles. Proc Natl Acad Sci USA 110(9):3270–3275
12. Baumgart T, Hess ST, Webb WW (2003) Imaging coexisting fluid domains in biomembrane models coupling curvature and line tension. Nature 425(6960):821–824
13. Beningo KA, Wang Y-l (2002) Fc-receptor-mediated phagocytosis is regulated by mechanical properties of the target. J Cell Sci 115(4):849–856

14. Brakke KA (1992) The surface evolver. Exp Math 1(2):141–165
15. Brewster R, Pincus PA, Safran SA (2009) Hybrid lipids as a biological surface-active component. Biophys J 97(4):1087–1094
16. Canton I, Battaglia G (2012) Endocytosis at the nanoscale. Chem Soc Rev 41(7):2718–2739
17. Champion JA, Mitragotri S (2006) Role of target geometry in phagocytosis. Proc Natl Acad Sci USA 103(13):4930–4934
18. Champion JA, Katare YK, Mitragotri S (2007) Making polymeric micro-and nanoparticles of complex shapes. Proc Natl Acad Sci USA 104(29):11901–11904
19. Chaudhuri A, Battaglia G, Golestanian R (2011) The effect of interactions on the cellular uptake of nanoparticles. Phys Biol 8(4):046002
20. Chithrani BD, Chan WCW (2007) Elucidating the mechanism of cellular uptake and removal of protein-coated gold nanoparticles of different sizes and shapes. Nano Lett 7(6):1542–1550
21. Chithrani BD, Ghazani AA, Chan WCW (2006) Determining the size and shape dependence of gold nanoparticle uptake into mammalian cells. Nano Lett 6(4):662–668
22. Cho EC, Zhang Q, Xia Y (2011) The effect of sedimentation and diffusion on cellular uptake of gold nanoparticles. Nat Nanotech 6(6):385–391
23. Churchman AH et al (2013) Serum albumin enhances the membrane activity of ZnO nanoparticles. Chem Commun 49(39):4172–4174
24. Copolovici DM et al (2014) Cell-penetrating peptides: design, synthesis, and applications. ACS Nano 8(3):1972–1994
25. Cowman AF, Crabb BS (2006) Invasion of red blood cells by malaria parasites. Cell 124(4):755–766
26. Crick AJ et al (2014) Quantitation of malaria parasite-erythrocyte cell-cell interactions using optical tweezers. Biophys J 107(4):846–853
27. Dan N et al (1994) Membrane-induced interactions between inclusions. J Phys II (France) 4(10):1713–1725
28. Dasgupta S, Auth T, Gompper G (2013) Wrapping of ellipsoidal nano-particles by fluid membranes. Soft Matter 9(22):5473–5482
29. Dasgupta S, Auth T, Gompper G (2014) Shape and orientation matter for the cellular uptake of nonspherical particles. Nano Lett 14(2):687–693
30. Dasgupta S et al (2014) Membrane-wrapping contributions to malaria parasite invasion of the human erythrocyte. Biophys J 107(1):43–54
31. Dasgupta S, Auth T, Gompper G (2015) Wrapping of ellipsoidal nano-particles by fluid membranes. Soft Matter 11:7441–7444
32. Dasgupta S, Auth T, Gompper G (2017) Nano-and microparticles at fluid and biological interfaces. J Phys Condens Matter 29:373003
33. Decuzzi P, Ferrari M (2006) The adhesive strength of non-spherical particles mediated by specific interactions. Biomaterials 27(30):5307–5314
34. Decuzzi P, Ferrari M (2007) The role of specific and non-specific interactions in receptor-mediated endocytosis of nanoparticles. Biomaterials 28(18):2915–2922
35. Decuzzi P, Ferrari M (2008) The receptor-mediated endocytosis of nonspherical particles. Biophys J 94(10):3790–3797
36. Decuzzi P et al (2009) Intravascular delivery of particulate systems: does geometry really matter? Pharm Res 26(1):235–243
37. Deserno M (2004) Elastic deformation of a fluid membrane upon colloid binding. Phys Rev E 69(3):031903
38. Deserno M (2004) When do fluid membranes engulf sticky colloids? J Phys Condens Matter 16(22):S2061
39. Deserno M, Bickel T (2003) Wrapping of a spherical colloid by a fluid membrane. Europhys Lett 62(5):767
40. Deserno M, Gelbart WM (2002) Adhesion and wrapping in colloid-vesicle complexes. J Phys Chem B 106(21):5543–5552
41. Ding H-m, Tian W-de, Ma Y-q (2012) Designing nanoparticle translocation through membranes by computer simulations. ACS Nano 6(2):1230–1238

42. Ehrig J, Petrov EP, Schwille P (2011) Near-critical fluctuations and cytoskeleton-assisted phase separation lead to subdiffusion in cell membranes. Biophys J 100(1):80–89
43. Ewers H et al (2010) GM1 structure determines SV40-induced membrane invagination and infection. Nat Cell Biol 12(1):11–18
44. Fish et al MB (2015) Emergence and utility of nonspherical particles in biomedicine. Ind Eng Chem Res 54(16):4043–4059
45. Florez L et al (2012) How shape influences uptake: interactions of anisotropic polymer nanoparticles and human mesenchymal stem cells. Small 8(14):2222–2230
46. Fošnarič M et al (2009) Monte carlo simulations of complex formation between a mixed fluid vesicle and a charged colloid. J Chem Phys 131(10):105103
47. Gao Y, Yu Y (2013) How half-coated janus particles enter cells. J Am Chem Soc 135(51):19091–19094
48. Gao H, Shi W, Freund LB (2005) Mechanics of receptor-mediated endocytosis. Proc Natl Acad Sci USA 102(27):9469–9474
49. Ge P et al (2010) Cryo-em model of the bullet-shaped vesicular stomatitis virus. Science 327(5966):689–693
50. Gompper G, Kroll DM (2004) Triangulated surface models of fluctuating membranes. In: Nelson DR, Piran T, Weinberg S (eds) Statistical mechanics of membranes and surfaces. World Scientific, Singapore
51. Gózdz WT (2007) Deformations of lipid vesicles induced by attached spherical particles. Langmuir 23(10):5665–5669
52. Hamada T et al (2012) Size-dependent partitioning of nano/microparticles mediated by membrane lateral heterogeneity. J Am Chem Soc 134(34):13990–13996
53. Hansen JC et al (1997) Influence of network topology on the elasticity of the red blood cell membrane skeleton. Biophys J 72(5):2369
54. Hashemi SM, Sens P, Mohammad-Rafiee F (2014) Regulation of the membrane wrapping transition of a cylindrical target by cytoskeleton adhesion. J R Soc Interface 11(100):20140769
55. Helfrich W (1973) Elastic properties of lipid bilayers: theory and possible experiments. Z Naturforsch C 28(11–12):693–703
56. Herant M, Heinrich V, Dembo M (2006) Mechanics of neutrophil phagocytosis: experiments and quantitative models. J Cell Sci 119(9):1903–1913
57. Herant M et al (2011) Protrusive push versus enveloping embrace: computational model of phagocytosis predicts key regulatory role of cytoskeletal membrane anchors. PLoS Comput Biol 7(1):e1001068
58. Hoffmann I et al (2014) Softening of phospholipid membranes by the adhesion of silica nanoparticles–as seen by neutron spin-echo (NSE). Nanoscale 6(12):6945–6952
59. Huang C et al (2013) Role of nanoparticle geometry in endocytosis: laying down to stand up. Nano Lett 13(9):4546–4550
60. Hurley et al JH (2010) Membrane budding. Cell 143(6):875–887
61. Ivask A et al (2014) Size-dependent toxicity of silver nanoparticles to bacteria, yeast, algae, crustaceans and mammalian cells in vitro. PLOS One 9(7):e102108
62. Jaskiewicz K et al (2012) Incorporation of nanoparticles into polymersomes: size and concentration effects. ACS Nano 6(8):7254–7262
63. Jaskiewicz K et al (2012) Probing bioinspired transport of nanoparticles into polymersomes. Angew Chem 124(19):4691–4695
64. Killian JA (1998) Hydrophobic mismatch between proteins and lipids in membranes. Biochim Biophys Acta Rev Biomembr 1376(3):401–416
65. Koltover I, Raedler JO, Safinya CR (1999) Membrane mediated attraction and ordered aggregation of colloidal particles bound to giant phospholipid vesicles. Phys Rev Lett 82(9):1991
66. Le Bihan O et al (2009) Cryo-electron tomography of nanoparticle transmigration into liposome. J Struct Biol 168(3):419–425

67. Lesniak A et al (2012) Effects of the presence or absence of a protein corona on silica nanoparticle uptake and impact on cells. ACS Nano 6(7):5845–5857
68. Li S, Malmstadt N (2013) Deformation and poration of lipid bilayer membranes by cationic nanoparticles. Soft Matter 9(20):4969–4976
69. Lin J et al (2010) Penetration of lipid membranes by gold nanoparticles: insights into cellular uptake, cytotoxicity, and their relationship. ACS Nano 4(9):5421–5429
70. Lipowsky R (1992) Budding of membranes induced by intramembrane domains. J Phys II (France) 2(10):1825–1840
71. Masters TA et al (2013) Plasma membrane tension orchestrates membrane trafficking, cytoskeletal remodeling, and biochemical signaling during phagocytosis. Proc Natl Acad Sci USA 110(29):11875–11880
72. Michel R et al (2014) Internalization of silica nanoparticles into fluid liposomes: formation of interesting hybrid colloids. Angew Chem Int Ed 53(46):12441–12445
73. Mihut AM et al (2013) Tunable adsorption of soft colloids on model biomembranes. ACS Nano 7(12):10752–10763
74. Möller J et al (2012) The race to the pole: how high-aspect ratio shape and heterogeneous environments limit phagocytosis of filamentous escherichia coli bacteria by macrophages. Nano Lett 12(6):2901–2905
75. Monopoli MP et al (2012) Biomolecular coronas provide the biological identity of nanosized materials. Nat Nanotechnol 7(12):779–786
76. Monticelli L et al (2009) Effects of carbon nanoparticles on lipid membranes: a molecular simulation perspective. Soft Matter 5(22):4433–4445
77. Nicolson GL (2014) The fluid—mosaic model of membrane structure: still relevant to understanding the structure, function and dynamics of biological membranes after more than 40 years. Biochim Biophys Acta Rev Biomembr 1838(6):1451–1466
78. Noda T et al (2006) Assembly and budding of ebolavirus. PLoS Pathog 2(9):e99–e99
79. Nowak SA, Chou T (2008) Membrane lipid segregation in endocytosis. Phys Rev E 78(2):021908
80. Nowak SA, Chou T (2009) Mechanisms of receptor/coreceptor-mediated entry of enveloped viruses. Biophys J 96(7):2624–2636
81. Osaki F et al (2004) A quantum dot conjugated sugar ball and its cellular uptake. on the size effects of endocytosis in the subviral region. J Am Chem Soc 126(21):6520–6521
82. Park J-G, Forster JD, Dufresne ER (2010) High-yield synthesis of monodisperse dumbbell-shaped polymer nanoparticles. J Am Chem Soc 132(17):5960–5961
83. Pletikapić G et al (2012) Atomic force microscopy characterization of silver nanoparticles interactions with marine diatom cells and extracellular polymeric substance. J Mol Recognit 25(5):309–317
84. Pogodin S, Baulin VA (2010) Can a carbon nanotube pierce through a phospholipid bilayer? ACS Nano 4(9):5293–5300
85. Raatz M, Lipowsky R, Weikl TR (2014) Cooperative wrapping of nanoparticles by membrane tubes. Soft Matter 10(20):3570–3577
86. Reynwar BJ, Deserno M (2011) Membrane-mediated interactions between circular particles in the strongly curved regime. Soft Matter 7(18):8567–8575
87. Reynwar BJ et al (2007) Aggregation and vesiculation of membrane proteins by curvature-mediated interactions. Nature 447(7143):461–464
88. Richards DM, Endres RG (2014) The mechanism of phagocytosis: two stages of engulfment. Biophys J 107(7):1542–1553
89. Roiter Y et al (2008) Interaction of nanoparticles with lipid membrane. Nano Lett 8(3):941–944
90. Rossi G, Monticelli L (2014) Modeling the effect of nano-sized polymer particles on the properties of lipid membranes. J Phys Condens Matter 26(50):503101
91. Sackmann E (1995) Biological membranes architecture and function. In: Lipowsky R, Sackmann E (eds) Structure and dynamics of membranes. Elsevier, Amsterdam

92. Šarić A, Cacciuto A (2011) Soft elastic surfaces as a platform for particle self-assembly. Soft Matter 7(18):8324–8329
93. Šarić A, Cacciuto A (2012) Fluid membranes can drive linear aggregation of adsorbed spherical nanoparticles. Phys Rev Lett 108(11):118101
94. Šarić A, Cacciuto A (2012) Mechanism of membrane tube formation induced by adhesive nanocomponents. Phys Rev Lett 109(18):188101
95. Šarić A, Cacciuto A (2013) Self-assembly of nanoparticles adsorbed on fluid and elastic membranes. Soft Matter 9(29):6677–6695
96. Schäfer LV et al (2011) Lipid packing drives the segregation of transmembrane helices into disordered lipid domains in model membranes. Proc Natl Acad Sci USA 108(4):1343–1348
97. Smith KA, Jasnow D, Balazs AC (2007) Designing synthetic vesicles that engulf nanoscopic particles. J Chem Phys 127(8):084703
98. Sondi I, Salopek-Sondi B (2004) Silver nanoparticles as antimicrobial agent: a case study on e. coli as a model for gram-negative bacteria. J Colloid Int Sci 275(1):177–182
99. Taturet S et al (2013) Effect of functionalized gold nanoparticles on floating lipid bilayers. Langmuir 29(22):6606–6614
100. Tian F, Zhang X, Dong W (2014) How hydrophobic nanoparticles aggregate in the interior of membranes: a computer simulation. Phys Rev E 90(5):052701
101. Tollis S et al (2010) The zipper mechanism in phagocytosis: energetic requirements and variability in phagocytic cup shape. BMC Syst Biol 4(1):149
102. Tzlil S et al (2004) A statistical-thermodynamic model of viral budding. Biophys J 86(4):2037–2048
103. Upadhyaya A, Sheetz MP (2004) Tension in tubulovesicular networks of golgi and endoplasmic reticulum membranes. Biophys J 86(5):2923–2928
104. Vácha R, Martinez-Veracoechea FJ, Frenkel D (2011) Receptor-mediated endocytosis of nanoparticles of various shapes. Nano Lett 11(12):5391–5395
105. Van Lehn RC, Alexander-Katz A (2014) Fusion of ligand-coated nanoparticles with lipid bilayers: effect of ligand flexibility. J Phys Chem A 118(31):5848–5856
106. Van Lehn RC, Alexander-Katz A (2014) Membrane-embedded nanoparticles induce lipid rearrangements similar to those exhibited by biological membrane proteins. J Phys Chem B 118(44):12586–12598
107. Van Lehn RC et al (2014) Lipid tail protrusions mediate the insertion of nanoparticles into model cell membranes. Nat Commun 5:Article No 4482
108. van Zon JS et al (2009) A mechanical bottleneck explains the variation in cup growth during fcγr phagocytosis. Mol Syst Biol 5(1):298
109. Vandoolaeghe P et al (2008) Adsorption of cubic liquid crystalline nanoparticles on model membranes. Soft Matter 4(11):2267–2277
110. Vasir JK, Labhasetwar V (2008) Quantification of the force of nanoparticle-cell membrane interactions and its influence on intracellular trafficking of nanoparticles. Biomaterials 29(31):4244–4252
111. Verma A et al (2008) Surface-structure-regulated cell-membrane penetration by monolayer-protected nanoparticles. Nat Mater 7(7):588–595
112. Wang T et al (2012) Cellular uptake of nanoparticles by membrane penetration: a study combining confocal microscopy with FTIR spectroelectrochemistry. ACS Nano 6(2):1251–1259
113. Welsch S et al (2010) Electron tomography reveals the steps in filovirus budding. PLoS Pathog 6(4):e1000875
114. Werner M, Sommer J-U, Baulin VA (2012) Homo-polymers with balanced hydrophobicity translocate through lipid bilayers and enhance local solvent permeability. Soft Matter 8(46):11714–11722
115. Wu H-J et al (2012) Membrane-protein binding measured with solution-phase plasmonic nanocube sensors. Nat Methods 9:1189–1191
116. Yang K, Ma Y-Q (2010) Computer simulation of the translocation of nanoparticles with different shapes across a lipid bilayer. Nat Nanotechnol 5(8):579–583

117. Yi X, Gao H (2015) Cell membrane wrapping of a spherical thin elastic shell. Soft Matter 11(6):1107–1115
118. Yi X, Shi X, Gao H (2011) A universal law for cell uptake of one-dimensional nanomaterials. Nano Lett 107(9):098101
119. Yi X, Shi X, Gao H (2014) Cellular uptake of elastic nanoparticles. Phys Rev Lett 14(2):1049–1055
120. Yuan H et al (2010) Variable nanoparticle-cell adhesion strength regulates cellular uptake. Phys Rev Lett 105(13):138101
121. Yue T, Zhang X (2013) Molecular modeling of the pathways of vesicle–membrane interaction. Soft Matter 9(2):559–569
122. Zemel A, Ben-Shaul A, May S (2005) Perturbation of a lipid membrane by amphipathic peptides and its role in pore formation. Eur Biophys J 34(3):230–242
123. Zhang S et al (2009) Size-dependent endocytosis of nanoparticles. Adv Mater 21(4):419–424
124. Zhang Y et al (2012) Permission to enter cell by shape: nanodisk vs nanosphere. ACS Appl Mater Interfaces 4(8):4099–4105

Adhesion of Biological Membranes

Kheya Sengupta and Ana-Sunčana Smith

Abstract One of the most important triggers of cell activity is adhesion, a process by which cells and their organelles interact and attach to substrates, internal scaffolds, external interfaces, or other cells. The physiological and pathological significance of cell adhesion is hard to exaggerate, and adhesion is ubiquitous in the living world. Adhesive contacts need to be able to function in widely varying circumstances and must be established in an extremely noisy environment. For these reasons, the control mechanisms of adhesion have had to develop so as to be able to permanently monitor and correct cellular performance. While a lot of effort has been invested into understanding the biochemical aspect of these processes, the underlying physical principles of adhesion regulation have obtained significantly less appreciation. Only in recent years have these two approaches begun to converge in a unified view. Due to the strong coupling of the biochemical reactions to the spatial coordination provided by membranes and the cytoskeleton, biological signaling is subject to a plethora of physical constraints. Indeed, many signaling pathways, particularly those involving the adhesion, involve protein diffusion and aggregation guided by membranes. It is these aspects of adhesion that can be understood in the framework of statistical physics, as we intend to demonstrate in this short review. Here we summarize the developments in understanding cell and membrane adhesion from a theoretical point of view and support it with experiments in model systems as well as with living cells.

Keywords Cell adhesion · Artificial cell · Ligand–receptor interactions · Competitive binding · Multiscale approaches to adhesion

K. Sengupta
Aix-Marseille Université, CNRS, CINaM UMR 7325, Marseille cedex 9, France
e-mail: sengupta@cinam.univ-mrs.fr

A.-S. Smith (✉)
PULS Group, Institut für Theoretische Physik and the Excellence Cluster: Engineering of Advanced Materials, Universität Erlangen-Nürnberg, Erlangen, Germany

Institute Ruđer Bošković, Division of Physical Chemistry, Zagreb, Croatia
e-mail: smith@physik.fau.de

P. Bassereau, P. Sens (eds.), *Physics of Biological Membranes*,
https://doi.org/10.1007/978-3-030-00630-3_18

1 Introduction

Biological cells are small-scale machines that permanently process a large amount of input signals in order to perform their normal activities [1]. One of the most important triggers of cell activity is adhesion, a process by which cells and their organelles interact and attach to substrates, internal scaffolds, external interfaces, or other cells. The physiological and pathological significance of cell adhesion is hard to exaggerate. Bacteria and viruses need to adhere and attach themselves to the cell membrane in order to invade it and in turn, dynamic initiation of adhesion intervenes at various points in the immune response of the body. Cell adhesion is essential for the integrity of tissues and needs to be dynamically controlled during embryogenesis. Adhesion is a prerequisite for fusion of, for example, endocytic vesicles to the cell membrane. It is equally important in phagocytosis and is a first step for migration to which it is intimately linked. Importantly, cells communicate in various ways across adhesive junctions, the propagation of nerve signals being a striking example. While adhesion is important for both prokaryotes and eukaryotes, the discussion below will be focused on animal cells, with examples taken mostly from mammalian cells.

Animal cells (Fig. 1) and their organelles are bound by phospholipid membranes [3]. Naturally therefore, the membrane plays a central role in adhesion. Apart from having amazing material properties which can be exploited beyond pure biological aspects, membranes provide a working environment for proteins which are responsible for establishing specific contacts [4]. In the context of adhesion-mediated cell recognition process, the plasma membrane carries specialized receptors called cell adhesion molecules (CAMs) that are usually transmembrane proteins with an

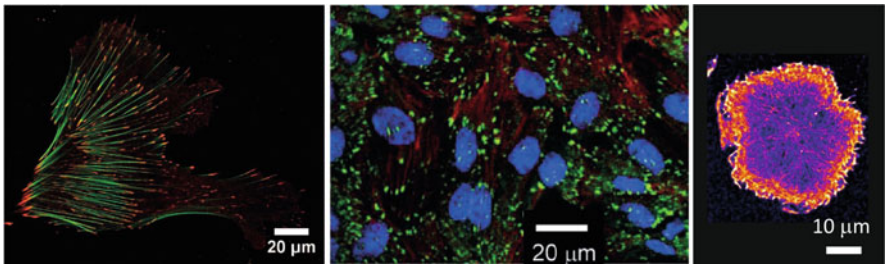

Fig. 1 Fluorescence images of specific ligand–receptor-mediated adhesion in living cells. Left: Primary cardiac fibroblasts from embryonic (E19) rat heart. Cells are stained for actin (green) and vinculin (red) and imaged in confocal mode. They clearly show focal adhesions, which are typically associated with integrin-mediated adhesion on immobilized ECM ligands. Image courtesy of R. Merkel and B. Hoffman. Middle: MDCK cell monolayer adhering to collagen I-coated glass. The nuclei (DAPI, blue), the actin cytoskeleton (red), and the focal adhesions (paxillin, green) are stained and imaged in confocal mode [2]. Right: a single T cell adhering to glass coated with ligand against the TCR–complex (anti-CD3) imaged in total internal fluorescence microscopy, with the actin stained and visualized in pseudo-color. No focal adhesions are formed in these cell types. Image courtesy of P. Dillard and L. Limozin

extracellular, an intracellular, and a transmembrane domain [3]. The extracellular domain forms specific bonds with the counter-receptor, often called the ligand. Typically, the ligand is either embedded into the extracellular matrix (ECM) and is immobile, or is carried on the surface of another cell in which case it is mobile in the plane of the cellular membrane. On its outer surface, the membrane carries long sugars and proteoglycans, called the glycocalyx, one of whose primary role is to prevent unspecific adhesion and merger of the cells. On the inner surface of the cell, the membrane is connected to a scaffold called the cortex which is made up of a network of the semiflexible polymer actin. When a receptor binds to its ligand, a chain of events are triggered and it is often accompanied by a drastic reorganization of the membrane at a local or cellular scale. This process is partly a result of passive thermodynamics of the membrane and is partly actively modulated by the cell [5–7]. Most receptors are sites of cell signaling: upon binding to a ligand on the extracellular side, the receptor transmits a biochemical signal towards the cell interior which then usually leads to a whole cascade of biochemical processes that culminate in a biological action [3]. The importance of the ensemble of these proteins is captured in the concept of "adhesome"—a term used to describe the entirety of proteins and signaling network triggered by a specific adhesion event.

Adhesive contacts need to be able to function in widely varying circumstances and must be established in an extremely noisy environment. For these reasons, the control mechanisms of adhesion have had to develop so as to be able to permanently monitor and correct cellular performance. While a lot of effort has been invested into understanding the biochemical aspect of these processes, the underlying physical principles of adhesion regulation have obtained significantly less appreciation. Only in recent years have these two approaches begun to converge in a unified view. Due to the strong coupling of the biochemical reactions to the spatial coordination provided by membranes and the cytoskeleton, biological signaling is subject to a plethora of physical constraints. Indeed, many signaling pathways, particularly those involving the adhesion, involve protein diffusion and aggregation guided by membranes. It is these aspects of adhesion that can be understood in the framework of statistical physics, as we intend to demonstrate in this short review.

1.1 Establishment of a Minimal System

Many features of cell-to-cell and cell-to-ECM adhesion have been, and continue to be, studied in vitro using single cells interacting with a functionalized surface. However, even with such simplified systems, due to the complexity of the cell and its natural regulation mechanisms, it is often difficult to repeatedly reproduce exactly the same experimental conditions in adhesion experiments. This was the main incentive for the development of a variety of model systems in which "ideal conditions" could be achieved. These ideal conditions comprise a fluid membrane, discernible ligand–receptor interactions, and the ability to mimic the control of the

glycocalyx [5, 7, 8]. At least one of the participants in the specific interaction should be mobile and the total number of ligand and receptors controlled.

To achieve these goals, giant unilamellar vesicles (GUVs) with about 30 μm diameter are used to mimic the cell [4, 5, 7–9]. GUVs are made of double-chained phospholipids arranged as a bilayer, with additional cholesterol, glycolipids, and/or embedded proteins to capture one or more essential property of the plasma membrane. The second cell can be simulated by another vesicle or a cell as, for example, in the case of experiments with micropipettes. This technique allows for a macroscopic view of the adhering vesicles whereas the information about adhesion events is obtained from the response function of the applied suction pressure [10, 11].

While the experimental methods for studying adhering membranes in three dimensions are quite limited, the variety of surface-sensitive optical techniques and electrical measurements that can be applied to planar systems is vast. Besides confocal microscopy [12], reflection interference contrast microscopy (RICM) is the most commonly used technique in studies of adhesion [13–16]. This technique allows direct measurement of the average membrane shape and fluctuations and thus provides information on the formation of protein complexes without the use of fluorescent labels [5]. Over the years, the capabilities of RICM were improved and enhanced, including the multiwavelength setups [17–19], or dynamic-RICM [1, 13, 20]. The development of these and other surface-sensitive optical imaging techniques is the reason that, flat, functionalized glass interfaces are often used as a cell or ECM mimic, and counterpartner for an adherent GUV (Fig. 2).

Functional surfaces rely on anchoring of active molecules, often to supported lipid bilayers (SLB). Flat bilayers can be assembled either by Langmuir–Blodgett lipid deposition or by rupturing of pretensed unilamellar vesicles on hydrophilic surfaces (see reviews by Sackmann and Tanaka [22] or Groves et al. [23] or Richter et al. [24] and references therein). When a bilayer is deposited directly on the surface, a thin film of lubricating water layer (thickness of 1 nm) forms separating the membrane from the support. This layer usually ensures that the lipids remain mobile in the plane of the bilayer. However, large transmembrane proteins such as integrins may become immobile, due to interactions with the surface.

A different strategy for separating the membrane from the substrate involves the inclusion of intercalating water-swelled polymers. This film can be achieved by the chemical grafting or physical absorption of water-soluble polymers or polyelectrolyte multilayers [25–27], the reconstitution of lipopolymers covalently bound to lipids in the bilayer [28, 29], or by the deposition of multilayers of amphiphilic molecules such as cellulose with alkyl side chains [30]. Though somewhat more elaborate for preparation and control, these systems ensure that a large proportion of proteins remain mobile and fully functional, and are hence suitable for adhesion assays.

In the context of cells, recently even more sophisticated substrates have been used that are chemically patterned at the nano-/submicron scale [31–34], or those that form diffusive barriers [35, 36]. Such approaches offer a wealth of possibilities for gaining new insights over the adhesion process by meticulously controlling

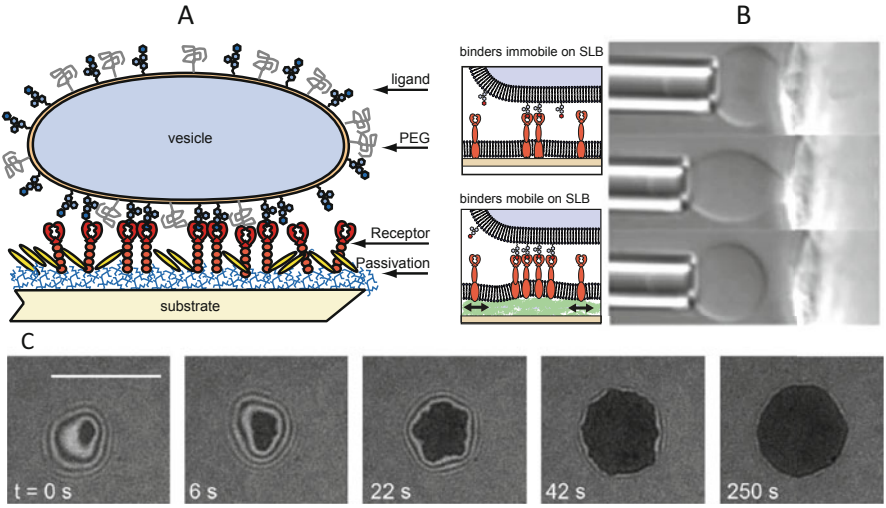

Fig. 2 Model systems for studying membrane-mediated adhesion. (**a**) Ligand-decorated GUV adhering to a functionalized substrate, which can expose mobile or immobile binders. (**b**) Unbinding of a vesicle specifically adhered to a cell, manipulated by the micropipette technique and observed in a differential interference contrast. Image adapted from Prechtel et al. [10]. (**c**) Interference contrast reflection microscopy can be used when the vesicle is brought in contact to a flat substrate and is more appropriate for detailed studies of the adhesion zone. Due to a very good height resolution of such setups, fluctuations of the membrane in the contact zone can be recorded in real time. This allows the determination of the mean-square amplitude of the fluctuations, and thus the distinction between weakly and strongly adhered (the growing dark patch) parts of the membrane can be obtained [16, 21]. Image courtesy S. Fenz [8]

the microenvironment in which cells or vesicles adhesion takes place. These highly advanced systems are particularly useful for the comparison with theoretical modeling and simulations, which can now be performed in precisely defined conditions that reproduce the experimental situation [37].

Despite the growing appreciation for mimetic approaches, however, a challenge remains to combine insight from these soft matter model systems with molecular specificity and activity found in real cells: The physical mechanisms isolated need to be translated into the realm of biology, and thus, put into the context of active processes and signaling. This is a challenging task already on the level of a single cell, and even more so in vivo. Yet, the prospect of understanding normal and pathological cell function should outweigh the immense work required to take into account the complexity of the system and through a multidisciplinary effort lead ultimately to deep understanding of the cell recognition process.

2 General Mechanisms of Adhesion

2.1 Protein-Mediated Adhesion in Cells and Tissues

Cell adhesion relies on selective binding of receptors which typically belong to one of five major families of cell adhesion proteins, namely cadherins, integrins, selectins, mucines, and immunoglobulins [38]. These proteins either establish homophilic contact as in case of cadherins, or they interact with specific ligands on the opposing surface. Their interactions rely on the so-called lock-and-key principle: the interplay of numerous low-energy interactions is established to produce a binding that is sufficiently strong to be useful in the recognition and adhesion process. The weakness of the individual interactions also conveys the ability to spontaneously dissociate without the need for further control mechanisms to be developed by the cell. These weak intermolecular contacts can be formed by different mechanisms. Specifically, electrostatic interactions between two complementarily charged domains in molecules lead to binding energies of 2–4 $k_{\mathrm{B}}T$. Hydrogen bonds are somewhat weaker and contribute with energies of 1–2 $k_{\mathrm{B}}T$. Furthermore, van der Waals energy can be considerable if the complementarity of protein shapes is large, yielding a large number of low-energy (0.2–0.5 $k_{\mathrm{B}}T$) contacts. Finally, as the proteins are exposed to water, domains in molecules with similar affinity to water will feel attractive forces due to the hydrophobic effect. Overall binding energy measured in solution, i.e. the three-dimensional binding affinity, amounts to 5–10 $k_{\mathrm{B}}T$, where the lower bounds are typical for selectins and cadherins, while larger values are associated with integrins. The affinity measured in solution can be as large as 30 $k_{\mathrm{B}}T$ in the case of the unusually strong, avidin–biotin recognition.

2.1.1 Focal Adhesion, Integrins, and Mechanotransduction

Receptors of the integrin family are one of the most prevalent adhesion molecules in animal cells [3]. Cells typically use integrins to bind to the extracellular matrix but integrins may occasionally also participate in cell–cell adhesion, the integrin LFA1 in T cells being a prime example [39]. On biding to its ligand, the intracellular part binds to talin which in turn binds to vinculin and other actin-binding proteins. At the same time, integrins cluster in the plane of the membrane. The resulting complex eventually links to actin and is capable of transmitting forces. In many cells, notably fibroblasts, the mature adhesion comprising integrins and the associated proteins takes the form of focal adhesions, linked to actin bundles called stress fibers [3] (see Fig. 1). Integrins are particularly intriguing because of their participation in both inside-out and outside-in signaling [40, 41].

Over the last couple of decades, it was shown that cells sense the mechanics of their surroundings by application of force, along the actin bundles and through the talin–integrin complex in focal adhesions. Intriguingly, the size of a focal adhesion

grows with application of physical force [42–45]. In general, cells tend to reinforce their adhesive contacts under force, and it is now well known that mechanical forces direct a host of cellular and tissue processes. It is believed that cell adhesion complexes may act as force sensors, in concert with the actin cytoskeleton, which also transmits the forces. Cells were shown to spread more on hard and less on soft substrates, and in turn, well spread cells are stiffer than less spread cells [46]. All these considerations link the adhesion state of cells to their mechanics. Today, it is impossible to discuss cell mechanics and cell adhesion separately from each other.

In addition to the actin-mediated mechanosensing, adhesion molecules are themselves force sensitive at the molecular level, often becoming weaker under force [47, 48]. In these "slip" bonds, the bond lifetime is shortened by tensile forces acting on the bond. More recently, integrins have been shown to form "catch bonds", responding in the opposite manner—in a certain force range, their lifetime increases with tensile force applied to the bond [49, 50]. It is now increasingly clear that integrins are not unique—the mechanosensitivity at single bond level is seen in many other adhesion molecules as well.

2.1.2 Cadherins and Tissue Formation

The cadherin superfamily of receptors is another class of cell adhesion molecules which participate in cell–cell adhesion. They are responsible for the integrity of tissues and are therefore dynamically reorganized during embryogenesis [51–56]. Because of this key role, they are also implicated in many forms of cancers [57]. Cadherins exist in different subtypes and form type-specific homodimers, which ensures agglomeration of cells containing only a particular cadherin type [58–60]. In addition to forming trans-bonds that connect cells, cadherins are also known to form cis-bonds in the plane of the membrane, which leads to the aggregation of trans-bonds—a phenomenon with clear biological importance [61–66]. Interestingly, unlike trans-bonds, cis-interactions have been detected only in membrane-bound cadherins [64], and the origin of cis-interactions remained elusive until recently. Based on computational studies, it has been suggested that the origin of cis-interactions resides in entropic reasons related to mechanics of the monomeric and dimeric states operating at very short distance range [60, 67]. New work, however, points to the intriguing possibility that in addition, long range cis-interactions may in fact be driven purely by membrane entropy related to bending fluctuations [37].

2.1.3 The Immune Synapse and Hybrid Systems

Adhesion of Lymphocytes is an example of a highly dynamic reorganization of the membrane following adhesion. T lymphocytes (also called T cells) undergo repeated adhesion and de-adhesion in order to fulfill their physiological role of recognition of "foreign" peptide fragments displayed on the membrane of specialized cells called antigen presenting cells (APCs) (see, for example, [68] for a review). T cells carry

specific receptors called T cell receptors (TCR) on their membrane which bind to their ligand present on the membrane of the APC. This binding or "recognition" triggers a cascade of signals, leading to the initiation of actin polymerization as well as activation of integrins (in this case LFA1 or $\alpha_L\beta_2$), which subsequently bind to their ligand, ICAM1, also present on the surface of the APC. Adhesion in T cells is rapid and is accompanied by dramatic reorganization of the cell membrane both in terms of molecular distribution and in terms of membrane topography. Upon binding to their ligands, the TCRs first form nano- to micron-size agglomerations [69, 70], the so-called micro-clusters, and then are later actively centralized by actin [36, 70]. Meanwhile, the LFA1 form separate, smaller clusters and ultimately are excluded from the center, forming a concentric ring with the TCR central cluster. Thus, though T cells adhere through a molecule of the integrin family, there is no focal adhesion formation (see Fig. 1).

A particularly successful experimental approach to study T cell activation and reorganization of the receptors has been to use hybrid systems where the APC is mimicked by a functionalized supporting lipid bilayer (SLB) exhibiting mobile ligands [35, 36, 70–72]. Such studies have revealed drastic receptor reorganization at the interface, leading to the formation of the immunological synapse, itself formed by coalescence of receptor micro-clusters that are transported along the T cell/APC interface [70]. Experiments connecting adhesive molecules of the substrate within micron-size corrals [35] or submicron patches [34], as much as the systematic comparison between mobile and immobile ligands [72], have emphasized the importance of receptor reorganization in signaling.

2.2 Nonspecific Adhesion

2.2.1 Generic Potentials and Fluctuations

While specific protein interactions were identified a long ago as the key players in cell adhesion, a new understanding has emerged during the past two decades that the cell membrane itself, being a "floppy" sheet, adds another unavoidable, yet not fully understood, interaction with the opposing surface it binds to. Although this interaction does not at all depend on any specific proteins, it can have a major impact on the protein-mediated adhesion and can be viewed as a mechanism that controls the binding affinity to the cell adhesion molecules [73].

A membrane, like any other interface, has different, omnipresent interaction types. Prominent examples include intrinsically continuous potentials of Coulomb, hydration [74], and van der Waals origin [30, 75]. Furthermore, due to their small bending rigidity of 10–100 k_BT, membranes experience relatively strong, fluctuations. As first argued by Helfrich, the suppression of these fluctuations by another interface gives rise to a steric repulsion which quadratically diverges close to a wall [76]. In cells, these fluctuations [77–82] may be of thermal origin, or may arise as a result of active processes [83–88]. Overall, the balance between attractive and

repulsive interactions typically results in an effective potential, which has at least one minimum separating two membranes by 5–150 nm [1, 16, 18, 21, 30, 73, 89–91].

The difficulty in measuring and modeling this nonspecific potential is that the tension in the cell or vesicle membrane renormalizes the fluctuations and thus the repulsive contribution to the effective potential [92]. In turn, this affects the position of the minimum of the potential and its strength. Consequently, all these parameters should be determined self-consistently [89, 91–93], as a function of the membrane stiffness. However, the coupling between the strength of the repulsion, the tension, and the fluctuation spectrum is still not fully understood when the system is of a finite size and away from the unbinding transition [94–97].

A common way to deal with the effective surface interactions of the membrane is to introduce a harmonic potential, whose strength and position are defined by the curvature γ and the position h_0 of the true minimum [4, 21, 73, 98–100]. In this case, the energetics of the membrane of bending stiffness κ and projected area S, put under tension σ, is given by:

$$\mathcal{H}_{\mathrm{m}} = \int_S \mathrm{d}\mathbf{x} \left[\frac{\kappa}{2} \left(\nabla^2 h(\mathbf{x}) \right)^2 + \frac{\sigma}{2} \left(\nabla h(\mathbf{x}) \right)^2 + \gamma \left(h(\mathbf{x}) - h_0 \right)^2 \right]. \tag{1}$$

Here, the membrane profile is parameterized in the Monge representation, whereby the membrane height $h(\mathbf{x})$ is determined for every vector $\mathbf{x}$ residing in the plane of the substrate. The first term in the Hamiltonian in Eq. (1) is the contribution due to the bending of the membrane. The second term accounts for the surface tension, while the last term in Eq. (1) is related to the discussed membrane–substrate interaction potential.

The validity of this model was only recently confirmed [91] in experiments where the vesicle membrane was pinned to square pattern [18, 90], within which the membrane–substrate interaction is purely nonspecific (Fig. 3). In this geometry, the membrane shape and fluctuations could be measured with Dual Wavelength Reflection Interference Contrast Microscopy [91] or with the Dynamic Optical Displacement Spectroscopy [88, 101]. Because the size of the patterned square is much larger than the lateral correlation length of the membrane [21], the membrane in the central part of the square is flat on average, and fluctuates around the minimum of the membrane–substrate interaction potential. These measurements showed that even in this weak interaction limit, the fluctuations are not purely Gaussian (Fig. 3). A holistic description requires abandoning the harmonic approximation, particularly for the reconstruction of the membrane average shape. However, the harmonic approximation for the potential seems sufficient for the description of the power spectral density [102].

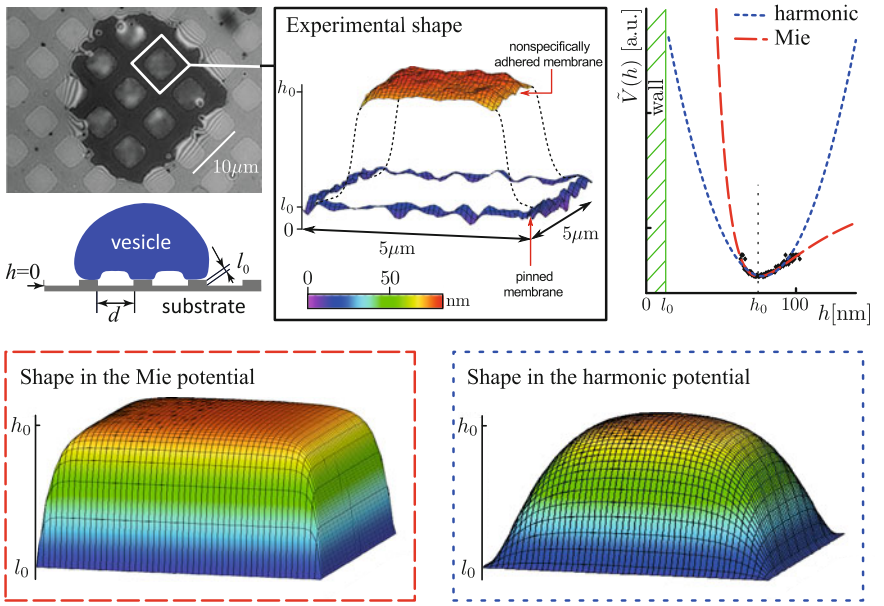

Fig. 3 Nonspecific potentials and the harmonic approximation. Top left: RICM image of a GUV, partly adhering via a pattern of ligands stamped on the substrate, as is shown schematically just below. The nonadhered parts of the GUV are seen in lighter shade of gray here and are seen to flicker in a dynamic movie. The experimental data can be fitted well with a Mie potential (top right). Bottom: Theoretically generated shapes with either Mie or harmonic potential—it is seen that the nonlinear Mie potential fits the experimental shape. Adapted from [91]

2.2.2 Steric Repulsion of the Glycocalyx

In most cells, the plasma membrane is decorated with a layer of long sugars and proteoglycans, variously called glycocalyx, cell coat, or pericellular matrix (Fig. 4a). This coat may be several microns thick [105–107] and can essentially have a repulsive role (see [108] for review). Cells are believed to be able to regulate their adhesion by modulating the glycocalyx, which needs to be expelled from the zone of contact. The glycocalyx has been modeled in GUVs with PEG as a repeller, where variation of the PEG concentration was shown to clearly change the weak nonspecific potential [109]. The concentration of the PEG layer also directly impacts specific adhesion (Fig. 4b–d), especially when the adhesion is mediated by very weak specific interactions [104]. Hyaluronan was used as a more realistic mimic (Fig. 5), but in conjunction with strong nonspecific adhesion [13]. In this case, the system can be switched from nonadhering to weakly or strongly adhering, depending on the thickness of the polymer layer (top vs bottom panels in Fig. 5), as well as the membrane tension [13, 19]. While in the case of membrane-coupled PEG [104], the repellers are thought to be expelled from the adhesion zone, both

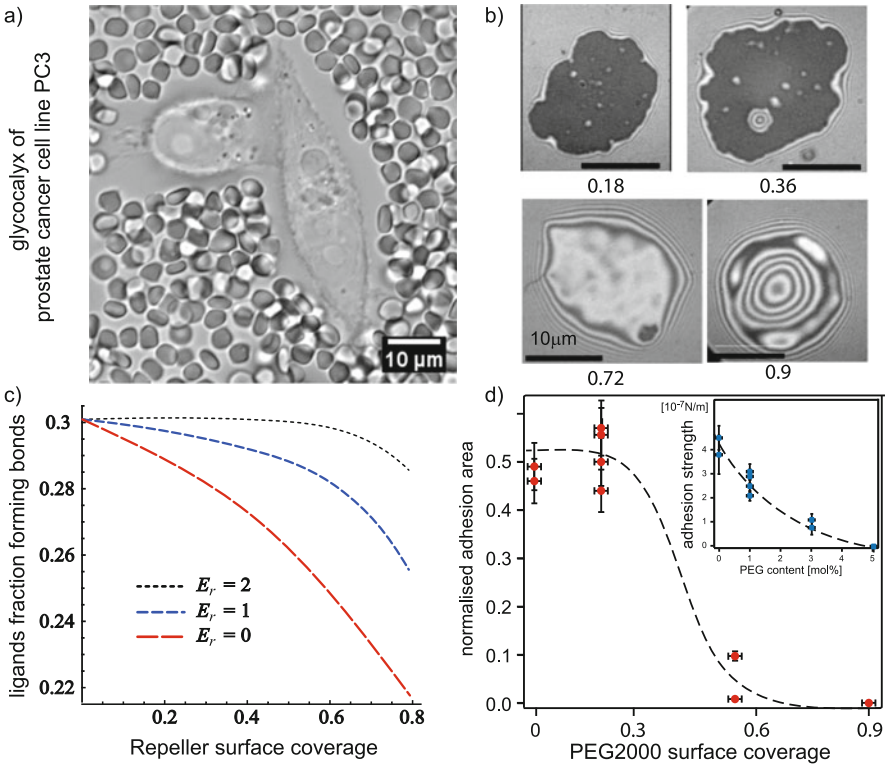

Fig. 4 Density and thickness of repelling molecules building the cell glycocalyx affect adhesion. (**a**) The glycocalyx, visualized by the exclusion of red blood cells, significantly changes in the adhesion zone between two cells. Image contributed by J. Curtis. (**b**) Variation in the surface coverage (denoted below micrographs) of the glycocalyx reconstituted into the vesicle membrane affects the E-selectin-mediated adhesion as seen by a decrease of the size of the black patch in the micrographs. The latter is an adhesion domain built by E-selectin attachments to sLex in the vesicle. The number of bonds, and the spreading pressure of the vesicle decrease with the increased density of the glycocalyx, as predicted by (**c**) a thermodynamic theory [103] (E_r denotes the enthalpic cost per repeller in the contact zone), and observed experimentally [104]. Notably, reconstituted glycocalyx which is shorter than the sLex construct did not affect adhesion

in case of surface bound hyaluronan [13, 19] and DNA [110, 111] repellers, they are crushed and flattened by the strong membrane interactions. Similar effects are observed in cells on PEG cushions. However, repellers rich in amino acids, which are often mimicked by BSA or HSA very successfully screen adhesion-inducing separation distances between membrane of over 100 nm [91, 104].

Modeling efforts showed that the effect of the glycocalyx can be integrated as a contribution to the nonspecific adhesion [112], with two competing states of adhesion: initial weak adhesion is followed by slower aggregation of the adhesion molecules into small, tightly bound clusters that coexist with the regions of weak adhesion. If on the other hand cluster of bonds grow extensively, the glycocalyx

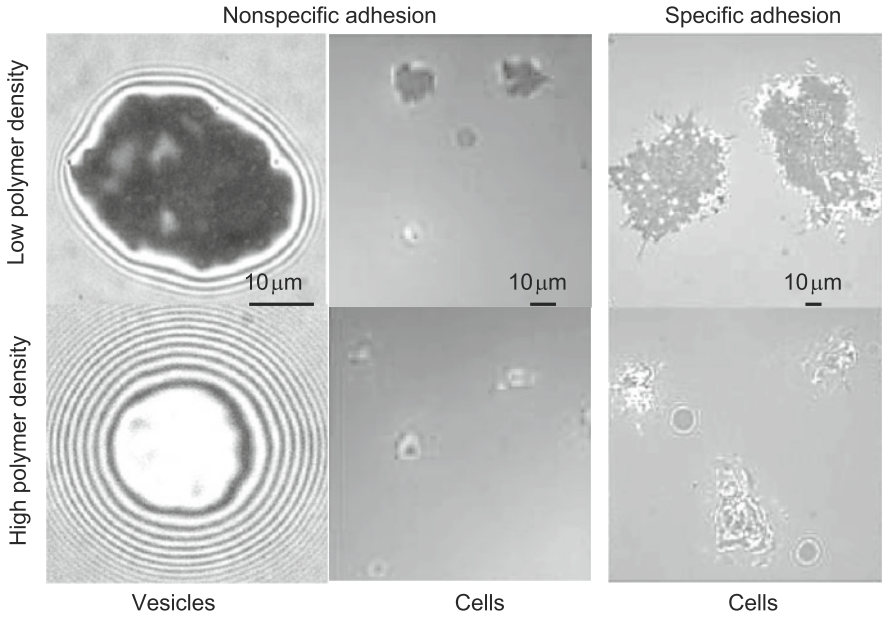

Fig. 5 Adhesion on repelling polymer layers of low (top) and high (bottom) density. Nonspecific adhesion in GUVs (left) and in cells (middle) is stronger on sparse layers. The same effect is also visible for cells that bind utilizing protein-mediated adhesion. Image adapted from [13, 34]

molecules will be expelled from the zone of contact, with small, nonspecifically bound islands where the molecules of the glycocalyx remain trapped [113]. Naturally, thermodynamics will also play a role, as expulsion of the glycocalyx from the zone of contact will act as a pressure on the adhesion domains. Reversely, after expulsion, competition for space in the nonadherent parts of the vesicle may lead to increase of binders in the contact zone, and strengthening of adhesion sites due to finite size effects [82, 103]. Interestingly, these effects were recently found to play a role in cells [114].

3 Modeling Adhesion

Despite several decades of intensive research [5, 22, 99, 115–119] and the pressing need to find the underlying principles governing the establishment of intracellular contacts in various circumstances [71, 120], the growth of macromolecular structures in membranes is still poorly understood. The complexity emerges from the coupling of molecular diffusion and formation of bonds (occurring with characteristic times of $10^{-5} - 10^{-2}$ s) to fast membrane fluctuations ($10^{-9} - 10^{-6}$ s). Moreover, several length scales are involved—from angstrom separations necessary

for molecular recognition, cooperative effects between proteins in membranes occurring on the length scale of the membrane correlation length [121], to the micron-sized macromolecular structures that develop over time.

3.1 Nonspecific Adhesion

On the macroscopic scale, adhesion of membranes can be regarded as a wetting phenomenon [9]. A number of features associated with the process of cell spreading were identified in experiments [122–124] and could be modeled on this continuous level [124], where a fluid bilayer vesicle is treated as a finite system with, for all practical purposes, a fixed true area (i.e. including residual fluctuations), and enclosed volume [115]. On this scale, it is possible to account for vesicle adhesion by introducing a single parameter W, the effective adhesion strength, which is assumed to be known [125]. Minimizing curvature and adhesion energy subject to the geometrical constraints leads to a two-dimensional phase diagram where regimes of strong adhesion (spherical cap-like shapes), weak adhesion (smooth shapes), and no adhesion can be identified [115, 125]. Similar methodology was used to study the de-adhesion processes induced by an apical force. In this case, depending on the adhesion strength, continuous unbinding through tethering [126] and discontinuous detachment of smoothly deformed shapes [127, 128] were identified and characterized.

In experiments, the emphasis has usually been on screening the nonspecific interactions in order to study specific binding [129–131]. Nevertheless, in controlled nonspecific adhesion, salient features could be identified like formation of bubbles [132] or even motion [133] due to electrostatic interactions [12]. Very strong adhesion was used for studies of controlled pore opening [134, 135], as well as the competition between adhesion and hydrodynamic dissipation [19, 136].

3.2 Specific Adhesion: Mechanisms Governing Protein Binding

Early attempts to theoretically model the formation of macromolecular clusters in the adhesion process involved analogies with classical theories of growth [137–140]. Furthermore, a number of scaling laws were suggested after the analysis of the relationship between various stochastic processes involved [141]. However, only limited experimental confirmation has been obtained to support these arguments [136, 142–144].

In experiments, actually, the focus from the earliest time was on specific adhesion in a minimal system. Formation of adhesion plaques was already observed in the earliest experiments with specific linkers [130, 131]. These plaques are domains

of closely packed bonds that, in case of strong and numerous bonds eventually, coalesce and fill the entire zone of adhesion. Such behavior was later observed with mammalian adhesion proteins like integrins [20, 142, 145, 146], cadherins [37, 147], and selectins [104]. Interestingly, these plaques can be destroyed by putting competitive antibodies as antagonists for the receptor into the surrounding solution [14].

3.2.1 Mobility and Density of Proteins

Another important aspect of adhesion is the transport of proteins from the regions of a membrane that are not participating in adhesion to regions in contact with another membrane or a cell. This transport is secured by the fluidity of the membrane as well as the membrane-anchoring or transmembrane nature of most cell adhesion proteins that exhibit two-dimensional diffusion. Importantly, the friction coefficient for this motion is dominated by the hydrodynamic coupling between the protein and the fluid bilayer [148]. Further effects arise due to the coupling of the protein motion with the local membrane curvature [149–152]. However, in the context of adhesion so far, these effects have been considered as small, and it is typically assumed that proteins perform a random walk with a rescaled diffusion coefficient [151, 153].

While it is intuitively clear that the diffusion of proteins will affect the dynamics of adhesion, it is perhaps less appreciated that both the equilibrium and steady-state adhesion depend on the density (Fig. 6) and mobility (Fig. 7) of binders. Namely, immobilization prior to adhesion, strong frictional coupling upon the formation of a bond, and trapping effects induced by preexisting bonds may immobilize newly formed complexes [102], the consequence of which is an entropic cost for binding. This entropic cost depends on the density of binders and has a different impact if one or both binding partners are mobile [20]. The loss of entropy is compensated by the enthalpic gain associated with the binding affinity of the pair [116]. The balance between these two contributions to the free energy [116], which naturally depends on the actual number of proteins available (Figs. 6 and 7e), in turn defines the final concentration of formed bonds [34, 104, 154, 155], and the spreading pressure of the cell or the vesicle (Fig. 6b). This highlights the importance of the correct choice of the thermodynamic ensemble—to explain the experimentally observed behavior, a cell or a vesicle must be treated as a finite reservoir of binders, while mobile receptors on the SLB should be coupled to a reservoir of a constant chemical potential.

As a consequence of the interplay between enthalpy and entropy of binding, complex thermodynamic response can be recovered, including the passive growth of adhesion domains subject to retracting force [20]. This increase in adhesion, which is usually reflected in the increase of the cell or vesicle spreading pressure (Fig. 6b, top right panel), couples with the deformation of the macroscopic membrane shape [128, 156]. Furthermore, even in the absence of any signaling or cytoskeleton, repeated pulling on a vesicle strengthens adhesion by compaction of dilute and growth dense agglomerates of bonds, which is reminiscent of mechanotransduction.

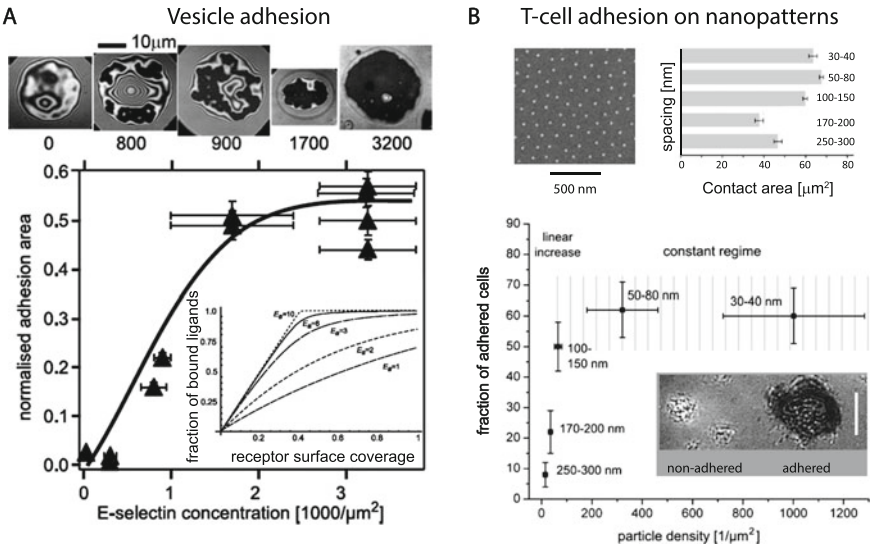

Fig. 6 Role of the density of receptors immobilized on the passivated glass support in GUV and cell adhesion. (**a**) Vesicle adhesion mediated by the binding of a lipid-anchored sialyl-Lewis^X (sLeX) motive to E-selectin receptors. As the concentration of E-selectin on the surface increases, the size of the domains grows linearly until saturation, as seen in the graph and in the associated RICM snapshots above the graph [104]. No adhesion was observed on substrates with less than 800 E-selectins per μm^2. Inset: Fraction of bound ligands as a function of receptor density for increasing binding affinity, as calculated from the entropy–enthalpy balance, shows the same linear increase and saturation [116]. (**b**) T-cell adhesion on substrates which are decorated with pMHC-functionalized nanoparticles with well-defined spacing (top left micrograph). Coupling of the density to the spreading pressure is evident from the change in the contact area as a function of spacing between ligand-coated beads (top right). Furthermore, adhesion versus particle density shown in the graph displays a rapid quasi-linear increase until the density reaches 300 particles per μm^2. As suggested by theory, and experiments with vesicles, this regime is followed by the saturation at higher particle densities. At low densities (spacing greater than 150 nm), most cells failed to adhere (micrographs in the inset). Image adapted from [154]. Similar dependence on ligand density is also reported in [34]

Furthermore, if both, the ligand and the receptor, are mobile, a disjointing force acting on the membranes results in displacement of intact ligand–receptor bonds between a vesicle and the SLB, without breaking. This mimics similar observations in T cell adhesion on mobile ligands of T cell receptor complex [72] and explains the observation that cells have significant difficulties to produce traction on supported bilayers if both binders are mobile. The role of ligand mobility has also been emphasized in integrin-mediated adhesion of fibroblasts where the formed adhesion structures on mobile or immobilized tripeptide Arg-Gly-Asp motive (RGD) spread on were very different [157].

Another aspect of the interplay between different contributions to the overall free energy is the accumulation of ligand–receptor pairs in the contact zone between two adherent membranes (Fig. 7) that leads to reorganization of the membrane molecular

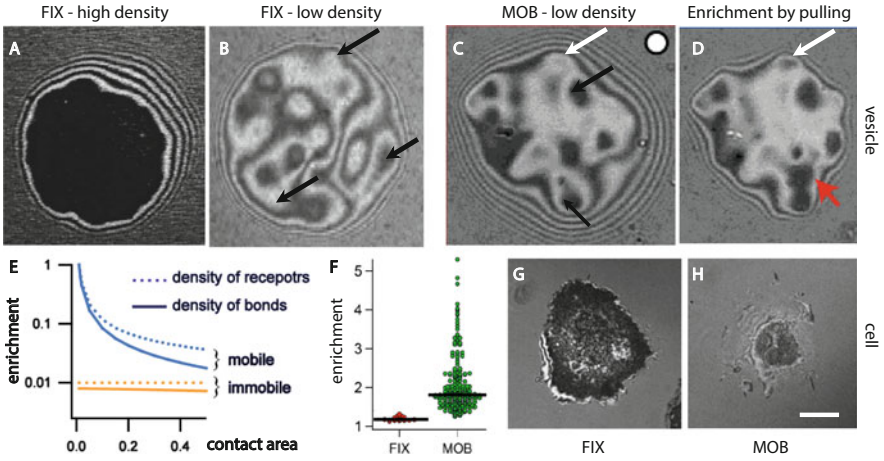

Fig. 7 Role of ligand/receptor mobility in GUV and cell spreading. Top: GUVs carrying the tripeptide Arg-Gly-Asp motive (RGD) spread on SLB carrying integrins. (**a**) When the integrins are immobile and abundant, the GUVs adhere tightly with a large adhesion zone [137]. (**b**) At low concentrations of integrins, the vesicles are not visibly adhered but nevertheless they resist being pulled off at the points shown with arrows [20, 145]. (**c**) On mobile integrins at comparably low integrin concentrations, dark, compact adhesions (black domains) are formed (black arrows). (**d**) If the contact zone is made smaller, compact adhesions grow (red arrow). In addition, dilute domains (white arrows in (**c**) and (**d**)), which densify under force could be identified by mapping membrane fluctuations [1, 20]. (**e**) The difference in baseline increased density between mobile and immobile, as well as the increase of enrichment for decreased contact can be captured by a thermodynamic theory. [116]. (**f**)–(**h**) T cells spreading on SLBs carrying anti-CD3 ligands. Image adopted from [72]. (**f**) Similar enrichment is seen between cells binding to immobile and mobile receptors, reminiscent to observations in vesicle adhesion. (**g**) Immobilized ligands can sustain traction-inducing cell spreading. No local increase in ligand/receptor density is observed. (**h**) When the ligands are mobile, the substrate is unable to sustain traction forces, and the cells are unable to spread. As in the case of GUVs, ligand–receptor pairs are pulled towards the cell interior, thus increasing their local density (see [72] for images of receptor distribution)

components [103, 113, 116, 156]. Combined with steric hindrance from molecules, this accumulation can lead to both the formation of unexpected patterns [1], and the self-assembly of adhesion corals, as observed first in vesicles [102, 158] and than in cells [66]. Recently, it was shown that not only proteins but also associated lipids phase separates upon adhesion [159].

From the point of view of dynamics, if the time to find a binding partner exceeds the time to bind, the growth is considered diffusion limited, and in the opposite case, reaction limited. In the context of radial growth, when there is no unbinding from immobilized receptors, these two regimes are associated with universal power laws describing the growth of the adhesion area as a function of time. The exponents adopt values of one or two for diffusion and reaction limited aggregation, respectively [137–140]. The transition from the reaction- to diffusion-dominated regime, induced by the depletion of binders, was demonstrated in

vesicles [104, 137] and cell spreading experiments [124]. More recently, the change of regime could be exploited to estimate the reaction rate for RGD–integrin, sLex-E-selectin, and biotin–neutravidin binding [121]. More complex growth exponents are, however, expected in the presence of unbinding [160], and when both partners are mobile [144]. This was demonstrated experimentally when some nonuniversal growth exponents were measured [136], showing that membrane adhesion is an ideal playground for studying the rich growth phase space in the presence of weak to strong fluctuations and short- to long-range interactions.

3.2.2 Stochastic Binding Rates and Explicit Membrane Simulations of Adhesion

Understanding adhesion requires dealing with local stochastic interactions associated with ligand–receptor binding. A common way to model these interactions is to consider the proteins as thermalized springs with stiffness λ and rest length l_0, contributing to the energy $\mathcal{H}_B$ associated with the membrane profile $h(\mathbf{r})$ by:

$$\mathcal{H}_B[h(\mathbf{r})] = \sum_{\mathrm{i}=1}^{N_b} \delta(\mathbf{r} - \mathbf{r_i}) \left[\frac{\lambda}{2} (h(\mathbf{r}) - l_0)^2 - \epsilon_b \right]. \tag{2}$$

Here, N_b is the number of formed bonds, ϵ_b accounts for the bond enthalpy gain for forming a bond, and $\delta(\mathbf{r})$ is the Dirac-delta function for a bond at the position $\mathbf{r}$.

If one assumes that the structural fluctuations of free receptors occur on faster timescales than the membrane dynamics (femtoseconds compared to nanoseconds), each bond should fulfill a local detailed balance condition for the transitions between the bound and unbound states, given by the instantaneous rates $k_{\mathrm{off}}(h(\mathbf{r}, t))$ and $k_{\mathrm{on}}(h(\mathbf{r}, t))$:

$$\frac{k_{\mathrm{off}}(h(\mathbf{r}, t))}{k_{\mathrm{on}}(h(\mathbf{r}, t))} = \exp\left[\left(\frac{\lambda}{2} (h(\mathbf{r}, t) - l_0)^2 - \epsilon_b \right) - \frac{1}{2} \ln\left(\frac{\lambda \alpha^2}{2\pi} \right) \right]. \tag{3}$$

Here, α is the range of the interaction potential of the ligand–receptor bond.

Condition (3) naturally includes the stretching energy associated with the slow structural changes of the protein due to binding (first term in the exponent) and the intrinsic binding affinity (second term) [161]. The last term accounts for the entropic cost associated with the suppression of structural fluctuations of a protein upon binding[140, 162]. Following such defined detailed balance, each bond is locally in thermal equilibrium with the instantaneous membrane shape.

Starting from (3), one can use arguments by Dembo et al. [49] and weigh in the intrinsic reaction rate k_0 with the Boltzmann factor that depends on the energy of protein structural fluctuations allowing ligands and receptors to come in the binding

range [49, 149, 163]:

$$k^{\text{on}}\left(h(\mathbf{r},t)\right) = k_0\sqrt{\frac{\lambda\alpha^2}{2\pi}}\exp\left[-\frac{\lambda}{2}\left\{\left(h(\mathbf{r},t)-l_0\right)-\alpha\right\}^2\right], \tag{4}$$

From this, the local off-rate can be determined readily using Eq. (3):

$$k^{\text{off}}\left(h(\mathbf{r},t)\right) = k_0\exp\left[-\epsilon_b\right]\exp\left[\lambda\left(h(\mathbf{r},t)-l_0\right)\alpha-\frac{\lambda\alpha^2}{2}\right], \tag{5}$$

This off-rate recovers the dependence of the unbinding rate on the force $\lambda\left(h(\mathbf{r},t)-l_0\right)$ acting on a bond, which was suggested by the Bell in one of the first models for protein recognition occurring between membranes [161]. While it is easy to physically motivate the rates equations (4) and (5) from the physics perspective, their development from a minimal model is still missing. Nevertheless, the simplicity of these rates secured their broad usage in modeling the dynamics of binding, in the framework of adhesion as discussed in the next section, but also in a much broader context [108, 164].

3.2.3 Simulating Adhesion with High Accuracy

The development of accurate mesoscopic schemes within which the membrane and the proteins are explicitly treated became possible with the increase in computing power. An example are kinetic Monte Carlo approaches [165–168]. An alternative are Langevin simulations [99, 149, 169–171], which have the advantage of coupling the complexation rates with the instantaneous membrane shape. Specifically, the membrane described by Eqs. (1) and (2) is propagated in time by means of the Langevin equation in the Fourier space spanned by modes $\mathbf{k}$ [99, 140, 149]:

$$\begin{aligned}\frac{\partial h(\mathbf{k},t)}{\partial t} =& -\Lambda(\mathbf{k})\Bigg\{\left[\kappa k^4+\gamma\right]\left(h(\mathbf{k},t)-\delta_{\mathbf{k},0}Ah_0\right)\\ &+\sum_{i=1}^{N_b(t)}\lambda\left(h(\mathbf{r}_i,t)-l_0\right)\exp\left(-\mathrm{i}\mathbf{k}\cdot\mathbf{r}_i\right)\Bigg\}+\xi(\mathbf{k}).\end{aligned} \tag{6}$$

Here, the tension is set to zero, $\Lambda(\mathbf{k}) = (4\eta k)^{-1}$ is the Oseen tensor, describing the hydrodynamic interaction between membrane and surrounding fluid of a viscosity η, and A is the area of the membrane. The stochastic force $\xi(\mathbf{k})$ is set by the temperature of the surrounding fluid by the fluctuation–dissipation theorem:

$$\left\langle\xi(\mathbf{k})\xi(\mathbf{k}')\right\rangle = 2k_{\text{B}}T\Lambda(\mathbf{k})\delta(\mathbf{k}+\mathbf{k}'). \tag{7}$$

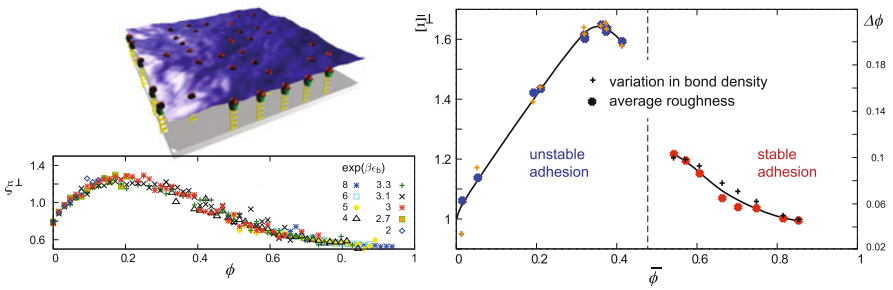

Fig. 8 Phase behavior of the adhered membrane and the relation between membrane roughness and bond density as obtained from explicit membrane simulations. Top left: Snapshot from a Langevin simulations of a membrane (blue), adhered to a substrate (gray) by elastic ligand–receptor bonds (yellow springs and red beads). Bottom left: Instantaneous roughness $\zeta_\perp$ (mean-square deviation from a flat shape in a particular moment of time), as a function of the instantaneous bond density ϕ, is found to be non-monotonous and independent of the bond strength (symbols as shown in the legend). Right: Mean fluctuation amplitude of a membrane segment $\bar{\Xi}$ obtained after temporal and spatial averaging (left axis, dots) is directly proportional to the fluctuation in bond concentration $\Delta\phi$ (right axis, crosses). Results are presented as a function of the mean bond density $\bar{\phi}$. A branch of stable adhesion (red dots and black crosses, high mean bond density) is separated from a branch of unstable adhesion (blue dots and yellow crosses at low mean density) by a dashed perpendicular line denoting a first-order-like phase transition. Figure adopted from [171]

This, and similar schemes, allowed for the direct comparison of the simulated shape of a pinned membrane with the experiment [99]. Furthermore, they were instrumental for the understanding that the affinity of the protein binding depends on the membrane fluctuations [149]. Furthermore, these simulations showed that the instantaneous roughness of the membrane reflects the instantaneous density of bonds, independently on their strength (bottom left panel in Fig. 8) [171]. Since the roughness is a non-monotonous function of the bond density, nucleation of an adhesion domain is accompanied by the appearance of a hot spot on the membrane, a fact first noticed in the context of cells [82], and rationalized by the comparison of experiments in GUVs and Langevin simulations [172]. Since the bonds are the main contributor to the roughness, spatially and temporally averaged roughness is directly proportional to the overall variance in the number of bonds (right panel in Fig. 8), both for unstable and stable adhesion.

While these insights contribute to deeper understanding of the adhesion process, only relatively small membrane segments (sizes of a single focal adhesion) can be explored for relatively short times. Consequently, long-timescale dynamics associated with the formation of adhesion structures and diffusion-limited processes remained out of reach with these techniques, which prompted the development of coarse-grained simulation methods based on mapping of adhesion to a lattice gas or Ising-like systems of bonds [100, 173–175]. While providing valuable understanding of cooperative dynamics in membranes, these approaches are, however, accurate only in a limited range of parameters.

3.2.4 Implicit Membrane Adhesion Dynamics: From Nucleation to Growth Patterns

A breakthrough in modeling the adhesion process was the realization that there is a clear separation of timescales between protein binding and diffusion on one hand, and membrane fluctuations on the other hand [73]. Accordingly, the mean membrane shape can be regarded as fixed, as long as the configuration of bonds pulling on the membrane remains unchanged. During this time, the membrane, and with it, the proteins sample the entire probability distribution of distances between ligands and receptors by means of membrane fluctuations.

Coarse Graining the Complexation Rates

The separation of timescales permits the integration of the effects of the membrane into effective rates for the (de)complexation of proteins. Consequently, the explicit treatment of the membrane can be fully circumvented with a negligible loss of accuracy. The averaging of the instantaneous rates equations (3)–(5) should be performed over all possible, and appropriately weighted configurations of the membrane at the position of the receptor, as height distribution $\{p\}$. Naturally, $\{p\}$ is sensitive to a configuration of bonds in the neighborhood of the receptor of interest. Accordingly,

$$K_{\rm off} \equiv \int {\rm d}h^b\; p(h^b) k_{\rm off}(h^b) = k_0 \exp\left[\frac{\lambda\alpha}{2}\left(2\left(\bar{h}^b - l_0\right) + \alpha\lambda\left(\sigma^b\right)^2 - \alpha\right) - \epsilon_b\right],$$
$$K_{\rm on} \equiv \rho_l \int {\rm d}h^r\; p(h^r) k_{\rm on}(h^r) = k_0 \frac{\sqrt{\lambda\alpha^2}}{\sqrt{2\pi(1+\lambda\,(\sigma^r)^2)}} \exp\left[\frac{\lambda\left[\bar{h}^r - (\alpha + l_0)\right]^2}{2(1+\lambda\,(\sigma^r)^2)}\right], \tag{8}$$

where h^b and h^r signify the height of the membrane at the position of a bond, and above a free receptor, respectively. The distribution $\{p\}$ can be calculated analytically for an arbitrary configuration of bonds in the surrounding [162], which permits to obtain effective rates (Eq. (8)) as a function on the average $\overline{h}$ (local mean membrane height) and the variance σ (local fluctuation amplitude) of the relevant distribution $\{p\}$ [73].

The analysis of the dependence of rates on properties of the membrane shows that typically membrane fluctuations and deformation increase the binding rate. This is because the probability for the encounter between a ligand and a receptor increases in average. Since stronger fluctuations can exert stronger stochastic forces, the unbinding rate is also increased, albeit to a lesser extent than the binding rate (Fig. 9a). Somewhat surprisingly, the overall effect is the effective stabilization of bonds by fluctuations.

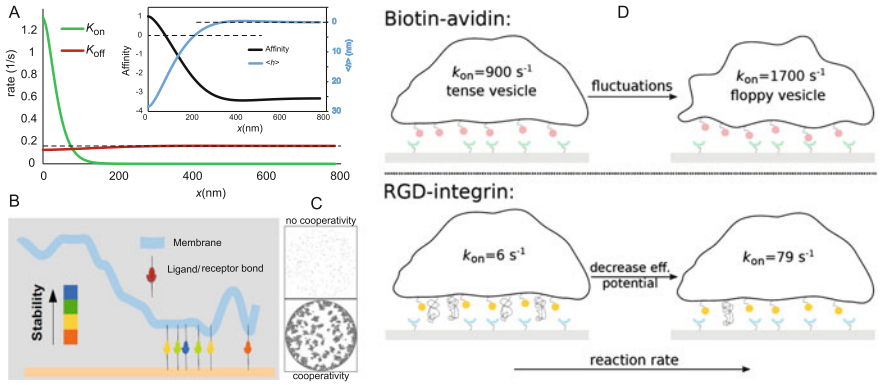

Fig. 9 Complexation rates and stability of bonds strongly depend on membrane-mediated, cooperative effects. (**a**) Binding (green) and unbinding (red) rates for a ligand receptor pair at distance x from a preexisting bond, showing appreciable changes up to 400-nm separations. Inset: Deformation of a bond (blue), and the affinity of a second bond as a function of the separation the bond inducing the deformation. At short distances (positive affinity), the second bond is stable, unlike at larger distances when the formation of a bond is associated with a free energy loss (negative affinity). Graph contributed by J. Vlajcevic. (**b**) Fluctuations of the membrane destabilize isolated bonds, thus leading to stabilization of bond clusters as shown in the cartoon. (**c**) Snapshots acquired at identical time from simulations run with cooperative effects switched off (top) and on (bottom). (**d**) Association rate determined from the radial growth of a domain [121]. In the case of biotin–avidin recognition, increasing the residual fluctuations increases the binding rate for a factor of two. Similarly, for RGD–integrin binding, decrease in density of the glycocalyx (weakening of the nonspecific potential) may increase the binding rate for over an order of magnitude. Sketch contributed by T. Bihr

The validity of the concept of average membrane-dependent rates could be independently verified by an alternative approach. Specifically, the binding rate K_{on}^{1} to form a bond in a neighborhood of an already existing bond can be extracted by fitting the time evolution of the area of a radially growing domain with a growth law obtained from a solution of a modified Stefan's equation [121]. The associated experiments show clearly that membrane fluctuations can change the binding rate by an order of magnitude in the case of RGD–integrin, or biotin–avidin pairing (Fig. 9d). Similar stabilization of biotin–neutravidin bonds was observed in switching from ultra-weak to strong adhesion, which takes place with the suppression of fluctuations within mature adhesion domains [172].

An important consequence of such a description is the strong sensitivity of the effective rates (Eq. (6)) to the neighboring distribution of bonds, which is equivalent to cooperative effects that may enhance or prevent further (de)complexation (Fig. 9b–c). This is best demonstrated for a scaffold comprising a domain of densely packed receptors. Deep within the domain, where each bonded receptor is surrounded by other bonds, the unbinding rate is nearly zero. The bonds at the smooth edge of the domain unbind with a probability that is several times larger, while fully exposed bonds are even more unstable. Likewise, compared to receptors

far away from the cluster, where the binding probability is very low, free receptors at the edge of the cluster have a significantly larger probability to form a bond [162].

Binding Affinity

As a consequence of the above argument, the binding affinity E_b is also a function of the local membrane environment (Fig. 9a). Such a finding is consistent with the significant spread in the values measured for binding energies of membrane-embedded proteins, where the membrane environment could not be strictly controlled in cells [176–178]. This spread, on the other hand, may be relevant physiologically, since it implies a subtle means of controlling binding affinity either by thermal or by active fluctuations, which have already been found to be important in the case of cadherin junction formation in cells [179] and in model membranes [37].

At a level of an individual bond, membrane fluctuations affect the affinity, which is, in principle, quadratic [162] and in units of $k_{\mathrm{B}}T$ takes the form:

$$E_b = \frac{1}{2}k_{eff}(\overline{h} - l_0)^2 + \frac{1}{2}\ln\left[\frac{2\pi}{\alpha^2 k_{eff}}\right] - \epsilon_b, \tag{9}$$

with the effective elastic stiffness of the bond-membrane construct being:

$$k_{eff} \equiv \left(\frac{1}{\lambda} + \sigma_f^2\right)^{-1}. \tag{10}$$

Here, the stiffness of the receptor–ligand bond is denoted by λ, and the fluctuation amplitude of the unbound membrane σ_f and ϵ_b signifies the (3D) binding affinity in solution.

The first term on the right-hand side of Eq. (9) is the deformation energy stored in the bond-membrane construct and is a quadratic function of the average vertical distance between the ligand and receptor $(\overline{h} - l_0)$. Here, $\overline{h}$ is the distance between the two membranes before the bond is formed and l_0 is the typical size of the protein assembly. The second term on the right-hand side of Eq. (9) is the entropic penalty associated with the suppression of the membrane fluctuations and the structural conformational space of the ligand–receptor pair [162]. It is important to notice that this 2D affinity is always smaller than its 3D counterpart, but also that the affinity of an ensemble of several bonds is larger (Fig. 9a). This is because a group of bonds which are separated by less than a couple of membrane correlation lengths cooperatively share the cost of bending the membrane and suppressing its fluctuations.

More detailed analysis of the free energy for the bond formation [162] shows that the affinity depends on the distance between bonds. In principle, there is a global minimum at zero distance between bonds, which suggests that densely packed domains should be most commonly observed, and that an effective attractive force acts between bonds in the membrane. However, depending on the details of

the system, an additional minimum appears in the free energy at finite distance between bonds, suggesting that a sparse configuration of bonds may be meta-stable, as observed experimentally in several experiments [8, 20].

The conclusion which arises from the present discussion is that because of strong cooperative effects induced by the membrane, the mass action law is inapplicable, except in some particular limits where cooperative effects play no role. The affinity (free energy gain per bond) is, in principle, nonadditive with the bond number, due to the nonadditive effect of fluctuations. The affinity can be evaluated for fixed distribution of bonds. Affinity is, hence, a property of the steady state, and it adopts no universal value. Instead, it is a direct function of bond density, membrane elasticity, glycocalyx thickness, and the mobility of binders.

Nucleation Dynamics

It is natural to expect that the sensitivity of rates to membrane parameters reflects in the nucleation dynamics of adhesion domains. The process of nucleation is typically characterized by two parameters—the number of bonds forming the smallest stable adhesion domain N_c, and its characteristic formation time $\bar{\tau}$ (Fig. 10a, b). For the membrane associated nucleation [73], N_c is calculated within the capillary approximation:

$$N_c \approx 1 + \frac{(\bar{h} - l_0)^4 \sigma_f^{-4}}{4\pi \rho_b \xi_{||}^2 E_b^2}, \tag{11}$$

where $\xi_{||}$ is the lateral correlation length of the membrane and ρ_b is the bond density within the domain. The analysis of Eq. (11) shows that the minimal number of bonds within a stable adhesion site is typically small. Importantly, N_c increases with the fourth power of the separation between the unbound ligand and receptor, and decreases with the fourth power of the membrane fluctuation amplitude.

The average nucleation time $\bar{\tau}$ is directly related to effective association and dissociation rates of the first (K_{on}^0, K_{off}^1) and the second bond (K_{off}^1 and K_{on}^2), even if $N_c > 2$ [73], giving rise to:

$$\bar{\tau} \simeq \left[\binom{N_c + 2}{3} \right]^{-1} \frac{K_{\text{off}}^1}{K_{\text{on}}^0} \left(\frac{K_{\text{off}}^2}{K_{\text{on}}^1} \right)^{(N_c - 2)} \frac{1}{K_{\text{on}}^1}. \tag{12}$$

This expression, extracted as an analytic solution to the master equation was successfully compared to explicit membrane Langevin dynamics in which the bond formation is governed by instantaneous rates (Eqs. (3)–(5)), as well as to implicit membrane Monte Carlo simulations, where the formation of bonds is driven by coarse-grained rates (Eq. (6)) [140].

From the functional form of the effective reaction rates [73], one can conclude that in the regime of moderate fluctuations, the nucleation time is a decreasing

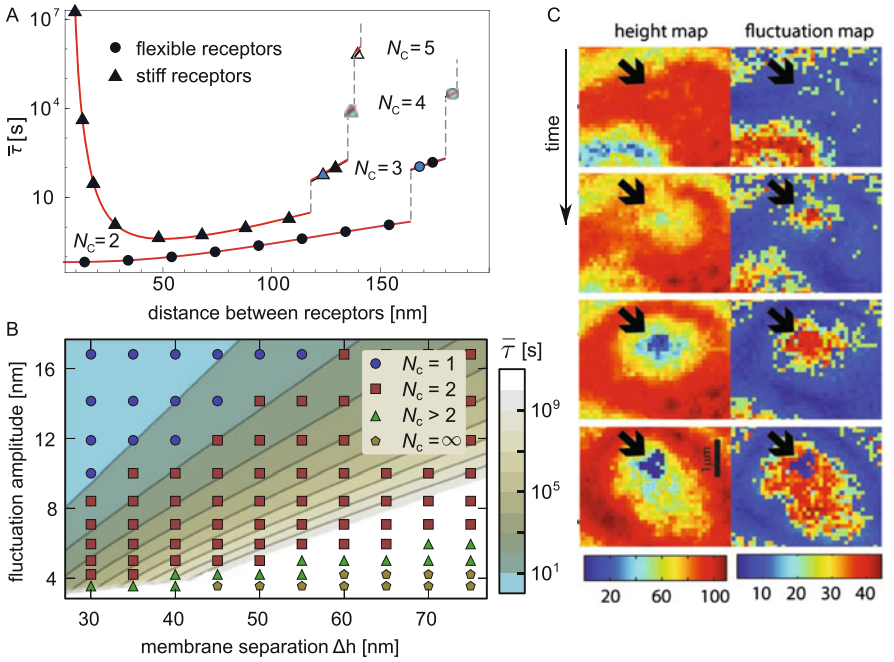

Fig. 10 Characteristics of the nucleation process in adhering membranes. (**a**) Dependence of the characteristic nucleation time $\bar{\tau}$ and the number of bonds forming a stable seed of the adhesion domain N_c, as a function of the distance between receptors. Strong sensitivity is observed with respect to the flexibility of the receptors, and small changes in receptor density may lead to large changes in the nucleation time. Results of an analytic approach (solid lines) are shown together with explicit membrane simulations (symbols). Panel reproduced from [73]. (**b**) Similar level of responsiveness is observed in the phase diagram for the nucleation time (colored background) and the number of bonds forming the seed (symbols), presented as a function of the membrane fluctuation amplitude and the initial separation between membranes (from [37]). (**c**) Dynamics of nucleation as observed by RICM height micrographs (left column), and Dy-RICM imaging the fluctuation amplitude of the membrane (right column). As the membrane gradually transitions from the nonspecific minimum to the bound state, the fluctuations show a non-monotonous behavior. Specifically, the site of nucleation appears initially as a hot spot in fluctuations as predicted by explicit membrane simulations presented in Fig. 8. Panel adopted from [172]

exponential function of the square of the fluctuation amplitude. On the other hand, $\bar{\tau}$ is an increasing exponential function of the square of the initial separation between ligands and receptors. This extreme sensitivity of both, the critical size and the characteristic nucleation time, is fully consistent with the experimentally observed variability of the number and size of growing adhesion junctions due to very small variations in the vesicle membrane fluctuation amplitude as well as in the initial height separation between the vesicle and the substrate [37].

In the model-membrane systems, the fluctuations are of thermal origin. Cells may, of course, locally regulate their activity, which is then reflected in the dynamic roughness of the membrane. Interestingly, locally increased fluctuations have been

observed in the early stages of the formation of adhesion contacts in vesicles [172] and in cells [82]. Moreover, a typical source of fluctuations are protrusions and retractions of filopodia which have been found necessary for the initiation of cell spreading through integrin-related adhesion, but also for the nucleation of cadherin junctions [66]. As expected, disruption of actin polymerization prevented adhesion [180], even though the association of cadherins with actin is not important for initial cadherin recruitment [179]. However, it is known that E-cadherin accumulation depends on transient activation of phosphatidylinositol 3-kinase and Rac1, the latter intensifying membrane fluctuations [179]. Upon the formation of tightly packed contacts equivalent to a nucleation site, fluctuations are suppressed within the domain, followed by a drop in the Rac1 activity. These findings, put in context of the theory of nucleation, suggest that there is a coupling between membrane mechanics and the signaling pathways already in the early stages of adhesion, prior to maturation of adhesion domain and the formation of the complete mechanosome.

Dynamics of Growth

Clearly, effective rates (Eq. (6)) can be also used within a Monte Carlo approach [140], in which systems of the size of a cell can be simulated for tens of seconds, because the membrane is no longer resolved explicitly. The simulation relies on determining the bond configuration around each binder (free or engaged) in each step. Because the binding rates decay very fast with increasing distance between the bonds, the current implementation explicitly checks only for first and second neighbors. Their configuration is used to determine the local mean shape and fluctuation amplitude for each binder. These rates are then applied in attempting to associate or dissociate each binder. After updating the bond configuration, all free proteins perform a diffusion step.

Even though the membrane is no longer explicitly treated, the described MC simulation operates without loss of accuracy, as shown by comparison to the 10^6 times more expensive Langevin simulations [171], which themselves were shown to agree very well with experiments in the context of the nucleation [172] and the morphology of adhesion domains [149]. As mentioned before, in this higher-level approach, the membrane deformations and fluctuations are explicitly simulated through a Langevin equation with the hydrodynamics fully resolved [140]. Furthermore, the scheme explicitly accounts for the diffusion and the complexation of binders, the latter modeled directly by Bell–Dembo's rates (Eq. (4)) [149]. This agreement fully validates the concept of the effective rates and enables studies of the early stages of the adhesion process in the regimes that are either not accessible to analytic modeling or are extremely demanding from the computational point of view. Examples of such regimes are fast nucleation, competitive growth of multiple seeds, or the diffusion-limited nucleation and growth. Actually, detailed analysis of the phase space shows a rich phase diagram that emerges from the competition between diffusivity, binding, cooperativity, and molecular crowding [37, 102] (Figs. 11 and 12). Furthermore, the spreading velocity of the membrane

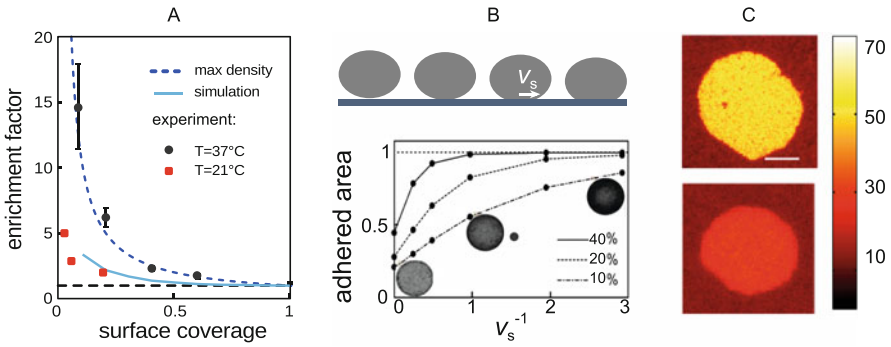

Fig. 11 Enrichment of mobile receptors in the adhesion zone. Figure adapted from [102]. (**a**) Enrichment factor as a function of the diffusion constant. At high temperature (fast diffusion, black dots), the adhesion zone is fully filled with receptors (blue dashed line), while for low diffusion constant enrichment factors are smaller in simulations (cyan full line) and in associated experiments (red squares), due to the buildup of corals at the edge of the adhesion zone. (**b**) Bond surface coverage (fraction of the adhesion zone occupied by bonds) as a function of the inverse of the velocity of spreading v_s, at various concentrations (surface coverage) of receptors. At small spreading velocities, migration of binders into the contact zone can lead to full filling, and the formation of the corals can be circumvented [8]. (**c**) As expected from simulations, at identical receptor densities, higher initial concentrations of ligands (top panel) lead to higher concentrations of bonds, compared to the system with small ligand concentration (bottom panel). In both systems, full filling is achieved due to small spreading velocities and corals are avoided. However, the enrichment factors differ considerably

and diffusivity was found to strongly affect the extent of binder accumulation (Fig. 11a), where large enrichment factors are obtained at fast spreading (Fig. 11b, c), both in simulations and experiments [102]. While this effect was demonstrated on relatively large scale, the mechanism applies also for small areas of contact. This would allow cells to regulate the density of binders in the forming adhesions by controlling the protruding and retracting speed of lamellipodia and filopodia that make the first adhesive contact with the environment.

Another interesting problem that this simulation can access is the formation of corals and patterns in the contact zone of vesicles and cells. Depending on the density of receptors, the adhesions may develop into peripheral ring-like structures [6]. The latter were found to be caused by the jamming of bulky proteins at the edge of the contact zone (Fig. 12a), and stabilized by membrane-transmitted correlations between bonds [102]. The simulations were able to recover the dependence of the ring thickness on the density of binders, as measured in experiments performed on biotinylated GUVs interacting with neutravidin-enriched SLBs, and show that the properties of the ring depend on the interplay between characteristic length of the path that protein makes upon entering the contact zone before forming a bond, and the mean free path of simple diffusion. Consequently, fast proteins reach the center of the contact zone prior to forming a bond, having a large dimensionless parameter:

$$\iota = D/(k_0 \rho_r). \tag{13}$$

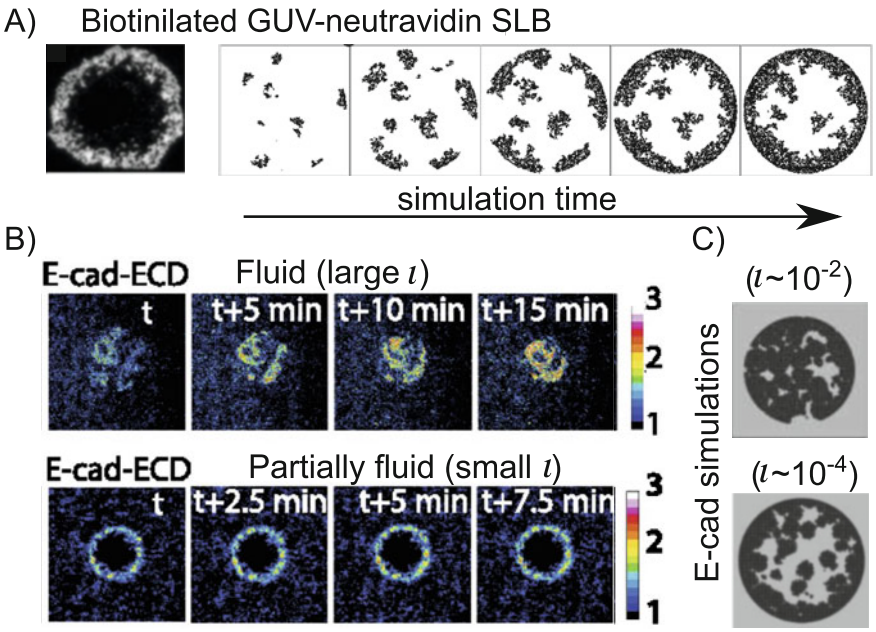

Fig. 12 Formation of ring-shaped coral in vesicles and cells. (**a**) Left panel shows an experimental fluorescent image of a ring formed by adhesion of a biotinylated GUV to an SLB decorated with mobile neutravidin as receptors. The sequence on the right shows the dynamics of the ring closure as obtained from implicit membrane simulations for the equivalent set of parameters. Stable ring was found to occur only at relatively small values of the parameters ι (Eq. (13)). Image adopted from [102]. (**b**) The formation of the ring was found to take place in cells only when the diffusion of binders is strongly suppressed relative to their characteristic binding time (decreasing ι). Panel reproduced from [66]. (**c**) Implicit membrane simulations of cadherin-mediated adhesion for various parameters ι. At high ι (fast diffusion, slow binding), full filling in a steady state is obtained an order of magnitude slower than a ring-like morphology at low ι (slow diffusion, fast binding)

The slow proteins (small ι) get recruited to adhesions at the edge of the contact zone, gradually building a coral. Similar effects have been observed in cell adhesion (Fig. 12b), where the fluidity (diffusivity) was found to affect the macroscopic organization of cadherins in cells [66]. At high cadherin diffusivity (high fluidity), the adhesions formed uniformly over the entire contact zone. At low diffusivity, a ring of cadherin junctions appeared spontaneously between two adherent cells [55], in cells binding to the substrate [66], and in analogous simulations as shown in Fig. 12c.

Another interesting system where the experiments and simulations showed a very good agreement is the cadherin-mediated GUV–SLB adhesion [37]. At small fluctuations and initial large separations between the GUV and the SLB, the cadherin agglomerate was a single, radially expanding domain with tightly packed bonds, consistently with strong, membrane-induced cooperative effects, recognized

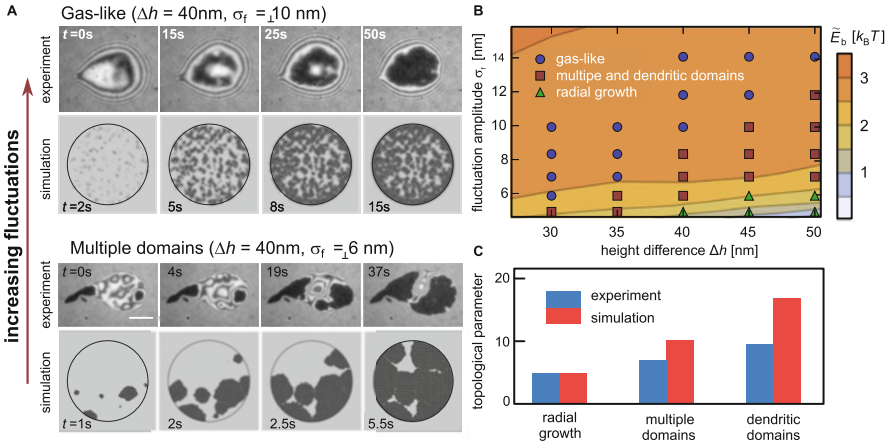

Fig. 13 Adhesion of GUV to SLBs via E-cadherin fragments. (**a**) An exceptionally good comparison of experiments and implicit membrane simulations demonstrates a particular sensitivity of the adhesion process to the fluctuation amplitude of the GUV membrane. Changes of only few nanometers can drive the system from growth via gas like distribution of bonds (top rows), where each individual bond is stable, to radial growth dominated by strong cooperative effects (bottom rows). (**b**) This sensitivity is captured in the phase diagram of growth patterns. Coarsening of the adhesion process occurs with the decrease of the effective binding affinity (background), e.g., the increase of the initial separation between the membranes and the decrease in the fluctuation amplitude. Parameters in this plot are identical to the ones used to plot the phase diagram for nucleation in Fig. 10b. (**c**) Topological parameter reflecting the edge roughness of adhesions, as obtained both in simulations and experiments. Image adopted from [37]

as *cis* interactions (bottom panels in Fig. 13a). Only 4-nm larger mean fluctuation amplitude of the GUV membrane resulted in a decrease of the characteristic nucleation time for three orders of magnitude. As a result, many domains developed simultaneously, producing a gas-like distribution of bonds (top panels in Fig. 13a). This is consistent with the finding that the critical number of bonds for stable nucleation has dropped to unity, even further decreasing the nucleation time (Fig. 10b), and the appearance of different patterns in the adhesion zone (Fig. 13b). At the same time, the affinity in the steady state for cadherin trans-binding grew by about 1–2 k_BTs (background in Fig. 13b) with increasing the fluctuations, as expected from the previous discussion.

These results together strongly challenge the paradigmatic idea that specific protein molecules embedded in the cell wall (or membrane) are alone responsible for cell adhesion. Instead, a new realization is emerging that the cell membrane itself, being a floppy and deformable, adds another unavoidable, but not yet understood interaction. Although this interaction does not depend on any specific proteins at all, it can have a major impact on the protein-mediated interactions and the organization on the membrane, which will have both dynamic and structural consequences.

3.3 Conclusion

Here, we have presented a framework for understanding GUV adhesion that has been constructed from experimental data as well as simulation and analytical modeling. To summarize, for nonspecific adhesion as well as abundant or strong linkers, the adhesion dynamics is determined by hydrodynamics and the final state from the competition between elastic deformation and adhesion; for specific adhesion with weak or sparse linkers, the dynamics can be reaction dominated, diffusion dominated or may show a transition between the two. The final state is usually a competition between adhesion enthalpy and entropy of different sort—positional entropy of the linkers, that of the repellers and the configurational entropy of the membrane expressed as fluctuations. The fluctuations can subtly control both the equilibrium state and the dynamics.

The model systems illustrated here are particularly adept at capturing specific aspects of cell adhesion. For example, the regulation of adhesion by the presence of polymers was modeled experimentally as well as theoretically, and has been long observed in cells, including in cancer invasion. Recently, this was quantified, and a very similar model was proposed for cells. The role of ligand mobility too was modeled in GUVs and using the theory, and its relevance was demonstrated later for cells. Crowding-induced pattern formation is another aspect that was first observed in GUV/SLB system and modeled as such and later also seen in the cellular context. Regulation of both in-plane bond clustering and out-of-plane bond formation by membrane fluctuations was demonstrated in model membranes, in analytical calculations as well as coarse-grained simulations using cadherins as example. These observations link up very well with recent reports on early stages of adhesion of cells, where the fluctuations are however active rather than thermal.

We hope to have demonstrated that while model membranes cannot be expected to simultaneously mimic all facets of cell adhesion, they can indeed capture and reproduce specific aspects, which can then be studied in detail and in isolation. This in turn facilitates clean and clear mathematical modeling that in turn can feed back into our understanding of the biology of cell adhesion.

Acknowledgements We are grateful to our mentors Erich Sackmann, Udo Seifert, and Rudolf Merkel for their insights and ongoing collaborations. We are thankful to our teams and colleagues who were instrumental in realizing the work summarized herein, especially Susanne Fenz, Cornelia Monzel, Daniel Smith, Timo Bihr, and Laurent Limozin. We thank Josip Augustin Janeš for the help with formatting and proofreading this chapter.

References

1. Smith A-S, Fenz SF, Sengupta K (2010) Inferring spatial organization of bonds within adhesion clusters by exploiting fluctuations of soft interfaces. EPL 89:28003:1–6
2. Kaliman S, Jayachandran C, Rehfeldt F, Smith A-S (2014) Novel growth regime of MDCK II model tissues on soft substrates. Biophys J 106(7):L25–L28

3. Alberts B, Johnson A, Lewis J, Raff M, Roberts K, Walter P (2008) Molecular biology of the cell. Garland Science, New York, 1392 pp
4. Lipowsky R (1995) Generic interactions of flexible membranes. In: Lipowsky R, Sackmann, E (eds) Structure and dynamics of membranes, Chapter 11. Elsevier, Amsterdam, pp 521–602
5. Smith A-S, Sackmann E (2009) Progress in mimetic studies of cell adhesion and the mechanosensing. ChemPhysChem 10(1):66–78
6. Fenz SF, Sengupta, K (2012) Giant vesicles as cell models. Integr Biol 4(9):982–995
7. Sackmann E, Smith A-S (2014) Physics of cell adhesion: some lessons from cell-mimetic systems. Soft Matter 10(11):1644–1659
8. Fenz SF, Smith A-S, Merkel R, Sengupta K (2011) Inter-membrane adhesion mediated by mobile linkers: effect of receptor shortage. Soft Matter 7(3):952
9. Bruinsma R, Sackmann E (2001) Bioadhesion and the dewetting transition. C R Acad Sci 2:803–815
10. Prechtel K, Bausch AR, Marchi-Artzner V, Kantlehner M, Kessler H, Merkel R (2002) Dynamic force spectroscopy to probe adhesion strength of living cells. Phys Rev Lett 89(2):028101
11. Evans EA (1980) Analysis of adhesion of large vesicles to surfaces. Biophys J 31(3):425
12. Steinkühler J, Agudo-Canalejo J, Lipowsky R, Dimova R (2016) Modulating vesicle adhesion by electric fields. Biophys J 111(7):1454–1464
13. Limozin L, Sengupta K (2007) Modulation of vesicle adhesion and spreading kinetics by hyaluronan cushions. Biophys J 93(9):3300–3313
14. Smith A-S, Lorz BG, Seifert U, Sackmann E (2006) Antagonist-induced deadhesion of specifically adhered vesicles. Biophys J 90:1064–1080
15. Rädler JO, Feder TJ, Strey HH, Sackmann E (1995) Fluctuation analysis of tension-controlled undulation forces between giant vesicles and solid substrates. Phys Rev E 51:4526–4536
16. Limozin L, Sengupta K (2009) Quantitative reflection interference contrast microscopy (RICM) in soft matter and cell adhesion. ChemPhysChem 10(16):2752–2768
17. Schilling J, Sengupta K, Goennenwein S, Bausch AR, Sackmann E (2004) Absolute interfacial distance measurements by dual-wavelength reflection interference contrast microscopy. Phys Rev E 69:021901
18. Monzel C, Fenz SF, Merkel R, Sengupta K (2009) Probing biomembrane dynamics by dual-wavelength reflection interference contrast microscopy. ChemPhysChem 10:2828–2838
19. Sengupta K, Limozin L (2010) Adhesion of soft membranes controlled by tension and interfacial polymers. Phys Rev Lett 104(8):088101
20. Smith A-S, Sengupta K, Goennenwein S, Seifert U, Sackmann E (2008) Force-induced growth of adhesion domains is controlled by receptor mobility. Proc Natl Acad Sci U S A 105(19):6906–6911
21. Rädler JO, Feder TJ, Strey HH, Sackmann E (1995) Fluctuation analysis of tension-controlled undulation forces between giant vesicles and solid substrates. Phys Rev E 51:4526–4536
22. Sackmann E (1996) Supported membranes: scientific and practical applications. Science 271(5245):43
23. Groves JT, Ulman N, Boxer SG (1997) Micropatterning fluid lipid bilayers on solid supports. Science 275(5300):651–653
24. Richter RP, Bérat R, Brisson AR (2006) Formation of solid-supported lipid bilayers: an integrated view. Langmuir 22(8):3497–3505
25. Elender G, Kühner M, Sackmann E (1996) Functionalisation of si/sio 2 and glass surfaces with ultrathin dextran films and deposition of lipid bilayers. Biosens Bioelectron 11(6):565–577
26. Fischlechner M, Zaulig M, Meyer S, Estrela-Lopis I, Cuéllar L, Irigoyen J, Pescador P, Brumen M, Messner P, Moya S, et al (2008) Lipid layers on polyelectrolyte multilayer supports. Soft Matter 4(11):2245–2258
27. Mulligan K, Jakubek ZJ, Linda JJ (2011) Supported lipid bilayers on biocompatible polysaccharide multilayers. Langmuir 27(23):14352–14359

28. Wagner ML, Tamm LK (2000) Tethered polymer-supported planar lipid bilayers for reconstitution of integral membrane proteins: silane-polyethyleneglycol-lipid as a cushion and covalent linker. Biophys J 79(3):1400–1414
29. Naumann CA, Prucker O, Lehmann T, Rühe J, Knoll W, Frank CW (2002) The polymer-supported phospholipid bilayer: tethering as a new approach to substrate-membrane stabilization. Biomacromolecules 3(1):27–35
30. Tanaka M, Sackmann E (2005) Polymer-supported membranes as models of the cell surface. Nature 437(7059):656–663
31. Ada Cavalcanti-Adam E, Volberg T, Micoulet A, Kessler H, Geiger B, Spatz JP (2007) Cell spreading and focal adhesion dynamics are regulated by spacing of integrin ligands. Biophys J 92(8):2964–2974
32. Spatz JP, Geiger B (2007) Molecular engineering of cellular environments: cell adhesion to nano-digital surfaces. Methods Cell Biol 83:89–111
33. Pi F, Dillard P, Alameddine R, Benard E, Wahl A, Ozerov I, Charrier A, Limozin L, Sengupta K (2015) Size-tunable organic nanodot arrays: a versatile platform for manipulating and imaging cells. Nano Lett 15(8):5178–5184. PMID: 26161675
34. Dillard P, Pi F, Lellouch AC, Limozin L, Sengupta K (2016) Nano-clustering of ligands on surrogate antigen presenting cells modulates t cell membrane adhesion and organization. Integr Biol 8(3):287–301
35. Mossman KD, Campi G, Groves JT, Dustin ML (2005) Altered TCR signaling from geometrically repatterned immunological synapses. Science 310(5751):1191–1193
36. Hartman NC, Nyeb JA, Groves JT (2009) Cluster size regulates protein sorting in the immunological synapse. Proc Natl Acad Sci U S A 106:12729–12734
37. Fenz S, Bihr T, Schmidt D, Merkel R, Seifert U, Sengupta K, Smith A-S (2017) Membrane fluctuations mediate lateral interactions between cadherin bonds. Nat Phys 13:906–913
38. Lodish H, Zipursky SL (2001) Molecular cell biology. Biochem Mol Biol Educ 29:126–133
39. Janeway C, Murphy KP, Travers P, Walport M (2008) Janeway's immunobiology. Garland Science, New York
40. Hynes RO (2002) Integrins: bidirectional, allosteric signaling machines. Cell 110(6):673–687
41. Kim M, Carman CV, Springer TA (2003) Bidirectional transmembrane signaling by cytoplasmic domain separation in integrins. Science 301(5640):1720–1725
42. Bershadsky A, Kozlov M, Geiger B (2006) Adhesion-mediated mechanosensitivity: a time to experiment, and a time to theorize. Curr Opin Cell Biol 18:472–481
43. Vogel V, Sheetz M (2006) Local force and geometry sensing regulate cell functions. Nat Rev Mol Cell Biol 7(4):265–275
44. Geiger B, Yamada KM (2011) Molecular architecture and function of matrix adhesions. Cold Spring Harb Perspect Biol 3(5):a005033
45. Iskratsch T, Wolfenson H, Sheetz MP (2014) Appreciating force and shape the rise of mechanotransduction in cell biology. Nat Rev Mol Cell Biol 15(12):825–833
46. Solon J, Levental I, Sengupta K, Georges PC, Janmey PA (2007) Fibroblast adaptation and stiffness matching to soft elastic substrates. Biophys J 93(12):4453–4461
47. Merkel R, Nassoy P, Leung A, Ritchie K, Evans E (1999) Energy landscapes of receptor–ligand bonds explored with dynamic force spectroscopy. Nature 397(6714):50–53
48. Evans EA, Calderwood DA (2007) Forces and bond dynamics in cell adhesion. Science 316(5828):1148–1153
49. Dembo M, Torney DC, Saxman K, Hammer D (1988) The reaction-limited kinetics of membrane-to-surface adhesion and detachment. Proc R Soc Lond B Biol Sci 234(1274):55–83
50. Kong F, García AJ, Paul Mould A, Humphries MJ, Zhu C (2009) Demonstration of catch bonds between an integrin and its ligand. J Cell Biol 185(7):1275–1284
51. Leckband DE, de Rooij J (2014) Cadherin adhesion and mechanotransduction. Annu Rev Cell Dev Biol 30:291–315
52. Lecuit T, Yap AS (2012) E-cadherin junctions as active mechanical integrators in tissue dynamics. Nat Cell Biol 17(5):533–539

53. Volk T, Cohen O, Geiger B (1987) Formation of heterotypic adherens-type junctions between l-cam-containing liver cells and a-cam-containing lens cells. Cell 50(6):987–994
54. Ayalon O, Sabanai H, Lampugnani MG, Dejana E, Geiger B (1994) Spatial and temporal relationships between cadherins and pecam-1 in cell-cell junctions of human endothelial cells. J Cell Biol 126(1):247–258
55. Engl W, Arasi B, Yap LL, Thiery JP, Viasnoff V (2014) Actin dynamics modulate mechanosensitive immobilization of E-cadherin at adherens junctions. Nat Cell Biol 16(6):587–594
56. Gumbiner BM (2005) Regulation of cadherin-mediated adhesion in morphogenesis. Nat Rev Mol Cell Biol 6(8):622–634
57. Jeanes A, Gottardi CJ, Yap AS (2008) Cadherins and cancer: how does cadherin dysfunction promote tumor progression? Oncogene 27(55):6920–6929
58. Bello SM, Millo H, Rajebhosale M, Price SR (2012) Catenin-dependent cadherin function drives divisional segregation of spinal motor neurons. J Neurosci 32(2):490–505
59. Katsamba P, Carroll K, Ahlsen G, Bahna F, Vendome J, Posy S, Rajebhosale M, Price S, Jessell TM, Ben-Shaul A, Shapiro L, Honig BH (2009) Linking molecular affinity and cellular specificity in cadherin-mediated adhesion. Proc Natl Acad Sci U S A 106(28):11594–11599
60. Wu Y, Vendome J, Shapiro L, Ben-Shaul A, Honig B (2011) Transforming binding affinities from three dimensions to two with application to cadherin clustering. Nature 475(7357):510–513
61. Hong S, Troyanovsky RB, Troyanovsky SM (2010) Spontaneous assembly and active disassembly balance adherens junction homeostasis. Proc Natl Acad Sci U S A 107(8):3528–3533
62. Taveau J-C, Dubois M, Le Bihan O, Trépout S, Almagro S, Hewat E, Durmort C, Heyraud S, Gulino-Debrac D, Lambert O (2008) Structure of artificial and natural ve-cadherinbased adherens junctions. Biochem Soc Trans 36(2):189–193
63. Ozaki C, Obata S, Yamanaka H, Tominaga S, Suzuki ST (2010) The extracellular domains of e- and n-cadherin determine the scattered punctate localization in epithelial cells and the cytoplasmic domains modulate the localization. J Biochem 147(3):415
64. Harrison OJ, Jin X, Hong S, Bahna F, Ahlsen G, Brasch J, Wu Y, Vendome J, Felsovalyi K, Hampton CM, Troyanovsky RB, Ben-Shaul A, Frank J, Troyanovsky SM, Shapiro L, Honig B (2011) The extracellular architecture of adherens junctions revealed by crystal structures of type I cadherins. Structure 19(2):244–256
65. Hong S, Troyanovsky RB, Troyanovsky SM (2013) Binding to f-actin guides cadherin cluster assembly, stability, and movement. J Cell Biol 201(1):131–143
66. Biswas KH, Hartman KL, Yu C, Harrison OJ, Song H, Smith AW, Huang WYC, Lin W, Guo Z, Padmanabhan A, Troyanovsky SM, Dustin ML, Shapiro L, Honig B, Zaidel-Bara R, Groves JT (2015) E-cadherin junction formation involves an active kinetic nucleation process. Proc Natl Acad Sci U S A 112(35):10932–10937
67. Brasch J, Harrison OJ, Honig B, Shapiro L (2012) Thinking outside the cell: how cadherins drive adhesion. Trends Cell Biol 22(6):299–310
68. Dustin ML, Groves JT (2012) Receptor signaling clusters in the immune synapse. Ann Rev Biophys 41:543
69. Varma R, Campi G, Yokosuka T, Saito T, Dustin ML (2006) T cell receptor-proximal signals are sustained in peripheral microclusters and terminated in the central supramolecular activation cluster. Immunity 25:117–127
70. Kaizuka Y, Douglass AD, Varma R, Dustin ML, Vale RD (2007) Mechanisms for segregating T cell receptor and adhesion molecules during immunological synapse formation in jurkat T cells. Proc Natl Acad Sci U S A 104(51):20296–20301
71. Grakoui A, Bromley SK, Sumen C, Davis MM, Shaw AS, Allen PM, Dustin ML (1999) The immunological synapse: a molecular machine controlling t cell activation. Science 285(5425):221–227
72. Dillard P, Varma R, Sengupta K, Limozin L (2014) Ligand-mediated friction determines morphodynamics of spreading t cells. Biophys J 107(11):2629–2638

73. Bihr T, Seifert U, Smith A-S (2012) Nucleation of ligand-receptor domains in membrane adhesion. Phys Rev Lett 109:258101
74. Pincus P, Joanny J-F, Andelman D (1990) Electrostatic interactions, curvature elasticity, and steric repulsion in multimembrane systems. Europhys Lett 11:763
75. Safinya CR, Roux D, Smith GS, Sinha SK, Dimon P, Clark NA, Bellocq AM (1986) Steric interactions in a model multimembrane system: a synchrotron X-ray study. Phys Rev Lett 57:2718
76. Helfrich W (1973) Elastic properties of lipid bilayers: theory and possible experiments. Z Naturforsch C J Biosci 28:693–703
77. Brochard F, Lennon JF (1975) Frequency spectrum of the flicker phenomenon in erythrocytes. J Phys Fr 36:11
78. Evans E, Rawicz W (1990) Entropy-driven tension and bending elasticity in condensed-fluid membranes. Phys Rev Lett 64:2094–2097
79. Zidovska A, Sackmann E (2006) Brownian motion of nucleated cell envelopes impedes adhesion. Phys Rev Lett 96(4):048103
80. Pelling AE, Veraitch FS, Chu CP-K, Nicholls BM, Hemsley AL, Mason C, Horton MA (2007) Mapping correlated membrane pulsations and fluctuations in human cells. J Mol Recognit 20:467
81. Auth T, Safran SA, Gov NS (2007) Fluctuations of coupled fluid and solid membranes with application to red blood cells. Phys Rev E 76:051910
82. Pierres A, Benoliel A-M, Touchard D, Bongrand P (2008) How cells tiptoe on adhesive surfaces before sticking. Biophys J 94:4114
83. Safran SA, Gov N, Nicolas A, Schwarz US, Tlusty T (2005) Physics of cell elasticity, shape and adhesion. Physica A 352:171
84. Betz T, Lenz M, Joanny J-F, Sykes C (2009) ATP-dependent mechanics of red blood cells. Proc Natl Acad Sci U S A 106(36):15320–15325
85. Loubet B, Seifert U, Lomholt MA (2012) Effective tension and fluctuations in active membranes. Phys Rev E 85:031913
86. Turlier H, Fedosov DA, Audoly B, Auth T, Gov NS, Sykes C, Joanny J-F, Gompper G, Betz T (2016) Equilibrium physics breakdown reveals the active nature of red blood cell flickering. Nat Phys 12:513–519
87. Smith A-S (2016) Biophysics: alive and twitching. Nat Phys 12(5):378–379
88. Monzel C, Schmidt D, Seifert U, Smith A-S, Merkel R, Sengupta K (2016) Nanometric thermal fluctuations of weakly confined biomembranes measured with microsecond time-resolution. Soft Matter 12(21):4755–4768
89. Netz RR, Lipowsky R (1995) Stacks of fluid membranes under pressure and tension. Europhys Lett 29:345–350
90. Monzel C, Fenz SF, Giesen M, Merkel R, Sengupta K (2012) Mapping fluctuations in biomembranes adhered to micropatterns. Soft Matter 8(22):6128
91. Schmidt D, Monzel C, Bihr T, Merkel R, Seifert U, Sengupta K, Smith A-S (2014) Signature of a nonharmonic potential as revealed from a consistent shape and fluctuation analysis of an adherent membrane. Phys Rev X 4(2):021023
92. Seifert U (1995) Self-consistent theory of bound vesicles. Phys Rev Lett 74:5060–5063
93. Mecke KR, Charitat T, Graner F (2003) Fluctuating lipid bilayer in an arbitrary potential: theory and experimental determination of bending rigidity. Langmuir 19:2080–2087
94. Lipowsky R, Leibler S (1986) Unbinding transitions of interacting membranes. Phys Rev Lett 56:2541–2544
95. Netz RR (1995) Complete unbinding of fluid membranes in the presence of short-ranged forces. Phys Rev E 51(3):2286–2294
96. Hategan A, Sengupta K, Kahn S, Sackmann E, Discher DE (2004) Topographical pattern dynamics in passive adhesion of cell membranes. Biophys J 87(5):3547–3560
97. Manghi M, Destainville N (2010) Statistical mechanics and dynamics of two supported stacked lipid bilayers. Langmuir 26:4057–4068

98. Bruinsma R, Goulian M, Pincus P (1994) Self-assembly of membrane junctions. Biophys J 67:746–750
99. Brown FLH (2008) Elastic modeling of biomembranes and lipid bilayers. Annu Rev Phys Chem 59:685–712
100. Speck T (2011) Effective free energy for pinned membranes. Phys Rev E 83:050901
101. Monzel C, Schmidt D, Kleusch C, Kirchenbüchler D, Seifert U, Smith A-S, Sengupta K, Merkel R (2015) Measuring fast stochastic displacements of bio-membranes with dynamic optical displacement spectroscopy. Nat Commun 6:8162
102. Schmidt D, Bihr T, Fenz S, Merkel R, Seifert U, Sengupta K, Smith A-S (2015) Crowding of receptors induces ring-like adhesions in model membranes. Biochim Biophys Acta Mol Cell Res 1853:2984–2991
103. Smith A-S, Seifert U (2007) Vesicles as a model for controlled (de-)adhesion of cells: a thermodynamic approach. Soft Matter 3:275–289
104. Lorz BG, Smith A-S, Gege C, Sackmann E (2007) Adhesion of giant vesicles mediated by weak binding of sialyl-LewisX to E-selectin in the presence of repelling poly(ethylene glycol) molecules. Langmuir 23:12293–12300
105. Boehm H, Mundinger TA, Boehm CHJ, Hagel V, Rauch U, Spatz JP, Curtis JE (2009) Mapping the mechanics and macromolecular organization of hyaluronan-rich cell coats. Soft Matter 5:4331–4337
106. McLane LT, Chang P, Granqvist A, Boehm H, Kramer A, Scrimgeour J, Curtis JE (2013) Spatial organization and mechanical properties of the pericellular matrix on chondrocytes. Biophys J 104(5):986–996
107. Chang PS, McLane LT, Fogg R, Scrimgeour J, Temenoff JS, Granqvist A, Curtis JE (2016) Cell surface access is modulated by tethered bottlebrush proteoglycans. Biophys J 110(12):2739–2750
108. Robert P, Limozin L, Benoliel A-M, Bongrand P (2006) Glycocalyx regulation of cell adhesion. Principles of cellular engineering: understanding the biomolecular interface. Academic, Boston, p 143
109. Marx S, Schilling J, Sackmann E, Bruinsma R (2002) Helfrich repulsion and dynamical phase separation of multicomponent lipid bilayers. Phys Rev Lett 88:138102
110. Hisette M-L, Haddad P, Gisler T, Marques CM, Schröder AP (2008) Spreading of bioadhesive vesicles on DNA carpets. Soft Matter 4(4):828–832
111. Nam G, Hisette ML, Sun YL, Gisler T, Johner A, Thalmann F, Schröder AP, Marques CM, Lee N-K (2010) Scraping and stapling of end-grafted DNA chains by a bioadhesive spreading vesicle to reveal chain internal friction and topological complexity. Phys Rev Lett 105(8):088101
112. Bruinsma R, Behrisch A, Sackmann E (2016) Adhesive switching of membranes: experiment and theory. Phys Rev E 61:4253–4267
113. Schmid EM, Bakalar MH, Choudhuri K, Weichsel J, Ann HS, Geissler PL, Dustin ML, Fletcher DA (2000) Size-dependent protein segregation at membrane interfaces. Nat Phys 12:704–711
114. Paszek MJ, DuFort CC, Rossier O, Bainer R, Mouw JK, Godula K, Hudak JE, Lakins JN, Wijekoon AC, Cassereau L, Rubashkin MG, Magbanua MJ, Thorn KS, Davidson MW, Rugo HS, Park JW, Hammer DA, Giannone G, Bertozzi CR, Weaver VM (2014) The cancer glycocalyx mechanically primes integrin-mediated growth and survival. Nature 511:319–325
115. Seifert U (1997) Configurations of fluid membranes and vesicles. Adv Phys 46:13–137
116. Smith A-S, Seifert U (2005) Effective adhesion strength of specifically bound vesicles. Phys Rev E 71:061902
117. Groves JT (2007) Bending mechanics and molecular organization in biological membranes. Annu Rev Phys Chem 58:697–717
118. Brown FLH (2011) Continuumsimulations of biomembrane dynamics and the importance of hydrodynamic effects. Q Rev Biophys 44:391–432
119. Schwarz US, Safran SA (2013) Physics of adherent cells. Rev Mod Phys 85:1327–1381

120. Dustin ML, Chakraborty AK, Shaw AS (2010) Understanding the structure and function of the immunological synapse. Cold Spring Harb Perspect Biol 2(10):a002311
121. Bihr T, Fenz S, Sackmann E, Merkel R, Seifert U, Sengupta K, Smith A-S (2014) Association rates of membrane-coupled cell adhesion molecules. Biophys J 107(11):L33–L36
122. Döbereiner H-G, Dubin-Thaler BJ, Hofman JM, Xenias HS, Sims TN, Giannone G, Dustin ML, Wiggins CH, Sheetz MP (2006) Lateral membrane waves constitute a universal dynamic pattern of motile cells. Phys Rev Lett 97(3):038102
123. Sengupta K, Aranda-Espinoza H, Smith L, Janmey P, Hammer D (2006) Spreading of neutrophils: from activation to migration. Biophys J 91:4638–4648
124. Cuvelier D, Théry M, Chu Y-S, Dufour S, Thiéry J-P, Bornens M, Nassoy P, Mahadevan L (2007) The universal dynamics of cell spreading. Curr Biol 17(8):694–699
125. Seifert U, Lipowsky R (1990) Adhesion of vesicles. Phys Rev A 42:4768–4771
126. Smith A-S, Sackmann E, Seifert U (2004) Pulling tethers from adhered vesicles. Phys Rev Lett 92:208101
127. Smith A-S, Sackmann E, Seifert U (2003) Effects of a pulling force on the shape of a bound vesicle. Europhys Lett 64:281–287
128. Smith A-S, Lorz BG, Goennenwein S, Sackmann E (2006) Force-controlled equilibria of specific vesicle-substrate adhesion. Biophys J 90:L52–L54
129. Feder TJ, Weissmüller G, Žekš B, Sackmann E (1995) Spreading of giant vesicles on moderately adhesive substrates by fingering: a reflection interference contrast microscopy study. Phys Rev E 51(4):3427
130. Albersdörfer A, Feder T, Sackmann E (1997) Adhesion-induced domain formation by interplay of long-range repulsion and short-range attraction force: a model membrane study. Biophys J 73:245–257
131. Kloboucek A, Behrisch A, Faix J, Sackmann E (1999) Adhesion-induced receptor segregation and adhesion plaque formation: a model membrane study. Biophys J 77(4):2311–2328
132. Nardi J, Bruinsma R, Sackmann E (1998) Adhesion-induced reorganization of charged fluid membranes. Phys Rev E 58(5):6340
133. Solon J, Streicher P, Richter R, Brochard-Wyart F, Bassereau P (2006) Vesicles surfing on a lipid bilayer: self-induced haptotactic motion. Proc Natl Acad Sci U S A 103(33):12382–12387
134. Sandre O, Moreaux L, Brochard-Wyart F (1999) Dynamics of transient pores in stretched vesicles. Proc Natl Acad Sci U S A 96(19):10591–10596
135. Bernard A-L, Guedeau-Boudeville M-A, Sandre O, Palacin S, di Meglio J-M, Jullien L (2000) Permeation through lipid bilayers by adhesion of giant vesicles on decorated surfaces. Langmuir 16(17):6801–6808
136. Puech P-H, Askovic V, De Gennes P-G, Brochard-Wyart F (2006) Dynamics of vesicle adhesion: spreading versus dewetting coupled to binder diffusion. Biophys Rev Lett 01(01):85–95
137. Boulbitch A, Guttenberg Z, Sackmann E (2001) Kinetics of membrane adhesion mediated by ligand–receptor interaction studied with a biomimetic system. Biophys J 81:2743–2751
138. Shenoy VB, Freund LB (2005) Growth and shape stability of a biological membrane adhesion complex in the diffusion-mediated regime. Proc Natl Acad Sci U S A 102:9
139. Gao H, Shi W, Freund LB (2005) Mechanics of receptor-mediated endocytosis. Proc Natl Acad Sci U S A 102:27
140. Bihr T, Seifert U, Smith A-S (2015) Multiscale approaches to protein-mediated interactions between membranes—relating microscopic and macroscopic dynamics in radially growing adhesions. New J Phys 17(8):083016
141. Brochard-Wyart F, De Gennes PG (2002) Adhesion induced by mobile binders: dynamics. Proc Natl Acad Sci U S A 99(12):7854–7859
142. Guttenberg Z, Lorz B, Sackmann E, Boulbitch A (2001) First-order transition between adhesion states in a system mimicking cell-tissue interaction. Europhys Lett 54(6):826
143. Cuvelier D, Nassoy P (2004) Hidden dynamics of vesicle adhesion induced by specific stickers. Phys Rev Lett 93(22):228101

144. De Gennes P-G, Puech P-H, Brochard-Wyart F (2003) Adhesion induced by mobile stickers: a list of scenarios. Langmuir 19:7112–7119
145. Goennenwein S, Tanaka M, Hu B, Moroder L, Sackmann E (2003) Functional incorporation of integrins into solid supported membranes on ultrathin films of cellulose: impact on adhesion. Biophys J 85(1):646–655
146. Streicher P, Nassoy P, Bärmann M, Dif A, Marchi-Artzner V, Brochard-Wyart F, Spatz J, Bassereau P (2009) Integrin reconstituted in guvs: a biomimetic system to study initial steps of cell spreading. Biochim Biophys Acta Biomembr 1788(10):2291–2300
147. Puech P-H, Feracci H, Brochard-Wyart F (2004) Adhesion between giant vesicles and supported bilayers decorated with chelated e-cadherin fragments. Langmuir 20(22):9763–9768
148. Saffman PG, Delbrück M (1975) Brownian motion in biological membranes. Proc Natl Acad Sci U S A 72:3111–3113
149. Reister-Gottfried E, Sengupta K, Lorz B, Sackmann E, Seifert U, Smith A-S (2008) Dynamics of specific vesicle-substrate adhesion: from local events to global dynamics. Phys Rev Lett 101(20):208103:1–4
150. Naji A, Atzberger PJ, Brown FLH (2009) Hybrid elastic and discrete-particle approach to biomembrane dynamics with application to the mobility of curved integral membrane proteins. Phys Rev Lett 102:138102
151. Reister-Gottfried E, Leitenberger SM, Seifert U (2010) Diffusing proteins on a fluctuating membrane: analytical theory and simulations. Phys Rev E 81:031903
152. Quemeneur F, Sigurdsson JK, Renner M, Atzberger PJ, Bassereau P, Lacoste D (2014) Shape matters in protein mobility within membranes. Proc Natl Acad Sci U S A 111(14):5083–5087
153. Bartossek T, Jones NG, Schäfer C, Cvitkovic M, Glogger M, Mott HR, Kuper J, Brennich M, Carrington M, Smith A-S, Fenz S, Kisker C, Engstler M (2017) Structural basis for the shielding function of the dynamic trypanosome variant surface glycoprotein coat. Nat Microbiol 2:1523–1532
154. Deeg J, Axmann M, Matic J, Liapis A, Depoil D, Afrose J, Curado S, Dustin ML, Spatz JP (2013) T cell activation is determined by the number of presented antigens. Nano Lett 13(11):5619–5626. PMID: 24117051
155. Deeg JA, Louban I, Aydin D, Selhuber-Unkel C, Kessler H, Spatz JP (2011) Impact of local versus global ligand density on cellular adhesion. Nano Lett 11(4):1469–1476. PMID: 21425841
156. Smith A-S, Seifert U (2005) Force-induced de-adhesion of specifically bound vesicles: strong adhesion in competition with tether extraction. Langmuir 21(24):11357–11367. PMID: 16285811.
157. Yu C-h, Rafiq NBM, Krishnasamy A, Hartman KL, Jones GE, Bershadsky AD, Sheetz MP (2013) Integrin-matrix clusters form podosome-like adhesions in the absence of traction forces. Cell Rep 5(5):1456–1468
158. Fenz SF, Smith A-S, Merkel R, Sengupta K (2011) Inter-membrane adhesion mediated by mobile linkers: effect of receptor shortage. Soft Matter 7(3):952–962
159. Shindell O, Mica N, Ritzer M, Gordon VD (2015) Specific adhesion of membranes simultaneously supports dual heterogeneities in lipids and proteins. Phys Chem Chem Phys 17:15598–15607
160. Bihr T, Sadafi F-Z, Seifert U, Taylor RK, Smith A-S (2017) Radial growth in 2d revisited: the effect of finite density, binding affinity, reaction rates, and diffusion. Adv Mater Int 4(1600310):1–7
161. Bell GI (1978) Models for the specific adhesion of cells to cells. Science 200:618–627
162. Schmidt D, Bihr T, Seifert U, Smith A-S (2012) Coexistence of dilute and densely packed domains of ligand-receptor bonds in membrane adhesion. Europhys Lett 99:38003
163. Erdmann T, Schwarz US (2006) Bistability of cell-matrix adhesions resulting from nonlinear receptor-ligand dynamics. Biophys J 91(6):L60–L62
164. Evans E, Leung A, Heinrich V, Zhu C (2004) Mechanical switching and coupling between two dissociation pathways in a p-selectin adhesion bond. Proc Natl Acad Sci U S A 101(31):11281–11286

165. Weikl TR (2001) Fluctuation-induced aggregation of rigid membrane inclusions. Europhys Lett 54:547–553
166. Weikl TR, Andelman D, Komura S, Lipowsky R (2002) Adhesion of membranes with competing specific and generic interactions. Eur Phys J E 8:59–66
167. Weikl TR, Lipowsky R (2004) Pattern formation during t-cell adhesion. Biophys J 87(6):3665–3678
168. Weikl TR, Asfaw M, Krobath H, Rózycki B, Lipowsky R (2009) Adhesion of membranes via receptor–ligand complexes: domain formation, binding cooperativity, and active processes. Soft Matter 5:3213–3224
169. Lin LC-L, Groves JT, Brown FLH (2006) Analysis of shape, fluctuations, and dynamics in intermembrane junctions. Biophys J 91:3600–3606
170. Lin LC-L, Gov N, Brown FLH (2006) Nonequilibrium membrane fluctuations driven by active proteins. J Chem Phys 124(7):074903
171. Reister E, Bihr T, Seifert U, Smith A-S (2011) Two intertwined facets of adherent membranes: membrane roughness and correlations between ligand–receptors bonds. New J Phys 13:025003:1–15
172. Fenz SF, Bihr T, Merkel R, Seifert U, Sengupta K, Smith A-S (2011) Switching from ultraweak to strong adhesion. Adv Mater 27:2622–2626
173. Farago O (2008) Membrane fluctuations near a plane rigid surface. Phys Rev E 78:051919
174. Farago O (2010) Fluctuation-induced attraction between adhesion sites of supported membranes. Phys Rev E 81(5):050902
175. Speck T, Reister E, Seifert U (2010) Specific adhesion of membranes: mapping to an effective bond lattice gas. Phys Rev E 82:021923
176. Dustin M, Bromley SK, Davis MM, Zhu C (2001) Identification of self through two-dimensional chemistry and synapses. Annu Rev Cell Dev Biol 17(3):133–157
177. Zhu D-M, Dustin ML, Cairo CW, Golan DE (2007) Analysis of two-dimensional dissociation constant of laterally mobile cell adhesion molecules. Biophys J 92(3):1022–1034
178. Hu J, Lipowsky R, Weikl TR (2013) Binding constants of membrane-anchored receptors and ligands depend strongly on the nanoscale roughness of membranes. Proc Natl Acad Sci U S A 110:15283–15288
179. Perez TD, Tamada M, Sheetz MP, Nelson WJ (2008) Immediate-early signaling induced by E-cadherin engagement and adhesion. J Biol Chem 283(8):5014–5022
180. Bazellières E, Conte V, Elosegui-Artola A, Serra-Picamal X, Bintanel-Morcillo M, Roca-Cusachs P, Muñoz JJ, Sales-Pardo M, Guimerà R, Trepat X (2015) Control of cell–cell forces and collective cell dynamics by the intercellular adhesome. Nat Cell Biol 17(4):409–420

Spatial and Mechanical Aspects of Signal Transduction in the Cell Membrane

Kabir H. Biswas and Jay T. Groves

Abstract Intercellular cognate receptor-ligand pairs are major players in cellular signal transduction. The fact that both the receptor and the ligand are present on the membrane in these juxtacrine signaling interactions presents distinct experimental difficulties in their study. One experimental platform that has proven particularly useful is the hybrid live cell-supported lipid bilayer system, wherein a live cell is allowed to interact with a synthetic supported membrane displaying ligands of interest. A synthetic membrane enables control over identity, density, mobility, and spatial patterning of the displayed ligands. This chapter provides insights gained from the reconstitution of the immunological synapse formed by T-cells, junction formed by ephrinA1-EphA2 receptor tyrosine kinase in breast cancer cells, and adhesion formed by E-cadherin in epithelial cells on synthetic supported lipid bilayers.

Keywords α-Catenin · Cell signaling · Cadherin · Ephrin · Eph receptor · Immunological synapse · Mechanical signaling · Peptide-major histocompatibility complex · Receptor-ligand clustering · Supported lipid bilayer · T-cell receptor

K. H. Biswas (✉)
School of Materials Science and Engineering, Nanyang Technological University, Singapore, Singapore

Mechanobiology Institute, National University of Singapore, Singapore, Singapore
e-mail: khbiswas@ntu.edu.sg

J. T. Groves
School of Materials Science and Engineering, Nanyang Technological University, Singapore, Singapore

Department of Chemistry, University of California, Berkeley, CA, USA
e-mail: jtgroves@lbl.gov

P. Bassereau, P. Sens (eds.), *Physics of Biological Membranes*,
https://doi.org/10.1007/978-3-030-00630-3_19

1 Introduction

Cells in a multicellular organism are constantly engaged with their microenvironment and alter their behavior according to the signals from the microenvironment. A large fraction of the signals originating from the cellular microenvironment are detected by cells through receptors that are expressed on their membranes. These include biochemical ligands such as growth factor hormones that bind to their cognate receptor and activate intracellular signaling. A significant fraction of the microenvironmental signals are, however, perceived by cells through the formation of cell-cell junctions involving interaction between receptor-ligand pairs that are present on the membranes of the two interacting cells. Some of the examples of juxtacrine interaction include the formation of the immunological synapse between a T-cell and an antigen-presenting cell (APC) during T-cell activation [1–3], junction formation by the Eph (erythropoietin-producing human hepatocellular) family receptors and the ephrin family of ligands [4, 5], the formation of E-cadherin mediated cell-cell adhesion in the epithelial tissue [6–8], or interaction formed by Notch and Delta/Serrate/LAG-2 (DSL) family of proteins [9, 10]. The resulting intercellular signaling complexes on the two-dimensional cell membrane (sometimes referred to as juxtacrine signaling) intrinsically integrate spatial and mechanical aspects of the cellular microenvironment in ways that are not possible with soluble ligands.

Studies of such juxtacrine signaling processes have been accelerated by the development of hybrid live cell—supported lipid bilayer experimental systems (Fig. 1a). Supported lipid bilayers consist of phospholipid membranes reconstituted

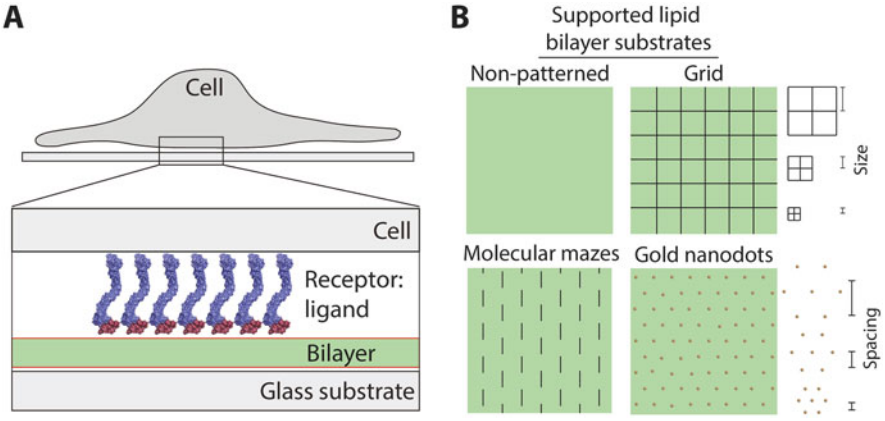

Fig. 1 The hybrid live cell-supported lipid bilayer system. (**a**) A schematic representation of a hybrid live cell-supported lipid bilayer system showing an adhesion formed between a live cell expressing a receptor of interest and a supported lipid bilayer displaying the cognate ligand for the receptor. (**b**) A schematic representation of either a non-patterned or different nanopatterned supported lipid bilayer substrates (grids, mazes, or nanodots) that are used for interrogating the role of spatial and mechanical features in juxtacrine signaling

on a solid substrate, such as glass or certain polymers [11, 12]. In a hybrid live cell-supported lipid bilayer assay, one of the cells is replaced with a synthetic, supported lipid bilayer functionalized with either a single or a few protein ligands, thus reducing the complexity of the system under study. Some of the advantages of using supported lipid bilayers for displaying ligands in this type of studies include preservation of the natural, two-dimensional characteristic of the cellular membrane, and retention of lateral fluidity of membrane components, which allows the assembly of ligand-mediated molecular complexes in the cells. The lateral fluidity, and hence the molecular mobility of the ligand, however, can be easily controlled by changing the lipid composition of the supported lipid bilayer at the same experimental conditions including temperature. Advances in micropatterning techniques have further increased their utility by allowing creation of solid barriers on the underlying substrate, which provides a control over the assembly of juxtacrine molecular complexes (Fig. 1b) [13–16]. Thus, the supported lipid bilayer platform has been successfully employed in understanding a number of juxtacrine signaling systems including the immunological synapse formed by T-cell receptor (TCR) and peptide-major histocompatibility (pMHC) [2, 3, 17–20], junction formed by B-cell receptor and antigen [21–23], junction formed by EphA2 and ephrinA1 [24–26], junction formed by the neuronal cell receptor neurexin and neuroligin [27, 28], adhesion formed by integrin and RGD peptide [29–32], and adhesion formed by E-cadherin [33, 34]. In the following sections of the chapter, we elaborate on the utilization of hybrid live cell-supported lipid bilayer assays for understanding the spatial and mechanical aspects of three different classes of juxtacrine signaling reactions.

2 Immunological Synapse Formation by T-Cells

As a part of the adaptive immunity, T-cells are responsible for the recognition of pathogen-derived peptide molecules displayed on the surface of APCs. This is achieved by the formation of an elaborate organization of molecular complexes called the immunological synapse at the interface between a T-cell and an APC (Fig. 2a, b). Key molecular players at the immunological synapse include the T-cell receptor (TCR) and the intercellular adhesion molecule 1 (ICAM-1), also known as the cluster of differentiation 45 (CD45) on the T-cell side, and pMHC complex and lymphocyte function-associated antigen 1 (LFA-1) integrin on the APC side. The interaction affinity between TCR and pMHC varies with the sequence of the peptide and is generally low for antigenic peptides [35]. Additionally, the molecular density of pMHC on the APC surface is very low [36]. Regardless of these, an interaction between a T-cell and an APC displaying specific pMHC results in the formation of a central supramolecular activation cluster (c-SMAC) constituted by the TCR-pMHC complex and peripheral supramolecular activation cluster (p-SMAC) constituted by the adhesion proteins ICAM-1-LFA-1 complex (Fig. 2b) [2, 3]. A sustained, juxtacrine association of the T-cell with the APC via the immunological synapse results in the activation of the T-cell.

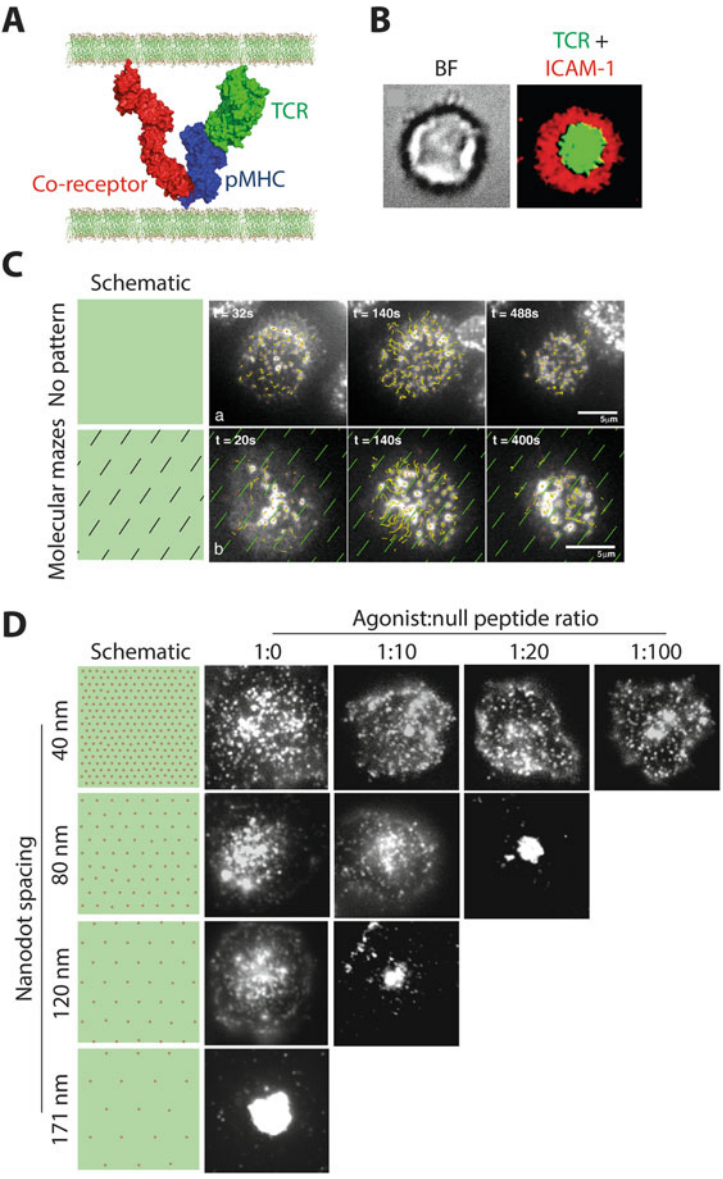

Fig. 2 Mechanical regulation of the T-cell immunological synapse. (**a**) Schematic of the pMHC-TCR (and a co-receptor) at the interface between two membranes. (**b**) Bright-field (BF) and epi-fluorescence images of a T-cell forming an immunological synapse on a supported lipid bilayer containing pMHC and ICAM-1. Adapted from [3]. (**c**) Actin cytoskeleton-mediated centripetal transport of pMHC-TCR on non-patterned and molecular maze patterned supported lipid bilayers. Adapted from [18]. (**d**) Cluster size-dependent pMHC-TCR microcluster transport by T-cells on substrates containing gold nanodots with the indicated spacing. Size of pMHC-TCR microclusters was controlled by titrating the density of agonist peptide on the bilayer by mixing with the null peptide at the indicated ratios. Adapted from [17]

2.1 Spatial Organization-Dependent Signaling at the Immunological Synapse

While a significant progress in this field was made with live cell assays, the spatial and mechanical regulation of the immunological synapse could only be appreciated with the utilization of hybrid live cell-supported lipid bilayer assays. In fact, the first usage of supported lipid bilayers for reconstitution of juxtacrine signaling with live cells was reported for studies related to the activation of T-cell by pMHC [37]. However, this initial study was limited by the immobilization of the ligand on the supported lipid bilayer, primarily due to the interaction of the lipid-embedded transmembrane region of the ligand with the solid support [38]. Utilization of a glycophosphatidylinositol (GPI)-linked pMHC complex on the supported lipid bilayer, thereby eliminating ligand immobilization, provided valuable new insights into the regulation of the immunological synapse formed by a T-cell and an antigen-presenting cell (APC) [2] and jumpstarted a much more widespread use of the technology. For instance, real-time imaging and quantitative analysis of fluorescently labeled pMHC indicated that the immunological synapse formation is a multistep process involving initial binding and clustering of pMHC-TCR followed by their translocation toward the center of the cell. Additionally, this assay system provided an understanding of how the number of pMHC and the kinetics of their interaction with TCR shape the T-cell activation outcome.

The evolution of the immunological synapse on the supported lipid bilayer platform suggested a role for the spatial arrangement of molecular complexes at the T-cell-APC interface into a "bull's eye" pattern in the signaling activity of the junction in the activation of T-cell [2]. This was confirmed by the introduction of nanopatterned supported lipid bilayers to guide and corral the mobility of lipids and proteins in the supported lipid bilayer [3, 18–20, 39, 40]. The nanopatterned substrates, in which metal structures of 100 nm width and 5 nm height are fabricated onto the underlying glass substrate, could be generated by a number of techniques including photolithography and electron beam lithography [41]. In this configuration, cells with different spatial arrangements of their receptor-ligand complexes are created without otherwise altering any chemical properties of the system. Such a perturbation of cell-cell junctions has been referred to as a "spatial mutation" [42] and has been productively used for probing other juxtacrine signaling systems including the ephrinA1-EphA2 receptor tyrosine kinase signaling system [24, 26], the integrin-RGD peptide-based adhesion [29–31], and the E-cadherin-based cell-cell adhesion [34]. The nanoscale physical barriers present on the nanopatterned substrates inhibit the free movement of the pMHC molecules that are functionalized to the lipid molecules in the bilayer thus inhibiting the inward transport of pMHC-TCR microclusters. The nanoscale physical barriers present on the nanopatterned substrate, however, do not affect the formation of these microclusters. Experiments with these substrates clearly established that the phosphotyrosine signaling from pMHC-TCR microclusters is dependent on their spatial location at the T-cell-APC interface. That is,

pMHC-TCR microclusters trapped at the cell periphery showed a prolonged colocalization with phosphorylated proteins as determined from staining the cells with an anti-phosphotyrosine antibody. This lead to an enhanced Ca^{2+} release indicative of an enhanced T-cell activation on the nanopatterned substrates compared to the non-patterned substrates. Importantly, the effects observed upon physically inhibiting pMHC-TCR microcluster translocation were different from a general reduction in the diffusion of the ligand, which resulted in a slower recruitment of key signaling molecules such as zeta-chain-associated protein of 70 kDa (ZAP70) kinase and a lower phosphotyrosine levels and intracellular Ca^{2+} elevation in T-cells [43]. The hybrid live cell-supported lipid bilayer system has also been instrumental in uncovering the polarized release of the microvesicles at the immunological synapse [44].

2.2 Mechanical Regulation of the Immunological Synapse

While these initial studies established a radially inward transport of pMHC-TCR microclusters as the basis of signaling and T-cell activation, the role and the nature of linkages of these pMHC-TCR microclusters with the actin cytoskeleton, which is required for transport of the microclusters [2, 45, 46], were not clear. This question was addressed with a differently nanopatterned supported lipid bilayer substrate in combination with quantitative single-particle tracking analysis. These substrates contained short, solid lines with intermittent gaps (referred to as "molecular mazes") that provided a control over the transport behavior of the microclusters (Fig. 2c) [18]. Based on the obstruction of the centripetal transport of pMHC-TCR microclusters by the metal lines on the substrate, it appeared that the pMHC-TCR microclusters are coupled by friction or viscous drag with actin flow, and this mechanism of coupling allows slip. In a direct extension of this study, the centripetal transport of pMHC-TCR microclusters by the actin cytoskeleton was monitored simultaneously with the flow of actin in T-cells by single-particle tracking [19]. This provided a detailed insight on the actin flow velocity vis-à-vis their relative spatial location at the T-cell-bilayer interface and revealed the deceleration of the centripetal actin flow toward the center of the immunological synapse. Further, the presence of physical barriers on the substrate resulted in a decrease in the velocity of actin flow associated with pMHC-TCR microcluster, while no difference was observed in the flow of actin in the absence of pMHC-TCR cluster. The gain of actin velocity immediately after traversing the physical barriers further strengthened the idea of a dynamic and dissipative coupling of the actin cytoskeleton with the pMHC-TCR microclusters. Another set of experiments mimicking protein chromatography performed using gold nanodot functionalized substrates revealed the size-dependent transport of pMHC-TCR microclusters by T-cells (Fig. 2d) [17]. Glass coverslips were coated with hexagonal arrays of gold nanodots (5–10 nm in diameter) with different inter-nanodot spacing ranging from 171 to 40 nm, while pMHC composition was varied on the bilayer. While cells formed a compact central

cluster of pMHC-TCR on substrates containing gold nanodots with a spacing of 171 and 145 nm, the centripetal transport of pMHC-TCR was inhibited on substrates containing gold nanodots with a spacing of 120 nm or less. Interestingly, including a null peptide, which, unlike the agonist peptides, does not activate T-cells, in the bilayer with 120 and 80 nm gold nanodot spacing relieved microcluster transport resulting in the formation of central cluster. However, the relative density of null peptide required for this relief varied with the nanodot spacing, i.e., a ratio of 1:10 of agonist vs. null peptide was required on substrates with 120 nm spacing, while a ratio of 1:20 was required on substrates with 80 nm. The inhibition of microcluster transport could not be completely relieved on substrates with 40 nm spacing even at an agonist/null peptide ratio of 1:100. Taken together, these experiments suggest that the size of pMHC-TCR microclusters depends on the density of ligand encountered by the cells and the actin cytoskeleton-mediated centripetal transport of these microclusters could be inhibited by physical obstacles on the substrate.

A combination of specialized tracking algorithms and image autocorrelation analysis further revealed the enrichment as well as assembly and disassembly dynamics of actin cytoskeleton at the pMHC-TCR microclusters [47]. Similar experiments have been performed to determine the role of myosin IIA in the formation of the immunological synapse [20]. These experiments revealed that myosin IIA drives the transport of pMHC-TCR microclusters in the early stages of immunological synapse formation, and inhibition of myosin IIA activity results in a reduction in the calcium influx (which is an indicator of T-cell activation). Moreover, myosin IIA inhibition also resulted in the reduced colocalization of ZAP70 and a reduced phosphorylation of the mechanically sensitive protein, CasL (Crk-associated substrate the lymphocyte type), which are the key signal transducers in the T-cell.

Sorting of the pMHC-TCR and ICAM-1-LFA-1 complexes at the immunological synapse has generally been proposed to be due to their physical dimensions, and perturbation of the length of the extracellular domain of TCR results in an artificial segregation of the molecules at the membrane interface [48–52]. A set of hybrid live cell-supported lipid bilayer experiments involving antibody cross-linking revealed that the LFA-1-ICAM-1 complex, which localizes to the periphery of the immunological synapse, can be transported to the central part of the synapse indicating a role for clustering (due to antibody binding-induced oligomerization) in the sorting of proteins at the immunological synapse [39].

An advance with regard to pMHC-TCR activation was made in experiments where single molecules of pMHC were tracked in concert with TCR [53]. This study showed that binding of a single pMHC molecule to a TCR resulted in the recruitment of ZAP70, and dwell-time analysis suggested a simple, stoichiometric binding that follows laws of mass action without any apparent cooperativity and signal amplification at the pMHC-TCR binding level. The binding kinetics obtained from this live cell study matched closely with surface plasmon resonance (SPR)-based measurements performed with purified proteins [54, 55]. However, this binding kinetics was slower than the rate of fluorescence resonance energy transfer (FRET) signal change observed in vitro [56] suggesting a cellular actomyosin

tension-dependent conformational change in the pMHC-TCR complex. But the fact that no change in the lifetime of the pMHC-TCR bond was observed upon disruption of the actin cytoskeleton induced by latrunculin A treatment of the cells [53] indicates the presence of other mechanisms for these differences in the pMHC-TCR binding.

3 Mechanical Force Sensing Through EphrinA1-EphA2

The Eph family of receptor tyrosine kinases is one of the largest families of receptor tyrosine kinases in the human genome. Unlike other receptor tyrosine kinases that bind soluble ligands, the Eph family of RTKs is special in that they bind membrane-localized ligands. Both the Eph receptor tyrosine kinases and their ephrin ligands have been divided into two classes, A and B, based on the biochemical binding characteristics as well as structural homologies. These receptor-ligand pairs are involved in the segregation of cells at tissue boundaries regulating processes such embryonic and neuronal development [57], remodeling of the epithelial tissue [58], or neuronal cell guidance [59].

The EphA2 receptor tyrosine kinase is expressed at low levels in epithelial cells and is involved in the regulation of cadherin-mediated cell-cell adhesion in these cells through other signaling proteins [58, 60]. More importantly, abnormally high expression of the EphA2 receptor tyrosine kinase has been implicated in diseases such as breast, lung, and ovarian cancer. Specifically, EphA2 is overexpressed in large fraction of breast cancers and is associated with poor prognosis and drug resistance [61, 62]. EphA2 consists of i) an extracellular part, which includes the ligand-binding domain, cys-rich Sushi and EGF domains followed by fibronectin repeats, and a transmembrane domain, ii) and an intracellular part, which consists of the tyrosine kinase, SAM (sterile α motif), and PDZ (Psd-95, Dlg, and ZO1) domains [63]. EphrinA1, on the other hand, consists of a receptor-binding domain in the extracellular part and is attached to the membrane via a glycosylphosphatidylinositol (GPI) anchor. Unlike the general model of dimerization of the receptor tyrosine kinases upon ligand binding, structural and cell-based studies have indicated that the interaction of the ephrinA1 to EphA2 could result in the formation of higher-order oligomers [63–65]. A monomeric, soluble ephrinA1, while able to bind to EphA2, is ineffective in activating EphA2 [66]. Instead, antibody-mediated clustering of ephrinA1 is required for the activation of EphA2 clearly indicating a role for physical organization of the receptor-ligand complex in the initiation of signaling by the kinase domain.

3.1 Physical Force Sensing Through EphrinA1-EphA2

Reconstitution of the EphA2-ephrinA1 junction with the highly invasive MDA-MB-231 breast cancer cell line that overexpresses EphA2 in a hybrid live cell-supported lipid bilayer format revealed a two-step process for junction formation (Fig. 3a,b)

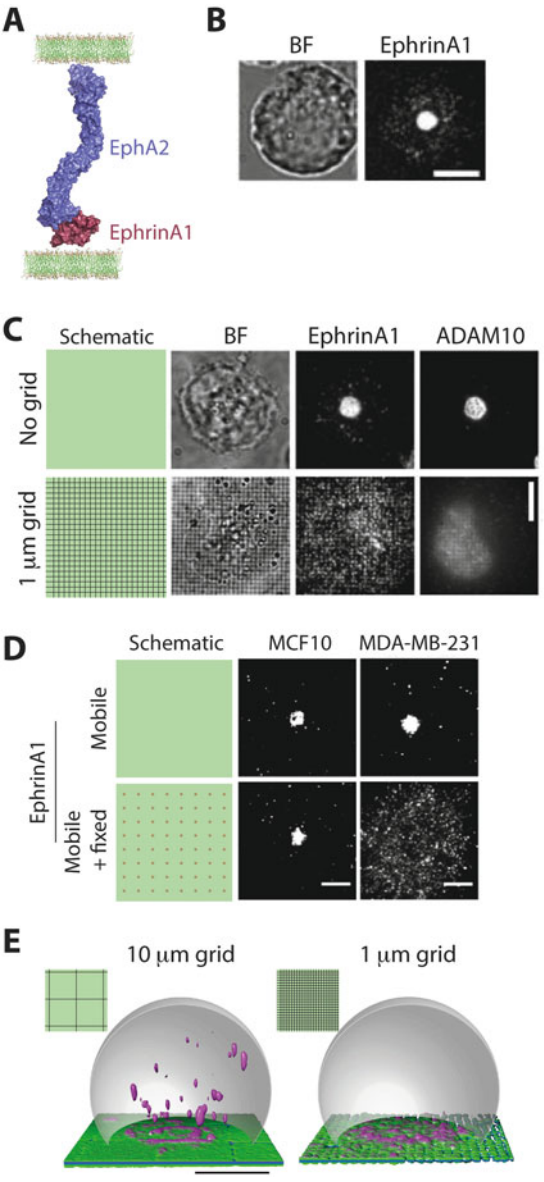

Fig. 3 Spatio-mechanical regulation of ephrinA1-EphA2 junction. (**a**) Schematic of ephrinA1-EphA2 complex at the interface between a live cell and a supported lipid bilayer membrane. (**b**) BF and epi-fluorescence images of an MDA-MB-231 cell on an ephrinA1-functionalized supported lipid bilayer showing the formation of a central cluster of ephrinA1-EphA2. Adapted from [26]. (**c**) Cells interacting with non-patterned or nanopatterned substrate showing inhibition of ADAM10 recruitment on nanopatterned substrates. Adapted from [26]. (**d**) Regulation of ephrinA1-EphA2 microcluster transport by MCF 10A and MDA-MB-231 cells on non-patterned or gold nanodot patterned substrates. Adapted from [25]. (**e**) Regulation of ephrinA1 trans-endocytosis by the spatial organization of the ephrinA1-EphA2 junction. Adapted from [24]

[26], in way similar to the pMHC-TCR-mediated junction formation by T-cells [2, 3]. Briefly, initial interaction of the cell with the ephrinA1-functionalized bilayer resulted in the formation of microclusters of ephrinA1-EphA2 within a few minutes. These microclusters are then transported toward the center of the cell-bilayer interface resulting in the coalescence of the microclusters into a large central cluster. It was clear that the transport of the ephrinA1-EphA2 microclusters

is dependent on the actomyosin tension as inhibition of the ROCK (Rho-associated coiled-coil forming protein serine/threonine) kinase, which phosphorylates myosin light chain, using Y-27632 resulted in a dose-dependent reduction in the centripetal transport of the microclusters. Further, the centripetal transport of the ephrinA1-EphA2 microclusters was quantitatively analyzed for a panel breast cancer cells with varying metastatic invasion potentials. This analysis revealed a higher correlation between invasion potential of these cells and the extent of centripetal transport of the ephrinA1-EphA2 microclusters in comparison to either the level of the EphA2 protein or its mRNA. This suggested that the central cluster formation is important for invasiveness of the cell lines tested and makes the hybrid live cell-supported lipid bilayer assay useful in predicting the invasiveness of cancer cells.

Unlike the position-dependent activity of pMHC-TCR in the immunological synapse [3], the catalytic activity of the kinase domain of EphA2 did not depend on the spatial localization of ephrinA1-EphA2 at the cell-bilayer interface. This was assessed by phosphotyrosine staining of cells forming junction on supported lipid bilayer substrates containing physical barriers [42] that effectively restricted the centripetal transport of ephrinA1-EphA2 microclusters. However, restriction of the centripetal transport of the microclusters by creating physical barrier on the substrate resulted in a reduction in the recruitment of A disintegrin and metalloproteinase domain-containing protein 10 (ADAM10) (Fig. 3c), which is instrumental in the proteolytic *trans*-cleavage of the ephrinA1-EphA2 complex [67, 68] and downstream signaling. Additionally, the restriction of the centripetal transport of ephrinA1-EphA2 microcluster resulted in an altered actin cytoskeleton morphology and large cell-bilayer contact area suggesting a strong association of the actin cytoskeleton with the microclusters. This was further investigated with substrates containing both fixed and mobile ephrinA1 (Fig. 3d) [25]. This was achieved by depositing a hexagonal array of gold nanoparticles on glass substrate by block copolymer lithography, followed by deposition of supported lipid bilayer [69]. Simultaneous functionalization of the gold nanodots and the supported lipid bilayer with ephrinA1 results in the production of substrates displaying fixed and mobile ephrinA1, respectively. Interaction of different breast cancer cell lines with this substrate resulted in the formation of ephrinA1-EphA2 microclusters. However, the centripetal transport of the microcluster was found to be dependent on the tumorigenic potential of the cell line. Non-tumorigenic cells, such as the MCF (Michigan Cancer Foundation) 10A breast epithelial cells, were still able to transport microclusters to the center of the cells and form the central cluster. In contrast, tumorigenic cells, such as the MDA-MB-231 breast cancer cells, showed a frustrated transport of the microclusters, perhaps due to a jamming of the mobile ephrinA1 molecules with the fixed ones, eventually leading to a failed central cluster formation. This suggests that the coupling of EphA2 with the actin cytoskeleton in these cell lines is dependent on the actomyosin contractility of the cell lines.

3.2 Spatial Organization-Dependent EphrinA1 Trans-endocytosis

In a manner similar to the T-cell immunological synapse, the ephrinA1-EphA2 junction formed by the MDA-MB-231 breast cancer cell also showed an elaborate spatial organization of intracellular proteins [24]. For instance, endocytosis-related proteins, clathrin and dynamin, and ADAM10 colocalized with ephrinA1-EphA2 clusters. In contrast, caveolin, Src, and anchors of other intracellular, membrane-associated signaling proteins such as Ras, PLC-PH, Lck, and RhoA were excluded from the eprhinA1-EphA2 central cluster. These proteins could be excluded from the ephrinA1-EphA2 clustered purely due to steric effects as seen in the case of clusters formed by the green fluorescent protein (GFP) present on synthetic unilamellar vesicles [70]. However, this does not appear to be the case for exclusion of proteins from ephrinA1-EphA2 clusters since the GPI anchor was homogenously distributed at the cell-bilayer interface. Unlike the organization of proteins at the T-cell immunological synapse in which the bilayer contained multiple ligands (pMHC and LFA-1) and the receptor-ligand complexes could be segregated due to their dimensions [48–52, 70, 71], the elaborate spatial organization of proteins observed at the ephrinA1-EphA2 junction appears to be solely driven by the ephrinA1-EphA2 clustering.

The colocalization of ADAM10 and clathrin with the ephrinA1-EphA2 clusters is indicative of a mechanical process wherein cleavage of ephrinA1 by ADAM10 allows clathrin-mediated *trans*-endocytosis of ephrinA1. Indeed, tracking of fluorescently labeled ephrinA1, initially bound to the supported lipid bilayer, by live cell, z-scan confocal microscopy revealed puncta of fluorescently labeled ephrinA1 inside the cell (Fig. 3e). The internalization of ephrinA1 was found to be due endocytosis since treatment of cells with Pitstop2, a clathrin terminal domain inhibitor [72, 73], resulted in a reduction of the number of internal ephrinA1 puncta. Further, treatment of cells with the small molecule INCB003619, which is an inhibitor of ADAM10 and ADAM17 [74, 75], resulted in a reduction in the relative levels of ephrinA1 internationalization. The fact that restriction of microcluster centripetal transport by physical barriers on the substrate resulted in the reduction of ADAM10 recruitment to the microcluster [26] suggests that the endocytosis of the ephrinA1-EphA2 could also be regulated by the spatial organization of the ephrinA1-EphA2 junction. Cells interacting with supported lipid bilayer substrate containing physical grids of 5 to 20 μm sizes showed fluorescent ephrinA1 puncta inside the cell. However, on substrates containing smaller grids of 1 or 3 μm, the process of ephrinA1 internalization was inhibited, thus confirming the idea that spatial organization and/or micron-scale clustering of ephrinA1-EphA2 complexes physically regulates the process of endocytosis-mediated internalization. This is likely happening due to a reduction in the local density of the ephrinA1-EphA2 protein complexes at the cell-bilayer interface.

4 E-Cadherin Adhesion

Cells in the epithelial tissue are physically organized by the formation of cell-cell junctions (also called adherens junction or zonula adherens), and this organization is required for the proper development of a variety of multicellular organisms [7, 76–78] (Fig. 4a). The primary component of the cell-cell junction is the calcium-dependent cell adhesion protein called E-cadherin. Aberrations in the function of E-cadherin have been implicated in the embryonic lethality [80, 81] as well as cancer metastasis [82–85].

Mature E-cadherin is expressed as a 120 kDa, glycosylated protein consisting of an extracellular domain (E-cad-ECD), a transmembrane domain, and an intracellular domain (E-cad-ICD) (Fig. 4b). E-cad-ECD is composed of a tandem repeat of 5 immunoglobulin-like domains, which are 110 amino acids long and have been named as EC1-5 (EC stands for extracellular cadherin) [76]. Structural studies have shown that the low-affinity (K_d values in the range of 100 to 700 μM) [86–91] homodimerization of E-cadherin is mediated by the "strand-swapping" interaction between their EC1 domains [79, 87]. Additionally, nuclear magnetic resonance (NMR)-based studies have shown that E-cadherin homodimerization occurs through a high activation energy barrier [88, 91] and sedimentation equilibrium centrifugation (SEC) studies have revealed a kinetically slow monomer-dimer interconversion [87]. Structural studies have also shown a weak *cis*-interaction between residues from the EC1 and EC2 domain [79] that impinges on the dynamics of E-cadherin at cell-cell junctions [79, 92]. This *cis*-interaction has been suggested to act cooperatively with the *trans*-interaction in molecular dynamic simulation studies leading to the formation of an ordered two-dimensional (2D) array of E-cadherin molecules, in which the *cis*-interaction acts as a "diffusion trap" for *trans*-interacting molecules [93, 94]. Importantly, structural and single-molecule force spectroscopy studies have shown that the E-cadherin homodimerization proceeds via the formation of a low-affinity intermediate X-dimer structure [87, 95–97] that plays a role in the assembly and disassembly of adhesion between live cells [98]. Single-molecule force spectroscopy experiments with the W2A mutant E-cadherin, which could only form the X-dimer intermediate, showed that lifetime of the bond increases with the increase in the applied force with a highest bond lifetime at 35 pN and then decreases with further increase in the applied force. This "catch bond" behavior has been confirmed with the wild-type E-cadherin in the presence of free tryptophan amino acid, which could compete for the docking of the tryptophan residue (W2) from one monomer to the other during the strand-swapped dimer formation. Additionally, bond lifetime and the nature of the bond formed between E-cadherin monomers in these experiments were shown to alter with the interaction time, i.e., short-lived, ideal bonds (which do not show a change in their lifetime with the application of force) were formed upon 0.3 s, while long-lived, slip bonds were formed upon 3 s of interaction [99]. These observations are suggestive of the presence of other intermediates in the formation of the X-dimer, and these intermediate steps are kinetically slow, perhaps due to high transition energy barriers [87, 91].

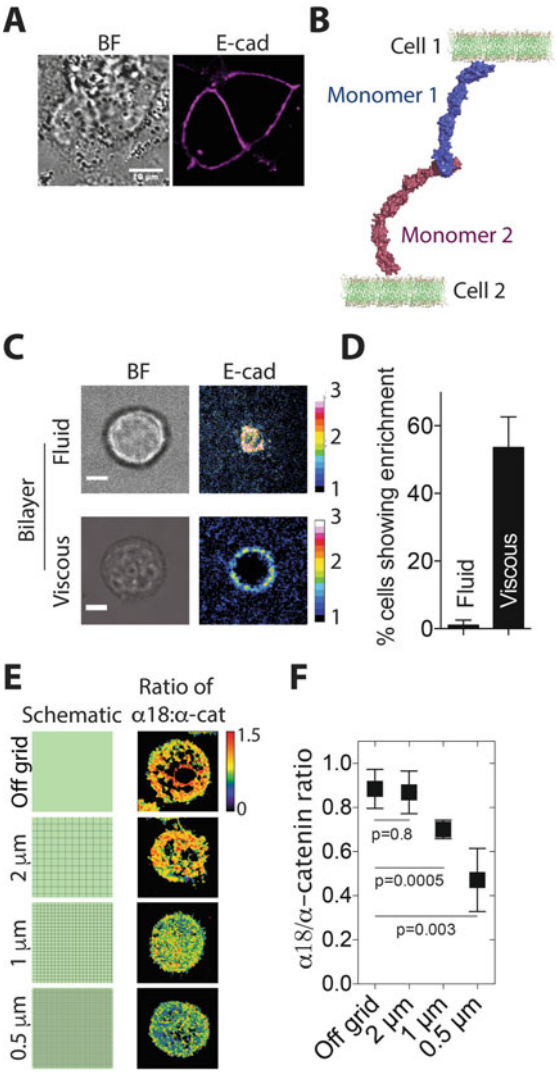

Fig. 4 Physico-spatial regulation of E-cadherin adhesion. (**a**) Bright-field (BF) and confocal microscopy images of E-cadherin-GFP-expressing cells in a monolayer showing the formation of E-cadherin adhesion between a pair of cells. (**b**) A schematic representation of a dimer of E-cadherin at the interface between two membranes [Protein Data Bank (PDB) code: 3Q2V] [79]. (**c**) BF and epi-fluorescence images of E-cadherin on fluid and viscous supported lipid bilayer showing molecular mobility-dependent E-cadherin adhesion formation. (**d**) Graph showing the frequency of cells forming junction on fluid vs. viscous bilayers. Both (**c**) and (**d**) are adapted from [33]. (**e**) Schematic and ratio of α18 and total α-catenin staining of cells adhering to substrates containing physical barriers (grids) of different sizes showing reduction in the activation of α-catenin upon inhibition of micron-scale clusters of E-cadherin on the substrate. The color code represents the relative level of activated α-catenin as determined from α18 and total α-catenin staining of cells. (**f**) Graph showing the ratio of α18 and total α-catenin staining from multiple cells on non-patterned and nanopatterned substrates. Both (**e**) and (**f**) are adapted from [34]

Unlike the structured ECD, the 150 amino acids long E-cad-ICD is unstructured. However, it interacts (directly as well as indirectly) with a large number of proteins including the actin cytoskeleton in the cytoplasm, thus enabling E-cadherin-based adhesion to function as a signaling hub in the cell [100–104]. Key among these interactions is the direct binding of p120- and β-catenin proteins. β-catenin, in turn, binds to α-catenin, which is a mechanically sensitive adaptor protein that has been proposed to shuttle between a "closed" and an "open" conformation depending on the application of mechanical force by the actin cytoskeleton [105]. Single-molecule force spectroscopy experiments with a trimeric complex of E-cad-ICD, β-catenin, and α-catenin have shown that the binding of α-catenin to F-actin is dependent on the mechanical force and is associated with a structural elongation of α-catenin [106]. This conformational activation of α-catenin has also been shown to uncover a cryptic vinculin binding site in α-catenin resulting in a dramatic increase in the affinity of α-catenin for vinculin in single-molecule force spectroscopy experiments [107]. Recruitment of vinculin, which also contains an F-actin binding domain, to the conformationally open α-catenin under conditions of increased cellular tension has been proposed to result in increased interaction with F-actin leading to strengthening of adhesion [108, 109].

4.1 Molecular Mobility-Dependent E-Cadherin Adhesion Formation

Initial attempts toward reconstituting E-cadherin adhesion in a hybrid live cell-supported lipid bilayer format employing a dimeric, Fc-fused E-cad-ECD showed enrichment of the E-cad-ECD on the bilayer, indicating the formation of adhesion [110]. A subsequent attempt was directed toward understanding the role of molecular mobility on the nature of adhesion formed by cells in a three-dimensional format [111]. The mobility of E-cadherin was altered by changing the temperature of the bilayer between 29 and 37 °C. Although the bilayer was largely mobile at 37 °C, a significant fraction (16%) of the protein on the bilayer was found to be immobile in a fluorescent recovery after photobleaching (FRAP) experiment. Nevertheless, these experiments revealed a difference in the way actin cytoskeleton was organized with respect to mobile vs. immobile display of E-cadherin on the bilayer. Another set of reconstitution experiments were directed toward understanding the apico-basal polarization of a key cell polarization marker, sodium, potassium (Na, K)-ATPase [112], which localized to the interface between the cell and bilayer [113].

A major advance in the field was reported when site specifically labeled, full-length E-cad-ECD was used for bilayer functionalization (Fig. 4b) [33]. Unlike the previous attempts, the protein was functionalized to the bilayer via the stable nickel-nitrilotriacetic acid (Ni-NTA)-poly-histidine interaction [114] allowing precise determination of the diffusion coefficient as well as density (observed to be a few hundred molecules per μm^2, which is in the range of densities observed in cells

[115]) of E-cadherin on the bilayer by z-scan fluorescence correlation spectroscopy (FCS) [116]. Photon counting histogram (PCH) analysis of the fluorescence fluctuation data indicated that E-cadherin is present on the bilayer in a monomeric form [117, 118]. Importantly, FRAP assays on these bilayers showed near-complete recovery of E-cadherin fluorescence within 90 s indicating the presence of close to 100% of the protein in the mobile form.

The key observation made with this hybrid system was that E-cadherin-mediated adhesion formation requires a low mobility supported lipid bilayer (Fig. 4c,d) [33]. That is, MKN28 epithelial cells seeded on highly fluid supported lipid bilayers prepared using 1,2-dioleoyl-sn-glycero-3-phosphocholine (DOPC) lipid rarely formed adhesion (<1%). In contrast, cells seeded on viscous supported lipid bilayers prepared using 1,2-dipalmitoyl-sn-glycero-3-phosphocholine (DPPC) doped with 1-acyl-2-[12-[(7-nitro-2-1,3- benzoxadiazol-4-yl)amino] dodecanoyl]-sn-glycero-3-phosphocholine (NBD-PC) readily formed adhesion (60%). A series of experiments ruled out the possibility that this difference in the frequency of adhesion formation was due to (1) a difference in the density of the protein, either on the bilayer or on the cell, (2) the cell line used in the experiments, or (3) engagement of the cytoskeleton with the E-cad-ICD [119, 120]. Further, the presence of physical barriers on the substrates that restrict free movement of molecules [26, 31, 42] or the presence of other types of adhesions such as the EphrinA1-EphA2 [24, 26] or the RGD integrin [29–31] did not induce the cells to form adhesion at high frequency on fluid bilayers. The fact that adhesion formation goes to completion on fluid bilayer, once initiated perhaps due to microscopic defects, suggested that E-cadherin adhesion formation involves a step of kinetic nucleation that is sensitive to the molecular mobility of E-cadherin. Therefore, the restricted diffusion of E-cadherin observed on live cell membranes [121–124] appears to be a key physical parameter that dictates E-cadherin adhesion formation. A requirement for a low molecular mobility appears to be unique to E-cadherin adhesion since no other cell-cell interaction system that has been studied so far in a hybrid live cell-supported lipid bilayer format showed such as a regulatory mechanism [2, 3, 26, 28, 29]. On the contrary, a reduction in molecular mobility of ligand on the supported lipid bilayer has generally been reported to negatively impact signaling. For example, a reduction in the diffusion of a stimulatory ligand resulted in a slower recruitment of key signaling molecules such as zeta-chain-associated protein of 70 kDa (ZAP70) kinase and a lower phosphotyrosine levels and intracellular Ca^{2+} elevation in T-cells [43]. Similarly, a reduction in the mobility of ligand on the bilayer resulted in reduced signaling by B-cells [21] or Fas-mediated death response of interacting cells [125].

The hybrid live cell-supported lipid bilayer system also revealed that cells cluster E-cadherin by extending and retracting filopodia on the bilayer substrate. This is agreement with the observation of E-cadherin clusters on filopodia in cells in monolayer culture [126, 127]. Further, an inhibition of filopodia formation by treating cells with Cdc42 inhibitor, ML 141 [128, 129], resulted in an inhibition of adhesion formation [33]. Importantly, the *cis*-interaction [79] was found to be redundant for adhesion formation on the viscous bilayers.

4.2 Micron-Scale Clustering-Dependent Activation of α-Catenin

The hybrid live cell-supported lipid bilayer platform has also been utilized to uncover the mechanism of conformational activation of the mechanosensory protein α-catenin at E-cadherin adhesions (Fig. 4e,f) [34]. The conformation of α-catenin was probed with either a conformation-specific antibody that specifically binds to the "open," activated conformation [105] or with a truncated version of vinculin containing only the head domain [107]. α-Catenin was found to be activated in E-cadherin adhesions and was sustained in the active conformation even after inhibition of cellular actomyosin tension by treating cells with ROCK kinase inhibitor, Y-27632. These results were confirmed in cells in the traditional monolayer cultures. However, the conformational activation of α-catenin in the hybrid assays was found to be dependent on the nucleation and micron-scale clustering of E-cadherin. This experiment was performed on nanopatterned supported lipid bilayer substrates containing physical barriers of different dimensions [42]. Cells adhering to non-patterned substrates or substrates containing grids of 2 μm size showed the formation of micron-scale clusters of E-cadherin, and similar levels of activated α-catenin, as determined from α18 antibody staining. However, cells adhering to substrates containing smaller grids of sizes 1 or 0.5 μm showed a reduction in the clustering of E-cadherin and a concomitant decrease in the levels of activated α-catenin. Thus, it appears that α-catenin is activated during the process of nucleation and micron-scale clustering of E-cadherin, and thus, the mechanical signal transduction from E-cadherin adhesions is dependent on the formation of the micron-scale clusters. This may take place through an alteration in the posttranslational modification, such as phosphorylation, of α-catenin [130]. Alternatively, the micron-scale clustering of E-cadherin could also change the interaction of α-catenin with other proteins [101, 104].

5 Conclusion

Biological cell membranes are active signaling platforms that play an essential role in efficient and appropriate signal transduction from juxtacrine signaling systems. They achieve this by not only allowing appropriate display of the receptor but also by controlling their physical properties such as mobility and assembly. This positions the hybrid live cell-supported lipid bilayer system to be an extremely useful technological platform to decipher specific mechanisms by which cell membrane regulates signal sensing and transduction by cellular receptors. Indeed, these systems have proven useful in understanding the spatio-mechanical regulation of receptor signaling such as in the case of pMHC-TCR, EphrinA1-EphA2, or E-cadherin adhesion as illustrated here. Key discoveries made with the hybrid T-cell assay system include spatial position-dependent signaling from TCR

and the actin cytoskeleton-mediated mechanical regulation of the immunological synapse. The ephrinA1-EphA2 hybrid setup provided insights into to the spatial organization-dependent downstream signaling and endocytosis of the receptor-ligand pair. Reconstitution of the E-cadherin adhesion on a hybrid platform revealed the role of molecular mobility on the frequency of adhesion formation and the role of micron-scale clustering on the activation of α-catenin.

At its core, the hybrid live cell-supported lipid bilayer platform integrates physical control of living cells, molecular specificity and mobility, and precision optical analysis. A tremendous wealth of biological processes occur at cell-cell interfaces, and we can anticipate this system to continue to play an enabling role in the advancement of this branch of quantitative cell biology.

References

1. Bromley SK, Burack WR, Johnson KG, Somersalo K, Sims TN, Sumen C, Davis MM, Shaw AS, Allen PM, Dustin ML (2001) The immunological synapse. Annu Rev Immunol 19:375–396. https://doi.org/10.1146/annurev.immunol.19.1.375
2. Grakoui A, Bromley SK, Sumen C, Davis MM, Shaw AS, Allen PM, Dustin ML (1999) The immunological synapse: a molecular machine controlling T cell activation. Science 285(5425):221–227. https://doi.org/10.1126/science.285.5425.221
3. Mossman KD, Campi G, Groves JT, Dustin ML (2005) Altered TCR signaling from geometrically repatterned immunological synapses. Science 310(5751):1191–1193. https://doi.org/10.1126/science.1119238
4. Klein R (2012) Eph/ephrin signalling during development. Development 139(22):4105–4109. https://doi.org/10.1242/dev.074997
5. Murai KK, Pasquale EB (2003) 'Eph'ective signaling: forward, reverse and crosstalk. J Cell Sci 116(Pt 14):2823–2832. https://doi.org/10.1242/jcs.00625
6. Leckband DE, de Rooij J (2014) Cadherin adhesion and mechanotransduction. Annu Rev Cell Dev Biol 30:291–315. https://doi.org/10.1146/annurev-cellbio-100913-013212
7. Patel SD, Chen CP, Bahna F, Honig B, Shapiro L (2003) Cadherin-mediated cell-cell adhesion: sticking together as a family. Curr Opin Struct Biol 13(6):690–698
8. Wheelock MJ, Johnson KR (2003) Cadherin-mediated cellular signaling. Curr Opin Cell Biol 15(5):509–514. https://doi.org/10.1016/S0955-0674(03)00101-7
9. Artavanis-Tsakonas S, Rand MD, Lake RJ (1999) Notch signaling: cell fate control and signal integration in development. Science 284(5415):770–776
10. Kopan R (2012) Notch signaling. Cold Spring Harb Perspect Biol 4(10). https://doi.org/10.1101/cshperspect.a011213
11. Sackmann E (1996) Supported membranes: scientific and practical applications. Science 271(5245):43–48. https://doi.org/10.1126/science.271.5245.43
12. Tanaka M, Sackmann E (2005) Polymer-supported membranes as models of the cell surface. Nature 437(7059):656–663. https://doi.org/10.1038/nature04164
13. Groves JT, Boxer SG (1995) Electric field-induced concentration gradients in planar supported bilayers. Biophys J 69(5):1972–1975. https://doi.org/10.1016/S0006-3495(95)80067-6
14. Groves JT, Boxer SG (2002) Micropattern formation in supported lipid membranes. Acc Chem Res 35(3):149–157. https://doi.org/10.1021/ar950039m
15. Groves JT, Ulman N, Boxer SG (1997) Micropatterning fluid lipid bilayers on solid supports. Science 275(5300):651–653. https://doi.org/10.1126/science.275.5300.651

16. Groves JT, Wulfing C, Boxer SG (1996) Electrical manipulation of glycan-phosphatidyl inositol-tethered proteins in planar supported bilayers. Biophys J 71(5):2716–2723. https://doi.org/10.1016/S0006-3495(96)79462-6
17. Caculitan NG, Kai H, Liu E, Fay N, Yu Y, Lohmuller T, O'Donoghue GP, Groves JT (2014) Size-based chromatography of signaling clusters in a living cell membrane. Nano Lett 14(5):2293–2298. https://doi.org/10.1021/nl404514e
18. DeMond AL, Mossman KD, Starr T, Dustin ML, Groves JT (2008) T cell receptor microcluster transport through molecular mazes reveals mechanism of translocation. Biophys J 94(8):3286–3292. https://doi.org/10.1529/biophysj.107.119099
19. Yu CH, Wu HJ, Kaizuka Y, Vale RD, Groves JT (2010) Altered actin centripetal retrograde flow in physically restricted immunological synapses. PLoS One 5(7):e11878. https://doi.org/10.1371/journal.pone.0011878
20. Yu Y, Fay NC, Smoligovets AA, Wu HJ, Groves JT (2012) Myosin IIA modulates T cell receptor transport and CasL phosphorylation during early immunological synapse formation. PLoS One 7(2):e30704. https://doi.org/10.1371/journal.pone.0030704
21. Ketchum C, Miller H, Song W, Upadhyaya A (2014) Ligand mobility regulates B cell receptor clustering and signaling activation. Biophys J 106(1):26–36. https://doi.org/10.1016/j.bpj.2013.10.043
22. Liu W, Won Sohn H, Tolar P, Meckel T, Pierce SK (2010) Antigen-induced oligomerization of the B cell receptor is an early target of fc gamma RIIB inhibition. J Immunol 184(4):1977–1989. https://doi.org/10.4049/jimmunol.0902334
23. Natkanski E, Lee WY, Mistry B, Casal A, Molloy JE, Tolar P (2013) B cells use mechanical energy to discriminate antigen affinities. Science 340(6140):1587–1590. https://doi.org/10.1126/science.1237572
24. Greene AC, Lord SJ, Tian A, Rhodes C, Kai H, Groves JT (2014) Spatial organization of EphA2 at the cell-cell interface modulates trans-endocytosis of ephrinA1. Biophys J 106(10):2196–2205. https://doi.org/10.1016/j.bpj.2014.03.043
25. Lohmuller T, Xu Q, Groves JT (2013) Nanoscale obstacle arrays frustrate transport of EphA2-Ephrin-A1 clusters in cancer cell lines. Nano Lett 13(7):3059–3064. https://doi.org/10.1021/nl400874v
26. Salaita K, Nair PM, Petit RS, Neve RM, Das D, Gray JW, Groves JT (2010) Restriction of receptor movement alters cellular response: physical force sensing by EphA2. Science 327(5971):1380–1385. https://doi.org/10.1126/science.1181729
27. Baksh MM, Dean C, Pautot S, DeMaria S, Isacoff E, Groves JT (2005) Neuronal activation by GPI-linked neuroligin-1 displayed in synthetic lipid bilayer membranes. Langmuir 21(23):10693–10698. https://doi.org/10.1021/la051243d
28. Pautot S, Lee H, Isacoff EY, Groves JT (2005) Neuronal synapse interaction reconstituted between live cells and supported lipid bilayers. Nat Chem Biol 1(5):283–289. https://doi.org/10.1038/nchembio737
29. Yu CH, Law JB, Suryana M, Low HY, Sheetz MP (2011) Early integrin binding to Arg-Gly-asp peptide activates actin polymerization and contractile movement that stimulates outward translocation. Proc Natl Acad Sci USA 108(51):20585–20590. https://doi.org/10.1073/pnas.1109485108
30. Yu CH, Rafiq NB, Cao F, Zhou Y, Krishnasamy A, Biswas KH, Ravasio A, Chen Z, Wang YH, Kawauchi K, Jones GE, Sheetz MP (2015) Integrin-beta3 clusters recruit clathrin-mediated endocytic machinery in the absence of traction force. Nat Commun 6:8672. https://doi.org/10.1038/ncomms9672
31. Yu CH, Rafiq NB, Krishnasamy A, Hartman KL, Jones GE, Bershadsky AD, Sheetz MP (2013) Integrin-matrix clusters form podosome-like adhesions in the absence of traction forces. Cell Rep 5(5):1456–1468. https://doi.org/10.1016/j.celrep.2013.10.040
32. Vafaei S, Tabaei SR, Biswas KH, Groves JT, Cho N-J (2017) Dynamic cellular interactions with extracellular matrix triggered by biomechanical tuning of low-rigidity, supported lipid membranes. Adv Healthc Mater 6(10):1700243–n/a. https://doi.org/10.1002/adhm.201770049

33. Biswas KH, Hartman KL, Yu CH, Harrison OJ, Song H, Smith AW, Huang WY, Lin WC, Guo Z, Padmanabhan A, Troyanovsky SM, Dustin ML, Shapiro L, Honig B, Zaidel-Bar R, Groves JT (2015) E-cadherin junction formation involves an active kinetic nucleation process. Proc Natl Acad Sci USA 112(35):10932–10937. https://doi.org/10.1073/pnas.1513775112
34. Biswas KH, Hartman KL, Zaidel-Bar R, Groves JT (2016) Sustained alpha-catenin activation at E-cadherin junctions in the absence of mechanical force. Biophys J 111(5):1044–1052. https://doi.org/10.1016/j.bpj.2016.06.027
35. Davis MM, Boniface JJ, Reich Z, Lyons D, Hampl J, Arden B, Chien Y (1998) Ligand recognition by alpha beta T cell receptors. Annu Rev Immunol 16:523–544. https://doi.org/10.1146/annurev.immunol.16.1.523
36. Wang W, Gulden PH, Pierce RA, Shabanowitz J, Man ST, Hunt DF, Engelhard VH (1997) A naturally processed peptide presented by HLA-A*0201 is expressed at low abundance and recognized by an alloreactive CD8+ cytotoxic T cell with apparent high affinity. J Immunol 158(12):5797–5804
37. Brian AA, McConnell HM (1984) Allogeneic stimulation of cytotoxic T cells by supported planar membranes. Proc Natl Acad Sci USA 81(19):6159–6163. https://doi.org/10.1073/pnas.81.19.6159
38. Salafsky J, Groves JT, Boxer SG (1996) Architecture and function of membrane proteins in planar supported bilayers: a study with photosynthetic reaction centers. Biochemistry 35(47):14773–14781. https://doi.org/10.1021/bi961432i
39. Hartman NC, Nye JA, Groves JT (2009) Cluster size regulates protein sorting in the immunological synapse. Proc Natl Acad Sci USA 106(31):12729–12734. https://doi.org/10.1073/pnas.0902621106
40. Manz BN, Jackson BL, Petit RS, Dustin ML, Groves J (2011) T-cell triggering thresholds are modulated by the number of antigen within individual T-cell receptor clusters. Proc Natl Acad Sci USA 108(22):9089–9094. https://doi.org/10.1073/pnas.1018771108
41. Yu CH, Groves JT (2010) Engineering supported membranes for cell biology. Med Biol Eng Comput 48(10):955–963. https://doi.org/10.1007/s11517-010-0634-x
42. Groves JT (2006) Spatial mutation of the T cell immunological synapse. Curr Opin Chem Biol 10(6):544–550. https://doi.org/10.1016/j.cbpa.2006.10.021
43. Hsu CJ, Hsieh WT, Waldman A, Clarke F, Huseby ES, Burkhardt JK, Baumgart T (2012) Ligand mobility modulates immunological synapse formation and T cell activation. PLoS One 7(2):e32398. https://doi.org/10.1371/journal.pone.0032398
44. Choudhuri K, Llodra J, Roth EW, Tsai J, Gordo S, Wucherpfennig KW, Kam LC, Stokes DL, Dustin ML (2014) Polarized release of T-cell-receptor-enriched microvesicles at the immunological synapse. Nature 507(7490):118–123. https://doi.org/10.1038/nature12951
45. Caplan S, Zeliger S, Wang L, Baniyash M (1995) Cell-surface-expressed T-cell antigen-receptor zeta chain is associated with the cytoskeleton. Proc Natl Acad Sci USA 92(11):4768–4772. https://doi.org/10.1073/pnas.1512331113
46. Wulfing C, Davis MM (1998) A receptor/cytoskeletal movement triggered by costimulation during T cell activation. Science 282(5397):2266–2269. https://doi.org/10.1126/science.282.5397.2266
47. Smoligovets AA, Smith AW, Wu HJ, Petit RS, Groves JT (2012) Characterization of dynamic actin associations with T-cell receptor microclusters in primary T cells. J Cell Sci 125(Pt 3):735–742. https://doi.org/10.1242/jcs.092825
48. Choudhuri K, Wiseman D, Brown MH, Gould K, van der Merwe PA (2005) T-cell receptor triggering is critically dependent on the dimensions of its peptide-MHC ligand. Nature 436(7050):578–582. https://doi.org/10.1038/nature03843
49. Cordoba SP, Choudhuri K, Zhang H, Bridge M, Basat AB, Dustin ML, van der Merwe PA (2013) The large ectodomains of CD45 and CD148 regulate their segregation from and inhibition of ligated T-cell receptor. Blood 121(21):4295–4302. https://doi.org/10.1182/blood-2012-07-442251
50. James JR, Vale RD (2012) Biophysical mechanism of T-cell receptor triggering in a reconstituted system. Nature 487(7405):64–69. https://doi.org/10.1038/nature11220

51. Lim HS, Cordoba SP, Dushek O, Goyette J, Taylor A, Rudd CE, van der Merwe PA (2015) Costimulation of IL-2 production through CD28 is dependent on the size of its ligand. J Immunol 195(11):5432–5439. https://doi.org/10.4049/jimmunol.1500707
52. Milstein O, Tseng SY, Starr T, Llodra J, Nans A, Liu M, Wild MK, van der Merwe PA, Stokes DL, Reisner Y, Dustin ML (2008) Nanoscale increases in CD2-CD48-mediated intermembrane spacing decrease adhesion and reorganize the immunological synapse. J Biol Chem 283(49):34414–34422. https://doi.org/10.1074/jbc.M804756200
53. O'Donoghue GP, Pielak RM, Smoligovets AA, Lin JJ, Groves JT (2013) Direct single molecule measurement of TCR triggering by agonist pMHC in living primary T cells. eLife 2:e00778. https://doi.org/10.7554/eLife.00778
54. Corse E, Gottschalk RA, Krogsgaard M, Allison JP (2010) Attenuated T cell responses to a high-potency ligand in vivo. PLoS Biol 8(9). https://doi.org/10.1371/journal.pbio.1000481
55. Newell EW, Ely LK, Kruse AC, Reay PA, Rodriguez SN, Lin AE, Kuhns MS, Garcia KC, Davis MM (2011) Structural basis of specificity and cross-reactivity in T cell receptors specific for cytochrome c-I-E(k). J Immunol 186(10):5823–5832. https://doi.org/10.4049/jimmunol.1100197
56. Huppa JB, Axmann M, Mortelmaier MA, Lillemeier BF, Newell EW, Brameshuber M, Klein LO, Schutz GJ, Davis MM (2010) TCR-peptide-MHC interactions in situ show accelerated kinetics and increased affinity. Nature 463(7283):963–967. https://doi.org/10.1038/nature08746
57. Mosch B, Reissenweber B, Neuber C, Pietzsch J (2010) Eph receptors and ephrin ligands: important players in angiogenesis and tumor angiogenesis. J Oncol 2010:135285. https://doi.org/10.1155/2010/135285
58. Miura K, Nam JM, Kojima C, Mochizuki N, Sabe H (2009) EphA2 engages Git1 to suppress Arf6 activity modulating epithelial cell-cell contacts. Mol Biol Cell 20(7):1949–1959. https://doi.org/10.1091/mbc.E08-06-0549
59. Bashaw GJ, Klein R (2010) Signaling from axon guidance receptors. Cold Spring Harb Perspect Biol 2(5):a001941. https://doi.org/10.1101/cshperspect.a001941
60. Fang WB, Ireton RC, Zhuang G, Takahashi T, Reynolds A, Chen J (2008) Overexpression of EPHA2 receptor destabilizes adherens junctions via a RhoA-dependent mechanism. J Cell Sci 121(Pt 3):358–368. https://doi.org/10.1242/jcs.017145
61. Pasquale EB (2008) Eph-ephrin bidirectional signaling in physiology and disease. Cell 133(1):38–52. https://doi.org/10.1016/j.cell.2008.03.011
62. Salaita K, Groves JT (2010) Roles of the cytoskeleton in regulating EphA2 signals. Commun Integr Biol 3(5):454–457. https://doi.org/10.4161/cib.3.5.12418
63. Seiradake E, Harlos K, Sutton G, Aricescu AR, Jones EY (2010) An extracellular steric seeding mechanism for Eph-ephrin signaling platform assembly. Nat Struct Mol Biol 17(4):398–402. https://doi.org/10.1038/nsmb.1782
64. Himanen JP, Yermekbayeva L, Janes PW, Walker JR, Xu K, Atapattu L, Rajashankar KR, Mensinga A, Lackmann M, Nikolov DB, Dhe-Paganon S (2010) Architecture of Eph receptor clusters. Proc Natl Acad Sci USA 107(24):10860–10865. https://doi.org/10.1073/pnas.1004148107
65. Seiradake E, Schaupp A, del Toro Ruiz D, Kaufmann R, Mitakidis N, Harlos K, Aricescu AR, Klein R, Jones EY (2013) Structurally encoded intraclass differences in EphA clusters drive distinct cell responses. Nat Struct Mol Biol 20(8):958–964. https://doi.org/10.1038/nsmb.2617
66. Davis S, Gale NW, Aldrich TH, Maisonpierre PC, Lhotak V, Pawson T, Goldfarb M, Yancopoulos GD (1994) Ligands for EPH-related receptor tyrosine kinases that require membrane attachment or clustering for activity. Science 266(5186):816–819. https://doi.org/10.1126/science.7973638
67. Atapattu L, Saha N, Llerena C, Vail ME, Scott AM, Nikolov DB, Lackmann M, Janes PW (2012) Antibodies binding the ADAM10 substrate recognition domain inhibit Eph function. J Cell Sci 125(Pt 24):6084–6093. https://doi.org/10.1242/jcs.112631

68. Janes PW, Saha N, Barton WA, Kolev MV, Wimmer-Kleikamp SH, Nievergall E, Blobel CP, Himanen JP, Lackmann M, Nikolov DB (2005) Adam meets Eph: an ADAM substrate recognition module acts as a molecular switch for ephrin cleavage in trans. Cell 123(2):291–304. https://doi.org/10.1016/j.cell.2005.08.014
69. Lohmuller T, Triffo S, O'Donoghue GP, Xu Q, Coyle MP, Groves JT (2011) Supported membranes embedded with fixed arrays of gold nanoparticles. Nano Lett 11(11):4912–4918. https://doi.org/10.1021/nl202847t
70. Schmid EM, Bakalar MH, Choudhuri K, Weichsel J, Ann H, Geissler PL, Dustin ML, Fletcher DA (2016) Size-dependent protein segregation at membrane interfaces. Nat Phys 12(7):704–711. https://doi.org/10.1038/nphys3678
71. Biswas KH, Groves JT (2016) A microbead supported membrane-based fluorescence imaging assay reveals intermembrane receptor-ligand complex dimension with nanometer precision. Langmuir 32(26):6775–6780. https://doi.org/10.1021/acs.langmuir.6b01377
72. Dutta D, Williamson CD, Cole NB, Donaldson JG (2012) Pitstop 2 is a potent inhibitor of clathrin-independent endocytosis. PLoS One 7(9):e45799. https://doi.org/10.1371/journal.pone.0045799
73. von Kleist L, Stahlschmidt W, Bulut H, Gromova K, Puchkov D, Robertson MJ, MacGregor KA, Tomilin N, Pechstein A, Chau N, Chircop M, Sakoff J, von Kries JP, Saenger W, Krausslich HG, Shupliakov O, Robinson PJ, McCluskey A, Haucke V (2011) Role of the clathrin terminal domain in regulating coated pit dynamics revealed by small molecule inhibition. Cell 146(3):471–484. https://doi.org/10.1016/j.cell.2011.06.025
74. Fridman JS, Caulder E, Hansbury M, Liu X, Yang G, Wang Q, Lo Y, Zhou BB, Pan M, Thomas SM, Grandis JR, Zhuo J, Yao W, Newton RC, Friedman SM, Scherle PA, Vaddi K (2007) Selective inhibition of ADAM metalloproteases as a novel approach for modulating ErbB pathways in cancer. Clin Cancer Res 13(6):1892–1902. https://doi.org/10.1158/1078-0432.CCR-06-2116
75. Zhou BB, Peyton M, He B, Liu C, Girard L, Caudler E, Lo Y, Baribaud F, Mikami I, Reguart N, Yang G, Li Y, Yao W, Vaddi K, Gazdar AF, Friedman SM, Jablons DM, Newton RC, Fridman JS, Minna JD, Scherle PA (2006) Targeting ADAM-mediated ligand cleavage to inhibit HER3 and EGFR pathways in non-small cell lung cancer. Cancer Cell 10(1):39–50. https://doi.org/10.1016/j.ccr.2006.05.024
76. Brasch J, Harrison OJ, Honig B, Shapiro L (2012) Thinking outside the cell: how cadherins drive adhesion. Trends Cell Biol 22(6):299–310. https://doi.org/10.1016/j.tcb.2012.03.004
77. Hiroki O (2012) Evolution of the cadherin-catenin complex. Subcell Biochem 60:9–35. https://doi.org/10.1007/978-94-007-4186-7_2
78. Biswas KH, Zaidel-Bar R (2017) Early events in the assembly of E-cadherin adhesions. Exp Cell Res 358(1):14–19. https://doi.org/10.1016/j.yexcr.2017.02.037
79. Harrison OJ, Jin X, Hong S, Bahna F, Ahlsen G, Brasch J, Wu Y, Vendome J, Felsovalyi K, Hampton CM, Troyanovsky RB, Ben-Shaul A, Frank J, Troyanovsky SM, Shapiro L, Honig B (2011) The extracellular architecture of adherens junctions revealed by crystal structures of type I cadherins. Structure 19(2):244–256. https://doi.org/10.1016/j.str.2010.11.016
80. Larue L, Ohsugi M, Hirchenhain J, Kemler R (1994) E-cadherin null mutant embryos fail to form a trophectoderm epithelium. Proc Natl Acad Sci USA 91(17):8263–8267. https://doi.org/10.1073/pnas.91.17.8263
81. Riethmacher D, Brinkmann V, Birchmeier C (1995) A targeted mutation in the mouse E-cadherin gene results in defective preimplantation development. Proc Natl Acad Sci USA 92(3):855–859. https://doi.org/10.1073/pnas.92.3.855
82. Guilford P, Hopkins J, Harraway J, McLeod M, McLeod N, Harawira P, Taite H, Scoular R, Miller A, Reeve AE (1998) E-cadherin germline mutations in familial gastric cancer. Nature 392(6674):402–405. https://doi.org/10.1038/32918
83. Onder TT, Gupta PB, Mani SA, Yang J, Lander ES, Weinberg RA (2008) Loss of E-cadherin promotes metastasis via multiple downstream transcriptional pathways. Cancer Res 68(10):3645–3654. https://doi.org/10.1158/0008-5472.CAN-07-2938

84. van Roy F (2014) Beyond E-cadherin: roles of other cadherin superfamily members in cancer. Nat Rev Cancer 14(2):121–134. https://doi.org/10.1038/nrc3647
85. Vasioukhin V (2012) Adherens junctions and cancer. Subcell Biochem 60:379–414. https://doi.org/10.1007/978-94-007-4186-7_16
86. Ciatto C, Bahna F, Zampieri N, VanSteenhouse HC, Katsamba PS, Ahlsen G, Harrison OJ, Brasch J, Jin X, Posy S, Vendome J, Ranscht B, Jessell TM, Honig B, Shapiro L (2010) T-cadherin structures reveal a novel adhesive binding mechanism. Nat Struct Mol Biol 17(3):339–347. https://doi.org/10.1038/nsmb.1781
87. Harrison OJ, Bahna F, Katsamba PS, Jin X, Brasch J, Vendome J, Ahlsen G, Carroll KJ, Price SR, Honig B, Shapiro L (2010) Two-step adhesive binding by classical cadherins. Nat Struct Mol Biol 17(3):348–357. https://doi.org/10.1038/nsmb.1784
88. Haussinger D, Ahrens T, Aberle T, Engel J, Stetefeld J, Grzesiek S (2004) Proteolytic E-cadherin activation followed by solution NMR and X-ray crystallography. EMBO J 23(8):1699–1708. https://doi.org/10.1038/sj.emboj.7600192
89. Katsamba P, Carroll K, Ahlsen G, Bahna F, Vendome J, Posy S, Rajebhosale M, Price S, Jessell TM, Ben-Shaul A, Shapiro L, Honig BH (2009) Linking molecular affinity and cellular specificity in cadherin-mediated adhesion. Proc Natl Acad Sci USA 106(28):11594–11599. https://doi.org/10.1073/pnas.0905349106
90. Koch AW, Pokutta S, Lustig A, Engel J (1997) Calcium binding and homoassociation of E-cadherin domains. Biochemistry 36(25):7697–7705. https://doi.org/10.1021/bi9705624
91. Li Y, Altorelli NL, Bahna F, Honig B, Shapiro L, Palmer AG 3rd (2013) Mechanism of E-cadherin dimerization probed by NMR relaxation dispersion. Proc Natl Acad Sci USA 110(41):16462–16467. https://doi.org/10.1073/pnas.1314303110
92. Bunse S, Garg S, Junek S, Vogel D, Ansari N, Stelzer EH, Schuman E (2013) Role of N-cadherin cis and trans interfaces in the dynamics of adherens junctions in living cells. PLoS One 8(12):e81517. https://doi.org/10.1371/journal.pone.0081517
93. Wu Y, Jin X, Harrison O, Shapiro L, Honig BH, Ben-Shaul A (2010) Cooperativity between trans and cis interactions in cadherin-mediated junction formation. Proc Natl Acad Sci USA 107(41):17592–17597. https://doi.org/10.1073/pnas.1011247107
94. Wu Y, Vendome J, Shapiro L, Ben-Shaul A, Honig B (2011) Transforming binding affinities from three dimensions to two with application to cadherin clustering. Nature 475(7357):510–513. https://doi.org/10.1038/nature10183
95. Nagar B, Overduin M, Ikura M, Rini JM (1996) Structural basis of calcium-induced E-cadherin rigidification and dimerization. Nature 380(6572):360–364. https://doi.org/10.1038/380360a0
96. Pertz O, Bozic D, Koch AW, Fauser C, Brancaccio A, Engel J (1999) A new crystal structure, Ca2+ dependence and mutational analysis reveal molecular details of E-cadherin homoassociation. EMBO J 18(7):1738–1747. https://doi.org/10.1093/emboj/18.7.1738
97. Sivasankar S, Zhang Y, Nelson WJ, Chu S (2009) Characterizing the initial encounter complex in cadherin adhesion. Structure 17(8):1075–1081. https://doi.org/10.1016/j.str.2009.06.012
98. Hong S, Troyanovsky RB, Troyanovsky SM (2011) Cadherin exits the junction by switching its adhesive bond. J Cell Biol 192(6):1073–1083. https://doi.org/10.1083/jcb.201006113
99. Rakshit S, Zhang Y, Manibog K, Shafraz O, Sivasankar S (2012) Ideal, catch, and slip bonds in cadherin adhesion. Proc Natl Acad Sci USA 109(46):18815–18820. https://doi.org/10.1073/pnas.1208349109
100. Bertocchi C, Wang Y, Ravasio A, Hara Y, Wu Y, Sailov T, Baird MA, Davidson MW, Zaidel-Bar R, Toyama Y, Ladoux B, Mege RM, Kanchanawong P (2017) Nanoscale architecture of cadherin-based cell adhesions. Nat Cell Biol 19(1):28–37. https://doi.org/10.1038/ncb3456
101. Guo Z, Neilson LJ, Zhong H, Murray PS, Zanivan S, Zaidel-Bar R (2014) E-cadherin interactome complexity and robustness resolved by quantitative proteomics. Sci Signal 7(354):rs7. https://doi.org/10.1126/scisignal.2005473
102. McEwen AE, Escobar DE, Gottardi CJ (2012) Signaling from the adherens junction. Subcell Biochem 60:171–196. https://doi.org/10.1007/978-94-007-4186-7_8

103. Van Itallie CM, Tietgens AJ, Aponte A, Fredriksson K, Fanning AS, Gucek M, Anderson JM (2014) Biotin ligase tagging identifies proteins proximal to E-cadherin, including lipoma preferred partner, a regulator of epithelial cell-cell and cell-substrate adhesion. J Cell Sci 127(Pt 4):885–895. https://doi.org/10.1242/jcs.140475
104. Zaidel-Bar R (2013) Cadherin adhesome at a glance. J Cell Sci 126(Pt 2):373–378. https://doi.org/10.1242/jcs.111559
105. Yonemura S, Wada Y, Watanabe T, Nagafuchi A, Shibata M (2010) Alpha-catenin as a tension transducer that induces adherens junction development. Nat Cell Biol 12(6):533–542. https://doi.org/10.1038/ncb2055
106. Buckley CD, Tan J, Anderson KL, Hanein D, Volkmann N, Weis WI, Nelson WJ, Dunn AR (2014) Cell adhesion. The minimal cadherin-catenin complex binds to actin filaments under force. Science 346(6209):1254211. https://doi.org/10.1126/science.1254211
107. Yao M, Qiu W, Liu R, Efremov AK, Cong P, Seddiki R, Payre M, Lim CT, Ladoux B, Mege RM, Yan J (2014) Force-dependent conformational switch of alpha-catenin controls vinculin binding. Nat Commun 5:4525. https://doi.org/10.1038/ncomms5525
108. le Duc Q, Shi Q, Blonk I, Sonnenberg A, Wang N, Leckband D, de Rooij J (2010) Vinculin potentiates E-cadherin mechanosensing and is recruited to actin-anchored sites within adherens junctions in a myosin II-dependent manner. J Cell Biol 189(7):1107–1115. https://doi.org/10.1083/jcb.201001149
109. Twiss F, Le Duc Q, Van Der Horst S, Tabdili H, Van Der Krogt G, Wang N, Rehmann H, Huveneers S, Leckband DE, De Rooij J (2012) Vinculin-dependent cadherin mechanosensing regulates efficient epithelial barrier formation. Biol Open 1(11):1128–1140. https://doi.org/10.1242/bio.20122428
110. Perez TD, Nelson WJ, Boxer SG, Kam L (2005) E-cadherin tethered to micropatterned supported lipid bilayers as a model for cell adhesion. Langmuir 21(25):11963–11968. https://doi.org/10.1021/la052264a
111. Andreasson-Ochsner M, Romano G, Hakanson M, Smith ML, Leckband DE, Textor M, Reimhult E (2011) Single cell 3-D platform to study ligand mobility in cell-cell contact. Lab Chip 11(17):2876–2883. https://doi.org/10.1039/c1lc20067d
112. McNeill H, Ozawa M, Kemler R, Nelson WJ (1990) Novel function of the cell adhesion molecule uvomorulin as an inducer of cell surface polarity. Cell 62(2):309–316. https://doi.org/10.1016/0092-8674(90)90368-O
113. Charnley M, Kroschewski R, Textor M (2012) The study of polarisation in single cells using model cell membranes. Integr Biol 4(9):1059–1071. https://doi.org/10.1039/c2ib20111a
114. Nye JA, Groves JT (2008) Kinetic control of histidine-tagged protein surface density on supported lipid bilayers. Langmuir 24(8):4145–4149. https://doi.org/10.1021/la703788h
115. Duguay D, Foty RA, Steinberg MS (2003) Cadherin-mediated cell adhesion and tissue segregation: qualitative and quantitative determinants. Dev Biol 253(2):309–323. https://doi.org/10.1016/S0012-1606(02)00016-7
116. Humpolickova J, Gielen E, Benda A, Fagulova V, Vercammen J, Vandeven M, Hof M, Ameloot M, Engelborghs Y (2006) Probing diffusion laws within cellular membranes by Z-scan fluorescence correlation spectroscopy. Biophys J 91(3):L23–L25. https://doi.org/10.1529/biophysj.106.089474
117. Chen Y, Muller JD, So PT, Gratton E (1999) The photon counting histogram in fluorescence fluctuation spectroscopy. Biophys J 77(1):553–567. https://doi.org/10.1016/S0006-3495(99)76912-2
118. Lin WC, Iversen L, Tu HL, Rhodes C, Christensen SM, Iwig JS, Hansen SD, Huang WY, Groves JT (2014) H-Ras forms dimers on membrane surfaces via a protein-protein interface. Proc Natl Acad Sci USA 111(8):2996–3001. https://doi.org/10.1073/pnas.1321155111
119. Hong S, Troyanovsky RB, Troyanovsky SM (2013) Binding to F-actin guides cadherin cluster assembly, stability, and movement. J Cell Biol 201(1):131–143. https://doi.org/10.1083/jcb.201211054

120. Ozono K, Komiya S, Shimamura K, Ito T, Nagafuchi A (2011) Defining the roles of alpha-catenin in cell adhesion and cytoskeleton organization: isolation of F9 cells completely lacking cadherin-catenin complex. Cell Struct Funct 36(1):131–143. https://doi.org/10.1247/csf.11009
121. Iino R, Koyama I, Kusumi A (2001) Single molecule imaging of green fluorescent proteins in living cells: E-cadherin forms oligomers on the free cell surface. Biophys J 80(6):2667–2677. https://doi.org/10.1016/S0006-3495(01)76236-4
122. Kusumi A, Nakada C, Ritchie K, Murase K, Suzuki K, Murakoshi H, Kasai RS, Kondo J, Fujiwara T (2005) Paradigm shift of the plasma membrane concept from the two-dimensional continuum fluid to the partitioned fluid: high-speed single-molecule tracking of membrane molecules. Annu Rev Biophys Biomol Struct 34:351–378. https://doi.org/10.1146/annurev.biophys.34.040204.144637
123. Kusumi A, Sako Y, Yamamoto M (1993) Confined lateral diffusion of membrane receptors as studied by single particle tracking (nanovid microscopy). Effects of calcium-induced differentiation in cultured epithelial cells. Biophys J 65(5):2021–2040. https://doi.org/10.1016/S0006-3495(93)81253-0
124. Sako Y, Nagafuchi A, Tsukita S, Takeichi M, Kusumi A (1998) Cytoplasmic regulation of the movement of E-cadherin on the free cell surface as studied by optical tweezers and single particle tracking: corralling and tethering by the membrane skeleton. J Cell Biol 140(5):1227–1240. https://doi.org/10.1083/jcb.140.5.1227
125. Sanchez MF, Levi V, Weidemann T, Carrer DC (2015) Agonist mobility on supported lipid bilayers affects Fas mediated death response. FEBS Lett 589(23):3527–3533. https://doi.org/10.1016/j.febslet.2015.10.009
126. Delanoe-Ayari H, Lenz P, Brevier J, Weidenhaupt M, Vallade M, Gulino D, Joanny JF, Riveline D (2004) Periodic adhesive fingers between contacting cells. Phys Rev Lett 93(10):108102. https://doi.org/10.1103/PhysRevLett.93.108102
127. Vasioukhin V, Bauer C, Yin M, Fuchs E (2000) Directed actin polymerization is the driving force for epithelial cell-cell adhesion. Cell 100(2):209–219. https://doi.org/10.1016/S0092-8674(00)81559-7
128. Jacquemet G, Hamidi H, Ivaska J (2015) Filopodia in cell adhesion, 3D migration and cancer cell invasion. Curr Opin Cell Biol 36:23–31. https://doi.org/10.1016/j.ceb.2015.06.007
129. Surviladze Z, Waller A, Strouse JJ, Bologa C, Ursu O, Salas V, Parkinson JF, Phillips GK, Romero E, Wandinger-Ness A, Sklar LA, Schroeder C, Simpson D, Noth J, Wang J, Golden J, Aube J (2010) A potent and selective inhibitor of Cdc42 GTPase. Probe Reports from the NIH Molecular Libraries Program, Bethesda, MD
130. Escobar DJ, Desai R, Ishiyama N, Folmsbee SS, Novak MN, Flozak AS, Daugherty RL, Mo R, Nanavati D, Sarpal R, Leckband D, Ikura M, Tepass U, Gottardi CJ (2015) Alpha-catenin phosphorylation promotes intercellular adhesion through a dual-kinase mechanism. J Cell Sci 128(6):1150–1165. https://doi.org/10.1242/jcs.163824

Protein-Induced Morphological Deformations of Biomembranes

P. B. Sunil Kumar and Mohamed Laradji

Abstract Many of the functions in living cells, such as endocytosis, cytokinesis, cell motility, and apoptosis, are mediated by the ability of the plasma membrane or organelles' membranes to deform. While it is well established experimentally that the highly curved deformations of lipid membranes in cells are the result of their interactions with proteins, the understanding of the mechanisms leading to these structures is still in its infancy. Conventional modeling of membranes using sheet elasticity cannot explain the stability and dynamics of many of the complex membrane structures in the cell. In this chapter, we present two studies based on two different numerical approaches, which show how complex structures in cell membranes can emerge from the interplay between membrane elasticity and protein–membrane interactions. The first study is focused on the effect of energy-consuming protein binding/unbinding onto membrane morphology, and the second study is focused on the effect of cytoskeletal proteins on regulating membrane shapes.

Keywords Lipids · Proteins · Cytoskeleton · Membrane morphogenesis · Blebbing · Simulation

Book Chapter in *Physics of Biological Membranes*, Eds. P. Sens and P. Bassereau.

P. B. Sunil Kumar
Department of Physics, Indian Institute of Technology Palakkad, Palakkad, India
e-mail: sunil@iitm.ac.in

M. Laradji (✉)
Department of Physics and Materials Science, The University of Memphis, Memphis, TN, USA
e-mail: mlaradji@memphis.edu

P. Bassereau, P. Sens (eds.), *Physics of Biological Membranes*,
https://doi.org/10.1007/978-3-030-00630-3_20

1 Introduction

A significant amount of research during the last few decades indicates that many functions of living cells necessitate local deformations of biomembranes in the form of protrusions as well as invaginations with curvatures much higher than those induced by thermal fluctuations. Much of the interest in this problem comes from our urge to understand the physical forces responsible for maintaining the morphologies of the plasma membrane and organelles such as the endoplasmic reticulum and Golgi body [1–3]. Such deformations are hypothesized to be mediated by activity of the cytoskeleton or peripheral proteins on the membrane.

Exoplasmic protrusions of the plasma membrane such as blebs are the result of mechanical forces exerted collectively by the actin filaments and myosin motors. These are important for processes such as cytokinesis, apoptosis, and cell motility. Likewise, interactions of microtubule motor complexes with membranes can induce tubular structures. Deformations of membranes into buds and tubules can also result from various peripheral proteins that are recruited to or are detached from them, through energy-consuming processes such as fusion and fission of vesicles [4]. Such actions can be due to curvature-sensing and curvature-generating proteins, which include a variety of BAR (Bin/Amphiphysin/Rvs) domain family of proteins [5], coat proteins [6], and GTPases [7–10]. In particular, proteins complexes such as Rabs–Snare and the Arf–Coatamer switch between membrane-bound and unbound states through energy-consuming processes that promote fusion and fission, respectively [11, 12]. The abovementioned activities are relevant in determining the shapes of membranes because the timescales of these processes are of the order of tens of seconds, which is comparable to membrane relaxation timescales of micron-sized compartments in the highly viscous environment of the cell [13, 14].

While there is detailed understanding of the molecular players involved in membrane remodeling, our understanding of the physical processes leading to large-scale morphogenesis is still poor. In this chapter, we will present two specific computational studies with the aim to understand the large-scale effects of proteins on the morphogenesis of lipid membranes. In Sects. 2 and 3, the collective effects of curvature-sensing proteins on the morphogenesis of biomembranes and the effect of the cortical cytoskeleton on blebbing of biomembrane are presented, respectively.

2 Protein-Induced Nonequilibrium Membrane Morphogenesis

Though membranes of different organelles have very different molecular compositions, many of the internal organelles exhibit similar ramified, tubular, or sheet-like shapes, suggesting that there may be a general physical mechanism giving rise to these common features. One such possible mechanism is the continuous flux of proteins and lipids between organelles, making the organelle membranes

highly dynamic [4]. How the large-scale morphology of the membrane-bound compartments could be influenced by the out-of-equilibrium processes of fission and fusion of material is intriguing. The steady-state shapes of the membranes, when they are subject to the binding–unbinding action of curvature-sensing and curvature-generating proteins, which modulate local membrane shape, is another aspect that will be considered here. Below, we discuss a model that incorporates the effect of curvature generation and removal, through the energy-consuming processes described above, to study the steady-state shapes of membrane compartments.

2.1 Model and Method

To be able to describe the ramified, strongly non-axisymmetric shapes of membrane organelles, over large spatiotemporal scales, we use a coarse-grained dynamical description of the membrane, governed by membrane elasticity, relaxational dynamics, and activity. The fluid membrane is represented as a triangulated closed surface with N vertices, denoted by $\{\vec{X}\}$, T triangles, and L links. This is represented by a triangulation map $\{\mathscr{T}\}$ (see Supplementary Section of reference [15] for a detailed description of the model). The elastic stresses can be described by the standard Canham–Helfrich energy functional, whose discrete form is given by:

$$\mathscr{H}_{\rm el} = \frac{\kappa}{2} \sum_{i=1}^{N} (H_i - H_{0i})^2 \, A_i - \Delta p_0 \, V \,, \tag{1}$$

where A_i is the area element associated with vertex i, H_i is the local mean curvature, and κ is the bending modulus, which we assume to be uniform for simplicity. H_{0i} is the local spontaneous curvature of the membrane and is nonzero only at the sites of activity. The presence of Δp_0 in this model sets the scale of the mean enclosed volume at equilibrium. This model has been used earlier to study non-axisymmetric multicomponent membranes both at equilibrium and when subject to nonequilibrium driving [16–19].

To model the active events of fission and fusion, which are driven by curvature-generating vesicle–protein complexes (cf. Fig. 1), we introduce a scalar field ϕ at every vertex i, which takes values $+1$ or -1, depending on whether this complex is bound to the membrane at i or not. The spontaneous curvature at vertex i is set to $H_{0i} = C_0(1 + \phi_i)/2$ in Eq. (1) such that the complex induces a local spontaneous curvature, C_0, when bound to vertex i ($\phi_i = 1$).

At every vertex i, the transition probabilities for $\phi_i \rightleftarrows -\phi_i$ are assumed to be independent of each other and are chosen as:

$$\mathcal{P}_{+\to-} = \epsilon_- \left(\frac{N_+}{N}\right) \frac{1}{1 + \exp(\zeta [N_+ - N_- - A_0])} \tag{2}$$

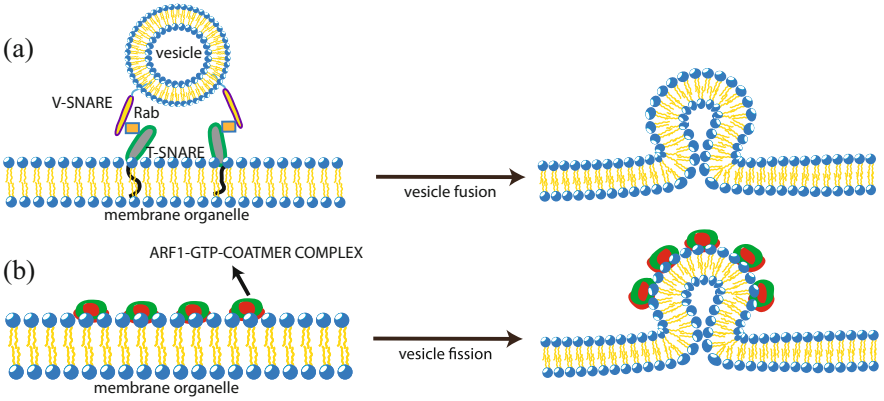

Fig. 1 Schematics of active fusion–fission-mediated curvature changes. (**a**) Fusion of a transport vesicle onto the organelle membrane is induced by energy-consuming Rabs–Snare complex and accompanied by membrane deformation. (**b**) Fission of transport vesicle from the organelle membrane is induced by energy-consuming Arf–Coat complex and accompanied by membrane deformation. Our study extends to other active membrane processes, such as the switching of membrane-bound pumps from their active to inactive forms. Reproduced from [15]

and

$$\mathcal{P}_{-\to+} = \epsilon_+ \left(\frac{N_-}{N}\right) \frac{1}{\eta + \exp(-\zeta[N_+ - N_- - A_0])}. \tag{3}$$

where $\epsilon_\pm$ denote the mean attempt rates for these nonequilibrium curvature changes, and $N_\pm$ denote the instantaneous numbers of vertices with $\phi_i = \pm 1$. For simplicity, we choose $\epsilon_- = \epsilon_+ = \epsilon$. These transition rates are determined by the preferred asymmetry parameter, $A_0 \equiv N_+^0 - N_-^0$, and the parameter ζ which sets the scale of fluctuations in $N_\pm$. N_+^0 and N_-^0 denote the steady-state mean values of N_+ and N_-; η is set to $(2\frac{N_-}{N_+} - 1)$ such that $N_\pm$ reaches $N_\pm^0$ at steady state. Note that the above transition probabilities do not depend on the energy change associated with a change in local configuration, $\phi \rightleftarrows -\phi$, and do not obey detailed balance. Detailed balance is however restored when we set the activity rate $\epsilon = 0$ or curvature–activity coupling $C_0 = 0$ [15].

In order to allow curvature generation resulting from the binding and unbinding of these complexes to be cooperative, the following Ising-type interaction is added to the Hamiltonian:

$$\mathscr{H}_\phi = -\frac{1}{2} \sum_{i=1}^{N} \sum_{j \in \Omega_i} J\, \phi_i \phi_j, \tag{4}$$

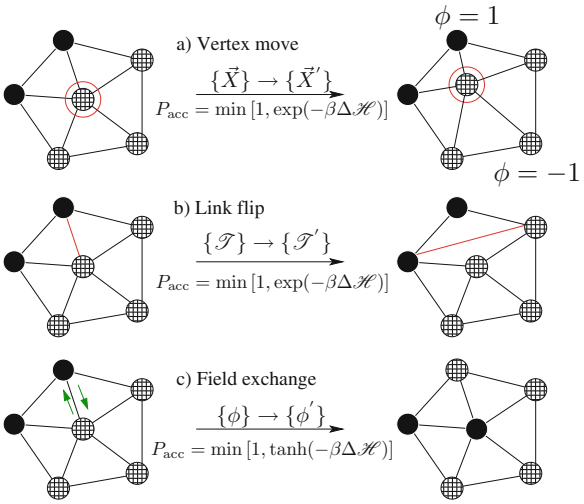

Fig. 2 DTMC of two-component fluid membranes. (**a**) A chosen vertex is randomly displaced in 3 dimensions keeping the connectivity $\{\mathscr{T}\}$ unchanged. (**b**) A link is flipped (red line) to change connectivity. (**c**) Kawasaki exchange of $\{\phi\}$ (green arrows) to enable diffusion of active protein complex on the surface (see text for notation). Here, $\beta \equiv 1/k_{\rm B}T$ ($k_{\rm B}$ is the Boltzmann constant and T is temperature) and $\Delta\mathscr{H}$ is the change in $\mathscr{H}$, Eq. (5), upon change in the conformational state of the membrane. In addition to the above moves, we carry out the active $\phi \rightleftarrows -\phi$ transitions at a rate set by ϵ. Reproduced from [15]

where the second summation is over sites $j \in \Omega_i$, the set of all vertices connected to i. Note that J can either be positive or negative. $J = 0$ corresponds to uncorrelated binding/unbinding of the complexes.

Figure 2 summarizes the full Dynamic Triangulation Monte Carlo (TDMC) dynamics including the active processes, the usual Kawasaki exchange moves of the field ϕ, and the Metropolis moves of membrane shape [16], using the full Hamiltonian:

$$\mathscr{H} = \mathscr{H}_{\rm el} + \mathscr{H}_{\phi}. \tag{5}$$

The unit of time is set by a Monte Carlo sweep (MCS), which corresponds to L attempts to flip links, N attempts to move vertices, N_+ attempts to exchange ϕ_i with neighboring vertices, and $N\epsilon$ attempts to flip the value of ϕ at vertices. Here, we present the results obtained for the case of $N_+^0 = 0.1N$. We vary ϵ, C_0, and J to explore the nonequilibrium steady-state morphologies of the membranes. κ and J are in units of $k_{\rm B}T$, and C_0 is in units of a_0^{-1}, where a_0 is the size associated with the coarse-grained vertices.

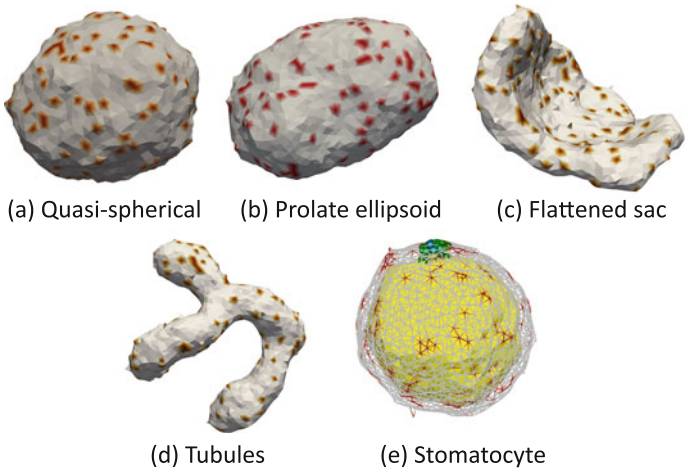

Fig. 3 Steady-state snapshots of the active vesicles. (**a**) Corresponds to $\epsilon = 0.1N/MCS$, $C_0 = 0.3$, and $J = 0$, (**b**) corresponds to $\epsilon = 0.25N/MCS$, $C_0 = 0.5$ and $J = 0$, (**c**) corresponds to $\epsilon = 0.1N/MCS$, $C_0 = 0.8$, and $J = 1$, (**d**) corresponds to $\epsilon = 0.1N/MCS$, $C_0 = 0.8$, and $J = 0$, and (**e**) corresponds to $\epsilon = 0.1N/MCS$, $C_0 = 0.8$, and $J = 5$

2.2 Dynamical Phase Diagram of Active Vesicles

Various steady-state shapes of the vesicle are obtained by changing the parameters ϵ, C_0, and J. These shapes can be broadly classified as: (a) quasi-spherical, (b) prolate ellipsoids, (c) flattened sacs, (d) tubules, and (e) stomatocytes, shown in Fig. 3. The steady-state morphologies for different parameters of $\epsilon - C_0$ and $\epsilon - J$ are summarized in the phase diagrams shown in Figs. 4 and 5, respectively.

From the $\epsilon - C_0$ phase diagram in Fig. 4, it is clear that the steady-state shapes depend strongly on the activity rate ϵ and that the effect of activity is higher for larger C_0. Similarly, as shown in Fig. 5 for $J > 0$, cluster formation *enhances* the effects of activity and curvature–activity coupling. As shown in Fig. 6a, cluster formation is more prominent when $J > 0$. However, we find that this cluster formation competes with activity which prevents larger clusters from forming. This is demonstrated by Fig. 6b, where we see that activity promotes small cluster formation while suppressing large clusters.

2.3 Activity-Induced Pressure

The ratio between the volume enclosed by the membrane V, and the volume V_0, of the sphere with the same surface area, collapses abruptly as the membrane shape transforms from a quasi-spherical conformation to a tubule or a disc, and thereafter smoothly approaches zero as the membrane transforms to a stomatocyte (Fig. 7). As

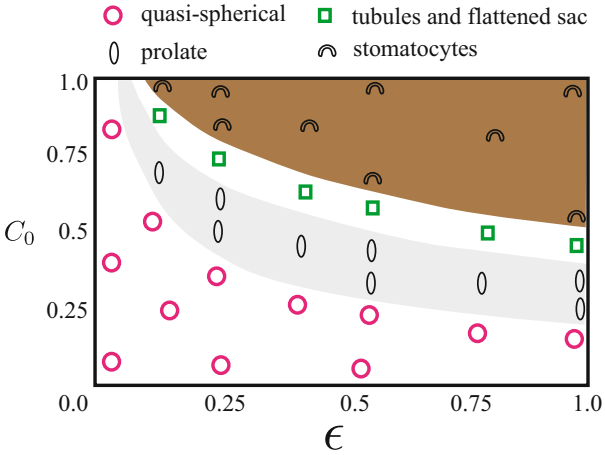

Fig. 4 Phases of the active closed membrane, for $J = 0$, as a function of C_0 and activity ϵ. The phase boundaries are mere guide to the eyes, determined by visual inspection of the dominant shape within an ensemble of morphologies simulated at each state point. Reproduced from [15]

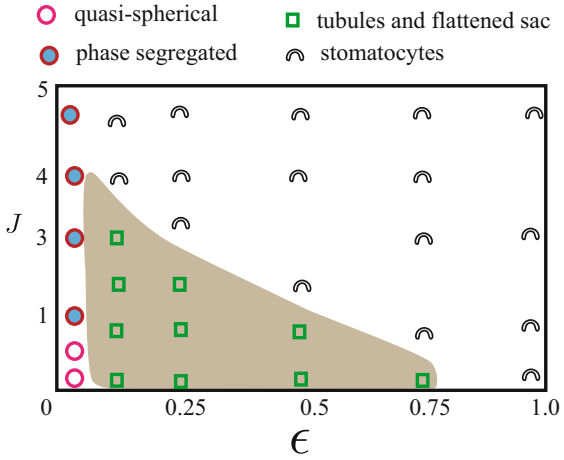

Fig. 5 Phase diagram of the closed active membrane as a function of J and activity ϵ, for a fixed $C_0 = 0.8$. Reprinted with permission from [15]. Reproduced from [15]

can be seen from the figure, this purely nonequilibrium *collapse transition* occurs at smaller value of C_0 when ϵ increases and is absent at equilibrium.

The volume enclosed by the membrane can also be changed by applying a pressure difference Δp_0 between the inside and the outside of the membrane. At large positive Δp_0, the membrane is an inflated sphere. The pressure required to fully inflate the membrane increases with C_0 and activity rate ϵ. The resulting V/V_0 vs. Δp_0 curves can be collapsed onto a single curve, when an activity-induced *dynamical pressure* Δp_a, which is negative, is added to Δp_0. This is shown in Fig. 8.

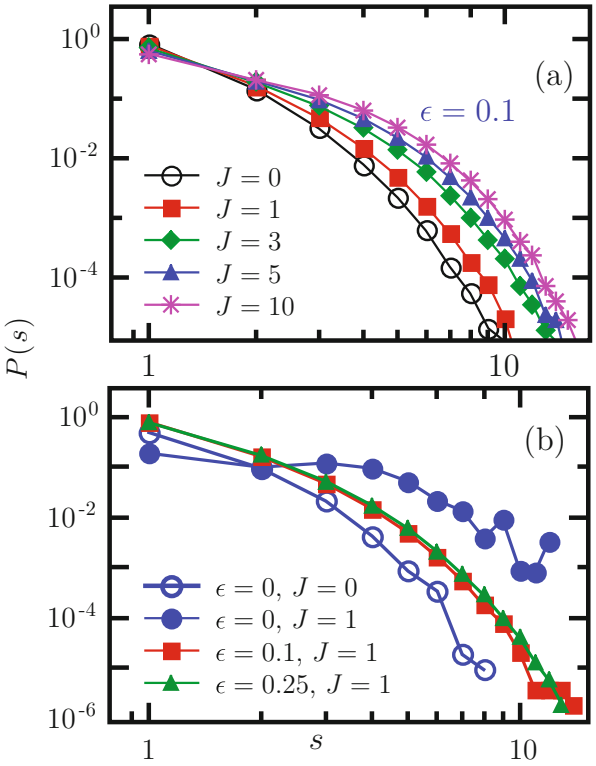

Fig. 6 Normalized cluster size distribution, $P(s)$, of the active species for different values of J at $\epsilon = 0.1N/MCS$ (**a**) and for different values of activity rate, ϵ in units of N/MCS (**b**). The equilibrium distributions ($\epsilon = 0$) for $J = 0$ and 1 are shown for comparison. Here, $N_+^0 = 0.1N$ and $C_0 = 0.8$. Reproduced from [15]

To calculate this dynamic pressure, we start with the steady-state configuration of the vesicle for a fixed activity rate and C_0, which will have $V/V_0 < 1.0$. We then find the pressure Δp needed to inflate the membrane such that $V/V_0 \approx 1.0$. This saturating pressure Δp is found to increase with activity rate and C_0 and when subtracted from Δp_0, the saturating pressure at equilibrium yields Δp_a, which is shown in the inset of Fig. 8. This additional pressure can be interpreted as arising from a dynamical tension $\sigma_a = -\epsilon\kappa C_0^2/(1+\epsilon)$ induced as the result of activity, which is consistent with the behavior of Δp_a shown in the inset of Fig. 8.

The results presented here establish a nonequilibrium mechanism through which membrane-bound organelles could maintain their shape. This mechanism could be acting at tandem with other equilibrium curvature generation processes by specialized proteins [10, 20].

The above results are pertinent to morphogenesis of cell organelle membranes as a result of their interaction with proteins. In the next section, we will present results for the morphogenesis of the plasma membrane as a result of its interaction with cytoskeletal proteins.

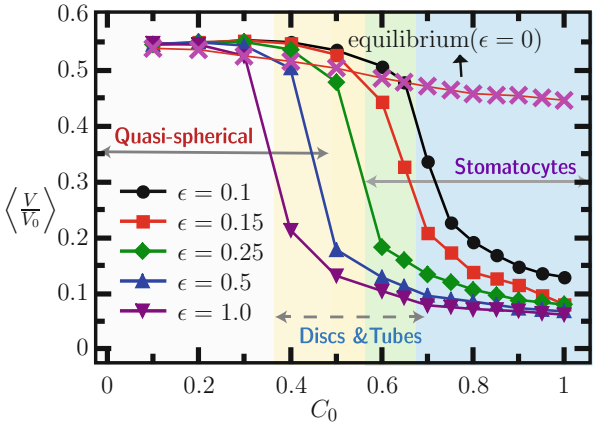

Fig. 7 Scaled enclosed volume (V/V_0) as a function of C_0 with $\kappa = 20$, $J = 0.0$, and $N_+^0 = 0.1N$ for different values of ϵ in units of N/MCS. The transition from quasi-spherical to tube, disc, and stomatocyte are shown by the various shaded regions for the specific case of $\epsilon = 0.1\, N/MCS$. The transition from a quasi-spherical vesicle to other shapes is characterized by a jump in the enclosed volume and gets sharper as ϵ increases. The equilibrium, $\epsilon = 0$, curve is when 10% of the vertices have a local spontaneous curvature C_0. Reproduced from [15]

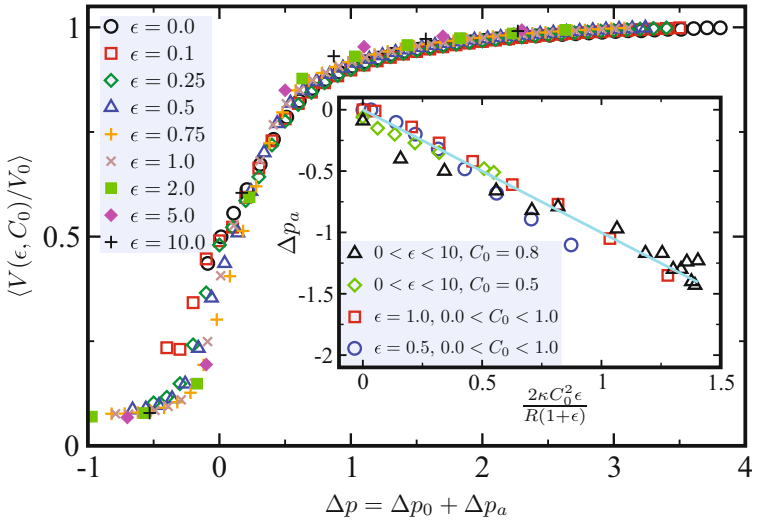

Fig. 8 Data collapse of the scaled enclosed volume versus the activity renormalized pressure, Δp. Data corresponds to $\kappa = 20$, $C_0 = 0.8$, $N_+^0 = 0.1N$ with $\epsilon = 0.0$, 0.1, 0.25, 0.5, 0.75, 1.0, 2.0, 5.0, and $10.0\, N/MCS$. *(Inset)* Computed values of the dynamic pressure Δp_a for different values of ϵ and C_0 show a good fit to $2\epsilon\kappa C_0^2/R(1+\epsilon)$, where $R \sim 19.4\, a_0$ is the radius of the fully inflated membrane. Reproduced from [15]

3 Cytoskeleton-Induced Membrane Morphogenesis

During processes such as cytokinesis, apoptosis, and cell migration, cells exhibit morphological changes in the form of spherical exoplasmic protrusion of their plasma membranes, known as blebs, that are mediated by the activity of the cortical cytoskeleton [21–28]. Blebs are triggered by a biochemical inhibition of myosin-II leading to the contraction of the cortical cytoskeleton [29] which then induces either a localized rupture of the cortex or a localized detachment of the lipid bilayer from the cortex (delamitation) [30–32]. Blebs can also be induced experimentally by a localized damage of the cortex via laser in suspended fibroblasts [30], by actin depolymerization [29], and by a rapid micropipette suction of cells [33]. Blebs are devoid of actomyosin, and grow into spherical shapes up to 2 μm in diameter. In cytokinesis and cell migration, actin and myosin recruitment and cortex reassembly within the bleb eventually leads to the retraction of the bleb [34]. While blebbing is mostly associated with nucleated cells, the suicidal death of red blood cells (erypotosis) is also characterized by blebbing of their plasma membrane [24]. Furthermore, during the late stages of the life of a red blood cell, a large fraction of its membrane is shed into small vesicles that are devoid of spectrin cytoskeleton. The fact that the shed vesicles are small, about 100 nm in diameter, suggests that their precursor blebs have a size of about the cytoskeleton corral size [32].

Despite the large amount of experimental studies of blebbing, only few theoretical and computational studies have been performed to investigate this phenomenon. Sens and Gov showed theoretically that blebbing is triggered when the compressive force of the cortical cytoskeleton overcomes the bending stress of the lipid bilayer [35]. Young and Mitran [36] and Strychalski and Guy [37] proposed a two-dimensional computational model for blebbing that accounts for the interactions between the cytosol, assumed to be Newtonian, and the elastic membrane and cortex. Other phenomenological models were later developed by Tozluoglu et al. [38] and Woolley et al. [39]. It is important to note that these phenomenological models consider the membrane as a stretchable surface in order to allow for the expansion of the bleb. Lipid bilayers, however, cannot sustain strains exceeding about 5%. In the present chapter, we will present the main results of a realistic molecular model for blebbing, based on self-assembled lipid bilayer vesicles with an explicit cortical cytoskeleton that is akin to that of red blood cells [40].

3.1 Molecular Model and Approach

In order to perform simulations over relatively large vesicles, a mesoscale implicit-solvent model for self-assembled lipids [41] is used to investigate membrane blebbing. A lipid molecule is coarse-grained into a semiflexible linear chain composed of one hydrophilic head bead (h) and two hydrophobic tail beads (t).

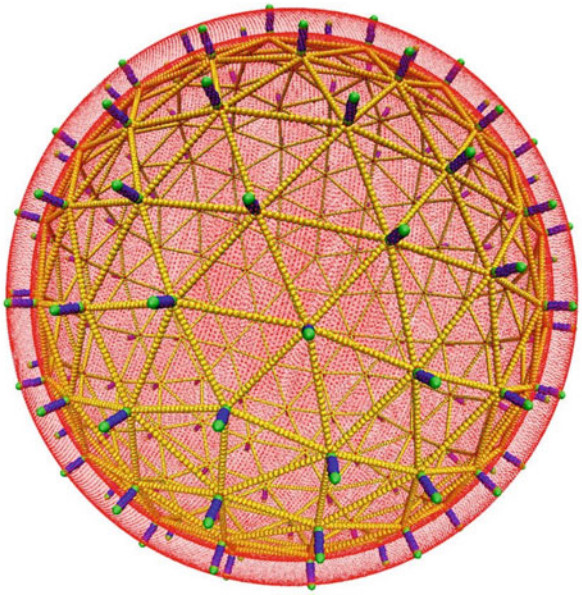

Fig. 9 The model of a lipid bilayer vesicle with cytoskeleton used in this study. Both head and tail beads of lipids are shown in red. Cytoskeleton beads are yellow. The vertices (black beads) connect the CSK to the lipid bilayer through bola-like lipids (green for their hydrophobic beads and orange for their hydrophilic beads)

Since the solvent in this model is implicit, the hydrophobic interaction that leads to the self-assembly of lipids is effectively accounted for by making $t - t$ interactions attractive. The inner (cytosolic) side of the self-assembled vesicle is apposed to a semiflexible polymer meshwork that is tessellated by triangles formed by linking the vertices with semiflexible polymer chains. The vertices themselves are connected to the bilayer by springs (see Fig. 9). In this model, beads interact with each other via two-body interactions, harmonic interactions for the bonds within each lipid or cytoskeleton, and three-body interactions to account for the bending rigidity of the lipid chains and the cytoskeleton [41]. The potential energy of the system can then be written as:

$$U\left(\{\mathbf{r}_i\}\right) = \sum_{i,j} U_0^{\alpha_i \alpha_j}\left(r_{ij}\right) + \sum_i U_{\text{bond}}^{\alpha_i \alpha_j}\left(r_{ij}\right) + \sum_i U_{\text{bend}}^{\alpha_i}\left(\mathbf{r}_{i-1}, \mathbf{r}_i, \mathbf{r}_{i+1}\right), \tag{6}$$

where $\mathbf{r}_i$ is the position of particle i, $r_{ij} = |\mathbf{r}_i - \mathbf{r}_j|$, and type of bead i, $\alpha_i = h, t$, or c for a lipid head bead, lipid tail bead, or a cytoskeleton bead, respectively. Details of the interaction potentials between particles are well described and discussed

in several articles by the authors [40–43]. The vesicle model with the apposed cytoskeleton meshwork in the inner side of the vesicle is shown in Fig. 9. Beads are moved using molecular dynamics with a Langevin thermostat [40].

3.2 Phase Behavior

To investigate the interplay between the lipid bilayer and tension of the cytoskeleton meshwork, a large number of simulations were performed for different values of the relaxed cytoskeleton corral area, $a^{(0)}_{\mathrm{CSK}}$, and a mismatch parameter defined as the ratio between the total area of the lipid vesicle, A_{LB}, and the total relaxed area of the cytoskeleton, $s = A_{\mathrm{LB}}/N_{\mathrm{cor}}a^{(0)}_{\mathrm{CSK}}$, where $N_{\mathrm{cor}} = 320$ is the number of the cytoskeleton corrals per vesicle. In the simulation, $a^{(0)}_{\mathrm{CSK}}$ is increased by increasing the number of beads per cytoskeleton strand between 8 and 22. For a given $a^{(0)}_{\mathrm{CSK}}$, the mismatch parameter, s, is increased by increasing the number of lipids per vesicle. Simulations were performed on vesicles composed of 3.5×10^4 to 2.5×10^5 lipids. $s = 1$ therefore corresponds to a vesicle with a relaxed cytoskeleton. $s < 1$ corresponds to a cytoskeleton that is compressed within the vesicle, and $s > 1$ corresponds to a cytoskeleton that is strained by the apposing lipid bilayer. The phase diagram of the system, depicted in Fig. 10, shows that the vesicle is uniform

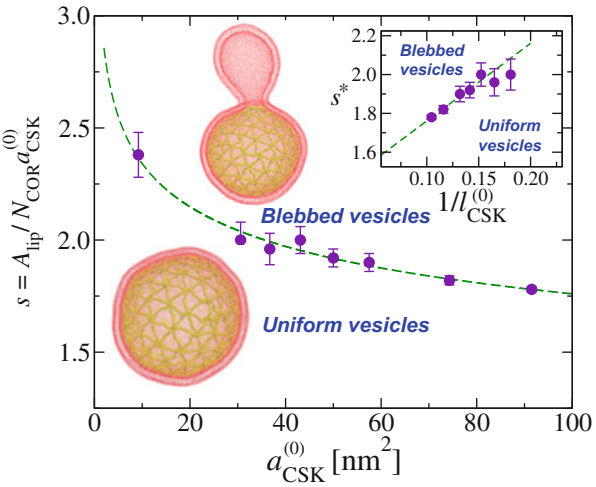

Fig. 10 Blebbing phase diagram in terms of the single corral relaxed area, $a^{(0)}_{\mathrm{CSK}}$, and the mismatch parameter. The inset shows the phase transition from the uniform phase to the blebbed phase versus the inverse of the linear size of the relaxed corral $1/l^{(0)}_{\mathrm{CSK}}$. The solid line is a fit with Eq. (9). The bottom and top snapshots are of a uniform and blebbed vesicle, respectively. Reproduced from [40]

for $s < s^*\left(a_{\mathrm{CSK}}^{(0)}\right)$, and is blebbed for $s > s^*\left(a_{\mathrm{CSK}}^{(0)}\right)$. The blebbing threshold, s^*, decreases with increasing the corral rest area. Within the uniform phase, the cytoskeleton conforms to the lipid bilayer. In the blebbing phase, however, the bleb is devoid of the cytoskeleton, in agreement with experimental observations.

The relationship between the threshold s^* and the corral relaxed area can be found using the following argument [35, 40]. The free energy of a vesicle in the uniform phase is the sum of the curvature energy of the lipid bilayer and the elastic energy of the cytoskeleton:

$$\mathcal{F}_{\mathrm{unif}} \approx 8\pi\kappa + \frac{e}{2} N_{\mathrm{cor}} a_{\mathrm{CSK}}^{(0)} \left(1 - \frac{a_{\mathrm{CSK}}}{a_{\mathrm{CSK}}^{(0)}}\right)^2, \tag{7}$$

where κ is the bending modulus of the lipid bilayer and e is the stretch modulus of the cytoskeleton. If the vesicle is blebbed, however, the cytoskeleton is relaxed, and the vesicle's free energy is therefore dominated by the curvature energy of the bleb and the main part of the vesicle (with apposed cytoskeleton):

$$\mathcal{F}_{\mathrm{bleb}} \approx 16\pi\kappa \left(1 - \frac{a_{\mathrm{CSK}}^{(0)}}{8\pi R_v^2} - \frac{a_{\mathrm{CSK}}^{(0)}}{8\pi R_b^2}\right), \tag{8}$$

where R_v and R_b are the radii of the main part of the vesicle and the bleb, respectively, both assumed to be spherical in shape. In Eq. (8), it is assumed that the area of the bleb's neck is almost equal to that of a relaxed corral. The transition point is obtained by equating the two free energies in Eqs. (7) and (8). In the case of $N_{\mathrm{cor}} \gg 1$, one then finds

$$s^* \approx 1 + \left(\frac{16\pi\kappa}{N_{\mathrm{cor}} e a_{\mathrm{CSK}}^{(0)}}\right)^{1/2}. \tag{9}$$

Therefore, s^* decreases linearly with $1/l_{\mathrm{CSK}}$, where l_{CSK} is the relaxed length of a cytoskeleton strand. This result is in very good agreement with Fig. 10, despite the relative small size of the corral size in this study.

To further understand the nature of blebbing in these simulations, the elastic energy of the cytoskeleton is shown as a function of the mismatch parameter for the case of $a_{\mathrm{CSK}}^{(0)} = 92 r_m^2$ in Fig. 11. This figure indicates that the elastic energy of the cytoskeleton is minimized around $s_{\mathrm{min}} \approx 1$ at which the cytoskeleton is tensionless. For $s < s_{\mathrm{min}}$, the elastic energy of the cytoskeleton is larger than its minimum value due to its confinement by the lipid vesicle. For $s_{\mathrm{min}} < s < s^*$, the elastic energy rises to a maximum value at which the cytoskeleton is very stretched by the conforming vesicle. The linear dependence of the $a_{\mathrm{CSK}}/a_{\mathrm{CSK}}^{(0)}$ for $s < s^*$ confirms that the cytoskeleton conforms to the lipid bilayer in this regime. The high

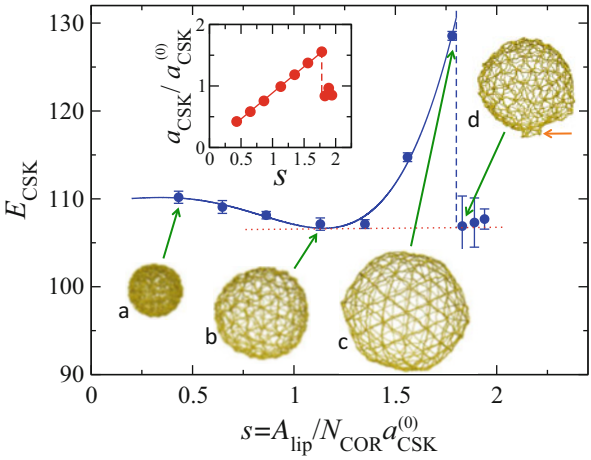

Fig. 11 Cytoskeleton elastic energy, per strand, vs. mismatch parameter, s, for the case of $a^{(0)}_{CSK} = 92r_m^2$. Inset shows the coral area, normalized by its rest area, vs. s, for the same system. Red (most right) arrow next to (d) points to the location of the bleb's neck. Reproduced from [40]

tension of the cytoskeleton for $s_{min} < s < s^*$ is compensated by the low curvature energy of the almost spherical vesicle.

The sharp discontinuity in the cytoskeleton elastic energy at s^* indicates the morphological transition of the vesicle from the uniform phase to the blebbing phase. At $s > s^*$, the elastic energy of the cytoskeleton is too high if it were to conform to a uniform vesicle. In this regime, the cytoskeleton retracts to release its tension and eventually conforms to a smaller portion of the vesicle. This is in line with Tininvez et al.'s findings [30]. At $s > s^* \approx 1.8$, the conformation of the cytoskeleton in the blebbing state (snapshot d in Fig. 11) is statistically identical to that of the cytoskeleton in the uniform phase in its relaxed state (snapshot b in Fig. 11). Figure 11 shows that the elastic energy of the cytoskeleton is minimized for $s > s^*$ implying that the cytoskeleton is essentially tensionless in the blebbed phase. The increase in the mismatch parameter therefore leads to an increase in the size of the bleb.

3.3 Kinetics of Bleb Formation and Expansion

The molecular model above is also used to investigate the kinetics of blebbing as a result of a localized rupture of the cytoskeleton. The rupture is initiated by arbitrarily selecting a vertex and dissociating it from its six neighbors. The numerical experiment is performed on a vesicle in the uniform phase with $a^{(0)}_{CSK} = 43.1r_m^2$ and $s = 1.9$, right below the transition line. The cytoskeleton is therefore initially under tension due to its conformity to the vesicle. Figure 12 shows that as soon as the vertex links are cleaved, the rest of the cytoskeleton undergoes compression, as demonstrated by the decrease in the average length of the cytoskeleton links (blue curve in Fig. 12). A small protrusion appears at the location where the cytoskeleton is cleaved. The velocity of the cap-shaped protrusion increases rapidly at early

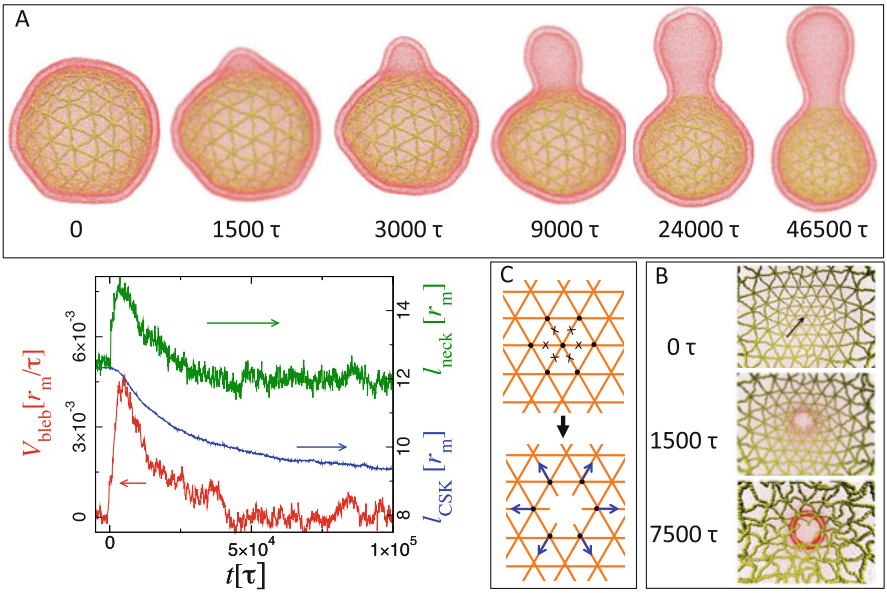

Fig. 12 Panel (**a**): Series of snapshots of a vesicle undergoing blebbing as a result of rupture of the cytoskeleton at the top. The initial state is at $a_{CSK}^{(0)} = 43.1 r_m^2$ and $s = 1.9$. Panel (**b**): Snapshots of the portion of the vesicle where the cytoskeleton rupture is applied. The arrow at $t = 0$ indicates the vertex cut from its six links. The dark red hallow indicates the neck of the bleb. Panel (**c**) schematically shows how a rupture of the links of a vertex leads to an imbalance of forces of the six neighboring vertices. The graph shows the bleb front velocity (red curve), the average length of a cytoskeleton strand between two neighboring vertices (blue curve), and the average length of a cytoskeleton strand in the neck (green curve). Reproduced from [40]

times (red curve in Fig. 12). This accelerated growth of the initial protrusion is accompanied by a rapid increase of the rim of its neck (blue curve in Fig. 12). At the same time, a cap appears at the location where the rupture is performed, as demonstrated by a positive velocity of the apex of the cap (red curve in Fig. 12). The velocity of the apex of the bleb reaches its maximum at about 5000τ, beyond which the neck size starts retracting, and the shape of the cap transforms into a bleb with a well-defined neck. The initial instability leading to the nucleation of a cap is the result of an imbalance of forces on the vertices linked to the cleaved links, as shown by Panel C in Fig. 12. The slowing-down of the bleb growth at intermediate times is associated with the reduction in the current of lipids flowing into the bleb from the main vesicle through the neck, which is proportional to the perimeter of the neck. It is interesting to note that here the growth of the bleb is due completely to the contraction of the cytoskeleton, since the solvent is implicit in this model. Nevertheless, the velocity of the bleb apex is in good qualitative agreement with that reported by Charras et al. [44].

In order to test what would happen if localized ruptures of the cytoskeletons happen at different locations and at different times, a series of simulations were

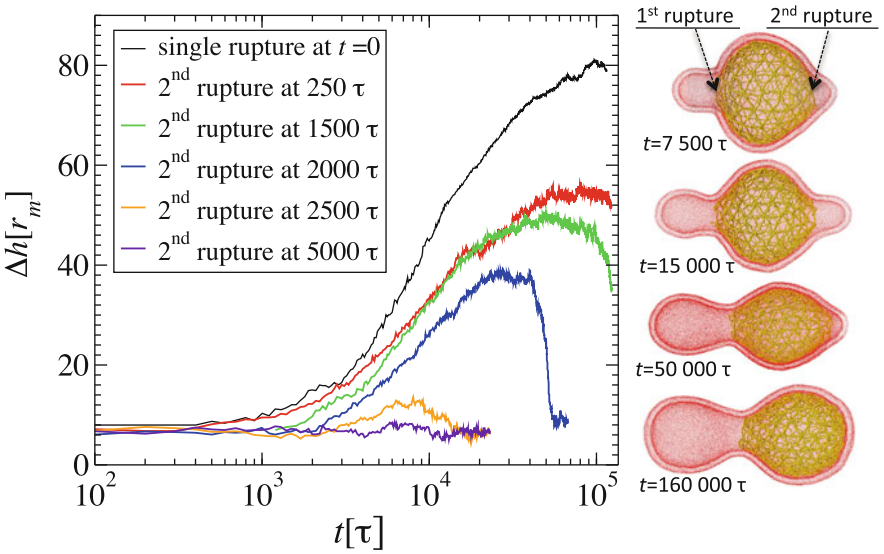

Fig. 13 This graph depicts the height of the second bleb when a vesicle is subjected to two consecutive localized cytoskeleton ruptures. The black curve shows the height of the bleb following a single rupture. The other curves from top to bottom correspond to a second rupture at $\Delta t = 250\tau$, 1500τ, 2000τ, 2500τ, and 5000τ, respectively. The series of snapshots on the right, which correspond to the case where the second rupture is applied at 2000τ, show the growth of the two blebs with time. The first and second ruptures are applied on the left and right, respectively. Reproduced from [40]

performed where a second rupture is applied at delayed time, Δt, at a location diametrically opposite to that of the first rupture. The height of the second bleb as a function of time together with a series of snapshots is shown in Fig. 13 monitored as a function of time.

The above study of blebbing is based on a model of self-assembled lipid bilayers with an explicit cytoskeleton model, while the cytosol is implicit in this model. Volume constraint and cytosol flow are not accounted for in this study. Cytosol flow has been assumed to be an essential ingredient of blebbing in several previous studies. The results above show that the equilibrium phase diagram of blebbing depends on the mismatch between the area of the membrane and the rest area of the cytoskeleton. Blebbing is triggered when the cytoskeleton is subjected to uniform contraction or localized damage, in line with experiments.

4 Concluding Remarks and Outlook

The above studies illustrate how simple models can capture aspects of morphogenesis of lipid membranes. It will be interesting to investigate the dynamics of the membrane in steady state using a model that accounts for hydrodynamics. This

will allow for the study of dynamical fluctuations at steady state which should be more accessible to experiments. In the case of blebbing, a generalized model that accounts for the effects of cytosol explicitly is warranted to understand how cytosolic flow affects formation and growth of blebs. In the case of the plasma membrane, it is believed that there are lipid reservoirs in the form of caveolae and other invaginations, which can dynamically control the excess area. Computational models that account for these effects would be highly desirable as well. With the current developments in computer power, such studies are plausible in the future.

Acknowledgements ML acknowledges financial support from NSF (DMR-0812470), NSF (DMR 0755447), and the Research Corporation (CC66879). PBSK acknowledges financial support from CSIR-India. The authors would like to thank N. Ramakrishnan, John Ipsen, Madan Rao, Eric Spangler, Cameron Harvey, and Joel Revalee for their contributions to the studies presented in this chapter.

References

1. Shibata Y, Hu J, Kozlov MM, Rapoport TA (2009) Mechanisms shaping the membranes of cellular organelles. Annu Rev Cell Dev Biol 25:329–354
2. Marshall WF (2011) Origins of cellular biology. BMC Biol 9:57
3. Martínez-Menárguez JA (2013) Intra-Golgi transport: roles for vesicles, tubules and cisternae. ISRN Cell Biol 2013:1–15
4. Alberts B, Johnson A, Lewis J, Raff M (2007) Molecular biology of the cell, 5th edn. Garland Science, New York
5. Frost A, Unger VM, De Camilli P (2009) The BAR domain superfamily: membrane-molding macromolecules. Cell 137:191–196
6. D'Souza-Schorey C, Chavrier P (2006) ARF proteins: roles in membrane traffic and beyond. Nat Rev Mol Cell Biol 7:347–358
7. Marks B, Stowell MHB, Vallis Y, Mills IG, Gibson A, Hopkins CR, McMahon HT (2001) GTPase activity of dynamin and resulting conformation change are essential to endocytosis. Nature 410:231–235
8. Baschieri F, Farhan H (2012) Crosstalk of small GTPases at the Golgi apparatus. Small GTPases 3:80–90
9. Harris KP, Littleton JT (2011) Vesicle trafficking: a Rab family profile. Curr Biol 21:R841–843
10. Zimmerberg J, Kozlov MM (2006) How proteins produce cellular membrane curvature. Nat Rev Mol Cell Biol 7:9–19
11. Chavrier P, Goud B (1999) The role of ARF and Rab GTPases in membrane transport. Curr. Opin. Cell Biol. 11:466–475
12. Turner M, Sens P, Socci N (2005) Nonequilibrium raftlike membrane domains under continuous recycling. Phys Rev Lett 95:168301
13. Wieland FT, Gleason ML, Serafini TA, Rothman JE (1987) The rate of bulk flow from the endoplasmic reticulum to the cell surface. Cell 50:289–300
14. Wirtz D (2009) Particle-tracking microrheology of living cells: principles and applications. Annu Rev Biophys 38:301–326
15. Ramakrishnan N, Rao M, Ipsen J, Sunil Kumar PB (2015) Organelle morphogenesis by active membrane remodeling. Soft Matter 11:2387
16. Sunil Kumar PB, Gompper G, Lipowsky R (2001) Budding dynamics of multicomponent membranes. Phys Rev Lett 86:3911–3914
17. Gompper G, Kroll D (1994) Phase diagram of fluid vesicles. Phys Rev Lett 73:2139–2142

18. Noguchi H, Gompper G (2005) Shape transitions of fluid vesicles and red blood cells in capillary flows. Proc Natl Acad Sci U S A 102:14159–14164
19. Ramakrishnan N, Sunil Kumar PB, Ipsen JH (2010) Monte Carlo simulations of fluid vesicles with in-plane orientational ordering. Phys Rev E 81:041922
20. Ramakrishnan N, Sunil Kumar PB, Ipsen JH (2013) Membrane-mediated aggregation of curvature-inducing nematogens and membrane tubulation. Biophys J 104:1018–1028
21. Paluch E, Sykes C, Prost J, Bronens M (2006) Dynamic modes of the cortical actomyosin gel during cell locomotion and division. Trends Cell Biol 16:5–10
22. Mills JC, Stone NL, Erhardt J, Pittman RN (1998) Apoptotic membrane blebbing is regulated by myosin light chain phosphorylation. J Cell Biol 140:627–636
23. Burton K, Taylor DL (1997) Traction forces of cytokinesis measured with optically modified elastic substrata. Nature (London) 385:450–454
24. Föller M, Huber SM, Lang F (2008) Erythrocyte programmed death. IUBMB Life 60:661–668
25. Barros LF, Kanaseki T, Sabirov R, Morishima S, Castrom J, Bittner CX, Maeno E, Anod-Akatsuka Y, Okada Y (2003) Apoptotic and necrotic blebs in epithelial cells display similar neck diameters but different kinase dependency. Cell Death Differ 10:687–697
26. Mercer J, Helenius A (2009) Vaccinia virus uses macropinocytosis and apoptotic mimicry to enter host cells. Science 320:531–535
27. Charras G, Palluch E (2008) Blebs lead the way: how to migrate without lamellipodia? Nat Rev Mol Cell Biol 9:730–736
28. Paluch EK, Raz E (2013) The role and regulation of blebs in cell migration. Curr Opin Cell Biol 25:582–590
29. Paluch E, Piel M, Prost J, Bornens M, Sykes C (2005) Cortical actomyosin breakage triggers shape oscillations in cells and cell fragments. Biophys J 89:724–733
30. Tinivez J-Y, Shulze U, Salbreux G, Roensch J, Joanny J-F, Paluch E (2009) Role of cortical tension in bleb growth. Proc Natl Acad Sci U S A 106:18581–18586
31. Charras GT, Coughlin M, Michison TJ, Mahadevan L (2008) Life and times of a cellular bleb. Biophys J 94:1836–1853
32. Sheetz MP, Sable JE, Döbereiner H-G (2006) Continuous membrane-cytoskeleton adhesion requires continuous accommodation to lipid and cytoskeleton dynamics. Annu Rev Biophys Biomol Struct 35:417–434
33. Merkel R, Simson R, Simson DA, Hohenadl M, Boulbitch A, Wallraff E, Sackmann E (2000) A micormechanic study of cell polarity and plasma membrane cell body coupling in Dictyostelium. Biophys J 79:707–719
34. Charras GT, Hu CK, Coughlin M, Mitchison TJ (2006) Reassembly of contractile actin cortex in cell blebs. J Cell Biol 175:477–490
35. Sens P, Gov N (2007) Force balance and membrane shedding at the red-blood-cell surface. Phys Rev Lett 98:018102
36. Young J, Mitran S (2010) A numerical study of cellular blebbing: a volume-conserving, fluid-structure interaction model of the entire cell. J Biomech 43:210–220
37. Strychalski W, Guy RD (2013) A computational model of bleb formation. Math Med Biol 30:115–130
38. Tozluoglu M, Tournier AL, Jenkins RP, Hooper S, Bates PA, Sahai E (2013) Matrix geometry determines optimal cancer cell migration strategy and modulates response to interventions. Nat Cell Biol 15:751–762
39. Woolley TE, Gaffney EA, Walters SL, Oliver JM, Baker RE, Goriely A (2014) Three mechanical models for blebbing and multi-blebbing. IMA J Appl Math 79:636–660
40. Spangler EJ, Harvey CW, Revalee JD, Sunil Kumar PB, Laradji M (2011) Computer simulation of cytoskeleton-induced blebbing in lipid membranes. Phys Rev E 84:051906
41. Revalee JD, Laradji M, Sunil Kumar PB (2008) Implicit-solvent mesoscale model based on soft-core potentials for self-assembled lipid membranes. J Chem Phys 128:035102
42. Sikder MKU, Stone KA, Sunil Kumar PB, Laradji M (2014) Combined effect of cortical cytoskeleton and transmembrane proteins on domain formation in biomembranes. J Chem Phys 141:054902

43. Spangler EJ, Sunil Kumar PB, Laradji M (2012) Anomalous freezing behavior of nanoscale liposomes. Soft Matter 8:10896–10904
44. Charras GT, Yarrow JC, Horton MA, Mahadevan L, Mitchison JT (2005) Non-equilibration of hydrostatic pressure in blebbing cells. Nature (London) 435:365–369

Fluctuations in Active Membranes

Hervé Turlier and Timo Betz

Abstract Active contributions to fluctuations are a direct consequence of metabolic energy consumption in living cells. Such metabolic processes continuously create active forces, which deform the membrane to control motility, proliferation as well as homeostasis. Membrane fluctuations contain therefore valuable information on the nature of active forces, but classical analysis of membrane fluctuations has been primarily centered on purely thermal driving. This chapter provides an overview of relevant experimental and theoretical approaches to measure, analyze, and model active membrane fluctuations. In the focus of the discussion remains the intrinsic problem that the sole fluctuation analysis may not be sufficient to separate active from thermal contributions, since the presence of activity may modify membrane mechanical properties themselves. By combining independent measurements of spontaneous fluctuations and mechanical response, it is possible to directly quantify time and energy-scales of the active contributions, allowing for a refinement of current theoretical descriptions of active membranes.

Keywords Lipid bilayer · Membrane physics · Non-equilibrium fluctuations · Active matter · Fluctuation–dissipation · Cytoskeleton

1 Introduction

Biological and biomimetic membranes consist in bilayers of phospholipids, which can embed various transmembrane or peripheral proteins. They constitute a selectively permeable barrier between distinct biological compartments, such as the

H. Turlier (✉)
Center for Interdisciplinary Research in Biology, Collège de France, PSL Research University, CNRS UMR7241, Inserm U1050, Paris, France
e-mail: herve.turlier@college-de-france.fr

T. Betz
Institute of Cell Biology, Center for Molecular Biology of Inflammation, Muenster, Germany
e-mail: timo.betz@uni-muenster.de

P. Bassereau, P. Sens (eds.), *Physics of Biological Membranes*,
https://doi.org/10.1007/978-3-030-00630-3_21

cytosol and extracellular medium. The stability of lipid bilayers in water is the result of an entropic effect, which combines non-covalent interactions between hydrophobic and hydrophilic parts of lipids. This leads to a large in-plane rigidity, making lipid bilayers almost incompressible: area strains of only 2–4% are generally enough to rupture a membrane. The non-covalent nature of interactions makes phospholipid bilayers moreover tangentially fluid. Any tangential force on a lipid or embedded protein will lead to lateral flows balancing almost instantly any density gradient. Bending a lipid bilayer, in contrast, requires only to slightly displace the polar heads, which are separated by a distance of the order of 0.5–1 nm [1, 2]. The bending modulus, generally denoted κ, is therefore not very large compared to thermal energy, of the order of a few tens of $k_B T$, which explains why membrane bending modes are readily excited at ambient temperatures. Hence, biological membranes are continuously fluctuating as a result of the thermal agitation of the surrounding medium, and this movement is directly observable using standard microscopy. However, besides thermal agitation, non-equilibrium active forces, of intrinsic or extrinsic origins, may also contribute and enhance membrane fluctuations. If such active fluctuations have random, uncorrelated sources, it remains however complicated to determine by simple observation to which extent membrane undulations are driven by thermal or by non-equilibrium effects.

One of the most prominent examples of fluctuating biological membranes is the "flickering" of red blood cells, already described in the nineteenth century [3]. Since its first observation, the origin of red blood cell flickering had been debated and only recently its possible active nature has been precisely investigated [4–7]. Initially, flickering was suggested to be passive, similar to the Brownian motion of microscopic particles [8, 9]. But in 1951, the amplitude of flickering was shown to be correlated to ion transport across the membrane [10], suggesting a possible active metabolic driving. However, this metabolic interpretation was soon revised as flickering was also observed in the absence of ATP in red blood cell ghosts [11]. After this finding, the pure passive origin of the flickering was generally accepted for more than 40 years [12], until in 1997 new experimental approaches revealed a change in the membrane fluctuations amplitude upon ATP starvation [4]. These new experiments, however, remained debated and a series of conflicting results were reported [13]. While most of the differences may be attributed to variations in preparation protocols, more and more indirect findings suggested that an active driving may contribute to the low frequency fluctuations spectrum [5, 14]. A conclusive experimental evidence for the active nature of red blood cell flickering was recently given by comparing directly flickering and mechanical response of the membrane [7]. The experimental observations could show that the flickering directly violates equilibrium statistical mechanics, proving the presence of non-equilibrium active forces driving membrane movement. This is an emblematic case of scientific controversy that took about 125 years to be conclusively resolved.

As this example attests, it remains difficult to evaluate to which extent active processes may contribute to membrane fluctuations. In general, active fluctuations are superimposing upon passive thermal fluctuations, and from an experimental point of view, active and passive fluctuations may share similar characteristics.

Hence, active contributions might not be visible, especially if thermal agitation dominates the fluctuation spectrum at the specific membrane position, length scale or timescale of interest. In this view, to answer the question whether fluctuations are active or passive, one should always define the relevant time and length scales involved.

From a mechanistic point of view, active membrane fluctuations originate from the conversion of metabolic energy into forces by proteins inserted in the bilayer, or connected to it (Fig. 1a). One may define active membrane fluctuations as intrinsic, when they are produced by proteins directly embedded in the membrane, or extrinsic when activity originates from an independent structure tethered to the membrane, like the cytoskeleton.

Active membrane fluctuations originating from ion pumps have been the focus of pioneering biophysics studies over the last decades, both from theoretical [15–17] and experimental perspectives [18–21]. These studies show that the activity of pumps leads to significant modifications in the fluctuation properties of reconstituted vesicles, measured as changes in the fluctuation amplitude, in the effective membrane tension or in the excess surface area. Besides ATP or photon driven ion pumps, lipid transport systems such as flipases and flopases [22] may also contribute to active fluctuations, as well as membrane fusion and fission of transport vesicles [23].

Active fluctuations can also originate from the interaction of the membrane with the underlying cytoskeleton, such as the spectrin network or the actomyosin cortex. In this case, the potential sources of active forces on the membrane are various: the proteins linking the membrane may change their binding affinity, or mechanical properties, upon phosphorylation, the cytoskeleton may exert tangential and normal forces on the bilayer under the action of molecular motors, or via polymerization of filaments.

The aim of this chapter is to present methods used to measure membrane fluctuations, to analyze their active and passive components, and to show how active membrane fluctuations may be modeled theoretically.

2 Experimental Observations of Active Membrane Fluctuations and Indications of Activity

A challenging experimental task is to show that the observed fluctuations are active by nature. This requires separating the active and passive contributions in the fluctuation spectrum. A typical approach proposed to detect active fluctuations was to remove the source of chemical energy, primarily ATP, and then to attribute possible differences to active processes. Unfortunately, biological membranes are complex systems, and the suppression of metabolic energy sources does not only remove active noise, but it may also change the mechanical properties of the membrane. For example, ion pumps do not only contribute to active fluctuations but are also important for maintaining the osmotic pressure in the cell. This is, in turn,

a key element determining membrane tension, and therefore influencing thermal fluctuations characteristics. It remains therefore generally challenging to disentangle fluctuations changes due to the suppression of activity from the ones due to passive mechanical variations. Another example is cytoskeletal softening or stiffening upon ATP depletion [24, 25]. In both cases, a simple removal of the energy source is not sufficient to pin down the contribution of active forces to the measured membrane fluctuations. In the following we will review different approaches that have been proposed to tackle this question in the context of membranes.

2.1 Micropipette Aspiration: Surface Tension and Excess Area

Surface tension is formally defined as the energy required to change surface area, but in lipid bilayers, the real surface can only be modified by a few percent before rupturing. However, a significant amount of membrane area is stored in the fluctuations, leading to clear difference between the total membrane area and its projected area (or apparent surface) (Fig. 1a). In other words, the apparent surface is always smaller than the real surface of the membrane, and this difference is called membrane excess area. When applying a tensile force to a membrane, the amplitude of the fluctuations is reduced and the apparent area increases, corresponding to a decrease of excess area (Fig. 1b). For a vesicle or a cell, where the volume and total membrane area are supposed constant, the excess area is on the contrary fixed. In

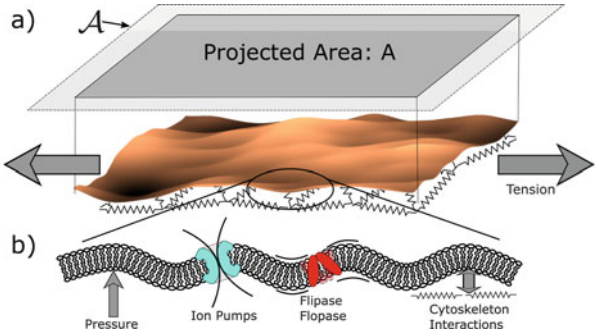

Fig. 1 Introduction of the concepts of membrane fluctuations, projected area surface tension and of the different active processes driving membrane fluctuations. (**a**) Thermal and active fluctuations buffer a significant fraction of the total membrane area, so that the projected area A is smaller than the real area $\mathcal{A}$. Lateral pulling forces effectively reduce the amplitudes of continuous fluctuations to extend the projected area. Hence these forces pull out the membrane reservoir that is stored in the fluctuations. The energy required to increase the projected area is used to define a membrane tension. It should be noted that this definition of tension depends on the entropic effect of thermally excited fluctuations. Biological membranes are typically connected to an underlying network of cytoskeletal elements such as F-actin or spectrin. (**b**) Beside thermal agitation, membrane fluctuations can be driven by active, force generating processes such as ion pumps or lipid transporters activity or via mechanical coupling to the underlying cytoskeleton

this case, active forces are expected to increase the fluctuations amplitude compared to pure thermal driving, leading to an increase of tension (see Sect. 4.2.4).

Building on this physical reasoning, one of the first experiments showing that an active process can change membrane fluctuations was done in biomimetic liposomes, combining classical micropipette aspiration techniques with purified bacteriorhodopsin proteins. Bacteriorhodopsin is a light-driven transmembrane pump, which transfers protons across the membrane when exposed to green–yellow light of wavelength around 566 nm [26]. Each time a proton is pumped, the membrane experiences a small active force. To measure this activity, micropipette aspiration was used. In this method the membrane area stored in fluctuations is measured by steadily increasing the aspiration pressure while following the changes in surface area. This change is calculated by following the length of the membrane tongue, while knowing the inner radius of the micropipette (Fig. 2a). In passive

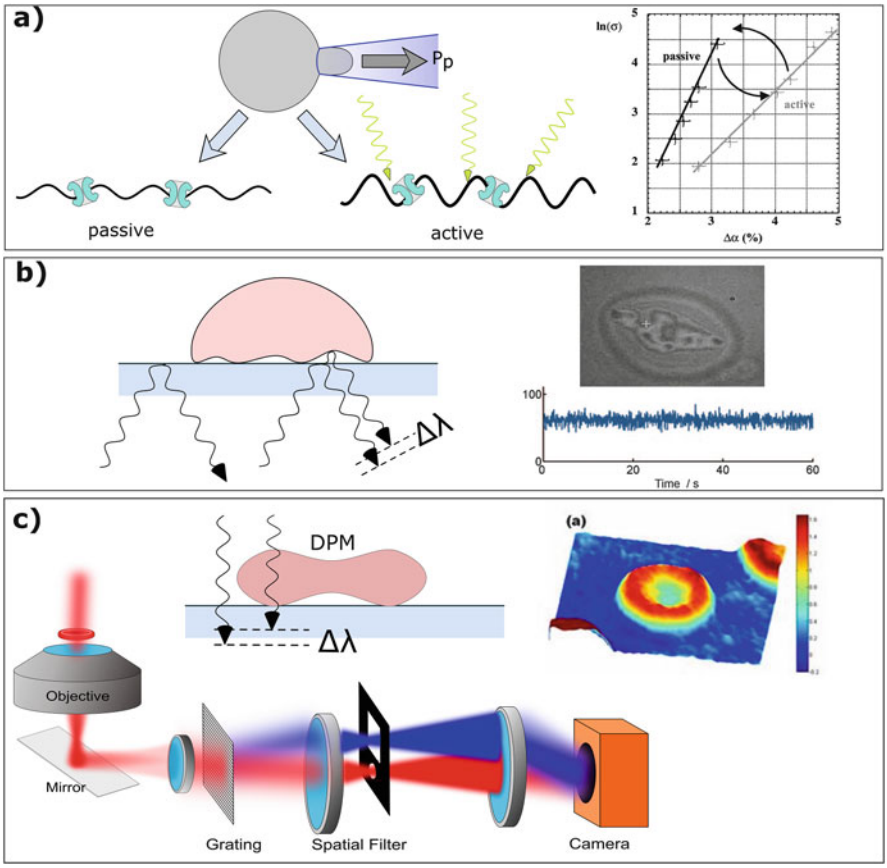

Fig. 2 Summary of the currently used techniques to study active and passive membrane fluctuations. (**a**) Active fluctuations can be measured as an increase of area stored in the membrane

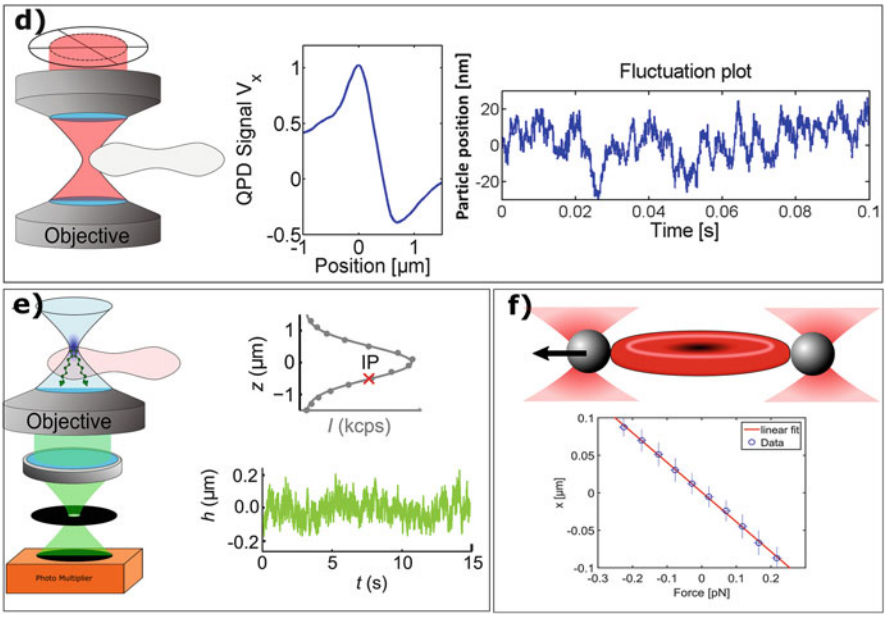

Fig. 2 (continued) fluctuations upon illumination with light (data reproduced with permission from [19]). (**b**) A further method to determine membrane fluctuations is based on RICM, where constructive and destructive interference from reflections at the glass and membrane surface are detected with a camera. (**c**) More recently DPM has been introduced which measures thickness changes by exploiting the change in optical path along the light propagation through the object to be measured (inset adapted from [27, Figure 2]). (**d**) By exploiting the phase shift of light partially touching a membrane, the lateral fluctuations can be measured using an interferometric approach using a quadrant photodiode. (**e**) Another new technique related to fluorescence correlation spectroscopy can measure height fluctuations of a membrane with excellent spatial and temporal resolution (data reproduced from [28]). (**f**) Finally, direct membrane mechanics can be measured using optical tweezer-based pulling on the membrane

membranes, equilibrium statistical mechanics allows to predict that the logarithm of the applied tension is a linear function of the excess area. For the equilibrium case, the slope of this curve is proportional to κ/k_BT (see Eq. (6)). Intuitively a larger bending rigidity will indeed decrease the area stored in fluctuations, and a smaller excess area should hence be measured at the same stretching force. Conversely, increasing temperature will increase the area stored in fluctuations. When light sensitive ion pumps are activated by exposing the liposome to yellow–green light, the slope of the logarithm of tension vs. excess area curve is significantly changed, indicating a larger excess area stored in fluctuations. To explain the experimental result, the real temperature can be simply replaced by an increased effective temperature. Hence, the difference between the real and the effective temperature can be used to estimate the energy injected to drive active membrane fluctuations.

In the case of bacteriorhodopsin the effective temperature was found to be about twice the real temperature [19]. In a further experiment using a calcium pump driven by ATP hydrolysis, the effective temperature was found to be in the same range [21]. In these experiments a clear dependence of the effective temperature on the pump concentration was observed.

Micropipette aspiration experiments provide hence a clear hint that membrane fluctuations are enhanced by active processes. Yet the actual fluctuations are only measured indirectly from the excess area. Other methods provide more direct access to membrane fluctuations and to possible active contributions.

2.2 Image-Based Contour Analysis

Video microscopy provides direct spatial and temporal access to membrane fluctuations. Brochard and Lennon have pioneered its use to determine relative thickness fluctuations in red blood cells, responsible for the flickering effect [12]. At the time, an equilibrium model was used to analyze the membrane fluctuation spectrum; however, as only relative amplitudes were measured it was not possible to extract mechanical properties from this model. This seminal work triggered a series of experiments aiming at inferring mechanical properties of biological and biomimetic membranes from precise measurement of their fluctuation spectrum. In a further improvement, image processing algorithms were developed to determine the time-dependent fluctuation amplitudes as a function of lateral modes in liposomes and red blood cells. This was used by Sackmann and coworkers to gain experimental access to membrane properties such as the bending modulus and, in later work, to infer an effective tension value in red blood cells [29, 30]. Over the following years, these techniques have been successfully refined, taking advantage of the rapid development in computer processing power and optical microscopy methods, paired with faster image acquisition methods [31]. However, in all these works, pure passive membrane models were used to analyze the data, including the case of red blood cells. First approaches to study the fluctuation dynamics of active membranes were done again on the bacteriorhodopsin system, where a mode-dependent enhancement of the fluctuations was confirmed [20]. More recently, optical tweezers have been used to systematically excite well-defined fluctuation modes and to subsequently study the mode-dependent relaxation behavior of the membrane [32]. Mode-dependent studies of active membranes allow to study possible complex mode-couplings due to activity or nonlinear interactions, which have remained overlooked so far. This approach may turn to be essential to study large biological membrane fluctuations, where the cytoskeleton may be the dominant source of active forces.

2.3 Interferometric Methods: Edge and Height Fluctuations

Video microscopy analysis of membrane movement still suffers from limited spatial and temporal resolution and from complex and long image processing. To overcome this, a number of alternative methods have been developed that exploit interferometric approaches to gain sub-nm precision, with sometimes even μs time resolution. Here we will briefly discuss different approaches and their application to active membranes. Among the first interferometric techniques applied to measure membrane fluctuations is the reflection interference contrast microscopy (RICM, Fig. 2b) which allows to determine the distance between a membrane and the glass substrate with a resolution down to 1 nm [33]. Monochromatic light is reflected at the glass–medium interface as well as at the medium–membrane interface. Both reflected waves interfere on the camera either destructively or constructively, depending on the phase shift $\Delta\lambda$ of the light. The interference represents the distance between the membrane and the glass, and is used to detect height fluctuations of a membrane in close proximity to the glass. RICM has been extensively used to study attachment phenomena in both equilibrium and non-equilibrium situations [34, 35].

A further interferometric method that was used to detect active membrane fluctuations in red blood cells is diffraction phase microscopy (DPM, Fig. 2c). Here the optical path of the light traveling through the object creates an interference pattern where the zero and first order diffracted beams are arranged to interfere on a camera chip. The final image has diffraction limited resolution in the image plane, and nm precise resolution of membrane height fluctuations. Combined with a fast camera this allows spatially resolved membrane height fluctuations with a time resolution that essentially depends on the camera acquisition speed. Using this method it was recently shown that the positional probability distribution of the red blood cell membrane height has non-Gaussian contributions that were proposed to result from active processes [5]. However, also other possible explanation can give rise to such non-Gaussian behavior in an equilibrium situation, such as nonlinear force–displacement relations often found in biological systems. Interestingly, these additional contributions depend on the local curvature, with increased fluctuations at more curved regions.

While RICM and DPM are sensitive to height fluctuations of passive and active membranes, another interferometric method was developed to determine the lateral fluctuations on a membrane at the rim of a cell or a liposome. The method is called time resolved membrane fluctuations spectroscopy and relies on a tight illumination of the membrane edge where part of the light penetrates the membrane and part is not interacting with the object (Fig. 2d). Typically this is done by a focused laser beam that is precisely positioned at the membrane interface [6]. As the common objects of interest provide a higher internal refractive index than the medium, the photons that traverse the object acquire a phase delay with respect to the photons that do not interact with the object. All the light is collected by a high numerical aperture condenser and the back focal plane of this condenser is imaged on a position sensitive detector or a quadrant photodetector. A calibration curve relates

the position of the membrane to the signal on the detector and allows to determine the membrane fluctuations with sub-nm and μs temporal precision. The advantage of this method is that it is very fast, it does not require complex post-processing, and it can be applied to any membrane oriented parallel to the axial direction of the laser focus. This technique was successfully used to determine the fluctuation spectra of red blood cells, growing membrane blebs and biomimetic liposomes [6, 36, 37]. A similar technique derived from dark field microscopy was previously used to determine the relative fluctuations amplitudes of membranes in the context of red blood cells [4]. In the absence of a calibration procedure, this initial approach was not able to determine the absolute membrane position, but the relative measurement gave the first insights into possible active effects on red blood cell membrane fluctuations.

2.4 Fluorescent Detection of Axial Fluctuations

Recently, a fluorescence-based method has been used to determine height fluctuations of red blood cells and other cell types by combining a confocal imaging method with a fast detector. Called dynamic optical displacement spectroscopy (DODS) this technique is in principle closely related to fluorescence correlation spectroscopy, with the difference that not the lateral diffusion of membrane bound molecules, but the out-of-plane movement of the full membrane is measured. When a high concentration of fluorescent molecules is present in the membrane, it is not the number of molecules in the focus that dominates the signal, but the position of the membrane with respect to the focal plane. Since the detector is placed behind a confocal pinhole, only the fluorescent signal originating from the focal region is detected. The resulting fluorescence intensity as a function of the axial (z) position corresponds to the point spread function of the pinhole. Hence, the fluorescent intensity can be translated into the axial position of the membrane. This results in a axial precision below 20 nm and a temporal resolution of 20 μs. DODS successfully verified the non-Gaussian behavior of the membrane fluctuations in red blood cells and the dependence of these fluctuations on the local curvature of the membrane [28]. In contrast to the DPM method introduced above, DODS has a superior time resolution similar to the time resolved membrane fluctuation spectroscopy. Furthermore, it is not limited to samples providing a homogeneous optical density, but can, in principle, be used on any object.

2.5 Optical Tweezers

A direct method to probe active membranes is based on optical tweezers (Fig. 2f). Here the momentum transfer of a highly focused laser generates a net force on arbitrary shaped particles if their refractive index is higher than the surrounding

medium. In a typical situation, micrometer sized beads are trapped, calibrated, and then used to apply well-defined forces on the object of interest. Initially, optical tweezers were used to measure the mechanical properties of red blood cells in the linear and nonlinear regimes [38, 39]. Many optical tweezer setups are also capable to detect the movement of single particles with very high precision. Here, the same methodology as for the time resolved membrane fluctuation spectroscopy is used, where a position sensitive detector measures asymmetries in the light deflected off the object in the beam path. The combination of these capabilities was used to determine both the mechanical response function of a red blood cell membrane and the spontaneous fluctuation spectrum of the same cell. For this, polystyrene beads are attached to the membrane and serve simultaneously as handles to fix the cell in space, as probe particles that can apply precise forces and as position sensors to follow the membrane deformation. In a first experimental system two beads were attached to a red blood cell, and both the mechanical properties and the fluctuations were studied. However, in this approach the fluctuations were not fully free as the beads needed to be still optically trapped, and hence the free membrane fluctuations were partially suppressed by the trapping potential created by the laser [40]. To explore the full fluctuation spectrum, a more complex four beads system was developed [7]. Here, four beads are attached on opposing sides on the rim of the red blood cell, and three of them are trapped by a tweezer and serve as handles to maintain the cell at a well-defined and stable position. The fourth bead is either forced to oscillate with a well-defined frequency, or simply allowed to move freely without any force to measure the free membrane fluctuations. In this setup the probe bead is not restricted in its movement by a laser trap. If the membrane fluctuations are purely thermal, equilibrium statistical mechanics connects the membrane fluctuation characteristics with the dissipative response of the membrane, and the tweezer setup was used to check this correspondence. The power of this approach is that it does not only provide clean experimental access to systematically study the active fluctuations and mechanical properties of a membrane, but it also results in precise frequency-dependent data. This permits comparison to detailed theoretical models, which include temporal characterization of the active membrane fluctuations.

3 Analysis of Active Membrane Fluctuation Data

The different experimental methods described above provide various determinations of membrane fluctuations, ranging from their indirect assessment by the excess area to direct spatio-temporal measurements using video microscopy. To give sense to these experimental data, analysis methods have been developed. They can be separated into static analysis that presents typically time averages or histograms without consideration of time-dependent aspects, and on the other hand dynamic analysis concepts such as the autocorrelation function and the power spectral densities, which directly quantify temporal variations in membrane position. In

general, dynamic analysis provides more extensive insight in fluctuations properties, but it requires stringent time resolution and a large number of datapoints to produce statistically relevant results.

Analysis of fluctuations requires to introduce an adapted theoretical formalism for the interpretation of quantitative data. The Helfrich's physical framework has proven its broad relevance to biological membranes since its introduction in 1973 [41], and is briefly overviewed in the following for a membrane at equilibrium.

3.1 Theoretical Framework for Equilibrium Membrane Fluctuations

3.1.1 Helfrich's Membrane Hamiltonian

Helfrich proposed a surface energy density of the form $\frac{\kappa}{2}(2C - C_0)^2$ for the bending energy of a lipid bilayer, where C is the local mean curvature and C_0 a spontaneous curvature (that we will generally ignore in the following). Note that we generally disregard an additional Gaussian curvature term, which reduces to a constant when integrated over a closed, or periodic surface. Since stretching lipids from one-another represents a high energy cost at the bilayer level, one may generally consider the membrane total area constant. From a theoretical point of view, this area constraint is enforced via a Lagrange multiplier denoted σ, and which is interpreted physically as the membrane surface tension. The Helfrich energy $\mathscr{H}$ is written as the sum of these bending and tension contributions, integrated over the total membrane area $\mathscr{A}$

$$\mathscr{H} = \int_{\mathscr{A}} \left\{ \frac{\kappa}{2}(2C - C_0)^2 + \sigma \right\} d\mathscr{A} \tag{1}$$

3.1.2 Static Membrane Fluctuations Spectrum

We consider here a quasi-planar membrane of bending modulus κ and surface tension σ, as sketched in Fig. 1a and we describe its shape in the Monge representation, where the position vector of the bilayer mid-plane is measured by the height vector $((x, y), h(x, y)) = (\mathbf{r}, h(\mathbf{r}))$. In the limit of small deformations $\left|\nabla h(\mathbf{r})\right| \ll 1$ the Helfrich Hamiltonian (1) can be written, to a constant

$$\mathscr{H} = \int_A d^2\mathbf{r} \left\{ \frac{\kappa}{2}\left[\nabla^2 h(\mathbf{r})\right]^2 + \frac{\sigma}{2}\left[\nabla h(\mathbf{r})\right]^2 \right\}, \tag{2}$$

where A denotes the projection of the membrane area $\mathscr{A}$ onto the plane (x, y).

Static Fluctuation Modes

To study fluctuations, it is more convenient to work in spatial Fourier space, and we consider hence a square piece of membrane with periodic boundary conditions. The membrane height in real space can be decomposed as $h(\mathbf{r}) = \frac{1}{A}\sum_{\mathbf{q}} h_{\mathbf{q}}\, e^{i\mathbf{q}\cdot\mathbf{r}}$ where $h_{\mathbf{q}} \equiv \int_A d\mathbf{r}\, h(\mathbf{r})\, e^{-i\mathbf{q}\cdot\mathbf{r}}$ is the Fourier component for the wave-vector $\mathbf{q}$ of membrane deformation. Inserting this expression in the Helfrich Hamiltonian (2) yields

$$\mathscr{H} = \frac{1}{2}\sum_{\mathbf{q}} \left(\sigma\mathbf{q}^2 + \kappa\mathbf{q}^4\right) |h_{\mathbf{q}}|^2 \,. \tag{3}$$

If the membrane is at thermal equilibrium, we can use the equipartition theorem, which assigns an average energy $k_{\mathrm{B}}T/2$ energy to each Fourier mode, yielding the static membrane fluctuation spectrum

$$\left\langle |h_{\mathbf{q}}|^2 \right\rangle = \frac{k_{\mathrm{B}}T}{\sigma\mathbf{q}^2 + \kappa\mathbf{q}^4} \,, \tag{4}$$

where $\langle . \rangle$ denotes a statistical average.

The modes of deformation are limited for a real membrane, which has a typical size $L \sim \sqrt{A}$ and is composed of lipids of microscopic size $a \sim 0.5\,\mathrm{nm}$. These two length scales allow us to define the following macroscopic and microscopic modes cut-offs: $q_{\min} \equiv 2\pi/L$ and $q_{\max} \equiv 2\pi/a$. In the reasonable limit $a \ll L$, the fluctuation spectrum amplitude can be calculated by integrating the static fluctuation spectrum (4) over all wave-vectors in the range $\left[q_{\min},\, q_{\max}\right]$, which yields

$$\left\langle |h|^2 \right\rangle = \frac{k_{\mathrm{B}}T}{4\pi\sigma} \ln\left(1 + \frac{\sigma}{\kappa q_{\min}^2}\right) \tag{5}$$

From Eq. (5), one readily observes that a characteristic length $\lambda_\sigma = \sqrt{\kappa/\sigma} = 2\pi\, q_\sigma^{-1}$ may be defined from the bending modulus and surface tension. Two membrane fluctuation regimes can be identified, depending on the amplitude of membrane wave-vector $q = |\mathbf{q}|$ relative to the intrinsic length scale q_σ:

- If $q \gg q_\sigma$, the fluctuations are controlled primarily by modes in q^4, corresponding to the membrane bending elasticity term. In this regime, membrane fluctuations are dominated by the longest deformation wavelength, and their squared amplitude scales as $\langle |h|^2 \rangle \sim \frac{k_{\mathrm{B}}T}{4\pi\kappa}\frac{A}{\pi^2}$.

  For a bilayer of typical size $L \sim 10\,\mu\mathrm{m}$, bending modulus $\kappa \sim 10\, k_{\mathrm{B}}T$, and vanishing tension, one would obtain $\sqrt{\langle h^2(L)\rangle} \approx 3\,\mu\mathrm{m}$.
- If $q \ll q_\sigma$, the tension modes in q^2 dominate fluctuations, and one can evaluate the fluctuation squared amplitude as $\langle |h|^2 \rangle \sim \frac{k_{\mathrm{B}}T}{4\pi\sigma} \ln(\frac{\sigma}{\kappa\, q_{\min}^2})$.

  For typical lipid size $a \sim 0.5\,\mathrm{nm}$ and membrane tension $\sigma \approx 10^{-5}\mathrm{N\,m^{-1}}$, one obtains an amplitude $\sqrt{\langle h^2(L)\rangle} \approx 60\,\mathrm{nm}$.

Excess Area and Membrane Tension

We see above that the amplitude of thermal fluctuations is strongly reduced when the membrane is tensed. As we mentioned before, the membrane tension is in fact intrinsically related to the constraint of conserved membrane area. To formalize this relation one may introduce the area excess α, which measures the difference between projected area A and total membrane area $\mathscr{A}$ [42] (see Fig. 1a)

$$\alpha = \frac{\mathscr{A} - A}{\mathscr{A}} \sim \frac{1}{2A} \int_A d\mathbf{r} \; |\nabla h(\mathbf{r})|^2 = \frac{k_B T}{8\pi\kappa} \ln\left(\frac{q_{\max}^2 + \sigma/\kappa}{q_{\min}^2 + \sigma/\kappa}\right) \tag{6}$$

For vanishing tension, this formula yields simply $\alpha = \frac{k_B T}{4\pi\kappa} \ln(\frac{L}{a})$. For intermediate tension values $q_{\min} \ll q_\sigma \ll q_{\max}$, tension is directly related to the excess area as $\alpha = \frac{k_B T}{8\pi\kappa} \ln(\frac{\kappa q_{\min}^2}{\sigma})$. Knowing the membrane excess area, one can therefore calculate the membrane tension directly by inverting this relation.

Note that for higher tension values one needs to consider an additional term $\frac{\sigma}{K_c}$ to the excess area to take into account the lipids stretching, characterized by a bulk modulus K_c [43].

3.1.3 Dynamic Fluctuation Spectrum

Membrane Langevin Dynamics

Biological or biomimetic membranes are embedded in aqueous solutions, which need to be displaced when the membrane deforms. Since inertia is negligible at this scale, fluid flow can be described by Stokes equations

$$-\nabla p(\mathbf{r}) + \eta \nabla^2 \mathbf{v}(\mathbf{r}) = -\mathbf{f}(\mathbf{r}) \tag{7}$$

$$\nabla \cdot \mathbf{v} = 0 \tag{8}$$

where $\mathbf{v}$, p, and η are, respectively, the fluid velocity, pressure, and viscosity, and $\mathbf{f}$ is a bulk force in the fluid.

The viscous force opposing membrane displacement can be inferred by calculating the flow generated by a point-like force $\mathbf{f}(\mathbf{r}) = \mathbf{F}\delta(\mathbf{r})$ and integrating this force along the membrane. The Stokes flow solution is related to the point-like force $\mathbf{f}$ through a Green's function $\Lambda(\mathbf{r})$, called the Oseen tensor [44] and defined in real space as $\mathbf{v}(\mathbf{r}) = \int \Lambda(\mathbf{r} - \mathbf{r}')\mathbf{f}(\mathbf{r}')d^3\mathbf{r}'$. Following the derivation proposed in [44], the diagonal part of the Oseen tensor may be calculated as

$$\Lambda(\mathbf{r}) = \frac{1}{8\pi\eta|\mathbf{r}|} \tag{9}$$

To obtain the membrane dynamics, we note that normal velocities of the fluid and of the membrane should coincide at the membrane surface $\mathbf{v} = \frac{\partial h}{\partial t}$, and that the membrane exerts an instantaneous elastic restoring force per area on the fluid $f^{\mathrm{el}}(\mathbf{r}, t) = -\frac{\delta \mathscr{H}}{\delta h(\mathbf{r},t)}$. By adding an additional white noise term in the force, to account for thermal agitation, we obtain an overdamped Langevin dynamics for the membrane height $h(\mathbf{r}, t)$

$$\frac{\partial h}{\partial t}(\mathbf{r}, t) = \int d^3\mathbf{r}'\, \Lambda(\mathbf{r} - \mathbf{r}') \left\{ -\frac{\delta \mathscr{H}}{\delta h(\mathbf{r}', t)} + \zeta^{\mathrm{th}}(\mathbf{r}', t) \right\} \tag{10}$$

In spatial Fourier space, this equation reads more concisely

$$\frac{\partial h_{\mathbf{q}}(t)}{\partial t} = \Lambda_{\mathbf{q}} \left[-\left(\kappa \mathbf{q}^4 + \sigma \mathbf{q}^2 \right) h_{\mathbf{q}}(t) + \zeta^{\mathrm{th}}_{\mathbf{q}}(t) \right] \tag{11}$$

The thermal noise term has zero mean and its correlations obey the fluctuation–dissipation relation

$$\left\langle \zeta^{\mathrm{th}}_{\mathbf{q}}(t) \zeta^{\mathrm{th}}_{\mathbf{q}'}(t') \right\rangle = 2 k_{\mathrm{B}} T\, \Lambda_{\mathbf{q}}^{-1} \delta(\mathbf{q} + \mathbf{q}') \delta(t - t') \tag{12}$$

where the Oseen tensor in Fourier space is given by $\Lambda_{\mathbf{q}} = \Lambda_q = 1/4\eta q$, with $q \equiv |\mathbf{q}|$.

Power Spectral Density

From the membrane dynamics (11), we can directly compute in temporal Fourier space the mode-dependent autocorrelation function for an equilibrium membrane

$$\left\langle \left| h_{\mathbf{q}}(\omega) \right|^2 \right\rangle = \frac{2 k_{\mathrm{B}} T\, \Lambda_q}{\omega^2 + \omega_q^2} \tag{13}$$

where ω_q is the typical membrane relaxation rate for the mode q, given by

$$\omega_q \equiv \Lambda_q \left(\kappa q^4 + \sigma q^2 \right) = \frac{\kappa q^3 + \sigma q}{4\eta} \tag{14}$$

To obtain the equilibrium membrane fluctuation spectrum (or power spectral density, noted PSD), one has to integrate the autocorrelation function (13) over all deformation modes explored by the membrane

$$\left\langle |h(\omega)|^2 \right\rangle = \int \frac{d\mathbf{q}}{(2\pi)^2} \frac{2 k_{\mathrm{B}} T\, \Lambda_q}{\omega^2 + \omega_q^2} = \frac{4\eta k_{\mathrm{B}} T}{\pi} \int_{q_{\min}}^{q_{\max}} \frac{dq}{(4\eta\omega)^2 + (\kappa q^3 + \sigma q)^2} \tag{15}$$

Supposing $q_{\min} \sim 0$ and $q_{\max} \sim \infty$, the PSD scales as $\omega^{-5/3}$ and ω^{-1} in the limit cases of, respectively, high and low frequency

$$\left\langle |h(\omega)|^2 \right\rangle \underset{\omega \to \infty}{\longrightarrow} \frac{k_B T}{6\pi (2\eta^2 \kappa)^{1/3} \omega^{5/3}} \tag{16}$$

$$\left\langle |h(\omega)|^2 \right\rangle \underset{\omega \to 0}{\longrightarrow} \frac{k_B T}{2\sigma\omega} \tag{17}$$

Fluctuation–Dissipation Relation

To write the fluctuation–dissipation relation, we have to determine the mechanical response function of the membrane, defined in temporal Fourier space as $\chi(\omega) \equiv h(\omega)/F(\omega)$, where F is an external driving force. Adding this external force to the mode-dependent Langevin dynamics (11), we obtain in temporal Fourier space

$$-i\omega h_{\mathbf{q}}(\omega) = \Lambda_q \left[-\left(\kappa q^4 + \sigma q^2\right) h_{\mathbf{q}}(\omega) + F_{\mathbf{q}}(\omega) + \zeta^{\text{th}}_{\mathbf{q}}(\omega) \right] \tag{18}$$

Supposing that the driving force F is much larger than thermal noise ζ^{th}, the mode-dependent response function is obtained as

$$\chi_{\mathbf{q}}(\omega) = \frac{\Lambda_q}{-i\omega + \omega_q} \tag{19}$$

The response function can be separated into real and dissipative parts $\chi_{\mathbf{q}}(\omega) = \chi'_{\mathbf{q}}(\omega) + i\,\chi''_{\mathbf{q}}(\omega)$, leading to

$$\chi'_{\mathbf{q}}(\omega) = \frac{\omega_q \Lambda_q}{\omega^2 + \omega_q^2} \qquad \chi''_{\mathbf{q}}(\omega) = \frac{\omega \Lambda_q}{\omega^2 + \omega_q^2} \tag{20}$$

By identification with the autocorrelation function (13), and after summing on the modes $\mathbf{q}$, we deduce the fluctuation–dissipation relation

$$C(\omega) \equiv \left\langle |h(\omega)|^2 \right\rangle = \frac{2k_B T}{\omega} \chi''(\omega) \tag{21}$$

3.2 Indirect Fluctuation Analysis

In micropipette aspiration experiments, tension and excess areas constitute inherent average measures of the fluctuations over the full liposome area. As introduced in Fig. 1 and in Eq. (6), the membrane fluctuations lead to a difference between the projected membrane area A, and the total membrane area $\mathscr{A}$. Experimentally

accessible is the change in excess area $\Delta\alpha \equiv \alpha_0 - \alpha$, obtained by measuring the radius of the liposome and the variation of the length of the membrane tongue δL while aspirating with a micropipette. Here α_0 is the excess area at the minimal tension σ_0 sufficient to suck up the liposome at the start of the experiment [19]. As long as the membrane fluctuations remain in the entropic regime, we have shown above that the excess area takes the form $\alpha = \frac{k_B T}{8\pi\kappa} \ln(\frac{\kappa q_{\min}^2}{\sigma})$, from which we easily deduce the excess area change upon aspiration

$$\Delta\alpha = \frac{k_B T}{8\pi\kappa} \ln\left(\frac{\sigma}{\sigma_0}\right) \tag{22}$$

The tension is controlled by the aspiration pressure and can be calculated using Laplace's law [19]. In the experimental procedure the tension is systematically increased and the resulting excess area change is plotted over the tension which is normalized to the initial tension. This leads to datasets such as presented in Fig. 2a. In the case of active ion pumps in the membrane one finds systematically a reduced slope of the experimental curve [19]. As the slope depends on the ratio between the temperature T and the bending modulus κ an initial analysis suggests investigation of these two parameters. To describe changes in the slope of the experimental data, an effective temperature T_{eff} is introduced. Since the physical reason for the excess area in passive systems is indeed a temperature dependent fluctuation, this intuitive modification provides a simple way to retain the analytical expressions. However, it should be mentioned that due to the spatial and temporal averaging any possible frequency dependence of T_{eff} is not accessible. This is important in the sense that the concept of temperature has no time dependence. Such an approach reflects the underlying assumption of statistical mechanics that thermal noise is a delta correlated stochastic variable with no inherent timescale. However, a dynamic analysis of the membrane fluctuations shows that the effective energy $E_{\text{eff}} = k_B T_{\text{eff}}$ may be a frequency-dependent quantity that is hence qualitatively different from the classical concept of temperature.

3.3 Static Analysis

In contrast to the micropipette experiment, the static analysis of the data is often based on time-dependent raw data, such as video images. To obtain better statistics, time-dependent data is condensed into histograms of the position or, in the extreme case, into a mean value and the standard deviation (Fig. 3a). This approach is very useful to reduce experimental noise if only a limited number of measurements are available. As the name points out, the static approach is fundamentally limited to static properties such as an elastic energy storage module that does not depend on timescales and that does not have inherent relaxation behavior. It should be mentioned that even such static measurements are still restricted to certain

timescales that are given by the total acquisition time and the sampling rate of the raw data. Typically it assumes that the total acquisition time is large enough for the system to explore all possible conformations. This is, for example, the case when a probability distribution of visited membrane positions does not change shape for longer measurement times. In this view, an important point is that changes in friction or viscous properties lead to slower dynamics, which might require a critical check of recording timescales: at higher viscosity it can take much longer to explore all possible configurations.

Regarding image analysis, the membrane position is commonly detected by image processing and the amplitude for the different modes is extracted using Fourier analysis or spherical harmonics decomposition. The average amplitude of the different modes is then plotted as a function of the mode number (Fig. 3b). Other possible analysis are cross-correlation curves, where distance-dependent correlation functions are calculated to understand the lateral length scale over which mechanical interaction is mediated by the membrane (Fig. 3c). In the case of active fluctuations initiated by bacteriorhodopsin, the activity enhances primarily lower modes (i.e., large wavelength) [20] (see Fig. 3b). This particular feature reflects in the time

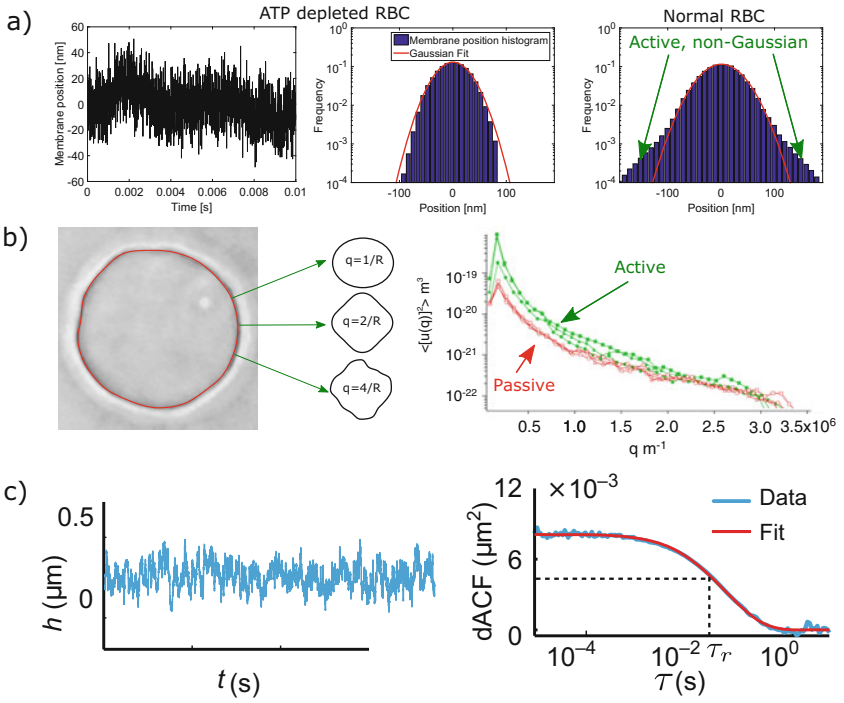

Fig. 3 Summary of the analysis methods to quantify active and passive fluctuations. (**a**) Using the histogram of the measured membrane fluctuations allows to quantify possible deviations from the expected Gaussian probability distribution. Commonly such non-Gaussian behavior

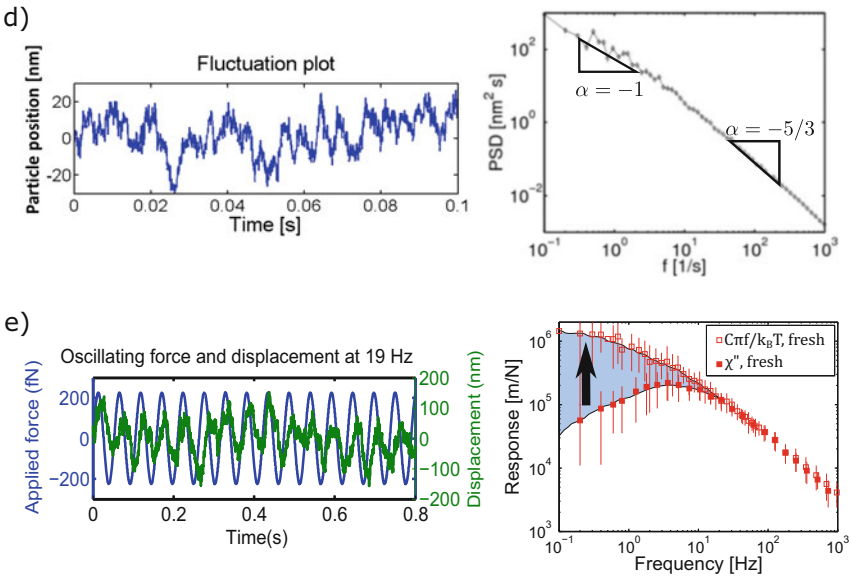

Fig. 3 (continued) is interpreted to result from active processes. (**b**) The detailed mode analysis of the fluctuation in membranes shows an increase of fluctuation amplitude and its characteristic mode dependence (data reproduced with permission from [20]). (**c**) If only time-dependent data is available, a common approach is to use the autocorrelation function and fit it with an exponential function, or more complex functions to describe the active component (data reproduced from [28]). (**d**) Another possible way to analyze time dependence membrane fluctuation is to determine the fluctuations spectrum. Membrane models can account for the different powerlaw observed in these measurements. (**e**) A direct check of activity can be achieved by comparing the directly measured response functions (e.g., via optical tweezers) with the expected response function that is obtained using the free fluctuations spectrum and applying equilibrium physics. The deviations between free fluctuations and membrane response are a direct measure of active membrane fluctuations (figures adapted from [7])

domain, where low frequency fluctuations—corresponding to low modes—are also predominately enhanced by activity.

Besides these direct observations of active fluctuations in model membranes, a static analysis was typically used to identify initial signs of active fluctuations in the red blood cell membrane. First measurements of relative membrane position showed relative changes in fluctuations upon ATP depletion, which was interpreted as a sign for activity. However, as the whole cell becomes stiffer upon depletion of intracellular ATP, a pure equilibrium interpretation may be proposed. Additional experimental results like changes of the static fluctuations amplitude when the buffer viscosity was changed did indeed hint for an active process [4]; however, these experiments could not been reproduced. It is possible that insufficient recording time may not allow the membrane to explore all possible conformations in this pioneering experiment.

More recently, the static analysis of membrane fluctuations was used to determine possible deviation from a Gaussian probability distribution of the membrane fluctuations. Such non-Gaussian contributions can be explained by active processes that generate membrane configurations hardly reachable from pure thermal agitation (Fig. 3a). A key feature of these non-Gaussian elements is that they are quite rare, which requires excellent statistics to be able to detect them. Using DRM a non-Gaussian parameter was indeed detected in the height fluctuations of red blood cells [5]. In the case of ATP depletion, this non-Gaussian behavior was reduced, which was interpreted as a sign for activity. These results have been later confirmed by DODS. While this was an intriguing result, such a non-Gaussian behavior cannot be a conclusive proof of active fluctuations, as any nonlinear behavior in the membrane could lead to similar results.

3.4 Dynamic Analysis

When a large number of time-dependent measurements with good temporal resolution are available, it becomes reasonable to exploit time as additional dimension. Temporal analysis is interesting as it provides access to dynamic variables such as processes related to energy dissipation and friction. These parameters are fundamental to understand and model the mechanical processes involved in both passive and active fluctuations. This becomes evident when considering energy dissipation as the fundamental reason for thermal fluctuations. Briefly, thermal excitation of a membrane fluctuation implies an energy transfer from the thermal bath to the membrane which in turn requires a reduction of the bath's temperature. However, driving a movement by cooling a reservoir is in contradiction to the rules of thermodynamics. The fluctuation–dissipation theorem states that the same amount of energy is returned to the thermal bath by dissipating the energy stored in the movement, thus leading to a heating that exactly compensates the "cooling" required to drive the fluctuations. Having this in mind, it becomes clear why the dissipation of active fluctuations gives a useful quantity to describe active processes, because it allows to measure the energy added to the system by the active process. Hence, to gain more information about the elastic but also dissipative properties of an active system, a time-dependent analysis is vital.

A common approach to look at time dependence is to study the autocorrelation function (ACF) of the position $x(t)$, typically denoted $\langle x(\tau)x(0)\rangle$. Depending on the type of analysis, the ACF is often normalized by subtracting the mean square of $x(t)$ and dividing by the variance of $x(t)$. When applying these normalizations the ACF becomes somewhat intuitive, as it varies only between ± 1, where a value of 1 marks a total correlation and -1 marks total anti-correlation. Often, an exponential decay of the ACF is found, which can be associated with a single relaxation process with timescale τ_r (Fig. 3c). In contrast, many systems show powerlaw behavior in the relaxation, which corresponds to a complex relaxation scheme with many processes. In the context of membranes, the ACF of a single mode typically relaxes

exponentially. Every fluctuation mode has a characteristic wavelength λ (typically reported: wavenumber $q = 2\pi/\lambda$) that corresponds to a characteristic relaxation frequency $\omega_q = (\kappa q^3 + \sigma q)/(4\eta)$, as introduced in Eq. (14), where η is the viscosity of the surrounding buffer solution. If the fluctuations are measured at one single position, they present the superposition of all accessible modes and hence the ACF results in a more complex powerlaw relaxation behavior. The overall advantage of the ACF lies in the visual and analytical interpretation of data containing a low number (1 to 3) of relaxation processes that are well separated in timescales, ideally by at least one order of magnitude. Also, the ACF can be efficiently calculated directly from the input data using dedicated hardware. It should be mentioned that the ACF function plays a key role in fluorescence correlation spectroscopy (FCS), which is a powerful tool in the study of lateral movements of lipids or membrane bound proteins. A key advantage of the correlation function is to combine temporal and spatial analysis by correlating two functions that represent the membrane movement at two different positions separated by a well-defined distance. This two-point correlation can give information about timescales and distances over which mechanical forces can act on the membrane. Such analysis was used to give direct hints for active processes representing force dipoles with characteristic length scales [5].

Besides the ACF, a second analysis type commonly used is the power spectral density (PSD), which is accessed by computing $C(\omega) = \frac{\tilde{x}(\omega)\times\tilde{x}(\omega)^*}{p\times s}$, where $\tilde{x}(\omega)$ is the Fourier transform of the time-dependent signal $x(t)$, and p and s are the sample rate and number of datapoints, respectively. The PSD refers to "power," as it was originally used to get the electrical power of voltage measurements. Hence, strictly speaking the PSD of the membrane position is not a mechanical power, but reflects the fluctuation amplitude. Figure 3d shows a typical PSD calculated from transverse fluctuations of a membrane. Important characteristic features are that the low frequencies provide large amplitudes while at high frequencies the amplitudes are small. This is qualitatively explained by friction which prevents large amplitudes at high frequencies. The quantitative behavior of the PSD can be easily described in the case of an equilibrium quasi-flat membrane, as we presented in Sect. 3.1.3: in the high-frequency regime, the spectrum is dominated by the bending modulus κ and shows a $-5/3$ powerlaw, while in the low-frequency regime, dominated by the tension σ, the exponent changes to -1 (see Eq. (16) and Fig. 3d). A quantitative model can be fit to the PSD to directly determine the mechanical properties of the membrane. In principle, the ACF and the PSD are exchangeable, as they are related to each other by a Fourier transformation in the time domain. Advantages of the PSD are that single frequency noise sources, such as electronic 50 Hz noise show up as delta peaks and can be easily eliminated. The ACF, however, allows to directly identify if a single or if multiple relaxation processes act on the system studied.

In both cases, activity typically shows up as an increase in fluctuation amplitudes and possible difference in the powerlaws from the equilibrium case. However, without a direct measure of the mechanical properties it is difficult to get a model-independent measure of active fluctuations.

3.5 Direct Measurement of the Mechanical Response Function

To experimentally prove the active nature of membrane fluctuations and to quantify the contribution of active forces to the fluctuations it is necessary to know the mechanical characteristics of the system. To measure mechanical properties, a well-defined force is applied and its resulting deformation is measured. Since typical systems of interest such as cells and liposomes are marked by viscoelastic characteristics, it is important to measure time-dependent response functions. In principle this can be done by measuring the time-dependent relaxation after application of a step force with an atomic force microscope, a magnetic tweezer, an optical tweezer, or a calibrated micropipette. The time resolution provided by step response is however generally not satisfactory in practice, and frequency response, where the system is probed successively for different frequencies, is generally preferred. For biological membranes we are interested in the mechanical properties at the micrometer scale, and hence the corresponding methods are called microrheology. Classically microrheology is separated into active and passive methods. In active microrheology, an external force is applied to the system to measure its response, while in passive microrheology, the spontaneous fluctuations of the system are used to infer its mechanical properties. It should be mentioned here again that for active and in particular living systems, passive microrheology may not be used to infer mechanical response, unless the properties of the active process are known and integrated in the analysis.

In the context of active membranes, optical tweezers-based microrheology has been used to measure the mechanical response of living cells, such as red blood cells and other eukaryotic cells [45]. In these measurements, the beads are attached to the plasma membrane and an oscillating force is applied while the response of the system is measured by following the bead movement. The advantage of the oscillatory driving is that noise and additional fluctuations can be removed by selecting the driving frequency $f = \omega/2\pi$ in the analysis. The response χ is then simply obtained by $\chi(f) = \tilde{x}(f)/F(f)$, where $F(f)$ is the oscillating driving force of frequency f. This experiment is repeated for driving forces of different oscillating period, to finally obtain the complex response function as a function of driving frequencies (Fig. 3e). This complex response function can be separated into its real and imaginary part, corresponding to the elastic ($\chi'(f)$) and dissipative ($\chi''(f)$) response. This approach was used to determine the dissipative response in the red blood cell membrane which was a key element to quantify active membrane fluctuations [7]. Furthermore, the same approach allowed to determine the active fluctuations of granules in mouse oocytes cells [46] and of particles embedded in biomimetic actomyosin systems [47].

3.6 Test of Fluctuation–Dissipation Theorem

Combining the dynamic fluctuations analysis with mechanical response measurements allows to decouple the active part from the thermal driving in the membrane fluctuations. This presents a key element to evaluate the pertinence of theoretical models describing active fluctuations. Here we use the example of active fluctuations in the red blood cell membrane [7], but the measurement principle can be equally applied to other systems. In the case of red blood cells, four beads are attached to the membrane, and the red blood cell is held in space by trapping three handle beads. The free fluctuations are measured by decreasing the laser intensity on the fourth bead (probe bead) to a level where the optical detection system works reliably, but where the trapping force on the particle is negligible compared to thermal fluctuations. In this situation the movement of the bead can be assumed to be purely thermally driven, while being precisely recorded. The PSD $C(f)$ is calculated as described in Sect. 3.4. In a second step of the experiment, the laser power on the probe bead is increased and the laser beam is moved in a sinusoidal fashion. The resulting oscillatory forces on the bead are recorded using the optical detection system. As described in Sect. 3.5, the frequency-dependent response function $\chi(f)$ is obtained.

In an equilibrium situation, the free fluctuations and the dissipation are connected by the fluctuation–dissipation theorem (21) that we rewrite here as function of the frequency f: $C(f) = \frac{2k_BT}{2\pi f}\chi''(f)$, where $\chi''(f)$ is the dissipative part of the response function. From an analysis point of view, the response function expected from an equilibrium system is obtained by measuring the PSD as $\chi''(f) = C(f)\pi f/k_BT$. Plotting this function and the response function directly measured on the system provides two curves, which shall collapse if, and only if the system is at thermodynamic equilibrium (Fig. 3e). Any discrepancy between the two curves is therefore a clear evidence for an additional, non-equilibrium process driving active fluctuations.

By analogy with the fluctuation–dissipation relation, one may define the effective energy and temperature as $E_{\text{eff}} \equiv C(f)\pi f/\chi''(f) \equiv k_BT_{\text{eff}}$. It becomes clear that the effective temperature is, in general, timescale dependent, which is somewhat contradictory to the concept of temperature itself. By measuring $\chi''(f)$ and $C(f)$, the effective energy becomes directly experimentally accessible, which is an interesting method to investigate active fluctuations from a thermodynamic perspective, and to detect the frequency onset of active energy input in the system. For the red blood cell membrane, metabolic activity is found to only excite the membrane at short timescales: for frequencies higher than 10 Hz, thermal fluctuations dominate the fluctuations, while at timescale lower than 100 ms, active contributions largely exceed thermal driving. Previous methods using the FDT, or passive microrheology, to infer the mechanical properties of red blood cell membrane have hence to be re-considered carefully.

4 Theoretical Models of Active Membrane

The advent of theoretical modeling of active membranes may surely be associated with the seminal work of Prost and Bruinsma in 1996 [15]. In this landmark paper, a hydrodynamic model predicts the influence of ion channels gating activity on membrane fluctuations. Since then, a large set of models were proposed to account for direct or indirect sources of active noise in biological membranes and to analyze their specific features. All these hydrodynamic models take essentially a similar general form, where active and thermal noise are uncorrelated and may therefore be split into two distinct contributions. A common structure for active membrane models is therefore proposed. Then we discuss intrinsically active membrane models, where the active sources of noise come from processes directly embedded in the bilayer, and extrinsically active membrane models, where activity is cytoskeleton based but may be transmitted to the bilayer through mechanical coupling. Note that we do not cover here electrokinetic active membrane models, which have been recently reviewed elsewhere [48].

4.1 General Structure of Active Membrane Models

Starting from the equilibrium Langevin dynamics in Fourier space (11), the height dynamics for an active membrane may in general be cast into the generic following form:

$$\frac{\partial h_{\mathbf{q}}(t)}{\partial t} + \omega_{\mathbf{q}} h_{\mathbf{q}}(t) = \Lambda_{\mathbf{q}} \zeta^{\mathrm{th}}_{\mathbf{q}}(t) + \Lambda_{\mathbf{q}} \zeta^{\mathrm{a}}_{\mathbf{q}}(t) \tag{23}$$

where $\omega_{\mathbf{q}}$ is the mechanical relaxation frequency of the membrane for the mode $\mathbf{q}$, $\zeta^{\mathrm{th}}_{\mathbf{q}}$ and $\zeta^{\mathrm{a}}_{\mathbf{q}}$ are thermal and active sources of noise, respectively, and $\Lambda_{\mathbf{q}}$ is a mode-dependent dissipative coefficient (e.g., the Oseen tensor for membranes surrounded by viscous fluids). In general, the membrane relaxation frequency takes the following form $\omega_{\mathbf{q}} = \Lambda_{\mathbf{q}}\, \delta\mathscr{H}/\delta h_{\mathbf{q}}(t)$, where $\mathscr{H}$ is the elastic energy of the membrane.

The characteristics of the active noise source term $\zeta^{\mathrm{a}}_{\mathbf{q}}(t)$ are not constrained a priori and may hence depend on the source of active forces, but as soon as this term is non-vanishing, one shall expect a violation of statistical equilibrium. We will hence describe in the following several models for the active source of noise in the membrane.

Note that Eq. (23) can be readily generalized to quasi-spherical membranes with the use of spherical harmonics instead of Fourier decomposition [49–51].

4.2 Intrinsically Active Membrane Models

4.2.1 Ion Channels Shot-Noise Activity

In the first active membrane model proposed by Prost and Bruinsma [15], active fluctuations originate from the shot-noise activity of ion channels freely diffusing in the membrane (see Fig. 1b).

By switching stochastically between open and closed states, under the action of metabolic energy, these channels produce an additional source of noise, described by a two-state variable $S_k(t) = 1$ if the ion channel k is active and 0 otherwise.[1] In agreement with single ion-channel gating measurements, the shot-noise is assumed to be exponentially correlated in time $g(t) = \langle S_k(t)S_k(0)\rangle - \langle S_k\rangle^2 = g(0)\, e^{-t/\tau_\mathrm{a}}$, with a typical correlation time τ_a.

By changing local osmolarity in the vicinity of the membrane, ion channels generate a local fluid pressure variation across the membrane of the form $\delta p(\mathbf{r}, t) \propto f \sum_k S_k(t)\, \delta(\mathbf{r} - \mathbf{R}_k(t))$, where $\mathbf{R}_k$ is the position of the ion channel k in the membrane plane, and $f \sim k_\mathrm{B}T/w$ is the typical force amplitude exerted on the membrane of thickness w. Supposing the membrane semi-permeable with a permeability denoted λ_p, the Langevin equation for the membrane height in Fourier space takes a similar form as (23)

$$\frac{\partial h_\mathbf{q}(t)}{\partial t} + \omega_\mathbf{q} h_\mathbf{q}(t) = \Lambda_q \zeta^\mathrm{th}_\mathbf{q}(t) + f\lambda_\mathrm{p} \sum_k S_k(t)\, e^{i\mathbf{q}\cdot\mathbf{R}_k(t)}\,, \tag{24}$$

where $\omega_\mathbf{q} = \frac{\kappa}{4\eta} q^3 + \kappa\lambda_\mathrm{p} q^4$ is the sum of the relaxation frequency for an impermeable membrane with vanishing tension and an additional permeation term. The dissipative coefficient is the membrane permeability $\Lambda_\mathbf{q} = \lambda_\mathrm{p}$, and we can identify the active noise term as $\zeta^\mathrm{a}_\mathbf{q}(t) = f \sum_k S_k(t) e^{i\mathbf{q}\cdot\mathbf{R}_k(t)}$.

In the long wavelength limit, the model predicts that area density fluctuations of ion channels of active nature shall dominate the membrane fluctuation spectrum $\langle |h_\mathbf{q}|^2\rangle \sim_{q\to 0} \frac{k_\mathrm{B}T}{\kappa}(q^{-4} + \xi^{-1}q^{-5})$, where ξ is a length scale proportional to the diffusion coefficient of channels in the membrane and inversely proportional to the shot-noise correlation.

This seminal work triggered a substantial theoretical interest for active membranes [7, 16, 18, 19, 50, 51, 53–60] that we aim to briefly overview in the following.

[1] Note that *ion channels* do not require metabolic energy consumption by definition and are hence generally considered as passive. However, when a non-zero (electro)chemical potential difference is maintained across the membrane (generally through the action of ion pumps), their gating activity is expected to be of non-equilibrium character [52].

4.2.2 Active Curvature Coupling

The first experimental realization of active membranes in vitro was done by reconstituting the transmembrane proton pump bacteriorhodopsin in giant unilamellar vesicles [18, 19]. A new theoretical model, considering the coupling between pumps activity and membrane curvature, was conjointly proposed by Ramaswamy, Toner, and Prost, to explain the experimental results [16]. The new ingredient added to the original model of Prost and Bruinsma [15] is an intrinsic asymmetry in the shape of ion pumps, inducing their preference either for positive or for negative membrane curvature regions (see Fig. 4a).

A signed density of proteins $\psi(\mathbf{r}, t) = n^{+}(\mathbf{r}, t) - n^{-}(\mathbf{r}, t)$, measuring the local difference between proteins with preference for positive curvature relative to proteins with preference to negative curvature, is introduced, and is coupled to the membrane elasticity in Eq. (2) up to second order in the variables

$$\mathscr{H}(h, \psi) = \frac{1}{2} \int_A d^2\mathbf{r} \left\{ \kappa \left[\nabla^2 h(\mathbf{r})\right]^2 + \sigma \left[\nabla h(\mathbf{r})\right]^2 + \mu \psi^2(\mathbf{r}) - 2\Xi \psi(\mathbf{r}) \nabla^2 h(\mathbf{r}) \right\} \tag{25}$$

where μ is the susceptibility for the imbalance between curvature positive and negative proteins and Ξ is the curvature coupling coefficient. To close the problem, a conservation law for $\psi(\mathbf{r}, t)$ is needed:

$$\frac{\partial \psi(\mathbf{r}, t)}{\partial t} \sim \Gamma \Delta \left(\frac{\delta \mathscr{H}}{\delta \psi} \right) + \nabla \cdot \boldsymbol{\zeta}_{\psi}^{\text{th}} \tag{26}$$

where $\Gamma = D/\mu$ is a mobility coefficient, with D is the diffusion coefficient of proteins in the membrane.

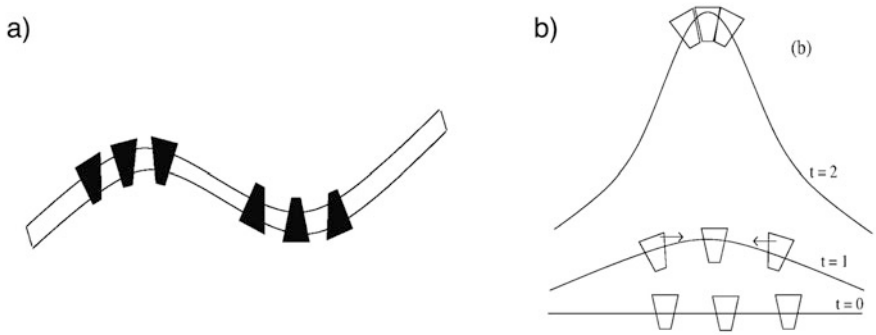

Fig. 4 Curvature coupling of ion pumps of asymmetric shape. (**a**) Asymmetric proteins are drawn to regions with curvature adapted to their shape. (**b**) An instability may develop if the curvature produced by local pumping has the right sign to attract more pumps (figures reproduced from [16])

The activity of positive and negative pumps leads essentially to two additional forces normal to the membrane :

- An active permeation term of the form $\lambda_p F_a \psi(\mathbf{r}, t)$ in Darcy's permeation equation across the membrane, where F_a is the elementary force transmitted to the membrane by the transfer of a proton.
- A hydrodynamic active dipolar force density $F_a\left[\delta(z - w^{\uparrow}) - \delta(z + w^{\downarrow})\right]\psi(\mathbf{r}, t)$ in the force balance equation between the membrane and the surrounding fluid, where $w_{\uparrow}$ and $w_{\downarrow}$ are the distances of the center of mass of the ion pump relative to the membrane mid-plane, which are supposed distinct (see Fig. 5).

A numerical estimation of these two effects shows that the active permeation term may be omitted, in comparison to the active dipolar force, for the typical micron to submicron length scales relevant to biological membranes [19].

This set of equations results in two coupled Langevin dynamics for h and ψ, which can be solved to obtain the membrane fluctuations autocorrelation and, eventually, an expression for the areal strain measured in micropipette experiments [19]:

$$\Delta\alpha = \alpha_0 - \alpha = \frac{k_B T_{\text{eff}}}{8\pi\kappa} \ln \frac{\sigma}{\sigma_0} \tag{27}$$

The model predicts that the effect of pumps activity on the areal strain can be cast simply into an effective temperature T_{eff}, in agreement with experimental results

$$\frac{T_{\text{eff}}}{T} = \frac{\kappa}{\kappa''}\left(1 + \mathscr{P}_a \frac{\mathscr{P}_a d^2 - \Xi d}{\kappa' d}\right) \tag{28}$$

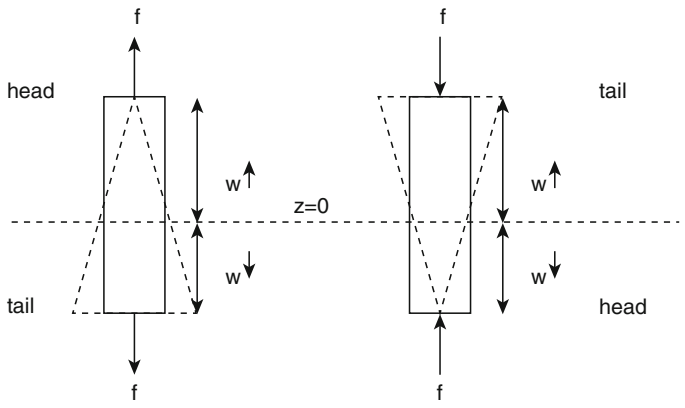

Fig. 5 Asymmetric dipole model used for active proteins: the center of mass of the pumps is displaced above the bilayer midline and force center lies at distances $w^{\uparrow}$ and $w^{\downarrow}$ from this midline. The shape asymmetry of the pump is represented by asymmetric triangles (figure reproduced from [60])

where κ' and κ'' are renormalized bending moduli and $\mathscr{P}_{\mathrm{a}} = F_a \frac{(w^{\uparrow})^2 - (w^{\downarrow})^2}{2w}$ is the work of active dipoles. This formula shows that ion pumps will give rise to active fluctuations in the membrane only in the presence of an asymmetry $w^{\uparrow} - w^{\downarrow} \neq 0$ in the protein configuration within the bilayer.

The coupling between mobile force centers and membrane curvature leads furthermore to a new and rich physical behavior, exhibiting localized instabilities and traveling waves [16]. For example, ion pumps with a preference for positive curvature regions may trigger an instability: by increasing local membrane curvature through their pumping activity, they will attract more pumps and amplify the curvature even greater, as sketched in Fig. 4b.

The model of Ramaswamy, Toner, and Prost does not consider, however, the random fluctuations in the pump activities (shot noise), introduced by Prost and Bruinsma [15]. In a subsequent paper, Lacoste and Lau addressed therefore simultaneously the effects of curvature couplings and pump activity fluctuations. While their model predicts similar local instability and traveling wave behaviors, it shows that shot-noise effects are essential to consider for dynamical measurements of membrane fluctuations, as they lead to different scaling laws at short timescales [59].

4.2.3 "Direct" vs. "Curvature Force" and Monopole vs. Dipole

If one neglects density fluctuation effects due to the diffusion of active proteins in the lipid bilayer, the active noise term can generally be assumed to be uncorrelated in space. In analogy with the shot-noise dynamics of ion channels, many models suppose active forces to be exponentially correlated in time, which is the property typically expected for a protein switching between "on" and "off" states [61]

$$\left\langle \zeta^{\mathrm{a}}_{\mathbf{q}}(t)\zeta^{\mathrm{a}}_{\mathbf{q}'}(t')\right\rangle = \Gamma^{\mathrm{a}}_q \delta_{\mathbf{q}+\mathbf{q}'} e^{-(t-t')/\tau_{\mathrm{a}}} \tag{29}$$

τ^{a} is a typical active timescale, which may be defined from "on" and "off" rates k_{on} and k_{off} for a two-state metabolic process $\tau^{\mathrm{a}} \sim (k_{\mathrm{on}} + k_{\mathrm{off}})^{-1}$, and Γ^{a}_q is the amplitude of the active noise, which may depend on the fluctuation mode $\mathbf{q}$.

Supposing that the elasticity of the membrane reduces to the Helfrich energy, the active membrane fluctuation spectrum can be calculated from Eqs. (12), (23), and (29):

$$\left\langle |h_q(\omega)|^2 \right\rangle = \frac{2k_{\mathrm{B}}T\Lambda_q}{\omega^2 + \omega_q^2} + \frac{1}{\omega^2 + \omega_q^2} \frac{2\tau_{\mathrm{a}} \Lambda_q^2 \Gamma^{\mathrm{a}}_q}{1 + \omega^2 \tau_{\mathrm{a}}^2} \tag{30}$$

where the intrinsic membrane relaxation ω_q was defined in Eq. (14).

In [55], Gov made an important distinction between two possible types of active forces, depending on whether the activity of proteins embedded in the membrane couples or not to the membrane curvature:

- For a so-called direct force, a random force of non-equilibrium origin is applied locally and directly to the membrane [55]. In this case, the active noise term $\zeta^{\mathrm{a}}_{\mathbf{q}}$ can be considered as an instantaneous "kick" on the membrane. The mean squared amplitude of the active noise is then independent of the mode $\mathbf{q}$ of membrane deformation and reads

$$\Gamma^{\mathrm{a}}_{q} = \rho_{\mathrm{a}} F_{\mathrm{a}}^2 \tag{31}$$

  F_a is the magnitude of the active force exerted on the membrane and $\rho_{\mathrm{a}} \sim N/A$ is the density of active proteins in the membrane.
- A "curvature force" is on a contrary an active random contribution $c(\mathbf{r}, t)$ to the spontaneous curvature, which may be introduced by generalizing the bending energy of the membrane as follows $\int_A d\mathbf{r}\{\frac{\kappa}{2}[\nabla^2 h(\mathbf{r}) - c(\mathbf{r}, t)]^2\}$ [17].

  As a result, an additional random force density term appears in the right-hand side of the Langevin equation for the membrane (23) in the form $\zeta^{\mathrm{a}}_{\mathbf{q}}(t) = -\kappa q^2 c_{\mathbf{q}}(t)$. Supposing that each active protein i may switch metabolically between positive and negative spontaneous curvatures $+c_0$ and $-c_0$, we can write the time correlation function for the curvature of a single protein i as $\langle c^i_0(t) c^i_0(t')\rangle = c_0^2 e^{-(t-t')/\tau_{\mathrm{a}}}$, where τ_{a} is, like previously, a typical active timescale for the switching process. Summing over the active proteins in the membrane, the mean squared amplitude of the active noise now depends explicitly on the mode q

$$\Gamma^{\mathrm{a}}_{q} = \rho_{\mathrm{a}} \left(\kappa c_0 b^2 q^2\right)^2 \tag{32}$$

  where b^2 is the typical surface area occupied by an active protein.

"Direct force" and "curvature force" activities are hence predicted to produce different scaling behaviors for the membrane fluctuation spectrum in the limits of large and small wavelengths [55]. In subsequent works, the same author and colleagues generalized the model to *diffusing* active proteins coupling to membrane curvature [17], and characterized the fluctuations of a membrane where the proteins are considered to be nucleators of actin filaments [57]. Other authors considered a generalization where the membrane curvature may feedback onto the conformational transition kinetics of the active inclusions [54].

An important distinction has to be made between monopolar, dipolar, or quadrupolar active contributions. "Direct forces" are typically force monopoles, which suppose essentially that an extrinsic agent, like the cytoskeleton, can push or pull locally on the membrane. Indeed, the spatial integral of the force over the system {protein + membrane + solvent} should vanish by force balance. If an active protein exerts a force on the membrane and solvent, the latter have to

exert an opposite force of same magnitude on the protein. This implies that the force density field of the proteins has zero monopole moment, unless the system is actually not isolated because extrinsic agents enter the force balance. In general, the first contribution of active membrane proteins is a force dipole [50], which can be idealized by two force centers of opposite sign but equal magnitude embedded in the membrane (see Fig. 5). A dipolar contribution is also expected from a permeation force [51]. In the absence of dipolar contribution, higher multipole moments may however contribute to the active membrane fluctuations, such as for "curvature forces," which can actually be considered as quadrupoles [50, 51].

4.2.4 Non-equilibrium Fluctuations and Excess Area

In the models described so far, the description of active fluctuations ignores the interplay between excess area and surface tension. As introduced by Seifert for passive membranes [62], membrane tension shall be formally regarded as a Lagrange multiplier for the conservation of total membrane area, and it is therefore intimately related to the excess area. The excess area is, by definition, a function of the fluctuation amplitude, which is itself a function of the tension. For a quasi-planar membrane, we can deduce from Eq. (6)

$$\alpha = \frac{1}{2A} \sum_{\mathbf{q}} q^2 \left\langle \left| h_{\mathbf{q}}(\sigma) \right|^2 \right\rangle \tag{33}$$

Setting the value of membrane excess area, the membrane tension is therefore controlled by the amplitude of fluctuations. The previous relation has, in general, to be inverted numerically, but analytic formula may been obtained from a perturbative approach for three different limit cases depending on the value of the dimensionless parameter $kT/\kappa\alpha$.

Generalizing this approach to active membranes, Loubet and colleagues show that, by increasing the fluctuations amplitude, the presence of activity in the membrane shall, in general, increase the bilayer surface tension [51]. Distinguishing short and long membrane relaxation times ω_q^{-1} relative to a typical active timescale τ_a, they derived analytical formula for the bilayer tension as function of the excess area of active membranes with either monopolar, dipolar, or quadrupolar types of active forces.

It should be noted that the phenomenological finding that the fluctuations increase due to activity may also be interpreted as a reduction in tension. This can be illustrated by recalling that with the same pulling pressure more hidden membrane can be pulled out of a vesicle [20] when active forces enhance membrane fluctuation. This shows that the interpretation of the activity in the context of classical equilibrium approach may be ambiguous.

4.3 Cytoskeleton-Based Active Membranes

4.3.1 Renormalization of Membrane Properties by the Cytoskeleton

The cell cytoskeleton being tightly coupled to the lipid bilayer, biological membranes are generally composite materials, where the mechanics is a combination of bilayer and cytoskeleton mechanics. A perturbative approach of the problem is to start with the Helfrich description of membranes, and to study how the presence of a cytoskeleton may renormalize endogenous properties, such as membrane tension or bending rigidity, or may create new types of mechanical response, such as resistance to shear or confinement of membrane deformations. Most of the work on the subject has been applied to the red blood cell membrane, where the cytoskeleton is, in comparison to other cell types, a more simple structure, made of a triangular network of extensible spectrin filaments, anchored to the bilayer at junction points via transmembrane protein complexes. Generalizations of these concepts may open new perspectives to characterize membrane fluctuations in cell types possessing an actomyosin cytoskeleton.

Membrane Confinement by the Cytoskeleton

The spectrin cytoskeleton in red blood cells has been proposed by Gov and colleagues to confine the bilayer fluctuations [63], an effect that can be rendered by the addition of a harmonic potential to the Helfrich energy (2)

$$V = \frac{1}{2}\int_A d\mathbf{r}\,\gamma\, h(\mathbf{r})^2 \tag{34}$$

The confinement term, of amplitude γ, constrains the mean squared amplitude of fluctuations to be equal to $d^2 = \frac{1}{8}k_\mathrm{B}T/\sqrt{\gamma\kappa}$. This is equivalent to consider that the spectrin cytoskeleton acts as a rigid plane at $h = 0$ that maintains the membrane at an average distance d via a harmonic restoring force. The static fluctuation spectrum of the confined membrane in Fourier space can be calculated at equilibrium as

$$\left\langle |h_\mathbf{q}|^2 \right\rangle = \frac{k_\mathrm{B}T}{\gamma + \sigma q^2 + \kappa q^4} \tag{35}$$

The confinement parameter γ defines a new characteristic length $\lambda_\gamma = (\kappa/\gamma)^{1/4}$, which determines the wavelength onset for membrane confinement. In their study, Gov et al. show that adding a confinement parameter of the order of $\gamma \sim 10^{-7}\,\mathrm{J\,m^{-4}}$ allows for a better fit of the mode-dependent experimental fluctuation spectrum measured by Zilker et al. in red blood cells [64], which displays an abrupt drop in fluctuations for wavelengths above 100 nm (see Fig. 6).

It should be noted that such confinement potential has been introduced originally in the context on membrane adhesion to a surface [65], to render the combined

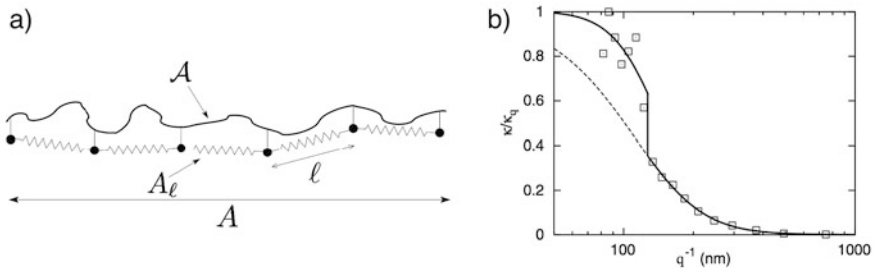

Fig. 6 Composite structure and static fluctuation spectrum of a quasi-planar red blood cell membrane. (**a**) Sketch of a nearly planar red blood cell membrane of total area, $\mathcal{A}$, of coarse-grained area A_ℓ and projected area A. The spectrin filaments are represented by linear springs of length ℓ anchored in the bilayer. (**b**) Fit (plain line) of the static fluctuation spectrum of a human red blood cell measured by Zilker et al. [64] with the model of Fournier et al. [67] predicting a tension jump at $q^{-1} \approx 125$ nm due to the spectrin cytoskeleton elasticity. The dashed line extrapolates the large wavelengths fit, without tension jump (figures adapted or reproduced from [67])

effect of electrostatic attraction and steric repulsion (by long glycocalyx chains) of membrane to the surface [66].

Effective Membrane Mechanics

A subsequent model was proposed by Fournier et al. to explain this jump in the fluctuation spectrum [67]. In this model, the composite red blood cell membrane energy is supposed to be the sum of the Helfrich energy (2) and an elastic contribution from the spectrin cytoskeleton $\mathscr{H}_{\rm el} = \frac{1}{2}Nk(\ell - \ell_0)^2$, supposed to be a perfect network of N entropic springs of stiffness k and of actual and resting lengths respectively ℓ and ℓ_0 (Fig. 6a). The authors show that this additional term leads to a jump in the membrane tension at wavelengths larger than the mesh size ℓ

$$\Delta\sigma \sim \frac{1}{2}gk\left(1 - \frac{\ell_0}{\ell}\right) \tag{36}$$

where g characterizes the topology of the network.

This model supposes fundamentally that the spectrin network is prestressed ($\ell \neq \ell_0$) and the best fit of the experimental data from Zilker et al. [64] is obtained for a spectrin network under extension $\Delta\sigma = \sigma^< - \sigma^> \sim 1.6 \times 10^{-6}\,\mathrm{N\,m^{-1}}$ and for a lipid bilayer under compression $\sigma^> = \sigma \sim -0.8 \times 10^{-7}\,\mathrm{N\,m^{-1}}$ (Fig. 6b). The authors suggest that the spectrin cytoskeleton may indeed lead to extra-folding of the bilayer, therefore regulating the membrane tension both directly at large scales compared to the mesh size and indirectly at shorter scales, via the membrane area constraint. In a following paper, a more detailed calculation at higher orders predicts that the bending modulus is also renormalized by the presence of the spectrin cytoskeleton [68].

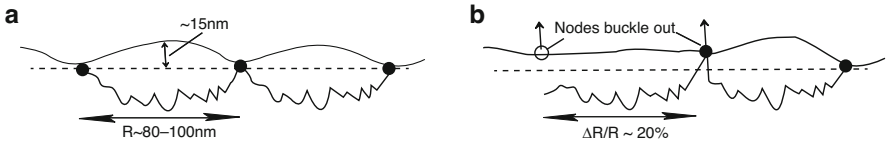

Fig. 7 Active spectrin dissociation model for the red blood cell membrane. (**a**) Schematic side view of the red blood cell composite membrane with fully connected spectrin filaments. (**b**) Sketch of the dissociation of a filament, which would generate a direct normal force on the bilayer (figures reproduced from [56])

4.3.2 Models of Active Red Blood Cell Membrane Fluctuations

In successive papers [55, 56, 58], Gov and Safran proposed a first model for active fluctuations in the red blood cell membrane, where the activity is supposed to originate from the spectrin cytoskeleton. Direct active forces ("kicks") on the membrane (see Eq. (31)) are suggested to be triggered by the detachment, under ATP hydrolysis, of spectrin filament ends from the lipid bilayer. In average, filament detachment is also predicted to soften the red blood cell membrane by decreasing the stiffness of the spectrin cytoskeleton, which is assumed to be naturally prestretched. Balancing the tension developed by a stretched filament with the energy needed to buckle the membrane, the authors predict a steady-state prestretch of the spectrin network of approximately 20% (see [56]). Assuming that detachment events are exponentially correlated in time, the non-thermal fluctuation spectrum originating from active direct forces is calculated in the same form as in Eq. (30). In a subsequent work, Auth, Safran, and Gov calculated the entropic pressure exerted on the lipid bilayer by fluctuations of the spectrin filaments themselves [69] and they derived the fluctuation spectrum of coupled solid and fluid membranes maintained at fixed distance. They showed that this composite system may be described as a single polymerized membrane with renormalized bending rigidity [70].

The model of Gov and Safran assumes that active detachment of spectrin filaments may drive direct normal forces onto the membrane (Fig. 7), but the precise microscopic mechanism of momentum transfer is not explicitly derived. In an alternative approach [7], Turlier et al. recently proposed a new active model for the composite red blood cell membrane, where the mechanical coupling between the lipid bilayer and the spectrin cytoskeleton is precisely derived, and the spectrin activity is described in a more generic manner.

Since all metabolic events identified in the spectrin network, or in its anchoring proteins, have been associated with a decreased mechanical strength of the membrane it is supposed that any phosphorylation shall lead to a local decrease of the network shear modulus, the single parameter necessary to characterize the spectrin network mechanics. A simple two-state dynamics is assumed for simplicity, and is characterized by two transition rates k_{on} and k_{off}, defining the active timescale $\tau_{\mathrm{a}} = (k_{\mathrm{on}} + k_{\mathrm{off}})^{-1}$ and the fraction of active sites $\langle n_{\mathrm{a}} \rangle = k_{\mathrm{on}}/(k_{\mathrm{on}} + k_{\mathrm{off}})$. The network shear modulus is then supposed to fluctuate around a mean value

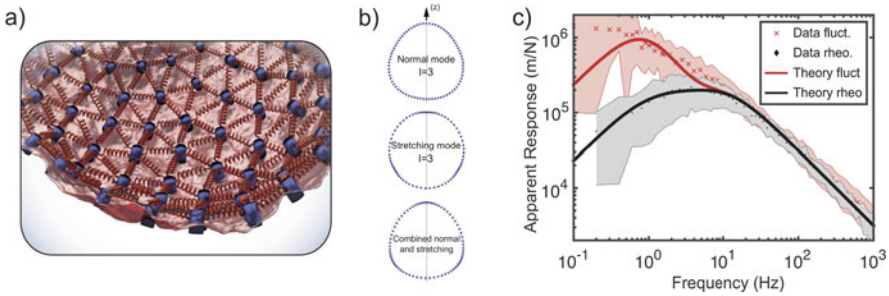

Fig. 8 Active quasi-spherical model of the composite red blood cell membrane. (**a**) Schematic representation of the red blood cell membrane composed of a lipid bilayer and a regular triangular network of spring-like spectrin filaments. (**b**) The composite membrane deformation can be separated in bending and stretching modes, illustrated for the spherical harmonic $l = 3$. (**c**) The analytic model (solid lines) can reproduce the experimental fluctuations and response data (crosses) (figures adapted from [7])

that decreases with metabolic activity $\langle \mu \rangle = \mu_0 (1 - \langle n_a \rangle)$. In line with previous studies, the spectrin cytoskeleton is idealized as a perfect triangular network of linear, prestressed springs (see Fig. 8a). As the prestress is supposed to be isotropic, the discrete elastic energy of the network can be homogenized into a continuous isotropic elastic membrane. Its energy is expressed as a function of the incremental deformation from the prestressed state and takes a Hookean form with an additional prestress term.

The mechanics of the prestressed network is characterized by an effective spectrin tension S and an incremental shear modulus M, which are functions of the original shear modulus μ_0, of the activity $\langle n_a \rangle$ and of a prestretch ratio. The membrane is supposed quasi-spherical and due to curvature, stretching and bending modes of deformations of the network are linearly coupled, as illustrated in Fig. 8b for the mode $l = 3$. Since the lipid bilayer is tangentially fluid, the proteins anchoring the network to the bilayer may have non-zero sliding velocity relative to lipids, which, in turn, exert a drag force on the network. This drag force is found to be the dominant dissipative contribution slowing down membrane stretching at large wavelengths. On the contrary, normal deformations are balanced by viscous forces from surrounding fluids. In this context, one has to calculate explicitly the lateral lipid pressure—or instantaneous surface tension—which acts as a Lagrange multiplier for local bilayer incompressibility (to distinguish from the global surface tension, which acts as a Lagrange multiplier for the total bilayer area). It turns out, from the calculation, that the lateral lipid pressure cancels systematically direct normal forces that may originate from active fluctuations in the spectrin mechanics. Since fluctuations in the network shear modulus lead to active forces in both tangential and normal directions, an indirect source of active noise is however conserved in the normal direction, thanks to the coupling between bending and stretching modes via the curvature. Decomposing the deformations in spherical harmonics modes (l, m), the membrane shape fluctuations appear classically as

a sum of thermal and active contributions, expressed here with the membrane response function and the spectrin metabolic activity, respectively:

$$C_{lm}(f) = \frac{2k_B T}{2\pi f}\chi''_{lm}(f) + \frac{2\langle n_a\rangle(1-\langle n_a\rangle)\tau_a}{1+(2\pi f\tau_a)}\left|N_{lm}(f)^2\right|^2 \tag{37}$$

where $f = \omega/2\pi$ is the frequency, and $N_{lm}(f)$ captures the complex mode- and frequency-dependent propagation of tangential active noise into membrane shape fluctuations.

The model predicts that spectrin-based active fluctuations should vanish for quasi-planar geometries, and it anticipates higher fluctuations in more curved regions of the red blood cell membrane, in agreement with recent spatial interferometric measurements [5]. It also shows clearly that a prestress in the network is the necessary ingredient for the emergence of spectrin-based active fluctuations, in agreement with previous hypotheses [56, 58]. It finally predicts that the network prestress may be maintained internally by an excess area of bilayer membrane, as suggested earlier by Fournier et al. [67]. Inverting the relation between excess area and bilayer tension (see Sect. 4.2.4), a negative bilayer tension of the order of $10^{-7}\,\mathrm{N\,m^{-1}}$ is found by fitting experimental data. This analytical model reproduces fairly both the response function and active membrane fluctuations measured in the red blood cell membrane [7], as shown in Fig. 8c.

5 Perspectives

5.1 A Physiological Role for Active Membrane Fluctuations?

An interesting and still overlooked question is the potential physiological role of active membrane fluctuations. The occurrence of active fluctuations does not substantiate by itself any functional role in biology, and active noise may be simply an unavoidable by-product of normal active processes in the cell. Yet, as noise is ubiquitous at this scale, cells may also control and take advantage of active noise, to actively facilitate or regulate other essential processes. It remains difficult, both experimentally and theoretically, to discriminate the potential role played by active fluctuations, from the main purpose of the active process considered. While still unproven, a number of possible physiological roles of membrane flickering have been suggested. As fluctuations increase membrane movement and fluidity, it should help mixing lipids and proteins within the membrane, an important property for cellular homeostasis (Fig. 9) [71]. Additionally, the fluctuations might help larger membrane bound proteins to be transported laterally as it can help to overcome possible steric obstacles such as intracellular cytoskeletal components that might prevent or reduce lateral transport [71]. A further possible role lies in the interaction with other, intracellular as well as extracellular membranes. Depending on the function, the fluctuations may help surface bound receptors to interact with other

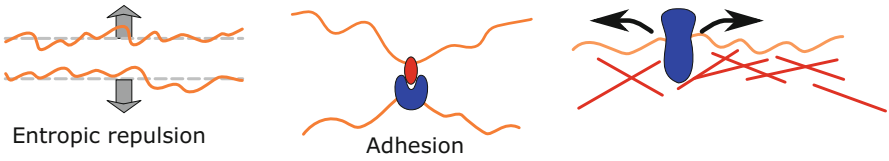

Fig. 9 Possible biological functions of enhanced fluctuations related to membrane adhesion, repulsion, and mixing. The fluctuations do create an effective potential barrier that can prevent uncontrolled membrane fusion. On the contrary, the large amplitudes of fluctuation may allow receptors and transmembrane proteins to explore larger volumes, and thus facilitate the controlled binding and adhesion between membranes. Additionally, the active forces might increase lipid mixing and help protein transport in the membrane again the cortical cytoskeleton (red lines)

membranes, as the fluctuations allow to explore a larger region (Fig. 9). On the other hand, active fluctuations may help to suppress nonspecific interaction by creating an effective repulsive force when an obstacle enters the region of the fluctuations [72, 73]. Finally, it was observed that active fluctuations modify the effective tension that is measured on membranes [6], while on the other hand, membrane tension is known to be an important mechanical parameter for a number of cellular functions ranging from cell motility to endo/exocytosis and mechanosensing.

5.2 Active Fluctuations in Membrane Adhesion Processes

Membrane adhesion is the physical process of interaction and attachment of a membrane to a surface, substrate, or another membrane (Fig. 9). In cells, membrane adhesion processes play essential roles in cell migration, cell–cell interaction, or bilayer-cytoskeleton coupling and are therefore tightly regulated by various membrane proteins (cadherins, integrins, ERM proteins) [66]. Membrane adhesion is, in general, controlled by a competition between attractive forces at short range (stickers), repulsive forces at intermediate distances (spacers) and elastic stresses coming from membrane deformation [74, 75]. Depending on their amplitude, membrane fluctuations may play antagonist roles towards adhesion: moderate fluctuations may assist the nucleation [76] and the expansion of adhesion domains, but at higher amplitudes fluctuations will compete with attractive forces and promote detachment of the membrane. The control of active fluctuations becomes in this context essential, but the role of activity in membrane adhesion has remained widely overlooked so far. Most of the theoretical models for membrane adhesion have considered membranes at equilibrium, which is justified when the focus is on biomimetic systems [76, 77]. To generalize these concepts to biological membranes, it will become critical to evaluate experimentally and theoretically the influence of active fluctuations on adhesion processes [78].

5.3 *Fluctuations of Membranes with an Actomyosin Cytoskeleton*

Most animal cell types possess a cortex of actomyosin, thin layer of actin filaments with embedded molecular motors, which lies beneath the membrane. The actomyosin cortex is tightly connected to the lipid bilayer via different proteins, the principal family being formed by the ERM (Ezrin-Radixin–Moesin) [79]. Regulated by phosphorylation, the connection between ERM and the cortex is dynamic and non-equilibrium by nature, providing a first possible source of active forces in the membrane. The active regulation of membrane-cortex adhesion is particularly important for the formation of blebs, membrane bulges originating from local cortex detachment [37, 80, 81]. But the cortex itself is notoriously very dynamic, with several processes requiring metabolic energy consumption, such as actin polymerization and myosin motor activity. All these processes constitute potential sources of active membrane fluctuations, covering a large spectrum of length and timescales. To disentangle and characterize precisely the various sources of activity in composite bilayer-cortex membranes, a substantial mutual effort from biologists, physicists, and theorists will be required over the next years, and precise numerical modeling will become critical [7, 82].

Acknowledgements H. Turlier acknowledges support from the CNRS/Inserm program ATIP-Avenir, from the Bettencourt-Schueller Foundation, and from the Collège de France. T. Betz is supported by the Deutsche Forschungsgemeinschaft (DFG), Cells-in-Motion Cluster of Excellence (EXC 1003-CiM), University of Münster, Germany.

References

1. Campelo F, Arnarez C, Marrink SJ, Kozlov MM (2014) Helfrich model of membrane bending: from Gibbs theory of liquid interfaces to membranes as thick anisotropic elastic layers. Adv Colloid Interface Sci 208:25–33
2. Hochmuth RM, Evans CA, Wiles HC, McCown JT (1983) Mechanical measurement of red cell membrane thickness. Science 220:101–102
3. Browicz T (1890) Further observation of motion phenomena on red blood cells in pathological states. Zbl med Wissen 28:625–627
4. Tuvia S, Almagor A, Bitler A, Levin S, Korenstein R, Yedgar S (1997) Cell membrane fluctuations are regulated by medium macroviscosity: evidence for a metabolic driving force. Proc Natl Acad Sci U S A 94:5045–5049
5. Park Y et al (2010) Metabolic remodeling of the human red blood cell membrane. Proc Natl Acad Sci U S A 107:1289–1294
6. Betz T, Lenz M, Joanny JF, Sykes C (2009) ATP-dependent mechanics of red blood cells. Proc Natl Acad Sci U S A 106:15320–15325
7. Turlier H et al (2016) Equilibrium physics breakdown reveals the active nature of red blood cell flickering. Nat Phys 12:513–519
8. Cabot RC (1901) A guide to the clinical examination of the blood, 4th edn. Longmans, Green & Co., London, p 52

9. Pulvertaft RJV (1949) Vibratory movement in the cytoplasm of erythrocytes. J Clin Path 2:281–283
10. Blowers R, Clarkson EM, Maizels M (1951) Flicker phenomenon in human erythrocytes. J Physiol 113:228
11. Parpart AK, Hoffman JH (1956) Flicker in erythrocytes. "vibratory movements in the cytoplasm"?. J Cell Comp Physiol 47:295–303
12. Brochard F, Lennon JF (1975) Frequency spectrum of the flicker phenomenon in erythrocytes. J Phys (Paris) 36:1035–1047
13. Evans J, Gratzer W, Mohandas N, Parker K, Sleep J (2008) Fluctuations of the red blood cell membrane: relation to mechanical properties and lack of ATP dependence. Biophys J 94: 4134–4144
14. Rodríguez-García R, López-Montero I, Mell M, Egea G, Gov NS, Monroy F (2015) Direct cytoskeleton forces cause membrane softening in red blood cells. Biophys J 108:2794–2806
15. Prost J, Bruinsma R (1996) Shape fluctuations of active membranes. Europhys Lett 33:321–326
16. Ramaswamy S, Toner J, Prost J (2000) Nonequilibrium fluctuations, traveling waves, and instabilities in active membranes. Phys Rev Lett 84:3494–3497
17. Lin LCL, Gov N, Brown FL (2006) Nonequilibrium membrane fluctuations driven by active proteins. J Chem Phys 124:074903
18. Manneville JB, Bassereau P, Lévy D, Prost J (1999) Activity of transmembrane proteins induces magnification of shape fluctuations of lipid membranes. Phys Rev Lett 82:4356–4359
19. Manneville JB, Bassereau P, Ramaswamy S, Prost J (2001) Active membrane fluctuations studied by micropipette aspiration. Phys Rev E 64:021908
20. Faris MEA, Lacoste D, Pécréaux J, Joanny JF, Prost J, Bassereau P (2009) Membrane tension lowering induced by protein activity. Phys Rev Lett 102:038102
21. Girard P, Prost J, Bassereau P (2005) Passive or active fluctuations in membranes containing proteins. Phys Rev Lett 94:088102
22. Hankins HM, Baldridge RD, Xu P, Graham TR (2015) Role of flippases, scramblases and transfer proteins in phosphatidylserine subcellular distribution. Traffic 16:35–47
23. Rao M, Sarasij RC (2001) Active fusion and fission processes on a fluid membrane. Phys Rev Lett 87:128101
24. Humphrey D, Duggan C, Saha D, Smith D, Käs J (2002) Active fluidization of polymer networks through molecular motors. Nature 416(6879):413–416
25. Koenderink GH, Dogic Z, Nakamura F, Bendix PM, MacKintosh FC, Hartwig JH, Stossel TP, Weitz DA (2009) An active biopolymer network controlled by molecular motors. Proc Natl Acad Sci USA 106:15192–15197
26. Wickstrand C, Dods R, Royant A, Neutze R (2015) Bacteriorhodopsin: would the real structural intermediates please stand up?. Biochim Biophys Acta Gen Subj 1850:536–553
27. Park Y et al (2006) Diffraction phase and fluorescence microscopy. Opt Express 14:8263–8268
28. Monzel C et al (2015) Measuring fast stochastic displacements of bio-membranes with dynamic optical displacement spectroscopy. Nat Commun 6:8162
29. Zilker A, Ziegler M, Sackmann E (1992) Spectral analysis of erythrocyte flickering in the 0.3–4μm^{-1} regime by microinterferometry combined with fast image processing. Phys Rev A 46:7998
30. Strey H, Peterson M, Sackmann E (1995) Measurement of erythrocyte membrane elasticity by flicker eigenmode decomposition. Biophys J 69:478
31. Pécréaux J, Döbereiner HG, Prost J, Joanny JF, Bassereau P (2004) Refined contour analysis of giant unilamellar vesicles. Eur Phys J E 13:277–290
32. Brown AT, Kotar J, Cicuta P (2011) Active rheology of phospholipid vesicles. Phys Rev E 84:021930
33. Rädler J, Sackmann E (1993) Imaging optical thicknesses and separation distances of phospholipid vesicles at solid surfaces. J Phys II 3:727–748
34. Monzel C, Sengupta K (2016) Measuring shape fluctuations in biological membranes. J Phys D Appl Phys 49:24

35. Schmidt D, Monzel C, Bihr T, Merkel R, Seifert U, Sengupta K, Smith AS (2014) Signature of a nonharmonic potential as revealed from a consistent shape and fluctuation analysis of an adherent membrane. Phys Rev X 4:021023
36. Betz T, Sykes C (2012) Time resolved membrane fluctuation spectroscopy. Soft Matter 8: 5317–5326
37. Peukes J, Betz T (2014) Direct measurement of the cortical tension during the growth of membrane blebs. Biophys J 107:1810–1820
38. Henon S, Lenormand G, Richert A, Gallet F (1999) A new determination of the shear modulus of the human erythrocyte membrane using optical tweezers. Biophys J 76:1145–1151
39. Mills JP, Qie L, Dao M, Lim CT, Suresh S (2004) Nonlinear elastic and viscoelastic deformation of the human red blood cell with optical tweezers. Mol Cell Biomech Tech Science Press 1:169–180
40. Yoon YZ, Kotar J, Brown AT, Cicuta P (2011) Red blood cell dynamics: from spontaneous fluctuations to non-linear response. Soft Matter 7:2042–2051
41. Helfrich W (1973) Elastic properties of lipid bilayers: theory and possible experiments. Z Naturforsch C 28:693–703
42. Helfrich WS, Servuss RM (1984) Undulations, steric interaction and cohesion of fluid membranes. Il Nuovo Cimento D 3:137–151
43. Fournier JB, Ajdari A, Peliti L (2001) Effective-area elasticity and tension of micromanipulated membranes. Phys Rev Lett 86:4970
44. Doi M, Edwards SF (1988) The theory of polymer dynamics. Oxford Science Publications, New York, pp 88–89
45. Schlosser F, Rehfeldt F, Schmidt C-F (2015) Force fluctuations in three-dimensional suspended fibroblasts. Philos Trans R Soc B 370:20140028
46. Almonacid M et al (2015) Active diffusion positions the nucleus in mouse oocytes. Nat Cell Biol 17:470–479
47. Mizuno D, Tardin C, Schmidt CF, MacKintosh FC (2007) Nonequilibrium mechanics of active cytoskeletal networks. Science 315:370–373
48. Lacoste D, Bassereau P (2014) An update on active membranes. In: Liposomes, lipid bilayers and model membranes. CRC Press, Boca Raton, pp 1–18
49. Milner ST, Safran SA (1987) Dynamical fluctuations of droplet microemulsions and vesicles. Phys Rev A 36:4371
50. Lomholt MA (2006) Fluctuation spectrum of quasispherical membranes with force-dipole activity. Phys Rev E 73:061914
51. Loubet B, Seifert U, Lomholt MA (2012) Effective tension and fluctuations in active membranes. Phys Rev E 85:031913
52. Gadsby DC (2009) Ion channels versus ion pumps: the principal difference, in principle. Nat Rev Mol Cell Biol 10:344–352
53. Chen HY (2004) Internal states of active inclusions and the dynamics of an active membrane. Phys Rev Lett 92:168101
54. Chen H-Y, Mikhailov AS (2010) Dynamics of biomembranes with active multiple-state inclusions. Phys Rev E 81:031901–031911
55. Gov NS (2004) Membrane undulations driven by force fluctuations of active proteins. Phys Rev Lett 93:268104–268104
56. Gov NS, Safran SA (2005) Red blood cell membrane fluctuations and shape controlled by ATP-induced cytoskeletal defects. Biophys J 88:1859–1874
57. Gov NS, Gopinathan A (2006) Dynamics of membranes driven by actin polymerization. Biophys J 90:454–469
58. Gov NS (2007) Active elastic network: cytoskeleton of the red blood cell. Phys Rev E 75:011921
59. Lacoste D, Lau AWC (2005) Dynamics of active membranes with internal noise. Europhys Lett 70:418–424

60. Sankararaman S, Menon GI, Sunil Kumar PB (2002) Two-component fluid membranes near repulsive walls: linearized hydrodynamics of equilibrium and nonequilibrium states. Phys Rev E 66:031914–031916
61. Gardiner CW (1985) Handbook of stochastic methods for physics, chemistry and the natural sciences. Springer, Berlin, p 77
62. Seifert U (1995) The concept of effective tension for fluctuating vesicles. Z Phys B 97:299–309
63. Gov N, Zilman A, Safran S (2003) Cytoskeleton confinement and tension of red blood cell membranes. Phys Rev Lett 90:228101
64. Zilker A, Engelhardt H, Sackmann E (1987) Dynamic reflection interference contrast (RIC) microscopy: a new method to study surface excitations of cells and to measure membrane bending elastic moduli. J Phys (Paris) 48:2139–2151
65. Rädler JO, Feder TJ, Strey HH, Sackmann E (1995) Fluctuation analysis of tension-controlled undulation forces between giant vesicles and solid substrates. Phys Rev E 51:4526
66. Sackmann E, Smith AS (2014) Physics of cell adhesion: some lessons from cell-mimetic systems. Soft Matter 10:1644–1659
67. Fournier J-B, Lacoste D, Raphaël E (2004) Fluctuation spectrum of fluid membranes coupled to an elastic meshwork: jump of the effective surface tension at the mesh size. Phys Rev Lett 92:018102–018104
68. Dubus C, Fournier JB (2007) A Gaussian model for the membrane of red blood cells with cytoskeletal defects. Europhys Lett 75:181–187
69. Auth T, Safran SA, Gov NS (2007) Filament networks attached to membranes: cytoskeletal pressure and local bilayer deformation. New J Phys 9:430–430
70. Auth T, Safran SA, Gov NS (2007) Fluctuations of coupled fluid and solid membranes with application to red blood cells. Phys Rev E 76:051910–051918
71. Lin L, Brown F (2004) Dynamics of pinned membranes with application to protein diffusion on the surface of red blood cells. Biophys J 86:764–780
72. Evans EA, Parsegian VA (1986) Thermal-mechanical fluctuations enhance repulsion between bimolecular layers. Proc Natl Acad Sci U S A 83:7132–7136
73. Prost J, Manneville JB, Bruinsma R (1998) Fluctuation-magnification of non-equilibrium membranes near a wall. Eur Phys J B 1:465–480
74. Bell GI (1988) Physical basis of cell-cell adhesion. CRC Press, Boca Raton, p 227
75. Evans E (1985) Detailed mechanics of membrane-membrane adhesion and separation. I. Continuum of molecular cross-bridges. Biophys J 48:175–183
76. Bihr T, Seifert U, Smith AS (2012) Nucleation of ligand-receptor domains in membrane adhesion. Phys Rev Lett 109:258101
77. Bruinsma R, Behrisch A, Sackmann E (2000) Adhesive switching of membranes: experiment and theory. Phys Rev E 61:4253–4267
78. Weikl TR, Asfaw M, Krobath H, Rózycki B, Lipowsky R (2009) Adhesion of membranes via receptor–ligand complexes: domain formation, binding cooperativity, and active processes. Soft Matter 5:3213–3224
79. Fehon RG, McClatchey AI, Bretscher A (2010) Organizing the cell cortex: the role of ERM proteins. Nat Rev Mol Cell Biol 11:276–287
80. Charras GT (2008) A short history of blebbing. J Microsc 231:466–478
81. Alert R, Casademunt J (2016) Bleb nucleation through membrane peeling. Phys Rev Lett 116:068101
82. Fedosov DA, Caswell B, Karniadakis GE (2010) A multiscale red blood cell model with accurate mechanics, rheology, and dynamics. Biophys J 98:2215–2225

Postface

In the course of editing this book, our goal was to gather the current views and models of various aspects of biomembranes. The objective was not to produce an exhaustive catalogue of membrane-related biophysical problems. Some were already well covered in the 1995 book by R. Lipowsky and E. Sackmann, and others are not yet sufficiently mature to be addressed in this book. We rather chose to focus on a limited number of questions of clear biological relevance, and for which our physical understanding has significantly progressed over the last two decades. In some cases, but not always, this physical understanding has fed back into the biological realm and has led to a truly interdisciplinary understanding of a particular process. However, there are still, to our minds, relatively few examples of biomembrane-specific cellular mechanisms that are fully understood from their physical basis to their nature and their function *in vivo*. This might be due to the reductionist approach traditionally used in physics, which might be limiting when considering the exquisite complexity of cellular membranes and their interaction with their cellular environment. One future direction of research for physicists will likely be to increase the complexity of their model systems (both experimental and theoretical) to better mimic the interaction of cellular membranes with different matrices and filamentous networks and to consider the role of membranes as signal processing elements.

Listed below are a few of the different processes for which we feel that fundamental physical concepts or frameworks are still missing, although we are conscious the list is not complete:

- We have come a long way from the static mosaic picture of biological membranes, and it is now acknowledged that cellular membranes are not only highly heterogeneous but also highly dynamic. While these topics have been treated extensively in some chapters of this book, some areas are still relatively uncharted. Examples include the interlayer coupling of membrane heterogeneities, or, more generally, the transmission of signals across the two leaflets of the plasma membrane, the regulation of the lateral mobility of membrane

P. Bassereau, P. Sens (eds.), *Physics of Biological Membranes*,
https://doi.org/10.1007/978-3-030-00630-3

proteins and signal processing mediated by the cytoskeleton, or the importance of crowding in the statics and dynamics of cellular membranes.

- *In vitro* studies have yielded valuable information both on the collective effects of membrane components (e.g., protein clustering) and on the molecular coupling between proteins and membranes (e.g., curvature sensitive binding). Coupled with theoretical models, these studies have helped decipher many of the mechanisms described in this book. The next challenge is to reconstitute an entire complex biological step *in vitro,* and not only isolated elements thereof. An example would be to first form a vesicle from a donor membrane by coat-assisted budding and scission and then fuse it to a receiver membrane by SNARE-assisted fusion. This is a required step for constructing more global and complex biological functions *in vitro*, such as membrane trafficking.
- It is becoming increasingly clear that membrane mechanical properties, in general, and membrane tension, in particular, play an important role in many cellular functions. However, measuring membrane tension in cells is still a challenge, and different experimental setups may yield different answers and have their own limitations. Moreover, we still lack a generic framework that would allow us to properly interpret data from these different experimental approaches and to disentangle membrane tension from cortical cytoskeleton tension and membrane-cortex adhesion. It was one of our great regrets that this book could not contain a chapter on this question. The development of molecular probes that are able to locally measure membrane stress (e.g., through conformation changes) would be particularly valuable.
- More generally, the interaction between the cell membrane and the cytoskeleton, which this book does not fully address, is gaining a lot of attention. A multiscale description of complex cellular processes such as the formation of protrusions (filopodia, lamellipodia) requires the integration of membrane properties and structural and mechanical properties of the cytoskeleton and regulatory proteins, which has not yet been achieved.
- The homeostasis of biological membranes is a vast topic of general interest. This includes mechanical homeostasis (i.e., the way membrane tension can be maintained with cell shape changes or external perturbation), but also composition homeostasis via exchange processes (i.e., the budding and fusion of vesicles, lipid flip-flop between the two membrane leaflets). For instance, intracellular organization/compartmentalization and transport are emerging topics that should attract a growing interest from physicists in the coming years. The role that fluxes play in maintaining cellular organization is clear from the biological point of view, in particular those along the endocytic and secretory pathways. However, a deep physical understanding of such processes is still lacking and will involve the modeling of nonequilibrium processes and building up *in vitro* systems in which these fluxes can be mastered and controlled.

We are confident that in the coming years, membrane biology will provide exciting questions for physicists to explore, and in return, with the development of new tools, physicists will help biologists decipher the many aspects of membrane functions.

P. Bassereau
P. Sens